CRANFIELD UNIVERSITY

ALASTAIR CAMILLERI B. Eng. (Hons.) MSc. (Cranfield)

DEVELOPMENT OF MICROTUBULAR SOLID OXIDE FUEL CELLS
DESIGN, FABRICATION AND PERFORMANCE

SCHOOL OF AEROSPACE TRANSPORT AND MANUFACTURING (SATM)

PhD Thesis
Nov 2009 – Aug 2017

Supervisors: Prof. John Nicholls

Submission: 25th August 2017

Abstract

Solid oxide fuel cells (SOFCs) are the most efficient energy conversion devices known. Many designs exist, with most current ones based on planar, tubular or so-called hybrid geometries. Tubular designs have many advantages over planar ones, including robustness and simpler sealing. They suffer from somewhat lower area-specific power density and considerably lower volume-specific power density. The miniaturization of tubular cells offers great improvement to both, and more besides. Pushing the boundaries of state-of-the-art manufacture to ever thinner films increases performance further, greatly advancing the long road to large scale commercialisation of SOFCs. This is only possible via the rigorous selection of materials and careful design – both for optimal performance and for mass manufacture.

Previous work by the author established the potential of a novel anode fabrication route as well as showing that even un-optimized electron beam physical vapour deposition (EB-PVD) was capable of creating demonstrator cells. In this work these manufacturing processes receive at least two passes of optimization towards both reproducible fabrication and maximising microtubular SOFC performance. The former was achieved by creating statistically significant quantities to assess reproducibility and studying the underlying science, and the latter was investigated in three aspects: gas transport, electrical and electrochemical.

The unique oxidation-reduction route creates robust, highly reproducible anodes with excellent through porosity offering as much as 5 orders of magnitude superior gas permeance to published sources. Nickel tubes (Ni200 5.9 mm OD, 125 μm wall thickness, 100 mm long) were oxidised in air at 1,100℃ for 42 h and reduced in pure hydrogen at four different temperatures. The extremes (400 °C and 1,000 °C) proved sufficiently promising that both were considered in subsequent stages of experiments and analysis for the final anode design. The morphology of the electrolyte (in particular with respect to gas-tightness) is a critical aspect of SOFC miniaturisation, and a challenge to achieve via mass-manufacture-friendly EB-PVD. The yttria-stabilized zirconia (YSZ) electrolyte deposition was optimized as far as proved possible with the available equipment. While results are more than encouraging there are a number of important concerns to be addressed in future to assure successful commercialization of the design. Accurately measuring gas permeance through the anode-electrolyte tube (sometimes called a half-cell) provides quantified justification. Finally a porous platinum cathode film 300 nm thick was successfully magnetron-sputtered onto the YSZ electrolyte at $p_{Ar} = 100$ mTorr, demonstrating the fabrication process and creating complete cells for electrical and electrochemical characterisation.

Keywords:
nickel anode, yttria-stabilised zirconia electrolyte, YSZ electrolyte, platinum cathode, metal oxidation, nickel oxidation, metal reduction, nickel reduction, physical vapour deposition, pvd, permeance, permeametry, metal electrodes, metallic electrodes, solid oxide fuel cell, SOFC, anode-supported, tubular.

The early manufacturing aspects of the project were undertaken with EPSRC grant support (EPID 506638/1 “Nanoscale multifunctional ferroic materials and devices” 1/04/2006 – 31/03/2011).

www.linkedin.com/in/alastair-f-camilleri

Acknowledgements

The author would like to extend his gratitude to the array of people who provided assistance and support of one sort or another, without whom this project would certainly not have been completed. It may well be the most valuable lesson learned: the more ambitious the project the more daring your help needs to be. Andrew Stallard from microsystems and nanotech, the sister building to the National High Temperature Surface Engineering Laboratory, for checking the permeametry sensor design and letting me borrow some of his toys. Tracey Roberts, a former PhD student in the NHTSEL, now a researcher there, for her advice on the fine art of sample preparation and polishing, her ever-helpful nature and kind assistance that, on occasion, allowed me to be in two places at once. I am also indebted to Mark Craig, who completed is PhD as I started mine. Mark provided much helpful advice in the early stages and his thesis proved helpful in creating a novel seal between test rig and fuel cell. Xian Wei Liu and Christine Kimpton, both analytical staff of great experience, for their patience, analytical acumen, and training course on the SEM. Andrew Dyer for his help with FIB, and allowing me to be trained to fly solo, for his guidance on sample preparation when some of my samples proved reticent and a shared humor at the sometimes strange vagaries of university life. Christine Chalk for taking care of the CVD coatings needed as well as providing guidance on the aluminizing process. Simon Gray and Christine Chalk also kindly filled in for Tim whenever he was away. Of course, Sharon McGuire, in her role as John's PA did more than book meetings. Her efforts coordinating all thigns administrative was a great help.

I wish to thank Tim Pryor for his patience and sharing his ability to solve innumerable practical issues ranging from re-mapping gas lines to reach needed furnace installations to providing considerable practical advice on designing the fuel cell test rig to safely meet the needs of the project. Tim was always my first port of call for safety, too – from SHE paperwork to PPE and training. I am deeply indebted to Tony Gray for his understanding, flexibility and willingness to try things never done before on his beloved coater, for carrying out all the Pt sputtering, helping me build ever-improving jigging to use in coater 1, and some much-needed encouragement!

Though circumstances removed him from this project I would like to express my gratitude to Jeremy Ramsden. Second supervisor initially, his earnest fascination with nanotechnology has truly been an inspiration to me from our first meeting during my MSc. The weekly group meetings he organized and chaired brought together his many students, working in vastly differing fields, to share ideas and offer critique. Nanotechnology was the common thread, and in that multiethnic, multicultural, multi-faith, multidisciplinary environment we all grew as scientists and people.

John Nicholls, jokingly referred to as the shadow supervisor of my MSc, encouraged this project and took on the role of principal supervisor. I am humbled by the wealth of information at his fingertips and ideas that he so freely shared. I am especially grateful for John's enthusiastic support and time, even well after hours. Our meetings were always long, always encouraging, always productive, and sometimes stretched well past 2000. I would truly not have been able to stomach the final years of this project without his support. Every meeting led to new ideas, a few discoveries, potential solutions (even some unlikely-sounding ones) and renewed enthusiasm. We are two peas in a pod: sharing a passion for engineering and science. I only wish there had been more time to learn from him.

Last, but no means least, mention goes to my friends and family. They managed to make this very long, stressful and at times utterly disheartening journey tolerable. My parents especially supported me and held me together during the darkest months I have ever experienced – a lesson I have very much taken to heart.

Table of Contents

1 Introduction 1

1.1 Aims and Objectives 3

1.2 Project Scope 4

1.3 Classification of Fuel Cells 6

1.4 A Brief History of Solid Oxide Fuel Cells 7

1.5 Benefits of Solid Oxide Fuel Cell Power 9

1.5.1 Efficiency 9

1.5.2 Flexibility in Power Plant Design 10

1.5.3 Manufacturing Advantages 10

1.5.4 Maintenance 10

1.5.5 Power Density Advantages 11

1.5.6 Reduced Pollution 11

1.5.7 Waste Heat 11

1.5.8 Capacity 12

1.5.9 Power on Demand 12

1.5.10 Advantages of Miniaturisation 12

1.6 Limitations to Solid Oxide Fuel Cell Power 13

1.7 Applications 13

1.8 Stationary Power Generation 17

1.8.1 Large Scale Centralised Power Generation 19

1.8.2 Small Scale CHP Systems 19

1.8.3 Domestic CHP Systems 21

1.9 Solid Oxide Fuel Cell Commercialisation and Economics 23

1.10 Solid Oxide Fuel Cell Fuel Cycle Analysis 27

1.10.1 Large Scale Centralised Power Generation Fuel Cycle 30

1.10.2 Distributed Power Generation Fuel Cycle 31

1.10.3 Remote Power Generation Fuel Cycle 33

1.10.4 Large Scale CHP Fuel Cycle 34

1.10.5 Industrial Scale CHP Fuel Cycle 35

1.10.6 Interpretation of Fuel Cycle Analysis 37
2 General Background on Solid Oxide Fuel Cells 39
2.1 Fuel 39
2.2 Hydrogen Storage Technology 41
2.2.1 Pressure Cylinders 42
2.2.2 Liquid Hydrogen 43
2.2.3 Metal Hydrides 44
2.2.4 Carbon Fibres 45
2.3 Hydrogen Generation Technology 46
2.3.1 Reformer Technology 46
2.3.2 Steam Reforming 47
2.3.3 Partial Oxidation (POX) 48
2.3.4 Autothermal Reforming (ATR) 49
2.3.5 Comparison of Reforming Technologies 49
2.4 PalladiumMembrane Technology 51
2.5 Matching Fuel to Application 52
2.6 Renewable Fuels 53
2.6.1 Renewable Hydrogen from Electrolysis 53
2.6.2 Biomass, Syngas and Organic Waste 54
2.7 High Temperature Fuel Cells 55
2.8 The Basic Fuel Cell Components 55
2.8.1 Fuel Selection 56
2.8.2 Catalyst Selection, Evaluation and Optimization 56
2.8.3 Electrode Selection and Evaluation 57
2.8.4 Electrolyte Selection and Classification 59
2.9 Basic Operating Principles 59
2.10 Electrode Kinetics 61
2.11 Survey of Previous Tubular SOFC Designs 62
2.12 Patents Relating to Microtubular SOFC Development 66
2.13 Microtubular SOFC Design 71
3 Material Selection and Geometrical Design of a Microtubular SOFC 79
3.1 Anode Material 79

3.1.1 Anode Requirements 79
3.1.2 Nickel Anodes 81
3.1.3 Nickel Cermet Anodes 81
3.2 Anode Fabrication 83
3.2.1 Conventional 83
3.2.2 This Project 84
3.3 Electrolyte Material 85
3.3.1 Fluorite-Structured Electrolytes 86
3.3.2 Zirconia-Based Ionic Conductors 87
3.3.3 Electrolyte Stability 91
3.4 Electrolyte Fabrication 92
3.4.1 Conventional 92
3.4.2 Unconventional 93
3.4.3 This Project 96
3.5 Cathode Material 97
3.5.1 Cathode Requirements 97
3.5.2 Platinum Cathodes 98
3.6 Cathode Fabrication 98
3.6.1 Conventional 98
3.6.2 This Project 99
Interconnect Material 99
3.6.3 Interconnect Requirements 99
3.6.4 Metallic Interconnects 100
3.7 Interconnect Fabrication 101
3.8 Design for this Project 101
3.8.1 Microtubular Cell Stack 103
3.9 Design Specification 104
4 Theory of Operation: Review and Critique 105
4.1 Thermodynamics of Electrochemical Fuel Cells 106
4.1.1 Chemical Cells and Concentration Cells 107
4.1.2 Reversibility and Irreversibility 107
4.1.3 Free Energy and Enthalpy 108

4.1.4 Fuel Cell Work Output 109
4.1.5 The Open-Circuit Voltage (OCV) 110
4.1.6 Enthalpy of Reaction from OCV 111
4.2 Reversible Electrode Potential 111
4.2.1 The Nernst Equation and the Effect of Concentration 111
4.2.2 The Effect of Temperature 113
4.2.3 The Effect of Pressure 114
4.2.4 Gas Diffusion Electrodes and the Three-Phase Limit 115
4.2.5 Mechanisms for Broadening the Three-Phase Limit 116
4.3 Polarisation as a Measure of Irreversibility 118
4.3.1 The Closed-Circuit E.M.F. 118
4.3.2 Activation Polarisation 119
4.3.3 Concentration Polarisation of the Electrolyte 120
4.3.4 Concentration Polarisation of the Gases 121
4.3.5 Resistance Polarisation 122
4.4 Thermodynamic Losses in Fuel Cells 123
4.5 The Role of Catalysis in the Fuel Cell Reaction 124
4.6 Kinetics of Porous Electrodes 126
4.7 Fuel Cell Thermodynamics – the Phenomenological Perspective 130
4.8 Fuel Utilisation, Ohmic Voltage Losses and Mixing Effects 131
4.9 Electrode Polarisations 132
4.9.1 Ohmic or Resistance Polarisation 134
4.9.2 Concentration Polarisation 135
4.9.3 Activation Polarisation 139
4.10 Continuum-Level Electrochemistry Model 143
4.11 Efficiency Considerations 145
4.11.1 Electrical Conversion Efficiency 145
4.11.2 Faradaic Efficiency 147
4.11.3 Power Density 148
4.12 Thermomechanical Model 150
5 Summarised Critique of State-of-the-Art: Research Objectives 153
5.1 Anode 153

5.2 Electrolyte 154
5.3 Cathode 155
5.4 General 157
6 Methodology and Terminology 159
6.1 Paradigm 159
6.2 Ontology Aspect 159
6.3 Epistemology Aspect 162
6.4 Terminology 164
6.5 Current Sign Convention 165
7 Introduction to Fabrication and Characterization of Components 167
7.1 Contents, Organization and Objectives 167
7.2 Desired Outcomes 167
8 Anode Fabrication and Characterization 169
8.1 Oxidation Objectives and Background 169
8.2 Oxidation Experiments 181
8.3 Process Optimization 182
8.3.1 Results & Discussion 182
8.4 Parabolic to Modified Parabolic Transition and Mechanistic Study 211
8.4.1 Results & Discussion 212
8.5 Improving Data Resolution or Refining Transition Time 223
8.5.1 Results & Discussion 224
8.6 Modified Wagnerian Model for Through Thickness Oxidation 229
8.6.1 Carl Wagner's Original Model 230
8.6.2 Modified Oxidation Model 234
8.7 Oxidation Temperature Optimization 240
8.7.1 Results & Discussion 240
8.8 Oxidation Conclusions 245
8.9 Reduction Objectives and Background 247
8.9.1 Thermodynamics: Congruent and Incongruent Mechanisms 249
8.9.2 Thermodynamics: Condensation Energy Transfer to the Reactant 250
8.9.3 Thermochemical Calculation of the Reaction Enthalpy 251
8.9.4 Variation of Enthalpy with Temperature and the Extent of Reaction 251

8.9.5 Kinetics; Langmuir Equations for Evaporation of Simple Substances .. 252
8.9.6 Kinetics: Isobaric and Equimolar Regimes of Reduction 253
8.9.7 Reduction Rate Dependence on $pH2$ and Reaction Regime 255
8.9.8 Determining the Activation Energy, E 255
8.9.9 Advantages of the Second Law and Third Law Methods 256
8.9.10 Characteristics of NiO Reduction by $H2$ 256
8.9.11 Creep Mechanisms and Deformation Maps 257
8.10 Reduction Experiments 262
8.11 Process Optimization with 5 vol.% H_2 265
8.11.1 Results & Discussion 265
8.12 Process Optimization with 100 vol.% H_2 278
8.12.1 Results & Discussion 279
8.13 Reduction Conclusions 316
8.14 Anode Conclusions 318
9 Electrolyte Fabrication and Characterization 319
9.1 Electrolyte Fabrication Objectives and Background 320
9.2 Physical Vapour Deposition Mechanisms 320
9.2.1 Thermodynamic Potentials and the Dividing Surface 320
9.2.2 Surface Tension and Surface Energy 322
9.2.3 Thermodynamics of the Vapour Pressure 324
9.2.4 The Kinetics of Crystal Growth 325
9.2.5 Concepts of Surface Electronics 328
9.2.6 Mechanisms of Physical Vapour Deposition 330
9.2.7 Chemisorption and Physisorption 330
9.2.8 Film Growth 335
9.2.9 Highlights 353
9.3 Zirconia Electrolytes by EB-PVD 354
9.4 Deposition Experiments 358
9.5 Deposition Reproducibility 362
9.5.1 Results & Discussion 362
9.6 Process Optimization 371
9.6.1 Results & Discussion 373

9.7 Electrolyte Fabrication Conclusions 392
10 Cathode Fabrication and Characterization 395
10.1 Cathode Fabrication Objectives and Background 395
10.2 Resistance Measurements 396
10.3 Results & Discussion 396
10.4 Cathode Fabrication Conclusions 397
11 Complete Cell Fabrication and Characterization 399
11.1 Complete Cell Fabrication Objectives and Background 399
11.2 Synthesis of Fabrication Techniques 399
11.3 Fabrication Reproducibility 402
11.3.1 Results & Discussion 402
11.3.2 Conclusions 422
11.4 Material and Energy Audit 423
11.4.1 Anode 424
11.4.2 Electrolyte 425
11.4.3 Cathode 426
11.4.4 Summary 427
12 Permeameter 429
12.1 Concept 429
12.2 Design 431
12.3 Assembly, Testing and Calibration 434
12.4 Measurement Methodology 438
12.5 Permeametry Experiments 439
12.6 Anode 442
12.6.1 Results & Discussion 442
12.6.2 Conclusions 452
12.7 Anode-Electrolyte Complex 453
12.7.1 Results & Discussion 453
12.7.2 Conclusions 466
12.8 Summary 467
13 Design and Construction of Test Rig 471
13.1 Background 471

13.2 FC Test Rig Specifications and Design 471
13.2.1 Furnace and Temperature Control 472
13.2.2 Gas Metering 473
13.2.3 Electrical Connection 473
13.2.4 Furnace Temperature Profile 481
13.2.5 Sealing the SOFC to the Test Rig 483
13.3 Conclusions 499
14 Fuel Cell Electrical and Electrochemical Performance Testing 501
14.1 Objective and background 501
14.2 Electrical and Electrochemical Experiments 502
14.3 Results & Discussion 503
14.4 Conclusions 519
15 Conceptual Development and Manufacturing Vision 521
15.1 Production Scale Out Discussion 521
15.2 Concept Model for Multi-Chamber Machine Manufacture of Cells 523
15.3 Roadmap to Mass Manufacture 531
16 Conclusion 533
16.1 Anode 533
16.2 Electrolyte 535
16.3 Cathode 536
16.4 General 537
16.5 Overall Conclusions 538
17 Further Work 539
17.1 Further Development of the Anode 539
17.2 Further Development of the Electrolyte 541
17.3 Further Development of the Cathode 543
17.4 Further Permeametry 544
Bibliography and Reference List 545
Appendix A: Activity Coefficient Calculations 565
Appendix B: Characterisation of As-delivered Nickel (Ni200) Tubes 566
Appendix C: Complete Oxidation Results Tables 569
Appendix D: Oxidation Micrographs 575

Appendix E: Oxidation Sample Furnace Positions and Schedule 585
Appendix F: Horizontal Hydrogen Furnace SOP 589
Appendix G: Complete Reduction Results Tables 595
Appendix H: Reduction Micrographs 601
Appendix I: SOP for the Deposition of YSZ Coatings 641
Appendix J: DoE Factor Significance Plots 643
Appendix K: Permeameter SOP 657
Appendix L: All Permeametry Plots 663
Appendix M: Ni Plating Recipes 693
Appendix N: Material Data Tables 695
Appendix O: Thermodynamic Data for Selected Chemical Compounds 701
Appendix P: Electrochemical Impedance Spectroscopy 703
Appendix Q: OCV Arrhenius Plots 715
Appendix R: Sample Code 719

List of Figures

Figures are labelled as Figure C-#. where C is the chapter number and # the number of that figure in the sequence for the whole chapter.

Figure 1-1. Schematic of SOFC operation. 2
Figure 1-2. Anode-supported tubular SOFC [Camilleri 2009]..... 3
Figure 1-3. SOFC potential markets and applications [van Gerwen 2003]..... 24
Figure 1-4. Transition from early market to mainstream market [van Gerwen 2003]. . 27
Figure 1-5. Schematic of energy carrier [adapted from Hart and Bauen 2003]. 28
Figure 1-6. Schematic of fuel cell system End-Use Technology. 28
Figure 1-7. Fuel cycle analysis steps [adapted from Hart and Bauen 2003]. 29
Figure 1-8. Total systems emissions and primary energy use of baseload power generation [reproduced with data from Hart and Bauen 2003]. 31
Figure 1-9. Total systems emissions and primary energy use of distributed power generation [reproduced with data from Hart and Bauen 2003]. 32
Figure 1-10. Total systems emissions and primary energy use of remote power generation [reproduced with data from Hart and Bauen 2003]. 33
Figure 1-11. Total systems emissions and primary energy use of large commercial CHP [reproduced with data from Hart and Bauen 2003]. 35
Figure 1-12. Total systems emissions and primary energy use of industrial-scale CHP [reproduced with data from Hart and Bauen 2003]. 37
Figure 1-13. Summary of the principal advantages of fuel cell power by fuel cell type and application [after Larminie and Dicks 2003]. 38
Figure 2-1. Schematic representation of thermodynamic energy balance of an ideal fuel cell and its system boundary. H_{total} is the energy of the fuel, Q is the thermal energy input needed to heat the SOFC to its operating temperature, W_{rev} is the reversible work output (electrical energy generated by cell), and H_{out} is the enthalpy lost by the reaction process (most fuel cell reactions are exothermic). Adapted from [Winkler 2003]. 60
Figure 2-2. I-V characteristics of the three variant designs for tubular electrode by Siemens Westinghouse Power Corporation, operated at 1,000 °C [Kendall, Minh and Singhal 2003]..... 63
Figure 2-3. Schematic of Siemens Westinghouse tubular SOFC [Kendall, Minh and Singhal 2003]..... 64
Figure 3-1. Temperature dependence of the ionic conductivity of some common oxide ion conductors [Ishihara *et al.* 2003]. 86
Figure 3-2. (left) Ionic conductivity with Y_2O_3 concentration at 1,273 °K from molecular dynamics simulation and experiment and (right) accessible free space and vacancy numbers of YSZ with Y_2O_3 concentration at 1,273 °K from simulation [Chang *et al.* 2011]. 88
Figure 3-3. Comparison of the oxygen ion displacement of the simulations for M-07-YSZ and P-07-YSZ at 1,273 °K [Chang *et al.* 2011]. Categories shown are short,

medium and long displacements in addition to thermal vibration. Also shown are the respective paths through a unit cell for each displacement category. 89
Figure 3-4. Oxygen ion diffusivities of the simulations for M-07-YSZ and P-07-YSZ with temperature [Chang *et al.* 2011]. 90
Figure 3-5. Schematic of microtubular design. Also shown are fabrication steps. This was updated and improved from Camilleri (2009). 102
Figure 3-6. Schematics of parallel stacking (a) and series connection (b). 104
Figure 4-1. Model of contact between metal electrode (sphere) and solid electrolyte. Adapted from [Gorin and Recht 1963]. 116
Figure 4-2. Potential against current density and polarisation relationships in a fuel cell. Adapted from [Eisenberg 1963]. 118
Figure 4-3. Schematic of coupled (b) and successive (a) diffusion-electrode reaction mechanisms. Adapted from [Heath and Sweeney 1963]. 127
Figure 4-4. Diffusion and electrochemical reaction in a single pore. Adapted from [Heath and Sweeney 1963]. 127
Figure 4-5. Typical plot showing polarisation curve when cell voltage is a function of current density. Activation polarisation is usually dominant at low current densities, and concentration polarisation is dominant at high current densities (when the transport of reactive species becomes the limiting factor) as can be surmised from the curve itself [Ivers-Tiffée and Virkar 2003]. 134
Figure 4-6. Ideal efficiency of common fuel cell reactions. Adapted from [Gorin and Recht 1963]. 146
Figure 8-1. Growth stresses in the oxidation of curved surfaces for cation diffusion processes [Schütze 1997]. 179
Figure 8-2. The signs of cooling stresses on curved surfaces [Schütze 1997]. 179
Figure 8-3. Sample hung on Nichrome wire jig for ease of handling and the wire jig itself. 182
Figure 8-4. Plots of the mass fraction oxidized – ratio of the measured mass of the oxidized sample to its calculated mass when fully oxidized – against time. Oxidation at 1,100 °C (compensated for the most likely source of surface area error – tube length). 184
Figure 8-5. Plots of x (mass gain / surface area) against time for oxidation at 1,100 °C. This is often casually referred to as the oxidation rate. 188
Figure 8-6. Plots of $x2$ [(mass gain / surface area)^2] against time for oxidation at 1,100 °C. This is often casually referred to as the square of oxidation rate. Deviations from parabolic show up clearly on this type of graph – as deviations from a straight line... 188
Figure 8-7. Schema of oxidation process including both stages: (a) cations transport through thin naturally occurring surface oxide to oxidise at the surface; (b) cation transport-controlled oxidation continues leaving vacancies in the Ni substrate that coalesce to form pores at the Ni-NiO interface and deeper into substrate by vacancy flux; (c) NiO dissociates into its anion and cation, cation transport continues but is impeded by the thickness of the oxide, the oxygen partial pressure gradient forces the

dissociated oxygen towards the un-oxidised side of the pore; (d) the pores oxidise internally, when a large volume fraction of pores exists this becomes the dominant mechanism. 191
Figure 8-8. FIB micrographs of sample OT-A-15/07/10-125.1100-A.10 (90.4 wt.% oxidised) showing milled trench. FIB milling was necessary to obtain a representative cross-sectional area for high resolution SEM imaging (see below). Micrograph (a) shows the milled trench, (b) the upper portion, (c) the middle and (d) the lower part of the trench. Notice the large pores visible even at this magnification. Also note that (as expected) they appear in distinct layers parallel to the surfaces. Some areas show heavy waterfalling due to the great depth of the trench which was milled from the outer surface (top of images) to the inner surface of the tube (bottom of images). 195
Figure 8-9. FIB micrographs of sample OT-A-14/07/10-125.1100-E.11 (91.0 wt.% oxidised) showing milled trench. Similarity to above images confirms the reproducibility. 196
Figure 8-10. SEM micrographs showing surface morphology of sample OT-A.15/07/2010-125.1100-A.10 (90.4 wt.% oxidised). 197
Figure 8-11. SEM micrographs* showing pores near to the inside edge of sample OT-A.15/07/2010-125.1100-A.10 (90.4 wt.% oxidised). 198
Figure 8-12. SEM micrographs* showing pores around the middle of sample OT-A.15/07/2010-125.1100-A.10 (90.4 wt.% oxidised). 199
Figure 8-13. SEM micrographs* showing pores near the outside edge of sample OT-A.15/07/2010-125.1100-A.10 (90.4 wt.% oxidised). 199
Figure 8-14. SEM micrographs showing surface morphology of sample OT-A.15/07/2010-125.1100-E.11 (91.0 wt.% oxidised). 200
Figure 8-15. SEM micrographs* showing pores near the inside edge of sample OT-A.15/07/2010-125.1100-E.11 (91.0 wt.% oxidised). 201
Figure 8-16. SEM micrographs* showing pores around the middle of sample OT-A.15/07/2010-125.1100-E.11 (91.0 wt.% oxidised). 202
Figure 8-17. SEM micrographs* showing pores near the outside edge of sample OT-A.15/07/2010-125.1100-E.11 (91.0 wt.% oxidised). 202
Figure 8-18. SEM micrographs* showing pores near the inside edge sample OT-A.15/07/2010-125.1100-C.01 (79.2 wt.% oxidised). This particular sample had a large void near the surface; probably a manufacturing defect. It is interesting to observe the oxidation from both sides of the upper portion leaving an unoxidized part near the middle. 203
Figure 8-19. SEM micrograph* showing lack of porosity around the middle of sample OT-A.15/07/2010-125.1100-C.01 (79.2 wt.% oxidised)..... 203
Figure 8-20. SEM micrograph* showing pores very near the outside edge of sample OT-A.15/07/2010-125.1100-C.01 (79.2 wt.% oxidised). Note that past about 1 μm into the sample from the bottom edge (just visible below the information and scale bar) there was no observed porosity at any resolution. 204

Figure 8-21. SEM micrographs* showing pores and more importantly grains in the area of the large void taking advantage of the 'through section' it presents near the inside edge of sample OT-A.15/07/2010-125.1100-C.01 (79.2 wt.% oxidised). 204
Figure 8-22. SEM micrographs showing surface morphology of sample OT-A.15/07/2010-125.1100-D.01 (79.3 wt.% oxidised). 205
Figure 8-23. SEM micrographs* showing pores near the inside edge of sample OT-A.15/07/2010-125.1100-D.01 (79.3 wt.% oxidised). 205
Figure 8-24. SEM micrographs* showing lack of porosity around the middle of sample OT-A.15/07/2010-125.1100-D.01 (79.3 wt.% oxidised). 206
Figure 8-25. SEM micrographs* showing pores near the outside edge of sample OT-A.15/07/2010-125.1100-D.01 (79.3 wt.% oxidised). 206
Figure 8-26. SEM micrographs* showing pores near the inside edge of sample OT-A.13/07/2010-125.1100-A.07 (84.9 wt.% oxidised). 208
Figure 8-27. SEM micrographs* showing pores around the middle of sample OT-A.13/07/2010-125.1100-A.07 (84.9 wt.% oxidised). 208
Figure 8-28. SEM micrographs* showing pores near the outside edge of sample OT-A.13/07/2010-125.1100-A.07 (84.9 wt.% oxidised). 209
Figure 8-29. Plots of the mass fraction oxidised against time in the period 0 to 5 h. Oxidation temperature 1,100 °C (compensated for the most likely source of surface area error – tube length). 213
Figure 8-30. SEM micrographs showing the surface morphology of the inner (concave) surface of samples bracketing the time of transition from k_{p1} to k_{p2}. Images are ordered from top to bottom in order of increasing apparent magnification; left column is sample OT-A.10/06/11-125.1100-B.16 (1 h 40 min 83.9 wt.% oxidised), right column is sample OT-A.10/06/11-125.1100-B.17 (2 h 20 min 86.1 wt.% oxidised). 215
Figure 8-31. SEM micrographs showing the surface morphology of the outer (convex) surface of samples bracketing the time of transition from k_{p1} to k_{p2}. Images are ordered from top to bottom in order of increasing apparent magnification; left column is sample OT-A.10/06/11-125.1100-B.16 (1 h 40 min 83.9 wt.% oxidised), right column is sample OT-A.10/06/11-125.1100-B.17 (2 h 20 min 86.1 wt.% oxidised). 217
Figure 8-32. SEM micrographs* showing pores near the inside edge of samples bracketing the time of transition from k_{p1} to k_{p2}. Images are ordered from top to bottom in order of increasing apparent magnification; left column is sample OT-A.10/06/11-125.1100-B.16 (1 h 40 min 83.9 wt.% oxidised), right column is sample OT-A.10/06/11-125.1100-B.17 (2 h 20 min 86.1 wt.% oxidised). 218
Figure 8-33. SEM micrographs* showing pores around the middle of samples bracketing the time of transition from k_{p1} to k_{p2}. Images are ordered from top to bottom in order of increasing apparent magnification; left column is sample OT-A.10/06/11-125.1100-B.16 (1 h 40 min 83.9 wt.% oxidised), right column is sample OT-A.10/06/11-125.1100-B.17 (2 h 20 min 86.1 wt.% oxidised). 220
Figure 8-34. SEM micrographs* showing pores near the outside edge of samples, bracketing the time of transition from k_{p1} to k_{p2}. Images are ordered from top to bottom

in order of increasing magnification; left column is sample OT-A.10/06/11-125.1100-B.16 (1 h 40 min 83.9 wt.% oxidised), right column is sample OT-A.10/06/11-125.1100-B.17 (2 h 20 min 86.1 wt.% oxidised). Highlighted areas and insert show debris (Al tape) in B.17 trench from sample preparation for SEM. 221
Figure 8-35. Plots of $x2$ [i.e. (mass gain / surface area)^2] against time for oxidation at 1,100 °C of Batch B and Batch D. Note: the plots shown include all samples oxidised as grouped into these batches (Tier 1, Tier 2 and Tier 4). 223
Figure 8-36. Plots of the mass fraction oxidised – ratio of the measured mass of the oxidised sample to its calculated mass when fully oxidised – against time for all results up to and including Tier 4. Oxidation temperature 1,100 °C (compensated for the most likely source of surface area error – tube length). 226
Figure 8-37. Plots of $x2$ [i.e. (mass gain / surface area)^2] against time for oxidation at 1,100 °C. All results shown, up to and including Tier 4. Deviations from parabolic appear as deviations from a straight line. 227
Figure 8-38. Schematic representation of linear fitting whole data set (as opposed to one linear fit per parabolic rate constant). Relative proportions are exaggerated for clarity. 227
Figure 8-39. Plots of the mass fraction oxidised against time in the period 0 to 5 h for all results up to and including Tier 4. Oxidation temperature 1,100 °C (compensated for the most likely source of surface area error – tube length). 228
Figure 8-40. Plots of $x2$ [i.e. (mass gain / surface area)^2] against time in the period 0 to 5 h for oxidation at 1,100 °C. All results shown, up to and including Tier 4. Deviations from parabolic appear as deviations from a straight line..... 229
Figure 8-41. Modified Wagnerian model verification for oxidation at 1,100 °C showing envelope of maximum and minimum experimental values alongside calculated average and model results. 237
Figure 8-42. Modified Wagnerian model verification for oxidation at 1,100 °C showing envelope of maximum and minimum experimental values alongside average and model. All results shown, up to and including Tier 4. Note the changes from Figure 8-41. (above). 237
Figure 8-43. Fractional error against log time for model verification data for oxidation at 1,100 °C. All results shown, up to and including Tier 4. 239
Figure 8-44. Plot of mass fraction oxidised against time for all samples oxidised at 1,150 °C compared with average mass fraction oxidized for an 1,100 °C oxidation temperature. 241
Figure 8-45. SEM micrographs showing the surface morphology of the inner (concave) surface of sample OT-A.21/11/11-125.1150-AC.03 (16 h 92.9 wt.% oxidised). Images are ordered from left to right in order of increasing apparent magnification. 242
Figure 8-46. SEM micrographs showing the surface morphology of the outer (convex) surface of sample OT-A.21/11/11-125.1150-AC.03 (16 h 92.9 wt.% oxidised). Images are ordered from left to right in order of increasing apparent magnification. 242

Figure 8-47. SEM micrographs* showing pores near the inside edge of sample OT-A.21/11/11-125.1150-AC.03 (16 h 92.9 wt.% oxidised). Images are ordered from left to right and top to bottom in order of increasing apparent magnification. 243
Figure 8-48. SEM micrographs* showing pores around the middle of sample OT-A.21/11/11-125.1150-AC.03 (16 h 92.9 wt.% oxidised). Images are ordered from left to right and top to bottom in order of increasing apparent magnification. 244
Figure 8-49. SEM micrographs* showing pores near the outside edge of sample OT-A.21/11/11-125.1150-AC.03 (16 h 92.9 wt.% oxidised). Images are ordered from left to right and top to bottom in order of increasing apparent magnification. 245
Figure 8-50. Deformation mechanism map for NiO from Schütze (1997). 259
Figure 8-51. Deformation mechanism map for pure Ni (work hardened with obstacle spacing taken as 4×10^{-8}) from Frost and Ashby (1982). The shaded areas are dynamic recrystallisation. The map for annealed nickel was constructed with an obstacle spacing of 2×10^{-7} m [Frost and Ashby 1982]. 260
Figure 8-52. Schematic of micro-crack network growth and healing in oxide scales [Schütze 1997]. 261
Figure 8-53. Samples hung on wire jigs for ease of handling. Shown on alumina sheets placed on a stainless steel tray ready for loading into the furnace. 262
Figure 8-54. Plot of mass fraction reduced against dwell for all batches. The plot for 1,000 °C is emphasised both because it was the most meaningful and because it was the most promising of the three. 267
Figure 8-55. Residual oxygen mass fraction, $mgain - mlossmgain = 1 - mlossmgain$, against dwell for all batches. The plot for 1,000 °C is emphasised both because it was the most meaningful and because it was the most promising of the three. 268
Figure 8-56. Oxygen loss squared against dwell for 1,000 °C, akin to the square of the mass gained during oxidation previously. This was the most meaningful promising of the three so is given greater prominence. 269
Figure 8-57. Oxygen loss squared against dwell 600 °C and 800 °C. 270
Figure 8-58. Ellingham diagram showing graphical calculation for $H2H2O$ ratio as well as the threshold $pO2$ at 600 °C, 800 °C and 1,000 °C for Ni. Source: 271
Figure 8-59. Ellingham diagram showing graphical calculation for $H2H2O$ ratio as well as the threshold $pO2$ at 600 °C, 800 °C and 1,000 °C for Ti. Source: 277
Figure 8-60. Plot of residual oxygen mass fraction, $mgain - mlossmgain = 1 - mlossmgain$, against dwell for all batches reduced at 1,000 °C. 281
Figure 8-61. Plot of residual oxygen mass fraction, $mgain - mlossmgain = 1 - mlossmgain$, against dwell for all batches reduced at 800 °C. 282
Figure 8-62. Plot of residual oxygen mass fraction, $mgain - mlossmgain = 1 - mlossmgain$, against dwell for all batches reduced at 600 °C. 282
Figure 8-63. Plot of residual oxygen mass fraction, $mgain - mlossmgain = 1 - mlossmgain$, against dwell for all batches reduced at 400 °C. 283

Figure 8-64. Oxygen loss squared against dwell for all batches at 400 °C, akin to the square of the oxidation rate explained previously. The fitting was carried out based on the mean of the data points at each dwell. The error shown is the maximum (i.e. worst case) calculated standard deviation from this mean. Samples in parenthesis are outliers. 285
Figure 8-65. Oxygen loss squared against dwell for all batches at 600 °C and 800 °C, akin to the square of the oxidation per unit area explained previously. The fitting was carried out based on the mean of the data points at each dwell. The error shown for each temperature is the maximum (i.e. worst case) calculated standard deviation from this mean. Note: in some cases the standard deviation is too small to appear in error bars.286
Figure 8-66. Oxygen loss squared against dwell for all batches at 1,000 °C, akin to the square of the oxidation per unit area explained previously. The fitting was carried out based on the mean of the data points at each dwell. The error shown for each temperature is the maximum (i.e. worst case) calculated standard deviation from this mean. Samples in parenthesis are outliers. Note: in some cases the standard deviation is too small to appear in error bars. 287
Figure 8-67. SEM micrographs structuring example, showing a pair reduced at 400 °C. Images are ordered: from top to bottom in order of increasing magnification; left column is 0 h dwell (ramp only – the minimum possible) and right column is 15 h dwell (nominally fully reduced). Samples: RT-A.04/03/13-125.1100(400)-FH.01 (downstream) and RT-A.17/07/13-125.1100(400)-FI.06 (upstream). In this case there are two pairs if images at 5,000× and 10,000×. Note sequence from context to detail, highlighting larger features then smaller ones. 292
Figure 8-68. SEM micrographs of the surface morphology of samples reduced at 400 °C. Left column is 0 h dwell (ramp only – the minimum possible) and right column is 15 h dwell (nominally fully reduced). Samples: RT-A.04/03/13-125.1100(400)-FH.01 (downstream) and RT-A.17/07/13-125.1100(400)-FI.06 (upstream). 294
Figure 8-69. SEM micrographs showing the overall cross-section of samples reduced at 400 °C. Left column is 0 h dwell (ramp only – the minimum possible) and right column is 15 h dwell (nominally fully reduced). Samples: RT-A.04/03/13-125.1100(400)-FH.01 (downstream) and RT-A.17/07/13-125.1100(400)-FI.06 (upstream). 295
Figure 8-70. SEM micrographs showing the cross-section near the outer edge of samples reduced at 400 °C. Left column is 0 h dwell (ramp only – the minimum possible) and right column is 15 h dwell (nominally fully reduced). Samples: RT-A.04/03/13-125.1100(400)-FH.01 (downstream) and RT-A.17/07/13-125.1100(400)-FI.06 (upstream). The right-hand image is a composite, centred around the large pore in the top right of the left hand part (highlighted). 296
Figure 8-71. SEM micrographs showing the cross-section near the middle of samples reduced at 400 °C. Left column is 0 h dwell (ramp only – the minimum possible) and right column is 15 h dwell (nominally fully reduced). Samples: RT-A.04/03/13-125.1100(400)-FH.01 (downstream) and RT-A.17/07/13-125.1100(400)-FI.06 (upstream). 296

Figure 8-72. SEM micrographs showing the cross-section near the inner edge of samples reduced at 400 °C. Left column is 0 h dwell (ramp only – the minimum possible) and right column is 15 h dwell (nominally fully reduced). Samples: RT-A.04/03/13-125.1100(400)-FH.01 (downstream) and RT-A.17/07/13-125.1100(400)-FI.06 (upstream). 297
Figure 8-73. SEM micrographs of the surface morphology of samples reduced at 600 °C. Left column is 0 h dwell (ramp only – the minimum possible) and right column is 2 min dwell (nominally fully reduced). Samples: RT-A.19/02/13-125.1100(600)-V.01 (midstream) and RT-A.04/03/13-125.1100(600)-W.02 (downstream). 298
Figure 8-74. SEM micrographs of the surface morphology of sample RT-A.04/03/13-125.1100(600)-W.02 (downstream) showing the development of pores within surface cracks. 299
Figure 8-75. SEM micrographs showing the overall cross-section of samples reduced at 600 °C. Left is 0 h dwell (ramp only – the minimum possible) and right is 2 min dwell (nominally fully reduced). Samples: RT-A.19/02/13-125.1100(600)-V.01 (midstream) and RT-A.04/03/13-125.1100(600)-W.02 (downstream). 299
Figure 8-76. SEM micrographs showing the cross-section near the outer edge of samples reduced at 600 °C. Left column is 0 h dwell (ramp only – the minimum possible) and right column is 2 min dwell (nominally fully reduced). Samples: RT-A.19/02/13-125.1100(600)-V.01 (midstream) and RT-A.04/03/13-125.1100(600)-W.02 (downstream). Note that part of the trench appears to have become clogged with debris from an unknown source that was not removed by rinsing the sample with acetone prior to imaging by SEM. This obscures some images yet sufficient detail remains visible.300
Figure 8-77. SEM micrographs showing the cross-section near the middle of samples reduced at 600 °C. Left column is 0 h dwell (ramp only – the minimum possible) and right column is 2 min dwell (nominally fully reduced). Samples: RT-A.19/02/13-125.1100(600)-V.01 (midstream) and RT-A.04/03/13-125.1100(600)-W.02 (downstream). 301
Figure 8-78. SEM micrographs showing the cross-section near the inner edge of samples reduced at 600 °C. Left column is 0 h dwell (ramp only – the minimum possible) and right column is 2 min dwell (nominally fully reduced). Samples: RT-A.19/02/13-125.1100(600)-V.01 (midstream) and RT-A.04/03/13-125.1100(600)-W.02 (downstream). 302
Figure 8-79. SEM micrographs of the surface morphology of samples reduced at 800 °C. Left column is 0 h dwell (ramp only – the minimum possible) and right column is 1 h dwell (nominally fully reduced). Samples: RT-A.23/10/12-125.1100(800)-Q.01 (downstream) and RT-A.23/10/12-125.1100(800)-L.02 (upstream)..... 303
Figure 8-80. SEM micrographs of the surface morphology of sample RT-A.23/10/12-125.1100(800)-Q.01 (downstream) reduced at 800 °C emphasizing the surface crack shape. 304
Figure 8-81. SEM micrographs showing the overall cross-section of samples reduced at 800 °C. Left column is 0 h dwell (ramp only – the minimum possible) and right column

is 1 h dwell (nominally fully reduced). Samples: RT-A.23/10/12-125.1100(800)-Q.01 (downstream) and RT-A.23/10/12-125.1100(800)-L.02 (upstream)..... 305
Figure 8-82. SEM micrographs showing the cross-section near the outer edge of samples reduced at 800 °C. Left column is 0 h dwell (ramp only – the minimum possible) and right column is 1 h dwell (nominally fully reduced). Samples: RT-A.23/10/12-125.1100(800)-Q.01 (downstream) and RT-A.23/10/12-125.1100(800)-L.02 (upstream). 305
Figure 8-83. SEM micrographs showing the cross-section near the middle of samples reduced at 800 °C. Left column is 0 h dwell (ramp only – the minimum possible) and right column is 1 h dwell (nominally fully reduced). Samples: RT-A.23/10/12-125.1100(800)-Q.01 (downstream) and RT-A.23/10/12-125.1100(800)-L.02 (upstream). 306
Figure 8-84. SEM micrographs showing the cross-section near the inner edge of samples reduced at 800 °C. Left column is 0 h dwell (ramp only – the minimum possible) and right column is 1 h dwell (nominally fully reduced). Samples: RT-A.23/10/12-125.1100(800)-Q.01 (downstream) and RT-A.23/10/12-125.1100(800)-L.02 (upstream). 307
Figure 8-85. SEM micrographs of the surface morphology of samples reduced at 1,000 °C. Left column is 0 h dwell (ramp only – the minimum possible) and right column is 5 h dwell (nominally fully reduced). Samples: RT-A.12/06/12-125.1100(1000)-H.02 (downstream) and RT-A.09/10/12-125.1100(1000)-I.01 (upstream). I.01 was coated with a few nm of AuPd by sputtering to improve resolution. 308
Figure 8-86. SEM micrographs showing the overall cross-section of samples reduced at 1,000 °C. Left column is 0 h dwell (ramp only – the minimum possible) and right column is 5 h dwell (nominally fully reduced). Samples: RT-A.12/06/12-125.1100(1000)-H.02 (downstream) and RT-A.09/10/12-125.1100(1000)-I.01 (upstream). I.01 was coated with a few nm of AuPd by sputtering to improve resolution. 309
Figure 8-87. SEM micrographs showing the cross-section near the outer edge of samples reduced at 1,000 °C. Left column is 0 h dwell (ramp only – the minimum possible) and right column is 5 h dwell (nominally fully reduced). Samples: RT-A.12/06/12-125.1100(1000)-H.02 (downstream) and RT-A.09/10/12-125.1100(1000)-I.01 (upstream). I.01 was coated with a few nm of AuPd by sputtering to improve resolution. 310
Figure 8-88. SEM micrographs showing the cross-section near the middle of samples reduced at 1,000 °C. Left column is 0 h dwell (ramp only – the minimum possible) and right column is 5 h dwell (nominally fully reduced). Samples: RT-A.12/06/12-125.1100(1000)-H.02 (downstream) and RT-A.09/10/12-125.1100(1000)-I.01 (upstream). I.01 was coated with a few nm of AuPd by sputtering to improve resolution. 311
Figure 8-89. SEM micrographs showing the cross-section near the inner edge of samples reduced at 1,000 °C. Left column is 0 h dwell (ramp only – the minimum

possible) and right column is 5 h dwell (nominally fully reduced). Samples: RT-A.12/06/12-125.1100(1000)-H.02 (downstream) and RT-A.09/10/12-125.1100(1000)-I.01 (upstream). I.01 was coated with a few nm of AuPd by sputtering to improve resolution. 311
Figure 8-90. Deformation mechanism map for NiO from Schütze (1997). Repetition of Figure 8-50. for convenience. 312
Figure 8-91. Deformation mechanism map for pure Ni (annealed with obstacle spacing taken as 2×10^{-7}) from Frost and Ashby (1982). The shaded areas are dynamic recrystallisation. 313
Figure 8-92. Surface of oxidised 99.2% Ni deformed at 800 °C to $\varepsilon = -0.1$ and $\varepsilon = -10 - 3$ s^{-1} (a) showing oxide grain loosening' and (b) cross-section showing pores [Schütze 1997]. 314
Figure 8-93. Schematic of oxide grain loosening, displacement and rotation, as well as oxide regrowth (hatched area), termed 'quasi-grain-boundary sliding' or 'pseudo-plasticity' [Schütze 1997]. 315
Figure 9-1. Schematic representation of the 'dividing surface' in terms of macroscopic concentrations, after Venables (2000). 321
Figure 9-2. Schematic representation of creating a new surface by cleavage. If thermodynamically reversible the work done creating the new surface is 2γA. 322
Figure 9-3. Deposition in the presence of a screw dislocation – causing a double step [Venables 2000]. (a) is at equilibrium, (b) through (d) are given as a function of time with supersaturation $\beta\Delta\mu$ = 1.5. Bond strength expressed in terms of temperature as $LkT = 12$, equivalent to $\phi = 4kT$ [Venables 2000]. 328
Figure 9-4. Schematic representation of (a) the work function and (b) electron affinity and ionisation potential [Venables 2000]. 329
Figure 9-5. Schematic diagram after Venables [2000] of a surface state defined by wave vector $\boldsymbol{k} \parallel = \boldsymbol{kx} + \boldsymbol{ky}$ and $\boldsymbol{k} \perp = \boldsymbol{kz}$ for the $3 \times 3R30°$ structure plotted in the same orientation as a xenon lattice. 329
Figure 9-6. Schematic representation of the three growth modes by surface coverage in ML (the number of monolayers) [after Venables 2000]. 335
Figure 9-7. Adsorption isotherms of the three growth modes shown in Figure 9-6. Δμ is the chemical potential of the growing deposit relative to the bulk material and θ is the coverage (in ML). In SK mode two stable intermediate layers are shown [Venables 2000]. 336
Figure 9-8. (a) growth of A on B where $\gamma A < \gamma B$: misfit dislocations are initially introduced and subsequently form islands (b) growth of B on A directly as islands, $\gamma *$ (the interfacial energy) represents the energy in excess of bulk A and B integrated over the interface region (c) surface processes and characteristic energies in nucleation and growth of films [from Venables 2000]. 336
Figure 9-9. Free energy of nucleation ΔGj for 3D and 2D clusters (solid and dashed lines respectively). Curves are to scale for the surface free energy term X = 4, and $\Delta\mu$

(or $\Delta\mu'$ for 2D clusters) equal to -1, 0, 1, and 2. All three energies (ΔGj, X and $\Delta\mu$) are in arbitrary units, but may be taken as kT [from Venables 2000]. 338
Figure 9-10. Illustration showing the interactions between nucleation and growth phases [Venables 2000]. Adatom density $n1$ determines the critical cluster density ni. $n1$ itself is determined by the arrival z in conjunction with the various loss processes having characteristic times, τ, as described. 344
Figure 9-11. Calculated pre-exponential factors $\eta\theta, i$ in the complete condensation regime for: (a) 3D islands with i = 1, 2 and 3 and with σx evaluated in the lattice (solid line) and uniform depletion (dashed line) approximations; (b) 2D islands with i = 1–20 and with σx approximated by $4\pi - \ln\theta$, which is very close to the uniform depletion approximation [Venables 2000]. NB: in the cited source, and this graph, Z = θ..... 346
Figure 9-12. Nucleation density on point defects with trap density nt = 0.001 ML and trap energy Et (a) 0.5 eV (b) 1.0 eV; parameter Ed with Ea = 1.16 eV and Eb = 1.04 eV [Venables 2000]. 350
Figure 9-13. EB-PVD deposition jig and alumina support rods. 359
Figure 9-14. Diagram of cross-sections taken of EB-PVD deposition for image analysis and relative positions of mounted samples after sectioning. 361
Figure 9-15. EB-PVD updated deposition jig that is both simplified and holds the sample more securely while removing the risk of damage that existed with the previous version. 361
Figure 9-16. SEM micrographs showing columnar 7YSZ on Ni tube. Notice the remarkable conformity over surface defects (visible in these micrographs as pores at the interface (sample DT-E.24/04/12-125;10.1000-A.01). Note that a carbon coating was used to enable the high resolution imaging of the non-conductive zirconia electrolyte (particularly necessary because the samples are mounted in a cold-cure resin, also highly electrically insulating). 367
Figure 9-17. Testing the linearity of thickness variation from end to middle of sample DT-E.17/05/12-125;10.1000-A.04 and DT-E.05/07/12-125;10.1000-A.05. In these plots 'x' in the equation of the fitted line is the section number multiplied by the length of that section. Notice the excellent fit and strong linearity (evidenced by points off the fitted line remaining within ±s of the line). 369
Figure 9-18. Diagram of 3D DoE parameter space. 372
Figure 9-19. Diagram of 3D DoE parameter space showing ninth point and 'mid-step' parameter values. 373
Figure 9-20. Diagram showing EB-PVD Tier 2 (DoE) measurement positions for z (thickness). 375
Figure 9-21. Mass gain (m_{YSZ} in tables) per unit surface area against coating thickness. 377
Figure 9-22. SEM micrographs showing columnar 7YSZ on Ni tube. Notice the remarkable strength despite subsurface pores most likely caused by oxidation of the Ni substrate (sample DT-E.22/11/12-125;10.950-B.01). 379

Figure 9-23. SEM micrographs showing columnar 7YSZ on Ni tube. The micrographs show the only visible damage in the coating as well as subsurface pores visible throughout likely due to some small amount of oxidation (sample DT-E.27/11/12-125;10.950-B.02)..... 379
Figure 9-24. SEM micrographs showing columnar 7YSZ on Ni tube. The first pair of micrographs show subsurface damage and the high conformity of the coating as well as detailed column morphology at high magnification. The second pair show the worst damage visible on the sample (sample DT-E.28/11/12-125;10.950-B.03). 380
Figure 9-25. SEM micrograph showing columnar 7YSZ on Ni tube. This is typical appearance for this sample (sample DT-E.04/12/12-125;10.1050-B.04)..... 380
Figure 9-26. SEM micrographs showing columnar 7YSZ on Ni tube. This is typical appearance for this sample, with a handful of areas showing complete delamination, though this may have been caused by sample preparation (sample DT-E.06/12/12-125;10.950-B.05)..... 381
Figure 9-27. SEM micrographs showing columnar 7YSZ on Ni tube. This sample exhibits little damage and porosity (sample DT-E.17/01/13-125;10.1000-B.06). 381
Figure 9-28. SEM micrographs showing columnar 7YSZ on Ni tube. Site is representative of whole sample (sample DT-E.21/01/13-125;10.1000-B.07)..... 382
Figure 9-29. SEM micrographs showing columnar 7YSZ on Ni tube. Micrographs shown are representative of whole sample (sample DT-E.22/01/13-125;10.1050-B.08). 382
Figure 9-30. SEM micrographs showing columnar 7YSZ on Ni tube. Site is representative of whole sample (sample DT-E.23/01/13-125;10.1050-B.09)..... 383
Figure 9-31. SEM micrographs showing columnar 7YSZ on Ni tube. Site shown is representative of whole sample (sample DT-E.24/01/13-125;10.1050-B.10). A detached portion of coating from a damaged area of the section was observed. No micrograph is included as the damage was attributed to sample preparation for microscopy. 383
Figure 9-32. SEM micrographs showing columnar 7YSZ on Ni tube. The first pair of micrographs depict an area representative of most of the sample, while the second pair show the same substratum partial delamination under the NiO noted before (sample DT-E.04/03/13-125;10.850-B.11). This may have as much to do with pores due to thermal oxidation (see chapter 8) as with thermal stress. 384
Figure 9-33. SEM micrographs showing columnar 7YSZ on Ni tube. This site is significant because it shows the only visible crack in the coating running perpendicular to the surface; the shape of the upper portion of the subsurface pore below it suggests it may have been caused by a very large pore YSZ nucleation could not span (sample DT-E.05/03/13-125;10.850-B.12) from pores forming at the Ni/ZrO_2 interface. Image shows development of through-thickness crack linked to pores in the Ni. In samples cooled from 1,050 °C we have seen this lead to adhesive failure. 385
Figure 9-34. SEM micrographs showing columnar 7YSZ on Ni tube. The shown site is one of a small number of areas with long cracks parallel to the surface in the Ni

substrate just below the Ni/YSZ interface (sample DT-E.06/03/13-125;10.850-B.13). 385
Figure 9-35. SEM micrographs showing columnar 7YSZ on Ni tube. The polishing proved sub-par and the resulting micrographs somewhat unclear, however, no significant damage was in view on this sample, nor were there subsurface cracks immediately below the interface parallel to the surface (sample DT-E.05/04/13-125;10.850-B.14). 386
Figure 9-36. Exceedance probability plots of two exemplars showing the least and most linear samples (sample DT-E.24/01/13-125;10.1050-B.10 and sample DT-E.28/11/12-125;10.950-B.03). A total of fourteen similar plots were made and analysed, one for each sample. 387
Figure 9-37. EDX of the nickel-YSZ interface (sample DT-E.28/04/14-125;10.1050-C.01). This sample does not appear in the rest of the analysis. It was a one-off to investigate an apparent inconsistency in coating thickness. This experiment helped ascertain the importance of a shutter. 389
Figure 11-1. Final improvements to reduction and EB=PVD jigging (figures (a) through (c) and (d), respectively). In the latter both jigs are shown for scale. 402
Figure 11-2. Selected photographs showing the net improvement from a further iteration of the reduction and EB-PVD jigging. 405
Figure 11-3. Anode MFR normal probability plot (both 400 °C and 1,000 °C). The error is too small to be visible. 406
Figure 11-4. Electrolyte mass normal probability plot for 7YSZ deposited on anode reduced at 400 °C. 407
Figure 11-5. Electrolyte mass normal probability plot for 7YSZ deposited on anode reduced at 1,000 °C. 408
Figure 11-6. Cathode mass normal probability plot. NB: The error is the measurement error, which differs greatly from the batch to batch manufacturing variance. 408
Figure 11-7. Selected overall cross-sectional micrograph of sample PT-AEC.19/09/14-125.10.0.3.1100(400)[1000]-D.01. 409
Figure 11-8. Selected cross-sectional micrographs near the outer edge of sample PT-AEC.19/09/14-125.10.0.3.1100(400)[1000]-D.01. The final image (bottom right) highlights the influence of surface cracks on the gas-tightness of the electrolyte (see chapter 12). 410
Figure 11-9. Selected cross-sectional micrographs near the middle of sample PT-AEC.19/09/14-125.10.0.3.1100(400)[1000]-D.01. 411
Figure 11-10. Selected overall cross-sectional micrograph of sample PT-AEC.07/10/14-125.10.0.3.1100(1000)[1000]-I.02. 412
Figure 11-11. Selected cross-sectional micrographs near the outer edge of sample PT-AEC.07/10/14-125.10.0.3.1100(1000)[1000]-I.02. Note once more the effect of surface cracks on the gas-tightness of the electrolyte (see chapter 12). 413
Figure 11-12. Selected cross-sectional micrographs near the middle of sample PT-AEC.07/10/14-125.10.0.3.1100(1000)[1000]-I.02. 414

Figure 11-13. EBSD analysis of fractured edge cross-section of PT-AEC.19/09/14-125.10.0.3.1100(400)[1000]-D.01. Top left is the SE micrograph. The top right image shows phases (yellow is tetragonal zirconia; blue is monoclinic zirconia; red is nickel). Note pores were mis-indexed as Ni and Ni as tetragonal ZrO_2. The middle row is the inverse pole figure (IPF) direction key. The final three images are IPF X, IPF Y and IPF Z, respectively, corresponding to the tangential, radial and longitudinal directions of the cell. 416
Figure 11-14. BSE (top) of fractured edge cross-section of PT-AEC.19/09/14-125.10.0.3.1100(400)[1000]-D.01 showing areas analysed and the corresponding EDS spectra. Note that only spectra of interest were included. 417
Figure 11-15. EBSD analysis of fractured edge cross-section of PT-AEC.07/10/14-125.10.0.3.1100(1000)[1000]-I.02. Top left is the SE micrograph. The top right image shows phases (yellow is tetragonal zirconia; blue is monoclinic zirconia; red is nickel). Note the Ni was mis-indexed. The middle row is the inverse pole figure (IPF) direction key. The final three images are IPF X, IPF Y and IPF Z, respectively, corresponding to the tangential, radial and longitudinal directions of the cell. 418
Figure 11-16. BSE (top) of fractured edge cross-section of PT-AEC.07/10/14-125.10.0.3.1100(1000)[1000]-I.02 showing areas analysed and the corresponding EDS spectra. Note that only spectra of interest were included. 421
Figure 11-17. Grain distortion measured by EBSD (an indicator of local strain) for fractured edge cross-section of sample PT-AEC.19/09/14-125.10.0.3.1100(400)[1000]-D.01 (left) and sample PT-AEC.07/10/14-125.10.0.3.1100(1000)[1000]-I.02 (right). 422
Figure 12-1. Schematic of permeameter electronics (power supply and transducers). 431
Figure 12-2. Schematic of permeameter cell 'can'. All dimensions in mm. The can drawings were created by Tim Pryor using the DeltaCAD free software and edited here for clarity. A simplified rendition of the pipework is shown here; the complete schematic can be found in Appendix K: Permeameter SOP. While not shown in these schematics the cell is capped with a thin 1 cm long 316 SS end cap affixed with resin covering that portion that would remain uncoated by 7YSZ or Pt. 432
Figure 12-3. Photographs of the assembled power supply and sensors. 434
Figure 12-4. Photograph of the permeameter cell 'can'. Note the absence of a sample between threaded fittings just above the chamber itself. 435
Figure 12-5. Schematic of the permeameter setup showing valves, pressure take-offs and connections (adapted from Permeameter SOP). 436
Figure 12-6. Permeameter rig sample and fittings showing assembly prior to loading into rig. (a) cell assembled with end epoxy into permeametry fittings (b) commercial fittings to create seal with permeameter (c) end cap (d) components for lower seal (with 'can') slipped over cell fittings into place (e) components for upper seal (with pipe work) (f) lower seal finished and upper seal components slipped over top end of cell fittings (g) upper seal finished and ready to affix to pipe work with threaded fitting and copper O-ring. 437

Figure 12-7. Permeameter in use. NB the pressure reading is in Volts, directly from the sensor. The transfer function included in the relevant sensor datasheet was used to convert these into pressures in kPa in an Excel spreadsheet. 438
Figure 12-8. Pressure drop against time showing repeat variance for the same sample for each gas. Two exemplars are shown of a total of 25 plots (see Appendix L: All Permeametry Plots). The errors (based on measurement error) are too small to be visible. 445
Figure 12-9. Pressure drop against time for all gas mixes (mean of repeat measurements for all samples). The reduction schemes are labelled and the solid Ni tube given a linear fit to more clearly show the pressure drop limits. Note the different mathematical models for pressure drop with time that fit the two reduction schemes. 447
Figure 12-10. Pressure drop against time for all gas mixes (mean of all four measurements pre anode type) divided by reduction scheme. Note the different mathematical models for pressure drop with time that fit the two reduction schemes. 447
Figure 12-11. Mean permeance against atomic weight for samples A.03 (left) and A.04 (right). Both were reduced at 400 °C for 15 h. Note the differing behaviour of the 5 vol.% H_2 gas mix. 449
Figure 12-12. Mean permeance against molecular weight for all data points of all samples. 450
Figure 12-13. Pressure drop against time showing repeat variance for the same sample for each gas. Two exemplars are shown of a total of 24 plots (see Appendix L: All Permeametry Plots). The errors (based on measurement error) are too small to be visible. 458
Figure 12-14. Mean pressure drop with time through anode-electrolyte complex organised by gas showing data points by sample and repeat. Note the anode was included for reference (as a 0 μm electrolyte). 459
Figure 12-15. Mean pressure drop with time through anode-electrolyte complex organised by gas showing data points by electrolyte thickness. Note the anode was included for reference (as a 0 μm electrolyte). 460
Figure 12-16. Mean pressure drop with time through anode-electrolyte complex organised by electrolyte thickness showing data points by gas. Note the anode was included for reference (as a 0 μm electrolyte). 461
Figure 12-17. Mean gas permeance through AEC against molecular weight, organised by electrolyte thickness (note that the 0 m refers to data from anode samples A.01 and A.02). 463
Figure 12-18. Gas permeance against molecular weight for all gases, all samples and all repeats (measured data points, not means) including data from the solid Ni tube and anodes (samples A01 and A.02) for facile comparison. Graph on the right is log-scaled on the ordinate (in this case the data for solid tubes was omitted) and colour-coded to more easily distinguish different electrolyte thicknesses. 464

Figure 12-19. Gas permeance against kinetic diameter of several test gases for a series of 10 membranes with a SiO_2 top layer (that enhances selectivity) [Menzler *et al.* 2013]. 465
Figure 13-1. Photographs of furnace, support frame and controller..... 472
Figure 13-2. Air and fuel exhaust bubbles for overpressure control. 473
Figure 13-3. Sample after CVD aluminisation but without any interdiffusion heat treatment. (a) SFEG micrograph showing Al by CVD (in pack) on a cylindrical Ni substrate (a short 25 mm section of the conductor rod stock). (b) SEM micrograph of the same aluminised section of conductor rod stock material showing points for EDS composition analysis. (c) to (g) EDS spectra of same. 476
Figure 13-4. Sample after CVD aluminisation and interdiffusion heat treatment under vacuum. (a) SFEG micrograph showing Al by CVD (in pack) on a cylindrical Ni substrate (a short 25 mm section of the conductor rod stock). (b) SEM micrograph of the same aluminised section of conductor rod stock material showing points for EDS composition analysis. (c) to (g) EDS spectra of same. 477
Figure 13-5. Sample after CVD aluminisation and interdiffusion heat treatment in Ar atmosphere. (a) SFEG micrograph showing Al by CVD (in pack) on a cylindrical Ni substrate (a short 25 mm section of the conductor rod stock). (b) SEM micrograph of the same aluminised section of conductor rod stock material showing points for EDS composition analysis. (c) to (g) EDS spectra of same. 478
Figure 13-6. Anode electrical connections (cone and foil arrangement)..... 479
Figure 13-7. Cell gas and electrical connections. 480
Figure 13-8. End cap layout and connections (gas and electric). 481
Figure 13-9. Temperature profile with the addition of heat baffles. Note the uniformity of the hot zone. The distance is from the top of the furnace tube interior. The term compensated profile refers to correction for small variations in setpoint at the controller (in this case the controller proved very stable so correction was unnecessary). 482
Figure 13-10. Scanned part drawings showing evolution of adapter design (only the most pertinent iterations shown). All dimensions in mm. 483
Figure 13-11. Aremco 552 ceramic paste trials. Shown is the most successful attempt bonding a solid (as-delivered) Ni200 tube into a piece of SS bored to match the test rig adapters (Images taken with a Nikon optical microscope with camera and AcQuis image acquisition system). 485
Figure 13-12. The mechanism of diffusion bonding: (a) Initial 'point' contact and oxide contaminant layer; (b) Asperity yielding and some creep leading to a thinner oxide and large voids; (c) After the first yielding and creep, some voids remain with a very thin oxide layer; (d) Continued vacancy diffusion eliminates the oxide layer, leaving a few small voids till the final stage; (e) bonding process is complete [Dunkerton 1990]. ... 487
Figure 13-13. The Ni-Al binary phase diagram. Note the intermetallics $NiAl_3$, Al_3Ni_2 and $AlNi_3$. 490

Figure 13-14. SEM micrograph of cell-adapter seal with Al powder. Note the different phases visible by use of a back scatter detector (and the resulting atomic number contrast). 493
Figure 13-15. EDS of cell-adapter seal with Al foil. 494
Figure 13-16. The Ni-Sn binary phase diagram. Note the intermetallics Ni_3Sn_2 and Ni_3Sn_4. 495
Figure 13-17. EBSD of cell-adapter seal with Sn slurry. Note the presence of bonding slurry inside the fuel cell (above the porous Ni area at the top of the micrographs, especially visible with EBSD phase-colouring). 497
Figure 13-18. Burner test photographs. Top row: setup; Bottom row from low H_2 flow rate (just sufficient to maintain flame) to high H_2 flow rate (approximately 2 litres per min). Note: hydrogen flames are very difficult to observe in lit conditions. 500
Figure 14-1. Galvanostatic mode Nyquist plot at 1,000 °C of sample PT-AE.20/03/15-125;10;0.3.1100(1000)[1000]-G.04. Note that this repeat was identified statistically as an outlier despite its resemblance to a classic Nyquist plot for an SOFC. Furthermore, note the very high impedances recorded. 512
Figure 14-2. Arrhenius-type plot for OCV. Note due to the uncertainty of this data discussed previously no point was plotted for A.03 at 600 °C. 514
Figure 14-3. Arrhenius-type plot for OCV (excluding 800 °C from the lower temperature regime). Note due to the uncertainty of this data discussed previously no point was plotted for A.03 at 600 °C. 516
Figure 15-1. Examples of cell packing arrangements. 522
Figure 15-2. Single-Multi-Chamber-Machine Cell Manufacture process flow and schematic for a machine with rotating material handling feed and load locks..... 527
Figure 15-3. Single-Multi-Chamber-Machine Cell Manufacture Gantt-chart type depiction of manufacturing process. The figure shows the first batch of the week and one subsequent one (with the necessary process modifications). 528
Figure 17-1. Schematic cross-section of the metal supported cell created by Haydn *et al.* [after Haydn *et al.* 2014]. 542

List of Tables

Tables are labelled as Table C-#. where C is the chapter number and # the number of that table in the sequence for the whole chapter.

Table 1-1. Total systems emissions and primary energy use of baseload power generation [Hart and Bauen 2003]. 31
Table 1-2. Total systems emissions and primary energy use of distributed power generation [Hart and Bauen 2003]. 32
Table 1-3. Total systems emissions and primary energy use of remote power generation [Hart and Bauen 2003]. 34
Table 1-4. Total systems emissions and primary energy use of large commercial CHP [Hart and Bauen 2003]. 35
Table 1-5. Total systems emissions and primary energy use of industrial-scale CHP [Hart and Bauen 2003]. 37
Table 2-1. Theoretical E.M.F. of selected reactions and Gibbs free energy at 25°C and 1.013 bar. The superior fuels are separated from the inferior ones by an empty row (fully explained below). Adapted from [Mitchell 1963 and Gibbs Free Energy article accessed 2014]. 39
Table 2-2. Estimated cost of hydrogen produced by different methods [edited, after Shaikh *et al.* 2015]. 41
Table 2-3. H_2 storage in pressure cylinders. Comparative data for two cylinder types [Larminie and Dicks 2003]. 43
Table 2-4. LH_2 (liquid hydrogen) storage in cryogenic cylinders [Larminie and Dicks 2003]. 44
Table 2-5. Hydrogen storage properties for a range of metal hydrides [Hoogers 2003b]. 45
Table 2-6. A very small metal hydride container [Larminie and Dicks 2003]. 45
Table 2-7. Typical compositions of reformate from Steam Reformers (SRs), Partial Oxidation Reformers (POXs), and Autothermal Reformers (ATRs). In all cases the fuel was methanol [Hoogers 2003b]. 50
Table 2-8. Fuel/fuel cell combination options with most likely candidates shown in bold [extracted from Hoogers 2003b]. 52
Table 2-9. Electrode functions and requisite properties. 58
Table 3-1. Summary of major challenges and requirements of anode development. 81
Table 3-2. Relation between operating temperature, electrolyte thickness and conductivity for 9YSZ (9 mol.% $Y_2O_3 – ZrO_2$) [Ishihara *et al.* 2003]. 91
Table 3-3. Summary of major challenges to successful SOFC electrolyte development. 92
Table 3-4. Summary of major challenges to successful cathode development. 97
Table 3-5. Summary of major challenges to successful interconnect development. ... 100
Table 4-1. Theoretical E.M.F. and Gibbs free energy of the reaction $H_2 + 0.5O_2 \rightarrow H_2O$ at 1.013 bar for selected temperatures of interest. 114

Table 5-1. Anode objectives and contributions summary. 154
Table 5-2. Electrolyte objectives and contributions summary. 155
Table 5-3. Cathode objectives and contributions summary. 156
Table 5-4. General objectives and contributions summary. 158
Table 8-1. Mass gain, mass fraction oxidized and oxide thickness of Ni tube oxidation at 1,100 °C. All samples from two exemplar batches of Tier 1 shown: B and D. The whole table can be found in Appendix C: Complete Oxidation Results Tables. 183
Table 8-2. Grain size range and corresponding approximate MFO for early, transitional and late stage oxidation at 1,100 °C. 187
Table 8-3. Mass gain, mass fraction oxidised and oxide thickness of Ni tube oxidation at 1,100 °C. All samples from two exemplar batches of Tier 2 shown: A and E. The whole table can be found in Appendix C: Complete Oxidation Results Tables. 212
Table 8-4. Mass gain, mass fraction oxidized and oxide thickness of Ni tube oxidation at 1,100 °C. All samples from two exemplar batches of Tier 4 shown: A and E. The whole table can be found in Appendix C: Complete Oxidation Results Tables. 225
Table 8-5. Modified Wagnerian model verification comparing the values calculated using the model to the average (arithmetic mean) of experimental values. Also shown is the percentage error of the model (difference between calculated and average values expressed as a percentage) and the fractional error (ratio of the error to the calculated value, also as a percentage). 236
Table 8-6. Rate constants and transition time for all batches and for mean of experimental results. Nonlinear fitting by numerical solution with modified Wagnerian model and initial estimates of solved parameters. 239
Table 8-7. Mass gain and oxide thickness of Ni tube oxidation at 1,150 °C. All batches from Tier 3 experiment shown. 241
Table 8-8. Atomic properties of Ni, $H_2O(g)$ and N_2. 254
Table 8-9. Mass loss and mass fraction reduced of Tier 1 reduction. All temperatures reduced in 5 vol.% H_2 (balance Ar) shown. D, M, U after the sample code indicates whether it was downstream, in the middle or upstream with respect to the gas supply (respectively). Full table can be found in Appendix G: Complete Reduction Results Tables. 266
Table 8-10. The molar rate of hydrogen required for reduction of samples and corresponding minimum exposure time with 5 vol.% H_2 (balance Ar) gas mix (Tier 1). 272
Table 8-11. Titanium getters mass changes. 274
Table 8-12. Mass loss and mass fraction reduced of Tier 1 reduction with Ti getters at 800 °C. All temperatures reduced in 5 vol.% H_2 (balance Ar) shown. D, M, U after the sample code indicates whether it was downstream, in the middle or upstream with respect to the gas supply (respectively). 278
Table 8-13. Mass loss and mass fraction reduced of Tier 2 reduction. All temperatures reduced in 100 vol.% H_2 shown. U, M, D after the sample code indicates whether it was

upstream, in the middle or downstream with respect to the gas supply (respectively). Full table can be found inAppendix G: Complete Reduction Results Tables. 281
Table 8-14. Student T Test results of Tier 2 reduction at 400 °C. 284
Table 8-15. Minimum mass loss during reduction in 100 vol.% H_2 by temperature... 288
Table 8-16. The molar rate of hydrogen required for reduction of samples and corresponding minimum exposure time with 100 vol.% H_2 gas (Tier 2). 289
Table 9-1. Exact nucleation density parameter dependence by regime [Venables 2000]. 345
Table 9-2. Tier 1 coating thickness: average of eight points along the circumference of each of the three sections per sample, and the mean thickness per sample (including standard deviations: denoted by s since sample size < 10). ** indicates complete delamination; likely due to sectioning or mounting damage. 363
Table 9-3. Tier 1 deposition results including mass deposited, area coated, average coating thickness (as detailed in the discussion) and average coating density (also detailed in the discussion)..... 363
Table 9-4. Tier 1 deposition parameters by run. 363
Table 9-5. Tier 1 calculated coating densities (all cases considered). 365
Table 9-6. Student T Test results for Tier 1 coating density calculation (all cases considered)..... 365
Table 9-7. Tier 2 deposition z (thickness) measurements and sectional average (z). *Poor adhesion, coating continued to spall during and after unloading. The last four are the extension to the original DoE as remarked in the text. NB: While the measurement system was different than the first tier, the resulting error is very similar. 374
Table 9-8. Tier 2 deposition results. The last four are the extension to the original DoE as remarked in the text. *Poor adhesion, coating continued to spall during and after unloading. Area and mass deposited are only a rough indication. 375
Table 9-9. Tier 2 deposition z (sectional average thickness) measurements, absolute sectional standard deviation (s) and relative (normalized) standard deviation (s/z). *Poor adhesion, coating continued to spall during and after unloading. !Deemed an unusually large. NB: While the measurement system was different than the first tier, the resulting error is very similar..... 376
Table 9-10. EB-PVD 7YSZ deposition rates (compensating for oxidation)..... 378
Table 9-11. Microstructure classification by Thornton's model for each sample. Zone T is the transition zone constituting a transition structure consisting of densely packed fibrous grains. Zone II consists of columnar grains. 386
Table 9-12. Tier 2 DoE calculated factor significance based on thickness measurements, including factor interactions. Highlighted as follows according to my own judgement (and discussion with Professor John Nicholls): no highlight = modest effect, grey = negligible effect, yellow = strong effect. 388
Table 10-1. Porous Pt resistance by slide (25 mm wide). 397
Table 10-2. Calculated resistivity (ρ) and sheet resistance (R_s) including mean values and standard deviations (s rather than σ due to small number of measurements). 397

Table 11-1. Complete cell fabrication anode parameters and results (oxidation at 1,100 °C, 42 h dwell for all samples). 403
Table 11-2. Complete cell fabrication electrolyte parameters and results. 404
Table 11-3. Complete cell fabrication cathode parameters and results. 404
Table 11-4. Reduction step gas consumption and monetary cost of anodes. 424
Table 12-1. Permeameter components. 433
Table 12-2. Permeameter sample fabrication parameters. 442
Table 12-3. Tabulated pressure measurements in relevant gas mixes with pressures normalised to 20 °C. Repeat measurements are shown in adjacent columns for the same gas. *Uncertain temperature readings resulted from a loose wire. [§]Sample was draining much slower than expected..... 445
Table 12-4. Tabulated calculated gas fluxes (permeances) in relevant gas mixes. The values given use the average temperature and non-normalised pressure. Of the three variants calculated this was the least modified or corrected and therefore deemed most representative despite increased scatter. Permeances calculated with average temperature and normalised pressure or normalised temperature and normalised pressure (in effect compensating to STP) do not differ significantly and were considered less representative. 449
Table 12-5. Atomic weight, molecular weight, atomic radius and kinetic diameter for the gasses of interest. * The remaining 1.2% was treated as being only Ar since at high pressure CO_2 solidifies and the other gasses in air (Neon, etc.) are in very small quantities. n/a not applicable. 450
Table 12-6. Summary of permeameter AEC sample fabrication parameters. All samples reduced at 1,000 °C (ramp only). The m_{Ni}, m_{Ni+NiO}, MFO, $m_{reduced}$, m_{loss} and m_{Ni+YSZ} were omitted as they add nothing to the discussion hereunder. 454
Table 12-7. Permeameter measurements in relevant gas mixes. The pressures given are normalised to 20 °C. Repeat measurements are shown in adjacent columns for the same gas. 457
Table 12-8. Tabulated calculated gas fluxes (permeances) in relevant gas mixes for AEC. The values given use the average temperature and non-normalised pressure. Of the three variants calculated this was the least modified or corrected and therefore deemed most representative despite increased scatter. Permeances calculated with average temperature and normalised pressure or normalised temperature and normalised pressure (in effect compensating to STP) did not differ significantly but were deemed less representative. 462
Table 12-9. Hydrogen flux through manufactured anodes at 400 °C, 600 °C, 800 °C and 1,000 °C. 468
Table 12-10. Hydrogen flux through manufactured anode-electrolyte samples at 400 °C, 600 °C, 800 °C and 1,000 °C..... 469
Table 13-1. ICON Heat Treatment (at 5×10^{-6} mbar). 491

Table 14-1. Open circuit voltage data showing the 10 automated repeats divided by repeat measurement sets and temperature from the 3-probe measurement data. (Mean $\boldsymbol{\mu}$ and standard deviation $\boldsymbol{\sigma}$ included). 508
Table 14-2. Summary of mean OCV and standard deviation (data subsets in brackets). *These values are based on only three repeat sets, shortly prior to the failure of this sample and were considered unreliable. 509
Table 14-3. Summary of sample reproducibility testing (via independent, 2 sample, unequal sample size, equal variance Student T tests); excludes outliers and data subsets identified previously. 510
Table 14-4. Mean open circuit voltage and test parameters. One representative repeat was selected for each combination of sample and temperature for inclusion in the table from the 3-probe measurement data. The OCV in parenthesis was estimated based on the linear regression of an Arrhenius plot (explained later). 511
Table 15-1. Key to Figure 15-3. 529
Table 16-1. Anode contributions achieved. 533
Table 16-2. Electrolyte contributions achieved. 535
Table 16-3. Cathode contributions achieved. 536
Table 16-4. General contributions achieved. 537

A list of equations was not included as frequent reference to them out of sequence was not made. Equations are labelled (C.#.) where C is the chapter number and # the sequential number of the equation.

1 Introduction

Fuel cells in their many forms have garnered varying degrees of interest over the last century and three-quarters. The same technological principles that create batteries apply to high performance fuel cells capable of outstripping batteries in terms of power to weight and power to volume ratios as well as energy conversion efficiency. Interest has varied from very early experiments combining chemical and electrical phenomena [Grove 1839, Schœnbein 1839] to NASA's interest in fuel cell technology for space, predating the first lunar landing, to modern attempts to create an all-electric vehicle that uses fuel rather than batteries (with some very promising prototypes) [Honda 2014]. It is best to begin this introduction by concisely defining the fuel cell. The following include a general definition, with solid oxide fuels cells being a subset having their own definition.

General Definition [adapted from Mitchell 1963 and Yashima *et al.* 1996]:

> A fuel cell is defined as an electrochemical device composed of non-consumable anode and cathode, an electrolyte and balance of plant (pumps, controllers, heaters, and so on). This definition is for the fuel cell as a device. If the balance of plant is ignored the same definition is also applicable to the individual cells within such a system. Note that the non-consumable nature of the anode and cathode is in contrast to galvanic cells where the electrodes are consumed.

Operation [adapted from Mitchell 1963]:

> The free energy of the reactants (fuel and oxidant) stored outside the cell itself is converted directly into electrical energy with no intermediary conversion steps. Fundamentally, any oxidation-reduction type of reaction will work.

Solid Oxide Fuel Cell (SOFC) Operation [Yashima *et al.* 1996]:

> "A ceramic fuel cell is an all-solid state energy conversion device that produces electricity by electrochemically combining fuel and oxidant gases across an ionic conducting oxide."

Figure 1-1, below, shows a representative schematic for a solid oxide fuel cell and its operation. The solid electrolyte, most commonly an yttria-stabilised zirconia (YSZ) or gadolinia-doped ceria (GDC) ceramic, acts as a conductor of oxide ions at temperatures in excess of 400 °C. The solid electrolyte allows oxygen that has dissociated and ionised (reduced) at the porous cathode surface to be transported through to the porous anode. The anode is filled with fuel gas, itself dissociated and ionised. The reaction causes oxygen ions to lose their excess electrons by conducting them to an external circuit. For hydrogen fuel the resultant product is water vapour formed at the anode. The basic components of a solid oxide fuel cell are therefore the electrolyte, flanked by two porous electrodes intimate contact: an anode and a cathode.

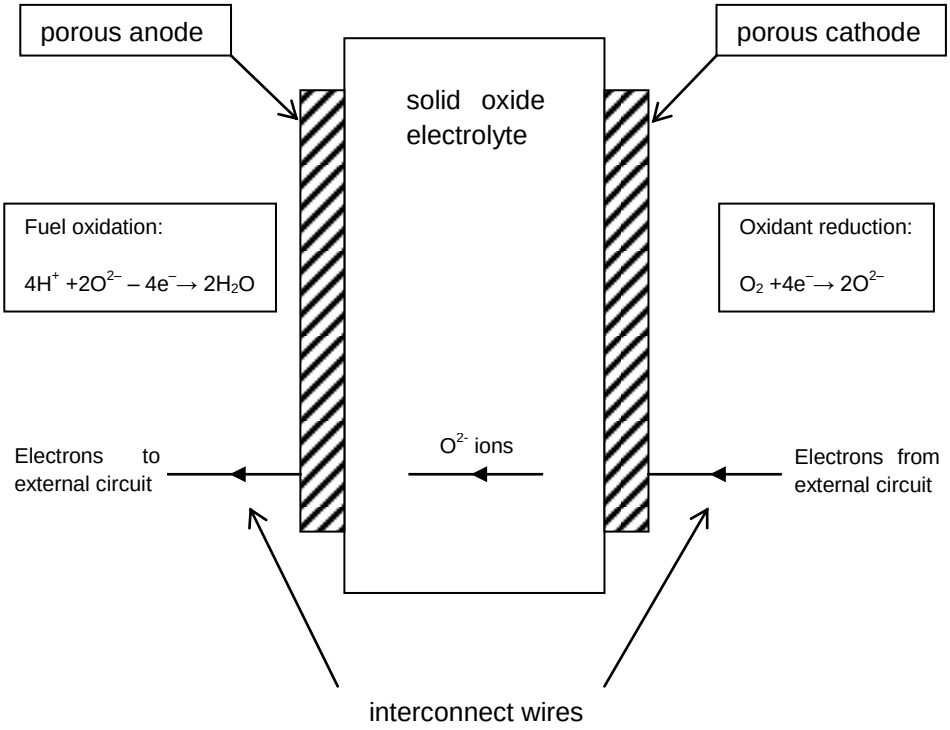

Figure 1-1. Schematic of SOFC operation.

The elegance of such a system is undeniable, especially when one considers it is a direct energy conversion with very low losses [Camilleri 2009]. Singhal and Kendal (2003) even go so far as to refer to it as “almost magical”, and find it astonishing the technology has not already been commercialized to such a degree as to supplant inefficient and polluting heat engines used for power generation. Market reluctance is probably a matter of economics that favour short term rather than long term improvement, and will be explored in greater detail later.

Solid oxide fuel cells (SOFCs) include high temperature versions, with tubular geometries a further specialisation and finally miniaturisation of these being an almost entirely new field. Also defined is the general operating principle of fuel cells. This

introductory chapter seeks to lay out the origins of fuel cell technology, its importance and potential, its limitations, as well as existing applications and potential future ones. The following provides a general discussion, much of which applies equally well to all types of fuel cells. However the focus is on the solid oxide fuel cell and its miniaturization.

1.1 Aims and Objectives

The theoretical and practical feasibility of the miniaturization of an alternative design for solid oxide fuel cell – the microtubular design – has already been demonstrated [Camilleri 2009]. This design has many advantages over the more conventional planar form that will be discussed below (section 1.5). A satisfactory route to fabrication (including an early demonstrator) has also been established. However, only two demonstrators were fabricated, far too little to truly assess the capability of this innovative fabrication route. Also, performance of this early demonstrator was not assessed and existing analytical models were found to be unsatisfactory [Camilleri 2009]. Furthermore, there is room for optimization in the fabrication techniques that is worth investigating.

This thesis aims to explore further microtubular fuel cell manufacture and establish at minimum a first-degree of optimization for the fabrication processes, assess fabrication process reproducibility and demonstrate the performance of the devices fabricated. Secondary to these is to assess whether it would be feasible to reach the EU target cost by the method described (chapter 15). Details are given in section 1.2.

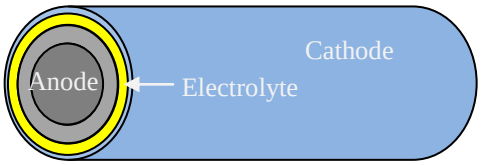

Figure 1-2. Anode-supported tubular SOFC [Camilleri 2009].

In addition, the further work set out hereunder, as suggested in Camilleri (2009) was addressed. Generally the work can be divided into three forms: (1) obtaining more data to support the findings of the previous project, (2) advancing the miniaturisation and the understanding of how this affects SOFCs and (3) working towards creating a commercially viable system. These tasks appear below arranged in order of priority.

1.2 Project Scope

- The miniaturisation of the components which is expected to allow for practical operation at lower temperatures (the so-called intermediate temperatures or IT-SOFCs) of around 400 °C to 600 °C. This has been investigated as part of the performance assessment of the design by operating at different temperatures spanning the IT and HT ranges, with special interest in finding lowest limit for adequate cell performance.
- Statistically significant numbers of experiments relating to the fabrication of the various components in order to verify the selected route. This is especially important for miniaturized devices, and becomes increasingly important as size is reduced since it is well known that the repeatability of processes is increasingly difficult with miniaturization.
- Precise measurements reflecting pore connectivity.
- Identification of the optimal oxidation time and creation of an accurate model based on oxidation by cation transport models found in the literature.
- Identification of the optimal reduction time (akin to the oxidation one) as well as establishing a body of evidence of the reduction mechanism (missing from the literature).
- Detailed investigation into fuel feasibility and the economics of fuel cells, taking into consideration infrastructure and economics. This is crucial because it concretely justifies an approach that does not follow current trends as well as defining the niche such products are able to fill in the energy market.

Those objectives that do not relate directly to improving the understanding of or building on the work of Camilleri (2009) were included to fill in voids in the current understanding of SOFCs. The economics of fuel cells is of secondary importance, and was in the form of a review. However, many authors in the literature tend to ignore this aspect, or treat it with simplistic sweeping statements. To date the author has found no quantitative justification in choosing tape-cast planar cells over other designs, and yet they dominate in both quantities produced and in perception as the most economically viable form of SOFCs. While at first glance it is obvious that such will be less expensive than say, PVD manufactured microtubular ones, just how much less expensive is unknown even on the most approximate of levels. It is certainly possible (and occurs regularly between competing products) that each design best fulfils a specific niche where one technology alone would be forced into excessive compromise. Therefore, an attempt has been made to enumerate the fundamental costs associated with manufacturing the cells described in this project in the hopes it will inspire others to do the same for their own work.

Generally the work outlined above can be divided into three main objectives: (1) obtaining more data to expand on the findings of my MSc project [Camilleri 2009] or

literature sources, (2) advancing SOFC miniaturisation and the understanding of its effects and (3) working towards creating a commercially viable microscale system.

Defining the objectives, or crudely what will be done, is obviously important. Equally important, however, is delineating what will not be done. In no small part because as Hoogers (2003) succinctly put it: "Another peculiarity of fuel cell technology is something I learned from my students which is that it is a very broad subject encompassing areas such as electrochemistry, chemical catalysts, materials science, polymer science, fluid dynamics, electrical and mechanical engineering, etc." Attempting to do everything in a single project would be foolish.

The following are aspects that will not be pursued in the current project:

1. Attempt to revise the fundamental theory of fuel cell operation. It is generally agreed that this is largely correct, and only certain details (such as exact reaction pathway of oxygen reduction) remain. What will be challenged is the way the relevant phenomena are modelled. While the way the fundamental phenomena are expressed may therefore differ from the conventional view the basic principles are in fact used to derive new equations.
2. Justification for the choice of design and the conceptual design itself has largely been set out in sufficient detail in Camilleri (2009) and little modification to this was envisaged. It should be noted, however, that all the fabrication techniques utilised and the model derived are equally valid for the so-called hybrid geometry. Some repetition regarding proposed manufacture methods is inevitable but this will be minimised.
3. While the previous discussion on the failures of older tubular designs is largely sufficient [Camilleri 2009] some more detail was added as part of this work since these details more clearly define the envisaged role of microtubular cells and hence what this project hoped to achieve.
4. Investigation of the performance of this design with different materials, the most relevant being strontium-stabilised manganates (LSM) for the cathode, ceria for the anode and alternative dopants for the electrolyte. Related to this last aspect is the choice of cathode material, which informed readers may question. The author concurs that the material selected does not conform to the state-of-the-art. The project is not intended to advance new cathode materials technology, which itself is undergoing dramatic changes as our understanding improves [Funahashi *et al.* 2007, Tsipis and Kharton 2008b, Suzuki *et al.* 2009b, Connor 2010]. Therefore a simple but largely 'uncommercialisable' platinum cathode is used (see Chapter 10). Given the minute quantities of platinum required this last point can be argued. It does provide the cathode as needed for performance testing and leaves the design open to further advances in cathode materials. Thus enabling a future incarnation to make full use of the most suitable cathode material(s) once

new developments are better understood, free of artificial constraints on cathode selection.

5. Further miniaturization taking a very different approach to that outlined. Rather than applying conventional techniques and miniaturizing the cells, working from the bottom up using more conventional micromachining technologies. This may lead to scaling down by a further order of magnitude to nanotubular fuel cells, opening a host of new possibilities and presenting new challenges.
6. Create a fully functional, directly commercialisable system encompassing the fuel cell itself and all necessary balance of plant.

The scope therefore is the analysis of the SOFC design adopted (fabricated as described in a previous MSc thesis [Camilleri 2009] and section 3.8), focussed on manufacturing processes and working towards further miniaturization. The intention furthermore, is to take the first steps in the creation of a commercially viable system based on the fabrication method route used. While its commercialization will not be the overriding principle of the project it will certainly be a considered need informing many design decisions. In other words, a weather eye was kept on manufacturing on a commercial scale. This is explained in chapter 6, Methodology and Terminology. Each objective is further expounded upon in chapter 5, listing the precise contributions to science this project aims to achieve. This thesis tackles the SOFC components in turn, each as a separate chapter with its own introduction and literature review as necessary. This is followed by performance analysis with the same format. Efforts were made to "divide and conquer" – further dividing component objectives into experiments, these in turn were optimized with respect to time and material resources and as much work as possible was carried out in parallel.

1.3 Classification of Fuel Cells

It is difficult to present a dimensionless definition of the fuel cell that will satisfactorily convey its functioning as a device while encompassing all relevant parameters. Therefore a range of classification systems are in use, often in combination, to adequately describe a particular type of cell.

Fuel cells can be classified by operating temperature, generally as high, medium or low. Solid electrolyte systems are representative of high temperature fuel cells, operating at 500 °C and above. Medium temperature cells are typified by the Bacon hydrogen-oxygen cell that operates at 200 °C. Finally, low temperature systems, mostly proton exchange membrane systems, operate at any temperature up to the boiling point of the aqueous electrolyte. There has been a recent trend to further divide high temperature cells into high temperature (above 700 °C) and medium or intermediate (nearer 500 °C or 600 °C) which can be confusing.

Classification by electrolyte divides fuel cells into basic or acidic systems. A variety of which have been investigated in the past [Mitchell 1963, Larminie and Dicks 2003]. Classification by physical form of electrolyte is also possible and includes solid electrolyte, liquid electrolyte or so-called contained electrolyte classifications. The latter refers to capillary membranes containing the electrolyte or ion exchange membranes (usually polymeric).

A similar division, separating fuel cells into those with metallic electrodes and ceramic ones, has also become commonplace. Occasionally this is even more specific, delineating whether the component providing the necessary mechanical support is one of the electrodes or the electrolyte. This results in very different designs of fuel cell, even with the same component materials, fuels, geometry, etc.

Fuel cells can also be classified by the type of fuel used. Gaseous fuel is typical and natural gas is the most common. Liquid fuels are normally alcohols, and solid fuels carbon or metals. It is possible, in a similar manner, to classify a fuel cell by the individual fuel itself rather than its type. So there are hydrogen fuel cells, and alcohol fuel cells, for instance. Since the fuel dictates much of the design including cell configuration, it has become common to classify fuel cells by the individual fuel. Generally there is much less flexibility in selecting the oxidant. This is usually limited to oxygen, air and hydrogen peroxide (H_2O_2).

Fuel cells can also be classified by their geometrical shape. While in the past many forms existed [Mitchell 1963] the most prevalent today are planar and tubular forms. The latter of which also has sub-types: microtubular and hybrid. Exceptions do exist, but they tend to be variants of one of these rather than an entirely new geometry. After the choice of fuel the geometry has been recognised as being the next most important feature of a fuel cell, determining many other parameters (such as the design of interconnects and support structure, sealing requirements and manifolding).

It is almost always most useful to describe a fuel cell using a combination of the classification types. A hybrid geometry, natural gas fuelled, solid oxide (both the form and type of electrolyte) fuel cell, for example.

1.4 A Brief History of Solid Oxide Fuel Cells

The first solid electrolyte gas cell was invented in 1853 and can therefore be considered the birth of much of the technology modern solid electrolyte fuel cells are based on. Yttria-stabilised zirconia (YSZ) was first used by Nernst in his patent for solid electrolyte-based incandescent light. Extensive studies on the doping of Zirconia were

carried out by Reynolds in 1902, solving the problem of the very short life of Nernst's incandescent light. Unfortunately, this long term stability problem led to the prevalence of the filament electric bulb we know today. Had things gone slightly differently we may have used fuel cell technology for household illumination. The first solid oxide fuel cell was developed by Haber and co-workers in 1905. Zirconia was first used as the solid electrolyte in 1937 by Baur and Preis, but its true potential and importance along with other forms of doped zirconia was not recognized till 1943 by Wagner. Micro-tubular cells, with improved performance and high thermal shock resistance (and therefore well suited for any rapid start-up application) were first investigated in 1994. The interested reader is referred to the review by Tsipis and Kharton (2008) and papers by Suzuki *et al.* (2008c) and Funahashi *et al.* (2009) for more.

As long ago as 1839 the basic operating principle of fuel cells was discovered by William Grove. He reversed the process of water electrolysis to generate electricity from hydrogen and oxygen, producing water. The operating principle remains unchanged since Grove's definition:

> "A fuel cell is a "device" that continuously converts chemical energy into electric energy (and some heat) for as long as fuel and oxidant are supplied."

Fuel cells therefore, resemble both batteries (electrochemical in nature) and combustion engines (work continuously as long as there is a supply of fuel – unlike batteries). The similarities end there. Unlike either batteries or combustion engines a fuel cell does not need charging, operates unrestricted by the Carnot cycle's limiting efficiency (and therefore very efficiently), and where hydrogen is used as the fuel it generates only water as "waste". Some have taken to referring to it as a *zero-emission engine* [Hoogers 2003a].

Important breakthroughs of the last decade include long operating life (>20,000 hours) by Siemens, high fuel efficiency (>45% without heat recovery) by Jülich, reducing operating temperature (down to 500 °C) by TOTO and the integration of auxiliary power units (APUs) into automobiles by BMW and Delphi [Wei 2008]. Considerable advances have been made since Nernst and his colleagues over a century ago. The optimization of fuel cell designs seems set to continue for some time to come.

Chen E. (2003), "History". In Hoogers G. (Ed.) *Fuel Cell Technology Handbook*, CRC Press, New York, USA (pg. 2-1–2-40) is highly recommended reading in addition to the two review papers by Tsipis and Kharton (2008a and 2008b).

1.5 Benefits of Solid Oxide Fuel Cell Power

SOFCs are the most efficient energy conversion devices currently known, even compared to other fuel cell types. Energy conversion efficiencies as high as 45% have been demonstrated in practice without waste heat recovery [Wei 2008]. Operating efficiencies of up to 70% are possible in conjunction with heat recovery or in combined cycle systems (e.g. with a gas turbine) [Pomfret, Eigenbrodt and Walker 2008]. The efficiency advantage and capability of operation with a wide variety of high molecular weight carbonaceous fuels in addition to hydrogen makes SOFC-based systems attractive as power sources [Pomfret, Eigenbrodt and Walker 2008, Coddet *et al.* 2014].

The following aspects inform all design decisions for this project:

1.5.1 Efficiency

Unlike power generation by combustion, chemical energy is converted directly into electricity without intermediate conversion to heat. Therefore, the limitations of the Carnot cycle in general, and the specific thermal cycles (Diesel, Brayton, Otto, etc) do not apply. This leads to very high theoretical efficiencies of up to 90% [Mitchell 1963, Larminie and Dicks 2003, Meng *et al.* 2008, Dal Grande *et al.* 2008, Cho and Choi 2009, Yang *et al.* 2009, Funahashi *et al.* 2009, Suzuki *et al.* 2009a, Coddet *et al.* 2014, Gadow *et al.* 2018]. In addition, fuel cells eliminate the need of the following energy conversions and their attendant inefficiencies: thermal-mechanical and mechanical-electrical (boiler to turbine and turbine to generator for example). Hence not only is the theoretical efficiency higher by circumventing the Carnot cycle (itself representing the best possible theoretical efficiency of all heat engines), but also losses inherent in multiple conversions are entirely avoided. Fuel cell efficiency has in the past been considered independent of the cell size [Mitchell 1963]. There are, however, other scaling effects including physical robustness and actual performance and efficiency as opposed to the ideal values that are at times not well explored nor particularly carefully defined in the literature. The definition for ideal thermodynamic efficiency (equation (4.85), defined more fully in section 4.11) is indeed independent of the cell size. It only considers however the energy conversion potential of a fuel (ratio of the Free-Energy change to the Enthalpy change), not the actual performance of a device; excluding, among other elements, reactant kinetics.

$$\eta_{ideal} = \frac{\Delta G}{\Delta H} \qquad (4.85)$$

To phrase things differently one could say that the claim is correct in literal terms, but not in practical ones. Furthermore, fuel cell efficiency is strongly affected by the amount of power produced [Mert *et al.* 2015] (the balance of output voltage and current density). Efficiency is an oft-quoted performance measure, and therefore its definition is

critical and must be rigorously adhered to if meaningful comparison between designs is to be made. The actual efficiency calculation is considered later on (section 4.11).

1.5.2 Flexibility in Power Plant Design

The voltage at the terminals of each cell is typically very low (~1 V), so it is nearly always necessary to connect them in series to obtain the desired voltage. The current delivered by each cell is proportional to the geometrical area of the electrode. Adding cells in parallel will hence increase the current output. The strategy then affords great flexibility enabling precise voltage and current outputs to be tuned by creating series parallel networks of cells [Mitchell 1963, Cho and Choi 2009, Soysal *et al.* 2013]. Ancillary to all this is that the cells can be grouped into convenient batteries, but the total power requirement can be met by a distributed system offering flexibility in weight distribution and space utilization. Furthermore, changes can be made *in situ* adapting to changing power requirements by having a system of switchable circuits that may be physically separated. SOFCs have the added advantage of not requiring an external fuel reformer [Larminie and Dicks 2003, Wei 2008], as described in section 2.1.

1.5.3 Manufacturing Advantages

The manufacturing cost of fuel cells is relatively low, principally because they have no moving parts that need to mate within stringent tolerances as would be the case with IC (internal combustion) engines. Fuel and oxidant manifolds can be machined (punched, etched or cast) directly in the manifold material with little difficulty using standard techniques from macro scaled machining to photolithographic processes and even strain engineering (also called strain epitaxy). Advanced, and especially miniaturised, designs benefit greatly from sophisticated manufacturing techniques such as the various forms of sintering and physical deposition. The same is unfortunately not true of the materials needed (see Limitations below). On the other hand SOFCs do not require precious metal catalysts [Larminie and Dicks 2003, Wei 2008]. The most desirable features of any production method are reproducibility, geometrical quality (the ability to make distortion free components) and scalability [Monzón *et al.* 2014]. “These standards are frequently not met by lab-scale methods and, in some cases, the lack of them can become performance limiting in the resultant cell.” [Monzón *et al.* 2014]

1.5.4 Maintenance

The lack of moving parts means there is nothing to wear so maintenance issues are limited to those related to high temperature corrosion and the aging that can come with thermal cycling of a material. With low (or at least lower) temperature cells this is less of a concern, concomitant with a reduced operating temperature. In both cases there is generally little maintenance needed over the fuel cell’s life [Mitchell 1963, Larminie and Dicks 2003]. Evaluation of the life of commercially viable systems is an ongoing challenge.

1.5.5 Power Density Advantages

Power per unit weight and power per unit volume are two very useful parameters to differentiate between power generation units. Fuel cells, when the weight and volume of fuel are also considered, prove to be considerably better performers than traditional generating sets [Mitchell 1963, Coddet *et al.* 2014]. Power per unit weight and power per unit volume are also frequently referred to in this thesis as weight specific and volume specific power density. The lack of a fuel reformer as additional plant is a benefit here also [Wei 2008].

1.5.6 Reduced Pollution

The exhaust products of a fuel cell contain no objectionable combustion products (SO_x, NO_x, CO and particulates), nor do they release any noxious gases [Larminie and Dicks 2003, Meng *et al.* 2008, Dal Grande *et al.* 2008, Cho and Choi 2009, Yang *et al.* 2009, Xing *et al.* 2012]. Waste is usually limited to one or two of the following (depending on the fuel): water, some carbon dioxide and nitrogen. Unspent fuel and oxidant can be re-circulated within the system. Finally, because there are no moving parts, fuel cells provide silent electrical power, even when electrical inverters are taken into account (convert DC to AC), particularly the modern solid state types. Of course the exact nature of the pollution depends on the fuel used. Ideally hydrogen is used as a fuel since water is the only by-product of the process. However, even the production of CO_2 may in fact be advantageous. Carbon dioxide is a greenhouse gas. However, methane is a much stronger greenhouse gas. As such using methane as a fuel has the additional effect of reducing the overall quantity of CO_2-equivalent greenhouse gases vented into the atmosphere. Unfortunately, methane and all other carbonaceous fuels have further disadvantages that will be outlined later. Greater detail can be found in section 1.10 (and the reference cited within).

1.5.7 Waste Heat

Electrical inefficiencies usually manifest themselves as heat. In better designs this can be considered as negligible, according to [Mitchell 1963]. For many applications minimising heat loss, not only in the sense that it constitutes a source of inefficiency, is very important. Examples include minimization of detectable heat loss (thermal signature) for military applications, as well as preventing creation of thermal drift and other losses where fuel cells are used in intimate proximity with sensitive electronics, for example cryogenically cooled satellite thermal imaging equipment. The need to operate SOFCs at elevated temperatures makes them inherently unsuited to such low thermal signature applications despite minimal waste heat generated. There are applications that make use of waste heat and the high operating temperature required by SOFCs (see sections 1.8.2, 1.8.3, 1.9 and 1.10).

1.5.8 Capacity

One of the major advantages of fuel cells for applications with unsteady loads is their high overload capacity thanks to the capacitive effect created by the double layer at the reacting surface (although this also is the source of the activation polarisation detailed later on) [Mitchell 1963, Larminie and Dicks 2003]. Generally a brief overload of 100% or more can be withstood safely [Mitchell 1963]. Thus the rating of a fuel cell can be based on average power and need not be rated for peak loads being able to cope with brief periods of overload without problems. This is the exact opposite of internal combustion type systems that must be rated for the peak power output, yet rarely operate at peak output, wasting capacity.

1.5.9 Power on Demand

Fuel cells only consume fuel and oxidant when power is drawn from the system [Mitchell 1963]. There is no consumption at all when the system is idle (no load). For large scale power generation systems this is a considerable boon, allowing fuel cells to be used to cope with peak demands with no consumption of fuel or oxidant when unloaded, unlike the systems used to drive turbines that suffer considerable losses in stop-start scenarios and when loads vary considerably. The greatest limitation in this aspect is the need to heat up solid oxide fuel cells to their operating temperature of anywhere between 600 °C and 1,200 °C. Smaller cells have an additional two advantages here over traditional designs: they heat up more rapidly both inherently due to a much smaller thermal mass and also because more rapid heating is allowable without the risk of causing damage, since small ceramic structures are far more resistant to thermal shock than larger ones (the deleterious effect of heterogeneous coefficients of thermal expansion and specific heat capacities is minimised by the small dimensions). Secondly, the energy needed to heat up small thermal masses is also far less than for conventional cells. Overall this reduces the power and time necessary to heat up cells for operation.

1.5.10 Advantages of Miniaturisation

Some of the benefits of miniaturisation have already been mentioned, these and others will be discussed alongside the relevant elements in their respective sections of the thesis. This makes for a smoother flow of discussion as well as facilitating direct comparison with models and experimental results where they are described in detail. Generally, there are three advantages: firstly, miniaturisation minimises material usage (and indirectly may permit more material-efficient mass manufacture), secondly losses are greatly reduced, and thirdly thermal cycling behaviour is improved.

Sections 1.5.2 and 1.5.4 (and others like 1.5.6) are defined by the nature of fuel cells in general; *viz.* Camilleri (2009). This thesis is interested in Efficiency, Manufacturing, Weight and Volume, Pollution, Waste Heat, Capacity and Power on Demand.

1.6 Limitations to Solid Oxide Fuel Cell Power

Many of these limitations apply to fuel cells generally. While the difficulty and cost of obtaining suitable fuels (hydrogen, hydrazine, alcohol and simple hydrocarbons) is not as difficult as it once was [Mitchell 1963] these fuels are not always commercially viable, and where needed catalysts are not always commercially available especially for lower temperature fuel cells where the need for catalysts is greater. In short there is no real infrastructure for most of the better fuels (those that do not poison the electrodes, have unfavourable kinetics or are more environmentally friendly). Furthermore, the materials needed for the cell components and the process of shaping these into a fuel cell is still expensive and requires specialised equipment. As Mitchell succinctly put it in 1963, "...from a technical standpoint fuel cells are here to stay. If their use is limited, it will be limited by economic factors rather than by technological difficulties." Even now it is accepted that high costs remain the single greatest limitation to the large scale commercialization of fuel cells in general and in particular of solid oxide fuel cells [Larminie and Dicks 2003, Tsipis and Kharton 2008, Piccardo *et al.* 2009, Connor 2010, Coddet *et al.* 2014]. "High production costs are linked to time consuming manufacturing techniques." [Coddet *et al.* 2014] Thus, large batch and rapid processes are an integral part of development towards successful commercialization.

Performance degradation over time is the second largest obstacle [Tsipis and Kharton 2008, Coddet *et al.* 2014]. SOFC reliability depends to a great extent on the chemical and microstructural stability of its components [Xing *et al.* 2012]. Lifetime limitations are linked to thermal stresses and thermally induced unwanted diffusion of components. Moving towards lower manufacturing and operating temperatures is considered very important to mitigate this [Coddet *et al.* 2014]. Therefore, thinner electrolytes that enable lower temperature operation are preferable. In order to reduce manufacturing temperatures, which cause unwanted interdiffusion, it is necessary to move away from green sintering based techniques [Coddet *et al.* 2014]. A significant disadvantage of solid oxide designs such as this one is that they require elevated operating temperatures (the inherent reasons for this are elucidated later). Fabrication difficulties and material as well as fabrication costs become even more of a limiting factor with miniaturised designs than with the larger variants. What must be ascertained is whether the performance advantages outweigh the increased cost in terms of commercial viability.

1.7 Applications

The applications that fuel cells of any given generation are suitable for is ultimately dictated by the following criteria: the capital cost, fuel cost and oxidant cost need to be competitive with rival technologies in that area. For example the steam turbine plant is best suited for general power generation while batteries and photovoltaic cells are more

suitable for high power density applications like consumer electronics, light industrial applications and satellites. To continue with this last example, hydrogen-oxygen fuel cell systems are used in space [Mitchell 1963, NASA Glenn Research Centre article] because of their high efficiency, superior power to weight and power to volume ratios, their reliability, low electrical and audible noise, minimal heat generation and useful reaction product (the only exhaust from such cells is water vapour). These are not usually SOFCs due to the high operating temperature requirement. Conversely the non-existent infrastructure to support fuel cells on a large scale currently precludes them from general power generation.

Fuel cells are used to power some material handling equipment and industrial movers like forklifts because of their efficiency, lack of noxious fumes, ability to take overload and provide high energy for initial motor torque (causes a voltage spike in electrical systems that fuel cells are easily able to cope with), and greater capacity than batteries. There is similar interest in military industries where the benefits are quiet operation, low heat (low thermal signature) and safe waste product [Mitchell 1963]. In the latter case SOFCs are unsuitable because of their thermal signature.

The need for portable, long shelf life, reliable emergency power has increased in rcent history. Such units are needed for emergency relief, as backup power for critical resources like hospitals and even at home in areas prone to lengthy power cuts. The standard today is the diesel electric generating set. Purpose designed ones are commercially available and as efficient as such a system is likely to get. Yet they remain prohibitively expensive for common use in third world countries and for emergency relief, let alone home use. They only see use with businesses of a certain size and hospitals. Fuel cells, which can be scaled more or less without loss of efficiency, may prove to be ideal both as small portable units and large plant to cover the basic needs of an entire hospital. This is especially true of SOFCs taking advantage of efficiencies even greater than other types of fuel cells, the ability to run on a wide range of fuel types with minimal to no modification and the possibility of running off the waste heat of other systems (more on this later).

A rather unusual area of application is in using the waste products of industrial chemical reactions as fuel, or the reactions themselves, to operate a fuel cell [Funahashi *et al.* 2007, Funahashi *et al.* 2009]. In the first case this reduces the waste to a more environmentally friendly form. In the second case this results in two useful outputs – the chemical synthesised by the reaction (original purpose of reactor) and electrical power (ancillary). Any synthesis reaction that produces carbon monoxide as a by-product of the process is a good example of this. This is very much like utilizing the primary heat generated by a boiler to drive a turbine and then the energy left in the steam is used for heating (called combined heat and power).

Scaling down to the millimetre and even micrometre scale yields several important benefits (including greatly improved performance by dramatically reducing losses), with only one major drawback. While the voltage output is unchanged (since it is a function of the chemical species involved) the current capacity of each individual cell is dependent upon its area and therefore may be greatly reduced depending on the design. This means a great many cells are needed to provide meaningful currents for general power applications, which is likely to make such systems even more costly than their larger brethren (in turn, already much more expensive than other power generation systems). Microtubular designs have a distinct advantage over their larger cousins in terms of usability. They can be placed in areas of high temperature, e.g. engine manifolds, near combustors, and so on, to generate power for sensors or other small electrical or electronic (probably microelectronic or MEMS) devices. These applications require very little current, so a handful of cells to achieve the right voltage makes these systems ideal if a suitable source of fuel is available (e.g. the carbonaceous gases exhausting through an engine manifold).

Fuel cells are possibly the strongest contender as a replacement for internal combustion engines (ICEs) in the transportation sector [Hoogers 2003a]. They are far more efficient than ICEs because they operate electrochemically rather than thermally (heat is the lowest grade of energy). Furthermore, fuel cells can help to reduce the consumption of primary energy and the emission of carbon dioxide. Both factors increasingly important in an evolving transport market. It is this last aspect (low-to-zero emissions) that inspired research in the 1980s and 1990s for the development of fuel cell powered cars and buses. Battery power is unacceptable both for its very limited range due to insufficient storage capacities, and because the electricity used to charge batteries depends solely on the power generation method used – often merely casting back pollution to the provider rather than the vehicle directly; also conventional fossil fuel power generation is only marginally more efficient than an ICE. There is much competition in this sector, but many expect the greatest market for fuel cells to be in transportation; fitted to buses initially and later cars once the hydrogen storage problem is more comprehensively solved [Hoogers 2003a]. With the Honda Clarity [Honda FCX Clarity accessed 2014] the hydrogen storage problem has been solved, or at least an effective compromise reached. So we seem to have reached the turning point identified by Hoogers. Unfortunately during this period hybrid technology has gained sufficient maturity to have already won over much of the market for non-fossil fuel transportation despite both the short-term and unsatisfactory nature of this technology (it is only a stop-gap measure and is still beholden to fossil fuels).

As noted, SOFCs are less well suited to mobile applications. The above paragraph is intended to illustrate the changing nature of the energy market, and the way an effective solution may replace an arguably superior one (hybrid commercial success and the slow implementation of fuel cell powered electric vehicles). The transport sector is

particularly competitive and demonstrates the importance of carefully selecting the target market for a fuel cell design.

The next largest market segment after transportation is stationary power generation, principally for the same reason – reducing emissions. Initially the reasoning had been that when fuel cells met automotive cost targets then power generation would benefit from the development and cheap multipurpose power sources would become available [Hoogers 2003c]. Currently, fuel cells are the only practical option for Combined Heat and Power (CHP) for domestic systems (5-10 kW; so-called micro-CHP) because a conventional CHP system (usually a compact gas turbine and generator set) is often impractical. The greater cost in domestic usage of a 'household' CHP unit using fuel cell technology is offset against savings in domestic energy supplies [Hoogers 2003c, Larminie and Dicks 2003]. In remote locations the use of fuel cell CHP negates the cost and complexity of power distribution to such areas [Hoogers 2003c]. In the 50–500 kW range fuel cell CHP systems will have to compete with more conventional systems. As the most credible markets for the adoption of fuel cell based power generation, particularly solid oxide varieties, fall under this category they will be explored in greater detail in the following section (section 1.8).

The portable applications market is less well defined [Hoogers 2003c]. Yet the potential for quiet fuel cell power in the 1 kW range is seen in the auxiliary-power unit (APU) concept. The loose term 'portable fuel cells' often includes grid-independent applications like camping, yachting, and traffic monitoring [Hoogers 2003c, Soysal *et al.* 2013, Coddet *et al.* 2014, Gadow *et al.* 2018], as well as sensor stations in remote locations (e.g. gas pipelines). The fuels considered as well as the type of fuel cell varies by application [Hoogers 2003a, Hoogers 2003c]; most of which would not be well served by solid oxide type cells.

Mert *et al.* (2015) carried out a multi-objective optimization, including economic factors, based on a genetic algorithm comparing polymer electrolyte membrane fuel cells (PEMFCs), direct methanol fuel cells (DMFCs), molten carbonate fuel cells (MCFCs) and SOFCs seeking to find the optimal application and cell design parameters with respect to maximum power output, maximum efficiency, and minimum cost. The selection of fuel cell systems spans the range from low to high temperature. Each system was modelled based on models and actual systems found in the literature. The modelled systems were stacks complete with balance of plant, so while efficiencies are calculated they represent real world efficiencies. Assuming the authors' assumptions on things such as cost per kW of power generated of pumps and so on is reasonable, and also that the relative objective weighting factors are realistic, then their observations hold true. Even with different cell configurations and optimized systems the overall trends observed likely would remain correct. Therefore, the following points are very useful:

- Temperature tends to have the highest effect on maximizing the power output and efficiency.
- Pressure has a fluctuating influence since it is tied into the reaction mechanism.
- Current density values tend to increase as the weighting for power production parameter is increased.
- An optimum set of parameters was reached. For SOFCs this entails an operating temperature of 1,253.8 °K, an operating pressure of 1.41 atm, a maximum membrane thickness of 330 nm (though it is unclear whether they mean the electrolyte or each component), and current density of 0.199 Wcm^{-2}.

For the low temperature fuel cell systems (PEM and DM) overall efficiency is in the range 10–30% and costs are $3–4/kW [Mert *et al.* 2015]. For the high temperature fuel cell systems (MC and SO) overall efficiency is in the range 15–45% and costs are $0.003–0.001/kW [Mert *et al.* 2015]. Recall that these systems are taken from literature data and many parts of the system were unoptimised. This excludes the potential of cogeneration, combined heat and power (CHP) or cogeneration and combined heat and power (CCHP). The low temperature systems studied were intended for transport applications so cogeneration or the like is unrealistic. However, the data the authors utilized for modelling high temperature systems was based on stationary power systems and may therefore be further improved in these ways. SOFCs in particular are well suited to stationary power generation since they offer high efficiency, power output and low costs compared to the others [Mert *et al.* 2015]. Interestingly, it appears that it is optimal for SOFCs to run at low current densities [Mert *et al.* 2015] for maximum efficiency.

1.8 Stationary Power Generation

The reasons for using fuel cells for power generation are quite different from those for using fuel cells for transport or mobile applications. The power generation market is a highly competitive business internationally. The single most important consideration for commercial power generation in terms of economic feasibility is maximization of the electrical power generated from the plant and fuel used (be it fossil fuel or another fuel), dependant primarily on three factors:

- The annual hours of operation
- The conversion efficiency of the electricity generation process used
- The capital investment

Fuel cells are likely to offer advantages for the first two of these factors. For instance they require less maintenance and therefore longer operation is possible and offer far higher conversion efficiency (especially for SOFCs).

Additionally many large consumers are turning towards investment in backup power sources (in regions where electricity supply is erratic), or even on-site power generation. On-site power generation has the added advantage of making available heat generated by the process which increases the overall efficiency by maximizing the fuel utilization. This is called combined heat and power generation, or, CHP. For large power stations the heat generated cannot normally be used because it is too great [Hoogers 2003c]. Therefore large quantities of low grade heat – that is to say relatively low temperature (not useful for power generation) – are dissipated to atmosphere, rivers, lakes or the sea.

In certain countries there exist remote locations that would be very difficult to connect to the national grid, including the USA, Canada and Scandinavia in particular where people often live far from major towns. In such places domestic or small scale fuel cell based power generation (1–20 kW) enters directly into competition with diesel generators. To a certain extent the same argument can be applied to developing countries where the demand for electricity grows too rapidly for the design and building of a traditional power station to be feasible.

In Europe however, very few areas are inaccessible to the grid. Therefore it is likely [Hoogers 2003c] that European customers would view domestic fuel cell systems as a replacement for their boiler with the added benefit of providing some or all of their electricity. It is expected that micro-CHP based on fuel cells is the best market approach in Europe as opposed to micro fuel cell systems providing only electrical power [Hoogers 2003c]. The vision for this market is customers replacing their conventional boilers with fuel cell-based CHP systems that cost somewhat more than their old boiler but generates both heat and electricity at very high conversion efficiency, potentially from the same fuel source, i.e. the domestic natural gas supply.

For stationary applications various types of fuel cell are close contenders, including proton exchange/polymer electrolyte membrane fuel cells (PEMFCs), phosphoric acid fuel cells (PAFCs), molten carbonate fuel cells (MCFCs) and solid oxide fuel cells (SOFCs). The characteristics of each are discussed in turn by Hoogers [Hoogers 2003c] and Larminie and Dicks (2003). The interested reader is advised to consult the cited references.

Kato *et al.* (2008) claim, and I agree, that there is no particular benefit (nor drawback) in the implementation of large or small scale systems (not the cells, but the systems) – or put differently SOFCs can be 'scaled out' to any desired scale of power output. Soysal *et al.* (2013) also emphasize SOFC technology's facile scale out. NB: This is different from scaling up in that the components are identical unlike a traditional scale-up or scale-down. Scale out is fundamentally the addition of parallel units, the sum of their effects is the desired greater output. See also section 1.5.2.

1.8.1 Large Scale Centralised Power Generation

For low temperature PAFC and PEMFC systems pilot plants generally have a maximum efficiency of 42% that decreases over the useful life of the cell to about 30% at the end of its life [Hoogers 2003c]. For high temperature fuel cell systems such as MCFCs and SOFCs efficiencies of around 46% are achievable in practice as demonstrated by MTU and Siemens-Westinghouse in pilot plants [Hoogers 2003c]. While the long term durability of MCFCs is still under investigation it appears that SOFCs are very durable, with Siemens-Westinghouse reporting 40,000 operating hours [Hoogers 2003c]. Both of these types of high temperature cells are being considered for use in combined cycle systems replacing the burner in a gas turbine. It is expected that this will lead to an overall energy conversion efficiency in excess of 70% [Hoogers 2003c].

In most industrialised countries the largest portion of electric power is generated using coal (or lignite where available), followed by nuclear and natural gas. France with its 60% generation from nuclear power, and Italy relying mostly on oil are the exceptions to this trend. Large central power plants conventionally are condensing-type systems having efficiencies of 30% to 40%, or as high as 50% with more modern techniques and equipment. The combined cycle (gas turbine followed by steam turbine) is capable of achieving conversion efficiencies of over 60% when run on natural gas [Hoogers 2003c]. It appears that only high temperature fuel cells have the capability to match and exceed the performance of conventional stationary large-scale power generation in terms of conversion efficiency. Their fuel flexibility and low maintenance are added advantages putting SOFCs ahead of competing technologies.

1.8.2 Small Scale CHP Systems

Small-scale combined heat and power is taken to be electrical power output of the order of 100 kW to several MW. In this range of power levels the heat generated is used *in-situ* for heating or other purposes (such as industrial processes). Where the waste heat is at higher temperatures this is even more valuable because it can be converted into steam which is both a common means of transporting thermal energy and also opens up the possibility of having a combined cycle CHP where fuel cell waste heat generates steam used in a steam turbine and the waste heat from this last is used for heating. The merits and demerits of the various types of fuel cells as applied to CHP are discussed in detail in [Hoogers 2003c] and outlined below.

Ballard Generation Systems have produced a small number (four by 2009) of 250 kW PEMFC CHP systems. These employ natural gas steam reforming to generate hydrogen and are capable of producing 250 kW of electrical power and 237 kW of heat at 74 °C (low grade heat) achieving an electric efficiency of 40%. Notice that PEMFCs operate at up to 100 °C so are not capable of generating anything but low grade heat. Also, because the main power generator is a fuel cell the electric efficiency (combines all the

efficiencies of conventional systems, e.g. boiler, turbine, generator) is the same as the conversion efficiency.

UTC Fuel Cells (formerly International Fuel Cells) is a leading developer of fuel cell systems for residential, stationary, transportation and space applications. The company developed a PAFC CHP called the PC25 and has been making it for close to two decades in collaboration with Toshiba. It was the sole supplier of fuel cells for U.S. manned space missions. The PC25 is the most successful fuel cell manufactured so far with hundreds of units delivered to customers in 19 countries on 6 continents since production began. It generates 200 kW of electrical power and 264 kW of heat at 60 °C. It may alternatively produce 132 kW of heat but at 120 °C [Hoogers 2003c]. In 2001 a PC25 power plant completed 40,000 hours of operation, which is considered the minimum useful life of a distributed power system [Hoogers 2003c]. The system is known to suffer from performance degradation although specific information has not been made publicly available. The fuel cells can be fuelled by a variety of fuels including natural gas, anaerobic digester gas, brewery sludge gas, and waste methanol from the electronics industry [Hoogers 2003c]. In January 2002 the PC25 system cost $90,000. This is reported [Hoogers 2003c] to be by far the least expensive system within this power range, although it is unclear whether the author refers to all such CHP generator sets or just those based on fuel cells. Interestingly the 1.2 kg of Pt that can be recovered from this system at the end of its useful life is worth some $15,000 indicating that while significant the cost of the platinum is not the controlling cost element [Hoogers 2003c]. Other manufacturers achieved even greater power outputs, including Mitsubishi Electric Corporation (500 kW systems) and Fuji Electric (50–100 kW PAFC systems). However, from 2001 none of the units larger than 500 kW remains operational [Hoogers 2003c].

MTU, a subsidiary of DaimlerChrysler and FuelCell Energy's European partner, developed a pilot MCFC CHP plant that underwent trials at the Rhön-Klinikum Hospital, Bad Neustadt, Germany providing 270 kW of electrical power and 160 kW of heat as steam at 200°C covering about a quarter of the hospital's energy demands [Hoogers 2003c]. Reported electrical efficiencies are 56% for the stack and 47% for the overall plant. It is expected to have a useful life of 20,000 hours and cost €3 million. The system makes use of internal reforming and runs on a multitude of fuels including natural gas, methanol, ethanol, biogas and any methane-containing fuel [Hoogers 2003c].

An alternative is CCP – combined cooling and power. This operates on the same principles as CHP but with the SOFC and GT driving chillers rather than providing direct power and heating. When demand for cooling is lower the excess power is fed to the grid. Improvements of 50–60% in both emissions and fuel efficiency over A/C systems powered by grid electricity are reported [Al-Qattan *et al.* 2014].

Compare the above with SOFC CHP systems. The SOFC is the most suitable candidate for large scale operation as part of combined cycle plants with the fuel cell replacing the gas turbine stage. Of this type of plant the Siemens-Westinghouse Power Corporation were the most advanced developer with many SOFC systems rated between 100 kW and 1 MW electric power with the optional utilization of high temperature steam [Hoogers 2003c]. They have successfully field-tested three systems generating 250 kW of electrical power. The cited source does not report the thermal power output, its temperature, electrical efficiency, cost, or expected life. However, it is likely based on Siemens-Westinghouse's previous work that a life of 10,000 hours is to be expected [cf. the following patents: Gillett *et al.* (1998), Holmes *et al.* (2003), Bischoff *et al.* (2007), Huang *et al.* (2012), Zafred *et al.* (2012), Gillett *et al.* (2013)].

1.8.3 Domestic CHP Systems

The majority of currently active fuel cell developers are focusing on the residential and small commercial power marker in the range 1–20 $kW_{el.}$ [Hoogers 2003c]. The target cost for domestic CHP systems, approximately $1,000 per kW, is perceived to be more readily achieved than the transport target of $50 per kW [Hoogers 2003c]. This belief, which is quite reasonable, is one of the principle reasons for targeting this market with fuel cells. Historically, this was not sufficiently attractive to convince leading developers of automotive fuel cells like Ballard and General Motors; probably because the potential market was deemed too small [Hoogers 2003c].

Performance targets for residential fuel cell systems vary in emphasis between grid-independent electrical power generation, micro-scale CHP, and combinations of electric power generation and adsorption chillers for cooling purposes [Hoogers 2003c]. Only two types of fuel cells have been considered suited to these applications: the PEMFC, which is clearly leading in terms of the number of developers, and the (planar) SOFC [Hoogers 2003c]. The author believes that the reason for this is that the technology developers see sufficient links between domestic CHP, portable applications, transport applications (for PEMFCs) and static power generation applications (for SOFCs) that they aim to use developments in one area as a spring board into others, thereby attaining maximum market share for the investment necessary to develop products. This is a clear testament to the flexibility of power delivered by fuel cell technologies – it can be scaled and adapted to a variety of applications.

The first domestic CHP units were based on PAFCs and made by UTC (the 12.5 kW PC-11 developed from 1967 to 1975). However, their performance proved inadequate (poor performance under intermittent loads) [Hoogers 2003c]. Also, Hoogers intimates that the cost advantage of PEMFC systems was another probable reason for the halting of PAFC development for household CHP.

PEMFCs are the primary competition for SOFCs in the domestic CHP market. Typical systems produce 3 kW to 5 kW of electrical power and 8 kW to 9 kW of thermal power [Hoogers 2003c]. Various manufactures were involved in this line of development including UTC (with Toshiba in Japan and Buderus Heiztechnik GmbH in Germany), Plug Power (an advanced, and very aggressive, development program in the late-1990s in collaboration with GE Fuel Cell Systems and Joh. Vaillant GmbH u. Co in Germany), Ballard Generation Systems (with Tokyo Gas, Ebara Ballard and Ebara Corporation) and others besides. The reader is referred to the extensive review by Hoogers [Hoogers 2003c] for more information. The only target price published was for the Plug Power system: $ 8,500 initially, falling to $ 4,000 by 2003 [Hoogers 2003c]. Virtually all of these systems used hydrocarbon fuels, with a couple using alcohol, in combination with steam reforming to generate hydrogen. As of 2014 none of these programs resulted in widespread commercial success, and a number of the developers involved no longer seem to exist. Some carry on under different names having been bought (UTC was bought by ClearEdge Power in 2011 for instance) or are no longer developing domestic CHP systems having shifted their focus to other applications for their PEMFCs and reformers (e.g. Plug Power, Nuvera Fuel Cells). More recently ClearEdge Power are offering a 5 kW domestic CHP system for $56,000 [ClearEdge Power article accessed 2014], but filed for bankruptcy in May 2014 [McCarty 2014].

Perhaps because of the additional need to heat them to high operating temperatures (generally 800 °C – 1,000 °C) there has been less interest in developing SOFC CHP systems. Sulzer Hexis (Switzerland) remains the leading developer of residential SOFC systems, using planar designs and taking full advantage of the inherent fuel flexibility of SOFCs in comparison to other types of fuel cell. Sulzer Hexis carried out field trials utilising natural gas, diesel, heating oil and gasified wood in conjunction with their 1 kW unit (with an approximate electrical efficiency of 30%) [Hoogers 2003c]. Development has continued, and their latest version is the Galileo 1000N, a 1 kW electrical power and 1.8 kW thermal power system operating on natural gas intended to replace household boilers [Hexis Galileo 1000N accessed 2014]. It is reported to have an electrical efficiency of 30–35% [Hexis Galileo 1000N accessed 2014]. Global Thermoelectric Inc. (Canada) developed a similar, planar, system aimed at the commercialization of technology acquired from Forschungszentrum Jülich [Hoogers 2003c]. In May 2001 they delivered a prototype system for residential energy to Canada's largest natural gas distributor, Enbridge Inc. [Hoogers 2003c]. Fuel Cell Technologies (Canada) developed a range of residential power systems from 5 kW to 15 kW in the early 2000s basing their domestic CHP systems on Siemens-Westinghouse's tubular fuel cell technology [Hoogers 2003c]. Ceramic Fuel Cells appear to have achieved commercial success with their BluGen SOFC CHP [Ceramic Fuel Cells BlueGen article accessed 2014]. It is a 1.5 kW electrical power system with a reported electrical efficiency of 60%, claimed to be the most efficient in the world. It is

optimised for electrical output providing only 0.5 kW of heat [Ceramic Fuel Cells BlueGen article accessed 2014].

The reader is again referred to the extensive review by Hoogers [Hoogers 2003c] as well as the other cited references for more information. SOFC based CCP is also possible at this scale, although the work reported by Al-Qattan *et al.* (2014) was of the larger MW scale. While initially the number of interested developers was smaller than for PEMFC technology SOFCs clearly have the advantage here as three of the companies mentioned are not only still extant but actively producing SOFC CHP systems and the number developing and field testing domestic CHP using SOFCs continues to grow. Planar designs dominate. I believe it is the relative maturity of planar systems over tubular ones combined with the relative ease of mass manufacture of planar cells using conventional ceramic forming technologies (compared to tubular cells) rather than the balance of advantages and disadvantages of the two designs that has led to planar systems being favoured.

Besides identifying the most suitable target markets for micro-tubular SOFCs the preceding information indicates there may be a significant advantage in moving away from conventional ceramic processing technology enabling the tubular designs to be manufactured economically on a large scale making full use of their unique benefits over their larger brethren and planar designs.

1.9 Solid Oxide Fuel Cell Commercialisation and Economics

In 2003 van Gerwen observed that there had yet to be a successfully implemented, commercially viable, cost-effective SOFC for power generation [van Gerwen 2003]. This is in spite of the fact that, according to Kato *et al.* (2008), SOFC systems have advanced enough through research carried out these last couple of decades to develop systems for commercial use. In recent years there has been a steady increase in the number of pilot projects, long term performance tests and field trials, and also a few commercial successes [Hexis Galileo 1000N and Ceramic Fuel Cells BlueGen warrant particular attention]. SECA (the solid state energy conversion alliance) projected solid oxide fuel cell costs of $ 400 per kW in 2010 would be achievable if production volumes are around 500,000 units annually [Wei 2008]. This is competitive with Li-ion batteries [Wei 2008]. As shown in Figure 1-3. below, however, plentiful commercial opportunities exist, some of which are beginning to be exploited as the interest generated by the METI and NEDO initiatives in Japan demonstrates [Kato *et al.* 2008], indicating we are perhaps closing in on van Gerwen's definition of successful commercialisation for large scale power generation also

At low power levels (~1–10 W) small, even micro, SOFC systems could replace conventional batteries especially for remote applications where the cost of replacing or recharging batteries is high but where suitable fuel is readily available [van Gerwen 2003]. Typical examples would be power sources for monitoring and control equipment for environmental surveying, on gas pipes where fuel can be tapped off the main line. At moderate power levels (~100 W – 1 kW) applications, especially military ones, requiring lightweight high portability power sources are a distinct possibility. Such applications may also encompass lightweight aircraft, refrigeration and electric supply modules for remote outposts, leisure (camping, yachts, especially for navigation, computer and telecommunication power) or anywhere that large scale battery use would be inefficient and cumbersome. For military applications costs of up to $ 30,000 per kW are considered acceptable [van Gerwen 2003]. However, the high operating temperature of SOFCs virtually precludes them from many such applications. Of course, this just strengthens existing motivation to lower operating temperatures.

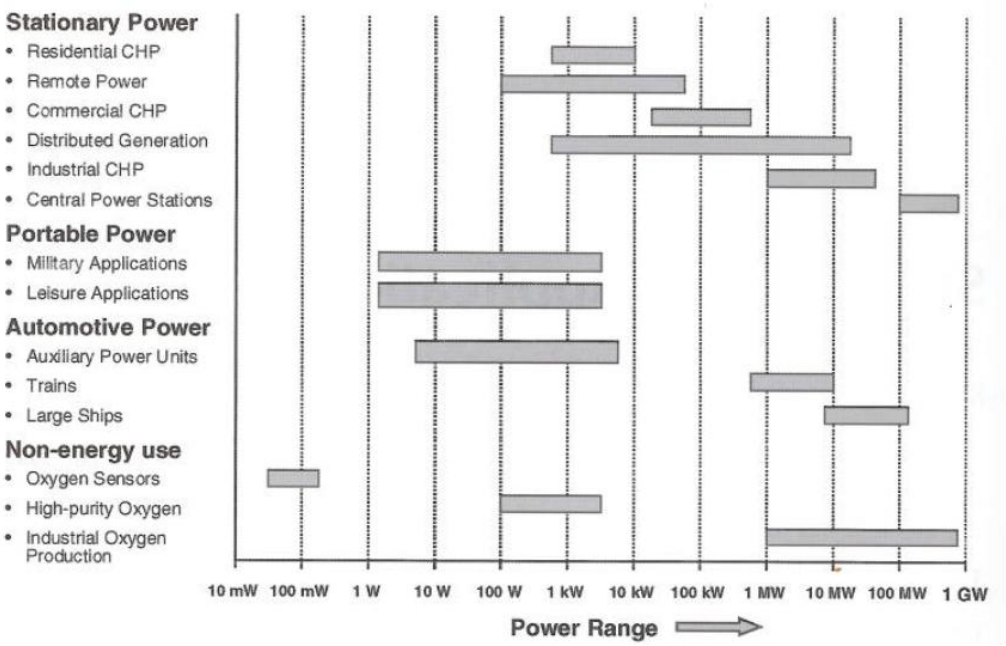

Figure 1-3. SOFC potential markets and applications [van Gerwen 2003].

Due to greatest likely profitability the commonly perceived main application areas for SOFCs are power systems to supply residential areas and power systems for mobile applications (auxiliary power units for vehicles) [Kato *et al.* 2008]. A number of current projects work towards this range (~1–10 kW), in particular demonstrating feasibility and long term stability. Their effectiveness as stationary power supplies has been demonstrated [Wei 2008]. The target cost for such systems is $ 400–1,000 per kW [van Gerwen 2003]. Potential markets are very large, up to hundreds of billions of dollars annually [van Gerwen 2003, Kato *et al.* 2008] if technical and economic requirements

are met. One of the greatest challenges is meeting the heating requirement of the cell for it to function.

On a similar vein the high operating temperatures of SOFCs usually complicates quick start and frequent start/stop cycles; often required by small power generators [Kato *et al.* 2008]. Kato *et al.* deduce that the first market application must chosen carefully such that any demerits of SOFCs do not emerge and their high efficiency is clearly represented as greatly advantageous over competing technologies. The 1–100 kW range has the added advantage of avoiding competition with low cost Diesel generators whose capacities are generally more than 100 kW – circumventing the main competition as it were for SOFC systems [Kato *et al.* 2008]. It is worth noting that for miniaturized systems (both planar and tubular) rapid start up is less problematic (in part due to far lower thermal masses involved) [Suzuki *et al.* 2008c, Funahashi *et al.* 2009]. There is still the issue of thermal cycling stability with cracks arising from repeated heating-cooling cycles. Tubular designs are at an advantage here also.

At the larger end of the scale are distributed power generation and combined heat and power (CHP) [van Gerwen 2003, Kato *et al.* 2008], although small scale CHP is also possible. At present, this market sector is filled by internal combustion engines, usually diesel generator sets or small scale gas or diesel turbines [van Gerwen 2003], ranging in power from tens of kW to a few MW. In order to be commercially viable in this sector SOFCs need to compete based on their strengths – low maintenance and low controlled emissions compared to diesel engines – in order to effectively offset the greater capital cost of SOFC systems compared to diesel gen-sets. It is possible [van Gerwen 2003] for SOFC systems of still larger scale (several MW) to work in conjunction with existing power generation systems. They can augment the performance of existing plants by improving efficiency and reducing emissions (assuming the augmentation takes the form of a CHP unit). Integrating SOFCs with gas turbines (GT) can lead to fuel conversion efficiencies (converting fuel input to electricity output) of up to 70% [van Gerwen 2003, Pomfret, Eigenbrodt and Walker 2008].

Installing a small SOFC system for supplying more than 5 GJ/year of heating energy will result in a cost saving of 60–90 kYen/year (GBP 450–670, USD 700–1050, or € 540–800) compared to the use of conventional gas boilers or electric boilers and greater savings compared to more expensive systems like GT-based CHP systems [Kato *et al.* 2008]. Money is saved even when compared to highly efficient systems based on electric heat pumps. While this analysis was carried out for the Japanese market, and therefore with local energy prices and usage data, it more than likely holds true for densely populated regions in Europe and North America. The authors [Kato *et al.* 2008] identify convenience stores (especially chains that are open for long hours – such as Cost Cutter, The Cooperative, and so on here in the UK) because of their long and constant electricity demands, small size business units (in Japan this is 100–150 m^2 for a

typical establishment) and the large number of such shops. The relatively low demand for heat energy indicates a considerable reduction in cost of SOFC systems is needed for sufficient market penetration into this sector in order to meet the stringent economic realities of convenience stores [Kato *et al.* 2008].

On similar lines the authors identify a certain types of small manufacturers (those surveyed are all food producers) as potential SOFC CHP customers because of their similar requirements to convenience stores but with often a larger need for heat and less stringent economics [Kato *et al.* 2008]. Possibly the best candidates are dairy manufacturers and other products with the need for reliable electricity supply in moderate to large quantities 24 hours a day and at least 250 days of the year (see also tabulated information in the cited paper).

The commercial CHP applications identified as suitable by Kato *et al.* (2008) tend to be of low heat to power ratio. This emphasises the electrical performance of the system, and by implication, the electrical efficiency.

The work of van Gerwen (2003) presents a lot of interesting, quite detailed energy market analysis including a detailed look at where SOFC fits in, particularly given US and EU power requirements. The discussion is lengthy and of only tangential interest to this project, but the reader is encouraged to read the cited documents for a better understanding of where SOFCs fit in the energy market. It is generally accepted that much more research is necessary [van Gerwen 2003, Tsipis and Kharton 2008, Kato *et al.* 2008, Suzuki *et al.* 2008c] to create SOFCs that are commercially viable and stable in the long term. Novel fabrication techniques coupled with microtubular designs is expected to benefit all the markets identified because of the facile scaling of such systems, in addition to specific benefits allaying concerns outlined above (e.g. rapid start-up is possible by means of low thermal mass and a design that is inherently better able to deal with rapid temperature cycling).

A market gap, termed a *chasm*, was identified between the early market and the mainstream market in the transition of novel technologies into mainstream use [van Gerwen 2003]. The early market consists of enthusiastic visionaries who see the potential of the technology and is quickly saturated being small in size. Across the *chasm* is the mainstream market consisting of pragmatists requiring dependable, economically-competitive systems and have little interest in future possible exploitation and development. Technologically fuel cells have advanced a great deal from their origins. The same cannot be said for their economics. Historically there has been a decreasing motivation to develop SOFCs for widespread use. This is partly based on the rapid growth of the hydrocarbon economy and partly on infrastructural developments. As recently as a decade ago there has been a slight shift, and an increasing interest in all renewable and non-conventional power generation techniques. This widely known and

broadly accepted change to our lives is yet to result in any large shifts towards a hydrogen economy, although the potential is there and awareness is growing as evidenced by the hydrogen filling stations implemented alongside hydrogen-powered vehicles [Camilleri 2009].

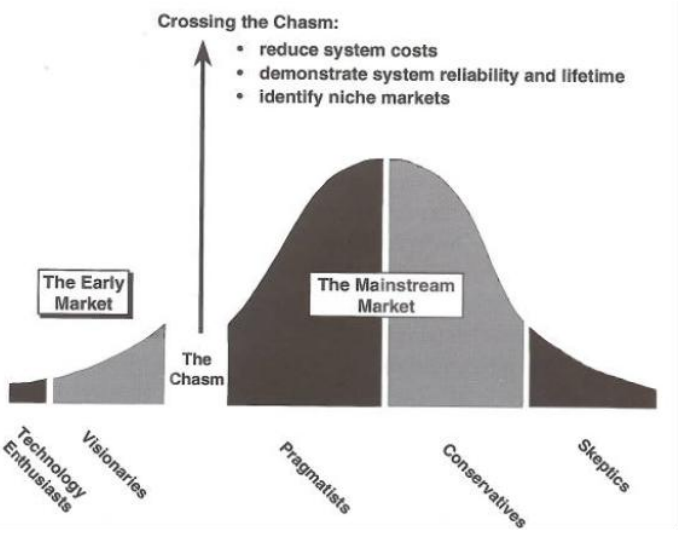

Figure 1-4. Transition from early market to mainstream market [van Gerwen 2003].

To gain traction in the mainstream market, therefore, it is crucial to identify suitable markets, demonstrate reliability, lifetime and cost-effectiveness of a SOFC system for that application sufficiently to convince the pragmatists. Crossing this conceptual *chasm* has proven to be the greatest challenge for SOFC technology.

1.10 Solid Oxide Fuel Cell Fuel Cycle Analysis

Fuel cycle analysis, also known as well-to-wheel analysis, is a method for considering the emissions and the energy use of a process from the extraction of the raw material to the motive power of a vehicle. The analysis is equally applicable to stationary applications. There is no specific emission that must be considered, the choice is up to the analyst. The most commonly analysed emissions are greenhouse gases (predominantly carbon dioxide and methane), and pollutants whose emissions are regulated by law (nitrogen oxides, sulphur oxides, particulates and volatile organic compounds). Energy use across the fuel cell cycle is also calculated for comparison in terms of efficiency of resource use between different fuel chains. Precisely what boundaries are applied (for instance which emissions are analysed, whether volatilization losses prior to processing are included, and so on) has an impact on the environmental effects considered and their magnitude [Hart and Bauen 2003]. Thus, a fuel cycle analysis is a form of life cycle analysis assessing the entire life cycle of a particular energy conversion route from fuel production through to use for power generation.

Complete fuel cycle analysis will include all the elements of the chain from raw material extraction, its processing, distribution and end use for a given application. According to Hart and Bauen (2003), however, accurate data for all the stages is not always available, necessitating the use of estimates. The accuracy required in performing the analysis is largely dictated by the reasons for carrying out the fuel cycle analysis in the first place. What follows, after definition and explanation of certain terms, is a comparison of SOFCs with competing technologies in terms of emissions and power output, from the aforementioned sole source.

The fuel cycle can be conveniently divided into two separate chains; useful when evaluating different fuel supply schemes. These are sometimes referred to as well-to-tank and tank-to-wheels cycles. Examples for a typical fuel cell system are shown below in Figure 1-5. and Figure 1-6.

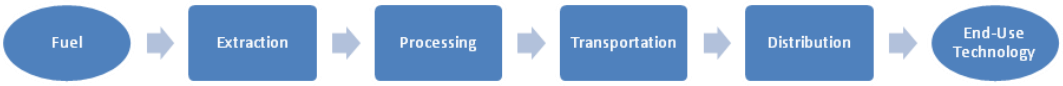

Figure 1-5. Schematic of energy carrier [adapted from Hart and Bauen 2003].

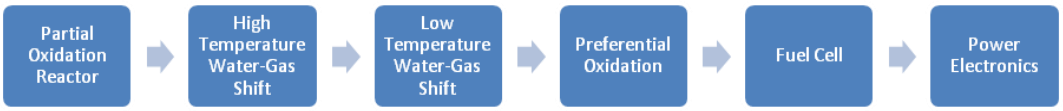

Figure 1-6. Schematic of fuel cell system End-Use Technology.

Usually fuel cycle analysis is carried out for a specific geographical location, though some are more generic. The location typically has a significant bearing on the outcome of the calculations since raw material composition, extraction technique, and equipment-specific performance vary considerably by location. Additionally the emissions of some energy carriers are highly dependent on transportation and distribution, while others less so. Typical examples are hydrogen for the former (very light and thus requires large amounts of energy to transport) and petroleum for the latter (high energy density and easily transported) [Hart and Bauen 2003]. Furthermore, the consideration of how emissions will affect the region in which they occur is not generally part of the fuel cycle calculations but needs to be evaluated for the analysis to be of practical use [Hart and Bauen 2003].

The comparison between various stationary power generation technologies greatly depends on the intended application. Where a lot of high temperature process heating is required and electricity is considered a secondary benefit, internal combustion engine solutions may be better suited than fuel cells. Where the heat generated is of little

interest or only secondary importance, the higher electrical conversion efficiency and lower heat output of a fuel cell will prove valuable. It is sometimes necessary, if unrealistic, to assume the same heat-to-power ratio for all applications for the sake of comparison [Hart and Bauen 2003].

The overall fuel cycle efficiency alone is not the best means to compare fuel chains or generation technologies. Which measure is most suitable will depend on the output of interest, for instance energy use, CO_2 emissions, or particulates: for example, if a solar-powered electrolysis unit produces hydrogen that is then used in an internal combustion engine vehicle, the efficiency of the process from well to wheels is probably a mere 1 – 2 %, compared with 15 % for a diesel internal combustion engine pathway. Yet CO_2 emissions will be zero, unlike with the diesel vehicle [Hart and Bauen 2003]. In practice, therefore, decisions will not be based exclusively on fuel chain efficiency. Other factors will be dominant. Such as local emissions (driven by local, national or international regulations or laws) and total cost.

Fuel cells require a clean hydrogen-rich fuel or pure hydrogen, and emissions are intrinsically low as a result [Hart and Bauen 2003]. However, considering the full cycle demonstrates that the fuel cycle emits pollutants from its various stages – all of which need to be evaluated for comparison between different fuels and power generation technologies. The primary energy source from which a fuel is derived largely dictates the fuel cycle and associated emissions [Hart and Bauen 2003].

The first step in the fuel cycle analysis consists of selecting the stationary (or transport) applications to be considered and defining the fuel cycles and their boundaries, as illustrated by Figure 1-7. below.

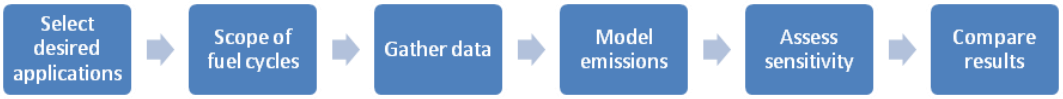

Figure 1-7. Fuel cycle analysis steps [adapted from Hart and Bauen 2003].

The step of defining the scope also provides a filtering step of the fuel cycle activities that are deemed significant and included in the analysis, while excluding those that are not, and determining the data required [Hart and Bauen 2003]. A few of the representative applications illustrated in the cited source are repeated here because of their significance to this project or to provide useful comparisons. The model includes all fuel cycle stages from acquiring the resource from which the fuel is derived to the end use application. Unlike a full life cycle analysis the model excludes the emissions and energy use associated with the manufacture and scrapping of the system elements [Hart and Bauen 2003]. The analysis does not model the effects of emissions, nor does it include the economic costs that are linked to either the pollution that is avoided or to

the development and implementation of the different generation technologies [Hart and Bauen 2003].

Stationary power systems considered include the phosphoric acid fuel cell (PAFC), solid oxide fuel cell (SOFC), combustion engine and turbine systems for commercial and industrial scale combined heat and power (CHP), and distributed, baseload, and remote power generation [Hart and Bauen 2003]. The UK electricity mix and electricity from combined cycle gas turbine (CCGT) plants are used as reference cases for distributed and baseload electricity generation [Hart and Bauen 2003]. Gas boilers are included as part of the reference systems for the provision of heat. The diesel engine based gen-set is the reference system for remote power [Hart and Bauen 2003]. The emissions evaluated from the different systems are regulated pollutants and greenhouse gases: nitrogen oxides (NO_x), sulphur oxides (SO_x), carbon monoxide (CO), non-methane hydrocarbons (NMHC), particulate matter (PM), carbon dioxide (CO_2), and methane (CH_4). The total use of primary energy for each system is included in the model [Hart and Bauen 2003].

The fuel cycles are modelled into the following stages: primary fuel production, fuel transport, fuel processing, end use [Hart and Bauen 2003]. Each calculation begins at the point of end use, and works backwards through the system to the source of primary energy [Hart and Bauen 2003]. Data and underlying assumptions were derived from several literature, industry sources and emission regulators [Hart and Bauen 2003]. The cited source also includes the organization and structure of the model; beyond the scope of this section, and indeed this project, but worthwhile reading.

“It is important to note that the state of the art in fuel cell technology is rapidly advancing, and that emissions and efficiency data are not known with great certainty over a range of operating conditions. The outcome of these calculations is therefore currently of greatest value in assessing the expected merits of the technologies and finding their sensitivity to a range of factors.” [Hart and Bauen 2003]

The fuel cycle emissions and primary energy consumption results are expressed per unit of electricity and useful heat produced. In all cases, some further analysis is presented in the original source, and the reader is directed there for additional comparisons.

1.10.1 Large Scale Centralised Power Generation Fuel Cycle

SOFCs operating in combined cycle with gas turbines (SOFC/GTs) or in triple cycle with gas and steam turbines (SOFC/GTCCs) have been selected for this application because of their potential for highly efficient and clean baseload power [Hart and Bauen 2003]. For capacities typical of baseload power generation (100 MW_e), the electrical efficiency is estimated to be around 74% for a SOFC/GT and 80% for a SOFC/GTCC

[Hart and Bauen 2003]. The UK electricity mix is taken as reference case, and CCGT electricity was also considered in the analysis [Hart and Bauen 2003].

Fuel cycle calculations regarding emissions and energy use for a typical baseload power plant are summarized in Figure 1-8. and Table 1-1. below, from [Hart and Bauen 2003]. As with distributed power, the emissions of NO_x and CO in particular are greatly reduced as well as reductions of some 50% in CO_2 compared to the UK grid and about 40% compared to CCGT [Hart and Bauen 2003]. In the case of the UK grid the reduction is mostly due to the avoided emissions from coal mining [Hart and Bauen 2003].

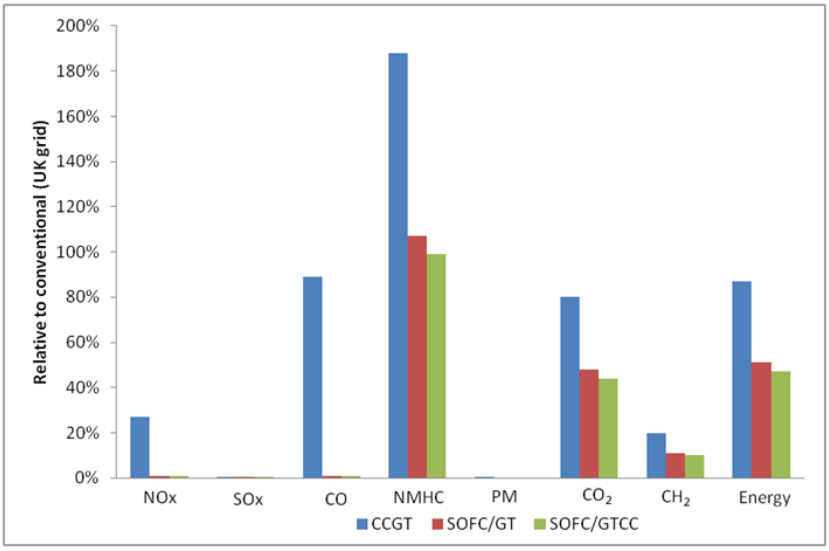

Figure 1-8. Total systems emissions and primary energy use of baseload power generation [reproduced with data from Hart and Bauen 2003].

	Regulated Pollutants					Greenhouse Gases		Energy
	NO_x	**SO_x**	**CO**	**NMHC**	**PM**	**CO_2**	**CH_4**	**(MJ/kWh$_e$)**
Application	**(g/kWh$_e$)**	**(g/kWh$_e$)**	**(g/kWh$_e$)**	**(g/kWh$_e$)**	**(g/kWh$_e$)**	**(g/kWh$_e$)**	**(g/kWh$_e$)**	
UK Grid	2.7	3.7	0.45	0.06	0.25	522	1.5	9.9
CCGT	0.73	0.01	0.4	0.11	0.0006	417	0.31	8.6
	27%	0.3%	89%	188%	0.3%	80%	20%	87%
SOFC/GT	0.02	0.005	0.005	0.06	0	251	0.17	5.1
	0.9%	0.1%	1.1%	107%	0%	48%	11%	51%
SOFC/GTCC	0.02	0.005	0.004	0.06	0	232	0.16	4.7
	0.8%	0.1%	1.0%	99%	0%	44%	10%	47%

Table 1-1. Total systems emissions and primary energy use of baseload power generation [Hart and Bauen 2003].

1.10.2 Distributed Power Generation Fuel Cycle

The SOFC was chosen as the system for modelling a distributed power generation application. Two systems are considered: the internally reforming-SOFC operated alone or in combined cycle with a gas turbine [Hart and Bauen 2003]. For capacities typical of

these applications (1–10 MW_e), the electrical efficiency of a SOFC system is estimated at 55% and 70% for a SOFC/GT [Hart and Bauen 2003]. The reference case consists of grid electricity supplied by a CCGT plant running on natural gas that is assumed to originate from UK continental shelf fields [Hart and Bauen 2003].

Fuel cycle calculations regarding emissions and energy use for a typical distributed power plant are summarized in Figure 1-9. and Table 1-2. below, from [Hart and Bauen 2003]. Using a large-scale SOFC plant for electricity generation rather than more conventional prime movers like CCGTs reduces the emissions of carbon monoxide and oxides of nitrogen to insignificant levels, and even carbon dioxide emissions are at most about 80% of the emissions of the reference system [Hart and Bauen 2003]. Emissions of all pollutants are reduced by a further 22% when using a SOFC/GT system because of its higher overall conversion efficiency [Hart and Bauen 2003]. The energy requirement is some 21% lower compared to the reference system for a SOFCs and 38% lower for SOFC/GT systems [Hart and Bauen 2003].

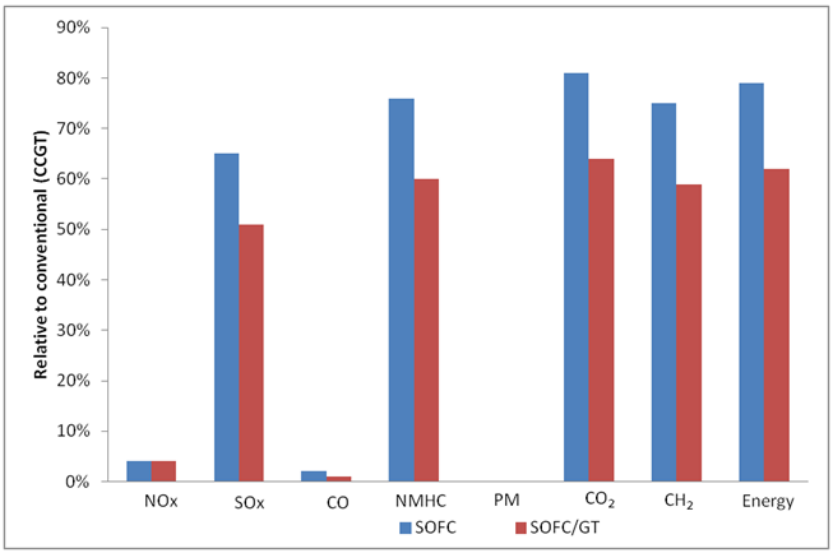

Figure 1-9. Total systems emissions and primary energy use of distributed power generation [reproduced with data from Hart and Bauen 2003].

	Regulated Pollutants					Greenhouse Gases		Energy
	NO_x	SO_x	CO	NMHC	PM	CO_2	CH_4	(MJ/kWh_e)
Application	**(g/kWh_e)**	**(g/kWh_e)**	**(g/kWh_e)**	**(g/kWh_e)**	**(g/kWh_e)**	**(g/kWh_e)**	**(g/kWh_e)**	
CCGT	0.73	0.01	0.4	0.11	0.0006	417	0.31	8.6
SOFC	0.03	0.01	0.01	0.08	0	338	0.23	6.8
	4%	65%	2%	76%	0%	81%	75%	79%
SOFC/GT	0.03	0.006	0.005	0.06	0	265	0.18	5.4
	4%	51%	1%	60%	0%	64%	59%	62%

Table 1-2. Total systems emissions and primary energy use of distributed power generation [Hart and Bauen 2003].

1.10.3 Remote Power Generation Fuel Cycle

Remote power applications are most often diesel generator sets. Methanol, diesel, and hydrogen powered fuel cells are an interesting, and cleaner, alternative. The cited source's study assumed the methanol to be derived from natural gas in large scale steam reforming plants and transported to the remote site. Road transport distances to the remote location was assumed to be 800 km (500 miles) round trip [Hart and Bauen 2003]. Hydrogen could be transported to the site or possibly even generated *in situ* for fuel cells integrated with renewable energy systems [Hart and Bauen 2003]. The efficiency of the methanol production process from natural gas is estimated to be 72% [Hart and Bauen 2003]. Emissions from the different components of the fuel cycles for remote power were based on similar equipment used in other transport and stationary fuel cycles [Hart and Bauen 2003].

Fuel cycle calculations regarding emissions and energy use for a typical remote power plant are summarized in Figure 1-10. and Table 1-3. below, from [Hart and Bauen 2003]. Adopting fuel cells for remote power applications rather than diesel engines would lead to important reductions in emissions, in particular with regard to greenhouse gases [Hart and Bauen 2003]. Opportunities for even greater reductions exist in the form of integrating fuel cell operation with hydrogen production by electrolysis powered by intermittent renewable energy sources such as wind and solar energy. The result is a zero emissions system. The only primary non-renewable energy would be that involved in production and installation of the system components [Hart and Bauen 2003].

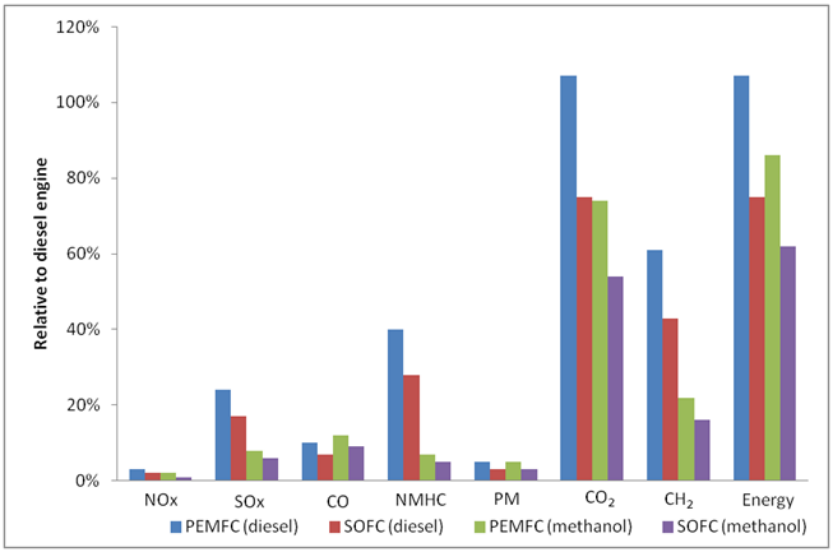

Figure 1-10. Total systems emissions and primary energy use of remote power generation [reproduced with data from Hart and Bauen 2003].

	Regulated Pollutants					Greenhouse Gases		Energy
	NO_x	SO_x	CO	NMHC	PM	CO_2	CH_4	(MJ/kWh_e)
Application	**(g/kWh_e)**	**(g/kWh_e)**	**(g/kWh_e)**	**(g/kWh_e)**	**(g/kWh_e)**	**(g/kWh_e)**	**(g/kWh_e)**	
Diesel Engine	12.6	2.0	0.65	2.1	0.15	906.8	0.26	13.7
PEMFC (diesel)	0.39	0.48	0.068	0.84	0.007	971.5	0.16	14.7
	3.0%	24%	10%	40%	5.0%	107%	61%	107%
SOFC (diesel)	0.27	0.34	0.048	0.59	0.005	680.1	0.11	10.2
	2.0%	17%	7.0%	28%	3.0%	75%	43%	75%
PEMFC (methanol)	0.24	0.16	0.077	0.15	0.007	675.3	0.06	11.8
	2.0%	8.0%	12%	7.0%	5.0%	74%	22%	86%
SOFC (methanol)	0.18	0.11	0.056	0.11	0.005	487.7	0.04	8.5
	1.0%	6.0%	9.0%	5.0%	3.0%	54%	16%	62%

Table 1-3. Total systems emissions and primary energy use of remote power generation [Hart and Bauen 2003].

1.10.4 Large Scale CHP Fuel Cycle

Typical capacity for large CHP systems is around 200 kW_e. The fuel cell systems selected are based on PAFC and SOFC systems. The SOFC systems internally reform natural gas to a hydrogen-rich gas called syngas. Diesel engines and natural gas combustion engines are used to represent conventional CHP systems [Hart and Bauen 2003]. The reference system has been defined as a conventional situation in which electricity is supplied from a CCGT plant and heat from a gas boiler.

The heat to power ratio is taken as 1.85, the average of the typical values in the UK that range from 1.5 to 2.2 [Hart and Bauen 2003]. The ratio chosen does not affect the emissions from CHP systems since these are a function of useful energy generated. The ratio does influence, however, the energy requirement and specific emissions of the reference system in which electricity production and heat generation are independent. Specific emissions for the reference system decrease as the heat to power ratio increases [Hart and Bauen 2003]. Whether it is in practice possible to achieve a given heat to power ratio depends on its electrical efficiency and the total system efficiency [Hart and Bauen 2003]. The fuel cell CHP plant is taken to be able to meet this heat to power ratio [Hart and Bauen 2003]. A ratio of 1.85 implies an electrical efficiency of 30% in the case of the co-generation systems considered, which are assumed to have a total efficiency of 85%. In the case of the SOFC, the heat to power ratio taken is likely to create a significant reduction in electrical efficiency [Hart and Bauen 2003], although this is not qualified or explained.

Fuel cycle calculations regarding emissions and energy use for a typical large commercial CHP plant are summarized in Figure 1-11. and Table 1-4. below, from [Hart and Bauen 2003]. The use of fuel cells reduces emissions by a substantial margin when compared to CCGT electricity and gas boiler heat systems (the reference system). The greatest reductions are for NO_x and CO emissions [Hart and Bauen 2003], reduced by a whole two orders of magnitude. Also of note is that fuel cell systems reduce the CO_2 emissions and energy consumption to about 80% of the reference system and perform even better when compared to diesel engines or natural gas engines. With

respect to these last two it is important to highlight that local emissions would increase compared with the reference case [Hart and Bauen 2003].

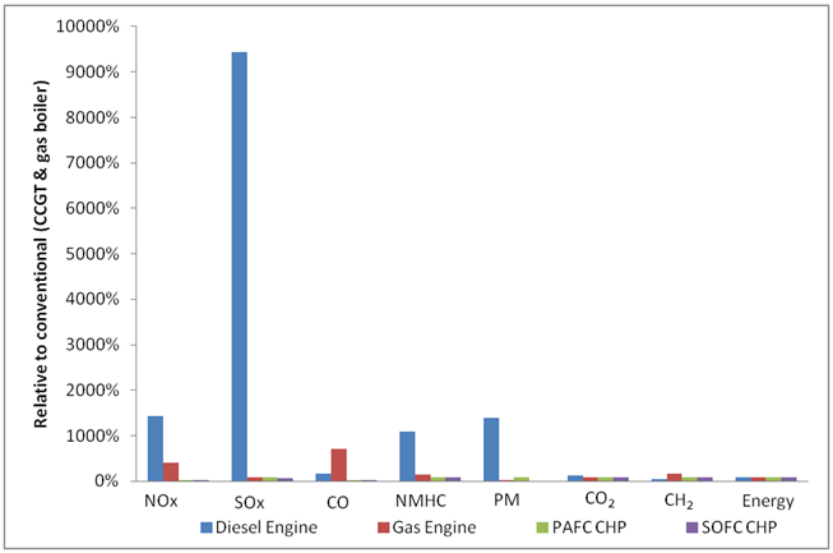

Figure 1-11. Total systems emissions and primary energy use of large commercial CHP [reproduced with data from Hart and Bauen 2003].

	Regulated Pollutants					Greenhouse Gases		Energy
	NO_x	**SO_x**	**CO**	**NMHC**	**PM**	**CO_2**	**CH_4**	**(MJ/kWh)**
Application	**(g/kWh)**	**(g/kWh)**	**(g/kWh)**	**(g/kWh)**	**(g/kWh)**	**(g/kWh)**	**(g/kWh)**	
CCGT & Gas Boiler	0.31	0.007	0.14	0.068	0.003	270	0.2	5.7
Diesel Engine	4.4	0.68	0.22	0.74	0.049	315	0.08	4.8
	1432%	9443%	158%	1086%	1390%	116%	40%	84%
Gas Engine	1.2	0.006	1.0	0.094	0.001	218	0.31	4.4
	402%	77%	706%	139%	21%	81%	157%	78%
PAFC CHP	0.027	0.006	0.01	0.058	0.003	218	0.15	4.4
	8.8%	77%	7%	85%	94%	81%	76%	78%
SOFC CHP	0.021	0.005	0.001	0.052	0	218	0.15	4.4
	6.8%	64%	1%	76%	0%	81%	76%	78%

Table 1-4. Total systems emissions and primary energy use of large commercial CHP [Hart and Bauen 2003].

1.10.5 Industrial Scale CHP Fuel Cycle

The SOFC is an interesting option for industrial scale CHP systems on the order of a few MW capacity where high-temperature heat is required. In these applications the SOFC could be utilized in a single cycle or combined cycle with a gas turbine (SOFC/GT). The combined cycle approach is best suited to a low heat to power ratio, taking advantage of the high electrical efficiency achieved by such systems [Hart and Bauen 2003]. Natural gas fuelled engines and natural gas fuelled turbines have been selected [Hart and Bauen 2003] as conventional options for industrial scale CHP systems. The reference system is the same as for large commercial CHP where

electricity is supplied by grid-connected CCGT and heat by gas boilers [Hart and Bauen 2003].

The heat to power ratio for industrial scale CHP is set as equal to unity [Hart and Bauen 2003]. Fuel cell systems are most likely to be used in industrial applications where heat to power ratios are less than about 1.2, or where there is the possibility for surplus electricity generation taking advantage of their high electrical efficiencies [Hart and Bauen 2003]. Once more it is claimed that fuel cell CHP systems could operate at higher heat to power ratios at the cost of electrical efficiency [Hart and Bauen 2003]. The minimum heat to power ratio in the case of a SOFC/GT system is 0.25, while for the natural gas turbine it is 2.27 based on the assumed electrical and total system efficiencies [Hart and Bauen 2003]. It seems the reasoning here is that by retaining more of the heat the fuel cell is not used at maximum conversion efficiency, and therefore its electrical efficiency is reduced.

The choice between SOFC and SOFC/GT will be largely dictated by the heat to power ratio characterising the system and the economics of the system. For heat to power ratios below about 0.55, SOFC/GT systems would be required [Hart and Bauen 2003]. This is because a conventional combined cycle gas turbine (CCGT) does not possess sufficiently high electrical conversion efficiency to achieve high electrical power output for low heat output.

Fuel cycle calculations regarding emissions and energy use for a typical industrial-scale CHP plant are summarized in Figure 1-12. and Table 1-5. below, from [Hart and Bauen 2003]. The smaller heat to power ratio (1 compared with 1.85) when compared with large commercial CHP results in increased emissions per unit of energy due to the greater portion of losses that can be attributed to the electrical power only generation [Hart and Bauen 2003]. The energy requirement is thus correspondingly greater [Hart and Bauen 2003]. Once more, the use of fuel cells (alone or in a combined cycle) yields considerably lower emissions than the base system. However, these reductions are smaller than for large commercial CHP systems. These calculations were made with the assumption that SOFC and SOFC/GT systems have the same total system efficiency – implying in turn that the SOFC/GT system has no advantages in terms of emissions per unit of useful energy [Hart and Bauen 2003]. This assumption is important because of the way emissions are allocated to energy products is a determining factor in drawing meaningful comparisons between systems [Hart and Bauen 2003]. In reality, the SOFC/GT has a higher electrical efficiency and will therefore be likely to be preferred in applications requiring low heat to power ratios. A similar analysis carried out for a MCFC-based system would show similar results leaving other factors such as economics and local conditions to favour one system or another [Hart and Bauen 2003].

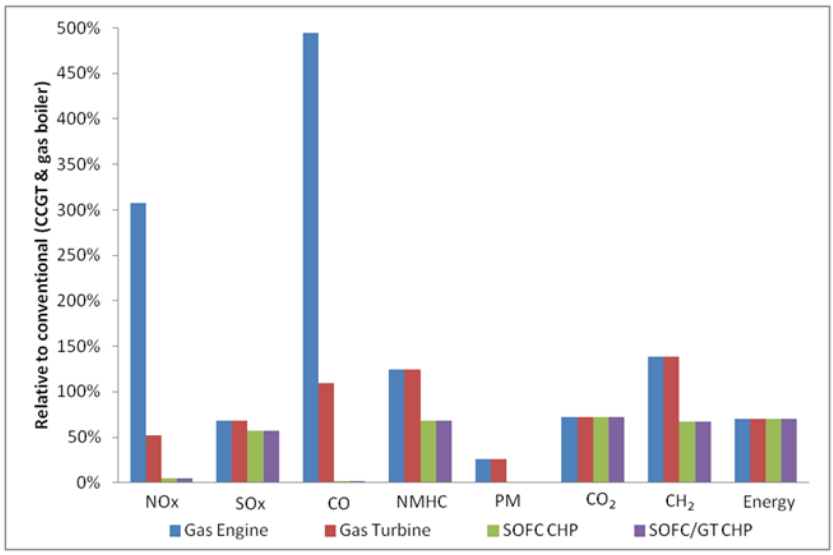

Figure 1-12. Total systems emissions and primary energy use of industrial-scale CHP [reproduced with data from Hart and Bauen 2003].

	Regulated Pollutants					Greenhouse Gases		Energy
	NO_x	**SO_x**	**CO**	**NMHC**	**PM**	**CO_2**	**CH_4**	**(MJ/kWh)**
Application	**(g/kWh)**	**(g/kWh)**	**(g/kWh)**	**(g/kWh)**	**(g/kWh)**	**(g/kWh)**	**(g/kWh)**	
CCGT & Gas Boiler	0.41	0.008	0.2	0.08	0.003	304	0.22	6.3
Gas Engine	1.2	0.006	1.0	0.09	0.001	218	0.31	4.4
	307%	68%	494%	124%	26%	72%	139%	70%
Gas Turbine	0.21	0.006	0.22	0.09	0.001	218	0.31	4.4
	52%	68%	109%	124%	26%	72%	139%	70%
SOFC CHP	0.021	0.005	0.004	0.052	0	218	0.15	4.4
	5%	57%	2%	68%	0%	72%	67%	70%
SOFC/GT CHP	0.02	0.005	0.004	0.05	0	218	0.15	4.4
	5%	57%	2%	68%	0%	72%	67%	70%

Table 1-5. Total systems emissions and primary energy use of industrial-scale CHP [Hart and Bauen 2003].

1.10.6 Interpretation of Fuel Cycle Analysis

The main conclusions drawn from fuel cycle calculations is that the widespread use of fuel cells in transport and stationary applications is highly likely to be greatly beneficial in terms of reduced energy consumption and reduced pollutants (at all levels, from global to local) [Hart and Bauen 2003]. While conventional technologies are evolving all the time, the nature of fuel cells and the fuels that can be used grant quite an edge in environmental terms [Hart and Bauen 2003] – even zero emission systems are possible if a renewable (even intermittent) energy source is used to produce hydrogen for use as fuel. The benefit of fuel cells in stationary applications is particularly noticeably for distributed and baseload power generation, where combining fuel cells with gas turbines increases the energy efficiency and reduces carbon dioxide emissions dramatically [Hart and Bauen 2003]. For combined heat and power (CHP) applications advantage should be taken of the high electrical efficiencies achievable with fuel cells.

An important consideration raised by Hart and Bauen (2003) is that any fuel cycle calculation is a "snapshot in time" based on a specific technology state of the art, assumptions on performance and emissions. Some of these technologies may develop only slowly, but there may be additional impacts that change with time requiring re-evaluation. For example a change in duty cycle for a diesel engine. This temporal aspect is especially important where the technology considered (resource extraction methods, fuel processing technology or the actual energy conversion technology such as gas turbines or fuel cells) is evolving rapidly, such as fuel cells. It is generally the case that once devices leave the laboratory or demonstrator stage performance improves considerably as dedicated power conditioning, and balance of plant are developed and then refined [Hart and Bauen 2003]. *Ergo*, comparison with conventional technology is inherently limited in accuracy at this stage and should perhaps be considered a good first approximation rather than a definitive analysis. Of course, the temporal aspect also applies to devices under dynamic (i.e. real world) loads as opposed to relatively static laboratory tests. Dynamic loading can have a very significant impact on overall performance [Hart and Bauen 2003].

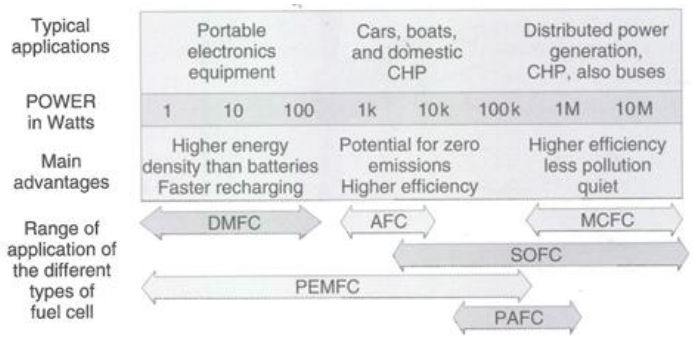

Figure 1-13. Summary of the principal advantages of fuel cell power by fuel cell type and application [after Larminie and Dicks 2003].

According to Hart and Bauen (2003) fuel cells in stationary applications are liable to use a variety of fuels, making the most of their flexibility, and the full environmental benefits will not be realised "until well into the future" once a hydrogen economy supplants the current fossil fuel one. SOFCs are a keystone of the future energy economy [Suzuki *et al.* 2009a].

Caeteris paribus the ideal target market for SOFCs appears to be in the 50 kW_e – 200 kW_e power range, aimed at a stationary application such as domestic or light commercial CHP and domestic power (or CHP) in remote regions. SOFC/GT combined cycles offer great potential in stationary power generation on a larger scale but face stiff competition from conventional generating systems and may therefore not be the optimal initial application for the technology.

2 General Background on Solid Oxide Fuel Cells

This chapter is a summary of the design and use of solid oxide fuel cells (SOFCs). It builds on material originally published in my MSc thesis [Camilleri 2009]. That review has been updated to provide the context to this study and background to SOFCs among fuel cells more generally.

2.1 Fuel

SOFCs offer great flexibility in the materials used as fuel. There are a few important considerations, however. The suitability of a material as fuel for a fuel cell is principally determined by two factors: thermodynamics of the oxidation-reduction reaction and its reaction kinetics. The former generally sets the maximum E.M.F. that can be generated while the latter determines the rate of transport of charge. In practical terms these correspond to cell voltage and current density, respectively. Kinetics is influenced by catalysis, the temperature and pressure of the reactants, and magnitude of the defined polarisations (losses). A number of potentially viable fuels, all of which have been used in experimental cells throughout the history of fuel cell development, are listed in Table 2-1. in their respective oxidation reactions along with the theoretical E.M.F. generated by the reaction with no load (the open-circuit voltage – OCV) and the Gibbs free energy of the reaction based on the Gibbs free energy of formation. The Gibbs free energy is a thermodynamic potential representing the maximum useable non-expansion work obtainable from a reversible process in a closed system. Gibbs free energy is also the chemical potential of a reaction that is minimized as the system reaches equilibrium at constant temperature and pressure.

Chemical Reaction	**E_{th} (Volts)**	**$\Delta G°$ (kJ mol^{-1})**
$H_2 + 0.5O_2 \rightarrow H_2O$	1.23	-237.53
$C + O_2 \rightarrow CO_2$	1.02	-394.95
$2C + O_2 \rightarrow 2CO$	0.70	-137.47
$2CO + O_2 \rightarrow 2CO_2$	1.33	-257.48
$C_3H_8 + 5O_2 \rightarrow 3CO_2 + 4H_2O$	1.10	-608.96
$2Na + H_2O + 0.5O_2 \rightarrow 2NaOH$	3.14	-302.96
$4NH_3 + 3O_2 \rightarrow 2N_2 + 6H_2O$	1.13	-241.82
$N_2H_4 + O_2 \rightarrow N_2 + 2H_2O$	1.56	-301.03
$CH_3OH + 1.5O_2 \rightarrow CO_2 + 2H_2O$	1.21	350.24
$CH_4 + 2O_2 \rightarrow CO_2 + 2H_2O$	1.51	-581.61

Table 2-1. Theoretical E.M.F. of selected reactions and Gibbs free energy at 25°C and 1.013 bar. The superior fuels are separated from the inferior ones by an empty row (fully explained below). Adapted from [Mitchell 1963 and Gibbs Free Energy article accessed 2014].

Even if a potential fuel is both thermodynamically and kinetically favourable it may not be economically viable for application in a fuel cell [Mitchell 1963]. Furthermore, many relevant fuels are not oxidised in a simple, single step but rather are a complex stepwise process. For example, the oxidation of methanol, frequently carried out in an alkaline electrolyte such as potassium hydroxide [Heath and Sweeney 1963], proceeds through formaldehyde (HCHO) and formic acid (HCOOH):

$$CH_3OH + 2OH^- \rightarrow [HCHO + 2H_2O + 2e^-]$$
$$[HCHO + 2OH^-] \rightarrow HCOOH + H_2O + 2e^-$$
$$HCOOH + 2OH^- \rightarrow CO_2 + 2H_2O + 2e^-$$

The products of any number of these steps may also have some effect on the overall cell reaction. The best known and most deleterious of these are anode sulphur poisoning and carbon fouling where some ancillary reaction of the fuel impedes correct operation of the anode – potentially until operation ceases entirely. Any carbonaceous fuel is known to cause this problem. The ancillary reaction is deposition of carbon on the electrodes, reducing the three-phase boundary (see later). Other culprits include impurities, such as sulphurous compounds, that tend to be included in some fuels. Therefore, generally speaking, all fuels save pure hydrogen require extensive pre-treatment and filtering for correct SOFC operation. For this reason hydrogen is favoured wherever possible, especially in experimental work where some base line needs to be established before work on auxiliary parts of the system (like pumps, insulation, control and so on) is undertaken.

Although hydrogen is an ideal fuel for fuel cells no global hydrogen infrastructure exists save for certain isolated industrial regions [Hoogers 2003b]. Furthermore hydrogen is usually generated from primary energy sources ~ typically fossil fuels. Even those cells that do not directly use hydrogen in its fuel gas form in fact do so indirectly, generating the needed hydrogen by *in situ* process like reformation and water shift reactions. A handful of fuel cells are also able to oxidise carbon monoxide thereby generating some power, although this is far less than for hydrogen [Hoogers 2003b, Larminie and Dicks 2003].

One can easily envisage, however, the use of more or less intermittent renewable power sources such as tidal energy and solar power that normally require some form of energy storage in order to be useful can instead be utilised to generate hydrogen from water by electrolysis. Thus the renewable energy generated by such intermittent sources that is not contributing to the grid is used to create fuel ~ locking the benefits of renewable energy in and empowering fuel cells for large scale generation (SOFCs) and for transport or mobile applications (PEMFCs).

Sources for H_2 production	Method	Cost (per kg)
Natural gas SOFC	Internal steam reformation	$ 1.47
Biomass syngas	Thermochemical and biochemical synthesis	$ 5.0 – 7.0
Coal	Coal gasification process	$ 2.0 – 2.5
Water	Electrolysis	$ 6.0 – 7.0
Methanol	Steam reformation	$ 2.0 – 5.0
Distributed wind power	Electrolysis	$ 7.26

Table 2-2. Estimated cost of hydrogen produced by different methods [edited, after Shaikh *et al.* 2015].

Generally the necessary purity of the hydrogen for a given application decreases with increasing operating temperature. For instance, PEMFCs can tolerate no more than a few ppm CO in the fuel gas before a significant drop in performance; phosphoric acid fuel cell (PAFCs), operating at higher temperatures, on the other hand tolerate up to 2% CO levels without significant loss in performance [Hoogers 2003b].

The presence of CO_2 in the fuel gas is another important consideration. Alkaline fuel cells (AFCs) are particularly vulnerable to this and are even prone to performance degradation when carbon dioxide is present in the oxidant [Hoogers 2003b]. This contrasts with PEMFCs, suffering only minor losses with up to 25% carbon dioxide in the fuel gas [Hoogers 2003b].

The fuels utilizable by high temperature cells (both SOFCs and MCFCs ~ Molten Carbonate Fuel Cells) are much more varied including hydrogen, carbon monoxide and small hydrocarbons (of which methane is usually considered the most important, closely followed by LPG ~ liquid petroleum gas) [Hoogers 2003b]. High temperature fuel cells are also somewhat tolerant of carbon dioxide [Hoogers 2003b].

Impurities in fuels such as halogens, sulphur and silicon compounds (common both in fossil fuels as well as renewable fuels such as biogas) are often highly deleterious to fuel cell performance [Hoogers 2003b]. Again, however, the higher the operating temperature the greater the tolerance for such impurities tends to be [Hoogers 2003b].

2.2 Hydrogen Storage Technology

The critical temperature of hydrogen, below which the gas is liquefied, is 33 °K, making this a difficult prospect [Hoogers 2003b, Larminie and Dicks 2003]. At ambient temperature hydrogen can only be stored in pressurised cylinders. Cryogenic cylinders maintain hydrogen at its boiling point of 20.39 °K at 1 atm to enabling higher storage density thanks to its liquid form at the expense of the additional complexity and power

load of the cryogenic process [Hoogers 2003b]. Other storage techniques do not store hydrogen as hydrogen at all but rather as absorbed into some carrier material. Metal hydride tanks use hydrogen penetrated into the interstitial lattice sites of a metal or metal alloy [Hoogers 2003b, Larminie and Dicks 2003]. In this manner the hydrogen is stored at very high density within the solid however the weight of the tank and the heat released during the storage process rule out this technique for mobile and most transport applications.

Less conventional, even exotic techniques, include the use of carbon fibres for their extraordinary hydrogen storage capacity and experimental approaches that aim to store hydrogen (among other things) inside large hollow molecules or nanoparticles including buckminsterfullerenes [Hoogers 2003b, Larminie and Dicks 2003].

2.2.1 Pressure Cylinders

Conventional gas cylinders made of steel are gradually being replaced by much lighter ones made from composite materials or designs like carbon-wrapped aluminium cylinders [Hoogers 2003b, Larminie and Dicks 2003]. These have a maximum operating pressure of up to 550 bar [Hoogers 2003b]. In practice national legislation and codes of practice limits this to 248 bar or 300 bar ~ a little over half capacity. At these pressures composite storage tanks are capable of containing a hydrogen mass fraction of about 3% (i.e. just 3% of the mass of the full cylinder is hydrogen) [Hoogers 2003b, Larminie and Dicks 2003]. Composite cylinders cost approximately three times as much as steel ones [Larminie and Dicks 2003]. Some interesting developments include “conformable” tanks with a 5.2% hydrogen mass fraction (also called storage density) designed by Thiokol Propulsion [Hoogers 2003b]. Pressurised storage has been used successfully by Ballard Power Systems, Californian Quantum Technologies and DaimlerChrysler among others, with pressures across the range from 248 bar to 700 bar in fuel cell powered vehicles (usually buses) giving a range of operation of 250 km to 400 km and weighing about 100 kg [Hoogers 2003b]. The reader is referred to the reference given as well as those cited within it for further detail.

	2 L steel cylinder (200 bar)	147 L composite cylinder (300 bar)
Mass of empty cylinder	3 kg	100 kg
Mass of hydrogen stored	0.036 kg	3.1 kg
Storage efficiency (% mass of H_2)	1.2 %	3.2 %
Specific energy	0.47 kWh kg^{-1}	1.2 kWh kg^{-1}
Volume of tank (approx.)	2,2 L (0.0022 m^3)	220 L (0.22 m^3)
Mass of H_2 per litre	0.016 kg L^{-1}	0.014 kg L^{-1}

Table 2-3. H_2 storage in pressure cylinders. Comparative data for two cylinder types [Larminie and Dicks 2003].

2.2.2 Liquid Hydrogen

Lowering the temperature of hydrogen to its boiling point of 20.39 °K at 1 atm requires 39.1 kJ kg^{-1} (or about 79 kJ mol^{-1}) – over a quarter of the higher heating value (HHV 286 kJ mol^{-1}) – thus already significantly reducing the energy efficiency by just filling the tank [Hoogers 2003b Larminie and Dicks 2003], Approximately 6 kJ kg^{-1} of this is consumed because of a quantum mechanical phenomenon called nuclear spin [Hoogers 2003b]. H_2 gas contains two atoms; spin-parallel ortho-hydrogen (o-H_2) and antiparallel para-hydrogen (p-H_2) species [Hoogers 2003b]. Ambient temperature hydrogen consists of about 25% p-H_2 and 75% o-H_2 [Hoogers 2003b]. Unfortunately p-H_2 is the stable form at cryogenic temperatures and the ortho- to para- conversion process takes several days [Hoogers 2003b]. In addition the conversion is highly exothermal leading to hydrogen losses by evaporation [Hoogers 2003b, Larminie and Dicks 2003]. Linde and Messer are both suppliers of cryogenic hydrogen storage tanks, capable of storing mass fractions of hydrogen of about 14.2% [Hoogers 2003b]. Safety of such tanks has already been assessed in Germany and has found not to be a problem [Hoogers 2003b, Larminie and Dicks 2003]. Filling the tanks (i.e. handling the liquefied hydrogen) on the other hand poses a problem at the filling station requiring rigidly adhered to procedures [Hoogers 2003b], particularly in order to prevent the ingress of air (which may form an explosive mixture) [Larminie and Dicks 2003].

	200 L cryogenic cylinder (3 bar)
Mass of empty cylinder	51.5 kg
Mass of hydrogen stored	8.5 kg
Storage efficiency (% mass of H_2)	14.2 %
Specific energy	5.57 kWh kg^{-1}
Volume of tank (approx.)	200 L (0.2 m^3)
Mass of H_2 per litre	0.0425 kg L^{-1}

Table 2-4. LH_2 (liquid hydrogen) storage in cryogenic cylinders [Larminie and Dicks 2003].

2.2.3 Metal Hydrides

Most elements are capable of forming ionic, covalent, metallic, or polymeric hydrides or mixtures of hydrides [Hoogers 2003b]. Of these the ionic and metallic hydrides are of most interest in fuel cell research because they are reversible [Hoogers 2003b, Larminie and Dicks 2003]. Alloys of chromium, iron, manganese, nickel and titatnium in particular readily form reversible metal hydrides [Larminie and Dicks 2003]. The formation of a hydride is an exothermal process that depends on the enthalpy of formation of the hydride ranging from several kJ mol^{-1} to several hundred kJ mol^{-1} [Hoogers 2003b]. The use of intermetallic compounds lowers this to practical values [Hoogers 2003b, Larminie and Dicks 2003]. The mass fraction of hydrogen varies from 1.4% to 7.7%, with many storing more than liquefied hydrogen systems [Hoogers 2003b, Larminie and Dicks 2003]. Some are unsuitable because of the large amount of heat released during the storage process lowering their energy efficiency. Furthermore, in order to release the hydrogen from hydrides a similar amount of heat has to be supplied to the hydride posing a major problem to the system [Hoogers 2003b]. However alloys can lower this even to room temperature [Larminie and Dicks 2003]. Gfe (Germany) and FeTi are two companies pursuing the metal hydride route, currently achieving mass storage fraction of about 0.7% to 1.4% [Hoogers 2003b].

Metal Hydride System	**Mg/MgH_2**	**Ti/TiH_2**	**V/VH_2**	**Mg_2Ni/Mg_2NiH_4**	**$FeTi/FeTiH_{1.95}$**	**$LaNi_5/LaNi_5H_{5.9}$**	**Liquid H_2**
H_2 content as mass fraction (%)	7.7	4.0	2.1	3.2	1.8	1.4	100.0
H_2 content by volume (kg/dm^3 = kg/l)	0.101	0.15	0.09	0.08	0.096	0.09	0.077
Energy content (based on HHV) (MJ/kg)	9.9	5.7	3.0	4.5	2.5	1.95	143
Heat of reaction (H_2) (kJ/Nm^3)	3360	5600	-	2800	1330	1340	-
Heat of reaction (H_2) (kJ/mol)	76.3	127.2	-	63.6	30.2	30.4	-
Heat of reaction (as fraction of HHV) (%)	26.7	44.5	-	22.2	10.6	10.6	-

Table 2-5. Hydrogen storage properties for a range of metal hydrides [Hoogers 2003b].

Metal hydride storage seems ideal for portable applications if suitable infrastructure for replacement is made available [Hoogers 2003b]. They are not suited to transport applications because of the significant decrease in fuel efficiency caused by the heat generated [Hoogers 2003b], although in cases where space is at a premium but weight is not (e.g. boats) they are potentially very useful [Larminie and Dicks 2003]. Metal hydride storage systems may be a practical alternative to liquid hydrogen (where no gas main exists) for SOFCs where the elevated temperatures can actually be of use to the system and where the loss of efficiency because of the storage process is less critical both because the application is stationary and also because the higher temperatures used by SOFCs make them more efficient than AFCs, MCFCs, PAFCs and PEMFCs. Probably the greatest disadvantage of this technology is that any impurities in the hydrogen react with the metal (or metal alloy) in an irreversible manner degrading storage capacity [Larminie and Dicks 2003]. Thus, metal hydride storage systems must only be used with very high purity hydrogen [Larminie and Dicks 2003].

	Small metal hydride container
Mass of empty cylinder	0.26 kg
Mass of hydrogen stored	0.0017 kg
Storage efficiency (% mass of H_2)	0.65 %
Specific energy	0.26 kWh kg^{-1}
Volume of tank (approx.)	0.06 L (0.00006 m^3)
Mass of H_2 per litre	0.028 kg L^{-1}

Table 2-6. A very small metal hydride container [Larminie and Dicks 2003].

2.2.4 Carbon Fibres

Hydrogen can be absorbed by carbon nanofibres [Larminie and Dicks 2003, Burchell *et al.* 2016, Hwang *et al.* 2016]. Early literature suggested that in excess of 67% of hydrogen could be absorbed at ambient temperature and pressure [Larminie and Dicks

2003]. These initial hopes proved erroneous and research is ongoing although no clear consensus on their utility for hydrogen storage beyond theoretical possibility has emerged [Larminie and Dicks 2003, Burchell *et al.* 2016, Hwang *et al.* 2016]. Measured absorptions vary from 1–2 wt.% to 5–10 wt.% [Larminie and Dicks 2003, Hwang *et al.* 2016]. Li doped variants may store as much as 20 wt.% [Larminie and Dicks 2003].

2.3 Hydrogen Generation Technology

An entirely different approach is to produce hydrogen when and where it is needed. One way of doing this is by using chemicals that can be used to produce hydrogen *in situ*. A number of liquid fuels have been of interest, and there are those who see this as the ultimate solution to the fuelling difficulties of fuel cell powered transport [Hoogers 2003b, Larminie and Dicks 2003]. The main contenders are: hydrocarbons including kerosene, gasoline, and diesel; methane; and LPG/propane [Hoogers 2003b]. Methanol is perhaps the most promising and as such has garnered the most interest [Hoogers 2003b, Larminie and Dicks 2003]. This is probably because it is relatively simple to process and can be made from any type of biomass with the correct thermal processing (unlike ethanol for instance) [Hoogers 2003b, Larminie and Dicks 2003].

The main benefits of this approach are high energy storage densities and the ease of transport and handling in part due to the existing infrastructure [Hoogers 2003b]. Also, their mass and volume are essentially determined by the fuel itself with the tank weighing only a fraction of the total since it has no special pressure or cryogenic requirements [Hoogers 2003b, Larminie and Dicks 2003]. The reader is referred to the cited references for more information on how such systems may be implemented.

2.3.1 Reformer Technology

Hydrogen is currently produced industrially for two main applications: some 50% of the world hydrogen production is used for the hydroformulation of oil in refineries producing automotive fuels, 40% is produced for subsequent reaction with nitrogen to create ammonia particularly for the manufacture of fertilizers [Hoogers 2003b, Larminie and Dicks 2003]. The cited source claims that the annual production volume of hydrogen in the USA is equivalent to somewhat over two days of average gasoline consumption. This puts the hydrogen economy, as it is often referred to, into perspective. Clearly the shift from a petroleum economy to a hydrogen one will not be a matter of a few years, even if the economic impetus exists.

Storage onboard of some alternative source of hydrogen, often a hydrocarbon followed by hydrogen generation *in situ* circumvents the need for a hydrogen transport/delivery infrastructure. This *in situ* generation may be on board a vehicle, inside a mobile device, or at a power station [Hoogers 2003b, Larminie and Dicks 2003]. Methanol, CH_3OH, has been the preferred fuel for striking a balance between fuel infrastructure and the

facility of fuel processing into hydrogen [Hoogers 2003b, Larminie and Dicks 2003]. This has been demonstrated by various prototype fuel cell vehicles by DaimlerChrysler, Toyota and General Motors [Hoogers 2003b, Larminie and Dicks 2003].

The last of these, GM, argue that in fact since methanol is generally accepted as an intermediary stage for establishing a hydrogen infrastructure (the best fuel for fuel cells) its use is actually detrimental since converting from a gasoline and diesel infrastructure would need to be done twice at immense expense ~ first to methanol and eventually to hydrogen [Hoogers 2003b]. As a result, GM has been dedicating more effort to using gasoline as a source of hydrogen making it a single conversion step to a hydrogen infrastructure [Hoogers 2003b]. Furthermore the existing infrastructure is also compatible with many renewable fuels enabling a smoother shift from fossil fuel hydrogen to renewable fuel hydrogen [Hoogers 2003b]. Omitting the intermediary methanol conversion allows more to be invested in developing a viable hydrogen economy [Hoogers 2003b]. The harshest criticism levelled against such an approach is that this argument, valid as it is, is strongly supported by major oil companies like ExxonMobil and Shell, who unsurprisingly are not keen on changing the existing fuel economy [Hoogers 2003b]. The technology of gasoline reforming is still immature compared with that of methanol reformation [Hoogers 2003b]. Without rapid development the use of hydrogen in transportation may well have to wait until hydrogen becomes widely available. Of course, none of this applies to stationary power generation and as such is expected to have little impact on the development of SOFCs and MCFCs.

2.3.2 Steam Reforming

Steam reforming of methanol (CH_3OH) is described by the following chemical equation [Hoogers 2003b, Larminie and Dicks 2003]:

$$CH_3OH(g) + H_2O(g) \longrightarrow CO_2(g) + 3H_2(g) \qquad \Delta H = 49\ kJ\ mol^{-1} \quad (2.1)$$

Methanol and water are evaporated in a catalytic reactor, reacting to produce carbon dioxide and hydrogen generally done between 200 °C and 300 °C using copper catalysts supported by zinc oxide [Hoogers 2003b]. One mole of methanol produces three moles of molecular hydrogen; the additional mole coming from the water [Hoogers 2003b, Larminie and Dicks 2003].

The exact kinetics is somewhat more complex with initial reformer output consisting of hydrogen, carbon dioxide and carbon monoxide [Hoogers 2003b, Larminie and Dicks 2003]. The carbon monoxide is fully oxidized to carbon dioxide and more hydrogen is produced in a high-temperature shift (HTS) stage followed by a low temperature shift

(LTS) stage [Hoogers 2003b, Larminie and Dicks 2003]. In both stages the water-gas shift reaction occurs:

$$CO + H_2O(g) \longrightarrow CO_2 + H_2 \qquad \Delta H = -41\ kJ\ mol^{-1} \quad (2.2)$$

The water-gas shift reaction is exothermal and eventually drives the reaction towards the reactant side (Le Chatelier's Principle) [Hoogers 2003b, Larminie and Dicks 2003]. In order to prevent this multiple stages with intercooling are used [Hoogers 2003b]. For the HTS stage the best catalyst is a mixture of iron and chromium oxides (Fe_3O_4 and Cr_2O_3) having good activity between 400 °C and 550 °C [Hoogers 2003b]. The LTS stage uses copper catalysts under similar conditions to those of steam reforming [Hoogers 2003b].

Steam reformation of methane is the standard industrial process used for the production of hydrogen on a large scale making it of importance to a hydrogen economy [Hoogers 2003b]. Steam reforming reactors have been scaled down to power generation at the building level [Hoogers 2003b]. The methane steam reforming reaction is [Hoogers 2003b]:

$$CH_4(g) + H_2O(g) \longrightarrow CO(g) + 3H_2(g) \qquad \Delta H = 206\ kJ\ mol^{-1} \quad (2.3)$$

This syngas reaction step as it is known, is again followed by the water-gas shift reaction [Hoogers 2003b] shown in equation (2.2). Methane steam reforming is usually catalysed by nickel and performed at temperatures between 750 °C and 1,000 °C with excess steam preventing carbon deposition on the nickel catalyst [Hoogers 2003b].

2.3.3 Partial Oxidation (POX)

Partial oxidation is generally used with heavier hydrocarbons than those used with that steam reforming reaction or when the particular situation makes certain species (pure oxygen for example) readily available [Hoogers 2003b, Larminie and Dicks 2003]. It is fundamentally oxidation with less than the stoichiometric amount of oxygen for full oxidation to the stable end products. In other words, it is partial oxidation creating metastable species [Hoogers 2003b]. For methane the chemical equation is [Hoogers 2003b, Larminie and Dicks 2003]:

$$CH_4(g) + \frac{1}{2}O_2(g) \longrightarrow CO(g) + 2H_2(g) \qquad \Delta H = -36\ kJ\ mol^{-1} \quad (2.4)$$

And/or:

$$CH_4(g) + O_2(g) \longrightarrow CO_2(g) + 2H_2(g) \qquad \Delta H = -319\ kJ\ mol^{-1} \quad (2.5)$$

Shell employ this process, as do Epyx (a subsidiary of Arthur D. Little) [Hoogers 2003b].

2.3.4 Autothermal Reforming (ATR)

There have been attempts to combine the benefits of steam reforming and partial oxidation [Hoogers 2003b, Larminie and Dicks 2003]. In an ideal scenario an exothermal reaction would be used at the initial phase thereby providing the heat needed by subsequent endothermal processes during steady state operation. The reactions can either be run in separate reactors with good thermal contact or in a single catalytic reactor [Hoogers 2003b, Larminie and Dicks 2003]. This combined process is known as autothermal reforming (ATR) [Hoogers 2003b, Larminie and Dicks 2003].

Johnson Matthey has developed a system they call the HotSpot fuel processor, initially for operation on methanol [Hoogers 2003b]. By running at a higher rate of partial oxidation during start-up, the HotSpot reaches 75% of its maximum hydrogen output within 20 seconds of cold start and 100% within a minute, making use of the exothermal nature of the first reaction [Hoogers 2003b]. During subsequent steady state operation a single 245 cm^2 reactor unit generates well over 750 litres of hydrogen per hour and is able to approximately provide the fuel requirements of a 1 kW fuel cell [Hoogers 2003b]. The units are very compact, made possible by the very effective heat exchange between the exothermal and endothermal reactions on a microscopic scale within the reactor [Hoogers 2003b].

The average stoichiometry corresponds to 2.4 moles of hydrogen generated from each mole of methanol [Hoogers 2003b]. Comparison with equation (2.4), (2.5) and (2.1) shows that as one would expect this yield is between the 2 and 3 moles of hydrogen per molecule for partial oxidation and steam reforming respectively.

2.3.5 Comparison of Reforming Technologies

In determining the most appropriate reforming technique the first consideration must be the ease with which the chosen fuel can be reformed. In general, methanol is the most readily reformed at low temperatures and can be handled well by any type of reformer [Hoogers 2003b]. Methane and LPG necessitate higher temperatures but once more are amenable to processing by any of the reformation techniques listed [Hoogers 2003b]. For higher (heavier) hydrocarbons one must usually resort to POX reactors [Hoogers 2003b]. The table below (Table 2-7.) shows typical gas compositions obtained from reformers. Steam reforming yields the highest hydrogen concentration. However, such a

system is best operated under steady state conditions as steam reforming does not lend itself to rapid dynamic systems, including frequent start-up shut-down cycles [Hoogers 2003b].

Output Composition (dry gas, vol.%)	**SRs**	**POXs**	**ATRs**
Hydrogen, H_2	67	45	55
Carbon Dioxide, CO_2	22	20	22
Nitrogen, N_2	-	22	21
Carbon Monoxide, CO	-	-	2

Table 2-7. Typical compositions of reformate from Steam Reformers (SRs), Partial Oxidation Reformers (POXs), and Autothermal Reformers (ATRs). In all cases the fuel was methanol [Hoogers 2003b].

Partial oxidation on the other hand offers compactness, rapid start-up and good dynamic response but yields lower concentrations of hydrogen [Hoogers 2003b, Larminie and Dicks 2003]. In addition to the different stoichiometries of SR and POX reformers, the output of a POX reformer is invariably diluted further by nitrogen since air is often the only practical source of oxygen [Hoogers 2003b, Larminie and Dicks 2003]. ATR offers a compromise as discussed in its description.

The fuel processor cannot be considered in isolation, however. Steam reforming is highly endothermal and this energy is usually supplied to the reactor by burning additional fuel [Hoogers 2003b, Larminie and Dicks 2003]. In a fuel cell system, catalytic oxidation of excess hydrogen exiting from the anode provides a convenient way of generating the requisite heat [Hoogers 2003b, Larminie and Dicks 2003]. It is worth noting that a PAFC operates at a sufficiently elevated temperature to generate its own steam to feed the fuel processor [Hoogers 2003b]. Steam reforming may be appropriate here while autothermal reforming is probably a better option for PEMFCs operating at lower temperatures and hence with only lower-grade heat available [Hoogers 2003b, Larminie and Dicks 2003]. In high temperature cells, especially SOFCs it is possible to conduct internal reformation because of the high temperatures of the cell itself.

Fuel efficiency also must be considered. Although always important the cost of fuel is the most important factor for stationary power generation (on a par with plant availability) [Hoogers 2003b]. For this reason the method offering the highest overall hydrogen output from the chosen fuel cell, usually natural gas, is selected [Hoogers 2003b]. Steam reforming delivers the highest hydrogen concentrations and therefore, the fuel cell stack efficiency at the higher hydrogen concentration may compensate for the additional fuel needed for steam generation.

In transport applications the dynamic behaviour of the reformer may control the whole power train [Hoogers 2003b]. A POX reformer offers the best dynamic behaviour and is also likely the best choice with heavier hydrocarbons [Hoogers 2003b]. For other fuels, particularly methanol, an ATR is likely to be the most appropriate [Hoogers 2003b].

2.4 PalladiumMembrane Technology

Different types of fuel cells are more or less tolerant to impurities in the fuel gas [Hoogers 2003b]. The removal of carbon monoxide is especially important for PEMFCs and less so for PAFCs, for example [Hoogers 2003b]. Ultra-pure hydrogen gas can be obtained using palladium membrane technology [Hoogers 2003b].

Permeation through palladium membranes are a well-established method for hydrogen (and only hydrogen) purification [Hoogers 2003b]. Palladium allows only hydrogen to permeate and retains any other gas species including nitrogen, carbon dioxide, carbon monoxide, and trace impurities on the upstream side [Hoogers 2003b]. CO absorbs strongly onto the surface since it is a noble metal, and therefore concentrations of just a few percent are deleterious to the hydrogen permeation through the membrane [Hoogers 2003b]. One way around this is to operate the membrane at a sufficiently high temperature in the presence of some added air or oxygen to oxidize the CO fully into CO_2 [Hoogers 2003b]. In practice, operating temperatures in excess of 350 °C and pressures of above 20 bar are frequently needed [Hoogers 2003b].

For economic reasons thin film membranes only a few microns thick consisting of Pd/Ag layers deposited onto a ceramic support are being developed [Hoogers 2003b]. Such thin films allow a reduction in the amount of Pd needed as well as improve the permeation rate [Hoogers 2003b]. The silver is needed to stabilize the desired metallic phase of palladium under the operating conditions [Hoogers 2003b]. Despite this stabilization, thermal cycling and hydrogen embrittlement are still a cause for loss of membrane integrity [Hoogers 2003b]. The high pressure difference across the membrane poses a significant barrier to the application of this technique to transportation or mobile applications [Hoogers 2003b]. On the other hand stationary power generators may benefit significantly from the low system complexity especially in the case of compact generators for remote areas [Hoogers 2003b].

A number of manufacturers including IdaTech and Mitsubishi Heavy Industries have developed or are developing reformers based on Pd membranes [Hoogers 2003b]. In these systems the reforming takes place inside the membrane chamber or in close contact with the Pd membrane, and only hydrogen passes into the cell [Hoogers 2003b]. IdaTech reported less than 1 ppm levels of CO and CO_2 in such systems [Hoogers 2003b]. Such pure hydrogen considerably enhances the viability of it as a fuel for fuel cells.

2.5 Matching Fuel to Application

Hoogers (2003b) presents a very useful table for the fuel/fuel cell combinations for both transportation and stationary power (portable applications are omitted since designs tend to be market sector specific rather than depending upon economic of ecological factors). Part of this table is reproduced here where it specifically relates to SOFCs in some guise. Interested readers are referred to the cited source for the full table and additional details [Hoogers 2003b].

Application	**High Temperature Fuel Cell - SOFC**
APU for conventional motor vehicles	**Gasoline**, **Diesel**
Domestic micro-scale electric power or cogeneration (CHP) (1-5 kW_{el})	**Natural Gas**, LPG, Fuel Oil
Small scale CHP (100 kW_{el} to 1 MW_{el})	**Natural Gas**, **Coal Gas**, LPG, Fuel Oil
Large central power station (multi-MW_{el})	**Natural Gas**, **Coal Gas**, Fuel Oil

Table 2-8. Fuel/fuel cell combination options with most likely candidates shown in bold [extracted from Hoogers 2003b].

An interesting crossover category exists, that of auxiliary power units (APUs) that are intended to supply electric power to vehicles for everything barring drive. Such systems are being developed by companies like Delphi in collaboration with BMW [Hoogers 2003b, Larminie and Dicks 2003]. One particularly beneficial aspect is removing the load of air conditioning systems from the internal combustion engine (several kW of power). Currently, due to difficulties of reforming gasoline, high temperature fuel cells (in particular SOFCs) are deemed the most suitable [Hoogers 2003b, Larminie and Dicks 2003].

Note that the arguments for and against hydrogen are given elsewhere and is intended for future development whereas Table 2-8. is referring exclusively to current infrastructure. As stated elsewhere hydrogen is the ideal fuel; only its production limits usage, so it tends to be avoided when an alternative exists.

For stationary power there will more often than not be natural-gas grid connections available. Where natural gas grid connection is not available (such as with micro-CHP in remote areas) similar fuels like LPG can be used. The use of fuel oil is possible but poses many challenges that are essentially similar to those of reforming gasoline or diesel [Hoogers 2003b].

2.6 Renewable Fuels

Despite the benefits of fuel cells, most notably in terms of reduced emissions, higher fuel efficiency and reduced maintenance, the choice of fuel is still a very important factor in determining the system's dependency or otherwise on fossil fuels and all that entails. Even should a hydrogen economy come fully into being relatively soon the production of hydrogen cannot depend solely on nuclear power because the amount of uranium left with current usage will last about as long as fossil fuels [Hoogers 2003b]. Therefore, the only truly complete long term solution includes the use of renewable energies. Fundamentally, there are just three primary sources for renewable energy [Hoogers 2003b]: the solar nuclear fusion process, heat emerging from the core of the earth (roughly half of this comes from heat of the early stages of the planet's formation as it continues to cool down and half from nuclear processes operating in the earth's crust), and the energy from the rotation of the earth and the moon [Hoogers 2003b]. All known renewable energies are traceable back to these fundamental sources, with solar energy exceeding all others by several orders of magnitude [Hoogers 2003b]. For example, the combination of solar energy evaporating water and the earth's rotation create wind [Hoogers 2003b]. According to Hoogers (2003b) there are two main routes for exploiting renewable energy for fuel cells:

- The production of hydrogen by water electrolysis powered by renewable sources (effectively turning renewable sources of energy into fuel).
- Generating biogas, syngas (CO and H_2), methanol or hydrogen from biomass.

2.6.1 Renewable Hydrogen from Electrolysis

"Electrolyzers have been available for a number of years to supply clean hydrogen to specialised industries. They have recently received a lot of attention as one option to generate CO_2-neutral hydrogen in conjunction with electric energy made from renewable." [Hoogers 2003b] Soysal *et al.* (2013) term the use of hydrogen generated from renewable sources for SOFC fuel a regenerative fuel supply.

Hydrogen fuelling stations have been or are going to be set up in such places as Sacramento, Las Vegas, Dearborn (Michigan), and Vancouver in North America; Hamburg, Munich, and Milan in Europe; and Osaka and Takamatsu in Japan [Hoogers 2003b, Larminie and Dicks 2003]. The Vancouver and Hamburg installations are going to use hydroelectric power as a renewable energy source, with Hamburg importing its hydrogen from Iceland [Hoogers 2003b].

A number of countries and islands are seeing their chance to be at the forefront of a hydrogen economy entirely based on renewables. Norway and Iceland have large resources of hydroelectric, wind, and geothermal power [Hoogers 2003b]. The Pacific islands of Vanuatu and Hawaii have plans to start building a hydrogen economy, with

Hawaii possibly exporting hydrogen to California [Hoogers 2003b]. Hydrogen generation will be based on wind, geothermal, and solar power. Elsewhere, in the emirate of Dubai, where the decline of Gulf oil reserves is first expected to become apparent, the government is working with BMW on a feasibility study to harness its share of the world's sunbelt for the generation of renewable hydrogen [Hoogers 2003b].

There is not much doubt that one day an energy economy based on renewable energy will exist. Yet, except for countries such as Norway with a large contribution of hydroelectric power, the amount of renewable electricity currently available is in the lower percent range of the overall national electric power consumption [Hoogers 2003b]. In indusrialised countries, the automotive sector alone consumes just as much primary energy again [Hoogers 2003b]. It is therefore debatable whether renewable electric power will be able to catch up fast enough in order to serve both purposes [Hoogers 2003b].

2.6.2 Biomass, Syngas and Organic Waste

Very interesting process in this route include the anaerobic digestion of biomass and the thermal processing of biomass to produce syngas. Biomass is available in large quantities, particularly as organic waste, throughout the year [Hoogers 2003b]. In the context of fuel for fuel cells, syngas from biomass can be processed to yield more hydrogen by the water-gas shift reaction or fed directly into the system (typically to a stationary high temperature fuel cell system based on MCFC or SOFC technology) [Hoogers 2003b, Larminie and Dicks 2003]. Perhaps the most noteworthy aspect is that waste biomass is turned into stored energy in the form of fuel [Hoogers 2003b]. This may be considerably more useful than the conventional approach of directly burning biomass to produce steam. Anaerobic digestion does not produce syngas, rather it generates so-called biogas; a mixture of about 50–75% methane, up to 35% CO_2, 0–10% water vapour, up to 5% N_2, up to 1% O_2, about 0.2% CO, less than 10 mg per m^3 of methane (CH_4) or siloxanes, and some 150 ppm H_2S [Hoogers 2003b, Larminie and Dicks 2003]. The composition is similar to natural gas, and *ergo*, all the reforming and purification techniques applicable to natural gas are also applicable to biogas [Hoogers 2003b, Larminie and Dicks 2003].

Dozens of practical plants have been built based on PAFC and biogas [Hoogers 2003b]. Some operate using sewage gas, and sulphur is removed by combination of cryogenic treatment to –20 °C to remove moisture that reduces the effectiveness of activated carbon filters and adsorption on activated charcoal [Hoogers 2003b]. A secondary advantage of the cryogenic treatment is that it freezes out siloxanes that are common in sewage and household waste [Hoogers 2003b].

This route is particularly attractive with MCFCs because of their tolerance to carbon dioxide [Hoogers 2003b]. Biomass is a cost-effective fuel source that is likely to

become increasingly important [Hoogers 2003b]. Another perspective that can be taken is that the waste can be used (via fuel cells) to provide the power needed by sewage treatment and waste processing plants [Hoogers 2003b].

2.7 High Temperature Fuel Cells

It is usual to define high temperature fuel cells as those operating above 500 °C. This lower bound is not rigid, and is intended to be representative of a range of operating temperatures [Gorin and Recht 1963]. Essentially there is no upper bound on operating temperatures for a high temperature cell provided suitable materials exist. The various parameters and component specification of any one particular fuel cell ultimately define its operating temperature [Gorin and Recht 1963, Wei 2008], so while temperature is a useful classification it is, in fact, subordinate to other elements (especially choice of fuel and geometry). Interest in such seemingly impractical devices derives from their potentially very high efficiency (highest of all fuel cells) with deleterious effects (especially the need to operate at elevated temperatures) offset by their potential for large scale power generation.

It is worth emphasising that conduction is electrolytic, so much so that any direct electrical path reduces fuel cell performance [Gorin and Recht 1963]. The electrolyte must, in addition to possessing a high electronic resistance, not undergo any compositional changes during operation or at the very least reach a steady state from which no further changes occur [Gorin and Recht 1963]. The problem of attaining adequate conductivity has relegated the use of solid electrolytes to higher temperatures within the high temperature fuel cell regime (generally above 750 °C). Such operation, however, is not without problems, as the operating temperatures used often call into question electrolyte stability (e.g. phase, microstructure) [Gorin and Recht 1963]. The high temperature requirement brings with it another benefit in the form of internal fuel reforming [Larminie and Dicks 2003, Wei 2008]. Most fuels must be processed prior to operation in a fuel cell (e.g. by steam reforming). High temperature fuel cells are capable of carrying out this reaction internally obviating the need for an external fuel reformer (one of the balance of plant components of a fuel cell system).

2.8 The Basic Fuel Cell Components

The six main components of all fuel cells are the fuel, oxidant, catalysts, electrodes, structural supports and electrolyte. The creation of a fuel cell thus necessitates the material specification and geometrical design of these six components from the range of available alternatives. Fuels and oxidants may be solid, liquid or gaseous, and a cell may actually employ a combination of these such as a liquid fuel and gaseous oxidant. A catalyst may or may not be deposited on the electrode surfaces to increase reaction

rates by improving the kinetics of the reaction. Electrodes can be porous or non-porous depending on the design of the cell. The electrolyte may be in a number of physical forms (solid, liquid impregnated matrix, etc.). In many instances the careful selection of one component 'sets' and defines much of the other components [Wynveen 1963]. Viable combinations tend to be restricted by the specifications imposed by the intended application. The following sections were used as guideline procedures to evaluate the various component characteristics. More detail on the design and material selection is given in Chapter 3.

2.8.1 Fuel Selection

Not all fuels are equally suited to any given fuel cell application; guidelines on suitability follow. The first step is calculation of the reversible electrode potential from standard free energy changes. This in no way expresses the kinetics of a reaction, but is useful to evaluate different anode and cathode reactants. This calculation will also often highlight any requirements placed on operating conditions for the reactants to be in the form desired (namely liquid or gas); namely pressure and temperature [Wynveen 1963, Larminie and Dicks 2003]. The table presented earlier (Table 2-1.) is sufficient for determining this. Secondly, the reversible electrode potential should be compared with the half-cell potential, capacity and efficiency of the selected anode and cathode reactions using data available in the literature [Wynveen 1963]. It is rare to achieve the reversible potential of an electrochemical reaction; the degree of irreversibility is dependent upon, among other things, the experimental operating conditions.

Other considerations need to come into play as part of the fuel selection process, especially since this informs subsequent material and even design considerations. This project includes several noteworthy examples of such additional considerations. Chief among these is the desire to use metallic electrodes (for processing reasons as well as for optimal conduction and catalysis). This requirement (a result of the excellent catalysis offered by metallic anodes) implies that carbonaceous fuels are likely to cause carbon fouling. Additionally metallic anodes tend to activate secondary reactions that both impede optimal operation of the fuel cell and complicate its evaluation. The only fuel that meets all these needs is pure hydrogen.

2.8.2 Catalyst Selection, Evaluation and Optimization

There are two main criteria a potential catalyst material needs to fulfil. First of all, it must activate the electrochemical reaction of the fuel without being itself unstable under the operating conditions (pH, temperature, pressure, low corrosion in electrolyte, and electrode potential). Secondly, the durability of the catalyst must be sufficient for use in the fuel cell at the particular operating conditions utilised. It is not enough for a material to be able to activate a reaction. It is important to determine its electrochemical behaviour over a range of potentials and under different operating conditions, since a catalyst that is active and stable under one set of operating conditions may be inactive or

unstable under another set of conditions [Wynveen 1963]. The literature is very helpful in this respect, suggesting catalysts with well known behaviour. For instance the cited source describes Pt as an excellent cathode for both electrodes (barring cost, naturally) and Ni is an excellent catalyst for the anode reaction.

The physical characteristics, namely the surface area, particle size/grain size, pore size, porosity, and crystal structure of a catalyst determine its catalytic activity and selectivity for a given reaction [Wynveen 1963]. Different preparation and deposition techniques, then, have a great impact on the effectiveness of the chosen catalyst.

The resistance of the catalyst to chemical attack varies by state; whether the material is used in solid form, as a fine powder, in liquid form and so on. The catalyst is in constant contact with the electrolyte, making even slow deterioration detrimental to the performance and life of the catalyst and therefore the whole fuel cell [Wynveen 1963]. Two changes are most commonly observed. First is dissolution of the catalyst and subsequent precipitation resulting from the differing solubility with particle size [Wynveen 1963]. The second typically observed phenomenon is permanent dissolution in the electrolyte occurring both during storage and while under load [Wynveen 1963].

For these reasons it was decided to use an anode material that was also a good catalyst for the fuel selected (hydrogen) in the case of the anode and a cathode material suitable for catalysis of the oxidant selected (air). The remaining challenge is selecting from the range of suitable catalytic materials one that meets the stability requirements given its state and form (a porous solid). At this stage it is worth delineating why air was selected as the oxidant. Air (rather than pure oxygen) is abundant, easily metered, needs no special precautions or considerations and can be pressurised easily if this is necessary. The same cannot be said for any other oxidant, making air the most suitable for eventual commercial application.

2.8.3 Electrode Selection and Evaluation

The functions an electrode must fulfil along with the properties necessary to fulfil these are tabulated below in Table 2-9. Fuel cells using gaseous reactant species necessitate porous electrodes to enable the fuel and oxidant to reach the three-phase boundary (more on this later).

Function	Property
Current carrier	Low electrical resistivity
Catalyst or catalyst support	Large electrochemically active area
Contain electrolyte between electrodes of opposite polarity	Chemical inertness toward the electrolyte
Cell structural support	Strong and resistant to fracture
Manifold fuel gas to reaction sites (gas electrodes only)	Adequate transport of relevant gases

Table 2-9. Electrode functions and requisite properties.

Depending on the particular choice of electrolyte and reactants several manufacturing techniques are applicable. The ideal electrode is made entirely of catalyst material. Electrode geometry is equally important. The planar (parallel plate) design appears to offer optimised cell performance [Wynveen 1963] based on volume. In general fewer, larger electrodes are more robust, can have greater overload capacity built into them, and for a given current operate at a more efficient (higher) potential and lower current density (fewer polarisation problems). However, tubular geometries offer many advantages also. Especially greater thermal cycling resistance, simpler gas distribution, simpler interconnect design (may not even need separate interconnects to be added). Finally, because tubular designs are more mechanically robust as well it is possible to miniaturise these far more practically than planar designs adding all the advantages of miniaturization including enhanced performance and less material usage. The only disadvantage that remains is a reduced overload tolerance because the electrodes are less bulky than in planar designs.

It is worth briefly justifying why tubular cells are more resistant to thermal-cycling-induced stresses. Coatings on tubes or cylinders have a more open structure, imposed by the convex curvature, and as a result are more compliant. This is especially true of coatings with a columnar texture. The other reasons for better thermal cycling performance of tubular cells are less directly related to the geometry. Tubular designs require virtually no sealing: only the ends need sealing and it may be possible to omit this if the coefficients of thermal expansion of the casing (or faceplate) and the tube are such that the tube expands to seal itself at operating temperature. That is the seals become an integral part of the stack design rather than an additional component. Similarly, very little clamping is needed to hold tubes in place. As a result the tubes are fairly free to expand minimizing any thermal stress forming and therefore avoiding damage by thermal cycling. A final note on this is that tubular structures are inherently stronger than planar ones, so are in fact better able to resist any stresses that do occur. The interested reader is directed to compare the principal stresses in a planar system to the stresses (hoop, radial and axial) of cylindrical systems.

2.8.4 Electrolyte Selection and Classification

The final component to be selected is the electrolyte. Electrical conductivity information is of interest; hence data of electrolyte resistance are a standard part of the evaluation procedure [Wynveen 1963]. With gaseous fuels electrolyte design is quite involved. If the electrolyte is a free flowing liquid it is necessary to ensure that flooding of the porous electrodes does not occur and reactant mixing is not possible in the electrolyte compartment [Wynveen 1963]. On these same lines, solid electrolytes, essentially ion-exchange membranes, are preferred and come in both organic forms as well as inorganic ones [Wynveen 1963]. Unfortunately inorganic solid electrolytes are only applicable in high temperature cells; or rather they generally impose the high temperature requirement on such cells. Achieving uniform contact between electrode and electrolyte with a minimum internal resistance is the path to optimization.

2.9 Basic Operating Principles

An ideal solid oxide fuel cell (SOFC) is an electrochemical device that converts the chemical energy of a fuel and an oxidant (usually air or pure oxygen) directly into electricity without irreversible oxidation [Winkler 2003, Larminie and Dicks 2003]. The oxygen ion, or other oxidizing ion or radical, is transported through the electrolyte to the anode, where it reacts with the fuel, typically forming water, carbon dioxide and carbon monoxide depending on the fuel. The zone in which oxidant ion, anode catalyst and fuel meet is called the three-phase boundary. Thermodynamically the process is dealt with in terms of the free enthalpy of reaction changes of the fuel with the oxidant.

The losses in SOFCs manifest as the lowest form of energy – heat. It is thus necessary to consider the cell as both a source of electrical power and heat [Winkler 2003]. This has been used in combined generation units (SOFC losses and waste heat generates steam to run a conventional turbine-generator set) and in combined heat and power units (waste heat is used to heat buildings, for instance). In most real systems excess air is often necessary to prevent overheating [Winkler 2003]. The energy inputs and outputs of an ideal SOFC are shown schematically in Figure 2-1.

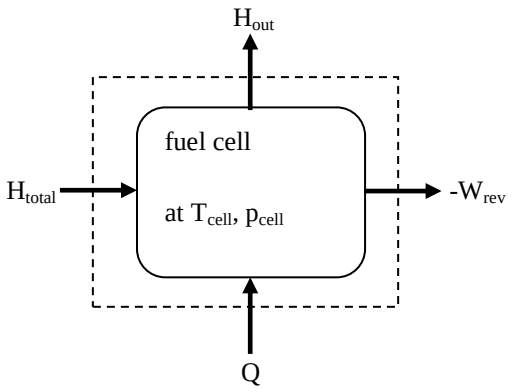

Figure 2-1. Schematic representation of thermodynamic energy balance of an ideal fuel cell and its system boundary. H_{total} is the energy of the fuel, Q is the thermal energy input needed to heat the SOFC to its operating temperature, W_{rev} is the reversible work output (electrical energy generated by cell), and H_{out} is the enthalpy lost by the reaction process (most fuel cell reactions are exothermic). Adapted from [Winkler 2003].

There are two conditions that must be fulfilled in order for a particular reaction to be a source of energy. Firstly, at least some of the reactants must be ionisable at the operating conditions (especially pressure and temperature) of the cell. It is the ionisation that creates the redox potential, ultimately the source of energy for any electrochemical fuel cell [Heath and Sweeney 1963]. Secondly, while the ionisable reaction is the source of energy for the system, a high electron flow rate is required for the cell to generate practically useful currents. Rapid reaction rates for the potential-determining, that is electron-supplying and electron-absorbing, reactions is the second condition.

Usually the first is considered pseudo-static in nature and is associated with thermodynamic equilibrium of the system. The second condition is dynamic in nature and associated with chemical kinetics [Heath and Sweeney 1963]. In reality, however, the rates for the forward and backward reactions are determined by the pseudo-static equilibrium. In other words, the kinetics is greatly affected by the thermodynamics.

The direction and magnitude of the free energy change in a reaction determines its usefulness in a fuel cell system. Yet even where this is favourable it is possible for the activation energy for that reaction to be too high to obtain useful currents at reasonable temperatures [Heath and Sweeney 1963]. This is even true of hydrogen oxidation, the least problematic of possible fuels. *Ergo*, catalysts are required to provide a low activation energy path that can be exploited to access the free energy change. Unfortunately, even with the availability of reliable data, the complex interaction of adsorption, kinetic, surface, electrical and solvent effects renders a general interpretation of catalysis exceedingly difficult. While perhaps overly complex to solve exactly it does help to identify performance limitations of a design and suggest improvements [Heath and Sweeney 1963]. So much so, that most discussions of suitable materials for the various components cite qualitatively the effectiveness of a

material as a catalyst for a particular reaction. See the material selection chapter for more details (Chapter 3).

2.10 Electrode Kinetics

The simplest fuel possible for a fuel cell is hydrogen. While details of the reaction are still debated [Gorin and Recht 1963, Tsipis and Kharton 2008] it is generally accepted that first hydrogen is adsorbed onto the electrode and then dissociated into hydrogen atoms. These atoms are either ionised or react with an anion containing oxygen from the electrolyte [Gorin and Recht 1963]. If the atomic hydrogen is ionised the transfer of one electron is implied possibly accounting for the relative ease with which hydrogen reactions occur at the electrode. These reactions can be written as:

$$H_2 + X \rightarrow H_2X \qquad (2.6)$$

$$H_2X + X \rightarrow 2HX \qquad (2.7)$$

$$HX \rightarrow Xe^- + H^+ \qquad (2.8)$$

$$2HX + O^{2-}(\text{in anion}) \rightarrow 2Xe^- + H_2O \qquad (2.9)$$

Where X represents the electrode surface material, equation (2.8) is the first case described and (2.9) is the second. If air or pure oxygen is the oxidant then the overall cell reaction is a simple combination of hydrogen and oxygen to form water. Generally for high temperature cells it is the reaction shown by equation (2.9) that occurs, with water produced at the anode [Gorin and Recht 1963, Larminie and Dicks 2003].

An excellent discussion on the kinetics of other important fuels such as carbon monoxide, alcohols and aldehydes (partially oxidised hydrocarbons), and low molecular weight hydrocarbons like methane as well as explanations of thermal cracking of carbonaceous fuels, steam reforming and the water-gas shift reaction and the Boudouard Equilibrium that leads to the evolution of solid carbon (carbon fouling) at the anode can be found in [Gorin and Recht 1963] and many others besides including recent papers [for example Conor 2010]. In all cases it is the hydrogen produced by these reactions that participates in the electrode process and remains the potential-determining species [Gorin and Recht 1963].

While it is certainly permissible to use more exotic oxidants and fuels, high temperature cells tend towards the utilisation of air or pure oxygen in combination with one of the fuels noted previously. This is further cemented by intended large scale power

generation applications for high temperature fuel cells. For such applications, clearly, hydrocarbons and air are the most economic reactants, and as production improves hydrogen is also becoming increasingly popular despite a general lack of infrastructure compared with fossil fuels [Gorin and Recht 1963, Singhal and Kendall 2003, Honda Clarity]. The use of air instead of pure oxygen lowers the cell potential, but only by 40 mV at 1,000 °K. The main limitation of air, as opposed to oxygen, is the presence of nitrogen. This relatively inert gas serves as a blanket, impeding the reaction, which oxygen must diffuse through to reach the reaction site. Therefore, the rate of the reaction is substantially reduced [Gorin and Recht 1963].

The electrode reaction rate increases exponentially with temperature (see the theory of operation, section 4.2.2). Therefore, with highly active fuels (like hydrogen) at elevated temperatures the chemical kinetics of the electrode reaction are no longer rate limiting. Rather, it is the physical conditions of the mass transport that become increasingly critical [Gorin and Recht 1963]. In polarisation terms it is not the activation polarisation that is dominant but the concentration polarisation. Ohmic polarisation does not relate very closely to the electrochemical process but rather the component and therefore is independent of the other two which are linked by reaction kinetics.

2.11 Survey of Previous Tubular SOFC Designs

From the early designs of the 1930s there have been many different geometrical designs, most have since fallen out of favour. Currently planar and tubular geometries dominate [Kendall, Minh and Singhal 2003, Larminie and Dicks 2003, Yang *et al.* 2009]. Typically an individual cell has an open-circuit voltage of somewhat less than 1 V. Obtaining practically significant voltages then requires many cells to be connected in series. This is usually achieved by connecting individual cells with interconnect material; the arrangement referred to as a stack in common parlance. Similarly, currents are relatively limited, so cells are stacked in parallel to achieve meaningful currents [Kendall, Minh and Singhal 2003, Larminie and Dicks 2003, Yang *et al.* 2009].

There are two forms of the tubular design currently pursued; cells with relatively large diameters of > 15 mm and so-called microtubular cells with relatively small diameters in the range of 1–5 mm. The author envisages an eventual further miniaturisation in the near future, to truly microtubular cells with diameters < 1 mm and perhaps even nanotubular designs with diameters of the order of a few hundred nm. Such likely would necessitate a complete rethinking of modelling and fabrication techniques currently employed. It should be possible to achieve this using physical vapour deposition (PVD). Of the tubular designs with larger diameters the best known and perhaps most successful design was pioneered by Westinghouse Electric Corporation, later Siemens Westinghouse Power Corporation [Kendall, Minh and Singhal 2003,

Hoogers 2003c, Larminie and Dicks 2003]. The design is cathode-supported and uses a doped $LaMnO_3$ tube usually of high aspect ratio onto which the other components are deposited as thin layers. Earlier designs had used a porous calcia-stabilised zirconia tube (PST – porous support tube) for structural support and as the air-manifold. It was found that both thick-walled PST (≈ 2 mm) and thin-walled PST (≈ 1.2 mm) created a significant impedance to air flow, so the decision was made to eliminate the use of a PST [Kendall, Minh and Singhal 2003]. The electrical performance of each of these three designs is shown in Figure 2-2.

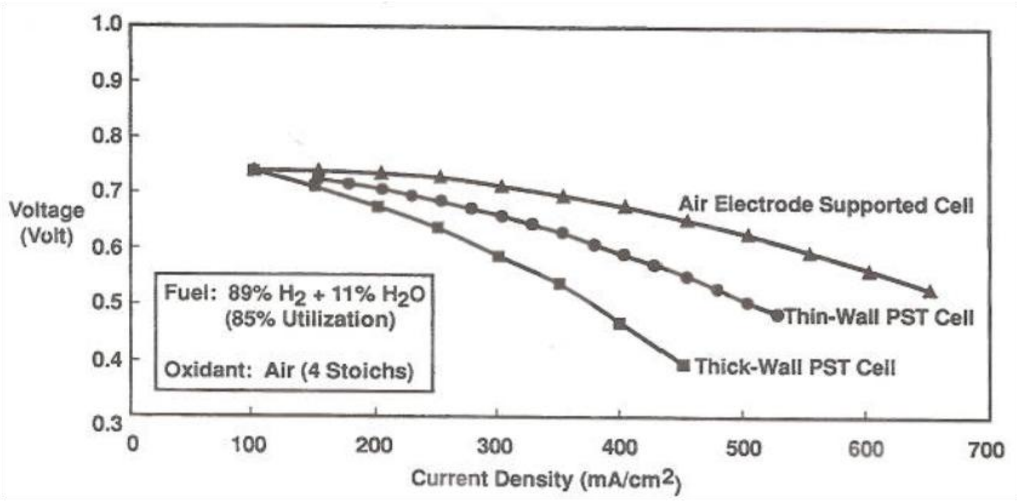

Figure 2-2. I-V characteristics of the three variant designs for tubular electrode by Siemens Westinghouse Power Corporation, operated at 1,000 °C [Kendall, Minh and Singhal 2003].

Each cell's length was continuously increased with development in order to increase the output (current is proportional to the active surface area) per cell, and therefore reduce the total number of cells per stack necessary. The result is better economics by minimising fabrication costs [Kendall, Minh and Singhal 2003]. The active length (the length of the interconnection) increased from 300 mm in 1986 to 1,500 mm in 2003. Also the diameter of each cell increased somewhat from 16 mm to 22 mm in order to accommodate the larger pressure drops experienced by longer length cells [Kendall, Minh and Singhal 2003, Hoogers 2003c], with a wall thickness of about 2.4 mm. The Siemens Westinghouse design is illustrated schematically below in Figure 2-3. Note the interconnect bar.

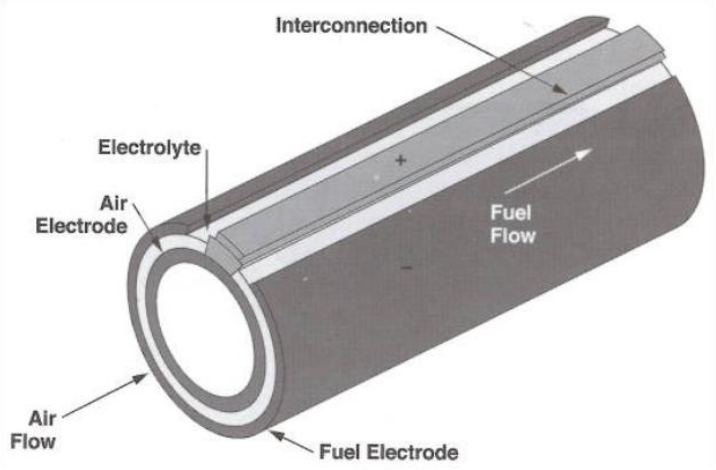

Figure 2-3. Schematic of Siemens Westinghouse tubular SOFC [Kendall, Minh and Singhal 2003].

The cathode (air-electrode) of the design shown is manufactured by green extrusion followed by sintering, obtaining a tube of wall 2.2 mm, about 1,800 mm in length (1,500 mm active length) and of 30–35 % porosity [Kendall, Minh and Singhal 2003, Hoogers 2003c]. The electrolyte is 40 μm thick 10YSZ deposited by electrochemical vapour deposition (EVD) [Kendall, Minh and Singhal 2003, Hoogers 2003c, Larminie and Dicks 2003]. EVD is complex, and the equipment has a high capital cost, as well as being inherently a batch process manufacturing technique [Kendall, Minh and Singhal 2003, Hoogers 2003c, Larminie and Dicks 2003]. In these aspects it is identical to EB-PVD (the route chosen for this project). The cathode tubes had an approximate value of £1,000 ($1,600) each [Hoogers 2003c]. Finally a Ni-YSZ cermet anode 100–150 μm thick is deposited onto the electrolyte by a hybrid technique combining slurry dip coating and EVD, subsequently co-fired in two different atmospheres for the cathode and anode [Kendall, Minh and Singhal 2003, Hoogers 2003c]. The equivalent active area of this patented design is 834 cm^2. Interconnects are formed by a strip of doped lanthanum chromite about 85 μm thick deposited by plasma spraying followed by a densification (sintering) stage [Kendall, Minh and Singhal 2003, Hoogers 2003c].

This design presents some safety concerns that could easily have been avoided. The first concern is that the fuel flows on the outside of each cell, meaning any leak in the stack is a fuel leak and commensurately hazardous. The second concern is the positioning of the current collection. Both are immersed in the fuel flow and any local overheating (due to local variations in internal resistance of the electrolyte, for instance) may cause ignition of the fuel should there be any air leaks (a small puncture of poor seal would allow air in to mix directly with the fuel, potentially very dangerous). Interestingly, the first tubular SOFC, with fuel on the inside and air on the outside was designed by Baur and Preis in the 1930s [Singhal and Kendall 2003a]. Already then the importance of the

fabrication technique and reducing electrolyte thickness to reduce ohmic losses was known. Why the Siemens Westinghouse design ignores this is not reported.

This design also results in very long conduction paths (already a problem with tubular cells in general and made worse by artificial constraints Siemens Westinghouse put on themselves). Long conduction paths lead to high ohmic losses, and since ohmic losses are the greatest single loss in SOFCs this is an intrinsically limiting design. Decisions made early on in the design created artificial constraints that restricted options later, creating a design that is far from optimal. The interested reader may benefit from reviewing the many patents filed by Siemens Westinghouse for their fuel cell designs [Gillett *et al.* 1998, Holmes *et al.* 2003, Zafred *et al.* 2012, Gillett *et al.* 2013 in particular].

This design generates 150 W of electrical power at an operating temperature of 950 °C, corresponding to an area-specific power density of 0.18 Wcm^{-2} [Kendall, Minh and Singhal 2003, Hoogers 2003c]. Detailed information on the performance of the Siemens Westinghouse design can be found in the cited reference and Hoogers (2003c) including fuel utilisation, lifetime, performance degradation, thermal cycling behaviour and power densities. They are not repeated here primarily because the Siemens Westinghouse design is quoted here to illustrate a typical prototype system that has achieved some commercial success. The design adopted in this project is not based on it, and in any case, in all ways save power densities, the microtubular designs are not directly comparable to their larger cousins.

An important advantage of tubular designs over planar ones is they require no high-temperature seals to separate the fuel gas and oxidant [Kendall, Minh and Singhal 2003, Hoogers 2003c, Larminie and Dicks 2003, Dal Grande *et al.* 2008, Yang *et al.* 2009]. However, the area power density is inferior, being only around 0.2 W cm^{-2} compared to planar cells with a power density of up to 2 W cm^{-2} [Kendall, Minh and Singhal 2003]. Additionally the manufacturing costs of tubular designs are intrinsically higher than for planar ones [Kendall, Minh and Singhal 2003, Hoogers 2003c, Larminie and Dicks 2003] due mostly to the increased complexity and labour-intensive manufacture. With larger diameter designs the volume power density is also lower than for planar designs so have conventionally not been suited to mobile and military applications [Kendall, Minh and Singhal 2003]. Hoogers (2003c) makes a similar point, yet completely overlooks the argument that volume-specific power density is inferior but area-specific power density is comparable (in no small part due to improved gas transport, hence lower concentration polarisation – see more on this in section 4.3.3 and 4.3.4) considerably mitigating any reduction in electrical performance of tubular cells compared with planar ones. The lower power density remains true today [Hussain *et al.* 2009], mostly due to the high electrical resistivity associated with longer current paths inherent in micro-tubular designs. There is then good reason to adopt tubular designs

over planar ones and even greater motivation to scale down tubular designs for both improved absolute performance (lower polarisation losses as explained previously) and for better area- and volume-specific power densities.

Other tubular SOFC developers [Hoogers 2003c, Larminie and Dicks 2003] include:

- TOTO Ltd., Kyushu Electric Power Co., and Nippon Steel Corporation, co-funded by the NEDO New Sunshine Project
- Mitsubishi Heavy Industries (MHI), in cooperation with Electric Power Development Co. (EPDC) and Chubu EPC.

The former consortium created 3 kW modules (36 cells) consisting of 22 mm diameter, 900 mm long tubes manufactured by sintering technology operating at an unreported temperature with atmospheric air and reformed natural gas (presumably also at or close to atmospheric pressure) that achieved an area-specific power density of 0.192 Wcm^{-2}. Performance is similar to the Siemens-Westinghouse design.

The latter group used segmented, staggered tubes 720 mm long consisting of 22 cells connected in series. This concept is also known as the "bell-and-spigot" design. The cells were manufactured by plasma spraying, and it is the inner electrode is the fuel electrode. By operating at higher pressures than atmospheric a 10 kW module was envisaged using coal gas as fuel.

2.12 Patents Relating to Microtubular SOFC Development

A search for patents relating to microtubular SOFCs yielded less than a dozen patents – mostly regarding fabrication of ceramic components (in particular of ceramic electrodes). A more general search for patents in the area of SOFCs yields an interesting statistic. The vast majority (about 98%) of patents are related to planar designs. These usually deal with a specific component – most often gas sealing and electrode fabrication. Most of these patents originate from the US, the remaining are divided about equally between the UK and Japan. A large number of these patents claimed to have developed the entire system [Tsunoda 2005, Hatada 2007, Tsunoda and Izumi 2009 and many others], creating integrated power generation systems using solid oxide fuel cells with a variety of carbonaceous fuels. The choices of fuel are dictated by practicality; initial research may be carried out using hydrogen for simplicity and to reduce the complexity of plant needed to run the experiments, but a practical cell must run on a practical fuel. The use of fossil fuels may be understandably convenient, but it is not very conducive to sustainable power generation and is rather short-sighted. SOFCs using natural gas and alcohol dominate the non-fossil-fuel-using patented devices.

Globally 121 patents were filed in this area.

Of the 55 tubular solid oxide fuel cell patents filed with the US Patent Office, ranging from interconnect designs, to heat exchanger designs that wrap around the cells without impeding gas manifolding, to electrodes, to complete cells [Fujinaga *et al.* 2004], and paired reformer-cell systems, only 4 were explicitly microtubular, or designed to work with microtubular cells (see the following paragraphs). It is possible as many as six others were of this order but such was left undisclosed in the patent. Of tangential interest is that two were of hybrid geometry (referred to as flat-tubular within the patents). Another proposes using injection moulding, though it is unclear what the dimensional limits of this would be [Maus *et al.* 2013].

The most relevant patents found are reviewed briefly. First, a micro-extrusion process for fabrication of a microtubular cell [Lee *et al.* 2008] that is interesting for its very challenging, but commercially viable, choice of fabrication route. A complex multi-pass extrusion process is used to fabricate all the components in green form. The final green is then sintered to create the device (co-sintering, or co-firing, all the components together). There are likely to be difficulties with the morphology due to co-sintering since the electrodes need to be porous while the electrolyte must be gas tight. The cited patent uses polymer binders and it can be inferred that the mixture is adjusted to create porosity where needed and minimize porosity in the electrolyte. The development of this type of fabrication process is exceedingly expensive and quite lengthy. However, once all the process variables are known it is possible to manufacture vast quantities of these cells with excellent repeatability and at relatively low cost. The fact that this technique is at the patent stage demonstrates its potential and commercial value. What is yet to be reported is the performance of cells made this way, and to what extent they can be miniaturized. It is likely that this technology is already operating at the smallest regime possible for green machining. A similar process is utilised by a patent titled "Method to fabricate high performance tubular solid oxide fuel cells" [Chen *et al.* 2013], with the addition of a phase inversion process to create remarkably porosity in the anode. The same technique was employed by Othman *et al.* [2010].

The patents filed by Huang and Ruka (2012) and Sarkar *et al.* (2004) are both metallic electrode-supported, with very thin ceramic electrolyte and non-support electrode layers. The former is anode-supported, with the all components sintered from powder mixes and intended for operation from 600 °C to 800 °C. The latter is similar, and made of similar materials, but unusually is constructed upon a wooden mandrel. Sarkar *et al.* (2004) created a Gadolinia-doped ceria electrolyte, and thus their design is aimed at the same temperature range as the device patented by Huang and Ruka (2012).

A similar search within the European Patent Office yielded just three patents, none of which related to microtubular designs. Two of these related to creating and connecting stacks and interconnect blocks. Fourteen were filed with the Canadian Intellectual

Property Office – most of which regarded stack arrangements. No patents for explicitly microtubular designs were found. However, an Acumentrics patent of an anode-supported design exists [Sammes *et al.* 2011], that was filed with the Canadian Intellectual Property Office. This particular design is of interest because it is anode-supported, and the components are created by machining the green which is then co-sintered. This complex processing is typical of all-ceramic designs that rely on sintering. It may be considered a microtubular design, however it is at the larger end of that range with component thicknesses of the range of 400 μm for the anode and half that for the electrolyte and cathode. Efforts to manage ohmic losses by material selection (adopting doped materials) led to a range of complex problems. The interested reader is referred to the cited reference for details.

Surprisingly no relevant patents were found to have been filed with the UK Patent Office.

Compare the patented designs described above to the ones below for macro-tubular cells, noting in particular comments and description given about complexity and design constraints, some of which appear arbitrary.

The two patents reviewed in some detail below are both the work of Siemens Westinghouse, and were selected as representative of the most commercially successful tubular SOFC system to date. The earlier patent [Gillett *et al.* 1998] is representative of the standard configuration of the Siemens Westinghouse work and contains a number of areas of interest. The system makes use of individually-insulated cells (referred to as "generators" in the document). This is hardly sound design. While the insulation *per se* might be optimised the overall arrangement seems unduly complex and as a result more costly than simpler insulation. The stack configuration consists of cells connected in series and in parallel arranged with their long axes parallel to one another in rectangular or circular groupings [Gillett *et al.* 1998]. Series connection was achieved by connecting the cathode of one cell to the anode of the adjacent one via a metallic coating and fibrous metal felt. The series-connected groups were then electrically connected in parallel with adjacent groups via cell interconnects extending axially along each cell. Needless to say this results in very long conduction paths when the dimensions of the cells manufactured is taken into account.

According to this patent [Gillett *et al.* 1998] conventional designs for SOFCs tend to have individual cells connected to pumps, reformers, and electrical leads individually because no overall casing/manifold system had been designed to collect them into convenient groupings and make each connection only once for each grouping. This is a very surprising statement, and while I do not contend its veracity at the time, it seems a singularly illogical approach. Westinghouse applied an approach that is not really

innovative but rather common sense. Raising the question as to why this is raised in the patent at all.

Designs, such as this, where direct handling of the cells is required for installation have a serious flaw in addition to sub-optimal usage of space (room needs to be left for workers to attach leads and so on) which is the much higher risk of breakage due to "self imposed handling loads" [Gillett *et al.* 1998]. The risk is further magnified by the need for fixtures to facilitate handling and assembly, removal of temporary support structures after mounting, and so on. Repair and replacement is equally impractical since the system needs to be disassembled to some degree to access the malfunctioning parts.

Gillett *et al.* (1998) opt for a very costly strategy for handling the balance of plant suggesting that auxiliary equipment like reformers and fuel and air distribution systems (pumps, filters and the like) are also to be mounted for each stack. This multiplies the cost of balance of plant tremendously as well as greatly increasing the number of things that can fail. It does however, permit great flexibility.

The design described by this patent has the following pertinent details:

- 500–2,300 mm long porous cathode, preferably self-supporting made of a doped perovskite ceramic, for example, lanthanum manganite doped with calcium, strontium, or cerium (approximately 1–3 mm thick).
- Thin, dense, gas-tight solid oxide electrolyte made of ceramic material, for example yttria-stabilised zirconia (approximately 1–100 μm thick) covering most of the outer periphery of the cathode, except a axial strip 9 mm wide extending along the entire active cell length.
- The exposed strip is covered by a thin, dense, gas-tight layer of an electrical interconnection ceramic material, for example, lanthanum chromite doped with calcium or strontium (approximately 30–100 μm thick), roughly similar in thickness to the solid electrolyte. This strip, termed the interconnection, is coupled by a conductor to an adjacent cell or power output contact.
- A porous anode made of a cermet material, for example, nickel-zirconia cermet, covers the outer periphery of the solid electrolyte surface (approximately 30–100 μm thick), except in the vicinity of the interconnection. Both the electrolyte and anode are spaced apart from the interconnection to avoid a short-circuit.
- An electrically conductive top layer of cermet material, for example nickel-zirconia cermet, also covers the outer periphery of the interconnection (approximately 30–100 μm thick), roughly similar in thickness to the fuel electrode. This prevents air from leaking to porous

cathode into the chamber filled with fuel (as would be the case because of the gap noted in the previous point).

- An optional porous calcia-stabilised zirconia support for supporting the inner periphery of the cathode tube can also be used, if necessary.
- Air is fed down a feeder tube to near the bottom of the cells, pre-heated to 1,000 °C.
- Gillett *et al.* (1998) claim that typically 25% of the air participates in the electrochemical reaction. However air is only 21 vol.% oxygen and it is unclear whether they meant that 25% of the oxygen is used.
- The fuel "concurrently directed to flow over the outside of the fuel cell" enters from the bottom closed end and moving upwards. This is a clever design element because even at room temperature hydrogen is light and may otherwise hardly react at all.
- The fuel is also preheated to 1,000 °C. Typically, 85% of the fuel is electrochemically oxidised. The remainder (spent fuel stream) is combusted with the spent air above the cell mixing it with the exhaust air in a combustion chamber. Note: One of the reasons SOFCs have low NOx is that the fuel reacts in a Nitrogen-free environment.

A further patent relating to the Siemens Westinghouse work is relevant. This is by Holmes *et al.* (2003) and aimed to improve the manifolding design of previous Siemens Westinghouse patented designs. Ancillary objectives included improvements to the insulation and designing power leads that require less cooling (apparently a problem in larger SOFC stacks) [Holmes *et al.* 2003]. This design is considerably improved, even over the rather clever modular system of Gillett *et al.* (1998). Yet it still has the same basic imitations that stem from the design of the cell tubes themselves, and is still rather bulky.

A typical system, as proposed by this patent, is comprised of stacks of 1,152, 22 mm OD, 1,500 mm active length tubular fuel cells, each generating 120 Watts, arranged in 12-bundle rows [Holmes *et al.* 2003]. Each stack would be fed from a fuel supply system including a recirculation system, ejector pumps, pre-reformer, and fuel manifold with riser tubes (that deliver raw fuel to the reformer and thence to the fuel manifold) [Holmes *et al.* 2003]. Air would be introduced through an inlet nozzle connected to a centrally located air manifold [Holmes *et al.* 2003]. The stack is intended to operate at temperatures "near 1,000 °C" according to the patent [Holmes *et al.* 2003].

Due to the high operating temperatures a significant amount of thermal insulation is required to prevent the outer metal casing from reaching unacceptable temperatures and to prevent high heat loss from the system. The patent proposes the use of bulk aluminosilicate ceramic fibres uniformly packed with a ceramic binder into different 'bricks' tailored to fit around other system components [Holmes *et al.* 2003]. In this way,

it is claimed reasonably enough, the outer container temperature can be maintained well below 60 °C by passive insulation alone without the added need for cooling jackets or air blowers. A metal liner divides the inner insulation and the system from the outer (lower grade) insulating material and the outer container [Holmes *et al.* 2003] serving both to limit fuel bypass and diffusion into the peripheral insulation system and to act as a radiative heat transfer shield minimising heat lost by that mode. *Caeteris paribus*, rather complex.

Despite its conceptual birth in the mid-1990s the microtubular design, while of immense interest academically, seems to be less attractive to those seeking to file patents in the area of SOFC technology. This is evidenced by the fact that only 10 out of 1,250 patents viewed related to the microtubular design directly (from 2000 to 2014), with a further 6 or so which may be but was undisclosed. Two of these were anode-supported designs [Huang and Ruka 2012, Sarkar *et al.* 2004]. Some display a tendency towards unnecessary complexity [Bischoff *et al.* 2007], often as a result of not being anode-supported designs. A particularly relevant design uses a separate metallic support tube on the outside, filed by Sarkar *et al.* (2004). The patent presents an ingenious technique for creating thin SOFC components on the inside of the support tube. The electrolyte, however, was 80 μm thick – eight times thicker than that achieved in this project using EB-PVD, as well as being on a separate support tube (an additional component). This patent illustrates the limitations of a sintering based approach and highlights the need to move to less conventional fabrication techniques to allow further miniaturization.

In summary therefore, the patents filed mostly related to the components of conventional planar stacks. A small number of patents relating to the tubular design were located, but few dealing with their miniaturization were found and all used sintering for fabrication. This shows quite clearly the magnitude of the hurdle that must be overcome for microtubular designs to become commercially viable. It is believed that academic publications on the performance of these designs and novel fabrication techniques will encourage institutions with the equipment and knowledge to venture into such designs, eventually increasing the number of patents filed and subsequently, it is hoped, the creation of a commercially viable system. This project, therefore, fits into an area of SOFC research that has seen much advancement of its components but not so for the fabrication of a miniaturised device.

2.13 Microtubular SOFC Design

The earliest reported microtubular designs appeared in the early 1990s with the, then emerging, technology that enabled the extrusion of thin-walled YSZ electrolyte tubes 1–5 mm in diameter with a wall thickness of 100–200 μm. The ionic conductivity and gas-tightness of such electrolyte tubes was reported to be good [Kendall, Minh and Singhal

2003] but is not quantified. The two major advantages of microtubular designs are as follows:

Firstly, there is a marked increase in volumetric power density compared with larger-diameter designs discussed previously. Power density scales with the reciprocal of tube diameter, *ergo* a 2 mm diameter microtubular SOFC provides ten times more power than a 20 mm diameter cell [Kendall, Minh and Singhal 2003, Funahashi *et al.* 2007, Suzuki *et al.* 2008b, Suzuki *et al.* 2009a, Yang *et al.* 2009]. While it may be possible to decrease diameters by another order of magnitude (increasing the power density by a further order of magnitude), such developments are difficult because connecting cells into stacks becomes increasingly problematic and the cells more fragile. Some sources [Kendall, Minh and Singhal 2003] cite the difficulty in applying and connecting the electrode and metal contact inside the bore of a very small diameter tube as the main concern. These authors seem to miss the great potential that exists in reversing the design, using an anode-supported cell having connection to the anode by masking deposition for a few mm at either end of the anode, and avoiding using wires to form electrical connections. Achieving this practically, then, is only a factor of correct jigging. Suzuki *et al.* (2008b, 2009a) expected that decreasing the diameter of tubular SOFCs will improve mechanical properties – a further reason to develop fabrication methods and technology for microtubular SOFCs with mm to sub mm diameters.

Secondly, tubular designs have better thermal shock resistance, but whereas the larger-diameter designs are still prone to cracking when rapidly heated [Kendall, Minh and Singhal 2003, Funahashi *et al.* 2007, Dal Grande *et al.* 2008, Suzuki *et al.* 2008b, Suzuki *et al.* 2009a, Yang *et al.* 2009, Monzón *et al.* 2014], microtubular designs do not crack even if heated to operating temperature over just a few seconds (making them far more capable of providing power on demand than other types of high temperature fuel cells – see section 1.5.9). This is by virtue of the nature of ceramics. Theoretical mechanical properties of ceramics are superlative, beyond even the best metallic alloys. The problem lies in the existence of defects. All ceramic parts contain defects, even if these are atomic in scale. The probabilistic nature means that ceramics are prone to fracturing at random sites with random frequency (according to a Weibull distribution). However, the smaller a ceramic part the greater the probability that it is virtually defect-free [Betts 2005], or at least the defects are small. As a result microtubular designs are likely to be near-defect-free structures and hence very resistant to thermal shock (stress caused by differential expansion and crack propagation from defect sites caused by large temperature gradients across the material) [Camilleri 2009]. This makes such designs of SOFC very useful where rapid start up or shut down would be a benefit, or indeed may be a requirement of the application. Load balancing modules in large central power stations or portable applications, for instance.

Typical microtubular SOFC designs are about 3 mm in diameter with a wall thickness of 150 μm, between 100 mm and 200 mm long. Many designs place the electrolyte on only a fraction of the length of the tube (some 30 mm) for an undisclosed reason [Kendall, Minh and Singhal 2003]. Possibly this is a performance testing issue; a short active length limits the output current. Papers and patents have been published in a steady stream since the early work in the 1990s, and a few companies (including Acumentrics Corporation, and Adelan Ltd.) have begun to develop microtubular SOFCs. "Efforts seem to focus on extrusion of the electrolyte, without exploring other fabrication methods. This narrow focus limits the potential of such microtubular SOFCs by *a priori* constraining the design without exploring alternatives, which is perhaps the reason they are not available on the market even after nearly two decades of development." [Camilleri 2009]

One major drawback with extrusion is the very high difficulty in developing electrolytes less than 100 μm thick, limiting performance [Kendall, Minh and Singhal 2003, Monzón *et al.* 2014]. Another major drawback is the length of time required by drying and debinding steps and all the preparation steps to create a suitable green. The state-of-the-art now permits 10 μm thick electrolytes to be extruded, though not without difficulty [see Connor 2010 for examples]. At this order of magnitude or smaller dip-coating is more facile [Suzuki *et al.* 2008a]. However, many opt for extrusion, advocating its well established technology and ability to mass produce cells [Monzón *et al.* 2014].

More on the state of the art is given here, from the work of Suzuki *et al.* (2009a). Their work led to the development of tubular SOFCs with diameters of 0.8–2.0 mm "operable at/under 550 °C."

Performance for single cells has been reported to achieve a maximum power density of over 1 Wcm^{-2} at 550 °C [Suzuki *et al.* 2009a]. A cubic bundle 1 cm^3 in volume was reported to achieve over 2 Wcm^{-3} at 0.7 V at 550 °C [Suzuki *et al.* 2009a]. The authors attribute the exceptional performance to optimisation of the electrode microstructure and the development of coating technology for fabrication of the electrolyte. I strongly agree with the authors' claim that "the key to realize such high-performance SOFCs lies in the design of the cell/bundle/stack and novel fabrication technology that can realize optimized electrode structures." In all cases the underpinning principle that makes this possible is miniaturisation.

Compare this to a typical, recent, microtubular cell made by extrusion: Monzón *et al.* (2014) created single cells that were 50 mm long and 700 μm thick with an OD of 3.4 mm. Layer thicknesses as follows: 50 vol.%/50 vol.% Ni-YSZ anode 644 μm (by extrusion), YSZ electrolyte 22 μm (by dip coating) and graded LSM-YSZ ceramic cathode 34 μm (also by dip coating) [Monzón *et al.* 2014]. Their best performing cells

had electrolytes sintered at 1,450 °C, and yielded 0.5 V and 0.7 Wcm^{-2} at 850 °C [Monzón *et al.* 2014]. These were however rather porous and also exhibited high ohmic resistance. From their EIS plots the optimal operating conditions for their cells at 850 °C would be at a current density of 0.7 Acm^{-2}, giving 0.5 Wcm^{-2} at 0.75 V, though the authors fail to mention this, opting to discuss only the maximum values of each in isolation. They report improved reproducibility and green strength for handling compared to isostatic pressing methods [Monzón *et al.* 2014].

Currently, there is much attention garnered by attempts to lower the operating temperature to the intermediate range, usually defined as below 650 °C. This shift is motivated by the attendant decrease in material degradation compared to higher temperatures, prolonging operating life and reducing cost (lower temperatures enables metals to be used for many components) [Suzuki *et al.* 2008b, Meng *et al.* 2009, Suzuki *et al.* 2009a], and potentially improving performance. Stratagems to reduce the operating temperature have been divided into three main groupings, following [Suzuki *et al.* 2008b, Suzuki *et al.* 2009a]:

1. Adopting new anode, electrolyte, and cathode materials.
2. Reducing the electrolyte thickness of conventional electrolyte materials (YSZ with different levels of doping). This is often constrained by the fabrication methods and technologies available.
3. Designing new structures for electrodes and electrolytes.
4. Novel system designs such as thermal self-sustainability where the reaction enthalpy of hydrocarbon oxidation over the anode is used to heat the cells.

One particularly well-known hurdle to reducing the operating temperature is the poor activity of the cathode material conventionally used (Lanthanum-doped Manganites – LSM) [Suzuki *et al.* 2009a]. The search for better cathode materials has seen considerable research interest, with some promising results. In particular a peak power density of 1.01 Wcm^{-2} at 600 °C was achieved using a (Ba, Sr) (Co, Fe)O_3 cathode with a ceria-based electrolyte [Suzuki *et al.* 2009a]. Some new anode and electrolyte materials have also been reported, including a Ru-Ni-ceria based anode and ceria electrolyte yielding a power density of 0.8 Wcm^{-2} at 600 °C, and over 1.9 Wcm^{-2} using a $LaGaO_3$-based electrolyte at the same temperature [Suzuki *et al.* 2009a]. For further details refer to the cited source and references therein. The introduction of doped ceria to electrodes and electrolytes seems to be of importance to enhance the performance of IT-SOFCs (intermediate temperature SOFCs) [Suzuki *et al.* 2009a]. Despite the higher electronic conductivity in reducing atmospheres, leading to losses across any ceria-based electrolyte that lowers the OCV to about 0.8 V from 0.9 V, the high power output has attracted considerable attention as electrolyte materials for operation at about 600 °C. Yet this is not the case for SOFCs intended for large scale, or even relatively large

scale, power generation, where the energy efficiency is paramount. Any losses (especially a drop in the already low OCV) are fundamentally unacceptable; all but precluding the use of ceria- and gadolinia-based electrolytes.

Thus far we may identify three basic designs of micro-SOFCs from the literature (see also the review paper by Wei [2008]): micro-tubular, micro-planar and honeycomb. The μ-planar designs are based on Si-wafer technology with dimensions down to the hundreds of nm (approaching the lithographic limits used in the microelectronics industry) [Wei 2008]. The μ-tubular designs have diameters from 0.8 mm to 2.5 mm (with a general trend towards smaller diameters) [Wei 2008]. These are usually arranged in stacks of 25 cells in a 5×5 array occupying a mere 1 cm^3 [Funahashi *et al.* 2007, Funahashi *et al.* 2008, Suzuki *et al.* 2008a, Suzuki *et al.* 2008b, Suzuki *et al.* 2008c, Wei 2008, Funahashi *et al.* 2009, Suzuki *et al.* 2009a, Suzuki *et al.* 2009b].

The AIST project in Japan that ran from July 2005 to March 2010 is one of the best-known recent examples developing millimetre-scale SOFC stacks [Wei 2008]. Under the aegis of this project 1 cm^3 cubical stacks were developed. Initially the SOFC tubes were cathode-supported having a 2 mm OD porous cathode tube onto which a 5–10 μm electrolyte and anode were layered [Wei 2008]. Such stacks have an OCV of 2.5 V and a peak volumetric power density of ~ 0.3 Wcm^{-3} at 400 °C (inlet fuel temperature rather than cell temperature) [Wei 2008]. Later the diameter was reduced to 0.8 mm seeing an increase in peak area specific power density to 0.5 Wcm^{-2} at 650 °C, and a volumetric power density for the whole stack of 3.0 Wcm^{-3} [Wei 2008].

In October 2006 NGK Insulators (associated with AIST) began a project to create a honeycomb-type micro-SOFC [Wei 2008]. Their design utilizes a LSM (strontium-doped lanthanum manganite) structure consisting of a square honeycomb of porous tubes. Each square-form hole was 0.7 mm on a side and coated with 20 μm of scandium zirconate (Sc ZrO_2) as the electrolyte and 10 μm of Ni-GDC cermet as the anode [Wei 2008]. Unfortunately some of the sources cited by Wei (2008) could not be found so the deposition technique is unknown. A similar design was created by Kyushu University using $La_{0.9}Sr_{0.1}Ga_{0.8}Mg_{0.2}O_3$ (LSGM) for the electrolyte, a Ni-Fe_3O_4 anode, and a $Sm_{0.5}Sr_{0.5}CoO_3$ (SSC55) cathode [Wei 2008]. These are fairly exotic materials and one cannot help but wonder how the material selection was justified. Both designs used a stainless steel manifold on both sides of the honeycomb to feed the fuel and oxidant [Wei 2008]. Power density is reported by Wei (2008) to be 0.4 Wcm^{-2} at 800 °C and 0.23 Wcm^{-2} at 700 °C. This corresponds to an estimated volumetric power density of 1.4 Wcm^{-3} [Wei 2008].

An interesting planar system, included for comparison with tubular ones, is the ONEBAT system developed by ETH (Europe) [Wei 2008]. It is a cigarette-sized cassette that comprises a planar fuel cell, thermal insulation, gas reformer, fuel canister

and thermal and power management systems [Wei 2008]. The planar cells were free-standing on a Si wafer reinforced by a Ni grid with 5 mm holes for fuel manifolding [Wei 2008]. The cathode was a mere 12 nm thick, the electrolyte 500 nm and the Pt anode 30 nm thick, with a Ni grid or mesh for current collection [Wei 2008].

Tube diameter determines the area available to the electrochemical reactions. State of the art extrusion techniques are capable of creating tubes with a diameter of 0.8 mm with a 200 micron wall thickness (i.e. a very narrow channel only some 400 microns across). Planar cells that function with thicknesses of the total cell at 680 nm or so point to the fact that there is still considerable improvement possible with tubular designs in terms of reducing thickness still further [Wei 2008].

Of concern for gas transport through narrow gaps is the mean free path (mfp) of the molecules relative to the gap size (S) given by [Wei 2008]:

$$mfp = \frac{1}{\sqrt{2\pi d 2n}} \qquad (2.10)$$

Where n is the number of molecules per unit volume, p/kT, d is the diameter of gas molecule (1.5×10^{-10} m), and k is Boltzmann's Constant (1.38×10^{-23} J atom^{-1} K^{-1}).

Example: Hydrogen diffusing at 600 °C (827 K) and at a pressure (p) of 2 atm (2.026×10^{5} Pa). The n value is 1.77×10^{25} atom m^{-3}, and the mfp is 5.65×10^{-7} m, or 0.565 microns. If the gap (S) is >5 mfp (>2.8 µm), then the diffusion of H_2 is normal diffusion.

The diffusion behaviour of gaseous species (hydrogen, oxygen, carbon monoxide, water, and others) is in the same order of magnitude [Wei 2008]. Therefore, the minimum gap for the transportation of the reactant gases by normal diffusion is in the range of a few micrometres. However, differential effects such as the size of gas species, the temperature distribution, the adsorption of gas molecules, and the pressure variation in the cells should be carefully addressed and studied since there is a lower bound to the suitable channel size [Wei 2008].

Suzuki *et al.* (2009a) acknowledge SOFCs as a keystone of the future energy economy, citing two further sources sharing this recognition. Their work on fabrication and stack integration focussed on improvement of the state-of-the-art through microtubular geometry and stack design with a mind to manufacturability. The salient point inferred from Suzuki *et al.* (2009a) is the benefit of reducing cell diameters to about 1 mm. However, this may require dropping the cell length to just 10 mm to prevent deleterious fuel pressure drops along the anode length causing performance loss and non-uniform

performance. In terms of aspect ratio the ideal seems around 10:1. The current cell design presented in this thesis has an aspect ratio of about 80:6, which is very close.

Their work also shows that the volumetric power density increases dramatically when the cell diameter is sub-millimetric [Suzuki *et al.* 2009a]. One of the principal reasons for this is the increase in the ratio of electrode area (tube surface) to cell volume (tube volume). The pressure drop becomes large only when diameters are below 100 microns [Suzuki *et al.* 2009a]. *Ergo*, microtubular SOFCs with diameters of a few mm to just sub-millimetric are highly advantageous for creating high power density energy sources.

During fabrication by the method described in Suzuki *et al.* (2009a) it is possible to control and optimise the anode microstructure by varying the sintering temperature and the amount of pore former added to the green. Changes in sintering behaviour due to the addition of a pore former may cause defects in the electrolyte layer during the co-sintering step, and therefore needs to be avoided [Suzuki *et al.* 2009a]. Suzuki *et al.* (2009a) found that PMMA beads (poly methyl methacrylate) as pore former in any proportion do not alter the sintering behaviour of the anode green, unlike carbon powder. The interested reader is referred to the cited reference; in particular the resulting microstructure of the sintered tubes. They report up to 51% porosity after reduction when sintering with 40 vol.% PMMA beads with a three dimensional network of (presumably connected) pores of predominantly 1 μm diameter [Suzuki *et al.* 2009a].

Their method suggests dip coating as a means to cost-effective mass manufacture [Suzuki *et al.* 2009a]. Dip coating permits facile control of layer thickness by controlling the pull speed, applying multiple coatings and changing the powder concentration in the slurry. By investigating the shrinkage of components at different sintering temperatures Suzuki *et al.* (2009a) determined that the GDC (gadolinia doped ceria) electrolyte was best sintered at temperatures at or above 1,300 °C, The shrinkage of the anode green during sintering also influences electrolyte densification, and the interested reader is encouraged to read the cited source for additional details on fabricating microtubular fuel cells by the state of the art conventional method (extrusion and/or dip coating ceramic greens followed by sintering and perhaps reduction also). The final manufacturing steps involved pre-calcination at 1,300 °C and sintering at 1,450 °C for 6 h, co-sintering all the components [Suzuki *et al.* 2009a].

After sintering the (GDC) electrolyte at 1,400 °C, for 1 h, deposited with pulling speeds of 1.0, 2.0, and 3.0 mm/s a thickness of 13–22 μm was obtained by changing the pulling speed of the dip coater [Suzuki *et al.* 2009a]. The thickness of the electrolyte layer also depends on upon the concentration of the powder in the slurry [Suzuki *et al.* 2009a]. Co-sintering anode and electrolyte as described in that work yielded a crack-free electrolyte without delaminating from the anode tube [Suzuki *et al.* 2009a]. Note however that no detail is given on the minimum layer thickness for the dip coating.

The first part (reviewed in above sections regarding fabrication) of the cited article is fundamentally the same sort of work I carried out for my MSc – creating and analysing a fabrication process and its control of microstructure. Other work by Suzuki *et al.* developed novel stack designs as well as testing the performance of their design [Funahashi *et al.* 2007, Funahashi *et al.* 2008, Suzuki *et al.* 2008a, Suzuki *et al.* 2008b, Suzuki *et al.* 2008c, Funahashi *et al.* 2009, Suzuki *et al.* 2009b].

3 Material Selection and Geometrical Design of a Microtubular SOFC

The objective of this chapter is to justify the choice of materials for each component, essentially forming a bill of materials. Also, because fabrication is virtually inseparable from material selection, especially for ceramic components, some additional notes on the fabrication of each component are included. The reviews by Tsipis and Kharton (2008a, 2008b) and Mahato *et al.* (2015) are comprehensive and recommended for further reading on the subject of available materials and their implementation. The final element is the geometrical design. Despite the apparent simplicity an explicit schematic and description were deemed essential for inclusion. An yttrium stabilised zirconia or gadolinia-doped ceria electrolyte with a Ni-YSZ anode and a strontium-doped lanthanum manganite (LSM) or gadolinia-and-strontium-doped-manganite (LSGM) cathode is the state-of-the-art for SOFCs, both planar and tubular [Larminie and Dicks 2003, Dal Grande *et al.* 2008, Mahato *et al.* 2015].

3.1 Anode Material

3.1.1 Anode Requirements

Anodes for SOFCs are required to possess a stringent combination of properties that makes material selection challenging. Required properties include: high electrical conductivity, high catalytic activity for fuel oxidation (hydrogen reduction) and chemical stability (particularly chemical expansion and cation interdiffusion) as well as thermomechanical compatibility with the other component materials under operating conditions [Larminie and Dicks 2003, Yokokawa and Horita 2003, Tsipis and Kharton 2008a, Tsipis and Kharton 2008b, Mahato *et al.* 2015].

The issue of long term stability is perhaps the most complex, and many factors combine increasing the difficulty in determining a suitable material. The anode must withstand thermal cycling between its operating temperature and ambient temperature, while also having a coefficient of thermal expansion that is not too dissimilar from the electrolyte's to prevent damage to the latter. The chemical equilibrium between fuel gas and reaction products inside the anode results in an oxygen partial pressure that, while low, varies over a range of several orders of magnitude [Camilleri 2009]. The anode material must be chemically and mechanically stable under these variable conditions.

This is especially true of metallic components that may be degraded by oxidation or corroded by reaction products. The electrical properties and lattice geometry of the anode may change due to variations in stoichiometry brought about by the anode

reaction as well as microstructural changes from mechanisms such as creep and grain coarsening, Finally, the chemical compatibility (part of the stability challenges) must be such that no solid solutions form during either fabrication or operation. Solid solutions are commonly caused by interdiffusion between the anode and electrolyte elements possible at elevated temperatures. Such interdiffusion creates new phases that increase electrical resistivity as well as reducing the available reaction sites [McEvoy 2003]. Note that this is different from a cermet. Should interdiffusion somehow result in mixing the anode and electrolyte phases (without creating a solid solution) at the interface the anode would actually be improved by extending the thee-phase boundary (see section 4.2.5). Many of these requirements also apply to the interface between anode and interconnect material if any is used. In most cases all the factors above must not only be considered for the operating environment but also for the fabrication technique employed. A brief note on electrocatalytic activity: while important for the anode reaction, such a material would ideally not be overly active as this leads to side reactions, such as the deposition of carbon from carbonaceous fuels [McEvoy 2003].

Only a handful of metallic and ceramic materials are therefore up to the task. Pure metals, as discussed above, are not generally seen as suitable in the long term due to oxidation in the partial oxygen pressure present at the anode, aggregation that effectively eliminates the three-phase boundary, or spalling under operating conditions [McEvoy 2003, Meng *et al.* 2009]. Pure ceramic anodes, on the other end of the scale, are a very recent development and much remains unknown. Of the noble metals platinum, palladium and rhodium offer the best performance as hydrogen catalysts [Heath and Sweeney 1963, Larminie and Dicks 2003]. They remain, however, exorbitantly expensive exacerbating the economic challenges that need to be overcome before commercialisable SOFCs are possible [Camilleri 2009]. Unfortunately group Ib metals and their oxides are not nearly as effective.

Reducing operating temperature to the intermediate range (IT-SOFCs) is of benefit here also in that it reduces degradation over time. Metallic-supported anodes have several advantages over ceramic ones in addition to reduced costs, including excellent catalysis, reduced concentration polarisation and easier fabrication [Meng *et al.* 2009].

At the very least electrode stability must be no worse than that of the electrolyte employed [Camilleri 2009]. The electrode must not react with the fuel or electrolyte in any way, in accordance with the definition of a catalyst. Fuel electrode (anode) stability is generally a trivial problem since many practically useful electrode materials of the transition metal type are resistant to corrosion in reducing atmospheres at the temperatures involved. Stability of the grains, pore structure, resistance to thermal stress and electrode insolubility in the electrolyte are again requirements for long term stability in operation of the fuel cell electrodes [Gorin and Recht 1963]. Table 3-1. summarises the major aspects (and requirements) of anode development.

Of Primary Importance	Of Secondary Importance
1. Porosity	1. CTE match with Electrolyte
2. Long term stability	2. Chemical compatibility with Electrolyte
3. Fabrication and processing costs	3. Electrical conductivity (must be sufficient material for conduction – but no more)
	4. Structural strength and thermal cycling resistance.

Table 3-1. Summary of major challenges and requirements of anode development.

3.1.2 Nickel Anodes

In much the same way as cathodes, early experiments used precious metals like platinum and gold, and transition metals like iron and nickel [Larminie and Dicks 2003, McEvoy 2003]. Unfortunately platinum anodes tend to spall off after a few hours, and porous nickel has a tendency to aggregate, reducing porosity and therefore long term effectiveness as an anode at high temperatures [McEvoy 2003].

The transition metals have varying degrees of performance as catalysts for hydrogen. Nickel is among the best, being only some 2% worse in terms of polarisation for a given current than platinum [McEvoy 2003]. For this reason nickel was deemed not only a suitable catalytic material for the anode but actually an excellent one [Dal Grande *et al.* 2008]. Additionally Ni has a high electrical conductivity. The greatest difficulty with metallic anodes made of Ni is the thermal expansion coefficient mismatch (13×10^{-6} $°K^{-1}$ compared to 11×10^{-6} $°K^{-1}$ for YSZ) and low wettability on YSZ. More on this is in section 3.2.1. Long term stability of a porous Ni electrode may also be problematic.

3.1.3 Nickel Cermet Anodes

The accepted alternative to a single-phase anode is a cermet; a porous composite of metallic and ceramic components sometimes called composite electrodes [Larminie and Dicks 2003, McEvoy 2003], or graded electrodes when the composition is varied (continuously or step-wise) from pure nickel at the outermost end of the anode to pure electrolyte material at the interface with the electrolyte. In these electrolyte particles are mixed in with the nickel matrix. Nickel cermet anodes suffer from carbon fouling when carbonaceous fuels are used, but otherwise provide adequate performance [Larminie and Dicks 2003, McEvoy 2003, Camilleri 2009]. Despite only adequate performance, nickel cermets have proved to be the most successful anode design for SOFCs to date [McEvoy 2003, Meng *et al.* 2009 and also refer to sections 2.12 and 2.13, regarding tubular fuel cell development and patents]. An interesting additional benefit is that Ni is known as a good catalyst for hydrocarbon cracking, giving it added fuel flexibility [Khaleel and Selman 2003].

The ceramic acts to inhibit aggregation by separating the nickel particles and preventing grain growth, maintaining the three-phase boundary and therefore achieving an adequate lifetime [Larminie and Dicks 2003, McEvoy 2003, Meng *et al.* 2009]. In

addition it helps adhesion between the anode and the electrolyte as well as acting to blur the boundary between the two so reducing the effective linear coefficient of thermal expansion mismatch – lowering thermally-induced stress and hence achieving greater thermal cycle resistance [Larminie and Dicks 2003, Meng *et al.* 2009]. McEvoy (2003) observed that the oxygen ion conductivity of the electrolyte particles in the anode has the secondary benefit of extending the three-phase boundary (the electrochemically active reaction zone). Ni-YSZ cermets do have one major drawback. These cermets are catalytically active to the point of allowing the deposition of solid carbon (called carbon fouling) with any carbonaceous fuel (e.g. hydrocarbons) [McEvoy 2003]. The carbon deposits obstruct pores, reduce available reaction sites and overall lower the cell performance. Unfortunately, anodes, especially in anode-supported cells, necessitate high metal content precluding the use of precious metals like platinum or rhodium that are more resistant to carbon deposition than nickel. Currently there is great interest in developing nickel-based anodes that are sufficiently active for hydrocarbon reforming under SOFC operating conditions while being suitably resistant to carbon deposition [Ormerod 2003, Connor 2010]. The incorporation of dopants including gold, molybdenum and copper and the addition of ceria to nickel-YSZ cermets are two possible routes mentioned in Ormerod (2003). Hydrogen was the fuel selected for this project eliminating any risk of carbon fouling (though that was not the main driver behind the choice). The reader is referred to the cited authors for the use of Ni-YSZ cermets with other fuels, the effect of carbon monoxide, sulphur poisoning and so on.

This may not be all there is to it, however. "Based on the review conducted, we find that cubic fluorite-structured compounds are the most promising anode materials reported thus far. Analyses of the structure and electrical performance of anode materials show as well that copper–gadolinium-doped cerium oxide (Cu–GDC) cubic fluorite-structured anodes exhibit higher electronic conductivity potential than yttria-stabilized zirconia-based anode materials." [Shaikh *et al.* 2015] The review by Mahato *et al.* (2015) is more cautious in outlook but reports similar findings. Once the novel anode fabrication technique developed for this project has been sufficiently refined the creation of a cermet is eminently desirable. Fortunately, this is relatively easily achieved using EB-PVD provided the system has the necessary elements (see electrolyte fabrication in section 3.4). In essence a base Ni anode is created as described in this thesis, then immediately prior to depositing the electrolyte a Ni cermet is deposited in the PVD chamber that smoothly grades to purely YSZ and thence some further thickness deposited as electrolyte. This could include elements of a Cu-GDC system also. Future work will enable optimization of a tubular anode suitable for large scale commercialization (see also chapter 17).

3.2 Anode Fabrication

3.2.1 Conventional

Nickel is the most widespread anode material used in SOFCs since 1964 because of a combination of known performance and economics [Singhal and Kendall 2003, Gorin and Recht 1963]. Unfortunately, metallic Ni does not adhere strongly to YSZ and flakes off unless it is mixed with zirconia when using conventional fabrication techniques (based on sintering). The flaking is caused by a large difference in expansion coefficient between YSZ and Ni: YSZ at around 11×10^{-6} °K^{-1} and Ni at 13.3×10^{-6} °K^{-1}. Powder mixing 30 vol.% NiO with YSZ and firing at 1,300 °C in hydrogen to creates a porous layer by reduction [Singhal and Kendall 2003]. The mismatch is greatly reduced – the nickel cermet having an expansion coefficient of 12.5×10^{-6} °K^{-1} – and adhesion is proportionally improved.

The conventional sintering-based route utilizes Spacil's formulation [McEvoy 2003] or a similar variant to create a cermet: NiO powder mixed with YSZ powder in an aqueous slurry of the type used for slip casting. The slurry is applied to the electrolyte surface and fired at a temperature of up to 1,550 °C [McEvoy 2003]. Subsequently it is heat treated again in a hydrogen atmosphere at a temperature in the range 850 °C – 1,000 °C reducing the NiO to metal in order to provide a percolation path for electrons through the [McEvoy 2003]. The volume is reduced by 25% during the reduction step, enhancing the porosity (advantageous for the anode) [Dal Grande *et al.* 2008]. The use of extrusion is also a popular fabrication technique that has enabled fairly thin SOFCs to be made [Cho and Choi 2009, Monzón *et al.* 2014]. However, such tubes have poor a microstructure leading to a large ohmic loss [Yang *et al.* 2009, Monzón *et al.* 2014].

An intimate bonding on the nanometre scale is necessary for the formation of the cermet and the establishment of the three-phase boundary necessitating some level of wetting (physicochemical interaction) between metal and ceramic [McEvoy 2003]. In an unmodified state the affinity of metallic nickel for zirconia is weak, with a contact angle of 120° [McEvoy 2003]. "In order to promote bonding in practice the powder specifications are chosen to ensure a sufficient surface activity." The limited affinity of zirconia for nickel is in fact rather useful as it prevents the formation of unwanted phases (solid solutions) that would increase electrical resistance and reduce the number of available reaction sites [McEvoy 2003].

The route to conventional anode optimization is control of the cermet morphology. The original formulation used by Spacil used a large proportion of nickel (some 50 vol.%), reduced from NiO of around 45 μm grain size with non-connected inclusions of 10 μm zirconia after sintering [McEvoy 2003]. The coefficient of thermal expansion was high, leading to a large mismatch with the electrolyte because there was more nickel than needed for electronic percolation conductivity (anything above this does not contribute

anything but increases the CTE mismatch). Furthermore, the low proportion of ceramic in the cermet, and its lack of connectivity, allowed nickel aggregation in the long run [McEvoy 2003]. For this formulation a temperature of 1,550 °C was reported to be necessary to sinter the anode to the electrolyte [McEvoy 2003]. Modern submicron ceramic powders sinter at 1,400 °C and provide a higher surface area to volume ratio – useful in enhancing anode reaction efficiency by providing more reaction sites [McEvoy 2003]. The powder mixture is typically applied onto the YSZ electrolyte (generally around 150 μm thick) [McEvoy 2003].

Lower temperature (800 °C), anode-supported cell designs have somewhat less stringent material requirements by virtue of the lower operating temperature. For such cell designs the YSZ electrolyte thickness must be reduced to just tens of microns or the power output will be unacceptably low due to its significantly lower conductivity at lower temperature [McEvoy 2003, Dal Grande *et al.* 2008]. *Ergo* the need for an anode supported design now that the electrolyte is too thin and fragile to provide any sort of structural support [Camilleri 2009]. Anodes for anode-supported designs tend to be a few hundred microns thick [Funahashi *et al.* 2007, Funahashi *et al.* 2008, Suzuki *et al.* 2008a, Suzuki *et al.* 2008b, Suzuki *et al.* 2008c, Funahashi *et al.* 2009, Suzuki *et al.* 2009b]. These, much thicker, anodes usually need to be graded with a higher porosity near the fuel gas supply and a lower porosity but higher catalytic activity (higher Ni content) nearer the electrolyte [McEvoy 2003, Yang *et al.* 2009].

For some examples of unconventional anode manufacturing methods the interested reader is referred to Camilleri [2009] and the review by Coddet *et al.* (2014).

3.2.2 This Project

For this project a cermet was not used because of the difficulty in creating one using EB-PVD. This requires a particular setup of coater (with two ingots, one of pure Ni and the other of YSZ) that was not available. An example of this fabrication technique in use can be found in the work of Meng *et al.* (2008, 2009). The author would like to emphasize that EB-PVD has exhibited characteristics marking it as clearly superior in the fabrication of such graded anodes [Meng *et al.* 2009]: can deposit a continuously varying composition, offers high deposition rates, large deposition area and good adhesion. Instead a pure nickel one was used because operation times would be very short and the fabrication technique is believed to yield highly porous anodes (only limited evidence prior to this project was available, see Camilleri (2009) for details) this limiting greatly the likelihood of porosity decreasing with time.

Further work is necessary both to assess the long term stability of purely metallic nickel anodes (particularly in terms of nickel aggregation) and to determine the optimal technique for creating a graded cermet using the same EB-PVD technique used to create the electrolyte. Another interesting possibility, for creating not only the anode but the

entire cell, is presented in the work by Yang *et al.* (2009) and is based on creation of a hollow fibre ceramic anode. However, the manufacturing technique is reported to take days and seems to be rather approximate (and not optimised at all). Furthermore, much of the fabrication was carried out manually in a complex and highly involved process exacerbating problems of repeatability.

One major challenge is creating a metallic support with controlled porosity both in terms of pore size and porosity [Panteix *et al.* 2009]. The cited paper presents an interesting discussion on grain morphology with respect to the effect on porosity, as well as a novel technique for achieving the porosity based on a metal slurry that is compacted, sintered, and finally reduced. In my MSc thesis [Camilleri 2009] I investigated a number of alternative anode fabrication techniques, eventually creating a heat treatment technique in part inspired by Panteix *et al.* (2009) that has great promise for SOFC miniaturisation and large scale manufacture (see 8.9).

3.3 Electrolyte Material

The electrolyte material must have good ionic conductivity yet possess a low (ideally zero) electronic conductivity at the cell operating temperature [Ishihara *et al.* 2003, Larminie and Dicks 2003, Tsipis and Kharton 2008a, Tsipis and Kharton 2008b]. In addition it needs to be of sufficient stability in both oxidising and reducing environments, unlike the electrodes which must each be stable under only one of those conditions. Also highly desirable from a purely material perspective is that the electrolyte material has a good thermal cycling resistance (some combination of high strength, good ductility, low CTE and compliant morphology). YSZ, a ceramic with the fluorite structure, has so far dominated as the state of the art material of choice for SOFC electrolytes [Yashima *et al.* 1996, Larminie and Dicks 2003, Yang *et al.* 2009]. Other fluorite structures such as doped ceria have also garnered interest for cells operating at intermediate temperatures. Other ceramic structures, including perovskites, brownmillerites and hexagonal close packed (HCP) oxides, possessing good ionic conductivity, have received some interest [Ishihara *et al.* 2003].

Oxide ion transport in a solid electrolyte was first observed in ZrO_2 (zirconia) doped with 15 wt.% Y_2O_3 (yttria), usually referred to as yttria-stabilised zirconia (YSZ) by Nernst in the 1890s [Ishihara *et al.* 2003]. In 1937 the first SOFC was constructed by Baur and Preis using YSZ as the electrolyte [Ishihara *et al.* 2003]. For more on the history of this type of oxides as used in SOFCs please refer to the cited reference, and the review quoted therein.

Ionic conductivity is temperature dependent, as shown in Figure 3-1. below. Notice that YSZ is not the best performer among the most commonly employed electrolyte materials.

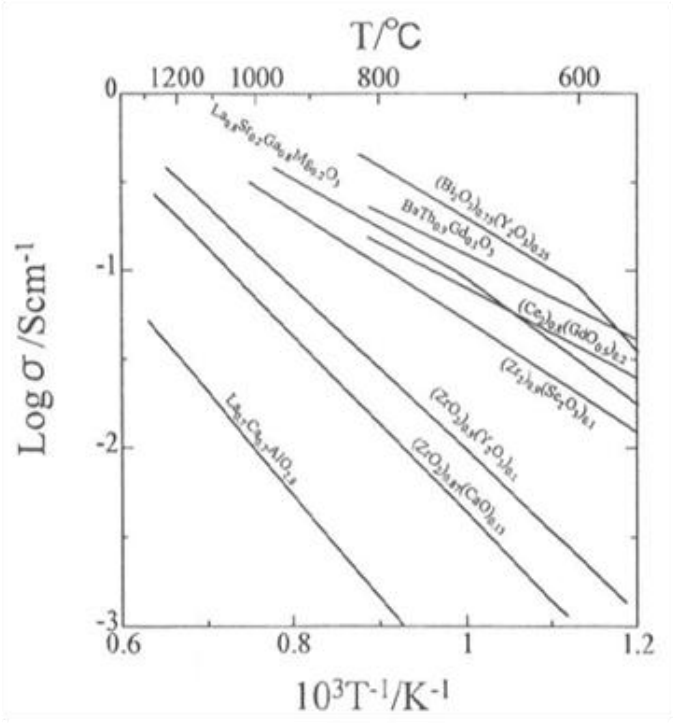

Figure 3-1. Temperature dependence of the ionic conductivity of some common oxide ion conductors [Ishihara *et al.* 2003].

Bismuth oxide compositions boast the highest ionic conductivity, and other compounds are also superior in this respect to YSZ particularly at the lower end of the temperature range and below 600 °C [Ishihara *et al.* 2003]. However, these other materials suffer from some serious disadvantages such as higher electronic conductivity, complex processing, rapid deterioration during use and higher cost.

3.3.1 Fluorite-Structured Electrolytes

The fluorite structure is a face centred cubic (FCC) crystal lattice of cations with anions occupying the tetrahedral sites. The resulting structure has a large number of octahedral interstitial voids [Ishihara *et al.* 2003, Betts 2005]. This, relatively open, structure is believed to lead to the rapid diffusion and high mobility of ions. At elevated temperatures zirconia naturally transitions to the fluorite (FCC) structure (often referred to as the cubic phase of YSZ) but requires stabilisation (doping) with aliovalent (that is can be both divalent and trivalent) cations like calcium (Ca) and yttrium (Y) to retain this ion-conducting structure at lower temperatures [Ishihara *et al.* 2003, Betts 2005]. Oxide ion conduction is provided by the oxide ion vacancies and interstitial oxide ions (in the aforementioned voids). Intrinsic defects (voids) are determined by

thermodynamic equilibrium of the pure compound, while extrinsic defects (interstitials and vacancies) are created by the presence of the aliovalent dopants. This occurs by the usual mechanisms where defects (e.g. Schottky defects) are introduced to maintain electrical neutrality in the presence of the aliovalent cations.

The lowest practical operating temperature for thin YSZ electrolytes is estimated to be about 700 °C from the ionic conductivity and mechanical properties for various temperatures [Ishihara *et al.* 2003]. It has been shown [Yashima *et al.* 1996, Ishihara *et al.* 2003] that the maximum ionic conductivity at 1,000 °C for YSZ of about $0.14\ S/\mathrm{cm}$ occurs at about 8–10 mol.% yttria, lower than predicted by the theoretical approach presented by Ishihara *et al.* (2003). This limiting effect has been attributed to the dopant ionic radius that influences the diffusion of oxide ion interstitials and oxide ion vacancies between the bulk and dopant cations [Ishihara *et al.* 2003]. The phase also has a marked effect with the metastable cubic phase preferred (8–10 mol.% yttria). The tetragonal-cubic phase boundary is strongly affected by oxygen stoichiometry [Yashima *et al.* 1996]. Refer to the cited text for more detail on conductivity as a function of dopant ionic radius and dopant concentration (mol.%) for the various dopants used to stabilise zirconia. It is likely porosity (as opposed to atomic vacancies) may also be of import to ionic conduction, but Ishihara *et al.* (2003) makes no mention of the porosity of the samples analysed so it is difficult to determine whether porosity was a factor leading to the lower ionic conductivity than predicted.

3.3.2 Zirconia-Based Ionic Conductors

A zirconia-based electrolyte was deemed the most suitable since according to the research highlighted above it is the least problematic, if not the best performing in terms of pure ionic conductivity. Of the possible zirconia-based systems, YSZ was selected since it is readily available and much experience is available at Cranfield University both in terms of understanding its material properties as well as its fabrication. The novelty of the deposition route selected for fabrication of the electrolyte and the extensive experience with its deposition using this technique to create TBCs (thermal barrier coatings) for aerospace at the National High Temperature Surface Engineering Laboratory at Cranfield further increased the attractiveness of YSZ as the electrolyte material, in accordance with my thoughts previously [Camilleri 2009].

YSZ exhibits good thermal stability, good chemical stability, high oxygen ion transfer, and excellent mechanical strength even at elevated temperatures [Yang *et al.* 2009, Coddet *et al.* 2014]. It also possesses an unusually high CTE for a ceramic ($2.0\times10^{-6}\ °K^{-1}$ according to Hass *et al.* 2001 and as much as $11.0\times10^{-6}\ °K^{-1}$ according to Zhao *et al.* 2006). This would normally be detrimental as a high CTE leads to large strains (and therefore high stresses), but in this case it means CTE of the metallic electrodes and the electrolyte are more closely matched than for other electrolytes.

The grain boundary (GB) exhibits a higher resistance to ionic transport than the grain interior (GI). This is attributed by Chang *et al.* (2011) to the aggregation of complex defects near the interfacial region between grains. That is grain boundaries reduce ionic transport because they are intrinsically unfavourable to ion transport [Chang *et al.* 2011]. It has been suggested that the paths created by GBs however, may facilitate rapid ionic conduction [Chang *et al.* 2011]: a fact that can be exploited through microstructural design of YSZ electrolytes. The authors note that it is difficult to investigate these molecular mechanisms experimentally and so molecular dynamics modelling was employed, and showed good agreement with experimentally reported results. These, and the importance of optimizing the YSZ composition, are discussed below.

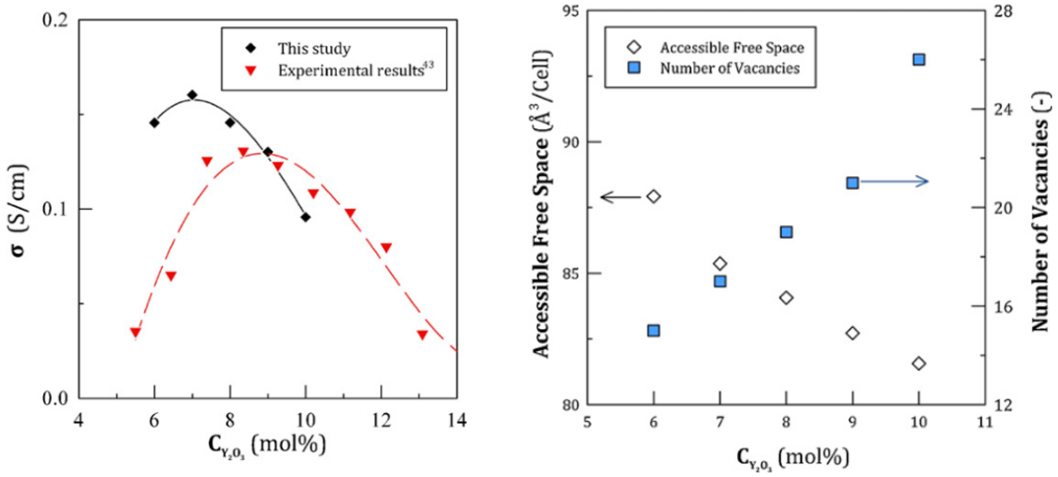

Figure 3-2. (left) Ionic conductivity with Y_2O_3 concentration at 1,273 °K from molecular dynamics simulation and experiment and (right) accessible free space and vacancy numbers of YSZ with Y_2O_3 concentration at 1,273 °K from simulation [Chang *et al.* 2011].

Increasing the concentration of the dopant (Y_2O_3) adds vacancies, which, in turn, form the pathways for oxygen ion transport [Chang *et al.* 2011]. However, at concentrations higher than 7 mol.%, paradoxically, the increasing vacancies no longer improve ion conduction but impede it [Chang *et al.* 2011]. The excess Y^{3+} in the YSZ system traps vacancies lowering their mobility and hence oxygen ion mobility and therefore oxygen ion transport rate (i.e. conduction) [Chang *et al.* 2011]. According to the model, therefore, the optimal composition for a doped zirconia electrolyte is 7 mol.% yttria. Chang *et al.* (2011) state that results of their simulation agree well with experiment and explain that the discrepancy can be attributed to the following factors: the size and duration of the simulation are less than in real systems due to computational limitations, and the selected potential function and parameters used in the model may contain errors.

The accessible free space represents the volume of pathways that is large enough for a hard sphere with radius equal to that of an oxygen ion to pass through the simulated

polycrystal [Chang *et al.* 2011]. A higher accessible free space value indicates a larger number of larger internal spaces or a greater connectivity among the vacancies in the structure (which may improve ionic conduction) [Chang *et al.* 2011]. Notice that the accessible free space decreased with increasing dopant concentration despite an increasing number of vacancies suggesting that vacancy connectivity may be reduced with increasing vacancy number [Chang *et al.* 2011]. It is also possible that the increasing concentration of yttira hinders the passage of oxygen ions [Chang *et al.* 2011]. Furthermore, at higher concentrations the distribution of vacancies may not be conducive to continuous ion transport [Chang *et al.* 2011].

The dislocations introduced with the addition of grain boundaries added a resistance to ion transport by hindering ionic hopping between vacancies across grains [Chang *et al.* 2011]. The authors compare this by means of two models, one with and the other without GBs, for the same composition (7 mol.% YSZ) and both at 1,273 °K. The former is labeled M-07-YSZ and the latter P-07-YSZ [Chang *et al.* 2011]. Note the substantially reduced displacements of oxygen ions in the simulation with grain boundaries included. For further details please refer to the cited source. For this thesis it is suffice to reproduce their graph of summarized results in Figure 3-3.

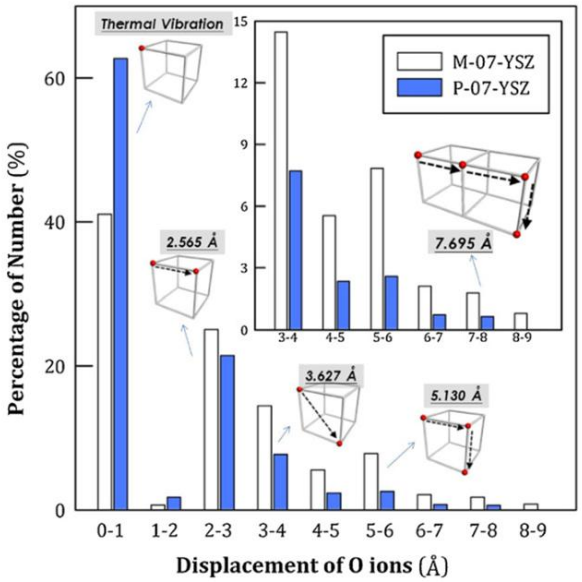

Figure 3-3. Comparison of the oxygen ion displacement of the simulations for M-07-YSZ and P-07-YSZ at 1,273 °K [Chang *et al.* 2011]. Categories shown are short, medium and long displacements in addition to thermal vibration. Also shown are the respective paths through a unit cell for each displacement category.

A similar situation arises when one considers oxygen ion diffusivity, as illustrated in Figure 3-4, below. Higher temperature increases the oxygen ion diffusivity in both cases. Higher temperature also increases kinetic energy that, in turn, increases ion velocity and directs ion motion [Chang *et al.* 2011]. Furthermore, the difference in ion

diffusivity in the presence and absence of GBs increases with increasing temperature [Chang *et al.* 2011]. The authors explain this is related to the fluorite structure: in a fluorite-structured electrolyte ionic conduction is induced when heated to 1,073 °K (for ceria based electrolytes) or 1,273 °K (for zirconia based electrolytes), at lower temperatures it is less clearly observable [Chang *et al.* 2011]. Since at elevated temperatures ion mobility is enhanced more ions displace larger distances and therefore interact with grain boundaries [Chang *et al.* 2011]. The probability of an ion interacting with a GB is therefore increased with temperature. So at elevated temperatures the intergrain resistance is dominant [Chang *et al.* 2011]. Note however, that elevated temperatures both impart greater migration velocity to ions as well as more easily overcomes the dissociation barrier that frees an ion to hop to the next site [Chang *et al.* 2011]. *Ergo*, the effect of grain boundary resistance decreases with temperature at very high temperatures [Chang *et al.* 2011].

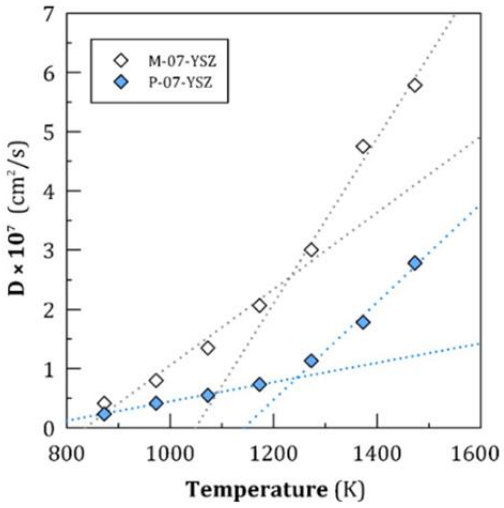

Figure 3-4. Oxygen ion diffusivities of the simulations for M-07-YSZ and P-07-YSZ with temperature [Chang *et al.* 2011].

For further detail on YSZ and other forms of doped zirconia, particularly phase diagrams and information about polymorphs, and comparison of different systems the interested reader is referred to Ishihara *et al.* (2003), Moulson and Herbert (2008), or any good ceramics textbook.

"To reduce ohmic losses, decreasing the electrolyte thickness and/or elaboration of alternative high-conductivity electrolytes is also inevitable." [Tsipis and Kharton 2008a] The same thought is expressed by Meng *et al.* (2008) and Ishihara *et al.* (2003). The latter recommend, for low ohmic polarisation (often the dominant polarisation loss in SOFCs), using an electrolyte no thicker than:

Temperature (℃)	Thickness (μm)	Conductivity (S/cm)
600	8.00	5.01×10^{-3}
650	20.00	10.00×10^{-3}
700	39.29	17.78×10^{-3}
750	56.25	33.98×10^{-3}
800	87.50	45.32×10^{-3}
850	140.00	69.78×10^{-3}
900	190.00	93.06×10^{-3}
950	285.71	133.35×10^{-3}
1,000	350.00	165.48×10^{-3}

Table 3-2. Relation between operating temperature, electrolyte thickness and conductivity for 9YSZ (9 mol.% $Y_2O_3 – ZrO_2$) [Ishihara *et al.* 2003].

Table 3-2. may be employed in two ways. Firstly, it can be used to determine the ionic conductivity of 9YSZ for all useful operating temperatures in the range shown (other temperatures can be determined by interpolation). Secondly it shows the thickness of electrolyte at any given temperature in the range with maximum ohmic polarisation acceptable for useful operation in a fuel cell (once more, intermediary values can be found by interpolation). It was assumed that 9YSZ is similar enough to 7YSZ (the composition available) that any differences in conductivity are negligible. This assumption is supported by the data given in Ishihara *et al.* (2003). While, of course, the values may be plotted as a graph the temperatures shown are the usual operating temperatures in the literature within this range, so it is more convenient to present the data in tabular form. There are significant discrepancies in values of CTE reported in the literature (see Appendix N: Material Data Tables for full listing and a solution to his problem).

A trade-off exists between higher ionic conductivity versus toughness. 8 mol.% YSZ is superior in terms of ionic performance, certainly suitable for planar systems and conventionally manufactured tubular ones (sintered). The situation is currently less well clear for EB-PVD coatings so toughness (4 mol.%) was emphasized with the potential to improve ionic performance later by adopting a different composition (one closer to fully stabilised; 8 mol.%).

3.3.3 Electrolyte Stability

For continuous operation the fuel cell reaction must not change once it has reached steady state. This imposes an additional restriction on the electrolyte material. The use of any solid oxide for extended periods of operation in a fuel cell invites recrystalisation of the oxide [Gorin and Recht 1963]. The high operating temperatures of SOFCs represent sufficient energy for the recrystallisation of the small grains into larger ones by ensuring sufficient mobility. The inherently higher energy of smaller grains compared to larger ones drives the process provided the energy barrier (energy needed for sufficient atomic, molecular and grain mobility) is available. While some grain

enlargement will always occur the problem is insignificant if the operating temperature is much lower than the melting point of the solid electrolyte, true of most ceramic electrolytes. Such conditions are less than optimal for performance, however, since higher ionic conductivity is naturally achieved at higher temperatures (high energy allows maximum mobility), and the maximum is *ergo* as close as possible to the melting point [Gorin and Recht 1963]. These opposing requirements complicate the design of any high performance fuel cell and necessarily imply some compromise between performance and long term stability must be reached. Recrystallisation is frequently accompanied by changes in geometry and crack formation, eventually leading to total cell failure [Gorin and Recht 1963]. Furthermore, the ionic species that carries the current by definition constitutes material transport. These changes in local composition instigate local recrystallisation events leading to continuous recrystallisation during operation [Gorin and Recht 1963]. Long term stability is a perennial problem with high temperature fuel cells [Camilleri 2009, Meng *et al.* 2009]. At best any solution is a compromise sacrificing performance; and yet long term stability is still inherently limited by the nature of ion transport in the solid electrolyte. The major aspects of electrolyte development are tabulated in Table 3-3., below.

Of Primary Importance	**Of Secondary Importance**
1. Ionic conductivity (for low polarisation)	1. CTE match with Anode and Cathode
2. Gas tightness	2. Chemical compatibility with Anode and Cathode
3. Fabrication and processing costs	3. Durability and thermal cycle resistance at elevated temperature
	4. Material costs

Table 3-3. Summary of major challenges to successful SOFC electrolyte development.

3.4 Electrolyte Fabrication

3.4.1 Conventional

From a fabrication viewpoint the electrolyte material must be capable of being fabricated as thin strong films, be gas tight, as well as ideally being relatively easy to fabricate and as low cost as possible [Ishihara *et al.* 2003, Larminie and Dicks 2003]. This is often achieved by extruding a green preform and sintering it, less commonly dip-coating or slurries are used – essentially employing methods traditionally associated with the fabrication of technical ceramics (all deposition methods eventually leading to a sintering step) [Ishihara *et al.* 2003]. It is worth noting that the widely-accepted sintering technique creates electrolytes some 150 μm thick – far thicker than envisaged for this design. The state of the art has settled at around 10 μm, with the best processes capable of achieving thicknesses of 1–3 μm (but reportedly only at considerable expense and often with unreported reproducibility). Sintering components (or more specifically creating self-supporting greens) thinner than a few hundred microns

becomes exceedingly difficult. Furthermore, Ni to YSZ adhesion (when they are deposited by dipping or as slurries then co-sintered) is known to be low [Chian and Li 2008]. The thinnest metallic anode, anode-supported SOFC reported at the time of my MSc (2009) that used a sintering process was 230 μm in total thickness [Cho and Choi 2009]. Compare these with the total thickness of 135 μm – 140 μm for this project. Other possibilities exist including sol-gel, chemical vapour deposition (CVD), and various physical vapour deposition (PVD) routes.

3.4.2 Unconventional

Over the last twenty years the PVD route has garnered much interest in the synthesis of solid electrolytes due to the excellent control of: film microstructure, porosity, stoichiometry (particularly if separate ingots for the yttria and zirconia are used) and deposition rate. Other advantages are less unique but no less valuable, including good adhesion, high deposition rate (as much as several microns per minute for an optimised process) and large deposition area. Whereas once costs greatly restricted use of the technology, these are now some 10% of what they were 40 years ago [Meng *et al.* 2008, Meng *et al.* 2009]. All this makes EB-PVD (electron beam physical vapour deposition, also called e-beam PVD) a very attractive technique for a wide range of applications, including fuel cells. In practice however, the PVD route has not been popular so far, probably due to complexity, capital expense and potential difficulties in electrolyte gas tightness. As a high energy process it is also expensive in terms of energy [Meng *et al.* 2009], though the falling capital costs mitigate this somewhat. For its highly relevant advantages and the possibility of integrating the whole manufacturing process to be performed by a single machine, EB-PVD (electron beam physical vapour deposition) was selected for fabrication. While the thickness of electrolyte required is not particularly difficult to achieve the equipment used had never been used to do so prior to my masters project [Camilleri 2009], and has certain unavoidable limitations (see section 1.1) that affect optimization and reproducibility

EB-PVD coatings of YSZ consist of collinear elongated single-crystal columns with a predominantly <100> orientation [Hass *et al.* 2001, Zhao *et al.* 2006]. They contain a small volume fraction of intercolumnar pores oriented perpendicular to the coating surface. The elongated pores make them more compliant to in plane stress, such as that caused by CTE mismatches and thermal cycling [Zhao *et al.* 2006]. If these pores form a diffusion pathway through the electrolyte gas tightness will obviously suffer, although whether this is the case is not clear from the literature alone. In any case, the small volume of material lost to pores does represent a fraction of oxygen ion conducting material lost and hence a drop in ion flux. However, unless the porosity is large it can be neglected.

Both experiments and modelling have shown that pore morphology in the coatings can be influenced by process variables that affect the incident angle of the vaporised atoms

and the mobility of the condensed species at the vapour-solid interface [Zhao *et al.* 2006]. Variables include substrate temperature, deposition rate, gas pressure and substrate roughness [Zhao *et al.* 2006, see also chapter 9; sections 9.2.9 and 9.7 in particular]. Highly porous columnar coatings are associated with low kinetic energy, oblique vapour incidence angles, low substrate temperatures, high deposition rates, rough substrates and high chamber pressures [Zhao *et al.* 2006]. These conditions are therefore to be avoided as much as possible since a gas tight coating is required. Unfortunately in order to obtain uniform coatings on tubes they must be rotated which may cause shadowing problems leading to increased porosity. Increasing the rate of rotation significantly (to about 30 rpm) is reported to reduce porosity [Hass *et al.* 2001, Zhao *et al.* 2006]. Column morphology changes from <111> to <001> in such cases, however. The tops of the columns are capped with pyramids (rather than tetrahaedra as is the case with <111> columns) [Hass *et al.* 2001, Zhao *et al.* 2006].

Another unconventional technique worth noting at this point is thermal spraying (TS). Thermal spraying, particularly the variant called suspension plasma spraying (SPS), has many of the advantages of EB-PVD (indeed these advantages are common to all PVD techniques) including the ability to create the whole cell [Coddet *et al.* 2014], high deposition rates [Soysal *et al.* 2013] (especially helpful because it helps reduce the thermal degradation of materisl, suppress temperature-dependent interdiffusion of components and reduce the closing of necessary prosity – especially important for metallic components whether separate supports or electrodes), much shorter overall processing time than green sintering based techniques [Soysal *et al.* 2013]. TS techniques can offer significant cost savings once scaled out to full production [Coddet *et al.* 2014]. Note that for the electrolyte (an oxide with high melting point) plasma spray systems are necessary, usually as APS (atmospheric plasma spraying) or the aforementioned SPS [Coddet *et al.* 2014]. It has proven ability to create tubular SOFCs as well as planar ones [Coddet *et al.* 2014], although the example given by Coddet *et al.* (2014), and discussed below, has a low performance probably due to a combination of being electrolyte supported, operating at low temperature (600 °C) and having a leaky electrolyte. The greatest limitation of TS techniques is the minimum thickness of the coating [Soysal et al. 2013].

The use of powders to create splats limits how thin the electrolyte can be to the particle diameter. Powders of 50 micron to 100 micron diameter are typical for thermal spraying, but as reported in Soysal *et al.* (2013) these can be closer to 20 microns. In either case post treatments are necessary to eliminate voids and cracks. These post treatments are typically at high temperature, risk undesired chemical interactions and undesired component interdiffusion, and result in anisotropic ionic conductivity with typically 50% of the surface value through the electrolyte thickness [Coddet *et al.* 2014]. Reducing powder size has its own limitations with a practical minimum to feed into the thermal plasma spray torch of 10 micron diameter [Coddet *et al.* 2014].

A modified process (e.g. from gas medium to liquid medium, resulting in Suspension Plasma Spraying; SPS in conjunction with a slurry consisting of water or alcohol and submicron powders) can allow further reduction of particle size [Coddet *et al.* 2014]. Post treatment by laser re-melting, solution infiltration (or even sol-gel), or sintering is still required to create a gas tight electrolyte [Coddet *et al.* 2014]. Soysal *et al.* (2013) report planar cells (8 mol.% YSZ electrolyte) with a performance of 800 $mWcm^{-2}$ at 800 °C and 0.7 V with a 1:1 mix of H_2 and N_2 as fuel and simulated air as oxidant after deposition parameter optimization for improved gas tightness. This group, based at DLR (Germany) found that these results were only achievable with SPS. Their electrolytes were 65 microns thick originally, but the DoE on manufacturing parameters allowed them to both reduce this to 35 microns and simultaneously reduce area-related leak by 72%.

The same group at DLR further improved their design by employing another variation of TS techniques: High Velocity Oxy Fuel (HVOF), reported by Gadow *et al.* (2018). The high kinetic energy of the impinging particles was found to be capable of producing dense coatings [Gadow *et al.* 2018]. Their group continued to work exclusively on planar SOFCs with APUs as the primary intended application, searching for modified plasma spray techniques after APS (Atmospheric Plasma Spraying), VPS (Vacuum Plasma Spraying), reduced particle sizes and SPS were found unsatisfactory. HVOF is cheaper than VPS as it is carried out in atmospheric conditions. In keeping with the rest of the development work at DLR the anodes were Ni-YSZ cermet deposited by VPS, the electrolyte was 8 mol.% YSZ, the cathode LSM deposited by screen printing, and the whole cell built onto porous metallic substrates 800 µm thick (a chrome ferritic steel composition most recently) [Gadow *et al.* 2018]. Unlike most reports in the literature they measure the gas tightness (same as previous DLR work). However, this was with synthetic air only and even then as merely a pressure difference across the membrane for constant gas flow [Gadow *et al.* 2018].

Their feedstock has surprisingly large particles; diameters of approximately 10 microns [Gadow *et al.* 2018]. The HVOF deposition parameters were optimised with DoE [Gadow *et al.* 2018]. They found that electrolytes 40 µm thick were required to achieve competitive gas tightness [Gadow *et al.* 2018]. HVOF, therefore, compares well with VPS but with lowered costs [Gadow *et al.* 2018] (probably quite considerable given the costs inherent in any vacuum process). The authors claim HVOF can be a cost-competitive alternative to sintering (without enumerating) but also note the critical role significant deleterious effect thermal gradients during spraying have on the homogeneity and porosity of the sprayed electrolyte [Gadow *et al.* 2018]. They note that the use of carefully optimised, robotically controlled, spray trajectories and appropriate substrates must be considered [Gadow *et al.* 2018]. This is an area EB-PVD is simpler requiring only the one-time setup of the re-usable jigging.

They perceived the minimum thickness that can be sprayed down is therefore 35 µm (by SPS [Soysal *et al.* 2013]) or 40 µm (by HVOF [Gadow *et al.* 2018]). *Ergo,* relative to state-of-the-art sintered electrolytes plasma sprayed methods are unable to match their 10 µm electrolytes. Thus, EB-PVD was preferred as an alternative technique to match the state-of-the-art bringing the advantages of PVD based (as opposed to sintering-based) techniques.

For planar examples the best performance was an electrolyte layer thickness of about 40-50 µm with a power density of 500 $mWcm^{-2}$ at 0.7 V and 800 °C; the OCV of the cell remained close to 950 mV with H_2 and air [Coddet *et al.* 2014]. Gas tightness remained the principal difficulty. With SPS it was possible to create YSZ electrolyte layers 10 µm thick using nanometre powder feedstock [Coddet *et al.* 2014], or via the High Velocity Oxy Fuel variant of SPS (HVOF) 20 µm thick with a cell performance of 700 $mWcm^{-2}$ at 700 °C and 0.7 V [Coddet *et al.* 2014] (fuel and oxidant gases and pressures unreported). Reportedly [Coddet *et al.* 2014] lifetime was low as CTE mismatch caused electrolyte delamination. EB-PVD (for thermal barrier coatings) is preferred as it provides excellent strain tolerance, on the other hand, so may result in acceptable lifetimes. In common with EB-PVD "the challenge of depositing a thin electrolyte layer on a porous substrate appears as a key point of the process" [Coddet *et al.* 2014].

3.4.3 This Project

The deposition technique selected, because it is a non-equilibrium process, inherently tends to favour porous structures, a mechanism known as the "shadowing effect" [Hass *et al.* 2001]. This is especially true at higher deposition rates. The electrolyte must be gas tight, so some post-treatment is often needed. Sol-infiltration and heat treatment has proven very effective in this [Meng *et al.* 2008, Meng *et al.* 2009]. The sol solution fills the pores and after heat treatment improves the density of the SOFC. The effect is a dramatic improvement in both open-circuit voltage (OCV) and current density at low polarisation. Sealants can reach depths of several hundred µm and generally improve other properties also – usually microhardness and properties characteristic of functional materials such as relative permittivity [Meng *et al.* 2008, Meng *et al.* 2009]. Should the deposited coatings prove too porous then a sol-infiltration treatment is considered to be the best solution, as recommended by Camilleri (2009). An interesting alternative is the use of a multilayer coating, alternating YSZ with zirconium-yttrium as proposed by Haydn *et al.* (2014). This is discussed in chapter 17 section 17.2.

The balance of advantages is in favour of EB-PVD as the chosen electrolyte deposition technique with the possible exception of capital cost. Furthermore, EB-PVD is an atomic-sale deposition process as opposed to the splats of SPS or HVOF so does not

have an inherent limitation to electrolyte thickness: the porosity in EB-PVD coatings comes from the shadowing effect and potentially its ultimately columnar structure.

3.5 Cathode Material

3.5.1 Cathode Requirements

As with the anode, the cathode must merge catalytic activity, electrical conductivity and chemical stability (particularly chemical expansion and cation interdiffusion) and thermomechanical stability under the operating conditions [Larminie and Dicks 2003, Yokokawa and Horita 2003, Thompsett 2003, Tsipis and Kharton 2008a, Tsipis and Kharton 2008b]. Early SOFCs used platinum cathodes since this material meets all requirements. However, platinum is expensive and has thus far proved impractical for cost-effective commercial power generation SOFC manufacture using conventional designs [Larminie and Dicks 2003, Yokokawa and Horita 2003].

Less expensive materials with promise include perovskites, but these degrade rapidly due to reactions with YSZ electrolytes. The degradation problem was reduced upon the introduction of lanthanum manganite based materials, yet these too suffer from some degree of degradation reaction when in contact with YSZ, particularly at higher temperatures, limiting the lifetime of such electrodes [Yokokawa and Horita 2003]. Recent developments concentrate on lanthanum deficient formulations to reduce the deleterious reactions with YSZ, with varying degrees of success [Larminie and Dicks 2003, Yokokawa and Horita 2003, Yang *et al.* 2009]. Perhaps the most successful of these has been a strontium-doped lanthanum manganite (LSM). The inclusion of Gadolina to create three-element-doped LSGM has benefits also [Liu *et al.* 2017]. Readers are encouraged to review the literature, particularly those references from the Lucerne 2010 SOFC Forum conference proceedings [Connor 2010]. Table 3-4., below, summarises the major aspects of cathode development.

Of Primary Importance	**Of Secondary Importance**
1. Porosity	1. CTE match with Electrolyte
2. Material costs	2. Chemical compatibility with Electrolyte
3. Long term stability	3. Electrical conductivity (must be sufficient material for conduction – but no more)
	4. Fabrication and processing costs

Table 3-4. Summary of major challenges to successful cathode development.

Microtubular designs are able to function with much thinner cathodes. Perhaps as thin as a few hundred nm, significantly reducing the cost compared to the mm thick films that prompted the shift to alternative cathode materials. There may be a shift back to platinum if miniaturised tubular designs become widely accepted and ongoing research into new cathode materials does not yield anything comparable to Pt.

3.5.2 Platinum Cathodes

The cathodic reaction requires the Pt to be porous, enabling the dissociated oxygen to reach the electrolyte. While not a material property *per se* the Pt must be amenable to suitable processing to create this porosity. Electrodes must not only be effective catalysts for the electrode reactions, but must have sufficient long term stability for meaningful cell operation. At the very least electrode stability must be no worse than that of the electrolyte employed. Rather obviously the electrode must not react with the oxidant or electrolyte in any way, in accordance with the definition of a catalyst. Oxygen electrode (cathode) stability is less certain than that of the fuel electrode and must be assessed for individual materials. Stability of the grains, pore structure, resistance to thermal stress and electrode insolubility in the electrolyte are also requirements for long term stability in operation of the fuel cell electrodes.

Unlike with anode catalysts the Group VIII metals are equalled by Group Ib metals and their oxides [Heath and Sweeney 1963, Gorin and Recht 1963], vastly increasing the range of options available should Pt still be unacceptably expensive. See the cited reference for more details on available catalysts and their reported performance. Generally, though, platinum is still the safest bet, offering the best overall performance irrespective of conditions both in terms of high current densities and low polarizations.

It is possible to improve Pt as cathode by using Pt alloyed with base metals like V, Cr and Ni. These nano-dispersed particles of Pt alloys possess improved intrinsic activity and stability over pure Pt [Thompsett 2003]. Such alloys are also more resistant to sintering, reducing the expected degradation of a purely metallic cathode at relatively high temperatures.

To meet the objectives of this project pure Pt was deemed ideal since others were conducting considerable research into cathode materials at the time. Platinum meets all the requirements of creating functional cells making it an excellent temporary solution till the optimal cathode material emerges.

3.6 Cathode Fabrication

3.6.1 Conventional

Fabrication is typically through powder processing routes followed by sintering [Yokokawa and Horita 2003]. Cathode material powders are usually synthesised either by solid state reactions of the constituent oxides or by the sol-gel route. The exact processing route, whether slurry, pressing, or green extrusion depends on the cell design. Tubular, anode-supported, cells are fabricated differently from cathode- or electrolyte-supported ones, and planar cells can even be fabricated by screen printing, tape casting and wet powder spraying [Yokokawa and Horita 2003]. These conventional

techniques restrict how thin the cathode can be made, exacerbating the problem of using Pt, an otherwise ideal material for the cathode.

Some examples of unconventional cathode manufacturing methods may be found in Camilleri [2009].

3.6.2 This Project

Sputtering was selected for fabrication for its flexibility, ability to deposit highly conformal films, ability to easily deposit films only nm thick (though up to several microns is feasible also), simplicity of operation, capability of varying porosity by changing chamber pressure (see Chapter 10) as well as availability of material, equipment and expertise. Furthermore, adopting novel fabrication techniques once more solves a difficulty with the conventional approach: in this instance the limited thickness possible via sintering routes (see section 3.6.1, above).

Interconnect Material

3.6.3 Interconnect Requirements

Interconnects serve two roles in HT-SOFCs (high temperature solid oxide fuel cells), namely electrical connection between cells and gas separation within cells for planar designs [Anderson and Tietz 2003, Larminie and Dicks 2003, Piccardo *et al.* 2009]. Inherently they are less important in tubular designs where their only purpose is electrical connection. Furthermore, such connections are innately simpler and can be more robust in tubular designs (see section 3.8). Naturally, any interconnect materials used must be compatible with any and all components they come into contact with (usually the electrodes and some type of enclosure) under both oxidising conditions (on the cathode side) and reducing conditions (on the anode side), all this at the relevant operating temperatures [Anderson and Tietz 2003, Larminie and Dicks 2003, Piccardo *et al.* 2009].

"Interconnect requirements are made even more stringent by the necessity of low cost raw material, economic fabrication and that a practicable fabrication route exists in the first place." [Camilleri 2009] As with the other SOFC materials these requirements can only be fulfilled by a handful of materials. Most commonly either perovskite-type ceramics based on rare earth chromites (for operation in the 900–1,000 °C range) or metallic alloys for lower temperatures [Anderson and Tietz 2003, Larminie and Dicks 2003, Piccardo *et al.* 2009].

The overall requirements of interconnect materials are: high electronic conductivity, low ionic conductivity, chemical stability in both fuel and oxidant, chemical compatibility with other SOFC materials, good CTE match with other SOFC materials,

good mechanical strength at operating temperatures, high thermal conductivity, feasible and economic fabrication route available, and preferably low raw material cost. Depending on the particular design of SOFC the interconnect material may also be required to supply gas-tightness and the ability to create gas-tight seals with other cell components.

The first four requirements greatly restrict the choices available. In particular components based on (La, Sr, Ca)(Cr,Mg)O_3 have proved eminently successful for HT cells. Other systems with compositions relating to (Y, Ca)CrO_3 are reported to be adequate [Anderson and Tietz 2003, Connor 2010]. Both systems suffer from fabrication difficulties and high cost. Metallic interconnects may solve both problems, but their lifetimes under operating conditions have not been verified conclusively [Anderson and Tietz 2003]. Table 3-5. summarises the major aspects of interconnect development.

Of Primary Importance	**Of Secondary Importance**
1. Fabrication and processing costs	1. CTE match with YSZ
2. Material costs	2. Chemical compatibility with YSZ and sealing glass or cement
	3. Expansion due to loss of oxygen
	4. Mechanical strength and durability in a reducing/oxidising atmosphere at elevated temperature
	5. Electrical conductivity in a reducing/ oxidising atmosphere at elevated temperature

Table 3-5. Summary of major challenges to successful interconnect development.

3.6.4 Metallic Interconnects

The benefits of replacing ceramic interconnects with metallic ones are obvious and very attractive. Metallic interconnects have both lower material and fabrication costs, they offer better formability and can easily take complex shapes, thermal and electrical conductivity are both superior to ceramic interconnects, and there is little risk of damage due to different gas atmospheres across the interconnection [Anderson and Tietz 2003, Piccardo *et al.* 2009].

Gas distribution through metallic interconnects is usually accomplished by creating parallel channel with ridges separating the channels to act as electrical connectors for the electrodes [Anderson and Tietz 2003, Larminie and Dicks 2003]. The gas manifolding requirement is irrelevant to tubular designs. To re-iterate, one of the greatest advantages of tubular designs is that the only function of the interconnect is electrical connectivity between cells – something easily accomplished.

The earliest examples of SOFCs using metallic interconnects were planar stacks reported in the early 1990s [Anderson and Tietz 2003]. These early attempts,

particularly using FeNiCr alloys, were not very successful due mostly to chromium poisoning of the cathode during operation – that is, chromium leeches from the interconnect at the operating temperatures and enters the electrode [Anderson and Tietz 2003]. The presence of Cr on the electrodes reduces the three-phase boundary and interferes with the catalytic activity of the electrodes. Another serious problem experienced by metallic interconnects is the high CTE mismatch [Anderson and Tietz 2003]. Chromium-based alloys are preferred, and in particular Ducrolloy (designed to have a good CTE match with 8YSZ). This is also the alloy used in the Siemens electrolyte-supported multi kW planar stack SOFCs, contain 5 wt.% Fe, and 1 wt.% yttria, balance Cr [Anderson and Tietz 2003]. The CTE matching benefit is reduced at operating temperatures above 800 °C, but is still acceptable up to around 1,000 °C (only an 8% difference) [Anderson and Tietz 2003]. Over a thousand hours of operation stability is reported to be excellent [Anderson and Tietz 2003].

Other popular systems (details for which can be found in the cited reference) include ferritic steels (low cost, very good formability, good weldability and good CTE match but unacceptable degradation in output power during operation), nickel-based alloys such as Inconel 600 and Ni 22Cr (investigated by Sanyo and Fuji Electric, good long term stability but poor thermal cycling resistance) and finally combinations such as FeCrAlY steels with silver pins to improve electrical contact. Unfortunately silver is not very stable above 700 °C, and the behaviour of such a material under thermal cycling is mostly unknown [Anderson and Tietz 2003].

Platinum suffers none of these drawbacks save perhaps long term stability issues that can only be conclusively resolved by further study. Recall that the only concrete reason not to use Pt is its cost.

3.7 Interconnect Fabrication

Suitable fabrication routes include conventional machining (though not really suitable for micro-SOFCs), pressing, or green body machining if powder metallurgy is the chosen route. CVD, sputtering or other PVD routes are also possible. Fabrication is usually via powder metallurgy (details in Anderson and Tietz [2003]).

3.8 Design for this Project

The design adopted (see Figure 3-5. below) has most dimensions constrained by external factors rather than any design intentions or constraints based on the nature of SOFCs. The length could be no more than 100 mm in order to fit in the various pieces of equipment needed, most importantly the EB-PVD coater. Similarly it could not be significantly shorter either to correctly fit the coater and ensure uniform coating

thickness. The diameter could not be less than about 5 mm OD for practical connecting and handling reasons. Any narrower and the manual handling needed (for jigging and electrical connection in particular) would become very difficult. Had it been possible to tailor make of modify certain pieces of equipment this would not have been nearly as restrictive. Such an ideal situation would also allow for dedicated jigging to ease handling issues. The wall thickness of the tubes that will eventually form the anode is ideally as thin as possible to minimize polarization losses. However, it was deemed that anything less than 50 μm wall thickness would be too delicate for manual handling and jigging. This was confirmed by other sources also [Cho and Choi 2009]. For all three dimensions (OD, wall thickness and length) there was the added factor of availability of tubes from commercial sources. The final design used tubes 100 mm long of 99.5% Ni, 5.9 mm OD with a wall thickness of 125 μm from Goodfellow Cambridge Ltd.

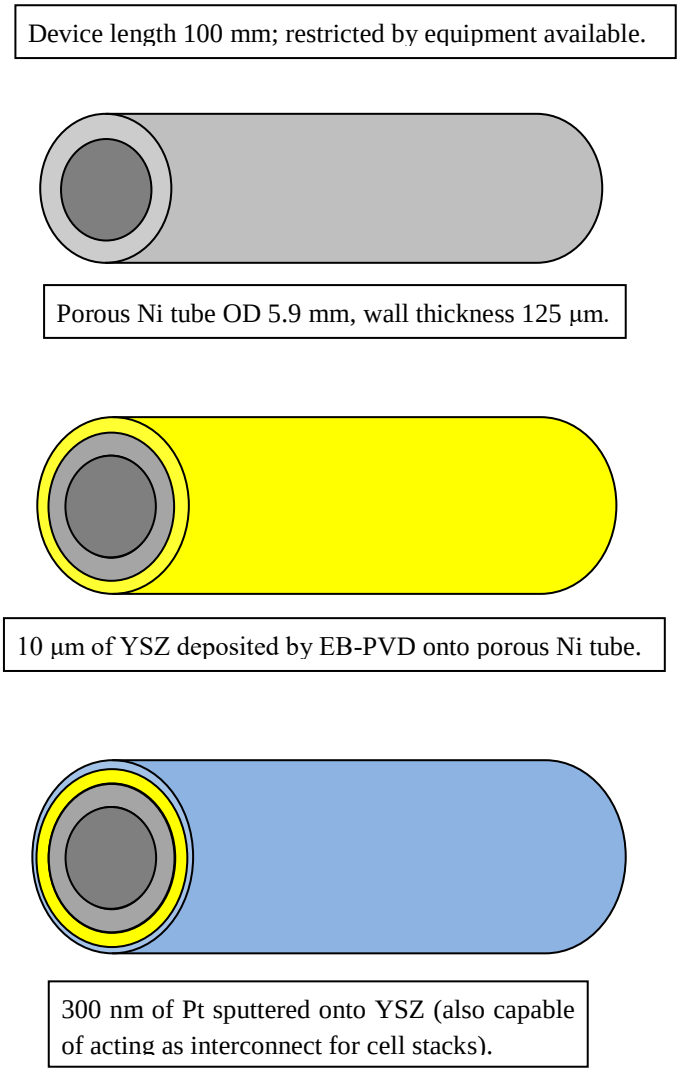

Figure 3-5. Schematic of microtubular design. Also shown are fabrication steps. This was updated and improved from Camilleri (2009).

Some reiteration of the design features is worthwhile. An anode-supported design was chosen to enable Pt to be used for the cathode (since this could be a very thin film), safety is improved (fuel flows inside rather than around the tubes), gas manifolding is simplified (it is simpler to have the outer surface exposed to air and flow hydrogen through the tubes than the converse), and also for fabrication reasons (creating a porous cathode of sufficient thickness would be difficult), nickel makes for a very good structural support and is also economical.

Gas transport occurs only by diffusion since convection in the pores of SOFC electrodes is negligible [Khaleel and Selman 2003]. Crucially, the oxygen partial pressure in the cathode pores near the cathode-electrolyte interface is lower than that in the air stream (see sections 4.3.3, 4.3.4 and 4.9.2). The greater the resistance to oxygen transport through the porous medium the greater the concentration polarization at the cathode will be. Thus, thick cathodes, as required by cathode-supported cells, lead to a high concentration polarization even at low-to-moderate current densities. Lowering concentration polarization requires the cathode to be as thin as possible with high porosity and large pore size [Khaleel and Selman 2003]. The ultra-thin sputtered platinum cathode of this design, with its high porosity, is therefore likely to have a very low concentration polarization even at high current densities.

The design was influenced by the theory of operation of fuel cells, in an effort to optimise the most basic aspect of the fuel cell – its geometry (see chapter 4 Theory of Operation: Review and Critique).

3.8.1 Microtubular Cell Stack

Creating stacks with previous tubular designs, even the mostly successful Siemens-Westinghouse design, is a non trivial design problem. A large part of this challenge is eliminated by adopting the anode-supported design, as evidenced by a very successful implementation of cell stacks with microtubular cells by one group in particular: Funahashi *et al.* (2007, 2008, 2009), Suzuki *et al.* (2008a, 2008b 2008c, 2009a, 2009b).

Creating parallel stacks with this form of tubular design is as simple as placing the cells such that their cathodes are firmly in contact. Or adopting something akin to the clever arrangement of cubes developed by the group referred to above. Series stacking is slightly more complex, and is best achieved by connecting parallel stacks rather than individual cells. This design is highly modular in this respect. Minor modifications (only outer casings and gas manifolds in fact) allow assembly of parallel stacks of fixed voltage and a range of currents: say a 200 mA stack, a 400 mA stack, an 800 mA stack and a 1 A one. These are then wired together (in series) to provide the needed voltage. Further standardised modules can be fabricated facilitating providing customers with the system they require. For instance one standard module might be a 1.2 kW stack of 10 A (consisting of ten 1 A stacks) at 120 V (one hundred and twenty series connected sets of

thirteen 1 A parallel stacks). Of course this means a lot of individual cells are needed (as many as 1,200 in the example given), but that is no different for large tubular designs or indeed planar ones. So there is no additional drawback for considerably simpler assembly (in no small part due to the lack of interconnects between individual cells) as illustrated in the figure below (Figure 3-6.).

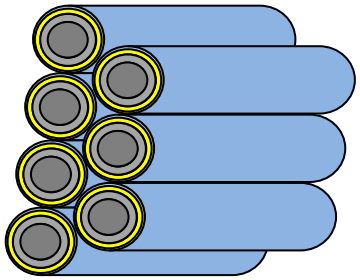

(a) Parallel stacking example: Pt acts as interconnect, leaving gap for air (oxidant) flow.

(b) Series "stacking": achieved by connecting subsequent modules (either parallel stacks or single cells) via electrical connections. For single cells (shown) the connection is from anode to cathode, for parallel stacks (closed units) it is from negative terminal to positive terminal. This allows any voltage to be built up in steps of around 1 V (the OCV).

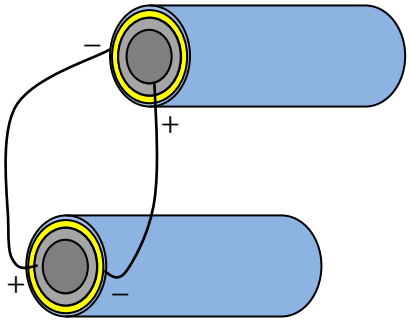

Figure 3-6. Schematics of parallel stacking (a) and series connection (b).

Naturally, a proof of concept for this scheme of cell stacking has its proper place after the development and optimization of individual cells is complete (refer to further work, chapter 17).

3.9 Design Specification

This section presents a simple design specification the wholly describes the fuel cell being developed. It loosely takes the form of a 'to do list' of components. The design consists of a porous metallic Ni anode made by an innovative (and to the author's knowledge unique) oxidation reduction process from commercially available Ni200 tube described previously. Over this a nominally 10 µm thick EB-PVD deposited 7YSZ electrolyte followed by a sputtered porous Pt cathode. The cell will operate on an artificial air mix for oxidant and pure H_2 for fuel.

4 Theory of Operation: Review and Critique

Several modelling approaches exist for SOFCs [Khaleel and Selman 2003] including modelling of thermo-mechanical, flow, chemical or electrochemical subsystems or integrated modelling of two or more coupled systems. Some of these models are characterised by their very different scales. This ranges from atomistic and molecular level modelling, to cell component level, to cell level, to stack level, and finally to system-level performance [Khaleel and Selman 2003, Larminie and Dicks 2003]. For the purposes of this project modelling will focus on cell electrochemistry, and principally intends to direct the thinking (and therefore optimization routes) rather than to validate experimental data.

This chapter aims to outline the salient phenomena of a fuel cell's operation. The operating principles presented are quite general, but directed towards HT-SOFCs (high temperature solid oxide fuel cells) for obvious reasons. Much of this theory at first glance appears to be a bit of a jumble. In truth, that is precisely what it is. Due to the complex nature of fuel cell operation and the great variety of physical phenomena involved it is a highly coupled problem touching upon various fields. To complicate matters further most electrochemical theory is based on liquid electrolytes, and there is rather less on solid ones [Camilleri 2009]. Adapting the various theories into something resembling a model of HT-SOFC operation results in several approaches (not to mention individual models).

Modern models have become increasingly sophisticated and complex. Many are indeed not solvable analytically and require the use of finite element analysis (FEA) software packages. Other models go a step further and present an atomistic view of the fuel cell reactions. The most popular approach is finite element analysis (FEA) of the coupled continuum-level electrochemical, flow and thermal models. FEA models of this sort (coupled problems) are time consuming and challenging to create, and while very informative tend to be beyond basic analytical needs. Therefore, they tend not to be used except in later developmental stages of SOFC design. For examples and reviews see Khaleel and Selmam (2003), Khaleel *et al.* (2004), Bove and Ubertini (2006), Hauch *et al.* (2008), Connor (2010), Chang *et al.* (2011), and Marino *et al.* (2011). A question arises here as to whether researchers undertake any preliminary modelling at all, given none was reported or even referred to in the sources reviewed, nor in any private communications the author has had on the topic.

Evident from the literature, as far as analytical models go (the subject of interest for initial modelling of this prototype) there are two possible philosophies. The first one approaches the problem from first principles, tracing the path of the oxygen as it ionizes at the cathode, diffuses through the electrolyte and reacts with hydrogen at the three-

phase boundary in the anode, calculating the relevant rate constants and energies as one progresses through the abstract device. The second approach proceeds from what is observable and measureable. Given the function of any fuel cell is to produce electrical energy it is generally deemed appropriate that this observed quantity is one or more of the following: power, current, voltage, electrical resistance. Most commonly graphs are plotted of current against voltage (I–V curves), and power against voltage, current or even fuel utilization. How one presents the information is not of the greatest importance. Rather it is the implication of this approach – that the cell can be treated as an electrical device evaluating fundamental electrical properties for the different components that result from the phenomena involved. This approach has been favoured because it is relatively straightforward to assemble a good model from the various components presented in the literature (often scattered across several sources), and also because each 'component' of the model, be it ohmic polarization or activation polarization, has been studied extensively.

Unfortunately the first-principles electrochemical approach, while didactically very useful, is rather too unwieldy for a practical analytical model. The greatest drawback with this approach is that the various segments are modelled individually with no clear route to integration. Therefore, no clear model for the entire cell can be assembled from the first principle partial models. The phenomenological model, on the other hand, is less useful didactically as it obscures somewhat the fundamental theory of operation that the first principles model sets out so clearly. It does, however, provide a more complete model of the entire cell in terms of fundamental, and measureable, performance characteristics. This chapter is therefore divided into three parts. The first is the first principles model, the second is the phenomenological model, and the final part includes models for efficiency and other (non-electrochemical) considerations. Much of this chapter refines and updates a review on SOFC theory of operation first published in the author's MSc thesis [Camilleri 2009]. Bin (2009) emphasised the advantages of nano-structuring electrolytes and condensed the principal elements of fuel cell theory into a review that is recommended.

Part I: First Principles Model

4.1 Thermodynamics of Electrochemical Fuel Cells

Ostwald (1894) stated that due to the fact that, for most chemical reactions useful in practice for fuel cells, the entropy term ($T\Delta S$) is small compared to the change in enthalpy (ΔH), the ideal thermodynamic efficiency for a direct energy conversion device is close to 100% [Eisenberg 1963]. On the other hand any heat engine or heat

pump has an ideal thermodynamic efficiency limited by the Carnot relationship: $\eta = 1 - \frac{T_{low}}{T_{high}}$ [Ghirlando 2004, Farrugia 2005].

An electrochemical fuel cell is a galvanic device for which the two half-reactions (at the individual electrodes) result in the direct conversion of the free energy of the reaction into electrical energy. *Ergo* the majority of thermodynamic aspects of electrochemical fuel cells are related to the thermodynamics of chemical galvanic cells [Eisenberg 1963, Larminie and Dicks 2003]. However, since in reality fuel cells are in a constant state of flux with entry and exit streams (fuel and oxidant and waste respectively) the relationships are somewhat more complex than for a typical galvanic cell (battery).

In reality the maximum fuel cell efficiency is $\frac{\Delta G}{\Delta H_f}$, where ΔH_f is the enthalpy of formation of the product of fuel and oxidant (e.g. water if hydrogen is the fuel and oxygen the oxidant). The ambiguity inherent in the difference between efficiency calculated from higher heating values (HHV) for condensation and lower heating values (LHV) for combustion are explained by Larminie and Dicks (2003). Suffice to add that at typical fuel cell temperatures (600 °C–1,000 °C) the maximum efficiency based on HHV (the more conservative option) for a hydrogen fuel cell (sometimes called the thermodynamic efficiency) is in the range 62% (1,000 °C) to 70% (600 °C) [Larminie and Dicks 2003].

4.1.1 Chemical Cells and Concentration Cells

Basically a galvanic cell consists of two electrodes in contact with an electrolyte such that a current will flow if the electrodes are connected by a conductor. The difference in potential at each electrode-electrolyte interface is called the reversible electrode potential (E_{rA} for the anode and E_{rC} for the cathode, in V). Their algebraic sum gives the total electro motive force (E.M.F.):

$$V_r = E_{rA} - E_{rC} \qquad (4.1)$$

Where V_r is the reversible cell potential (the E.M.F. of the cell, V), and E_{rA} and E_{rC} are as defined above. Depending on whether the E.M.F. results from a difference in concentrations of the potential-determining species or is the result of the overall chemical reaction the galvanic cell is referred to as a concentration cell or a chemical cell respectively [Eisenberg 1963]. In practice, nearly all electrochemical fuel cells are chemical cells [Eisenberg 1963], and therefore these will be discussed in more detail.

4.1.2 Reversibility and Irreversibility

Reversibility in galvanic cells is only in the thermodynamic sense. Thermodynamic reversibility implies that there is a state of equilibrium at every stage and that there is no spontaneous chemical reaction at the electrodes. In a thermodynamically reversible cell

the chemical reaction is proportional to the quantity of electricity passed by Faraday's Laws of Electrolysis. *Ergo*, for a reversible cell the application of an external E.M.F. to balance the E.M.F. of the galvanic cell will affect no chemical change when the net current flow is zero. Small changes to the applied (external) E.M.F. in either direction will shift the cell in the corresponding direction. Electrochemical equilibrium is not, however, static. Rather it is a dynamic equilibrium where at zero current at a given electrode there is a small amount of reaction proceeding in both directions at a rate corresponding to the exchange current density (i_0). The exchange current density is an important parameter in electrode kinetics. Once steady state is reached the dynamic equilibrium implies that the forward and backward electrode reactions are equal when there is no net current flow.

4.1.3 Free Energy and Enthalpy

For a reversible chemical cell or for a fuel cell in which the overall reaction can be written as:

$$A + B + \cdots \rightleftharpoons C + D + \cdots \qquad (4.2)$$

It can be shown from thermodynamics that the chemical potential or partial molar free energy for each species, i, can be expressed as:

$$\mu_i = \mu_i^\circ + RT \ln f_i \, x_i \qquad (4.3)$$

and the overall change in free energy is:

$$\Delta G = \Delta H - T\Delta S = \sum_i \nu_i \mu_i = \sum_i \nu_i \, \mu_i^\circ + RT \sum_i \nu_i \ln f_i \, x_i \qquad (4.4)$$

Where:

ΔG = change in Gibbs free energy of reaction (Jmol^{-1})
ΔH = change in enthalpy of reaction (Jmol^{-1})
ΔS = change in entropy of reaction (Jmol^{-1}K^{-1})
μ_i = chemcial potential of species i (Jmol^{-1})
μ_i° = chemical potential at the standard state, when the activity $f_i x_i$=1 (Jmol^{-1})
R = universal gas constant (8.314472 Jmol^{-1}K^{-1})
T = absolute temperature (K)
f_i= coefficient of activity of species i (no units) See Appendix A.
x_i= mole fraction of species i (no units)
ν_i = stoichiometric number of species i (no units)

When all reactants and products are at their standard states (activities all equal to one, denoted by superscript °), (4.4) simplifies to:

$$\Delta G^{\circ} = \Delta H^{\circ} - T\Delta S^{\circ} = \sum \nu_i \mu_i^{\circ} \qquad (4.5)$$

The stoichiometric numbers ν_i are to be taken as negative for the reactants $\{A + B + \cdots\}$ and positive for the reaction products $\{C + D + \cdots\}$ in equation (4.2).

For fuel cells operating at elevated temperatures, in which both the reactants and the products are gaseous, these may be treated as ideal gases, neglecting any deviations from behaviour described by the ideal gas laws, provided the operating pressure is relatively low. In such cases equation **Error! Reference source not found.** can be xpressed in terms of partial pressures, p_i, as follows:

$$\Delta G = \sum \nu_i \, \mu_i^{\circ} + RT \sum \nu_i \ln p_i = -RT \ln K_p + RT \sum \nu_i \ln p_i \qquad (4.6)$$

Where:

$\Delta G =$ change in Gibbs free energy of reaction (Jmol^{-1})
$\mu_i^{\circ} =$ chemical potential at the standard state, when the activity $f_i x_i$=1 (Jmol^{-1})
$R =$ universal gas constant (8.314472 J mol^{-1}K^{-1})
$T =$ absolute temperature (K)
$\nu_i =$ stoichiometric number of species i (no units)
$p_i =$ partial pressure of the species i (bar)
$K_p =$ equilibrium constant of the gas reaction (no units)

4.1.4 Fuel Cell Work Output

In thermodynamic terms the operation of an electrochemical cell usually corresponds to an isothermal process at constant pressure. The differential free energy change:

$$dG = dH - TdS \qquad (4.7)$$

Which may be combined with the expression for the internal energy change (from the 2nd Law of Thermodynamics):

$$dU = dQ - dW \qquad (4.8)$$

Where dQ is the heat absorbed by the system from the surroundings and dW is the work done by the system on the surroundings. Now the work done is:

$$dW = pdV + dW_{max} \qquad (4.9)$$

Where pdV is the work done in expansion and dW_{max} is the maximum useful work.

For a reversible process at constant pressure and temperature the heat absorbed, dQ, can be shown to be:

$$dQ = TdS \qquad (4.10)$$

Substituting equations (4.9) and (4.10) into (4.8) yields:

$$dU = TdS - pdV - dW_{max} \qquad (4.11)$$

Now the enthalpy change, dH, is given by:

$$dH = dU + pdV \qquad (4.12)$$

Therefore, combining equations (4.5), (4.11) and (4.12) gives:

$$dG = -dW_{max} \qquad (4.13)$$

Hence, the maximum useful work done at constant temperature and pressure from a galvanic cell is equal to the change in free energy of the system. The free energy change for a reversible isothermal cell is given by:

$$\Delta G = -n\mathcal{F}V_r \qquad (4.14)$$

Where:

$\Delta G =$ change in Gibbs free energy (Jmol^{-1})
$n =$ number of electrons per reacting ion or molecule (no units)
$\mathcal{F} =$ number of Faradays ($\mathcal{F} = 96484.56$ Coulombs/mol) per equivalent
$V_r =$ theoretical maximum cell voltage for the overall chemical reaction (V)

It may be useful to keep in mind that in chemical terms (as opposed to classical thermodynamics terms as given above) $\Delta G = G_{H_2O} - G_{H_2} - \frac{1}{2}G_{O_2}$.

4.1.5 The Open-Circuit Voltage (OCV)

The open-circuit voltage (i.e. when no current is flowing) is the highest voltage obtainable experimentally. For a reversible cell, the open-circuit or open-cell voltage is equal to the theoretical maximum voltage predicted by equation (4.14). See Table 2-1. for some examples (repeated here for convenience).

Chemical Reaction	E_{th} (Volts)	$\Delta G°$ (kJ mol^{-1})
$H_2 + 0.5O_2 \rightarrow H_2O$	1.23	-237.53
$C + O_2 \rightarrow CO_2$	1.02	-394.95
$2C + O_2 \rightarrow 2CO$	0.70	-137.47
$2CO + O_2 \rightarrow 2CO_2$	1.33	-257.48
$C_3H_8 + 5O_2 \rightarrow 3CO_2 + 4H_2O$	1.10	-608.96
$2Na + H_2O + 0.5O_2 \rightarrow 2NaOH$	3.14	-302.96
$4NH_3 + 3O_2 \rightarrow 2N_2 + 6H_2O$	1.13	-241.82
$N_2H_4 + O_2 \rightarrow N_2 + 2H_2O$	1.56	-301.03
$CH_3OH + 1.5O_2 \rightarrow CO_2 + 2H_2O$	1.21	350.24
$CH_4 + 2O_2 \rightarrow CO_2 + 2H_2O$	1.51	-581.61

Table 2-1. Theoretical E.M.F. of selected reactions and Gibbs free energy at 25 °C and 1.013 bar. The superior fuels are separated from the inferior ones by an empty row (fully explained below). Adapted from [Mitchell 1963 and Gibbs Free Energy article accessed 2014].

Note that the theoretical EMFs tabulated above are completely independent of cell processes since $V = E_{Th} - iR_{total}$.

4.1.6 Enthalpy of Reaction from OCV

According to the Gibbs-Helmholz equation, for a reversible process:

$$\Delta G = \Delta H + T\left(\frac{\partial(\Delta F)}{\partial T}\right)_p \qquad (4.15)$$

Where ΔH is the increase in enthalpy (Jmol^{-1}) for the cell reaction, i.e. the heat absorbed in the reaction at constant pressure. Substituting equation (4.14) into (4.15) results in:

$$\Delta H = -n\mathcal{F}\left[V_r - T\left(\frac{\partial V_r}{\partial T}\right)_p\right] \qquad (4.16)$$

Hence, the enthalpy of the cell reaction can be found from the E.M.F. and its temperature coefficient. Since in general the open-circuit E.M.F. (V_r) of a fuel cell can be described by its relation to the basic thermodynamic principles of enthalpy and entropy, the effect of temperature or pressure changes on the E.M.F. can be found by calculating the effect on the free energy or the equilibrium constant of the gas reaction.

4.2 Reversible Electrode Potential

4.2.1 The Nernst Equation and the Effect of Concentration

Any detailed discussion on the thermodynamics and the electrochemical kinetics of fuel cells must be referred to single electrodes: cathodes and anodes. The reversible single electrode potential, E_r, can be treated rigorously by application of the Nernst equation.

For a single electrode process whose net result can be presented by the following reaction:

$$M \rightarrow M^{n+} + ne^{-} \qquad (4.17)$$

$$H_2 + 0.5O_2 \rightarrow H_2O \qquad (4.18)$$

the single electrode potential can be expressed as:

$$E_r = E_r^{\circ} - \left(\frac{RT}{n\mathcal{F}}\right)\sum \ln a_i^{\nu_i} \qquad (4.19)$$

Where:

E_r = the reversible (single) electrode potential (V)

E_r° = the standard potential of the electrode when all species i are at unit activity (i.e. also in their standard states) (V)

R = universal gas constant (8.314472 $Jmol^{-1}K^{-1}$)

T = absolute temperature (K)

n = number of electrons participating in the overall reaction (no units)

$\mathcal{F}$ = number of Faradays ($\mathcal{F} = 96540$ Coulombs) per equivalent

a_i = activity of species i (no units)

ν_i = number of ions or molecules of species i for the reaction as written (no units)

Equation (4.19) is the generalised form of the Nernst equation. For a complete single cell the open-circuit E.M.F. (OCV), V_r, can be expressed as (provided both electrodes are reversible):

$$V_r = E_{rA} - E_{rC} = \left[E_{rA}^{\circ} - \left(\frac{RT}{n\mathcal{F}}\right)\sum \ln a_A^{\nu_A}\right] - \left[E_{rC}^{\circ} - \left(\frac{RT}{n\mathcal{F}}\right)\sum \ln a_C^{\nu_C}\right] \qquad (4.20)$$

Where: A and C refer to the anode and cathode respectively.

It needs to be reiterated that this expression for cell E.M.F. of a single cell can be verified experimentally only if both electrode are, in fact, thermodynamically reversible. Furthermore, in many experimental situations concerning fuel cells it is difficult to determine which is the primary electrode reaction and so becomes difficult to select the activities of the correct potential-determining species. Another problem that can arise with application of (4.20) to experimentally obtained data of the open-circuit potential in electrochemical fuel cells is due to the presence of several electrochemical reactions at one or both electrodes. This leads to mixed electrode potentials and the attendant complication of successfully applying the equation [Eisenberg 1963, Larminie and Dicks 2003].

Strictly speaking, the equations demonstrate that it is necessary to use individual activity coefficients for each species, i, that determines the potential. Theoretical rigidity notwithstanding the physical-chemical methods for determining activity coefficients yield mean activity coefficients for both ions into which a solute will disassociate [Eisenberg 1963, see also Appendix A:]. In practice, the mean activity coefficient is sufficient.

4.2.2 The Effect of Temperature

The effect of temperature on the reversible E.M.F. of a complete open-circuit cell, V_r, can be obtained by rearranging the Gibbs-Helmholz equation – that relates enthalpy gain to the E.M.F. [Eisenberg 1963, Khaleel and Selman 2003, Larminie and Dicks 2003] (4.16) to:

$$-n\mathcal{F}V_r = \Delta H - T\left[\frac{\partial(n\mathcal{F}V_r)}{\partial T}\right]_p \qquad (4.21)$$

Since the term $\left[\frac{\partial(n\mathcal{F}V_r)}{\partial T}\right]_p$ is the derivative of the free energy change for the overall reaction with respect to temperature at constant pressure, it is a measure of the change in entropy, ΔS. Thus,

$$T\left[\frac{\partial(n\mathcal{F}V_r)}{\partial T}\right]_p = T\Delta S = -q \qquad (4.22)$$

Where q represents the heat involved in the overall reaction. By utilising both of the equations above, i.e. (4.21) and (4.22) the effect of temperature on the overall cell open-circuit E.M.F., V_r, can be determined from experimental data of V_r and its temperature coefficient. Typical values of the temperature coefficient $\left[\frac{\partial V_r}{\partial T}\right]$ for galvanic elements around room temperature vary from -5×10^{-4} VK^{-1} to $+8 \times 10^{-4}$ VK^{-1}.

This method of determining the effect of temperature changes on the reversible E.M.F. of a complete galvanic cell, V_r, requires the use of experimentally obtained temperature coefficients with all their attendant inaccuracies. A more rigorous approach uses the expression of the standard free energy change in the form of an equation as a function of temperature. This uses well known thermodynamic functions and the calculation of the standard free energy change, ΔG°, at the desired temperature. The standard reversible open-cell E.M.F., V_r°, can then be calculated using a relationship similar to the one in equation (4.14). Since the inclusion of these functions does not further understanding of fuel cell operation the interested reader is referred to [Eisenberg 1963] for the details of this approach.

Tabulated below is the Gibbs free energy of the reaction $H_2 + 0.5O_2 \rightarrow H_2O$ at various temperatures of interest [ΔG data with temperature from Larminie and Dicks 2003], and the corresponding OCV (calculated as per equation (4.14) above).

Temperature (°C)	E_{th} (Volts)	$\Delta G°$ (kJ mol^{-1})
25	1.23	-237.53
80 (liquid)	1.18	-228.20
80 (gas)	1.17	-226.1
100	1.17	-225.2
200	1.14	-220.4
400	1.09	-210.3
600	1.03	-199.6
800	0.98	-188.6
1,000	0.92	-177.4

Table 4-1. Theoretical E.M.F. and Gibbs free energy of the reaction $H_2 + 0.5O_2 \rightarrow H_2O$ at 1.013 bar for selected temperatures of interest.

4.2.3 The Effect of Pressure

The effect of pressure change on V_r of a complete cell at a constant temperature is obtained from consideration of its effect on the partial molar free energy. That is the effect on the chemical potential $\mu_i = \left(\frac{\partial G}{\partial x_i}\right)$ for each component species, i, participating in the overall reaction. The total effect of pressure for all components can therefore be expressed as:

$$\sum \nu_i \frac{\partial}{\partial p}\left(\frac{\partial G}{\partial x_i}\right) = \sum \nu_i \frac{\partial}{\partial x_i}\left(\frac{\partial G}{\partial p}\right) \qquad (4.23)$$

Since at constant temperature $\left(\frac{\partial G}{\partial p}\right) = \nu$, it can be shown from equations (4.4), (4.14) and (4.23) that the effect of a pressure change on the reversible total cell E.M.F. (V_r) is:

$$-n\mathcal{F}\frac{\partial}{\partial p}(V_r) = \sum \nu_i \left(\frac{\partial \nu}{\partial x_i}\right) = \Delta\nu \qquad (4.24)$$

Where $\Delta\nu$ (m^3) is the change in volume resulting from the reaction. Integrating equation (4.24) between p_1 and p_2 yields the reversible E.M.F. of the total cell at the higher pressure, p_2. Hence:

$$(V_r)_{p_2} = (V_r)_{p_1} - \frac{1}{n\mathcal{F}}\int_{p_1}^{p_2} \Delta\nu \, dp \qquad (4.25)$$

Several interesting conclusions can be drawn from equation (4.25). For a fuel cell in which all products and reactants are condensed phases for which the volume change is negligibly small, changes in pressure have little to no effect on the E.M.F. of the total cell. On the other hand, fuel cells in which there are sizeable changes in volume (e.g.

hydrogen-oxygen cells), the correction, that is the change in E.M.F., becomes significant. However, calculation of this correction requires information on the volume change due to the reaction.

4.2.4 Gas Diffusion Electrodes and the Three-Phase Limit

A variety of different types of electrodes are used in conjunction with fuel cell systems [Eisenberg 1963, Larminie and Dicks 2003]. These are classified by the electrochemical characteristics of each type. Refer to the cited reference for detailed information on the different types. The most relevant of these is the gas diffusion electrode, which has taken on great importance with the development of fuel cells using gases as the reactants. Treatment of such electrodes is complex as it must account for the physics of gas transport through a porous matrix. In addition, analysis of the reactants equilibrium with the electrolyte, and the kinetics and thermodynamics of the transport mechanism are all complex.

The region of contact between the reactants, electrolyte and electrode is of obviously great interest in fuel cell research. All of the reactions take place here and it is in this region that electron transport occurs. The fuel must transfer electrons to or from the electrode simultaneously as it enters the electrolyte as an ion. Therefore, the region in which this takes place must be at the three-phase limit, a line [Gorin and Recht 1963]. There are mechanisms for broadening this limit to achieve practically significant rates for the electrode process. Possible mechanisms are considered later. An intimate contact between the electrolyte and the electrode (the intersection of the three phases) must perforce exist for electron transfer to be possible [Gorin and Recht 1963].

The useful operation of a gas diffusion electrode depends on maintaining the three-phase equilibrium between the electrode (porous matrix), the reactant gas, and the electrolyte mentioned above. In practice, for a real system, gas diffusion electrodes have a distribution of pore radii. This makes measurement of the three-phase boundary, the surface area over which the three-phase equilibrium is established, difficult. Furthermore, there is no restriction forcing pores to be normal to the surface of the electrode, and pores may or may not be connected. It is usual to assume some distribution function for the pore radii centred around the most frequent radius, r_0. Thus, if the number of operating pores is given by the distribution function:

$$n(r) = \phi(r - r_0) \qquad (4.26)$$

Assuming perfectly cylindrical pores of average length $l_{avg.}$, then the total internal surface area of the electrode per unit apparent area is:

$$S = 2\pi l_{avg.} \int_0^\infty r\,\phi(r - r_0)dr \qquad (4.27)$$

Inside each pore the three-phase boundary is ideally a circle of radius $2\pi r$ or $\frac{S}{l_{avg.}}$; therefore, the total (cumulative) length of the three-phase boundary per unit apparent area of the electrode is given by the integration of all pores over the distribution:

$$L_B = 2\pi \int_0^{\infty} r\,\phi(r - r_0)dr \qquad (4.28)$$

Obviously, an active gas diffusion electrode should have the highest possible value of L_B (a large three-phase boundary per unit apparent area of the electrode surface).

4.2.5 Mechanisms for Broadening the Three-Phase Limit

There are three possible mechanisms for broadening the three-phase limit: diffusion of the gas through a thin film in the vicinity of the interface, diffusion of gas through the bulk electrode material, and surface diffusion across the electrode surface [Gorin and Recht 1963, Larminie and Dicks 2003].

Diffusion of the gas through a thin film in the vicinity of the interface is unlikely [Gorin and Recht 1963] based on inadequate diffusion rate through electrolytes. The diffusion rate of gases through metals (the bulk electrode material) is both easier to obtain and more promising as a possible mechanism. For example, the diffusion rate of hydrogen through nickel at atmospheric pressure is $1.46 \times 10^{-6}\ exp\left(-\frac{13{,}100}{RT}\right)$ moles.cm^{-1}s^{-1}. At 750 ℃ this becomes 2.37×10^{-9} moles.cm^{-1}s^{-1}, a factor of 10^3 greater than the diffusion of hydrogen through even a molten electrolyte at room temperature [Gorin and Recht 1963]. This is of course, greater still for porous electrodes (see also section 4.6).

This second mechanism is therefore a likely candidate for broadening the three-phase limit. Below is a simplified model of the contact between metal electrode and electrolyte showing in cross section a spherical metal granule of radius r of the porous metal electrode.

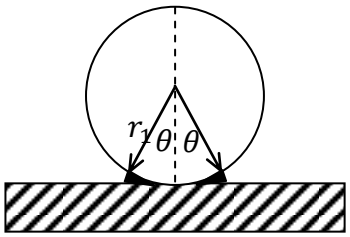

Figure 4-1. Model of contact between metal electrode (sphere) and solid electrolyte. Adapted from [Gorin and Recht 1963].

The angle, θ, is the portion of the cross section representing contact between the electrode granule and the electrolyte (Figure 4-1.). It is assumed that the rate of solution of gas into the electrode is controlled by the rate of penetration of the gas from an adsorbed layer of atoms, possibly dissociated, as described previously. Furthermore, the rate of dissolution is controlled by the rate of gas penetration into the metal surface to form said adsorbed layer [Gorin and Recht 1963]. It has been shown experimentally [Gorin and Recht 1963] that the rate of solution and dissolution of gas in metals is very rapid relative to the rate of diffusion through the bulk. Less is known conclusively about the rate determining step for adsorption and desorption. The available information shows that dissolved gases are present in their dissociated form when dissolved in metals. The adsorbed layer should therefore be considered to be the gas in its dissociated form [Gorin and Recht 1963].

Two more assumptions are now necessary. The rate of adsorption is assumed to be very rapid compared to the rate of solution such that the concentration in the adsorbed layer is in equilibrium with the gas phase (so adsorption is not rate limiting). It is further assumed that the electrode reaction occurs within the adsorbed layer, and that it is very rapid compared to the rate of desorption from the electrode. *Ergo*, the equilibrium electrode potential is maintained and is determined by the concentration of potential-determining species in the adsorbed layer. The mathematical treatment of this is detailed in the cited reference, but adds little to one's understanding of the three-phase limit and was therefore omitted.

As derived in the cited source the current density at constant polarisation drops only proportional to the square root of the pressure. This implies that this mechanism for broadening the three-phase boundary is favoured at low pressures [Gorin and Recht 1963]. Additionally the current density at constant polarisation is proportional to the permeation rate of the electrode and is fairly insensitive to the reaction rate at the electrode. This implies that even for non-insignificant activation polarisation this technique for broadening the three-phase limit will function. This treatment has a few anomalous results, indicating it is far from a complete explanation. One very relevant example is platinum. The permeability of hydrogen through platinum is known to be considerably smaller than through nickel or iron [Gorin and Recht 1963]. Despite this, however, platinum is demonstrably [Gorin and Recht 1963] superior as a hydrogen (fuel) electrode particularly at lower temperatures. The difference may arise from a difference in bulk permeation and thin film permeation, with the theory above applying only to the former [Gorin and Recht 1963].

4.3 Polarisation as a Measure of Irreversibility

4.3.1 The Closed-Circuit E.M.F.

All of the theory outlined above is based on the assumption of thermodynamic reversibility. However, in reality, some degree of irreversibility will always exist. Hence it is useful to explore the kinetics at the heart of the irreversibilities of electrochemical fuel cells. When a fuel cell that is reversible at open-circuit is loaded each of the two electrodes will undergo a shift in potential (polarisation) in opposite directions. The cathodes become less cathodic and the anodes less anodic, decreasing the available cell voltage. This is above and beyond the linear ohmic potential drop that is the normal operation of a cell or battery. Figure 4-2. below shows the ohmic potential drop (straight lines from cathode and anode potential) as well as two of four possible polarisations: concentration polarisation and activation polarisation.

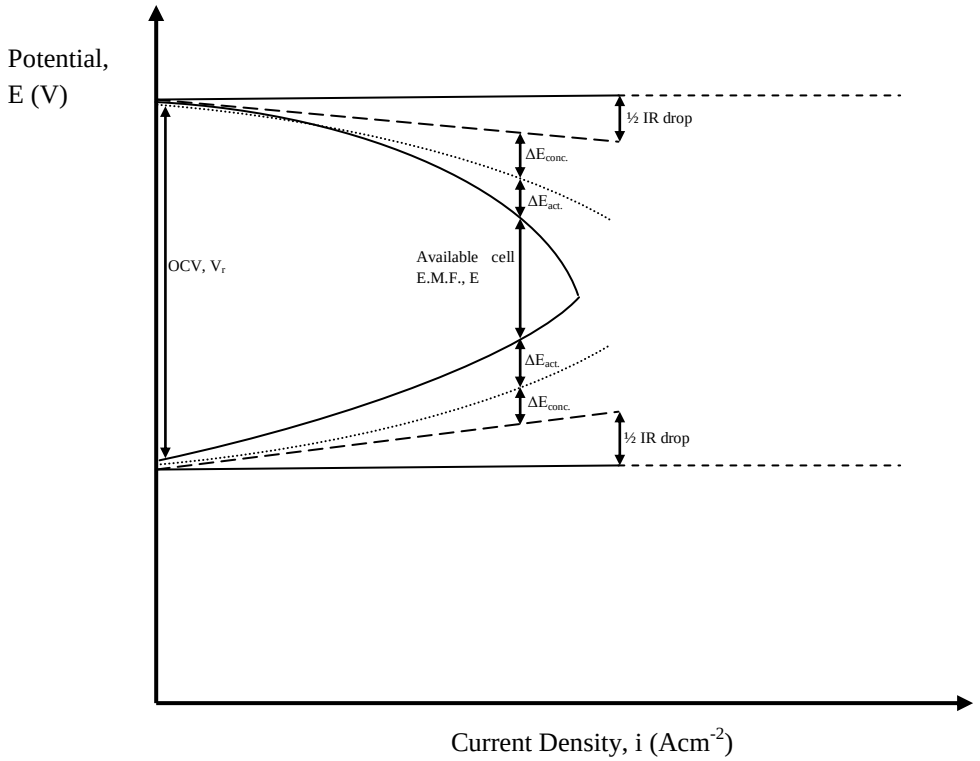

Figure 4-2. Potential against current density and polarisation relationships in a fuel cell. Adapted from [Eisenberg 1963].

The complete list of polarisations is: the concentration polarisation of the electrolyte, $\Delta E_{conc.,E}$, the chemical or activation polarisation, $\Delta E_{act.}$, gas side concentration polarisation (applicable to gas diffusion electrodes) $\Delta E_{conc.,G}$, and the resistance polarisation, ΔE_{ohmic}. The total polarisation of each electrode is determinable by the superposition principle to be:

$$\Delta E_{Total} = \Delta E_{act.} + \Delta E_{conc.,E} + \Delta E_{conc.,G} + \Delta E_{ohmic} \quad (4.29)$$

Hence the cell voltage is given by:

$$V = \left(E_{r,A} - \Delta E_{Total,A}\right) - \left(E_{r,C} - \Delta E_{Total,C}\right) - I\sum R_i \quad (4.30)$$

$$V = V_r - \Delta E_{Total,A} + \Delta E_{Total,C} - I\sum R_i \quad (4.31)$$

Where:

$V =$ cell voltage (V)
$\Delta E_{Total,A} =$ sum of components of anodic polarisation (a positive number) (V)
$\Delta E_{Total,C} =$ sum of all cathodic polarisations (a negative number) (V)
$I =$ load current (A)
$\sum R_i =$ sum of all internal cell resistances (usually electrolyte, electrode resistance and interconnect) (Ω)

The various components of polarisation of the electrodes and the ohmic potential drops inside the cell reduce the voltage of a closed-circuit cell from its thermodynamic open-circuit voltage, V_r. Polarisation increases proportional to increasing current density, leading to the drop in cell voltage as described by equation (4.31). Thus the thermodynamic irreversibility of a fuel cell increases with increasing current density (increasing reaction rate). Determination of each of the polarisations follows.

4.3.2 Activation Polarisation

Activation polarisation occurs because one or more of the steps of the overall reaction at a single electrode is kinetically slow – that is involves activation energy barriers to be overcome. This mode of polarisation is at times referred to as overpotential, overvoltage or chemical polarisation. The terms chemical or activation polarisation are preferred as they describe the total of all chemical kinetic effects in each individual electrode process [Eisenberg 1963, Heath and Sweeney 1963, Larminie and Dicks 2003, Winkler 2003]. For each electrode the activation polarisation can be expressed as:

$$\Delta E_{act.} = \left[\frac{RT}{\alpha n\mathcal{F}}\right]\ln\left(\frac{i}{i_0}\right) \quad (4.32)$$

Where:

$\alpha =$ fraction of the activation energy barrier acting in the forward direction
$i =$ applied current density (Acm^{-2})
$i_0 =$ exchange current density (Acm^{-2})

The exchange current density is of great importance being related to the height of the activation energy barrier, ΔF^*, in the following manner:

$$i_0 = \frac{n\mathcal{F}}{N_A}\left[\frac{kT}{h}\right] C^{\circ} e^{\left(-\frac{\Delta F^*}{RT}\right)} \qquad (4.33)$$

Where:

$N_A =$ Avogadro's number (6.0221418×10^{23} mol^{-1})
$k =$ Boltzmann's constant (1.3806504×10^{-23} JK^{-1})
$h =$ Planck's constant (6.626068×10^{-34} Js)

The exchange current density represents the rate of forward and backward reactions around equilibrium. The larger the value of i_0, the lower the chemical polarisation involved. Its value is influenced by the nature of the electrode reaction itself as well as any catalytic effects of the electrode surface.

Frequently, the activation polarisation is expressed in the form of the Tafel equation [Eisenberg 1963, Larminie and Dicks 2003, Winkler 2003]:

$$\Delta E_{act.} = a + b \log i \qquad (4.34)$$

Where:

$$a = \left[\frac{RT}{\alpha n\mathcal{F}}\right] \ln i_0$$
$$b = 2.303\left[\frac{RT}{\alpha n\mathcal{F}}\right]$$

Plotting equation (4.34) as $\Delta E_{act.}$ against $\log i$ allows the determination of the kinetic parameters α and i_0 from the intercept and gradient of the plot.

4.3.3 Concentration Polarisation of the Electrolyte

When an electrochemical reaction takes place at an electrode, changes in the concentration of the potential-determining species will occur in the immediate vicinity of the electrode surface. The resulting concentration gradient shifts the electrode potential an amount equal to the E.M.F. of a cell of corresponding concentration. Hence the concentration polarisation is defined as:

$$\Delta E_{conc.,E} = \left[\frac{RT}{n\mathcal{F}}\right] \ln\left(\frac{C_i}{C_0}\right) \qquad (4.35)$$

Where C_i and C_0 are the interfacial and bulk concentrations of the reacting species, respectively. If more than one species is potential-determining, two gradients will usually form as an increase in the concentration of one species and a decrease in the

concentration of the other. Thus, the ratios of concentrations of both species need to be considered in the application of equation (4.35) by superposition.

The maximum current density that can be passed depends on the rate of mass transfer of oxidant into fuel. This value, referred to as the limiting current density, i_L, is obtained when the difference in concentration is at its maximum. That is, when $\Delta C = C_0$, the bulk concentration. From equation (4.35) it can be shown that the concentration polarisation within the electrolyte of a fuel cell is:

$$\Delta E_{conc.,E} = \left[\frac{RT}{n\mathcal{F}}\right] \ln\left(\frac{i_L - i}{i_L}\right) \qquad (4.36)$$

Naturally, concentration polarisation will also take place at the other electrode, at which a species is generated and it concentration builds up to form a local concentration gradient with a different limiting current density at each electrode.

Concentration polarisation within the electrolyte of a fuel cell can be of great significance when either low bulk concentrations are involved, or when large concentration gradients result from poor mass transfer within the fuel cell [Eisenberg 1963, Heath and Sweeney 1963, Larminie and Dicks 2003]. The former is true of low fuel mixtures frequently used in research. The latter is mainly an issue of diffusion. Therefore, the thinner the section the gaseous species must permeate or diffuse through the better. Hence, it is expected that for micro designs, where the thickest component is the support structure (even then no more than 200 μm), there will be very little concentration polarisation and hence better performance than more conventional designs.

4.3.4 Concentration Polarisation of the Gases

When either a reactant or a product are gaseous and there is a change in the partial pressure of the potential-determining species in the vicinity of the reaction site compared with its partial pressure in the bulk of the gaseous phase, gas concentration polarisation becomes relevant. A representative example is an air electrode in a fuel cell [Eisenberg 1963, Heath and Sweeney 1963, Larminie and Dicks 2003]. When the reaction proceeds at a finite rate and current density, the partial pressure of oxygen near the reaction site within the pores of the electrode is reduced compared to the partial pressure of oxygen in the bulk of the air feed stream to the fuel cell. This change, according to thermodynamic equilibrium, causes a shift in the E.M.F. of the electrode dependent on the gas concentration. Concentration polarisation is therefore concerned with, and indeed a measure of, gas transport. This is what is meant by the term gas, or gas side, polarisation, and is equal to:

$$\Delta E_{conc.,G} = \left[\frac{RT}{n\mathcal{F}}\right] \ln \frac{(p_A)_1}{(p_A)_2'} \qquad (4.37)$$

For some types of fuel cells more than one gaseous concentration gradient is present and needs to be accounted for. This is achieved by using the ratios of partial pressures of all the relevant gaseous species present in the bulk and near the reaction site. On a similar note, the same equation must be applied to the fuel side and the total polarisations summed to yield the total gas concentration polarisation.

Catalysis and elevated temperatures may be employed to reduce the activation polarisation, but will not have any effect on concentration polarisation. In order to reduce concentration polarisation the diffusion thickness needs to be reduced [Mitchell 1963]. Ordinarily polarisation due to gas phase mass transfer is insignificant except at very high current densities (in excess of 200 mA cm^{-2}).

4.3.5 Resistance Polarisation

In some cases the electrochemical reaction taking place at the electrode causes a significant change in the specific conductivity of the electrolyte resulting in an additional loss of potential termed resistance polarisation [Eisenberg 1963]. Resistance (or ohmic) polarisation is found by integrating the potential drop across a diffusion boundary of thickness δ, giving:

$$\Delta E_{ohmic} = \int_0^{\delta} \frac{i}{\Lambda C_x} dx \qquad (4.38)$$

Where:

$\Lambda =$ equivalent conductance of the reacting ion (cm^2/ohm.equivalent)

$C_x =$ value of local concentration (moles.cm^{-3})

Mass transfer theory can be used to show that the lowered conductance near the boundary layer is given by [Eisenberg 1963]:

$$\Delta E_{ohmic} = \left[\frac{n\mathcal{F}D}{\Lambda(1-\mathrm{t_i})}\right] \ln\left(\frac{i_L - i}{i_L}\right) \qquad (4.39)$$

Where D is the diffusion constant. A similar relationship exists for the other electrode. Eisenberg (1963) makes the interesting observation that at times the decrease in conductivity at one electrode is accompanied by a nearly equal increase in conductivity at the other electrode so that the two resistance polarisations counter and even cancel each other.

Even where the above effect is small to negligible the high internal resistance of most fuel cells (especially the electrolyte) has been the most limiting factor, at least in terms

of polarisation-induced voltage losses under load, even in high temperature cells [Gorin and Recht 1963]. Practical cells should have a value of around 1 Ωcm^{-2} in order to be considered useful. It can be calculated according to:

$$R = \frac{t}{\kappa\alpha} \qquad (4.40)$$

Where:

$R =$ internal resistivity (Ωcm^{-2})
$t =$ thickness of electrolyte matrix (cm)
$\kappa =$ specific conductivity of electrolyte (cm2/Ω or Siemens, S)
$\alpha =$ porosity fraction of matrix (no units)

Reducing thickness of solid electrolyte is one of the best ways to lower the operating temperature and ohmic polarisation losses [Larminie and Dicks 2003, Meng *et al.* 2008].

4.4 Thermodynamic Losses in Fuel Cells

While the efficiency of fuel cells is typically very high, operating irreversibly at constant temperature and pressure means the electrical energy developed (the useful work done by the system) is always less than the decrease in free energy of the system. The loss is as heat energy, given by:

$$-Q_{cell} = -T\Delta S - \left(\frac{n\mathcal{F}}{4.185}\right)(V_r - V) \qquad (4.41)$$

Where V_r and V are the reversible E.M.F. and the actual E.M.F. respectively, and other symbols have their usual meaning. Notice that depending on the magnitudes of the two terms the resulting heat is either a net absorption of heat by the cell or a net increase in the heat that must be absorbed by the surroundings (has to be removed from the cell). Since the actual E.M.F. is highly dependent on current density it is possible that the direction of net heat changes with varying current density. Normally, however, the entropy term is smaller than the heat change due to thermodynamic irreversibility of the cell (that is polarisation and ohmic potential drops), so the heat is usually generated rather than absorbed [Eisenberg 1963, Larminie and Dicks 2003]. That is the fuel cell heats up, dissipating heat energy to its surroundings. The mechanisms governing this are as follows:

(a). In the bulk electrolyte resulting from the ohmic potential drop (IR) per unit cross-sectional area of the cell. This corresponds to resistive heating:

$$Q_R = I^2 \frac{t}{\kappa} \qquad (4.42)$$

Where:

Q_R = resistive heat generated (Watts.cm^{-2}mol^{-1})
I = current (A)
t = electrolyte thickness (cm)
κ = electrolyte specific conductivity (1/Ωcm)

(b). At the electrode surfaces and in their vicinity due to the polarisation and the reversible heat term $T\Delta S$. Per unit cross-sectional area of the cell the heat generated at both electrodes is:

$$Q_E = I\left[\sum \Delta E_A + \sum \Delta E_C + \left(\frac{4.185}{n}\right)(T\Delta S)\right] \qquad (4.43)$$

Where Q_E is the polarisation heat generated at the electrodes (Watts.cm^{-2}mol^{-1}), and other symbols have their usual meaning. Note that the summations include all modes of polarisation at the anode and cathode respectively.

Equations (4.42) and (4.43) are heat outputs (that is are negative if the usual sign convention is followed). They are expressed in this form for convenience, and since it is usual for the heat to be generated rather than absorbed then the sign convention is somewhat redundant. Far more critically the heat is per mole of reaction product produced in the particular cell. Since the cell operates at elevated temperature this heat generated is actually useful in maintaining the temperature.

4.5 The Role of Catalysis in the Fuel Cell Reaction

Catalysts are required to lower the activation energy rather than supplying large quantities of heat energy for activation. As such the catalysis of reactions important to electrochemical fuel cells is of paramount importance to the design of low temperature fuel cells [Heath and Sweeney 1963, Larminie and Dicks 2003]. The use of catalysts, as semi-empirical as the theory remains, is often of importance to other sorts of fuel cells also [Heath and Sweeney 1963] enabling the use of less rare (and therefore less costly) catalytic materials as well as introducing some scope for temperature reduction.

Any catalyst used participates in three or more reactions in the electrochemical process. These are adsorption, electron transfer, and surface reaction [Heath and Sweeney 1963].

The adsorption of a reactant should be strong enough for oxidation or reduction to take place on the surface of the electrode, and at the same time should be sufficiently quick to enable the generation of high currents. The adsorption mechanism is usually chemisorption rather than physisorption. The mechanism of chemisorption involves the creation of partially covalent bonds between adsorbent and adsorbate [Heath and Sweeney 1963]. It has been shown that electrode reactions depend on the free energy of adsorption of the reactants – making low to negligible adsorption activation energies desirable [Heath and Sweeney 1963].

The most popular catalysts for electrochemical fuel cells are the transition metals. Even more important than their free energy is the peculiar bonding of the *d* orbitals known as the *d*-band character. This is defined as the degree to which the *d* electron orbitals of a metal are filled, and has been related to both the adsorption energy and work function [Heath and Sweeney 1963]. Metals with a low percentage *d*-band character (many holes in the *d* orbital), have many unpaired electrons. These vacant sites may react with electron donors and thus adsorb the donor more strongly than one with less vacant sites (fewer holes) [Heath and Sweeney 1963]. This is true for catalysts when adsorption is slower than desorption. When desorption is slower than adsorption a metal with a higher percentage *d*-band character would probably be a better catalyst.

The electron work function of a metal increases with increasing percentage *d*-band character since electron spins are paired as the *d* orbital vacancies are occupied. These paired electrons are more stable than unpaired ones, and hence require more energy to be extracted from the orbital. The energy of adsorption, therefore, decreases as work function increases [Heath and Sweeney 1963]. As might be expected there is a relation between the work function and rate at which a reaction progresses. The exchange current increases exponentially [Heath and Sweeney 1963] with increasing work function. In a similar manner the exchange current increases with increasing percentage *d*-band character. Hence a lower work function leads to better catalysis, and in fact must be lower than the ionisation potential of the reactant for discharge to occur [Heath and Sweeney 1963]. This can be viewed from a slightly different perspective also: when the work function is decreased the energy for the reaction $A^+ + e^- \rightarrow A$, given by $\Delta F_0 \approx ionisation\ potential - work\ function$, is increased with respect to the ground state. The activation energy is reduced proportionally [Heath and Sweeney 1963]. The electron work function also influences surface reactions. Interactions with the outer orbital electrons and promotion of these electrons in the reactants causes the free energy of the activated complex to be reduced, accelerating the reaction [Heath and Sweeney 1963].

Electronic factors do not control catalysis exclusively. Geometric factors may also come into play – the spacing and crystallographic arrangement of the catalyst's crystal lattice. These principally affect the rate of adsorption and desorption. Larger interatomic

distances on the catalyst lattice require higher activation energy because the reactant molecule must dissociate before adsorption; conversely for very small lattice constants the repulsive forces inhibit and retard adsorption [Heath and Sweeney 1963].

It is generally accepted [Heath and Sweeney 1963, Larminie and Dicks 2003] that Group VIII transition metals, including nickel, palladium and platinum, are the most effective catalysts for the anodic oxidation of H_2, CO, hydrocarbons as well as alcohols. The examples cited require the lowest heats of activation for adsorption and are active catalysts for non-electrochemical heterogeneous hydrogenation-dehydrogenation reactions. Assuming they bond covalently with the fuel via the metal's *d* orbital (as noted previously) their catalytic behaviour is explained in more detail for both hydrogen and carbonaceous fuels in the cited reference.

In summary, many options are available for hydrogen-oxygen fuel cells, but things look less promising for fuel cells utilising carbonaceous fuels; adding to the list of hurdles that need to be overcome if carbonaceous fuels are to be employed successfully.

4.6 Kinetics of Porous Electrodes

The question whether the kinetics derived for nonporous electrodes can be applied to porous electrodes is eminently relevant. If the reaction rate at the surface is faster than the diffusion rate in the pores, then the pores will become depleted of reactants very rapidly. Of course, when a reaction step follows a diffusion step in a nonporous electrode the overall kinetics is controlled by the slower of the two steps. Some authors [Heath and Sweeney 1963] term this a successive diffusion-reaction mechanism. In a porous electrode, on the other hand, the overall kinetics are controlled by both steps irrespective of their relative rates [Eisenberg 1963, Heath and Sweeney 1963]. The influence of diffusion and reaction rates is complementary, both having an effect on overall electrode polarisation. Figure 4-3. shows these graphically based on quantitative analysis of this coupled diffusion and reaction control mechanism [Heath and Sweeney 1963, source adapted these from Tarmy 1961].

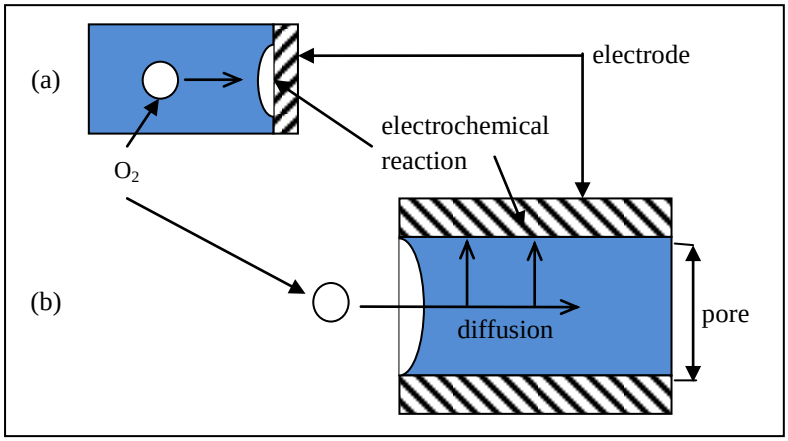

Figure 4-3. Schematic of coupled (b) and successive (a) diffusion-electrode reaction mechanisms. Adapted from [Heath and Sweeney 1963].

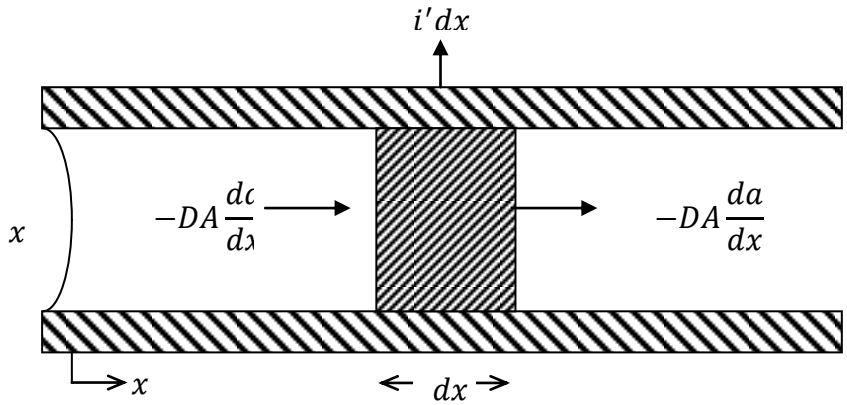

Figure 4-4. Diffusion and electrochemical reaction in a single pore. Adapted from [Heath and Sweeney 1963].

Consider a single pore of cross sectional area A and a gas-electrolyte interface at $x = 0$, the mouth of the pore (Figure 4-4.). The ratio of pore diameter to length is sufficiently large to satisfy the assumption that the pore is semi-infinite. Assuming that the polarisation through the pore is constant; implying all ion and reactant species activities are mostly constant and the ohmic loss within the pore is negligible [Heath and Sweeney 1963]. The activity of the gaseous reactant species within the electrolyte is taken to be low, with an activity at the pore mouth, $x = 0$, of a_0.

At any element, dx, inside the pore the net rate of gas diffusion into dx is $DA\left(\frac{d^2a}{dx^2}\right)dx$ and the rate of electrochemical reaction of the gas and rate at which it exits the element is $\left(\frac{1}{n\mathcal{F}}\right)i'dx$ where i' is the current length density in A/m of pore length. When steady state is reached:

$$\frac{d^2a}{dx^2} = \frac{1}{DAn\mathcal{F}} i' \qquad (4.44)$$

Now the current length density, i', is given by:

$$i' = i_0 A_s a \, exp\left(\ln \frac{I}{I_0}\right) \qquad (4.45)$$

Where:

$i_0 =$ exchange current density (A.cm^{-2})

$A_s =$ inside surface area of pore per unit length (m^2/m)

Hence, equation (4.44) becomes:

$$\frac{d^2a}{dx^2} = \frac{1}{DAn\mathcal{F}} i_0 A_s a \, exp\left(\ln \frac{I}{I_0}\right) \qquad (4.46)$$

Substituting $p = \frac{da}{dx}$ into equation (4.46) to solve the equation yields:

$$\int_0^p p \, dp = \frac{i_0 A_s \, exp\left(\ln \frac{I}{I_0}\right)}{DAn\mathcal{F}} \int_{a_{x=\infty}}^{a} a \, da \qquad (4.47)$$

Now if at $x = \infty$, the activity gradient is zero then $\frac{da}{dx} = p = 0$ and the activity becomes $a_{x=\infty}$. Integrating equation (4.47) gives:

$$\frac{da}{dx} = -\left[\frac{i_0 A_s \, exp\left(\ln \frac{I}{I_0}\right)}{DAn\mathcal{F}}\right]^{\frac{1}{2}} \sqrt{a^2 - a_{x=\infty}^2} \qquad (4.48)$$

The minus sign indicates that this is a negative gradient with activity decreasing as x increases. Solving and setting $x = \infty$ gives a numerical value for the activity at the end of an infinitely long pore; $a_{x=\infty} = 0$. The cited reference gives this as a relationship between pore depth and the activity of the limiting reactant.

The activity of a limiting gas reactant decreases rapidly with penetration into the electrode pore. This loss becomes even more severe at higher polarisations. Therefore, long pores in the order of a few mm serve no purpose as the activity is reduced to nearly zero [Heath and Sweeney 1963]. It appears, therefore that there is an inherent benefit in designing microstructured fuel cells from the kinetics aspect in addition to any others. The relationship referred to also demonstrates that in order to increase performance rather than increase the effect of pores by increasing their length (which in fact is highly

deleterious to performance) it is far more useful to increase the number of pores (i.e. the porosity of the electrodes).

The total current obtained by a single pore is found by multiplying both sides of equation (4.44) by dx and integrating over the pore depth (from $x = 0$ to $x = x$). For the theoretical semi-infinite pore considered this is [Heath and Sweeney 1963]:

$$I = \int_0^\infty i' \, dx = DAn\mathcal{F} \int_0^\infty \left(\frac{d^2a}{dx^2}\right) dx \qquad (4.49)$$

Finally, it can be shown that:

$$I = \sqrt{DAn\mathcal{F}a_0 I_0 A_s} \exp\left(\ln \frac{I}{I_0}\right) \qquad (4.50)$$

The result, calculated for one pore, can be applied to a porous electrode if the total number of pores and the pore diameter distribution are known. From equation (4.50) it is clear that the kinetics of a porous electrode are very different from a nonporous one. Hence, performance will differ significantly from that often reported in studies of kinetics since these tend to use nonporous electrodes [Heath and Sweeney 1963]. A porous electrode will polarise twice as fast as a nonporous one at the same load (i.e. the same current). Increasing the exchange current via catalysis or use of large surface areas increases the polarised current less than expected from a nonporous model. *Ergo* the improved performance of porous electrodes compared with their non-porous counterparts does not originate from a more efficient electrode process. Rather, higher current densities and lower polarisations are achieved by means of a larger active area.

Perhaps the greatest advantage of high temperature operation of a fuel cell is the accelerated kinetics [Gorin and Recht 1963, Winkler 2003]. This can be expressed in the form of an Arrhenius relationship as done in the cited sources. The expression shows that for a given reaction (and hence ΔH_a, the enthalpy of activation of the process) the reaction rate, k, increases exponentially with increasing temperature.

Part II: Phenomenological Model

Experimentally determined values of activity coefficients for solid electrolytes are not readily available in the literature. This lack of activity coefficient data specifically, and other information more generally (e.g. volume changes of reactions) really relegates the first principles model to purely didactic uses. The situation is exacerbated by the fact that solution of many of the equations that fall under the first principles model requires extensive experimental data relating to specific conditions of the researcher's cell over

and above difficult to find data for activity coefficients and the like. Furthermore, there is no clear way to integrate the various equations into an intelligible cell model rather than a collection of models for the various phenomena. That said it excels at clearly portraying the precise mechanisms of operation of fuel cells which is the reason for its inclusion here.

4.7 Fuel Cell Thermodynamics – the Phenomenological Perspective

The phenomenological model is best approached by establishing the relationship between flow of charge (current) and the electrochemical reaction. For a detailed review on the salient processes and their intricacies see Approach 1: the First-Principles model.

By definition [Winkler 2003]:

$$I = \dot{n}(-e^-)N_A = -\dot{n}\mathcal{F} = -xn_{fuel}\mathcal{F} \quad (4.51)$$

Where:

$\dot{n}$ = molar flow of electrons (mol.s^{-1})
n_{fuel} = molar flow of spent fuel (mol.s^{-1})
e^- = electronic charge 1.602178×10^{-19} $(Coulombs)$
$\mathcal{F}$ = Faraday's Constant $(Coulombs/mol)$
x = number of electron per mole of fuel $(no\ units)$

The above equation shows that the electric current is a measure of the fuel spent [Winkler 2003]. Now, matching the thermodynamic and electrical parameters can be done via the power but not the work [Winkler 2003]. This is because mass or substance transport is used in thermodynamic calculations and charge transport for electrical phenomena – power is the only common ground [Camilleri 2009]. The reversible power can be expressed in terms of the reversible potential difference and the current, as well as the product of the molar flow of fuel and the change in enthalpy of reaction (the Gibbs free energy change, $\Delta^r G$):

$$Power_{reversible} = V_r I = n_{fuel} w_r = n_{fuel}\Delta^r G \quad (4.52)$$

The reversible voltage can be deduced from equations (4.51) and (4.52):

$$V_r = \frac{-n_{fuel}\Delta^r G}{\dot{n}\mathcal{F}} \quad (4.53)$$

Now let n be the number of electrons that are released during the ionisation process of one fuel molecule. Therefore, the reversible voltage can be expressed as:

$$V_r = \frac{-\Delta^r G}{n\mathcal{F}} \qquad (4.54)$$

Notice that this is the same relationship between free energy change and the reversible open-circuit voltage as given by equation (4.14) despite the different approach in its derivation. The derivation is shown to establish that the phenomenological and first-principles models are indeed equivalent, but as will be seen from the following sections the phenomenological model is easier to work with and is also easily integrated into a model representative of the whole cell rather than isolated components and phenomena [Camilleri 2009].

4.8 Fuel Utilisation, Ohmic Voltage Losses and Mixing Effects

Fuel utilization, U_f, is the ratio of the spent fuel flow to the inlet fuel flow [Larminie and Dicks 2003, Winkler 2003]:

$$U_f = 1 - \frac{\dot{m}_{fuel\ outlet}}{\dot{m}_{fuel\ inlet}} \qquad (4.55)$$

Where:

$\dot{m}_{fuel\ outlet}$ = mass flow rate of fuel at the outlet of the anode (kg s^{-1})
$\dot{m}_{fuel\ inlet}$ = mass flow rate of fuel at cell inlet (kg s^{-1})

A similar definition can be written for molar flow rates. Notice that the reaction products (e.g. water) are mixed with the anode gas and its concentration increases with increasing fuel utilization [Larminie and Dicks 2003, Winkler 2003]. These mixing effects are irreversible. As a result they increase the entropy of the system. *Ergo*, reversible fuel cell operation is only possible as the limiting process of the real process with $U_f \to 0$ [Camilleri 2009].

The voltage is a measure of exergy, similar to the work done by a thermodynamic process. Exergy is defined as the potential of the reversible work of a system related to the ambient state 0 [Larminie and Dicks 2003, Winkler 2003]. The voltage loss due to the electrical resistance implies an additional increase in entropy, that is an increasingly irreversible process [Larminie and Dicks 2003, Winkler 2003].

$$\Delta V = IR \qquad (4.56)$$

Where:

ΔV = ohmic polarisation (voltage loss due to resistance) (V)
I = current drawn from cell (A)
R = electrical resistance of cell (Ω)

The voltage drop corresponds to a loss in total power generated, given by:

$$Power_{loss} = \Delta VI = I^2R = TU_f n_{f,in}\Delta S \quad (4.57)$$

Where:

$T =$ absolute temperature K
$n_{f,in} =$ molar flow of fuel at input (mol.s^{-1})
$\Delta S =$ entropy change JK^{-1}

Equation (4.57) shows that the irreversible entropy increase attendant with an ohmic power loss is smaller in fuel cells operating at lower temperatures [Winkler 2003]. The irreversible entropy can be calculated using:

$$\Delta S = \frac{U_f n_{f,in} R(n\mathcal{F})^2}{T} \quad (4.58)$$

It has been demonstrated [Winkler 2003] that the HT-SOFC has the best exergic efficiency, of about 55-65% (maximum theoretical is about 70–80%). Exergic efficiency, ζ, is defined as:

$$\zeta = \frac{Work_{real}}{Work_{reversible}} \quad (4.59)$$

Losses due to irreversibility (polarisation losses) are the cause behind the difference in efficiency of a reversible and a real fuel cell process [Larminie and Dicks 2003, Winkler 2003].

4.9 Electrode Polarisations

Polarisation is a voltage loss, and is a function of current density. Total polarisation is divided into three separate terms originating from different phenomena [Ivers-Tiffée and Virkar 2003]. The three dominant phenomena are: ohmic polarisation, concentration polarisation and activation polarisation. The greatest component of the fuel is normally hydrogen in one form or another (whether as pure hydrogen or in hydrocarbons such as alcohols), so the focus will be on the oxidation of hydrogen. The overall reaction is:

$$H_{2\ (gas,\ anode)} + \frac{1}{2}O_{2\ (gas,\ cathode)} \longrightarrow H_2O_{\ (gas,\ anode)}$$

At open-circuit, with the electrochemical potential of oxide ions balanced across the oxide-ion conductor (the electrolyte) a reversible voltage, V_r, between the anode and

cathode (called the Nernst potential), is given by the Nernst equation, one form of which is equation (4.60). The open-circuit voltage (OCV), that is the Nernst potential, can be expressed in terms of partial pressures [Ivers-Tiffée and Virkar 2003, Larminie and Dicks 2003]:

$$V_r = -\frac{\Delta G}{2\mathcal{F}} = -\frac{\Delta G^\circ}{2\mathcal{F}} - \frac{RT}{2\mathcal{F}}\ln\left(\frac{p_{H_2O}^A}{p_{H_2}^A p_{O_2}^{C\ 1/2}}\right) = V_r^\circ + \frac{RT}{4\mathcal{F}}\ln\left(\frac{p_{O_2}^C p_{H_2}^{A\ 2}}{p_{H_2O}^{A\ 2}}\right) \qquad (4.60)$$

Where:

V_r = theoretical maximum cell voltage for the overall chemical reaction (V)
ΔG = change in Gibbs free energy ($Jmol^{-1}$)
$\mathcal{F}$ = number of Faradays ($\mathcal{F} = 96484.56$ Coulombs/mol) per equivalent
R = universal gas constant (8.314472 $Jmol^{-1}K^{-1}$)
T = absolute temperature (K)
$p_{O_2}^C$ = partial pressure of oxygen in the cathode gas (bar)
$p_{H_2}^A$ = partial pressure of hydrogen in the anode gas (bar)
$p_{H_2O}^A$ = partial pressure of water in the anode gas (the exhaust stream) (bar)

It is generally assumed that the partial pressures in the vicinity of the electrodes is to all intents and purposes fixed [Ivers-Tiffée and Virkar 2003], regardless of current density (i.e. irrespective of load). This implies that the Nernst voltage, V_r, is not a function of current density. Figure 4-5. below shows a typical voltage versus current density plot demonstrating polarisation where the cell voltage is a function of current density. It is interesting to compare this to Figure 4-2. where it is divided into the respective electrodes.

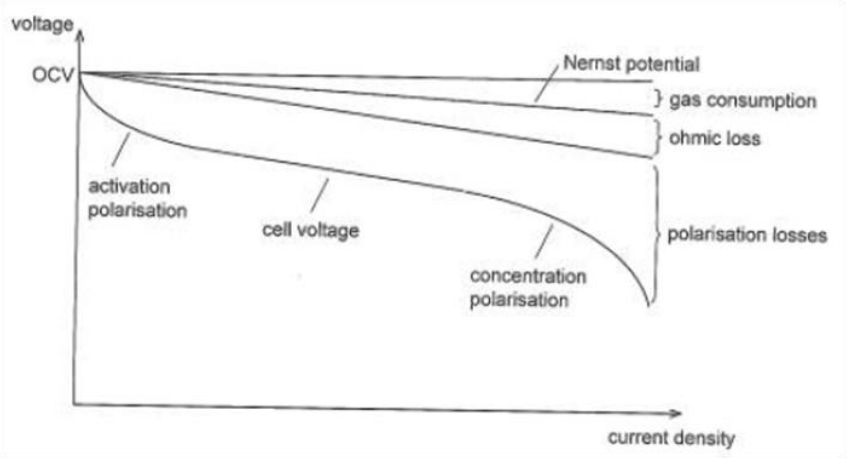

Figure 4-5. Typical plot showing polarisation curve when cell voltage is a function of current density. Activation polarisation is usually dominant at low current densities, and concentration polarisation is dominant at high current densities (when the transport of reactive species becomes the limiting factor) as can be surmised from the curve itself [Ivers-Tiffée and Virkar 2003].

The larger a cell the more likely local polarisations vary from point to point. Electrode overpotential (defined as the difference between local potential of the electrode when under load and the OCV) is also a local property as it depends on the bulk gas composition and current density in a given location [Khaleel and Selman 2003]. Similarly, in larger cells, there can be non-negligible differences from point to point in the current, with electrodes experiencing internal currents where local potentials vary. Such considerations are far less important for small cells where any variations would be minute. This is indeed an additional advantage of micro-designs since it implies they are less prone to internal losses in the form of internal currents than their larger counterparts.

4.9.1 Ohmic or Resistance Polarisation

For a complete definition of this please see the Part I: the First-Principles model (section 4.3.5). The relationship between voltage and current density is assumed to be linear, and is described by resistivity, a material property. In a similar manner the transport of oxide ions through the electrolyte can be said to be governed by the ionic resistivity of the electrolyte material. Secondary (insulating phases) formed in the electrodes and porosity both affect the electrical resistivity. The ohmic resistances at any given current density lead to a voltage loss given by:

$$\Delta E_{ohmic} = (\rho_A t_A + \rho_E t_E + \rho_C t_C + R_{contact})i \qquad (4.61)$$

Where:

$\rho_{A/E/C}$ = resistivity of the Anode, Electrolyte and Cathode respectively (Ωm)

$\rho_A = R\frac{A}{l}$ where R is the electrical resistance (Ω), A is the cross-sectional area (m^2) and l is the length (component thickness in this case) (m).

$t_{A/E/C}$ = thickness of the Anode, Electrolyte and Cathode respectively (m)

$R_{contact}$ = contact resistance (if any) (Ωm^2)

i = current density (Am^{-2})

In SOFCs the main contribution to the resistance polarisation comes from the electrolyte since its ionic resistivity is typically far greater than the electronic resistivities of the electrodes [Ivers-Tiffée and Virkar 2003, Larminie and Dicks 2003]. The presence of high resistivity secondary phases can change this, especially where electrode-supported cells with thin electrolytes are used, resulting in the increasing dominance of the electrode resistivity. This accounts, in some part at least, for the improved performance of metallic anode-supported cells compared with electrolyte supported ones (the thickest component has a very low ohmic loss) [Ivers-Tiffée and Virkar 2003].

4.9.2 Concentration Polarisation

In SOFCs the reacting species are gaseous. At the anode hydrogen must be transported from the fuel stream through the porous anode to the three-phase boundary at the electrode-electrolyte interface. Here the hydrogen reacts with oxygen ions transported through the electrolyte forming water and releasing electrons into the anode for subsequent transport to the cathode via an external circuit (the current flow). The water that is formed must be transported away from the reaction sites at the anode-electrolyte interface through the porous anode into the fuel stream (or combined fuel and exhaust stream). Naturally the transport of hydrogen must be consistent with the net current flowing through the cell adjusted for charge balance and mass balance [Ivers-Tiffée and Virkar 2003]. In steady state the following equality must be obeyed:

$$\left|j_{H_2}\right| = \left|j_{H_2O}\right| = 2\left|j_{O_2}\right| = \frac{iN_A}{2\mathcal{F}} \qquad (4.62)$$

Where:

j_{H_2} = hydrogen flux through porous anode to the anode-electrolyte interface ($mol\ s^{-1}$)

j_{H_2O} = water vapour flux from the anode-electrolyte interface through the porous anode ($mol\ s^{-1}$)

j_{O_2} = oxygen flux through the porous cathode to the anode-electrolyte interface ($mol\ s^{-1}$)

N_A = Avogadro's number ($6.0221418\times10^{23}\ mol^{-1}$)

For cases where the fuel is not pure hydrogen refer to the cited reference.

Transport of gaseous species is mostly by binary diffusion, where the effective binary diffusivity is a function of the fundamental binary diffusivity $D_{H_2-H_2O}$ and microstructural or morphological parameters of the anode [Ivers-Tiffée and Virkar 2003]. Convection in the pores of an SOFC is negligible [Khaleel and Selman 2003]. In typical electrode structures with very small pores the possible effects of Knudsen diffusion (fast diffusion through long narrow pores, akin to ballistic transport of electrons and phonons), adsorption/desorption and surface diffusion may also be present [Ivers-Tiffée and Virkar 2003] increasing the effective diffusivity above that predicted by fundamental binary diffusion. The physical resistance (not to be confused with the electronic/ionic resistance) to the transport of the gaseous species through the anode at a given current density manifests as a voltage loss. This is the phenomenon known as concentration polarisation, $\Delta E_{conc.}$, and is a function of several parameters and taking Knudsen diffusion, adsorption/desorption and surface diffusion to be negligible, can be expressed as [Camilleri 2009]:

$$\Delta E_{A,conc.} = f\left(D_{H_2-H_2O}, Microstructure, Partial\ Pressures, i\right) \qquad (4.63)$$

Notice that the increase with current density is not linear. In terms of derived functions to allow explicit calculation the anode-limiting current density, which is the current density at which the partial pressure of the fuel at the anode-electrolyte interface is near zero such that the cell is effectively starved of fuel, is one of the most important parameters [Ivers-Tiffée and Virkar 2003]. If this current density is reached during operation the voltage will rapidly drop to zero. The anode-limiting current density is given by:

$$i_{As} = \frac{2\mathcal{F} p_{A,H_2} D_{A(eff)}}{RT t_A} \qquad (4.64)$$

Where:

i_{As} = anode-limiting current density (Am^{-2})
$D_{A(eff)}$ = effective gas diffusivity through the anode (m^2s^{-1})

The effective anode diffusivity contains the binary diffusivity of the relevant species (H_2 and H_2O, i.e. $D_{H_2-H_2O}$), the volume fraction of porosity, $V_{V(A)}$, and the tortuosity factor, τ_A [Ivers-Tiffée and Virkar 2003]. The tortuosity is a measure of the tortuous nature of the anode pores through which diffusion must occur. In very fine microstructures the tortuosity as a phenomenological parameter might include the effect of Knudsen diffusion, surface diffusion and perhaps adsorption/desorption [Ivers-Tiffée and Virkar 2003]. The anodic concentration polarisation takes the form:

$$\Delta E_{A,conc.} = -\frac{RT}{2\mathcal{F}}\ln\left(1-\frac{i}{i_{As}}\right)+\frac{RT}{2\mathcal{F}}\ln\left(1+\frac{p_{A,H_2}i}{p_{A,H_2O}i_{As}}\right) \qquad (4.65)$$

Notice that as the current density approaches the anode limiting current density, that is when $i \longrightarrow i_{As}$, $-\frac{RT}{2\mathcal{F}}\ln\left(1-\frac{i}{i_{As}}\right) \longrightarrow \infty$. Of course, the maximum value of $\Delta E_{A,conc.}$ is limited by the OCV, so in practice the maximum achievable current will always be less than i_{As} [Ivers-Tiffée and Virkar 2003, Larminie and Dicks 2003]. In qualitative terms from the standpoint of physical dimensions and microstructural parameters, the lower the volume fraction of porosity the higher the tortousity factor, and the greater the anode thickness the higher the anodic concentration polarisation will be. From the standpoint of gas composition, the lower the partial pressure of hydrogen the higher the anodic concentration polarisation will be [Ivers-Tiffée and Virkar 2003].

The temperature dependence is far less clear and a lot more complicated. It is reported that $i_{As} \propto T^{1/2}$, since $D_{A(eff)} \propto T^{3/2}$, implying that the anodic concentration polarisation increases as temperature decreases [Ivers-Tiffée and Virkar 2003]. However, (4.65) shows that the anodic concentration polarisation increases or decreases linearly with temperature. In general it is taken that the anodic concentration polarisation is not very strongly dependent upon temperature [Ivers-Tiffée and Virkar 2003] in order to reconcile these contradictory temperature behaviours.

Gas transport through the porous electrodes cannot be described by first order kinetics; but a characteristic time constant can be approximated:

$$\theta_{characteristic,A} \approx \frac{t_A^2}{D_{A(eff)}} \qquad (4.66)$$

Where:

$t_A =$ anode thickness (m)
$D_{A(eff)} =$ effective gas diffusivity through the anode (m^2s^{-1})

If a typical cell is considered, with t_A between $0.5\ mm$ and $1\ mm$, and $D_{A(eff)}$ between $\sim 0.1\ cm^2s^{-1}$ and $\sim 0.5\ cm^2s^{-1}$, then the characteristic time is of the order of a few milliseconds to a few hundred milliseconds. Estimated tortousity factors, based on cell performance measurements vary from ~ 5 or ~ 6 to ~ 15 or even as high as ~ 20 [Ivers-Tiffée and Virkar 2003]. The lower values correspond to purely geometrical considerations, while the higher ones include other effects like Knudsen diffusion, adsorption/desorption and surface diffusion. These higher end values nevertheless crop up regularly in reports on cell performance through bodies with low porosity and small pore sized [Ivers-Tiffée and Virkar 2003].

The concentration polarisation at the cathode is, in a similar manner to the anode, related to the transport of oxygen and nitrogen through the porous cathode. The net flux of oxygen from the oxidant stream through the cathode to the cathode-electrolyte interface is linearly proportional to the net current density [Ivers-Tiffée and Virkar 2003]. As with the anode, gaseous transport is a function of diffusivity, in particular the binary diffusivity $D_{O_2-N_2}$ and cathode microstructure. As with the anode the physical resistance to oxygen transport is reflected as a voltage loss - the cathodic concentration polarisation [Camilleri 2009]:

$$\Delta E_{C,conc.} = f\left(D_{O_2-N_2}, Microstructure, Partial\ Pressures, i\right) \qquad (4.67)$$

Thus, the cathodic concentration polarisation increases with current density, but (as with the anode) the relationship is not linear [Ivers-Tiffée and Virkar 2003]. The time constant is a function of the diffusivity and a characteristic diffusion distance, corresponding to a finite non-zero time as for the anode. Similar to the anode, the characteristic time for the cathode is given by:

$$\theta_{characteristic,C} \approx \frac{t_C^2}{D_{C(eff)}} \qquad (4.68)$$

Where:

$t_C =$ cathode thickness (m)

$D_{C(eff)} =$ effective gas diffusivity through the cathode (m^2s^{-1})

For a typical anode-supported cell, of thickness ~ 200 μm, and effective cathode diffusivity of ~ 0.05 cm^2s^{-1}, the characteristic time is ~ 8 milliseconds [Ivers-Tiffée and Virkar 2003]. As with the anode, the cathode-limiting current density, which is defined as the current density at which the partial pressure of the oxidant at the cathode-electrolyte interface is near zero such that the cell is starved of oxidant, is an important parameter. Should this happen the voltage rapidly drops to zero, however in practice this does not usually occur. The cathode-limiting current density, i_{Cs}, can be expressed as [Ivers-Tiffée and Virkar 2003]:

$$i_{Cs} = \frac{4\mathcal{F}p_{C,O_2}D_{C(eff)}}{\left(\frac{p - p_{C,O_2}}{p}\right)RTt_C} \qquad (4.69)$$

The cathodic concentration polarisation takes the form:

$$\Delta E_{C,conc.} = -\frac{RT}{4\mathcal{F}}\ln\left(1 - \frac{i}{i_{Cs}}\right) \qquad (4.70)$$

The oxygen partial pressure at the cathode-electrolyte interface will be lower than in the air stream [Khaleel and Selman 2003]. Gas transport resistance increases with increasing electrode thickness [Khaleel and Selman 2003], and therefore the thicker the cathode the greater its concentration polarisation will be. The thick cathodes are needed for cathode-supported designs have inherently higher concentration polarisation. The thinnest possible cathode therefore, with the highest gas permeance (high porosity and large pores [Khaleel and Selman 2003]) minimizes cathodic concentration polarisation.

For similar electrode thicknesses and microstructures the anodic concentration polarisation is usually much lower than the cathodic concentration polarisation for two principle reasons: First, the binary diffusivity $D_{H_2-H_2O}$ is four to five times greater than the binary diffusivity of $D_{O_2-N_2}$ due to the much lower molecular weight of hydrogen compared to the other species; Second, the typical partial pressure of hydrogen in the fuel is much larger than the typical partial pressure of oxygen in the oxidant [Ivers-Tiffée and Virkar 2003]. Hence, the anode-limiting current density is much greater than the cathode-limiting current density.

For practical cells one of the electrodes is usually thicker than the other as it must also form the structural support for the cell. In anode-supported designs, where the anode is much thicker than the cathode (around a factor of ten), the concentration polarisations is correspondingly greater. However, even in these cases the two concentration polarisations remain comparable in magnitude [Camilleri 2009].

For instance, with hydrogen as a fuel relatively thick anodes on the order of $\sim$1 mm still have very high anode-limiting current densities of as much as 5 Acm^{-2} at an operating temperature of 800 °C enabling the fabrication of structurally strong relatively thick anode-supported designs without significant increase in concentration polarisation. This favours anode-supported over cathode-supported designs (or more specifically fuel-electrode-supported designs over oxidant-electrode-supported ones) [Camilleri 2009]. The ultrathin sputtered platinum cathode employed for this project, with its high porosity, is likely to offer a very small contribution to cell polarisation even at high current densities.

4.9.3 Activation Polarisation

Charge transfer is a fundamental part of the electrode reactions. At the cathode the charge transfer reaction is the conversion of oxygen molecules into oxide ions. At the anode the charge transfer reaction is the conversion of hydrogen molecules into protons (hydrogen ions). In solid state electrochemical devices the electrodes may be exclusively electronic conductors or they may be both electronic and ionic conductors (called mixed ionic electronic conduction, or MIEC) [Ivers-Tiffée and Virkar 2003, Larminie and Dicks 2003]. In addition, electrodes are either single phased or composites

of (usually) two phases such as graded electrodes. This discussion considers only a single phase electrode that is purely an electronic conductor.

Oxygen reduction involves a number of possible steps, usually comprising several parallel reaction paths. This multiplicity of reaction paths has, thus far, confounded researchers and no exact understanding of the elementary processes in SOFC cathodes under realistic conditions has been achieved [Ivers-Tiffée and Virkar 2003]. Therefore, it is all but impossible to select one of the numerous potential reaction mechanisms as the definitive answer. Microstructure and material considerations further complicate the issue [Ivers-Tiffée and Virkar 2003]. Likewise it is difficult to determine a single rate-determining step for any of the proposed mechanisms due to the presence of a series of steps. It is, however, possible to describe the overall process from a phenomenological or quasi-empirical point of view [Ivers-Tiffée and Virkar 2003]. Below is one possible mechanism, but is by no means definitive.

Step 1: Surface adsorption of oxygen, molecules on the electronic conductor (electrode), which either is also the electrocatalyst or has some catalyst material deposited on the surface. Surface adsorption of oxygen molecules may also occur on the surface of the electrolyte followed by dissociation into oxygen atoms and their surface diffusion to the three-phase boundary.

$$\frac{1}{2}O_2(gas) \longrightarrow \frac{1}{2}O_{2_{ads.}}(electrocatalyst)$$

This is further support for the use of films only just sufficient for the cathode to provide catalysis, provided they are also sufficient to conduct the generated current. It may be most desirable to employ a catalyst layer of minimal thickness topped by a conduction layer that may be patterned (i.e. not continuous).

Step 2: Dissociation of adsorbed oxygen molecules into adsorbed atoms.

$$\frac{1}{2}O_{2_{ads.}}(electrocatalyst) \longrightarrow O_{ads.}(electrocatalyst)$$

Step 3: Surface diffusion of adsorbed oxygen atoms to a three-phase boundary (TPB) between the electrocatalyst, electrolyte and gas phase.

$$O_{ads.}(electrocatalyst) \longrightarrow O_{ads.}(electrocatalyst/electrolyte/gas\ phase)$$

Step 4: Formation of oxide ions by electron transfer with incorporation of these ions into the electrolyte.

$$O_{ads.}(TPB) + 2e^{-}(electrocatalyst) + V_O^{\bullet\bullet}(oxygen\ vacancy\ /\ electrolyte) \longrightarrow O_O^x(electrolyte)$$

Where $V_O^{\bullet\bullet}$ represents the electron deficiency of the oxygen vacancy (i.e. the positive charge associated with that vacancy), and O_O^x represents an oxygen ion in the electrolyte lattice with neutral charge using the Kroger-Vink notation. The charge transfer step, central to the ionisation of oxygen, has been confirmed experimentally [Ivers-Tiffée and Virkar 2003]. The slowest of these steps is then the rate-determining step. It may be that two or more steps have similar kinetic barriers and so are similarly slow putting the process up to several steps from equilibrium at any given time rather than the single step for a single rate-determining step [Ivers-Tiffée and Virkar 2003]. The remainder of the steps are assumed to be at equilibrium at any given time.

The net current density is proportional to the rate of the cathodic reaction – making fast cathode kinetics eminently desirable. Associated with the reaction rate (or rather the current flow) is the voltage drop called the cathodic activation polarisation [Ivers-Tiffée and Virkar 2003], which is a function of:

$$\Delta E_{C,act.} = f\begin{pmatrix} Material\ Properties, Microstructure, \\ Temperature, Atmosphere, i \end{pmatrix} \qquad (4.71)$$

As with concentration polarisations there is a dependence on the current density but this is by no means linear. A quantitative relationship between the cathodic activation polarisation and the current density derived from phenomenological considerations is given, called the Butler-Volmer equation:

$$i = i_{C,0}\left\{exp\left[\frac{\beta z\mathcal{F}\Delta E_{C,act.}}{RT}\right] - exp\left[-\frac{(1-\beta)z\mathcal{F}\Delta E_{C,act.}}{RT}\right]\right\} \qquad (4.72)$$

Where β, the transfer coefficient, is a dimensionless positive number that takes a value of less than one for a one-step charge transfer process. $i_{C,0}$ is the exchange current density. Notice that the relationship between cathodic activation polarisation and current density is implicit – that is equation (4.72) does not allow explicit determination of cathodic activation polarisation as a function of current density. There are, however, limiting forms of the Butler-Volmer equation that express cathodic activation polarisation as a function of current density [Ivers-Tiffée and Virkar 2003]. For this purpose two current density regimes are identified; the low current density regime and the high current density regime.

In the low current density regime it is possible for $\left|\frac{\beta z\mathcal{F}\Delta E_{C,act.}}{RT}\right| \ll 1$ and $\left|\frac{(1-\beta)z\mathcal{F}\Delta E_{C,act.}}{RT}\right| \ll 1$. In such cases the Butler-Volmer equation simplifies to:

$$i \approx i_{C,0} \left| \frac{z\mathcal{F}\Delta E_{C,act.}}{RT} \right| \qquad (4.73)$$

or

$$\left|\Delta E_{C,act.}\right| \approx \frac{RT}{z\mathcal{F} i_{C,0}} i \qquad (4.74)$$

The term $\frac{RT}{z\mathcal{F} i_{C,0}}$ has the same units as area-specific resistance, Ωm^2, and is referred to as the charge transfer resistance. It is sometimes denoted by $R_{C,ct}$, given by $R_{C,ct} = \frac{RT}{z\mathcal{F} i_{C,0}}$.

It is important to note that while the relationship depicted by equation (4.73) and equation (4.74) is linear in the low current density regime this in no way implies an ohmic relationship since the response time of the process is long [Ivers-Tiffée and Virkar 2003].

In the high current density regime, $\left|\frac{\beta z\mathcal{F}\Delta E_{C,act.}}{RT}\right| \gg 1$ and the Butler-Volmer equation simplifies to:

$$\Delta E_{C,act.} \approx \frac{RT}{\beta z\mathcal{F}} \ln i_{C,0} - \frac{RT}{\beta z\mathcal{F}} \ln i \approx a + b \ln i \qquad (4.75)$$

which is known as the Tafel equation.

The TPB is characterised by a line along the electrolyte surface with dimensions m/m^2 or m^{-1}. This indicates that the electrode kinetics depend on the TPB length, as well as physical parameters such as the catalytic activity and the partial pressure of the reactant. This in turn implies that the exchange current density, $i_{C,0}$, depends on the electrode microstructure (physically defines the TPB), and the number of electrocatalyst particles per unit area of the electrolyte surface:

$$i_{C,0} = f\left(\begin{array}{c} Partial\ Pressure\ of\ Oxygen\ in\ the\ atmosphere, \\ Oxygen\ Vacancy\ Concentration\ in\ the\ Electrolyte, \\ Oxygen\ Vacancy\ Mobility\ in\ the\ Electrolyte, \\ Electron\ Concentration\ in\ the\ Electrocatalyst \\ TPB, \quad Temperature \end{array}\right) \qquad (4.76)$$

Similar to the cathodic activation polarisation, the anodic activation polarisation depends on material properties, atmosphere, microstructure, temperature and current density:

$$\Delta E_{A,act.} = f\begin{pmatrix} Material\ Properties, Microstructure, \\ Temperature, Atmosphere, i \end{pmatrix} \quad (4.77)$$

Once more, assuming a phenomenological model anodic activation polarisation can be described by the Butler-Volmer equation in either the low current density regime (linear limit) or the high current density regime (Tafel form) [Ivers-Tiffée and Virkar 2003]. The anodic exchange current density, $i_{A,0}$, in a manner not dissimilar to the cathodic exchange current density, depends on a number of parameters:

$$i_{A,0} = f\begin{pmatrix} Partial\ Pressure\ of\ Hydrogen\ in\ the\ atmosphere, \\ Oxygen\ Vacancy\ Concentration\ in\ the\ Electrolyte, \\ Oxygen\ Vacancy\ Mobility\ in\ the\ Electrolyte, \\ TPB, Temperature \end{pmatrix} \quad (4.78)$$

4.10 Continuum-Level Electrochemistry Model

At the continuum-level, or the effective property level, the modelling of SOFC performance requires only a parameterised electrochemical model [Khaleel and Selman 2003]. This is usually in the form of a current-voltage relationship (often in the form of an I-V curve) for a single cell in terms of parameters that are effectively cell properties as well as operational parameters. Such I-V relationships show the potential loss (the polarisation losses) at a specific current (usually expressed as current density) with respect to the ideal thermodynamic performance of the cell.

As noted elsewhere the maximum possible electrical work that can be drawn from the cell is equal to the change in Gibbs Free energy. The rate at which this work can be extracted is zero for open-circuit conditions since no current flows. Upon connecting an external load a finite current flows and a finite amount of work is done. The process is carried out irreversibly. At a given current density, i, some part of the OCV is lost due to the sum total of polarisation. This usually appears as heating. If the voltage drop across the external load is $V(i)$ and the voltage loss is $\Delta E(i)$ then:

$$V_r = V(i) + \Delta E(i) \quad (4.79)$$

If the assumption that the reversible voltage is not valid (the cell voltage is dependent upon the current) then the above equation becomes [Ivers-Tiffée and Virkar 2003, Larminie and Dicks 2003]:

$$V_r(i) = V(i) + \Delta E(i) \quad (4.80)$$

The difference $V_r - V_r(i)$ is a measure of the change in gas phase compositions in the vicinity of the electrodes [Ivers-Tiffée and Virkar 2003], that must be accounted for in the overall model of cell performance. The voltage loss term, $\Delta E(i)$, is the total

polarisation loss and is a function of the current density as noted in the above two equations. This concept is more fully developed by listing all the separate polarisation and combining them into a potential balance for the fuel cell analogous to its mass balance [Khaleel and Selman 2003]:

$$V(i) - V_r - iR_i - \Delta E_C - \Delta E_A = E_{eq} - iR_i - \Delta E_{Ca} - \Delta E_{Cc} - \Delta E_{Aa} - \Delta E_{Ac} \quad (4.81)$$

Where:

$V_r =$ reversible equilibrium (open-circuit) voltage or E.M.F. of the cell (V)
$i =$ current density (Am^{-2})
$iR_i =$ total Ohmic polarisation (V)
$\Delta E_C =$ cathode polarisation (V)
$\Delta E_A =$ anode polarisation (V)
$\Delta E_{Ca} =$ cathode activation polarisation (V)
$\Delta E_{Cc} =$ cathode concentration polarisation (V)
$\Delta E_{Aa} =$ anode activation polarisation (V)
$\Delta E_{Ac} =$ anode concentration polarisation (V)

The thermodynamic cell potential, V_r, depends on the reactant and product partial pressures as well as the operating temperature. For hydrogen as the fuel gas and oxygen as the oxidant [Khaleel and Selman 2003]:

$$V_r = -\frac{\Delta G^0}{2\mathcal{F}} + \frac{RT}{4\mathcal{F}} \ln \frac{p_{O_2} p_{H_2}^2}{p_{H_2O}^2} = E^0 + \frac{RT}{4\mathcal{F}} \ln \frac{p_{O_2} p_{H_2}^2}{p_{H_2O}^2} \quad (4.82)$$

Generally, the thermodynamic (or theoretical) open-circuit voltage can be determined from the Nernst equation as explained above. It should be noted that the Nernst equation unequivocally demonstrates the deleterious nature of an oxygen leak into the anode; it reduces the open-circuit voltage.

Part III: Non-Electrochemical Models

4.11 Efficiency Considerations

4.11.1 Electrical Conversion Efficiency

The electrical efficiency of a cell or stack is defined as:

$$\eta_{elec.} = \frac{electrical\ power\ output}{chemical\ energy\ input\ per\ unit\ time} = \frac{VI}{\Delta H\left(\frac{dn}{dt}\right)} \qquad (4.83)$$

The electrical efficiency is somewhat dependent on the definition of input energy for the fuel and whether ancillary equipment like pumps have their power consumption subtracted from the numerator or not. The electrical efficiency (or overall conversion efficiency) can be considered to be the product of three fundamental efficiencies [Eisenberg 1963, Khaleel and Selman 2003], the multiplication of which is the standard procedure for determining the overall efficiency of a system. These components are: the ideal (theoretical) thermodynamic efficiency $(\Delta G/\Delta H)$, the voltage efficiency (V/V_r), and the fuel utilisation (U_f):

$$\eta_{elec.} = \left[\frac{\Delta G}{\Delta H}\right]\left[\frac{V}{V_r}\right]\left[U_f\right] = \left[\frac{-n\mathcal{F}V_r}{\Delta H}\right]\left[\frac{V}{V_r}\right]\left[U_f\right] \qquad (4.84)$$

An ideal fuel cell operates reversibly and isothermally, as described previously. Under these idealised conditions the voltage generated is equal to the free energy change of the reaction. In a thermal cycle the ideal efficiency depends on the enthalpy change. For a fuel cell, however, it depends on the free energy change. Therefore, the ideal thermal efficiency can be defined as the ratio of the electrical work done to the heat of combustion of the fuel [Eisenberg 1963, Gorin and Recht 1963, Larminie and Dicks 2003]:

$$\eta_T = 1 - \frac{T\Delta S}{\Delta H} = \frac{\Delta G}{\Delta H} = \frac{-n\mathcal{F}V_r}{\Delta H} \qquad (4.85)$$

The ideal thermal efficiency is the theoretical limit, never reached in practice, that acts as a benchmark for evaluating a high temperature fuel cell [Gorin and Recht 1963, Larminie and Dicks 2003]. The primary reason ideal efficiencies are never reached is that fuel cells operate with some degree of irreversibility as quantified by its polarisation losses [Eisenberg 1963, Gorin and Recht 1963, Heath and Sweeney 1963, Larminie and Dicks 2003]. The graph below, Figure 4-6., shows the ideal thermal efficiency at various temperatures for a variety of commonly employed gaseous fuels.

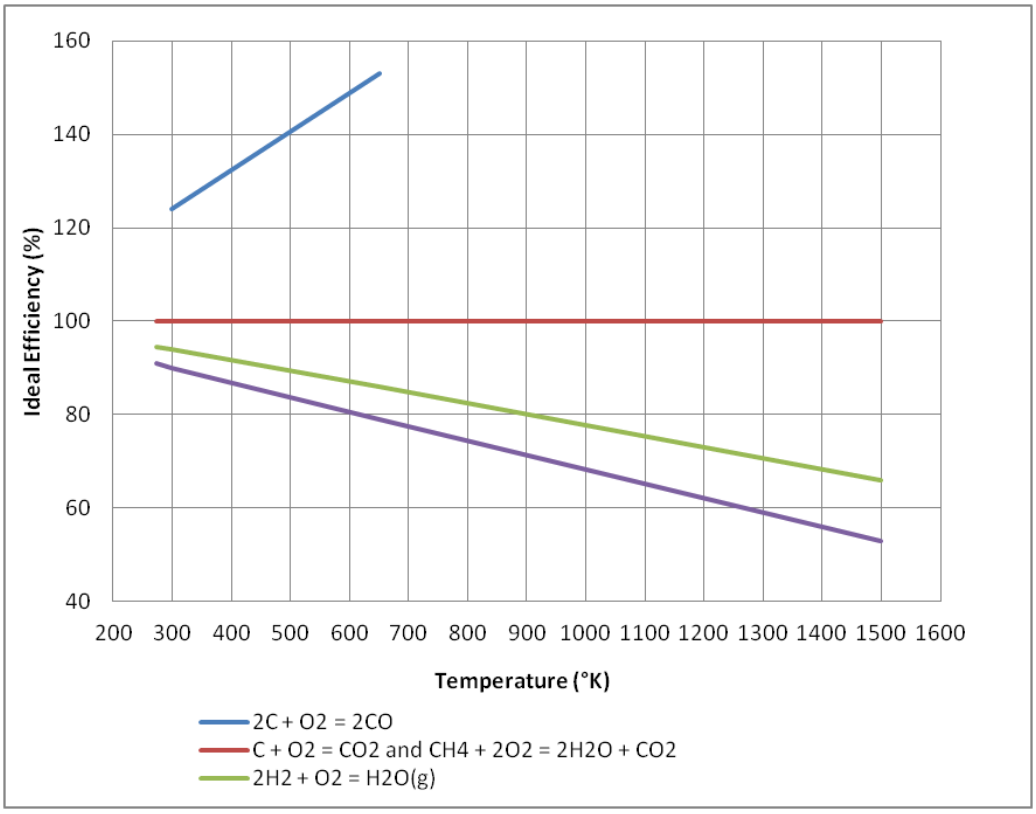

Figure 4-6. Ideal efficiency of common fuel cell reactions. Adapted from [Gorin and Recht 1963].

The voltage efficiency is simply the ratio of voltage obtained to theoretical voltage output.

Finally, the fuel utilisation is defined as the ratio of the delivered current to the stoichiometric current equivalent to the fuel flow rate [Khaleel and Selman 2003]:

$$U_f = \frac{I}{2\mathcal{F}\left(\frac{dn}{dt}\right)} \qquad (4.86)$$

The fuel utilisation is sometimes quoted in terms of Faradaic efficiency (see below), with that efficiency replacing the fuel efficiency term. This is however a rather unwieldy and impractical alternative, little used in modern research.

The ideal thermodynamic efficiency is a measure of the thermodynamic reversibility of the potential-determining reactions taking place in the cell. It depends only upon the operating temperature and the fuel used and is generally between 80% and 100% [Khaleel and Selman 2003]. The voltage efficiency and fuel utilisation are useful measures of cell performance in their own right, not just in the combined from as the overall electrical efficiency.

4.11.2 Faradaic Efficiency

Not all reactant available at a given electrode is used electrochemically in accordance to Faraday's laws [Eisenberg 1963]. Often this is due to other reactions occurring that reduce the potential-determining species and so reduce the overall electron-equivalents (hydrogen ions - protons) per mole of consumed reactant. There are, however, other physical and chemical processes that may lower the electrochemical efficiency. Losses in Faradaic efficiency are due to one or two situations [Eisenberg 1963]:

1. The non-electrochemical decomposition/dissociation of a reactant in a heterogeneous reaction catalysed by the electrodes, or catalysed by the materials used in constructing the cell enclosure itself and related components. This situation is not very likely where hydrogen is used as the fuel;
2. A direct chemical reaction between the two electrode reactants taking place either as a result of their incomplete separation in the fuel cell, or as a result of the particular reactant and electrolyte feed mechanism employed. Sometimes this type of reaction involves an intermediate form of the reactant, such as peroxide ions created at the cathode when oxygen is the cathodic reactant. The archetypal example of this is a leak (insufficient separation of fuel and oxidant) leading to some fuel oxidation by combustion rather than electrochemically.

Faradaic efficiency is defined as:

$$\eta_F = \frac{(coulombs\ obtained)}{(total\ moles\ consumed)n\mathcal{F}} \qquad (4.87)$$

This can differ at the two electrodes, and normally at least one will be less than 100%. If both are lower than 100%, and not the same, it becomes necessary to make adjustments in material balance calculations.

The non-electrochemical reaction described in 1. above has a decomposition rate given by:

$$N_D = k_D A C \qquad (4.88)$$

Where:

k_D = rate constant depending on the catalytic properties of the electrode and surface porosity (cm s^{-1})

A = apparent area of the electrode (cm^2)

C = concentration (mol cm^{-3})

Now for an electrode of apparent area A the electrochemical rate is $A\left(\frac{i}{n\mathcal{F}}\right)$. Substituting in to equation (4.66) gives the Faradaic efficiency for a single electrode:

$$\eta_F = \frac{{}^{i}/_{n\mathcal{F}}}{{}^{i}/_{n\mathcal{F}} + k_D C} \qquad (4.89)$$

Note that as might be expected for a given concentration of the electrode reactant, C, an increase in applied current density improves Faradaic efficiency without changing the reaction rate N_D.

When the Faradaic efficiency of both the anodic and cathodic reactions are considered, and given that the closed-circuit cell potential is given by:

$$V = E_C + (-E_A) - i\frac{t}{\kappa} \qquad (4.90)$$

Where:

E_C = closed-circuit cathode potential (V)
E_A = closed-circuit anode potential (V)
i = apparent current density (A/cm^2)
t = electrolyte thickness (cm)
κ = electrolyte specific conductivity (1/Ωcm)

Therefore the general form of the overall energy conversion efficiency is expressed as:

$$\eta_0 = \left(-\frac{n\mathcal{F}}{\Delta H}\right)\left[\frac{(E_C - E_A)}{2}\eta_{F,C} + \frac{(E_C - E_A)}{2}\eta_{F,A} - i\frac{t}{\kappa}\right] \qquad (4.91)$$

Which is a modified form of the base equation for overall efficiency that is used when the numerical values of the individual electrode potentials (E_C and E_A) are very close to zero, in order to give proper weighting to the individual Faradaic efficiencies [Eisenberg 1963]. This relationship is far more relevant to micro designs where polarisations (particularly ohmic and concentration) are very low by design rather than the unmodified version also presented in the cited reference.

4.11.3 Power Density

Another oft quoted performance figure for SOFCs is the power density of the cell (or stack). It is grouped here with efficiency because it is also a measure of the efficiency of the device, only rather than considering the electrical conversion efficiency power density concerns itself with the spatial efficiency of the device as a convenient way to

compare one system to another. The power density of a cell is often defined on the basis of cell or electrode area [Khaleel and Selman 2003, Larminie and Dicks 2003]:

$$\dot{P}_{cell} = \frac{voltage \times current}{cell\ or\ electrode\ area} = \frac{VI}{A} \qquad (4.92)$$

Where:

$\dot{P}$ = power density of cell (Wm^{-2})
V = cell voltage (V)
I = cell current (A)
A = cell or electrode area (m^2)

A Sulzar type planar stack has a power density of around 0.5 Wcm^{-2}. The Westinghouse tubular cell has a power density slightly lower, about 0.46 Wcm^{-2}.

For stacks the volumetric power density works slightly differently. In a tubular stack packed in a square array the volumetric power density depends on the diameter, D, of the cells and the gap, g, between them according to [Singhal and Kendall 2003]:

$$Volumetric\ power\ density = \frac{\pi DP}{(D+g)^2} \qquad (4.93)$$

Where:

P = power per unit area of membrane (Wcm^{-2})

For Westinghouse tubes 2 cm in diameter, separated by 0.2 cm gaps the volumetric power density is therefore 0.6 Wcm^{-3}. This is lower than for the planar stack quoted (Sulzar type planar stack has a volumetric power density of around 1 Wcm^{-3}) [Singhal and Kendall 2003] because of the relatively large diameter of the tubes. Micro-tubular designs give far better volumetric power densities by having smaller diameters and less spacing between cells. For instance, with a 150 μm diameter cell and 100 μm spacing the result is about 3.8 Wcm^{-3} – four times better.

Power density is a convenient way of improving understanding of the complex interactions (thermal, chemical, electrochemical and fluidic) that make up a SOFC. This is more or less true also of the electrical conversion efficiency (the other most quoted performance characterisation). Modelling these phenomena in another way is complicated by the coupled nature of the problem. The convenience of this approach makes it the *de facto* favoured modelling route for cell performance characterisation [Khaleel and Selman 2003]. The same approach is used to evaluate stacks. The only change is the power density which is defined as a volumetric power density for stacks (rather than being based on area). Unfortunately most sources quote a single value for

both power density and electrical conversion efficiency, and not all state the current density alongside these values. This is more than a little deceptive. A more rigorous approach would be to plot calculated power densities and efficiencies against current density.

4.12 Thermomechanical Model

The mismatched coefficient of thermal expansion (CTE) of the various cell components combined with the high temperature processing typically necessary to fabricate cells, means that upon cooling to room temperature a strain will develop. The strain leads to stresses forming in the cell, which are compounded by any residual stresses introduced by assembly and sealing processes [Khaleel and Selman 2003]. The magnitude of the thermomechanical stress depends on: difference in CTEs of the materials used; the differential between the processing temperature (no stress since deposition / sintering occurs at this temperature and grains have sufficient energy to move relieving induced strains), room temperature and operating temperatures; cell component thicknesses. The thickness is far less than the lateral dimensions and therefore the stress field is often assumed to be two dimensional [Khaleel and Selman 2003]. Typically the electrolyte (YSZ or other ceramic) will have the lowest CTE, and metallic electrodes and interconnects have a far higher CTE with graded anodes or cathodes, or other cermet structures, falling somewhere in between. Consideration of the relative CTE mismatch indicates the type of stress generated. Fortuitously the structure of a SOFC means that the fragile, brittle YSZ is under compression since upon cooling it shrinks less than the metallic or cermet anode and cathode. This is favourable (since ceramics are strong in compression) so long as adhesion is strong, otherwise blistering and delamination of the YSZ will occur [Camilleri 2009]. Conversely the anode and cathode (as well as interconnects) tend to be under tensile loads, which may or may not be problematic depending on their magnitude, material and the adhesion strength of the various components.

Residual stress when cooled from the stress-free temperature to any other lower temperature (e.g. room temperature) is given by [Khaleel and Selman 2003]:

$$\sigma_1 = \frac{(\alpha_2 - \alpha_1)E_1\Delta T}{\left[1 + \frac{h_1 E_1}{h_2 E_2}\right]} \qquad (4.94)$$

Where:

σ = residual stress (Pa)
α = coefficient of thermal expansion ($°C^{-1}$)
E = elastic or Young's modulus (Pa)
ΔT = change in temperature (°C)
h = layer thickness (m)
Subscripts 1 and 2 denote two neighbouring layers of the cell.

As equation (4.94) demonstrates, thinner layers are subject to higher residual stresses and therefore are of greater concern. While fortunately ceramics are strong in compression and therefore this should not be a problem for the electrolyte (as described above), this becomes a concern in the non-structurally-supporting electrode. For instance, to reduce polarisation losses an anode-supported cell would have a thin cathode, making residual stress a concern for this component but not the thicker anode. Of course, the material's elastic modulus also comes into play so a particular anodic material may be more vulnerable than a cathodic material of the same thickness. Residual stresses are highest in electrolyte-supported cells [Khaleel and Selman 2003]. The probability of failure for a given residual stress can be estimated from the Weibull function [Khaleel and Selman 2003, Betts 2005], however doing so requires the definition of a shape parameter and a scale parameter. No indication is given for how this can be done for SOFC.

Mechanical failure can occur by any of several mechanisms. For thin coatings under compressive stress (typical of thin ceramic electrolytes on thicker metal or cermet electrodes) a common failure mode is buckling of the coating and subsequent delamination, often called blistering [Khaleel and Selman 2003 and personal discussion with J. Nicholls]. The mechanism proceeds as follows. First, the coating will fail and buckle (perpendicularly) away from some local area where adhesion is poor. The buckling of the film relieves the stress between the coating and the substrate, but loads the interface between the coating and the substrate where there is still adhesion. This causes the crack to propagate outwards in a roughly circular pattern from the original local delamination (adhesion failure). Another common failure mode is thermal shock spalling [Khaleel and Selman 2003]. Thermal cycling of the SOFC introduces a tensile surface stress in the surface layer, leading to spalling of this surface layer [Camilleri 2009].

Related to these failure modes is the important consideration that materials are of significantly lowered mechanical strength at elevated temperatures, especially metals. This reduced strength becomes an issue needing due consideration for all metallic components particularly thin coatings (prone to high residual stresses) and metallic structural supports such as with anode- and cathode-supported cells. With regard to the former while it is possible, if the temperature is high enough, to relieve the stress by

annealing, this is unlikely to occur for two reasons: firstly the temperature is not high enough to rapidly anneal the metal, and secondly (linked to the first reason) is that the part would fail before any significant annealing could occur. Another possible mode of failure is also due to differential thermal stresses. Since the anode side materials are exposed to different conditions than the cathode side materials (reducing as opposed to oxidising) and ceramics will tend to reduce or oxidise according to the local oxygen partial pressure [Khaleel and Selman 2003], then the electrolyte may locally change composition at the opposite surfaces (anode-side and cathode-side). This differential expansion can lead to significant stresses, which may lead to crack formation. In extreme cases this leads to the formation of new phases with different structures (that is the reduction or oxidation changes the ceramic to a new stoichiometric composition – effectively transforming into a different ceramic made of the same base materials).

5 Summarised Critique of State-of-the-Art: Research Objectives

In order to clearly address this project's contributions to science this section sets out the major requirements for each component in tabular form defining the gaps in knowledge and those areas this thesis will contribute to the extension of knowledge beyond the state-of-the-art, together with what the expected contribution is. See the aims and scope of the thesis in chapter 1.

5.1 Anode

Anode (chapter 8)			
Requirements	**Gaps in Knowledge/ Novelty in this Project**	**Objectives/Planned Contributions**	**Well Understood Aspects (i.e. excluded from project)**
Porous (min. 30%-40%)	Oxidation-reduction is a novel way to create anodes with a connected network of pores.	Elaboration of this technique past the proof of concept in Camilleri (2009). See chapter 8. While working on the fuel cell analytical model it became apparent that porosity *per se* is unimportant. What matters is the permeability to the fuel gas and exhaust gases (see permeability measurement in 12.6).	Basic oxidation mechanism (via cation transport alone) and thence Wagnerian model.
	Complete oxidation not well understood (actual oxide thickness, mass and oxidation rate strays from classical model).	Modifying model to account for deviations from the classical models (section 8.6 onwards).	
	No model for reduction process.	Create one based on the oxidation model.	
Provide electronic conduction	Overall resistivity of a structure created this way needs to be assessed (since the technique is new).	Carrying out resistance measurements and compare to bulk Ni (useful to determine ohmic polarization also).	
Catalyst for hydrogen dissociation	Catalyst performance	It is possible that the very fine porosity will lead to very large surface areas and better catalyst performance (seen as a lower anodic activation polarisation). This is incidental to the technique for making the structure, not separate work.	No deterioration of catalyst performance caused by interaction with YSZ. Ideal solution is used since in fact entire anode is made of catalytic material.
	Anode and cathode kinetics are only generally understood. Very complex	None.	The general reaction pathways are acceptable even if the specifics are not well understood currently. The

	problem.		knowledge is sufficient to assess activation polarization of the anode and cathode.
Cell mechanical support	Resistance to thermal cycling of metallic anode supported cell with very thin electrolyte.	Unless experiments show obvious thermomechanical damage this will not be explored.	Well understood that the problem exists, however, these cells use a unique combination of techniques AND very thin electrolytes so thermal cycling performance is unknown. Comprehensive assessment would require many hundreds (at least) of cycles.
Extend reaction zone (TPB)	Creation of a Ni-YSZ nanocomposite (nano-cermet?). NB: This is a second stage of development. Initially the simpler base cells were tested to set baseline performance.	It is exceedingly difficult to create a nano-structured cermet using conventional SOFC manufacture techniques. EB-PVD may be set up to facilitate cermet (even with a graded composition) creation. Main contribution would be optimizing the microstructure (see 17.1 within Further Work).	The use of a cermet is in itself not new (it also improves long term stability and thermal cycling resistance). Published literature reports use of NiO and YSZ which is then reduced.
Fabrication/ processing costs	No quantified assessment of the manufacturing cost (or material for that matter) exists, merely claims.	None.	Fabrication / processing costs are more important than material ones particularly when using a Ni-based anode.

Table 5-1. Anode objectives and contributions summary.

5.2 Electrolyte

Electrolyte (chapter 9)			
Requirements	**Gaps in Knowledge/ Novelty in this Project**	**Objectives/Planned Contributions**	**Well Understood Aspects (i.e. excluded from project)**
Gas tight (to both H_2 and O_2).	Disorder in the first few µm leads to a non-columnar structure which is believed be gas tight.	Confirm/refute hypothesized gas tightness of EB-PVD manufactured electrolyte (see section 12.7 permeametry of anode-electrolyte complex).	EB-PVD deposition is well understood (particularly at Cranfield).
	Having demonstrated it is possible to manufacture 10 µm. Next is optimization of the process and pushing to find lower limit (thinner electrolyte leads to lower losses).	Demonstrate the ability of EB-PVD to make exceedingly thin electrolytes (aiming for some 3-5 µm). Refer to chaper 9.	Deposition in this technique is not often in such thin layers (more usual is hundreds of µm), but the principles do not change.
High ionic conductivity.	Effect of columnar texturing on cathode side unknown. Possibly will enhance conductivity (large surface area).	Determine the influence on performance of the columnar texturing (comparing bulk resistivity to the ohmic resistance of the deposited electrolyte from EIS)	The oxygen ion conduction within bulk YSZ is well researched.
	A high operating temperature is	Thinner electrolyte implies short path, and therefore a	Generally to operate at temperatures below 700 °C

	needed for sufficient ionic conduction (hence the HT requirement of YSZ electrolyte cells). Thinner electrolytes relieve this requirement.	faster process. Will determine the lowest suitable operating temperature for these thinner electrolytes.	different materials are used (which usually have significant disadvantages). There are calculated estimates for minimum operating T for a given thickness, but these are only down to 8 µm and to my knowledge have not been confirmed experimentally [see Table 3-2. and Ishihara *et al.* 2003].
Low (ideally zero) electronic conductivity.	None relevant.	None.	YSZ is acceptable in this aspect (and better than all the ceria-based materials for sub-700 °C operation).
Intimate contact with electrodes.	Behaviour of EB-PVD YSZ electrolyte deposition onto porous Ni anode.	Both assessed as part of the relevant deposition experiments. However, performance is also an indicator of uniformity and intimacy of electrolyte-electrode contact.	Both EB-PVD (electrolyte onto anode) and sputtering (cathode onto electrolyte) yield strongly adhering, conformal coatings. NiO-YSZ coatings have been successfully deposited by EB-PVD.
	Behaviour of sputtered Pt cathode deposition onto columnar YSZ electrolyte.		
	Nobody has created a cermet or graded cermet of YSZ and Ni using EB-PVD for SOFCs to date.	Establishing a technique for creating the cermet (can be seen as an evolution of the single phase deposition used in MSc)	
Stable in oxidising and reducing atmospheres at operating temperature.	None.	None.	It is well known that YSZ performs well under both these conditions even at operating temperatures in excess of 1,000 °C.
Good thermal cycling resistance.	The compliant morphology of the columnar YSZ is liable to greatly increase thermal cycling resistance under SOFC operating conditions.	None (will not be investigated since it requires many thousands of cycles each taking many hours – for which there is no room in addition to the rest of the project).	Good thermal cycling resistance requires a combination of high strength, good ductility, CTE match with anode and cathode, and compliant morphology. These aspects are well understood, but usually in different applications.
Fabrication/ processing costs.	No quantified assessment of the manufacturing costs (or material for that matter) exist, merely claims.	Due to the complications of the coater using several three-phase power supplies only the material costs will be assessed.	Fabrication / processing costs are more important than material ones.

Table 5-2. Electrolyte objectives and contributions summary.

5.3 Cathode

Cathode (chapter 10)			
Requirements	**Gaps in Knowledge/ Novelty in this Project**	**Objectives/Planned Contributions**	**Well Understood Aspects (i.e. excluded from project)**
Porous (min. 30%-40%).	Is a very thin (c. 300 nm) layer of Pt sufficient for gas transport?	Outside of answering these basic questions I will not be working on alternative cathode materials / designs. Many others are already doing so. Refer to chapter 10	Layer will be sputtered, nothing needs to be developed (outside of selecting correct parameters).

		as well as discussion in sections 3.6.2 and 17.3.	
	Is the cathodic activation polarization as low as expected?		
Provide electronic conduction.	Is a very thin (c. 300 nm) layer of Pt adequate for electronic conduction?	Carrying out resistance measurements and compare to bulk Pt (useful to determine ohmic polarization)	
Catalyst for oxygen dissociation.	Catalyst performance.	It is expected that the very fine porosity will lead to very large surface areas and better catalyst performance (seen as a lower cathodic activation polarisation). This is incidental to the technique for making the structure, not separate work.	Pt is accepted as the ideal catalyst for the cathode and is only restricted by its high cost. Ideal solution is used since in fact entire cathode is made of catalytic material.
	Anode and cathode kinetics are only generally understood. Very complex problem.	None	Same as for anode.
Mechanical Strength.	Resistance to damage in handling and quality of adhesion (given high thin film stresses)	Unless experiments show obvious damage this will not be explored.	Reason why thin films have high stresses, and the accepted 'delicacy' of thin films (sticky tape can strip them off) are well known.
Extend reaction zone.	Creation of a Pt-YSZ nanocomposite (nano-cermet?). To my knowledge this has not been done in any way before (and before pursuing I will determine why). NB: Will be done as a third stage once the base cells and those with cermet anodes have been tested. NB: This is an idea I first had about 3 years ago. Will only explore after similar work on the anode is finished.	Finding a way of doing this in a way that can be easily ported to large scale manufacture (i.e. in keeping with the commercialization-friendly theme of the project).	The use of a cermet is in itself not new, however, it has never been attempted for the cathode. As noted this is something that only occurred to us recently, and may not be pursued at all.
Fabrication/ processing costs.	No quantified assessment of the manufacturing cost (or material for that matter) exists, merely claims.	None.	Generally fabrication / processing costs are more important than material ones. Since the project will not deal with the cathode beyond needing one to test the cells, this is not directly relevant, but it is definitely of great importance for cathode developers!

Table 5-3. Cathode objectives and contributions summary.

5.4 General

General (i.e. not component-specific)			
Requirements	**Gaps in Knowledge/ Novelty in this Project**	**Objectives/Planned Contributions**	**Well Understood Aspects (i.e. excluded from project)**
Evaluate performance of cells by experiment.	The performance of these particular cells obviously was unknown.	Comprehensive analysis of cell performance including I-V curves, impedance spectroscopy, power-current density plots, fuel utilization plotted against both current density and power output and probably more besides.	The final experimental phase. See schedule section later. Possible, though unlikely, before moving on to a more sophisticated design with EB-PVD cermets.
Analytical model of all relevant physical and electrochemical phenomena.	No satisfactory, complete analytical model was found in the literature. Furthermore, treatment of cathode processes is less than satisfactory. The model under development aims to mitigate or circumvent this difficulty and present a quasi-one-dimensional model aiming to be convenient for initial performance analysis and prediction.	Detailed strategy. Carefully define all terms and assumptions. Develop analytical model of components and phenomena with the largest contributions to performance (phase I of the modelling process). Add terms to model detailing remaining components and phenomena (phase II).	
Economics of fuel cells.	Detailed investigation into fuel feasibility and the economics of fuel cells, taking into consideration infrastructure and economics. This is crucial because it concretely justifies an approach that does not follow current trends as well as defining the niche such products are able to fill in the energy market.	Will take the form of a review and will include any estimates of costs found in the literature (though these are only very general rather than design-specific) and whatever cost estimates I can provide based on my own work.	

Assessing fabrication process consistency.	Reproducibility is an acknowledged weakness in the fabrication of micro- and nano-scaled devices, and becomes increasingly important as size is reduced. No relevant literature source so much as makes mention of this, l*et al.*one attempt to assess it.	Statistically significant numbers of experiments relating to the fabrication of the various components.	
		Statistically significant numbers of experiments relating to the fabrication of complete cells.	

Table 5-4. General objectives and contributions summary.

The scope therefore is the establishment of a fabrication routine for a microtubular solid oxide fuel cell (with at least one level of optimisation for both anode and electrolyte) and the demonstration of this manufacturing capability, analysed statistically. An analysis of the SOFC design adopted will be presented along the lines suggested in Camilleri (2009) *mutatis mutandis*, the establishment of a framework for the creation of a new analytical model and work towards further miniaturization. The intention, furthermore, is to take the first steps in the creation of a commercially viable system based on the fabrication method used. While its commercialization will not be the overriding principle of the project the capability to commercialize will certainly be a priority.

Chapters 6 and -1441529855 describe the strategy employed to achieve these objectives, the results of the work carried out is reported on a by-component basis in chapter 8 through 11, with additional performance measures undertaken reported in chapters 1, 13, 14 and 16. The way forward, from further research to mass manufacture, is suggested in chapters 15 and 17.

6 Methodology and Terminology

Methodological description and remarks are integrated into the experimental sections of each chapter. This is to ensure clarity as I have carried out a range of experiments with widely differing objectives and test methods, testing different hypotheses, under a variety of constraints and using different materials. Therefore, it did not seem logical to combine all the methodological elements into sections of a single chapter; rather they are introduced at the start of every relevant portion of the thesis. This chapter instead deals only with the overall methodology adopted as well as any general comments on methodology and a few remarks on terminology.

6.1 Paradigm

There are two primary experimental paradigms: Positivism – the traditional undertaking of experiments to test hypotheses; and Interpretavism – rather than approach the data with a hypothesis the experiments are exploratory. I actually use both throughout my PhD. Mostly positivism, but there are cases where an exploratory interpretavist paradigm is more useful.

6.2 Ontology Aspect

The object of this research is set out explicitly in great detail in the Aims and Objectives and Project Scope (sections 1.1 and 1.2), as well as the Summarised Critique of State-of-the-Art: Research Objectives (chapter 5). Here I discuss the larger scale development of SOFCs and where my work fits into this. Broadly, we may class development of SOFCs by three length-scales: macro, micro and hybrid. The first refers to mostly earlier examples with cells of the order of a metre or more in the largest dimension [Gillett *et al.* 1998, Holmes *et al.* 2003, Siemens-Westinghouse Research Archives accessed 2010, Huang and Ruka 2012]. Micro I am here using to refer only to those with the largest dimension of the order of a few hundred μm [Funahashi 2007, Funahashi 2008, Suzuki *et al.* 2008a, Suzuki *et al.* 2008b, Suzuki *et al.* 2008c, Sammes *et al.* 2009, Monzón 2014]. These are often created by traditional microfabrication techniques and are little different from MEMS (Micro Electro-Mechanical systems). Perhaps we could term them MECS (Micro Electro-Chemical systems). The hybrid type has their largest dimensions of the order of a few to a few tens of centimetres but their component layers are of the order of a few hundred microns at most in total. It is these that are most commonly referred to as μ-SOFCs.

The first type has been implemented successfully both in the laboratory and in pilot projects but proved to be very expensive both in terms of capital expenditure and unit

cost (expensive materials used in relatively large quantities, complex ancillary systems, poor area and volume specific power output). Commercial implementation remains elusive. The underlying reason is uncommonly straightforward: the single greatest loss in SOFCs is the electrolyte with thinner electrolytes vastly outperforming the thicker ones created at this scale (with each layer approaching 1 cm in thickness). Notably, however, the only patents the author has seen for complete systems (i.e. including ancillary systems and insulation) have been of this type and these systems have performed well over their lifetime. For these large scale systems, the target market is large scale power generation (mostly load balancing and in competition with large diesel generators).

The second type is a rather more exotic incarnation; they take full advantage of microfabrication techniques to create very thin component layers reducing losses significantly. Often alternative materials to traditional SOFCs are utilised with these SOFC-on-a-chip devices in order to lower the operating temperature as much as possible. The reason for prioritising lowering the operating temperature is that this type is targeted at providing power on the same scale as contemporary batteries. They are still a long way from commercial development and are in competition with other micro electrical supply systems ranging from improved batteries (conventional and carbon-nanotube types) to other fuel cell types (e.g. in particular PEMFCs – polymer electrolyte membrane fuel cells), and even energy harvesting technologies, many of which have important advantages over μ-SOFCs including lower complexity and room temperature or near-room temperature operation (as well as greater public acceptance).

Hybrid type SOFCs fit nearly anywhere in the range between the two. Indeed one of their greatest strengths is their scalability – it is very easy to have systems utilising small stacks to clusters of distributed stacks numbering hundreds or thousands (or even hundreds of thousands) individual cells. In addition, their small component thicknesses lead to the most efficient energy conversion devices known to date, outperforming even other types of fuel cells. Much of the preceding information is summarised from the literature review. Details on each type can be found there. The most credible target market, at least initially, is medium size diesel generator replacement (for small commercial use in case of power failure) and domestic combined heat and power use (a single unit replacing domestic boilers providing both heat and power; known as CHP); examples of both applications are given in Kato *et al.* (2008) including detailed discussion. The author is in complete agreement with this reasoning, and this thesis will focus on μ-tubular SOFCs, with an emphasis on a comprehensive view of a target market.

This project had two ambitious and intimately connected aims: to further develop microtubular SOFC technology (with an emphasis on materials and fabrication techniques) and to do so with a weather eye to future commercial development.

The project explores a unique method for creating metallic anodes motivated by the desire to move away from traditional labour intensive and rather slow sintering-based methods in an effort to improve manufacturability on an industrial scale. The whole is designed to integrate with possible future work on creating graded anodes. This last is important because graded anodes (and to a lesser extent graded cathodes) provide significant improvement in energy conversion efficiency. This is a built-in desirable for the design even if there is no opportunity to explore it as part of this PhD. This, and a few other elements, would form part of a next iteration of the design bringing it closer to production. In addition, exploring a wide temperature range for the reduction step of the process was deemed important not just for modelling purposes but also to explore options for mass manufacture (i.e. determine a process minimising consumable usage that operates with the lowest possible energy input).

For the project a conventional electrolyte material was used – because it was deemed the most suitable for intended applications and its major limitations are mitigated greatly through design and applying innovative fabrication techniques to create the thinnest practical electrolyte. Initially the electrolyte experiments were intended to only assess reproducibility of the process with deposition parameters based on the literature, including findings of my MSc [Camilleri 2009]. Results were unsatisfactory with unacceptable delamination and variations in colouration and discolouration indicating deposition parameters were not optimal and the processing window was rather narrow. In light of this, the objective was extended to a deposition parameter optimization. The last tier of electrolyte experiments is of an exploratory nature (an example of the aforementioned interpretavist paradigm): making batches with identical (optimised) deposition parameters attempting to create thinner still electrolyte layers, in a controlled process.

The performance testing part of this thesis follows a similar methodology. For the permeametry it is the permeance of the relevant gases (fuel, oxidant and exhaust) through the various components that is of interest. A study that does not seem to have been carried out previously (the rare instances of measured permeance in the literature used argon; in most papers only porosity was estimated/measured). Essentially, this part is another method of characterization for the anode helping to ascertain the effectiveness of the selected fabrication parameters (which are optimised for fabrication). Unsatisfactory results would necessitate investigating less than optimal sets of fabrication parameters to ensure optimal gas permeance. For the electrolyte the permeametry represented a final verification stage ensuring the electrolytes (optimised both for reproducible fabrication and fuel cell performance) are fit for purpose; an especially important consideration given the drive to create the thinnest possible electrolyte. Permeametry also serves other purposes, though neither are part of this PhD:

valuable data for testing fuel cell models (whole or component-level) and, further down the development cycle, an in-line test for quality control during manufacture.

The final stage tested the fuel cells themselves. Each cell underwent electrochemical characterization, electrical performance characterization, and exhaust gas analysis supplemented with calculations for energy conversion efficiency, as well as area and volume specific output. The data collated in this part mirrors the *de facto* standard performance data experimentalists have published for their fuel cells.

6.3 Epistemology Aspect

In developing the anode, a systematic approach is taken with a relatively large number of samples for both the oxidation and reduction experiments. The reasons are: this scale is notoriously tricky when it comes to achieving reproducible results (unfortunately a consideration often overlooked in the literature), *ergo* sufficient data for statistical analysis are necessary (both repeats and sufficient set-points for variables to understand the mechanisms). The oxidation temperature was determined from careful reading of the literature. Careful, insomuch as it must be sufficiently rapid to be useful for producing anodes on a large scale, must yield suitable microstructure both in terms of desirable surface texture and in terms of significant porosity. In this instance the number of samples was required to produce a statistically-backed model and at the same time determine optimal time for oxidation. Modification of the traditional Wagner based diffusion oxidation model was necessary as it was found to not represent the process very well when completely oxidising thin nickel tubes. See section 8.1 for an in-depth review of the literature and details on oxidation temperature selection. Metal oxidation is a topic with a great deal more subtlety when studied at the micro scale than is generally accepted.

For this task intelligently chosen set-points are necessary with at least 5 repeats per point. A similar situation occurs with the reduction. However, in this case not even a suitable reduction temperature is known. Authors describing reducing anodes sintered from oxide powders to metallic structures have not once justified their choice of reduction conditions (temperature, partial pressure of hydrogen or other reducing gas, and duration of dwell). Finding a combination that works is relatively facile; finding one that is optimal is rather more of a challenge (see section 8.9). While the possibility of using some Design of Experiments schema was considered, in the end I opted for a simple systematic approach in the interest of wider scientific discovery than testing a strict set of factors. Furthermore, recall that the main objective was to determine a suitable process for the reduction step, complementing the oxidation step and thus creating a metallic nickel anode.

The approach for producing the electrolyte was use of a design of experiments schema as described in that chapter, rather than a simple systematic approach, because of the very large number of experiments such would entail. This formal design of experiments approach was not used elsewhere since the rest of the experimental work did not involve selection of alternative sets of manufacturing parameters with quite so many factors. In creating even thinner electrolyte layers the only important epistemological consideration was the need for statistically significant quantities of samples.

While experiments on the cathode were not needed *per se* it was necessary to conduct a few brief trials for two reasons: 1) verify that the sputtering parameters used for the MSc were reasonably reproducible and 2) create samples for the measurement of resistance of the porous platinum film for use with the fuel cell analytical performance model.

In measuring the permeance both for the anode and for the electrolyte the same experimental approach to gathering the information was used. A number of samples were created using the appropriate techniques (established in the fabrication chapters of this thesis) in sufficient quantity to be statistically significant. Each was then subjected to an identical set of measurements carried out in sequence with the gases of interest. This is another instance in this project where in my view it is more valuable to set experiments with reproducibility in mind, rather than repeat measurements on the same samples, because of the nature of this length scale. Once more, the setup can be conveniently adopted as part of quality control once scaled to actual manufacturing quantities.

A statistically significant number of experiments with different cells would ideally be carried out testing the performance of the completed cells. Unfortunately it was only possible to undertake a small number of such experiments. The priority would ideally be reproducibility of performance, rather than repeatability. However, at this stage it is worthwhile considering repeatability also because it would encompass a form of reliability for the devices (i.e. do they behave the same way when used on different occasions?).

In all cases the worst of measurement error and standard deviation was given in results tables and both were taken into account when interpreting the results. Error bars were frequently too small to be visible on plots. Furthermore, in many cases all data points are shown on plots so there is no need to add error bars since the scatter is plainly visible.

As a final epistemological addendum I'd like to remark on the usefulness of applying Pareto's Rule (also known as the 80/20 rule) as a timesaver. I did so extensively throughout the project in an effort to avoid uselessly investing time in experiments or

samples, “over-engineering” them. For instance, I generally polished samples for the SEM to a ‘good enough for the job’ standard, with only those samples intended for high quality imaging done to an ‘excellent’ standard – saving approximately 3 h per sample. With creating cross-sections using the FIB gains are even more significant. Additional ‘cleaning cross-sections’ (as they are called) to reduce waterfalling would have added a minimum of 4 h per sample.

6.4 Terminology

There are a few elements of terminology it is worth elaborating on. First of all, throughout this thesis, reference is made to microtubular and µ-tubular SOFCs interchangeably. In either case this refers to the conventional usage (termed hybrid in this chapter's introduction). The reason I do not refer to them as hybrid is because conventionally with fuel cells hybrid refers to a particular design that is geometrically a hybrid of planar and tubular cells. In short, I utilise conventional fuel cell terminology with one or two exceptions where it is necessary to draw a stricter delineation.

Secondly, it is common practice to label one electrode the anode and the other the cathode. While in reality the names are interchangeable according to whether one follows the electrochemical convention or the physics convention for fuel cells, it is generally the fuel electrode that is termed the anode and the oxidant electrode that is termed the cathode. Both conventions are often used in fuel cell literature, although the author has avoided this to prevent confusion. Throughout the text anode and cathode will be used in reference to specific electrodes (fuel and oxidant electrodes respectively).

Lastly, I at times refer to batches of samples that are not true batches. Normally the term batch refers to samples/parts processed together. That is, they are undergoing the same treatment simultaneously. I use the term to refer to a somewhat arbitrary grouping of samples done for convenience or clarity in analysis. For instance, the oxidation batches are differing durations of exposure and the term instead refers to common furnace positions. At times I will refer to batch-to-batch variations. In these cases they are true batches treating samples undergoing processing together. For instance comparing three samples (from different arbitrarily grouped 'batches') reduced together to another set of three. Each run is considered individually for batch-to-batch variation. To avoid ambiguity these were frequently referred to as runs rather than batches when meaning ‘processed together’.

All other specific terminology, whether conventional or traditional to an area of interest or merely a term I utilise, is elucidated in the relevant chapter.

6.5 Current Sign Convention

As the reader will have realised by this point electrons flow from the anode to the cathode (and oxygen ions travel in the reverse direction – it is convenient to think of these as holes in the traditional electronic sense). The current sign convention is thus that the cathode is the electrically positive terminal since electrons flow from – to +. This convention is often a source of confusion, indeed as Larminie and Dicks (2003) point out there are two seemingly contradictory definitions for the cathode:

I. "The negative electrode in an electrolyte cell or electron valve or tube"
II. "The positive terminal of a primary cell such as a battery"

Notice that the cathode is the positive terminal of all primary batteries; in essence the confusion is caused by whether in the circuit of interest one is referring to the power source or a load. It is helpful to remember that cations are positive ions, such as the Ni^{2+} cations discussed in Chapter 1. Anions, such as O^{2-} are negative ions. The cathode is therefore the electrode into which electrons flow while the anode is the electrode from which electrons flow. This convention applies to fuel cells, electrolysers (electrolysis cells), diodes, etc.

Recall that the true current described by this convention (electrons flow from – to +, from anode to cathode). There is also the widely used 'conventional positive current' [Larminie and Dicks 2003] that flows the other way. This is the second source of confusion, potentially the more insidious one.

7 Introduction to Fabrication and Characterization of Components

The preceding chapters lay out the context of this project and define both its framework and goals. What follows are chapters detailing the experimental work carried out to fill those gaps in knowledge identified (most explicitly given in Chapter 5). This is a brief preamble to those experimental chapters, and should be read in context of Chapter 6.

7.1 Contents, Organization and Objectives

The experimental chapters form two broad subdivisions: the first detailing fuel cell fabrication and the second performance testing (permeametry, electrochemical and electrical). All experimental chapters employ a common format, following the accepted template one might expect.

The fuel cell fabrication chapters (8 through 11) are organised by fuel cell component with an additional chapter dedicated to the fabrication of complete fuel cells – forming the core of this thesis. The anode (Chapter 8) combines two experimental activities into a single chapter for consistency with this logical layout of the experimental work, and is therefore the longest chapter. Furthermore, the cathode (Chapter 10) is more akin to an addendum to the preceding two chapters for reasons explained elsewhere, and is commensurately brief.

The performance testing chapters are arranged in no particular order with each chapter detailing one of the performance aspects, more or less on a by-technique basis. An additional chapter details fabrication of the electrochemical-electrical test rig. Critical issues relate to the transport of fuel gas and oxidant to the three-phase boundary (the anode-electrolyte interface), a vital part of this is gas permeance (chapter 1). This must be assessed in conjunction with an assessment of the microstructure of components given in the respective fabrication chapters. Electrochemical aspects are covered in chapter 14. In addition to these performance related chapters, an additional one details the fabrication of an electrochemical and electrical performance test rig (chapter 13).

7.2 Desired Outcomes

Omitting the specifics detailed in chapter 5, these experiments aim to define a processing route capable of creating a complete microtubular SOFC and establishing its performance using typical performance measures for solid oxide fuel cells. The anode fabrication method was optimised in two iterations, though there is still potential for further optimization of this component by altering the basic design, and perhaps also by

investigating additional oxidation and reduction temperatures. The electrolyte was deposited based on knowledge of thermal barrier coating deposition and conformed to state-of-the-art electrolyte thicknesses. The process itself received one step of optimization focussing on discovering the optimal set of parameters for deposition. A second step was planned, attempting to create thinner electrolytes beginning at 5 µm, but aborted for reasons discussed in that chapter. Thinner electrolytes would offer improved performance, but how thin can they be made by EB-PVD? The Pt cathode is deposited using a modification of established practice in general Pt coating by sputtering (high pressure to induce porosity) and was not further optimised. Recall the cathode used is not intended as final but rather a temporary solution in the face of evolving cathode materials.

8 Anode Fabrication and Characterization

It is proposed to create porous Ni anodes using an oxidation-reduction cycle. It is believed this route offers significant potential and provides a new and novel method of anode manufacture with great benefits possible. Following on from the concepts introduced in my MSc thesis [Camilleri 2009] this method is based on the combination of phenomena inherent to both the oxidation and reduction mechanisms to create porosity through coalescence of vacancies and in combination to create sufficient porosity for correct functioning of the anode. The porosity deemed sufficient is usually estimated to be around the percolation limit of 35–40% [Tsipis and Kharton 2008a, Cho and Choi 2009, Meng *et al.* 2009, Suzuki *et al.* 2009a – it is unclear from some of these sources if by mass or by volume, it has been assumed to be volumetric due to the nature of fabrication via a sintering route]. The first phenomenon of note is a side effect of the mechanism of nickel oxidation [Hancock 1976, Rosa 1982, Haugsrud 2001, Haugsrud 2003, Chuprina and Shalya 2004, Huntz *et al.* 2006, Zhou *at al.* 2008]. This chapter's organisation mirrors the two processes: the first part details the development and optimization of the oxidation step followed by a second part on the reduction step completing the process.

Step 1: Oxidation

8.1 Oxidation Objectives and Background

While previous work by the author [Camilleri 2009] has demonstrated the effectiveness of the oxidation-reduction treatment for creating porosity only a few experiments were carried out due to time constraints on the cited masters thesis study. The objective of these current experiments is to optimise the oxidation process by obtaining a body of data and modifying the model if necessary thus determining the minimum time necessary for sufficient oxidation to create the requisite level of porosity. The first tier of experiments (section 8.3) deals mostly with gathering sufficient data to confirm or refute that the process is repeatable and obtaining a first estimation of the time required for complete oxidation. The second tier of experiments (section 8.4) aims to refine the transition time between the two rates of oxidation identified in Tier 1. The third tier was carried out to improve the resolution of the transition time (section 8.5). Finally, Tier 4 (section 8.7) expands the experimental envelope investigating oxidation at higher temperature than previously. The model used previously [Camilleri 2009, Appendix C] for predicting the oxidation time for the nickel tubes is given its own section as it was modified in order to correctly model the new experimental results (section 8.6).

Nickel oxidises principally by cation transport. Nickel cations (Ni^{2+} ions) diffuse through the surface oxide to oxidise when they come into contact with the oxidising medium (usually oxygen or air). The oxide layer grows via outward diffusion of Ni^{2+}

ions via cation vacancies and electron hopping between Ni^{2+} located in normal lattice sites to ionise the chemisorbed oxygen atoms [Rosa 1982]. The cation transport depends on the presence of vacancies and also leaves vacancies behind. If there are sufficient such vacancies, these coalesce to form pores that are nominally circular but in reality their shape depends on factors such as strain state of the sample and the time oxidation has proceeded for. Observed pores tend to be a few hundred nanometres to a few microns in diameter, though both smaller and larger ones have occasionally been observed. Vacancies can also arise at the Ni/NiO interface [Pieraggi and Rapp 1988, Huntz *et al.* 2006], this is likely to be caused by grains moving in order to accommodate the changing grain size of the oxidized grains (explained in the following paragraph). Naturally, this interface moves as oxidation progresses through the sample and is nonexistent in fully oxidised samples, but is likely to induce increased porosity compared to cation diffusion alone.

The eventual exhaustion of the vacancy sinks (existing defects in grains or at grain boundaries, as well as dislocations and Schottky type defects) is thought to lead to vacancy condensation and thence void formation by vacancy diffusion at the interface of the metal and oxide [Pieraggi and Rapp 1988]. The annihilation of vacancies occurs in tandem with the advancing interface of metal-oxide through the sample and in the creation of additional vacancy sinks from scale growth [Pieraggi and Rapp 1988]. "During the growth of a cation-vacancy diffusing [oxide] scale, cation vacancies are attracted elastically to the interfacial sites of highest stress where the vacancy exchanges with a metal atom at the instant of its ionization (oxidation)." [Pieraggi and Rapp 1988] As the elastic strain in the metal and oxide increases the fraction of dislocations that climb or glide elastically also increases, as does the spacing between dislocations. A graph (Fig. 4. in Pieraggi and Rapp 1988) demonstrates this. Once the strain is sufficient the spacing between dislocations will deform plastically, in the form of deformation glide, on both sides of the Ni/NiO interface [Pieraggi and Rapp 1988].This is the most plausible explanation for the relatively small number of vacancies that coalesce into pores (i.e. are not eliminated by vacancy sinks) [Pieraggi and Rapp 1988].

The mechanism is therefore a balance of cation transport (diffusion and hopping) and oxidation of the surface atomic layer exposed to the oxidant (a chemical reaction, kinetics may be rate-limiting). At the elevated temperature used the chemical reaction kinetics (that is, of nickel becoming NiO on contact with oxygen) can be generally considered to be non rate-limiting, and therefore may be neglected. It is important to note that the cation transport, however, is a rate-limiting factor in the process because of the thickness of oxide involved (complete oxidation as opposed to a scale a few μm thick which the model and any oxidation theory are based on).

It is generally assumed in the literature (for example the previously-cited sources) that there is a semi-infinite source of Ni, and infinite source of oxygen, and that the inward transport of oxygen (by diffusion or in solution in the Ni) can be neglected implying

that the only operating mechanism – as well as only rate-limiting factor – is the outward transport of Ni^{2+} cations. For this work the first of these assumptions is clearly violated nearing complete oxidation, though what influence this has is unknown. The second assumption is reasonable and is also assumed here. It would, in practice, only be violated if the oxidant-containing medium has a very low concentration of oxidant or the oxidation proceeds in a closed environment without replenishment of the oxidant medium. The final assumption is often noted to be somewhat violated even in existing literature, here too it is a possible explanation for the discrepancies between the model and experimental results. That said, the solubility of O_2 in Ni is very low [Rosa 1982] and can be safely neglected. A final assumption, noted separately due to its lesser importance, is that at high temperatures (> 1,000 °C) stoichiometric NiO is formed since the Ni-O system has only one stable oxide at this temperature [Haugsrud 2001]. Furthermore, the non-stoichiometry of NiO in general is very low [Haugsrud 2003].

It was initially assumed (for calculations and initial experimental work) that nickel atoms are always available at the surface for oxidation. In truth it is possible that, at the temperature used, the oxidation chemical reaction kinetics are more rapid than the cation transport despite improved diffusion rates at elevated temperatures and evidence of rapid intergranular diffusion [Douglass 1995, Li *et al.* 1997, Khalid *et al.* 1999, Haugsrud 2003, Huntz *et al.* 2006, Zhou *et al.* 2008]. The implication is that at the free surfaces available for Ni oxidation an oxygen concentration gradient exists which would then potentially become the controlling (slowest) kinetics compared to the cation transport. The self-diffusion in oxygen is unlikely to be slow enough for this to be the case (hence the assumption was made). Furthermore, the degree of vacancy coalescence and hence porosity formation is dependent on a large number of factors including:

1) nickel morphology (including grain crystallographic orientation, grain size, vacancy defect concentration, and line defects like twinning – although this last has the least influence) [Atkinson *et al.* 1978, Pieraggi and Rapp 1988, Li *et al.* 1997, Thomson and Randle 1997, Khalid *et al.* 1999, Huntz *et al.* 2006].
2) surface roughness, sometimes referred to as surface condition [Pieraggi and Rapp 1988, Haugsrud 2003, Huntz *et al.* 2006, Zhou *et al.* 2008].
3) impurity/inclusion/alloying element quantities [Pieraggi and Rapp 1988, Haugsrud 2003, Huntz *et al.* 2006, Zhou *et al.* 2008].
4) impurity/inclusion/alloying element type [Khalid *et al.* 1999, Haugsrud 2003, Huntz *et al.* 2006].
5) stress state [Pieraggi and Rapp 1988, Khalid *et al.* 1999, Haugsrud 2003, Zhou *et al.* 2008].

All the factors listed above control the cation transport by diffusion in some respect, whether the effect accelerates or decelerates the oxidation rate. Some of these factors will increase the oxidation rate but reduce the porosity formed (e.g. stress). Huntz *et al.*

(2006) attribute discrepancies of the nickel oxidation mechanisms reported in the literature to differences in the purity of samples (including the presence of alloying elements), the surface preparation, the surface roughness, the furnace atmosphere and the heating procedure (e.g. heating rate).

At the oxidation conditions chosen the chemical reaction kinetics are more rapid than the cation transport (so are not rate limiting, and in fact are so rapid their effect can be neglected). The cation transport is in turn more rapid than the various dislocation slip or creep mechanisms possible for eliminating defects (notably pores). The end result is the most rapid possible oxidation with minimal reduction in porosity. The overall oxidation kinetics (including both the chemical reaction and transport) are essentially parabolic, with rates higher in alloyed or doped Ni than in the pure metal [Haugsrud 2001]. The exception is the presence of the oxides of so-called reactive elements such as CeO_2, La_2O_3 and Y_2O_3 [Haugsrud 2003]. Generally, the reactive element oxides segregate to grain boundaries either as oxides or as ions, resulting in a decreased outward flux of cations along grain boundaries [Haugsrud 2003]. The result is a reduced oxidation rate, typically by two orders of magnitude [Haugsrud 2003].

The work by Huntz *et al.* (2006) contradicts this, claiming that oxidation of pure Ni is faster. This sort of confusion continues with defining the exact mechanism. It is generally accepted that temperature and partial pressure of oxygen have the greatest influence on the oxidation rate of Ni (k_p). Of the two factors temperature has the most influence on k_p. Furthermore, the effect of the oxygen partial pressure decreases with increasing temperature [Haugsrud 2001].

Before continuing I wish to interject a brief comment on the conclusion drawn by Huntz *et al.* (2006) referred to in the above paragraph. It seems highly likely that the defect mobility is indeed greater in pure nickel since there are fewer obstructions to impede it. However, the presence of impurities may well increase the overall rate of oxidation by increasing the number of defects and dislocations creating a higher strain state and a greater concentration of vacancies increasing both the vacancy injection rate (high strain) and cation transport (larger number of available sites), *ergo* accelerating the oxidation rate. Additionally, in the work of Huntz *et al.* (2006) the samples were as-delivered in a high strain, and therefore very likely high stress state (barring a low temperature creep mechanism) because they were cold-rolled. This makes it difficult to determine from her work whether the purity or strain state has the greater influence. However, by comparing to the work of others it seems that the strain state has the greater effect on oxidation rate. Of note is that for all the experimental results reported this probably means that the work of Huntz *et al.* (2006) is most similar to mine (see Appendix B: Characterisation of As-delivered Nickel (Ni200) Tubes), enabling some degree of direct comparison.

While seemingly straightforward the oxidation mechanism of nickel has many subtleties which must be taken into account if any porosity at all is to be achieved. The oxidation mechanism of Ni has been studied for over a century [Haugsrud 2003, Huntz *et al.* 2006], yet, there remain discrepancies and important unanswered questions with reference to the details of the oxidation mechanism. There has been significant research into the oxidation of Ni, not least because of the large number of applications and alloys. Also the Ni-O system has been of scientific interest because it is a relatively simple system with only one stable oxide forming at high temperatures [Haugsrud 2001]. Much of the work in this area is based on Carl Wagner's theory for high-temperature oxidation of metals, including nickel. For details the reader is referred to the works cited in the preceding paragraphs as well as the following ones. The more important points that are relevant to the current study are collated below.

The high-temperature oxidation mechanism for commercially pure nickel (Ni 200) may, crudely, be considered to be of two types or regimes. At higher temperatures, bulk/lattice diffusion of nickel cations through the nickel oxide lattice determines the oxidation rate, while at lower temperatures other mechanisms (not all of which are clear to this day; presumably includes short circuit mechanisms) come into effect. This includes grain boundary diffusion, becoming more dominant than lattice diffusion. Over which range in temperature this change in growth mechanism occurs, depends mostly on the purity of Ni [Haugsrud 2003, Huntz *et al.* 2006].

At temperatures of 1,100 °C and above the rate is parabolic, which is to say that plotting mass gain or oxide thickness against time yields a plot, in Cartesian terms, of the form $y^2 = ax + b$, controlled by lattice diffusion (almost all sources agree, even the exceptions appear to implicitly accept it offering no explicit contradiction). Indeed it is only at temperatures in excess of 900 °C that the grain size sufficiently large for lattice diffusion to be dominant over grain boundary transport [Young 2016]. Oxide scales grown at these temperatures reportedly consist of columnar grains through the entire scale with some microporosity at the oxide-metal interface [Haugsrud 2003]. Huntz *et al.* (2006) only note the microporosity, making no mention of the presence of columnar grains, adding that the oxidation creates many small pores throughout the oxide layer often with a non-spherical shape. Furthermore, they add, there is typically no detectable internal oxidation, indicating the mechanism was solely one of cation transport and surface oxidation. They failed to consider the possibility of a vapour phase transport mechanism, which can only occur at the metal-oxide interface, which is not a cation transport mechanism, and entails no surface oxidation. As the temperature of oxidation decreases below 1,000 °C, the overall kinetics gradually change into a sub-parabolic behaviour meaning that the oxidation rate decreases faster as a function of time than as for high-temperature parabolic kinetics [Haugsrud 2003, Zhou *et al.* 2008]. Plotting mass gain or oxide thickness against time therefore becomes of the form $y^{(2-\delta)} = ax + b$. A convenient technique for checking whether data is in the parabolic or sub-parabolic regime is to plot the square of the oxidation rate coefficient (k_p) against time. Parabolic

behaviour yields a straight line, with subparabolas curling off the straight. Unusually at about 600 °C the oxidation rate returns to parabolic kinetic behaviour [Haugsrud 2003].

At lower temperatures the sample condition (grain size, roughness, existing porosity, purity, stress state and so on) has a great influence on the oxidation rate. At higher temperatures this is somewhat less so. In summary, the high temperature oxidation mechanism for unalloyed Ni may be broadly divided into two categories:

1) At higher temperatures ($T \geq 1{,}100$ °C) lattice diffusion determines the oxidation rate
2) At lower temperatures ($T \leq 1{,}000$ °C) short-circuit transport mechanisms are the dominant contributor

The above may be attributed to the difference in activation energy for the transport mechanisms. The exact temperature this change occurs at depends on factors influencing the grain size of the oxide (Ni purity, surface preparation) [Haugsrud 2003].

Experimentally Atkinson and Taylor (1978) introduced the importance of crystal face, and thus surface orientation, in oxidation. It is something not accounted for in Wagner's theory. The cited study was mostly interested in oxidation in the range 700–1,000 °C [Atkinson and Taylor 1978]. However, the relative contributions of oxygen transport along grain boundaries and of Ni transport along the same remains important even at higher oxidation temperatures. Their work was on single crystals of NiO in 1 atmosphere of pure oxygen. Ni tracer was used to measure Ni diffusion in the system [Atkinson and Taylor 1978]. As grain boundaries are excluded they measured only intragranular diffusion of Ni in NiO ($D_{Ni\text{-}NiO}$). Atkinson and Taylor (1978) were the first to show that lattice diffusion alone cannot account for measured oxidation in the range 700–1,000 °C. Subsequently it has become accepted that a $D_{Effective}$ is needed combining lattice and short-circuit diffusion contributions; the specific balance of which depends on temperature. Calculating (using Wagner's model) with $D_{Ni\text{-}NiO}$ omits the other important diffusion mechanisms from the overall oxidation rate (which is what would be measured experimentally).

The 'computer model' (a Monte Carlo-generated microstructure and followed by 2D solution of diffusion equations) by Li *et al.* (1997) shows that grain boundary diffusion is the dominant transport mechanism during metal oxidation at temperatures less than half the melting point of the oxide (727.5 °C for Ni) [Li *et al.* 1997]. The cited source notes that this is particularly evident with the oxidation of Ni crystal faces. The Monte Carlo-based technique used by Li *et al.* (1997) to generate a random Ni microstructure yields very realistic microstructures, close in appearance to actual observed ones both in the literature and from my own work. According to Li *et al.* (1997) the higher contribution of grain boundary diffusion compared to lattice diffusion leads to a small deviation from parabolic behaviour, although this seems to be also a function of the

crystal face of NiO that Ni is moving through. For instance, it was more marked at the (100) than (111) face. Complicating matters further is that there is also diffusion from grain boundaries into the lattice, not simply transport along grain boundaries through the oxide [Li *et al.* 1997]. NiO grain boundary diffusion is anisotropic, with about an order of magnitude difference between (111) and (100) crystal faces [Li *et al.* 1997].

Atkinson *et al.* (1982) continued their studies in 1 atmosphere of oxygen in the temperature range 500–800 °C on polycrystalline samples. Their samples were 250 µm thick and had work-hardened surfaces [Atkinson *et al.* 1982] and are therefore not dissimilar to my own work. Their choice of lower temperatures would suppress bulk diffusion so that the major contributing mechanism was grain boundary diffusion – *a priori* assuming that grain boundary transport was dominant. They claimed that it is well known that <1,000 °C measured oxidation is far more rapid than the Wagnerian model suggests implying that cationic bulk diffusion cannot be the primary mechanism [Atkinson *et al.* 1982]. While it is generally accepted that Wagner's model underestimates (often greatly) the oxidation rate the infrerral is hardly indisputable. Wagner's model does not specify lattice diffusion rather a $D_{Effective}$. That said, short-circuit diffusion is likely the dominant mechanism at relatively low temperatures in protective scales (500–1000 °C is suggested) whether it occurs by Ni atom/ion diffusion or oxygen molecule/ion diffusion and whether this is along dislocations, grain boundaries, cracks or interconnected porosity [Atkinson *et al.* 1982]. The authors conclude that this is "widespread and may well be dominant in all [oxide] systems at sufficiently low temperatures." [Atkinson *et al.* 1982] The resulting microstructure observed at 800 °C is very similar to my results (see the following sections) possibly indicating the same microstructural evolution at 800 °C as at 1,100 °C for samples with significant work-hardening. Atkinson *et al.* (1982) conclude that "the oxidation temperature must be above 1,100 °C for the lattice diffusion flux to exceed grain boundary diffusion flux."

Generally, an increase in grain size results in a decrease in the density of short-circuit diffusion paths and *ergo* a reduced oxidation rate [Atkinson *et al.* 1982, Li *et al.* 1997]. However, as noted by Li *et al.* (1997), these changes are dramatic for very small grain sizes (around 100 nm) and become increasingly insignificant for large grains – and therefore can be safely neglected. The cited source includes a graph demonstrating this as well as an equation describing the relationship between metal alloy grain size and the parabolic rate constant of oxide growth, k_p. The Ni tubes utilised in the cited study have far smaller grains than the tubes utilised throughout this project (see also Appendix B: Characterisation of As-delivered Nickel (Ni200) Tubes), *ergo* this particular phenomenon can be neglected, calculating the oxidation rate as normal.

Furthermore, the surface morphology of oxidised Ni changes as a function of temperature. In the low temperature regime (T < 600 °C) a fine-grained structure, sometimes with platelets and whiskers, is formed [Haugsrud 2003]. This is generally

considered the characteristic surface morphology for NiO and originates from surface preparation, oxygen partial pressure, water vapour concentration or the presence of impurities [Zhou *et al.* 2008]. Increasing the temperature to between 700 °C and 900 °C results in ridges at the surface [Haugsrud 2003]. Above temperatures of 1,000 °C to 1,100 °C faceted NiO grains dominate the surface morphology [Haugsrud 2003, Zhou *et al.* 2008]. The faceting of NiO grains is attributed by Zhou *et al.* (2008) to the flux of nickel cations by diffusion from the centre of grains outwards combined with the minimisation of surface energy. At temperatures above around 900 °C duplex scales tend to form. That is, an outer columnar layer over an inner, finer, equiaxed structure. Unlike Haugsrud's observations of purely columnar oxides at 1,100 °C! Some authors attribute this to the presence of impurities [Huntz *et al.* 2006] while others make no such connection [Haugsrud 2003]. Yet others report that a duplex scale did not form in the range 500–800 °C [Atkinson *et al.* 1982]. The oxidation temperature chosen was 1,100 °C both to take advantage of a predictable mechanism as well as to accelerate the process as far as possible without having to raise the partial pressure of oxygen – a far more complex prospect, and one that would unnecessarily raise production costs with eventual scale-out.

The picture so far is a complex one, and there is more to come. Schütze (1997) expressed the reason for this eloquently indeed: "In practice, components in high temperature technology often experience not only thermomechanical conditions but also complex thermal-chemical-mechanical demands. [...] The synergistic effects arising from the three types of condition are often neglected. These effects can markedly influence the performance of the material and lead to service lives much shorter than would be expected from the results of simple thermochemical or thermomechanical investigations." [Schütze 1997]

Regarding the stress of the oxide; both compressive loads and tensile loads accelerate the oxidation rate [Zhou *et al.* 2008], with compressive loads having a greater effect. Diffusion creep decreases the concentration of vacancies at the oxide-metal interface under tensile loads, increasing the oxidation rate [Zhou *et al.* 2008] but decreasing the porosity. The thin oxide scale that is growing has high in-film stresses precisely because it is a thin film. If adhesion is poor or the oxide exceedingly porous spallation (i.e. detachment of part or all of the film as flakes) may occur. For nickel the oxide is generally compact, dense and adherent to surface of sample when oxidised at 1,000 °C [Khalid *et al.* 1999]. Spallation of the external oxide surface when oxidised at 1,200 °C was noted by Khalid *et al.* (1999) who attribute this to stresses developed in the oxide upon cooling. They also note that it is possible that the inclusion of several elements in the two alloys studied contribute to causing spallation. In particular Si is noted to form an oxide that increases the likelihood of spalling in the external oxide. There are four sources for stress in the oxide film: growth-associated, temperature-associated (both upon heating and more usually upon cooling), initial stresses (for instance due to sample manufacturing or preparation), and finally sample/substrate curvature. These are all

important in that they affect the oxidation rate, and in many cases the resulting microstructure (including porosity) of the oxide.

Regarding the stresses arising from oxide growth; for NiO on Ni compressive stresses in the oxide scale are usually attributed to the diffusion of oxygen inward towards the base metal beneath the scale along oxide grain boundaries simultaneously with Ni cation diffusion within the lattice, resulting in growth of new oxide in the grain boundaries of the oxide. Originally it was believed this should lead not only to lateral oxide growth but also an increase in oxide thickness, demonstrated by the observed raised level of NiO over the grain boundaries. This was disputed for some time, and later disproven. In fact, what occurs is that oxygen penetrates through micro cracks (probably due to growth stresses) rather than by grain boundary diffusion [Schütze 1997].

The stress resulting from temperature changes is due to two factors: coefficient of thermal expansion (CTE) mismatch and changes in phase as the sample heats up or cools down. During heating both metal and oxide atoms and molecules are far more mobile than at room temperature so the strain from phase changes and CTE mismatch is usually mitigated at least partially by dislocation glide, creep, grain rotation and similar mechanisms. Upon cooling there is far less mobility resulting in high strains and hence elevated stresses. To elucidate, the equation below gives the film stress due to temperature changes for an adherent oxide, originally presented in [Schütze 1997]:

$$\sigma_{oxide} = \frac{-E_{oxide}\Delta T(\alpha_{metal} - \alpha_{oxide})}{\frac{E_{oxide}}{E_{metal}}\frac{d_{oxide}}{d_{metal}}(1 - \nu_{metal}) + (1 - \nu_{oxide})} \qquad (8.1)$$

Where:

σ_{oxide} is the stress in the oxide [MPa]
E_{metal} is the elastic modulus of the metal substrate [GPa]
E_{oxide} is the elastic modulus of the oxide [GPa]
ΔT is the temperature change [°K]
α_{metal} is the coefficient of thermal expansion (CTE) of the metal [$°K^{-1}$]
α_{oxide} is the coefficient of thermal expansion (CTE) of the oxide [$°K^{-1}$]
d_{metal} is the thickness of the metal substrate [m]
d_{oxide} is the thickness of the oxide scale [m]
ν_{metal} is the Poisson's ratio of the metal [none]
ν_{oxide} is the Poisson's ratio of the oxide [none]

The elastic modulii, and in some cases the CTEs also, are temperature dependant. In such cases equation (8.1) is only valid for small temperature changes (the limiting case). For larger temperature changes a more accurate calculation of σ_{oxide} is possible by taking the summation of calculated values over small temperature intervals such that the small intervals add up to the desired total temperature change [Schütze 1997].

Where several layers with different CTEs exist, equation (8.2) developed by Metcalfe and Manning should be used [Schütze 1997]. The stress σ_i in an individual layer i of n layers is given by:

$$\sigma_i = \frac{E_i}{1-\nu_i}\Delta T\frac{\alpha_m - \alpha_i}{1-\alpha_i\Delta T} \qquad (8.2)$$

Where α_m is the mean coefficient of thermal expansion of the combined scale and is given by:

$$\alpha_m = \frac{\frac{\sum_i^n d_i E_i \alpha_i}{(1-\nu_i)(1-\alpha_i\Delta T)}}{\frac{\sum_i^n d_i E_i}{(1-\nu_i)(1-\alpha_i\Delta T)}} \qquad (8.3)$$

At the edges of the block (or ends of the tube), shear stresses (τ) rather than simple tensile/compressive stresses are developed due to temperature changes at the oxide/metal phase boundary [Schütze 1997]:

$$\tau_{max} = \frac{4d_{oxide}E_{oxide}\Delta T(\alpha_{metal}-\alpha_{oxide})}{L\left(1+\frac{E_{oxide}}{E_{metal}}\frac{d_{oxide}}{d_{metal}}\right)}\frac{1}{1-\nu} \qquad (8.4)$$

Where L is the lateral dimension of the finite scale/substrate block (or circumference for a tube). The equation shows that the shear stress for thin scales on a thick substrate increases with oxide thickness and that it reaches a maximum at the end of the composite system (at the edges) [Schütze 1997]. The shear stress drops linearly from the edges to the centre [Schütze 1997]. L can also be the distance between two perpendicular through-cracks in the oxide film [Schütze 1997].

All the equations presented assume linear elastic behaviour of the oxide scale and substrate, and their validity becomes questionable when stress-reducing mechanisms come into play (which is common) [Schütze 1997]. However, they represent a conservative start to calculating the stress in an oxide scale [Schütze 1997].

The effect of surface curvature on the development of stresses in the oxide scale is relevant because of the way stress affects oxide growth. Therefore for tubes (as is the case in this project) contribution of curvature to stress, and thence to k_p, cannot be ignored. In particular because, unlike growth and temperature-dependent stresses, curvature-induced stress can be controlled to some degree by utilising different diameter cells.

Convex surfaces give rise to tangential compressive stresses in the oxide scale and radial tensile stresses at the oxide/metal phase boundary. This is because the consumption of metal by oxidation causes the oxide/metal interface to recede further and further into the metal substrate while contact between the oxide and the metal is maintained [Schütze 1997]. This holds as long as the oxide layer remains adherent and no significant stress relieving mechanisms take place [Schütze 1997]. With increasing oxidation time these stresses increase, so that a portion of the tangential stress in the oxide (or resultant tensile stress in the metal) is relieved by injection of vacancies into the metal as a consequence of the oxidation process [Schütze 1997], leading to the formation or increased formation of pores.

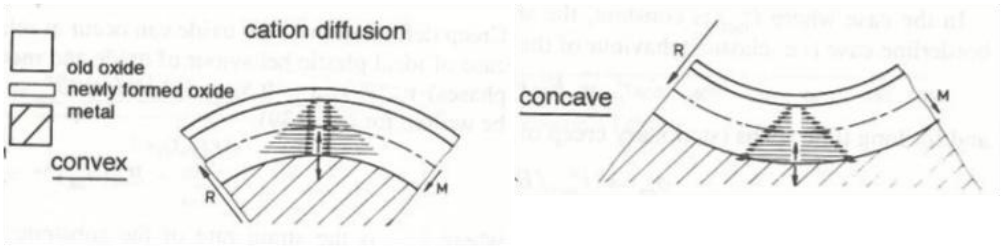

Figure 8-1. Growth stresses in the oxidation of curved surfaces for cation diffusion processes [Schütze 1997].

Curvature also affects strains due to temperature changes [Schütze 1997]. The directions of the tangential and radial stresses from cooling from the oxidation temperature for concave and convex surfaces are shown in Figure 8-2, below, after Schütze (1997), depending on whether the CTE (α) of the oxide is greater than that of the metal or *vice versa*.

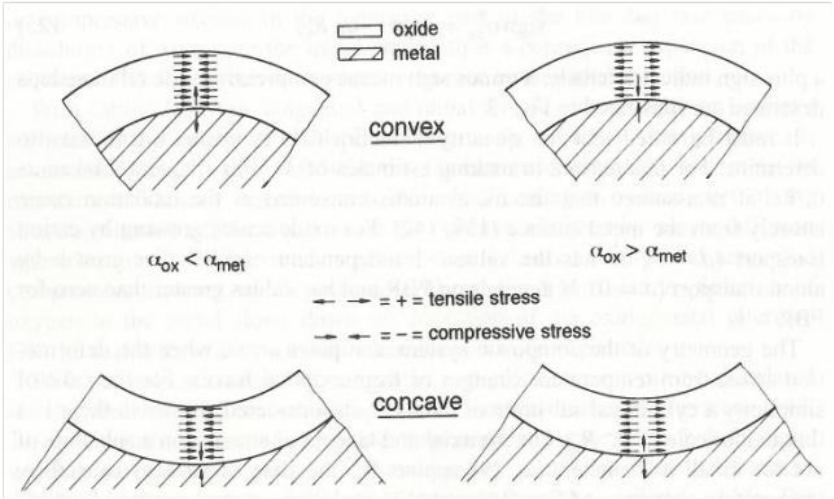

Figure 8-2. The signs of cooling stresses on curved surfaces [Schütze 1997].

Ergo, considering only the stress induced by oxide growth the greatest stress regardless of the type of curvature, will be at the metal-oxide interface. Indicating oxidation will be fastest here. Upon cooling both the convex oxide and concave oxide experience

additional compressive stress, for the more common case (including Ni and its oxide) where $\alpha_{oxide} < \alpha_{metal}$. Any stress tends to increase oxidation rate as described above, with compressive stresses having the greater effect. Thus with both convex and concave surfaces the curvature is helpful in accelerating the oxidation rate. Perhaps more importantly the oxidation rates can be assumed to be enhanced to the same degree — so stress due to temperature changes in the oxide is relatively uniform.

Concluding the background information and its review are additional facts about the oxidation of Ni, collected here because they have only ancillary importance in the use of this oxidation-reduction technique to create porous anodes, but are included for completeness' sake and for possible higher-order interactions with other factors not relating directly to the manufacturing of the anode.

At higher oxygen partial pressures the oxide is a metal-deficient ($Ni_{1-x}O$) p-type semiconductor [Rosa 1982, Haugsrud 2003] with Ni vacancies as the most common defect type [Haugsrud 2003]. These vacancies may be singly or doubly charged as reflected by the oxygen pressure dependency of the various point defect-governed processes [Haugsrud 2003]. Concentration of nickel vacancies at 1,000 °C in 1 atm of oxygen is of the order 10^{-3} to 10^{-4} (atomic fraction) [Haugsrud 2003]. Self-diffusion lattice diffusivity of oxygen in NiO at temperatures above 1,100 °C to 1,600 °C is more than five orders of magnitude lower than the self-diffusion lattice diffusivity of Ni [Haugsrud 2003]. The activation energy for oxygen diffusion in NiO was found to be up to 530 kJ/mol. While there is some uncertainty regarding the oxygen point defect type, interstitials appear to be favoured [Haugsrud 2003]. Activation energies for oxidation at 1,100 °C and above is in the order of 220–250 kJ/mol, reported quite consistently [Haugsrud 2003]. At 600 °C for different surface pretreatments the differences in oxidation rate constant are as high as 4 orders of magnitude. Attributed to varying amounts of short-circuit paths (like grain boundaries and dislocations). The different surface pretreatments also lead to variations in the apparent activation energy for oxidation [Haugsrud 2003]. These other characteristics, as well as characteristics mentioned previously relating to transport mechanisms are affected by the nature of point defects in Ni [Haugsrud 2003].

Returning to the matter of creating anodes; if the whole anode is transformed into NiO then there should be some porosity right through the structure that is fairly uniformly, if randomly, distributed throughout. Of course, such a material is no longer suitable as the anode since all the nickel (needed for hydrogen catalysis and adsorption as well as conducting the resulting current) is fully oxidised. Also, the porosity created by vacancy coalescence is small, certainly less than the recommended minimum of 35–40 vol.% for successful SOFC operation noted previously. A second phenomenon can be used to create porosity, one which also restores the useful properties of Ni – the reduction of oxide to metal (see section 8.9 onwards).

8.2 Oxidation Experiments

The fuel cell tube is 99.5% pure nickel (Ni 200) OD 5.9 mm, wall thickness 125 μm from Goodfellow Cambridge Ltd., cleaned in an acetone ultrasonic bath for 5 min prior to oxidation. See Appendix B: Characterisation of As-delivered Nickel (Ni200) Tubes for sample composition and manufacture details as well as geometry (thickness variation, roundness). Normally the tube is 100 mm long for the device, however for these experiments a short tube 25 ±1 mm long was deemed sufficient. A total of 60 samples were used initially, separated into 5 batches of 12. The samples were oxidized in air in a Carbolite 1200 C rapid heating box furnace at 1,100 °C. Micrographs presented in [Khalid *et al.* 1999] show that at higher temperatures, above 1,200 °C, the oxidation process creates fewer voids, and the grains are larger and more densely packed, leaving little room at grain boundaries. It is likely, therefore, that porosity can be enhanced by oxidising at nearer 1,000 °C than 1,200 °C; hence, the chosen temperature. Once fully oxidised the samples become very fragile, a fact occasionally noted in the literature: oxides are prone to brittle fracture, and in all practical cases are usually stressed either due to growth stresses (from the oxide growth itself), or stressed thermally, or by external loading [Zhou *et al.* 2008]. Therefore, they were placed in ceramic boats made of Alumina-Silicate (Fisher Scientific) for ease of handling.

In order to establish an experimental plot for the oxidation twelve time intervals were chosen (keeping in mind the parabolic nature of the curve) that would give a good spread of data points. The samples were loaded with those to be oxidised longest at the back, and the first to be removed – having shorter oxidation times – in the front. It was then a simple matter of rapidly unloading each sample in turn at the correct time using long tongs.

The calculations, and hence experiment, are based on mass gain (that is, the mass of oxygen added to the sample by the oxidation process). Each sample was weighed before and after oxidation, taking care to extract the correct sample (known by its position in the furnace). The mass gain was used to calculate oxide thickness and fraction of mass oxidised. A number of plots were used to compare the predicted results with the experimental ones. Note that these experiments amount to a classic thermogravimetric study but on samples of tubular geometry, with multiple repeat samples. One advantage of ensuring sufficient numbers of samples for statistical robustness is that it minimised the resulting human error. Naturally, steps were taken to keep these to a minimum and overall results show consistent accuracy.

Characterization was also by visual inspection (for quality and uniformity of oxide) and using SEM imaging, of both the surface and cross-sections (trenches created by FIB, frequently after coating with gold-palladium or carbon by sputtering to improve sample

conductivity). The FIB used was a FEI XP200 and the SEM utilized was an FEI XL30 SFEG.

This method was employed for all subsequent tiers of oxidation experiments with the following changes. The second experimental tier consisted of a total of 25 samples, separated into 5 batches of 5. Unlike the first experiment, the samples were hung on wire jigs made of NiCr alloy (80/20 Ni/Cr by mass; commercial name Nichrome) for ease of handling (Figure 8-3.). This resolved the issue of contamination from the ceramic boats used initially (section 8.3.1), an explicit objective of the second tier of experiments (section 8.4).

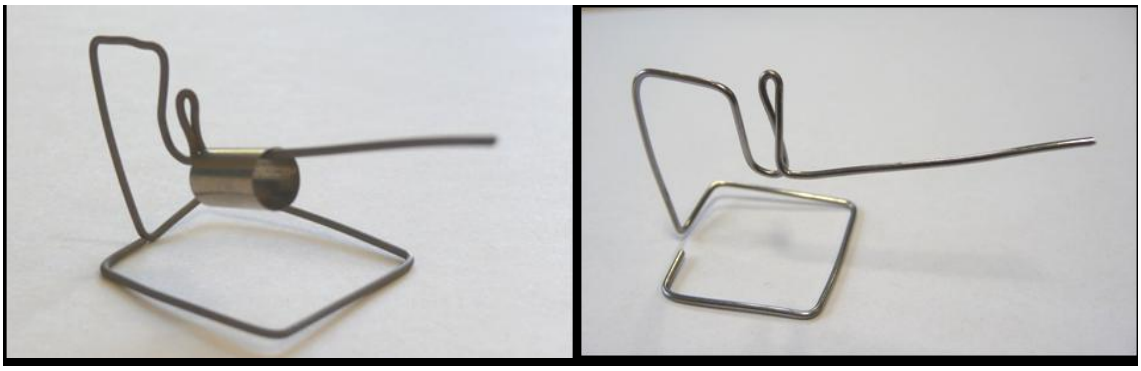

Figure 8-3. Sample hung on Nichrome wire jig for ease of handling and the wire jig itself.

Later, a further 35 samples were added to improve data resolution, separated into 7 batches of 5. The purpose of this tier, as described in detail in section 8.5, was to further understand the oxidation process through to complete oxidation. The NiCr wire jigs noted above were used for ease of handling.

A total of 15 samples were used in the third experiment, separated into 3 batches of 5, oxidised at 1,150 °C. The objective for this experimental tier was exploring potentially reduced process time, as described in section 8.7. The NiCr jigs were used once more.

8.3 Process Optimization

The objective of this experiment was to optimise the oxidation process by obtaining a statistically significant body of data and modifying the model as necessary to determine the minimum time for sufficient oxidation to create the required porosity. This first tier of experiments deals mostly with gathering sufficient data to confirm, or refute, that the process is repeatable and to obtain a first approximation of the time to complete oxidation of the nickel tubes.

8.3.1 Results & Discussion

Table 8-1. below summarises the results and gives the mass gain of each sample, the mass fraction oxidised (mass of oxide gained divided by the maximum possible mass of

oxygen gained based on sample's initial unoxidized mass) as well as the calculated oxide thickness, z. Figure 8-4. shows a plot of experimental results and the calculated bounds. Errors have been estimated using linear approximation by partial differentiation [Error Propagation article accessed 2013] where an equation was used or based purely on measurement equipment error otherwise.

Sample	**t (h)** ±0.01 h	**m_{Ni} (mg)** ±1 mg	**m_{Ni+NiO} (mg)** ±1 mg	**m_{gain} (mg)** ±2 mg	**Mass fraction oxidized** ±0.001	**z (µm)** ±0.23 µm
Batch B						
OT-A.13/07/10-125.1100-B.01	0.017 (1 min)	478.9	481.8	2.9	0.791	2.23
OT-A.13/07/10-125.1100-B.02	0.033 (2 min)	475.4	480.9	5.5	0.795	4.22
OT-A.13/07/10-125.1100-B.03	0.083 (5 min)	468.6	477.0	8.4	0.800	6.45
OT-A.13/07/10-125.1100-B.04	0.167 (10 min)	508.4	520.4	12.0	0.804	9.21
OT-A.13/07/10-125.1100-B.05	0.333 (20 min)	464.8	480.2	15.4	0.812	11.82
OT-A.13/07/10-125.1100-B.06	1.000	486.9	514.6	27.7	0.830	21.27
OT-A.13/07/10-125.1100-B.07	2.000	487.4	526.1	38.7	0.848	29.71
OT-A.14/07/10-125.1100-B.08	5.000	536.2	583.1	46.9	0.855	36.00
OT-A.15/07/10-125.1100-B.09	9.000	536.0	591.2	55.2	0.867	42.38
OT-A.15/07/10-125.1100-B.10	16.000	541.2	616.2	75.0	0.895	57.58
OT-A.14/07/10-125.1100-B.11	20.000	464.2	559.0	94.8	0.946	72.78
OT-A.15/07/10-125.1100-B.12	42.000	544.7	673.5	128.8	0.972	98.88
Batch D						
OT-A.13/07/10-125.1100-D.01	0.017 (1 min)	503.7	508.2	4.5	0.793	3.46
OT-A.13/07/10-125.1100-D.02	0.033 (2 min)	476.6	482.1	5.5	0.795	4.22
OT-A.13/07/10-125.1100-D.03	0.083 (5 min)	492.4	500.4	8..0	0.799	6.14
OT-A.13/07/10-125.1100-D.04	0.167 (10 min)	494.1	506.3	12.2	0.805	9.37
OT-A.13/07/10-125.1100-D.05	0.333 (20 min)	502.0	517.3	15.3	0.810	11.75
OT-A.13/07/10-125.1100-D.06	1.000	492.9	519.0	26.1	0.827	20.04
OT-A.13/07/10-125.1100-D.07	2.000	494.7	531.3	36.6	0.844	28.10
OT-A.14/07/10-125.1100-D.08	5.000	542.8	583.4	40.6	0.845	31.17
OT-A.15/07/10-125.1100-D.09	9.000	553.6	609.6	56.0	0.865	42.99
OT-A.15/07/10-125.1100-D.10	16.000	538.2	611.8	73.6	0.893	56.50
OT-A.14/07/10-125.1100-D.11	20.000	529.0	606.0	77.0	0.900	59.11
OT-A.15/07/10-125.1100-D.12	42.000	530.4	656.6	126.2	0.973	96.88

Table 8-1. Mass gain, mass fraction oxidized and oxide thickness of Ni tube oxidation at 1,100 °C. All samples from two exemplar batches of Tier 1 shown: B and D. The whole table can be found in Appendix C: Complete Oxidation Results Tables.

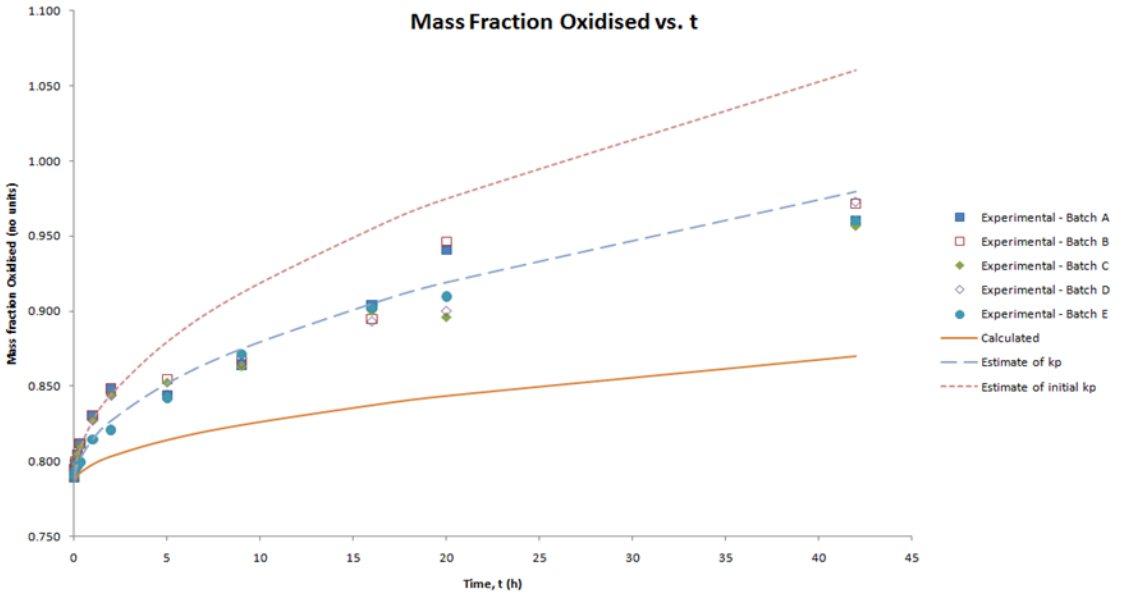

Figure 8-4. Plots of the mass fraction oxidized – ratio of the measured mass of the oxidized sample to its calculated mass when fully oxidized – against time. Oxidation at 1,100 °C (compensated for the most likely source of surface area error – tube length).

Samples at the front of the furnace were under somewhat different conditions that those at the back because they were nearer the end of the hot zone and were more exposed to sudden cooling while the door of the furnace was open to extract samples (a periodic occurrence). The net effect would be oxidation at a slightly lower temperature. It is assumed that there is no variation side-to-side within the furnace, only front-to-rear. The full details, in the form of a pair of tables, are given in Appendix E: Oxidation Sample Furnace Positions and Schedule. First of all, the samples from batches A and B, and C and D were paired in ceramic boats. That is A.01 and B.01 were in the same boat, and C.01 and D.01 were in the same boat, and so on. All samples from batch E were in the middle of the boat, each having its own. The ceramic boats were placed side-by-side in the furnace. A and C were always towards the door of the furnace, and B and D towards the back. This is represented on the graph by using common symbols, one filled and the other empty. The rest is tabulated in the appendix referred to previously for clarity. There is also a second table, outlining the oxidation schedule.

The combination of the position in the furnace and schedule gives complete sample traceability. Comparing these tables to the plots (particularly of mass fraction) shows that: Behaviour in a given boat does not vary (for instance all samples of batch A and B show the same trends), but do vary from boat to boat (samples from batch A and D show different trends) with batch A gaining more mass than batch D. Specifically, I refer to samples 7, 8 and 11 of all batches.

Regarding sample 11 of all five batches: The behaviour with batches A and B is at odds with the rest, however the boats were at the front of the furnace. Similarly, all sample

11s were put into the furnace and removed simultaneously. With reference to Figure 8-4., the two samples without contamination (A.11 and B.11) show a higher fraction oxidised than the others. Therefore A and B must be considered representative of an important process (a jump in oxidation rate) rather than outliers or simple stochastic differences or human error. The periodic cooling appeared unimportant.

Regarding sample 8 of all batches there is a similar trend. The behaviour of A and B is at odds with the rest. All were at the front of the furnace and put in and removed together. Considering Figure 8-4. closely, the differences are small and not consistent. The samples from batch B (rear of boat) and C (front of boat) have a slightly higher mass fraction than the rest. Therefore while the behaviour seems odd at first, given the difference is of only 1.3 % at most it can be treated as random variance and not significant.

Regarding sample 7 of all batches: All save E were at the back of the furnace. Once more behaviour within boats is consistent (with A and B showing the same trend and C and D another). The differences are of only 0.5 % at most for A, B, C, and D. However, batch E shows significantly lower oxidised thickness and a 2.8 % lower mass fraction oxidised. This is consistent with its position as any sample near the furnace door is more exposed to changing conditions (especially temperature) when the door is opened to extract samples or add new ones. Note that the apparent transition from principal mechanism to a secondary one occurring somewhere between samples 7 and 8 is also evident here, only exaggerated because E.07 has not quite oxidised as much as it should have.

In conclusion to the issue of differences between batches A through to E, particularly with regards to potential bias due to furnace position it appears that the planned approach in having samples as far as possible under the same conditions was successful in eliminating batch to batch bias. Where significant deviation was noted this is due to a change in furnace position for that sample (due to space and/or time considerations). There is some bias in one sense: samples were not oxidised in the same exact position within the furnace – so the nominal conditions were not in fact applied to all samples. However, these differences are the same because there was no batch to batch bias (only sample to sample for those samples oxidised at the front compared to those at the back).

Initially, the actual oxidation rate is far higher than the theoretically predicted one calculated from literature values for k_p (0.864 $mg^2cm^{-4}h^{-1}$) as can be seen in Figure 8-4. and discussed in detail over the coming pages. This increased initial oxidation rate has been observed before [Haugsrud 2003] with an early oxidation following the parabolic law but at much higher rate than anticipated. So at 1,100 °C these results are consistent with the observations of Haugsrud (2003), conforming to the first type of behaviour reported in the cited source despite the higher temperature in this study, thus extending the temperature range of these observations. Specifically, Haugsrud's own experimental

work revealed that in the temperature range 700 – 1,000 °C two distinct oxidation behaviours are encountered [Haugsrud 2003]:

1) Oxidation rate is initially rapid, decreasing to become parabolic
2) Oxidation rate never conforms to parabolic rate law, but decreases more rapidly with time (sub-parabolic behaviour).

In the current work at 1,100 °C, there is a consistent deviation from the parabolic model for exposures longer than 2 h giving rise to a significant mass gain at 1,100 °C, greater than 5 mg cm^{-2}. Furthermore, no work the author has read specifically set out to completely oxidise a sample, but to controllably oxidise one to some degree (extent measured by the weight gain which clearly does not necessitate complete oxidation). Therefore, the model itself it not designed to accurately reflect through oxidation (and therefore the depleting reserve of available Ni cations). Curvature is known to alter oxidation rate, although usually concave and convex curvatures are considered separately [Schütze 1997]. In this work one would have to simultaneously consider the effects of oxidation on the inner concave tube surface and outer convex tube surface.

The oxidation rate also varies for different orientations between the oxide and the metal grains [Haugsrud 2003]. This may explain why thin scales, generally, are more non-uniform than thicker scales (high temperatures versus low temperatures and short exposures versus longer exposures). The faster growing orientations will eventually dominate over the slower-growing orientations, but at low temperatures this may take some time [Haugsrud 2003]. The competing processes of nucleation and growth result in a situation where initially (near the surface) nucleation dominates and the number of grains is high with small grain sizes. Subsequently it is growth that dominates and the number of grains decreases but their size increases [Douglass 1995].

A by-eye estimate from the tier 1 data indicates the initial $k_p \approx 9$ $mg^2\,cm^{-4}\,h^{-1}$ and after the transition to sub-parabolic/another parabola (at around 2 h) $k_p \approx 4.5$ $mg^2\,cm^{-4}\,h^{-1}$ (for sub-parabolic the units are $mg^{(2-x)}\,cm^{-(4-2x)}\,h^{-1}$). At this stage it is not clear whether the transition is to a sub-parabolic second rate law or to another parabolic mechanism, see Figure 8-5. The factor of two change from initial to second oxidation rate suggests some mechanistic connection.

The possibility of a grain boundary transport dominated mechanism with the added influence of grain growth needs to be considered. However, the path for Ni transport along grain boundaries to diffuse from the un-oxidised bulk to the surface (potentially over 60 µm of NiO for the tubular anodes created in this work) is much longer than the path for oxygen in pores from dissociated NiO to reach the un-oxidised side of the pore. At high temperatures (≥1,100 °C, see section 8.1) the bulk contribution should furthermore be more significant than grain boundary diffusion also since the available sites are proportional to the cube rather than the square for surface sites. Also the

activation energies for the mechanisms have different slopes – associated with the energy to hop in the lattice as opposed to the grain boundary. As oxidation temperature increases lattice vibration increases making site hopping much easier within the lattice. Eventually as temperature increases the two end up as similar rates [Atkinson and Taylor 1979, private communication with John Nicholls].

It has been observed that the measured oxidation rate may not remain perfectly parabolic at later stages of oxidation with scales about 25 microns thick [Atkinson *et al.* 1982]. Atkinson *et al.* (1982) show that (at least in the range 500–800 °C) the oxidation rate drops to sub-parabolic because of grain growth. This is likely true at higher temperatures also – provided no significant pore network exists [Atkinson *et al.* 1982]. Pores, of course, mean that grain boundary diffusion is highly constrained by areas inaccessible to atomic vacancy hopping. It follows, then, that at any given section parallel to the outer surface: the larger the pore volume the less contiguous material (Ni or NiO) is present and therefore there are fewer overall grain boundaries to act as short-circuit paths. Schütze (1997) attributes the presence of pores with longer cation diffusion paths to near-surface areas. My results show that with through-thickness oxidation at 1,100 °C the later stages of oxidation are also parabolic rather than becoming sub-parabolic (see Figure 8-6., the discussion after it and section 8.4). Furthermore, grain size increases slowly with time (Table 8-2.), but it is approximately equal to the spread of grain size data and this at 1,100 °C grain growth is not dominating oxidation, unlike the situation seen at lower temperatures in the work of Atkinson *et al.* (1982). It was therefore concluded that the dominant mechanism was not grain boundary diffusion.

	Early (<2 h 15 min)	**Transitional**	**Late**
Grain size (µm)	0.5-8	1-5	2-7
Mass Fraction Oxidised (%)	c.80	c.84-85	up to 97

Table 8-2. Grain size range and corresponding approximate MFO for early, transitional and late stage oxidation at 1,100 °C.

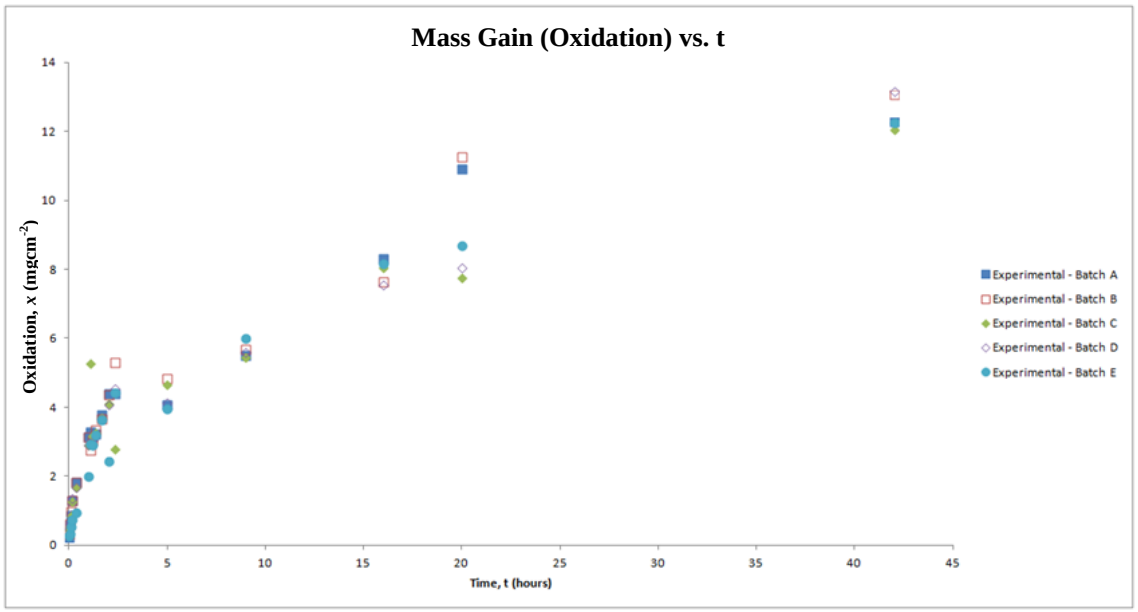

Figure 8-5. Plots of x (mass gain / surface area) against time for oxidation at 1,100 °C. This is often casually referred to as the oxidation rate.

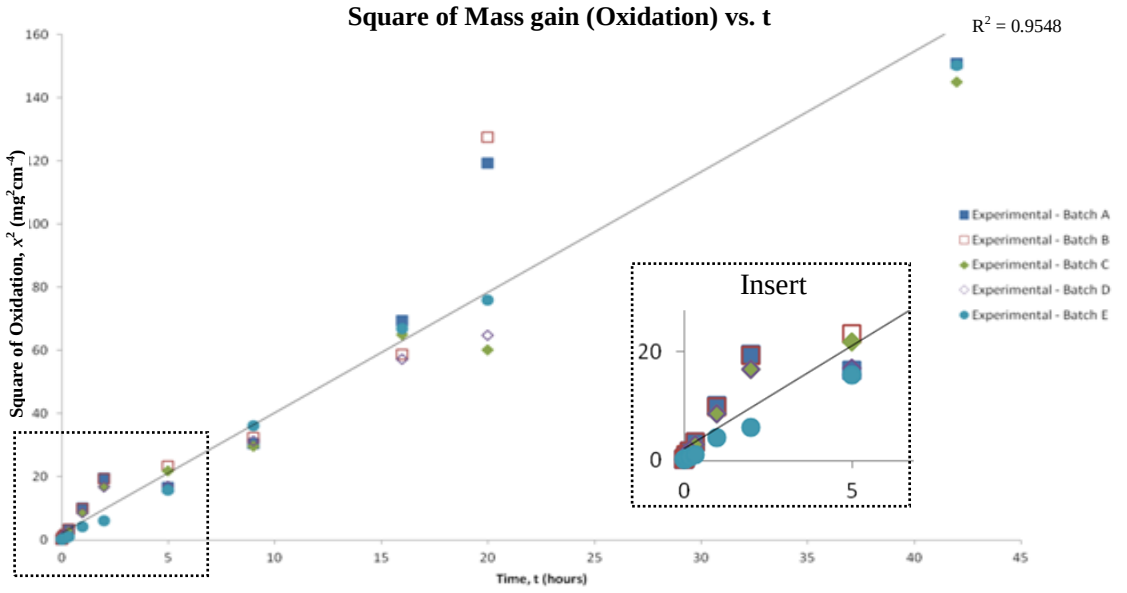

Figure 8-6. Plots of x^2 [(mass gain / surface area)^2] against time for oxidation at 1,100 °C. This is often casually referred to as the square of oxidation rate. Deviations from parabolic show up clearly on this type of graph – as deviations from a straight line.

The preceding graph (Figure 8-6.) is particularly useful because it allows us to determine whether the cationic oxidation mechanism is indeed parabolic during early oxidation under these conditions and whether the second mechanism is parabolic or sub-parabolic. This is achieved by fitting a pair of straight lines through to origin for each batch of data. The first covers the initial cationic-transport-dominated phase and the second covers the second mechanism (discussed later). For parabolic processes the data should closely fit a straight line. If the data deviates upwards from the straight line then

it fits a superparabolic law ($y = ax^{\frac{1}{(2+b)}} + c$). If the data deviates downwards from the straight line then it fits a subparabolic law ($y = ax^{\frac{1}{(2-b)}} + c$). Straight lines of different gradients simply describe different parabolas (for example, $y = ax^{\frac{1}{2}}$ as opposed to $y = bx^{\frac{1}{2}}$). This exercise demonstrates the mechanisms are both parabolic, albeit with different rate constants. The conventional (and algebraically equivalent of course) format used in oxidation studies is $y^n = ax + c$.

A batch to batch comparison was made by plotting graphs similar to Figure 8-6. for each batch individually, highlighting any deviation from straight lines. There were no significant deviations suggesting the mechanism is parabolic. All five batches shown here on a single plot for brevity; each was analysed individually as separate plots.

The most likely explanation for the two, more-or-less distinct, diffusion-controlled mechanisms (parabolas) is that there are two stages of oxidation; a first dominated by cation transport followed by a stage dominated by another transport mechanism rather than proceeding throughout by cation transport. The second was thought, following metallographic observation, to be vapour phase partial pressure gradients across the pores. Identifying these mechanisms is the next thing to address.

Due to the oxidation temperature being 1,100 °C duplex scales will not normally form, and also the high purity of the samples means the advancing front of internal oxidation will be thin according to Haugsrud (2003), and is supported by the micrographs shown below. Three possible causes of the creation of micropores have been put forward [Haugsrud 2003]:

1) Dissociation of the scale into and along defects (porosity and line defects). Cations and cation vacancies diffuse in opposite directions while the scale is growing outwards, and the vacancies must be annihilated at or close to the oxide-metal interface [Haugsrud 2003]. If the process for annihilating vacancies is slower than the outward cation diffusion (i.e. the formation of vacancies) then the vacancies coalesce into pores at the metal-oxide interface [Haugsrud 2003]. The result is discontinuities of outward metal diffusion. Something observed in all samples for which SEM micrographs have been taken. Still cations continue to diffuse outwards from the surface of the pore nearest the sample surface due to the gradient in concentration of the chemical potential across the scale [Haugsrud 2003]. Similarly, metal activity decreases, while oxygen activity increases, at the surface of the pore nearest the sample surface. This results in oxygen dissociating into the pore with a net inward transport of oxygen due to the oxygen partial pressure gradient noted previously. It has been suggested that pores open up along grain boundaries caused by the preferential outward cation

transport along these boundaries (as rapid diffusion paths), allowing a direct ingress of oxygen, far more direct than by dissociation alone.

2) Stress-induced fissuring in the oxide. Generally, any oxide scale growing by outward diffusion of cations will be under compressive load parallel to the oxide-metal interface and tensile load perpendicular to the interface [Haugsrud 2003, Zhou *et al.* 2008]. The formation of fresh oxide within the growing scale develops large compressive stress that, in an ideal oxide growing homogeneously, prevents the formation of microfissures [Haugsrud 2003]. The non-uniformity at grain boundaries may well allow local tensile stress fields to exist opening microfissures [Haugsrud 2003]. The as-delivered Ni is in a high strain state (see Appendix B: Characterisation of As-delivered Nickel (Ni200) Tubes), and is under tension parallel to the surface. Therefore this particular mechanism is quite likely to occur.

3) Differential rates of deformation across the growing oxide scale leading to opening of microfissures. Strains are usually accommodated by dislocation glide. However, it is likely that too few slip systems are available during oxidation at low and intermediate temperatures; creep is then the only mechanism to relieve strain [Haugsrud 2003]. Deformation in growing oxide scales then will be by diffusional flow and grain boundary sliding mechanisms [Haugsrud 2003]. Combined tensile and compressive forces elongate oxide grains in regions of the scale growing by outwards diffusion. Should the scale remain dense and structurally sound, grain boundary sliding must occur [Haugsrud 2003]. If creep is more highly dependent on oxygen partial pressure than grain boundary sliding microfissures will have a tendency to form on the interior region of the scale [Haugsrud 2003]. The presence of columnar layers renders the combined effect of the aforementioned deformation mechanisms less likely. However, once an equiaxed layer has formed in the inner region the mechanism of differential rates of deformation will be valid as long as there is an electrochemical potential gradient across the scale [Haugsrud 2003]. This last was included for completeness's sake since it is limited to oxidation at lower temperatures (at higher temperatures creep is relatively facile), and some degree of deformation can be accommodated by grain rotation if there is insufficient energy for creep [Thomson and Randle 1997]. At 1,100 °C Nabarro-Herring creep (controlled by lattice diffusion; of nickel in this instance) is the primary creep mechanism operating within the NiO [Schütze 1997] with a yield rate ($\dot{\gamma}$) of approximately 10^{-7} s^{-1}.

Haugsrud (2003) notes that it is yet unknown, and quite interesting, to study what sort of influence inward oxygen transport changes have as a function of oxidation time.

Within the scale, if the deformation/dislocation processes (dislocation climb, creep, etc.) are fast enough, cavities (from coalesced pores) at the oxide-metal interface will be taken up by the oxide and either eliminated by sintering or moved outwards by dissociation and deformation [Haugsrud 2003]. Clearly this is a situation best avoided, and it seems that 1,100 °C is a good compromise here too if the oxidation progresses rapidly enough. The balance is between time to complete oxidation and the time required for the desired pores coalescing from vacancies to close up again.

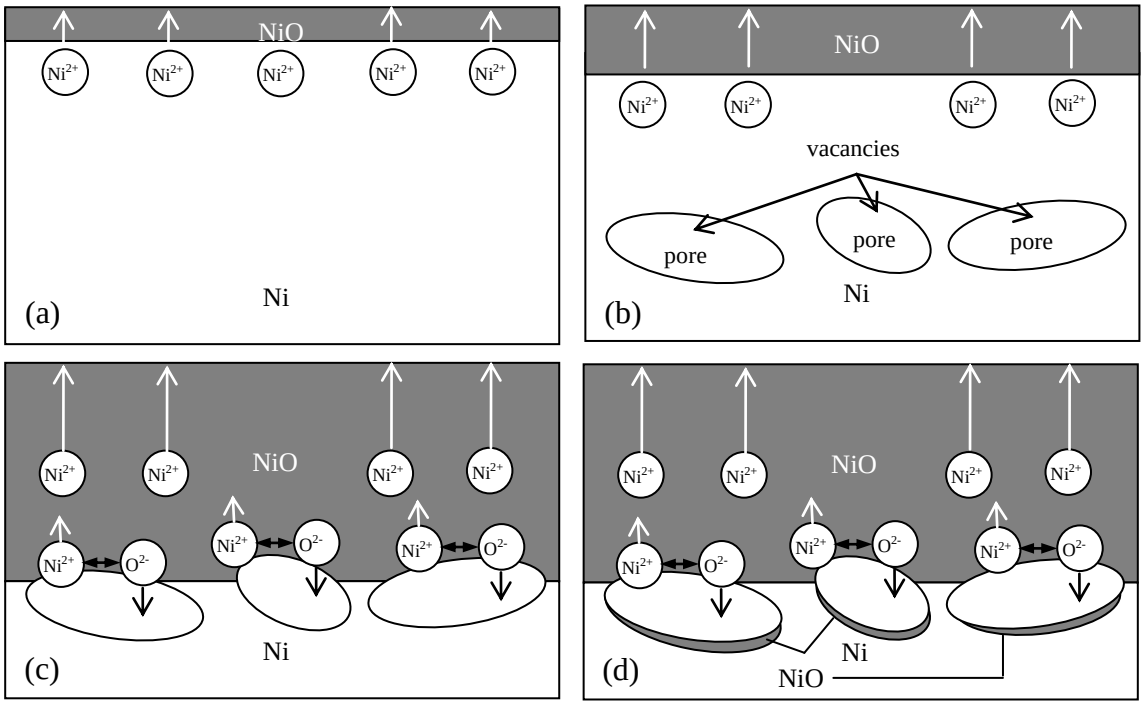

Figure 8-7. Schema of oxidation process including both stages: (a) cations transport through thin naturally occurring surface oxide to oxidise at the surface; (b) cation transport-controlled oxidation continues leaving vacancies in the Ni substrate that coalesce to form pores at the Ni-NiO interface and deeper into substrate by vacancy flux; (c) NiO dissociates into its anion and cation, cation transport continues but is impeded by the thickness of the oxide, the oxygen partial pressure gradient forces the dissociated oxygen towards the un-oxidised side of the pore; (d) the pores oxidise internally, when a large volume fraction of pores exists this becomes the dominant mechanism.

The vapour phase transport mechanism is as follows: Within the pores NiO breaks down again into Ni and oxygen, the Ni cation diffuses towards the surface (continuing that oxidation mechanism) and the oxygen travels inwards to the un-oxidised surface inside the pore due to the oxygen partial pressure gradient across the pore (higher concentration of oxygen towards the outward-facing oxide surface in the form of oxygen bonded into the oxide to the lower concentration on the un-oxidised side of the pore), where it oxidises the underlying Ni [Schütze 1997]. Internal oxidation (presumably by vapor phase transport and a small amount of oxygen diffusion along grain boundaries) was noted by two sources in the literature; both samples oxidized at 1,000 °C and 1,200 °C [Khalid *et al.* 1999] display internal oxidation, in the vicinity of

1,000 °C [Haugsrud 2003]. It is associated with the formation of so-called duplex scales [Haugsrud 2003]. Duplex NiO scales form at oxidation temperatures below about 1,000 °C [Haugsrud 2003]. The inner region is associated with inward (probably gaseous) oxygen transport [Haugsrud 2003]. For pure Ni the inner layer is generally thinner than the outer, columnar, part of the oxide scale and its relative thickness with respect to the outer region increases with decreasing temperature [Haugsrud 2003]. This indicates that in the vicinity of 1,000 °C, at least for pure Ni, the inward oxidation rate (by gaseous oxygen transport) is slower than the outward cation transport-controlled mechanism. It has been shown, furthermore, that the relative thickness of the inner region decreases for increasingly pure Ni [Haugsrud 2003]. Inward diffusion of oxygen is slow in NiO, even at grain boundaries [Haugsrud 2003]. It has been concluded [Haugsrud 2003] that the oxidation of the inner region is due to oxygen transport down a continuous network of micropores in the scale. Evidence suggests that the nature of these pores is transient, rather than permanently-open, that are continuously generated and terminated.

In a vacuum NiO reduction occurs as the decomposition (or dissociation) of NiO as $NiO \rightarrow Ni + 0.5O_{2\,(g)}$ at the interface between NiO and existing Ni [Xing *et al.* 2012]. This strongly supports the vapour phase transport mechanism. The decomposition occurs despite the thermodynamic improbability suggested by an Ellingham diagram because that treats only bulk solid Ni, while the cation transport during oxidation will result in voids (as discussed); defects that enable the decomposition of NiO to Ni under vacuum (in the pores formed from coalesced vacancies) [Xing *et al.* 2012].

Since the vaporisation and re-condensation/re-oxidation is far slower than the cation transport it becomes the rate determining step during the second stage [also see the conclusions of Haugsrud (2003) above]. It is likely that both mechanisms act simultaneously, but the cation transport is dominant initially and the vapour process becomes dominant after about 2 h.

One should keep in mind that the mechanisms discussed here are the principal ones. The classic, purely cation transport, model mentioned above, for instance, neglects such aspects as vapour-phase transport, relative contribution of lattice and short-circuit diffusion and even the effect of stress (and nearly all samples will be stressed as the oxide scale grows due to thermal stresses from CTE mismatch and the volume change inherent in the transformation from medal to metal oxide since oxides invariably have a greater volume). On this vein it is worth noting the following fact. Internal oxidation is more likely if the grains are smaller (more grain boundaries for grain boundary oxidation) [Li *et al.* 1997, Khalid *et al.* 1999]. Grain size is expected to have no effect on internal oxidation by vapour phase transport since this depends on the presence of relatively large pores not grains. However, it depends on the grain boundary cross sectional area as diffusion along grain boundaries can be many times faster than through grains providing a rapid sink for Ni^{2+} cations resulting from dissociation inside pores. It is possible that a large area of grain boundaries may allow rapid grain boundary

diffusion of cations (similar to what occurs to Cr in the cited paper). Hence, in a modified oxidation model accounting for the vapour phase transport we may safely neglect grain boundary diffusion. A modified Wagnerian model is likely to be sufficient since cation transport and vapour-phase transport are both diffusion-type processes.

Such a model is described later (Modified Wagnerian Model, section 8.6). Pertinent to the current discussion is firstly, the model is strong mathematical evidence that the process consists of two parabolas – two diffusion-controlled mechanisms each with their own parabolic rate constant. Secondly, a model of verified accuracy would allow the statistical derivation of the two parabolic rate constants, based on parabolic curve fitting to the data from the first two tiers of experiments (sections 8.3 and 8.4). The average initial $k_p \approx 8.9$ mg^2 cm^{-4} h^{-1} and after the transition to the second parabola (at 0.93 h on average) the average $k_p \approx 4.2$ mg^2 cm^{-4} h^{-1} (calculation shown in section 8.6). Recalling my initial by-eye estimates from the plots themselves it is interesting to note how similar they are to those derived using the model – the statistics confirm our estimates and indeed expectations despite the imperfect modelling of the transition from the first to second mechanisms as described in the Modified Wagnerian Model (see section 8.6 below).

Further to the above discussion consider the following information from Young (2016): NiO nonstoichoimetry (δ) as noted previously is low, c.10^{-3} at.% (metal-deficient type, $\delta > 0$). The vacancy concentration fraction (C_V) is 10^{-5} at 1,000 °C, and the calculated diffusion coefficient of these vacancies at that temperature (D_V) is 1×10^{-6} cm^3 s^{-1}. Recall that $D = D_0 exp\left(\frac{-Q}{RT}\right)$. The self diffusion coefficient for Ni in NiO is $D_0 = 1\times10^{-10}$ cm^3 s^{-1}; the self diffusion coefficient for O in Ni is $D_0 = 0.049$ cm^3 s^{-1}. The latter is particularly of interest, with a self diffusion of $D = 5.78\times10^{-17}$ cm^3 s^{-1} at 1,100 °C (Q = 164 kJ mol^{-1}).

The overall accelerated oxidation observed experimentally compared to that predicted by calculation from published pure nickel oxidation rates can be explained as follows: The curvature introduces stress with a magnitude in part dependent on scale thickness and tensile or compressive based on curvature leading to an accelerated oxidation [Haugsrud 2001, Haugsrud 2003, Zhou *et al.* 2008]. Furthermore, the tubes are delivered in hard temper from cold extrusion, implying high initial (as delivered) strain state, *ergo* accelerated oxidation once more (see also Appendix B: Characterisation of As-delivered Nickel (Ni200) Tubes for microstructure and radius deviation measurements from nominal). The combination evidently accounts for the far greater oxidation rate than obtained from Haugsrud (2001, 2003). The relatively thin (125 μm) wall thickness of the tubes means that inevitable in-film stresses are magnified (inherent part of mathematical relationship of stress and strain as thickness approaches zero) resulting in an even more marked effect on oxidation rate. Both compressive loads and

tensile loads accelerate the oxidation rate [Zhou *et al.* 2008] with compressive loads having a larger effect.

Thermal stresses in oxides are due to the CTE mismatch between the metal substrate and the oxide scale. Thermal stresses develop in both the oxide and the substrate [Zhou *et al.* 2008]. The oxide experiences a compressive stress while the metallic substrate experiences a tensile one. Growth stresses in oxides are generally compressive due to the combination of oxide volume change (from metal to oxide) and the simultaneous consumption of the underlying metal [Zhou *et al.* 2008]. In the case of compressive stresses the surface morphology is often rumpled, and the substrate contains discontinuous cavities (very large non-spherical pores) at the oxide-metal boundary [Zhou *et al.* 2008]. This can be observed in the following micrographs prepared as part of this study: Figure 8-12. and Figure 8-16. Because of the way concave surfaces influence the stresses at the oxide-metal boundary the large discontinuous cavities noted will tend to be towards the inner edge (although not necessarily adjacent to it). Naturally as the oxidation progresses this interface advances leaving parallel layers of such large cavities.

In the case of tensile stresses the surface morphology often displays many parallel cracks, containing a mix of accumulated cavities at the oxide-metal boundary and transgranular cracks in the oxide scale [Zhou *et al.* 2008]. This was not observed however, and in agreement with other sources the areas under tensile loading (the outer edges of the tube) display less oxidation than those under compressive loading (the inner edges) due to the inferior increase of the oxidation rate of tensile strain compared to compressive strain described above.

Stress affects grain boundary diffusion and causes excessive vacancies to accumulate at the oxide-metal boundary, possibly altering the behaviour of diffusing cations [Zhou *et al.* 2008]. The stress at the boundary (which under no external load is controlled by growth and thermal stresses) is altered by the application of an external load. Zhou *et al*. (2008) have determined that there is a minimum threshold tensile stress for any effect on oxidation rate to occur. There are no evident sources of such external load on the samples in this study, so there is no modification of the boundary microstructure.

The reason stress increases oxidation rate, proposed by Zhou *et al.* (2008) is given here by way of explanation. The observed increased oxidation rate may be dependent upon a greater vacancy flux injection into the metal substrate; a decrease in the vacancy supersaturation at the boundary between oxide and metal would increase oxidation rate [Zhou *et al.* 2008]. Any cavities formed at the boundary under compressive loading might be expected to decrease oxidation rate by impeding cation diffusion. However, because the pores extend into the metal, gradients in the activity in the scale create partial pressure gradients in the cavities [Zhou *et al.* 2008]. The vaporised metal in the porous inner scale (that is to say the scale in the vicinity of the oxide-metal boundary)

allows continued oxide growth [Zhou *et al.* 2008]. Furthermore, the presence of stresses affects the oxide-gas interface stress distribution near grain boundaries, increasing the diffusion rate of nickel ions resulting in accelerated oxidation [Zhou *et al.* 2008].

Unless otherwise noted the following micrographs are ordered from lower to higher magnifications by this arrangement: left to right and top to bottom. Note that the lowest mass fraction oxidised observed (at 1 min) was about 79 wt.% due to the rapidity of the process and the maximum (at 42 h) was approximately 96 wt.%. See also Table 8-1. (above). As oxidation progresses pores formed bands more-or-less parallel to the surfaces.

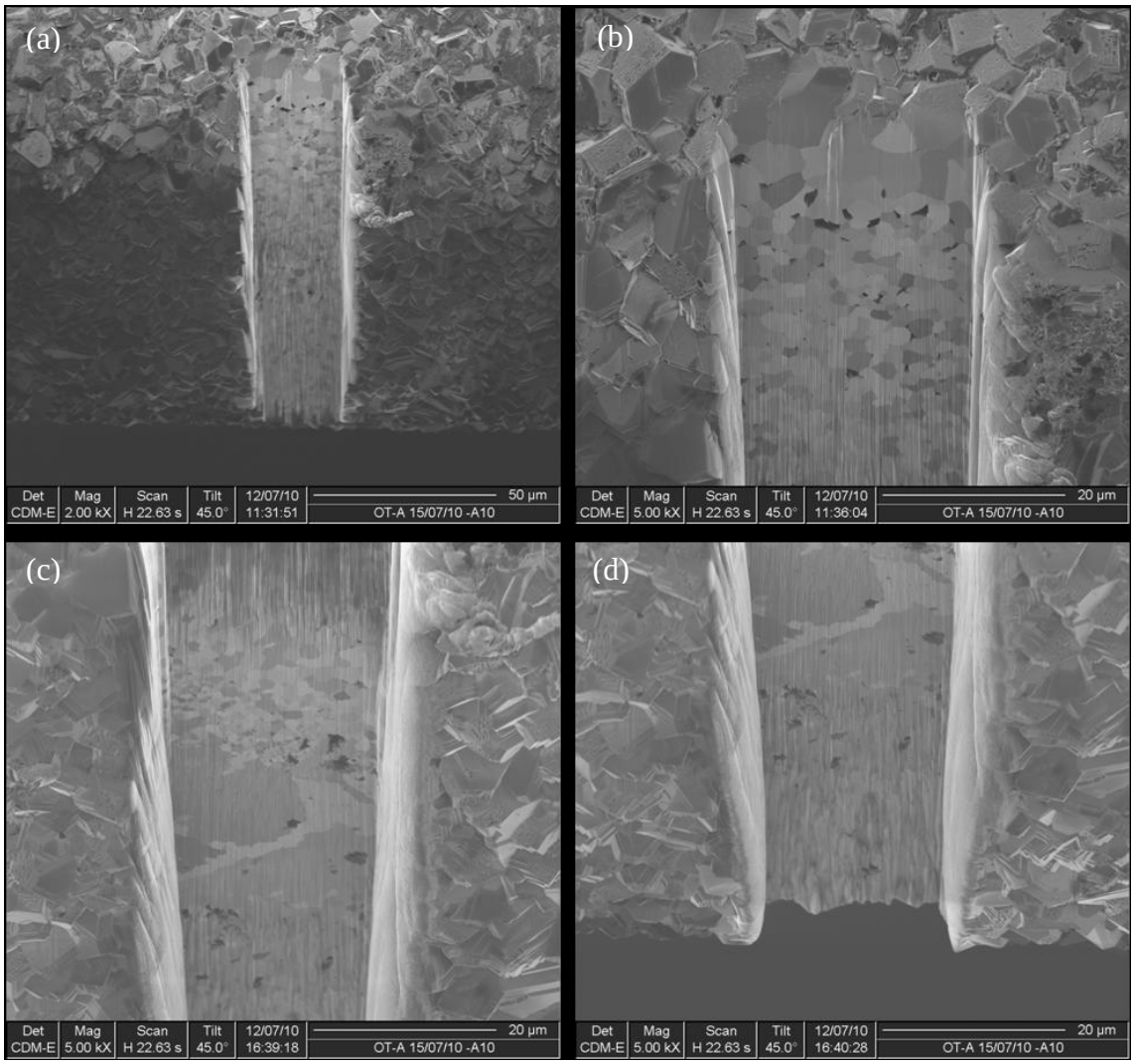

Figure 8-8. FIB micrographs of sample OT-A-15/07/10-125.1100-A.10 (90.4 wt.% oxidised) showing milled trench. FIB milling was necessary to obtain a representative cross-sectional area for high resolution SEM imaging (see below). Micrograph (a) shows the milled trench, (b) the upper portion, (c) the middle and (d) the lower part of the trench. Notice the large pores visible even at this magnification. Also note that (as expected) they appear in distinct layers parallel to the surfaces. Some areas show heavy waterfalling due to the great depth of the trench which was milled from the outer surface (top of images) to the inner surface of the tube (bottom of images).

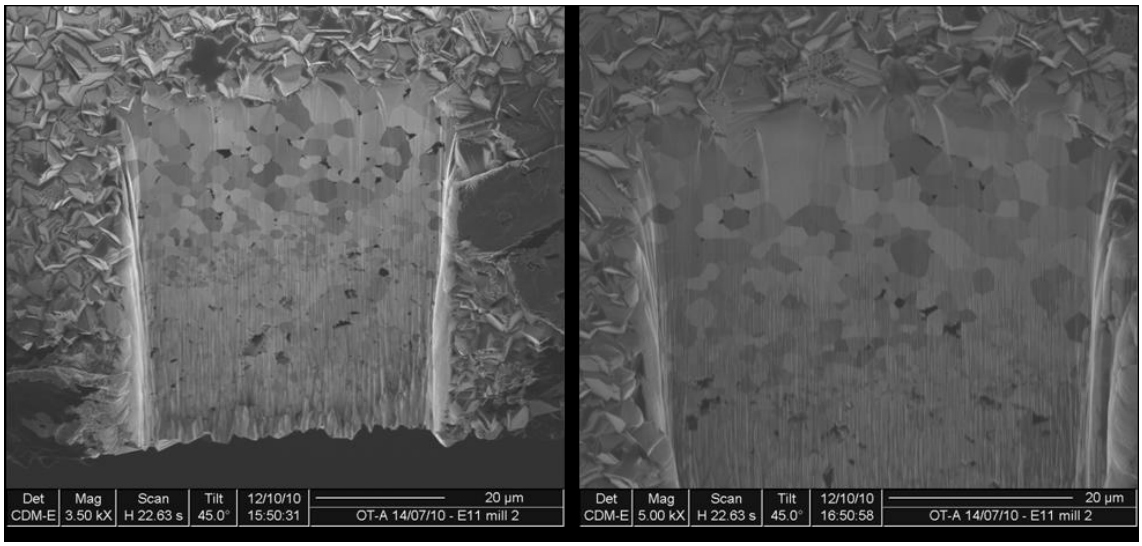

Figure 8-9. FIB micrographs of sample OT-A-14/07/10-125.1100-E.11 (91.0 wt.% oxidised) showing milled trench. Similarity to above images confirms the reproducibility.

In order to fully oxidise (~96 wt.%) the samples a heat treatment at 1,100 ℃ in air for ~42 hours is sufficient. However, whether the full time is necessary for sufficient oxidation for the anode fabrication is less obvious.

Four samples selected to be representative of early oxidation and virtually complete oxidation were inspected visually and using ultra-high resolution scanning electron microscope (SEM) imaging, of both the surface and cross-sections (trenches created by FIB). A Au-Pd coating was used to enable the high resolution imaging. The grains of the coating are visible in some images appearing somewhat as scales. The characterization was subsequently repeated with a sample representative of an intermediate time close to the transition from kp_1 to kp_2.

The goals of the characterization were as follows: confirm the presence of small pores created by vacancy coalescence, confirm uniformity of oxidation through section taken, inspect grains and grain boundaries for damage or signs of a different mechanism that may have affected the predicted oxidation, ascertain reproducibility of oxidation. Each objective will be treated in turn.

At each site of interest a sequence of images was taken at increasing magnification, usually with the site of interest centred in all micrographs. These sets of micrographs with multiple levels of magnification are shown in Appendix D: Oxidation Micrographs. For the remainder of this chapter only images at one or two magnifications are generally shown. For cross sections this is typically 10,000× or greater. This particular magnification was selected based on studying the micrographs as a whole: it clearly shows all the larger features and even smaller pores remain visible while showing a relatively large area that demonstrates that the features occur consistently in a region rather than being highly localised. The only drawback is a loss

of context (exact location within the oxide scale), a feature only possible with lower magnification images. Detail of very small features visible may be shown at 20,000× and higher. Naturally, all images were used interpreting the microstructure with representative examples given in the following figures. Extensive waterfalling due to the depth of the trenches mulled by FIB is marked with an * in the relevant figure captions.

Oxidation was confirmed to occur as an advancing front from the near-surface region to the sample interior with little to no sign of preferential grain boundary oxidation. Oxidation was confirmed to be right through the A.10 and E.11 samples by EDS analysis of a trench milled by FIB at an edge. The trench showed uniform oxidation with fairly monodisperse grain sizes. While there does appear to be some morphological difference between the outer strata and inner oxide the presence of the columnar outer structure mentioned in some sources of the literature was not noted.

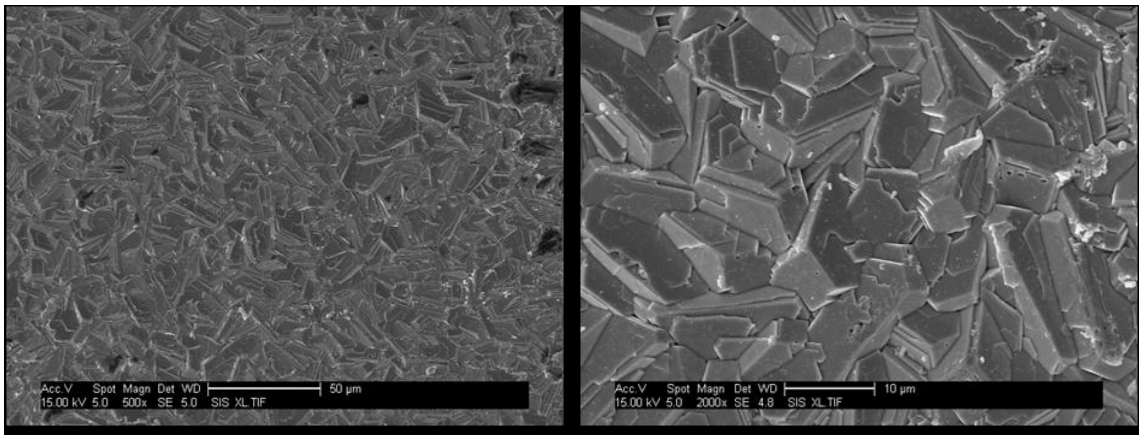

Figure 8-10. SEM micrographs showing surface morphology of sample OT-A.15/07/2010-125.1100-A.10 (90.4 wt.% oxidised).

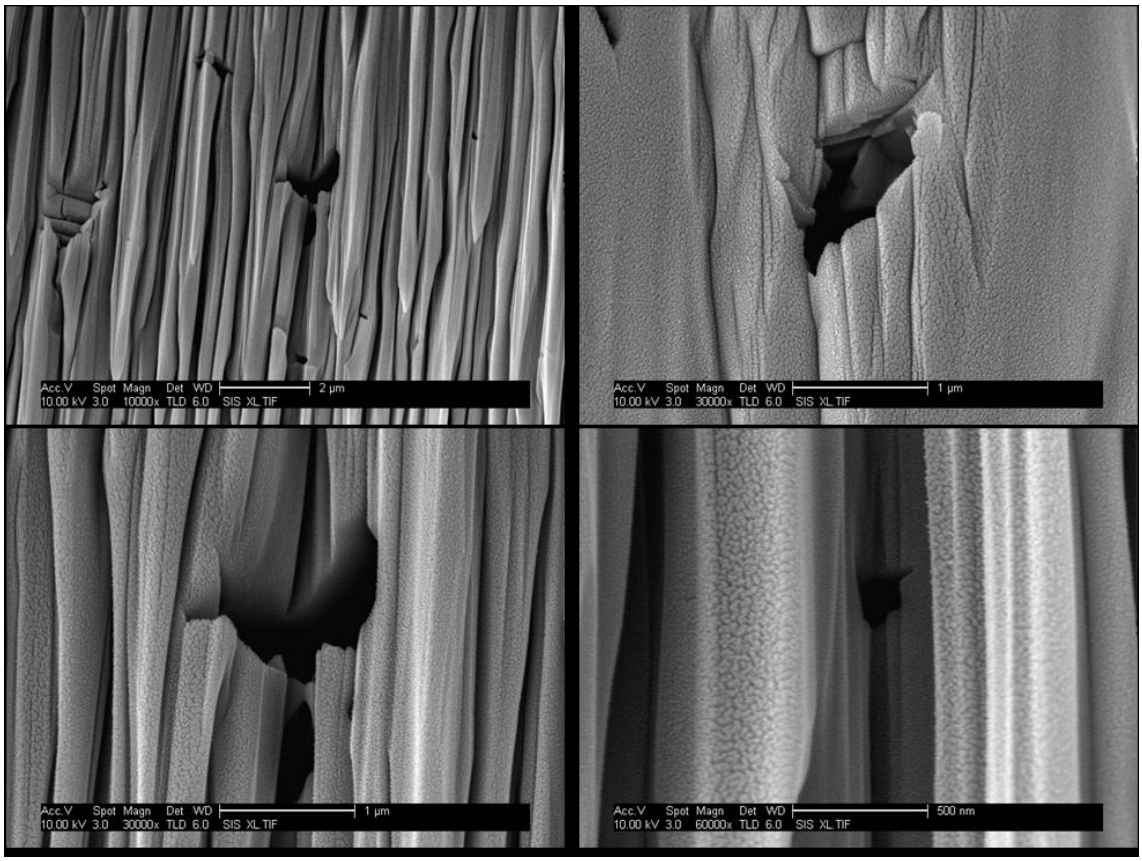

Figure 8-11. SEM micrographs* showing pores near to the inside edge of sample OT-A.15/07/2010-125.1100-A.10 (90.4 wt.% oxidised).

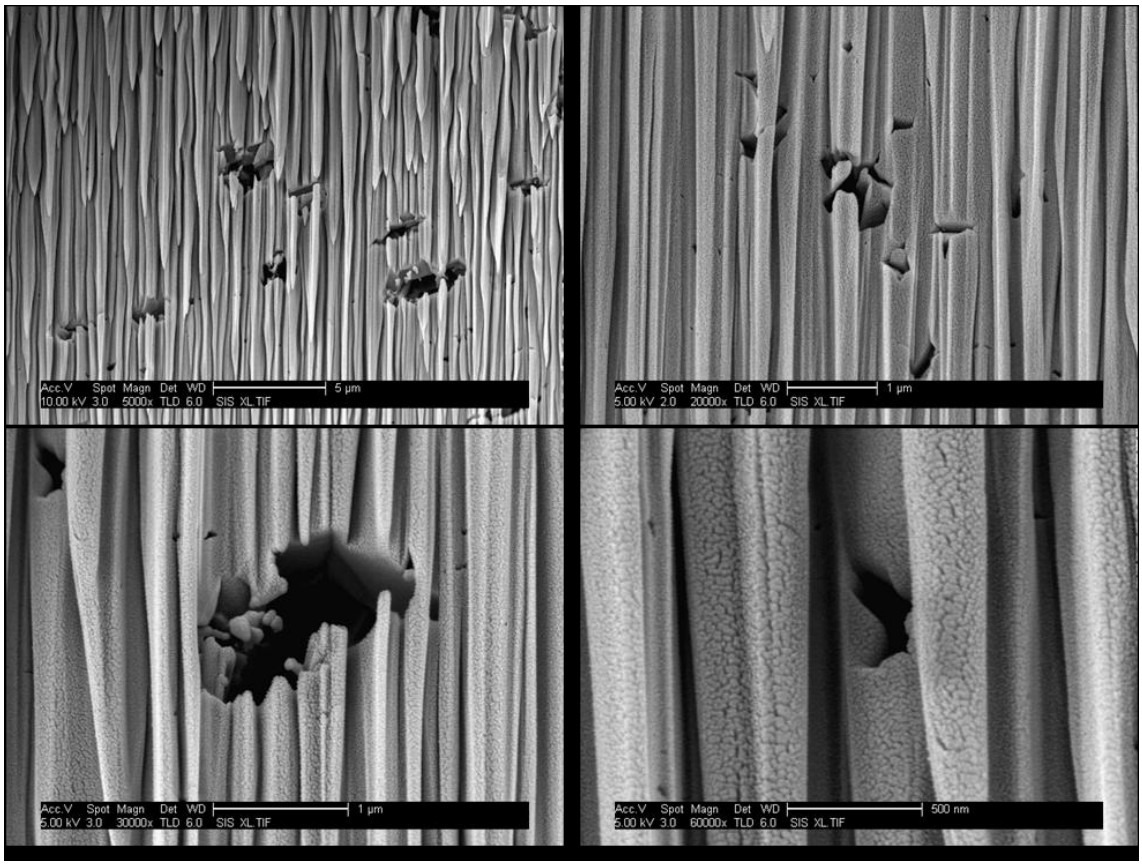

Figure 8-12. SEM micrographs* showing pores around the middle of sample OT-A.15/07/2010-125.1100-A.10 (90.4 wt.% oxidised).

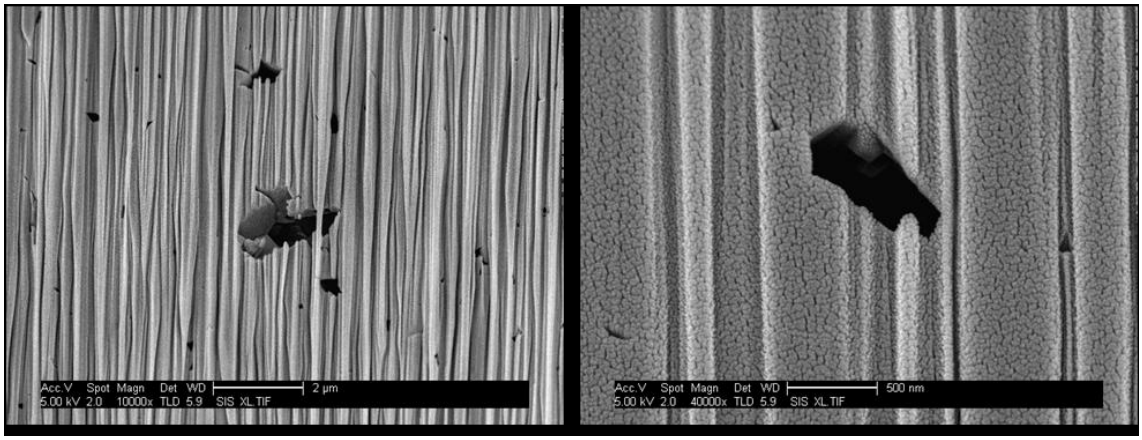

Figure 8-13. SEM micrographs* showing pores near the outside edge of sample OT-A.15/07/2010-125.1100-A.10 (90.4 wt.% oxidised).

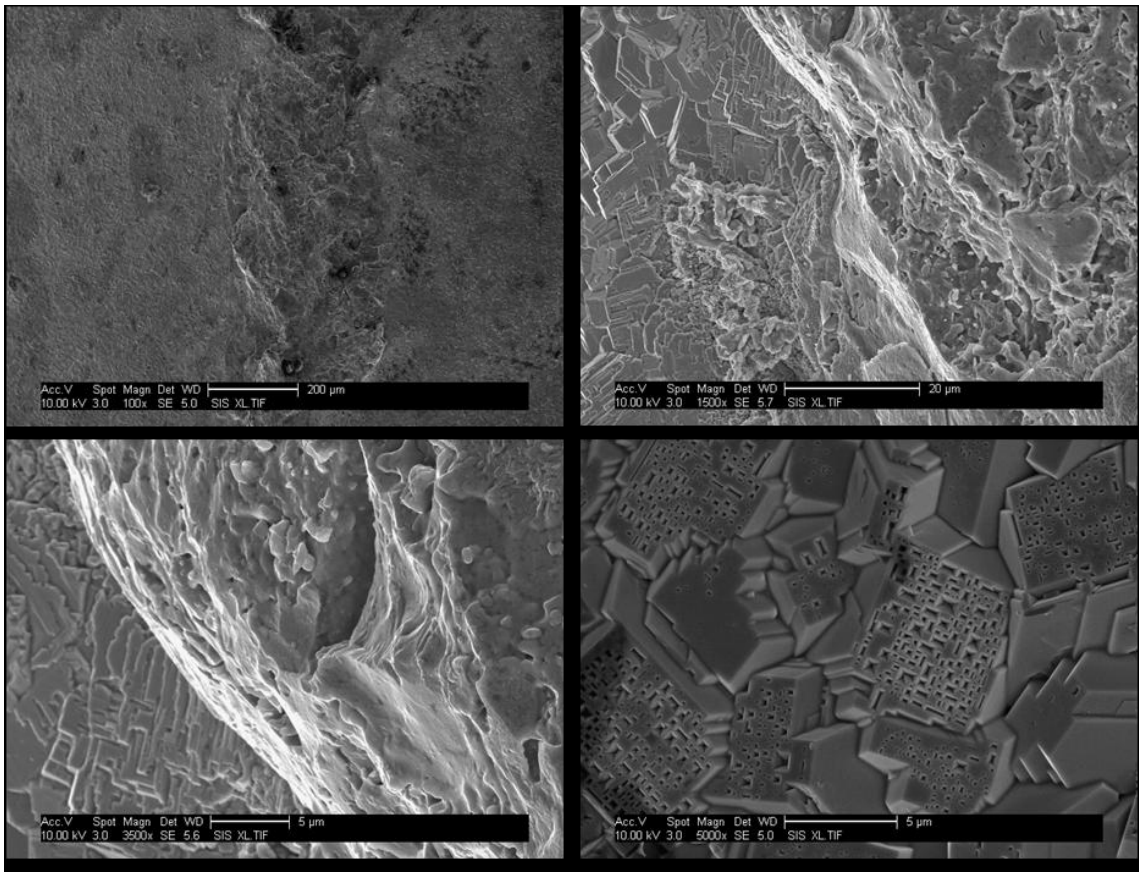

Figure 8-14. SEM micrographs showing surface morphology of sample OT-A.15/07/2010-125.1100-E.11 (91.0 wt.% oxidised).

The surface of all samples at or near complete oxidation is not rumpled as observed in the literature [Zhou *et al*. 2008], but a large surface feature appears on the surface of E.11., shown in Figure 8-14. Some surface undulations were visible, however, also associated with compressive loading. Otherwise, the surface morphology is identical to A.10.

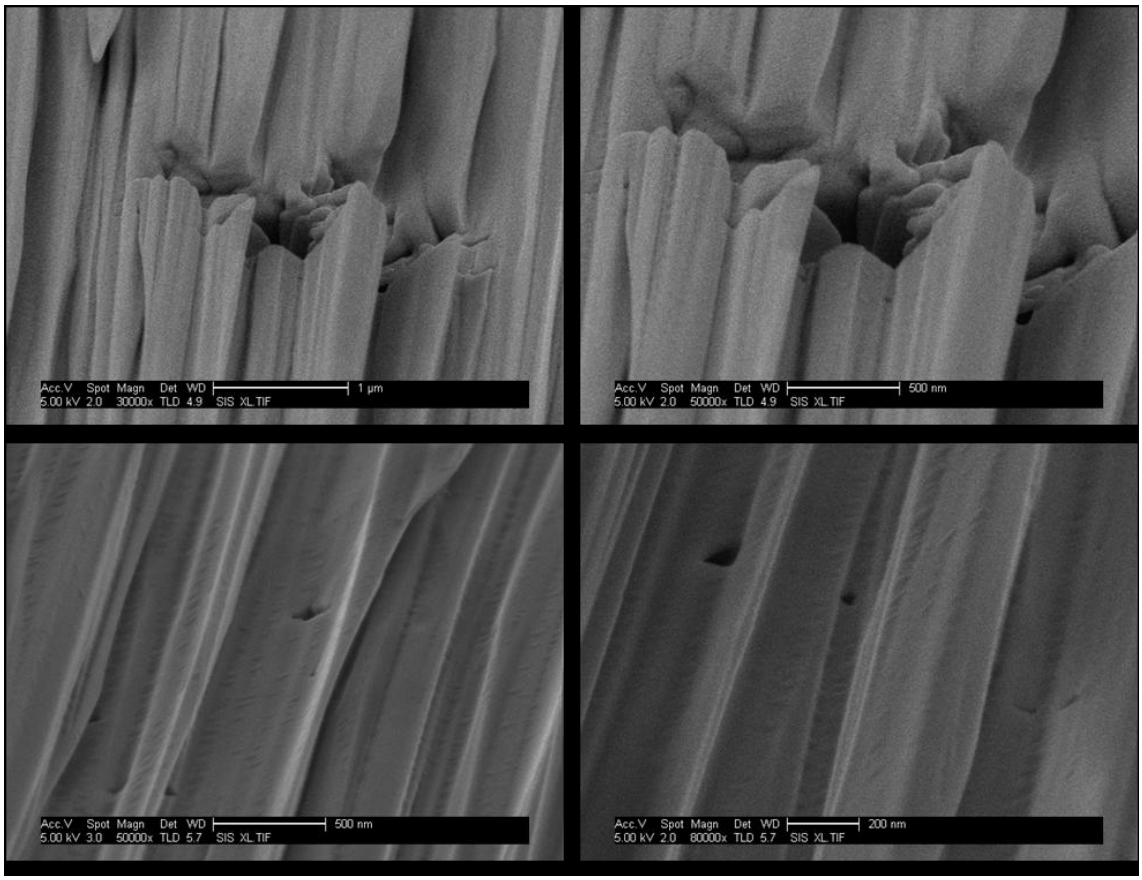

Figure 8-15. SEM micrographs* showing pores near the inside edge of sample OT-A.15/07/2010-125.1100-E.11 (91.0 wt.% oxidised).

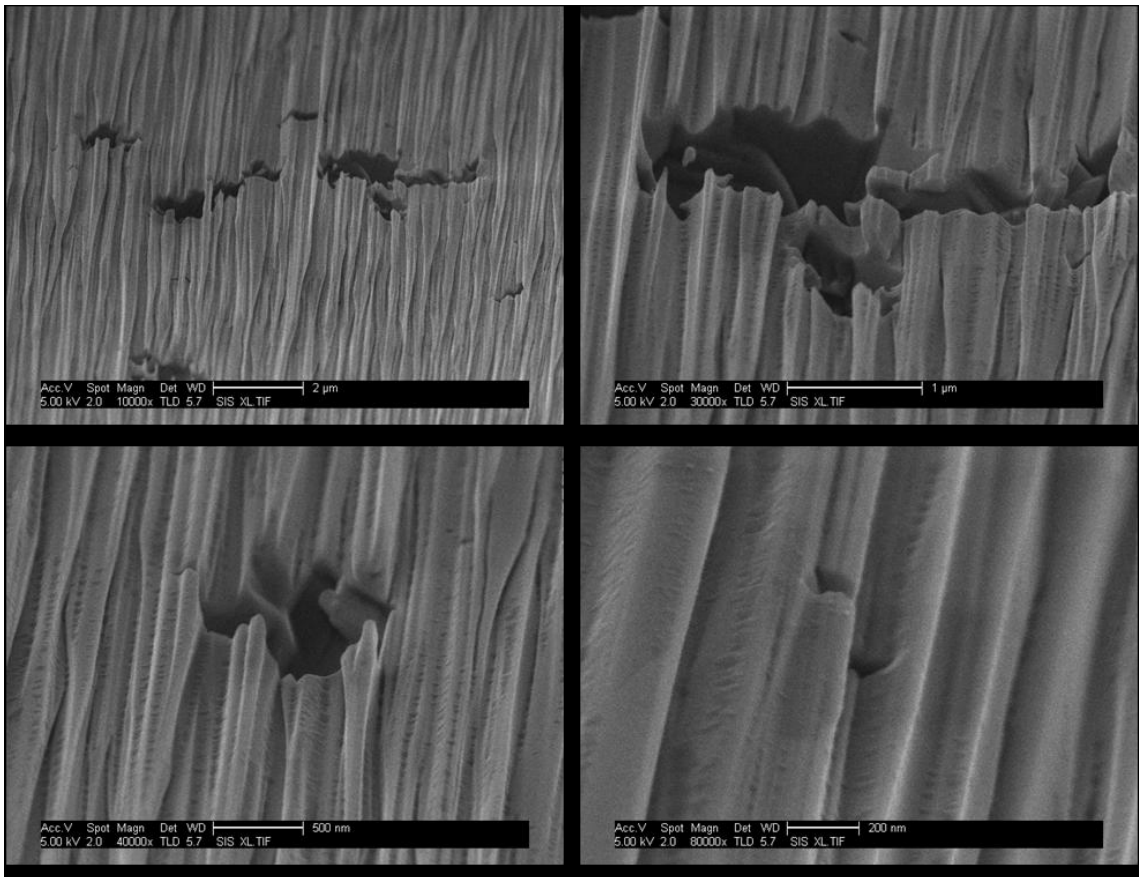

Figure 8-16. SEM micrographs* showing pores around the middle of sample OT-A.15/07/2010-125.1100-E.11 (91.0 wt.% oxidised).

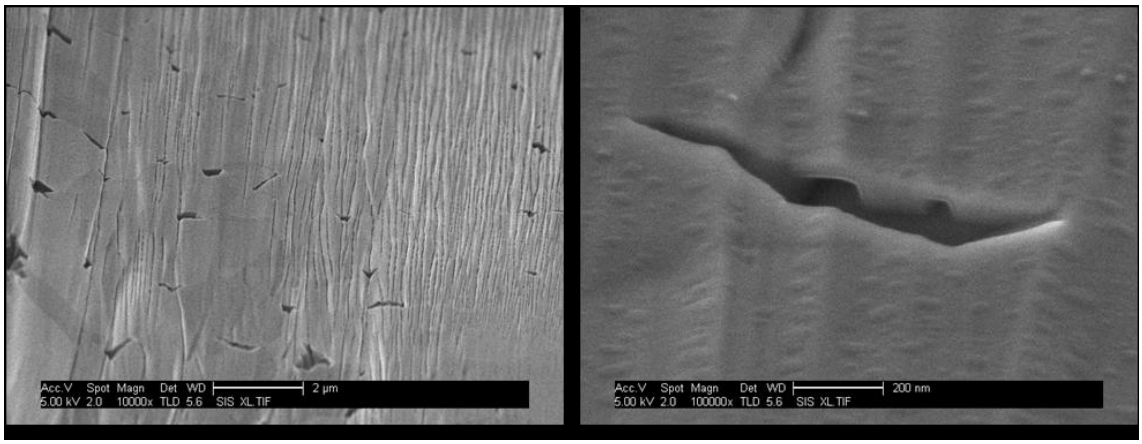

Figure 8-17. SEM micrographs* showing pores near the outside edge of sample OT-A.15/07/2010-125.1100-E.11 (91.0 wt.% oxidised).

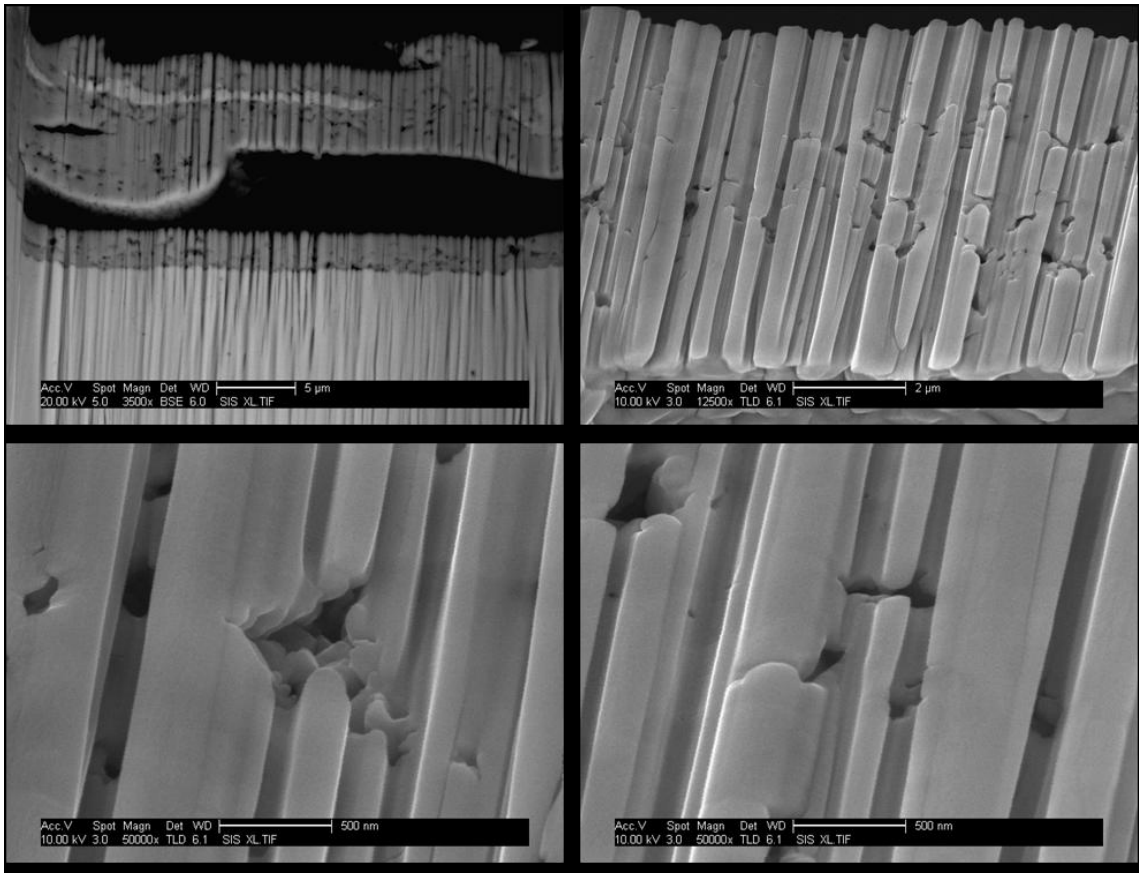

Figure 8-18. SEM micrographs* showing pores near the inside edge sample OT-A.15/07/2010-125.1100-C.01 (79.2 wt.% oxidised). This particular sample had a large void near the surface; probably a manufacturing defect. It is interesting to observe the oxidation from both sides of the upper portion leaving an unoxidized part near the middle.

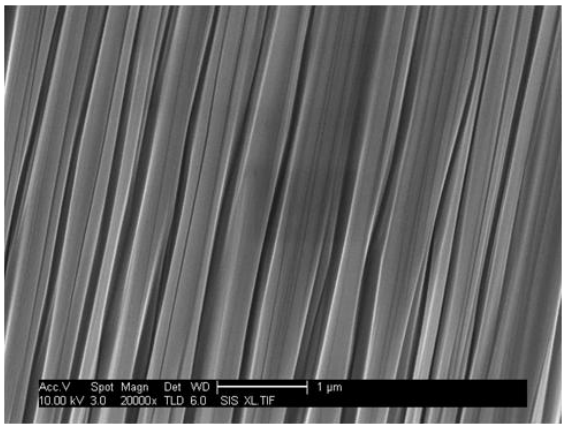

Figure 8-19. SEM micrograph* showing lack of porosity around the middle of sample OT-A.15/07/2010-125.1100-C.01 (79.2 wt.% oxidised).

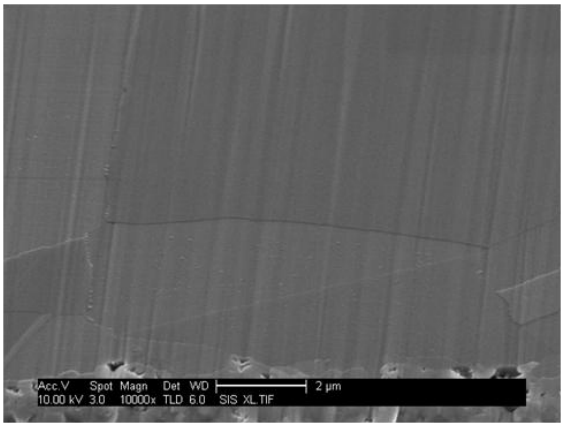

Figure 8-20. SEM micrograph* showing pores very near the outside edge of sample OT-A.15/07/2010-125.1100-C.01 (79.2 wt.% oxidised). Note that past about 1 µm into the sample from the bottom edge (just visible below the information and scale bar) there was no observed porosity at any resolution.

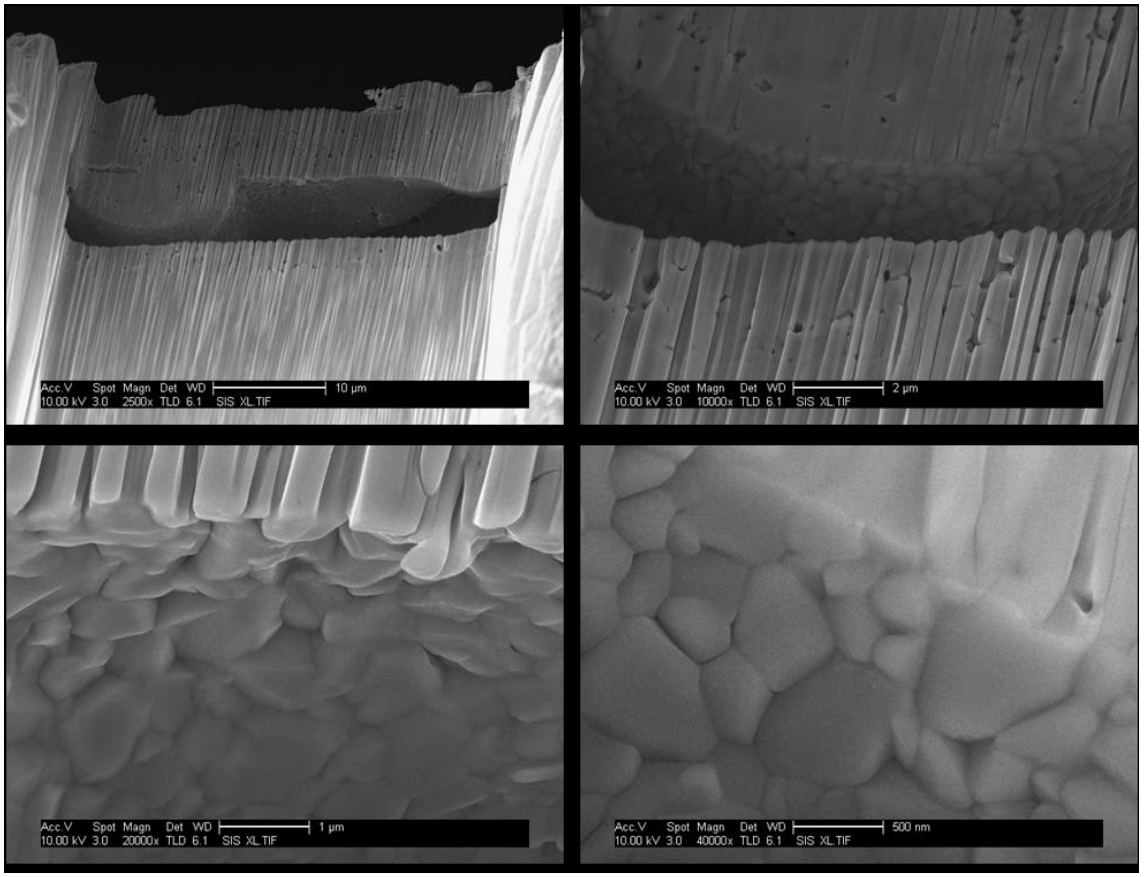

Figure 8-21. SEM micrographs* showing pores and more importantly grains in the area of the large void taking advantage of the 'through section' it presents near the inside edge of sample OT-A.15/07/2010-125.1100-C.01 (79.2 wt.% oxidised).

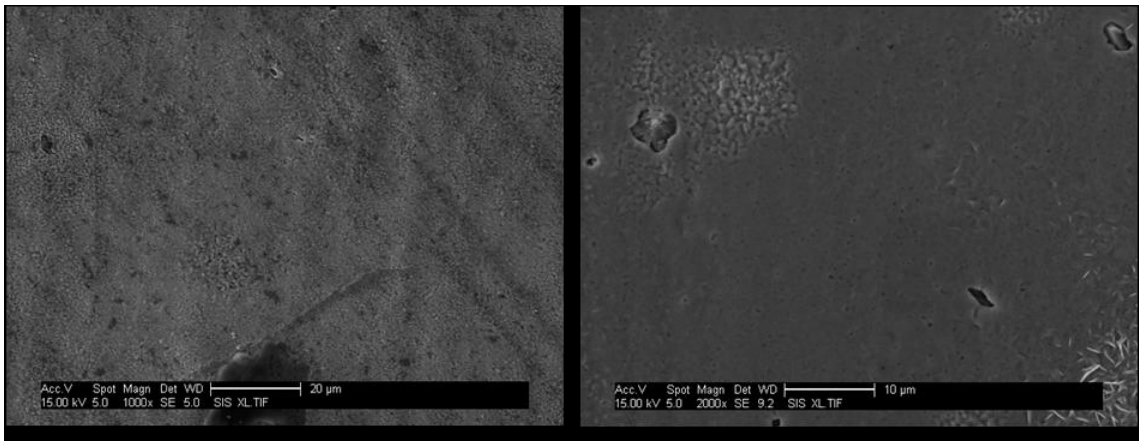

Figure 8-22. SEM micrographs showing surface morphology of sample OT-A.15/07/2010-125.1100-D.01 (79.3 wt.% oxidised).

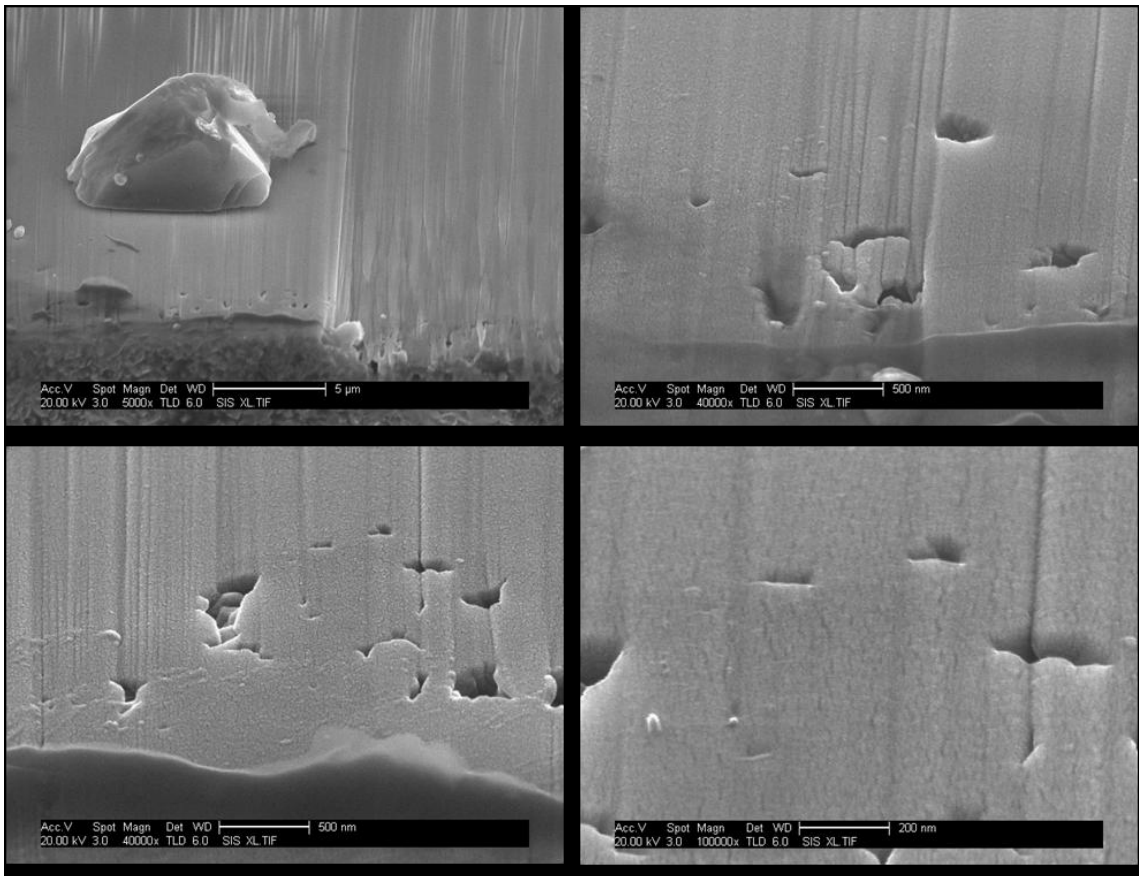

Figure 8-23. SEM micrographs* showing pores near the inside edge of sample OT-A.15/07/2010-125.1100-D.01 (79.3 wt.% oxidised).

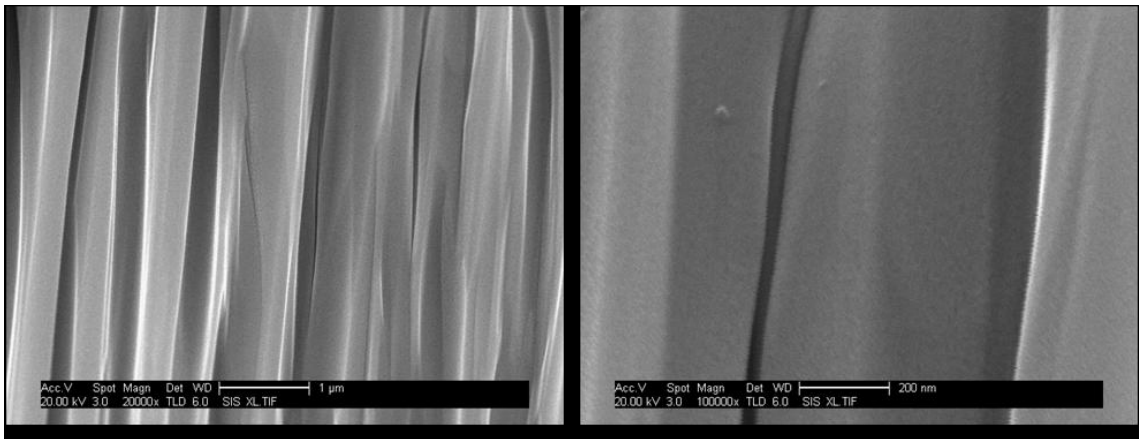

Figure 8-24. SEM micrographs* showing lack of porosity around the middle of sample OT-A.15/07/2010-125.1100-D.01 (79.3 wt.% oxidised).

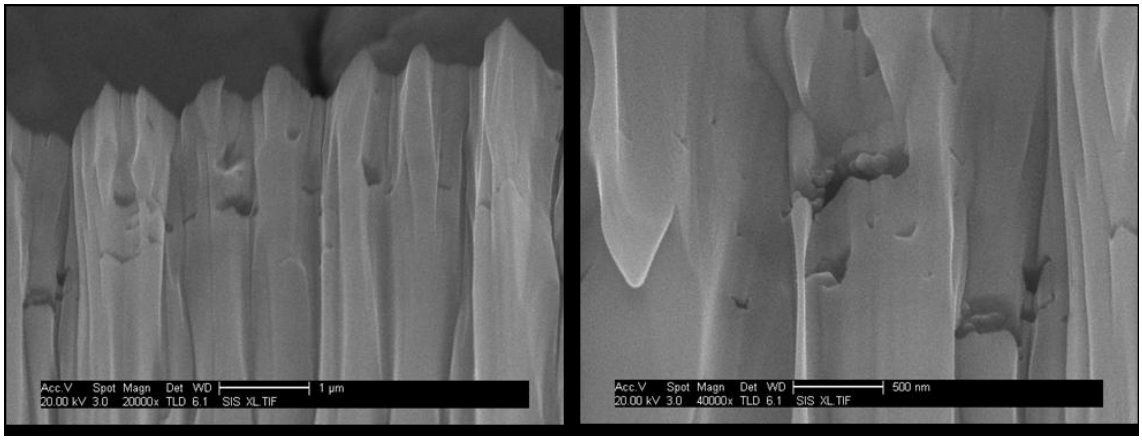

Figure 8-25. SEM micrographs* showing pores near the outside edge of sample OT-A.15/07/2010-125.1100-D.01 (79.3 wt.% oxidised).

As can be seen in the micrographs above, showing cross-sections of samples oxidised for just 1 minute, pores are more prevalent and of a smaller size than at later oxidation stages. This observation is wholly consistent with the mechanism proposed whereby vacancies have sufficient mobility to coalesce into small pores given sufficient time (very rapid, evidenced by early stage samples) and eventually coalesce into fewer much larger voids with oxidation continuing through the substrate by cation transport but with the addition of vapour phase transport. The latter become increasingly dominant as the area at any given in-plane section of metal decreases and that area of pores increases with time. Similarly consistent with the proposed modification to the oxidation mechanism is the lack of observable pores (of any size) around the middle of early stage sampled. The oxidation prgresses as an advancing front, which in the early stages had not yet reached the centre of the sample from the free surfaces exposed to oxygen.

The consistent behaviour remarked on in the preceeeding paragraph extends to the surface morphologies of the samples. Early stage samples exhibit a notable number of surface-connected pores, mostly at triple points, whereas the surface of late stage

samples appear tightly compacted. At high magnifications the surface of samples that were approximately completely oxidised display highly facted, tightly-packed, grains (compare early and late stage oxidation micrograph sets in Appendix D: Oxidation Micrographs). The interior of these grains is in most cases perforated by a large number of 50 nm – 500 nm faceted pores. While studying the cause behind the appearance of these structures in any detail is beyond the scope of this project, the regular faceting suggests crystallographic orientation and lowering surface energies have a stong influence. The fact that the honeycomb-like structure does not appear in all grains to the same extent suggests that a grain's orientation with respect to particular crystallographic planes is also an important factor. The most likely explanation is that cation transport is more rapid along certain crystallographic planes resulting in preferentail outward growth of the oxide on those planes and slower growth on others. Haugsrud (2003) reported on preferential oxide growth in certain crystallographic directions.

Furthermore, the tightly packed grains of late stage as opposed to earlier samples indicates that the surface layer is under compression during oxidation, in agreement with the observations of [Zhou *et al.* 2008]. A possible explanation, in excess of any residual stress in the as-delivered material, is that NiO crystals are larger than Ni ones [Camilleri 2009]. Hence, as the surface oxidizes the nickel metal below will tend to compress the oxide. The absence of surface cracks of any sort also supports the compression theory (see Zhou *et al.* (2008) for micrographs of cracks in oxide scale on nickel induced by and indicative of tensile loading). The effect can be extrapolated to explain the relative lack of porosity near the surfaces for samples with a longer dwell.

The three figures below (Figure 8-26, Figure 8-27 and Figure 8-28) show a sample that is representative of an intermediate time close to the transition from k_{p1} to k_{p2}. The sample in question was charging up, resulting in poor image quality. The images shown were therefore re-taken with a different SEM than the rest of this project, courtesy of the characterization lab at the University of Malta's Department of Metallurgy and Materials Engineering within the Faculty of Engineering. That state-of-the-art SEM in concert with remounting the sample resulted in far more manageable levels of surface charge and therefore sharper images even at very high magnification.

The observed features fit, as one might reasonably expect, between the early and late stages (see discussion above). *Ergo*, there are no additional mechanisms or interactions at work during oxidation.

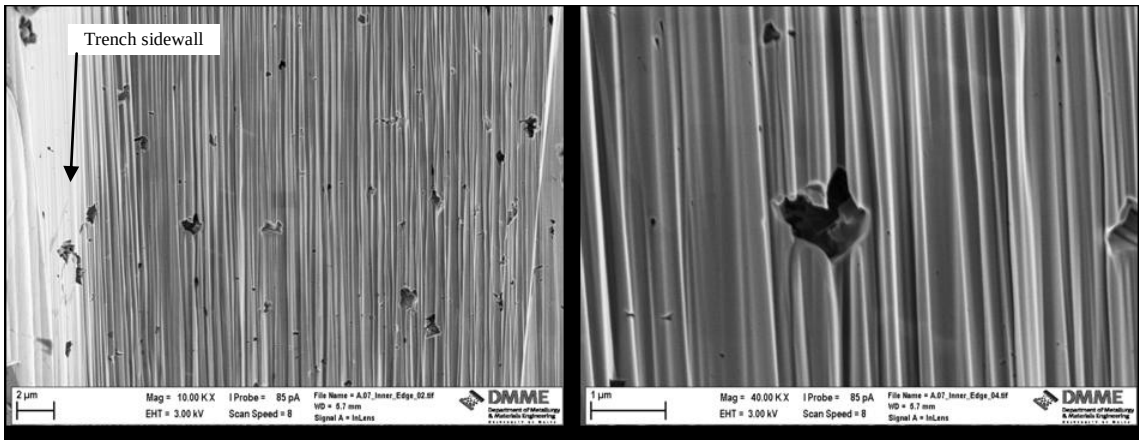

Figure 8-26. SEM micrographs* showing pores near the inside edge of sample OT-A.13/07/2010-125.1100-A.07 (84.9 wt.% oxidised).

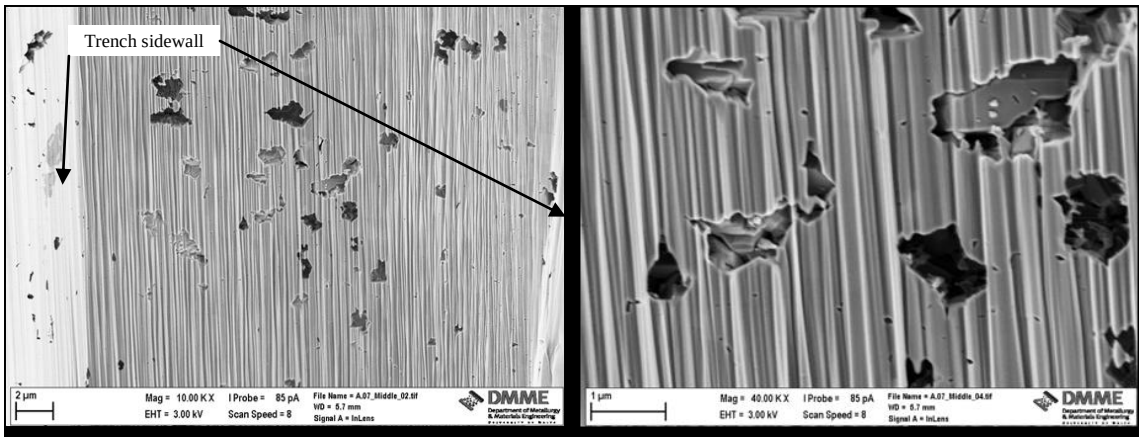

Figure 8-27. SEM micrographs* showing pores around the middle of sample OT-A.13/07/2010-125.1100-A.07 (84.9 wt.% oxidised).

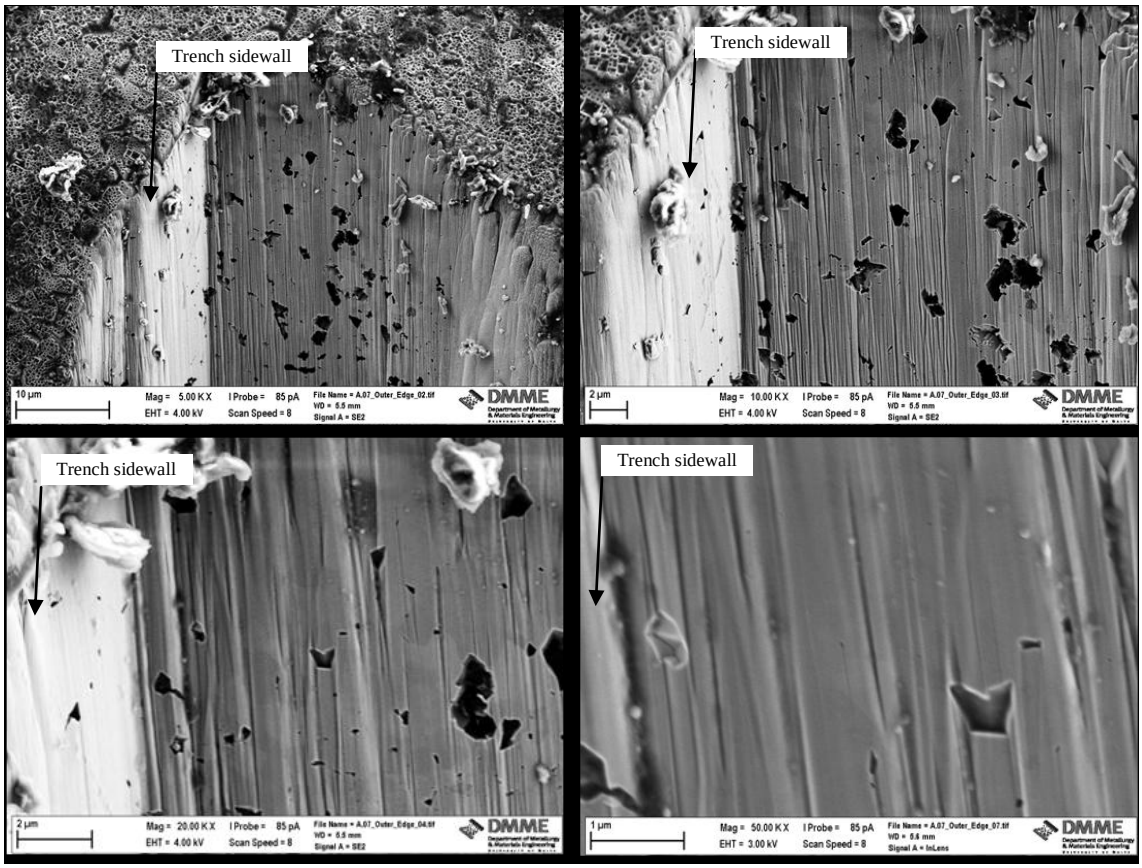

Figure 8-28. SEM micrographs* showing pores near the outside edge of sample OT-A.13/07/2010-125.1100-A.07 (84.9 wt.% oxidised).

The micrographs shown previously demonstrate that the porosity was detectable using the SEM; including ultra-high resolutions that reveal pores less than 25 nm across (e.g. Figure 8-26.), to some pores over 2 µm across (e.g. Figure 8-27.). The FIB micrographs show clearly the grain structure. Both types of images demonstrate that the pores form in layers parallel to the surfaces as expected due to the advancing oxidation front consuming metal and creating vacancies that coalesce into pores at the metal-oxide interface.

There is relatively little porosity visible. Likely reasons are: In general, oxide scales will be in a state of compressive stress parallel to the oxide–metal interface and tensile stresses normal to the oxide-metal interface. Formation of new oxide within a growing scale induces large compressive stresses (since the film is very thin). For an ideal oxide with a uniform stress distribution, compressive stresses should prevent formation of microfissures [Haugsrud 2003]. Given the high temperature and the fact that the process starts out as creating a thin film of oxide means high temperature creep may account for the lack of porosity. For the pure Ni, creep of the substrate as it is still oxidizing can occur and compensates the vacancies, closing them. This is also evidenced by the very tightly compacted grains – a sign of the high compressive stresses induced during oxidation [Huntz *et al.* 2006]. Finally there is the nature of the reported experiments – in which only thin oxide scales are grown and the Ni-NiO interface (where the vacancies

appear) is visible. The samples of this study were fully oxidized through the entire thickness. It is likely therefore that the situation is sufficiently different from that reported in the literature that the lack of porosity far from the interface was not observed in the experimental work cited. The curvature induced stress and the resulting effect on the porosity has already been described. The micrographs support this.

The oxide layer is uniform but there is no evidence of the columnar texturing reported by some. Micropores as in Huntz *et al.* (2006) are in evidence. Does this indicate that the oxide is still in a disordered growth mode prior to columns (a preferred growth texture) being seeded? I believe this is unlikely given the oxide thickness. I think the presence or absence of columnar texturing in NiO is a factor of strain state, with high strain (such as with the cold extruded as-delivered nickel tubes utilised throughout this project) suppressing the texturing. This is consistent with Huntz *et al.* (2006), also using samples with a high initial strain. The oxide-metal interface advances as a front remarkably uniformly across the sample. For samples completely oxidised the resulting NiO tubes have a uniform microstructure with pores 25 nm – 2 μm across that are non-spherical and oriented with their longer axis parallel to the nearest surface. While this is in stark contrast to Wagner's assumptions it is, in fact, the norm for NiO.

Given the quantity of samples studied it is reasonable to claim the process shows excellent reproducibility in both microstructure and mass fraction oxidised (hereafter I abbreviate this to MFO).

There is no evidence of other mechanisms of oxidation taking place in addition to the two noted (cation transport and vapour phase transport) and other features conform to those reported in the literature [Zhou *et al.* 2008, Khalid *et al.* 1999, Haugsrud 2003, Huntz *et al.* 2006]. The reasons for the discrepancies in oxidation rate inferred from the mass gain versus time curves and the literature appear to be correct, or at least no contradictory evidence is offered by the SEM analysis.

The nickel was oxidised without stresses accumulating sufficiently to cause spallation or fracture. Oxidation progresses as expected with an advancing front from each surface moving inwards until full oxidation. The oxidation rate appears modified by the curvature-induced stress and thermally induced stress. Some porosity was observed with pores ranging from a few nm to a few μm across.

There is a significant deviation from the behaviour predicted by the unaltered model (Figure 8-4.). This deviation can be attributed partly to one of the assumptions of the theory of oxidation – that a semi-infinite reservoir of nickel cations is available. While such an assumption is certainly valid when thin oxide scales are investigated it is clearly no longer valid if a sample is being fully oxidised. This (only valid for the later stages) along with the described shift in dominant mechanism from cation transport to vapour phase transport explains the sharper drop in oxidation compared to Wagnerian model

predictions. For the earlier stages of oxidation the great increase in effective oxidation rate, both when cation transport is dominant and when gas phase transport is dominant, may be attributed to the stressed state of the Ni tubes. Even in their as-delivered condition they are in a high strain state due to their mode of manufacture (see Appendix B: Characterisation of As-delivered Nickel (Ni200) Tubes). Oxidation normally induces strain, and combined with the effect of curvature, the samples are in a highly strained state compared to typical samples used in oxidation studies. *Ergo* the oxidation rate is greatly accelerated compared to annealed, flat samples as typified in the literature.

There is evidence (Figure 8-4.) for the change in dominant mechanism at around 2 h from cation-transport-dominated to vapour-phase-transport-dominated. In order to fully oxidise (~96 wt.%) the samples a heat treatment at 1,100 ℃ in air for ~42 hours is sufficient. Unfortunately, because oxidation progresses as an advancing front, the samples must be fully oxidised to ensure there is NiO to reduce and create porosity right through the anode. This is a great pity: the parabolic nature of Ni oxidation means that after a few minutes ~80% oxidation by mass is achieved. Had this been distributed through the entire anode it would have been possible to create a sufficiently permeable anode with just a few minutes of oxidation – highly advantageous in the economical fabrication of fuel cells.

Finally, it was noted in the background section that it is generally assumed in the literature that there is a semi-infinite source of Ni and that this assumption is violated in any oxidised sample where the amount of oxide is greater than about one tenth of the total quantity of Ni available. This was the case in most (if not all) of the samples since complete oxidation was of interest. It appears that the violation of this assumption does not affect the oxidation progressing through the sample towards complete oxidation. Indeed, the model presented later as well as the micrographs support this showing no appreciable difference in mass gain or quality of oxide – only of rate.

8.4 Parabolic to Modified Parabolic Transition and Mechanistic Study

Gathering more data on the switch from parabolic to sub-parabolic/modified parabolic around the 2 h mark was the objective of this tier of oxidation experiments. Specific goals included a more accurate estimate of the time when the switch in dominant mechanism occurs, and strategically oxidising more samples to improve the understanding of the microstructure as oxidation progresses (especially regarding pore evolution, advancing oxide front, and signs of strain relief mechanisms deleteriously affecting porosity). Ancillary to this is attempting to eliminate the cause of contamination while ensuring samples are adequately supported.

In order to establish an experimental plot of the oxidation, five time intervals were chosen that would give a good spread of data points (keeping in mind the parabolic nature of the curve, and the area of interest for this experiment – around 2 h). The samples were loaded and unloaded, and weighed before and after oxidation as described in section 8.2.

8.4.1 Results & Discussion

Table 8-1. summarises the results giving the mass gain of each sample, the mass fraction oxidised (mass of oxide gained divided by the maximum possible mass of oxygen gained based on sample's initial unoxidised mass) as well as the calculated oxide thickness, z. Figure 8-29. shows graphically calculated and experimental results. Errors estimated using linear approximation by partial differentiation where an equation was used or based purely on measurement equipment error otherwise.

Sample	**t (h)** ±0.01 h	**m_{Ni} (mg)** ±1 mg	**m_{Ni+NiO} (mg)** ±1 mg	**m_{gain} (mg)** ±2 mg	**Mass fraction oxidised** ±0.001	**z (µm)** ±0.23 µm
Batch A						
OT-A.10/06/11-125.1100-A.13	1.083 (65 min)	493.2	522.6	29.4	0.833	22.57
OT-A.10/06/11-125.1100-A.14	1.167 (70 min)	492.6	520.6	28.0	0.830	21.50
OT-A.10/06/11-125.1100-A.15	1.333 (80 min)	492.4	521.4	29.0	0.832	22.26
OT-A.10/06/11-125.1100-A.16	1.667 (100 min)	478.0	510.9	32.9	0.840	25.26
OT-A.10/06/11-125.1100-A.17	2.333 (140 min)	494.9	534.5	39.6	0.849	30.40
Batch E						
OT-A.29/07/11-125.1100-E.13	1.083 (65 min)	487.7	513.7	26.0	0.828	19.96
OT-A.29/07/11-125.1100-E.14	1.167 (70 min)	478.1	503.4	25.3	0.827	19.42
OT-A.29/07/11-125.1100-E.15	1.333 (80 min)	497.6	526.4	28.8	0.831	22.11
OT-A.29/07/11-125.1100-E.16	1.667 (100 min)	499.4	532.3	32.9	0.838	25.26
OT-A.29/07/11-125.1100-E.17	2.333 (140 min)	507.9	548.7	40.8	0.849	31.32

Table 8-3. Mass gain, mass fraction oxidised and oxide thickness of Ni tube oxidation at 1,100 °C. All samples from two exemplar batches of Tier 2 shown: A and E. The whole table can be found in Appendix C: Complete Oxidation Results Tables.

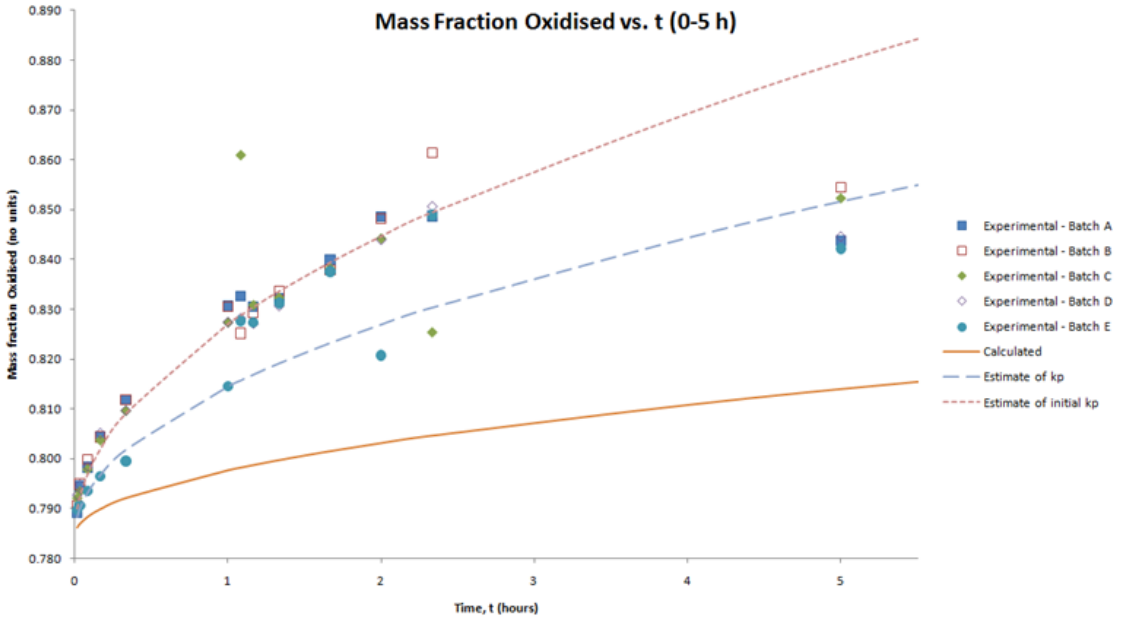

Figure 8-29. Plots of the mass fraction oxidised against time in the period 0 to 5 h. Oxidation temperature 1,100 °C (compensated for the most likely source of surface area error – tube length).

Figure 8-29. shows a sudden change at ~2 h 15 min. From this figure and Figure 8-4. alone it is difficult to ascertain whether the shift is from one parabola to another or from a parabolic law to a subparabolic one. What is certain however is that excepting large errors and ignoring obvious outliers or bias induced by the sample position in the furnace (see the discussion immediately following Figure 8-4.) there is a shift in the dominant mechanism, most likely from one dominated by cation transport to one dominated by vapour phase transport as explained previously. For Batches A and B change is between 2 h 15 min and 5 h; for Batches C and D change is between 2 h and 2 h 15 min; for batch E change is unclear because almost immediately results deviate from the rest. Possibly batch E is controlled from early oxidation times by the lower oxidation rate constant. The fact that the time the change from initial k_p to the subsequent (nominally also parabolic) rate occurs at is split evenly between batches A and B on one hand and C and D on the other is notable. In order to draw further conclusions sample position must be considered once more.

The reason behind the incongruent behaviour of the samples from Batch E is unclear. There is no underlying bias in the position in the furnace, and as the batches are arbitrary groupings, the particular segment of as-delivered tube cannot be the root cause for the divergent behaviour. It is plausible, although difficult to assess, that these samples were exposed to a greater temperature drop when the furnace door was opened than other samples. As temperature has a very strong effect on oxidation rate a difference of just 10 °C could actually account for the difference observed. A common rule of thumb is that the oxidation rate for Ni (and other fast-growing oxides) doubles every 30 °C increase in oxidation temperature.

As with previous oxidation experiments, the full sample positioning and schedule details for this tier was tabulated for complete sample traceability (Appendix E: Oxidation Sample Furnace Positions and Schedule). As with the Tier 1 (Process Optimization) oxidation experiments samples at the front of the furnace were under somewhat different conditions that those at the back because they were nearer the end of the hot zone and were more exposed to sudden cooling while the door of the furnace was open to extract samples. As before, and since there is no clear evidence otherwise, it is assumed that there is no variation side-to-side within the furnace, only front-to-rear.

With the exception of Batch E there appears to be no bias in the results. A few samples do display behaviour at odds with the trend of the rest for a given time period (in particular from Batch C). However, there is no evidence as to a cause so they are most likely simply due to stochastic error or defects in the as-delivered material (for instance large voids or unusually high strain). As with the process optimization experiments there is some bias in one sense: samples were not oxidised in the same exact position within the furnace – so the nominal conditions were not in fact applied to all samples. However, these differences are slight as all samples fit within the hot zone with a temperature variation of 1–2 °C. Additionally, there was no batch to batch bias (only sample to sample for those samples oxidised at the front compared to those at the back).

The results obtained are consistent with tier 1. Based on parabolic curve fitting the tier 2 data fits the estimated k_p from the tier 1 data. Both sets of data are therefore combined in any subsequent analysis.

The following micrographs (Figure 8-30. to Figure 8-34.) show milled cross-sections through two samples and their surface morphologies; one sample either side of the transition time identified. They are both, therefore, intermediate stages of oxidation (approximately 85%). Images were created by scanning electron microscope (SEM), and cross-sections were trenches created by focused ion beam (FIB) milling. A Au-Pd coating was used to enable the high resolution imaging. The grains of the coating are visible in some images (appearing somewhat as scales).

The micrographs were used to look for microstructural changes around the approximate time of transition in oxidation rate (from k_{p1} to k_{p2}). Some changes are expected as the transition is expected to be from cation transport dominated to vapour phase transport dominated regimes.

To facilitate comparison the micrographs are presented in pairs with the left hand images pertaining to sample B.16 and the right hand ones to B.17. Images are also ordered by apparent magnification: from lower magnifications (top) to higher ones (bottom). A special note of sample B.17 warrants mention. For this sample a second, deeper, trench was also milled (to roughly double the depth of other milled trenches).

This was done to check whether the trenches created in this and other samples were indeed representative of the cross-sectional microstructure or were influenced by near-surface effects. The micrographs taken are not shown but demonstrate quite clearly that the procedure for creating and imaging the cross-section is indeed representative of the sample. The micrographs presented below for sample B.16 are all of the deeper trench as it exhibited less waterfalling and sample charging, resulting in an overall enhancement of image quality.

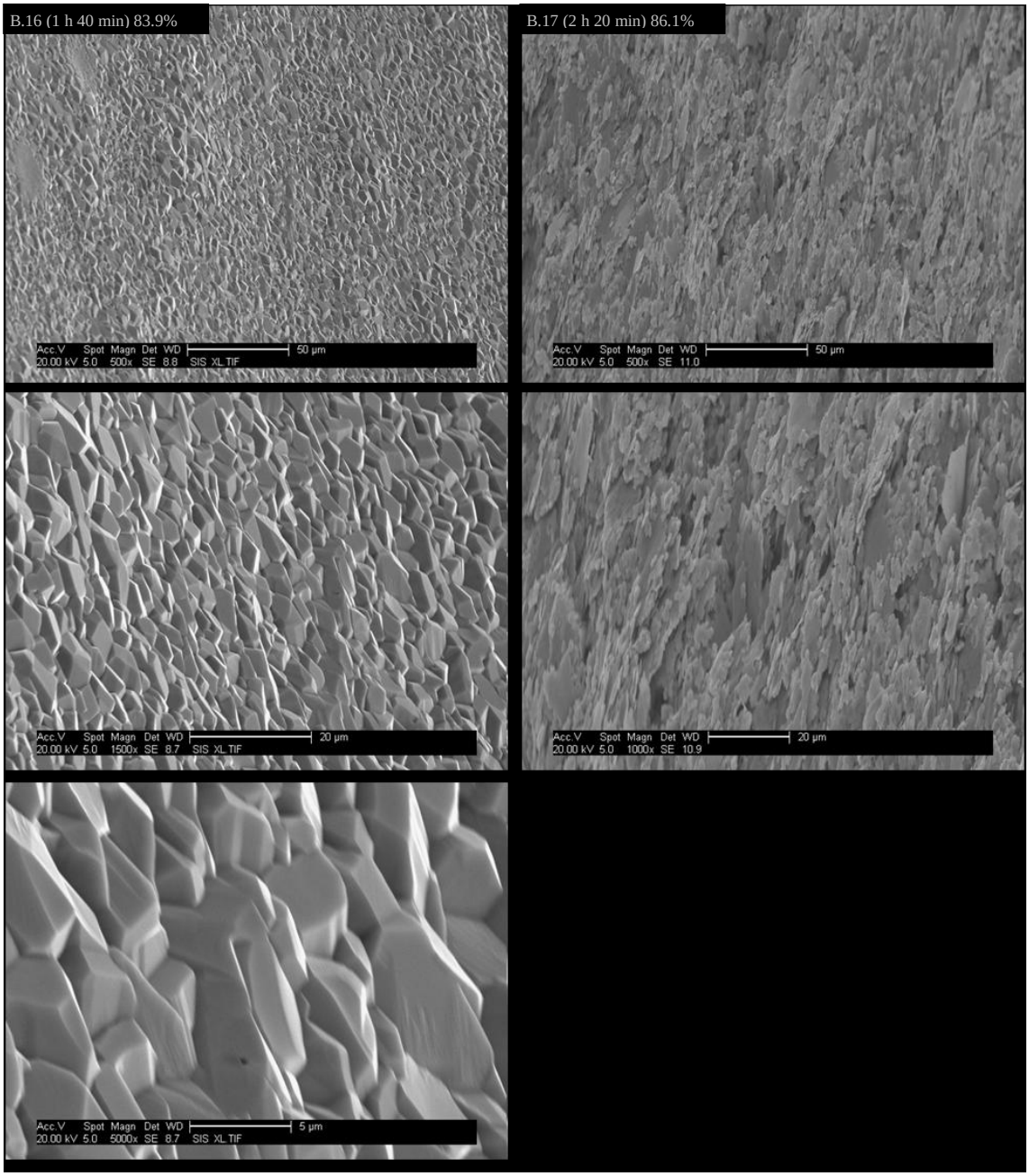

Figure 8-30. SEM micrographs showing the surface morphology of the inner (concave) surface of samples bracketing the time of transition from k_{p1} to k_{p2}. Images are ordered from top to bottom in order of increasing apparent magnification; left column is sample OT-A.10/06/11-125.1100-B.16 (1 h 40 min 83.9 wt.% oxidised), right column is sample OT-A.10/06/11-125.1100-B.17 (2 h 20 min 86.1 wt.% oxidised).

The inner surface of the tube appears to be in a high stress state with grains becoming deformed from their usual sharp crystalline appearance once the dominant mechanism becomes vapour phase transport. The micrographs and oxidation mechanism suggest an additional possible mechanism: I hypothesise that at longer oxidation times, as cation transport of nickel cations to the surface slows, so does strain relief by diffusion controlled plastic deformation. Furthermore, as vacancies coalesce into larger pores grain mobility (especially rotation to relieve stress) becomes increasingly restricted with the vacancies acting as, relatively weak, anchors akin to large precipitates.

There were no visible signs of significant surface cracks. Therefore the tube retains its structural integrity (and suitability for continued processing into anodes) despite being in a highly stressed state. Larger surface channels and pores are no longer visible on the inner surface.

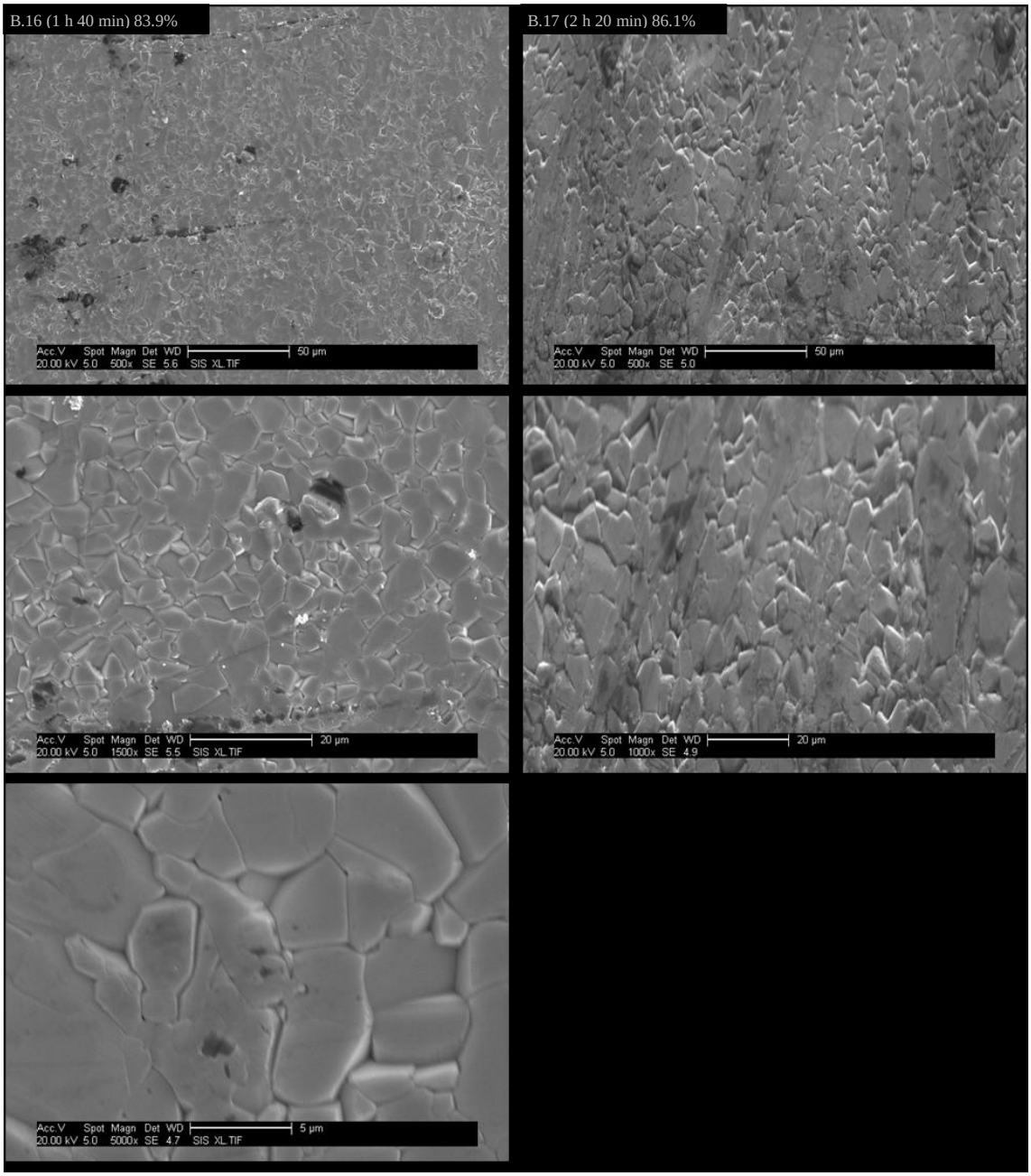

Figure 8-31. SEM micrographs showing the surface morphology of the outer (convex) surface of samples bracketing the time of transition from k_{p1} to k_{p2}. Images are ordered from top to bottom in order of increasing apparent magnification; left column is sample OT-A.10/06/11-125.1100-B.16 (1 h 40 min 83.9 wt.% oxidised), right column is sample OT-A.10/06/11-125.1100-B.17 (2 h 20 min 86.1 wt.% oxidised).

The convex (outer) surface has the expected morphology. Sharp-edged highly crystalline grains, becoming less rounded with increasing oxidation time. In both cases some surface fissuring remains visible, though this closes at longer oxidation times. The overall surface morphology is slightly more open for B.17 than B.16. This is likely due to a combination of the tensile strain on the convex side of the neutral plane (the stress plane bisecting the tube, parallel to both surfaces, at which the strain – and therefore stress – is zero) and the transition to a vapour phase dominated mechanism in which

there is greatly reduced movement of cations (movement of material) and hence reduced diffusion type creep to accommodate growth-induced strain.

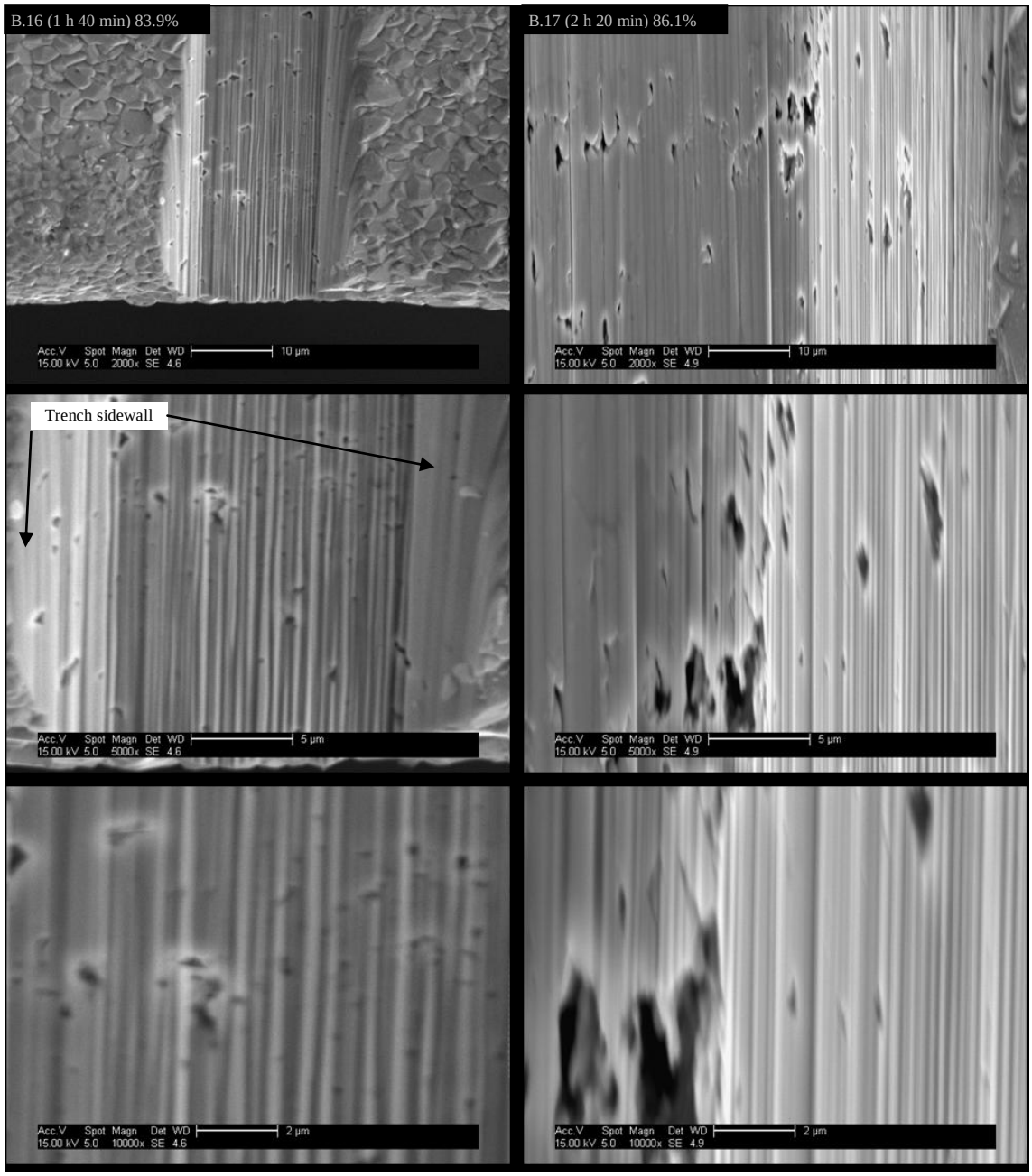

Figure 8-32. SEM micrographs* showing pores near the inside edge of samples bracketing the time of transition from k_{p1} to k_{p2}. Images are ordered from top to bottom in order of increasing apparent magnification; left column is sample OT-A.10/06/11-125.1100-B.16 (1 h 40 min 83.9 wt.% oxidised), right column is sample OT-A.10/06/11-125.1100-B.17 (2 h 20 min 86.1 wt.% oxidised).

The evolution of the microstructure through the sections shown in Figure 8-32., Figure 8-33. and Figure 8-34. is consistent with previous observations. Of particular note is the reduction in the number density of visible pores but the coalescence of vacancies and small pores into larger ones, more often at triple points.

The difficulty in producing reliable spatially resolved proportions of nickel and oxygen by EDS means it proved not possible to observe the vapour phase transport mechanism in progress. This would have been achieved by sampling the material composition at several points near a large pore – one group nearer the sample surface and the other at the area farther from the sample surface. Points near the edge towards the nearest sample surface should exhibit an increasing proportion of nickel with respect to oxygen. Those farther from the sample surface should show a decreasing proportion of nickel with respect to oxygen (as this becomes oxidised). Given the 2–3 μm diameter teardrop volume sampled by the x-rays in EDS analysis a very large pore would have had to be located and the detector would perforce be required to have accurate, calibrated, oxygen detection beyond what was available.

An alternative, also sadly not possible for this project, is to oxidise with a gas containing some known proportion of an oxygen isotope and use isotope analysis to track the movement of oxygen through the samples (oxidised for different durations). Refer to the further work section 17.1 for details.

There is microstructural evidence for the change in dominant mechanism, however. The majority of pores remain at triple points (stable positions) and the pore density does not increase noticeably from 2 h 20 min (B.17) to 16 h (A.10) and 20 h (E.11). Some small pores do appear with oxidation after the transition from k_{p1} to k_{p2}, most likely created by the movement of Ni cations from the innermost, as yet unoxidised, portions of the sample. Recall that and these cations must diffuse to a surface with available oxygen (large pores: vapour phase transport or one of the external surfaces: surface oxidation) which may require them to move a relatively long distance.

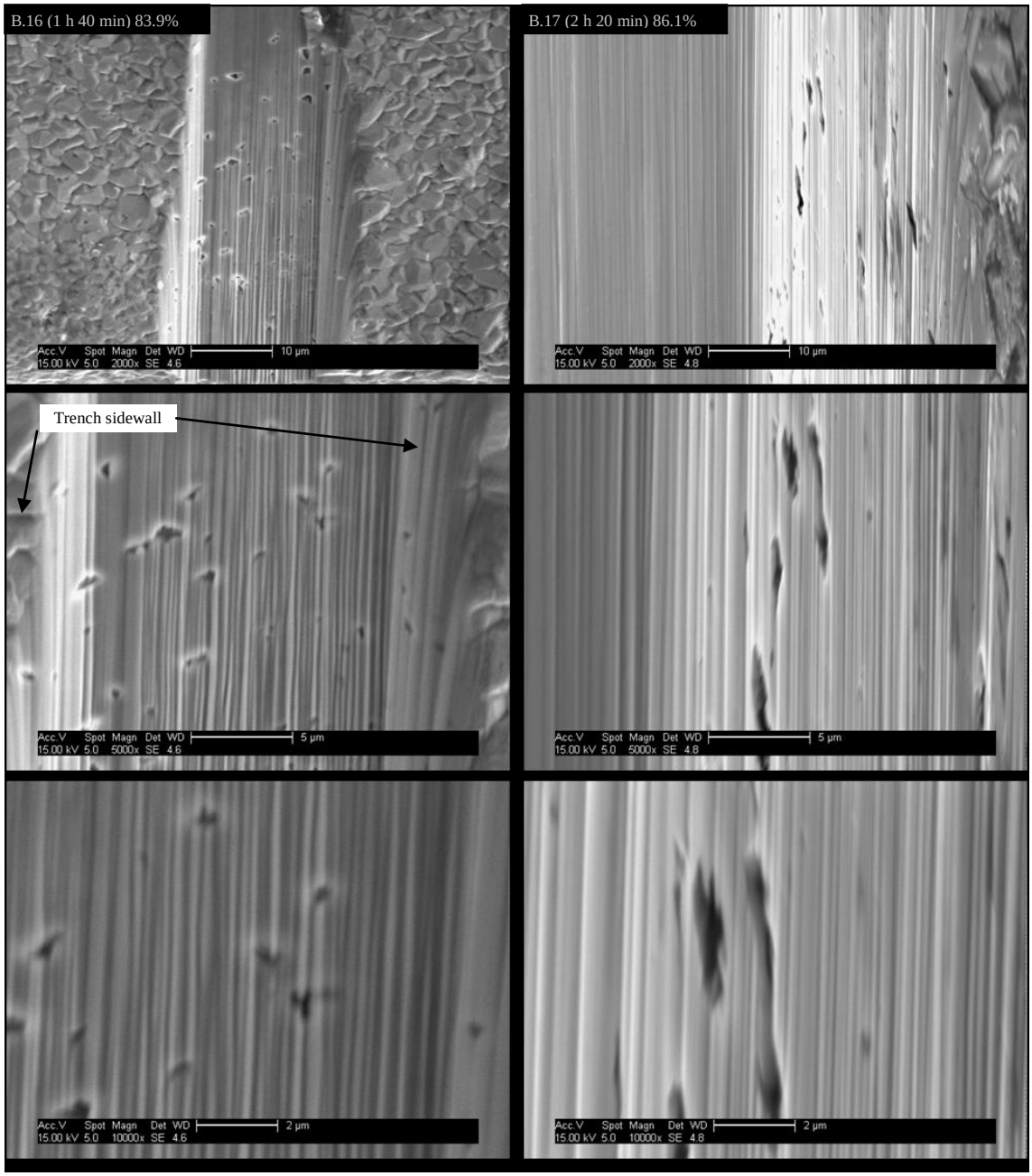

Figure 8-33. SEM micrographs* showing pores around the middle of samples bracketing the time of transition from k_{p1} to k_{p2}. Images are ordered from top to bottom in order of increasing apparent magnification; left column is sample OT-A.10/06/11-125.1100-B.16 (1 h 40 min 83.9 wt.% oxidised), right column is sample OT-A.10/06/11-125.1100-B.17 (2 h 20 min 86.1 wt.% oxidised).

The lack of visible pores in the main face of the section of B.17 (Figure 8-33.) above is unexpected. Yet the expected mix of pore sizes and density was to be found on the side walls of the trench. It is these that are shown, as can be determined from the first image for B.17 in the sequence. The reason for this not known with any certainty, though waterfalling hiding pores is unlikely, and it may be a coincidence. If this is the case, and random volumes of the sample are either not oxidising or undergoing some form of microstructural change or effect that eliminates pores, it is worth further investigation.

Given that this is the only appearance for this unexplainable exception I am foregoing further investigation and treating it as an anomalous occurrence.

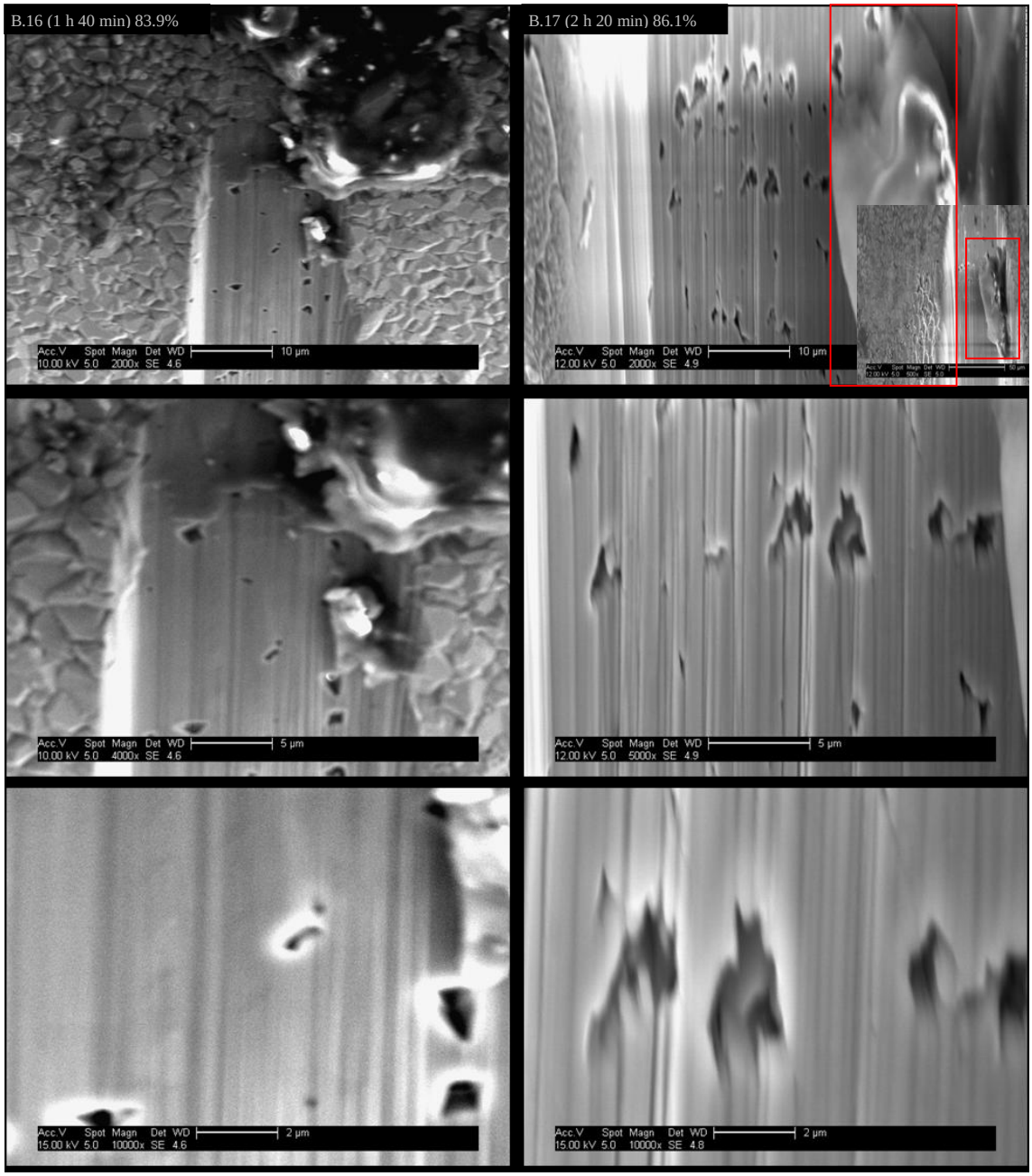

Figure 8-34. SEM micrographs* showing pores near the outside edge of samples, bracketing the time of transition from k_{p1} to k_{p2}. Images are ordered from top to bottom in order of increasing magnification; left column is sample OT-A.10/06/11-125.1100-B.16 (1 h 40 min 83.9 wt.% oxidised), right column is sample OT-A.10/06/11-125.1100-B.17 (2 h 20 min 86.1 wt.% oxidised). Highlighted areas and insert show debris (Al tape) in B.17 trench from sample preparation for SEM.

The micrographs near the outer surface of sample B.16 charged up noticeably more than other areas. The reason is that this area was imaged last during a relatively long SEM session. Highly non-conductive samples (such as this) may eventually accumulate

significant charge during a long session. Much of this can be successfully conducted away as normal for a well prepared sample, however, at sharp edges were any charge is concentrated image quality will be affected. There may also be a somewhat reduced overall quality also [from discussions with Christine Kimpton and Xian Wei Liu, characterization suite analytical officers]. In light of this, rather than the image at 5000× magnification one at 4000× was used, as shown in figure above. The pores towards the outer surface are larger, although the pore number density is roughly the same.

EDS results proved unreliable for quantitative oxygen detection; far less oxygen than possible was detected (as little as 0.7 at.%, with a mean of approximately 10 at.%). The EDS results were not consistent with the mass of oxygen gained. While I cannot say so with certainty I think the discrepancy is due to a very large number of atomic defects and pores too small for the SEM to resolve. It is likely that voids in the sampled volume of EDS (a teardrop shape into the material, with the largest diameter of the order of 2–3 μm) are interfering with electron scattering. As a result, EDS will accurately detect the presence of Ni, O, Mn (and other impurity elements in the nickel) but quantification will be unreliable. It is plausible that only oxygen is affected this way because compared to the other elements of interest (Ni and the impurity elements) oxygen has a much lower atomic mass. Finally, according to the analytical suite staff, oxygen is notoriously tricky to quantify accurately. Otherwise results conform to those of the tier 1 experiments.

After observing that first, the actual point (chronologically speaking) during oxidation at which the switch from the first rate of oxidation (the first parabola) to the second varies slightly, and second, by plotting each batch of mass gain data individually it appears that the process plateaus briefly between parabolas. The significance of this incubation period is currently unknown. An example (Figure 8-35.) is shown below, comparing Batch D (as tabulated above) with Batch B.

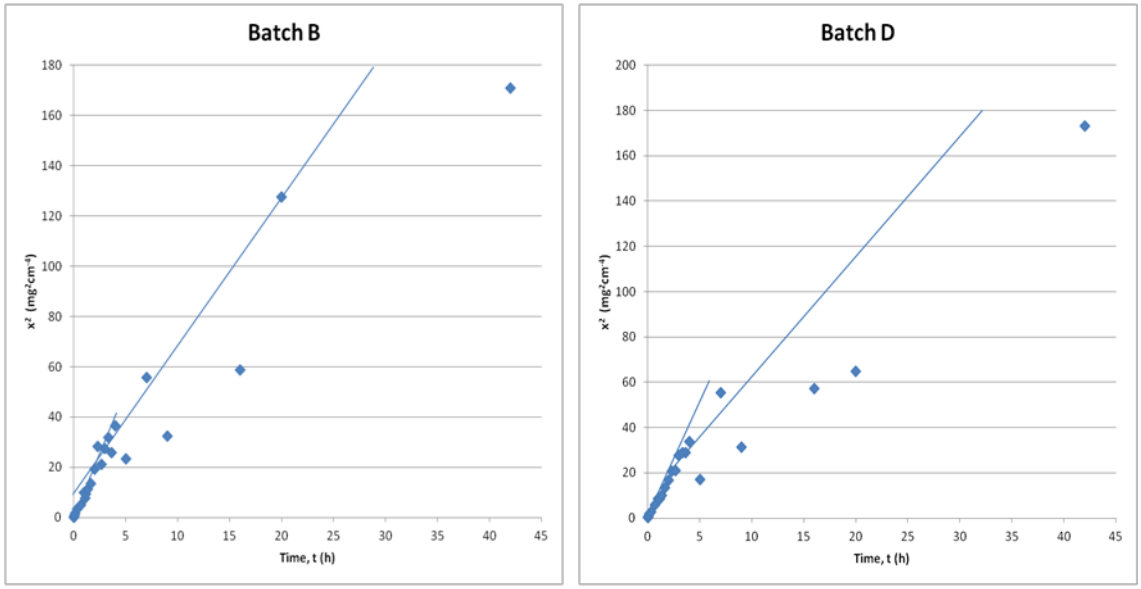

Figure 8-35. Plots of x^2 [i.e. (mass gain / surface area)^2] against time for oxidation at 1,100 °C of Batch B and Batch D. Note: the plots shown include all samples oxidised as grouped into these batches (Tier 1, Tier 2 and Tier 4).

For Batch B the transition time is approximately 2 h 15 min, while for Batch D it is nearer to 1 h. The batches are semi-arbitrary as explained previously, making associating any changes in transition time with batch futile. Consistently, however, batches with a higher initial oxidation rate (k_{p1}) exhibit an earlier transition, while a lower initial oxidation rate is associated with a later transition. The opposite is true for the second oxidation rate (k_{p2}): a higher k_{p2} is associated with later transition times. The association of a higher initial rate with an earlier transition to the second rate could be explained by these samples more rapidly reaching a critical state (e.g. oxide thickness or strain energy) than others.

Unfortunately, even with the added samples described below, data resolution was insufficient to confirm or refute the presence of a brief plateau in transitioning from cation dominated (k_{p1}) to vapour phase transport dominated oxidation (k_{p2}).

8.5 Improving Data Resolution or Refining Transition Time

The addition of a third set of oxidation experiments at 1,100 °C (tier 4) was intended to reduce ambiguity in and around oxidation times near the transition from the first to second stage of oxidation or where previous results seemed to diverge from the majority for a given oxidation time. The reasons were twofold: first, more data points means a smoother plot in which outliers are more obvious, step changes highlighted and the overall process clearer; second, the oxidation times chosen are designed to help improve 'resolution' clarifying more precise times for the change in mechanism and whether this is indeed as a step change as it appears to be.

Chronologically this was the fourth and final set of oxidation experiments. The third tier (see 8.7 below) was to answer the question whether accelerating the process by means of an increased temperature would result in deleterious microsturcture changes (particularly those resulting in greatly decreased porosity and large cracks or delamination reducing structural integrity of the tubes).

The objective was to improve the resolution of the data, especially for determining the transition from k_{p1} to k_{p2} and for fitting purposes. This was achieved by closely studying the data plotted thus far and indentifying potentially useful time intervals between existing points, as always keeping in mind the parabolic nature of the curve.

8.5.1 Results & Discussion

The results are summarised in Table 8-4. giving the mass gain of each sample, the mass fraction oxidised (mass of oxide gained divided by the maximum possible mass of oxygen gained based on sample's initial unoxidised mass) as well as the calculated oxide thickness, z. Figure 8-36. shows a plot of calculated and experimental results, including the first two sets of experiments presented previously. Errors estimated using linear approximation by partial differentiation where an equation was used or based purely on measurement equipment error otherwise.

Sample	t (h) ±0.01 h	m_{Ni} (mg) ±1 mg	m_{Ni+NiO} (mg) ±1 mg	m_{gain} (mg) ±2 mg	Mass fraction oxidised ±0.001	z (µm) ±0.23 µm
Batch A						
OT-A.15/11/12-125.1100-A.18	0.667 (40 min)	499.5	519.4	19.9	0.817	15.28
OT-A.16/11/12-125.1100-A.19	2.667 (160 min)	494.4	535.8	41.4	0.852	31.78
OT-A.27/11/12-125.1100-A.20	3.000	472.3	517.0	44.7	0.860	34.32
OT-A.05/02/13-125.1100-A.21	3.333 (200 min)	496.9	547.7	50.8	0.866	39.00
OT-A.07/02/13-125.1100-A.22	4.000	487.4	539.5	52.1	0.870	40.00
OT-A.22/02/13-125.1100-A.23	3.667 (220 min)	492.1	540.9	48.8	0.864	37.46
OT-A.27/02/13-125.1100-A.24	7.000	494.9	558.4	63.5	0.887	48.75
Batch E						
OT-A.15/11/12-125.1100-E.18	0.667 (40 min)	492.5	513.4	20.9	0.819	16.04
OT-A.16/11/12-125.1100-E.19	2.667 (160 min)	484.6	526.5	41.9	0.854	32.17
OT-A.27/11/12-125.1100-E.20	3.000	478.7	523.8	45.1	0.860	34.62
OT-A.05/02/13-125.1100-E.21	3.333 (200 min)	498.2	546.2	48.0	0.861	36.85
OT-A.07/02/13-125.1100-E.22	4.000	483.1	534.6	51.5	0.870	39.54
OT-A.22/02/13-125.1100-E.23	3.667 (220 min)	496.0	544.3	48.3	0.862	37.08
OT-A.27/02/13-125.1100-E.24	7.000	493.4	556.0	62.6	0.885	48.06

Table 8-4. Mass gain, mass fraction oxidized and oxide thickness of Ni tube oxidation at 1,100 °C. All samples from two exemplar batches of Tier 4 shown: A and E. The whole table can be found in Appendix C: Complete Oxidation Results Tables.

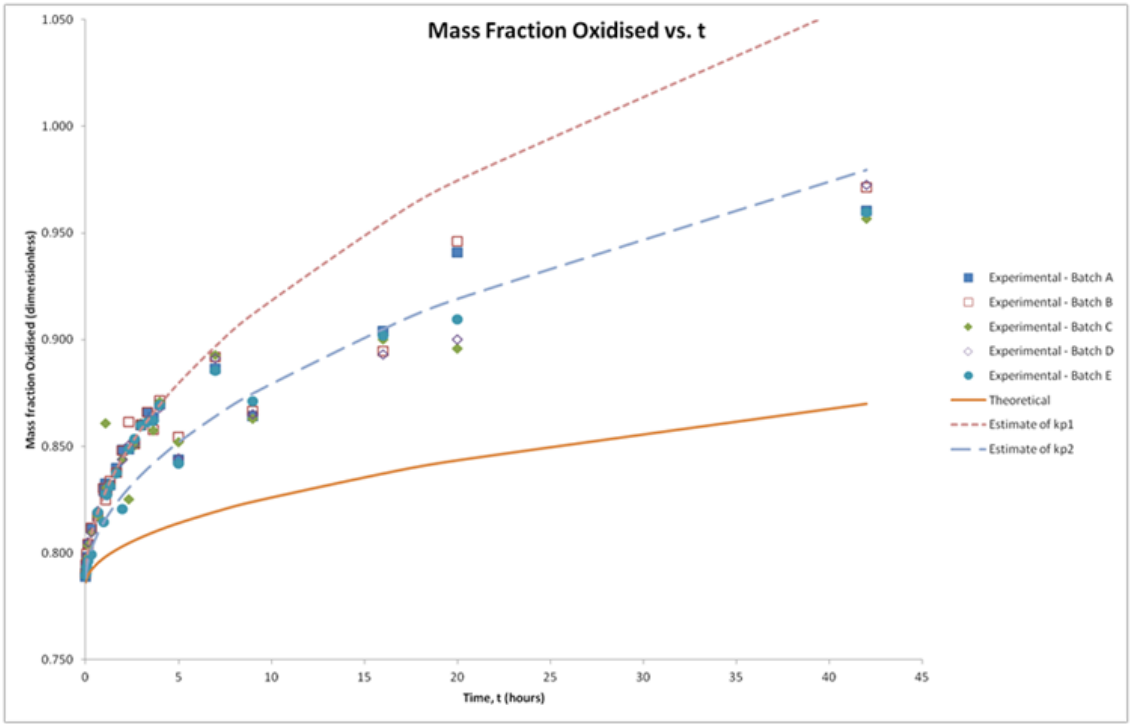

Figure 8-36. Plots of the mass fraction oxidised – ratio of the measured mass of the oxidised sample to its calculated mass when fully oxidised – against time for all results up to and including Tier 4. Oxidation temperature 1,100 °C (compensated for the most likely source of surface area error – tube length).

The graph below plots x^2 for all samples (all three preceding sets of data) combined onto one graph for each (Figure 8-37.). Compare this to Figure 8-6. (square of oxidation rate for first set of data), and Figure 8-35. (square of oxidation rate for selected batches highlighting the differing transition times).

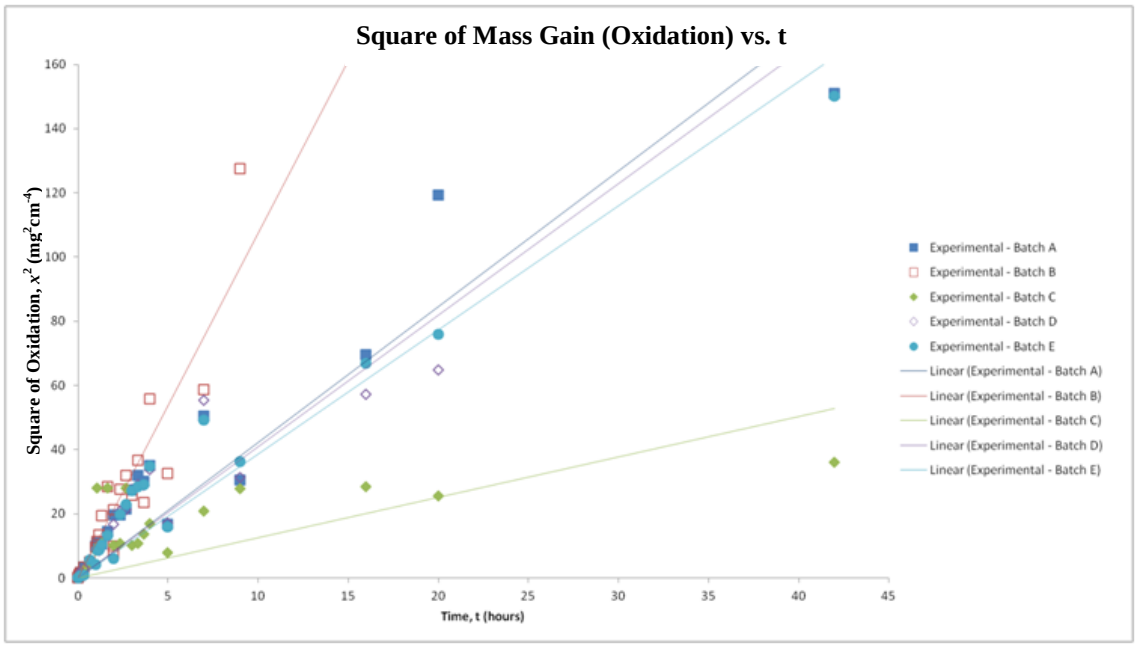

Figure 8-37. Plots of x^2 [i.e. (mass gain / surface area)^2] against time for oxidation at 1,100 °C. All results shown, up to and including Tier 4. Deviations from parabolic appear as deviations from a straight line.

The approximate linear fits utilise all the data points for each batch. Strictly speaking each batch should have two linear fits; one for each parabolic rate (k_p). However, for the purposes of determining whether the data may be considered parabolic it was deemed acceptable to consider each batch as one data set for linear fitting since both rates were expected to be parabolic (and indeed prior linear fitting with fewer data points was consistent with two parabolas). This can be explained schematically (Figure 8-38.).

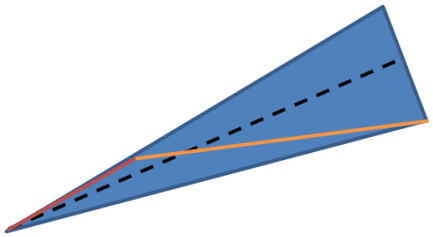

The red line represents the initial rate, the orange the second rate. The dotted line represents linear fit to the whole data set. The filled blue triangle illustrates the effective difference between treating each as separate plots of the square of the area specific mass gain and a linear fit of the same. The density of data points is assumed to be greater initially (as was the case with the actual data).

Figure 8-38. Schematic representation of linear fitting whole data set (as opposed to one linear fit per parabolic rate constant). Relative proportions are exaggerated for clarity.

In plotting the entire data set this way it became apparent that Batch B and Batch C contain a larger number of outliers and are therefore, overall, somewhat less representative. The other three batches, arbitrary as they may be, display tightly grouped trends. In turn these trends closely fit the data. *Ergo*, conclusions based on Batch A, Batch D and Batch E are built on a solid foundation of representative, reproducible experiments.

Unfortunately, however, the addition of further points (7 per batch in the period up to 5 h) does not serve to clarify the transition time from the initial parabolic rate constant to the next. This is due to an unexpectedly high number of outliers and many of the added points having greater scatter than for previous experiments (see Figure 8-39.). Subsequently it was noticed that the furnace had been refurbished, replacing the heating elements and the electronic controller resulting in an altered hot zone. Otherwise results conform to previous observations.

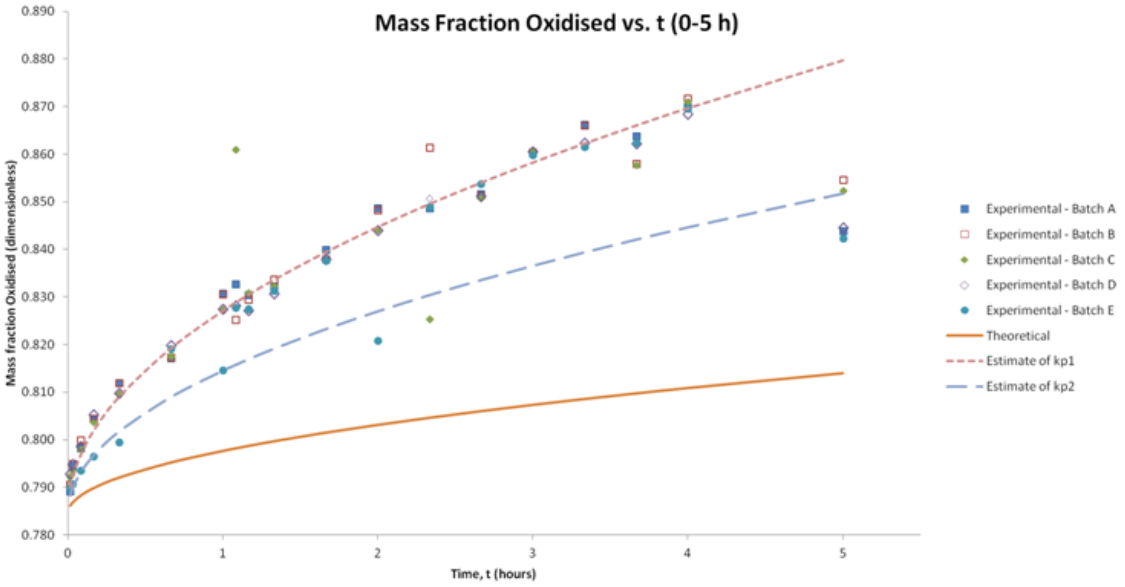

Figure 8-39. Plots of the mass fraction oxidised against time in the period 0 to 5 h for all results up to and including Tier 4. Oxidation temperature 1,100 °C (compensated for the most likely source of surface area error – tube length).

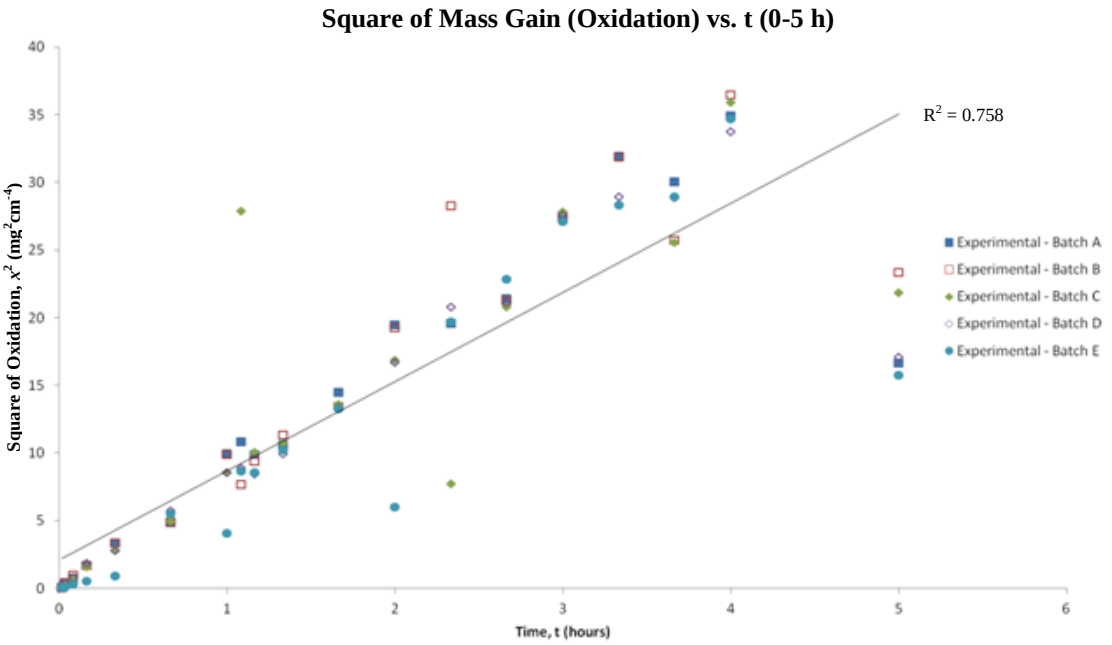

Figure 8-40. Plots of x^2 [i.e. (mass gain / surface area)^2] against time in the period 0 to 5 h for oxidation at 1,100 °C. All results shown, up to and including Tier 4. Deviations from parabolic appear as deviations from a straight line.

The thicknesses for the early stage oxide prior to the transition in mechanism (<2 h 15 min; <0.84 MFO) is close to the work of Atkins *et al.* (1982). The best degree of fit obtained (excluding the outliers from the Tier 4 data) was R^2=0.9487 to a parabolic fit. Fitting to a general power law resulted in the same degree of fit and an $x^{2.03}$ law. This shows that early stage oxidation at 1,100 °C follows parabolic kinetics for MFO up to 0.84 and oxide thickness of about 40 µm. So in the early stage oxidation is controlled by lattice diffusion transport. After the transition the mechanism remains parabolic as shown with no significant difference when modelled with a general power law (R^2=0.95 to parabolic fit, R^2=0.97 for sub-parabolic) again excluding the Tier 4 data outliers.

8.6 Modified Wagnerian Model for Through Thickness Oxidation

From experimental work it is clear that there is more than one process, the effects of which are observed in the varying k_p as shown by the plots for mass gain against time of oxidation. Two broad regions have been identified, each having their own k_p – named here k_{p_1} (initial) and k_{p_2}. The Wagner model has been modified to reflect this as will be explained below.

Chronologically the first iteration of the model was immediately following Process Optimization (section 8.3). However, this was in unmodified form and sought only to derive an average k_p and compare this to the literature and my own estimates from previous work in my MSc thesis [Camilleri 2009]. It was during this analysis that I

began to suspect a second rate controlling mechanism as discussed in the noted section. The second iteration was created after the mechanistic study (section 8.4), entirely by design. This, in the modified form has been discussed here, and then further refined with the data gathered explicitly to improve resolution (section 0). The model is presented here only in its final form since those few notable remarks or points for discussion emerging from earlier iterations could be readily added to the experimental discussions. The modified Wagnerian Model and the discussion of its creation and verification rests in this section, an important addendum to all of the oxidation work detailed preceding it.

8.6.1 Carl Wagner's Original Model

Carl Wagner first derived the theory for the high temperature oxidation of metal based on the availability and mobility of the rate-controlling ionic conduction. For some of the transition metal oxides (including NiO) the relation between point defects in the oxide and oxidation kinetics has been studied extensively [Haugsrud 2003]. Wagner thoroughly analysed and formalised the theory of internal oxidation in 1959. Here internal oxidation is taken to mean that a diffusing species from the surface reacts with a less-noble solute in the alloy to form discrete particles [Douglass 1995]. The diffusing species is usually oxygen, nitrogen, hydrogen, sulphur or carbon. By measuring the oxygen pressure dependence of grain boundary diffusion of oxygen in nickel it has been proposed that transport occurs according to a vacancy mechanism in which singly charged vacancies predominate [Haugsrud 2003]. This is contradicted by molecular dynamic simulations of Ni ions along grain boundaries, which indicate that doubly charged Ni vacancies are responsible for cation grain boundary diffusion [Haugsrud 2003]. The measurement of creep rates in NiO supports the conclusion that oxygen transport requires a high activation energy, but suggests that oxygen diffusion occurs via vacancies rather than defects (supporting evidence of vapour phase transport) [Haugsrud 2003].

The diffusion rate of oxygen along grain boundaries is much slower than Ni grain boundary diffusion; with an activation energy of 240 kJ mol^{-1} this is comparable to the diffusivity of Ni in the NiO lattice [Haugsrud 2003]. Lattice diffusion is an order of magnitude slower than diffusion along dislocations; the coefficient of diffusion of Ni in NiO $D_{Ni\text{-}NiO} = 128\times10^{-13}$ cm^2 s^{-1} at 1,100 °C (other temperatures are given also; it roughly trebles for every +100 °C) [Rosa 1982]. The grain boundary diffusion coefficient is twice that of diffusion across grain boundaries; and therefore 20 times the lattice diffusion coefficient [Li *et al.* 1997]. Exact coefficients are not quoted here because these are highly dependent upon the operating temperature and the oxygen partial pressure.

Wagner made a number of assumptions in his work that are valid for the growth of thin scales but may not for through thickness oxidation. Those assumptions need revisiting in order to explain observed discrepancies from his theory seen in this work and others.

These include [Douglass 1995]: stoichiometric oxide precipitated at the reaction front, the formation of low-solubility product oxides caused virtually all of the reactive solute to precipitate leaving a matrix of "pure" solvent, precipitation was complete at the reaction front and no further precipitation occurred within the internal-oxidation zone subsequently, uniform planar fronts existed, a constant mole fraction of solute oxide existed across the reaction zone, and thickening of the front was controlled primarily by oxygen diffusion in the substrate.

Contrary to Wagner's assumption, spherical particles of oxide are the exception rather than the rule [Douglass 1995]. Furthermore, according to the cited source there seems to be a limitless variation in oxide morphologies with each alloy having its own virtually unique morphology. I would extend this even further by stating that based on the behaviour of NiO it is probable that different morphologies exist for oxides made under different conditions of initial strain state, temperature and perhaps even oxidant concentration.

Since the non-stoichiometry is low aliovalent impurities that dissolve in NiO change the native defect concentration. According to point defect chemistry, ions with a higher valence than Ni(II) increase the concentration of metal vacancies and, in turn, the oxidation rate, whereas ions with a lower valence than Ni(II) should decrease the oxidation rate [Haugsrud 2003]. There are discrepancies in the reported rate constants (and the derived physicochemical properties) of NiO at oxidation temperatures below 1,000 °C [Haugsrud 2003].

Prior to moving on to the model itself and its modification and verification it is worthwhile reviewing in some detail the nature of the parabolic rate constant, k_p. The parabolic rate constant is proportional to the oxygen partial pressure, somewhere in the range $k_p \propto p_{O_2}^{1/6}$ (at 1,000 °C) to $k_p \propto p_{O_2}^{1/4}$ (at 1,300 °C) [Haugsrud 2003]. The high temperature (1,000 °C – 1,300 °C) k_p varies in a linear fashion with oxygen partial pressure, when plotted logarithmically against the partial pressure of oxygen. At 700 °C the oxidation rate is observed to be independent of oxygen partial pressure. [Haugsrud 2003; see Fig. 2. of this paper]. Young (2016) is in agreement with this range of oxygen partial pressure.

Assuming that the diffusion proceeds through native Ni vacancies, *verbatim* "the dependence indicates that the relative ratio between doubly and singly charged vacancies decreases with increasing temperature" [Haugsrud 2003]. This contradicts measurements taken using electrical conductivity where the number of doubly charged vacancies increases with increasing temperature [Haugsrud 2003]. Haugsrud (2003) suggests an alternative interpretation of the $p_{O^{2-}}$ dependence is to assume that doping affects the oxidation at lower temperatures and that its influence gradually disappears as the native defect concentration increases with increasing temperature. Furthermore, the

overall oxidation rate may no longer be affected by grain boundary transport at 1,000–1,100 °C, where the point defect structure in the grain boundaries dominates rather than in the oxide lattice – corresponding to the pressure dependence expected on basis of simulations of the grain boundary defect structure [Haugsrud 2003]. However, the fact that the oxidation rate is essentially independent of oxygen pressure at 700 °C may indicate the effect of doping.

The temperature dependence of k_p shows three different regimes: At lower (<800 °C) and higher temperatures (>1,000 °C) the oxidation rate is of Arrhenius-type behaviour with high activation energy [Haugsrud 2003]. The values of the activation energies reflect transport along grain boundaries and/or dislocations at the lower temperature, and transport in the oxide lattice at the higher temperatures. There is an intermediate regime between the two linear ends where the oxidation rate shows weak temperature dependence [Haugsrud 2003]. One combination of processes that is proposed [Haugsrud 2003] to explain this is: lattice diffusion — grain boundary diffusion — grain growth. Grain growth is slow at the lower temperatures and the oxidation rate would essentially be parabolic but governed by transport at the grain boundaries. At higher temperatures the rate of grain growth increases. At the higher temperatures, lattice diffusion dominates the process, and a 'normal' Arrhenius behaviour occurs even if grain growth is rapid. Another possible scenario is that the influence of inward short circuit oxygen transport decreases faster than the diffusional processes (cation transport through the lattice, vapour phase transport, grain boundary cation or oxygen diffusion) contributing to the overall oxidation.

The oxidation rate is strongly dependent on the surface morphology and texture of Ni. At 600 °C the initial oxidation rate varies by as much as 4 orders of magnitude for different sample pre-treatments [Haugsrud 2003]. This is reflected in the results presented in this chapter where the high strain of the as-delivered tubes due to the cold extrusion manufacturing process is anticipated to modify early oxidation behaviour. The far higher than expected k_p is, in this instance, beneficial rather than detrimental since it ensures a more rapid process when using this technique to create porous structures than would be the case for annealed samples. *Verbatim* [Haugsrud 2003] "During the initial period of the oxidation when a continuous layer has been formed, the ratio between the rate of growth and nucleation of new oxide grains are important. As long as the scale is very thin, the grain boundary area may actually not be important to the overall oxidation rate, even though the grain boundary diffusivity is much higher than bulk diffusion. However, once a quasi steady state has developed, the grain size of the scale becomes important. Measurements of the rate of oxygen dissociation during the initial oxidation show that after the first 5-10 nm of oxide scale has formed, the rate of oxygen dissociation is faster than the instantaneous consumption of oxygen by the oxidation reaction. This means that after the first 150 s of the oxidation, the Wagnerian parabolic conditions are satisfied with respect to equilibrium at the oxide-gas interface."

The oxide growth rate is given by [Schütze 1997, Huntz *et al.* 2006, Young 2016]:

$$\frac{dx}{dt} = \frac{k_p}{x} \qquad (8.5)$$

Upon integration equation (8.5) becomes:

$$x^2 = 2k_p t + a \qquad (8.6)$$

Where:

$x = \left(\frac{m}{A}\right)$ [mg cm^{-2}]
$m =$ mass of oxygen [mg]
$A =$ area of sample exposed to oxygen [cm^2]
$k_p' = \frac{k_p}{2}$ [mg^2 cm^{-4} h^{-1}]
$k_p =$ average parabolic rate constant of oxidation (literature) [mg^2 cm^{-4} h^{-1}]
$t =$ time [h]
$a =$ constant of integration [no units]

Note: It is customary to give the units in this (non-SI form). This is done here to facilitate comparison with the majority of sources dealing with nickel oxidation. In publication what is labelled for convenience as k_p is usually a rate constant measured experimentally from a plot of x^2 against t, and is therefore not truly k_p, but k_p' (i.e. $\frac{k_p}{2}$).

Equation (8.6) is known as the Parabolic Oxidation Law, and applies to the majority of oxide systems. Normally the integration constant a is zero, reflecting that at time zero there is no oxide. However, I have been considering whether it has any meaning. Perhaps it accounts for the common observation that initial oxidation in particular progresses in a faster-than-parabolic fashion. It is sometimes assumed that early non-protective oxidation may follow linear or a faster parabolic kinetics before transitioning to the steady-state parabolic rate of the mode [private communication with Professor John Nicholls]. Although I believe this to be due to the shift from one parabolic rate to anther slower one as formerly discussed (the basis of the modified model presented below). What meaning, if any, can be attributed to a is uncertain, but I believe it cannot be neglected.

Slow oxidation occurs when the diffusion coefficients of ions in the scale are low (i.e. low self-diffusion). The migration of ions in the scale is a function of the degree of non-stoichiometry of the oxide. Oxides with a high degree of defects have a higher oxidation rate. High scale growth rates are observed in highly defective structures like FeO. Furthermore the rapid oxide growth of CoO and NiO is due to a large number of defects in the cation lattice (leading to a high self-diffusion) [Schütze 1997]. Foreign ions (dopants) can change the defect concentration and hence the diffusion rate in the oxide.

For instance, dissolved Cr in NiO increases the number of cation vacancies increasing the diffusion rate and hence the oxidation rate [Schütze 1997].

While normally lattice diffusion dominates one cannot neglect grain boundary diffusion. This is especially true in conditions where lattice diffusion is slow or where the grain size is small and there is therefore a large volume fraction of grain boundaries. In this case, too, doping can affect behaviour. It is even possible for different components (metal or oxide) to travel preferentially by one mode: lattice or grain boundary, and the other preferentially by the other mode [Schütze 1997].

The oxide thickness is given by [Huntz *et al.* 2006, and an equivalent in Young 2016]:

$$z_{NiO} = x \frac{M_{NiO}}{M_O \rho_{NiO}} \qquad (8.7)$$

Where:

$z_{NiO} =$ oxide thickness [cm]
$x = \left(\frac{m}{A}\right)$ [g cm^{-2}]
$m =$ mass of oxygen [g]
$A =$ area of sample exposed to oxygen [cm^2]
$M_{NiO} =$ molar mass of nickel oxide [g mol^{-1}]
$M_O =$ molar mass of oxygen [g mol^{-1}]
$\rho_{NiO} =$ density of nickel oxide [g cm^{-3}]

The above equations assume that all of the incorporated oxygen forms a scale at the surface and there is no isolated internal oxidation.

An interesting comment is to be made on the utility of Wagner's theorem (and equations) [*verbatim* from Young 2016] "From a practical point of view, it is easier to measure a parabolic rate constant than to predict it by determining diffusion coefficients and deviations from stoichiometry as functions of oxygen activity. The real value of the theory is in providing a fundamental understanding of the oxidation mechanism."

8.6.2 Modified Oxidation Model

In order to most clearly present the reasoning behind the creation of this modified-Wagnerian oxidation model the basic model is best given by the differential form of the widely known equation $x^2 = k_p' t$ (equation (8.5)). This is given by:

$$\int_{x=0}^{x} x\, dx = \int_{t=0}^{t} k_p^{'}\, dt \qquad (8.8)$$

Where:

$x = \left(\frac{m}{A}\right)$ [mg cm^{-2}]

$m =$ mass of oxygen [mg]

$A =$ area of sample exposed to oxygen [cm^2]

$k_p' = \frac{k_p}{2}$ [mg^2 cm^{-4} h^{-1}]

$k_p =$ average parabolic rate constant of oxidation (literature) [mg^2 cm^{-4} h^{-1}]

$t =$ time [h]

For a process occurring in two distinct stages with respect to oxidation time (as proposed in the Tier 1 oxidation discussion; section 8.3), the above equation's RHS can be split to match these processes:

$$\int_{x=0}^{x} x\,dx = \int_{t=0}^{t_1} k_{p_1}^{'}\,dt + \int_{t_1}^{t_2} k_{p_2}^{'}\,dt \qquad (8.9)$$

$$\frac{x^2}{2} = k_{p_1}^{'}[t_1 - 0] + k_{p_2}^{'}[t_2 - t_1] \qquad (8.10)$$

$$\frac{1}{2}m^2 = A^2\left(k_{p_1}^{'}t_1 + k_{p_2}^{'}[t_2 - t_1]\right) \qquad (8.11)$$

Verifying the validity of this modified-Wagnerian model was done by inputting experimental results into equation (8.11). This is accomplished by using the rate constants approximated from the results to calculate the mass of oxygen in the oxidised samples for various times in the range $t = 0$ to $t = t_2$. It was estimated that t_1 (that is the shift from cation transport dominated to vapour phase transport dominated oxidation) occurs at 2.25 h. These three estimates (initial k_p ≈9 mg^2 cm^{-4} h^{-1}, second k_p ≈ 4.5 mg^2 cm^{-4} h^{-1} and 2.25 h transition time) were made by eye from the mass fraction with time plots.

t (h) ±0.01 h	**m_{gain} (mg) [calculated]** ±2 mg	**m_{gain} (mg) [average]** ±2 mg	**Error (%)**	**Fractional Error (%)**
0.017 (1 min)	3.5	3.3	7.36	2.1
0.033 (2 min)	5.0	4.9	2.88	0.58
0.083 (5 min)	7.9	7.3	7.63	0.97
0.167 (10 min)	11.2	10.8	4.09	0.37
0.333 (20 min)	15.8	14.0	13.02	0.82
1.000	27.4	25.2	8.82	0.32
1.083 (65 min)	28.5	30.7	-7.29	-0.26
1.167 (70 min)	29.5	27.4	7.59	0.26
1.333 (80 min)	31.6	29.3	7.92	0.25
1.667 (100 min)	35.3	32.9	7.23	0.2
2.000	38.7	35.2	9.94	0.26
2.333 (140 min)	42.5	38.7	9.82	0.23
5.000	53.0	43.6	21.56	0.41
9.000	65.6	55.4	18.41	0.28
16.000	83.2	77.2	7.8	0.09
20.000	91.7	84.7	8.32	0.09
42.000	129.0	124.2	3.85	0.03

Table 8-5. Modified Wagnerian model verification comparing the values calculated using the model to the average (arithmetic mean) of experimental values. Also shown is the percentage error of the model (difference between calculated and average values expressed as a percentage) and the fractional error (ratio of the error to the calculated value, also as a percentage).

The whole table can be found in Appendix C: Complete Oxidation Results Tables. A by-batch comparison was made in addition to one based on the average of experimental data that can be found in the aforementioned appendix.

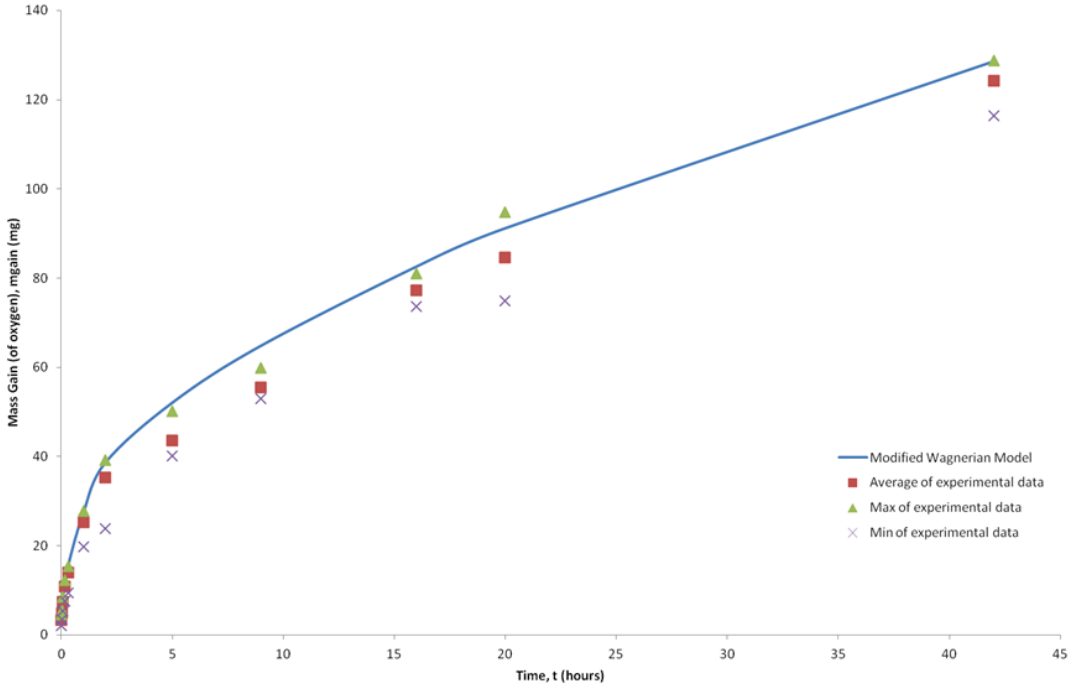

Figure 8-41. Modified Wagnerian model verification for oxidation at 1,100 °C showing envelope of maximum and minimum experimental values alongside calculated average and model results.

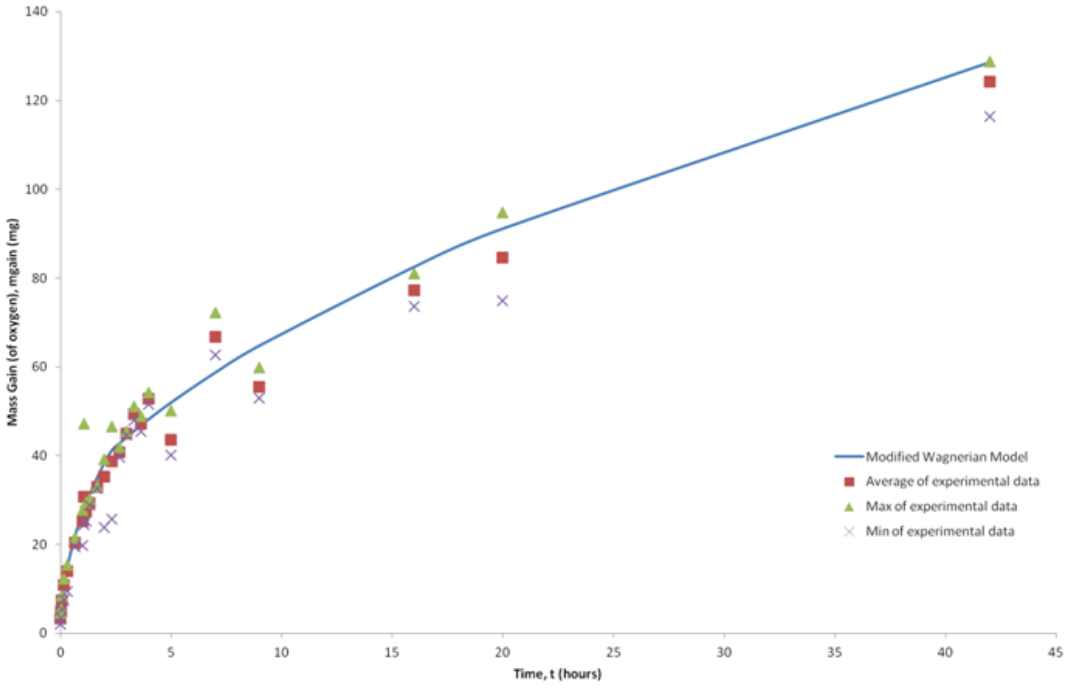

Figure 8-42. Modified Wagnerian model verification for oxidation at 1,100 °C showing envelope of maximum and minimum experimental values alongside average and model. All results shown, up to and including Tier 4. Note the changes from Figure 8-41. (above).

As can be seen from Table 8-5. the error is for the most part below 10% and as low as 3%. The only three exceptions occur at 20 minutes, 5 h and 9 h. However, upon

considering the fractional error, which is in some ways more useful because it is a measure of relative error, the points at which the model would greatly benefit from improvement are considerably different. According to the fractional error the 1 min, 5 min, 20 min and 2 min are the largest discrepancies (in order from largest to smallest). Based on the error alone it appears there are only a few isolated portions of the model, mostly later dwells, which would benefit from improvement. Contrary to this, the fractional errors indicate that most benefit is to be had by modifying the earlier portion of the model. It is worth reiterating that the earlier points are liable to include greater experimental error than later ones so the significant deviation highlighted by the fractional error may not be truly representative. This is shown rather clearly in Figure 8-41.

Further examination of the figure shows that the model deviates from the envelope of experimental results only between about 4 h and 16.5 h. Between 9 h and 16.5 h the model consistently overestimates the mass of oxygen gained. Otherwise, the model fits within the experimental data envelope, albeit yielding a higher mass gain estimate than the experimental data mean. The apparent overestimation of mass gain of the model noted may be due to the bahviour (discussed previously) of batch E and could be corrected by adding more data (and an improved mean). Therefore, modifying the way the transition is modelled may bring the model closer to experimental results.

Plotting the fractional error against time or log time (for more compactness) shows that the fractional error declines rapidly over the first few minutes and reaches a steady minimum with one exception at 5 h where the fractional error is inexplicably higher (Figure 8-43.). However, the decline itself is not steady. All the samples oxidised for 5 h were positioned at the front of the furnace and therefore possibly exposed to more changeable conditions during oxidation, which may account for the sudden increase in fractional error for these samples. This seems to imply that it is worth reconsidering how the earliest part of the process is modelled. However, as stated earlier, the short oxidation times suffer from larger stochastic error than the rest so while Figure 8-43. confirms this I do not believe it indicates the best optimization path for the model. Revisiting Wagner's original work based on chemical activity gradients, ion concentrations and ion mobilities may be required to revise the model to account for violation of the semi-infinite metal cation source assumption but is beyond the scope of the current work.

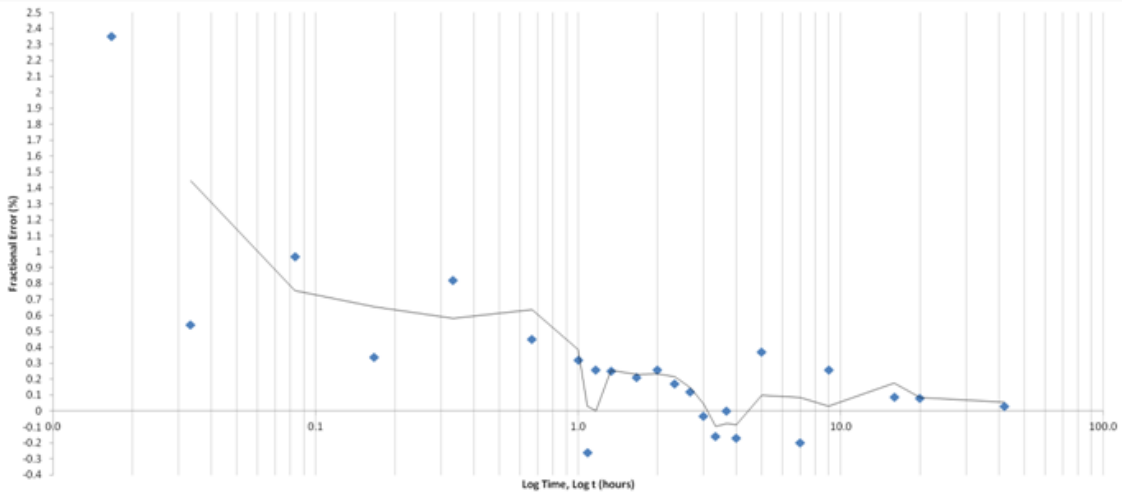

Figure 8-43. Fractional error against log time for model verification data for oxidation at 1,100 °C. All results shown, up to and including Tier 4.

The calculations used to verify the data have a further use, one referred to earlier: k_p and transition time estimates. These can be found using a numerical solver (in this case the one included with Microsoft Excel 2007) and solving to minimise error between the model and experimental results – or put differently it is a nonlinear fit of the model to the data, adjusting specified constants (k_{p_1}, k_{p_2} and t_1 in this instance) from initial estimates iteratively till the best possible fit is achieved. The results of this numerical solution are tabulated below.

Data	**k_{p_1} (mg^2 cm^{-4} h^{-1})**	**k_{p_2} (mg^2 cm^{-4} h^{-1})**	**t_1 (h)**
Batch A	8.43	4.34	1.40
Batch B	8.20	4.34	2.25
Batch C	10.20	3.65	1.08
Batch D	10.20	3.94	0.90
Batch E	10.20	3.94	0.61
Mean of data	8.90	4.20	0.93

Table 8-6. Rate constants and transition time for all batches and for mean of experimental results. Nonlinear fitting by numerical solution with modified Wagnerian model and initial estimates of solved parameters.

Following Wagner's original approach one obtains a predicted k_p at 1,100 °C of between 4×10^{-10} g^2 cm^{-4} s^{-1} and 9×10^{-10} g^2 cm^{-4} s^{-1} [obtained from an aggregate plot of data from various sources presented in Young 2016]. Elsewhere Young (2016) has included a measured value for NiO k_p of 9×10^{-11} g^2 cm^{-4} s^{-1} at 1,000 °C. I have associated the range, or rather a change from 9×10^{-10} g^2 cm^{-4} s^{-1} to 4×10^{-10} g^2 cm^{-4} s^{-1} (4.5 mg^2 cm^{-4} h^{-1} and 9 mg^2 cm^{-4} h^{-1} respectively in my own work), with a changing microstructure and the emergence of significant vapour phase transport across large pores.

8.7 Oxidation Temperature Optimization

The previous two tiers of oxidation experiments determined the time to full oxidation of the Ni200 tubes is approximately 42 h when oxidized at 1,100 °C. This temperature yields acceptable microstructure and surface morphology for further processing of the nickel tubes into anodes. The literature did not provide detailed information on the characteristics of NiO between 1,100 °C and 1,200 °C, yet this is of considerable interest since even a modest increase in temperature is known to greatly accelerate the oxidation rate (a common rule of thumb being that for every 30 °C increase in temperature the rate of oxidation doubles – private communication with Professor John Nicholls).

The aim is therefore to optimise the oxidation process with respect to oxidation time with the proviso that there should be no deleterious effects on either the surface morphology of the oxide nor its cross sectional microstructure, in particular porosity. The objectives of the tier 3 oxidation experiments were to oxidise a number of samples at 1,150 °C for three time intervals and compare the mass fraction oxidised with that of the previous experiments carried out at 1,100 °C. A crucial second objective was to observe the surface morphologies and cross sectional microstructures for changes compared to the lower temperature oxide.

8.7.1 Results & Discussion

Table 8-7. summarises the results giving the mass gain of each sample, the mass fraction oxidised (mass of oxide gained divided by the maximum possible mass of oxygen gained based on sample's initial unoxidised mass) as well as the calculated oxide thickness, z. Figure 8-44. shows a plot of calculated and experimental results. Errors estimated using linear approximation by partial differentiation where an equation was used or based purely on measurement equipment error otherwise.

Sample	t (h) ±0.01 h	m_{Ni} (mg) ±1 mg	m_{Ni+NiO} (mg) ±1 mg	m_{gain} (mg) ±2 mg	Mass fraction oxidised ±0.001	z (µm) ±0.23 µm
Batch AA						
OT-A.21/11/11-125.1150-AA.01	5	592.4	651.9	59.5	0.865	45.68
OT-A.21/11/11-125.1150-AA.02	9	570.2	646.2	76.0	0.891	58.34
OT-A.21/11/11-125.1150-AA.03	16	574.8	676.0	101.2	0.924	77.69
Batch AB						
OT-A.21/11/11-125.1150-AB.01	5	499.2	568.2	69.0	0.894	52.97
OT-A.21/11/11-125.1150-AB.02	9	557.3	633.4	76.1	0.893	58.42
OT-A.21/11/11-125.1150-AB.03	16	623.1	735.7	112.6	0.928	86.44
Batch AC						
OT-A.21/11/11-125.1150-AC.01	5	577.8	634.6	57.0	0.863	43.76
OT-A.21/11/11-125.1150-AC.02	9	554.1	631.6	77.5	0.896	59.50
OT-A.21/11/11-125.1150-AC.03	16	544.3	643.7	99.4	0.929	76.31
Batch AD						
OT-A.21/11/11-125.1150-AD.01	5	560.3	618.4	58.1	0.867	44.60
OT-A.21/11/11-125.1150-AD.02	9	554.6	631.5	58.9	0.869	45.22
OT-A.21/11/11-125.1150-AD.03	16	573.6	676.2	102.6	0.926	78.76
Batch AE						
OT-A.21/11/11-125.1150-AE.01	5	581.2	639.6	58.4	0.865	44.83
OT-A.21/11/11-125.1150-AE.02	9	563.7	642.8	79.1	0.896	60.72
OT-A.21/11/11-125.1150-AE.03	16	570.9	674.6	103.7	0.929	79.61

Table 8-7. Mass gain and oxide thickness of Ni tube oxidation at 1,150 °C. All batches from Tier 3 experiment shown.

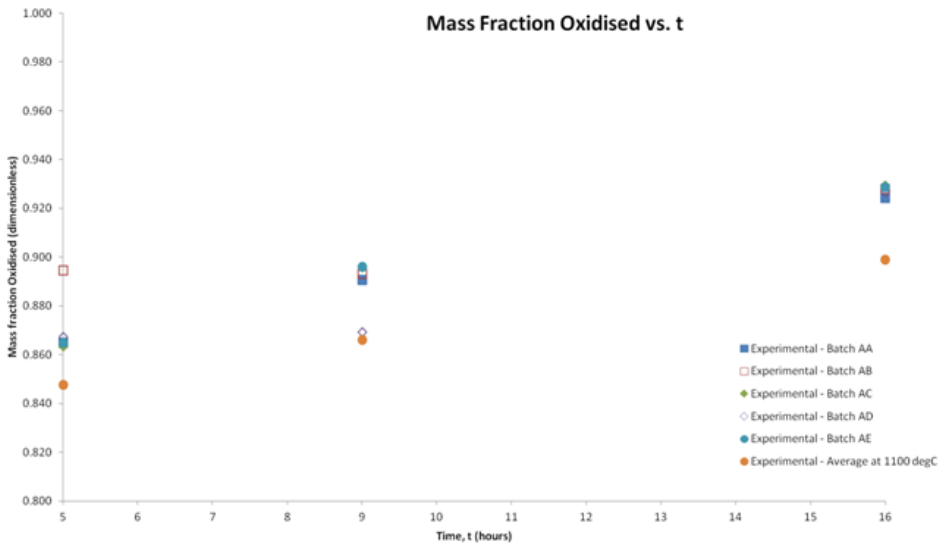

Figure 8-44. Plot of mass fraction oxidised against time for all samples oxidised at 1,150 °C compared with average mass fraction oxidized for an 1,100 °C oxidation temperature.

The results presented in Table 8-7. and Figure 8-44. clearly indicate there was an increase in the MFO of at least 20 wt.% in all cases. Or, put differently, a sample

oxidised at 1,150 °C for 5 h is equivalent (in terms of mass gain) to one oxidised at 1,100 °C for 9 h (similarly 1,150 °C for 9 h is equivalent to 1,100 °C for nearly 16 h and 1,150 °C for 16 h is equivalent to 1,100 °C for somewhere around 20 h).

The following micrographs were used to look for deleterious microstructural changes that could be attributed to an increase in oxidation temperature. These consist, as previously, of milled cross-sections through the sample and its surface morphology. Images were created by scanning electron microscope (SEM), and cross-sections were trenches created by focused ion beam (FIB) milling. A Au-Pd coating was used to enable the high resolution imaging. However, unlike previous instances the grains of the coating are not visible because the coating was thinner.

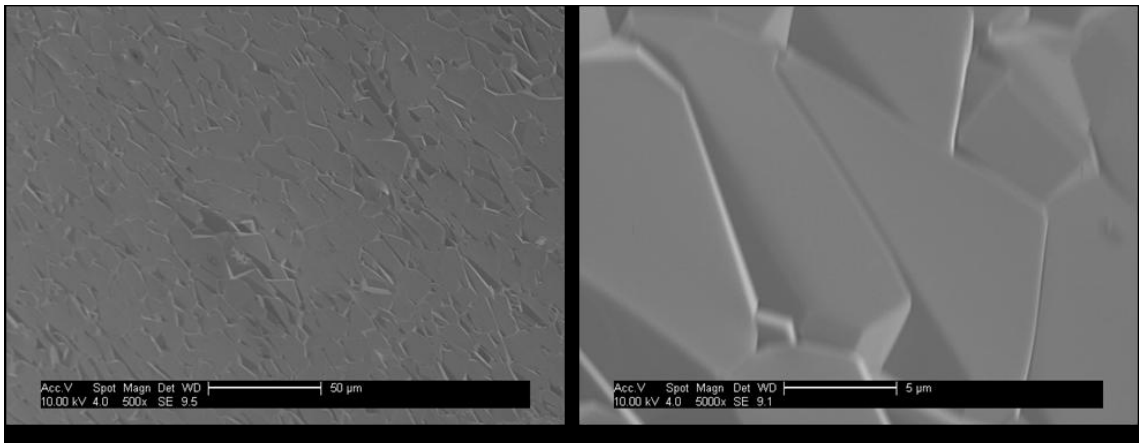

Figure 8-45. SEM micrographs showing the surface morphology of the inner (concave) surface of sample OT-A.21/11/11-125.1150-AC.03 (16 h 92.9 wt.% oxidised). Images are ordered from left to right in order of increasing apparent magnification.

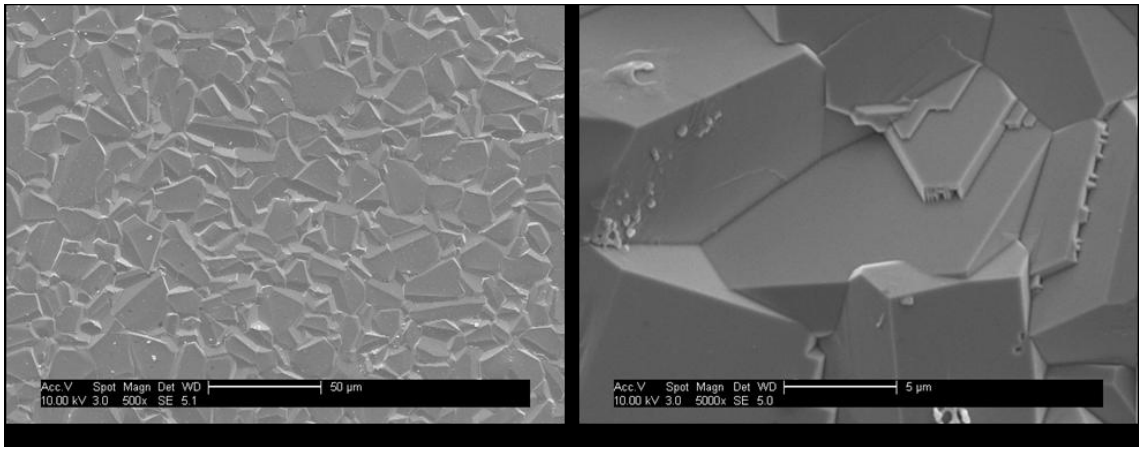

Figure 8-46. SEM micrographs showing the surface morphology of the outer (convex) surface of sample OT-A.21/11/11-125.1150-AC.03 (16 h 92.9 wt.% oxidised). Images are ordered from left to right in order of increasing apparent magnification.

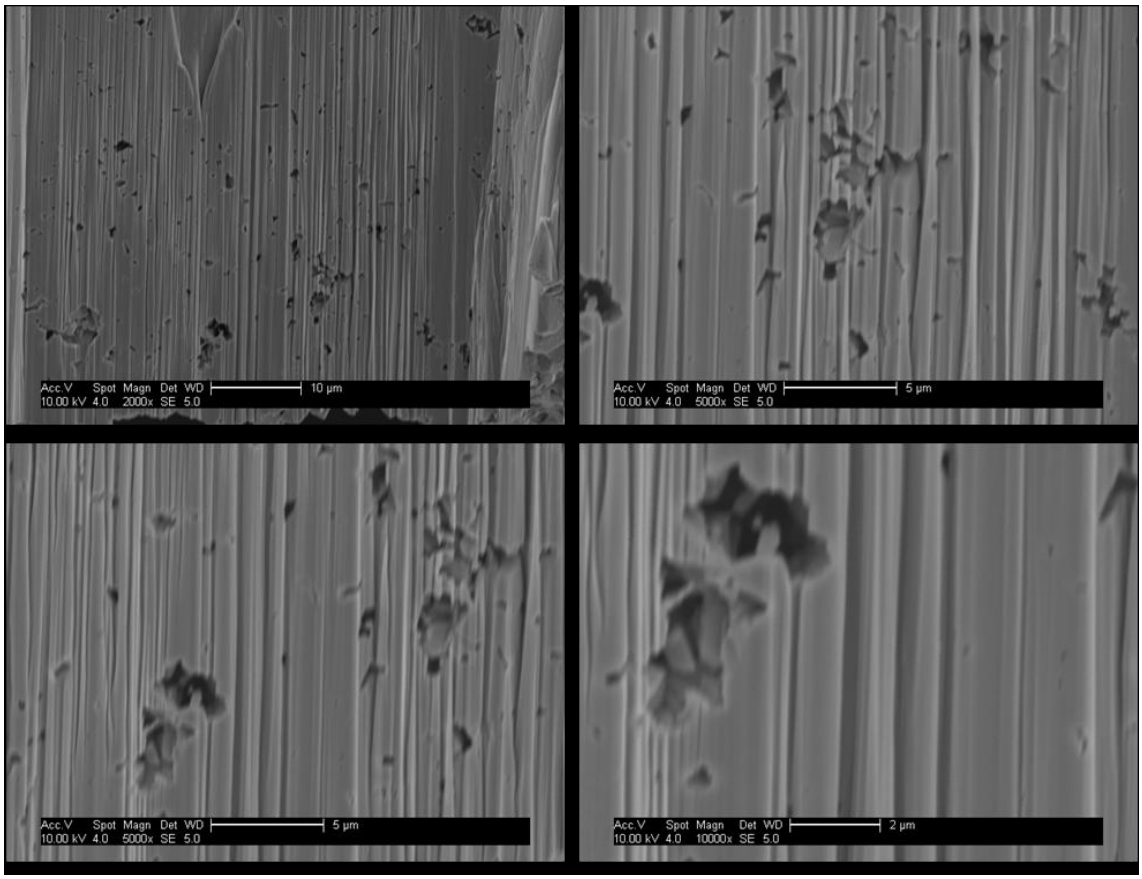

Figure 8-47. SEM micrographs* showing pores near the inside edge of sample OT-A.21/11/11-125.1150-AC.03 (16 h 92.9 wt.% oxidised). Images are ordered from left to right and top to bottom in order of increasing apparent magnification.

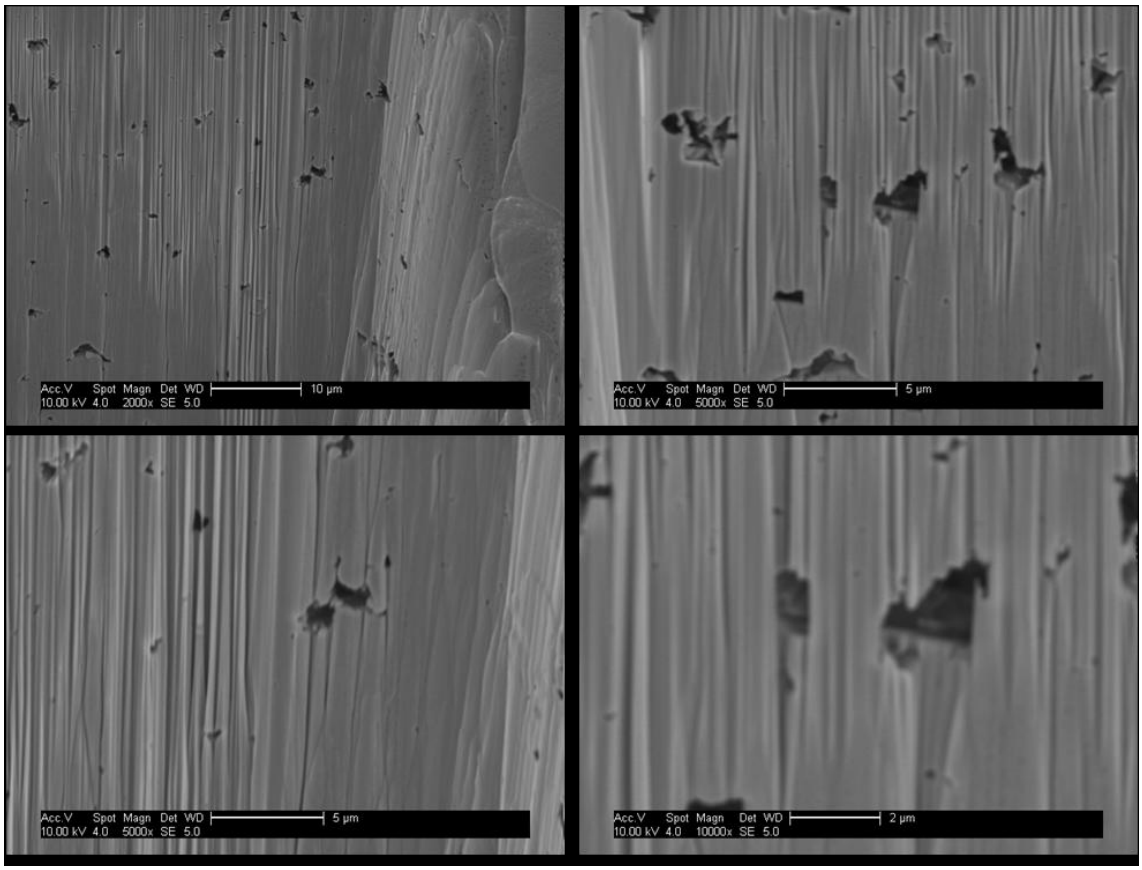

Figure 8-48. SEM micrographs* showing pores around the middle of sample OT-A.21/11/11-125.1150-AC.03 (16 h 92.9 wt.% oxidised). Images are ordered from left to right and top to bottom in order of increasing apparent magnification.

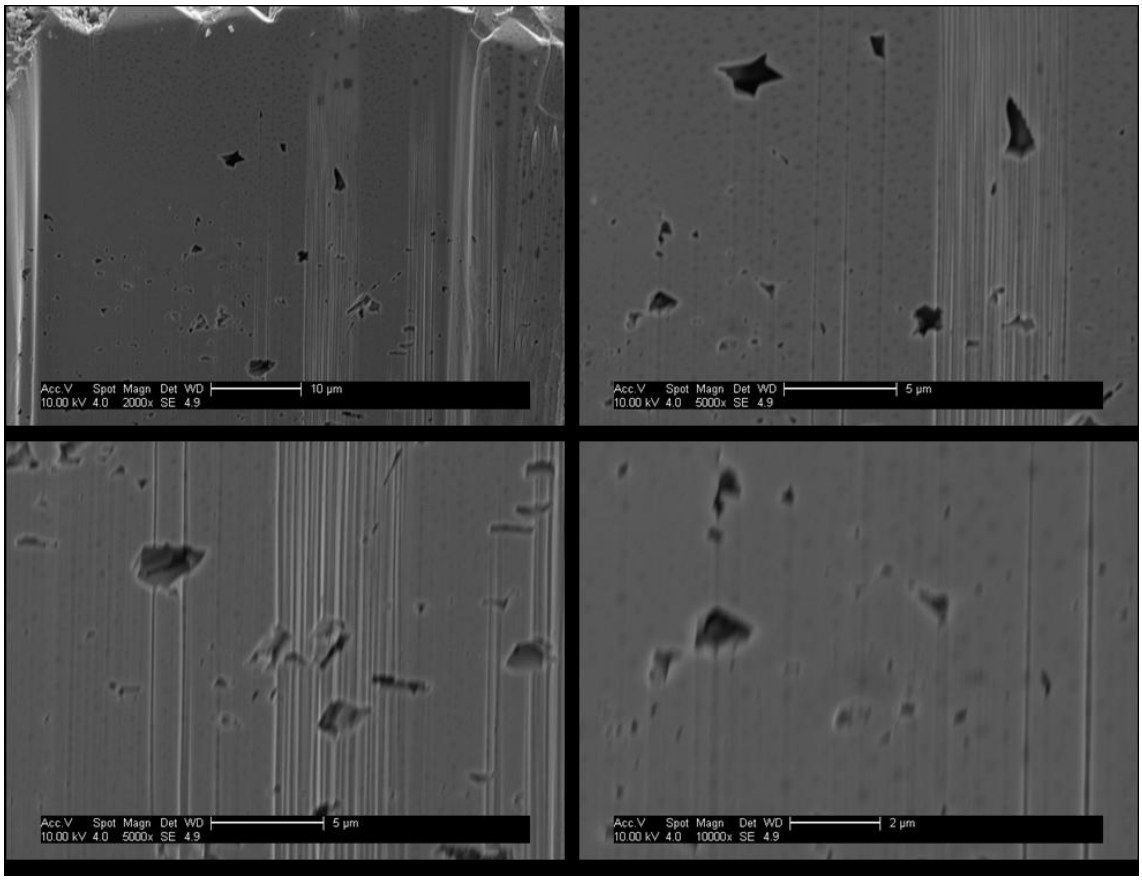

Figure 8-49. SEM micrographs* showing pores near the outside edge of sample OT-A.21/11/11-125.1150-AC.03 (16 h 92.9 wt.% oxidised). Images are ordered from left to right and top to bottom in order of increasing apparent magnification.

The sample characterised showed no significant deleterious changes in microstructure compared to samples oxidised at the lower temperature. Conclusive results require additional data in the form of both further samples oxidised for different periods of time and more imaging especially to compare to the nearest equivalent oxidised at the lower temperature (by time and/or mass fraction oxidised). Greater data would also be required to look for more subtle differences, both potentially negative changes as well as exploitable opportunities.

The benefit, a 20% increase in mass fraction oxidised for the same oxidation period, ensures this is a valuable area of research to pursue. For the purposes of this work the reduction in time to complete oxidation is less important. I wish to stress that for commercialization it is far more significant and should be pursued vigorously.

8.8 Oxidation Conclusions

Oxidation alone is unlikely to result in sufficient fuel and exhaust gas permeance for anodes. The potential of this route depends greatly on whether reduction creates sufficient useful porosity to attain a reasonable fuel and exhaust gas permeance.

There is no evidence of additional oxidation mechanisms taking place beyond the two noted (cation transport with no short-circuit paths and vapour phase transport). Other features conform to those reported in the literature [Khalid *et al.* 1999, Haugsrud 2001, Haugsrud 2003, Huntz *et al.* 2006, Zhou *et al.* 2008]. The reasons for the discrepancies in oxidation rate inferred from the mass gain versus time curves and the literature appear to be correct, or at least no contradictory evidence is offered by the SEM analysis.

It appears that violating the assumption that there exists a semi-infinite supply of Ni cations has a single outcome: the emergence of vapour-phase transport as the dominant mechanism once the assumption is violated. This is reflected in the modified Wagnerian model. The paucity of experiments concerned with a high degree of oxidation, and complete lack hitherto of ones dealing with through oxidation, explains why this second stage of the process (taking the role of dominant mechanism) reflecting the effect of violating an assumed semi-infinite source of mobile Ni cations went unnoticed thus far.

Oxidation was confirmed to occur as an advancing front from the near-surface region to the sample interior with little to no sign of any short circuit processes or preferential grain boundary oxidation. Oxidation was confirmed to be right through the A.10 and E.11 samples by EDS analysis of a trench milled by FIB at an edge. The trench showed uniform oxidation with fairly monodisperse grain sizes. While there does appear to be some morphological difference between the outer strata and inner oxide the presence of the columnar outer structure mentioned in some sources was not noted.

Unfortunately because oxidation progresses as an advancing front the samples must by fully oxidised to ensure there is NiO to reduce and create porosity right through the anode. This is a great pity: the parabolic nature of Ni oxidation means that after a few minutes ~80% oxidation by mass is achieved. Had this been distributed through the entire anode it would have been possible to create a sufficiently permeable anode with just a few minutes of oxidation – highly advantageous in the economical fabrication of fuel cells.

Higher temperature oxidation was trialled, yielding enough benefit for a modest increase in oxidation temperature, from 1,100 °C to 1,150 °C, to be noteworthy. No deleterious changes to microstructure were noted although further study is warranted. This optimization route (minimising time to complete oxidation), while not strictly beyond the scope of this thesis, was deemed of lesser interest than others and therefore not pursued further.

Inclusions of some 3 wt.% Mo causes NiO to break down very rapidly at 1,200 °C, resulting in a very porous oxide [Khalid *et al.* 1999]. This is most likely due to the preferential oxidation of such inclusions at the metal grain boundaries (the inclusions

may be forced there by changing solubility of in the Ni and hence segregation) and because M_2O_3 is volatile at 1,200 °C. The scale in such a case is layered, as one might expect from the vapour phase transport mechanism taking over across large pores creating more oxide (and more large pores parallel to the surface) and so on. In these cases there is however some risk of spallation [Khalid *et al.* 1999]. It may therefore be greatly advantageous to utilize an alloy of Ni containing some 3 wt.% Mo. There do not appear to be any such commercial alloys.

In order to fully oxidise (~96 wt.%) the samples a heat treatment at 1,100 ℃ in air for ~42 hours is sufficient. However, whether the full time is necessary for sufficient oxidation for the anode fabrication still has to be determined.

Step 2: Reduction

8.9 Reduction Objectives and Background

The reduction step is the second process required to create porous anodes in accordance with this project's design. The aim of this work is to mirror the oxidation. While my earlier work [Camilleri, 2009] demonstrated the feasibility of an oxidation-reduction treatment for creating porosity, only a few experiments were carried out as part of this MSc study due to time constraints. The objectives of this experiment are to optimise the reduction process by obtaining a body of data and developing a suitable model for the process. Special consideration is given to attaining some combination of shortest process time, lowest temperature reduction, maximum porosity, and complete reduction, with the aim of achieving the most efficient processing times. The same basic procedure, developed previously [Camilleri 2009], was used.

The reduction process (removing the oxygen from a metal oxide) leaves behind vacancies in those lattice sites previously occupied by oxygen. If the temperature is high enough and sufficient time allowed the now disconnected particles of metal will tend to sinter in order to minimise their surface energy reducing the desired porosity – in a manner analogous to the vacancy elimination mechanisms for the oxide. A balance between fully reducing the fully oxidised nickel anode and minimal sintering is necessary to obtain useful anodes. The total porosity, the sum of that attained by reduction and the porosity created in oxidising the nickel, should be sufficient for successful SOFC operation. The result, intuitively, should be a metallic structure with sufficient connected porosity to serve as the anode of a SOFC (see discussion on permeability later, in particular fuel permeability – chapter 1).

Historically Volmer discovered that thermal decomposition occurs in the now familiar two stages of reactant dissociation and subsequent metal condensation from a supersaturated vapour [Galwey 2012]. This is the same rate determining process as

proposed by L'vov 60 years later in the CDV (congruent dissociative vapourisation) mechanism [Galwey 2012, see also L'vov and Galwey 2012]. Ostwald and Langmuir are identified by Galwey (2012) as identifying the essential role of the contact interface between phases (metal and its oxide for instance) in thermal decomposition.

The Arrhenius approach was adopted not long after these initial discoveries but its use continues without adequately demonstrated theoretical underpinning [Galwey 2012]. It is eminently suited to kinetic processes in homogeneous material but remains unproven for heterogeneous reactions (such as thermal decomposition) [Galwey 2012]. Further detail on the development of this science can be found in the comprehensive review by Galwey (2012).

Research into the mechanisms of NiO reduction in hydrogen has an 85 year history, originating with Benton and Emmet [L'vov and Galwey 2012]. The traditional theoretical approach is based on the kinetic Arrhenius equation and the mechanism of direct reduction of solid oxide to solid metal provided an insufficiently reliable quantitative interpretation of the kinetic characteristics [L'vov and Galwey 2012]. The authors cite the induction period and autocatalytic behaviour in particular. The authors cited used a thermochemical approach to interpret the kinetics and mechanism of NiO reduction by H_2. The technique has developed over the last 20 years to explain the kinetics and mechanisms of thermal decomposition of solids [L'vov and Galwey 2012].

Two different kinetic models are proposed for the reduction of oxides: the nucleation model and the interface-controlled model [Chatterjee *et al.* 2012]. In the nucleation model the rate-limiting step is the generation of small aggregates of the new (reduced) phase [Chatterjee *et al.* 2012]. In the interface-controlled model the rate of metal oxide reduction is proportional to the surface area of the metal-oxide interface [Chatterjee *et al.* 2012]. This interface is changing continuously during reduction. A parallel may be drawn to cationic oxidation, proceeding as it does as an advancing front (the metal-oxide interface changing continuously). However, the oxidation mechanism (cation transport) and the reduction mechanism are not directly related.

There are a number of significant differences between the conventional approach and the thermochemical one [L'vov and Galwey 2012]. Mechanism, kinetics and methodology are treated in turn, first in summary then in full.

Conventional approach	**Thermochemical approach**
Regarding mechanism:	
Congruent reduction of oxides of volatile metals and incongruent reduction of oxides of the low-volatility metals.	Congruent reduction of any oxides to gaseous products, followed by condensation of supersaturated metal vapour in the case of low-volatility metals.
Regarding kinetics:	
Arrhenius kinetic equation.	Langmuir quasi-equilibrium equations for the vapourisation in vacuum and in a foreign gas, including the concepts of equimolar and isobaric reduction modes.
Regarding methodology:	
Arrhenius-plot method (differential).	The third-law method (absolute) and the second-law method (differential).

The magnitude of T_{in} / E (the temperature of onset of the reaction in Kelvin divided by the activation energy in kJ mol^{-1}) is nearly unvarying for the thermal decomposition of 50 compounds yielding both gaseous and solid products [Galwey 2012]. This fairly conclusively indicates that there is a common, simple, initial vapourisation step for all thermal decomposition reactions [Galwey 2012]. This disproves the earlier concept held by application of the Arrhenius model that the reactants form a so-called transition complex (a transitory compound on the way to the final products). The most likely candidate for such a common initial step is surface species sublimation [Galwey 2012] without any intermediate activation – "the energetic entity simply volatilizes." [Galwey 2012]

8.9.1 Thermodynamics: Congruent and Incongruent Mechanisms

Conventionally there are two interpretations of oxide reduction kinetic data: congruent reduction forming gaseous metal for volatile metals, or incongruent reduction directly forming solid products for low-volatility metals [L'vov and Galwey 2012]. The thermochemical approach is based upon congruent formation of gaseous products for all metal oxides. For low-volatility metals this is followed by condensation of the supersaturated metal vapour [L'vov and Galwey 2012]. Thus, the thermal decomposition of NiO can be described by the following equation (among a range of metal oxides described by similar equations):

$$NiO\ (s) + H_2 \leftrightarrow Ni\ (g) + H_2O \rightarrow Ni\ (s) + H_2O \qquad (8.12)$$

The two step equation can be conveniently expressed as [L'vov and Galwey 2012]:

$$NiO\ (s) + H_2 \leftrightarrow Ni\ (g) \downarrow + H_2O \qquad (8.13)$$

"The condensation of a supersaturated Ni vapour explains the formation of finely divided metallic product (in the form of nanoparticles) on the oxide (reactant) surface."

[L'vov and Galwey 2012] In the thermal decomposition of solids this mechanism is termed congruent dissociative vapourisation of reactant (CDV) [L'vov and Galwey 2012].

The radius r of a spherical particle of liquid or solid formed by vapour condensation, at supersaturation S and temperature T, is expressed by the Gibbs-Thomson equation [L'vov and Galwey 2012]:

$$r = \frac{2M\gamma}{\rho RT \ln S} \qquad (8.14)$$

Where:

M is molar mass

γ is surface tension (or formation energy / unit surface area)

ρ is the density of the substance

S is the supersaturation, the ratio of the actual pressure, p_{act}, of metal in the equilibrium part of the reaction equation (8.12) to its saturated vapour pressure, p_{sat}: $S = \frac{p_{act}}{p_{sat}}$

8.9.2 Thermodynamics: Condensation Energy Transfer to the Reactant

Another important distinction between the CDV mechanism and the conventional incongruent mechanism lies in the portion of condensation energy transferred to the reactant within the thin reaction zone formed at the contact of the two solid phases (i.e. the interfacial zone between reactant and product, NiO and Ni in this instance) [L'vov and Galwey 2012, Galwey 2012]. According to the cited sources this energy accounts for the increased rate of reaction inside the interfacial zone in comparison to the open reactant surface. That is, reduction proceeds more rapidly at the interface of NiO and Ni than it would at a free NiO surface. "In the absence of an interface, most of the condensation energy is scattered/released to the open space above the reactant oxide surface." [L'vov and Galwey 2012]

This effect explains both the induction period during which the reaction is limited to highly localized areas of the surface and the subsequent autocatalytic behaviour leading to the formation of a layer of product across all oxide surfaces [L'vov and Galwey 2012].

To calculate the enthalpy of the reduction reaction a supplementary term is introduced that takes into account the partial transfer of condensation energy to the reactant (oxide). This supplementary term is [L'vov and Galwey 2012, Galwey 2012]:

$$\tau = \Delta_c H_T^0(M) \qquad (8.15)$$

Where:

τ is the transfer coefficient, representing the fraction of the $\Delta_c H_T^0(M)$ energy that is transferred to the oxide during thermal decomposition.

Thus we have the relationship [L'vov and Galwey 2012]:

$$\Delta_c H_T^0 = \Delta_f H_T^0(M) + \Delta_f H_T^0(H_2O) - \Delta_f H_T^0(MO) - \Delta_f H_T^0(H_2) + \tau\Delta_c H_T^0(M) \quad (8.16)$$

Where:

$\Delta_f H_T^0$ terms represent the enthalpy of formation of each component of the reaction

$\tau\Delta_c H_T^0(M)$ is the enthalpy of oxide reduction including the effect of metal condensation, i.e. the heat of Ni sublimation with the opposite sign

The authors of the cited source found that τ was linked to the degree of supersaturation (S) of the low-volatility product during decomposition [L'vov and Galwey 2012], expressed by:

$$\tau = 0.351[\log(\log S)] + 0.017 \quad (8.17)$$

"The above dependence is very weak: variation of supersaturation by an order of magnitude (at the average value, S = 1032) changes τ by only 0.1 %. Unfortunately, no physical explanation for this dependence has yet been found." [L'vov and Galwey 2012]

8.9.3 Thermochemical Calculation of the Reaction Enthalpy

The procedure is as follows [edited for clarity from L'vov and Galwey 2012]:

1) Find the saturated vapour pressure of Ni at the desired temperature, P_{act} is about 10^{-5} bar.
2) Calculate the supersaturation, S.
3) Calculate τ using equation (8.17).
4) Find the relevant enthalpies of formation (Ni, H_2O, NiO and H_2).
5) Find the heat of sublimation for the metal (Ni) at the desired temperature; this is $\Delta_c H_T^0(M)$ – the enthalpy change due to metal condensation.

8.9.4 Variation of Enthalpy with Temperature and the Extent of Reaction

The increase in enthalpy with temperature corresponds to the observed rise in E [L'vov and Galwey 2012]. It is associated with the transfer of condensation energy from the metal vapour to the reactant. The numerical value of τ decreases with increasing temperature and therefore its contribution to the overall enthalpy (and to a lesser extent the condensation energy itself) decreases [L'vov and Galwey 2012]. Thus, instead of a small enthalpy decrease with increasing temperature there is a small increase.

At a hydrogen partial pressure of 1 bar the equilibrium constant, including the contribution of vapour condensation, lies in the range 10^{-13} to 10^{-8} bar; corresponding to partial pressures of gaseous products between 10^{-6} and 10^{-4} bar, exhibiting good agreement with experimentally measured values of P_{H2O} [L'vov and Galwey 2012]. Should the condensation energy contribution be excluded then the equilibrium constant lies in the range 10^{-23} to 10^{-14} bar [L'vov and Galwey 2012]. The change is indicative of the origin and extension of the induction period: during the initiation of the reduction reaction most of the condensation energy is scattered in the open space above the reactant oxide surface [L'vov and Galwey 2012]. The reduction rate only reaches its maximum value gradually, when the number and size of nuclei increases sufficiently to form a complete layer of metal product, covering all reactant surfaces [L'vov and Galwey 2012].

The reaction of hydrogen with metal oxide occurs at the interface between the two solid phases: reactant and product, via the interaction of H_2 molecules with oxygen released by the congruent dissociation of the metal oxide (NiO in this instance) [L'vov and Galwey 2012]. Oxygen molecules are adsorbed at the oxide surface such that the enthalpy of this exothermic reaction ($H_2 + 0.5O_2 = H_2O$) is a part of the total enthalpy of NiO reduction by hydrogen [L'vov and Galwey 2012]. The energy of condensation of gaseous Ni atoms (Ni(g) → Ni(s)), however, is distributed almost equally between both solid phases as evidenced by τ [L'vov and Galwey 2012]. Furthermore, τ decreases with increasing reduction temperature; so a larger proportion of the condensation energy is distributed to the reactant phase [L'vov and Galwey 2012].

8.9.5 Kinetics; Langmuir Equations for Evaporation of Simple Substances

The thermochemical approach uses Langmuir's equations for the evaporation of simple substances rather than the Arrhenius equation ($k = Ae^{-E/RT}$) [L'vov and Galwey 2012]. Langmuir's quasi-equilibrium equations for the evaporation of a simple substance (e.g. a metal) in vacuum or an inert gas are [L'vov and Galwey 2012]:

$$J = \frac{Mp}{\sqrt{2\pi MRT}} \qquad (8.18)$$

$$J = \frac{MDp}{zRT} \qquad (8.19)$$

$$J = \frac{MDp}{rRT} \qquad (8.20)$$

Where:

J is the absolute evaporation rate [kg m^{-2} s^{-1}]. This is directly proportional to the equilibrium vapour pressure of the substance.

M is the molar mass [kg mol^{-1}]

D is the diffusion coefficient of the vapour in an inert gas [m^2 s^{-1}]

z is the distance from the vapourisation surface to the sink (where the vapour concentration is zero) [m]

r is the radius of a spherical particle of the substance [m]

p is the vapour pressure of the substance [Pa]

8.9.6 Kinetics: Isobaric and Equimolar Regimes of Reduction

In determining which of the above Langmuir equations to apply one must determine the regime of reduction. In thermal decomposition and in reduction of solid reactants two reaction regimes exist: isobaric and equimolar [L'vov and Galwey 2012].

The equilibrium constant is given as:

$$K_p = \frac{p_{Ni} p_{H_2O}}{P_{H_2}} \qquad (8.21)$$

The calculated values, both including and excluding the effect of metal vapour condensation from the supersaturated Ni vapour, agree with experiment [L'vov and Galwey 2012]. One would expect this equilibrium constant, more explicitly, to be $K_{const.P_{H_2}}$ (that is the equilibrium constant at constant hydrogen pressure) and to be given in terms of partial pressures (p) of Ni and water and absolute pressure of hydrogen (P). However, the cited source does not make this clear. Indeed elsewhere partial pressures are used. As such (8.21) may indicate an equilibrium constant that is not time-invariant.

The isobaric regime (designated by superscript ^{iso}) refers to reaction in excess (that is, added) water vapour, i.e. $p_{H_2O}^{external} > p_{H_2O}^{internal}$. The equimolar mode (designated by superscript ^{eq}) refers to reaction in the absence of excess (added) water vapour, i.e. $p_{H_2O}^{internal} > p_{H_2O}^{external}$. The importance of the distinction, first made by L'vov [L'vov and Galwey 2012], is that in the presence of its gaseous product (water vapour) in the reaction zone equation (8.21) becomes [L'vov and Galwey 2012]:

$$K_p = \frac{p_{Ni}^{internal}\left(p_{H_2O}^{internal} + p_{H_2O}^{external}\right)}{P_{H_2}} \qquad (8.22)$$

Where:

$p_{Ni}^{internal}$ is the equilibrium partial pressure for the metal (Ni in this case) determined by the reaction itself (internal) [Pa]

$p_{H_2O}^{internal}$ is the equilibrium partial pressure for water vapour determined by the reaction itself (internal) [Pa]

$p_{H_2O}^{external}$ is the externally introduced (constant) partial pressure of water vapour [Pa]

When the reaction is congruent and yields equal molar quantities of product, i.e. $\frac{J_{Ni}}{M_{Ni}} = \frac{J_{H_2O}}{M_{H_2O}}$, equation (8.22) yields [L'vov and Galwey 2012]:

$$\frac{p_{H_2O}^{internal}}{p_{Ni}^{internal}} = \sqrt{\frac{M_{H_2O}}{M_{Ni}}} = \beta^{eq} \qquad (8.23)$$

Similarly, under this condition equation (8.22) for the equimolar mode becomes [L'vov and Galwey 2012]:

$$K_p^{eq} = \frac{\left(p_{H_2O}^{internal}\right)^2}{\beta^{eq} p_{H_2}} \qquad (8.24)$$

For the isobaric regime equation (8.20) under the congruence condition becomes [L'vov and Galwey 2012]:

$$\frac{p_{H_2O}^{internal}}{p_{Ni}^{internal}} = \frac{D_{H_2O}}{D_{Ni}} = \beta^{iso} \qquad (8.25)$$

Similarly, under this condition equation (8.22) for the isobaric mode is [L'vov and Galwey 2012]:

$$K_p^{iso} = \frac{\left(p_{H_2O}^{internal}\right)\left(p_{H_2O}^{external}\right)}{\beta^{iso} p_{H_2}} \qquad (8.26)$$

	Ni	**H_2O(g)**	**N_2**
Molar Mass (kg mol^{-1})	0.0587	0.018	0.028
Radius (Angstroms)	2.06	0.96	1.09

Table 8-8. Atomic properties of Ni, H_2O(g) and N_2.

In the case of NiO reduction by hydrogen in an inert environment consisting of nitrogen L'vov and Galwey (2012) calculate β^{eq} = 0.554 and β^{iso} = 3.1 [L'vov and Galwey 2012].

8.9.7 Reduction Rate Dependence on p_{H_2} and Reaction Regime

The relationships derived above delineate the reduction rate's dependence on hydrogen partial pressure, both in the absence and in the presence of excess water vapour in the reaction zone [L'vov and Galwey 2012]. Reported values in the absence of water vapour range from rate ~ $p^{0.35}$ to rate ~ $p^{1.0}$, and in the presence of water the reaction rate is reported to have a higher dependence rate ~ $p^{1.5}$.

Under the CDV mechanism when an oxide is reduced in hydrogen (pure or diluted with an inert gas) the vapour of the low-volatility metal is condensed and the reduction rate is limited solely by the diffusion of water vapour away from the oxide surface [L'vov and Galwey 2012]. Hence, for reactions in the equimolar regime described the diffusion equations (8.19) and (8.20) are valid. In the isobaric regime with a constant pressure of excess water vapour, diffusion limitations are eliminated such that the relationship between the reaction rate and $p_{H_2O}^{internal}$ in vacuum is defined by (8.18) [L'vov and Galwey 2012]. Thus, the two reaction regimes correspond to the following relations for $p_{H_2O}^{internal}$ [L'vov and Galwey 2012]:

$$\left(p_{H_2O}^{internal}\right)^{eq} = J^{eq}\left(\frac{zRT}{MD}\right) \qquad (8.27)$$

$$\left(p_{H_2O}^{internal}\right)^{eq} = J^{eq}\left(\frac{rRT}{MD}\right) \qquad (8.28)$$

$$\left(p_{H_2O}^{internal}\right)^{iso} = J^{iso}\left(\frac{\sqrt{2\pi MRT}}{M}\right) \qquad (8.29)$$

The relationship between the absolute reduction rate J and the rate constant k for spherical particles of initial radius r_0 and density ρ is [L'vov and Galwey 2012]:

$$J = \rho r_0 k \qquad (8.30)$$

CDV may also explain the autocatalytic behaviour of the thermal decomposition of certain compounds because of the re-absorption of the energy of condensation upon condensation of the metal vapour [Galwey 2012]. This recycled energy, to paraphrase Galwey (2012) lowers the activation energy for further sublimation of the reactant.

8.9.8 Determining the Activation Energy, E

The equilibrium constant k_p for the oxide reduction may be used with the Second Law method to find the reaction enthalpy ΔrH^0T via equation (8.31), a well-known thermodynamic relationship [L'vov and Galwey 2012].

$$\Delta rH^0T = T\left(\Delta rS^0T - R\ln k_p\right) \qquad (8.31)$$

Using the Arrhenius method the reaction enthalpy is calculated from the $\ln J$ vs. $^1/_T$ plot. Its magnitude is the slope of the plot (a straight line). The magnitude of ΔrS^0T is the plot's intercept with the ordinate (vertical) axis [L'vov and Galwey 2012].

L'vov's innovative Third Law method for calculating the activation energy, E, yields more precise magnitudes than the graphical Arrhenius method [Galwey 2012]. Note, however, that in CDV theory E is the total reaction enthalpy – which is also the vapourisation enthalpy – rather than the energy to activate a transition complex (the conventional meaning) [Galwey 2012]. While this is potentially ambiguous and possibly confusing the symbol was retained as it is commonly accepted as a measure of the temperature coefficient of the reaction rate [Galwey 2012].

This method also accounts for the consequences of reactant self-cooling as a consequence of endothermic sublimation [Galwey 2012].

8.9.9 Advantages of the Second Law and Third Law Methods

The second-law method enables both thermodynamic parameters (reaction enthalpy ΔrH^0T and ΔrS^0T) to be determined [L'vov and Galwey 2012]. In addition, the second-law method allows explicit calculation of the dependence of the absolute reduction rate J (or rate constant k) on temperature [L'vov and Galwey 2012]. Alternately, if the equilibrium constant k_p can be determined then the reaction enthalpy may be calculated directly as described above using equation (8.31) in which the entropy is known [L'vov and Galwey 2012]. Absolute values of the standard entropy S°298 and the corresponding temperature increments S°T - S°298 for most substances of interest may be found in the literature [L'vov and Galwey 2012]. This is referred to as the third-law method. Values calculated by the third-law method are more precise and reliable than by the differential Arrhenius plot or second-law methods [L'vov and Galwey 2012]. The cited source describes this, and the reduced errors, of third-law calculations in some detail to which interested readers are referred.

8.9.10 Characteristics of NiO Reduction by H_2

NiO reduction by H_2 has the following characteristics: (1) reduction proceeds in a boundary layer consisting of the solid phases NiO and Ni; (2) autocatalytic behaviour is due to changes in the area of this layer during the reaction; (3) the induction (or incubation) period before onset of the reaction depends on temperature and on the nature of the sample; (4) the presence of water vapour in the reaction zone decreases the reduction rate and increases the induction period [Galwey 2012, L'vov and Galwey 2012]. Interestingly (4) indicates that a process with a flow of hydrogen can be reasonably expected to be significantly more rapid than in a static volume of gas since the concentration of any water vapour is kept low by the flowing gas.

Arrhenius activation energy, *E*, values show considerable variation (E = 97±28 kJ mol^{-1}) in studies published 1950–1976 but far less variation in more recent studies (1989-2009; 93 ± 4 kJ mol^{-1}) due to improvements in measuring techniques and equipment [L'vov and Galwey 2012]. Chatterjee *et al.* (2012) report an activation energy of 90 kJ mol^{-1} in the temperature range 400 °C to 600 °C. The value of *E* increases in the presence of water vapour [L'vov and Galwey 2012]. In the presence of water vapour the dependence of the reduction rate on hydrogen partial pressure is $v \approx p^{1.5}$ [L'vov and Galwey 2012]. It is less in the absence of water: $v \approx p^{0.5}$ [L'vov and Galwey 2012].

A correlation was found [Chatterjee *et al.* 2012] between the concentration of oxygen vacancies in the NiO lattice and the reduction rate. The reduction mechanism is influenced by the quantity of oxygen vacancies in the NiO lattice and their transport (from bulk to the reducing surface). This must be driven by a vacancy concentration gradient: higher concentration of pores near the reducing surface and lower concentration within the bulk lattice.

Oxygen vacancies possess different potential energies and hence have different adsorption energies for hydrogen adsorption leading to a range of activation energies rather than a single one [Chatterjee *et al.* 2012].

Three steps have been identified [Chatterjee *et al.* 2012] for the reduction of NiO by dry hydrogen gas:

> (1) An induction period associated with the initial reduction of NiO and the appearance of Ni metal aggregates (initial Ni metal nucleation – from Ni vapour [Chatterjee *et al.* 2012, L'vov and Galwey 2012]). This is the dominant mode initially, and is proportional to the square root of the hydrogen pressure.
> (2) An accelerated reduction rate as the size of aggregates increases (Ni phase growth).
> (3) A pseudo-first-order process in which NiO disappears and Ni appears simultaneously until reduction slowed at fractional conversion (m.f.r. in this author's writings) of approximately 0.8.

Experimental studies also revealed that [Chatterjee *et al.* 2012] reduction occurs at the Ni-NiO interface (the first metallic Ni created by surface reduction followed by nucleation, as mentioned above), and is autocatalytic. There is an induction (i.e. nucleation) period that depends on the nature of the sample and the reduction temperature. Also, added water impedes reduction, reducing the reduction rate and increasing the induction period [Chatterjee *et al.* 2012].

8.9.11 Creep Mechanisms and Deformation Maps

High temperature oxide systems may not behave in a linear-elastic fashion in response to applied stress – particularly the metal substrate at high temperature. At high

temperature plastic deformation of the metal substrate, by creep, plays a significant role in stress reduction without macroscopic damage [Schütze 1997]. The oxide itself raises the question of the extent of plasticity of an oxide, and a distinction must be made between a bulk oxide and a growing oxide (termed by Schütze as ‘dead’ and ‘living’ respectively) [Schütze 1997]. The deformation of the growing oxide can be regarded as a superimposition of the deformation mechanisms of bulk oxides and the growth mechanism of the oxide [Schütze 1997]. While we are here interested in creep mechanisms the reader is referred to the discussion on so-termed elastic creep in oxides in the cited source for a discussion on potentially surprisingly high tolerance to strain of the system due to the presence of micro-cracks (cracks of the order of 20 μm).

Plastic deformation in the absence of diffusion processes – low temperature plasticity – occurs by the usual mode of dislocation movement (also called dislocation glide or dislocation slip) along slip systems. In oxides there are generally only two (of a possible five) slip systems; oxides are more likely to crack than take up strain by plastically deforming [Schütze 1997]. There are in addition up to three secondary slip systems for a total of five [Schütze 1997].

However, at intermediate temperatures cracks will normally begin to occur at stresses below those required to initiate secondary slip systems because of dislocation pile-ups in the primary slip system at grain boundaries [Schütze 1997]. The stress to activate secondary slip systems (thereby preventing the onset of cracks) decreases more rapidly with increasing temperature than the stress necessary to initiate micro-cracks [Schütze 1997]. Thus, at higher temperatures considerable plastic deformation by dislocation glide of both primary and secondary slip systems is possible [Schütze 1997]. Twinning may also provide a degree of plasticity preventing crack formation [Schütze 1997].

The temperatures at which some oxides of interest exhibit fracture strains greater than 0.2% was measured for bulk oxides [Schütze 1997]. Generally the temperature is above a homologous temperature of 0.5 implying that for strains without cracking above 0.2% plastic deformation by creep is the major contributor. There is one important exception: NiO. In the case of NiO it is only 0.34 homologous [Schütze 1997]; this implies that it is likely secondary slip systems are also active at lower temperature than for the other oxides considered.

However, it has been shown that the onset of micro-cracks is coincident with deviation from the linear region of the stress-strain plot, and is therefore less certain whether the significant deformation is due to elastic creep or genuine plastic deformation [Schütze 1997]. The greater strains evident during the plastic deformation of oxides at intermediate to high temperatures cannot be accounted for solely through dislocation glide [Schütze 1997].

High temperature plasticity (creep deformation) can occur as dislocation glide combined with dislocation climb (dislocation creep), recrystallisation (also called dynamic recrystallisation) and diffusion creep [Schütze 1997]. The last of these is a spectrum between two extremes: Nabarro-Herring creep (controlled by lattice diffusion) and Coble creep (controlled by grain boundary diffusion) [Schütze 1997]. Additional detail on the mechanisms as well as equations can be found in the cited source (except dynamic recrystallisation for which no suitable equation exists), and are not repeated here.

Diffusion creep, and the diffusion creep rate (also called the yield rate), is determined by the diffusion rate of the slowest species along its fastest diffusion path [Schütze 1997]. Using the equations referred to deformation maps for various oxides can be constructed [further details on this process as well as examples can be found in Schütze 1997]. Fields are demarcated on deformation maps designating the corresponding dominant deformation mechanism at a given temperature and shear stress; the resulting yield rate (constant shear rate) is commonly included also [Schütze 1997]. The estimated stress is conservative compared to real cases [Schütze 1997].

An important limitation is that crack formation is omitted, so it is possible for no significant deformation to occur under a tensile load because of earlier failure due to crack formation [Schütze 1997]. Despite the relatively simple equations the maps are based on "they are a good basis for estimating the deformation behaviour of oxides." [Schütze 1997]

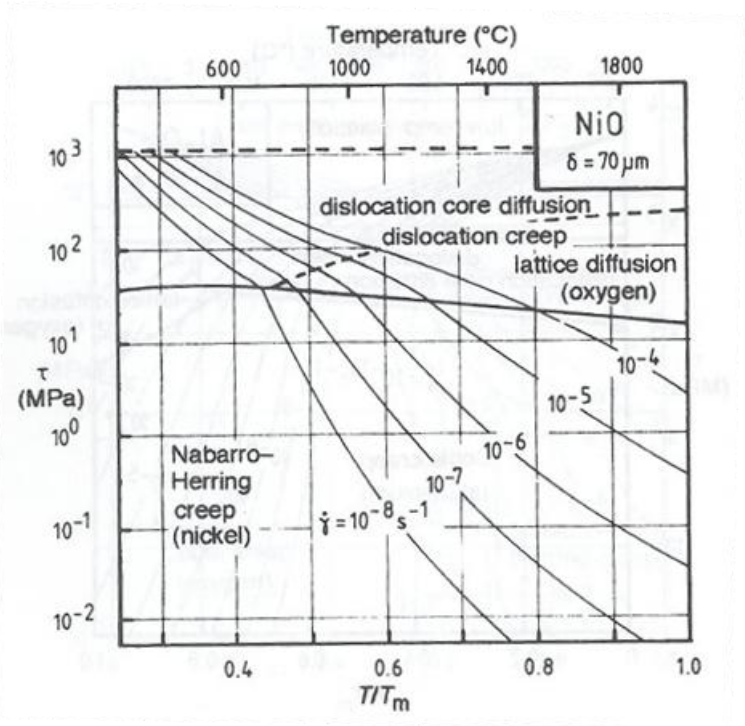

Figure 8-50. Deformation mechanism map for NiO from Schütze (1997).

Grain size has an influence on creep rate and the effect lies between $\dot{\varepsilon} \propto \delta^{-2}$ (Nabarro-Herring creep) and $\dot{\varepsilon} \propto \delta^{-3}$ (Coble creep); where δ is the grain size [Schütze 1997]. Smaller grain sizes favour Coble creep, larger ones Nabarro-Herring creep [Schütze 1997]. Compare the figure for NiO above to the two for Ni shown hereunder (of different grain sizes).

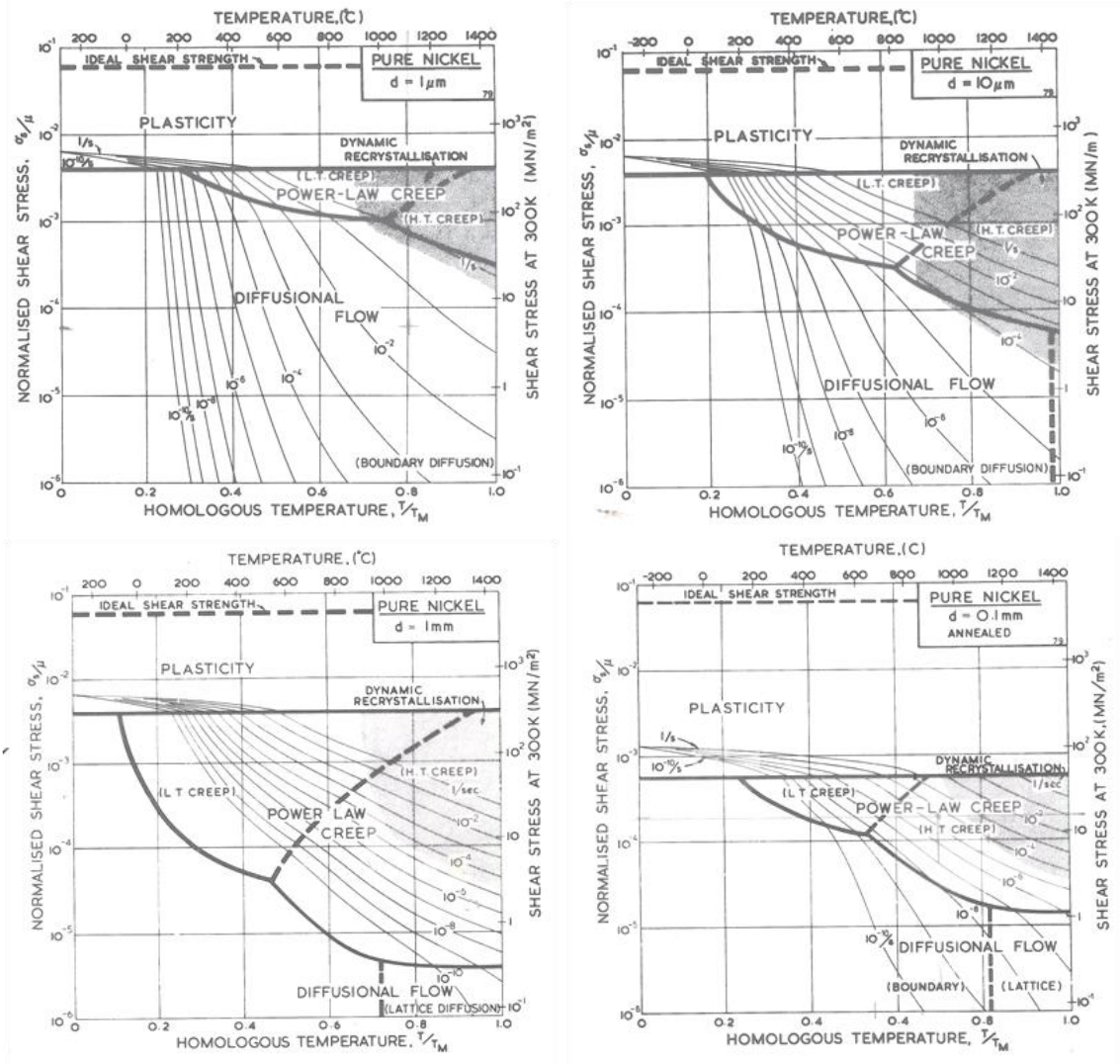

Figure 8-51. Deformation mechanism map for pure Ni (work hardened with obstacle spacing taken as 4×10^{-8}) from Frost and Ashby (1982). The shaded areas are dynamic recrystallisation. The map for annealed nickel was constructed with an obstacle spacing of 2×10^{-7} m [Frost and Ashby 1982].

In pure f.c.c. metals such as Ni the density and arrangement of dislocations determines the yield strength and plastic behaviour, and therefore the work hardening strongly impacts this [Frost and Ashby 1982].

Diffusion in oxides is greatly influenced by lattice disorder, and since the diffusion rates in the oxide determine the creep rate (dislocation creep as well as both types of diffusion creep), it follows that the degree of lattice disorder affect the deformation behaviour [Schütze 1997]. The oxygen partial pressure of the atmosphere in which the oxide resides influences the degree of disorder of the oxide [Schütze 1997]. Generally the degree of lattice disorder increases in oxygen-deficient (or metal-excess) oxide systems with decreasing oxygen partial pressure [Schütze 1997]. Conversely the lattice disorder increases with increasing oxygen partial pressure in metal-deficient oxides such as FeO, CoO and NiO [Schütze 1997]. At temperatures of 1,070 °C to 1,550 °C and a stress of 10–159 MPa stress has a strong influence on creep rate and the oxygen partial pressure has a relatively small negative effect or no effect at all [Schütze 1997]. This led to the conclusion that the dominant creep mechanism in NiO is dislocation creep [Schütze 1997]; this study was carried out on NiO single crystals, however. Thus, no oxide grain boundaries were included.

Porosity has a marked effect on creep deformation [Schütze 1997], greatly increasing the strain rate for a given stress state and temperature. This has been formulated, at least for compressive loading to be $\dot{\varepsilon} \propto \frac{1}{1-p^{2/3}}$ (see equation (55) in cited source).

High fracture strains (that is to say surprising apparent plasticity) in oxide scales can be created by a mechanism in which the formation of micro-cracks is superimposed with healing of those crack to result in rapid oxidation and the production of perfect oxide scales at low deformation rates [Schütze 1997]. It is assumed that the micro-cracks present in the growing oxide have already formed (due to growth stresses for example) and is subjected to a tensile load (due to ongoing oxide formation for instance) [Schütze 1997]. At a critical strain (or equivalent critical stress) the micro-cracks grow creating a crack network open to the atmosphere at the surfaces as shown in Figure 8-52. Given sufficient oxygen partial pressure and the continuation of cation transport the oxide will continue to grow – on the faces of the cracks [Schütze 1997].

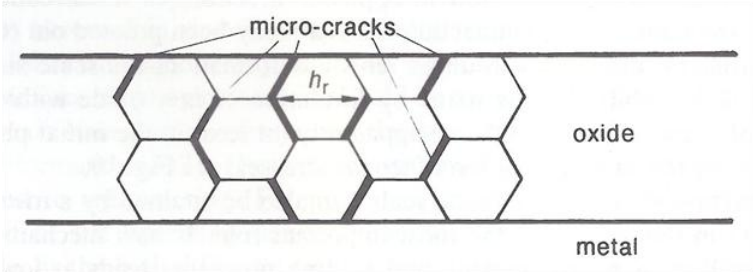

Figure 8-52. Schematic of micro-crack network growth and healing in oxide scales [Schütze 1997].

This results in a reduction in the length and width of cracks, leading to local crack healing/closure [Schütze 1997]. Further tensile deformation expands the crack network by lengthening existing cracks or seeding new ones [Schütze 1997]. A critical strain rate

can be calculated (see cited source for method) above which the crack network continues to grow and below which it heals [Schütze 1997].

8.10 Reduction Experiments

A number of samples were oxidised as described in section 8.2 for 42 h in accordance with the results for the oxidation experiments; fully oxidised having a mass fraction of Ni converted to NiO of >95%. All samples were tubes of 99.5% pure nickel OD 5.9 mm, wall thickness 125 μm from Goodfellow Cambridge Ltd., cleaned in an acetone ultrasonic bath for 5 min prior to oxidation. A short tube 10 ±1 mm long was deemed sufficient for these experiments. Forty-eight samples were used initially. The samples were reduced at different temperatures (600 °C, 800 °C and 1,000 °C) for different periods of time, the range of these estimated based on the rapidity of the process noted previously [Camilleri 2009]. The gas mixture consisted of 5 vol.% H_2, balance Ar with a total pressure of 1 atm (absolute) and gas flow rate (measured by a rotameter) of 0.6 litres per min.

The fully oxidised samples are very fragile. Therefore, they were reduced on wire holders made of NiCr alloy (80/20 Ni/Cr by mass; commercial name Nichrome) for ease of handling. These formed a separate set from those used for oxidising samples since an oxidised jig may interfere with the sample reduction by providing a p_{O_2} additional to that of the samples.

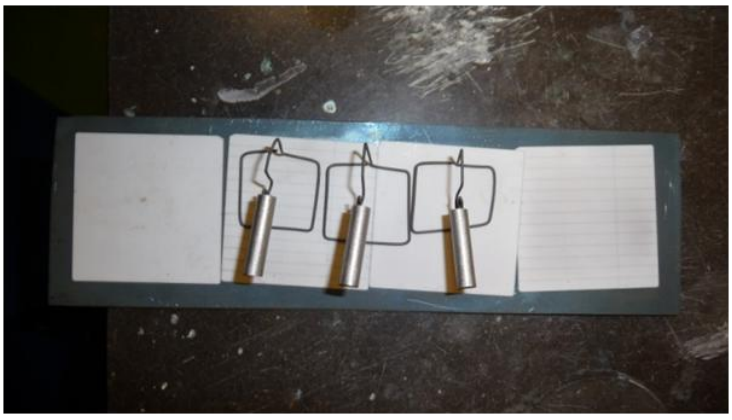

Figure 8-53. Samples hung on wire jigs for ease of handling. Shown on alumina sheets placed on a stainless steel tray ready for loading into the furnace.

In order to establish an experimental plot for the reduction process akin to that for oxidation of metals several time intervals were chosen for each temperature that would give a good spread of data points (although in fact few were used for reasons explained later). It was expected that the results would conform to a parabolic law, assuming the process is diffusion-controlled. Due the precise time to complete reduction being initially unknown, the first time interval was a 0 h dwell (i.e. heating up to reduction

temperature then cooled) followed by a 2 h dwell, the dwell times of the remaining samples was revised accordingly.

Unfortunately, the nature of the experiment precludes simply opening the furnace when a particular sample's dwell is complete and removing only that sample while leaving the remainder inside. Instead each time interval was run as a separate experiment with three of the samples at a time (so each dwell time was run twice giving some indication of run-to-run reproducibility). It is worth noting that as a result of this the samples are exposed to a varying temperature (from room temperature to the reduction temperature) for the 2 h to 4 h 15 min required to heat the furnace to the reduction temperature, and approximately three times that period for the cooling cycle. It is expected this will have some effect on the reduction process and resultant microstructure, albeit one not possible to determine precisely.

The specific heating rates follow: ramp at 5 °C min^{-1} to 600 °C then at 3 °C min^{-1} to higher temperatures. Cooling nominally occurs at the same controlled rates although in practice it was noticed that cooling takes three to four times longer. The SOP (Standard Operating Procedure, see Appendix F: Horizontal Hydrogen Furnace SOP) dictates that the reducing gas is introduced with the furnace cold and only switched to Ar (the purge gas) once the furnace has cooled to near room temperature. As a result of this safety requirement some reduction is expected to occur during the ramp to the desired reduction temperature and ramp back down to room temperature.

The first experiment for each temperature was a ramp up to reduction temperature followed by a ramp down to room temperature with no dwell time (referred to as the ramp only or 0 h dwell run). This is very useful since it both sets the point of least dwell in building a mass loss plot for reduction akin to Figure 8-4. and Figure 8-36. for oxidation, as well as providing some calibration by indicating to what degree a sample is reduced at the specified temperature simply due to the process requirements of ramping to temperature exposed to the reducing gas prior to being reaching the desired dwell temperature rather than an isothermal exposure.

The final choice of reduction temperature is based on three factors. Firstly, from thermodynamics an elevated temperature will yield a more rapid reduction than a lower temperature, advantageous from a mass manufacture standpoint. Secondly, since the creation of a model similar to that for oxidation is eminently desirable the spread of temperatures should yield useful insight into the kinetics of the mechanisms involved (which may be modified significantly by the nature of the samples, as was noted regarding oxidation). Finally, it was initially important to avoid fully reducing the samples, instead reducing to ideally somewhere between 25% and 50% reduction in oxygen content. By fully reducing a sample the only information gained is that it is fully reduced. By partially reducing samples a reduction rate plot can be constructed. For

similar reasons the use of a second hydrogen partial pressure was planned for a later tier of experiments.

It is worth reiterating that unlike previous work [Camilleri 2009], the purpose of this experiment is both to determine a reasonably accurate rate constant for the reduction and optimise it by identifying the best time for the reduction process to yield a good compromise in performance and properties between shortest time, lowest temperature, maximum porosity, and complete reduction.

As with the oxidation work, analysis is based on mass change: uptake of oxygen from the oxidation step and loss of oxygen from the reduction step. Each sample was weighed before and after oxidation, and finally after reduction. These measurements were used to plot mass loss from the oxidised samples against reduction time to determine the time necessary to fully reduce a given (completely oxidised) sample that has gained a known mass of oxygen.

Characterization was also by visual inspection and using SEM imaging, of both the surface and cross-sections (trenches created by FIB). The FIB used was a FEI XP200 and the SEM utilized was an FEI XL30 SFEG.

This method was followed for all subsequent tiers of reduction experiments, with the following modifications. Longer, 25 ±1 mm, tubes were used. Even at the lowest temperature used in this tier of experiments the dramatically greater concentration of hydrogen available reduces process times to the order of a few seconds (see calculations below) making it somewhat challenging to obtain meaningful results with the system available. Furthermore, I had found the smaller 10 mm samples suffer far more frequent breakage.

The second experimental tier consisted of a total of 78 samples, reduced in trios as before separated into two runs per temperature-dwell combination. The samples were reduced at different temperatures (1,000 °C, 800 °C, 600 °C and 400 °C) for different periods of time, the range of these estimated based on the rapidity of the process noted previously [Camilleri 2009]. The gas mixture was pure H_2 (minimum 99.995 vol.% with N_2, H_2O and O_2 the most likely contaminants, BOC Industrial Gases) at 1 atm (absolute). In all cases the gas flow rate (measured by rotameter) was 0.8 litres per min. This is a greater volumetric flow rate than for tier 1 as it was found to be the minimum necessary for the Davey lamp fitted to the furnace to burn off the exhaust (unnecessary with the non-flammable mix utilised previously).

In order to establish an experimental plot for the reduction process akin to those for oxidation of metals time intervals were chosen for each temperature (keeping in mind the expected parabolic nature of the curve) that would give a good spread of data points. The exact number varies as it was adapted from experiment to experiment according to

the degree of reduction measured by mass loss. The ramp to temperature varied from 1 h 20 min to 4 h 15 min, and three to four times that for cooling, as before. Ramp rates were unchanged.

The purpose of this experiment remained the same: determine a reasonably accurate rate constant for the reduction and identify the best time for the reduction process to yield a good compromise between shortest process time, lowest temperature reduction, maximum porosity, and complete reduction.

8.11 Process Optimization with 5 vol.% H_2

This first tier of experiments aims to gather sufficient data to determine the effect of temperature on microstructure and the time required for complete reduction of the samples as well as to assess the repeatability of the reduction process.

8.11.1 Results & Discussion

Table 8-9. summarises the results of the experiment, and gives the mass gain from oxidation of each sample, the mass fraction oxidised, the mass loss from reduction and the mass fraction reduced (the mass of oxygen lost divided by the mass of oxygen gained; so a mass fraction reduced of unity means all the oxygen gained by oxidation was removed by hydrogen reduction) for each dwell. Notice that the time is dwell at the indicated temperature. This differs from oxidation where samples are loaded hot so the oxidation time is the entire dwell in the furnace. Furthermore, the samples undergo some reduction in the ramp to and from the dwell temperature as noted previously; the dwell does not constitute the entire time undergoing reduction. Figure 8-54. shows a plot of experimental results. Errors estimated based on linear approximation by partial differentiation where an equation was used [Error Propagation article accessed 2013], or based purely on measurement equipment error. In all cases errors represent the worst case scenario. Due to a small problem with the rotameter samples F.03, G.03 and H.03 replace F.02, G.02 and H.02 (these last are not displayed in this document).

Sample	**m_{gain} (mg)** ±2 mg	**Mass fraction oxidised** ±0.001	**t_{dwell} (h)** ±1 s	**m_{loss} (mg)** ±2 mg	**Mass fraction reduced** ±0.034
Reduction at 600 °C					
RT-A.23/03/11-125.1100(600)-F.01 D	53.7	1.000	ramp	6.8	0.126
RT-A.23/03/11-125.1100(600)-G.01 M	49.8	1.000	ramp	7.1	0.143
RT-A.23/03/11-125.1100(600)-H.01 U	56.1	1.000	ramp	6.8	0.120
RT-A.30/03/11-125.1100(600)-I.01 D	54.9	0.999	ramp	4.9	0.089
RT-A.30/03/11-125.1100(600)-J.01 M	56.1	1.001	ramp	5.1	0.090
RT-A.30/03/11-125.1100(600)-K.01 U	56.7	1.000	ramp	5.1	0.090
RT-A.21/06/11-125.1100(600)-F.03 D	53.5	1.000	2	8.1	0.152
RT-A.21/06/11-125.1100(600)-G.03 M	54.3	1.000	2	8.4	0.154
RT-A.21/06/11-125.1100(600)-H.03 U	52.4	0.999	2	7.8	0.149
RT-A.09/05/11-125.1100(600)-I.02 D	54.7	1.000	2	23.1	0.423

RT-A.09/05/11-125.1100(600)-J.02 M	54.5	1.000	2	24.0	0.440
RT-A.09/05/11-125.1100(600)-K.02 U	53.1	1.000	2	31.1	0.586
Reduction at 800 °C					
RT-A.25/05/11-125.1100(800)-L.01 D	54.6	1.000	ramp	35.6	0.652
RT-A.25/05/11-125.1100(800)-M.01 M	49.7	1.000	ramp	36.0	0.723
RT-A.25/05/11-125.1100(800)-N.01 U	58.5	1.001	ramp	50.7	0.867
RT-A.01/06/11-125.1100(800)-O.01 D	53.0	1.000	ramp	10.7	0.201
RT-A.01/06/11-125.1100(800)-P.01 M	55.9	0.999	ramp	11.5	0.206
RT-A.01/06/11-125.1100(800)-Q.01 U	54.2	0.999	ramp	11.4	0.210
RT-A.08/06/11-125.1100(800)-L.02 D	54.4	1.000	2	8.9	0.164
RT-A.08/06/11-125.1100(800)-M.02 M	52.7	1.000	2	9.3	0.176
RT-A.08/06/11-125.1100(800)-N.02 U	52.2	1.000	2	11.3	0.216
RT-A.08/06/11-125.1100(800)-O.02 D	53.0	1.001	2	8.4	0.158
RT-A.08/06/11-125.1100(800)-P.02 M	51.8	1.000	2	8.2	0.159
RT-A.08/06/11-125.1100(800)-Q.02 U	57.1	1.000	2	9.0	0.157
Reduction at 1,000 °C					
RT-A.13/07/11-125.1100(1000)-R.01 D	55.2	0.999	ramp	11.3	0.204
RT-A.13/07/11-125.1100(1000)-S.01 M	57.5	0.999	ramp	12.2	0.212
RT-A.13/07/11-125.1100(1000)-T.01 U	59.9	0.999	ramp	13.0	0.217
RT-A.20/08/13-125.1100(1000)-U.01 D	55.8	1.000	ramp	11.9	0.214
RT-A.20/08/13-125.1100(1000)-V.01 M	50.2	0.999	ramp	11.7	0.232
RT-A.20/08/13-125.1100(1000)-W.01 U	50.9	1.000	ramp	11.4	0.224
RT-A.18/07/11-125.1100(1000)-R.02 D	55.4	1.000	2	23.9	0.431
RT-A.18/07/11-125.1100(1000)-S.02 M	55.3	0.999	2	26.4	0.477
RT-A.18/07/11-125.1100(1000)-T.02 U	56.7	1.000	2	26.1	0.461
RT-A.20/08/13-125.1100(1000)-U.02 D	56.8	1.000	2	26.6	0.468
RT-A.20/08/13-125.1100(1000)-V.02 M	48.4	1.000	2	24.8	0.512
RT-A.20/08/13-125.1100(1000)-W.02 U	51.2	1.000	2	26.9	0.526
RT-A.01/10/13-125.1100(1000)-R.04 D	57.3	1.000	10	55.4	0.967
RT-A.01/10/13-125.1100(1000)-S.04 M	51.8	1.000	10	50.5	0.975
RT-A.01/10/13-125.1100(1000)-T.04 U	51.6	1.000	10	49.2	0.954
RT-A.09/10/13-125.1100(1000)-U.04 D	53.3	1.000	10	43.0	0.807
RT-A.09/10/13-125.1100(1000)-V.04 M	57.8	1.001	10	47.7	0.826
RT-A.09/10/13-125.1100(1000)-W.04 U	56.4	1.001	10	47.0	0.834
RT-A.18/09/13-125.1100(1000)-R.03 D	53.2	1.000	15	53.1	0.999
RT-A.18/09/13-125.1100(1000)-S.03 M	51.7	1.000	15	51.7	1.000
RT-A.18/09/13-125.1100(1000)-T.03 U	52.9	1.000	15	52.9	1.000
RT-A.24/09/13-125.1100(1000)-U.03 D	53.4	1.000	15	53.2	0.996
RT-A.24/09/13-125.1100(1000)-V.03 M	56.0	1.000	15	55.8	0.997
RT-A.24/09/13-125.1100(1000)-W.03 U	52.0	1.000	15	51.8	0.996

Table 8-9. Mass loss and mass fraction reduced of Tier 1 reduction. All temperatures reduced in 5 vol.% H_2 (balance Ar) shown. D, M, U after the sample code indicates whether it was downstream, in the middle or upstream with respect to the gas supply (respectively). Full table can be found in Appendix G: Complete Reduction Results Tables.

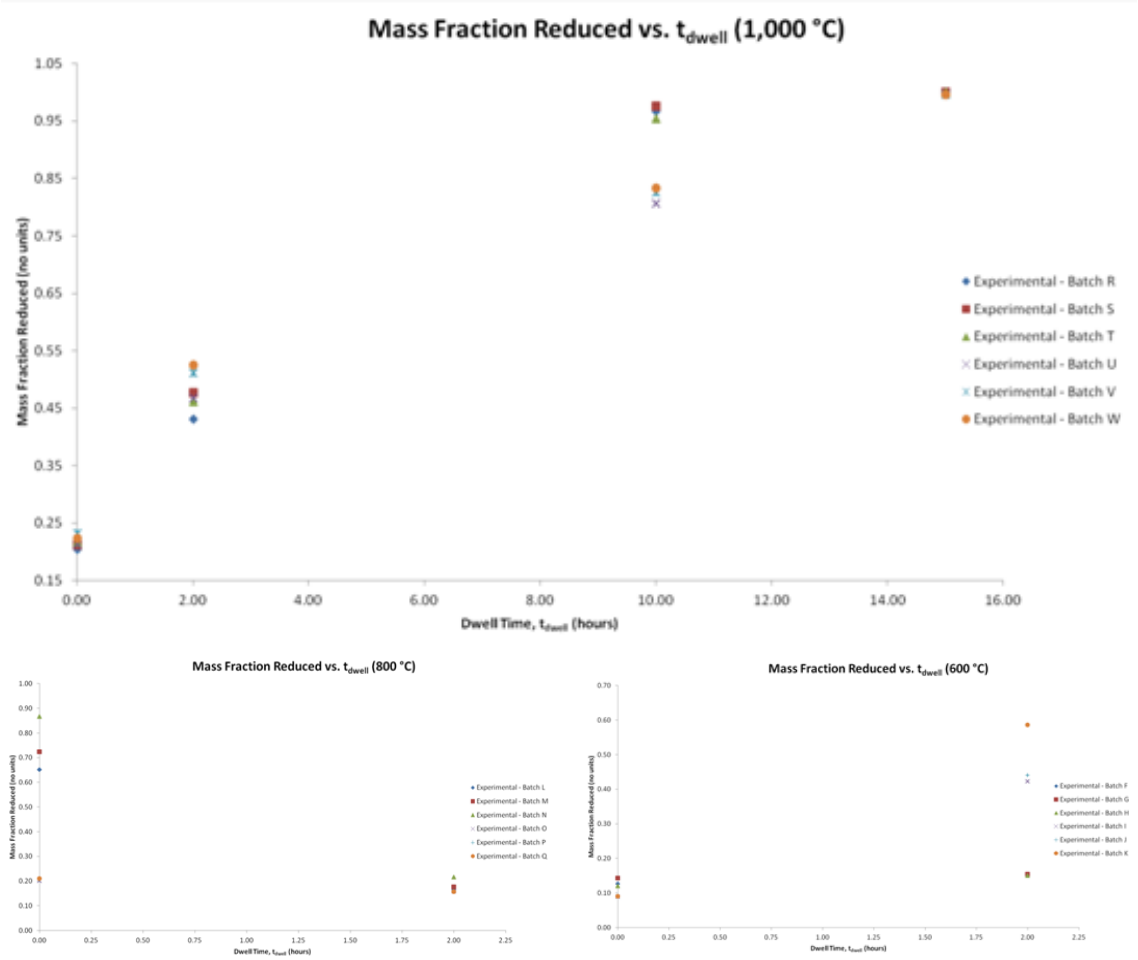

Figure 8-54. Plot of mass fraction reduced against dwell for all batches. The plot for 1,000 °C is emphasised both because it was the most meaningful and because it was the most promising of the three.

Initially results appeared promising with the ramp (0 h dwell) showing some reduction. As the results unequivocally show, however, even at the highest temperature investigated the kinetics are very slow. It was expected that those samples closest to the gas source would show somewhat greater reduction than those farthest downstream. This did not prove to be the case for all but one run at 600 °C, the majority of runs at 800 °C, and half the runs at 1,000 °C. There appears to be no discernible pattern as to reduction temperature or dwell for this behaviour other than some influence of the reduction temperature on the mass fraction reduced during heat up. I believe this to conform to the behaviour described by L'vov and Galwey (2012) and Galwey (2012) whereby the incubation period is longer in the presence of a diluting gas (water vapour and also argon in this case).

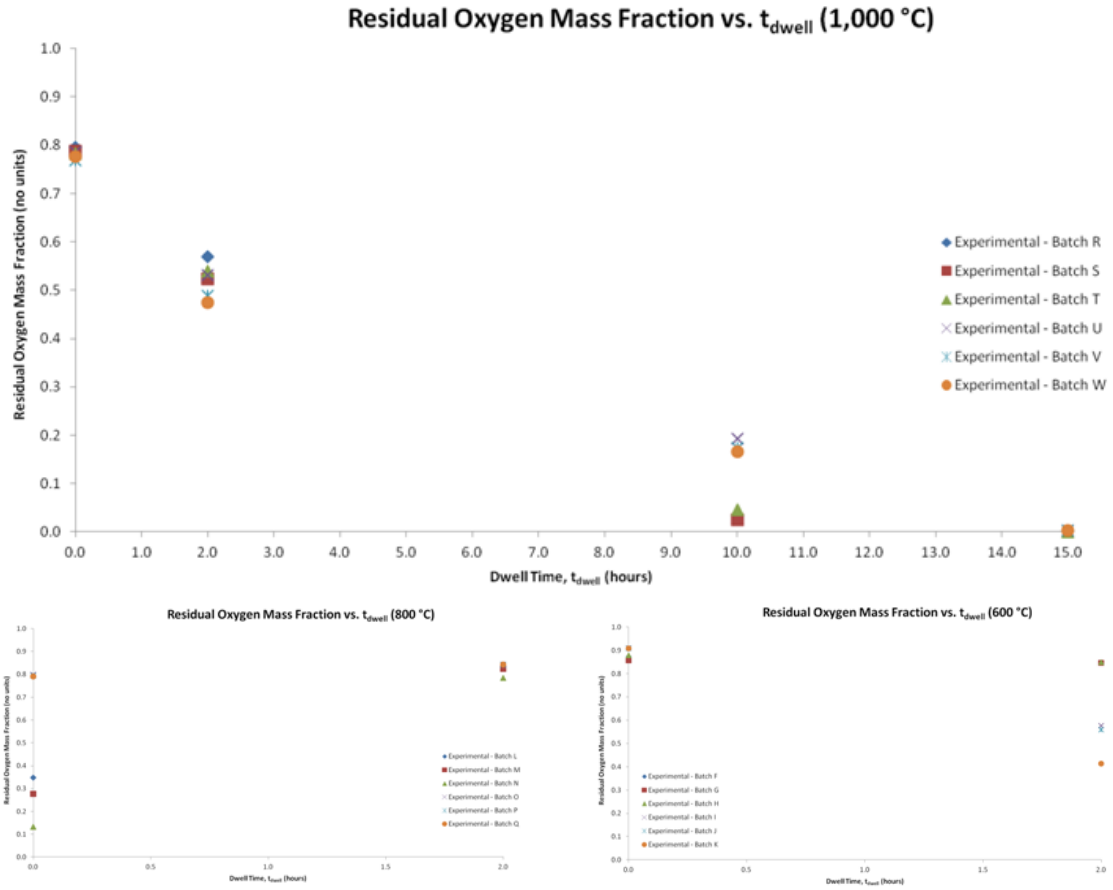

Figure 8-55. Residual oxygen mass fraction, $\frac{(m_{gain}-m_{loss})}{m_{gain}} = 1 - \frac{m_{loss}}{m_{gain}}$, against dwell for all batches. The plot for 1,000 °C is emphasised both because it was the most meaningful and because it was the most promising of the three.

The residual oxygen mass fraction, plotted above in Figure 8-55, varies from 1 to 0. It is the fraction, by mass, of oxygen that remains after the reduction step, representing the converse of the mass fraction reduced. It is another way to conveniently portray the progressing of reduction through the samples. It is perhaps particularly clear in its depiction of this because it continues the thread of tracking the gain and loss of oxygen by mass. The mass fraction reduced, on the other hand, is essentially a percentage completion for the reduction, a subtly different metric. As with the plots of mass fraction reduced there is little can be determined for those samples reduced at 600 °C and 800 °C due to the somewhat erratic behaviour as discussed already. One observation of interest is that the scatter tends to be minimal or relatively large, although the trend from small to large scatter with dwell is reversed for some unknown reason at 800 °C. What instead shows very clearly is that the ramp alone accounts for approximately 20% of the oxygen mass fraction removed from the samples, regardless of reduction temperature. This implies that reduction starts at a considerably lower temperature and then slows: it is the same across all reduction temperatures because during ramp up some reduction occurs in a surface-and-near-surface region, common regardless of the final reduction temperature. The change in temperature is not

instantaneous and thus there will be some sites whose surface energy state (e.g. due to local defects) results in a lower activation energy for reduction to occur at those local sites and therefore a local combination of chemisorption and physisorption (or desorption) will exist contributing over time to the mass of oxygen removed even at low temperatures.

The rate calculation that gives the plots in the figure below (Figure 8-56.) could have been based on the mass fraction reduced, the residual oxygen mass fraction or the mass loss. The last of these was preferred as it conveniently is mass per unit surface area, comparable to similar work carried out in analysis of the oxidation experiments (see section 8.3 onwards). More crucially the mass loss is not a derived variable, but a measured one.

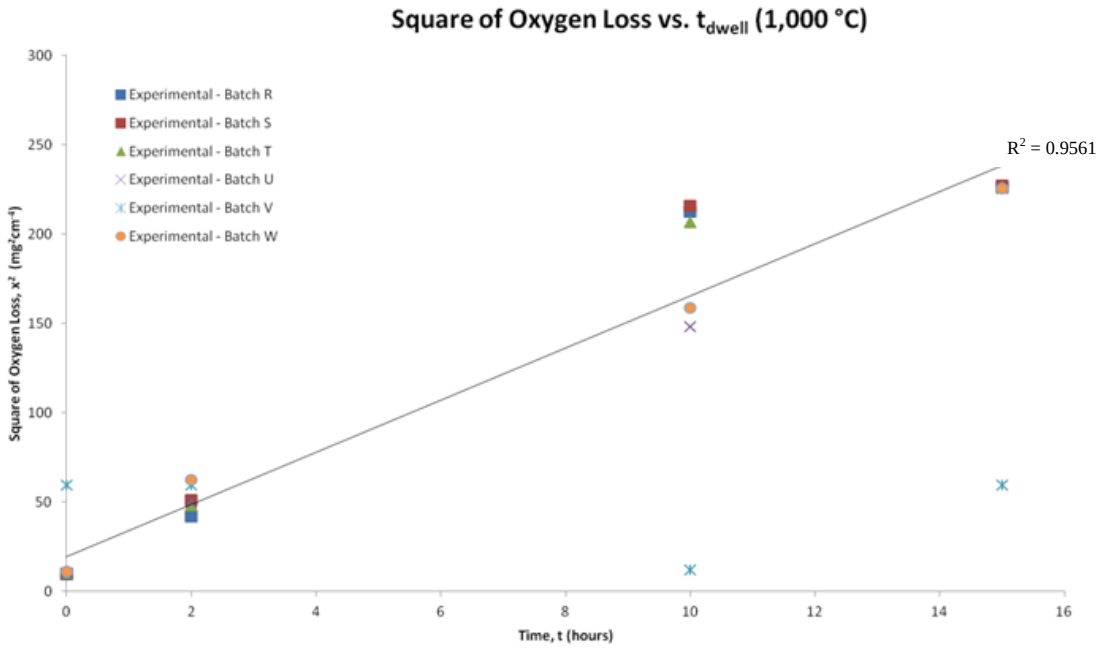

Figure 8-56. Oxygen loss squared against dwell for 1,000 °C, akin to the square of the mass gained during oxidation previously. This was the most meaningful promising of the three so is given greater prominence.

Based on Figure 8-55. it appears that reduction behaviour is parabolic with dwell, agreeing with my earlier assumption – essentially confirmed by Figure 8-56. (note the excellent parabolic fit with an index of 1.8; recall that the square was plotted). An index of 1 indicates linear (and therefore surface and near surface transport) while a 2 indicates bulk transport. Values in between proportionally indicate behaviour that combines both mechanisms. The most facile technique to determine this is by plotting the log of both axes. The inverse of the gradient is the index (a gradient of 0.5 would be parabolic for example). The previous statement applies strictly at 1,000 °C, the comparative lack of data at the lower temperatures (for reasons explained subsequently)

means the behaviour at other temperatures is not known for certain. I think it will also be linear, though subject to large scatter.

About half the runs at 600 °C and 800 °C exhibited inconsistent results; one or more samples per run for a given dwell time exhibited very different results (20–40% more reduction for instance) with no pattern discernible (e.g. had they all been in the same position with respect to the gas flow there may have been a pertinent phenomenon to observe). Samples with large differences in mass fraction reduced yielded no explanations for this. This is made especially clear once the scatter on the plots (and concomitantly poor fit of the linear fit to match a parabolic law) is taken into account. Hence, the initial experimental plan, presented above in its original format, was suspended before commencing the runs at 1,000 °C and an investigation into the cause of these seemingly anomalous results undertaken. It was expected that this would also reveal possible methods to alleviate the slow kinetics somewhat since eliminating all possible sources of oxygen other than the samples would result in a greater concentration of hydrogen available for reduction as well as larger concentration gradients to accelerate diffusion (although the differences would be small).

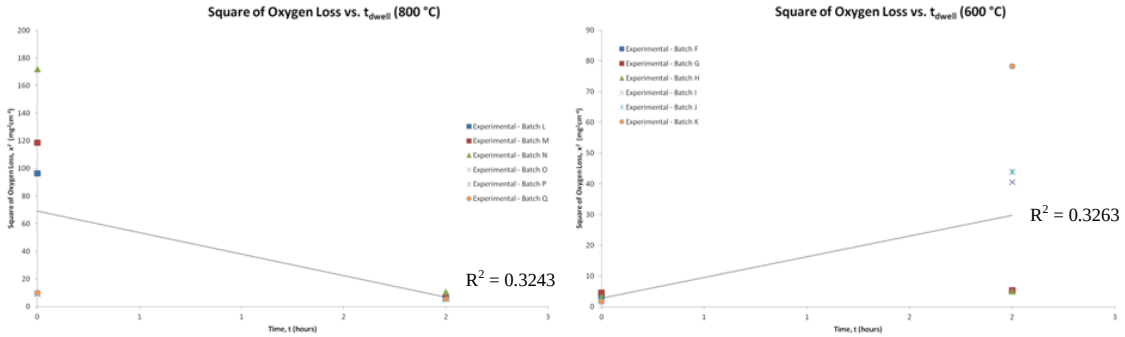

Figure 8-57. Oxygen loss squared against dwell 600 °C and 800 °C.

The first part of this investigation involved a careful analysis of the thermodynamics involved by use of an Ellingham Diagram (shown below). For each temperature of interest the minimum H_2/H_2O ratio was calculated as well as the threshold p_{O_2} (any partial pressure of oxygen above results in oxidation of the samples, while any partial pressure of oxygen below the threshold results in reduction). Note these are equilibrium values.

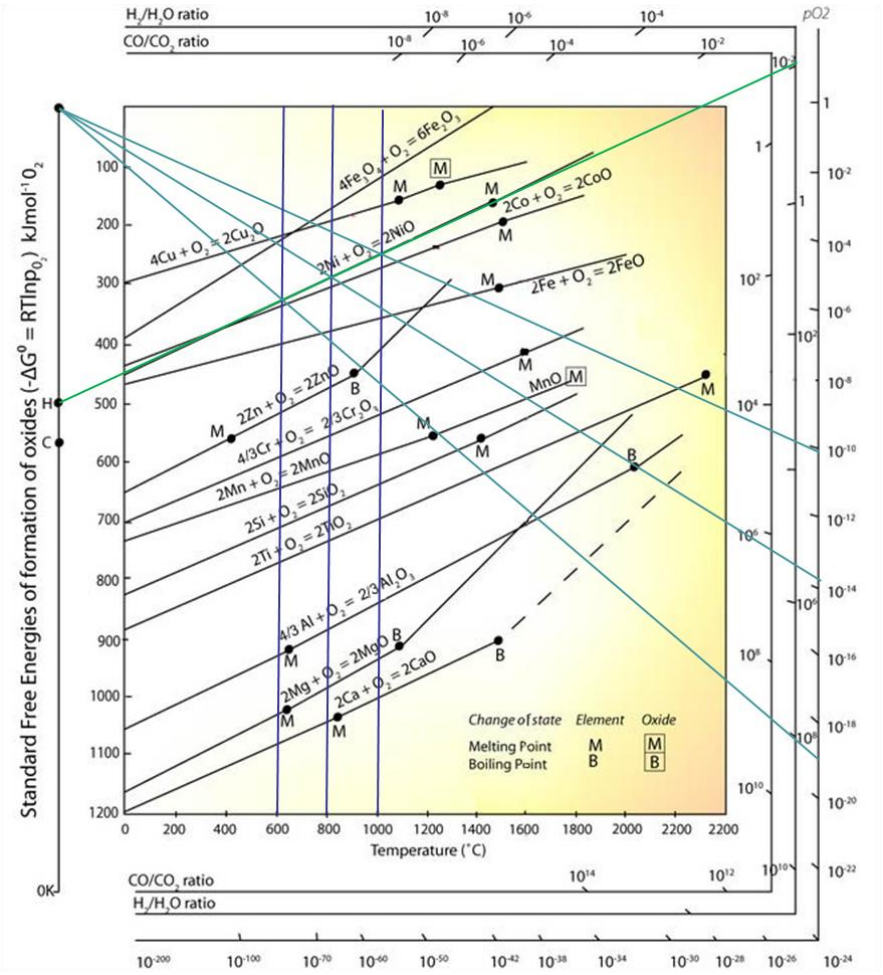

For Nickel:		
At 600 °C	—	$H_2/H_2O \approx 1\%\ p_{O_2} \approx 2 \times 10^{-19}$ atm
At 800 °C	—	$H_2/H_2O \approx 1\%\ p_{O_2} \approx 2 \times 10^{-14}$ atm
At 1,000 °C	—	$H_2/H_2O \approx 1\%\ p_{O_2} \approx 8 \times 10^{-11}$ atm

Figure 8-58. Ellingham diagram showing graphical calculation for H_2/H_2O ratio as well as the threshold p_{O_2} at 600 °C, 800 °C and 1,000 °C for Ni. Source: http://www.doitpoms.ac.uk/tlplib/ellingham_diagrams/ellingham.php

Ergo, while a 5 vol.% hydrogen reducing gas is indeed sufficient to achieve complete reduction it is exceedingly challenging to remain below the threshold p_{O_2}. The most likely scenario explaining how this is the case and yet significant reduction occurs anyway is that the system is highly dependent on local conditions that themselves change over time; at a random moment in time local gas fluxes will result in a p_{O_2} below the threshold, enabling reduction to occur at the local temperature, only for the balance to shift as the gas flows over the sample. It is the combination of NiO/Ni and the gas phase that defines the local p_{O_2} at each thermobaric condition. Even a very small arrival of oxygen will cause the H_2/H_2O ratio to increase slightly.

It is helpful to estimate the minimum time for complete reduction assuming the reduction itself is instantaneous, hydrogen diffusion to the reaction site is not rate-limiting and the availability of hydrogen is the dominant mechanism. This represents the absolute minimum time necessary to completely reduce the samples.

A 10 mm long Ni tube contains $\frac{0.202}{58.69} = 3.44181 \times 10^{-3}$ moles of nickel.

Assuming the oxide is stoichiometric there will be a like number of oxygen atoms to remove by reduction. This is a very solid assumption as there is no evidence in the literature that Ni forms anything but its stoichiometric oxide. Assuming further that the reduction reaction is also perfectly stoichiometric, twice as many hydrogen atoms as oxygen atoms will be needed to reduce the sample.

This means 6.8836×10^{-3} moles of hydrogen are needed to reduce one sample.

Now, the flow rate used was 0.6 litres per minute, 5 vol.% of which is hydrogen (balance Ar). Hence, the flow of hydrogen is 5×10^{-7} $m^3 s^{-1}$.

At each temperature we use a slightly modified version of the common thermodynamic relationship $PV = nRT$ to determine the number of moles per second of hydrogen that are available. The only modification is converting it to deal with rates rather than constant values:

$$P\dot{V} = \dot{n}RT \qquad (8.32)$$

Where:

P = pressure (Pa)
$\dot{V}$ = volumetric flow rate of hydrogen ($m^3 s^{-1}$)
$\dot{n}$ = molar flow rate of hydrogen (mol s^{-1})
R = universal gas constant (8.314472 J $mol^{-1} K^{-1}$)
T = absolute temperature (K)

Reduction Temperature (°C)	Molar Flow Rate (mol s^{-1})	Minimum Exposure (min)
600	6.9784×10^{-6}	16.4
800	5.6773×10^{-6}	20.2
1,000	4.7854×10^{-6}	24.0

Table 8-10. The molar rate of hydrogen required for reduction of samples and corresponding minimum exposure time with 5 vol.% H_2 (balance Ar) gas mix (Tier 1).

Thus a minimum of 16.4 minutes of exposure are needed to reduce the sample (at the lowest temperature – 600 °C). The effect of hydrogen depletion can be neglected given the times samples are typically reduced for. In just a ramp-only run (8 h for a 600 °C,

no-dwell, ramp-only run start to finish – the shortest possible) 0.2 moles of hydrogen are available, but only 0.007 moles are needed.

As shown above the availability of hydrogen is more than sufficient (and indeed enough to replace any local depletion rapidly). Efforts were made, therefore, to lower the overall system p_{O_2} below the threshold. To achieve the desired conditions and consistency of results a number of possible additions and/or modifications to the system were made, detailed below.

The potential sources of oxygen in the system are:

- the small quantity of impurities in the hydrogen gas include water vapour and oxygen (limited to about 100 ppm)
- at high temperatures the water vapour that results from reduction of the NiO samples may readily dissociate
- the furnace itself may be out-gassing despite the use of an alumina furnace tube
- the furnace utilises porous borosilicate heat shields which may absorb and/or adsorb water vapour from the atmosphere while loading or unloading the furnace (or possibly even when it is not in use via very small leaks through the seals)
- while no leaks through the seals has ever been detected even after repeated extended tests in excess of process pressures it is possible a minute leak exists

Possible solutions include:

- adding getters (ideally very near the samples) to absorb oxygen
- passing the process gas (5 vol.% H_2, balance Ar plus impurities of the order of a few hundred ppm) over a separate oxygen getter before flowing into the furnace inlet
- rather than flowing hydrogen over the samples the furnace is instead filled to a fixed pressure, so the reduction is carried out without introducing any additional sources of oxygen via the gas impurities

A series of experiments was undertaken to identify and eliminate all possible sources of oxygen in the system other than the oxidised samples themselves. Ti getters were utilised to measure the mass of oxygen gained from these unwanted p_{O_2} sources (no NiO sample was present so any oxidation came from other sources – sources that must be eliminated for the atmosphere in the reduction furnace to be conducive to completely reducing the NiO samples as intended).

Titanium is an ideal oxygen getter because it readily absorbs up to approximately a third of its mass in oxygen. Based on the average mass of oxygen absorbed by the Ni samples during oxidation it was possible to determine that 180 mg of oxygen are to be removed

from all three samples per batch during reduction. Allowing for up to 100 reduction runs to ensure the same getters may be reused throughout the project, combined with the available Ti sheet the size of the necessary getter was calculated. This total volume was divided into seven sections: one under each sample, two between the samples and one upstream of the samples and one downstream. Dividing the getter in this way allows discreet determination of where oxygen is being absorbed – possibly indicating its source.

The procedure was modified stepwise; at each step all 7 getters were weighed. The details of the stepwise modification to the process and the mass change of the getters are shown below. The stainless steel tray and alumina sheets were also weighed but no significant weight changes were measured (a mere 270 μg for the alumina and 40 mg from the stainless steel: note for the latter a less accurate balance had to be used because the tray did not fit on the usual one, in both cases the total mass change over the period is within the measurement error of the relevant electronic balance).

Getter	**Upstream**			**→**			**Downstream**
	1	**2**	**3**	**4**	**5**	**6**	**7**
m_0 **(mg)** ±1 mg	6,755.2	6,730.3	6,684.5	6,698.7	6,861.9	6,735.9	6,818.4
m_1 **(mg)** ±1 mg	6,794.7	6,753.4	6,704.0	6,716.3	6,878.6	6,751.8	6,838.4
m_2 **(mg)** ±1 mg	6,832.5	6,737.4	6,778.9	6,739.3	6,900.9	6,776.4	6,866.7
m_3' **(mg)** ±1 mg	6,770.1	6,732.9	6,895.2	6,818.2	6,759.6	6,689.7	6,722.6
m_3 **(mg)** ±1 mg	6,789.2	6,749.8	6,912.4	6,831.9	6,772.7	6,729.9	6,729.2
m_4 **(mg)** ±1 mg	6,806.3	6,765.3	6,927.6	6,846.1	6,787.1	6,743.6	6,747.5
m_5 **(mg)** ±1 mg	6,812.5	6,771.6	6,935.6	6,855.9	6,797.3	6,758.0	6,759.1
m_6 **(mg)** ±1 mg	6,825.6	6,782.9	6,945.0	6,863.9	6,805.2	6,766.0	6,771.6
m_7 **(mg)** ±1 mg	6,842.4	6,795.4	6,955.8	6,874.0	6,814.8	6,776.8	6,784.1
m_8 **(mg)** ±1 mg	6,850.9	6,802.0	6,961.7	6,878.9	6,820.4	6,784.0	6,792.3
m_9 **(mg)** ±1 mg	6,855.5	6,805.8	6,964.5	6,881.0	6,822.7	6,786.9	6,796.2
m_{10}' **(mg)** ±1 mg	6,854.5	6,805.5	6,964.3	6,880.9	6,822.5	6,786.8	6,795.8
m_{10} **(mg)** ±1 mg	6,859.6	6,808.6	6,966.4	6,882.3	6,823.9	6,789.4	6,800.1

Table 8-11. Titanium getters mass changes.

m_0 is the initial mass of the getter and m_n where n is an integer are the measured masses of the getters after different reduction runs. An apostrophe marks that the samples were grit blasted or cleaned ultrasonically to remove oxide scale and establish a new datum. An oxide scale is undesirable as the Ti absorbs the oxygen and such a scale would impede this eventually eliminating their utility as oxygen getters.

Reduction run and process alteration index:

m_1	is for samples L.03, M.03 and N.03.
m_2	is for samples L.04, M.04 and N.04.
m_3	was a run with the getters only, on alumina sheet, at 800 °C, ramp only, 0.6 litres per minute gas flow (5% H_2, balance Ar). The usual porous ceramic brick was replaced with an austenitic stainless steel sheet (unsure whether 304 or 316). Stainless steel was selected by means of an Ellingham diagram ensuring that even under conditions where Ni is not reducing the stainless steel does not act as a source of oxygen.
m_4	was identical to m_3 but with an additional drying step under high Ar flow at 150 °C for 60 minutes. The run was ramp only (no dwell).
m_5	was similar to m_4 but with a modified drying step: before ramping to temperature the samples were dried at the same temperature and for the same duration but with no gas flow. Instead it was carried out under vacuum. The run was ramp only (no dwell).
m_6	was similar to m_5 but with no flow of reducing gas mix. The furnace was filled to slightly above atmospheric pressure and left unchanged the entire run. This indicated whether the remaining source of p_{O_2} was the water vapour in the gas bottles. This obviously cannot be eliminated via drying the furnace, being introduced by the gas supply.
m_7	was the same as m_6 with the addition that the stainless steel sample tray and alumina plates were also weighed from this point on.
m_8	was similar to m_7 with the introduction of a longer drying stage before the furnace was loaded. The furnace was heated as per normal ramp rates to 800 °C with no gas flow and under vacuum. The exhaust line of the hydrogen furnace was checked every hour and was found to remain cool to the touch up till 800 °C and therefore safe it was deemed safe to leave the vacuum pump switched on for the entire drying sequence. This now consisted of heating to 150 °C and 1 h dwell, then ramp to 800 °C and a 6 h dwell followed by cooling to room temperature. Once cool the furnace was back filled to a small overpressure (~ 0.2 bar) under Ar and all valves then closed. It was then loaded as quickly as possible followed by reduction with the normal procedure including the added short drying step as in m_5 onwards.
m_9	was similar to m_8 but with a new 5 vol.% H_2 (balance Ar) gas bottle was used eliminating any potential problems of gas separation that may have occurred with the older bottle (which had previously been in storage for some time). In addition, switching to a fresh gas mix would show whether any gas separation did, in fact, occur with the old bottle.
m_{10}	added an external getter furnace. This consisted of a Ti tube independently heated to 700 °C and added in-line between the gas supply and the hydrogen furnace utilised for reduction treatments. The addition of an external getter furnace necessitated some modification of the usual procedure. The high pressure leak test was carried out as normal, but the vacuum leak test was carried out with the introduction of a valve between the reduction furnace and the getter furnace. This was closed during pre-run leak testing to avoid including gas leaks in the getter furnace into the test. Subsequent to the leak tests the reduction furnace was back filled with Ar to atmospheric pressure, then the exhaust valve was opened and the getter furnace switched on. Once the getter furnace reached 700 °C the Ar flow was continued for a further 20 minutes to purge it.

	This traditional purge replaced the vacuum-assisted purge cycled adopted thus far because the getter furnace requires a gas flow inside it to prevent excessive oxidation. After purging, the gas was switched to the usual process gas with the getter furnace (at 700 °C) to remove p_{O_2} from the purge then the process gasses. The process gas was flowed for 20 minutes, venting to atmosphere. During this period the reduction furnace was switched on, carrying out the programmed 1 h drying stage at 150 °C. The exhaust valve was then closed, the furnace filled with process gas to slightly above atmospheric pressure, gas glow shut off and getter furnace switched off. Then reduction process then continues as described previously. Note that since post-process purge before unloading is carried out at room temperature any p_{O_2} introduced by the Ar purge gas will not affect samples. *Ergo*, the getter furnace is not necessary when purging prior to unloading.

Figure 8-59. below shows just how effective the addition of Ti getters is in modifying the atmosphere of the reduction furnace to favour reduction even with the low concentration of hydrogen.

Ellingham diagrams (Figure 8-58. and Figure 8-59.) quickly revealed that for the reduction furnace to have an atmosphere, even at 1,000 °C, that would reduce the NiO samples as intended the overall p_{O_2}must be so low that the mass of oxygen taken up by the Ti getters in these experiments becomes too small to measure on the microbalances available. This has conclusively demonstrated that with the initial 5 vol.% H_2 (balance Ar) gas mix it will never be possible to reduce the samples in an acceptable time with the current system regardless of what modifications to the furnace or procedure are made. Therefore, the only way forward is to change to a gas mix to one with a greater hydrogen content, despite the increased hazard (although of course the furnace was designed to run under these conditions at up to 1,300 °C continuous or 1,400 °C peak).

Hydrogen mixes with 10 vol.% H_2 or less are very safe (not even flammable), although plotting the conditions out on an Ellingham diagram combined with the experience gained earlier makes moving to the 10 vol.% unlikely to provide the sort of improvement in process time desired. Unusually intermediate H_2-content gas mixes are more explosive than pure H_2 so it is in fact safer to use the latter than any other hydrogen rich gas (ideal for the goal of reducing NiO). See section 13.2.2 for more.

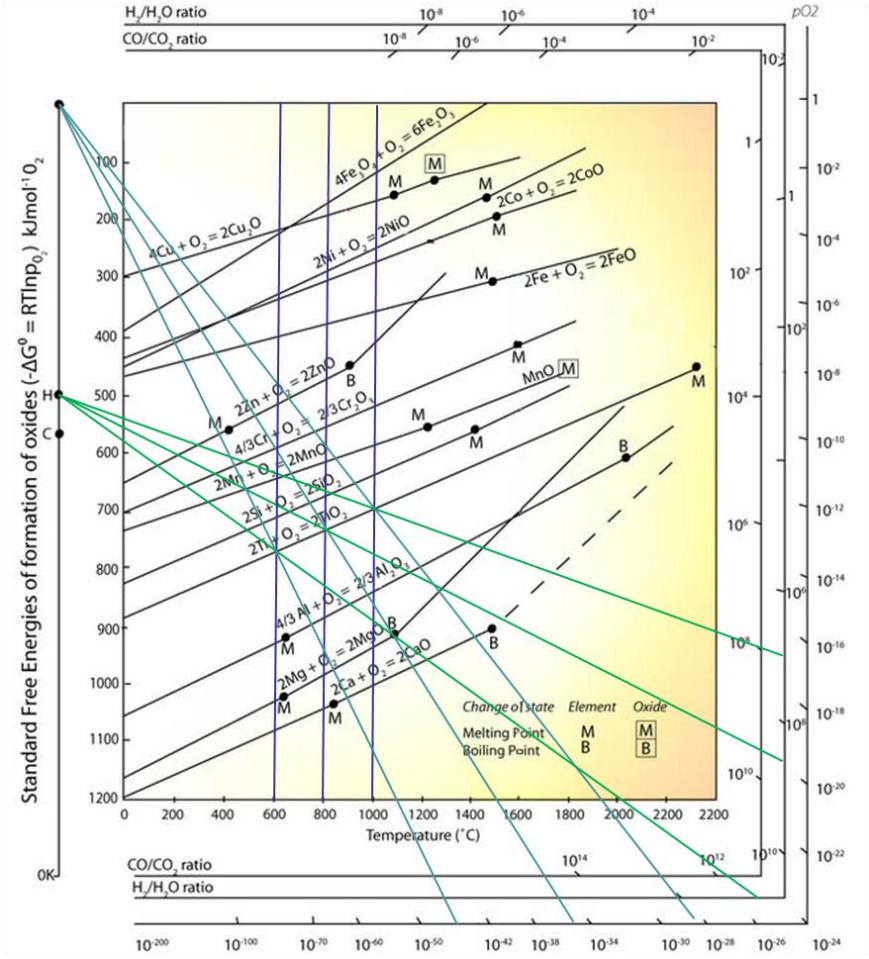

For Titanium:			
At 600 °C	—	$H_2/H_2O \approx 1 \times 10^{10}$	$p_{O_2} \approx 1 \times 10^{-46}$ atm
At 800 °C	—	$H_2/H_2O \approx 5 \times 10^{8}$	$p_{O_2} \approx 9 \times 10^{-35}$ atm
At 1,000 °C	—	$H_2/H_2O \approx 2 \times 10^{7}$	$p_{O_2} \approx 5 \times 10^{-28}$ atm

Figure 8-59. Ellingham diagram showing graphical calculation for H_2/H_2O ratio as well as the threshold p_{O_2} at 600 °C, 800 °C and 1,000 °C for Ti. Source: http://www.doitpoms.ac.uk/tlplib/ellingham_diagrams/ellingham.php

Sample	$t_{oxidised}$ (h) ±0.01 h	m_{Ni} (mg) ±1 mg	m_{Ni+NiO} (mg) ±1 mg	m_{gain} (mg) ±2 mg	Mass fraction oxidised ±0.0011	$t_{reduced}$ (h) ±1 s	$m_{reduced}$ (mg) ±1 mg	m_{loss} (mg) ±2 mg	Mass fraction reduced ±0.0046-0.0344
Reduction at 800 °C									
RT-A.31/08/11-125.1100(800)-L.03 D	42	188.6	240.0	51.4	1.000	ramp	233.3	6.7	0.131
RT-A.31/08/11-125.1100(800)-M.03 M	42	210.41	267.6	57.2	0.999	ramp	260.0	7.8	0.136
RT-A.31/08/11-125.1100(800)-N.03 U	42	210.2	267.4	57.2	1.000	ramp	258.6	8.9	0.156
RT-A.31/08/11-125.1100(800)-L.04 D	42	207.4	263.8	56.4	0.999	2	254.3	9.6	0.171
RT-A.31/08/11-125.1100(800)-M.04 M	42	184.8	235.1	50.3	1.000	2	224.2	11.0	0.218
RT-A.31/08/11-125.1100(800)-N.04 U	42	228.7	291.0	62.3	1.000	2	281.0	10.0	0.161

Table 8-12. Mass loss and mass fraction reduced of Tier 1 reduction with Ti getters at 800 °C. All temperatures reduced in 5 vol.% H_2 (balance Ar) shown. D, M, U after the sample code indicates whether it was downstream, in the middle or upstream with respect to the gas supply (respectively).

Unfortunately, as Table 8-12. shows, the addition of Ti getters and modifications to the reduction procedure described failed to improve the reduction kinetics significantly. Clearly, the H_2/H_2O balance established with the flowing 5 vol.% H_2 (balance Ar) gas was sufficient to establish a low enough p_{O_2} within the gas phase to support the reduction of NiO to Ni. Therefore, the slowness of the reduction kinetics must be attributed in significant part or wholly to shallow diffusion gradients established between the reduction gas and the NiO bulk. Localised surface reduction is evident with 13–16% reduction observed while heating to temperature; therefore, the slow kinetics is more likely associated with the transport of H_2O within the metal away from the NiO/Ni reaction zone.

8.12 Process Optimization with 100 vol.% H_2

The tier 1 work (section 8.11) revealed a fundamental hurdle to be overcome before it was possible to reduce the fully oxidised tubes to metallic nickel once more; completing the oxidation-reduction route to create porosity sufficient for use as anodes. An identical set of experiments using a higher hydrogen partial pressure had been planned all along in order to evaluate behaviour of the reduction with partial pressure of hydrogen. However, tier 1 demonstrated that a 5 vol.% hydrogen (balance Ar) mix only yields partial reduction and is therefore insufficient. Thus tier 2 is a repeat of tier 1; identical in all ways save the higher hydrogen concentration used (in the form of 100 vol.% H_2 process gas) and the addition of a low temperature set of experiments anticipating that a lower temperature will be sufficient given the greater availability of H_2 compared to tier 1. The objectives, therefore, remain the same as those of tier 1: optimise the reduction

process by obtaining a body of data to determine the effect of temperature on microstructure, determine the time to complete reduction, assess the reproducibility of the process and develop a model for the process. Special consideration is given to attaining some combination of shortest time/lowest temperature reduction, maximum porosity, and complete reduction. It is worth repeating that the change in process gas means a 20 fold increase in available hydrogen.

8.12.1 Results & Discussion

Table 8-13. summarises the results of the experiment, and gives the mass gain from oxidation of each sample, the mass fraction oxidised, the mass loss from reduction and the mass fraction reduced (the mass of oxygen lost divided by the mass of oxygen gained; so a mass fraction reduced of unity means all the oxygen gained by oxidation was removed by hydrogen reduction). Figure 8-60., Figure 8-61., Figure 8-62. and Figure 8-63. show plots of experimental results. Errors estimated using linear approximation by partial differentiation where an equation was used [Error Propagation article accessed 2013], or based purely on measurement equipment error. In all cases errors represent the worst case scenario.

Sample	**m_{gain} (mg)** ±2 mg	**Mass fraction oxidised** ±0.0005	**t_{dwell} (h)** ±1 s	**m_{loss} (mg)** ±2 mg	**Mass fraction reduced** ±0.0042
Reduction at 400 °C					
RT-A.04/03/13-125.1100(400)-FF.01 U	136.0	1.000	ramp	125.2	0.920
RT-A.04/03/13-125.1100(400)-FG.01 M	136.1	1.000	ramp	110.0	0.809
RT-A.04/03/13-125.1100(400)-FH.01 D	134.5	1.000	ramp	122.1	0.908
RT-A.05/04/13-125.1100(400)-FI.01 U	129.8	1.000	ramp	123.2	0.949
RT-A.05/04/13-125.1100(400)-FJ.01 M	132.2	1.000	ramp	125.0	0.942
RT-A.05/04/13-125.1100(400)-FK.01 D	131.3	1.000	ramp	124.5	0.948
RT-A.26/03/13-125.1100(400)-FF.02 U	133.5	1.000	0.017 (1 min)	125.1	0.937
RT-A.26/03/13-125.1100(400)-FG.02 M	135.4	1.000	0.017 (1 min)	127.8	0.944
RT-A.26/03/13-125.1100(400)-FH.02 D	133.3	1.000	0.017 (1 min)	125.2	0.939
RT-A.05/04/13-125.1100(400)-FI.02 U	132.6	1.000	0.017 (1 min)	124.5	0.939
RT-A.05/04/13-125.1100(400)-FJ.02 M	133.0	1.000	0.017 (1 min)	123.7	0.930
RT-A.05/04/13-125.1100(400)-FK.02 D	133.7	1.000	0.017 (1 min)	124.3	0.929
RT-A.07/05/13-125.1100(400)-FF.03 U	134.5	1.000	0.167 (10 min)	127.9	0.951
RT-A.07/05/13-125.1100(400)-FG.03 M	135.4	1.000	0.167 (10 min)	129.2	0.954
RT-A.07/05/13-125.1100(400)-FH.03 D	133.9	1.000	0.167 (10 min)	127.2	0.950
RT-A.07/05/13-125.1100(400)-FI.03 U	137.8	1.000	0.167 (10 min)	130.1	0.944
RT-A.07/05/13-125.1100(400)-FJ.03 M	132.9	1.000	0.167 (10 min)	126.4	0.951
RT-A.07/05/13-125.1100(400)-FK.03 D	133.4	1.000	0.167	126.8	0.950

Sample	m_{gain} (mg) ±2 mg	Mass fraction oxidised ±0.0005	t_{dwell} (h) ±1 s	m_{loss} (mg) ±2 mg	Mass fraction reduced ±0.0042
			(10 min)		
RT-A.17/05/13-125.1100(400)-FF.04 U	131.9	1.000	1	124.9	0.947
RT-A.17/05/13-125.1100(400)-FG.04 M	133.1	1.000	1	126.2	0.949
RT-A.17/05/13-125.1100(400)-FH.04 D	129.5	1.000	1	122.8	0.949
RT-A.17/05/13-125.1100(400)-FI.04 U	132.5	1.000	1	125.8	0.950
RT-A.17/05/13-125.1100(400)-FJ.04M	127.4	0.996	1	124.9	0.981
RT-A.17/05/13-125.1100(400)-FK.04 D	127.8	1.000	1	120.8	0.946
RT-A.12/06/13-125.1100(400)-FF.05 U	129.5	1.000	5	124.0	0.957
RT-A.12/06/13-125.1100(400)-FG.05 M	130.6	1.000	5	125.2	0.958
RT-A.12/06/13-125.1100(400)-FH.05 D	134.4	1.000	5	128.6	0.957
RT-A.12/06/13-125.1100(400)-FI.05 U	132.8	1.004	5	125.0	0.941
RT-A.12/06/13-125.1100(400)-FJ.05 M	133.4	1.003	5	125.6	0.942
RT-A.12/06/13-125.1100(400)-FK.05 D	134.1	1.001	5	127.8	0.953
RT-A.17/07/13-125.1100(400)-FF.06 U	132.2	1.000	15	128.5	0.972
RT-A.17/07/13-125.1100(400)-FG.06 M	133.4	1.000	15	129.7	0.972
RT-A.17/07/13-125.1100(400)-FH.06 D	136.4	1.000	15	132.6	0.972
RT-A.17/07/13-125.1100(400)-FI.06 U	136.8	1.000	15	132.9	0.972
RT-A.17/07/13-125.1100(400)-FJ.06 M	135.9	1.000	15	132.0	0.971
RT-A.17/07/13-125.1100(400)-FK.06 D	137.8	1.000	15	133.8	0.971
Reduction at 600 °C					
RT-A.28/11/12-125.1100(600)-R.01 U	126.7	1.000	ramp	124.4	0.982
RT-A.28/11/12-125.1100(600)-S.01 M	136.2	1.000	ramp	133.7	0.982
RT-A.28/11/12-125.1100(600)-T.01 D	134.6	1.000	ramp	132.1	0.981
RT-A.19/02/13-125.1100(600)-U.01 U	136.8	1.000	ramp	134.6	0.984
RT-A.19/02/13-125.1100(600)-V.01 M	135.3	1.000	ramp	133.2	0.985
RT-A.19/02/13-125.1100(600)-W.01 D	134.1	1.000	ramp	131.9	0.983
RT-A.19/02/13-125.1100(600)-R.02 U	137.2	1.000	0.033 (2 min)	135.0	0.984
RT-A.19/02/13-125.1100(600)-S.02 M	137.3	1.000	0.033 (2 min)	135.3	0.985
RT-A.19/02/13-125.1100(600)-T.02 D	134.5	1.000	0.033 (2 min)	132.4	0.984
RT-A.04/03/13-125.1100(600)-U.02 U	129.9	1.000	0.033 (2 min)	127.6	0.983
RT-A.04/03/13-125.1100(600)-V.02 M	136.7	1.000	0.033 (2 min)	134.4	0.983
RT-A.04/03/13-125.1100(600)-W.02 D	133.5	1.000	0.033 (2 min)	131.7	0.986
Reduction at 800 °C					
RT-A.16/10/12-125.1100(800)-L.01 U	134.8	1.000	ramp	134.1	0.995
RT-A.16/10/12-125.1100(800)-M.01 M	130.2	1.000	ramp	129.3	0.993
RT-A.16/10/12-125.1100(800)-N.01 D	133.9	1.000	ramp	133.4	0.996
RT-A.23/10/12-125.1100(800)-O.01 U	134.3	1.000	ramp	133.6	0.995
RT-A.23/10/12-125.1100(800)-P.01 M	133.0	1.000	ramp	132.4	0.996
RT-A.23/10/12-125.1100(800)-Q.01 D	134.8	1.000	ramp	134.3	0.997
RT-A.23/10/12-125.1100(800)-L.02 U	131.0	1.000	1	130.8	0.999
RT-A.23/10/12-125.1100(800)-M.02 M	132.3	1.000	1	131.6	0.995
RT-A.23/10/12-125.1100(800)-N.02 D	131.2	1.000	1	131.0	0.999
RT-A.05/10/13-125.1100(800)-O.02 U	133.0	1.000	1	132.8	0.999
RT-A.05/02/13-125.1100(800)-P.02 M	136.6	0.999	1	137.2	1.004
RT-A.05/02/13-125.1100(800)-Q.02 D	136.8	1.000	1	136.7	0.999

Sample	m_{gain} (mg) ±2 mg	Mass fraction oxidised ±0.0005	t_{dwell} (h) ±1 s	m_{loss} (mg) ±2 mg	Mass fraction reduced ±0.0042
Reduction at 1,000 °C					
RT-A.12/06/12-125.1100(1000)-F.02 U	134.1	1.000	ramp	134.0	0.999
RT-A.12/06/12-125.1100(1000)-G.02 M	134.6	0.997	ramp	137.1	1.019
RT-A.12/06/12-125.1100(1000)-H.02 D	137.0	1.002	ramp	134.9	0.985
RT-A.09/10/12-125.1100(1000)-I.02 U	135.1	1.000	ramp	134.8	0.998
RT-A.09/10/12-125.1100(1000)-J.02 M	133.5	1.000	ramp	133.9	1.003
RT-A.09/10/12-125.1100(1000)-K.02 D	129.2	1.000	ramp	129.1	0.999
RT-A.02/07/12-125.1100(1000)-F.03 U	113.8	0.975	1	141.1	1.240
RT-A.02/07/12-125.1100(1000)-G.03 M	134.5	1.000	1	134.3	0.999
RT-A.02/07/12-125.1100(1000)-H.03 D	133.3	0.997	1	136.9	1.027
RT-A.16/10/12-125.1100(1000)-I.03 U	130.7	1.000	1	130.6	0.999
RT-A.16/10/12-125.1100(1000)-J.03 M	131.7	1.000	1	131.8	1.000
RT-A.16/10/12-125.1100(1000)-K.03 D	133.1	1.000	1	133.1	1.000
RT-A.06/06/12-125.1100(1000)-F.01 U	134.0	1.000	5	133.7	0.998
RT-A.06/06/12-125.1100(1000)-G.01 M	132.4	0.996	5	136.1	1.028
RT-A.06/06/12-125.1100(1000)-H.01 D	119.9	0.981	5	140.4	1.171
RT-A.09/10/12-125.1100(1000)-I.01 U	132.4	0.998	5	133.9	1.011
RT-A.09/10/12-125.1100(1000)-J.01 M	138.2	1.000	5	138.2	1.000
RT-A.09/10/12-125.1100(1000)-K.01 D	131.6	1.000	5	131.6	1.000

Table 8-13. Mass loss and mass fraction reduced of Tier 2 reduction. All temperatures reduced in 100 vol.% H_2 shown. U, M, D after the sample code indicates whether it was upstream, in the middle or downstream with respect to the gas supply (respectively). Full table can be found inAppendix G: Complete Reduction Results Tables.

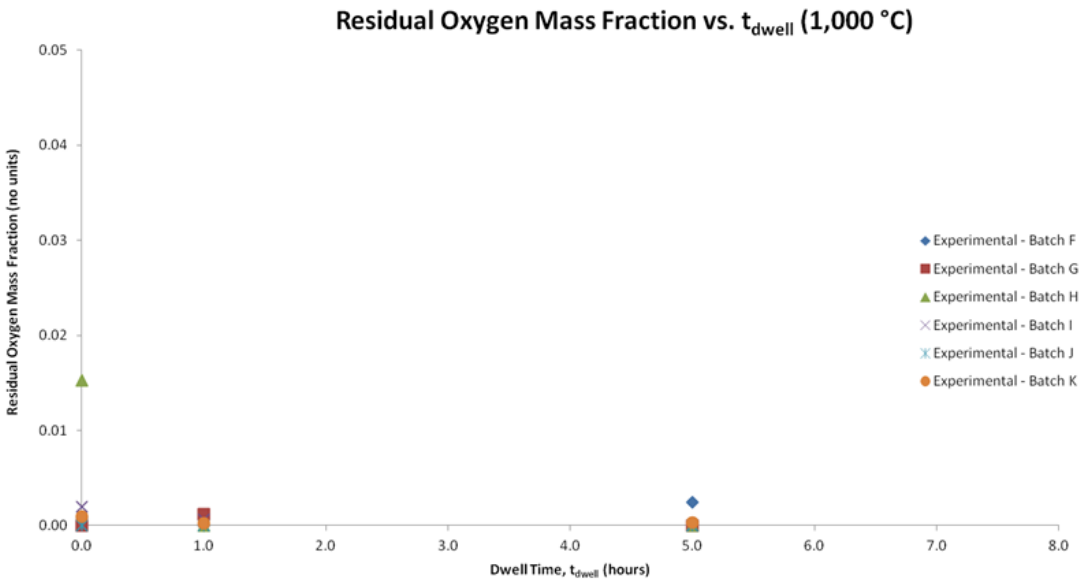

Figure 8-60. Plot of residual oxygen mass fraction, $\frac{(m_{gain}-m_{loss})}{m_{gain}} = 1 - \frac{m_{loss}}{m_{gain}}$, against dwell for all batches reduced at 1,000 °C.

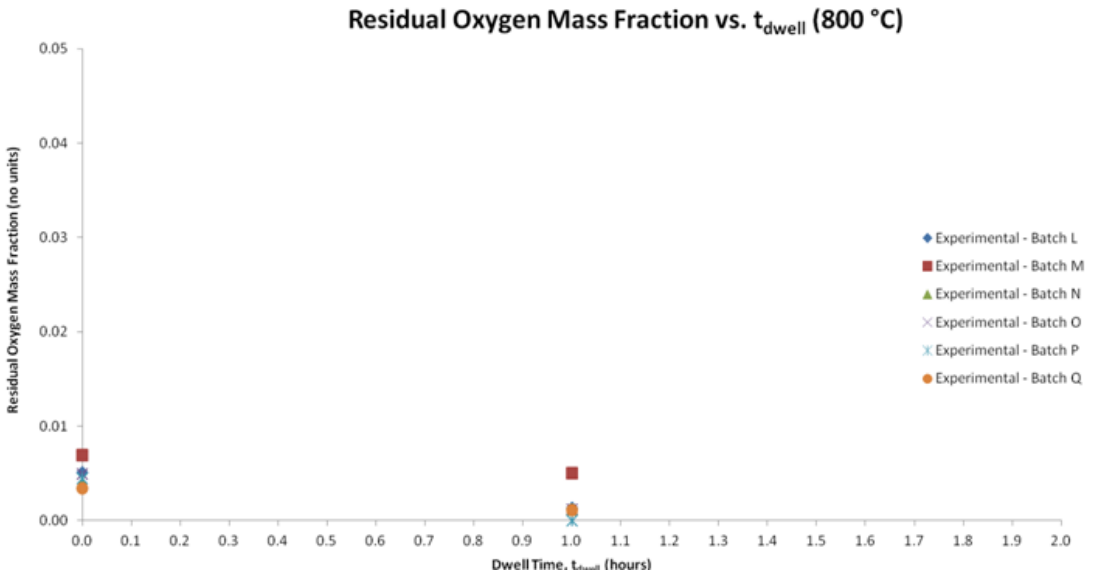

Figure 8-61. Plot of residual oxygen mass fraction, $\frac{(m_{gain}-m_{loss})}{m_{gain}} = 1 - \frac{m_{loss}}{m_{gain}}$, against dwell for all batches reduced at 800 °C.

At both 1,000 °C and 800 °C reduction is very rapid, proceeding to completion with just the ramp to and from temperature. Note that instances where calculated reduction exceeds unity is for samples where a small piece broke off exaggerating the apparent reduction. The one exception is sample P.02 (in this case the excess over complete reduction falls within the calculated error).

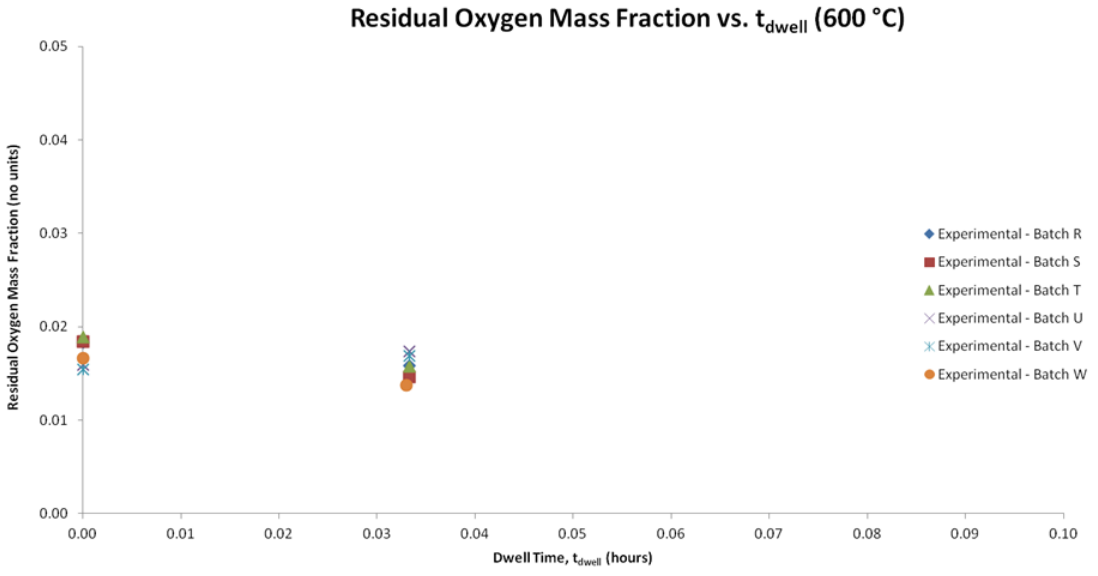

Figure 8-62. Plot of residual oxygen mass fraction, $\frac{(m_{gain}-m_{loss})}{m_{gain}} = 1 - \frac{m_{loss}}{m_{gain}}$, against dwell for all batches reduced at 600 °C.

The situation is a little less clear at 600 °C. Did the dwell increase the mass fraction reduced by any significant quantity? In order to test the hypothesis that the dwell further reduces samples the Student T test (a form of statistical null hypothesis test) was employed. With a (standard) 95 % confidence interval we may assert that the dwell is not statistically significant (but only just). *Ergo*, we may consider the ramp alone sufficient to fully reduce samples. It is often helpful to bracket results with a lower and a higher confidence interval. At 90 % confidence interval the dwell significantly adds to reduction while at 99 % confidence interval it does not. From all this we conclude that the 2 min dwell does not further reduce samples beyond what a ramp-cycle alone achieves (in this case a 1 h ramp to reach 600 °C, measured to less than 1 min precision). This is false (i.e. we are wrong, a Type I Error – a false positive) only if the confidence interval is below 94 %. Put differently in only 6 % of cases will we encounter a false positive correlation.

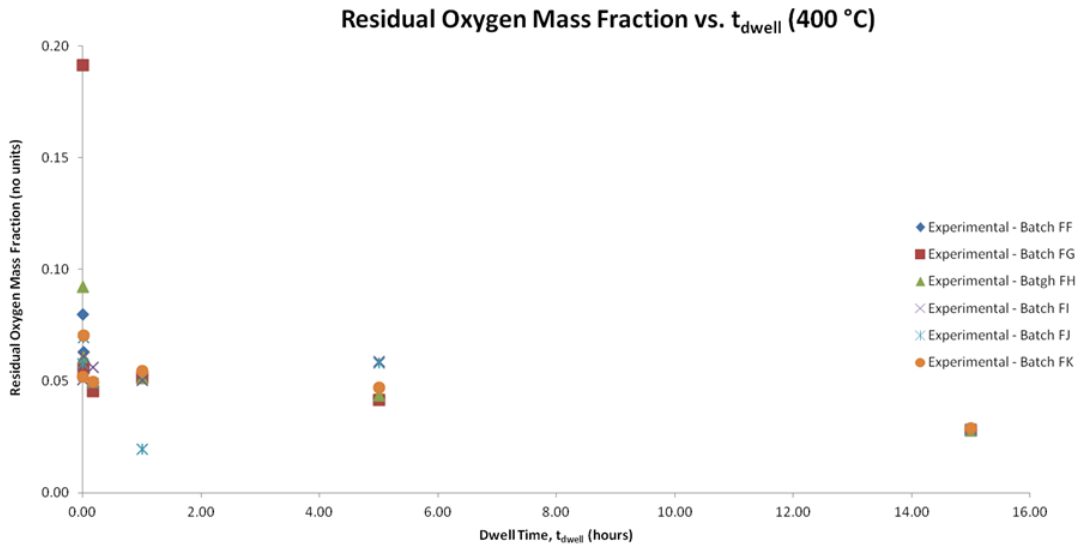

Figure 8-63. Plot of residual oxygen mass fraction, $\frac{(m_{gain}-m_{loss})}{m_{gain}} = 1 - \frac{m_{loss}}{m_{gain}}$, against dwell for all batches reduced at 400 °C.

At 400 °C reduction is 91 % complete on average from just the ramp-cycle. This rises to a mean MFR (mass fraction reduced) of 94 % after a 1 min dwell, 95 % after a 10 min dwell, 95.4 % after a 1 h dwell, 95.1 % after a 5 h dwell, and 97.2 % after a 15 h dwell. Applying Student T tests pair-wise (comparing ramp to 1 min dwell, 1 min dwell to 10 min dwell, etc.) results in the following:

Dwell	Student T Test results	Conclusions
1 min	At 90 % confidence interval the difference is NOT statistically significant. At 95 % confidence interval the difference is NOT statistically significant. The threshold confidence interval is 85 %.	Even with a lower than normal confidence interval of 90 % (i.e. a 1 in 10 chance of a false positive correlation) one may safely consider the dwell to not significantly add to the sample reduction over the ramp alone.
10 min	At 90 % confidence interval the difference IS statistically significant. At 95 % confidence interval the difference is NOT statistically significant. The threshold confidence interval is 94 %.	This dwell does not significantly increase the reduction of the sample over the ramp alone. A false positive correlation will occur only if the confidence interval is below 95 % (i.e. in 6 % of cases the dwell will actually be significant).
1 h	At 95 % confidence interval the difference IS statistically significant (just). At 99 % confidence interval the difference is NOT statistically significant. The threshold confidence interval is 95 %.	At the typical confidence interval of 95 % the dwell significantly increases the reduction over the ramp alone. However, at greater confidence interval the ramp alone is considered sufficient. Given the test results on shorter dwells I am inclined to consider that this dwell is not significant. There is a 5 % chance this is false.
5 h	At 95 % confidence interval the difference is NOT statistically significant. At 99 % confidence interval the difference is NOT statistically significant. The threshold confidence interval is 94.5 %.	Literal interpretation of the test result is that at the typical confidence interval of 95 % this dwell does not significantly increase the reduction of the sample compared to the ramp alone. However, given the threshold is 94.5 % the result is somewhat ambiguous with a 5.5 % chance this conclusion is a false negative.
15 h	At 95 % confidence interval the difference IS statistically significant. At 99 % confidence interval the difference is NOT statistically significant. The threshold confidence interval is 99 %.	The dwell significantly increases the reduction compared to ramp alone at any confidence interval below 99 %. In 1 % of cases the conclusion will be false (a false positive correlation).

Table 8-14. Student T Test results of Tier 2 reduction at 400 °C.

Taking into consideration all the results of the Student T tests and the conclusions made above, one can confidently state that a dwell of up to 15 h at 400 °C does not significantly increased the reduction of the samples over that observed in the ramp up period. In other words the ramp alone should be sufficient to fully reduce the NiO into anodes at 400 °C. However, some dwell (at least 1 h) may be beneficial increasing the confidence interval of success to 95%.

Perhaps the most practical conclusion is that other factors may determine which the better anode production method is; whether to reduce samples for (ramp + 15 h) or ramp alone. Energetically a ramp-only process is favourable unless the furnace is of sufficient size that it is more economical to process very large batches – in which case, assuming the furnace has excellent thermal insulation and sufficient thermal mass to require next

to no additional heating (i.e. very low heat loss rate), it seems wise to take advantage and expose samples to an isothermal dwell for one or more hours.

Also of interest is the identical maximum MFR for all samples reduced at 400 °C for 15 h. This implies that the remaining 0.029 % of the mass of oxygen absorbed by the samples is in solution and inaccessible by diffusion in the time scale considered. This can be confirmed by the nickel-oxygen binary phase diagram, where the oxygen solubility in Ni at 400 °C is less than 0.5 mol%.

As before by plotting the square of the oxygen mass loss per unit area we may infer whether the reduction is primarily surface controlled (linear behaviour) or primarily diffusion, or bulk process, controlled (parabolic behaviour).

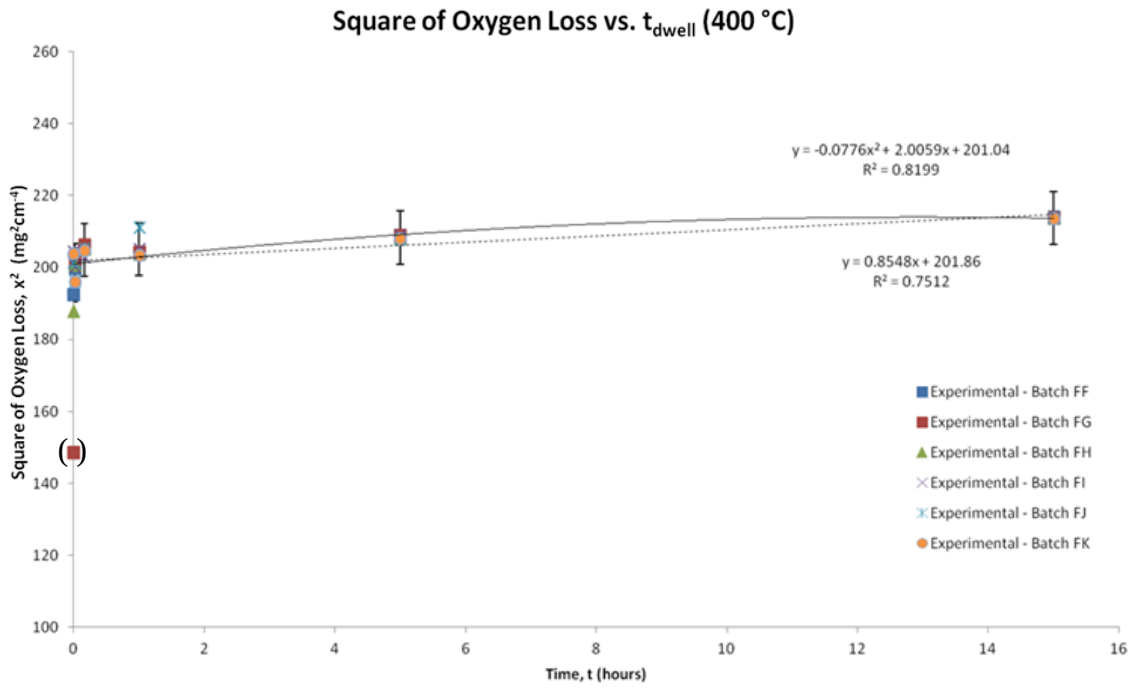

Figure 8-64. Oxygen loss squared against dwell for all batches at 400 °C, akin to the square of the oxidation rate explained previously. The fitting was carried out based on the mean of the data points at each dwell. The error shown is the maximum (i.e. worst case) calculated standard deviation from this mean. Samples in parenthesis are outliers.

The data for reduction at 400 °C was fitted to both a power law model (solid line) and a parabolic one (dashed line). The deviation from a straight line in the case of the latter indicates the data conforms to a superparabolic (i.e. $x^{(2+a)}$, a power law). It is apparent that sample FG.01 is an outlier. This is evidenced by both the extent to which the fitting improved once it was excluded and, more rigorously, upon considering the maximum error as it lies more than two standard deviations outside of the mean. The maximum standard deviation should FG.01 be included is 21.25 mg (reduced to 7.37 mg once it is excluded). Both linear and parabolic models fit well. However, there is a noticeable

improvement with the parabolic fit. This indicates that while there is a strong linear character (or alternatively a significant linear component contributes to the mechanism) it is dominated by a parabolic process. *Ergo*, the reduction process at 400 °C is bulk diffusion controlled (but with a strong surface diffusion component). Contrast this with 1,000 °C, discussed below. The uncharacteristically large standard deviation at 0 h dwell (7.37) rapidly drops to 2.56 at the next point then to a mere 0.14 with the final point. Larger standard deviation at low dwells indicates that in the initial stages of reduction small stochastic variances has a strong influence on the outcome, but only when the process is at the slowest considered (the lowest temperature).

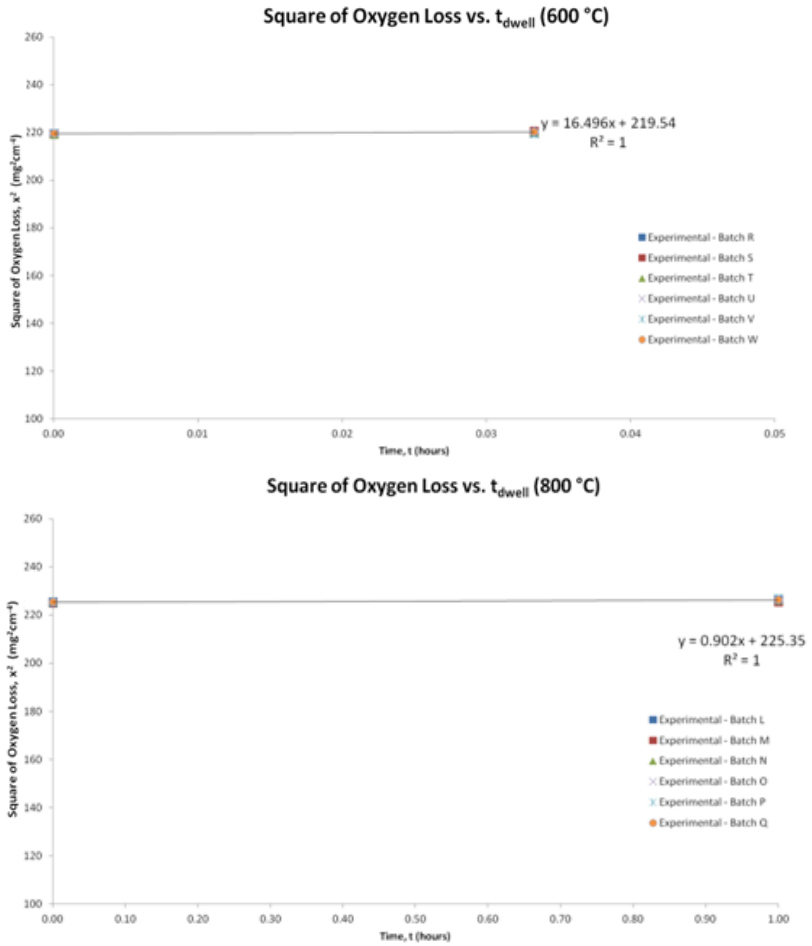

Figure 8-65. Oxygen loss squared against dwell for all batches at 600 °C and 800 °C, akin to the square of the oxidation per unit area explained previously. The fitting was carried out based on the mean of the data points at each dwell. The error shown for each temperature is the maximum (i.e. worst case) calculated standard deviation from this mean. Note: in some cases the standard deviation is too small to appear in error bars.

There is relatively little to be said about plots of the square of mass loss against dwell for 600 °C and 800 °C. In both cases the fit is obviously limited to being linear (only two sets of data). As was discussed previously once it became clear that even with the minimum dwell (0 h) complete reduction would be achieved there was no point carrying out further experiments (note chronologically the 1,000 °C was carried out earlier,

initially with a 5 h dwell then 0 h and finally 1 h). The only element of note is the tight grouping of data points and commensurately small standard deviation.

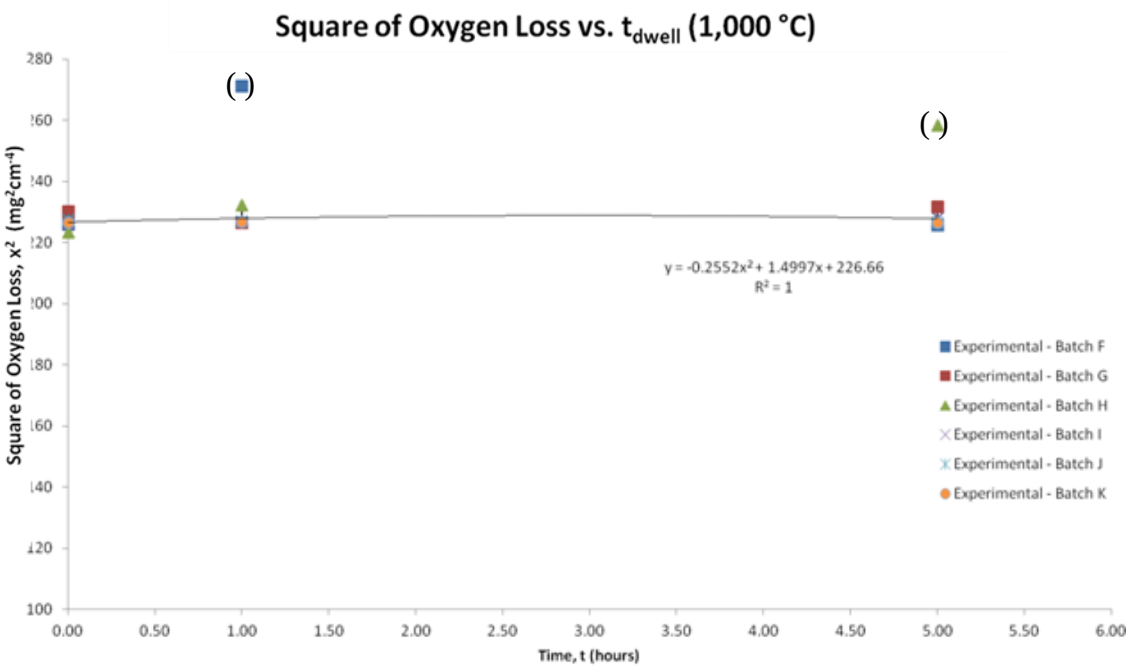

Figure 8-66. Oxygen loss squared against dwell for all batches at 1,000 °C, akin to the square of the oxidation per unit area explained previously. The fitting was carried out based on the mean of the data points at each dwell. The error shown for each temperature is the maximum (i.e. worst case) calculated standard deviation from this mean. Samples in parenthesis are outliers. Note: in some cases the standard deviation is too small to appear in error bars.

The data for reduction at 1,000 °C has two outliers: H.01 and F.03. Both lay more than two standard deviations outside of the mean and excluding them improved the fitting quality. Reduction at this temperature is bulk diffusion controlled (a parabolic model fits well). Contrast this with 400 °C, discussed previously. The standard deviation is approximately 2.4 mg increasing very slightly with dwell (from 2.17 to 2.43 and finally 2.47).

Overall the square of mass loss against dwell time plots reveal a process that has strong contributions by both surface and bulk diffusion. As temperature decreases the surface processes become the larger contributor although even then bulk diffusion remains very important. I would expect reduction at even lower temperature of such samples to show an increasing linear character and the parabolic contribution to continue to drop. The plots also show clearly in the models to what extent at each temperature samples are reduced during heating to process temperature. This is tabulated below. As expected it increases with increasing temperature.

Temperature (°C)	Minimum mass loss (mg)
400	201
600	220
800	225
1,000	227

Table 8-15. Minimum mass loss during reduction in 100 vol.% H_2 by temperature.

According to [Xing *et al.* 2012] in a hydrogen atmosphere at 600 °C reduction at the NiO surface dominates, evidenced by the interconnected pores they observed. Their results show a similar surface and cross-sectional microstructure to my anodes, supporting my conclusion that the reduction is surface process dominated at lower temperatures. The process they describe is as follows [Xing *et al.* 2012]: H_2 is adsorbed and then dissociated. Ni is a good catalyst for hydrogen dissociation any pockets of unoxidised Ni will readily promote the dissociation. The hydrogen atoms on the NiO surface then diffuse to a reactive zone and capture oxygen atoms in NiO to produce water, which is subsequently desorbed. The presence of oxygen vacancies in the NiO lowers the energy barrier for the dissociation of hydrogen and aids in adsorption [Xing *et al.* 2012]. Furthermore, adsorbed hydrogen can induce the migration of oxygen vacancies from inside to the surface (it is unclear if the authors mean of the sample or of grains – I am inclined to think grains) [Xing *et al.* 2012]. The resulting vacancies enhance the adsorption and dissociation of hydrogen further on Ni atoms adjacent to these vacancies perpetuating the reduction reaction [Xing *et al.* 2012].

The minimum time for complete reduction (assuming the reduction itself is instantaneous and the availability of hydrogen is the dominant mechanism) is estimated as before (see 8.11.1; the text accompanying equation (8.32) above). This represents the absolute minimum time necessary to completely reduce the samples.

A 25 mm long Ni tube contains $\frac{0.504}{58.69} = 8.59 \times 10^{-3}$ moles of nickel.

Taking the same assumptions as before yields 17.18×10^{-3} moles of hydrogen to reduce one sample.

Now, the flow rate used for tier 2 was 0.8 litres per minute, 100 vol.% of which was hydrogen. Hence, the flow of hydrogen is 1.33×10^{-5} $m^3 s^{-1}$. Applying (8.32) and tabulating the results gives:

Reduction Temperature (°C)	Molar Flow Rate (mol s^{-1})	Minimum Exposure (min)
200	3.43×10^{-4}	0.83
400	2.41×10^{-4}	1.19
600	1.86×10^{-4}	1.54
800	1.51×10^{-4}	1.89
1,000	1.28×10^{-4}	2.24

Table 8-16. The molar rate of hydrogen required for reduction of samples and corresponding minimum exposure time with 100 vol.% H_2 gas (Tier 2).

Thus a minimum of 1.19 minutes of exposure are needed to reduce the sample (at the lowest temperature utilised – 400 °C). As before, the effect of hydrogen depletion can be neglected given the times samples are typically reduced for and that additional twentyfold increase in the quantity of hydrogen available for runs of the same duration (5.33 h for a 400 °C, no-dwell, ramp-only run start to finish – the shortest possible). In just a ramp-only run 4.64 moles of hydrogen are available, but less than 0.02 moles are needed.

A simplistic model for the thermodynamics it may be, but it is certainly sufficient to demonstrate that the thermodynamics and availability of hydrogen are not limiting factors to the rapidity of reduction. Rather, therefore, it is most likely the kinetics rather than thermodynamics are critical. Further evidence of this is that at 400 °C complete reduction takes 15 h (and even then appears limited to a MFR of 0.972 by oxygen in solution) but is considerably faster at higher temperatures – the opposite of what Table 8-16. suggests. Note that while statistically the dwell does not significantly increase reduction in this instance the samples are not yet fully reduced. A reasonable interpretation is that while reduction may not be complete without a dwell the benefit gained is not significant (although certainly an important part of my analysis!).

There are two final elements worthy of discussion following on the above calculations. Firstly, had 10 mm long samples been utilised the calculated dwell for complete reduction would be just 2 s. Secondly, the astute reader will have noticed that Table 8-16. includes data for a run at 200 °C. This was theoretical only, no such experiment having been carried out. It is included here because there may be further gains to be made in investigating the lowest feasible reduction temperature. I have not gone quite that far because already at 400 °C the reduction time is approaching practical limits for a process intended to be used for mass manufacture.

The morphology, both surface and sectional, of the extreme dwells (0 h and that resulting in nominally complete reduction) for each temperature was analysed. Each sample was selected at random from among the six possible for each relevant combination of temperature and dwell. The cross-sections were created by FIB. Surface images were taken near the FIB-milled section with additional sets at increasing distances along the length of the tube towards the other end. At least one of the areas

imaged for surface morphology was always near the end of the tube furthest from the milled trench. The sectional micrographs are given in four distinct groupings: overall, micrographs from near the outer edge of the sample, micrographs from near the middle, and micrographs from near the inner edge of the tube (viewed sectionally). Images are oriented so that the top of the image corresponds with the direction towards the outer edge of the section. The depth of the milled trenches combined with the poor electrical conductivity of NiO leads to a build up of charge at the surface caused by the impacting Ar^+ ions. This charge deflects and diffuses the accelerated beam of ions causing what is known as waterfalling (and contributes to re-deposition of milled material also), evident on all samples to some degree towards the bottom of the trench. This is an artefact of milling deep trenches that only slightly reduces visual clarity of the samples. The micrographs below are a selection intended to showcase and support my observations. A more complete set can be found in Appendix H: Reduction Micrographs.

First is an example demonstrating the structure of the micrographs displayed. At each site of interest a sequence of images was taken at increasing magnification, usually with the site of interest centred in all micrographs. These sets of micrographs with multiple levels of magnification are shown in full in the aforementioned appendix. For the remainder of this chapter (excepting the example below and a few special instances) only images at one magnification are shown. For cross sections this is 5,000×. This particular magnification was selected based on studying the micrographs as a whole: it clearly shows all the larger features and even smaller pores remain visible while showing a relatively large area that demonstrates that the features occur consistently in a region rather than being highly localised. The only drawbacks are a loss of context possible with lower magnification images and loss of detail of very small features visible on those at 10,000× and higher. Naturally, all images were used in my analysis even if not shown. In those cases where multiple magnifications are shown they are ordered from top to bottom in order of increasing magnification.

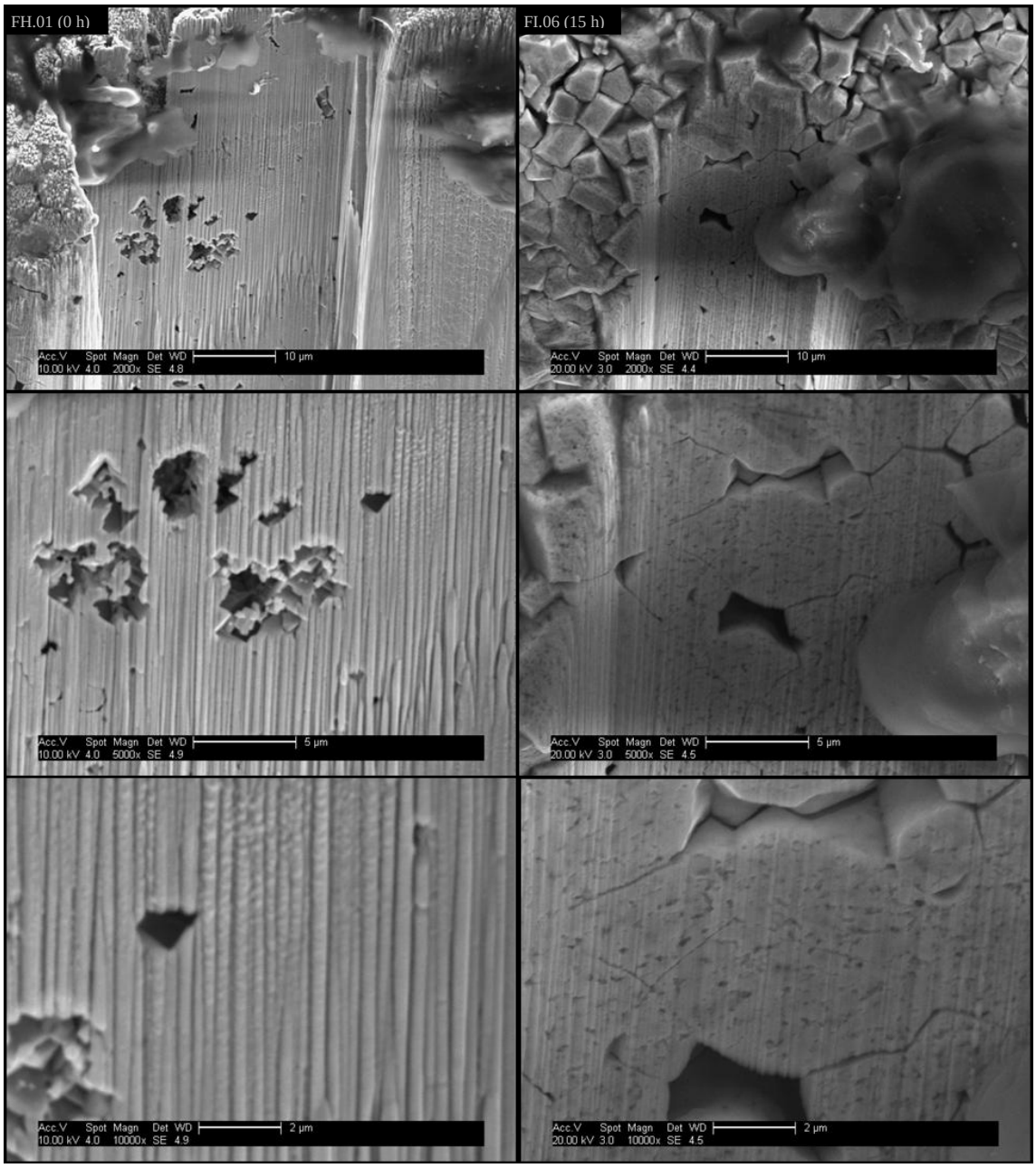
FH.01 (0 h)
FI.06 (15 h)
Acc.V Spot Magn Det WD 10 µm
10.00 kV 4.0 2000x SE 4.8
Acc.V Spot Magn Det WD 10 µm
20.00 kV 3.0 2000x SE 4.4
Acc.V Spot Magn Det WD 5 µm
10.00 kV 4.0 5000x SE 4.9
Acc.V Spot Magn Det WD 5 µm
20.00 kV 3.0 5000x SE 4.5
Acc.V Spot Magn Det WD 2 µm
10.00 kV 4.0 10000x SE 4.9
Acc.V Spot Magn Det WD 2 µm
20.00 kV 3.0 10000x SE 4.5

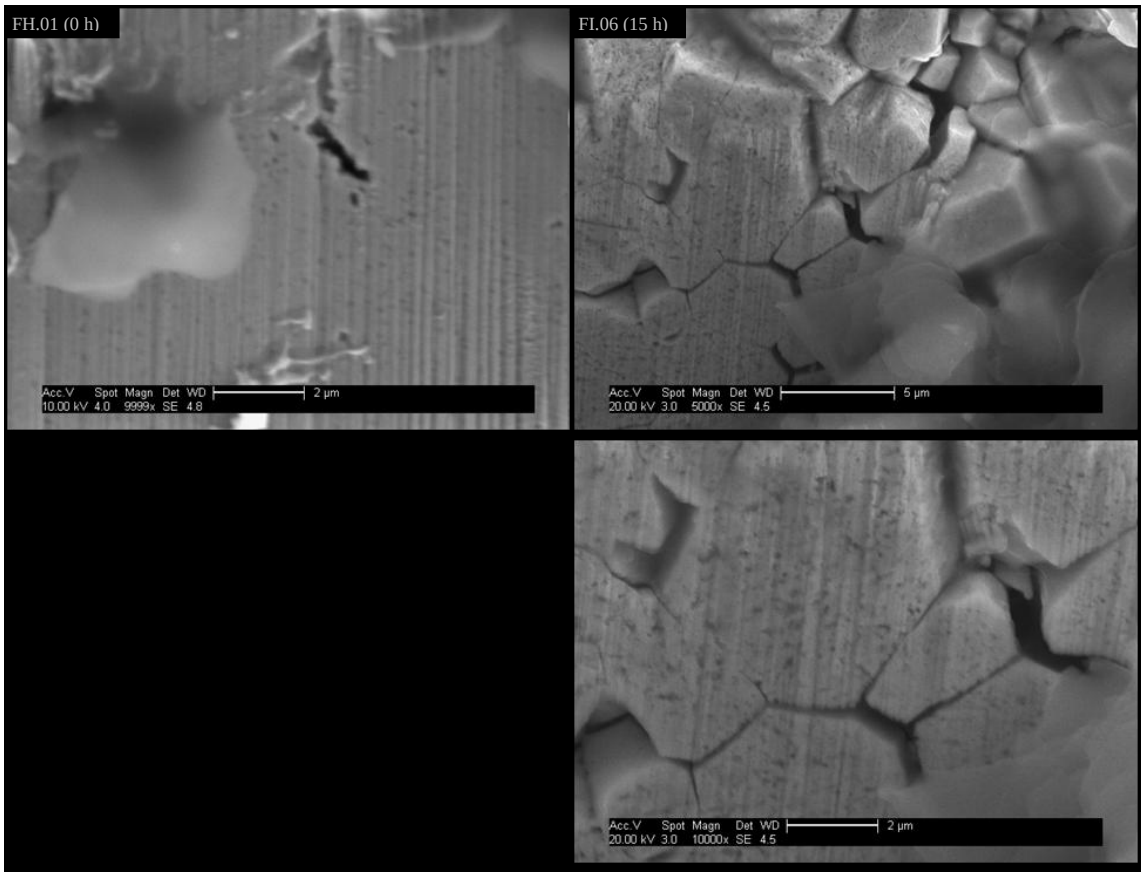

Figure 8-67. SEM micrographs structuring example, showing a pair reduced at 400 °C. Images are ordered: from top to bottom in order of increasing magnification; left column is 0 h dwell (ramp only – the minimum possible) and right column is 15 h dwell (nominally fully reduced). Samples: RT-A.04/03/13-125.1100(400)-FH.01 (downstream) and RT-A.17/07/13-125.1100(400)-FI.06 (upstream). In this case there are two pairs if images at 5,000× and 10,000×. Note sequence from context to detail, highlighting larger features then smaller ones.

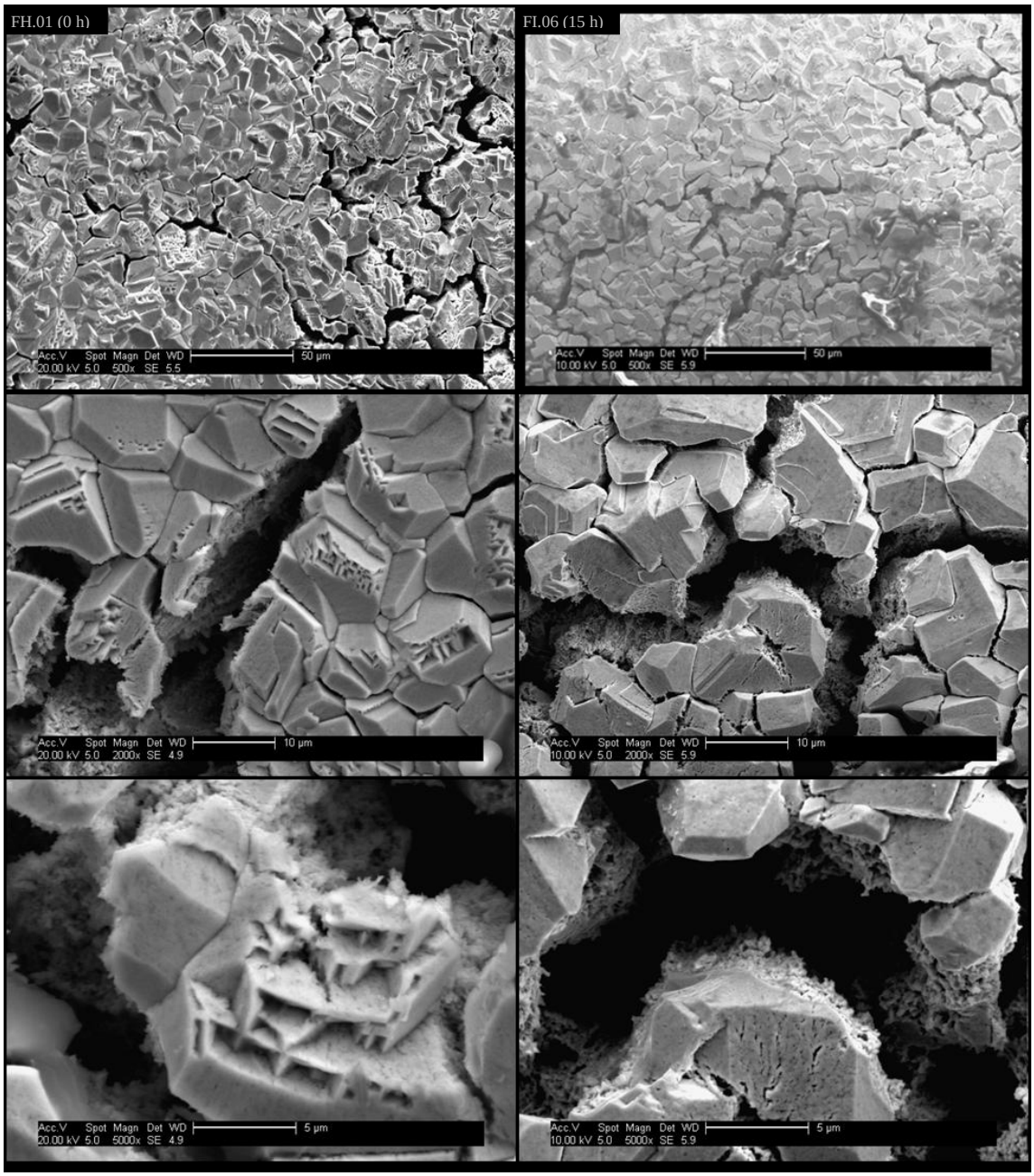
FH.01 (0 h)
Acc.V Spot Magn Det WD 50 µm
20.00 kV 5.0 500x SE 5.5
FL.06 (15 h)
Acc.V Spot Magn Det WD 50 µm
10.00 kV 5.0 500x SE 5.9
Acc.V Spot Magn Det WD 10 µm
20.00 kV 5.0 2000x SE 4.9
Acc.V Spot Magn Det WD 10 µm
10.00 kV 5.0 2000x SE 5.9
Acc.V Spot Magn Det WD 5 µm
20.00 kV 5.0 5000x SE 4.9
Acc.V Spot Magn Det WD 5 µm
10.00 kV 5.0 5000x SE 5.9

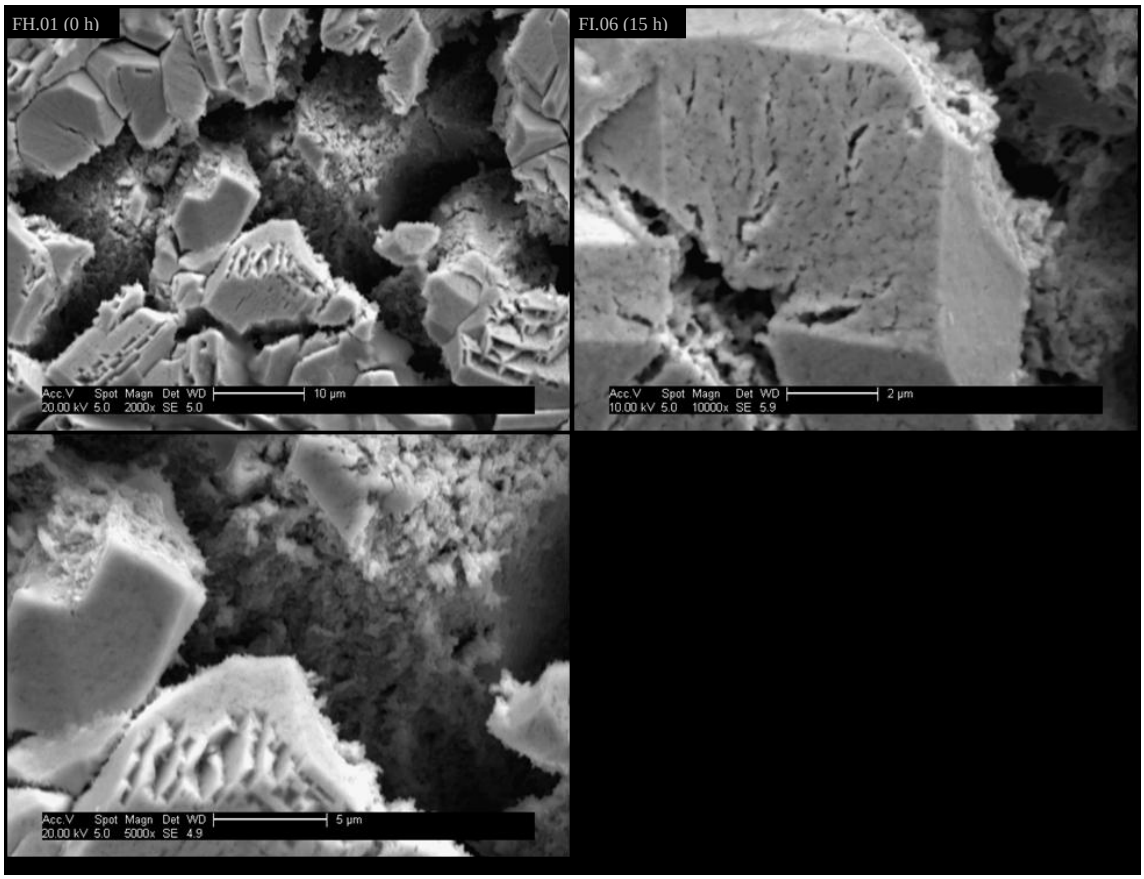

Figure 8-68. SEM micrographs of the surface morphology of samples reduced at 400 °C. Left column is 0 h dwell (ramp only – the minimum possible) and right column is 15 h dwell (nominally fully reduced). Samples: RT-A.04/03/13-125.1100(400)-FH.01 (downstream) and RT-A.17/07/13-125.1100(400)-FI.06 (upstream).

The NiO grains of sample FH.01 appear tightly packed and c.10 μm across in the largest dimension. This is consistent with the slightly smaller grains of sample FI.06, due to the volume lost as a consequence of the removal of oxygen over the 15 h dwell. The sub-surface grains, visible in the larger cracks, appear different. They are smaller (<5 μm, more accurate measurement not possible), lack the unusual trapezoidal pores, and, as far as could be determined, have only intergranular pores. FH.01 shows re-arranged grains due to dislocation creep, appearing as protruding terraces that indicate preferred slip planes. Some feathering is visible in sub-surface grains that indicates local plastic deformation (in dislocation creep mode) splitting pores as a crack propagates. While these grains appear different to the surface ones with a similar pore structure the pores became distorted as the crack propagates through them. FI.06 exhibits some important changes to surface morphology with the increased dwell: a larger number of pores, pores are substantially smaller on average (submicron), intergranular cracks are enlarged, grains take on a more cubic appearance. For both samples the only variation in surface morphology across the entire surface is that the larger cracks are wider in the near vicinity of the tube ends. This last was observed across all samples; *ergo* it is likely an effect of the additional exposed surfaces (the tube end faces) rather than an inherent microstructural difference. It is also interesting to note the apparent fractal nature of the

surface cracking, most clearly visible in the lower magnification micrographs. The larger cuboid-trapezoidal pores are caused by the minimization of surface energy due to boundaries of a preferred orientation. EBSD was used to get crystal orientation and crystal structure information using complete cells (see section 11.3).

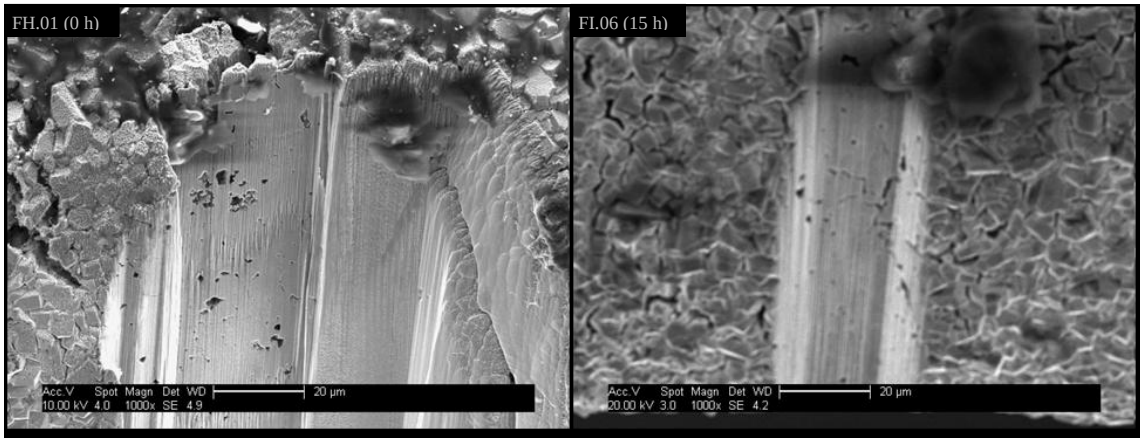

Figure 8-69. SEM micrographs showing the overall cross-section of samples reduced at 400 °C. Left column is 0 h dwell (ramp only – the minimum possible) and right column is 15 h dwell (nominally fully reduced). Samples: RT-A.04/03/13-125.1100(400)-FH.01 (downstream) and RT-A.17/07/13-125.1100(400)-FI.06 (upstream).

FH.01 exhibits a range of pore sizes from submicron to approximately 10 μm. No cracks or elongated pores. The distribution is mostly random, the exception being larger pores are more common near the outer edge of the tube (top of images). It is difficult to ascertain with any certainty but the pores seem to aggregate in bands parallel to the outer and inner edges of the sample. Overall the sample is quite porous, but is not completely reduced (MFR = 0.908). Sample FI.06 is overall similar to FH.01. Unlike the 0 h dwell sample, however, elongated crack-like pores appear. Of those visible all are intergranular and may be created as grains lose oxygen and shrink.

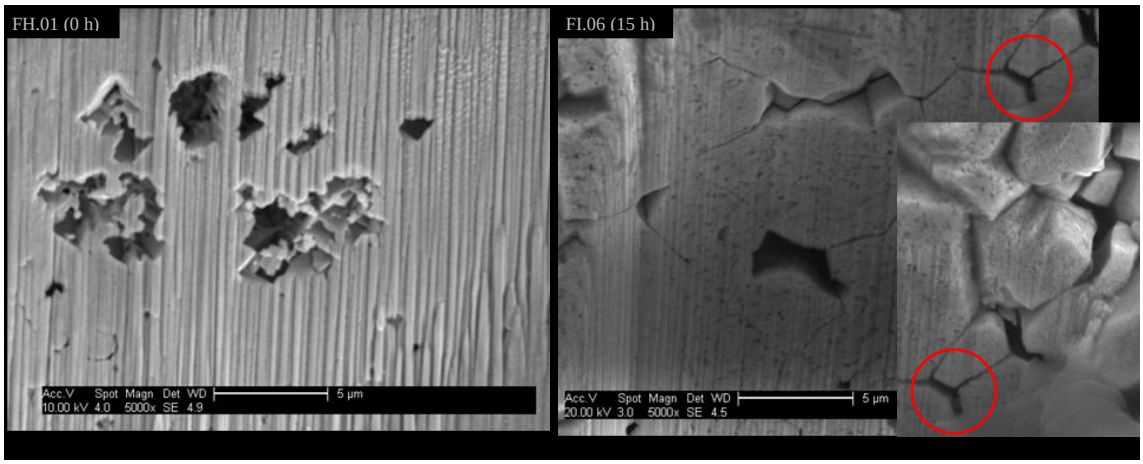

Figure 8-70. SEM micrographs showing the cross-section near the outer edge of samples reduced at 400 °C. Left column is 0 h dwell (ramp only – the minimum possible) and right column is 15 h dwell (nominally fully reduced). Samples: RT-A.04/03/13-125.1100(400)-FH.01 (downstream) and RT-A.17/07/13-125.1100(400)-FI.06 (upstream). The right-hand image is a composite, centred around the large pore in the top right of the left hand part (highlighted).

The same observations made regarding the surface morphologies of these two samples also apply to their sectional microstructures in the vicinity of the outer edge. FI.06 shows the majority of the pores occur inside grains. Their small diameter is surprising given the dwell. Normally such small pores would coalesce, forming larger ones with time, in order to progressively reduce the energy of the system. It may be surmised that at 400 °C the pores have insufficient mobility to do so. One may also observe that in FI.06 the intergranular pores/cracks connect to the surface of the samples (top right of the image). The composite of the two micrographs highlights the two behaviours: small intragranular pores and larger intergranular pores and cracks.

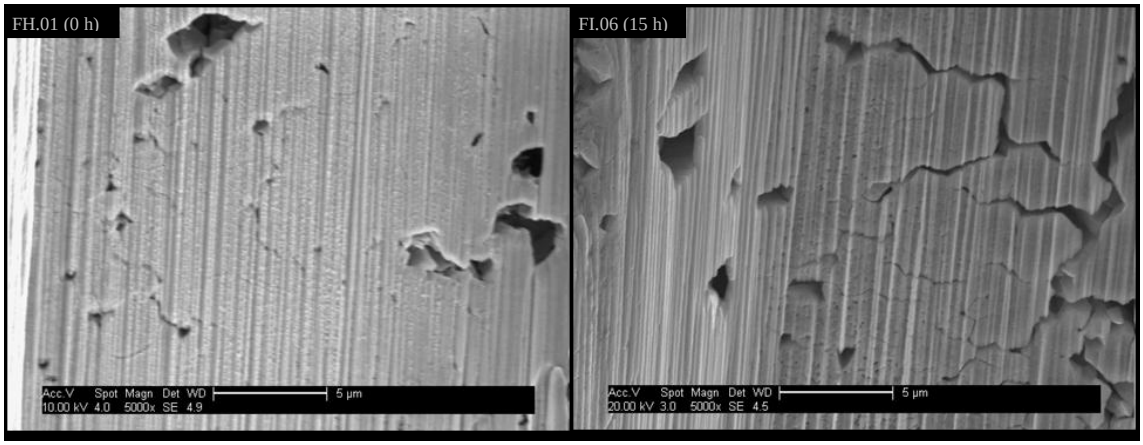

Figure 8-71. SEM micrographs showing the cross-section near the middle of samples reduced at 400 °C. Left column is 0 h dwell (ramp only – the minimum possible) and right column is 15 h dwell (nominally fully reduced). Samples: RT-A.04/03/13-125.1100(400)-FH.01 (downstream) and RT-A.17/07/13-125.1100(400)-FI.06 (upstream).

The middle section is the most similar between these two samples. The most notable difference being that after the 15 h dwell all intergranular cracks are enlarged as noted previously. The remarks made above for these two samples also apply here. FI.06 exhibits an increased number of submicron pores and a lessening of pores c.1 μm across.

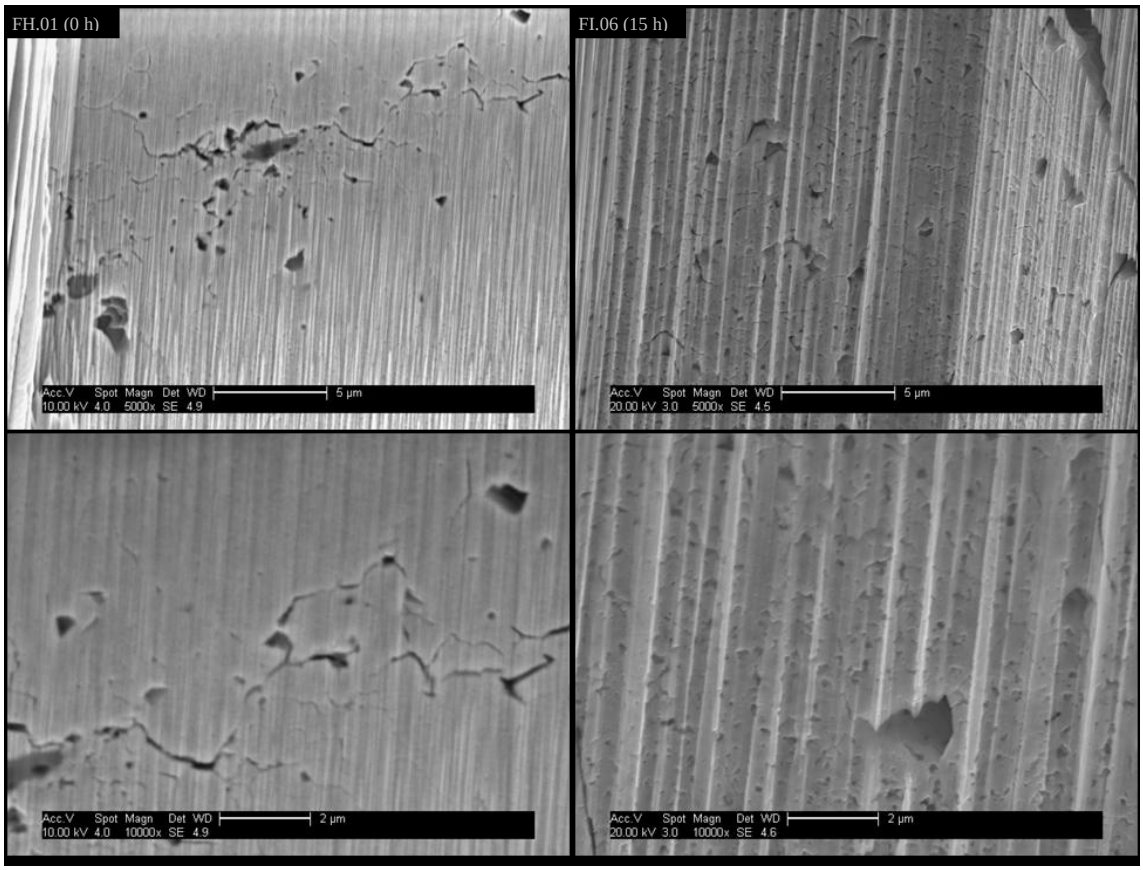

Figure 8-72. SEM micrographs showing the cross-section near the inner edge of samples reduced at 400 °C. Left column is 0 h dwell (ramp only – the minimum possible) and right column is 15 h dwell (nominally fully reduced). Samples: RT-A.04/03/13-125.1100(400)-FH.01 (downstream) and RT-A.17/07/13-125.1100(400)-FI.06 (upstream).

The same comments made for the previous sectional micrographs of these two samples apply here also. The only addition being that, upon close inspection of the micrographs at an apparent magnification of 5,000×, it becomes apparent that pores tend to be smaller very near the inner edge. Cracks (intergranular pores/voids/gaps) are prevalent away from the inner edge (towards the middle of the cross-section). This is true for both FH.01 (0 h dwell) and FI.06 (15 h dwell), but is more marked for the longer dwell. It is possible that a similar acceleration effect due to compressive loads in the region from the neutral plane to the inner edge as with oxidation has occurred, favouring pore nucleation (see section 8.3.1, 8.4.1 and 8.5.1).

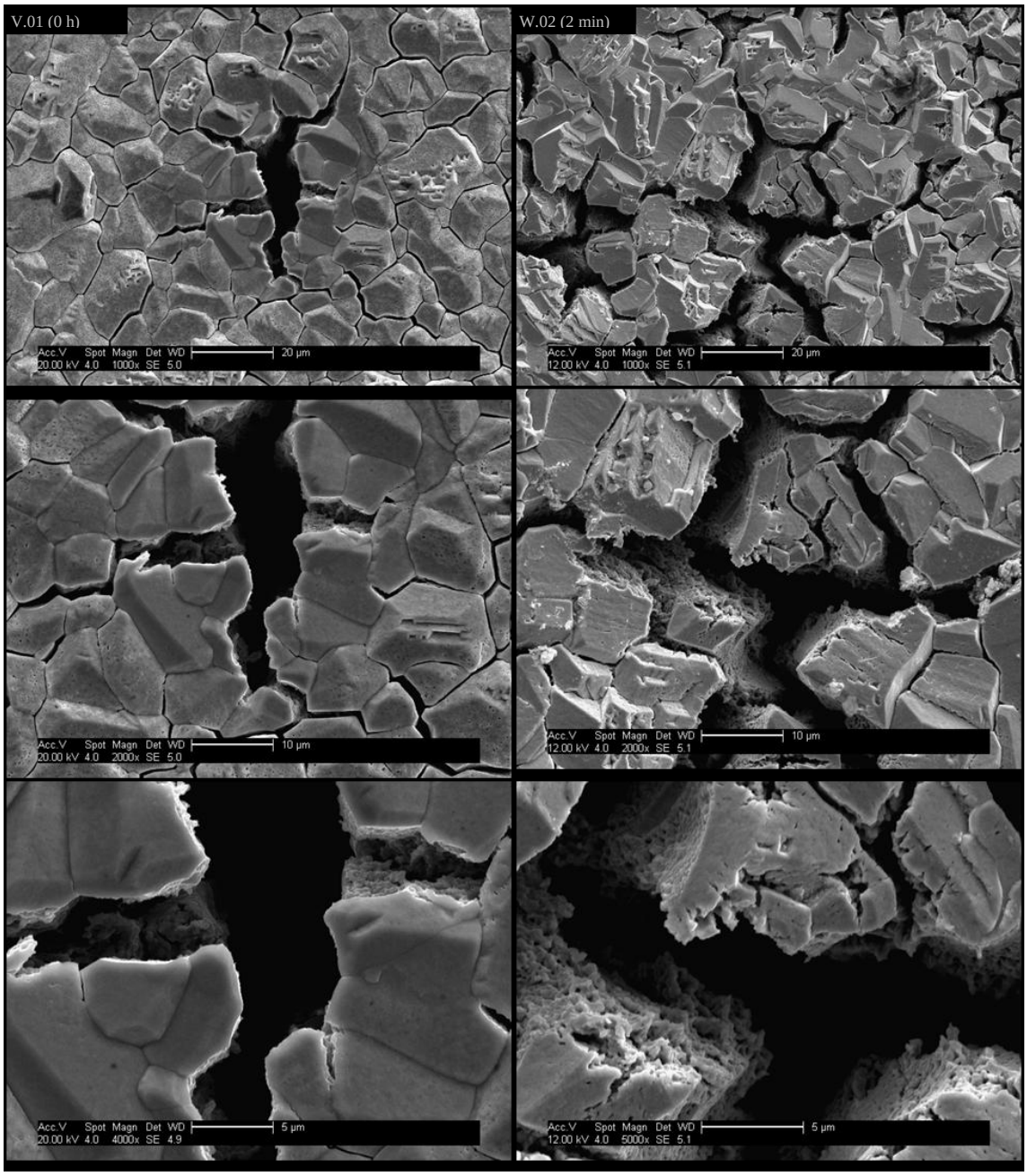

Figure 8-73. SEM micrographs of the surface morphology of samples reduced at 600 °C. Left column is 0 h dwell (ramp only – the minimum possible) and right column is 2 min dwell (nominally fully reduced). Samples: RT-A.19/02/13-125.1100(600)-V.01 (midstream) and RT-A.04/03/13-125.1100(600)-W.02 (downstream).

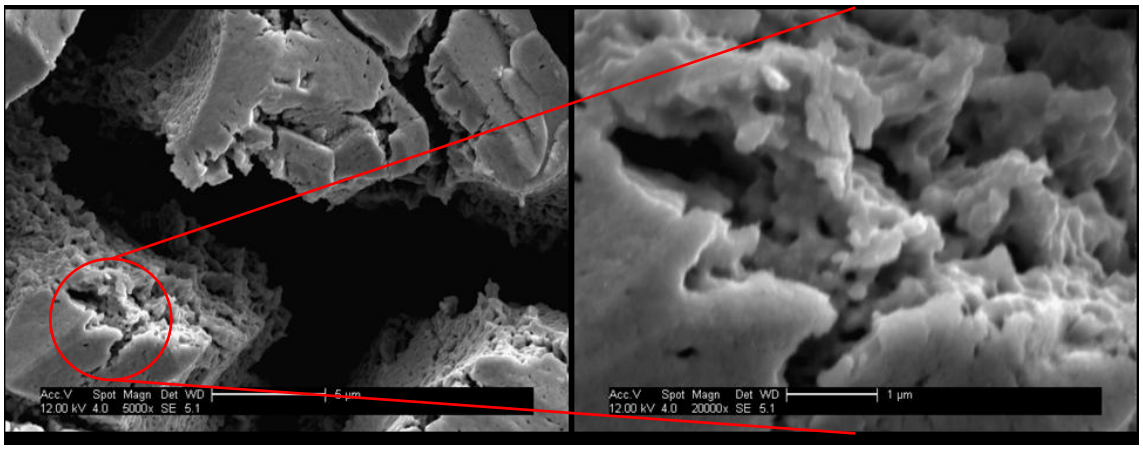

Figure 8-74. SEM micrographs of the surface morphology of sample RT-A.04/03/13-125.1100(600)-W.02 (downstream) showing the development of pores within surface cracks.

The same commentary regarding surface morphology made for the samples reduced at 400 °C as these reduced at 600 °C. There is one notable difference however. W.02's surface microstructure still has a small number of the unusual trapezoidal pores where at 400 °C (and after 15 h to fully reduce) they disappeared. Consistent with overall pore formation behaviour discussed so far the number of randomly distributed submicron pores increases with increasing dwell.

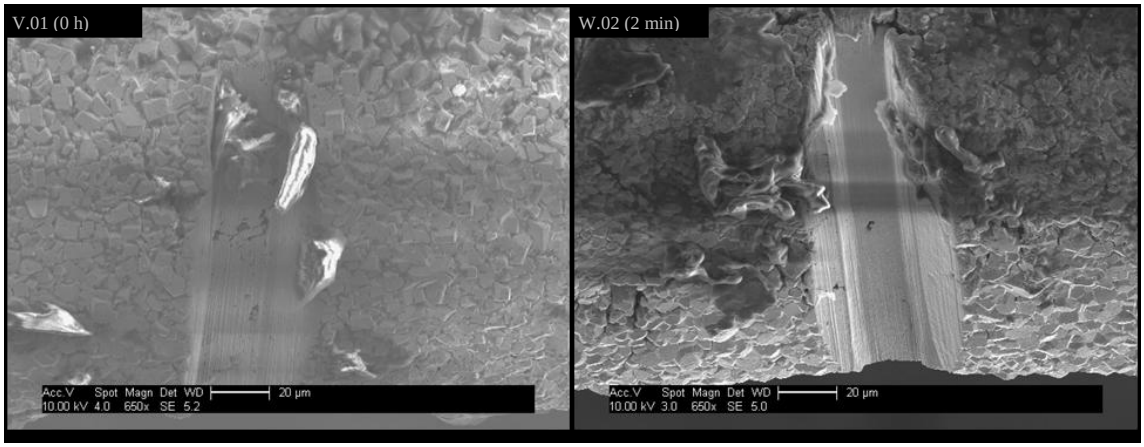

Figure 8-75. SEM micrographs showing the overall cross-section of samples reduced at 600 °C. Left is 0 h dwell (ramp only – the minimum possible) and right is 2 min dwell (nominally fully reduced). Samples: RT-A.19/02/13-125.1100(600)-V.01 (midstream) and RT-A.04/03/13-125.1100(600)-W.02 (downstream).

The sectional micrographs (Figure 8-75.) show that V.01 has a greater quantity of larger pores than W.02. In both cases the larger pores are concentrated towards the middle of the cross-section. Virtually no cracks or intergranular gaps are visible at this magnification, however as subsequent micrographs will show both samples exhibit a not inconsiderable number of these, all rather fine (barely 100 nm wide).

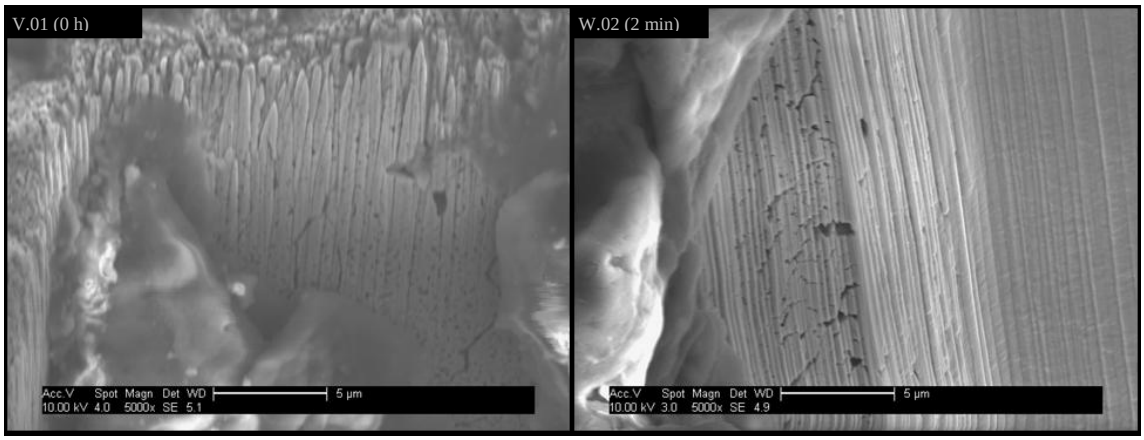

Figure 8-76. SEM micrographs showing the cross-section near the outer edge of samples reduced at 600 °C. Left column is 0 h dwell (ramp only – the minimum possible) and right column is 2 min dwell (nominally fully reduced). Samples: RT-A.19/02/13-125.1100(600)-V.01 (midstream) and RT-A.04/03/13-125.1100(600)-W.02 (downstream). Note that part of the trench appears to have become clogged with debris from an unknown source that was not removed by rinsing the sample with acetone prior to imaging by SEM. This obscures some images yet sufficient detail remains visible.

The sectional microstructure for samples V.01 (ramp) and W.02 (2 min dwell) in the vicinity of the outer edge is very similar. Unlike with those samples reduced at 400 °C there is no notable difference in number, size or shape of pores, nor in which type (pores or cracks) is more numerous. This is to be expected due to the relatively short reduction dwell. The relative scarcity of larger pores is unsurprising given the short dwells – pore coalescence into larger ones is time-dependent. It is notable that the pore structure is very fine even for sample V.01. This may indicate that the formation of the submicron pores (themselves the result of coalesced atomic vacancies caused by the removal of oxygen from the lattice) increases with increasing temperature. The formation of such pores is continuous throughout reduction.

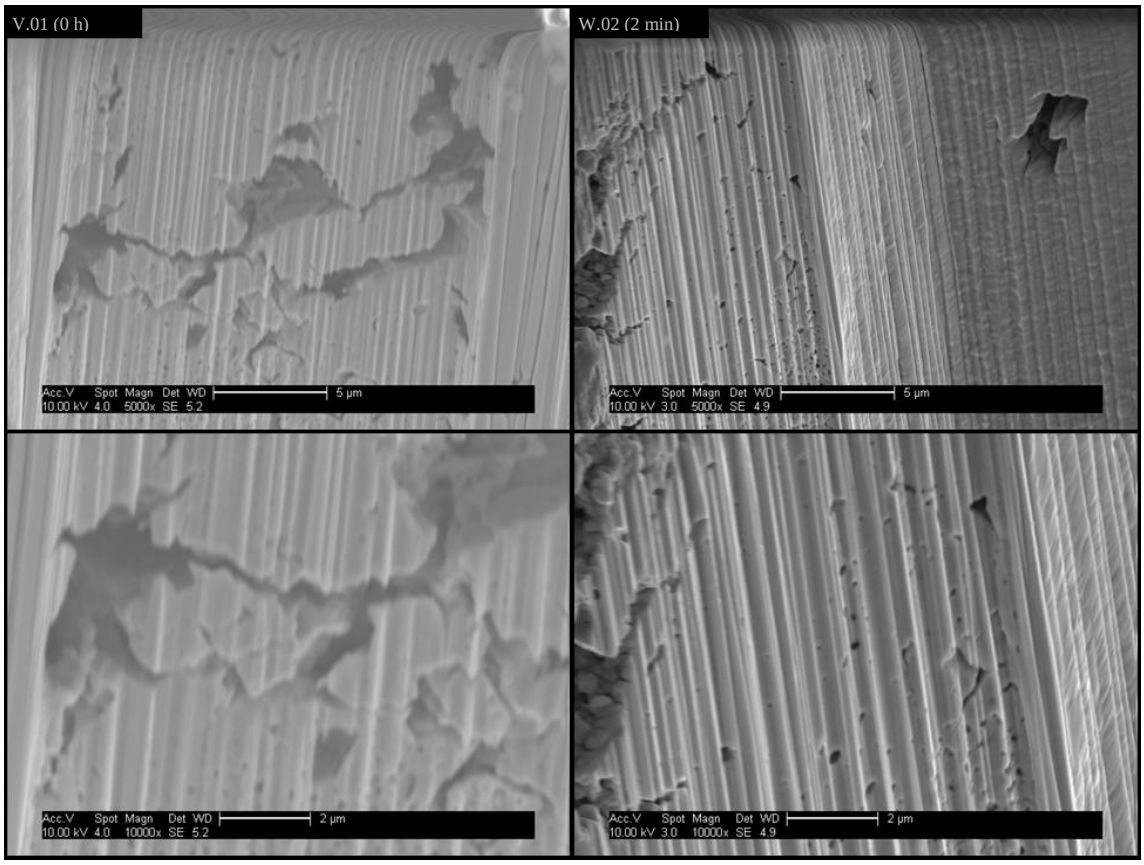

Figure 8-77. SEM micrographs showing the cross-section near the middle of samples reduced at 600 °C. Left column is 0 h dwell (ramp only – the minimum possible) and right column is 2 min dwell (nominally fully reduced). Samples: RT-A.19/02/13-125.1100(600)-V.01 (midstream) and RT-A.04/03/13-125.1100(600)-W.02 (downstream).

The middle third of the section of V.01 is very porous; a combination of pores in the range submicron, 1–2 μm, intergranular cracks/gaps and large (~5 μm) intergranular spaces (irregular pores not merely widened grain boundaries). W.02 is similar but lesser in all aspects. It is possible that the greater porosity exhibited by V.01 in this area of the cross-section is coincidental. However, the similarity between the two samples otherwise (surface morphology, sectional microstructure in the vicinity of the outer edge and inner edge) does not suggest this.

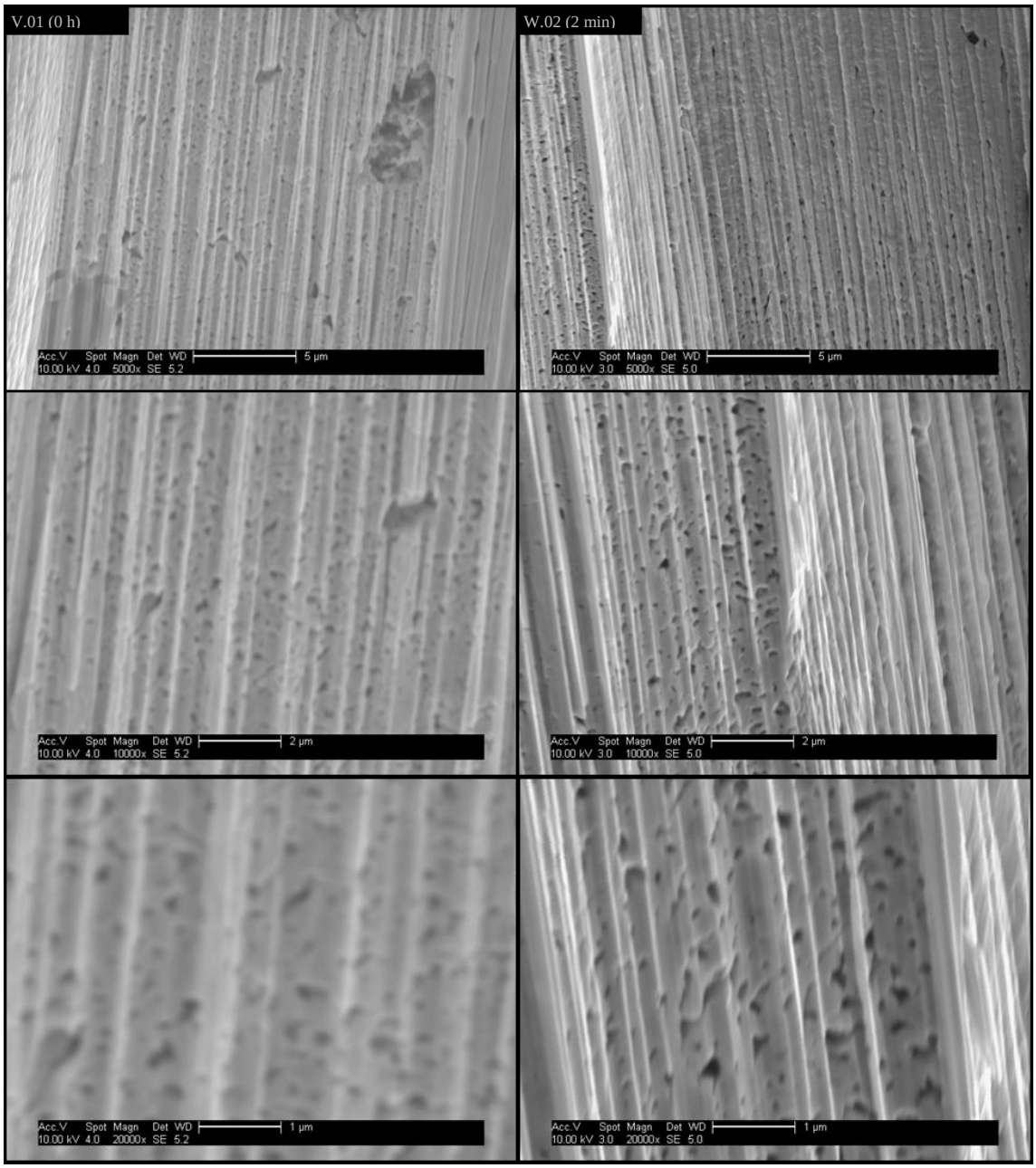

Figure 8-78. SEM micrographs showing the cross-section near the inner edge of samples reduced at 600 °C. Left column is 0 h dwell (ramp only – the minimum possible) and right column is 2 min dwell (nominally fully reduced). Samples: RT-A.19/02/13-125.1100(600)-V.01 (midstream) and RT-A.04/03/13-125.1100(600)-W.02 (downstream).

The very small (100 nm to 250 nm), evenly and randomly distributed pores visible in the above set of micrographs are virtually the same for both sample V.01 and sample W.02. This is, once more, not unexpected given the short duration of both dwells and is consistent with all the micrographs for these two samples discussed. The large pore visible in the V.01 micrographs was probably there prior to reduction. I infer this from its drastic difference (size and morphology) when compared to the other pores visible in this section.

On a tangential note the high degree of similarity of all the samples' microstructures (particularly pore morphology) indicates that the most suitable tool to discern any significant differences in reduction schemas (particular combinations of temperature and dwell) is permeametry.

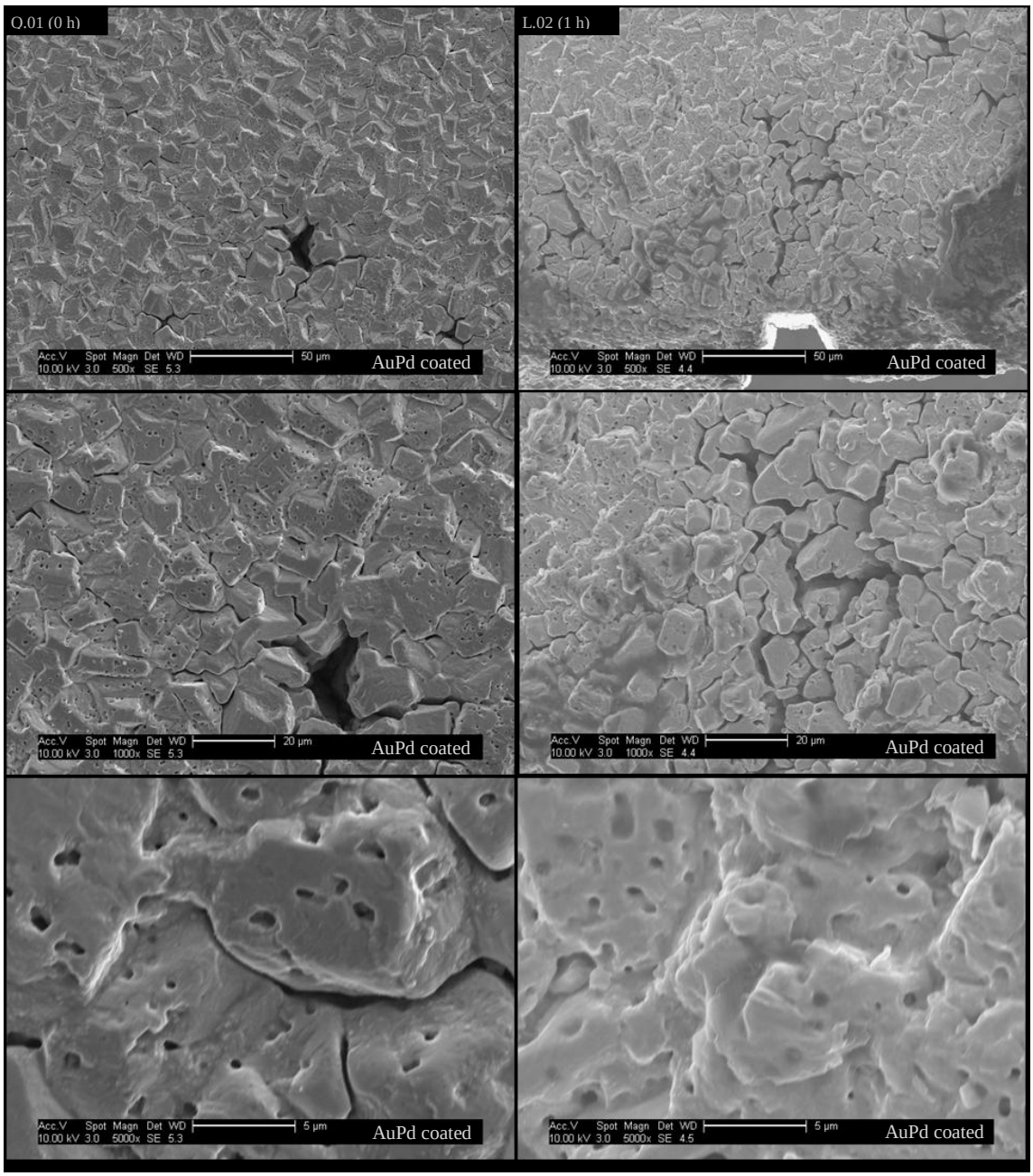

Figure 8-79. SEM micrographs of the surface morphology of samples reduced at 800 °C. Left column is 0 h dwell (ramp only – the minimum possible) and right column is 1 h dwell (nominally fully reduced). Samples: RT-A.23/10/12-125.1100(800)-Q.01 (downstream) and RT-A.23/10/12-125.1100(800)-L.02 (upstream).

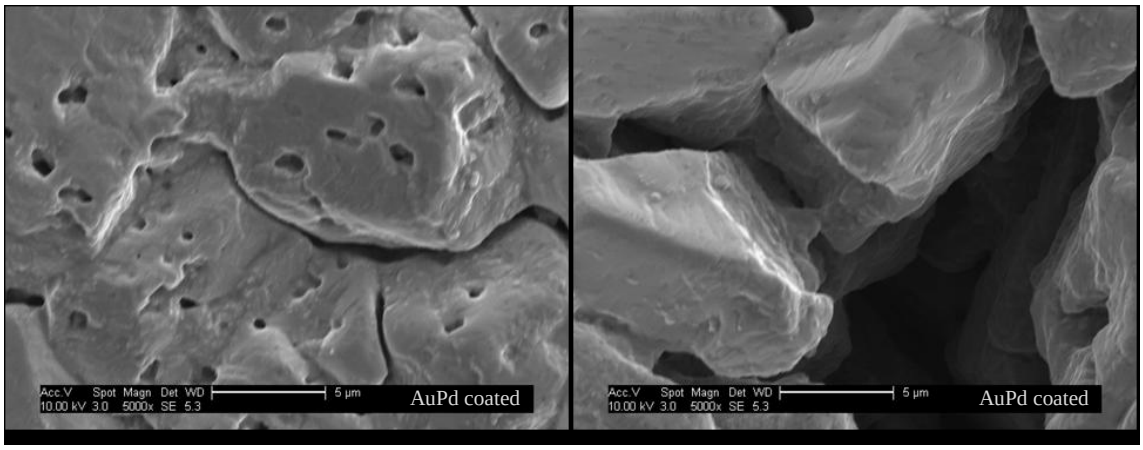

Figure 8-80. SEM micrographs of the surface morphology of sample RT-A.23/10/12-125.1100(800)-Q.01 (downstream) reduced at 800 °C emphasizing the surface crack shape.

Both samples were coated with a few nm of AuPd by sputtering to improve resolution. The coating was omitted on those samples analysed initially because previous experience showed such coatings are visible at higher magnifications (appearing similar to reptile scales) potentially obscuring pores 100 nm across or smaller. A new coater enabled coatings to be deposited that are not visible in these micrographs (and a few others) and do not obscure even very small pores.

The surface morphology of sample Q.01 is very similar over its entire surface. The only noteworthy variation is one already described; a difference between areas in the immediate vicinity of the tube ends and the rest of the surface (see discussion after Figure 8-67.). At lower magnifications L.02 and Q.01 have the same surface morphology. However, from approximately 1,250× magnification it becomes apparent that as reduction progresses submicron pores appear, randomly distributed, through grains (intragranular rather than intergranular). Q.01 has a small scattering of such small pores close to 1 μm in diameter, whereas L.02 exhibits a large number of closely distributed pores ranging in size from c.100 nm to just below 1 μm. There was a notable paucity of pores on the surface of L.02 in the vicinity of cracks; virtually all pores on this sample were intragranular. It is unclear whether there is any significant increase in the number of cracks forming at the surface after the 1 h dwell (i.e. from sample Q.01 to L.02).

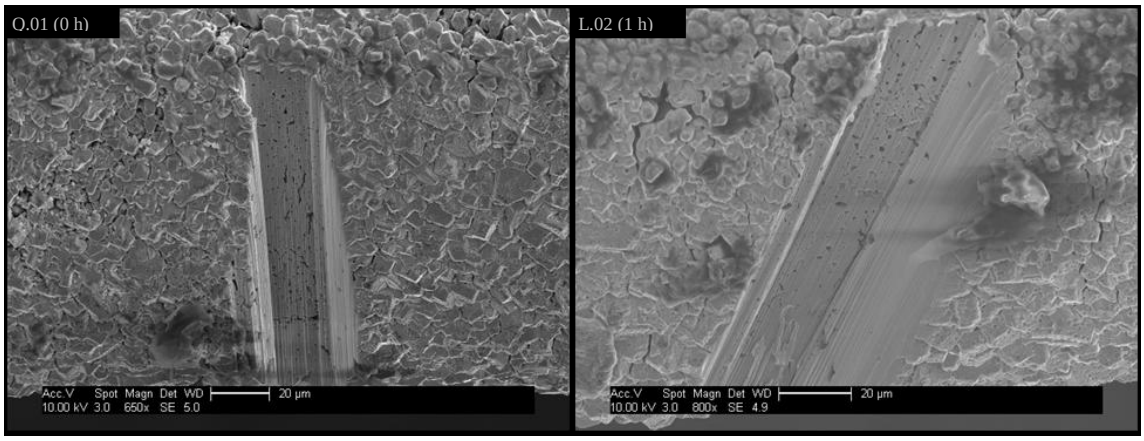

Figure 8-81. SEM micrographs showing the overall cross-section of samples reduced at 800 °C. Left column is 0 h dwell (ramp only – the minimum possible) and right column is 1 h dwell (nominally fully reduced). Samples: RT-A.23/10/12-125.1100(800)-Q.01 (downstream) and RT-A.23/10/12-125.1100(800)-L.02 (upstream).

Both sample Q.01 and sample L.02 show similar cross sectional microstructures. There are both larger pores (for both samples of about 2 µm at the largest) and intergranular gaps or cracks, with a preponderance of pores over cracks. Unlike samples shown previously the random distribution of cracks and pores is uniform from outer edge to inner edge for both of these samples. Refer to Figure 8-69. and Figure 8-75., and their respective analyses, for comparison.

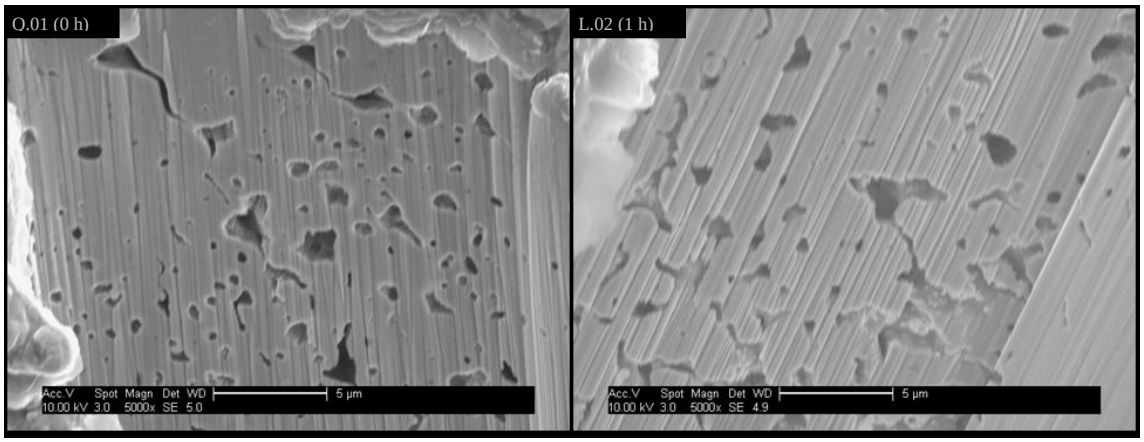

Figure 8-82. SEM micrographs showing the cross-section near the outer edge of samples reduced at 800 °C. Left column is 0 h dwell (ramp only – the minimum possible) and right column is 1 h dwell (nominally fully reduced). Samples: RT-A.23/10/12-125.1100(800)-Q.01 (downstream) and RT-A.23/10/12-125.1100(800)-L.02 (upstream).

The two samples represented in Figure 8-82. above exhibit the combination of crack-like pores and roughly two sizes of circular pores (c. 2 µm and submicron) that is consistent with the other reduction samples. The random distribution, pore geometries are also essentially analogous. Q.01, furthermore, undergoes a change in microstructure as discussed earlier: fewer, larger pores. In this case, however, the change is rather subtle. There may also be greater interconnection between pores, although this may be by chance.

The mechanism forming the pores is not altered by the reduction temperature. As a result the cross-section of Q.01 near the outer surface of the tube is particularly interesting because it demonstrates how pores are interconnected into a network, with channels from the interior to the oxide.

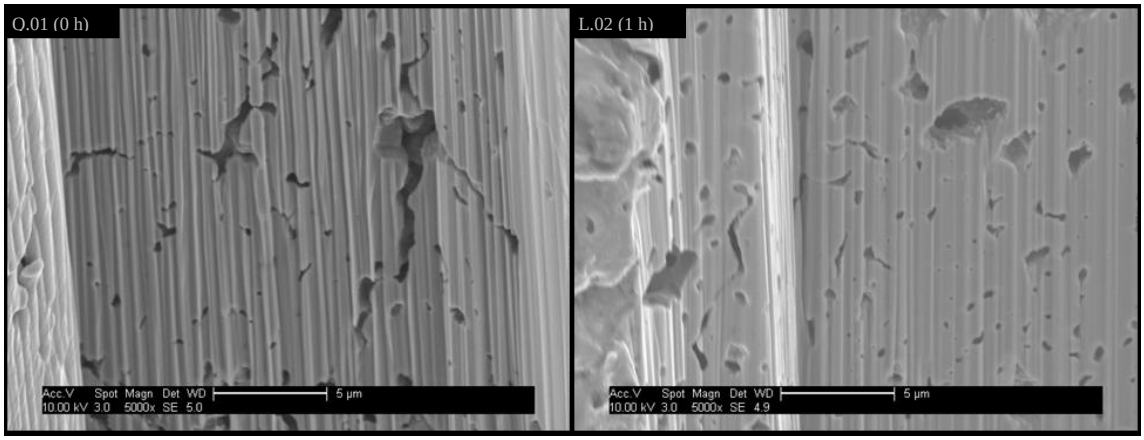

Figure 8-83. SEM micrographs showing the cross-section near the middle of samples reduced at 800 °C. Left column is 0 h dwell (ramp only – the minimum possible) and right column is 1 h dwell (nominally fully reduced). Samples: RT-A.23/10/12-125.1100(800)-Q.01 (downstream) and RT-A.23/10/12-125.1100(800)-L.02 (upstream).

For sample Q.01 there is no noticeable change in microstructure from the sectional micrographs of the area near the outer edge and the middle. Both Q.01 and L.02, considering the middle section, exhibit greater visible porosity than samples reduced at 400 °C and 600 °C. The microstructure is more similar to that seen at 600 °C, only with smaller cracks and larger and more numerous pores. Samples H.02 and I.01 (reduced at 1,000 °C) are both more porous showing a great deal of combination of small vacancies and pores into larger roughly circular pores. The effect of dwell is consistent throughout. Sample L.02 exhibits a lower pore density and a greater number of pores in the 1 μm (or slightly submicron) range rather than of around 2 μm.

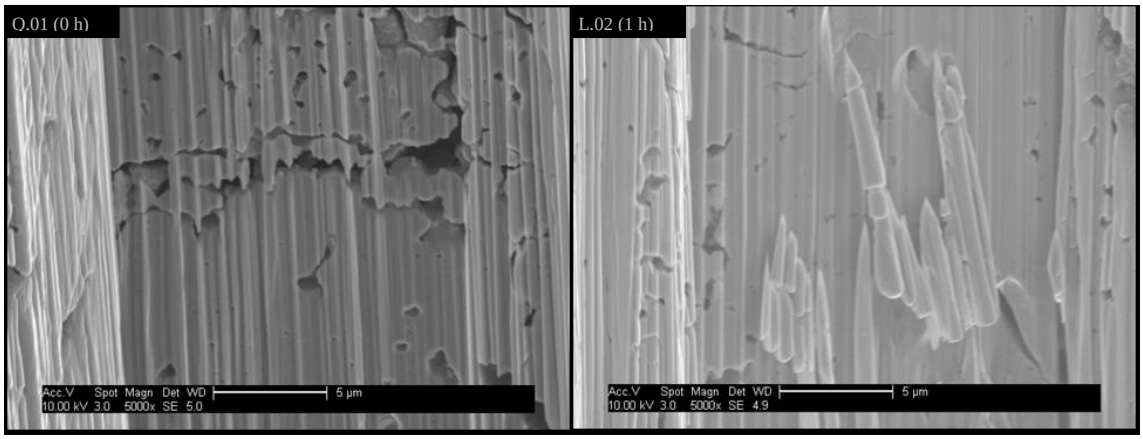

Figure 8-84. SEM micrographs showing the cross-section near the inner edge of samples reduced at 800 °C. Left column is 0 h dwell (ramp only – the minimum possible) and right column is 1 h dwell (nominally fully reduced). Samples: RT-A.23/10/12-125.1100(800)-Q.01 (downstream) and RT-A.23/10/12-125.1100(800)-L.02 (upstream).

The microstructure of the areas near the inner edge of the tube of sample Q.01 is similar to that near the outer edge and towards the middle of the FIB-milled section. The one difference of note is that nearest the inner edge there were few pores observed (all approximately 1 μm in diameter). Regarding sample L.02 the microstructure near the inner edge is similar to that near the outer edge and towards the middle of the milled section. However, the majority of pores are intergranular and crack-like. It is possible that the significant waterfalling evident (caused by the FIB milling) obscured some of the finer pores. Some submicron pores, in small clusters of three or four, are visible. They are among the smallest observed for any of these samples being approximately 80 nm in diameter. The 1 h dwell seems to have little to no effect on the microstructure.

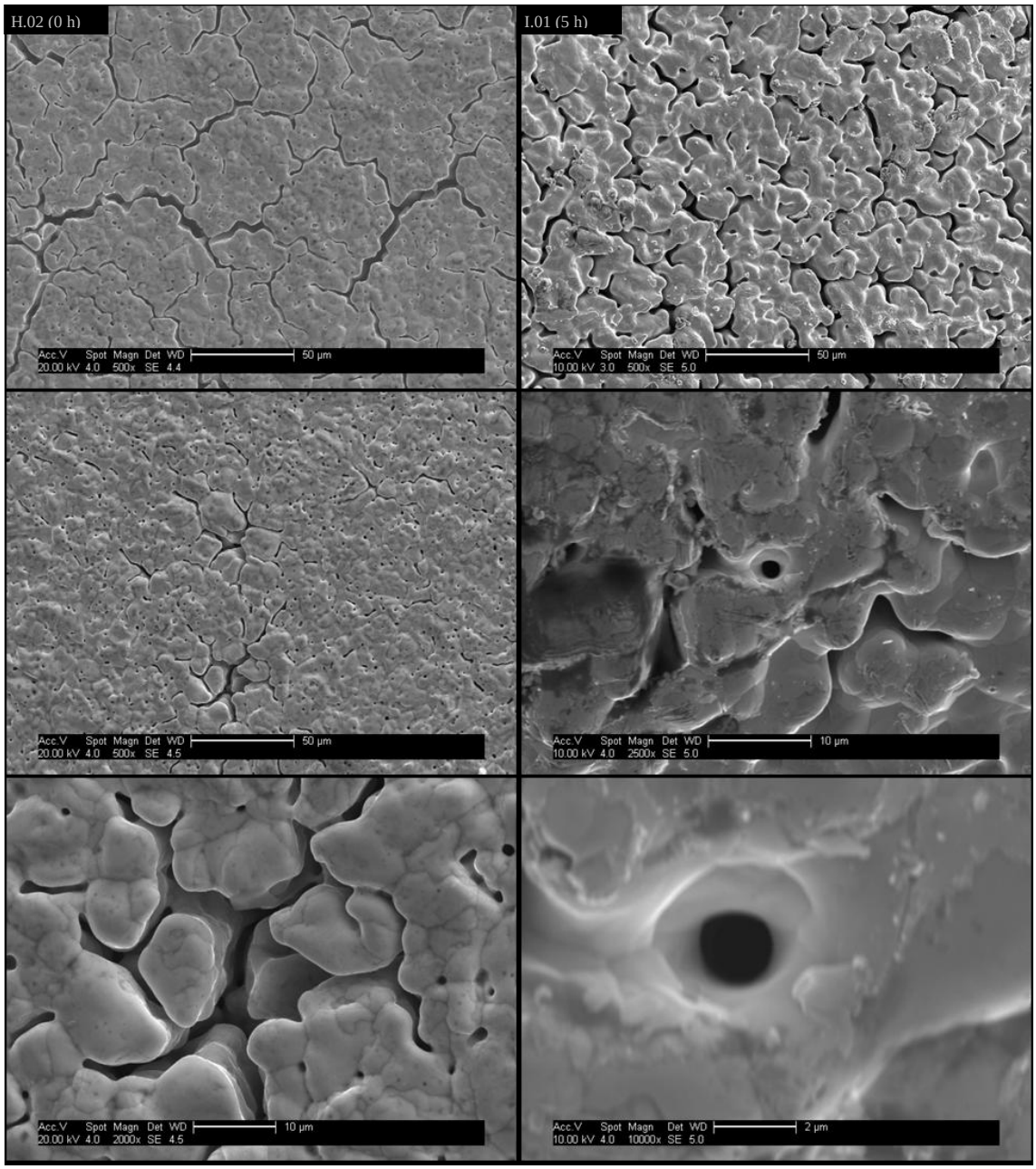

Figure 8-85. SEM micrographs of the surface morphology of samples reduced at 1,000 °C. Left column is 0 h dwell (ramp only – the minimum possible) and right column is 5 h dwell (nominally fully reduced). Samples: RT-A.12/06/12-125.1100(1000)-H.02 (downstream) and RT-A.09/10/12-125.1100(1000)-I.01 (upstream). I.01 was coated with a few nm of AuPd by sputtering to improve resolution.

I.01 was coated with a few nm of AuPd by sputtering to improve resolution. The coating was omitted on those samples analysed previous to this because past experience showed such coatings are visible at higher magnifications (appearing similar to reptile scales) potentially obscuring important details such as pores 100 nm across or smaller. However, it was found needful in this instance to achieve acceptable resolution. This set of images (and others in the aforementioned appendix) show good detail of the cracks

becoming more rounded due to the high reduction temperature. There are also fewer circular pores evident than on other samples, but these are larger.

The relatively large, very circular, pore visible on the surface of I.01 was an isolated an unusual feature. It is assumed this site is a triple point, and the unusually circular nature of the pore is due to fusion of the grains making it appear to be an isolated large pore in the centre of a surface grain. However, elsewhere on the sample (as seen in Figure 8-85.) pores to indeed break through to the surface. This example may have been closed from the surface and spallation during cooling exposed it to the surface. Pores with a similar appearance on the surface of H.02 are more obviously located at triple points.

As noted earlier the curvature parallel to the long axis of the tubes near its ends results in more cracks and intergranular gaps (particularly at triple points) more pronounced than elsewhere on the surface of a given sample. While this applies to both H.02 and I.01 the effect is far less noticeable than on samples reduced at lower temperatures. The obvious inference here being that the greater mobility of material at higher temperatures enables grains to adjust more readily to the additional surface strain (and attendant surface energy) caused by the additional axis of curvature near the tube ends rather than having energy sufficient only for grain rotation. This is discussed in more detail later.

H.02 and I.01 show very similar surface morphologies. As reduction progresses grain edges become more rounded, and the small, mainly circular, intragranular pores grow and simultaneously intergranular ones extend and connect forming a distinctive ‘ant farm’-like network compared to the predominance of small pores of H.02.

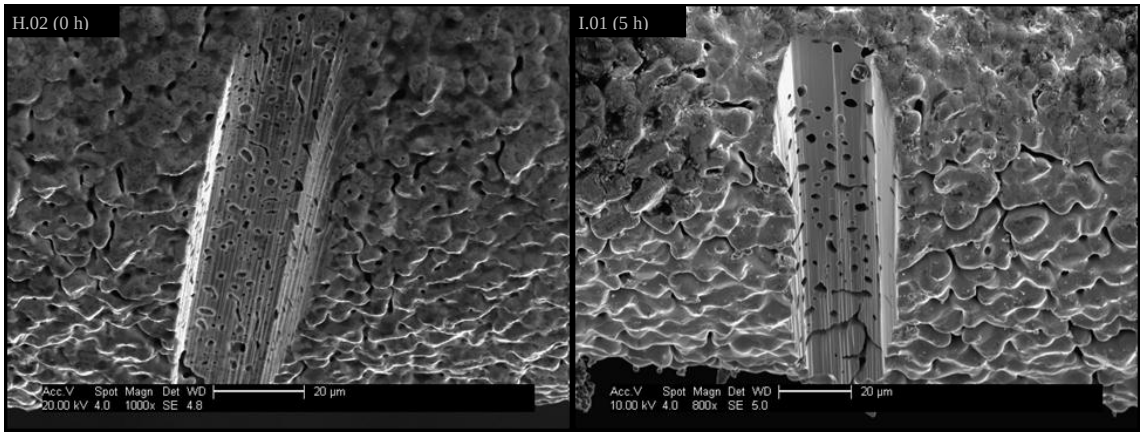

Figure 8-86. SEM micrographs showing the overall cross-section of samples reduced at 1,000 °C. Left column is 0 h dwell (ramp only – the minimum possible) and right column is 5 h dwell (nominally fully reduced). Samples: RT-A.12/06/12-125.1100(1000)-H.02 (downstream) and RT-A.09/10/12-125.1100(1000)-I.01 (upstream). I.01 was coated with a few nm of AuPd by sputtering to improve resolution.

H.02 shows a uniform, random, distribution of large pores and a few intergranular cracks. As expected the sectional microstructure of I.01 is very similar to H.02.

However, as reduction progresses vacancies, pores and even the relatively large intergranular cracks will sinter closed (at least partially). I.01 has next to no smaller pores, only those in the range approximately 2 μm to 4 μm.

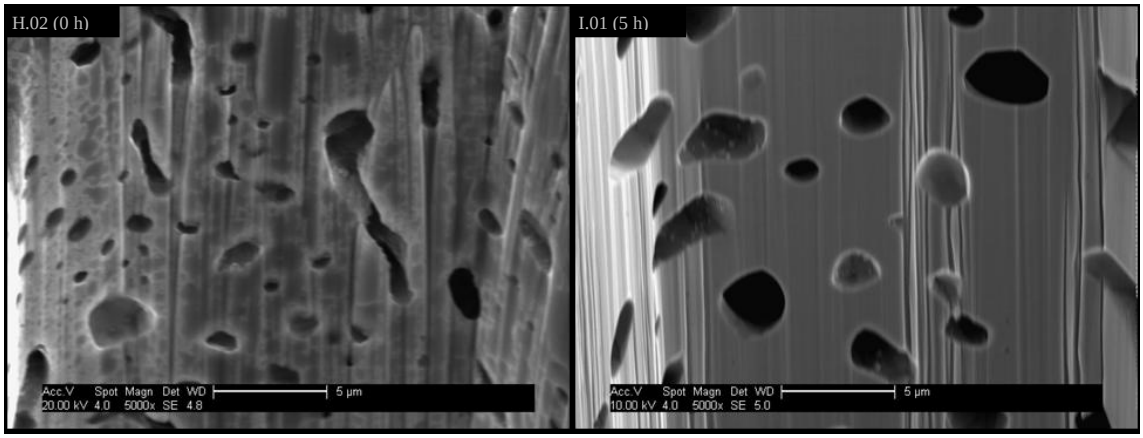

Figure 8-87. SEM micrographs showing the cross-section near the outer edge of samples reduced at 1,000 °C. Left column is 0 h dwell (ramp only – the minimum possible) and right column is 5 h dwell (nominally fully reduced). Samples: RT-A.12/06/12-125.1100(1000)-H.02 (downstream) and RT-A.09/10/12-125.1100(1000)-I.01 (upstream). I.01 was coated with a few nm of AuPd by sputtering to improve resolution.

The pores visible in the sectional micrograph of sample H.02 (0 h dwell) near the outer edge range in size from approximately 500 nm to over 2 μm. On the other hand the same area of sample I.01 shows only two pore sizes: approximately 1.5 μm and 3.5 μm. It appears as though the reduction temperature has a greater influence on microstructure than the dwell. Both samples reduced at 1,000 °C seem to show the end result of pores coalescing into larger, rounded ones. The dwell only seems to reduce the appearance of intergranular gaps, consistent with expected behaviour of materials at high temperature minimising surface energy.

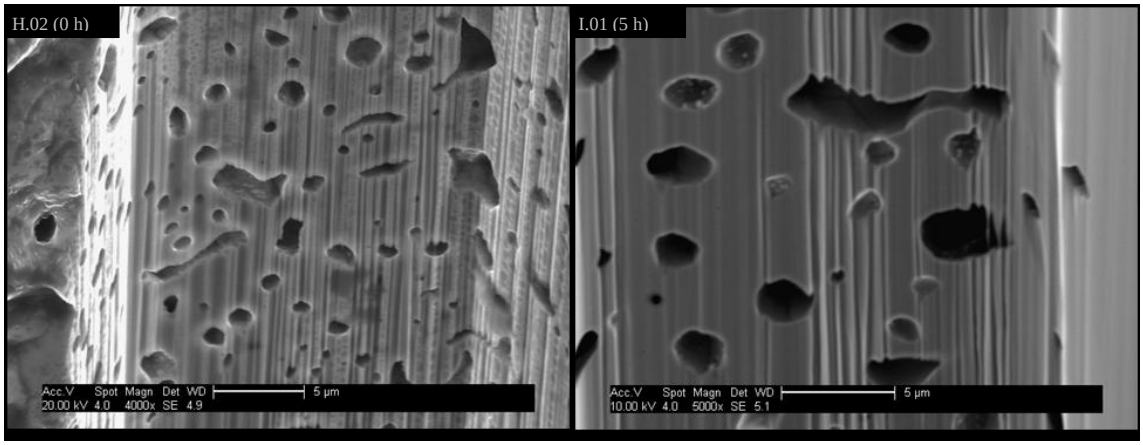

Figure 8-88. SEM micrographs showing the cross-section near the middle of samples reduced at 1,000 °C. Left column is 0 h dwell (ramp only – the minimum possible) and right column is 5 h dwell (nominally fully reduced). Samples: RT-A.12/06/12-125.1100(1000)-H.02 (downstream) and RT-A.09/10/12-125.1100(1000)-I.01 (upstream). I.01 was coated with a few nm of AuPd by sputtering to improve resolution.

The sectional micrographs of the middle area of samples H.02 and I.01 are very similar to those near the outer edge. The overall density and distribution of pores is also very similar. In fact, there are no distinguishable differences between the two sections (for both samples).

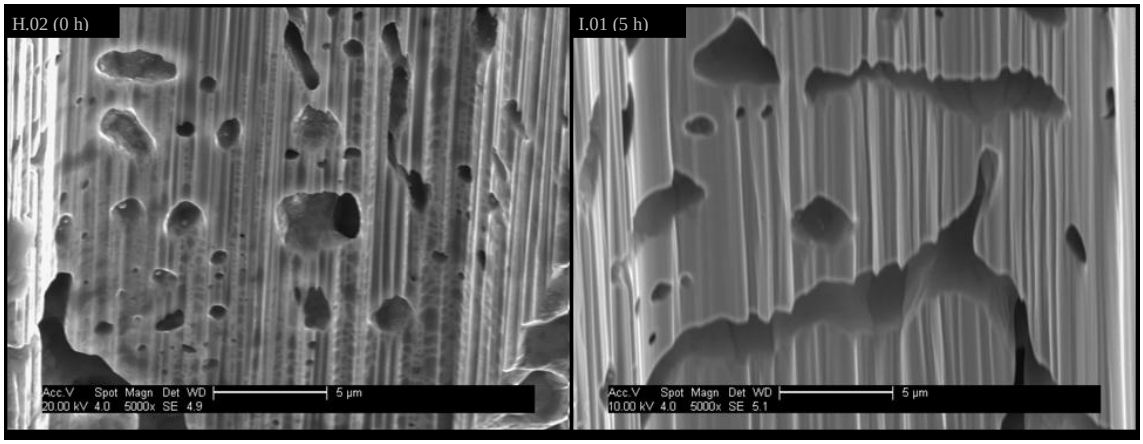

Figure 8-89. SEM micrographs showing the cross-section near the inner edge of samples reduced at 1,000 °C. Left column is 0 h dwell (ramp only – the minimum possible) and right column is 5 h dwell (nominally fully reduced). Samples: RT-A.12/06/12-125.1100(1000)-H.02 (downstream) and RT-A.09/10/12-125.1100(1000)-I.01 (upstream). I.01 was coated with a few nm of AuPd by sputtering to improve resolution.

As may be seen in the micrographs of Figure 8-86. the reduction in quantity and increase in size of the pores with dwell is greater near the inner edge of the sample than other areas. Notice that, as discussed earlier, the dwell does not increase MFR (at least not with statistical significance at any reasonable confidence interval). Instead it alters the microstructure.

High temperature deformation was a significant contributor to the final microstructure observed. Determining what type(s) of creep influence the anodes greatly improves our understanding of the resulting microstructure as well as improving the understanding of the mechanisms at work during reduction. Please refer to section 8.9.11 (above) for details on the types of creep mechanisms and the utilization of deformation maps.

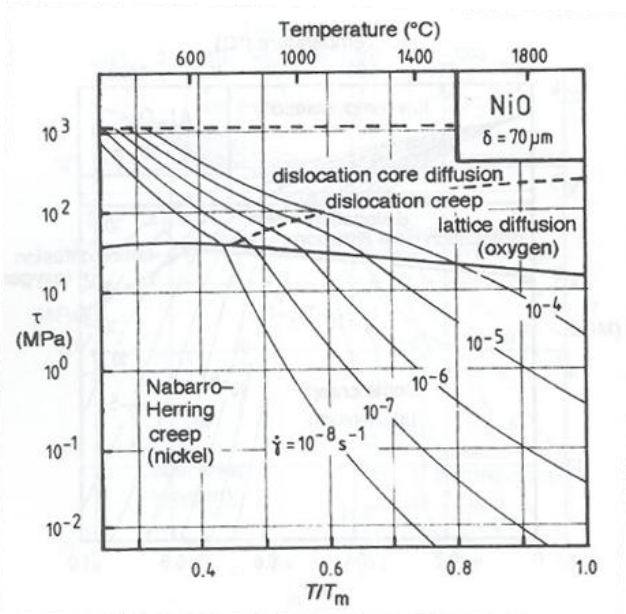

Figure 8-90. Deformation mechanism map for NiO from Schütze (1997). Repetition of Figure 8-50. for convenience.

During the reduction of the samples, the map in Figure 8-90. indicates, assuming stresses are low due to effectively high temperature annealing in the latter stages of oxidation, high temperature deformation will be dominated by Nabarro-Herring creep (controlled by lattice diffusion) at all temperatures considered. Extrapolating to the observed reduction behaviour of the samples one may conclude that the microstructure is altered by the removal of oxygen leaving voids as discussed previously but also that the grains reshape themselves by high temperature creep and grain rotation controlled by the diffusion of Ni cations (higher diffusion rate than oxygen). It is apparent, from the pores within grains, that the resulting slip systems open up routes for the ingress of hydrogen and egress of water vapour resulting in internal reduction facilitated by the creep deformation.

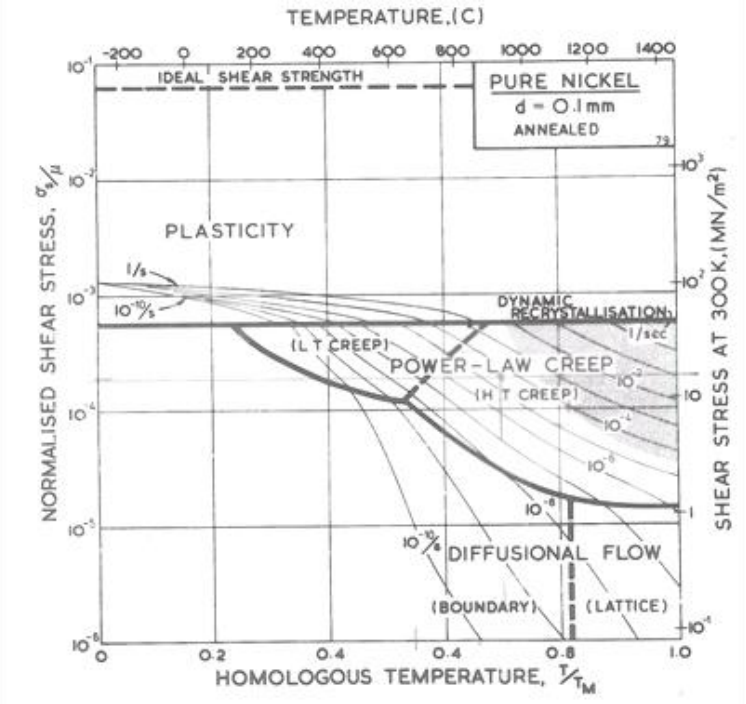

Figure 8-91. Deformation mechanism map for pure Ni (annealed with obstacle spacing taken as 2×10^{-7}) from Frost and Ashby (1982). The shaded areas are dynamic recrystallisation.

In pure f.c.c. metals such as Ni the density and arrangement of dislocations determines the yield strength and plastic behaviour, and therefore the work hardening strongly impacts this [Frost and Ashby 1982]. Recall the tubes are delivered in a work hardened state. The final map shown in Figure 8-49. (repeated here for convenience as Figure 8-91.) is for annealed Ni. The samples anneal as they oxidise relieving some growth strain, then again as they are reduced, almost certainly causing the distortion in full length samples when insufficiently supported (see chapter 11). The matter is complicated of course by the presence of both Ni and NiO in proportions according to the state of oxidation or reduction. Annealing lowers the yield strength, facilitating creep (and low temperature creep).

Recall from 8.9.11 that stress greatly affects creep rate. Given the manner in which curvature alters stress the anodes therefore exhibit different creep behaviour towards the convex or concave surfaces. During reduction the inner, concave, surface and the volume in its vicinity experience greater stress since during oxidation the convex parts have a higher creep rate to deform plastically. In turn, this leads once again to differential creep rates either side of the neutral plane and potential macroscopic deformation. It also implies that during reduction the first areas to be reduced will thereafter be dominated by Nabarro-Herring diffusion creep (Ni cations) and the still-to-be-reduced oxide by dislocation creep. *Ergo* it will be dictated by $T_{homologous}$ (Ni) and $T_{homologous}$ (NiO) (i.e. $\frac{T}{T_{melting}}$ of the metal and oxide, respectively).

In the pure metal creep begins at approximately 0.3 T_m [Frost and Ashby 1982], and is diffusion controlled yet slower in the more closed f.c.c. structure than the more open b.c.c. one [Frost and Ashby 1982]. "This low temperature creep is predominantly at grain boundaries for $T < 0.4T_m$ and will be some form of lattice creep for $T > 0.6T_m$." (private communication with Professor John Nicholls). For Ni the two boundaries are 418 °C and 764 °C respectively. Therefore, at the low reduction temperature of 400 °C creep is dominated by boundary diffusion and at 1,000 °C by lattice diffusion.

The grain boundary separation observed by Schütze and others is shown in the figure below in which a 99.2% Ni sample was deformed at 800 °C [Schütze 1997]. Note the virtually identical appearance of the anode convex surface (the curvature induces a tensile loading) after oxidation but prior to reduction pictured in micrographs in that section of this chapter. Schütze (1997) terms this process oxide grain boundary loosening (Figure 8-93.).

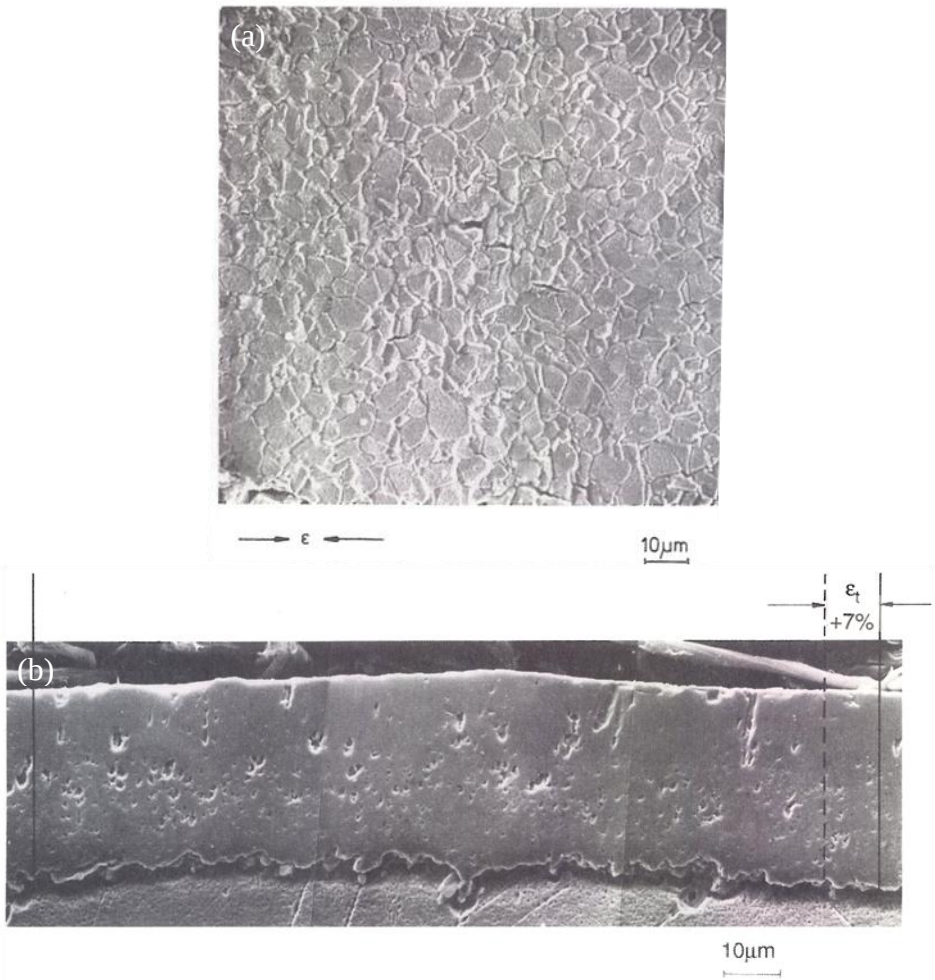

Figure 8-92. Surface of oxidised 99.2% Ni deformed at 800 °C to $\varepsilon = -0.1$ and $\dot{\varepsilon} = -10^{-3}$ s^{-1} (a) showing oxide grain loosening' and (b) cross-section showing pores [Schütze 1997].

Schütze (1997) also observed the lack of subsurface cracks and the presence of small, somewhat rounded, pores instead. This is attributed to longer cation diffusion paths to the near-surface areas and, hence, a lower local healing rate [Schütze 1997] and therefore more pronounced cracks remain. Cracks deeper into the oxide only remain if the transport paths for oxygen are impeded by local healing [Schütze 1997]. The combination of crack surrounding grains (the grain loosening Schütze (1997) refers to) and local strain fields (particularly tensile ones and stresses induced by the oxide growth on neighbouring grains) could lead to grains in the oxide becoming sufficiently mobile to shift and rotate. Should it occur continually (including attendant oxide regrowth) in the oxide this type of deformation process to plastically accommodate strains in the oxide is termed 'quasi-grain-boundary sliding' or 'pseudo-plasticity' by Schütze (1997).

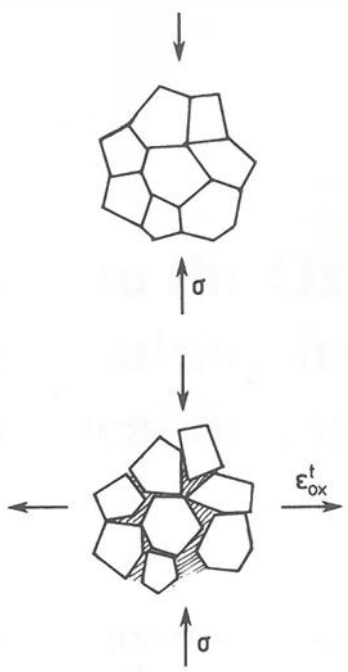

Figure 8-93. Schematic of oxide grain loosening, displacement and rotation, as well as oxide regrowth (hatched area), termed 'quasi-grain-boundary sliding' or 'pseudo-plasticity' [Schütze 1997].

From the deformation map of Figure 8-91. we may estimate creep rates ($\dot{\varepsilon}$) at each temperature of interest for Ni. It was assumed that the stress would be low, taking the normalised shear stress ($^{\sigma_s}/_{\mu}$) as 1×10^{-5}. At $0.39T_m$ (400 °C) the effective $\dot{\varepsilon} = <10^{-12}$ s^{-1}. At $0.51T_m$ (600 °C) the effective $\dot{\varepsilon} = 3\times10^{-11}$ s^{-1}. At $0.62T_m$ (800 °C) the effective $\dot{\varepsilon} = 5\times10^{-10}$ s^{-1}. Finally, at $0.74T_m$ (1,000 °C) the effective $\dot{\varepsilon} = 3\times10^{-9}$ s^{-1}. At higher shear stress the creep rates are significantly greater, so these numbers correspond to a state in which a relatively low amount of grain re-arrangement occurs; in practice it may well be greater. While the estimated creep rates are not especially rapid it is clear that once reduced creep is an important mechanism resulting in microstructural modification once reduced to nickel.

One might reasonably expect some analysis to follow of pore sizes, pore size distribution and approximate pore density (number of pores visible per m^2 of milled section surface). However, for the purposes of creating anodes a more qualitative analysis of the pore structures was deemed sufficient for the following reasons: a simple typography of what sorts of pores (pore sizes, shapes, and distributions through the sample) is sufficient to differentiate the different reduction profiles; permeametry (see chapter 1) is a far better tool than any analysis of the pores visible by SEM to ascertain usefulness of the process for creating anodes and selecting the optimal reduction profile. Also, it would require micrographs to be taken of additional sections along the tube, and repeating this for several samples at the same dwell for such a quantitative analysis to be valid. At this juncture reproducibly making anodes optimised for permeance is the priority. Scientific investigation of the correlation between temperature and dwell on pore sizes, pore size distribution, and pore density with the statistical backing to ensure validity is outside the scope of my thesis.

8.13 Reduction Conclusions

The reduction experiments of Chatterjee *et al.* (2012) with porous NiO pellets (a close analogue of my own NiO tubes) reduced at 300–700 °C resulted in a maximum MFR of 0.95, similar to my own experience where the maximum was 0.97. The remaining oxygen is in solution, as discussed previously, corresponding to the solubility of oxygen in nickel at the reduction temperature.

The 5 vol.% hydrogen (balance Ar) mix used is sufficient to attain the desired reduction but its kinetics are unacceptably slow both for further experiments and for any practical fabrication, laboratory or otherwise, of anodes. Changing to 100 vol.% H_2 dramatically hastened the kinetics.

The majority of the tier 1 (5 vol.% H_2) objectives were aborted because of the unacceptably slow kinetics, as discussed above. These were re-instated as the goals of tier 2 (100 vol.% H_2) and met. Two feasible reduction processes were found: either at 400 °C for 15 h or at 1,000 °C with no dwell (i.e. ramp only). The intermediate temperatures did not offer any advantages compared to low temperature or low dwell. The relatively low porosity observed in certain areas is of some concern. However, the rapidity of the reduction process suggests that there is sufficient gas transport through the oxide morphology for successful implementation as a SOFC anode. The energy costs are another factor in deciding optimal reduction scheme for the creation of anodes by this method, and are discussed later (section 11.4.1). Reproducibility is excellent despite safety constraints on the loading/unloading and temperature ramp procedures.

The rapidity of the reduction even at temperatures as low as 400 °C is key. It is indicative of a surface-, rather than bulk-, controlled process. There are two identifiable

modes for the progression or surface-process dominated reduction: 1) hydrogen reacts with surface oxygen at surfaces including grain boundaries and the pore network already in place after oxidation 2) at sites where oxygen has been removed by the hydrogen the local oxygen partial pressure is reduced allowing oxygen to diffuse to the surface and be reduced in turn. The combination of these two sub-mechanisms has an important implication. As the reduction progresses the surface area available for further reduction continually increases, nearing an exponential type behaviour. The implication is that the surface available for reduction, and therefore, the overall reduction rate increases with time. This is due to the formation of additional surface available for reduction.

Both alloy (Ni with dissolved oxygen) and NiO creep and vacancy movement in the alloy and oxygen vacancy in the oxide are diffusion controlled, specifically grain boundary controlled. This suggests that the actual reduction is more or less linear, dependent only on the availability of oxide to reduce. $T_{0.7}$ for Ni is 1,000 °C, and $T_{0.4}$ is 400 °C, these two homologous temperatures are associated with long range and short range (surface) diffusion respectively. So the two temperature extremes of interest from a manufacturing standpoint are also the limits at either end of long and short range diffusion within nickel, whose influence on creep behaviour (and it likely affect on microstructure evolution) was discussed in the preceding paragraphs. Similarly $T_{0.7}$ for NiO is 1,287 °C, and $T_{0.4}$ is 618 °C.

For reduction at 400 °C a 5 h dwell results in an average MFR of 0.95. This may reasonably be considered to be complete reduction. However, there is far less scatter in the data for reduction with a 15 h dwell, resulting in an average MFR of 0.97 (variance is only 0.001 ~ 0.1%). For this reason it was decided that the 15 h dwell was preferable despite at first glance it hardly seems worth an additional 10 hours of dwell for just an 0.02 increase in the mass fraction reduced. Additional data from new samples and perhaps further refinements to the process may alter this in the future. Should further data prove that a 5 h dwell is sufficient this would be a significant change from a manufacturing perspective.

Increasing the performance of SOFCs depends in no small part on optimising the microstructure of the electrodes, since this is where gases diffuse and the electrochemical reactions take place [Suzuki *et al.* 2009a]. The ideal electrode is made entirely of catalyst material (section 2.8.3); a criterion fulfilled by this design of anode. The synthesis of the results discussed above is therefore that while the optimal reduction scheme between the two extremes is yet to be assessed in terms of gas transport the optimised process produces anodes with excellent potential. To determine which anode is optimal it is necessary to consider the manufacturing (material and energy) cost (see chapter 11), the gas transport performance (see chapter 1) and the resulting electrical and electrochemical performance (see chapter 14) of anodes from the two reduction schemes.

According to the calculations Zaitsev and Zaitseva (2002) the enthalpy of sublimation calculated by third law method, $\Delta sH°_0$ (III), for nickel varies somewhat; 425.5 kJ mol^{-1} at 1,273 °K to 425.1 kJ mol^{-1} at 1,373 °K. They recommend utilising a value of $\Delta_sH°_0$ = 425.3 + 2 kJ/mol for the enthalpy of sublimation. The corresponding saturation pressures of nickel vapour are $p_{s\ (Ni)} = 0.154\times10^{-4}$ Pa and $p_{s\ (Ni)} = 3.040\times10^{-4}$ Pa, respectively. The Ni partial pressure will therefore be very low. *Ergo*, the Ni vapour will have far less impact on the microstructure than the oxygen transport.

8.14 Anode Conclusions

Investigating oxidation-reduction as a potential route to create the desired porosity was carried out in the MSc project. The work done as part of this PhD sought to assess the reproducibility of the process, refine the parameters for full oxidation and full reduction, modify the Wagner model to better represent the process, create a model for the reduction similar to that of the oxidation, and closely monitor any changes in microstructure.

Oxidation-reduction has advantages that become evident when fabrication of SOFCs is envisioned on a production scale as briefly outlined here (and in more detail in section 15.1). The most common means of creating porous anodes is sintering a Ni or NiO powder with the aid of pore-formers. Several separate manufacturing processes are needed to create the electrolyte on top of this and the cathode on top of the electrolyte, and finally any interconnects needed will have to be deposited. By creating porosity in the manner described, and following the electrolyte deposition approach described in chapter 9 it is possible to create all or most of the SOFC in a single machine as described elsewhere (section 15.2). This is of obvious benefit both in terms of ease of automation and significant time savings (by eliminating lengthy drying and sintering steps and all changeover and jigging time after the initial material is loaded).

9 Electrolyte Fabrication and Characterization

Over the last twenty years the PVD route has garnered much interest in the synthesis of solid electrolytes due to its excellent control of film microstructure, porosity, stoichiometry and growth rate [Meng *et al.* 2008]. Other advantages are less unique but no less valuable; including good adherence, high deposition rate and large deposition area. Conversely, the deposition of a ceramic coating suitable for use as an electrolyte is highly dependent on processing parameters including deposition (i.e. substrate) temperature, rotation speed and deposition rate [Matsumoto *et al.* 2008]. Once costs greatly restricted use of the technology, but they are now some 10% of what they were 40 years ago [Meng *et al.* 2008]. All these factors make e-beam PVD a very attractive technique for a wide range of applications, including fuel cells.

EB-PVD coatings of YSZ consist of collinear elongated single-crystal columns with a predominantly <111> orientation on stationary samples but a <100> orientation on rotated samples [Zhao *et al.* 2006]. In the latter case, which is that of this project, the columns are capped by four {111} planes [Zhao *et al.* 2006]. They contain a small volume fraction of intercolumnar pores oriented perpendicular to the coating surface [Zhao *et al.* 2006]. As the EB-PVD technique is a non-equilibrium process it inherently tends to favour such porous structures in a mechanism known as the "shadowing effect," especially at higher deposition rates [Meng *et al.* 2008]. The elongated pores make them more compliant to in plane stress, such as that caused by CTE mismatches and thermal cycling [Zhao *et al.* 2006].

However, if these pores form a diffusion pathway through the electrolyte gas tightness will obviously suffer, although whether this is the case or not is not clear from the literature alone. Investigating this was another novel aspect of my work (see Permeametry Chapter 1). In any case, the small volume of material lost to pores does represent a fraction of oxygen ion conducting material lost and hence a drop in ion flux. However, unless the porosity is large the reduction in ionic conducting paths will be small and can be neglected.

Improving electrolyte gas tightness can be achieved by a post-treatment. Sol-infiltration and heat treatment has proven very effective in this regard [Meng *et al.* 2008]. The sol solution fills the pores and combined with a subsequent heat treatment improves the density of the electrolyte [Meng *et al.* 2008]. In performance terms the effect is a dramatic improvement in both open-circuit voltage (OCV) and current density at low polarisation [Meng *et al.* 2008]. Sealant can reach depths of several hundred μm and generally improves properties other than density – usually microhardness and properties characteristic of functional materials such as relative permittivity [Meng *et al.* 2008].

It is also possible, albeit with a different PVD technique, to improve gas tightness by creating a multilayer structure (multi-beam or jumping beam evaporation) or a zigzag columnar microstructure by alternating substrate rotation.

Meng *et al.* (2008) observe that when a coating is about 10 μm thick a denser top surface forms above a columnar structure. Does this hold true for this project also? What about thinner coatings? If it is visibly less porous it might make sense to use fewer infiltration treatments. The aforementioned authors do not elaborate on the causes for this. Furthermore, this seems to contradict the oft-observed disordered, apparently denser, initial few microns with a columnar morphology on top.

9.1 Electrolyte Fabrication Objectives and Background

Camilleri (2009) successfully demonstrated the creation of a 7YSZ electrolyte by EB-PVD, depositing directly onto tubular Ni anodes. However, only two such demonstrators were fabricated (as a single batch) due to time constraints. It is well known that one of the major hurdles of miniaturisation is achieving acceptable reproducibility. As such, the objective of this chapter is twofold: optimise the deposition process and gather a body of data to assess in detail electrolyte quality and deposition reproducibility.

9.2 Physical Vapour Deposition Mechanisms

What follows is a detailed exposition on the mechanisms relevant to physical vapour deposition and the creation of thin films. First a number of useful concepts will be described followed by elucidation of the mechanisms in a more-or-less atomistic-mechanistic format. Finally parameters influencing deposition will be discussed as far as they are relevant to the creation of electrolyte films on tubes.

9.2.1 Thermodynamic Potentials and the Dividing Surface

Gibbs pioneered applying thermodynamics to surfaces in the 1870s and 1880s [Venables 2000]. The central idea is that of the ‘dividing surface’. At the boundary between phases 1 and 2, the concentration profile of any elemental or molecular or atomic species changes continuously from one level c_1 to another c_2 (see Figure 9-1.). This enables the thermodynamic potentials (including the internal energy U, the Helmholtz free energy F, or the Gibbs free energy G) to be written as contributions from the two phases plus a surface term [Venables 2000].

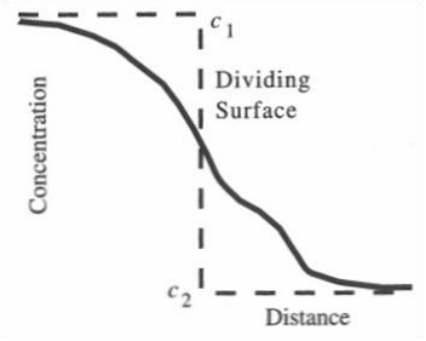

Figure 9-1. Schematic representation of the 'dividing surface' in terms of macroscopic concentrations, after Venables (2000).

In thermodynamics of bulk matter the Helmholtz free energy $F_b = F(N_1, N_2)$ [Venables 2000]. Also (applicable at constant temperature, pressure and particle number):

$$dF_b = -SdT - pdV + \mu dN = 0 \qquad (9.1)$$

Where:

F_b is the Helmholtz free energy [J]
S is the bulk entropy [J]
T is the temperature [°K]
p is the pressure [Pa]
V is the volume [m^3]
μ is the chemical potential [J $mole^{-1}$]
N is the particle number [dimensionless] = n/N_A
n is the number of moles [dimensionless]
N_A is Avogadro's number

Similar equations exist for the other thermodynamic potentials.

It is of interest to derive changed relations for conditions when the system is characterized by a surface area A in addition to the volume [Venables 2000]. With a surface present the total free energy $F_{total} = F(N_1, N_2, A)$, and, assuming that the total number of atomic or molecular entities in the two phases, N_1 and N_2, remain constant [Venables 2000]:

$$dF_{total} = dF_b(N_1, N_2) + f_{surface}dA \qquad (9.2)$$

Where:

$f_{surface}$ is the additional Helmholtz free energy per unit area due to the presence of the surface [J m^{-2}]

Gibbs' concept of the 'dividing surface' is as follows. Although the concentration may vary in the neighbourhood of the surface, the system is considered as uniform up to this ideal interface: $f_{surface}$ is then the surface excess free energy [Venables 2000].

In concrete terms one can think of a one-component solid-vapour interface where c_1 is high and c_2 is very low; the exact concentration profile in the vicinity of the interface is typically unknown [Venables 2000]. While not entirely accurate one can define an imaginary dividing surface, such that the system behaves as uniform solid or uniform vapour up to this dividing surface, and the surface itself has thermodynamic properties scaling with its area [Venables 2000].

9.2.2 Surface Tension and Surface Energy

Surface tension, γ, is defined as the reversible work done in creating unit area of a new surface at constant temperature and volume [Venables 2000]:

$$\gamma = \lim_{dA \to 0} \frac{dW}{dA} = \left(\frac{dF_{total}}{dA}\right)_{T,V} \qquad (9.3)$$

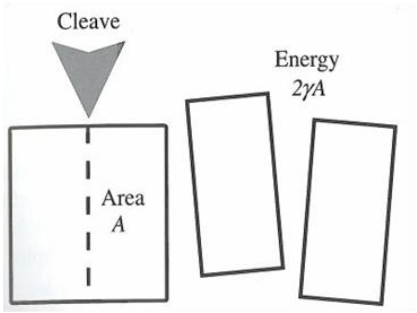

Figure 9-2. Schematic representation of creating a new surface by cleavage. If thermodynamically reversible the work done creating the new surface is 2γA.

As illustrated in Figure 9-2., $\Delta F = F_1 - F_0 = 2\gamma A$; $dF_{total} = \gamma dA$. At constant temperature and volume [Venables 2000]:

$$dF_{total} = -SdT - \rho dV + \sum \mu_i dN_i + f_{surface} dA = f_{surface} dA + \sum \mu_i dN_i \qquad (9.4)$$

Therefore [Venables 2000],

$$\gamma dA = f_{surface} dA + \sum \mu_i \, dN_i \qquad (9.5)$$

In a system with a single component, e.g. metal-vapour, the dividing surface can be selected such that $dN_i = 0$, so γ and $f_{surface}$ are equal [Venables 2000]. This is the manner in which the terms surface energy and surface tension are ordinarily employed

in the literature [Venables 2000]. For more complex systems the introduction of a new surface may cause changes in N_i ($N_1 + N_2$ in the bulk and $dN_i \rightarrow$ surface, so that the change in bulk number of atoms in phase i, dN_i, is negative). For these complex systems the following applies [Venables 2000]:

$$dN = -\Gamma dA \quad \text{and} \quad \gamma = f_{surface} - \sum \Gamma_i \mu_i \qquad (9.6)$$

Where:

the second term is the free energy contribution of atoms changing from bulk to surface [J]

Γ is the surface density of $(F - G)$ [kg m^{-2}]

An equivalent view is that γ is the surface excess density of Kramer's grand potential $\Omega = -\rho(V_1 + V_2) + \gamma A$, which is minimised at constant T, V and μ [Venables 2000].

Realistic models at $T > 0\ K$ must map onto the relevant statistical distribution to make accurate predictions at the atomic or molecular level. In summary, $\gamma = f_{surface}$ for one-component systems [Venables 2000]. It seems reasonable to consider the EB-PVD coating a one component system; the deposition temperatures considered are not so high that the Ni vaporises so there should be only YSZ vapour and condensing YSZ present in the system.

One can then define a surface excess internal energy, $e_{surface}$ and entropy $s_{surface}$, using various thermodynamic equations [Venables 2000]:

$$e_{surface} = f_{surface} + T s_{surface} = \gamma - T\left(\frac{d\gamma}{dT}\right)_V \qquad (9.7)$$

$$\text{and} \quad s_{surface} = -\left(\frac{df_{surface}}{dT}\right)_V$$

The surface entropy, s_s, is typically positive and has a value of a few Boltzmann's constant (k) per atom [Venables 2000]. "One reason, not the only one, is that surface atoms are less strongly bound, and thus vibrate with lower frequency and higher amplitude than bulk atoms; another reason is that the positions of steps on the surface are not fixed. Hence $e_{surface} > f_{surface}$ at $T > 0$ K." [Venables 2000]

A note on surface energy and surface stress. They may share units, but surface stress is a vector quantity (two-dimensional matrix, aka a second rank tensor) while surface tension is a scalar quantity. The two are the same for fluids but may be substantially different for solids. Furthermore, surface stresses and thin film stresses are not identical, and may be caused by different factors [Venables 2000].

9.2.3 Thermodynamics of the Vapour Pressure

The sublimation of a pure solid under equilibrium conditions is given by the condition $\mu_v = \mu_s$ [Venables 2000] where μ_v is the chemical potential of the vapour and μ_s that of the solid. From the theory of perfect gases one can use the standard result that the chemical potential of the vapour at low pressure is [Venables 2000]:

$$\mu_v = -kT \ln\left(\frac{kT}{p\lambda^3}\right) \qquad (9.8)$$

Where:

μ_v is the chemical potential of the vapour [J mole^{-1}]
k is Boltzmann's constant [J K^{-1}]
T is the temperature [°K]
p is the pressure [Pa]
$\lambda = \frac{h}{(2\pi mkT)^{\frac{1}{2}}}$ is the thermal de Broglie wavelength [m]
In which:
h is Planck's constant [approx. 6.62606957×10^{-34} J s]
m is the particle mass [kg]

This can be rewritten as follows to yield the equilibrium vapour pressure, p_e, in terms of the chemical potential of the solid [Venables 2000]:

$$p_e = \left(\frac{2\pi m}{h^2}\right)^{\frac{3}{2}} (kT)^{\frac{5}{2}} e^{\left(\frac{\mu_s}{kT}\right)} \qquad (9.9)$$

Therefore, to calculate the vapour pressure one needs a model for the chemical potential of the solid. A typical μ_s at low pressure is the 'quasi-harmonic' model, which assumes harmonic vibrations of the solid at its given lattice parameter [Venables 2000]. This free energy per particle is [Venables 2000]:

$$\frac{F}{N} = \mu_s = U_0 + \left(\frac{3hv}{2}\right) + 3kT \langle \ln\left[1 - e^{\left(\frac{-hv}{kT}\right)}\right] \rangle \qquad (9.10)$$

Where:

$\langle \ldots \rangle$ signifies average values
v is the lattice vibration frequency [Hz]

The (positive) sublimation energy at zero temperature is $L_0 = -\left(U_0 + \langle\frac{3hv}{2}\rangle\right)$, where the first term is the (negative) energy per particle in the solid relative to vapour and the second term is the (positive) energy due to zero-point vibrations [Venables 2000].

The vapour pressure is significant at higher temperature usually, where the Einstein model of the solid is surprisingly realistic provided thermal expansion is taken into account in U_0 [Venables 2000]. Within this model (all $3N$ lattice vibration frequencies are the same), in the high temperature limit [Venables 2000]:

$$\langle \ln\left[1 - e^{\left(\frac{-h\nu}{kT}\right)}\right]\rangle = \langle \ln\left(\frac{h\nu}{kT}\right)\rangle \qquad (9.11)$$

Such that $e^{\left(\frac{\mu_S}{kT}\right)} = \left(\frac{h\nu}{kT}\right)^3 e^{\left(\frac{-L_0}{kT}\right)}$.

This gives [Venables 2000]:

$$p_e = (2\pi m v^2)^{\frac{3}{2}}(kT)^{\frac{-1}{2}} e^{\left(\frac{-L_0}{kT}\right)} \qquad (9.12)$$

$p_e T^{\frac{1}{2}}$ follows an Arrhenius law, and the pre-exponential depends on the lattice vibration frequency $\propto \nu^3$ [Venables 2000]. The absence of Planck's constant in (9.12) shows that this is a classical effect (as opposed to a quantum one), where the equipartition of energy applies [Venables 2000]. That is to say that the temperature of the system is derived from its average energies.

The $T^{\frac{1}{2}}$ term is slowly varying, and many tabulations of vapour pressure in the literature simply express $\log_{10}(p_e) = A - \frac{B}{T}$ and give the constants A and B [Venables 2000]. In practice the model follows real behaviour very closely over many decades of pressure [see Venables (2000) for some examples].

A crucial point at this juncture is that in the above calculation the vapour pressure does not depend on the structure of the surface. The surface simply acts as an intermediary, in equilibrium with both the solid crystal and the vapour [Venables 2000].

9.2.4 The Kinetics of Crystal Growth

Under equilibrium conditions the image so far is of a fluctuating surface that does not influence the vapour pressure, but now we consider non-equilibrium cases [Venables 2000]. "The classic paper is by Burton, Cabrera & Frank (1951), known as BCF, and much quoted in the crystal growth literature." [Venables 2000] One has to consider the presence of kinks and ledges as well as extrinsic defects (in particular screw dislocations) [Venables 2000]. Presumably screw dislocations are important because of the way they alter the surface introducing new ledges, although this is not explained by Venables. Other defects have been found to terminate ledges, even those of sub-atomic height, that have their own importance in the mechanisms of crystal growth [Venables 2000].

An important concept is that of supersaturation $S = \left(\frac{p}{p_e}\right)$ [Venables 2000]. Another is the thermodynamic driving force, $\Delta\mu = kT \ln S$ [Venables 2000]. At equilibrium $\Delta\mu = 0$; during condensation $\Delta\mu > 0$; and $\Delta\mu < 0$ during sublimation or evaporation [Venables 2000]. Thus, the variable that enters into exponents is $\frac{\Delta\mu}{kT}$, often written as $\beta\Delta\mu$ (i.e. $\beta = \frac{1}{kT}$) considered standard notation in statistical mechanics [Venables 2000].

The deposition rate or flux ($\dot{z}$ in monolayers per minute and J respectively) is related, using kinetic theory, to p as $\dot{z}\ (or\ J) = \frac{p}{(2\pi mkT)^{1/2}}$ [Venables 2000].

An atom can adsorb on the surface becoming an adatom, with an adsorption energy E_a, positive relative to zero in the vapour [Venables 2000]. Occasionally this is referred to as desorption energy, and the symbols for both terms vary wildly [Venables 2000].

The rate at which the adatom desorbs is approximately $\nu_a e^{\left(\frac{-E_a}{kT}\right)}$ [Venables 2000]. It is helpful to specify this frequency as ν_a in order to distinguish it from other frequencies [Venables 2000]. "It may vary relatively slowly (not exponentially) with T." [Venables 2000]

An adatom can diffuse over the surface with energy E_d and corresponding pre-exponential ν_d. One can reasonably expect $E_d < E_a$ maybe $E_d \ll E_a$ [Venables 2000]. Adatom diffusion is derived by considering a 2D random walk; the 2D diffusion coefficient, D, is then given by [Venables 2000]:

$$D = \left(\frac{\nu_d a^2}{4}\right) e^{\left(\frac{-E_d}{kT}\right)} \qquad (9.13)$$

Where:

a is a special parameter defined below (after Figure 9-3.)

Also, the adatom lifetime before desorption, τ_a, is [Venables 2000]:

$$\tau_a = \left(\frac{1}{\nu_a}\right) e^{\left(\frac{E_a}{kT}\right)} \qquad (9.14)$$

BCF showed that $x_s = \sqrt{D\tau_a}$ is a characteristic length that governs what happens to the adatom and defines the role of ledges (steps) in evaporation and condensation [Venables 2000].

Two useful concepts are introduced here: local equilibrium and one-dimensional diffusion. Local equilibrium can be defined either in terms of differential equations or of chemical potentials [Venables 2000]. This is demonstrated in the cited book problems 1.2 and 1.4 should the reader wish to see the difference. One dimensional diffusion requires the use of differential equations or a Monte Carlo simulation [Venables 2000]. The relevant points regarding these are summarised below:

1) Crystal growth (or sublimation) is difficult on a perfect terrace requiring substantial supersaturation (or undersaturation for sublimation) [Venables 2000]. Growth, when it occurs, proceeds in two distinct stages; nucleation and growth. Monolayer islands (or pits for sublimation) must be nucleated before growth (or sublimation) is able to proceed [Venables 2000]. This can be seen as the need for some anchor point to adhere to for arriving adatoms that contribute to the growth of a crystal. The analogy is not so clear with sublimation, however.
2) A ledge or step on the surface of a crystal captures arriving adatoms within a zone of influence of width x_s to either side of the step [Venables 2000]. If only individual steps exist across the terrace then these will eventually grow out, and the resulting terrace will grow slowly (as explained in point 1. above) [Venables 2000]. In general, rough surfaces grow faster than smooth ones; the final structure of a growing crystal will consist entirely of slow growing (smooth) surfaces [Venables 2000].
3) The presence of screw dislocations provides additional steps providing a mechanism for continuous growth at modest supersaturation since they form spirals as they grow [Venables 2000].

Detailed studies [Venables 2000] have demonstrated that the growth rate depends quadratically upon the supersaturation for mechanism 3. and exponentially for mechanism 1. [Venables 2000]; implying that screw dislocations are dominant at low supersaturation [Venables 2000].

Crystal growth from liquid phases and solutions has been treated similarly [Venables 2000], emphasizing the internal energy change upon melting, L_m (i.e. latent heat of fusion for melting), and a parameter labelled α [Venables 2000]. $\alpha \propto \frac{L_m}{kT}$, where $\alpha < 2$ is typical for melt growth of elemental solids and corresponds to rough liquid-solid interfaces [Venables 2000].

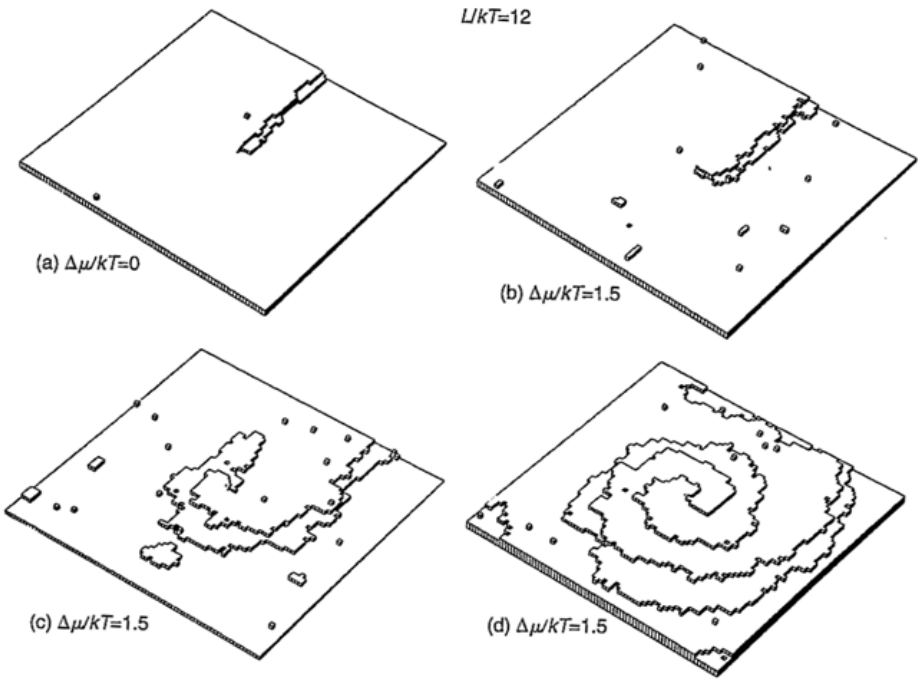

Figure 9-3. Deposition in the presence of a screw dislocation – causing a double step [Venables 2000]. (a) is at equilibrium, (b) through (d) are given as a function of time with supersaturation $\beta\Delta\mu$ = 1.5. Bond strength expressed in terms of temperature as $^{L}/_{kT} = 12$, equivalent to $\phi = 4kT$ [Venables 2000].

Growth from a vapour via smooth interfaces is characterised by larger values of α; either because the sublimation energy $L_0 \gg L_m$ and/or the growth temperature (i.e. the deposition temperature, for example, the operating temperature during evaporation) is much lower than the melting temperature [Venables 2000].

9.2.5 Concepts of Surface Electronics

In addition to the above concepts it is useful to define a few terms relating to surface electronics which will be used in a general context. The following definitions are after Venables (2000).

Work Function, ϕ

The work function is the energy required to move an electron from the Fermi Level, E_F, to the vacuum level, E_0, as shown in Figure 9-4. (a). The work function depends on the crystal face {hkl} and rough surfaces typically have lower ϕ. It is typically of the order of a few electronvolts.

Electron affinity, χ, and ionisation potential Φ

Both of these are the same for a metal, and equal to ϕ; for a semiconductor or insulator they differ. The electron affinity is the difference between the vacuum level, E_0, and the bottom of the conduction band, E_C, as shown in Figure 9-4. (b). The ionisation potential

$\Phi = E_0 - E_V$, where E_V is the top of the valence band. These terms are not specific to surfaces: they are also used for atoms and molecules generally, as the energy level which (a) the next electron goes into, and (b) the last electron comes from.

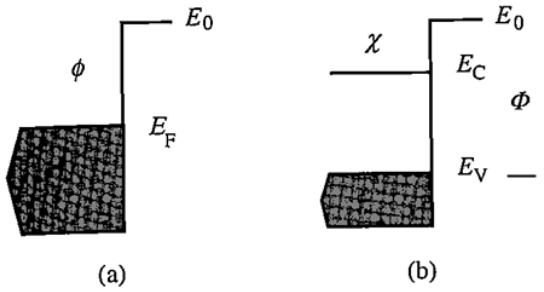

Figure 9-4. Schematic representation of (a) the work function and (b) electron affinity and ionisation potential [Venables 2000].

Surface states and related ideas

A surface state is a state localised at the surface which decays exponentially into the bulk, but which may travel along the surface. The wave function is typically of the form

$$\psi = u(r)e^{(-ik_\perp|z|)}e^{(ik_\parallel r)} \qquad (9.15)$$

where, for a state in the band gap, $k_\perp$ is complex, decaying away from the surface on both sides, as shown in Figure 9-5. (a). Such a state is called a resonance if it overlaps with a bulk band, as then it may have increased amplitude at the surface, but evolves continuously into a bulk state. A surface plasmon is a collective excitation located at the surface, with frequency typically of $\frac{\omega_p}{\sqrt{2}}$, where ω_p is the frequency of a bulk plasmon. A plasmon is a quantum of plasma oscillation, a quasiparticle due to the quantization of plasma oscillations equivalent to phonons from quantisation of mechanical (lattice) vibrations.

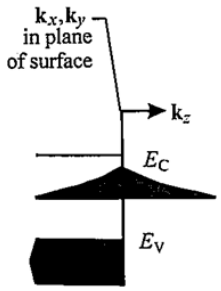

Figure 9-5. Schematic diagram after Venables [2000] of a surface state defined by wave vector $\boldsymbol{k}_\parallel = \boldsymbol{k_x} + \boldsymbol{k_y}$ and $\boldsymbol{k}_\perp = \boldsymbol{k_z}$ for the $\sqrt{3} \times \sqrt{3}R30°$ structure plotted in the same orientation as a xenon lattice.

9.2.6 Mechanisms of Physical Vapour Deposition

The vapour pressure of the source material is exponentially dependent on the temperature [Venables 2000]. The deposition rate is determined by the source area and temperature, and by the distance between source and substrate [Venables 2000]. Different materials have vastly different relations between the vapour pressure and the melting point. Thus, a satisfactory deposition rate is only obtained if the material is liquid [Venables 2000].

It is relatively simple to devise a crucible such that the evaporant does not evaporate in all directions but emerges as a more or less directed beam [Venables 2000]. This can be further collimated so the source material is directed preferentially onto the substrate [Venables 2000]. Sources can be characterised as effusion sources (with a relatively large opening) or as Knudsen sources (where a small hole is used) [Venables 2000]. "In practice, considerable thought and effort is required to achieve a uniform temperature enclosure, via careful design of the crucible, heater windings, radiation shields and water cooling, and by the use of anticipatory electronic control of heater currents based on thermocouple measurements." [Venables 2000]

For the deposition of high temperature materials, or materials that interact with the crucible, electron beam evaporation is required [Venables 2000]. The e-beam is directed onto the sample surface by a shaped magnetic field, typically using an inbuilt permanent magnet [Venables 2000]. The heating produced this way is very localised, and care is required to ensure it is localised where it should be [Venables 2000]. This is also the case when using pulsed UV eximer lasers instead of an e-beam for heating [Venables 2000].

Laser ablation, which is sometimes also called pulsed laser deposition (PLD), has typically been used to deposit ceramic materials including high temperature superconductors [Venables 2000]. "PLD produces very rapid deposition in which whole chunks of material can break off and be deposited during the immense peak powers which typically last for 10–20 ns." [Venables 2000]

"A particular advantage of rapid evaporation [so presumably applies to e-beam and PLD] is the control of stoichiometry, since the different species do not have time to segregate to the surface during the evaporation phase." [Venables 2000]

9.2.7 Chemisorption and Physisorption

In chemisorptions a strong 'chemical bond' is formed between the adsorbate atom or molecule and the substrate. The adsorption energy, E_a, of the adatom will be a significant fraction of the sublimation energy of the substrate, or even more, e.g. $E_a = 2$ eV for an adatom on f.c.c. (100) surface when the sublimation energy $L_0 = 3$ eV [Venables 2000]. Energies of 1–10 eV/atom are typical for chemisorption.

Physisorption involves no strictly chemical (in the usually understood sense of the word) interaction making it weaker. The energy of interaction is due to the (physical) van der Waals force; arising from fluctuating dipole and higher-order moments on the interacting adsorbate and substrate [Venables 2000]. “Typical systems are rare gases or small molecules on larger compounds or metals, with experiments performed below room temperature.” [Venables 2000] Physisorption energies are about 50–100 meV/atom; comparable to the sublimation energies of rare gas solids [Venables 2000].

Reactive molecules may be adsorbed in two stages that proceed either in series or as alternatives to one another. “A first, precursor, stage has all the characteristics of physisorption, but the resulting state is metastable. In this state the molecule may reevaporate, or it may stay on the surface long enough to transform irreversibly into a chemisorbed state. The second stage is rather dramatic, usually resulting in splitting the molecule and adsorbing the individual atoms: dissociative chemisorption. The adsorption energies for the precursor phase are similar to physisorption of rare gases, but may contain additional contributions from the dipole, quadrupole, and higher moments, and from the anisotropic shape and polarisability of the molecules. The dissociation stage can be explosive – literally. The heat of adsorption is given up suddenly, and can be imparted to the resulting adatoms.” [Venables 2000] For instance, bulk solid F_2 has an alarming tendency to explode by reacting dissociatively with its container [Venables 2000].

Venables (2000) presents information about the energy of adsorption E_a, adsorption potential μ_a the Langmuir model of adsorption and 2D coverage that may interest the reader but is not relevant to understanding the deposition mechanisms for an EB-PVD electrolyte.

A given phase, i.e. combination of ρ and structure, is described by the Equation Of State (EOS) [Venables 2000]:

$$\rho = f(p,T) \qquad (9.16)$$

For surfaces (i.e. 2D rather than bulk 3D) the EOS is [Venables 2000]:

$$\theta = f(p,T) \qquad (9.17)$$

Where:

ρ is the density of the phase [kg m^{-3}]
p is the pressure [Pa]
T is the absolute temperature [°K]
θ is the coverage of the adsorbate on the substrate [fraction, no units]

Since $\mu_v = \mu_0 + kT\ln(p)$ and $\mu_v = \mu_a$, then [Venables 2000].

$$\theta = f(\mu, T) \qquad (9.18)$$

As a 2D gas or localised adlayer (an adsorbed layer of material) is compressed by increasing the gas pressure p, the adatoms will come within range of their mutual attractive or repulsive forces, and phase transitions may result, first within the forming monolayer and subsequently from monolayer to multilayer [Venables 2000]. If the substrate and absorbate are well ordered, condensation may proceed in well defined steps at monolayer and sub-monolayer coverages (i.e.$0 \leq \theta \leq 1$) [Venables 2000].

The existence of 2D solid, liquid and gaseous layers has been established [Venables 2000], and the (p,T) coordinates of the phase transitions (including multilayer transitions) and fixed points such as triple points and critical points measured for certain cases where substrate and adsorbate are well ordered [Venables 2000]. This is to say that these are not theoretical or conceptual constructs utilised to model deposition-growth but real physical processes.

Some good points on the graphs that can be plotted [all quoted from Venables 2000]: "An isotherm is a graph of θ against $\ln(p)$ or μ, with T as the parameter... A phase diagram using $\log(p)$ and $1/T$ axes is very convenient for (physisorption) experimentalists, because the pressure can be varied over many orders of magnitude, and this plot results in straight lines for phase transitions (e.g. gas-solid or monolayer-bilayer transitions) which show Arrhenius behaviour – the slope of these lines give the corresponding energies. But typically the coverage information is lost. Theorists are fond of phase diagrams as a function of T and μ: this gives them the chance to investigate the adsorbed phase, and ignore the 3D gas phase, which provides the value of μ, typically $\Delta\mu$ with respect to the bulk 3D phase, when the comparison with experiment is made later."

"An isobar is a graph/cut/contour at constant pressure, giving a plot of $\theta(T)$, with $\ln(p)$ or μ as the parameter. The meaning is the same used on weather charts, but the context is a little different (is the weather an equilibrium phenomenon?). In many single surface experiments, a more or less directed beam is aimed at the substrate to establish a steady state concentration which is almost a true equilibrium, but not quite. In particular, the temperature of the beam T_b is typically not the same as that of the adsorbate T_a: the question of whether or not to correct the pressure for this thermo-molecular effect, of order $\left(\frac{T_a}{T_b}\right)^{1/2}$, recurs in experimental literature."

"An isostere is a contour on a $p(T)$ plot at constant coverage. Typically $\log(p)$ varies as $\frac{1}{T}$, and the energy associated with such an Arrhenius plot is called the isosteric heat of adsorption. This is the energy associated with the adsorbed phase at that coverage, and it comprises the adsorption energy and lateral binding energies, their derivatives with respect to coverage, and various terms related to the atomic vibrations."

Understanding the thermodynamics of the 2D gas-solid transition enables the determination of the "cohesive energy of the 2D adsorbed solid" (i.e. its sublimation energy), and the pre-exponential factor, which can be related to the entropy of adsorption. This last one would expect to be lower than in the unordered vapour since the material has crystallised onto the surface [Venables 2000].

"This results in an estimate of the change in vibration frequencies between the adsorbed 2D phase and the bulk 3D phase." A negative entropy [change?] corresponds to the effective vibration frequencies being higher in the adsorbed state than in the bulk phase.

The above arises from considering the vapour phase equation and the behaviour of monolayer vibrations. The 2D gas-solid phase transition line on an Arrhenius plot corresponding approximately to the sublimation energy L_2 of the 2D solid phase [Venables 2000]. Note that this will typically be considerably higher than the (T=0) sublimation energy L_0 of the 3D bulk vapour. This is the basic reason why an adsorbed layer is stable [Venables 2000].

The intercept of this 2D transition line on the $\log(p)$ axis at $T^{-1} = 0$ is actually higher than that of the 3D bulk sublimation line intercept, and the difference in $\ln(p) = \frac{-\Delta S}{K}$, where ΔS is the entropy difference between 2D and 3D solids.

In the high temperature limit of the Einstein model [Venables 2000]:

$$\frac{\Delta S}{K} = 3 \ln\left(\frac{\nu}{\nu_e}\right) \qquad (9.19)$$

Where:

ν_e is the geometric average of three vibration frequencies in the 2D adsorbed solid.

"Consequently, the thermodynamic $\frac{\Delta S}{K}$ estimate implies that the lateral vibrations in the completed solid monolayer are also higher than bulk values." Venables [2000]

The adsorbate will tend to form a phase matching the lattice parameters of the substrate, at least when it is just as monolayer (called an incommensurate phase – because it does

not have the normal lattice parameters). This I-phase has a modulated lattice parameter (i.e. is epitaxial); this has increased energy from having more of the adsorbate in the potential wells of the substrate, but costs energy in the alternating compression and rarefaction of the adsorbate [Venables 2000].

"Chemisorption in practice is strongly linked to the study of catalytic reactions, and the onset of irreversible reactions such as oxidation." [Venables 2000] There are essentially two classes of chemisorptions: weak (Lorentzian) and strong [Venables 2000].

1) Weak chemisorption is characterised by the metal states projected by the substrate (i.e. unfilled states forming a conduction band) onto the adsorbate are independent of energy. The local density of states (LDOS) takes on a Lorentzian distribution of an unshifted atomic energy level. The substrate has a broad band of energy levels and LDOS (e.g. s-p band metal) [Venables 2000].
2) The second case involves a narrow band of energy levels and LDOS of the substrate (e.g. insulator, semiconductor, or d-band metal) [Venables 2000] – creating bonding and antibonding states on the adatom [Venables 2000]. In strong bonding the projected energy states of the substrate onto the adsorbate are essentially a delta function in energy; these are the only sites (energetically speaking) in which the adsorbate may chemisorb onto the substrate. The interaction gives rise to essentially discrete bonding and antibonding states [Venables 2000].

Nickel has two outer shell electron configurations: $[Ar]4s^2 3d^8$ and $[Ar]4s^1 3d^9$. So it probably forms both weak and strong chemisorptions bonds. When oxygen bonds with Ni in the first configuration the Ni donates the $4s^2$ electrons. Bonding to the second configuration the Ni will lose the 4^{th} shell and the $3d^9$ becomes $3d^8$. In these ways the Kossel-Lewis idea of octets is preserved. Now the subshells of lower orbital quantum number are at lower energies (i.e. electrons in s subshells have less energy than in p subshells and so on) and are therefore more energetically favourable to fill/empty during electrovalent (i.e. ionic) bonding. The implication is that the first Ni configuration is more favourable energetically since both of the electrons lost come from an s subshell (for the second configuration one electron comes from the d subshell). Ni lattice parameter is 0.352 nm, NiO has a lattice parameter of 0.417 nm and cubic zirconia (i.e. stabilised) has a lattice parameter of 0.517 nm. The oxygen terminated bonding between Ni and the YSZ electrolyte will be under considerably less interfacial strain (compressive in this case), therefore, than bonding directly Ni to YSZ.

It is very important to realise that the strong bonding to the surface creates disturbances in the substrate [Venables 2000]. If the substrate is a metal the disturbances will be

strongly screened via Friedel oscillations (discussed later) [Venables 2000, section 6.1 of the book].

9.2.8 Film Growth

There are three growth modes for epitaxial films [Venables 2000]:

- Layer by layer (or Frank-van der Merwe) that arises because the atoms of the deposit material are more strongly attracted to the substrate than to themselves.
- Island growth (or Volmer-Weber) which occurs under the opposite conditions; i.e. when the deposit material atoms are more strongly attracted to each other than to the substrate.
- Finally, there exists an intermediate case called layer-plus-island (or Stranski-Krastanov, SK for short); layers form first, but then the system switches to island growth for some reason or another. It is more common than one might think [Venables 2000].

In terms of surface tension / surface energy: if depositing material A on B layer growth occurs if $\gamma_A < \gamma_B + \gamma^*$ where γ^* is the interface energy. Island growth occurs if $\gamma_A > \gamma_B + \gamma^*$ [Venables 2000].

The SK mode of growth occurs because the interface energy (increasing with thickness as per normal) increases such that islands form instead of layers [Venables 2000]. Typically the layer is under strain to fit the substrate, contributing to the interface energy [Venables 2000]. Should the layer fit exactly it is called pseudo morphic growth [Venables 2000].

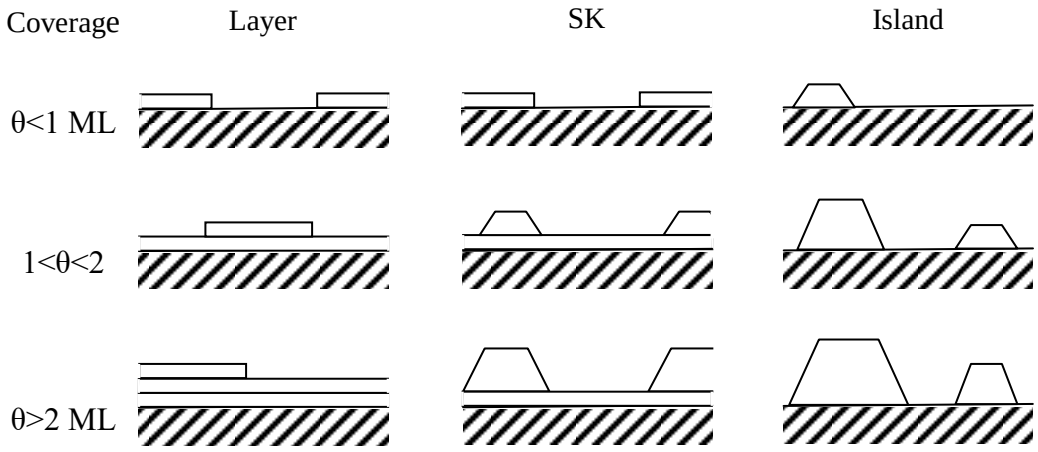

Figure 9-6. Schematic representation of the three growth modes by surface coverage in ML (the number of monolayers) [after Venables 2000].

A corresponding adsorption isotherm exists for each growth mode.

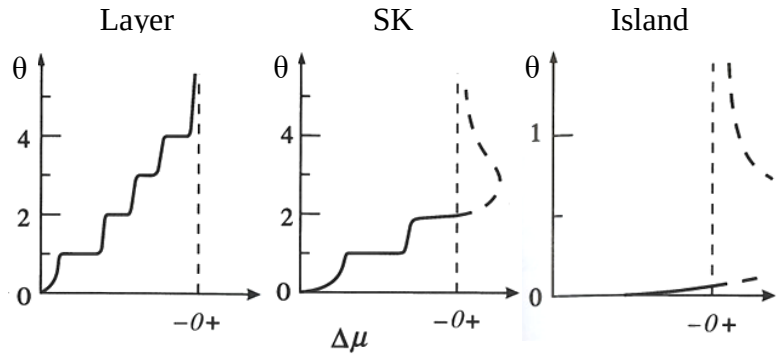

Figure 9-7. Adsorption isotherms of the three growth modes shown in Figure 9-6. Δμ is the chemical potential of the growing deposit relative to the bulk material and θ is the coverage (in ML). In SK mode two stable intermediate layers are shown [Venables 2000].

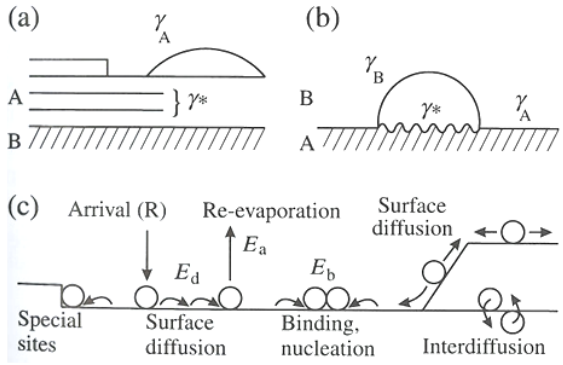

Figure 9-8. (a) growth of A on B where $\gamma_A < \gamma_B$: misfit dislocations are initially introduced and subsequently form islands (b) growth of B on A directly as islands, γ^* (the interfacial energy) represents the energy in excess of bulk A and B integrated over the interface region (c) surface processes and characteristic energies in nucleation and growth of films [from Venables 2000].

For island growth adatom concentration on the surface is small at the equilibrium vapour pressure of the deposit material. This implies that no deposition occurs at all without a large supersaturation. For layer growth, the vapour pressure is approached from below so that all the kinetic growth processes require undersaturation to occur (as with the creation of adsorbed monolayers). For SK growth, a finite number of layers are on the surface in equilibrium. A new element is introduced here: the nucleation barrier concept [Venables 2000]. The barrier indicates that a finite supersaturation is required to nucleate the 3D deposit [Venables 2000]. Since epitaxial growth mechanisms are kinetic phenomena, metastable (supersaturated) layers can coexist with islands [Venables 2000].

In atomistic terms there are many kinetic processes at the interface which can occur at the surface of either material (deposit or substrate): arrival of atoms (characteristic energy R), surface diffusion (characteristic energy E_d), re-evaporation (characteristic

energy E_a), binding / nucleation (characteristic energy E_b), and interdiffusion [Venables 2000]. In general only a few of the possible processes can be modelled quantitatively at the same time [Venables 2000].

There is only one (possible combination) of these kinetic processes that will be rate-limiting and thus responsible for the nucleation barrier [Venables 2000]. These processes can be investigated in both classical microscopic surface energy terms or in atomistic terms [Venables 2000].

Classical nucleation theory proceeds as follows [Venables 2000, note this section of the book chapter contained a few errors and inconsistencies, corrected here]. If we consider the case where $\gamma_A < \gamma_B$, producing 3D islands it is possible to construct a free energy diagram $\Delta G(j)$ for islands containing j atoms:

$$\Delta G(j) = -j\Delta\mu + j^{\frac{2}{3}}X \qquad (9.20)$$

Where:

$\Delta\mu$ is the supersaturation [J]

X is a surface energy term [J] of the form:

$$X = \sum_k C_k\gamma_k + C_{AB}(\gamma^* - \gamma_B) \qquad (9.21)$$

The first term represents the surface energy of the various faces of the islands of A. The second represents the interfacial energy between A and B. The geometrical constants C_k and C_{AB} depend on the shape of the islands [Venables 2000].

Note that the reference state for which $\Delta G(j) = 0$ is both a cluster containing no atoms (i.e. $j = 0$) and also the bulk solid B in equilibrium with its own adsorbed layer and vapour, but where the surface energy is neglected, such that $\Delta\mu$ and X are zero [Venables 2000]. This is the case used previously to define $\Delta\mu = kT \ln\left(\frac{p}{p_e}\right)$.

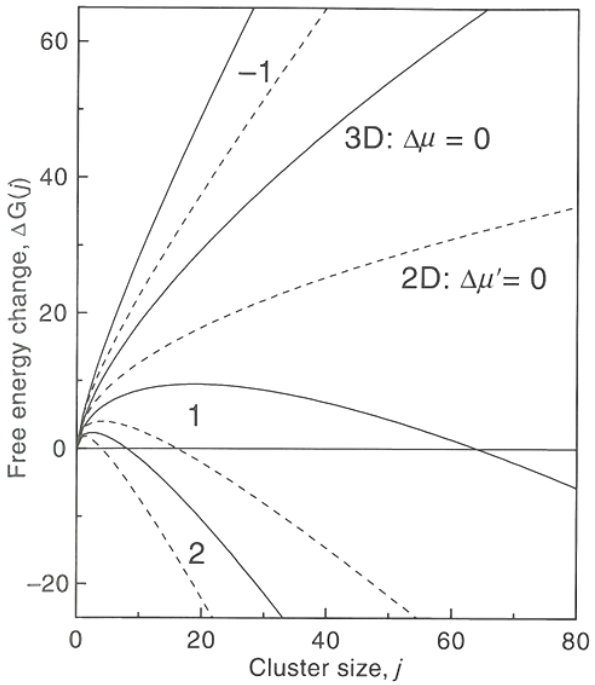

Figure 9-9. Free energy of nucleation $\Delta G(j)$ for 3D and 2D clusters (solid and dashed lines respectively). Curves are to scale for the surface free energy term X = 4, and $\Delta\mu$ (or $\Delta\mu'$ for 2D clusters) equal to -1, 0, 1, and 2. All three energies ($\Delta G(j)$, X and $\Delta\mu$) are in arbitrary units, but may be taken as kT [from Venables 2000].

The shape of the free energy curves for differing $\Delta\mu$ and X (in arbitrary units, but think kT) are shown in Figure 9-9. The nucleation barrier occurs because the curves possess a maximum at which the gradient is zero. Differentiating $\Delta G(j) = -j\Delta\mu + j^{\frac{2}{3}}X$ with respect to j demonstrates that the maximum is when $j = the\ critical\ cluster\ size,\ i$ [Venables 2000]:

$$i = \left(\frac{2X\Delta\mu}{3}\right)^3 \quad \text{and} \quad \Delta G(i) = \frac{4X^3}{27\Delta\mu^2} \qquad (9.22)$$

The same derivation can be followed for 2D clusters (i.e. monolayer thick islands). Here, the supersaturation is expressed in relation to the corresponding step in the adsorption isotherm [Venables 2000]: $\Delta\mu' = kT \ln\left(\frac{p}{p_1}\right)$ for nucleation of the monolayer. The free energy equation becomes:

$$\Delta G(j) = -j\Delta\mu' + j^{\frac{1}{2}}X \qquad (9.23)$$

In the equation above the term containing the square root results from the extra edge energy X [Venables 2000].

Similarly differentiating to locate the maximum yields [Venables 2000]:

$$i = \left(\frac{X}{2\Lambda\mu'}\right)^2 \quad \text{and} \quad \Delta G(i) = \frac{X^2}{4\Delta\mu'} \qquad (9.24)$$

Where:

$$\Delta\mu' = \Delta\mu - \Delta\mu_c$$

in which $\Delta\mu_c = (\gamma_B + \gamma^* - \gamma_A)\Omega^{2/3}$

Ω is the atomic volume of the deposit

In the atomistic formulation therefore a measurement of the pressure of the steps in the adsorption isotherm directly determines the surface energy difference $(\gamma_B + \gamma^* - \gamma_A)$ [Venables 2000]. The atomistic model is less than completely realistic [Venables 2000] as it is rather artificial to consider the surface energies of monolayers and very small clusters in terms of macroscopic concepts like surface energy.

Numerically, the critical cluster size, i, can be quite small, even a single atom [Venables 2000]. For this reason an atomistic model was developed (discussed next). The form of the free energy in an atomistic calculation is very similar to the figure noted previously but has a discrete character that can show secondary minima at particularly stable cluster sizes – sometimes referred to as magic clusters [Venables 2000]. In the large i limit the atomistic model should remain consistent with the macroscopic thermodynamic viewpoint [Venables 2000].

The rate equations derived below begin as simple rate equations for adatom concentrations. To these are added non-linear terms to describe the clustering and nucleation of 2D or 3D islands [Venables 2000]. These equations are governed by energies appearing as exponential terms and by frequency and entropic pre-exponential factors [Venables 2000]. The most important energies are [Venables 2000]: E_a and E_d controlling desorption and diffusion of adatoms (linear), E_j and E_i are binding energies that control clustering (non-linear).

For a simple three parameter model the cluster energies are constructed out of pair bonds of strength E_b [Venables 2000]. “Without this simplifying assumption, we can’t make explicit predictions; but with it, we can develop models which describe nucleation and growth processes over a large range of time and length scales.” [Venables 2000] This is a type of mean field model, describing large ranges of time and length scales but does not describe fluctuations accurately [Venables 2000]. Also, such models do not accurately describe quantities like size distribution of clusters [Venables 2000].

An atomistic model emerges from consideration of rate equations for the various sized clusters, which are then simplified [Venables 2000]. If only isolated adatoms are mobile on the surface [Venables 2000]:

$$\frac{dn_1}{dt} = \dot{z}(or\ J) - \frac{n_1}{\tau_a} - 2U_1 - \sum U_j \qquad (9.25)$$

For larger clusters of adatoms [Venables 2000]:

$$\frac{dn_j}{dt} = U_{j-1} - U_j \qquad (j \geq 2) \qquad (9.26)$$

Where:

U_j is the net rate of capture of adatoms by j-clusters [no units]

The above is not very useful in isolation, requiring further development. Particularly expressions for the net capture rate of adatoms by clusters, U_j, is needed as well as the simplification of introducing the concept of a critical nucleus size, i [Venables 2000]. In its simplest form this entails [Venables 2000]:

(a). Considering all clusters of size $> i$ to be stable in the sense that on average another adatom usually arrives before the clusters decay. The opposite holds true for clusters of size $< i$ (i.e. below the critical nucleus size).
(b). Subcritical clusters are in local equilibrium with the adatom population.

(a). leads to the definition of a stable cluster density or nucleation density n_x by means of the nucleation rate:

$$\frac{dn_x}{dt} = \sum\nolimits_{j \geq i} (U_j - U_{j+1}) \qquad (9.27)$$

$\frac{dn_x}{dt} = U_i$ ... (since all the other terms cancel out in pairs)

The ... means that it is possible to add other terms such as the loss of clusters caused by coalescence.

(b). leads to arguments about detailed balance and the Walton relation [Venables 2000]. These detailed balance considerations lead to all the $U_j = 0$ $(j < i)$ separately. Hence $\frac{dn_j}{dt} = 0$. However, this does not signify steady state because $U_{j-1} = U_j$ making it more stringent than broader conditions of steady state [Venables 2000].

A typical expression for U_j includes both growth and decay terms. In local equilibrium these two terms are numerically equal [Venables 2000]. The growth term due to adding single adatoms by diffusion to $j-1$ clusters is of the form $\sigma_j D n_1 n_{j-1}$, where σ is known as the capture number [Venables 2000]. The decay term is of the form $-\nu_d n_j e^{\left[-\frac{(E_d+\Delta E)}{kT}\right]}$ where ΔE is the binding energy difference between j and $j-1$ clusters [Venables 2000].

Therefore if there is a local equilibrium, the ratio [Venables 2000]:

$$\frac{n_j}{n_{j-1}} = n_1 C e^{\left[\frac{\Delta E}{kT}\right]} \qquad (9.28)$$

Where:

C is a statistical weight factor (constant for a particular size and configuration of cluster)

Note that this equilibrium does not depend on D which is concerned exclusively with kinetics [Venables 2000].

The above can be extended to subcritical clusters, yielding an equation known as the Walton relation [Venables 2000]:

$$n_j = (n_1) \sum_m C_j\,(m) e^{\left[\frac{E_j(m)}{kT}\right]} \qquad (9.29)$$

Where:

m denotes the mth configuration of the j-sized cluster.

In analogy to physical chemistry the Walton relation gives the equilibrium constant of the polymerisation reaction j adatoms <=> 1 j-mer [Venables 2000]. So far n_j has been considered in monolayer units. Sometimes N_0 (the number of sites on the lattice) is used explicitly, in which case n_j are area densities, modifying n_j to $\frac{n_j}{N_0}$ and n_1 to $\frac{n_1}{N_0}$ in equation (9.29) [Venables 2000].

From here the rate equations can be simplified into something useful; two coupled equations [Venables 2000]. The first is:

$$\frac{dn_1}{dt} = \dot{z} - \frac{n_1}{\tau_a} - \left(2U_1 + \sum_{j<i} U_j\right) - \sigma_x D n_1 n_x \qquad (9.30)$$

Where:

$\left(2U_1 + \sum_{j<i} U_j\right)$ is almost always numerically insignificant.

The last term describes the capture of adatoms by stable clusters.

It can be written as $\frac{n_1}{\tau_c}$

The other equation is:

$$\frac{dn_x}{dt} = \sigma_1 D n_1 n_i - U_{cl} \qquad (9.31)$$

Which assumes the local equilibrium for n_i (which is only a first approximation) will make the first term explicit and proportional to the $(i+1)^{th}$ power of the adatom concentration. This is highly non-linear if the critical nucleus size, i, is large [Venables 2000]. In the above equation U_{cl} is typically due to the coalescence of islands and is proportional to $n_x \frac{d\ddot{\theta}}{dt}$ where $\ddot{\theta}$ is the coverage of the substrate by stable islands [Venables 2000]. Thus $\frac{d\ddot{\theta}}{dt}$ is related to the shape (2D or 3D) of the islands and how they grow [Venables 2000].

In the simplified case of 2D islands the two terms $\left(2U_1 + \sum_{j<i} U_j\right)$ and $\sigma_x D n_1 n_x$ equal $N_a \frac{d\ddot{\theta}}{dt}$ where N_a is the 2D density of atoms in the deposit [Venables 2000]. NB: $\ddot{\theta}$ is measured in monolayers and is therefore dimensionless.

The capture numbers, U, depend on the size, stability and spatial distribution of islands [Venables 2000]. The simplest mean field model, referred to as the uniform depletion approximation, considers a typical cluster size K immersed in the average density of islands of all sizes [Venables 2000]. From this point an ancillary diffusion equation is written for the adatom concentration in the vicinity of the K-cluster (size specific) or X-cluster (the average size cluster) which has a Bessel Function solution [Venables 2000].

Such a model, in the incomplete condensation limit, gives exactly [Venables 2000]:

$$\sigma_K = \frac{2\pi X_K K_1(X_K)}{K_0 X_K} \qquad (9.32)$$

and

$$\sigma_X = \frac{2\pi X K_1(X)}{K_0(X)} \qquad (9.33)$$

Where [Venables 2000]:

$X_K^2 = \frac{r_K^2}{D\tau_a}$ and $X^2 = \frac{r_X^2}{D\tau_a}$

r_K and r_X being the corresponding island radii
K_0 and K_1 the Bessel Functions

For complete condensation the mean field expressions are the same, but the arguments of the Bessel Function contain τ_c instead of τ_a [Venables 2000]. In general the definition of τ that follows is used.

For complete condensation the capture numbers are just functions of the coverage of the substrate by islands, $\ddot{\theta}$ [Venables 2000]. Note the capture numbers are simply numbers with σ_i in the range 2–4 and σ_x often in the range 5–10 [Venables 2000]. Using the expressions given here one can compute the evolution of the nucleation density with time $\left(\frac{dn_X}{dt}\right)$ or more readily with $\ddot{\theta}$ as the independent variable [Venables 2000]. There are also other approximations for the various σs such as the lattice approximation [Venables 2000]. However, Venables explains, the sustainability of any approximation for condensation depends on the spatial correlation between islands developing as nucleation proceeds [Venables 2000].

Regimes of condensation: the rate equation for adatoms can be written as [Venables 2000]:

$$\frac{dn_1}{dt} = \dot{z} - \frac{n_1}{\tau} \qquad (9.34)$$

Where:

$$\tau^{-1} = \tau_a^{-1} + \tau_n^{-1} + \tau_c^{-1} + \cdots \qquad (9.35)$$

The various time constants, τ, can be defined by comparison with (9.30) [Venables 2000]:

$$\tau_n^{-1} = \frac{1}{n_1}\left(2U_1 + \sum\nolimits_{j<i} U j\right) \qquad (9.36)$$

$$\tau_c^{-1} = \sigma_X D n_X$$

The term in parenthesis is the nucleation term and can be expected to be almost always numerically insignificant since $U_i \approx 0$ for subcritical clusters [Venables 2000].

The ratio $r = \frac{\tau_a}{\tau_c} = \sigma_X n_X D \tau_a$ determines the regime; $r \gg 1$ is complete condensation and $r \ll 1$ is incomplete condensation [Venables 2000]. At high temperatures $\tau \Rightarrow \tau_a$ and at low temperatures (and/or high deposition rates) $\tau \Rightarrow \tau_c$ [Venables 2000]. Therefore usually high temperatures are under the complete condensation regime and

low temperatures (and/or high deposition rates) are under the incomplete condensation regime.

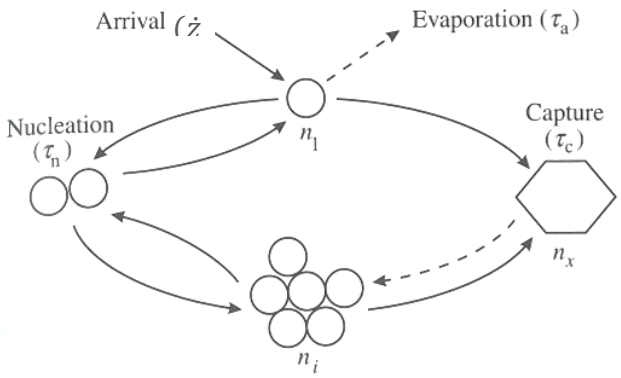

Figure 9-10. Illustration showing the interactions between nucleation and growth phases [Venables 2000]. Adatom density n_1 determines the critical cluster density n_i. n_1 itself is determined by the arrival $\dot{z}$ in conjunction with the various loss processes having characteristic times, τ, as described.

It is helpful to think of competitive capture, described by equation (9.35) and (9.36) for processes in which all the adatoms end up somewhere and the different competing processes (or channels) add as parallel resistances [Venables 2000].

Condensation often starts as incomplete, becoming complete by the end of the deposition [Venables 2000]. This can be termed the initially incomplete regime [Venables 2000]. If the diffusion distance on the surface is so short that only atoms impinging directly on the islands condense, then this is termed the extreme incomplete regime [Venables 2000].

In both of the limiting cases described above the two coupled rate equations (9.30) for n_1 and (9.31) for n_X can be evaluated explicitly. They give the nucleation density in the form $n_X \approx \dot{z}^p e^{\left(\frac{E}{kT}\right)}$, with p and E dependent on the regime considered [Venables 2000]. Summarised in tabular format as:

Regime	3D Islands	2D Islands
Extreme incomplete	$p = \frac{2i}{3}$ $E = \frac{2}{3}[E_i + (i+1)E_a - E_d]$	$p = i$ $E = [E_i + (i+1)E_a - E_d]$
Initially incomplete	$p = \frac{2i}{5}$ $E = \frac{2}{5}(E_i + iE_a)$	$p = \frac{i}{2}$ $E = E_i + iE_a$
Complete	$p = \frac{i}{(i+2.5)}$ $E = \frac{(E_i + iE_d)}{(i+2.5)}$	$p = \frac{i}{(i+2)}$ $E = \frac{(E_i + iE_d)}{(i+2)}$

Table 9-1. Exact nucleation density parameter dependence by regime [Venables 2000].

Perhaps the most important regime is complete condensation [Venables 2000]. Re-evaporation is absent in this regime (notice E_a, the adsorption energy, is absent in the expression for cluster density in the above table) [Venables 2000]. The absence of re-evaporation can perhaps be expected given the name of this regime, with complete condensation indicting lack of re-evaporation.

In the complete condensation regime the non-linear interplay between nucleation and growth is most marked [Venables 2000]. In general, it is clear that if different processes are included then different power laws and energies will be obtained [Venables 2000].

A final derivation regarding cluster density is an attempt to achieve a generalised equation for the maximum cluster density, yielding the regimes described previously [Venables 2000]. Equation (9.31) will lead to a maximum in the stable cluster density at the point where the (positive) nucleation term is balanced by the (negative) coalescence term [Venables 2000]. At this point $\frac{dn_X}{dt} = 0$ and the coverage of the substrate by islands $\ddot{\theta} = \ddot{\theta}_0$ [Venables 2000]. Substituting $\ddot{\theta} = \ddot{\theta}_0$ gives an explicit expression for $n_X(\ddot{\theta}_0)$.

For the sake of practicality, the θ-dependence of n_X is calculated within each of the condensation regimes, obtaining pre-exponential terms $\eta(\ddot{\theta}, i)$ for each regime [Venables 2000].

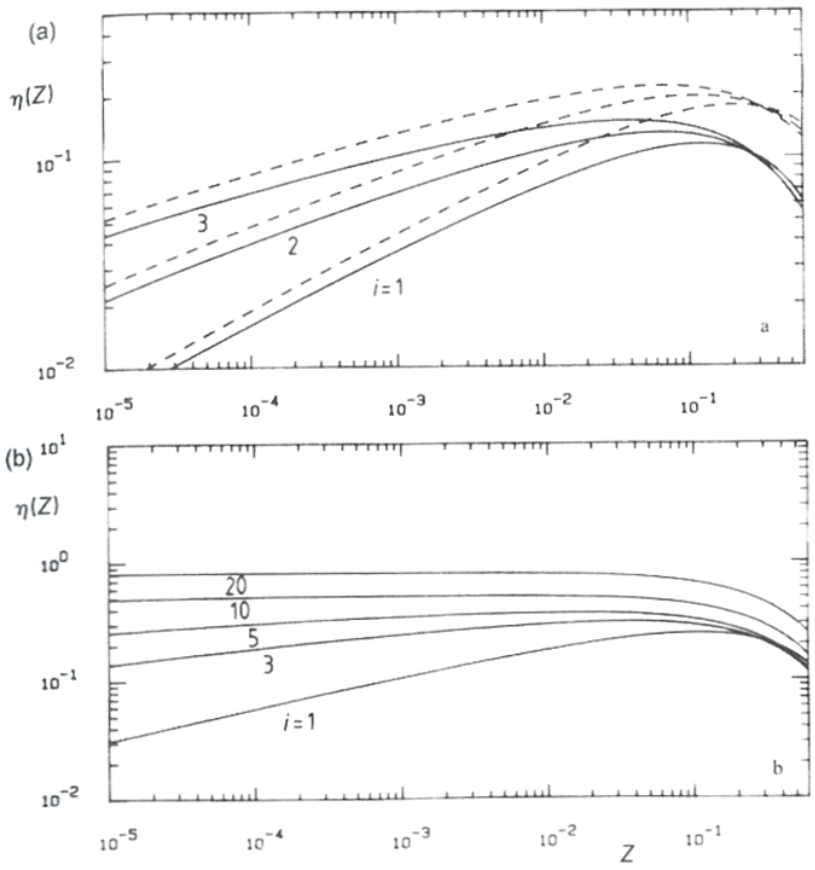

Figure 9-11. Calculated pre-exponential factors $\eta(\ddot{\theta}, i)$ in the complete condensation regime for: (a) 3D islands with i = 1, 2 and 3 and with σ_x evaluated in the lattice (solid line) and uniform depletion (dashed line) approximations; (b) 2D islands with i = 1–20 and with σ_x approximated by $4\pi/(-\ln \ddot{\theta})$, which is very close to the uniform depletion approximation

[Venables 2000]. NB: in the cited source, and this graph, Z = $\ddot{\theta}$.

These pre-exponentials, which multiply the 2D and 3D parameters tabulated earlier (Table 9-1.), are only weakly dependent on $\ddot{\theta}$ and the critical cluster size i [Venables 2000]. Similarly, although the coverage $\ddot{\theta}_0$ depends on the relation chosen for the coalescence term U_{cl}, in turn dependent upon the spatial correlations that develop during growth, none of this influences the exponential terms in the equations [Venables 2000].

Using the coalescence expression $U_{cl} = 2n_X \frac{d\ddot{\theta}}{dt}$, starting from equation (9.31) and inserting the Walton equation (9.29) for n_i, the steady state equation (9.36) for n_1 (neglecting the nucleation term $\dot{z}\tau_n$), and working for 2D islands, n_X is given by [Venables 2000]:

$$n_X(g+r)^i\left(\ddot{\theta}_0+r\right)=f\left(\frac{\dot{z}}{D}\right)^i\left[e^{\left(\frac{E_i}{kT}\right)}\right](\sigma_x D\tau_a)^{i+1} \qquad (9.37)$$

The slowly-varying numerical functions f and g involve the capture numbers σ_i and σ_X [Venables 2000].

With 3D islands, n_X is changed to $n_X^{\frac{3}{2}}$ on the left hand side of (9.37), and the constants altered slightly [referenced within Venables, 1987].

All the arguments above concerning general equation for the maximum cluster density assume that the critical nucleus size is i. The actual critical nucleus size is that which produces the lowest nucleation rate and density [Venables 2000]. Only under such conditions is the critical nucleus consistent with the highest free energy $\Delta G(j)$, for $j=i$ [Venables 2000]. The critical nucleus size is thus determined self consistently as an output (not input) of an iterative calculation for all feasible assumed critical sizes [Venables 2000].

For the complete condensation regime the ratio $r=\frac{\tau_0}{\tau_c}$ is much greater than both g and $\ddot{\theta}_0$, corresponding to adatom capture being much more probable than re-evaporation [Venables 2000]. For the incomplete condensation regime both r and g are much less than $\ddot{\theta}_0$ [Venables 2000]. In the range $\ddot{\theta}_0<r<g$ most cluster growth occurs by diffusion capture, at least initially [Venables 2000].

The generalisation of minimum cluster density equations are only soluble if E_i is known (for use in equation (9.31) or (9.37)); and also the value of i is itself determined implicitly. Hence, predictions are only explicit if within the model the binding energy E_j for all sizes j is calculated [Venables 2000]. This is the reason a pair binding model is invoked [Venables 2000]: the equations are not soluble otherwise without too much complication to be practically useful.

For 2D clusters the simplification allows the estimation of $E_j=b_jE_b$, where b_j is the number of lateral bonds in the clusters, each of strength E_b [Venables 2000]. However, retaining E_a as the vertical binding to the substrate there is sufficient freedom to model large differences between vertical and lateral binding, within a three-parameter fit to the nucleation and growth data [Venables 2000]. Venables adds that this feature of the pair binding model is important as it creates enough latitude to mirror, albeit in a simple manner, the different types of bonding actually occurring in the growth of one material on another [Venables 2000].

Defect-induced nucleation on oxides and fluorides: There are many examples where defect nucleation seems to be needed. Transitioning from $i=0$ to $i=1$ in such cases occurs by defect sites being used initially followed by nucleation proceeding upon

perfect terraces in the initially incomplete condensation regime [Venables 2000]. Examples [Venables 2000] include Au on mica, and Fe and Co on CaF_2. The usual adatom capture is superseded (at least initially) by defect trapping [Venables 2000].

It is possible to include various types of defects into analytical models (of interest here) or numerical simulations (such as kinetic Monte Carlo). This is at the cost of adding at least two parameters: the defect trap density n_t and the defect trap binding energy E_t, or the binding energy of adatoms to terrace steps E_s [Venables 2000].

The nucleation density of islands on defective surfaces can be derived by considering the origin of the terms in equation (9.37) [Venables 2000]. The right hand side of the equation is proportional to the nucleation rate via the term $e^{\left(\frac{E_i}{kT}\right)}$, which is enhanced by a ratio $B_t = 1 + A_t$ when defects are included [Venables 2000].

Consider point defect traps. These can be occupied by adatoms with a nucleation density of n_{1t}, occupied by clusters with a nucleation density of n_{Xt}, or can be unoccupied [Venables 2000]. Consider the number of adatoms attached to defect traps n_{1t} [Venables 2000]:

$$\frac{dn_{1t}}{dt} = \sigma_{1t} D n_1 n_{te} - n_{1t} \nu_d e^{\left[\frac{-(E_t + E_d)}{kT}\right]} \qquad (9.38)$$

Where:

n_{te} is the number of empty defect traps, given by $n_{te} = n_t - n_{1t} - n_{Xt}$.

In steady state conditions $\frac{dn_{1t}}{dt} = 0$.

Substituting the 2D diffusion coefficient given by $D = \left(\nu_d \frac{a^2}{4}\right) e^{\left(\frac{-E_d}{kT}\right)}$ (ν is the vibrational Einstein frequency) we can deduce [Venables 2000]:

$$\frac{n_{1t}}{(n_t - n_{Xt})} = \frac{A}{(1 + A)} \qquad (9.39)$$

Where:

$$A = n_1 C_t e^{\left(\frac{E_t}{kT}\right)}$$

in which C_t is an entropic constant, normally taken as equal to 1.

Equation (9.39) shows that the defect traps are full ($n_{1t} = n_t - n_{Xt}$) in the strong defect trapping limit, but depend exponentially on $\left(\frac{E_t}{kT}\right)$ in the weak defect trapping limit [Venables 2000].

Equation (9.39) is a Langmuir-type isotherm for the occupation of defect traps [Venables 2000]. It can be thought of as having a defect trapping time constant τ_t analogous to equation (9.35) to reach the steady state described [Venables 2000]. τ_t is very short unless E_t is very large. However, if this is the case then all the defect traps are full anyway [Venables 2000].

The total nucleation rate is the sum of the nucleation rate on the terraces and at surface defects [Venables 2000]. The nucleation rate equation without coalescence (equivalent to equation (9.31)) becomes [Venables 2000]:

$$\frac{dn_X}{dt} = \sigma_i D n_1 n_i + \sigma_{it} D n_1 n_{it} \qquad (9.40)$$

Where the second term on the right hand side is the nucleation rate on defects and n_{it} is the density of critical clusters attached to defects, with a corresponding capture number σ_{it}.

In simple cases defect traps are considered to act only on the first atom which binds to them, and also entropic effects are neglected [Venables 2000]. Then:

$$A_t = \frac{n_{1t}}{n_1} = (n_t - n_{Xt}) A \frac{1}{n_1(1+A)} \qquad (9.41)$$

A high value of A yields a strong trapping effect with almost all the sites unoccupied by clusters being occupied by individual adatoms [Venables 2000]. In this, simplest, model it is assumed that clusters cannot leave the defect traps [Venables 2000]. Note that even this model is nonlinear.

The adatom clusters that form on the defect sites are nucleated early on in the process, thereby depleting the adatom density on the atomic terraces that are the nominal sites for nucleation [Venables 2000]. *Ergo,* the overall nucleation density, $n_X(g+r)\left(\ddot{\theta}_0 + r\right)$, as given by equation (9.37), grows only as a fractionional power of the defect trap density, typically as $(i + 2.5)$ for complete condensation [Venables 2000]. In this weak defect-trapping limit the main result is a reduced diffusion constant, D, due to the time adatoms spend at defect traps [Venables 2000].

Nucleation on terrace sites is strongly suppressed due to adatom capture by clusters that have already nucleated at point defect sites [Venables 2000]. However, when $n_X > n_t$ there is minimal effect on the overall nucleation density, shown graphically in the s-shaped curves of Figure 9-12. for $FeCaF_2$ (111) [Venables 2000].

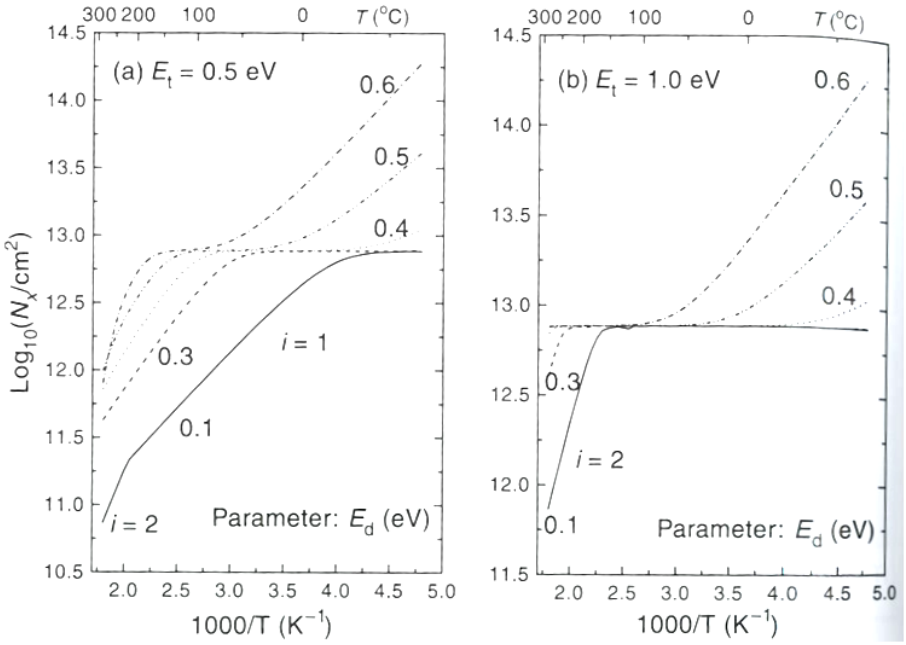

Figure 9-12. Nucleation density on point defects with trap density n_t = 0.001 ML and trap energy E_t (a) 0.5 eV (b) 1.0 eV; parameter E_d with E_a = 1.16 eV and E_b = 1.04 eV [Venables 2000].

If the defect trapping is very strong (high E_t) and the diffusion energy is low there is a large band or regime where $n_X = n_t$ [Venables 2000]. Conversely, if the defect trapping is weak (low E_t) there will be a single point of inflection (and the attendant change of gradient) at the trap density [Venables 2000].

Experiments have shown that the energies E_a, E_b and E_t are all bounded at $\approx 1\ eV$ and E_d at 0.1–0.3 eV [Venables 2000]. Notice that a low E_d is required so that adatoms are able to migrate far enough at low temperatures to reach defect sites [Venables 2000]. The other energies have relatively large values required to prevent something else from intervening at high temperatures [Venables 2000]. Or, put more explicitly [after Venables 2000], if E_t is as low as 0.5 eV the nucleation density does not reach n_t over a sufficiently broad temperature range; if E_a is too low then condensation will become incomplete too early. Note also that the transition from $i = 1$ to $i = 2$ is observed for 0.1 eV < E_d < 0.3 eV at the highest temperature meaning that the limiting process can become the breaking up of the cluster (on a defect trap) rather than the removal of the adatom from the defect trap; E_t is consequently not itself important provided that it is sufficiently large [Venables 2000].

This defect trap model contains a number of sub-cases depending on the values of various parameters. For instance the remarkable example of Pd/MgO (001): it requires a high trapping energy, E_t, in agreement with the model, for trapping Pd at surface vacancies, and a low E_d for adequate adatom mobility [Venables 2000].

Models involving point defects are typically indicative rather than fully quantitative because the possibility exists that the defects occurring have a range of binding energies rather than a single one [Venables 2000].

Qualitatively it is trivial to recognise that a moderate E_t and facile dimer movement (low E_d) implies that defect traps may become reusable at sufficiently high temperatures [Venables 2000]. This further complication, necessitating even more parameters be introduced to the model, has been thought necessary on occasion [Venables 2000]. In practice equation (9.37) is solved iteratively using the complete condensation solution as a starting point [Venables 2000].

Step defects often act as one-dimensional sinks, with most interest, historically, on incomplete condensation in island growth systems [Venables 2000]. In this case both E_a and E_d are usually small, the mean diffusion length before desorption is the Burton, Cabrera and Frank length (usually occurring in abbreviated BCF form), x_s, given by [Venables 2000]:

$$x_s = (D\tau_a)^{\frac{1}{2}} = \left(\frac{a}{2}\right)\left(\frac{\nu_d}{\nu_a}\right)^{\frac{1}{2}} e^{\left[\frac{(E_a - E_d)}{2kT}\right]} \qquad (9.42)$$

At moderate deposition temperatures steps (statistically) capture atoms arriving in a zone of width x_s to either side of the step [Venables 2000]. A cluster's position relative to the step involves long range elastic interactions and other atomic forces [Venables 2000], discussed relatively extensively in the literature.

The effect of adatom capture by step defects can be modelled by the extension of equations (9.35) and (9.36) in one of two ways:

I. Looking at a scale between the steps, in which case the steps provide the boundary conditions for a rate-diffusion equation of the form [Venables 2000]:

$$\frac{dn_1}{dt} = \dot{z} - \frac{n_1}{\tau} + \frac{\partial}{\partial x}\left(D\frac{\partial n_1}{\partial x}\right)$$
$$\left[i.e.\frac{dn}{dt} = a + n + \frac{\partial^2 n}{\partial x}\right] \qquad (9.43)$$

II. Taking the average over many steps, in which case adatom capture by step defects (pit, edge, and spiral dislocations) adds an additional loss term to equation (9.35) having a characteristic time τ_s [Venables 2000].

It can be shown from the equivalence of these two options in complete condensation that the average adatom density, n_1, is [Venables 2000]:

$$n_1 = n_{1e} + \dot{z}\tau_s \qquad (9.44)$$

Where:

n_{1e} is the concentration in equilibrium with the steps

$\tau_s = \frac{d^2}{12D}$ where d is the distance between steps

Steps can also act as one-dimensional sources of adatoms [Venables 2000]. The emission of adatoms in this way forms part of any discussion on sublimation, and occurs if $n_{1e} > 0$ in equation (9.44). In this case adatoms are expelled at kink sites and are able to diffuse over the terrace and be incorporated into other steps [Venables 2000]. When the adatom concentration is low this process has an effective diffusion constant given by [Venables 2000]:

$$D_e = n_1 D = Ke^{\left[-\frac{(L-E_a)}{kT}\right]}D \qquad (9.45)$$

So that the activation energy $Q = (L - E_a + E_d)$, with K an entropic constant [Venables 2000].

At high temperatures other mechanisms may become active, including surface vacancies, "indeed one of the difficulties of studying surface diffusion is that there are so many mechanisms which may need to be considered." [Venables 2000] However, during annealing at moderate temperatures equation (9.45) or a variant allowing for small amounts of clustering, should be a good approximation [Venables 2000].

Note that $n_1 D$ is an expression of the mass transport or chemical diffusion coefficient D^*. At higher adatom concentrations some adatoms will spend part of the time in small clusters of size j. These have typically small (even zero) intrinsic hopping diffusion coefficients D_j [Venables 2000]. In this way, at higher adatom concentration, the chemical diffusion coefficient is concentration [Venables 2000]:

$$D^*\{= n_1 D \; in \; (10.45)\} = \sum_j D_j \frac{j^2 n_j}{\left[\sum_j j^2 n_j\right]} \qquad (9.46)$$

Combining the above with the Walton equation (9.29), in the latter's simplest form, for non-zero concentrations yields a D^* that is exponentially dependent upon $\frac{E_b}{kT}$ as well as $\frac{E_d}{kT}$. It may further depend on other energies due to the diffusion of small clusters [Venables 2000].

At elevated temperatures surface vacancies are generated in addition to adatoms, and as the temperature increases the surface may have a roughness of several layers [Venables 2000]. In alloys exchange diffusion may become a factor where species trade positions [Venables 2000]. These factors must all modify how D^* is interpreted in terms of individual surface (and near surface) processes [Venables 2000]. NB: throughout the cited source processes referred to were only studied at a few degrees Kelvin – so any reference to high temperatures refers to anything more elevated than room temperature.

Ostwald ripening is a term that refers to situations where large clusters grow or coarsen and small clusters shrink or disappear [Venables 2000]. In the case of Ostwald ripening controlled via adatom surface diffusion, equation (9.45) gives the effective diffusion coefficient with an activation energy $Q = (L - E_a + E_d)$ [Venables 2000].

In the high temperature limit of the nucleation model in the complete condensation regime yields this same activation energy since $L = E_a + 3E_b$ for large 2D (hexagonal) cluster [Venables 2000]. The nucleation density expression given in Table 9-1. has $E_i = 3E_b$ for large critical nucleus sizes i, yielding a corresponding activation energy of $E_d + 3E_b$ once more [Venables 2000]. *Ergo* this is an internal check on the validity of the nucleation model [Venables 2000].

9.2.9 Highlights

This chapter, however, does not concern itself with modelling the deposition process, but rather utilising existing models to guide the development of a technique to create 10 micron thick 7YSZ electrolytes by EB-PVD on tubular substrates. What the above literature highlights is:

- The important distinction between nucleation and growth, and the concept that deposition can be nucleation-dominated or growth-dominated and that as conditions change it can shift from one to the other. This change may be local rather than global.
- The energy binding adatoms together is not the same as that binding them to the surface (i.e. the binding energy) giving explicit definition to the distinction between surface- and self-adhesion of the coating.
- The importance of defect-induced nucleation on oxides; important because the Ni tube substrate (the anode) will have a thin oxide, possibly discontinuous, or at the very least oxygen chemisorbed onto the surface.

9.3 Zirconia Electrolytes by EB-PVD

"The electrolyte is that component that separates the fuel from the oxidant and forces the oxidation to proceed electrochemically rather than by combustion." [Camilleri 2009] There are several requirements it must fulfil as a result. For anode-supported designs such as this one there are no structural requirements to fulfil beyond good adhesion to the anode. Ancillary to this is sufficient robustness for handling, subsequent processing steps, and operation (related primarily to resistance to thermally-induced forces during thermal cycling of the SOFC between room temperature and the operating temperature). The other requirements revolve around the electrolyte's role as an ionic conductor and separator between fuel and oxidant. Once a suitable material has been identified there are two parameters that describe its capability as an ionic conductor and its capability as a gas separator – thickness and porosity respectively. Porosity is also a function of morphology, in turn influenced by the thickness and surface conditioning. So in many ways the thickness is critical.

The Ohmic polarization is partly an indication of the ionic conductance of the electrolyte since it includes electrical components from the electrodes and the ionic component from the electrolyte. This last is accepted to be the greatest contributor to the total ohmic polarization [Meng *et al.* 2008] since its conductivity tends to be far lower than the metallic electrodes (anode and cathode). "Recall also that the definition of current is flow of charge – both electronic and ionic are taken together." [Camilleri 2009] A thinner electrolyte reduces ohmic polarization, and hence offers superior performance (lower voltage drop when current is drawn from the device). Key to the development of metal-supported SOFCs is the manufacturing of gas tight thin-film electrolytes [Haydn *et al.* 2014, Coddet *et al.* 2014].

The above only holds if the electrolyte is also gas-tight. As mentioned here and elsewhere the electrolyte also serves to separate the fuel and oxidant to drive electrochemical oxidation rather than combustion (thermal oxidation). *Ergo*, a compromise must be reached between the thinnest possible electrolyte (thereby minimising ohmic polarization) and the minimum possible thickness needed to ensure gas tightness. In the case of ceramics the matter is further complicated because they tend to form a large number of phases and possible textures according to the combination of pressure, temperature, composition, stabilizing agents, and even nucleation and the particular route of crystallisation. This is certainly true of YSZ, despite the stabilisation resulting in the cubic phase to form almost exclusively [Stevens 1986, Yashima *et al.* 1996]. The comprehensive paper by Yashima *et al.* (1996) was an invaluable resource in understanding the metastable nature of doped zirconia and its subtleties. Previous experience (Ken Lawson and Professor John Nicholls, personal communication) and literature sources [Matsumoto *et al.* 2008] show that at higher deposition temperatures in the range 850 °C – 1,000 °C, as described in section 3.3.1,

takes on (as a fluorite type ceramic) a FCC (face centred cubic) structure with columnar texturing.

At lower deposition temperatures texturing is absent. This is usually also true for thinner coatings. Even when the structure is columnar it is not so through the entire thickness of the coating. The first few microns are a randomly oriented FCC (possibly containing some tetragonal) phase, then, when the coating is thick enough, after sufficient time for subsequent grains to orient themselves forming columns. These may sinter slightly at the top, closing them off at the surface. The process that leads to this is referred to as shadowing, and is a preferential growth mechanism based in the direction of the incoming material flux. As a result the first few layers and possibly the column tops have no texturing. While the columnar structure appears more open, it is in fact more gas tight than phases deposited at temperatures close to 600 °C – 700 °C, such as those oft quoted in the literature. High deposition temperature coatings also exhibit better thermal cycle resistance due to superior compliance [Matsumoto *et al.* 2008].

Previous experience has shown (Ken Lawson and Professor John Nicholls, personal communication) this to be especially true of high operating temperatures when the thermal expansion of the columns compacts them together. The author believes it would be advantageous (in terms of improved gas tightness and hence improved performance) to exploit the columnar structure if permitted by the electrolyte thickness and its growth mechanism. Unfortunately, this is likely to entail a minimum thickness (less than ideal from the ohmic polarisation standpoint) and also entails using higher deposition temperatures. The use of higher temperatures complicates equipment significantly, so much so that the coater used is in fact the only one of its kind in UK academia capable of reaching the necessary temperatures under vacuum. Requiring a bespoke high-temperature design and the increased energy needed, translates into more expensive devices at the consumer end. “Since cost has always been the Achilles’ heel of SOFCs the increase in performance would have to be significant to justify it.” [Camilleri 2009]

Both experiments and modelling have shown that pore morphology in the coatings can be influenced by process variables that affect the incident angle of the vapourised atoms (the vapour incident angle or VIA) and the mobility of the condensed species at the vapour-solid interface [Zhao *et al.* 2006]. Variables include substrate temperature, deposition rate, gas pressure and substrate roughness.

Highly porous columnar coatings are associated with low kinetic energy, oblique vapour incidence angles, low substrate temperatures, high deposition rates, rough substrates and high chamber pressures [Hass *et al.* 2001, Zhao *et al.* 2006]. These conditions are therefore to be avoided as much as possible since a gas tight coating is required. Unfortunately in order to obtain uniform coatings on tubes these must be rotated which may cause shadowing problems leading to increased porosity. Increasing the rate of

rotation significantly (to about 30 rpm) is reported to reduce porosity [Zhao *et al.* 2006]. Column morphology changes from <111> to <001> in such cases, however, and the tops of the columns are capped with pyramids (rather than tetrahaedra as is the case with <111> columns) [Zhao *et al.* 2006].

It has been shown [Matsumoto *et al.* 2008] that columnar structures with columns of intermediate width have longer lives than narrower or thicker ones (unfortunately without defining a range that can be considered intermediate). On a fabrication note the work of Matsumoto *et al.* (2008) shows that the columns are more dense when the VIA (vapour incident angle) is perpendicular to the substrate, and more porous when the VIA is more oblique. A high rotation rate was used to attempt to keep the VIA as near to 90° as possible during deposition. Matsumoto *et al.* (2008) observe that a very slow rotation rate (0–1 rpm) yields c.95% theoretical density, and faster rotation rate of around 20 rpm yield c.70–80% theoretical density.

An interesting benefit to employing a higher rotational speed is that it results in a more uniform temperature distribution across the sample, especially if the substrate temperature is maintained by additional heating (as in this case), which has been observed to reduce cracking during deposition [Matsumoto *et al.* 2008]. Matsumoto *et al.* (2008) present a graph showing the cycles to failure (life) versus the rotation speed. The general conclusion is that higher speeds yield improved coating life, at least when applied as thermal barrier coatings or other applications with significant cycling of temperatures (not necessarily the case with SOFCs for large scale power generation). The effect has been attributed, at least in part, to the lower residual stress of the compliant coatings made at higher rotational speeds [Matsumoto *et al.* 2008]. The columnar microstructure of EB-PVD coatings is accepted as the reason for high strain compliance that results in superior thermal shock resistance [Matsumoto *et al.* 2008].

The high temperature morphological stability of YSZ, crucial to its role as a solid electrolyte at high temperature, is explored by Thome *et al.* (2004). Those authors studied YSZ surface morphology (on (100) single crystals) with temperature (up to 1,500 °C) in air at the nanometric scale using AFM. They are however, 9.5 wt.% rather than 7 wt.% as with the deposited YSZ for this project. AFM is necessary when studying YSZ at this scale because of its strongly insulating properties. Something observed in my own SEM microscopy with an effective limit of approximately 10,000 times magnification.

At 0.43 T homologous (1,000 °C for YSZ) the surface morphology of YSZ forms 0.5 nm tall steps separated by 160 nm [Thome *et al.* 2004]. The step height corresponds to the height of a unit cell and therefore each step is a monolayer. For a discussion on the great stability of the surface morphology of YSZ at high temperature the reader is referred to the cited paper [Thome *et al.* 2004]. What is important to note for the

purposes of forming thin electrolytes for microtubular SOFCs is that at the maximum operating temperature of interest the only change from room temperature morphology is the formation of monolayer steps uniformly distributed along the (100) surface. Notice this is for the (100) crystal faces – the larger scale surface morphology remains that of tetrahedron-topped columns.

Three important implications are:

I. no substantial change in surface morphology that may interfere with the electrolyte-cathode interface
II. perhaps a small improvement in performance (lower interfacial loss) due to increased surface contact at a nanoscopic scale
III. no change that may dislodge the cathode (particularly important with cathode materials considerably less adhering than sputtered platinum).

Should adhesion prove poor in all cases (recall deposition was without the aid of a bondcoat or interlayer) the samples would be pre-oxidised. The oxide would facilitate the adhesion of YSZ onto the nickel since oxides usually adhere well to other oxides. A little oxidation occurs upon introducing oxygen (opening the oxygen valve) immediately prior to commencing zirconia deposition (the processes are mere seconds apart). It is believed that this would be sufficient, and pre-oxidation the best solution should this not be so. The thicker oxide, that deleteriously affects performance, can be removed by a brief reduction treatment. The use of an interlayer (often referred to colloquially as a bond coat), while standard for depositing YSZ and similar ceramics onto materials where adhesion is problematic, is unacceptable in this case because it would drastically reduce performance by essentially blocking off the three phase boundary.

Quoting from the abstract of Menzler *et al.* (2013) is an excellent summary: "The implementation of thin-film technologies [...] is essential in terms of enhancing the functionality, reducing operating temperatures, and increasing lifetime. Introducing thin electrolyte layers into solid oxide fuel cells (SOFCs) decreases the internal cell resistance and thus drastically enhances the power density. This supports the goal of reducing the operation temperature from 800 °C to temperatures below 700 °C. As the operation temperature is lowered, the temperature-activated degradation processes are slowed down, and 40,000 h of operation becomes feasible. [...] Thinner functional layers possess higher permeabilities [in this instance the authors are referring to oxygen ion conduction through the electrolyte] but also involve a risk of more layer defects. [...] Thus, the manufacturing of the supports and the intermediate layers is also very important."

9.4 Deposition Experiments

The fuel cell tube is 99.5% pure nickel (Ni 200) OD 5.9 mm, wall thickness 125 μm from Goodfellow Cambridge Ltd., cleaned in an acetone ultrasonic bath for 5 min prior to deposition. The full fuel cell length of 100 mm is needed for these experiments since the variation of coating thickness with length is an important factor to investigate (recall that the deposition distance from source to substrate increases from the middle of the tube towards the ends because there is a single source, a pseudo point-source). The deposited 7 wt.% YSZ will cover 80 mm of the tube (frequently referred to as the active length) leaving the ends uncoated by utilising a Ni foil mask. The porosity of anodes was demonstrated [Camilleri 2009] to have neither adverse nor beneficial effect on deposition. Thus, it was deemed most expedient and economical to use as delivered tubes (i.e. solid Ni tubes rather than porous anodes) for these experiments. Unless otherwise noted the abbreviation 7YSZ refers to the mass fraction of yttria stabilizing the zirconia.

Deposition was carried out using Nimonic 75 jigs purpose made for this project with alumina support rods (see Figure 9-13.), cleaned as per the samples prior to each deposition. A total of 10 samples were used, separated into 5 batches of 2 (the maximum that can be coated simultaneously in this particular coater) – deemed acceptable for determining the reproducibility of the results. The equipment used was a modified Electrotech CL 680 (Cubic Line with a 680 mm^3 chamber) ion plater delivered to Cranfield University in 1980 with three guns. It is called an Ion Plater because it has the ability to place a large bias on the substrate causing ion bombardment. Its initial job was to produce graded MCrAlY bond coats. It was modified in 1994 to a single hearth ceramic coater by drilling a hole in the crucible of a standard Temescal 15 cc single pot gun and building an ingot rotation and lift system. The gun is driven by a Temescal 14 kW power supply. A 1,000 °C furnace was installed along with a substrate rotation system these were both produced by Severn Furnaces to National High Temperature Surface Engineering Laboratory (B57 of Cranfield University) design. It is given the designation of Coater 1 to distinguish it from other coaters in the University. It is unique in the world of EB-PVD academia. The ingots were 7 wt.% Y_2O_3-ZrO_2 (approximately 4 at.%), 33.5 mm ±0.5 mm diameter, 200 mm ±5 mm length, 3.6–4.0 gcm^{-3} density from Phoenix Coating Resources, Inc., Florida, USA.

Based on my MSc [Camilleri 2009] and the literature regarding EB-PVD deposition of YSZ the deposition parameters are as follows: overnight evacuation without heating followed by rapid heating to 850 °C immediately before deposition. Then the electron gun is switched on to evaporate the ingot, also raising the temperature to the desired deposition temperature of 1,000 °C. The chamber is then filled with a 90 vol.% O_2 (balance Ar) mix to a nominal pressure of $1–1.5x10^{-2}$ mbar at a volumetric flow rate of 80–100 sccm. In order to obtain the desired nominal thickness of 10 μm deposition

proceeds for 4 min 6 s, at which point the electron gun is switched off and the system allowed to cool. The mounting points for the samples (referred to as paddles) rotate ensuring even coverage of each sample. Rotation rate was 10 rpm. Once cool the chamber is brought to atmospheric pressure for unloading. It is worth noting that the gas system operates under pressure control, the volumetric flow rate is provided for completeness (and possibly to monitor gas consumption).

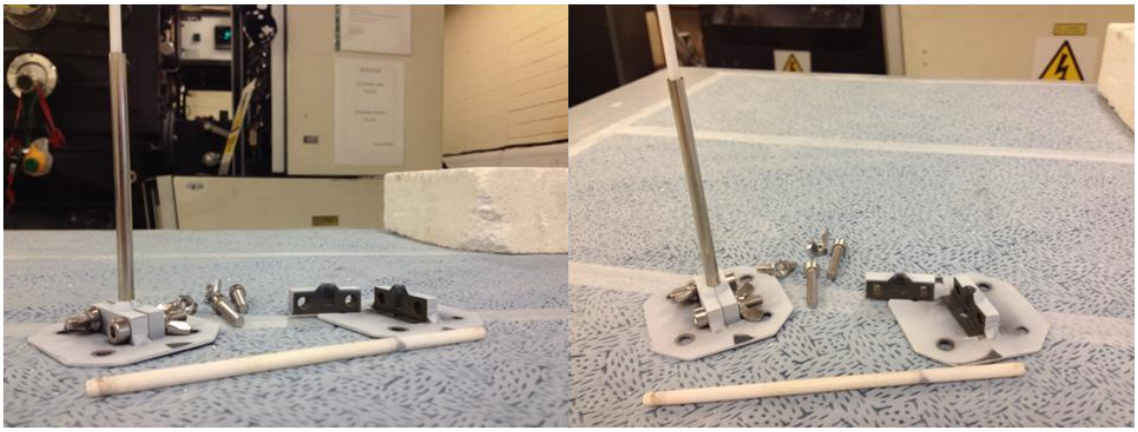

Figure 9-13. EB-PVD deposition jig and alumina support rods.

A sure sign of a successful, strongly adhering, high quality coating is that the tubes can be handled with little worry of damaging the electrolyte. Cracks and delamination are signs of unsuccessful deposition. Some discolouration is possible (samples appear yellow-brown or have areas that are this colour rather than grey). This is caused by oxygen deficiency and can be corrected (ensuring the entire electrolyte is stoichiometric) by a heat treatment at 700 °C for 1 h. This can be done as part of the start-up for cell operation and is of little concern.

For this tier of deposition experiments 10 µm of 7YSZ were deposited to confirm or refute the findings published in my MSc thesis [Camilleri 2009]. It is additionally the current state of the art electrolyte thickness for thin electrolyte SOFCs as discussed previously (sections 2.13).

Each sample was weighed before and after deposition, taking care to extract the correct sample (known by its position in the coater – left paddle or right paddle). The mass gain gives a quantitative measure of how much 7YSZ adhered to the Ni200 tubes. The end nearest the furnace door was marked with a permanent marker while unloading. Knowing the orientation of each sample allows the assumption that the thickness profile is symmetrical (i.e. that the evaporator is symmetrical) to be tested.

Characterization was also by visual inspection (for quality, conformity, reproducibility and uniformity of electrolyte) and using SEM imaging, of both the surface and cross-sections (sectioned, mounted and polished conventionally). Frequently carbon or gold

sputtering was used to improve sample conductivity. The SEM utilized was an FEI XL30 SFEG. Reproducibility was quantified using a series of thickness measurements as described immediately below.

Samples were prepared as follows post-deposition: In order to obtain sufficient data points from each tube at least four sections need to be taken along the length (each end, and two sections in between – to either side of the mid-point). Ideally a total of six sections are used allowing a non-linear profile to be generated; this also means we are able to test whether any long-axis variation in coating thickness is linear or not. However, since the deposition source is directed to the mid-point (lengthwise) of the tubes the deposition profile (variation in coating thickness from middle to ends) should be symmetrical. As a result only two sections per sample are needed. Three were used to account for a possibly non-linear profile. It was necessary to take sections from both samples despite being coated simultaneously because the left and right paddles are offset somewhat – sitting at different distances to the source – and therefore resulting in slightly different coating thicknesses. The work of James *et al.* (1995) indicates a symmetrical bell-shaped profile is to be expected, with marginally reduced overall coating thickness for samples deposited on the paddle further form the source. While the equations are for a point source [James *et al.* 1995], the distributed-source nature of a real coater merely modifies the bell-curve, widening it. The symmetricity is preserved.

Each of the three sections per sample were: 26 mm (including 10 mm uncoated at the very end), 12 mm and 12 mm long segments cut using a precision saw. Each trio of sections (from a single deposition sample) were mounted together in resin (Struers Epofix resin and hardener – room temperature cure), and polished to 2400 grit and finally finished with colloidal silica paste. An autopolisher (Buehler Motopol automatic grinder/polisher) was used to ensure flatness of the mounted samples. The procedure resulted in samples well suited to image analysis having excellent contrast between the mounting material and the samples. Contrast between the substrate (Ni tube) and deposited coating was considerably poorer. Measurements were taken at eight positions around the circumference of each section, equally spread 45° apart. Unfortunately the semi-automated IA system available on campus had insufficient magnification to clearly distinguish the coating from the substrate. An optical microscope fitted with a digital camera and measurement software was used instead (Nikon Eclipse ME600 with AcQuis software from Syncroscopy), 50× magnification was found to be adequate. As a result there is likely to be some operator error in positioning the samples for measurement, despite the relative ease of using the eight compass points. The data were analysed using a spreadsheet and collated in section 9.5 (Deposition Reproducibility), below.

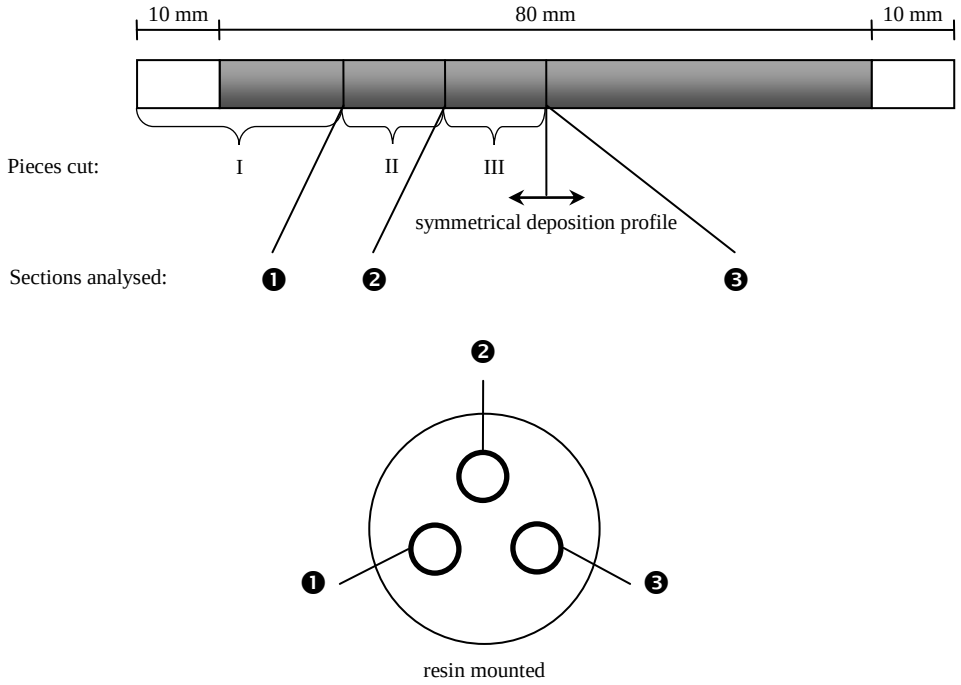

Figure 9-14. Diagram of cross-sections taken of EB-PVD deposition for image analysis and relative positions of mounted samples after sectioning.

Following the results of the first experiments, most notably the unacceptable delamination, it became apparent that the parameters were not as optimal as had been believed. Deposition parameter optimization was therefore a necessary adjunct. This was carried out on a second iteration jig made of NiCr and Inconel obviating the need for alumina support rods (see Figure 9-13. and Figure 9-15.). A total of 14 samples were used, coated singly in the same coater and using the same ingots as previously. All samples were mounted on the left hand paddle of the coater. The same method as tier 1 was employed.

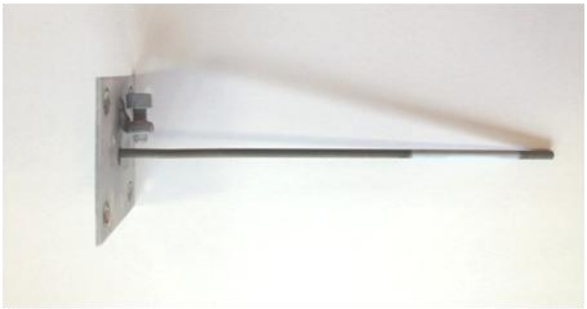

Figure 9-15. EB-PVD updated deposition jig that is both simplified and holds the sample more securely while removing the risk of damage that existed with the previous version.

For this tier of deposition experiments 10 µm of 7YSZ were deposited with different deposition parameters according to the DoE schema detailed in section 9.6.1 (also see

Table 9-7.). Each sample was weighed before and after deposition, for a quantitative measure of the mass of 7YSZ adhering to the Ni200 tubes. The actual order the experiments was carried out in was randomised as shown in the table. This avoids any systematic bias and is standard practice in DoE.

Characterization was also by visual inspection (for quality, macro-conformity, reproducibility and uniformity of electrolyte) and using SEM imaging, of both the surface and cross-sections (trenches created by FIB where necessary but samples otherwise sectioned, mounted and polished conventionally). Frequently, carbon or gold sputtering was used to improve sample conductivity. The batch of resin used appeared to be somewhat defective (or at the very least it behaved noticeably differently than on previous, and subsequent, occasions). Specifically, the cured resin frequently separated from the sample in at least a few areas (testament to how strong the bonding between coating and substrate is there was rarely damage to the coating itself!). The result proved exceedingly difficult to polish, and (because of the gaps) the use of colloidal silica to achieve a high polish was not possible. Colloidal silica would infiltrate the gaps and then be drawn out while pumping down the SEM chamber utterly obscuring details. It took months of trial and error and repeated re-polishing (six times in one case, three in most others) to achieve adequate results, exacerbated further by further unusual behaviour of the cured resin which pitted if left unattended for a few weeks. Images are still not entirely satisfactory, but for the purpose of measuring coating thickness are adequate. The section used is equivalent to ❶ for the Tier 1 experiments (see Figure 9-14.). The FIB used was a FEI XP200 and the SEM utilized was an FEI XL30 SFEG.

9.5 Deposition Reproducibility

The objective for this tier of experiments was to assess (quantitatively, via thickness) the reproducibility of the deposition process using the parameters previously established [Camilleri 2009]. This was conceived as the only optimization necessary for 10 μm thick coatings; the next step would be optimization of the electrolyte itself by reducing thickness further.

9.5.1 Results & Discussion

Table 9-3. summarises the results of the tier 1 experiments giving the initial mass of the sample, the mass after deposition, mass of 7YSZ deposited, measured area coated, the average coating thickness (average of the mean thicknesses at each section along the length of the sample, detailed in Table 9-2.) and the average coating density. It is assumed that the coating density does not vary for a given sample, only the thickness. In addition, the deposition parameters for each deposition run (including the electron gun voltage and current) are given in Table 9-4. to enable comparison between results and deposition parameters for the purpose of process optimization.

The actual, as opposed to nominal, coating thickness is a very important parameter. In many ways it is the outcome that the other parameters are judged by. The average coating thickness (see also Table 9-3.) was determined as described in the section 9.4. The results are displayed in Table 9-2. below. The thicknesses z_I, z_{II} and z_{III} are the mean of the measured thicknesses around the circumference of the substrate of the deposited 7YSZ coating of each of the three sections from the sample end to middle respectively as shown in Figure 9-14., $\bar{z}$ is the average of these three, i.e. the average mean coating thickness of a given sample.

Sample	$z_I \pm s_I$ **(µm)**	$z_{II} \pm s_{II}$ **(µm)**	$z_{III} \pm s_{III}$ **(µm)**	$\bar{z} \pm \bar{s}$ **(µm)**
DT-E.24/04/12-125;10.1000-A.01	8.4 ± 0.7	9.6 ± 0.7	10.6 ± 0.5	9.5 ± 1.1
DT-E.24/04/12-125;10.1000-A.02	6.9 ± 0.7	7.8 ± 0.6	9.2 ± 0.7	8.0 ± 1.2
DT-E.17/05/12-125;10.1000-A.03	11.7 ± 0.6	13.4 ± 0.7	15.2 ± 0.6	13.4 ± 1.6
DT-E.17/05/12-125;10.1000-A.04	9.3 ± 0.5	10.8 ± 1.1	12.3 ± 0.6	10.8 ± 1.5
DT-E.05/07/12-125;10.1000-A.05	8.4 ± 0.6	10.1 ± 0.5	12.5 ± 1.4	10.3 ± 1.9
DT-E.05/07/12-125;10.1000-A.06	10.7 ± 0.6	10.2 ± 0.3	9.0 ± 0.2	10.0 ± 0.8
DT-E.12/09/12-125;10.1000-A.07	7.0 ± 0.4	8.2 ± 0.5	9.3 ± 0.3	8.2 ± 1.0
DT-E.12/09/12-125;10.1000-A.08	**	11.1 ± 0.4	10. ± 0.4	10.7 ± 0.6
DT-E.01/10/12-125;10.1000-A.09	**	11.4 ± 0.9	10.8 ± 0.5	11.1 ± 0.8
DT-E.01/10/12-125;10.1000-A.10	7.3 ± 0.4	8.8 ± 0.5	9.9 ± 0.4	8.6 ± 1.2
Arithmetic mean	8.7 ± 0.6	10.1 ± 0.6	10.9 ± 0.5	10.1 ± 1.2

Table 9-2. Tier 1 coating thickness: average of eight points along the circumference of each of the three sections per sample, and the mean thickness per sample (including standard deviations: denoted by s since sample size < 10). ** indicates complete delamination; likely due to sectioning or mounting damage.

Sample	$\mathbf{m_{Ni}}$ **(mg)** ±1 mg	$\mathbf{m_{YSZ}}$ **(mg)** ±1 mg	**A (cm^2)** ±1x10^{-4} cm^2	$\bar{z}$ **(µm)** ±1.9 µm	$\bar{\rho}$ **(gcm^{-3})** ±0.6 gcm^{-3}
DT-E.24/04/12-125;10.1000-A.01	2,006.3	80.0	18.1647	9.5	4.68
DT-E.24/04/12-125;10.1000-A.02	2,023.8	70.8	17.0526	8.0	5.29
DT-E.17/05/12-125;10.1000-A.03	1,976.4	117.4	16.0715	13.4	5.52
DT-E.17/05/12-125;10.1000-A.04	1,970.8	89.0	15.2015	10.8	5.50
DT-E.05/07/12-125;10.1000-A.05	2,028.4	73.8	15.5694	10.3	4.68
DT-E.05/07/12-125;10.1000-A.06	2,004.0	70.8	15.2914	10.0	4.60
DT-E.12/09/12-125;10.1000-A.07	1,968.9	57.9	13.6900	8.2	5.25
DT-E.12/09/12-125;10.1000-A.08	2,015.3	55.6	13.7600	10.7	6.31
DT-E.01/10/12-125;10.1000-A.09	2,024.9	64.2	15.6680	11.1	6.17
DT-E.01/10/12-125;10.1000-A.10	1,972.4	66.1	15.6540	8.6	4.97

Table 9-3. Tier 1 deposition results including mass deposited, area coated, average coating thickness (as detailed in the discussion) and average coating density (also detailed in the discussion).

Run	**T (°C)** ±2 °C	**Duration** ±1 s	$\mathbf{P_{chamber}}$ **(mbar)** ±1x10^{-4} mbar	**Gas Flow (sccm)** ±5 sccm	***f*** **(rpm)** ±1 rpm	**V (kV)** ±10%	**I (A)** ±10 %
1 (A.01 & A.02)	1,018	4 min 6 s	1.38 x10^{-2}	110	10	10	0.4
2 (A.03 & A.04)	1,019	4 min 6 s	1.44 x10^{-2}	80	10	10	0.4
3 (A.05 & A.06)	1,040	4 min 6 s	1.03 x10^{-2}	60	10	10	0.4
4 (A.07 & A.08)	1,024	4 min 6 s	1.08 x10^{-2}	80	10	10	0.4
5 (A.09 & A.10)	1,029	4 min 6 s	1.02 x10^{-2}	70	10	10	0.4

Table 9-4. Tier 1 deposition parameters by run.

Calculating coating density was itself not a trivial problem. Short of employing FIB tomography assumptions must be made and the data treated accordingly. We might select one section as representative and calculate the coating volume (and thence density) based on that. Alternatives include using the global average coating thickness tabulated above (arithmetic mean of average coating thicknesses), or take the mean of all 24 data points (i.e. not distinguishing between points of different segments of the tube, I, II and III), or we may treat each section individually summing the total volume (i.e. $V = 2(A_I z_I + A_{II} z_{II} + A_{III} z_{III})$). The volume can also be calculated accurately by multiple integration for each sample using the linear thickness variation plots and a triple integration in cylindrical coordinates.

Three cases were considered:

1) Case 1 Uses the average thickness of the whole sample (i.e. of 24 data points).
2) Case 2 Treats each section individually, summing up the total coating volume of a given sample to calculate its density (i.e. $V = 2(A_I z_I + A_{II} z_{II} + A_{III} z_{III})$). The areas are determined proportionally to that section's length with respect to the whole sample.
3) Case 3 Uses the global average thickness of 10.1 ± 1.2 μm for all samples.

In each case the density was computed, and expressed both in gcm^{-3} as well as a percentage of the maximum (nominal) density of 7YSZ. The latter is 6.025 gcm^{-3} (at 0% porosity) or 5.925 gcm^{-3} (overall average of data, see Appendix N: Material Data Tables).

Sample	Case 1		Case 2		Case 3	
	ρ (gcm^{-3}) ±0.6 gcm^{-3}	$\frac{\rho}{\rho_{max}}$ (%)	ρ (gcm^{-3}) ±0.6 gcm^{-3}	$\frac{\rho}{\rho_{max}}$ (%)	ρ (gcm^{-3}) ±1.0 gcm^{-3}	$\frac{\rho}{\rho_{max}}$ (%)
DT-E.24/04/12-125;10.1000-A.01	4.64	76.95	4.68	77.62	4.38	72.73
DT-E.24/04/12-125;10.1000-A.02	5.19	86.14	5.29	87.77	4.13	68.57
DT-E.17/05/12-125;10.1000-A.03	5.45	90.48	5.52	91.65	7.27	120.64
DT-E.17/05/12-125;10.1000-A.04	5.42	89.98	5.50	91.29	5.83	96.69
DT-E.05/07/12-125;10.1000-A.05	4.60	76.38	4.68	77.69	4.72	78.28
DT-E.05/07/12-125;10.1000-A.06	4.63	76.85	4.60	76.42	4.61	76.47
DT-E.12/09/12-125;10.1000-A.07	5.16	85.61	5.25	87.13	4.21	69.85
DT-E.12/09/12-125;10.1000-A.08	3.78	62.68	6.31	104.71	4.02	66.73
DT-E.01/10/12-125;10.1000-A.09	3.69	61.27	6.17	102.35	4.08	67.67
DT-E.01/10/12-125;10.1000-A.10	4.91	81.49	4.97	82.46	4.20	69.74

Table 9-5. Tier 1 calculated coating densities (all cases considered).

A 65–75% dense film would be typical [discussion with Professor John Nicholls, Zhao *et al.* 2006]. This production scheme, then, results in greater density films than is typical by EB-PVD. Not unexpectedly the results are very similar. To determine which case is more representative Student T Tests (a form of statistical null hypothesis test) were carried out comparing cases pairwise (a restriction of the test) for significant difference.

Comparison	Student T Test results	Conclusions
Case 1 and Case 2	At 95 % confidence interval the difference IS statistically significant. At 99 % confidence interval the difference is NOT statistically significant. The threshold confidence interval is 97 %.	While there is a small chance of a false positive correlation treating each segment separately yields more accurate results.
Case 1 and Case 3	At 90 % confidence interval the difference is NOT statistically significant. At 95 % confidence interval the difference is NOT statistically significant. The threshold confidence interval is 50 %.	Indicates that there is no statistically significant difference between using the mean thickness for each sample and the global average thickness.
Case 2 and Case 3	At 90 % confidence interval the difference IS statistically significant. At 95 % confidence interval the difference is NOT statistically significant. The threshold confidence interval is 92 %.	Unless we accept a larger-than-usual chance of an incorrect assessment it is fair to say that there is no significant difference between treating each segment differently and using the global average thickness.

Table 9-6. Student T Test results for Tier 1 coating density calculation (all cases considered).

Based on the confidence intervals the comparison between Case 1 and Case 2 is the most precise. Among these two options the Student T Test shows that Case 2 is the most representative technique for calculating coating density, with only a 3% chance of a false positive correlation. The calculated densities labelled as Case 2 were therefore selected as the most representative coating density (Table 9-3.). Unsurprisingly the coating is not fully dense 7YSZ. This was entirely expected because of the columnar nature. In three instances the density is perhaps somewhat too low (<80%) and may indicate improvement is required. However, the mean density was 87.91 ± 9.93 % of max which may well prove adequate.

By ordering sample data by sample average thickness it is possible to detect trends in coating density with increasing thickness. No such trend was observed in this data, with a random variation in density with coating thickness.

Many of these samples exhibited O_2 deficiency, not uncommon with this process and something that can be corrected with a heat treatment as noted in the section 9.4. Oxygen deficiency in 7YSZ appears as yellow-brown discolourations rather than the grey characteristic of stabilized zirconia of this thickness (the hue of the discolouration is also characteristic of O_2 deficiency in stabilized zirconia).

The samples could be handled without concern and, with the exception of a handful of areas, the first and third batches show no delamination (A.01, A.02, A.05 and A0.6). The second shows considerable delamination (A.03 and A.04), although most of the coating is intact and strongly adhering. The reason is hypothesised below.

Sample A.01 was subsequently heat treated in air at 700 °C for 1 h to fully oxidise the electrolyte. Ni200 foil was used to seal the tube ends much like a sweet wrapper reducing oxidation of the Ni substrate. The results are: m_{Ni+YSZ} = 2,090.7 mg; m_{YSZ} = 84.1 mg. To obtain realistic values for mass gain the sample was sectioned to measure electrolyte thickness *after* the heat treatment. *Ergo*, the electrolyte density of A.01 is not directly comparable to the rest. It does, however, give a useful measure of the extent to which samples are depleted in oxygen and what effect this has. The added foil is certainly not sufficient to prevent anode oxidation. The small increase in mass does suggest it helped, however, and that this result is not conclusive but a useful guide.

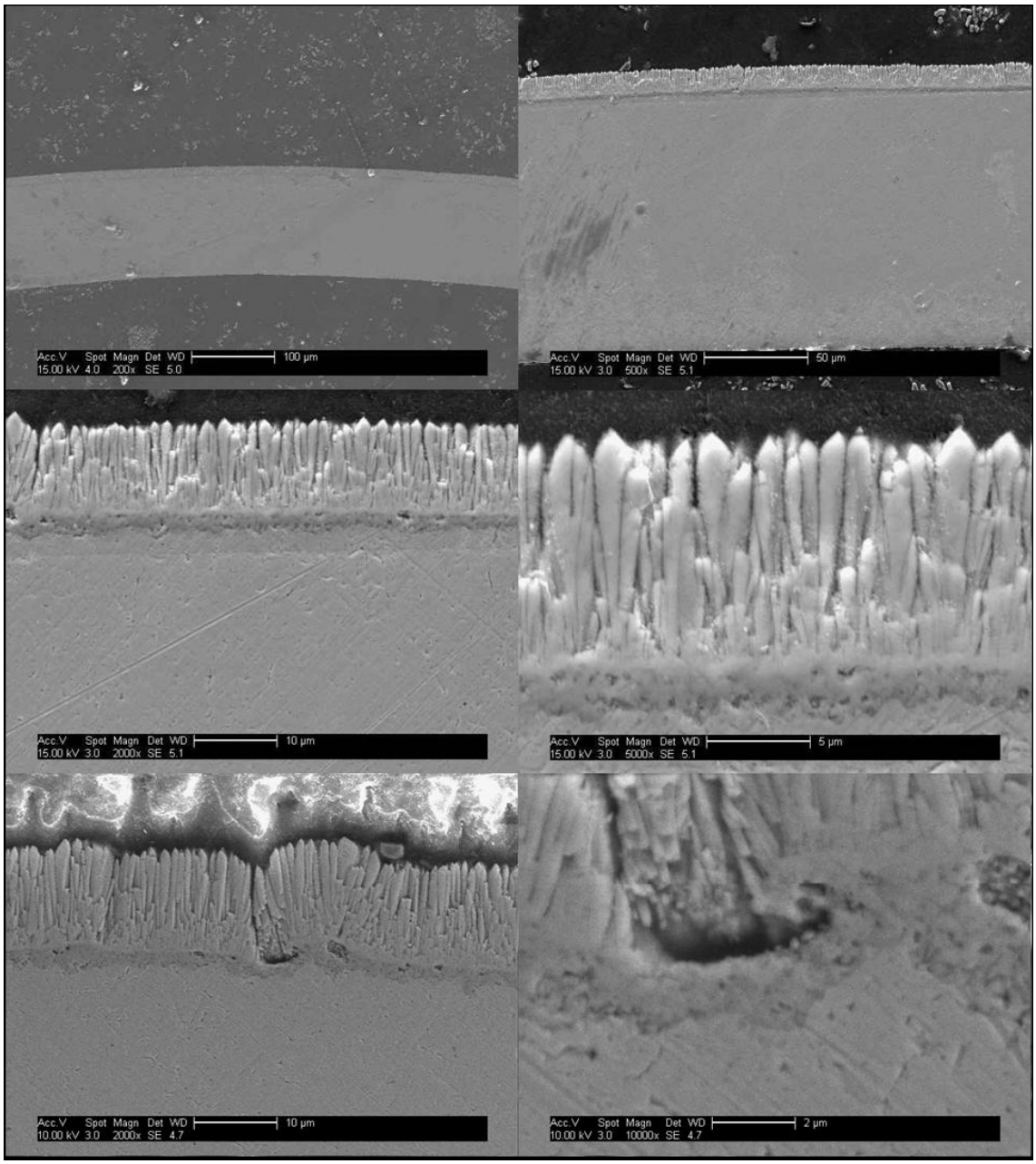

Figure 9-16. SEM micrographs showing columnar 7YSZ on Ni tube. Notice the remarkable conformity over surface defects (visible in these micrographs as pores at the interface (sample DT-E.24/04/12-125;10.1000-A.01). Note that a carbon coating was used to enable the high resolution imaging of the non-conductive zirconia electrolyte (particularly necessary because the samples are mounted in a cold-cure resin, also highly electrically insulating).

The batch containing samples A.03 and A.04 was of markedly inferior quality than those preceding it. Both samples have small areas exhibiting complete delamination of the electrolyte although otherwise appear of adequate quality. There is also a greater area of discoloured YSZ than on A.01 and A.02. The area covered recorded in Table 9-3. takes this into account with approximate areas of the delaminated sections subtracted from the total surface coated.

For batch 3 (A.05 and A.06) a higher temperature and lower pressure were intentionally used in an effort to determine the direction for investigation into optimising the deposition process. The resulting electrolytes were of noticeably better quality than batch 2, yet were still oxygen deficient. A systematic approach is necessary to fully understand the relationship between deposition parameters and electrolyte quality. However, batch 3 successfully demonstrates that altering, even slightly, the deposition temperature (increasing) and chamber pressure (decreasing) has a noticeable effect (beneficial in both cases).

The average sectional coating thickness is thinnest at the end and thickest in the middle of each sample; there are just two definite exceptions A.06 and A.07 (batch 3 right paddle and batch 4 left paddle, respectively). Of these two there is a case to be made based on the standard deviation of the end section for sample A.06. This is double the value of the rest of the sample. Factoring the standard deviation(s) into the assessment A.06's coating may, in fact, vary from thinnest at the ends to thickest in the middle as predicted by the positioning of the source. Two further samples may, or may not, also exhibit greatest thickness not in the middle section: A.08 (batch 4 right paddle) and A.09 (batch 5 left paddle). In both cases the end section yielded no data points as it appeared the coating was stripped during preparation for microscopy. Normally this sort of localised damage is simply ground away and a 'deeper' section is imaged instead. However, in this instance that did not work even after removing about half the sample's 10 mm total length. The standard deviations are uniform per sample (in all cases bar three, ~10% of total), overall low (effectively the same as the estimated measurement accuracy of ±0.5 μm) and with no bias along the sample length, paddle-to-paddle or batch-to-batch – all good news for optimising the deposition process for reproducibility.

Table 9-2. also shows the arithmetic mean and standard deviation of the average thickness per section, by section (which is to say it is the mean of the sectional-average thicknesses given for each section I, II and III). While for certain specific samples it may not be so clear cut the global averages show that the ends have the thinnest coating and the middles the thickest with an s of ±0.6 μm (considered excellent given the precision of the measurement software employed with the optical microscope is ±0.5 μm). Similarly, quantifying the reproducibility of the coatings by thickness yields a global average thickness of 10.05 ± 1.16 μm. This is excellent conforming near perfectly to the nominal value chosen for the deposition experiment. Were this the only criterion used to judge coating quality no further work would be necessary. However, the delamination was considerably worse than expected warranting further assessment of coating quality (refer to continuing discussion below, after linearity of thickness variation from ends to middle of the samples is covered).

The average sectional thicknesses for each sample were plotted against section number (1, 2, or 3) to test linearity. Two such plots are shown hereunder (Figure 9-17.).

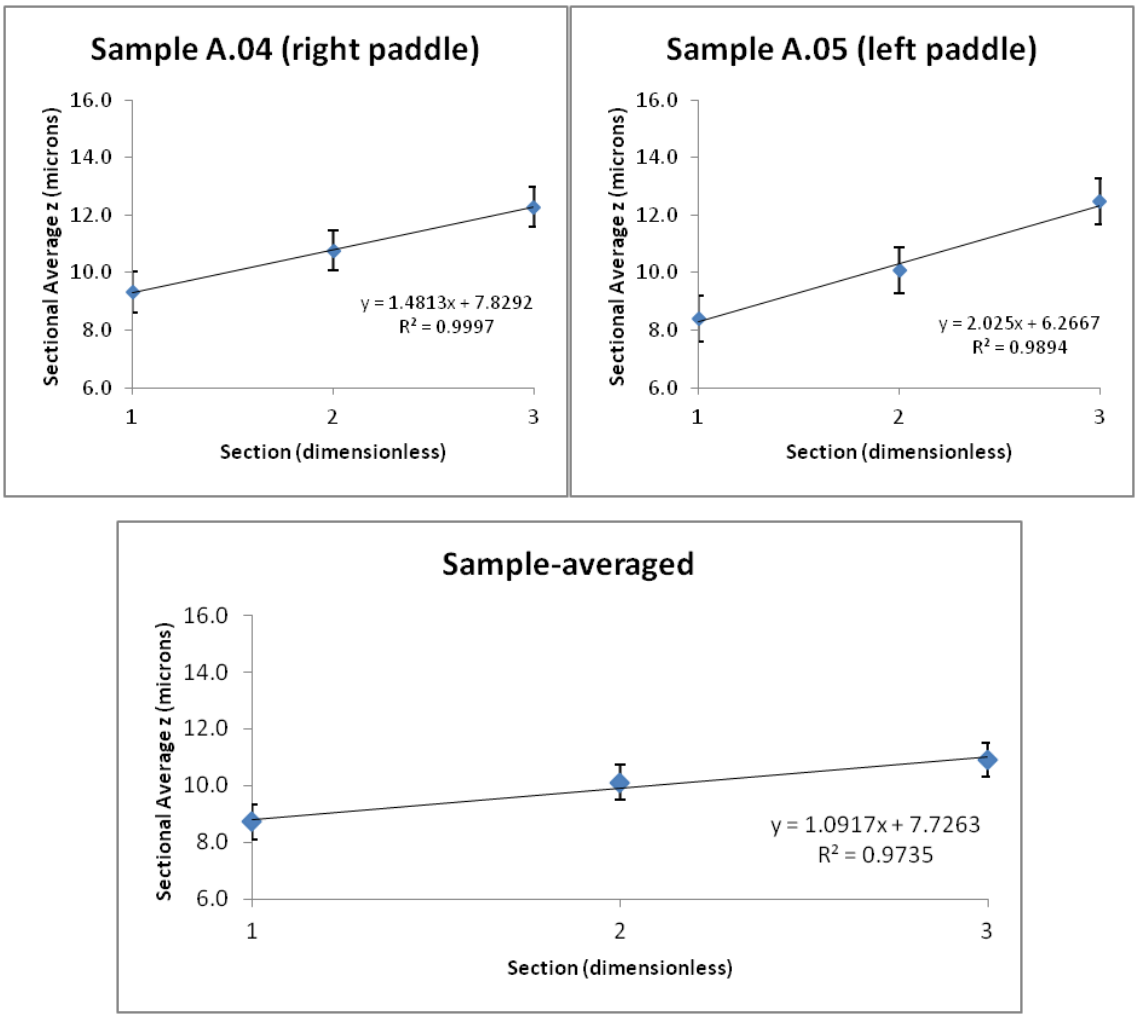

Figure 9-17. Testing the linearity of thickness variation from end to middle of sample DT-E.17/05/12-125;10.1000-A.04 and DT-E.05/07/12-125;10.1000-A.05. In these plots 'x' in the equation of the fitted line is the section number multiplied by the length of that section. Notice the excellent fit and strong linearity (evidenced by points off the fitted line remaining within ±s of the line).

The worst fit has $R^2 = 0.938$ (the average is 0.9735). The excellent fit is the most important thing to notice as this confirms the variation is linear from the ends to the middle of each sample, independent of paddle or detailed considerations of thickness or quality.

There was no evidence to suggest that the assumption of a symmetrical thickness profile (thinnest at the ends of the tubes) due to the varying distance from the source was violated. A wholly expected outcome provided no issues arose with the jigging.

Although the thickness and density are within acceptable tolerances the coatings display an unacceptable level of delamination, which raises the question of adhesion with the nickel substrate (anode). Since delamination is not total and results are otherwise excellent it is my view that another tier of optimization is needed before finalising the deposition parameters to make the electrolytes for the final cells.

It is worth emphasising that the nickel surfaces were not keyed (i.e. used in as delivered state) and that no bond coat or binding aids of any kind were used. This last fact alone makes the results remarkable since traditionally when depositing an yttria stabilised zirconia formulation onto a metallic or alloy part, particularly one with any curvature, an oxide bonding layer, formed by the bond coat is needed. This is due to the nature of YSZ bonding, which is via oxygen bonds (one can think of it as oxygen-terminated) [Marino *et al.* 2011].

The work by Marino *et al.* (2011) forms part of a group effort directed and coordinated by Emily Carter (the third author of the cited work). It supports with atomistic modelling and quantum mechanics calculations the theory that zirconia bonding is oxygen-terminated via the 2*p* shell that is not filled. The presence of yttrium helps to strengthen this bond since transition metal additives/dopants such as Si, Y, or Ti enhance the covalent character of the bond. Its ionic character creates a repulsion between the nearly filled 3*d* shell in Ni and the zirconia atoms at the interface reducing bond strength. The cited paper is highly recommended, as it provides considerable insight into the bonding characteristics all principle layers of a thermal barrier coating (namely Ni superalloy, alumina, thermally grown oxide and YSZ) via separation work (work done to delaminate). My working hypothesis as to why a bond coat was not required is that the YSZ bonds to surface NiO that provides the necessary oxygen sites for YSZ bonding. Testing this hypothesis was beyond the scope of the current work, however.

I hypothesise that the reason behind the variance in amount of discolouration and small areas of delamination evident on some batches whilst overall results are of excellent quality is due to system and process tolerances. It is likely that the exact combination of parameters yielding high quality 7YSZ electrolytes is rather stringent, and stochastic variation from batch to batch resulting in batches, or parts of batches, not quite at the nominal conditions – an effect not evident in other work with this coater because typically coatings are of the order of 200 microns thick, remedying the problem by simple dint of available material for deposition. In short, I believe a narrow processing window was the root cause. Correlating electrolyte discolouration and delamination with deposition outside a narrow processing window caused by system tolerances proved impractical at this stage as it requires modification of the current system to narrow those tolerances.

9.6 Process Optimization

Partly in response to the above hypothesis that the exact combination of deposition parameters yielding high quality 7YSZ of acceptable reproducibility is rather stringent and partly as just general good practice a second tier of deposition experiments was carried out with the objective of systematically (and statistically) optimising the deposition parameters. This was achieved by means of applying statistical design of experiments (DoE), in a modified form of the full factorial schema. The objective of statistical design of experiments is to identify those parameters (often called factors) having a relevant impact and optimise these using the minimum number of experiments possible. What follows is some discussion on the selection of parameters for optimization, the responses measured to ascertain whether an electrolyte is acceptable or not, and the DoE itself.

The parameters influencing the deposition of ytrria partially stabilised zirconia by EB-PVD are:

1. Deposition temperature
2. Chamber pressure
3. Substrate rotation speed
4. Deposition rate (cannot normally be controlled directly)
5. Type of bonding (oxide-oxide, metal-oxide, etc.)
6. Substrate geometry
7. Substrate surface roughness
8. CTE mismatch between 8YSZ and substrate
9. Distance between source and substrate

Possible responses (measured outcomes):

1. Uniformity of the coating thickness at any given section (i.e. around the circumference of the substrate)
2. Linearity of thickness variation from middle sections to the ends
3. Width of YSZ columns (a measure of the morphology)
4. Coating density
5. Mass of 7YSZ adhering to substrate
6. ...[any other measureable quantity that can ‘measure’ a successful coating run]

It is well known that deposition temperature and chamber pressure have the greatest influence on coating morphology [Thome *et al.* 2004, Zhao *et al.* 2006, Meng *et al.* 2008, and see chapter 9 introduction]. Substrate rotation is also known to be influential on more complex geometries and/or non-planar substrates [Hass *et al.* 2001, Zhao *et al.* 2006, Matsumoto *et al.* 2008, and see introduction above]. While theoretically the type of bonding (altered by choice of bond coat – or its absence as in this case), substrate geometry, CTE mismatch and substrate surface roughness are of critical importance in

ensuring adequate adhesion [Zhao *et al.* 2006, Meng *et al.* 2008, Cho and Chio 2009, and see introduction above]. Previous work on this by the author [Camilleri 2009] demonstrated that with the nominal deposition parameters used then and more recently for this thesis, adequate adhesion is indeed possible on the very low R_A Ni200 tubes used as substrates. The tier 1 deposition experiments reported above reveal that reproducibility needs improving and the deposition parameters may not yet be optimal.

Given prior success with this exact combination of bond type, substrate geometry and substrate surface roughness these three parameters have been excluded from the DoE. Of the many other parameters, these are either known to have less influence on the outcome or cannot be altered without significant modification to the EB-PVD coater itself. Therefore, the parameters (often called factors in formal DoE language) to be varied for optimising 7YSZ deposition for electrolytes are: deposition temperature, chamber pressure and substrate rotation speed.

Even just three steps per parameter would entail performing 27 individual experiments (deposition runs). Two steps per parameter results in a far more practicable 8 experiments. These can be visualised as a three dimensional space with one dimension per factor and one vertex per step, or setting, of each parameter.

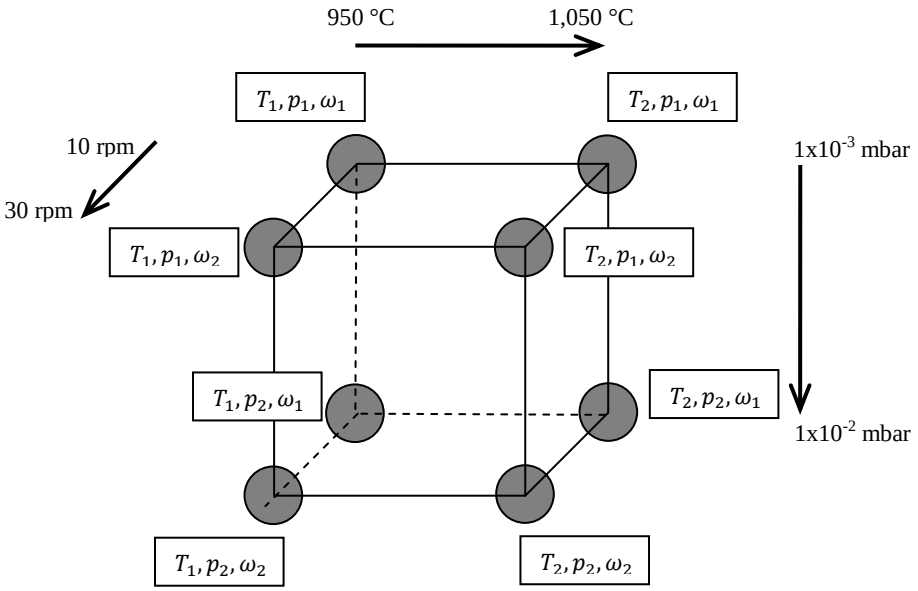

Figure 9-18. Diagram of 3D DoE parameter space.

For deposition temperature the two steps were 950 °C and 1,050 °C (i.e. one point below and one above 0.43T homologous; the range 850 °C – 1,000 °C was identified as optimal by my MSc project [Camilleri 2009]; 0.43T homologous equates to 1,000 °C). For chamber pressure the high step was $1x10^{-2}$ mbar and the low step is $1x10^{-3}$ mbar.

For substrate rotation speed the two steps were 10 rpm (corresponding to previous depositions) and 30 rpm.

Now adding a ninth vertex, set with each deposition parameter at mid value (1,000 °C, $3x10^{-3}$ mbar accounting for logarithmic pressure scale and 20 rpm assuming linear variation) allows interpolation on all three dimensions, in essence almost adding the information yielded by having three steps per factor without necessitating 27 experiments. This allows quadratic rather than purely linear plots to be created revealing any nonlinear behaviour and allowing sensible optimisation whilst adding only one experiment (rather than adding 19 for a full factorial approach).

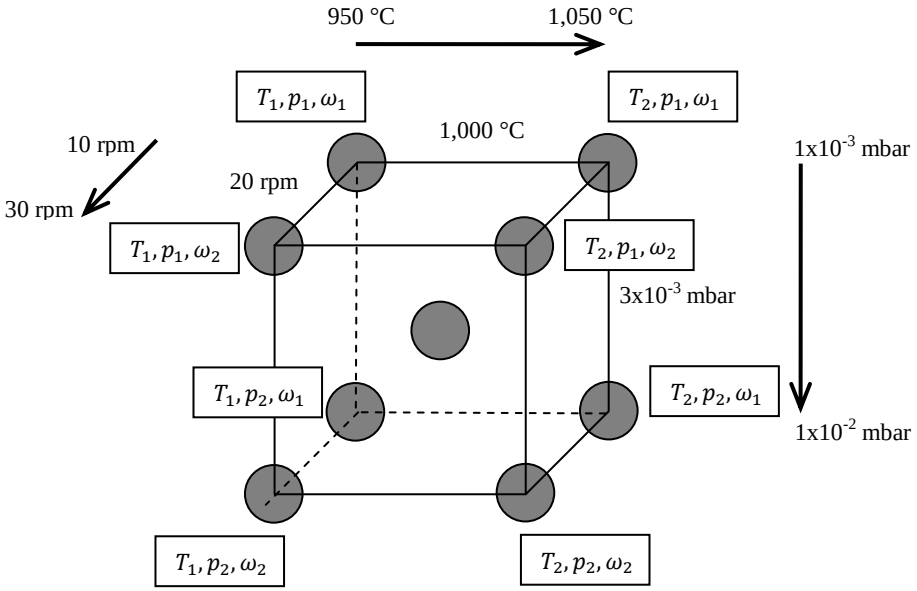

Figure 9-19. Diagram of 3D DoE parameter space showing ninth point and 'mid-step' parameter values.

It is worth repeating this ninth vertex experiment (deposition run) as doing so gives an approximate idea of the overall reproducibility without needing to carry out multiple runs for each of the 8 vertices (overall since the 'middle' vertex uses mean values for all factors). Credit must go to Professor John Nicholls for teaching me these little add-ons that can squeeze even more information out of statistical DoE without necessitating a dramatic increase in the number of experiments required. The parameters for the 10 experiments to be carried out are tabulated in Table 9-8. below, under Results & Discussion (section 9.6.1).

9.6.1 Results & Discussion

Table 9-7. and Table 9-8. summarise the results of the Tier 2 experiments. Table 9-7. gives measurements of coating thickness while Table 9-8. gives the initial mass of the sample, the mass after deposition, mass of 7YSZ deposited, measured area coated, the

average sectional coating thickness and the average coating density for each combination of deposition parameters (also in Table 9-8.) and the measured thicknesses for each combination of deposition parameters. See also Figure 9-20. illustrating the positions of the measurements taken. These are relative rather than absolute positions (i.e. it did not prove possible to use the same datum across all samples – the marking on the tubes became concealed in the cloudy resin). The deposition parameters have nominal values as described above (Figure 9-19.), the values recorded in Table 9-8. are those measured *in situ* by coater instrumentation.

Sample	z_1**(µm)** ±1%	z_2**(µm)** ±1%	z_3**(µm)** ±1%	z_4**(µm)** ±1%	z_5**(µm)** ±1%	z_6**(µm)** ±1%	z_7**(µm)** ±1%	z_8**(µm)** ±1%	$\bar{z}$ **(µm)** ±1%
DT-E.22/11/12-125;10.950-B.01	5.1	5.2	4.2	4.5	4.5	4.4	5.2	5.5	4.83
DT-E.27/11/12-125;10.950-B.02	6.7	6.3	6.3	6.2	6.7	6.4	6.5	6.7	6.48
DT-E.28/11/12-125;10.950-B.03	8.5	8.1	8.3	7.9	8.3	8.8	8.7	8.4	8.38
DT-E.04/12/12-125;10.1050-B.04	6.3	5.8	4.6	4.8	6.4	5.8	5.0	5.3	5.50
DT-E.06/12/12-125;10.950-B.05*	2.2	2.3	2.3	2.0	2.1	2.4	2.4	2.4	2.26
DT-E.17/01/13-125;10.1000-B.06	6.0	5.8	5.9	6.1	6.1	6.0	5.7	5.9	5.94
DT-E.21/01/13-125;10.1000-B.07	4.7	4.7	4.7	4.3	4.5	4.9	4.5	4.7	4.63
DT-E.22/01/13-125;10.1050-B.08	6.9	6.3	7.1	6.6	7.2	6.9	6.5	7..1	6.83
DT-E.23/01/13-125;10.1050-B.09	5.3	5.5	5.3	5.9	6.0	6.0	5.8	5.5	5.66
DT-E.24/01/13-125;10.1050-B.10	5.7	5.8	6.0	6.1	6.3	5.7	5.8	5.8	5.90
DT-E.04/03/13-125;10.850-B.11	6.4	6.0	6.3	6.5	7.1	6.8	6.3	6.3	6.46
DT-E.05/03/13-125;10.850-B.12	4.6	4.4.	3.6	3.7	4.4	4.2	4.5	4.8	4.28
DT-E.06/03/13-125;10.850-B.13	8.6	8.9	8.0	9.1	6.5	7.5	8.7	7.9	8.15
DT-E.05/04/13-125;10.850-B.14	4.9	5.3	5.0	5.1	5.2	4.9	4.9	5.1	5.05

Table 9-7. Tier 2 deposition z (thickness) measurements and sectional average ($\bar{z}$). *Poor adhesion, coating continued to spall during and after unloading. The last four are the extension to the original DoE as remarked in the text. NB: While the measurement system was different than the first tier, the resulting error is very similar.

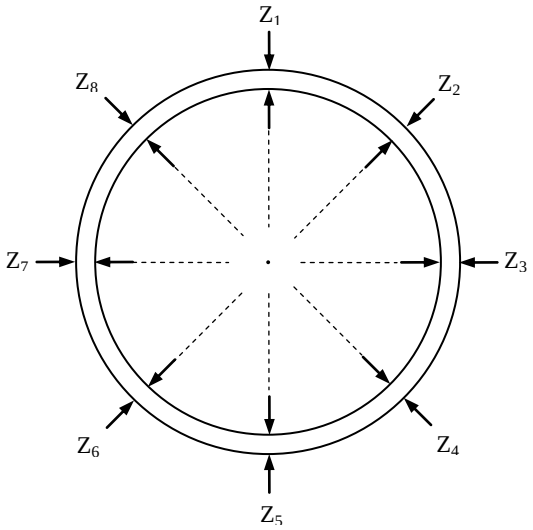

Figure 9-20. Diagram showing EB-PVD Tier 2 (DoE) measurement positions for *z* (thickness).

Sample	**T (°C)** ±2 °C	**$P_{chamber}$ (mbar)** ±1x10^{-4} mbar	***f* (rpm)** ±1 rpm	**m_{Ni} (mg)** ±1 mg	**m_{YSZ} (mg)** ±1 mg	**A (cm^2)** ±1x10^{-4} cm^2	**$\bar{z}$ (µm)** ±1%	**$\bar{\rho}$ (gcm^{-3})** ±1 gcm^{-3}
DT-E.22/11/12-125;10.950-B.01	955	3.80x10^{-3}	30	2,049.4	48.9	15.39	4.83	6.83
DT-E.27/11/12-125;10.950-B.02	959	5.10x10^{-3}	10	2,056.6	68.3	16.76	6.48	7.11
DT-E.28/11/12-125;10.950-B.03	958	1.04x10^{-2}	10	2,010.2	88.9	16.39	8.38	7.15
DT-E.04/12/12-125;10.1050-B.04	1,057	1.01x10^{-2}	10	1,998.2	67.3	16.31	5.50	8.24
DT-E.06/12/12-125;10.950-B.05*	961	1.06x10^{-2}	30	1,991.2	66.5	15.84	2.26	9.83
DT-E.17/01/13-125;10.1000-B.06	1,022	2.94x10^{-3}	20	2,009.2	63.7	15.99	5.94	7.23
DT-E.21/01/13-125;10.1000-B.07	1,022	3.01x10^{-3}	20	1,977.7	47.4	15.53	4.63	6.91
DT-E.22/01/13-125;10.1050-B.08	1,059	1.38x10^{-3}	30	2,011.2	55.1	16.28	6.83	5.44
DT-E.23/01/13-125;10.1050-B.09	1,056	1.18x10^{-3}	10	2,026.4	61.0	15.33	5.66	7.26
DT-E.24/01/13-125;10.1050-B.10	1,057	1.06x10^{-2}	30	2,033.1	57.1	16.49	5.90	6.52
DT-E.04/03/13-125;10.850-B.11	873	1.03x10^{-2}	10	2,008.8	59.3	16.35	6.46	6.18
DT-E.05/03/13-125;10.850-B.12	880	1.56x10^{-3}	10	2,018.5	49.6	16.39	4.28	7.82
DT-E.06/03/13-125;10.850-B.13	887	1.04x10^{-2}	30	2,030.7	79.3	16.61	8.15	6.55
DT-E.05/04/13-125;10.850-B.14	872	1.04x10^{-3}	30	2026.9	54.6	15.97	5.05	7.29

Table 9-8. Tier 2 deposition results. The last four are the extension to the original DoE as remarked in the text. *Poor adhesion, coating continued to spall during and after unloading. Area and mass deposited are only a rough indication.

Sample B.09 and B.10 are worth separate mention. Both show excellent adhesion, the right texture (as far as human fingers can ascertain), virtually no spalling. The only such spalling evidenced is at the tube ends where the deposition process interacts with the

mask that blanks off 10 mm from each extremity. This was the site of the worst spallation in almost all cases so, one may infer, it is most likely a jigging or masking effect that should be solvable by using different masks. However, B.09 was the expected grey colouration and B.10 was yellow-green with additional white-yellow discolourations. Also, B.09 is the only sample where the masking foil (adhesive Ni foil) worked as intended and didn't shift: clean borders and exactly correct active length. Furthermore, the yellow 'seam line' discolouration running lengthwise observed previously (tier 1) has disappeared.

Sample	$\bar{z}$ **(µm)** ±1%	**Sectional s** (absolute)	**Relative s** (normalized)
DT-E.22/11/12-125;10.950-B.01	4.83	0.48 !	0.099
DT-E.27/11/12-125;10.950-B.02	6.48	0.21	0.032
DT-E.28/11/12-125;10.950-B.03	8.38	0.30	0.035
DT-E.04/12/12-125;10.1050-B.04	5.50	0.68 !	0.123
DT-E.06/12/12-125;10.950-B.05*	(2.26)	0.15	0.067
DT-E.17/01/13-125;10.1000-B.06	5.94	0.14	0.024
DT-E.21/01/13-125;10.1000-B.07	4.63	0.18	0.040
DT-E.22/01/13-125;10.1050-B.08	6.83	0.32	0.047
DT-E.23/01/13-125;10.1050-B.09	5.66	0.30	0.053
DT-E.24/01/13-125;10.1050-B.10	5.90	0.21	0.036
DT-E.04/03/13-125;10.850-B.11	6.46	0.34	0.053
DT-E.05/03/13-125;10.850-B.12	4.28	0.42 !	0.099
DT-E.06/03/13-125;10.850-B.13	8.15	0.86 !	0.106
DT-E.05/04/13-125;10.850-B.14	5.05	0.15	0.030

Table 9-9. Tier 2 deposition $\bar{z}$ (sectional average thickness) measurements, absolute sectional standard deviation (s) and relative (normalized) standard deviation ($s/\bar{z}$). *Poor adhesion, coating continued to spall during and after unloading. !Deemed an unusually large. NB: While the measurement system was different than the first tier, the resulting error is very similar.

Unlike the previous (tier 1) experiments the sectional and sample average thicknesses are the same in this case as there was only one section per sample. Sectional average is used for consistence of terminology. Since the sample size is smaller than 10 standard deviation is denoted by s (rather than σ).

As will have been noted four of the sectional standard deviations are marked with an exclamation mark. This indicates that these were deemed unusually large by my own judgement and necessitated further investigation. I was advised (private communication with Professor John Nicholls) to calculate a relative error term consisting of s normalized for the average thickness of that section. Normalizing in this way is useful in this instance since each experiment results in varying deposition thickness due to the deposition parameters rather than stochastic error. Normalization shows that these four still have greater than typical relative s, but it is not all that much greater. It also shows that the deviation is stochastic in nature (not connected to coating thickness). It is worth noting that the calculated sectional s is in all cases within or very close to the accepted measurement error for the SFEG of 1%.

The density was calculated as per case 2 described earlier. The nominal density for 7YSZ is usually given as 6.025 gcm^{-3} (at 0 vol.% porosity) or 5.925 gcm^{-3} (overall average from multiple sources, see Appendix N: Material Data Tables). In all cases the calculated density is overestimated, exceeding even the maximum theoretical density of 7YSZ. It is likely that the oxidation of the Ni tube, particularly the inner – uncoated – surface during deposition adds sufficient mass to exaggerate the density. A powerful tool is available to help resolve the likely density of the coating and also estimate the amount of oxidation by mass that is occurring during deposition. This is as simple as plotting the mass gain post-deposition (m_{YSZ} in the tables) per unit surface area against coating thickness (see Figure 9-21. below).

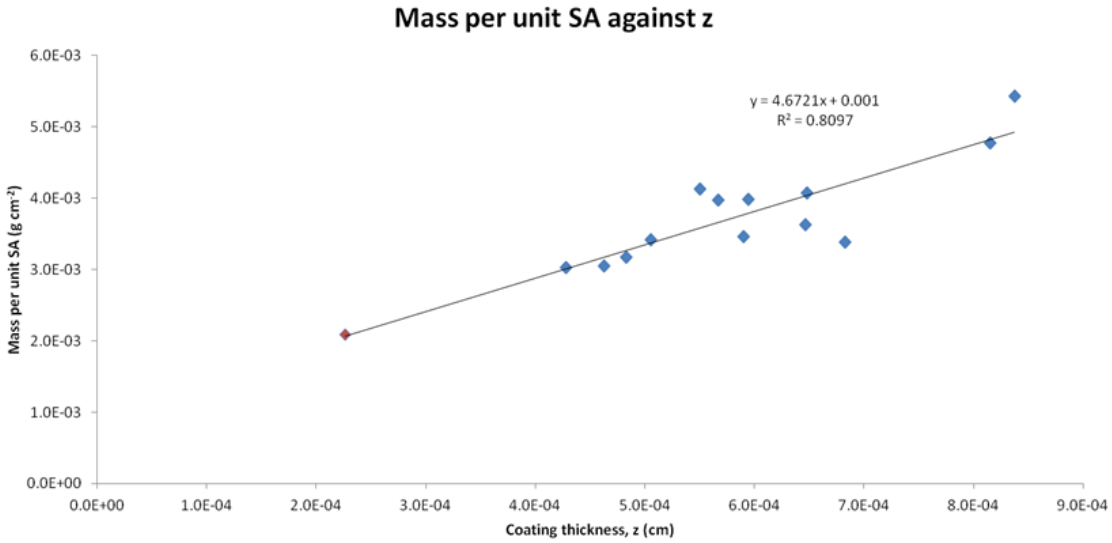

Figure 9-21. Mass gain (m_{YSZ} in tables) per unit surface area against coating thickness.

The gradient of the plot gives the density and the intercept the mass of oxygen added by oxidation per unit surface area. Extrapolating the fitted line to a coating thickness of 0 without forcing it to intercept the origin shows the actual electrolyte density was 4.67 gcm^{-3}; there was 1.0 mg cm^{-2} worth of oxidation occurring during deposition. The goodness of fit is certainly adequate for these estimates to be made, though they may not be entirely accurate. Although the data shows some scatter it is most likely, given the relatively small temperature range and narrow processing windows considered for chamber pressure and substrate rotation speed, that the source of the scatter is measurement error of the length the coating extends over and imperfect masking rather than any significant deviation in density of the deposited 7YSZ. This density matches the high density tier 1 structure so the objective of creating electrolyte in tier 2 at the maximum density achieved in tier 1 was fulfilled (though still somewhat lower than nominal values in the literature).

Sample B.05 had a very thin coating (marked in Table 9-8. as showing significant spalling of the coating) and is clearly not where it should be in terms of mass after deposition. A more correct mass would be 33 mg.

The deposition rate is a frequently referred to parameter that is mostly of use in comparing processes that are otherwise equivalent (for instance two different techniques that result in equivalent coatings). Two rates were calculated, shown in Table 9-10, the mass deposition rate and a deposition thickness rate using the surface area of each sample measured individually and compensating for the mass of oxidation.

Sample	**Deposition Rates**	
	By Mass (mg min^{-1})	**By z_{AVG} (µm min^{-1})**
DT-E.22/11/12-125;10.950-B.01	8.17	1.177
DT-E.27/11/12-125;10.950-B.02	12.57	1.579
DT-E.28/11/12-125;10.950-B.03	17.69	2.043
DT-E.04/12/12-125;10.1050-B.04	12.44	1.341
DT-E.06/12/12-125;10.950-B.05*	4.19	0.552
DT-E.17/01/13-125;10.1000-B.06	11.64	1.448
DT-E.21/01/13-125;10.1000-B.07	7.77	1.128
DT-E.22/01/13-125;10.1050-B.08	9.47	1.665
DT-E.23/01/13-125;10.1050-B.09	11.14	1.381
DT-E.24/01/13-125;10.1050-B.10	9.91	1.439
DT-E.04/03/13-125;10.850-B.11	10.48	1.576
DT-E.05/03/13-125;10.850-B.12	8.10	1.043
DT-E.06/03/13-125;10.850-B.13	15.29	1.988
DT-E.05/04/13-125;10.850-B.14	9.42	1.232

Table 9-10. EB-PVD 7YSZ deposition rates (compensating for oxidation).

A carbon coating was frequently required to enable the high resolution imaging of the non-conductive YSZ electrolyte (particularly necessary because the samples are mounted in a cold-cure resin, also highly insulating).

Before beginning the detailed discussion on the analysis of these experiments there is an important point to make on the choice of responses (the measured variables of the experiments). There are several possible orders of variables; first order (directly measured), second order (variables derived from first order values), and higher order (variables derived from lower-ordered derived variables). Usually first and second order are of interest. For these experiments m_{gain} and z are the primary measured variables. Coating density is the most important derived one. However, analysing all three is redundant since the derived variable is a function of the two measured ones. I have opted to focus my analysis on the coating thickness and density (analysing the mass deposited separately would be redundant). My choice is based on the utility and frequent reference in literature to these variables across the spectrum of coating technologies and applications.

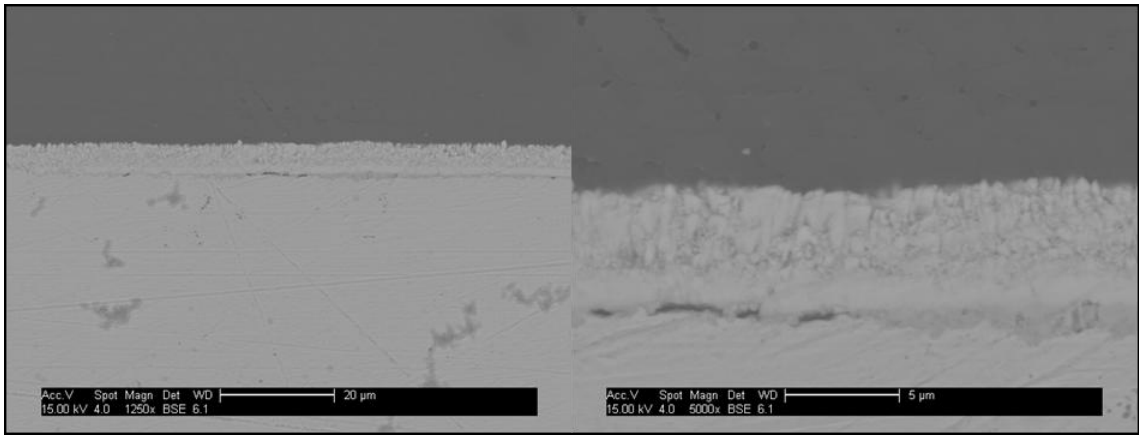

Figure 9-22. SEM micrographs showing columnar 7YSZ on Ni tube. Notice the remarkable strength despite subsurface pores most likely caused by oxidation of the Ni substrate (sample DT-E.22/11/12-125;10.950-B.01).

Sample B.01 exhibits mostly uniform columns with a considerable disordered portion visible in the first few microns. The micrograph shows a nucleation dominated deposition (many narrow columns as opposed to fewer wider ones), in line with the deposition conditions.

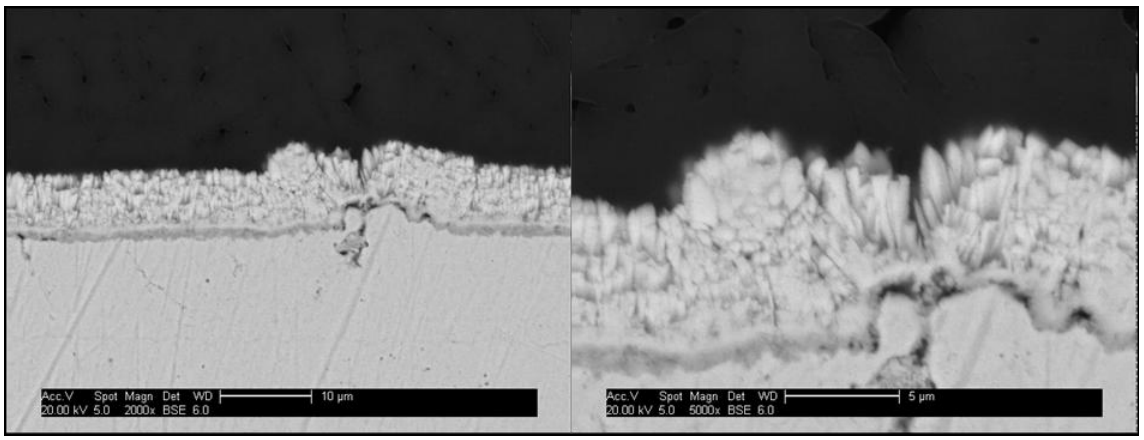

Figure 9-23. SEM micrographs showing columnar 7YSZ on Ni tube. The micrographs show the only visible damage in the coating as well as subsurface pores visible throughout likely due to some small amount of oxidation (sample DT-E.27/11/12-125;10.950-B.02).

The columns of sample B.02 are thicker than B.01. The only change in deposition parameters was a reduction in substrate rotation speed from 30 rpm to 10 rpm. This appears to have been sufficient to push the regime more towards a growth dominated one.

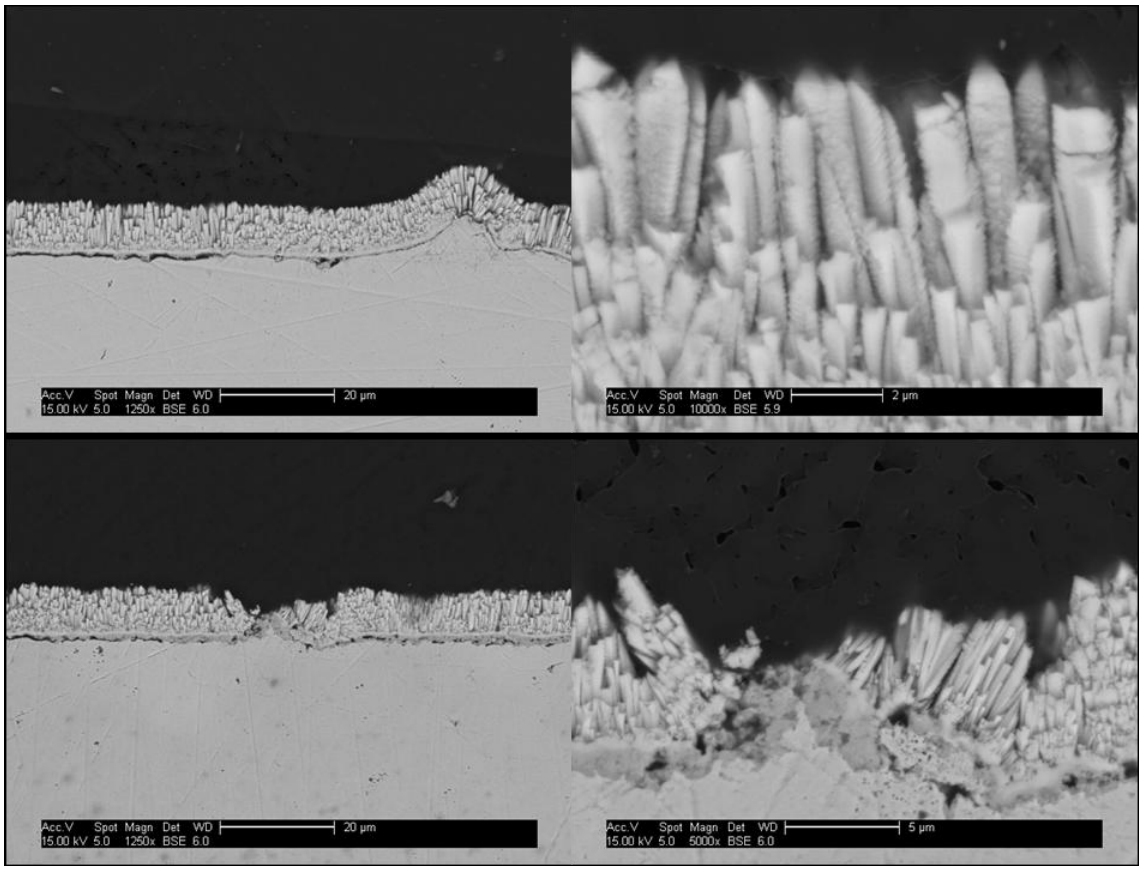

Figure 9-24. SEM micrographs showing columnar 7YSZ on Ni tube. The first pair of micrographs show subsurface damage and the high conformity of the coating as well as detailed column morphology at high magnification. The second pair show the worst damage visible on the sample (sample DT-E.28/11/12-125;10.950-B.03).

Compare the micrographs of B.03 above to those of B.02 (Figure 9-23.). The increase in chamber pressure, the only change in deposition conditions between these two samples, results in an increase in the appearance of new columns and corresponding reduction in column width.

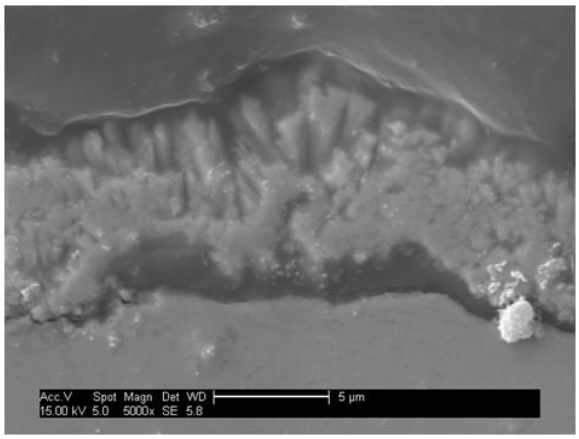

Figure 9-25. SEM micrograph showing columnar 7YSZ on Ni tube. This is typical appearance for this sample (sample DT-E.04/12/12-125;10.1050-B.04).

The higher temperature at which sample B.04 was deposited compared to B.03 results in an increased dominance of growth over nucleation as can be seen by the increase in column width and the tendency for columns to be wider near the surface.

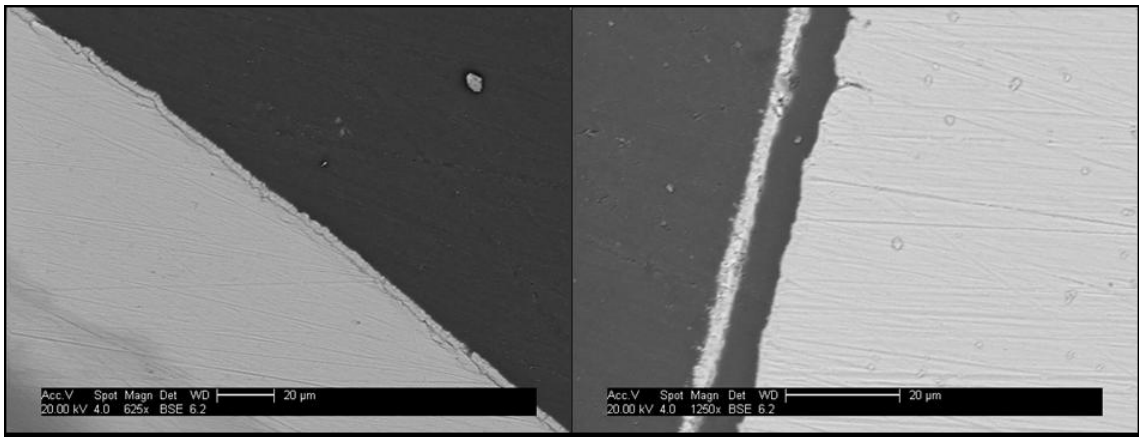

Figure 9-26. SEM micrographs showing columnar 7YSZ on Ni tube. This is typical appearance for this sample, with a handful of areas showing complete delamination, though this may have been caused by sample preparation (sample DT-E.06/12/12-125;10.950-B.05).

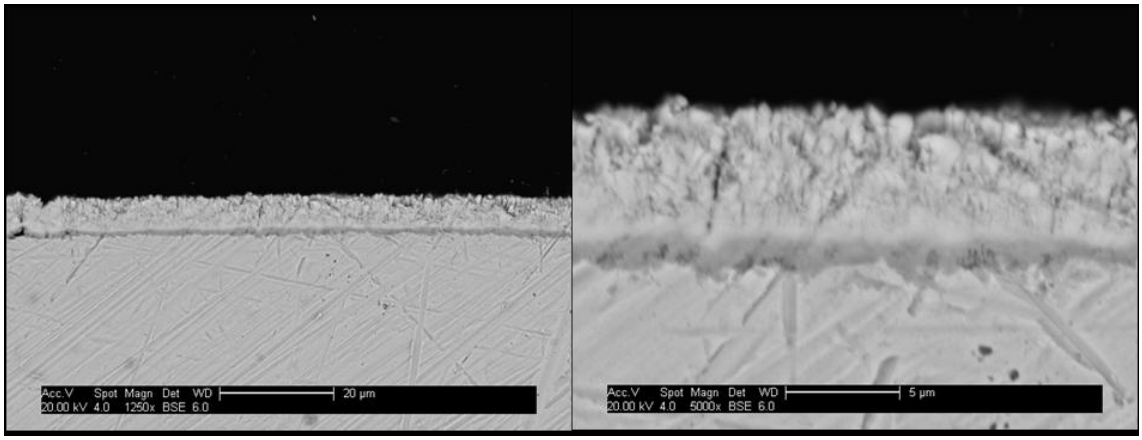

Figure 9-27. SEM micrographs showing columnar 7YSZ on Ni tube. This sample exhibits little damage and porosity (sample DT-E.17/01/13-125;10.1000-B.06).

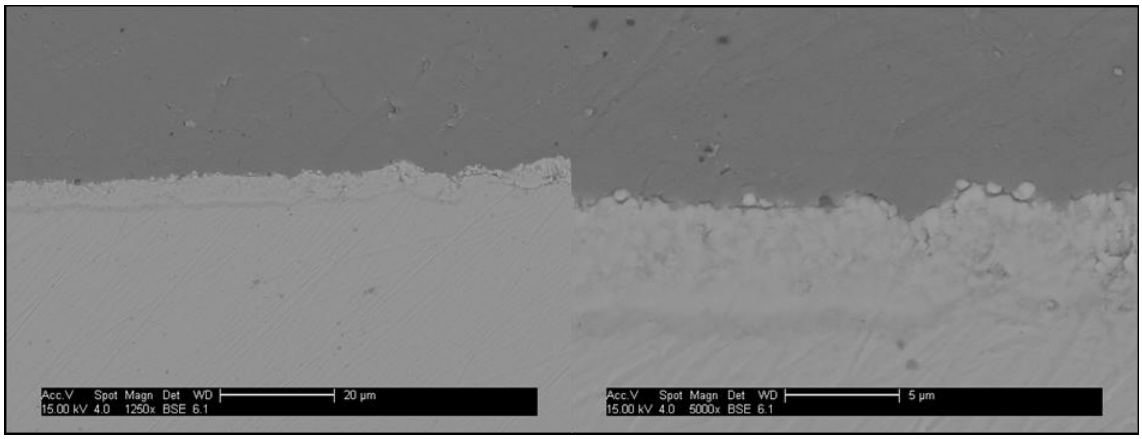

Figure 9-28. SEM micrographs showing columnar 7YSZ on Ni tube. Site is representative of whole sample (sample DT-E.21/01/13-125;10.1000-B.07).

B.06 and B.07 (Figure 9-27. and Figure 9-28. respectively) were deposited at the same conditions; the mid-way values for the 950 °C – 1,050 °C 'unit cell'. It comes as no surprise the microstructure is very similar.

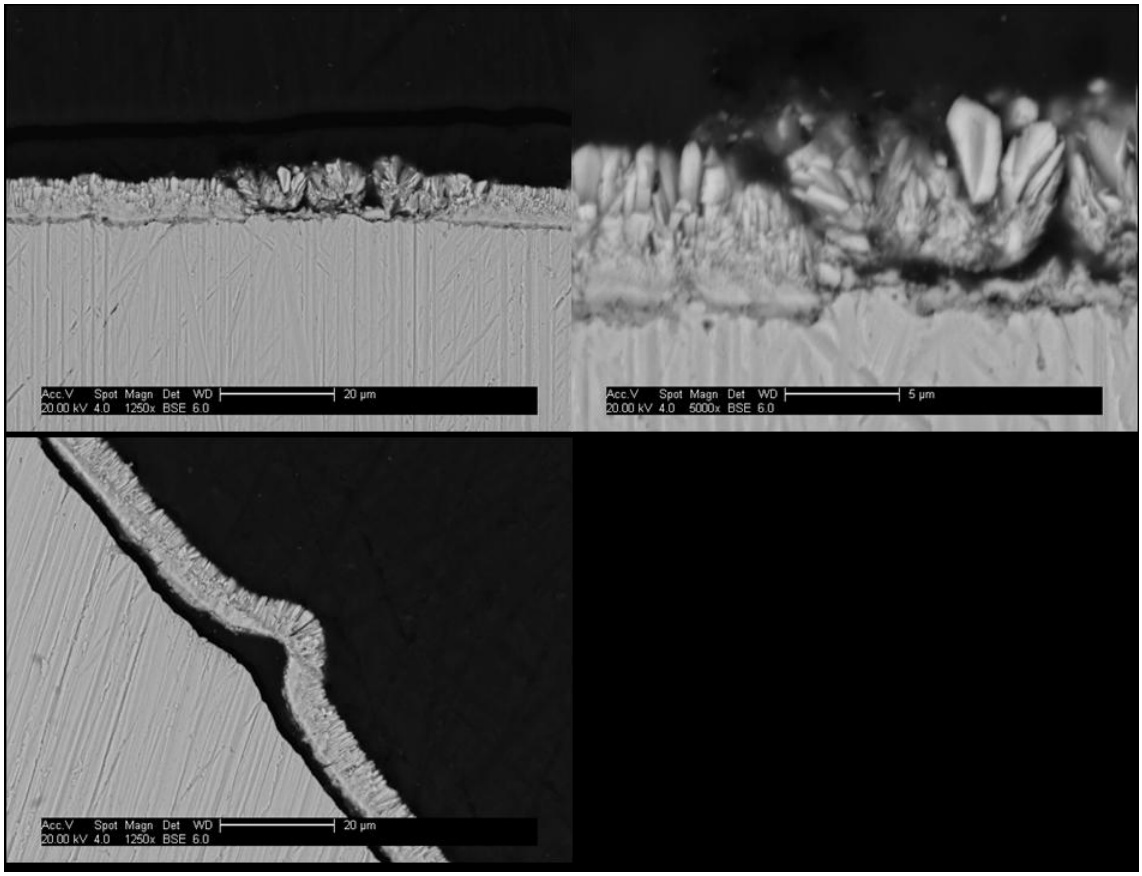

Figure 9-29. SEM micrographs showing columnar 7YSZ on Ni tube. Micrographs shown are representative of whole sample (sample DT-E.22/01/13-125;10.1050-B.08).

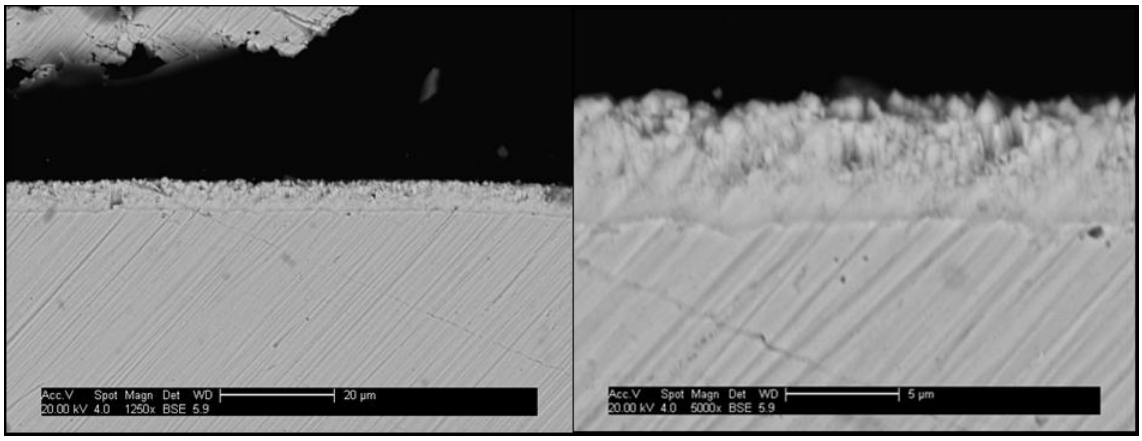

Figure 9-30. SEM micrographs showing columnar 7YSZ on Ni tube. Site is representative of whole sample (sample DT-E.23/01/13-125;10.1050-B.09).

Once more we see the same sort of microstructural changes from B.08 to B.09 (Figure 9-29. and Figure 9-30. respectively) as was seen previously in Figure 9-22. and Figure 9-23., their analogous pair deposited at 950 °C in place of 1,050 °C. Figure 9-29. elegantly demonstrates the types of thermal-strain-induced failures possible with the coating, with some interesting corollaries. Top left is an excellent example of wedge cracking (cracks at 45° angles to the free surface). This wedge cracking occurs in the YSZ rather than at the interface. This type of cohesive failure (that is within the ceramic as opposed to the far more common adhesive failure, that is, failure at the interface) shows areas of high stress and very strong adhesion to the substrate. The bottom image shows buckling failure of the coating. The compressive strain was such that after adhesive failure the coating compressed into a more pronounced spur than the initial one instigated by the surface morphology of the Ni substrate. Neither of these are relevant to the DoE discussion but are interesting enough to highlight.

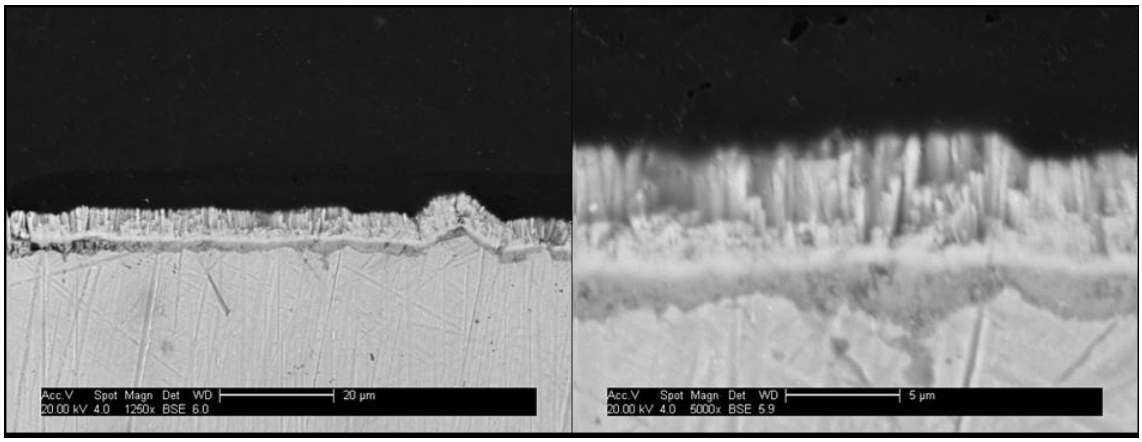

Figure 9-31. SEM micrographs showing columnar 7YSZ on Ni tube. Site shown is representative of whole sample (sample DT-E.24/01/13-125;10.1050-B.10). A detached portion of coating from a damaged area of the section was observed. No micrograph is included as the damage was attributed to sample preparation for microscopy.

The high rotation speed results in a nucleation dominated deposition regime, with the same resulting microstructure visible for sample B10 above as for others like B.01 and B.08.

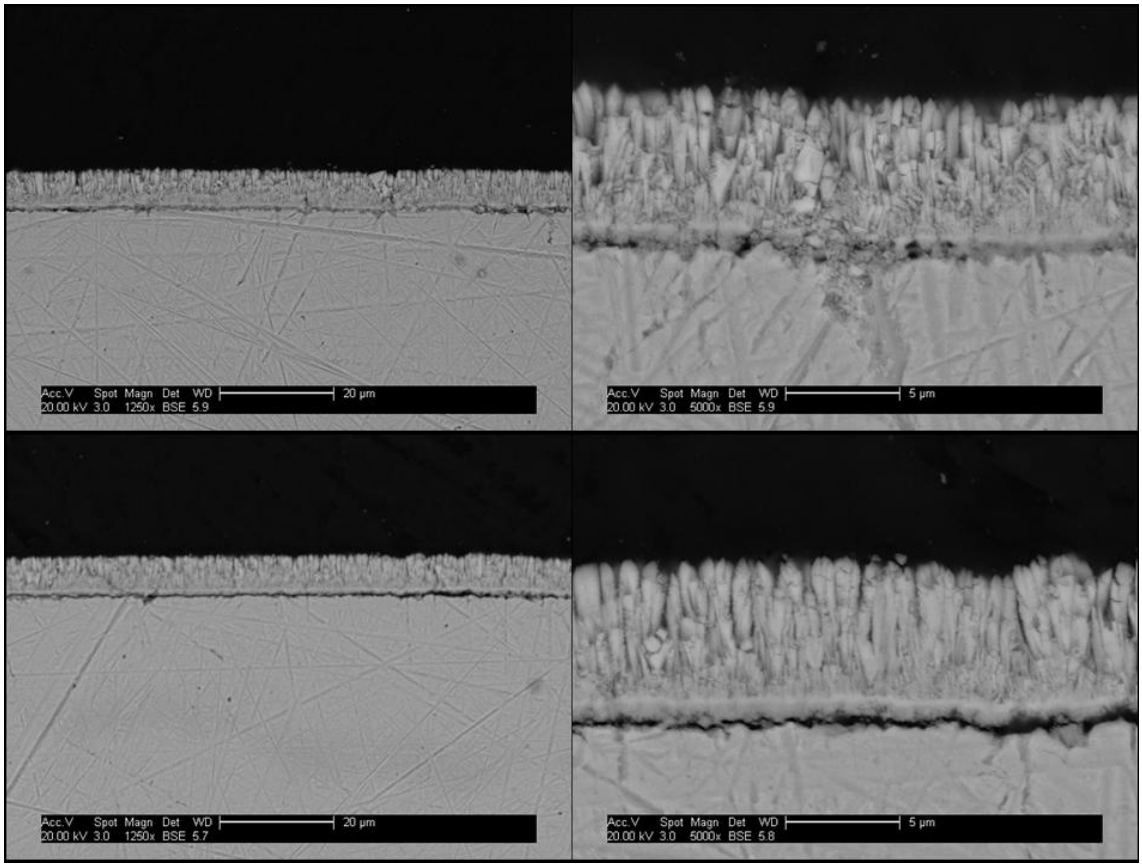

Figure 9-32. SEM micrographs showing columnar 7YSZ on Ni tube. The first pair of micrographs depict an area representative of most of the sample, while the second pair show the same substratum partial delamination under the NiO noted before (sample DT-E.04/03/13-125;10.850-B.11). This may have as much to do with pores due to thermal oxidation (see chapter 8) as with thermal stress.

Once more the effect of decreasing the deposition temperature in conjunction with a decrease in substrate rotation speed can be seen in comparing B.10 (Figure 9-31.) and B.11 above. Thicker columns that are wider at the surface can be attributed to these alterations in deposition parameters (favouring growth over nucleation).

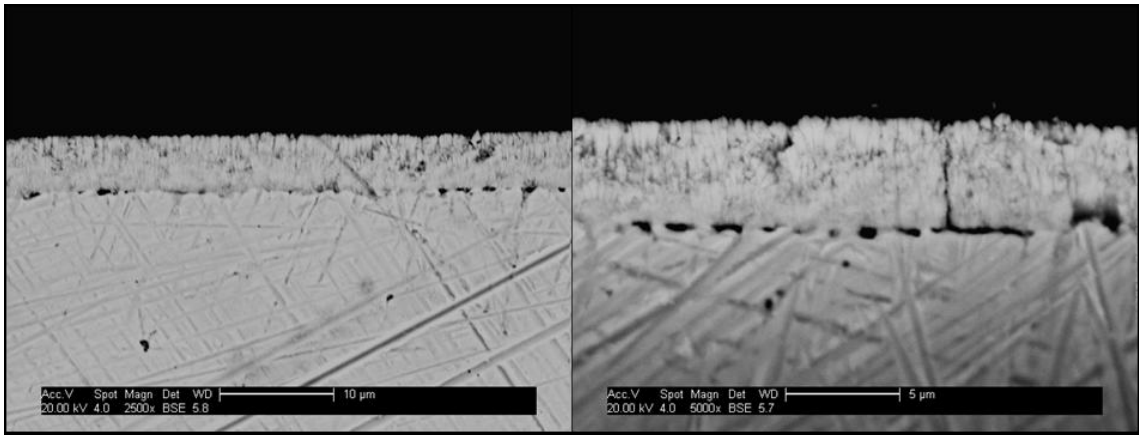

Figure 9-33. SEM micrographs showing columnar 7YSZ on Ni tube. This site is significant because it shows the only visible crack in the coating running perpendicular to the surface; the shape of the upper portion of the subsurface pore below it suggests it may have been caused by a very large pore YSZ nucleation could not span (sample DT-E.05/03/13-125;10.850-B.12) from pores forming at the Ni/ZrO_2 interface. Image shows development of through-thickness crack linked to pores in the Ni. In samples cooled from 1,050 °C we have seen this lead to adhesive failure.

Decreasing the chamber pressure to the low setting changes the microstructure from B.11 to B.12: presumably the reduction in scattering events contributes directly to an increase in uniformity of column dimensions. These conditions (850 °C and 10 rpm) result in an expected shift in position on the Thornton diagram to a coating type that is once more nucleation dominated compared to the growth dominated coatings seen at the low temperature.

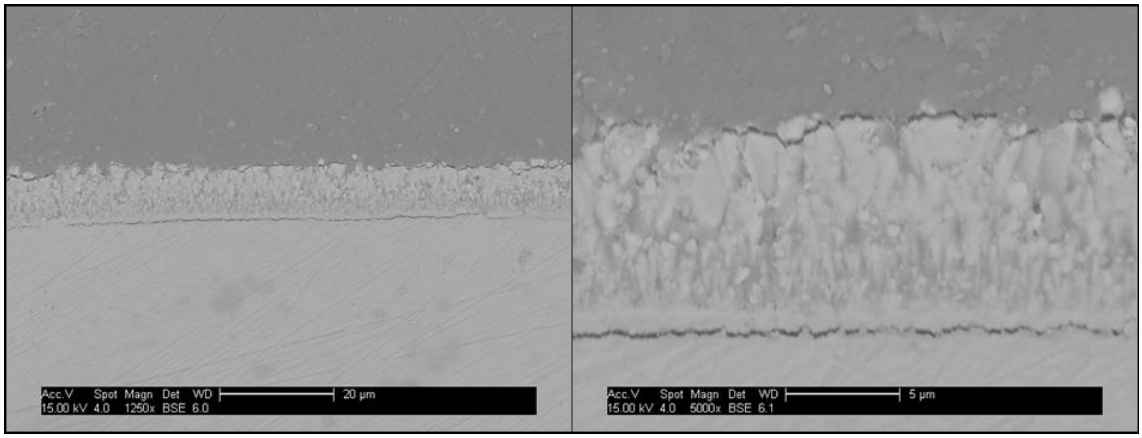

Figure 9-34. SEM micrographs showing columnar 7YSZ on Ni tube. The shown site is one of a small number of areas with long cracks parallel to the surface in the Ni substrate just below the Ni/YSZ interface (sample DT-E.06/03/13-125;10.850-B.13).

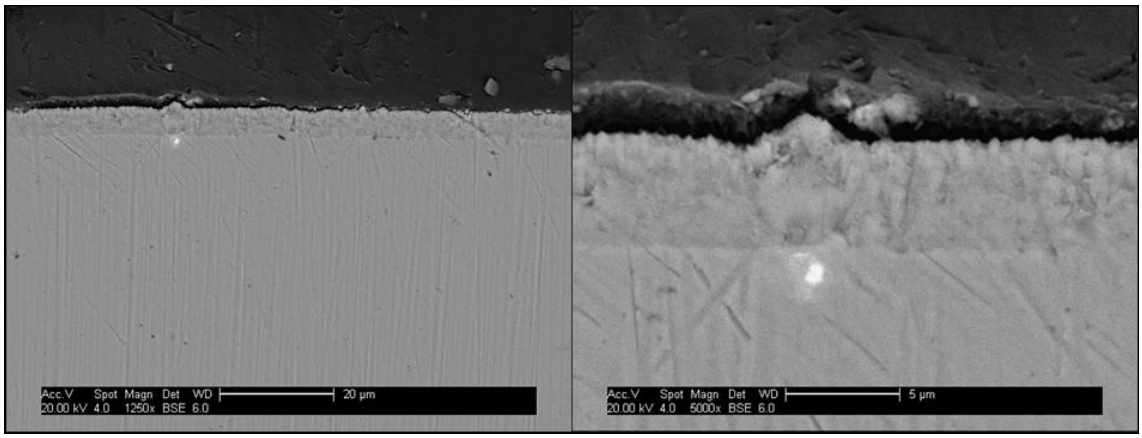

Figure 9-35. SEM micrographs showing columnar 7YSZ on Ni tube. The polishing proved sub-par and the resulting micrographs somewhat unclear, however, no significant damage was in view on this sample, nor were there subsurface cracks immediately below the interface parallel to the surface (sample DT-E.05/04/13-125;10.850-B.14).

The very different microstructure evident in Figure 9-34. and Figure 9-35. is attributable to the order-of-magnitude-change in chamber pressure between these two experiments. This has a considerable influence on the resulting coating microstructure at any deposition temperature and substrate rotation speed.

Below is tabulated the deposition zone for the electrolyte of each sample according to Thornton's model, factoring in the ratio of deposition temperature to melting point and chamber pressure. For 8YSZ the melting point, T_m, is 2,325 °C.

Sample	**T (°C)**	**T/T_m (°K)**	**P (mbar)**	**Structure**
DT-E.22/11/12-125;10.950-B.01	955	0.4727	0.00380	Zone T
DT-E.27/11/12-125;10.950-B.02	959	0.4742	0.00510	Zone T
DT-E.28/11/12-125;10.950-B.03	958	0.4738	0.01040	Zone T
DT-E.04/12/12-125;10.1050-B.04	1,057	0.5119	0.01010	Border of Zone T and Zone II
DT-E.06/12/12-125;10.950-B.05*	961	0.4750	0.01060	Zone T
DT-E.17/01/13-125;10.1000-B.06	1,022	0.4985	0.00294	Zone T
DT-E.21/01/13-125;10.1000-B.07	1,022	0.4985	0.00301	Zone T
DT-E.22/01/13-125;10.1050-B.08	1,059	0.5127	0.00138	Zone T
DT-E.23/01/13-125;10.1050-B.09	1,056	0.5115	0.00118	Zone T
DT-E.24/01/13-125;10.1050-B.10	1,057	0.5119	0.01060	Border of Zone T and Zone II
DT-E.04/03/13-125;10.850-B.11	873	0.4411	0.01030	Zone T
DT-E.05/03/13-125;10.850-B.12	880	0.4438	0.00156	Zone T
DT-E.06/03/13-125;10.850-B.13	887	0.4465	0.01040	Zone T
DT-E.05/04/13-125;10.850-B.14	875	0.4419	0.00104	Zone T

Table 9-11. Microstructure classification by Thornton's model for each sample. Zone T is the transition zone constituting a transition structure consisting of densely packed fibrous grains. Zone II consists of columnar grains.

Table 9-11. suggests it is optimal to deposit at or below 1,000 °C. As the deposition temperature approaches 1,050 °C more open Zone II structures may form that are less useful for creation of an electrolyte.

Probability plots (examples shown in Figure 9-36.) were created to test whether the 8 measurements taken from each sample were a random distribution or whether there is some biasing effect. A probability plot consists of plotting an outcome (thickness in this case) in ascending or descending order on the y axis against the exceedance probability. Exceedance probability (usual symbol for which is Z) is found by looking up probability values for the normal distribution for the probability of each measurement occurring. The probability of each measurement occurring is given by $^{1}/_{(n+1)}$, with a value of 0.11 for these experiments. This will almost certainly require some linear interpolation as it did for these DoE experiments. A straight line on the resulting plot signifies a random distribution of events. Therefore, they may be treated as statistically independent and as such may be utilised as repeat experiments for the purposes of statistical analysis.

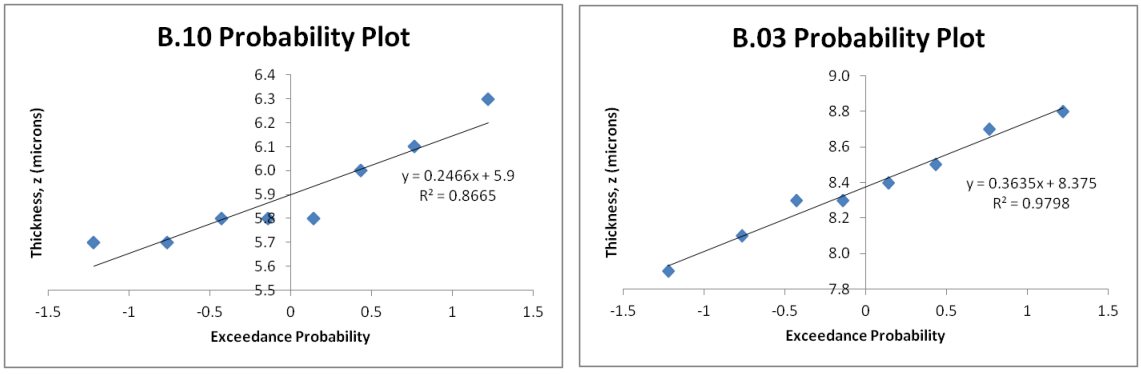

Figure 9-36. Exceedance probability plots of two exemplars showing the least and most linear samples (sample DT-E.24/01/13-125;10.1050-B.10 and sample DT-E.28/11/12-125;10.950-B.03). A total of fourteen similar plots were made and analysed, one for each sample.

The measurement error is only approximately 1%, and therefore error bars are too small to be clearly visible on these plots (making them visible would render the points themselves too small). The error is sufficiently small that there are no overlapping errors and the plotted linear fits can be taken as is. The average fit for all samples was R^2 = 0.9173, with minimum and maximums displayed in the above figure. Overall excellent linearity, *ergo*, the measurements taken on each sample may be considered independent experiments for the purposes of statistical analysis, and that the variation is normally distributed.

It is admissible to treat the section z measurements as separate responses because local conditions during deposition vary around the circumference of the sample. This means that measurements are effectively taken sufficiently far apart to be essentially independent samples with respect to the points at which z was measured. This is useful because it means the sectional average z ($\bar{z}$) can be treated as the average response of several independent measurements, ideal for classic DoE.

Factor Significance	Factors			Factor Interactions			
	T (°C) ±2 °C	**$P_{chamber}$ (mbar)** ±1x10^{-4} mbar	***f* (rpm)** ±1 rpm	**T.$P_{chamber}$**	**T.*f***	**$P_{chamber}$.*f***	**T. $P_{chamber}$.*f***
'Unit cell' 1 (950–1,050 °C)	+1.95	-1.75	-6.20	+0.30	+9.50	-5.30	+2.70
'Unit cell' 2 (850–950 °C)	-2.00	+7.86	-5.30	-4.80	-8.60	-5.40	-2.60

Table 9-12. Tier 2 DoE calculated factor significance based on thickness measurements, including factor interactions. Highlighted as follows according to my own judgement (and discussion with Professor John Nicholls): no highlight = modest effect, grey = negligible effect, yellow = strong effect.

A few important points regarding the calculation of factor significance must be made here. First, the average response was used (sectional average thickness, $\bar{z}$, in the previous tables). Second, experiments with factors set to the middle value were ignored in the calculation (e.g. B.06 and B.07 for T significance). Third, the results are divided into two rows: top row for the original 'unit cell', bottom for the additional one at lower temperature (850 °C – 950 °C). Finally note that in the tables (both as presented here and in the single table form original in Excel) the data is ordered by sample number for ease of referencing. As such identifying the '-' (low) and '+' (high) setting was entirely manual. With DoE one analyzes factors and their significance by simple calculations or plots. I elected to do both for internal verification and because each approach can reveal information the other does not. The factor significance plots are collated in Appendix J: DoE Factor Significance Plots.

Overall the most significant factor is the interaction of deposition temperature and rotation speed (T.*f*). It is the most significant factor for each 'unit cell' considered individually and also considering both at once.

It is worth re-emphasising that the nickel surfaces were not keyed (i.e. used in as delivered state) and that no bond coat or binding aids of any kind were used. This last fact alone makes the results remarkable since traditionally when depositing a yttria stabilised zirconia formulation onto a metallic or alloy part an oxide or oxide-forming bond coat is needed, confirming my earlier assertion on the oxygen-terminated nature of YSZ bonding to a Ni/NiO surface.

Performing EDX on the Ni-YSZ interface (Figure 9-37.), in this case of sample C.01, strongly makes the case that not only did it prove possible to deposit YSZ directly onto Ni without a bond coat but the interface is a blend of the two oxides both facilitating oxygen ion conduction and providing oxygen for the oxygen terminated bonding that joins ZrO_2 to Ni.

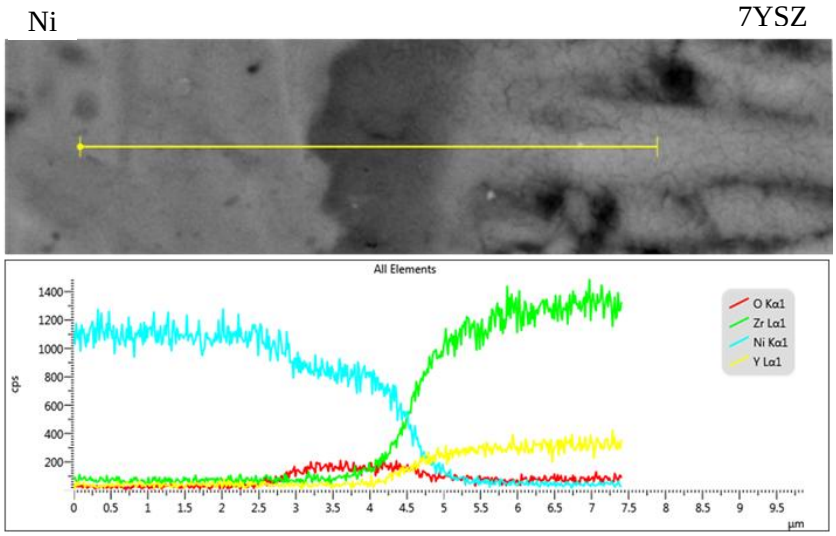

Figure 9-37. EDX of the nickel-YSZ interface (sample DT-E.28/04/14-125;10.1050-C.01). This sample does not appear in the rest of the analysis. It was a one-off to investigate an apparent inconsistency in coating thickness. This experiment helped ascertain the importance of a shutter.

What remains is to systematically select the deposition parameters for fuel cell fabrication.

For temperature the calculated factor significance is low, except in the interaction term with rotation speed. Plotting the significance of this factor for chamber pressure confirms this and also reveals that there is less scatter at the highest temperatures considered. Plotting the significance of temperature sorted for rotation speed shows the same results: temperature is not significant but higher temperatures have less scatter in the data. Referring to the calculated factor significances once more, one notes a weak interaction effect of deposition temperature and chamber pressure at the lower temperatures, decreasing dramatically at the high ones. The interaction of temperature and rotation speed is very strong; in fact the strongest effect of any factor in both temperature ranges as well as overall.

For chamber pressure the calculated factor significance indicates a strong effect at the lower temperatures weakening in the higher temperature range. As expected, the lower chamber pressures show considerably less scatter in the results than the mid and high settings when considering the plotted significance of the chamber pressure sorted for deposition temperature. It seems as though the scatter is worst at 950 °C, which may indicate that this is a transition temperature of sorts in the chamber pressure-deposition temperature interaction factor. Plotting the significance of chamber pressure sorted for rotation speed shows the same trend as before with higher chamber pressures exhibiting more scatter in both temperature regimes and at all rotation speeds but showing no obvious relationship in the results between temperature regimes, or chamber pressures

and no notable interaction effect with rotation speed. However, the calculated factor significances for chamber pressure show an interaction effect between chamber pressure and rotation speed in both temperature ranges.

Regarding rotation speed the calculated factor significance is negative and (probably) significant in both temperature ranges. Plotting the significance of this factor sorted for temperature indicates much the same, but displays notable scatter. Plotting the same but sorted for chamber pressure again shows a potentially significant negative relationship between rotation speed and chamber pressure for both temperature ranges. For both of these plots the higher temperature range displays somewhat lower scatter than the lower one.

The interaction term of temperature, chamber pressure and rotation speed is not significant and may represent random error. The main effect is likely through the interaction with temperature.

As noted elsewhere, all fall in the transition zone of the Thornton diagram. We are therefore able to optimise for maximum deposition rate within the processing window described by this DoE without fear of depositing an unsuitable microstructure. The higher temperature range is advantageous as in this range all results exhibited reduced scatter (or no change) when compared to the lower temperature range, the effect of chamber pressure is minimised (desirable since this is a difficult parameter to control with precision), the positive interaction term T.f is maximised and the negative interaction term $P_{chamber}.f$ is minimised (considering the rest to be not sufficiently significant relative to these). The only drawbacks are that the negative impact of rotation speed is larger at the higher temperatures than at the lower ones and that of course, this is a higher energy manufacturing route than at a lower deposition temperature.

A lower chamber pressure is preferable as it offers reduced scatter of the resulting coating thickness and minimises the negative effect on thickness of increasing chamber pressure. The author initially posited that the higher scatter (physical not statistical) of incoming material caused by a greater number of gas molecules, and therefore higher nucleation rate, would be advantageous in terms of microstructure, but from the micrographs one can see that this is not so. A higher deposition temperature (1,050 °C) gives somewhat lower statistical scatter and slightly thicker coatings (or more accurately the actual coating thickness is closer to the nominal for the deposition duration utilised). It also has the effect of producing the least statistical scatter in results whether considering deposition temperature or rotation speed while simultaneously giving rise to the thickest thermally grown oxide on the Ni.

A lower rotation speed results in a somewhat lessened effect of T.f (i.e. coating thickness may reduce), but also lowers the impact of $P_{chamber}.f$, itself reducing coating thickness. Perhaps because the chamber pressure is already low the $P_{chamber}.f$ interaction can be neglected? A higher rotation speed leads to maximised deposition rate, but increases the significance of $P_{chamber}.f$.

The final selection of deposition parameters is: 1,050 °C, 0.001 mbar and 30 rpm. This results in a 7 µm thick electrolyte (sample B.08 $\bar{z}$ 6.83 µm, sectional s 0.32, relative s 0.047). Notice, however, that there is a substantial range of deposition rates (recall all coating runs were carried out with the same deposition duration) as evidenced by the range of electrolyte thicknesses measured. *Ergo,* while the DoE optimised the deposition process for coating quality and thickness (really deposition rate) by itself it does not optimise for coating thickness reproducibility.

The T.f Interaction changes with temperature. The strong negative interaction in the lower temperature range indicates that many clumps are nucleating but there is no material arriving in the vicinity of, and being captured by, existing nuclei for growth (see sections 9.2.4, 9.2.6 and 9.2.8). It is almost entirely a nucleation process under these conditions. The vicinity is governed by the surface mobility of the arriving material, and the lower temperature range seems to offer insufficient energy to allow effective transport to nucleation sites for growth. At the higher temperatures considered and the same elevated rotation speed the effect is the opposite: a strong positive interaction. The high rotation speed ensures a steady stream of arriving material at fresh sites and the temperature allows for sufficient surface mobility for the nuclei to grow rapidly.

The results show poor reproducibility in terms of electrolyte thickness (as can be inferred from the middle setting and its repeat, B.06 & B.07). As discussed earlier, this means the journey is not quite finished – an optimal set of deposition parameters has been found but the deposition duration clearly has further room for improvement in order to reproducibly attain coatings of the desired thickness (initially 10 µm). At this point one would expect a further tier of experiments to optimise the reproducibility for 10 µm thick electrolytes and a further one exploring thinner still electrolytes. However, this coater lacked a shutter. The significance of this is discussed here.

PVD systems can be equipped with control systems that measure coating thickness *in situ*. These can be linked in a feedback loop to automated deposition rate control to achieve the desired thickness. Measurement is carried out either optically (for example via an infrared laser and detector that measures the change in reflected or absorbed frequencies) or via mass (a crystal oscillator's harmonic frequency changes as mass is deposited onto the substrate). Unfortunately, neither of these techniques is suitable for ceramic deposition because the temperatures required are simply too elevated (for

instance crystal oscillators – most commonly based on quartz – have a maximum operating temperature of 300 °C for high temperature variants).

Creating a suitable melt pool and the attendant vapour that deposits material onto the substrate is not instantaneous and requires considerable operator skill when automated controls are not viable. This leads to some uncontrolled and largely un-measureable amount of material deposited that varies with the time taken to stabilise the vaporization of the source material. Very effective control can be achieved using a shutter between the substrate and the source, even a manually operated one. Coater 1 once had such a system but it was removed many years ago. Other work on the coater obviated the possibility of installing a new system. Therefore, it did not prove feasible to fully assess the reproducibility nor to attempt thinner coatings. It is testament to Mr. Tony Gray's skill that the results are as consistent as they are.

In terms of creating electrolytes for this project the significance is twofold: first, coatings were 6.8 ± 0.32 µm thick (based on B.08) rather than the nominal 10 µm (of course the lack of a shutter meant a reproducibility study to refine this and the disposition rate further would be less than reliable); second, although it was deemed unwise given the relatively poor reproducibility to attempt thinner coatings and assess their impact on performance some of the coatings measured under 5 µm thick demonstrating that the process is certainly capable of achieving this. Both experimental areas could be tackled with the re-introduction of a shutter.

9.7 Electrolyte Fabrication Conclusions

A 65–75% dense film would be typical [Zhao *et al.* 2006 and discussion with Professor John Nicholls]. The tier 1 production scheme results in greater density films than is typical by EB-PVD (mean density 87.91 ± 9.93 %). The samples could be handled without concern and, with the exception of a handful of areas, the first and third batches show no delamination (A.01, A.02, A.05 and A0.6). The second shows considerable delamination (A.03 and A.04), although most of the coating is intact and strongly adhering.

Quantifying the reproducibility of the coatings by thickness yields a global average thickness of 10.05 ± 1.16 µm. This is excellent conforming near perfectly to the nominal value chosen for the tier 1 experiments focused on establishing base parameters and assessing reproducibility. The variation in coating thickness from the ends to the middle of each sample is linear, independent of paddle or detailed considerations of thickness or quality.

It is worth emphasising that the nickel surfaces were not keyed (i.e. used in as delivered state) and that no bond coat or binding aids of any kind were used. This last fact alone makes the results remarkable. Performing EDX on the Ni-YSZ interface (Figure 9-37.) strongly makes the case that not only did it prove possible to deposit YSZ directly onto Ni without a bond coat but the interface is a blend of the two oxides both facilitating oxygen ion conduction and providing oxygen for the oxygen terminated bonding that joins ZrO_2 to Ni.

A systematic approach is necessary to fully understand the relationship between deposition parameters and electrolyte quality – necessary even with the small alterations to the basic parameters from literature and past experience being considered for optimization. It is believed that the exact combination of parameters yielding high quality 7YSZ electrolytes is rather stringent, and stochastic variation from batch to batch resulting in batches, or parts of batches, not quite at the nominal conditions.

For tier 2 the relative coating density was 77–78%. This density matches the high density tier 1 structure so the objective of creating electrolyte in tier 2 at the maximum density achieved in tier 1 was fulfilled. The microstructure is in all but two cases firmly Zone T, with reference to Thornton's model. These two cases are on the border between Zone T and Zone II. Zone II structures may form at temperatures in excess of 1,000 °C that are less useful for creation of an electrolyte.

The most significant factor is the interaction of deposition temperature and rotation speed ($T.f$). For temperature alone the calculated factor significance is low. Regarding rotation speed the calculated factor significance is negative and (probably) significant in both temperature ranges. The interaction term of temperature, chamber pressure and rotation speed is not significant and may represent random error. The main effect is likely through the interaction with temperature. The $T.f$ Interaction changes with temperature. The strong negative interaction in the lower temperature range indicates that many clumps are nucleating but there is no material arriving in the vicinity of existing nuclei for growth. It is almost entirely a nucleation process under these conditions.

The higher temperature range is advantageous as in this range all results exhibited reduced scatter (or no change) when compared to the lower temperature range, the effect of chamber pressure is minimised (desirable since this is a difficult parameter to control with precision), the positive interaction term $T.f$ is maximised and the negative interaction term $P_{chamber}.f$ is minimised (considering the rest to be not sufficiently significant relative to these). The only drawbacks are that the negative impact of rotation speed is larger at the higher temperatures than at the lower ones and that of course, this is a higher energy manufacturing route than at a lower deposition temperature. A lower chamber pressure is preferable as it offers reduced scatter of the

resulting coating thickness and minimises the negative effect on thickness of increasing chamber pressure.

The final selection of deposition parameters is: 1,050 °C, 0.001 mbar and 30 rpm. This results in a 7 µm thick electrolyte (sample B.08 $\bar{z}$ 6.83 µm, sectional s 0.32, relative s 0.047). An optimal set of deposition parameters was identified but there is clearly room for improvement in reproducibly in order to attain coatings of the desired thickness (initially 10 µm). This requires a shutter between the substrate and the source, even a manually operated one. The large variation in coating thickness and quality from relatively small variations in processing parameters supports my earlier hypothesis of a stringent processing window.

Though by accident rather than design the electrolytes resulting from this step will surpass my initial goal of matching that state of the art (10 µm) being 6.8 ± 0.32 µm thick, though for the reasons discussed it proved unfeasible to push this any further.

For comparison consider a state-of-the-art planar solid oxide fuel cell with proven capability and 40,000 h operation: The paper by Menzler *et al.* (2013) is based on the work at Forschungszentrum Jülich GmbH (Germany) on planar cells consisting of a Ni-YSZ support over 130 µm thick, 7 µm Ni-YSZ anode, 10 µm YSZ electrolyte, GDC (gadolinea doped ceria) diffusion barrier (to prevent Co degrading the electrolyte) and 50 µm LSCF cathode [Menzler *et al.* 2013]. The support was tape cast the rest screen printed, and sintered in three steps taking over 8 h in all, at temperatures from 1,080 °C to 1,400 °C [Menzler *et al.* 2013]. The miniaturization efforts at Jülich focused on reducing the electrolyte thickness by using PVD (evaporation and sputtering) and sol-gel techniques, achieving electrolytes over 6 µm and approximately 1 µm thick, respectively [Menzler *et al.* 2013]. In the former case considerable porosity was present. Though closed (no effect on gas tightness) this would have had a negative impact on electrolyte polarization. Of particular interest is their observation that "If [...] the electrolyte is applied as a very thin film (<2 µm), the current density of single cells increases markedly, but in stack testing, the difference is negligible." [Menzler *et al.* 2013] The resulting microstructure of the work by Menzler *et al.* (2013) is very different to the microstructure shown here. Gas tightness appears excellent (it was not measured in the cited work), certainly superior to those created at this stage of development of the design presented in this thesis. However, their manufacture is far more involved and takes much longer also – both important factors to the successful commercialization of SOFCs.

10 Cathode Fabrication and Characterization

Little needs to be done regarding the cathode to fulfil this project's aims, as discussed earlier (in particular the reader is referred to sections 1.2, 3.5, 3.6 and 5.3). A technique to create a porous Pt cathode on top of the 7YSZ electrolyte was developed as part of my MSc project [Camilleri 2009]. In summary this process consists of sputtering 300 nm of Pt with a high chamber pressure (100 mTorr in this case) in an argon atmosphere. The high pressure leads to a great number of scattering events preventing the formation of a dense coating. This creates the porosity necessitated by fuel cell cathodes. Camilleri (2009) estimates the porosity at or near 50%.

As anything relating to the cathode under this project is required only to test the electrical and electrochemical performance of fabricated cells, the only areas of interest are the cathode's electrical resistivity and its reproducibility. The former is the subject of this chapter while the latter (given the nature of sputtered coatings) is not practical to explore.

10.1 Cathode Fabrication Objectives and Background

This is one of a number of relatively minor experimental areas. It is worth showing to continue building a cogent picture of the author's fuel cell design. As discussed elsewhere (sections 3.5 and 3.6) Pt was selected for the cathode material. The concentration and activation polarizations of the cathode are the smallest contributions to the overall polarization losses in the specific case of anode supported SOFCs (refer to section 4.3 and beyond). Measuring the resistance of porous Pt is of inherent scientific interest and also is an important parameter for fuel cell analytical modelling. Resistance further serves as a quantified performance measure of the cathode to compare Pt to other cathode materials that have been and continue to be developed for SOFCs. In practice one is unlikely to opt for platinum commercially as discussed previously; primarily because of cost concerns even if mitigated by thin film technology.

Resistivity is given by:

$$\rho = R\frac{A}{l} \qquad (10.1)$$

Where:

ρ is the resistivity [Ω.m]
R is the electrical resistance [Ω]
A is the sample cross sectional area perpendicular to the flow of current [m^2]
l is the sample length, parallel to the flow of current [m]

Sheet resistance (i.e. taking the assumption that the majority of current flows along the film rather than through it) is given by the equation:

$$R_s = R\frac{l}{w} = \frac{\rho}{t}\frac{l}{w} \qquad (10.2)$$

Where:

R_s is the sheet resistance [Ω/□]
R is the electrical resistance [Ω]
l is the sample length, parallel to the flow of current [m]
w is the sample width, perpendicular to the flow of current [m]
ρ is the resistivity [Ωm]
t is the sample (film) thickness, perpendicular to the flow of current [m]

10.2 Resistance Measurements

Three glass slides were prepared with a porous Pt film 300 nm thick in a rectangle, nominally 60 mm by 25 mm. Pt was sputtered at 0.1 mbar for 15 minutes at 393 V with a current of 0.7 A. The coater was a Cranfield-modified Electrotech type 840 (840 cm cube magnetrons manufactured by Teer Coatings, and are of the internal type where the entire magnetron is contained within the vacuum chamber rather than attached to the side). The coater was served by a high-vacuum pump manufactured by Leybold (model 1100 cryo pump). The system was controlled by a bespoke computer system designed by Cametrics. Substrates can be rotated individually or as a whole carousel, and also indexed from magnetron to magnetron (coater has a total of three) manufactured by Teer Coatings to Cranfield specifications. Five repetitions were made of the resistance measurement on each slide, all carried out at room temperature (20 ±1 °C at the time). In order to make robust contacts with the minimum contact resistance silver dag (Agar Electrodag 1415) was used, painted onto opposite ends of the slide three layers thick. A separate glass slide had the Ag dag only in order to measure its own resistivity. Ten resistance measurements were taken in two sets measured at perpendicular axes on the blob of Ag dag. The average resistance for the silver dag was found to be 0.21 ± 0.15 Ω.

10.3 Results & Discussion

Table 10-1. (below) shows the results of the measurements described above for each slide (25 mm wide), including mean resistance, standard deviation (s rather than σ due to small number of measurements), area of Pt (assumed uniformly 300 nm thick), average length of sputtered conductor and cross sectional area of film (CSA).

Slide	R (Ω)							L (cm)	A (cm^2)	CSA (m^2)
	1	2	3	4	5	Mean	s	±0.05	±0.005	±1.25×10-^{10}
Slide 1	82.9	82.9	82.9	82.9	82.9	82.9	0.000	6.18	15.44	7.5×10^{-9}
Slide 2	216.5	216.5	216.5	216.5	216.6	216.5	0.045	6.10	15.25	7.5×10^{-9}
Slide 3	590	590	591	591	591	590.6	0.548	6.03	15.06	7.5×10^{-9}

Table 10-1. Porous Pt resistance by slide (25 mm wide).

In order to measure the resistance of thin films four point probe measurements are normally taken to eliminate the contact resistance as this can be of the same magnitude as the sheet resistance of the film. However, in this case the combination of Ag dag and contact resistance is negligible so both the 'bulk' resistivity and sheet resistance are valid without needing to use 4 probe measurements. The average resistance for the porous Pt was found to be 296.67 ± 213.87 Ω.

Slide	ρ (Ωm)	R_s (Ω)
Slide 1	1.006×10^{-5}	204.929
Slide 2	2.662×10^{-5}	528.260
Slide 3	7.346×10^{-5}	1,424.527
Mean	3.671×10^{-5}	719.239
s	3.288×10^{-5}	631.830

Table 10-2. Calculated resistivity (ρ) and sheet resistance (R_s) including mean values and standard deviations (s rather than σ due to small number of measurements).

The average 'bulk' resistivity of porous Pt is $3.65\times10^{-5} \pm 2.63\times10^{-5}$ Ωm.
The sheet resistance of porous Pt is 724.27 ± 522.13 Ω.

Compare the above results with the bulk resistivity of dense (i.e. non-porous) Pt: 1.06×10^{-7} Ωm.

The very high standard deviation is indicative of thickness variation between the three slides, violating the assumption of uniform thickness (the same is likely for the silver dag resistance). An unsurprising situation as sputtered samples may exhibit relatively large (30–40%) variations in thickness across the same sample or multiple smaller samples with a common target as was the case here [private communication with Dr. Jeff Rao and Miroslav Kula].

The highly conformal nature of sputtered coatings strongly suggests there will be no effects of introducing curvature (i.e. moving from glass slides to the fuel cells).

10.4 Cathode Fabrication Conclusions

At this stage the important outcomes are that while the resistance measurement error and/or the film thickness exhibit large standard deviation the sputtered Pt forms an adequate cathode. Determining correct cathode thickness is best left to cross-sectional

analysis of complete cells. Outside of modeling it makes little difference for this project what the exact cathode thickness and porosity achieved by this process are as long as they prove adequate for operation. The author believes that with such a thin coating and elevated operating temperatures the porosity is liable to be in constant flux: sintering will tend to close pores, while the combination of defects and diffusion gradient injects oxygen through the cathode which will tend to coalesce into pores as well as rapid grain boundary diffusion in conjunction with the opening of triple points creating new pores (see chapter 8 for more detailed discussion on these mechanisms and phenomena).

11 Complete Cell Fabrication and Characterization

The preceding fabrication chapters delved in detail into each of the three components of a single fuel cell (stacks require a fourth component – the interconnect – tying cells together). This chapter serves to both verify the additive manufacture of complete cells as well as prepare cells for performance testing (see sections 13.2 and 14.2). Regarding electrochemical and electrical performance testing: a full week is required per sample including loading and unloading (each a task requiring several hours) *ergo* it is vital to maximise both the utilization of each tested cell as well as ensure they are as representative as possible. To achieve the latter a relatively large, statistically sensible quantity was manufactured. From this sample individual cells for performance testing were selected at random to ensure no bias.

11.1 Complete Cell Fabrication Objectives and Background

Camilleri (2009) demonstrated that this suite of techniques exhibits no underlying incompatibilities that would result in failure to create complete cells and successfully fabricated a small number of demonstrators. This chapter assumed the same lack of incompatibilities and instead dealt with manufacture reproducibility. A statistically sound number of cells was fabricated for the reasons introduced in the preceding section (24 in all). This chapter also serves to link the techniques developed and/or optimised into a manufacture 'recipe' that could also see use as the starting point for further optimization prior to development into mass manufacture.

11.2 Synthesis of Fabrication Techniques

Each sample was a 100 mm long 99.5% pure nickel tube (Ni200 from Goodfellow Ltd.) 5.9 mm OD, 125 µm wall thickness, in as-delivered condition. Samples were prepared immediately prior to processing by cleaning in an ultrasonic bath in acetone for 5 minutes. Jigging components that were in direct contact with samples (and where possible those one step removed also) were treated in the same manner immediately prior to the respective step; immediately preceding oxidation for the oxidation jigging, immediately prior to reduction for the reduction rigging, and so on. Samples were oxidised as described earlier, in section 8.2, at 1,100 °C for 42 h. Subsequently samples were subjected to a reduction treatment as described in section 8.10 in a 100% H_2 atmosphere at atmospheric pressure in two separate schemes, each considered equally capable of producing an excellent anode as the reader may recall from that chapter (in effect the two reduction schemes may represent the limiting conditions of a possible spectrum of suitable reducing conditions): 1,000 °C with no dwell or 400 °C with a 15 h dwell. Both were promising for anode fabrication but with no clearly superior version

(based on microstructure) to continue with it was decided to carry both forward as the different microstructures may have specific benefits on performance, explored in chapter 1. In both cases the gas flow was 0.8 litres per minute. An equal number of samples (twelve) were subjected to the two different reduction treatments. The electrolyte was deposited as explained in section 9.4; this was performed at nominally 1,050 °C, 1×10^{-3} mbar and 30 rpm (see also section 9.7), in the same pairs as reduction, keeping careful record of which paddle the sample was loaded onto. The cathode was prepared as described in chapter 10 at 0.1 mbar and 6 rpm substrate rotation for 15 minutes, determined by a prior rate run, sputtering at 393 V and 0.7 A. Prior work was on glass slides and therefore no rotation was necessary. For the fuel cells, substrates (anode-electrolyte tubes), were rotated via the coater's planetary gear system. Both the turntable and sample holders rotate synchronously at the rate given.

Comparison with previous results, each treating one of the three components, can be conveniently carried out via monitoring sample mass changes. As such, samples were weighed prior to and after oxidation, after reduction, after EB-PVD and after sputtering. Characterization was also by visual inspection.

Oxidation was carried out on 4 samples simultaneously, grouped accordingly in the anode table below (Table 11-1.). Four was found to be the maximum practical as any more in the oxidation furnace would mean some are outside the most uniform part of the hot zone and also more than four become unwieldy to load or unload rapidly – recall that samples are loaded at temperature and therefore it is important to do so as swiftly as possible because of the attendant temperature drop (samples would begin oxidising at a lower temperature than desired) and because the process is parabolic, and initially very rapid, it will result in uneven mass fractions oxidised. While a longer dwell corrects this (after all, a sample cannot be more oxidised than completely oxidised) it will mean some samples may have slightly different microsturctures if they reach MFO = 1 earlier than others. As it is unknown what effect this has on the reduction step or more generally on the creation of anodes, it was deemed best avoided by ensuring the most rapid loading possible.

Next, samples were processed together for the reduction and EB-PVD steps. Reduction and EB-PVD coating of 7YSZ in sequence on each of the pairs combined into a batch (again shown in the respective table, Table 11-2.). Finally sputtering was done on just four samples for reasons explained below. Up to four can be conveniently loaded into the coater simultaneously. Also, for the two steps carried out in batches of 2 (reduction and PVD) sample 01 was on the left hand side and 02 on the right within the respective furnaces.

These samples were intended to be the only complete cells made for this project. However, unforeseeable and costly difficulties arose in bonding these to the stainless

steel adapters necessary to connect the cells into the FC test rig (see 13.2.5). These difficulties effectively consumed the most viable manufactured cells, others had become out of true during processing (generally the ends were out of round, tending to form a rounded triangular cross-section, and occasionally the entire sample bowed). Such deformations had not been observed previously. EB-PVD or reduction are the most likely culprits. From early results it appeared to be a random occurrence. A trend was soon noted, however. The worst always occurred after the reduction step (no deformation at all was observed after oxidation). As a result additional complete cells were required. The second set of samples does not constitute a new experimental tier because it was not a new experiment, rather a repeat separated chronologically by 6 months.

In direct consequence of these factors the author re-assessed the existing jigging utilised for each step and additional complete cells were fabricated. A small modification to the order of processing steps was made also. Previous to this point, the cells were complete before being bonded to the adapters. In order to ensure minimal cathode degradation prior to performance testing the sputtering was subsequently carried out after bonding to the adapters. The reduction jigs were replaced with a single more substantial one offering greater support along the entire length of the tubes eliminating the appearance of bowed samples and greatly reducing both the number of samples that were out of round as well as the degree to which they were such. This was further refined later on with the addition of alumina tubes 5 mm OD, 3 mm ID of 99.7% purity from Multi-Lab (Figure 11-1. (a)). No further samples were out of round after reduction from the introduction of this change. The EB-PVD jigs were similarly modified with the addition of the same type of alumina tubes eliminating the slight out of roundness that occurred with some samples (Figure 11-1. (b)). Note the thin rods of the deposition jigs were replaced with thinner 2 mm diameter ones to fit inside the alumina tubes. These were prevented from slipping off the jigs with beads of weld at the top.

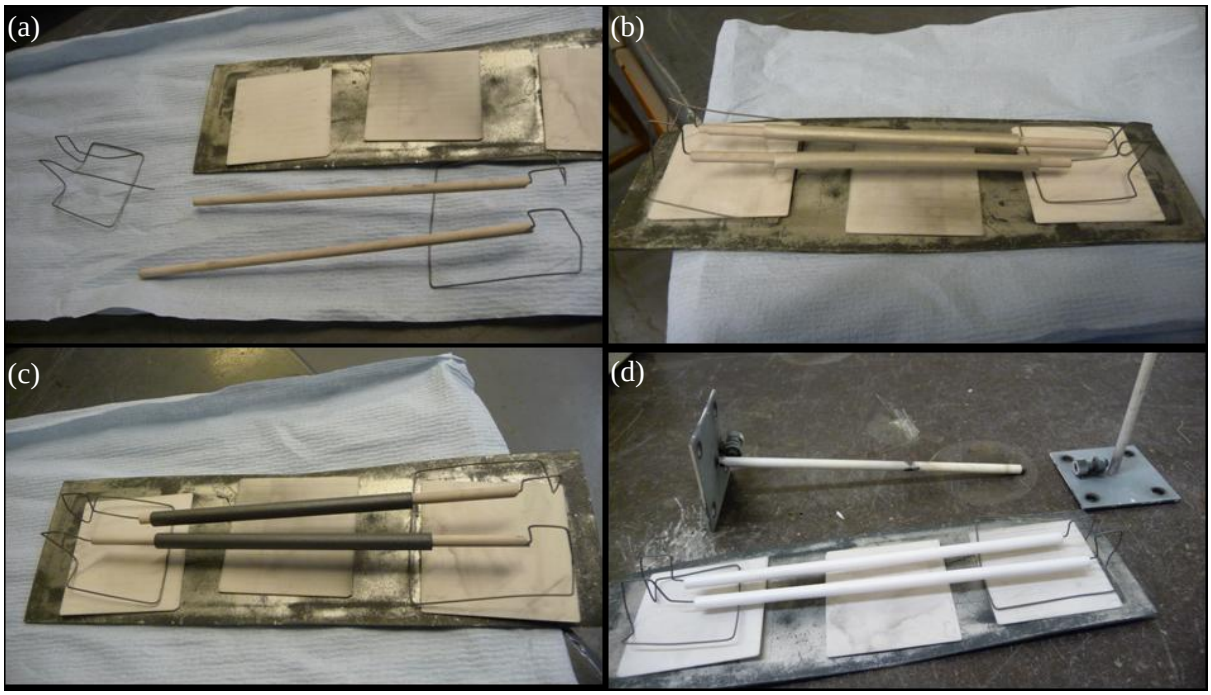

Figure 11-1. Final improvements to reduction and EB=PVD jigging (figures (a) through (c) and (d), respectively). In the latter both jigs are shown for scale.

11.3 Fabrication Reproducibility

While the purpose of this step was principally to create sufficient samples for representative electrical and electrochemical performance testing it proved to be a convenient juncture to also assess reproducibility of the fabrication process as a whole.

11.3.1 Results & Discussion

The results of the fabrication runs are summarised in the tables hereunder (Table 11-1., Table 11-2. and Table 11-3.), having the same format as those tables summarising the results of chapters 8, 9 and 10, respectively. Errors estimated using linear approximation by partial differentiation [Error Propagation article accessed 2013] where an equation was used or based purely on measurement equipment error otherwise.

Anode							
Sample	**m_{Ni} (mg)** ±1 mg	**m_{gain} (mg)** ±2 mg	**Mass fraction oxidized** ±0.0001	**$T_{reduced}$ (°C)** ± neg.	**$t_{reduced}$ (h)** ±1 s	**m_{loss} (mg)** ±2 mg	**Mass fraction reduced** ±0.0001
PT-AEC.12/09/14-125;10;0.3.1100(400)[1000]-A.01	1,978.3	538.3	1.000	400	15	521.0	0.968
PT-AEC.12/09/14-125;10;0.3.1100(400)[1000]-A.02	1,970.5	536.4	1.000	400	15	517.9	0.966
PT-AEC.12/09/14-125;10;0.3.1100(400)[1000]-B.01	1,989.9	542.4	1.000	400	15	523.8	0.966
PT-AEC.12/09/14-125;10;0.3.1100(400)[1000]-B.02	1,953.7	532.0	1.000	400	15	512.9	0.964
PT-AEC.16/09/14-125;10;0.3.1100(400)[1000]-C.01	2,028.1	551.5	0.999	400	15	535.1	0.970
PT-AEC.16/09/14-125;10;0.3.1100(400)[1000]-C.02	1,953.9	532.0	1.000	400	15	513.5	0.965
PT-AEC.16/09/14-125;10;0.3.1100(400)[1000]-D.01	1,938.7	528.0	1.000	400	15	510.2	0.966
PT-AEC.16/09/14-125;10;0.3.1100(400)[1000]-D.02	2,011.4	547.9	1.000	400	15	528.0	0.964
PT-AEC.17/10/14-125;10;0.3.1100(1000)[1000]-F.01	2,020.5	550.7	1.000	1,000	0	550.0	0.999
PT-AEC.17/10/14-125;10;0.3.1100(1000)[1000]-F.02	1,964.6	535.0	1.000	1,000	0	534.4	0.999
PT-AEC.17/10/14-125;10;0.3.1100(1000)[1000]-G.01	1,997.1	543.9	1.000	1,000	0	543.5	0.999
PT-AEC.17/10/14-125;10;0.3.1100(1000)[1000]-G.02	2,058.7	560.9	1.000	1,000	0	560.6	1.000
PT-AEC.07/10/14-125;10;0.3.1100(1000)[1000]-H.01	2,031.4	539.2	0.994	1,000	0	561.8	1.042
PT-AEC.07/10/14-125;10;0.3.1100(1000)[1000]-H.02	1,989.4	530.4	0.995	1,000	0	550.8	1.039
PT-AEC.07/10/14-125;10;0.3.1100(1000)[1000]-I.01	1,992.5	532.3	0.996	1,000	0	551.4	1.036
PT-AEC.07/10/14-125;10;0.3.1100(1000)[1000]-I.02	2,001.2	536.0	0.996	1,000	0	551.2	1.028
PT-AEC.13/03/15-125;10;0.3.1100(400)[1000]-A.03	1,974.3	538.2	1.000	400	15	519.9	0.966
PT-AEC.13/03/15-125;10;0.3.1100(400)[1000]-A.04	1,984.7	541.0	1.000	400	15	522.2	0.965
PT-AEC.13/03/15-125;10;0.3.1100(400)[1000]-B.03	1,984.8	541.2	1.000	400	15	523.0	0.966
PT-AEC.13/03/15-125;10;0.3.1100(400)[1000]-B.04	2,017.3	550.0	1.000	400	15	532.4	0.968
PT-AEC.20/03/15-125;10;0.3.1100(1000)[1000]-F.03	1,998.9	544.0	1.000	1,000	0	545.0	1.002
PT-AEC.20/03/15-125;10;0.3.1100(1000)[1000]-F.04	2,006.4	546.2	1.000	1,000	0	546.7	1.001
PT-AEC.20/03/15-125;10;0.3.1100(1000)[1000]-G.03	1,982.8	538.8	0.999	1,000	0	541.2	1.005
PT-AEC.20/03/15-125;10;0.3.1100(1000)[1000]-G.04	1,967.0	535.6	1.000	1,000	0	536.2	1.001

Table 11-1. Complete cell fabrication anode parameters and results (oxidation at 1,100 °C, 42 h dwell for all samples).

Electrolyte				
Sample	**$T_{EB\text{-}PVD}$ (°C)** ±2 °C	**$P_{chamber}$ (mbar)** ±1x10^{-4} mbar	***f*** **(rpm)** ±1 rpm	**m_{YSZ} (mg)** ±2 mg
PT-AEC.12/09/14-125;10;0.3.1100(400)[1000]-A.01	1,051	0.00125	30	53.6
PT-AEC.12/09/14-125;10;0.3.1100(400)[1000]-A.02	1,051	0.00125	30	48.9
PT-AEC.12/09/14-125;10;0.3.1100(400)[1000]-B.01	1,045	0.00114	30	53.0
PT-AEC.12/09/14-125;10;0.3.1100(400)[1000]-B.02	1,045	0.00114	30	47.9
PT-AEC.16/09/14-125;10;0.3.1100(400)[1000]-C.01	1,050	0.00107	30	61.0
PT-AEC.16/09/14-125;10;0.3.1100(400)[1000]-C.02	1,050	0.00107	30	54.6
PT-AEC.16/09/14-125;10;0.3.1100(400)[1000]-D.01	1,047	0.00107	30	55.5
PT-AEC.16/09/14-125;10;0.3.1100(400)[1000]-D.02	1,047	0.00107	30	49.8
PT-AEC.17/10/14-125;10;0.3.1100(1000)[1000]-F.01	1,040	0.00093	30	80.8
PT-AEC.17/10/14-125;10;0.3.1100(1000)[1000]-F.02	1,040	0.00093	30	74.2
PT-AEC.17/10/14-125;10;0.3.1100(1000)[1000]-G.01	1,053	0.00111	30	79.9
PT-AEC.17/10/14-125;10;0.3.1100(1000)[1000]-G.02	1,053	0.00111	30	74.6
PT-AEC.07/10/14-125;10;0.3.1100(1000)[1000]-H.01	1,045	0.00148	30	81.2
PT-AEC.07/10/14-125;10;0.3.1100(1000)[1000]-H.02	1,045	0.00148	30	75.3
PT-AEC.07/10/14-125;10;0.3.1100(1000)[1000]-I.01	1,047	0.00107	30	86.6
PT-AEC.07/10/14-125;10;0.3.1100(1000)[1000]-I.02	1,047	0.00107	30	79.2
PT-AEC.13/03/15-125;10;0.3.1100(400)[1000]-A.03	1,048	0.00218	30	49.8
PT-AEC.13/03/15-125;10;0.3.1100(400)[1000]-A.04	1,048	0.00218	30	45.0
PT-AEC.13/03/15-125;10;0.3.1100(400)[1000]-B.03	1,048	0.00118	30	48.3
PT-AEC.13/03/15-125;10;0.3.1100(400)[1000]-B.04	1,048	0.00118	30	53.1
PT-AEC.20/03/15-125;10;0.3.1100(1000)[1000]-F.03	1,048	0.00163	30	56.8
PT-AEC.20/03/15-125;10;0.3.1100(1000)[1000]-F.04	1,048	0.00163	30	72.8
PT-AEC.20/03/15-125;10;0.3.1100(1000)[1000]-G.03	1,051	0.00149	30	74.4
PT-AEC.20/03/15-125;10;0.3.1100(1000)[1000]-G.04	1,051	0.00149	30	70.2

Table 11-2. Complete cell fabrication electrolyte parameters and results.

Cathode							
Sample	**$P_{chamber}$ (mbar)** ±1x10^{-4} mbar	***f*** **(rpm)** ±1 rpm	**T_{sputt} (min)** ±1 s	**V (V)** ±5%	**I (I)** ±5%	**m_{cell} (mg)** ±1 mg	**m_{Pt} (mg)** ±2 mg
PT-AEC.16/09/14-125;10;0.3.1100(400)[1000]-C.02	0.1	6	15	393.0	0.7	2,033.2	5.5
PT-AEC.16/09/14-125;10;0.3.1100(400)[1000]-D.01	0.1	6	15	393.0	0.7	2,017.5	5.0
PT-AEC.07/10/14-125;10;0.3.1100(1000)[1000]-I.01	0.1	6	15	393.0	0.7	2,077.5	6.6
PT-AEC.07/10/14-125;10;0.3.1100(1000)[1000]-I.02	0.1	6	15	393.0	0.7	2,081.0	6.2
PT-AEC.13/03/15-125;10;0.3.1100(400)[1000]-A.03	0.1	6	15	399.0	0.7	2,048.3	5.9
PT-AEC.20/03/15-125;10;0.3.1100(1000)[1000]-F.03	0.1	6	15	399.0	0.7	2,060.6	5.0
PT-AEC.20/03/15-125;10;0.3.1100(1000)[1000]-G.04	0.1	6	15	397.0	0.7	2,042.8	5.6

Table 11-3. Complete cell fabrication cathode parameters and results.

To demonstrate the effectiveness of the improvements made on the jigging consult Figure 11-2. below. The photographs show a sample with the initial jigging (H.02), one after the improvements to the reduction jig (A.02), a third after the addition of alumina tubes to the reduction jig (B.04) and the final photo shows a sample after the addition of

alumina tubes to the EB-PVD jigs also (G.03). As can be seen in these photographs out or roundness was not necessarily equal at both ends of a given fuel cell. The end of the set screw of the EB-PVD was in all cases somewhat more out of round (or slightly out of round in cases where the other end was not). This is surprising because as a single point constraint one would expect the cell to be able to expand and contract freely. However, by constraining axial movement it may well be forcing radial movement to deform the cells as noted. Sample A.02 is an excellent example with one end sufficiently unmarred for testing bonding methods while the other is severely out of round, appearing crushed. One can be certain these samples have not been subjected to any significant mechanical loading at room temperature (i.e. separate from the heat treatments) that may have caused the distortions by their brittle nature. Any such loading would quite literally shatter the porous Ni tubes and thin electrolyte layer rather than cause visible plastic deformation.

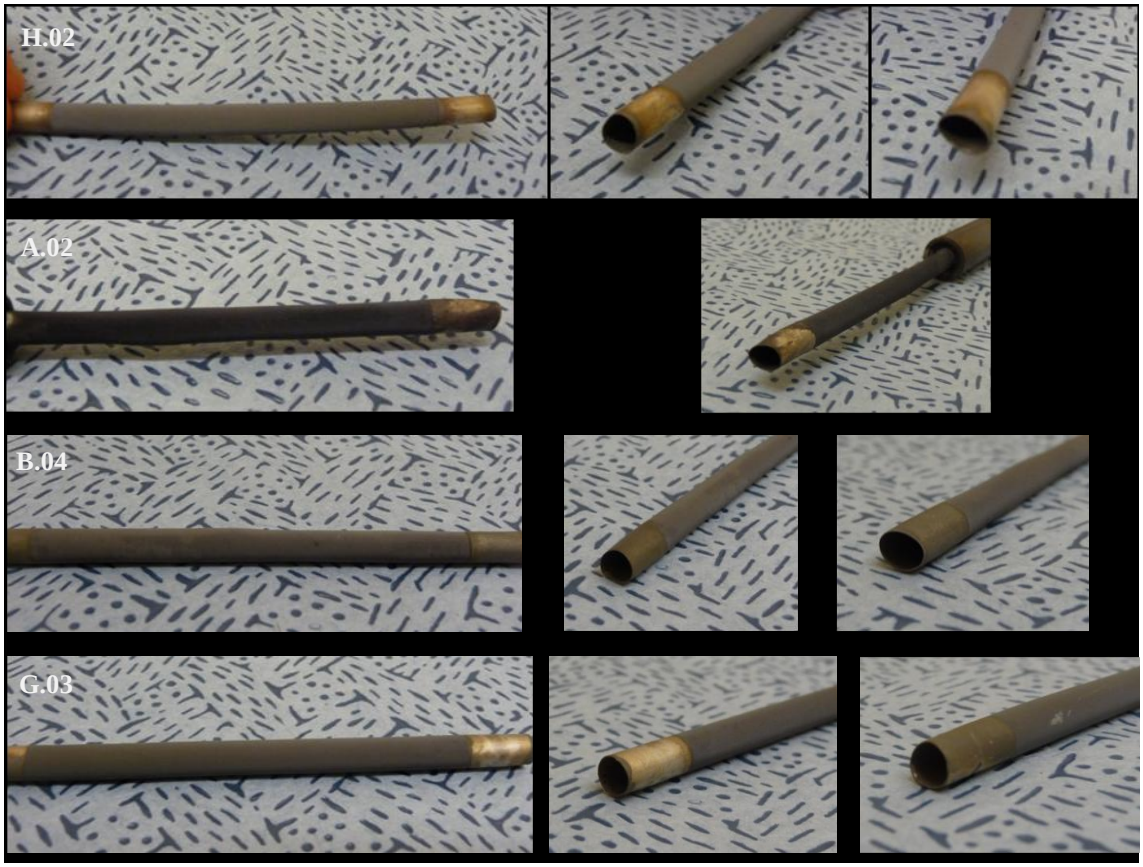

Figure 11-2. Selected photographs showing the net improvement from a further iteration of the reduction and EB-PVD jigging.

Inspection of the tables shows little difference between each sub-group of samples. However, probability plots can be conveniently employed to better compare the two datasets. In this instance it is practical to show all these comparisons, divided by component: see Figure 11-3. through Figure 11-6. Straight lines indicate a normal distribution, and overlapping points indicate that the two sets exhibit only stochastic

differences with no systemic changes to results and therefore are highly reproducible. Notice that this is essentially the same sort of statistically analysis carried out in section 9.6.1, only with a different purpose.

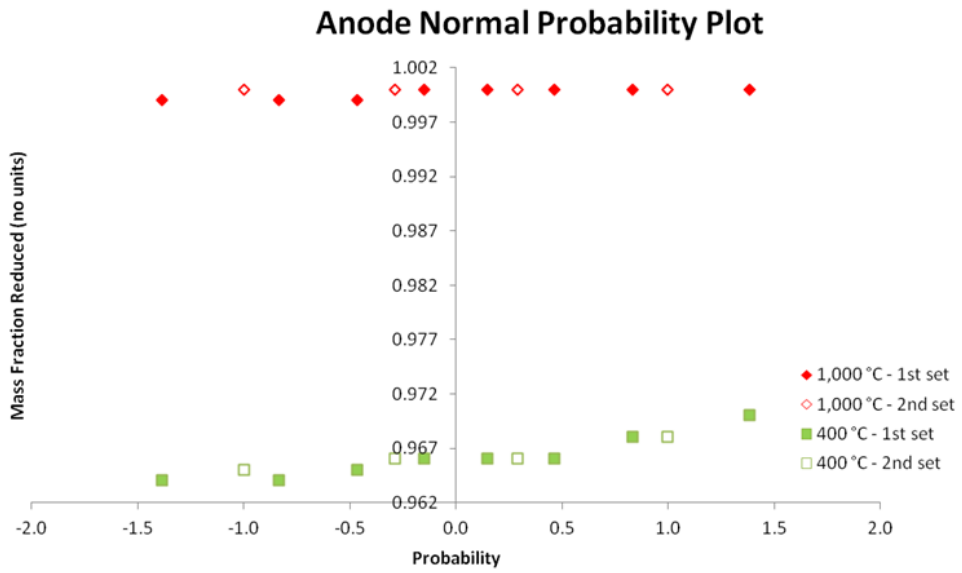

Figure 11-3. Anode MFR normal probability plot (both 400 °C and 1,000 °C). The error is too small to be visible.

The probability plots in Figure 11-3. clearly show that at both temperatures the reproducibility is such that the first and second sets of fabrication are essentially the same. They also conform to a Gaussian distribution: all deviations are stochastic. Comparing their medians with the results of the fabrication optimization experiments (see chapter 8) shows excellent reproducibility at both temperatures. The results at each temperature conform perfectly to previous experiments. At 400 °C samples achieve a median MFR of 0.97 and at 1,000 °C they achieve a median MFR of 1.0.

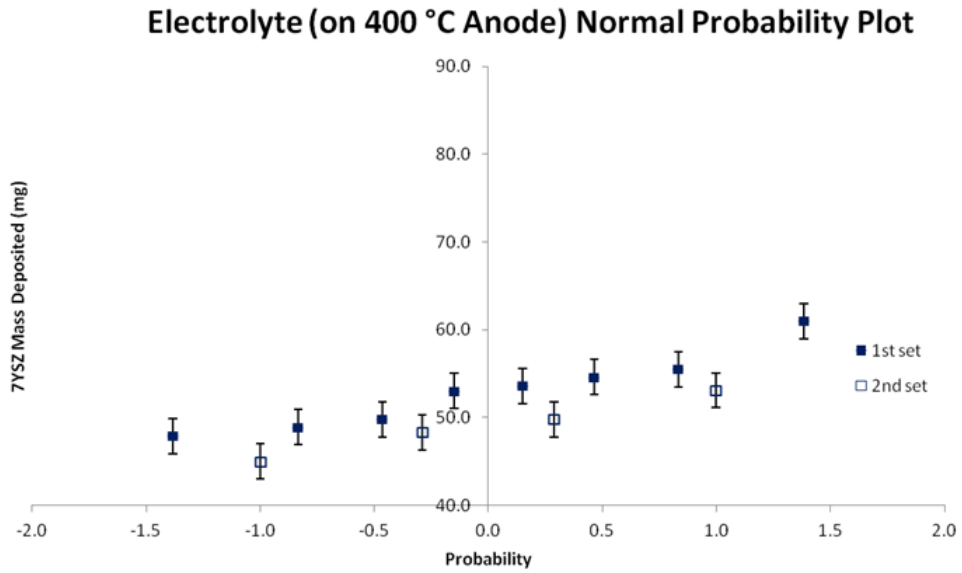

Figure 11-4. Electrolyte mass normal probability plot for 7YSZ deposited on anode reduced at 400 °C.

When deposited on an anode reduced at 400 °C both sets demonstrate excellent reproducibility as with the anodes discussed above. The distribution is Gaussian. Recall from chapter 9 that the deposition optimization experiments were carried out on solid Ni tubes; here we compare the results of depositing an electrolyte on anodes of each reduction scheme with the optimization results (especially the DoE). From the DoE results sample B.08 was selected as optimal for deposition parameters. It resulted in 55 mg of 7YSZ deposited onto the solid Ni tube. The median in Figure 11-4. agrees very well with this: 53 mg. Thus, one may conclude that the deposition process exhibits a very high degree of reproducibility and deviations are stochastic as opposed to a persistent bias (deterministic element).

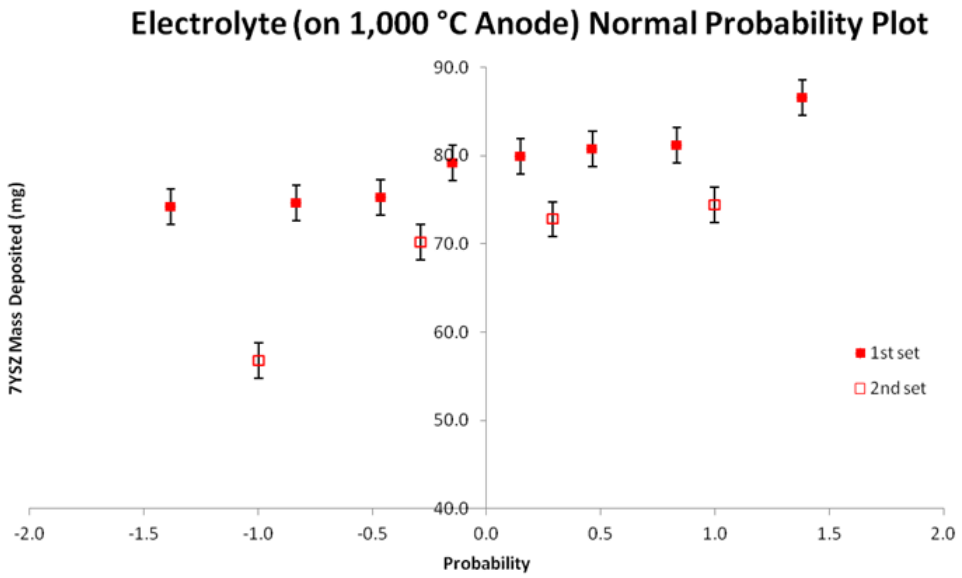

Figure 11-5. Electrolyte mass normal probability plot for 7YSZ deposited on anode reduced at 1,000 °C.

While the scatter is greater than for deposition on 400 °C anodes the data still conforms to a Gaussian distribution and shows excellent reproducibility (no significant differences between the first and second set). However, it does result in significantly higher deposited mass: median of 80 mg. Compare this to the 55 mg deposited onto B.08 from the DoE experiments. Referring back to chapter 8 there is an increased surface roughness for those samples with an anode made with the 1,000 °C reduction scheme. I believe this to be the reason for an increase in the median deposited mass of YSZ.

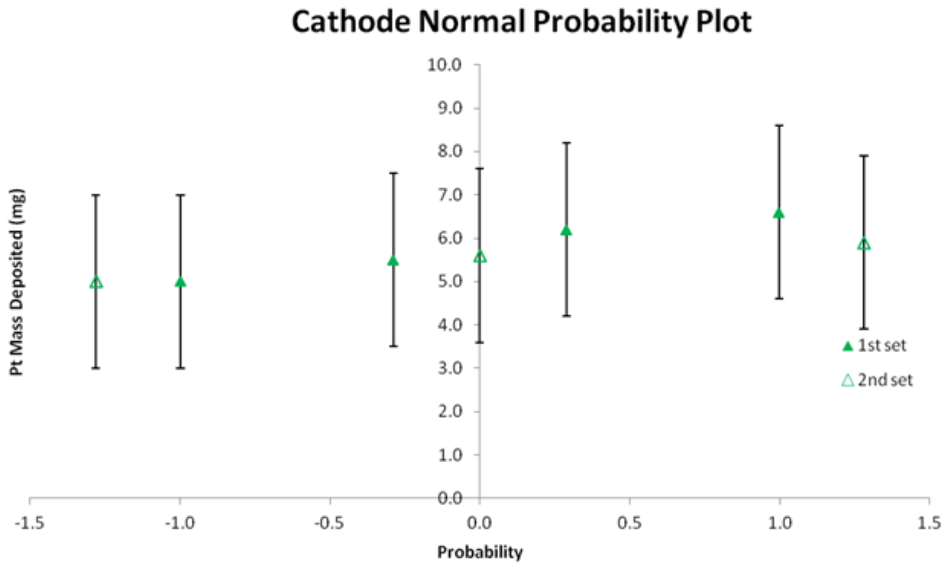

Figure 11-6. Cathode mass normal probability plot. NB: The error is the measurement error, which differs greatly from the batch to batch manufacturing variance.

In the case of the cathode, Figure 11-6., the measurement error dominates over the stochastic variation during deposition. Both data sets conform to a Gaussian distribution and show excellent reproducibility (no significant differences between the first and second set). The total variance of the cathode probability plot data is considerably less than the (measurement) error; by a factor of approximately four. From this we may infer that the reproducibility is in fact significantly better than even the measurement error using a microbalance.

Cross-sectional micrographs of two samples (PT-AEC.19/09/14-125.10.0.3.1100 (400)[1000]-D.01 and PT-AEC.07/10/14-125.10.0.3.1100(1000)[1000]-I.02), selected at random to represent one complete cell manufactured with each reduction route, follow. These micrographs include both secondary emission (SE) and back scatter electron (BSE) imaging, following the same pattern as the oxidation and reduction cross-sectional images (overall, outer edge and middle only in this instance since the microstructure towards the inner edge of the anode is of less interest here). SE images are on the left hand side, BSE on the right (not necessarily the same site). Cross-sections were achieved via fractured edge; clean fractures were obtained thanks to the very high porosity of the anode.

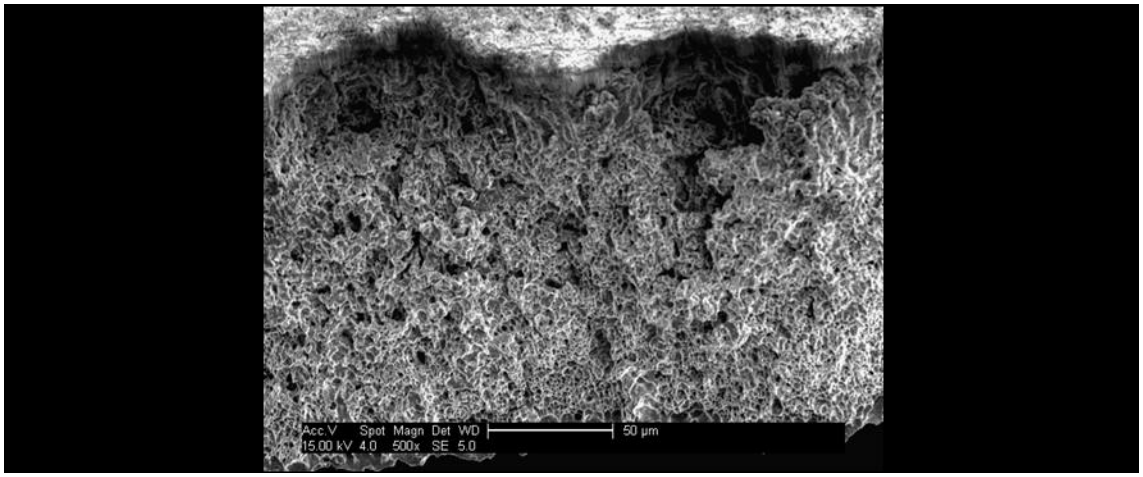

Figure 11-7. Selected overall cross-sectional micrograph of sample PT-AEC.19/09/14-125.10.0.3.1100(400)[1000]-D.01.

The additional processing at elevated temperature subsequent to completing the anode (electrolyte deposition) has not significantly altered the microstructure. Much the same combination of larger pores (mostly at triple points) and a dispersed matrix of small pores is visible in the anode. The sharp asperities created by fracturing the sample quite visible as bright spots in Figure 11-7**.**

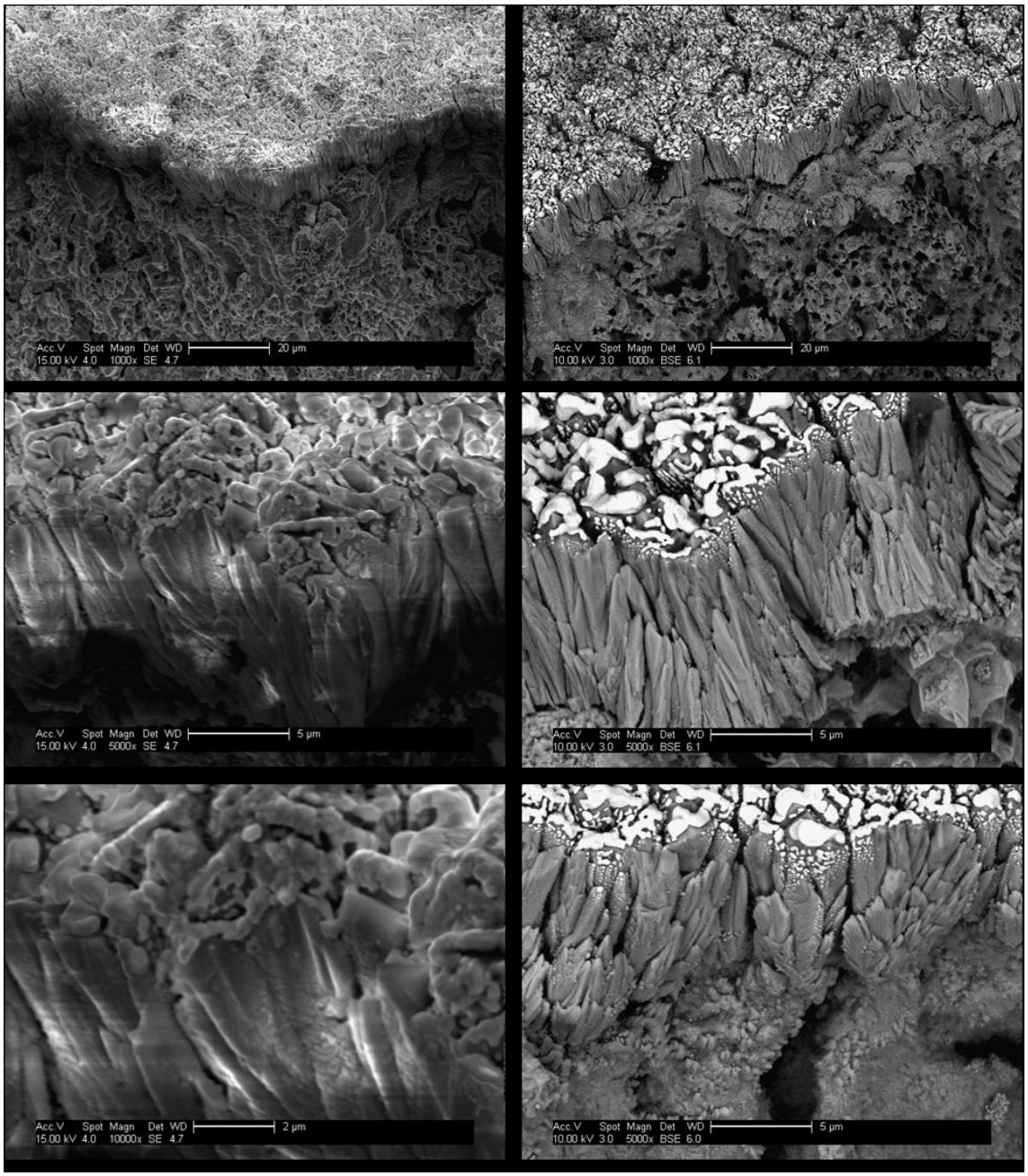

Figure 11-8. Selected cross-sectional micrographs near the outer edge of sample PT-AEC.19/09/14-125.10.0.3.1100(400)[1000]-D.01. The final image (bottom right) highlights the influence of surface cracks on the gas-tightness of the electrolyte (see chapter 1).

Whereas the SE images in Figure 11-8. show clearly the sputtered clumps of Pt on the surface, the BSE ones yield greater detail. Both image types highlight the very high conformability of a metallic cathode deposited in this way. To make best use of this feature modifications to the electrolyte itself are necessary; whether this is an alteration to the EB-PVD technique employed or the addition of a further manufacturing step to overcome the unintended and indeed undesirable side-effect of the extremely high anode porosity at the anode-electrolyte interface that led to large cracks through the

electrolyte and thence cathode. These cracks propagate through the electrolyte from surface cracks in the anode all the way to the cathode. There is some subsurface cracking appearing at the anode-electrolyte interface. It is, however, unclear whether this occurred during fabrication or as a result of fracturing the samples for imaging purposes. In either case manual handling did not result in the delamination of the electrolyte in these areas indicating strong adhesion without a bondcoat.

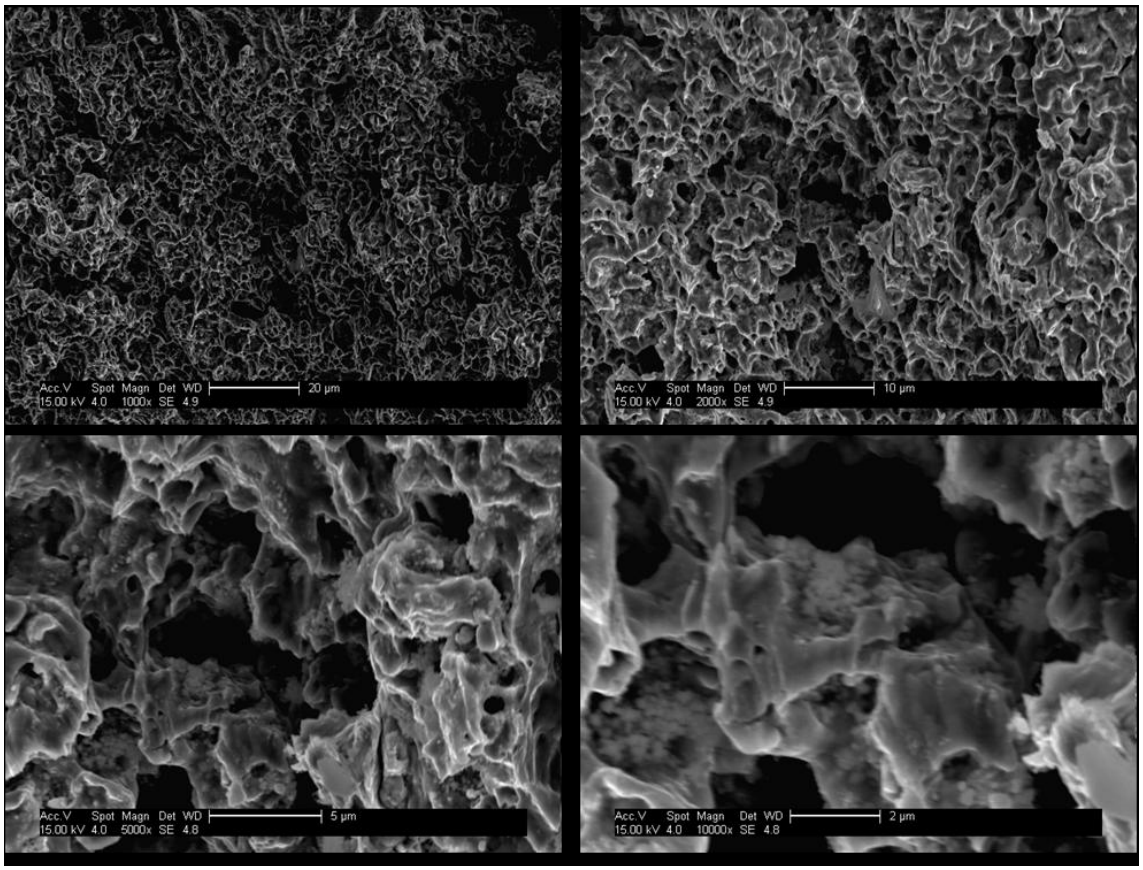

Figure 11-9. Selected cross-sectional micrographs near the middle of sample PT-AEC.19/09/14-125.10.0.3.1100(400)[1000]-D.01.

The micrographs above (in Figure 11-7., Figure 11-8. and Figure 11-9.) show unambiguously a highly connected network of anode pores ranging in size as noted previously. Figure 11-9. in particular showcases a degree of porosity achieved throughout the sample's anode that is remarkable. It is expected the anode concentration polarisation will be minimal, perhaps even inconsequential.

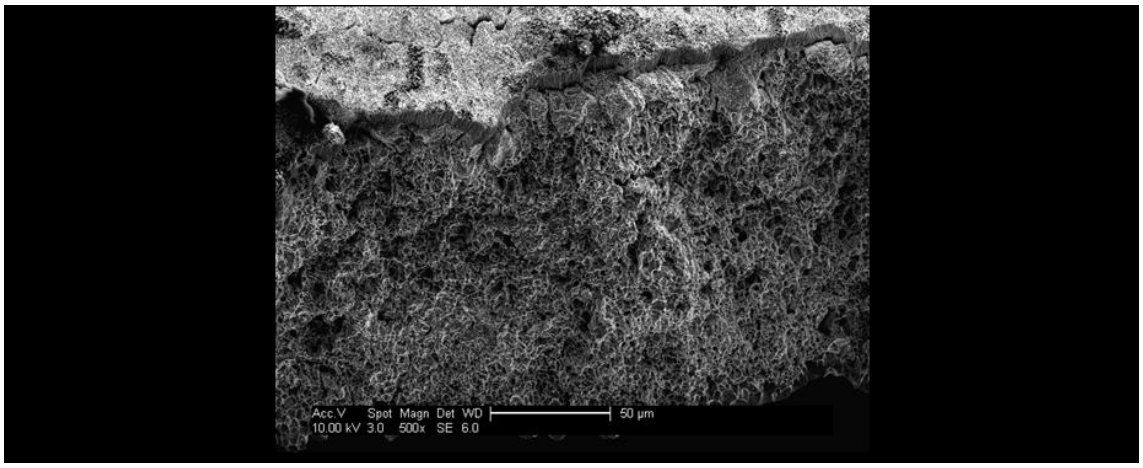

Figure 11-10. Selected overall cross-sectional micrograph of sample PT-AEC.07/10/14-125.10.0.3.1100(1000)[1000]-I.02.

The overall cross-section shown in Figure 11-10. is much the same as Figure 11-7. with a somewhat different distribution of pore sizes (discussed further below). Clearly then both reduction schemes are tenable routes for the creation of complete cells.

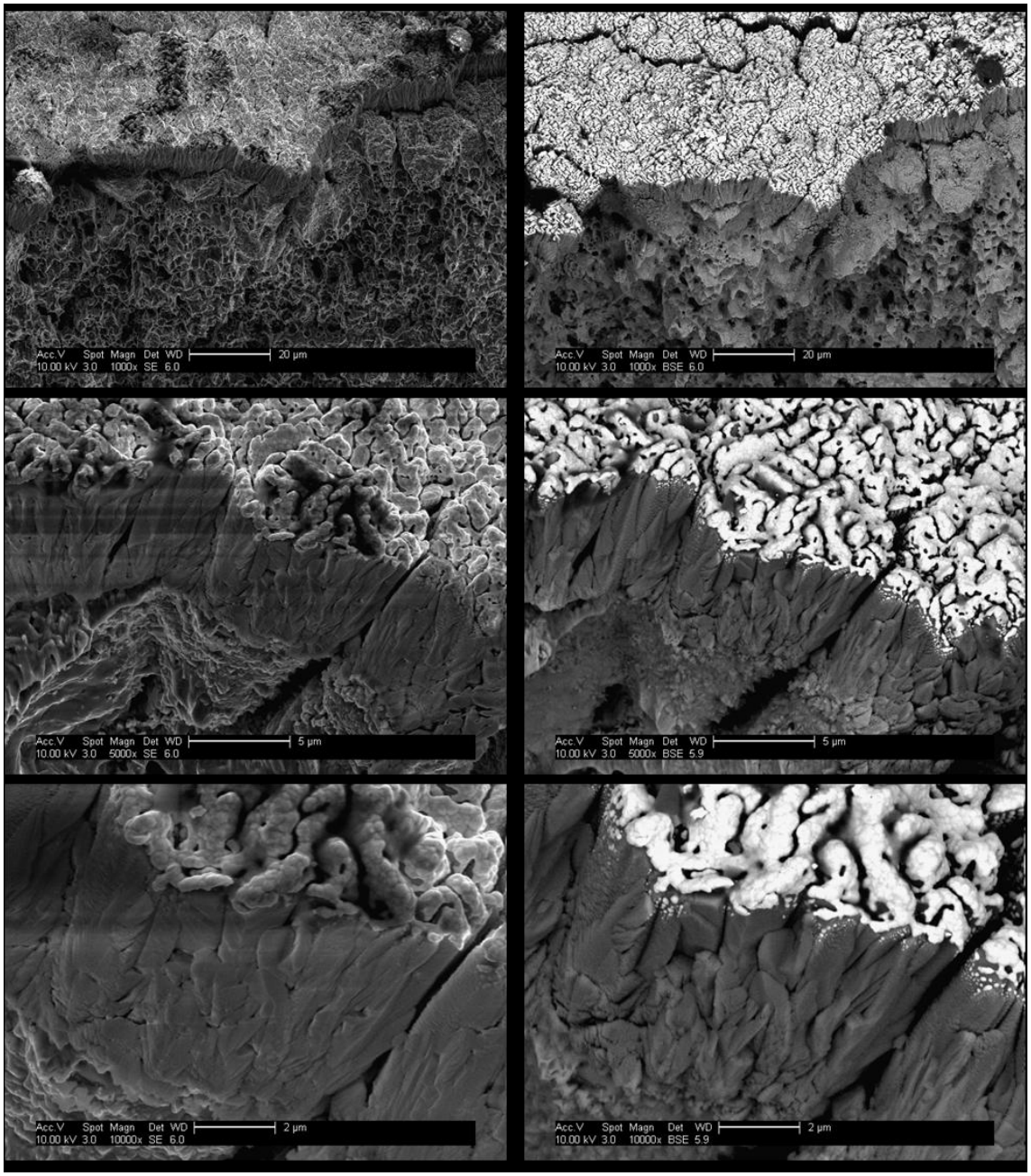

Figure 11-11. Selected cross-sectional micrographs near the outer edge of sample PT-AEC.07/10/14-125.10.0.3.1100(1000)[1000]-I.02. Note once more the effect of surface cracks on the gas-tightness of the electrolyte (see chapter 1).

The results visible in Figure 11-11. are very similar to those of Figure 11-7. There are a few notable differences. First, there is a reduction in the proportion of smaller pores and a concomitant increased proportion of larger ones distributed throughout the anode compared to the previous. Secondly, there appear to be fewer surface cracks in the anode (and therefore fewer cracks propagating through the electrolyte to the cathode on the surface). These are, however, larger overall both in width and length. Third, likely as a consequence of the preceding observation, the YSZ columns are more tightly packed between large cracks than for samples where the electrolyte was depsoited onto

an anode reduced by the other scheme (400 °C, 15 h dwell). By simple observation it is not possible to determine which resulting microstructure is best suited for fuel cell operation (i.e. which electrolyte is more gas tight). That is best determined by permeametry experiments (see chapter 1).

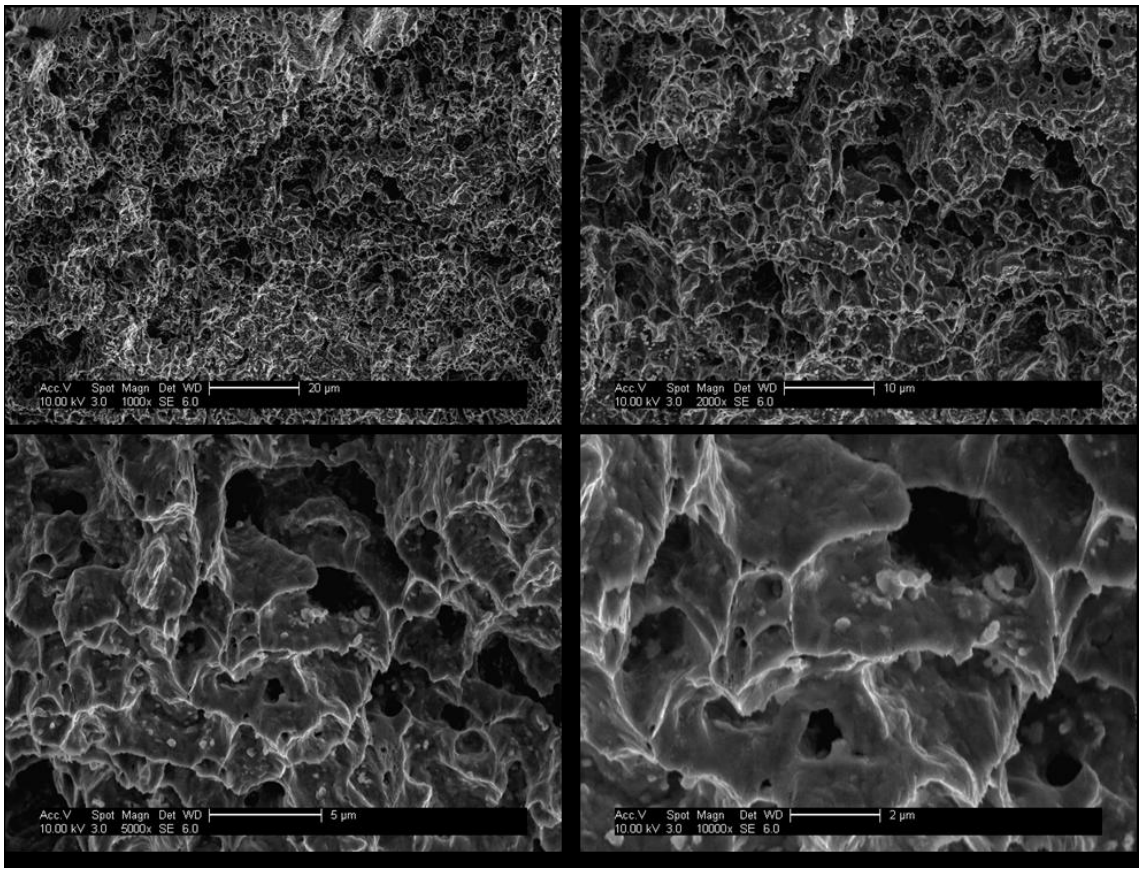

Figure 11-12. Selected cross-sectional micrographs near the middle of sample PT-AEC.07/10/14-125.10.0.3.1100(1000)[1000]-I.02.

As noted before, sample I.02 (reduced at 1,000 C with a 0 h dwell) has a greater concentration of larger pores and a proportionally smaller concentration of small pores. The pore network evident in Figure 11-11. can be clearly seen to be equally widely connected and evenly dispersed throughout the microstructure.

EBSD was used to gather information about grain texturing. In particular grain boundaries and grain orientation (especially of YSZ) – global and local texture – were of interest. The results of this analysis are discussed hereunder. First however, it is necessary to comment on a number of innate characteristics of EBSD as well as make a few observations common to both imaged samples. EBSD takes only an extremely shallow slice of the sample in analysis. The affected zone is about 100 nm; unlike the 2–5 µm for EDS. For both samples the Ni phase was mis-indexed (i.e. mis-identified). The very small pores (c.100 nm) dispersed throughout the anode and electrolyte were identified as Ni. We may discern this because the dispersion matches observed pores

seen in cross-sectional micrographs and also because it is exceedingly unlikely for Ni to diffuse that far through the ceramic given the time required at sufficiently elevated temperatures for significant diffusion to occur at each manufacturing step. In addition, no other Ni phase is detected in the anode (which is 99.95% Ni). Mis-indexing of phases is always a problem with EBSD analysis but rarely to a large scale. The precise reason in the case of these two samples is unknown but distortion of the crystal structure or strain could be causes [personal communication with Xianwei Liu, Analytical Technical Officer in SATAM at Cranfield University]. Note also that all the EBSD micrographs are oriented such that the top of the image is the anode and the bottom is the outer surface.

In conjunction EDS analysis was carried out, confirming the various components were located where expected – indicating no significant diffusion occurred during subsequent steps, even at high temperature.

While the Ni phase of the fractured edge cross-section from sample D.01 was mis-indexed as discussed above, the phase contrast remains informative. First of all the very shallow area imaged (c.100 nm) highlights the interconnected nature of the pore structure; compare the SE and phase contrast images. Secondly, the phase contrast highlights the nature of the columnar YSZ and its growth as was discussed in sections 9.2.8, 9.2.9, 9.5.1 and 9.6.1, but made even more clear here since EBSD is an excellent tool for identifying grain boundaries. Third, pores are mis-indexed as Ni, and Ni as tetragonal YSZ. The correct phases were identified through EDS to be consistent with previous analysis demonstrating that the mis-indexing is restricted to the EBSD. A reasonable conclusion is that the problem rests with the Ni and pores. One would expect the YSZ to be almost entirely tetragonal with some monoclinic phases (as may be seen in Figure 11-13.) based on the deposition parameters (temperature, chamber pressure, rotation speed, etc.) and was therefore correctly indexed by EBSD. The IPF data shows that the Ni and Pt have no texturing, whereas the YSZ is textured with the [010] direction perpendicular to the anode surface. This is consistent with expectations. The microstructure of the electrolyte evolves as deposition progresses: from random nucleation to growth in preferential directions. Such was expected based on the literature, of course, but the inverse pole figures from EBSD analysis show this with impressive clarity thanks to grain orientation contrast.

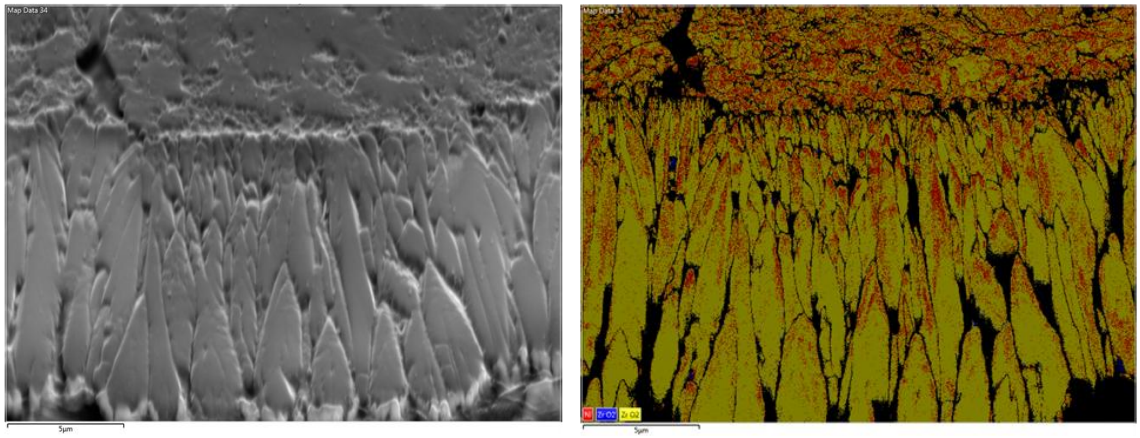

Inverse Pole Figure (IPF) Direction Key

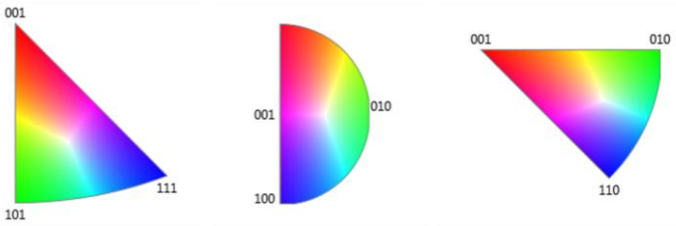

Ni monoclinic ZrO_2 tetragonal ZrO_2

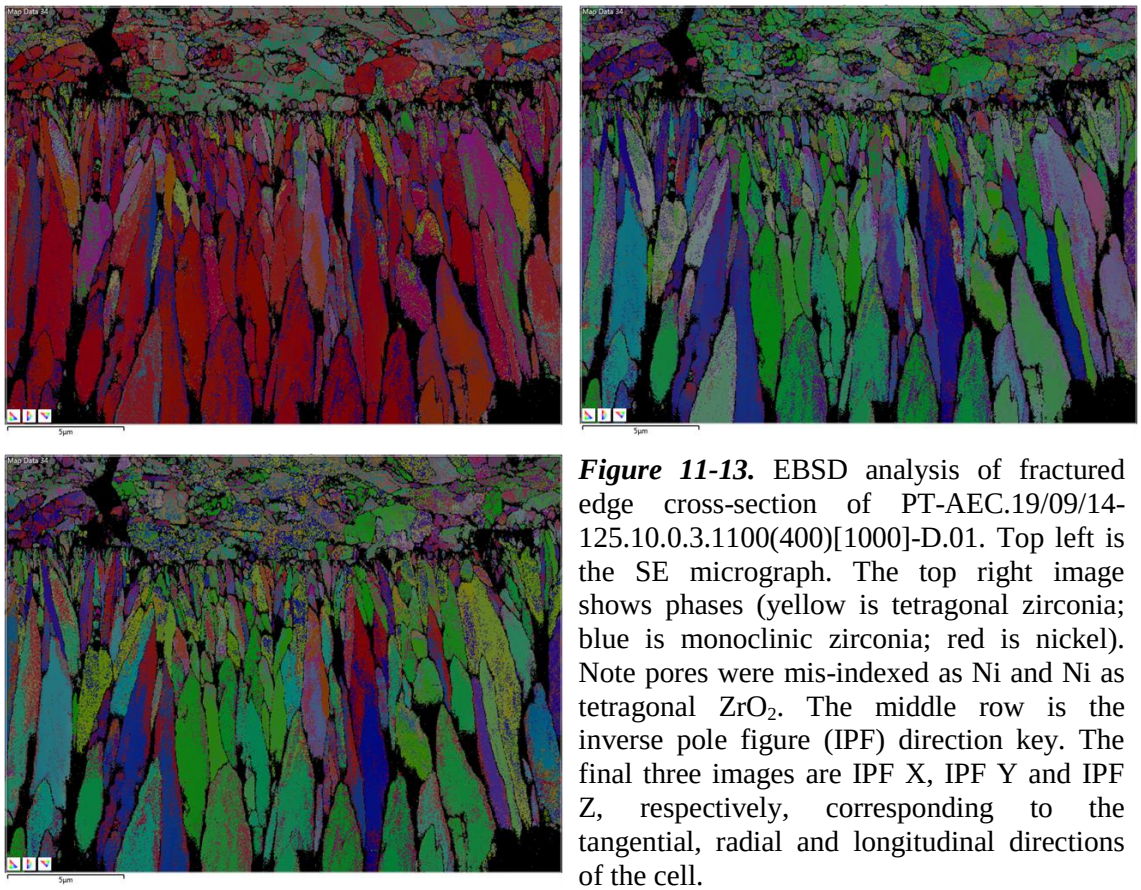

Figure 11-13. EBSD analysis of fractured edge cross-section of PT-AEC.19/09/14-125.10.0.3.1100(400)[1000]-D.01. Top left is the SE micrograph. The top right image shows phases (yellow is tetragonal zirconia; blue is monoclinic zirconia; red is nickel). Note pores were mis-indexed as Ni and Ni as tetragonal ZrO_2. The middle row is the inverse pole figure (IPF) direction key. The final three images are IPF X, IPF Y and IPF Z, respectively, corresponding to the tangential, radial and longitudinal directions of the cell.

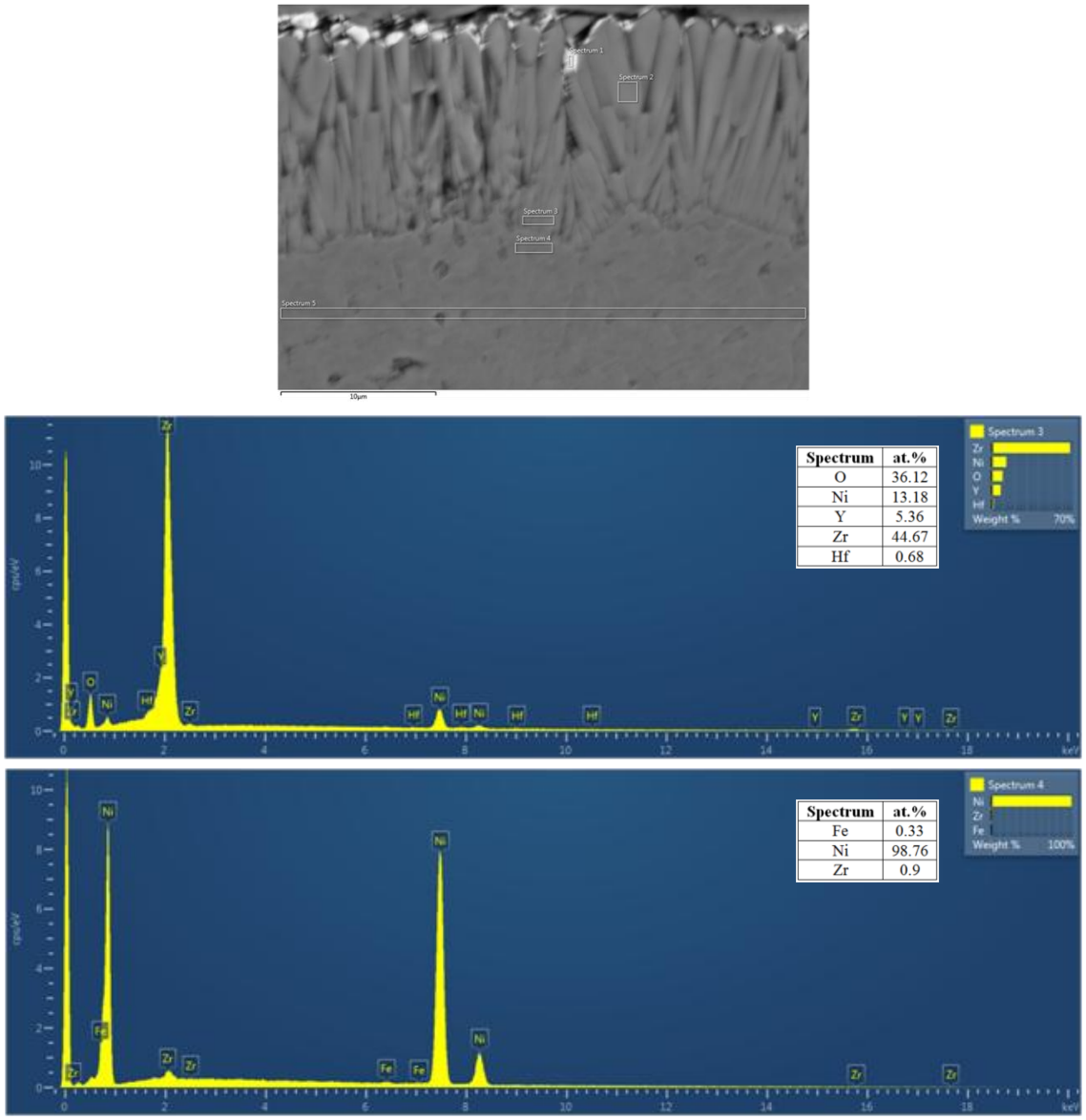

Figure 11-14. BSE (top) of fractured edge cross-section of PT-AEC.19/09/14-125.10.0.3.1100(400)[1000]-D.01 showing areas analysed and the corresponding EDS spectra. Note that only spectra of interest were included.

For sample D.01 the electrolyte is oxygen-deficient at the interface, not an uncommon or unexpected result as was previously discussed. A Pt phase was detected by EDS (in spectrum 1, although this is not shown as the spectrum is otherwise uninteresting) despite none being found by EBSD. Perhaps the grains were too small and therefore characterization was below detection limits. Also of interest is the relatively sharp transition across the narrow interfacial zone with little to no material diffusing across it. Given processing temperatures more was expected.

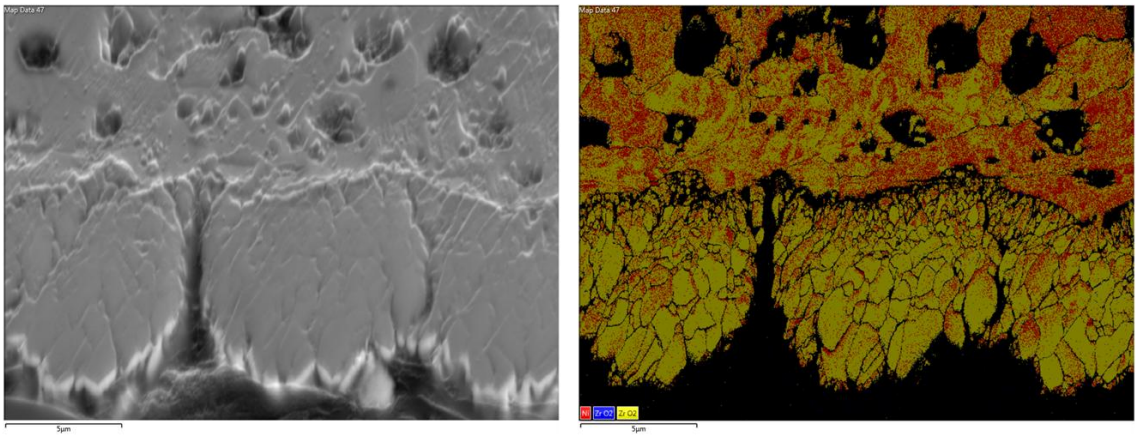

Figure 11-15. EBSD analysis of fractured edge cross-section of PT-AEC.07/10/14-125.10.0.3.1100(1000)[1000]-I.02. Top left is the SE micrograph. The top right image shows phases (yellow is tetragonal zirconia; blue is monoclinic zirconia; red is nickel). Note the Ni was mis-indexed. The middle row is the inverse pole figure (IPF) direction key. The final three images are IPF X, IPF Y and IPF Z, respectively, corresponding to the tangential, radial and longitudinal directions of the cell.

Sample I.02 (Figure 11-15.) exhibits many of the same features as D.01 did, including the same mis-indexing, with a few additional features of note. The pore network visible

from this fractured edge cross-section has larger pores and wider intragranular gaps that are highlighted especially well due to the shallow depth to which EBSD penetrates. The microstructural differences between anodes created via the 400°C reduction scheme and the 1,000 °C reduction scheme discussed in chapter 8 (from section 8.10 onwards) are brought into sharp focus by Figure 11-13. and Figure 11-15. Unlike D.01, which appeared to have a growth-dominated electrolyte, I.02's electrolyte appears nucleation-dominated. The electrolyte is furthermore somewhat less textured in the direction perpendicular to the anode surface than for sample D.01. Notice the microstructural evolution with growth of the electrolyte.

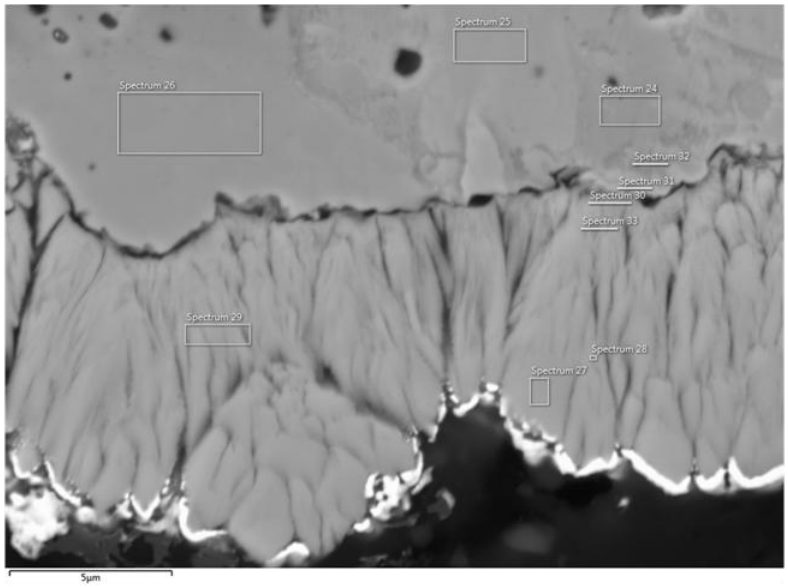

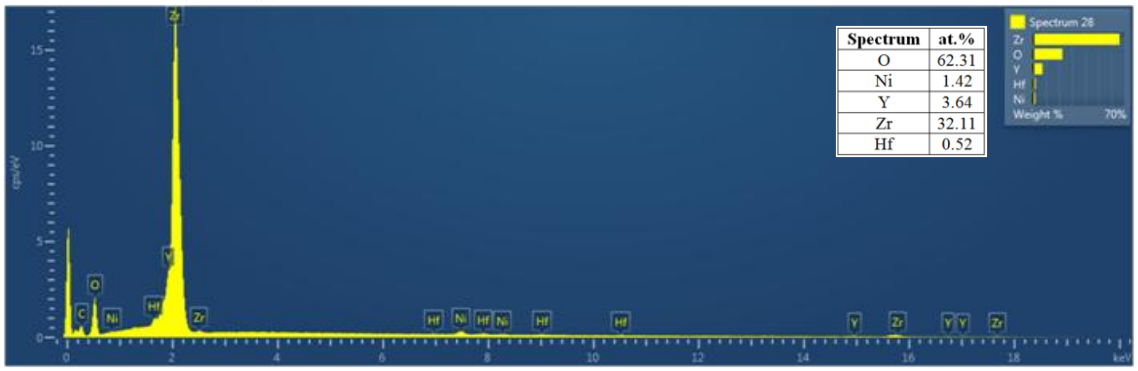

Spectrum	at.%
O	62.31
Ni	1.42
Y	3.64
Zr	32.11
Hf	0.52

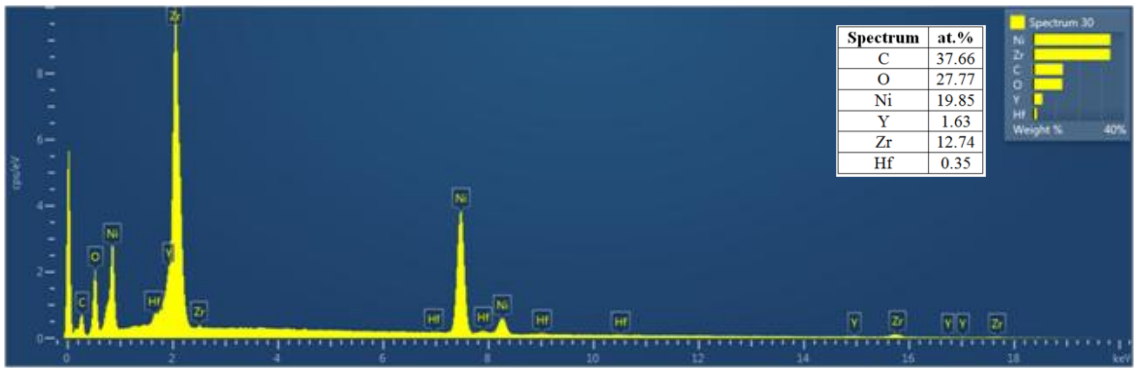

Spectrum	at.%
C	37.66
O	27.77
Ni	19.85
Y	1.63
Zr	12.74
Hf	0.35

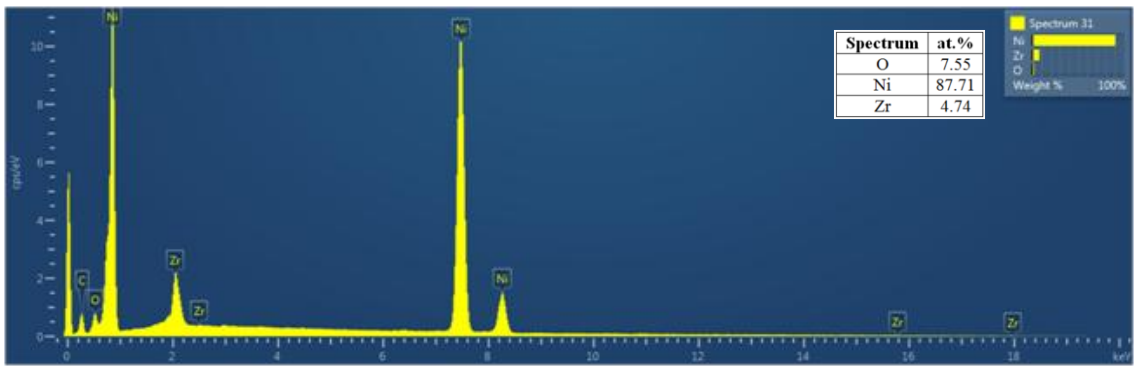

Spectrum	at.%
O	7.55
Ni	87.71
Zr	4.74

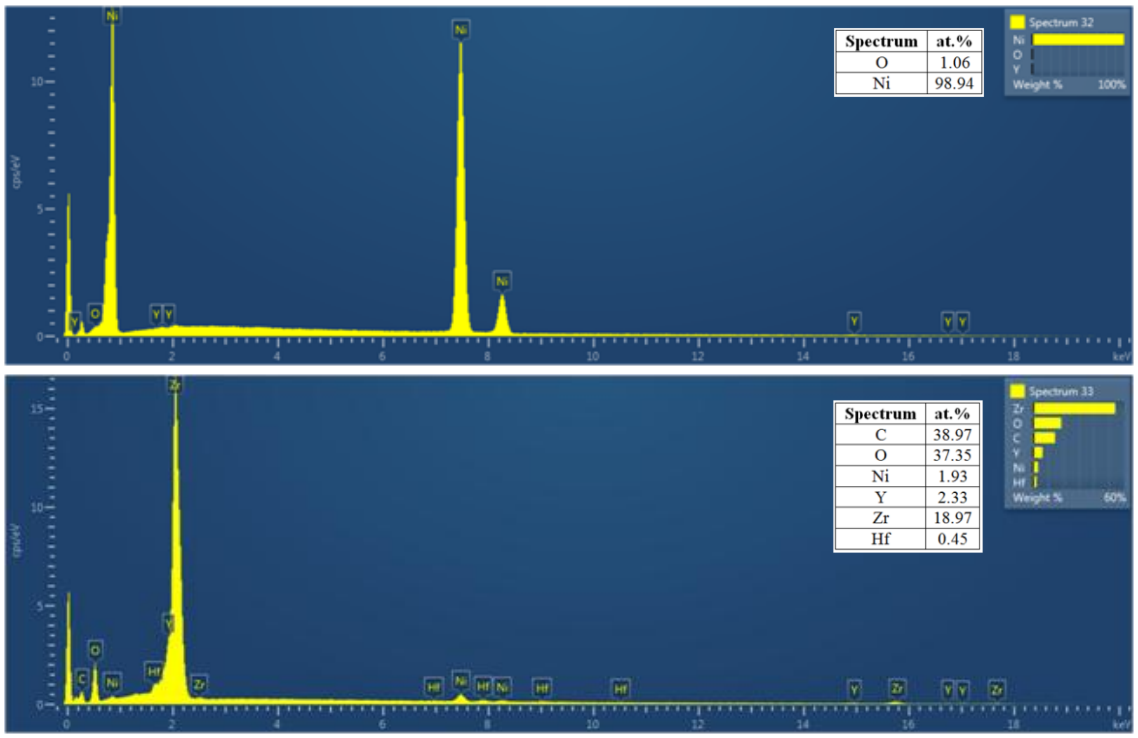

Figure 11-16. BSE (top) of fractured edge cross-section of PT-AEC.07/10/14-125.10.0.3.1100(1000)[1000]-I.02 showing areas analysed and the corresponding EDS spectra. Note that only spectra of interest were included.

The spectra for areas labelled 24, 25 and 26 detected only Ni – as would be expected for the anodes – and were not included in Figure 11-16. Spectrum 28 is representative of the three taken towards the centre of the electrolyte. The oxygen content is consistently over-estimated by this particular EDS system for unknown reasons. This is systemic and hardware driven, occurring in samples analysed across a considerable interval of time (more than 6 years) and is something experienced by several users. Therefore, the oxygen content must be taken with a pinch of salt. Otherwise these spectra conform to expectations and previous analysis. The YSZ had the expected quantity of Hf, a result of the raw material processing. Some Ni was detected near the interface but this may be due to the EDS affected zone (teardrop shaped area that is sampled) rather than the diffusion of Ni into the electrolyte. The EDS also detects the small amount of dissolved oxygen in the Ni anode, this is dissolved into the Ni as noted during the anode manufacture. A little Ni does diffuse into the electrolyte but only about 2 µm whereas, even at just 100 nm from the interface, no zirconia was detected in the Ni.

Another useful tool within EBSD is measurement of grain distortion which is a useful indicator of strain. Note, however, that while mis-indexing may be indeed caused by sample strain, measurements of grain distortion may be skewed by mis-indexing. *Ergo*, the following plots may well have significant error.

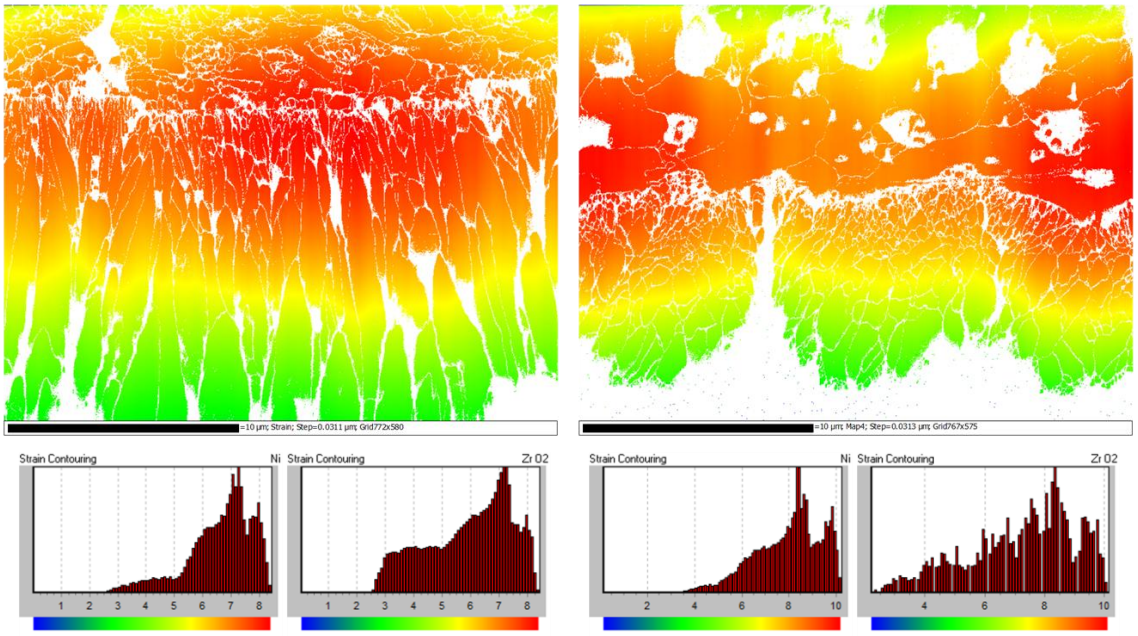

Figure 11-17. Grain distortion measured by EBSD (an indicator of local strain) for fractured edge cross-section of sample PT-AEC.19/09/14-125.10.0.3.1100(400)[1000]-D.01 (left) and sample PT-AEC.07/10/14-125.10.0.3.1100(1000)[1000]-I.02 (right).

Notwithstanding any error linked to mis-indexing it remained plausible to make some determinations based on Figure 11-17. Within the electrolyte the transition from a high level of distortion to a much lower one occurs over a very short distance; the border roughly corresponding to an increase in column width. Grain distortion indicates strain is likely high at the interface, normalizing to low strain further away. This is consistent with PVD coatings of all types. Of particular interest is the strain-relief afforded by surface cracks of the anode and concomitant electrolyte microstructure (visible in sample D.01), gaps in the electrolyte not caused by the anode surface morphology (visible in sample I.02) and around pores (visible throughout in both the anode and the electrolyte). Finally, one may also observe that the tubular nature of the substrate likely contributes to lowering strain towards the outer surface of the electrolyte (bottom part of images) due to the structure becoming more open as was hypothesised earlier in this thesis. The zone of high distortion in the Ni is narrower than in the electrolyte, with the high temperature anode, furthermore, having a narrower-still high distortion band. This may indicate some strain relief in the anode during electrolyte deposition as well as during reduction (see creep discussion). While not a strain effect the colouration helps greatly in highlighting the increase in grain size with increased reduction temperature (see sections 8.11.1 and 8.12.1 for more on anode microstructure).

11.3.2 Conclusions

The fabrication route developed exhibits excellent reproducibility, demonstrating a route that is eminently suitable to scale out is also capable of manufacture to narrow tolerances despite the use of equipment designed for experimental use that is therefore

not optimised for manufacture. This is especially remarkable in the case of the electrolyte deposition given the lack of a shutter to precisely control deposition thickness. The excellent reproducibility also reveals that randomly selecting from the samples fabricated is an acceptable way to obtain representative cells for further testing.

Bonding YSZ directly onto Ni shows excellent adhesion if manufactured by the described procedure – the processing window appears narrow as was discussed in chapter 9. The strong adhesion is evident from the fractured edge cross-sectional micrographs with no fractures originating at the electrolyte-anode interface. Indeed, there are numerous areas where it appears parts of YSZ columns became detached from the electrolyte and snapped away during fracture with little damage to remaining columns (either of the columns themselves or at the interface); Figure 11-11. is one such example. The pattern of cracks that propagate through the electrolyte to the free surface remain clear despite the cathode (which is too thin and too conformal to bridge them) closely resembling the cracks in the surface of the underlying anode layer. This is unlikely to be coincidental. Most likely it is, in fact, causal, with the surface cracks in the anode resulting in cracks – or more accurately gaps (i.e. not a result of a damage mechanism) – in the electrolyte. Recall that EB-PVD is highly conformal and unable to bridge across surface cracks of the anode. Rather the nucleation is on a discontinuous surface.

The EBSD showcases very effectively the changing grain structure of the electrolyte – transition from nucleation-dominated early stages to growth-dominated later ones, the fine nature of the pore network and the strongly adhering 300 nm cathode atop the YSZ columns. With regards to the pores, EBSD micrographs in Figure 11-13. and Figure 11-15. show the degree of in-plane porosity that is at the submicron size (from chapter 8 the anode is known to contain a very large quantity of ~100 nm pores). While considerable mis-indexing of materials was noted EDS of several areas through the cross-section at different sites of the fractured edge reveal no anomalous interdiffusion; indeed there is little interdiffusion at all. EBSD additionally yields some useful information on texturing of the fuel cell microstructure: the anode and cathode display no texturing whereas the electrolyte is strongly textured in the radial direction (the primary growth direction). This result is in accordance with expectations, confirming the fabrication methods employed function as intended.

11.4 Material and Energy Audit

The material and energy usage of the manufacturing processes forms an integral part of any discussion on fuel cells intended for commercialization. More the pity there are no examples in the literature. Even excluding ancillary costs such as lighting for workspaces, consumables used (e.g. distilled water, acetone, absorbent paper) and

materials used in creating jigging, a reasonable estimate of the costs to fabricate a functioning SOFC of my design is possible. The audit will be tackled on a per component basis. Note that in this case Pt is included both for completeness and as a useful benchmark for cathode costing. Energy costs were calculated based on the annual reporting by the UK Department for Business, Energy & Industrial Strategy of fuels and energy price for non-domestic consumers in the UK, including the climate change levy (accessed 19/05/2017). The average cost of electricity (excluding VAT) was £ 0.1088 per kWh. Given the high energy costs associated with many of the manufacturing process involved it is possible, even likely, that a lower rate might apply (for the extra large consumer bracket, i.e. with an annual consumption of >150,000 MWh, the price drops to £ 0.0976 per kWh). The mean was used in the calculations to represent a less-than-optimal scenario.

11.4.1 Anode

The most cost-effective way to procure the Ni tube for the anodes, given only rough initial estimates for the number required, is to buy them as 200 mm long sections in packs of 10 pieces for £ 243 from Goodfellow Ltd. (excluding VAT but including shipping). Each anode therefore costs £ 12.15.

The oxidation was carried out in atmospheric air, so this is not considered a material cost. The hydrogen is shared across the whole lab and sees frequent enough usage that short of purchasing local metering for the reduction furnace it did not prove practical to measure gas consumption. It is possible to estimate it, however. In all cases the flow rate of hydrogen was approximately 0.8 litres per minute, measured by a rotameter close to the furnace. Each gas cylinder contained 8,884.5 litres of pure hydrogen compressed to 45 litres at 200 bar and cost approximately £ 50 (BOC Ltd.). Tabulated below is the gas consumption and attendant approximate cost for the two reduction schemes. The process time is calculated by heating and cooling rate and dwell for that reduction temperature.

Reduction Temperature (°C)	1,000	400
Dwell Time (h)	0	15
Total Process Time (min)	1,013.33	1,220.00
Gas Consumption per run (litres)	810.67	976.00
Cost per anode (2 per run) (£)	2.28	2.75

Table 11-4. Reduction step gas consumption and monetary cost of anodes.

For oxidation it was not possible to measure power consumption because of the temperature control program that very rapidly pulsed power to the elements. Furthermore, in line power meters rated at the necessary voltage and up to 32 A are expensive. This increases approximately fourfold if data logging is required; which in this case would be required because of the way the furnace controller pulses power to the heating elements. Thus, an in line power meter was deemed too expensive for just

this project. The maximum voltage was 240 V and maximum current 22 A for a maximum power of 5.28 kVA.

For the reduction step an in line power meter was a feasible purchase although considerably more than those rated for household supply (13 A). It must be rated at 230 V and 16 A, however versions with data logging capabilities are once more four times more expensive at over £ 400 and deemed too expensive for use on just one project. *Ergo*, one without the data logging capability was purchased. Unfortunately, although the reduction furnace controller does not rapidly pulse power to the heating elements its duty cycle was such that accurate measurement was impossible; the furnace controller ramped currents up and then down in a saw-tooth duty cycle rapidly enough that it was not possible to take sufficiently accurate readings to mathematically recreate this and calculate power usage. However, by taking several approximate readings during ramping to temperature over many reduction runs it was possible to calculate a reasonable average max current usage observed. The same was also done for power required to maintain temperature during dwell. For reduction at both 1,000 °C (0 h dwell) and 400 °C (15 h dwell) an average maximum of 19.0 A was observed during heating and an average maximum of 1.1 A during the dwell. The steady state power consumption during heating is therefore 4.56 kVA; the steady state power is taken to be 264 VA.

Oxidation was carried out in batches of four, while reduction was limited by furnace size to just two samples at a time. Larger batches are not only possible but eminently desirable due to the great deal of power required in heating to the desired processing temperature.

11.4.2 Electrolyte

Each ingot of 7YSZ for use in Cranfield University's EB-PVD coater was priced at approximately £ 76.27 (118.34 USD) at the time. Prices have been on the rise with increasing cost of the raw materials. Each ingot is 35 mm in diameter, 200 mm long and weighs approximately 700 g. Two samples can be coated at once, for a total mass deposited of 110–150 mg (approximately 10 microns in thickness). However, there is a significant mass of zirconia deposited on all exposed surfaces, not just the samples. There is also some wastage because it is not possible to use the entire ingot due to gun geometry: approximately 50 mm. As such, each ingot is usable to deposit a total of approximately 400 microns (on up to two samples simultaneously). This is equivalent to about 40 electrolyte deposition runs (80 samples) as opposed to over 4,600 deposition runs as the mass alone would suggest; or an approximately 1% yield. The material efficiency of the process can be greatly increased by modifying the sample rotation mechanisms to hold two carousels with planetary gears rather than two samples. For research purposes the expense would be unnecessary, but it is a common technique for optimising material efficiency in commercial PVD.

The three-phase power supply rendered any attempts to measure power consumption impractical. The multiple, non-integrated (i.e. don't share the main power supply) pumps complicates assessing power utilization, as does the computer control system. However, needless to say, power consumption is high (so much so that B57 has its own substation to cope with the power demands of a multitude of coaters). An estimate could be reached using the peak power consumption of the primary elements: the electron gun (4 kW), the coater furnace (4 kW) and the diffusion pumps (two at 4 kW each). If we consider furnace insulation to require no additional power to maintain the chamber temperature of 850 °C (quite reasonable especially given the high vacuum) the furnace component is approximately 32 kWh. The electron gun is only in use for the 4 min and 6s deposition duration, for an approximate power consumption of 0.27 kWh. It is unclear without detailed study for how long the diffusion pumps operate at close to peak power but we may safely assume the power consumption to be no greater than approximately 64 kWh. The total power consumption per batch is therefore 96.27 kWh (2 samples per batch with current jigging) at a cost of £ 10.47.

11.4.3 Cathode

The coater was a highly modified Electrotech 840 with PLC (programmable logic controller) control by Cametrics Ltd. A Pt target for sputtering in conjunction with the equipment used cost £ 70,000 at the time of usage (99.95% purity). This type of Pt sputtering target is the standard for small sized internal magnetrons (such as the Teer Coatings one used by the coater). They are 178 mm × 78 mm × 4 mm (thickness) and weigh 1.19 kg. An average of 5.825 mg of Pt create each cathode (up to four can be coated simultaneously), or just £ 0.343 per cathode. However, this assumes 100% deposition efficiency, which is not the case. The deposition efficiency can be determined by weighing the target between depositions for a sufficient number of coating runs, a procedure that did not prove viable at the time because heavy use of the coater demanded minimum down time between deposition runs precluding de-mounting the target to weigh it. Deposition efficiency may be as low as ~1% (based on a line-of-sight deposition estimate), in which case each cathode would cost approximately £ 34.3. Should a costly material like platinum prove suitable by the expedient of ultrathin cathodes (50–500 nm) investigating and improving deposition efficiency assumes a critical importance. However, it is well known that in coaters with a large number of samples on suitable holders deposition efficiency is greatly improved, mitigating the concern once transitioned from laboratory scale fabrication to large scale manufacture.

Sputtering takes place under argon flowing at 275 sccm from gas bottles that contained 11,100 litres of Ar that cost £ 86.64 (BOC Ltd.); the actual cost for the project was considerably lower – £ 13.74 at university discounted rates. The gas consumption per run was 4.125 litres at a cost, based on the non-discounted price, of £ 0.032 per run (4 cathodes per run).

Once more the use of a three-phase power supply rendered attempts to measure power consumption impractical. Furthermore the sputtering coater has the same setup as the EB-PVD coater with the same power consumption complications. Sputtering uses far less power than EB-PVD, and 5 kW is a sound estimate (from private communications with Tony Gray). The power consumption per run is therefore approximately 1.25 kWh (£ 0.138).

11.4.4 Summary

One may reasonably consider the fuel cells fabricated throughout this project to cost approximately £ 15.73 ea. (1,000 °C reduction scheme) to £ 16.20 ea. (400 °C reduction scheme) in materials (including gases). The energy audit remains somewhat incomplete, though a fairly cogent conclusion may be drawn: energy costs are high on a processing step basis. The obvious optimization from a manufacturing standpoint is then to increase batch sizes as much as is practical. The required jigging for coaters will become highly complex as a result but the benefits outweigh increased complexity and expense of jigging.

12 Permeameter

The main objective of this part of the project is to measure the permeance of relevant gas mixes through the electrodes and the electrolyte as part of the fundamental characterization of this fuel cell design. A necessary sub-objective is the design and fabrication of a suitable instrument to accurately and precisely measure permeability of tubular samples including both a cell or chamber and sensor system. Ancillary to this is the design and implementation of a measurement procedure and a calibration/rig testing procedure.

12.1 Concept

Often the porosity and gas tightness of SOFC components will be discussed in the literature. This arises from the importance of having sufficient gas transport at the electrodes (requiring porosity) and the impermeability – or gas tightness – of the electrolyte to ensure fuel is consumed electrochemically rather than via combustion. However, it is my belief that measuring the porosity is somewhat unhelpful if not incorrect. The reasons are as follows: firstly, the porosity does not, in and of itself, offer any information on how much gas (or what flow or partial pressure) is actually available at the TPB or at the cathode-electrolyte interface for reaction or conduction. Secondly, measuring porosity by any technique has a non-negligible setback. For instance, if using image analysis or impedance techniques all porosity is included in the measurement yet only connected pores are relevant in SOFCs; using gas or mercury porosimetry often requires high pressure that may damage or destroy delicate structures and most importantly may be in no way representative of the actual gases being transported through the component.

A bit of lateral thinking soon reveals that it is in fact the permeability to the relevant gases that is of interest, not the porosity. What is needed therefore is an experiment that allows the measurement of gas permeance with great precision and the equipment to carry out such measurements. I wish to extend my gratitude here to Othman M. H. D, at the time working on his PhD at Imperial College (London), for his assistance in finding a suitable experiment and the associated equations. The permeameter described below (also referred to as the permeance rig) is based on the following relationship [Othman *et al.* 2010]:

$$J = \frac{Q \ln\left({}^{D_o}/_{D_i}\right)}{\pi L (D_o - D_i) \Delta P} \qquad (12.1)$$

Where:

J is the gas permeability [mol m^{-2} s^{-1} Pa^{-1}]
Q is the total permeation rate [mol s^{-1}]
D_o is the outer diameter of the tube [m]
D_i is the inner diameter of the tube [m]
L is the tube length [m]
ΔP is the partial pressure difference across the membrane [Pa]

The above equation was used to determine the gas permeation through a single layer structure anode made of a Ni-CGO composite [Othman *et al.* 2010]. In the cited work nitrogen was flowed through the anode, measuring the flow rate with a bubble flow meter. The anode tube was glued into a stainless steel sample holder with an epoxy resin (UKR-135 resin with UKH-136 hardener; UK Epoxy Resins, Lancashire, UK). The sample holder was then assembled into a cylinder of known internal volume (300 cm^3). The gas feed was at one end of the tube, and the permeate gas was collected at the shell side of the anode tube.

The gas tightness on the other hand is measured based on pressure change with time [Othman *et al.* 2010]. Once again the cited source employed nitrogen as the test gas. For the gas tightness measurement the pressure change with time of the tube is measured using a pressure gauge connected to the tube. The gas permeance is thus obtained based on the cylinder pressure change with time:

$$J = \frac{V}{RTA_m t} \ln\left(\frac{p_o - p_a}{p_t - p_a}\right) \qquad (12.2)$$

Where:

J is the permeance of the membrane [mol m^{-2} s^{-1} Pa^{-1}]
V is the volume of the test cylinder [m^3]
R is the gas constant [8.314 J mol^{-1} $°K^{-1}$]
T is the measured temperature [°K]
p_o is the initial measured pressure in the test cylinder (i.e. the sample) [Pa]
p_t is the final measured pressure in the test cylinder (i.e. the sample) [Pa]
p_a is the atmospheric pressure [Pa]
A_m is the membrane area [m^2], where $A_m = \frac{[2\pi L(R_o - R_i)]}{\ln\left({R_o}/{R_i}\right)}$, R_o is the outer radius of the tube [m], R_i is the inner radius of the tube [m], L is the tube length [m]
t is the time for the measurement [s]

Note that throughout this work permeance is not given a special symbol. It is a mass flux, symbol J, and labelled as such for consistency. P for permeance may appear in some sources, such as [Othman *et al.* 2010].

A positive sign signifies that the test cylinder is draining (loosing gas) whereas a negative sign indicates filling (the test cylinder is being pressurised). As such, all gas fluxes (i.e. permeances) for the experiments carried out here will be positive values. This can be thought of as the same sort of sign convention as used in stress calculations where a positive sign denotes tension in the direction of the applied force and a negative one compression.

12.2 Design

A simple schematic of the permeameter is shown below. Notice that this rig has the added features of being readily expandable by adding more pressure gauges (preferably using the installed DC-DC converters) and there is plenty of power available from the switch mode power supply to add more DC-DC converters for additional voltages as needed, or integrate a panel meter rather than use an external one as was opted for here (a precise desktop meter was available). The second pressure sensor with a higher pressure range enables accurate gas tightness measurements of the electrolyte to be made. The reason a different pressure transducer is required is that, as with most transducers, a larger range reduces the accuracy and often the sensitivity also. Therefore, for the permeance measurements where one would expect a relatively low pressure difference due to the permeability of the material, a sensor with a very small range allows for great accuracy – ideal for permeance. Where it is gas tightness that is of interest a larger pressure differential is to be expected inherently limiting the accuracy of the transducer used. A differential pressure sensor is used in each case obviating the need to separately measure the atmospheric pressure.

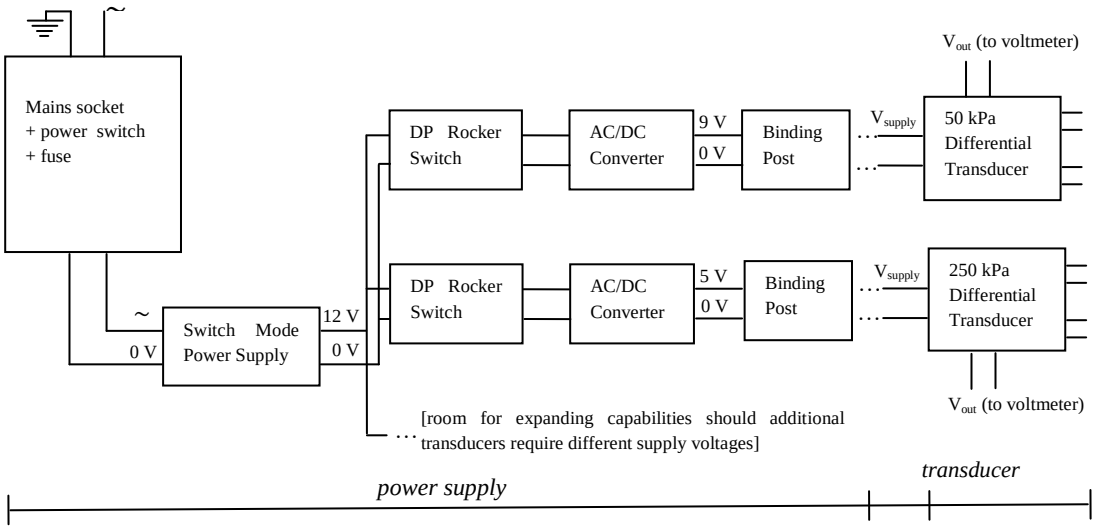

Figure 12-1. Schematic of permeameter electronics (power supply and transducers).

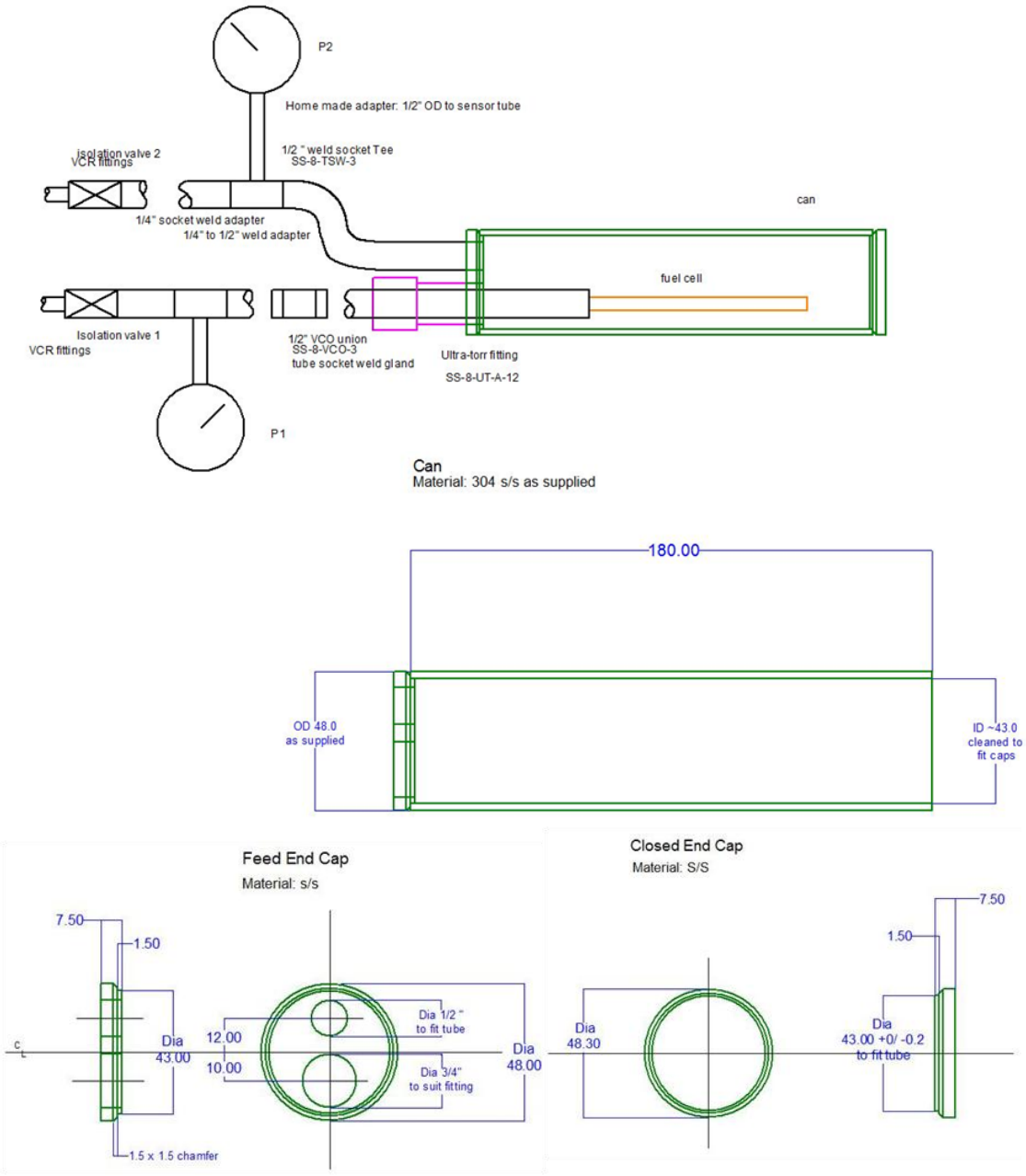

Figure 12-2. Schematic of permeameter cell 'can'. All dimensions in mm. The can drawings were created by Tim Pryor using the DeltaCAD free software and edited here for clarity. A simplified rendition of the pipework is shown here; the complete schematic can be found in Appendix K: Permeameter SOP. While not shown in these schematics the cell is capped with a thin 1 cm long 316 SS end cap affixed with resin covering that portion that would remain uncoated by 7YSZ or Pt.

What follows is a listing of all the components used and stock numbers where available and a set of photographs showing the assembled power supply and transducer elements with the necessary wiring and filter circuitry.

Component (Quantity)	Manufacturer and Part Number [Supplier and Stock Number]	Notes
Sensors		
250 kPa differential pressure sensor (for gas tightness) (1)	Freescale Semiconductor MPX4250DP [RS 719-1077]	Supply 5.1 V, 53.5 mW_{max}
50 kPa differential pressure sensor (for gas permeance) (1)	Freescale Semiconductor MPX2050DP [RS 719-1033]	Supply 10 V, 96 mW_{max}
1.0 µF capacitor (any type) (1)	[Maplin N24CN]	Rated for 50 V
0.01 µF capacitor (any type) (1)	[Maplin N15CN]	Rated for 63 V
470 pF capacitor (any type) (1)	[Maplin N02CN]	Rated for 100 V
Cable gland (4)		
80x40x20 mm Enclosure (2)	Hammond 1551 KBK [Onecall 3536439]	ABS, black
3.2 mm bored flexible tubing (15 m total length)	Tygon R3603 [Fisher Scientific TWT-700-070LAAC00007]	
Strip Board	Vero Technologies 01-3939 [RS 433-826]	Two pieces cut to fit sensor enclosures.
Mains cable 8 m (secured in cable glands)		Two 2 m lengths per sensor enclosure.
Spade connector (4)		Two per sensor enclosure.
Banana connector (4)		Two per sensor enclosure.
Power Supply		
Switch Mode Power Supply (12 V_{DC}, 25 W) (1)	RS RS-25-12 [RS 621-0578]	
DC-DC Converter (12 to 5 V) (1)	Murata Power Solutions NDL1205SC [RS 689-4854]	
DC-DC Converter (12 to 9 V) (1)	Murata Power Solutions MEV351209SC [RS 689-5740]	
2.2 µF capacitor (ceramic) (1)		Rated for 25V, for MEV351209SC
22 µH inductor (1)		Rated for 350 mA, Resonant Frequency >20 MHz, for MEV351209SC
100 µF capacitor (any type) (2)	[Maplin KQ70M]	Rated for 25V, for NDL1205SC
DPST on-off rocker switch (2)	Arcoelectric C1250APAAD [RS 811-800]	Two-position double pole switch
Chassis plug mains rated switched and fused – horizontal with red neon	Bulgin [RS 211-1001]	Double pole switch
Binding post (black) (2)	Abbatron 1517-103B [RS 2508937124]	Gold plated
Binding post (red) (2)	Abbatron 1517-102R [RS 2508937118]	Gold plated
220x125x95 mm Instrument case (1)	Hammond 513-0900 [RS 232-926]	Painted mild steel

Table 12-1. Permeameter components.

12.3 Assembly, Testing and Calibration

In all cases the circuits needed were fairly straightforward and carried out making frequent reference to the relevant datasheets. A conventional circuit diagram was not deemed necessary.

Figure 12-3. Photographs of the assembled power supply and sensors.

Finally we come to the permeametry cell 'can' itself. This was made in house out of stainless steel (alloy not known but either 304 or 316, as such it is unimportant) with all joints welded to ensure a good seal. Figure 12-2. shows the design and below are photographs of the test cell (Figure 12-4.). While it can be operated either way the

system is designed for the pressurised port to be that holding the porous tube as opposed to pressurizing the test cell chamber. Also shown (in Figure 12-5.) is a schematic of the permeameter setup showing valves, pressure take-offs and connections, from the SOP developed for the rig.

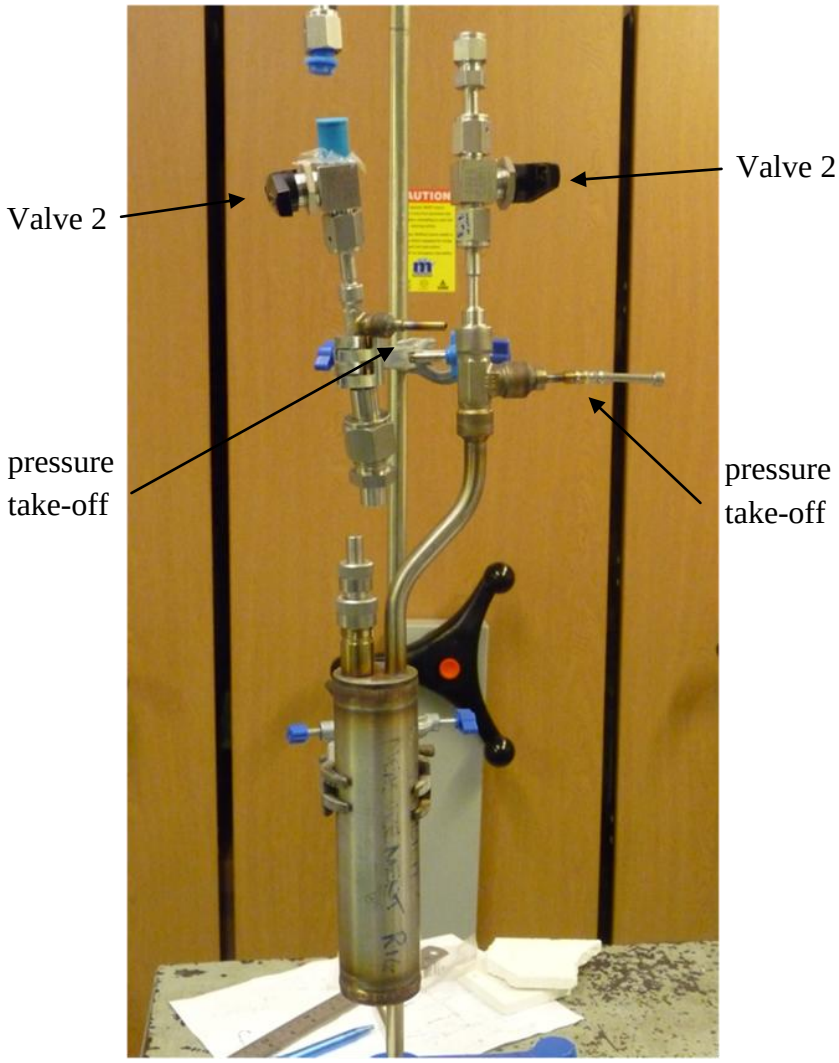

Figure 12-4. Photograph of the permeameter cell 'can'. Note the absence of a sample between threaded fittings just above the chamber itself.

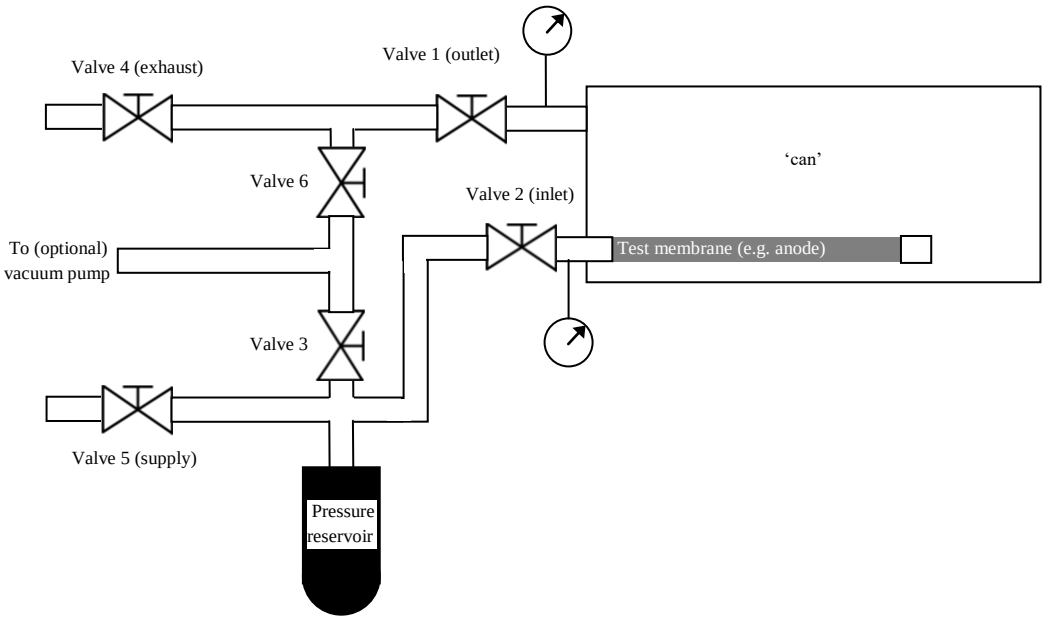

Figure 12-5. Schematic of the permeameter setup showing valves, pressure take-offs and connections (adapted from Permeameter SOP).

The 'can' has an internal volume of 251.58 cc measured with a 60 mm length of SS rod, 3/8" OD plugging the aperture for the tubular membrane (for these experiments this is the fuel cell in varying stages of completion), measured from the outside edge of the fitting.

Each sample is glued into the necessary SS fittings with epoxy resin (Araldite) and connected to the rest of the rig using fittings that integrate high grade seals (Swagelok fittings, mostly stainless steel with some brass; vacuum rated because these offer the best possible sealing and can withstand a few bar of pressure). These seals are a threaded body with rubber O-ring and the same set of fittings was used throughout. The photographs below (Figure 12-6.) show all fittings along with a sample as it is assembled ready for loading into the main portion of the rig.

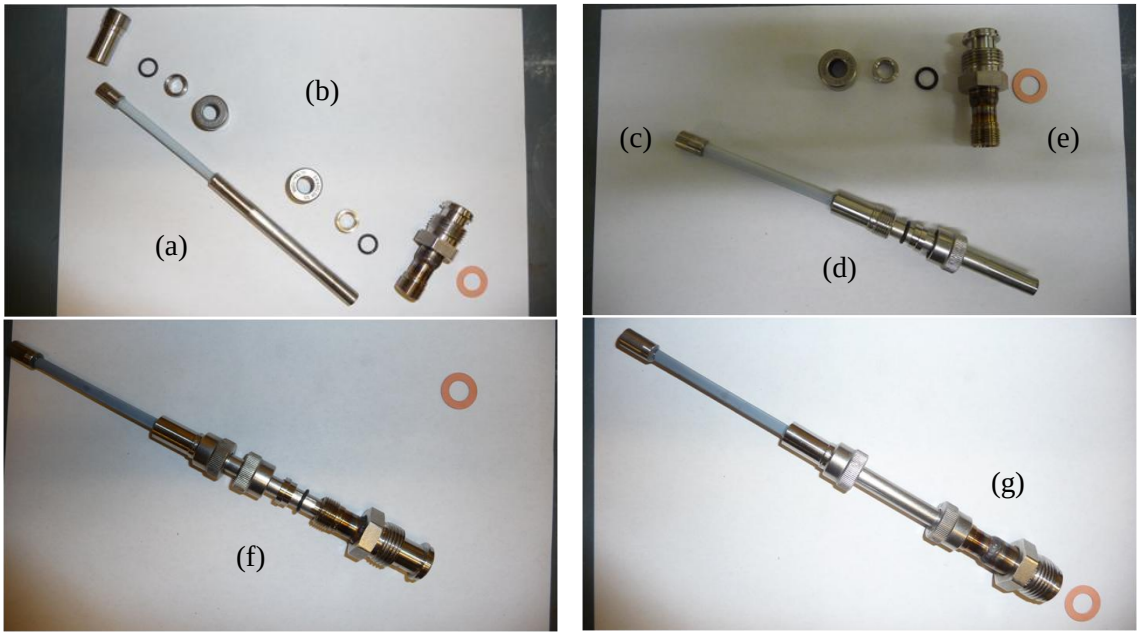

Figure 12-6. Permeameter rig sample and fittings showing assembly prior to loading into rig. (a) cell assembled with end epoxy into permeametry fittings (b) commercial fittings to create seal with permeameter (c) end cap (d) components for lower seal (with 'can') slipped over cell fittings into place (e) components for upper seal (with pipe work) (f) lower seal finished and upper seal components slipped over top end of cell fittings (g) upper seal finished and ready to affix to pipe work with threaded fitting and copper O-ring.

The copper O-ring pictured seals the end fitting into the Permeameter. It is compressed by tightening the nut on the barrel onto the corresponding threaded fitting on the rig, forming a gas tight connection. The complete setup is pictured in Figure 12-7., below, during one of the measurements.

Figure 12-7. Permeameter in use. NB the pressure reading is in Volts, directly from the sensor. The transfer function included in the relevant sensor datasheet was used to convert these into pressures in kPa in an Excel spreadsheet.

A brief test regime to proof and calibrate the rig was carried out before the first measurements were made following standard procedures for testing pressure vessels. The results of the initial calibration test with a dummy (impermeable) Ni tube of the same sort used to create the anode instead of a porous tube (anode, anode and electrolyte, etc) are shown alongside the experimental results. These values set the baseline for any system leaks – anything above these values represents actual gas permeances through the porous tubes under test.

12.4 Measurement Methodology

The samples were securely attached to the fittings and permeameter leak tested prior to taking any measurements. After a purge step the supply valve was opened and the entire permeameter pressurised to the desired pressure. The supply valve was then closed,

valves 2 and 3 opened then and valve 4 opened to vent the exhaust line. The pressure is allowed to drop to atmospheric then valve 2 was opened and timer started simultaneously to begin the test. The pressure drop between immediately prior to opening valve 2 and just before the chamber reaches atmospheric gives the pressure-drop-over-time permeametry. The second measurement, taken before the pressures have completely equalised, allows calculation of the volume of gas passed to be determined. After measurements valves 1, 2 and 4 are open and valves 3, 5 and the supply valve are closed. The system then undergoes another purge using argon. Appendix K: Permeameter SOP contains greater detail, including alternative uses for the permeametry rig and the hydraulic pressure testing procedure to ensure the rig was safe for operation.

12.5 Permeametry Experiments

The permeabilities of particular interest are the following: hydrogen through anode; water vapour through anode; oxygen through cathode; hydrogen through the electrolyte (deleterious so minimal permeance is desired). The gas mixes utilised mean the following experiments were carried out (with repeats for better quantification): 100 vol% H_2 through anode; 5 vol.% H_2 balance Ar through anode; 100 vol.% He through anode (intended to later replace pure hydrogen in similar experiments for improved safety if behaviour proves sufficiently similar); water vapour through anode; air mix (dried compressed air) through anode (oxygen leaking into the anode rather than being transported as ions through the electrolyte would deleteriously affect performance); 5 vol.% H_2 balance Ar through electrolyte; 100 vol.% H_2 through electrolyte or 100 vol.% He through electrolyte (depending whether the anode results demonstrate they are equivalent). The volume fractions given exclude impurities – which were a few 100 ppm at most. Some modelling will be necessary since it will not be possible to test on a free standing electrolyte because it is far too fragile.

There were no measurements conducted for the cathode. This project did not seek an improved cathode since it is an area that throughout the project was under extensive study elsewhere. Of course, in order to test the electrochemical performance and power output of the fuel cell a cathode was necessary. As described in detail elsewhere a conventional (though not optimal from an economic standpoint) Pt cathode was utilised. Therefore, measuring permeance through the cathode was of limited interest – limited to usage in modelling – and therefore left to further work.

It did not prove feasible to conduct the measurements with water vapour. These would be far too time consuming because to ensure the accuracy of subsequent measurements with other gases (including repeats with water vapour) the rig would need to be partially disassembled and dried between each measurement. The drying would involve a lengthy

(preferably overnight) period in a drying cabinet and/or under vacuum. This procedure would of course need to be carried out for each sample. Even at the most efficient (i.e. leaving the water vapour measurements for last ensuring only one such drying procedure is needed per sample with an additional one before setting up the next sample) this would mean nine overnight drying periods. Unfortunately repeated lengthy delays in other areas not directly associated with this project, which were both unexpected and unforeseeable, contributed to severely delaying the construction of the permeametry rig (approximately one year all told) leaving barely enough time to carry out any permeametry at all. Furthermore, at any given time the measurement was made there will be slight variations in the atmospheric pressure, and therefore a different vapour pressure so each water vapour measurement will contain a different quantity of water vapour when the carrier gas passes through the water bubbler. No practical solution to this was found. In addition, accurate permeance of water vapour would be best done at the temperatures of interest since unlike the other gasses treating it as an ideal gas to calculate behaviour at temperature is not as robust. Such elevated temperatures are well beyond the measurement range of economical pressure sensors with the sort of accuracy and precision desired as well as considerably complicating sealing the rig (see section 13.2.5. for how this was solved for the fuel cell testing rig).

The samples were the full size of the fuel cells; including using the 10 mm at each end for sealing into the test rig mirroring conditions under operation in the fuel cell test rig. This left an 80 mm long segment of the tube through which gases permeate.

For the anode permeametry samples were oxidised at 1,100 °C for 42 h prior to reduction (see chapter 8 sections 8.3–8.7). In order to fully explore the effect of different reduction schemes samples were reduced at the two extremes explored in the reduction chapter (refer to chapter 8 sections 8.10–8.13): low temperature long dwell (400 °C, 15 h, 97% reduced) and high temperature short dwell (1,000 °C, no dwell – ramp only, 100% reduced). Of course both schemes produced samples one may reasonably consider completely reduced. Exploring the parameter space in this way is another type of optimization. In the reduction work the focus was on complete reduction and optimization for manufacture; the focus here was on measuring actual gas permeance as part of characterising the performance of this fuel cell design and optimising for performance (high permeance is desirable through the electrodes and low permeance is desirable through the electrolyte). Combining the knowledge gained will reveal the best overall combination of processing parameters to create anodes optimised for both production and performance. Samples were weighed before and after oxidation and after reduction. This ensures the result of the process is in line with prior findings. It is a simple measure that can be adopted to mass manufacture.

The electrolyte is too fragile to be used by itself for permeametry, so there are no measurements of stand-alone gas permeances through the electrolyte. Instead

measurements were carried out on the combined anode and electrolyte (often referred to as an anode-electrolyte complex, or AEC, in the literature). These experiments were carried out after those on the anode as it was necessary to determine which anode reduction scheme resulted in a more permeable component. Thus, the electrolyte was deposited on anodes reduced at 1,000 °C with no dwell (see section 12.7). The nominal electrolyte deposition parameters were in accordance with the conclusions of chapter 9 (section 9.7). After the initial results with (nominally) 10 μm thick electrolytes two further sets of measurements were made with thicker electrolytes (50 μm and 150 μm).

The most time- and material-efficient way of carrying out the requisite measurements combined with necessary purging cycles and safety precautions (refer to Appendix K: Permeameter SOP) is to run them in the following order for each sample: a sample is loaded in to the rig and all the measurements are taken, including repeats, before switching to another sample and repeating the process. The order for the measurements is:

1. Ar
2. H_2
3. Ar (purge cycle and repeat of the Ar measurement)
4. 5% H_2 mix
5. Ar (purge cycle)
6. He
7. Ar (purge cycle)
8. Air mix
9. Ar (purge cycle)
10. H_2 (repeat of the H_2 measurement)
11. Ar (purge cycle)
12. 5% H_2 mix (repeat of the 5% H_2 measurement)
13. Ar (purge cycle)
14. He (repeat of the He measurement)
15. Ar (purge cycle)
16. Air mix (repeat of the air mix measurement)
17. Ar (purge cycle)

This results in 2 repeat measurements with each gas for every sample. Additionally carrying out this measurement scheme for two nominally identical samples indicates whether there may be any reproducibility issues (requiring further measurements to be carried out). The one exception was the blank cell; in this case 3 repeat measurements were made but there was only one sample (the only advantage of a second would be testing the reproducibility of the epoxy resin).

The times recorded are not separate dwells but cumulative time from measurement start. In other words, each pressure measurement was a snapshot in time, with the time at which that measurement was recorded (as well as ambient temperature) being recorded also. Measurement was begun from 1 s. The data point at 1 s is the starting pressure for the measurement; picked because it is the limiting resolution of the time measurements.

12.6 Anode

The first set of measurements dealt with anodes, testing among other things the resulting permeance (the gas transport performance) of anodes made at the extremes tested for manufacture; that is those reduced at 1,000 °C (no dwell) and those at 400 °C (15 h dwell).

12.6.1 Results & Discussion

Table 12-3. summarises the results of the measurements on the anodes, recording ambient temperatures at the time of each measurement, time under pressure, and differential pressures (the difference of sample pressure and atmospheric pressure) for each time interval for each gas mixture of interest. The calculated permeances through the membranes are tabulated in Table 12-4. Also included are the fabrication parameters of the samples (Table 12-2.). Errors estimated using linear approximation by partial differentiation where an equation was used [Error Propagation article accessed 2013], or based purely on measurement equipment error otherwise. In all cases errors represent the worst case scenario.

Note that before carrying out any measurements, including the baseline with the dummy cell, the chamber itself was leak tested. No leak was detected over 5 days under pressure with periodic measurements. A shorter leak test (overnight) was carried out after each sample change.

Sample	**m_{Ni} (mg)** ±1 mg	**m_{Ni+NiO} (mg)** ±1 mg	**m_{gain} (mg)** ±2 mg	**Mass fraction oxidised** ±0.0005	**$\theta_{reduced}$ (°C)**	**$t_{reduced}$ (h)** ±1 s	**$m_{reduced}$ (mg)** ±1 mg	**m_{loss} (mg)** ±2 mg	**Mass fraction reduced** ±0.0042
A.01	2,008.9	2,556.2	547.3	1.000	1,000	ramp	2,009.6	546.6	0.999
A.02	2,013.9	2,562.5	548.6	1.000	1,000	ramp	2,014.5	548.0	0.999
A.03	2,020.9	2,568.2	547.3	0.999	400	15	2,038.8	529.4	0.967
A.04	2,015.3	2,564.5	549.2	1.000	400	15	2,033.9	530.6	0.966

Table 12-2. Permeameter sample fabrication parameters.

The fabrication data presented in Table 12-2. was included to emphasize the reproducibility of the fabrication process. Compare these results with those presented in section 8.12.1 and section 11.3. The samples utilised for permeametry are therefore representative of anodes fabricated by each of the two reduction schemes.

Gas	Ar		H_2		He		5 vol.%H_2		Air mix	
Sample solid Ni tube										
t_0 [s] ± 1 s	0	0	0	0	0	0	0	0	0	0
$p^{0,Norm}$ [kPa] ± 0.064 kPa	199.9*	199.9	153.2*	154.4	200.6	147.3*	102.6	113.6	98.0	120.5
t_1 [s] ± 1 s	11,520 (3 h 12 min)	6,711,100 (186 h 25 min)	7,200 (2 h)	259,800 (72 h 10 min)	7,200 (2 h)	336,000 (93 h 20 min)	7,200 (2 h)	498,300 (138 h 25 min)	7,200 (2 h)	148,980 (41 h 23 min)
$p^{t1,Norm}$ [kPa] ± 0.064 kPa	200.2*	197.8	153.2*	154.9	201.0	147.0*	103.0	112.4	98.3	119.4
Sample A.01										
t_0 [s] ± 1 s	0	0	0	0	0	0	0	0	0	0
$p^{0,Norm}$ [kPa] ± 0.064 kPa	100.5	100.8	101.8	100.4	100.6	100.6	100.4	100.5	100.3	100.3
t_1 [s] ± 1 s	30	30	30	30	30	30	30	30	30	30
$p^{t1,Norm}$ [kPa] ± 0.064 kPa	30.39	30.44	13.19	11.88	19.80	12.58	49.97	32.19	23.45	26.02
t_2 [s] ± 1 s	60	60	60	60	60	60	60	60	60	60
$p^{t2,Norm}$ [kPa] ± 0.064 kPa	8.575	8.518	0.543	0.380	1.845	0.108	15.468	8.564	4.885	5.041
t_3 [s] ± 1 s	129	131	87	84	100	78	143	131	111	140
$p^{t3,Norm}$ [kPa] ± 0.064 kPa	-0.326	-0.326	-0.380	-0.380	-0.326	-0.325	-0.326	-0.325	-0.380	-0.379
Sample A.02										
t_0 [s] ± 1 s	0	0	0	0	0	0	0	0	0	0
$p^{0,Norm}$ [kPa] ± 0.064 kPa	100.2	100.6	100.7	100.5	100.3	100.3	100.5	100.6	100.1	100.1
t_1 [s] ± 1 s	30	30	30	30	30	30	30	30	30	30
$p^{t1,Norm}$ [kPa] ± 0.064 kPa	45.52	47.04	29.13	30.36	36.59	36.44	46.91	47.31	42.53	44.90
t_2 [s] ± 1 s	60	60	60	60	60	60	60	60	60	60
$p^{t2,Norm}$ [kPa] ± 0.064 kPa	23.39	23.44	9.81	9.36	14.45	14.02	23.92	23.87	19.26	20.63
t_3 [s] ± 1 s	320	307	210	189	228	225	287	285	235	252
$p^{t3,Norm}$ [kPa] ± 0.064 kPa	-0.325	-0.326	-0.326	-0.325	-0.325	-0.325	-0.325	-0.325	-0.325	-0.325
Sample A.03										
t_0 [s] ± 1 s	0	0	0	0	0	0	0	0	0	0
$p^{0,Norm}$ [kPa] ± 0.064 kPa	100.3	99.76	100.2	99.63	99.54	99.83	99.96	100.8	100.5	100.6
t_1 [s] ± 1 s	30	30	30	30	30	30	30	30	30	30

Gas	**Ar**		**H_2**		**He**		**5 vol.%H_2**		**Air mix**	
$p^{t1,Norm}$ [kPa] ± 0.064 kPa	98.09	98.30	94.80	93.07	95.78	95.42	97.70	98.58	97.99	97.91
t_2 [s] ± 1 s	60	60	60	60	60	60	60	60	60	60
$p^{t2,Norm}$ [kPa] ± 0.064 kPa	96.58	96.02	91.07	87.56	92.73	91.86	96.16	97.11	96.31	96.27
t_3 [s] ± 1 s	300	300	300	300	300	300	300	300	300	300
$p^{t3,Norm}$ [kPa] ± 0.064 kPa	85.95	85.34	68.65	53.33	71.59	62.49	85.17	86.03	83.94	83.92
t_4 [s] ± 1 s	600	600	600	600	600	600	600	600	600	600
$p^{t4,Norm}$ [kPa] ± 0.064 kPa	74.15	73.53	50.48	28.83	52.42	46.42	73.10	73.95	70.69	70.68
t_5 [s] ± 1 s	3600	3600	3600	3600	3600	3600	3600	3600	3600	3600
$p^{t5,Norm}$ [kPa] ± 0.064 kPa	16.78	16.14	21.26	-0.214	2.086	0.966	15.56	16.76	12.61	12.91
t_6 [s] ± 1 s	13,663 (3 h 47 min 43 s)	15,254 (4 h 14 min 14 s)	8,567 (2 h 22 min 47 s)	3,807 (1 h 3 min 27 s)	7,449 (2 h 4 min 9 s)	6,932 (1 h 55 min 32 s)	11,471 (3 h 11 min 11 s)	15,369 (4 h 16 min 9 s)	12,056 (3 h 20 min 56 s)	12,772 (3 h 32 min 52 s)
$p^{t6,Norm}$ [kPa] ± 0.064 kPa	-0.214	-0.215	-0.268	-0.267	-0.267	-0.268	0.107	-0.162	-0.161	-0.161
Sample A.04										
t_0 [s] ± 1 s	0	0	0	0	0	0	0	0	0	0
$p^{0,Norm}$ [kPa] ± 0.064 kPa	100.2	100.5	100.7	100.9	101.3	101.8	101.4	100.9	101.2	101.5
t_1 [s] ± 1 s	30	30	30	30	30	30	30	30	30	30
$p^{t1,Norm}$ [kPa] ± 0.064 kPa	97.90	98.52	95.61	96.12	96.92	97.63	98.03	98.55	98.48	98.85
t_2 [s] ± 1 s	60	60	60	60	60	60	60	60	60	60
$p^{t2,Norm}$ [kPa] ± 0.064 kPa	96.43	96.95	92.11	92.80	93.65	94.07	97.38	96.885	96.60	97.117
t_3 [s] ± 1 s	300	300	300	300	300	300	300	300	300	300
$p^{t3,Norm}$ [kPa] ± 0.064 kPa	85.30	88.20	69.32	70.96	72.33	72.92	85.70	85.17	83.72	84.21
t_4 [s] ± 1 s	600	600	600	600	600	600	600	600	600	600
$p^{t4,Norm}$ [kPa] ± 0.064 kPa	73.26	73.01	50.26	52.17	53.46	54.03	73.00	72.83	70.06	70.48
t_5 [s] ± 1 s	3600	3600	3600	3600	3600	3600	3600	3600	3600	3600
$p^{t5,Norm}$ [kPa] ± 0.064 kPa	15.44	15.35	2.007	2.396	2.663	2.842	15.08	14.77	11.68	11.60
t_6 [s] ± 1 s	14,058 (3 h 54 min 18 s)	13,532 (3 h 45 min 32 s)	6,143 (1 h 42 min 23 s)	7,712 (2 h 8 min 32 s)	7,389 (2 h 3 min 9 s)	7,724 (2 h 8 min 44 s)	10,605 (2 h 56 min 45 s)	7,452 (2 h 4 min 12 s)	9,128 (2 h 32 min 8 s)	9,094 (2 h 31 min 34 s)
$p^{t6,Norm}$ [kPa] ± 0.064 kPa	-0.270	-0.271	-0.271	-0.327	-0.272	-0.273	0.109[§]	-0.270	-0.271	-0.272

Table 12-3. Tabulated pressure measurements in relevant gas mixes with pressures normalised to 20 °C. Repeat measurements are shown in adjacent columns for the same gas. *Uncertain temperature readings resulted from a loose wire. [§]Sample was draining much slower than expected.

In addition to the calculated gas fluxes (shown later in Table 12-4.) the pressure drop over time is a useful tool in understanding gas permeation. The pressure drop was plotted against time for each pair of repeats, a different graph for every combination of gas type and sample, including the solid Ni tubes. Figure 12-8. shows two such plots (of a total of 25; all shown in Appendix L: All Permeametry Plots).

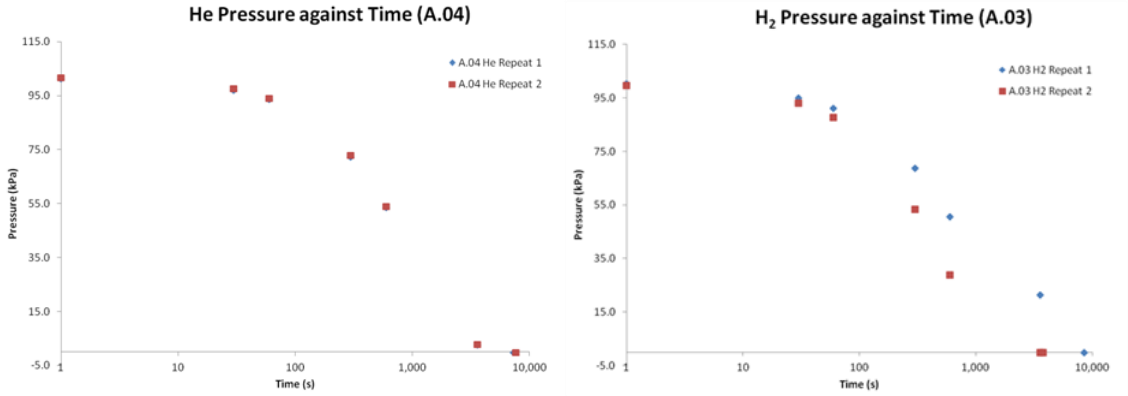

Figure 12-8. Pressure drop against time showing repeat variance for the same sample for each gas. Two exemplars are shown of a total of 25 plots (see Appendix L: All Permeametry Plots). The errors (based on measurement error) are too small to be visible.

The plot on the left is a typical exemplar from the set of graphs, while the plot on the right shows the largest scatter in the data among the 25 graphs. Notice the clear trends even with the largest scatter. In almost all instances the repeat measurements show excellent repeatability, being virtually indistinguishable. However, where there is scatter no obvious explanation presents itself: the error calculated according to the sensor manufacturer's error analysis does not account for it. The error is calculated via an equation on the sensor's datasheet that is strongly dependent on the supply voltage. Yet, even modifying the calculated error to present a worst case with a large error (20 %) on the supply voltage does not fully account for the scatter noted, which is up to ±15.309 kPa at the maximum. There is a possible contribution by the temperature measurement error that factors into the normalisation of the data to 20 °C, though this will also be rather small. Likely the explanation is in the manner time was recorded: manually with a digital stopwatch. Recording temperature, time and pressure at once may lead to greater errors than the measurement error of each individually. As these are pressure-drop-over-time experiments the time taken to record data may lead to differing pressure readings, more different than measurement error alone would suggest. It is unfortunate that an automated, or semi-automated, system was not deemed cost-effective for data collection. There is an additional potential source of error: manufacturing variance.

Stochastic variation during manufacture of the anodes, particularly the reduction step, may contribute significantly to the error. A small change in the surface area available for adsorption (prior to gas transport) and similarly desorption of the permeating gas species will impact the gas flux. This also applies (perhaps even more so) to the electrolyte deposition step in creating anode-electrolyte complexes for permeametry, discussed later.

Despite this, the overwhelming majority of the data suggests repeatability is very good. Furthermore, recall that A.01 and A.02 were made by one reduction scheme while A.03 and A.04 by another. Comparison of the results with the same reduction scheme shows they are also very similar; suggesting reproducibility of the results is also excellent. One may then reasonably treat the four data points for each time interval (two samples with two repeats each) as a single set and plot the mean. Essentially, the repeats are acting as stand-ins in lieu of additional samples. Results are so similar, however, that it was deemed more informative to present those graphs with the mean of repeat measurements but all samples are shown separately to graphically demonstrate the reproducibility. See Figure 12-9. (below).

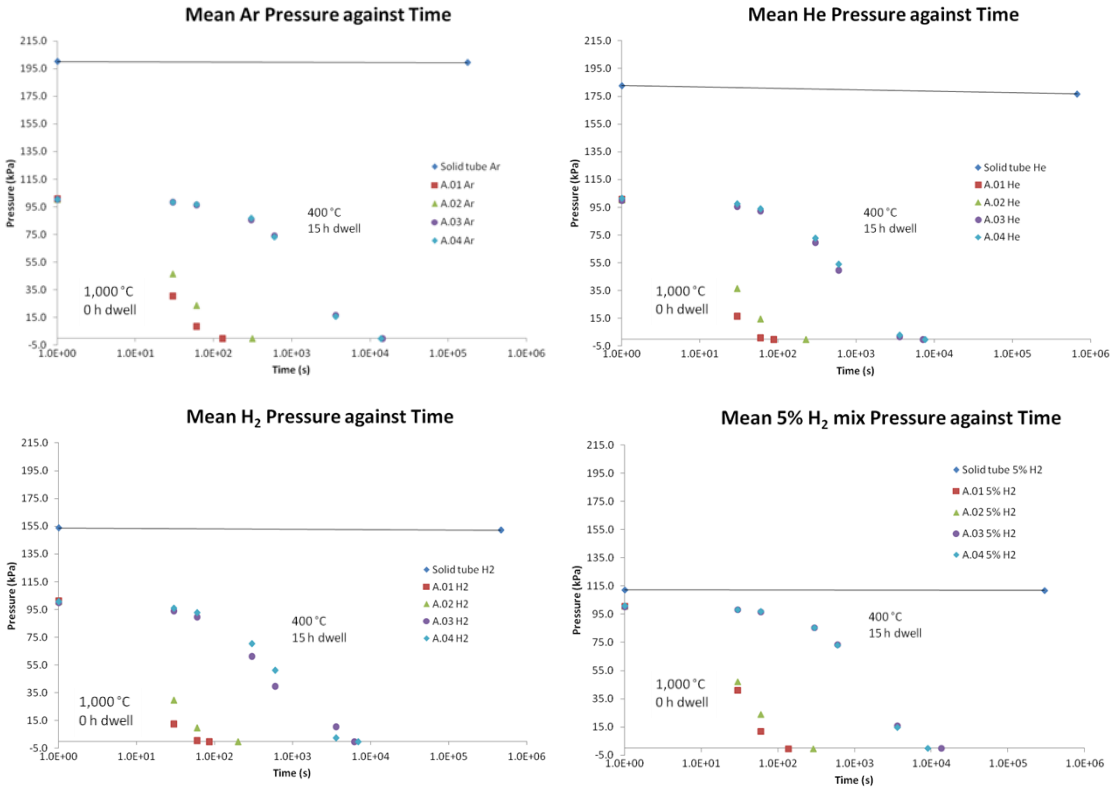

Figure 12-9. Pressure drop against time for all gas mixes (mean of repeat measurements for all samples). The reduction schemes are labelled and the solid Ni tube given a linear fit to more clearly show the pressure drop limits. Note the different mathematical models for pressure drop with time that fit the two reduction schemes.

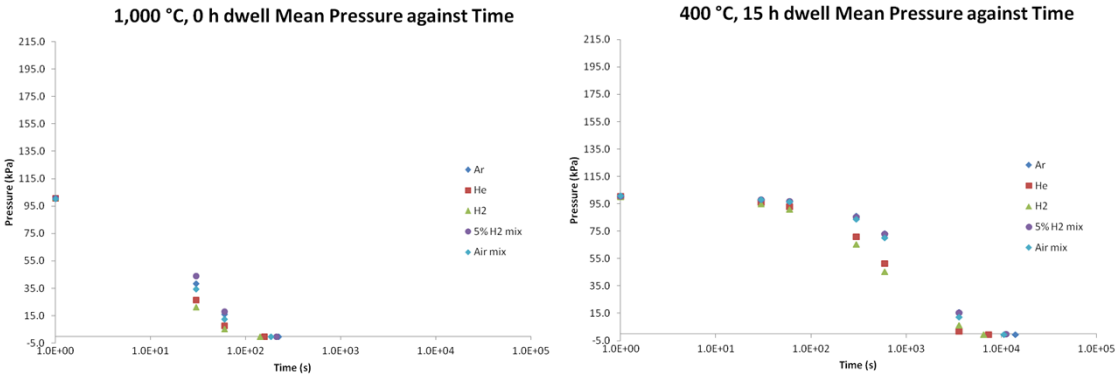

Figure 12-10. Pressure drop against time for all gas mixes (mean of all four measurements pre anode type) divided by reduction scheme. Note the different mathematical models for pressure drop with time that fit the two reduction schemes.

From the plots of mean pressure over time, where each of the five plots are arranged to show all samples of a single gas, it is clear that the two manufacturing routes not only result in two very different pressure drops (and permeances) but also that they conform to different mathematical models. Furthermore, while those samples reduced at 1,000 °C with no dwell (A.01 and A.02) show some variance in the pressure data there is little to no such variance in the case of the pair reduced at 400 °C for 25 h. Broadly we may consider gas transport to be in three phases: physisorption onto the membrane surface, diffusional transport through the membrane and desorption. The "membrane" in this case is the porous anode or anode-electrolyte complex. On the graphs this is visible as an initial plateau, a middle linear segment, and a final plateau when it tails off.

By plotting the same data but arranged such that each plot shows all gases for a single sample a clear trend appears, with Ar, 5% H_2 (balance Ar) and the air mix draining slower than the others, as expected. Of note is that this trend is only visible where scatter is greater (at the later times), otherwise the data is clustered very closely together. It appears as though the hydrogen in the 5% H_2 (balance Ar) mix is impeding the transport of Ar resulting in a slower pressure drop with time than pure Ar or the air mix. This is either because a hydroxyl-type compound is forming or the H_2 in the 5% H_2 mix physisorbs onto the surface more rapidly than Ar, occupying the physical space Ar requires to do the same. All in all this indicates that the anodes are exceedingly permeable but the microstructure offers some resistance, more in the case of those samples reduced at the lower temperature.

The same methodology applied to analysis of the pressure drop with time data was adopted for the calculated permeances so the steps shown for the pressure drop analysis will not be repeated. The following pair of graphs show that the 5% H_2 gas mix behaved somewhat differently to the other gases. Some microstructural effect (a difference between the two samples due to stochastic variations in manufacture) results in about half an order of magnitude difference in permeance. As the effect was only observed with this gas mix it is likely something to do with the nature of the mixture containing a small and light gas and a relatively larger and far heavier one. Both plots show that the gas permeance dependence on weight (atomic or molecular) is relatively weak, but very clearly exponential (linear behaviour with a logarithmic ordinate). The phenomenon was most clearly visible for the lower temperature reduction scheme; for the higher temperature reduction scheme the difference is insignificant.

Gas	Mean Permeance ±s ($molm^{-2}s^{-1}Pa^{-1}$)		Mean by reduction scheme ±s
Sample	*solid Ni tube*		
Ar	$1.459\times^{-10}$ ±$2.611\times^{-10}$		*n/a*
H_2	$4.526\times^{-11}$ ±$7.840\times^{-11}$		*n/a*
He	$1.173\times^{-11}$ ±$1.726\times^{-11}$		*n/a*
5 vol.%H_2	$5.327\times^{-12}$ ±$9.226\times^{-12}$		*n/a*
Air mix	$1.855\times^{-11}$ ±$3.213\times^{-11}$		*n/a*
Sample	*A.01*	*A.02*	*1,000 °C, ramp*
Ar	$3.490\times^{-5}$ ±$4.862\times^{-8}$	$2.021\times^{-5}$ ±$4.915\times^{-7}$	$2.755\times^{-5}$ ±$8.485\times^{-6}$
H_2	$7.616\times^{-5}$ ±$3.056\times^{-6}$	$3.239\times^{-5}$ ±$2.731\times^{-7}$	$5.428\times^{-5}$ ±$2.534\times^{-5}$
He	$7.564\times^{-5}$ ±$2.714\times^{-5}$	$2.663\times^{-5}$ ±$4.474\times^{-7}$	$5.113\times^{-5}$ ±$3.234\times^{-5}$
5 vol.%H_2	$3.034\times^{-5}$ ±$5.503\times^{-6}$	$1.952\times^{-5}$ ±$1.117\times^{-7}$	$2.493\times^{-5}$ ±$7.008\times^{-6}$
Air mix	$4.215\times^{-5}$ ±$9.155\times^{-7}$	$2.203\times^{-5}$ ±$4.668\times^{-7}$	$3.209\times^{-5}$ ±$1.164\times^{-5}$
Sample	*A.03*	*A.04*	*400 °C, 15h*
Ar	$3.479\times^{-7}$ ±$3.547\times^{-9}$	$4.078\times^{-7}$ ±$2.501\times^{-8}$	$3.779\times^{-7}$ ±$3.751\times^{-8}$
H_2	$8.311\times^{-7}$ ±$7.484\times^{-6}$	$9.075\times^{-7}$ ±$1.565\times^{-8}$	$8.693\times^{-7}$ ±$4.345\times^{-7}$
He	$8.398\times^{-7}$ ±$1.309\times^{-7}$	$9.103\times^{-7}$ ±$5.270\times^{-8}$	$8.751\times^{-7}$ ±$9.108\times^{-8}$
5 vol.%H_2	$1.942\times^{-7}$ ±$2.747\times^{-7}$	$4.484\times^{-7}$ ±$2.927\times^{-8}$	$3.213\times^{-7}$ ±$2.167\times^{-7}$
Air mix	$4.478\times^{-7}$ ±$2.519\times^{-9}$	$5.290\times^{-7}$ ±$2.382\times^{-8}$	$4.884\times^{-7}$ ±$4.887\times^{-8}$

Table 12-4. Tabulated calculated gas fluxes (permeances) in relevant gas mixes. The values given use the average temperature and non-normalised pressure. Of the three variants calculated this was the least modified or corrected and therefore deemed most representative despite increased scatter. Permeances calculated with average temperature and normalised pressure or normalised temperature and normalised pressure (in effect compensating to STP) do not differ significantly and were considered less representative.

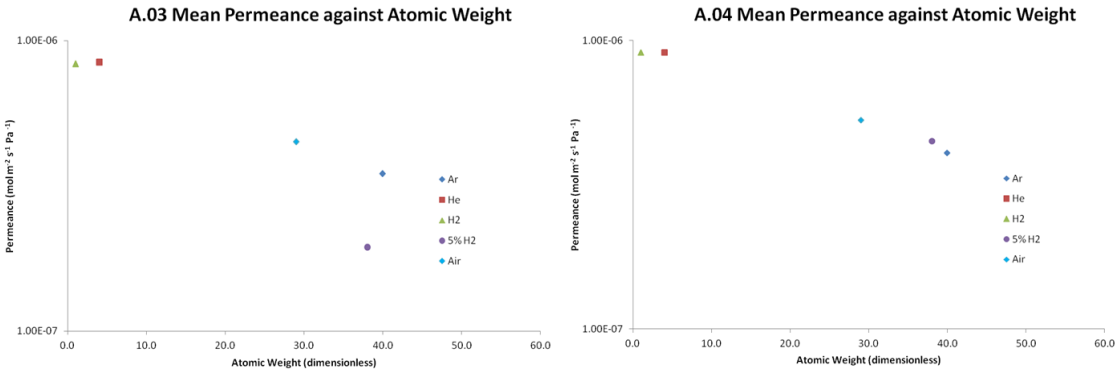

Figure 12-11. Mean permeance against atomic weight for samples A.03 (left) and A.04 (right). Both were reduced at 400 °C for 15 h. Note the differing behaviour of the 5 vol.% H_2 gas mix.

Tabulated in Table 12-5. are the values of atomic weight, molecular weight, atomic radius (also, and perhaps more properly, called the Van der Waals radius) and kinetic diameter for each gas of interest, including gas mixes. In the case of gas mixes the molecular weight had to be calculated. This was simply a weighted function, e.g. for the 5% H_2 (balance Ar) gas mix this is calculated as 0.05[molecular mass of hydrogen] +

0.95[molecular mass of Ar]. The components considered for the air mix (compressed dry air) are also given in addition to the effective values used in analysis. In certain cases this was not a sensible approach, indicated as not applicable in the table. For instance, atomic radius cannot be handled in this way. Finally, for the gas mixes, the molecular weight value was also used in place of the atomic weight since atomic weight holds little meaning for a gas mix that includes molecules. In this imperfect but practical manner we are able include the gas mixes when analysing the data with respect to atomic weight.

Gas / Gas Mix	**Ar**	**He**	**H_2**	**5 vol.% H_2**	**Air**	**N_2** (78 vol.%)	**O_2** (20.8 vol.%)	**Other*** (1.2 vol.%)
Atomic No. (dimensionless)	18	2	1	n/a	n/a	7	8	18
Atomic Weight (dimensionless)	39.9480	4.0026	1.0080	n/a	n/a	14.0070	15.9998	39.9480
Molecular Weight (dimensionless)	n/a	n/a	2.0160	38.0514	29.0182	28.0140	31.9996	n/a
Atomic Radius (pm)	188	140	120	n/a	n/a	155	152	188
Kinetic Diameter (pm)	340.00	260.00	289.00	337.45	360.24	364.00	346.00	340

Table 12-5. Atomic weight, molecular weight, atomic radius and kinetic diameter for the gasses of interest. * The remaining 1.2% was treated as being only Ar since at high pressure CO_2 solidifies and the other gasses in air (Neon, etc.) are in very small quantities. n/a not applicable.

Figure 12-12., below plots permeance against molecular weight for all gases, all samples and all repeats (measured data points, not means). The graph on the right hand side has a log-scale ordinate that more clearly shows the separation between solid Ni tubes and the two reduction schemes. Two sets of permeance plots were created and analysed against weight: atomic weight and molecular weight. There was no difference in behaviour between the two, and the molecular weight was deemed 'more correct' due to the presence of gas molecules and gas mixes containing molecules, and hence is shown here. While it is not strictly true that Ar or He possess a molecular weight this is less relevant than the difference between monotonic hydrogen and H_2, and so on.

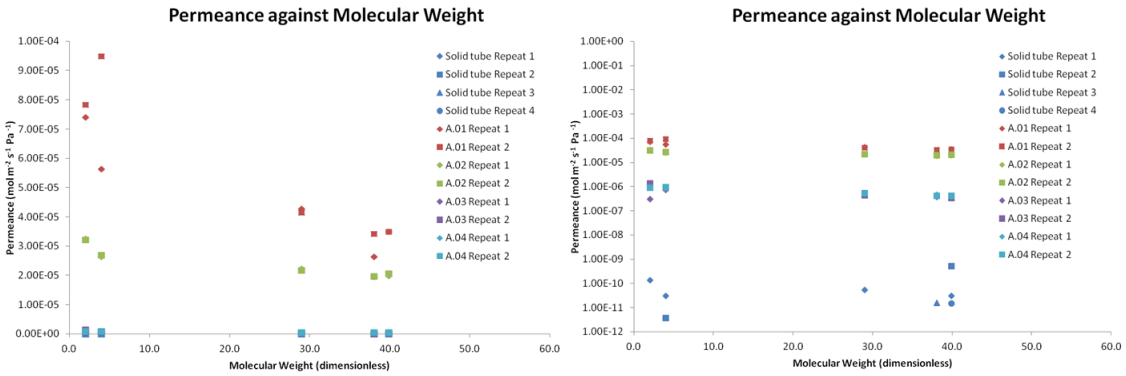

Figure 12-12. Mean permeance against molecular weight for all data points of all samples.

The same analysis was also carried out with sets of graphs with atomic radius (in pm) and kinetic diameter (in pm) for the abscissas. Atomic radius reveals no new information and is also less representative than molecular weight (especially at lower temperatures where the gasses are unlikely to dissociate). The kinetic diameter, while a good measure of atomic/molecular size (or perhaps more correctly its "sphere of effect") did not fit the data very well; the simpler exponential model was preferred.

Inspection of both plots indicates that the permeance behaviour is exponential with molecular weight (and atomic weight); with a logarithmic ordinate axis the trend is linear. As expected the least permeance is through the solid Ni tubes, and both reduction schemes result in significant gas flux through the anode, with samples reduced at 1,000 °C having markedly greater permeance.

For solid Ni tubes the scatter in the data is from approximately 5×10^{-12} to 7×10^{-10}, about 2 orders of magnitude. This is the gas flux measurement limit of the permeametry rig, and while 2 orders of magnitude may seem a significant scatter the actual permeance difference is very small.

For samples reduced with the 400 °C scheme the data scatter is approximately from 3×10^{-7} to 1×10^{-6}, or about half an order of magnitude. Overall the gas flux is 5 orders of magnitude greater than the solid tube.

For samples reduced with the 1,000 °C scheme the permeance data varies from about 2×10^{-5} to 1×10^{-4}, still less than 1 order of magnitude. Overall the gas flux is 8 orders of magnitude greater than the solid tube.

The right hand side plot, with logarithmic ordinate axis, shows that the gas has little effect on the permeance – rather it was the manufactured permeance that dominated – implying that chasms are sufficiently wide for permeance not to be influenced much by the size of the transported atoms. The gases were free to hop from site to site through the anode without restriction by the microstructure (at the atomic scale). This suggests that it is the number of channels that determines gas permeance rather than the nature of the gas. The measurement deviation of sample repeats was much less than the scatter in the measured permeances for different samples. Thus, the measured differences in permeance for samples fabricated by the same reduction scheme are due to stochastic variation in the manufacture.

The same analysis (via the same set of some 48 graphs) was repeated with ionic radius and then also covalent radius as the abscissa. There were no further observations to make; the results were the same as discussed above.

Othman *et al.* (2010) only used nitrogen as the test gas in measuring the permeance of their anode design and in verifying the gas tightness of their electrolyte. However, as observed during this study, the gas species has a limited influence on permeance. The most appropriate comparison to this work is, therefore, the measurements made with the air mix. The maximum reported anode permeance is 4.5×10^{-9} mol m^{-2} s^{-1} Pa^{-1} [Othman *et al.* 2010]. Compare this to an air permeance 4.4×10^{-5} mol m^{-2} s^{-1} Pa^{-1} of air for anodes manufactured with the 1,000 °C reduction scheme and 2.2×10^{-5} mol m^{-2} s^{-1} Pa^{-1} for those at 400 °C. The anodes made by this design are some 4 orders of magnitude more permeable.

Is the exponential behaviour of the permeance with atomic and molecular weight related to chemisorption changes with atomic/molecular weight? Or the changes in so-called strong atomic force with atomic/molecular weight?

The rig is common to all the measurements, the solid tube constituting the baseline measurement limits of the rig. These limits are very small, better, in fact, than predicted during construction and proofing of the rig, demonstrating the effectiveness of a relatively simple rig built almost entirely from off-the-shelf components, and also highlighting its potential in similar studies.

Helium was omitted from subsequent permeametry measurements for the anode-electrolyte complex because it proved significantly different from H_2 which it was intended to be representative of and replace for improved safety. Furthermore, the combination of flash back protection, relatively small quantities of gas, room temperature operation, exhaust extraction and carefully designed SOP resulted in a very reliable measurement system that produced highly repeatable and reproducible data with negligible risk; making measurements with He redundant.

12.6.2 Conclusions

Repeat measurements of the anode pressure drop with time show excellent repeatability, repeats being virtually indistinguishable. Comparison of the results with the same reduction scheme shows they are also very similar; suggesting reproducibility of the results is also excellent. Furthermore, while those samples reduced at 1,000 °C with no dwell (A.01 and A.02) show some variance in the pressure data there is little to no such variance in the case of the pair reduced at 400 °C for 25 h. *Ergo,* the anodes are exceedingly permeable but the microstructure offers some resistance, more in the case of those samples reduced at the lower temperature. The two reduction schemes have been found to result in greatly differing gas fluxes.

Anode permeance plots show a relatively weak, but very clear, gas permeance dependence on atomic/molecular weight. This was most clearly visible for the lower temperature reduction scheme; for the higher temperature reduction scheme the

dependence was rather weak. The two reduction schemes are clearly distinguishable by the measured permeances. Inspection of both sets of plots indicates that the permeance behaviour is exponential with molecular weight (and similarly atomic weight). As expected the permeance was all but negligible through the solid Ni tubes, and both reduction schemes result in significant gas flux through the anode, with samples reduced at 1,000 °C having markedly greater permeance.

For solid Ni tubes the scatter in the data is approximately 2 orders of magnitude, which may seem significant but the actual permeance difference is very small. The range 5×10^{-12} to 7×10^{-10} mol m^{-2} s^{-1} Pa^{-1} represents the gas flux measurement limit of the permeametry rig. Those samples reduced with the 400 °C scheme displayed a gas flux 5 orders of magnitude greater than the solid tube with a scatter of about half an order of magnitude. Samples reduced with the 1,000 °C scheme had an overall gas flux 8 orders of magnitude greater than the solid tube (three orders of magnitude more permeable than those reduced at 400 °C) with a scatter of less than 1 order of magnitude. The anodes made by this design are some 4 orders of magnitude more permeable than those reported by Othman *et al.* (2010).

The gas (specifically its molecular mass) has little effect on the permeance. The sample microstructure dependent on manufacture dominated the measured permeances implying that chasms are sufficiently wide for permeance not to be influenced much by the size of the transported gas atoms. Therefore, it is the number of channels that determines gas permeance rather than the nature of the gas.

12.7 Anode-Electrolyte Complex

The second set of measurements dealt with electrolytes of three different thicknesses deposited on the most permeable anode identified from the first set of measurements).

12.7.1 Results & Discussion

Table 12-7. summarises the results on the anode-electrolyte samples but is otherwise the same as Table 12-3. Fabrication parameters for these samples are given in Table 12-6. Working with undiluted hydrogen proved entirely satisfactory in terms of safety (both near the permeances rig and in the lab in general) due to the combination of flashback orifice on the exhaust valve and procedures established (Appendix K: Permeameter SOP). As a result He, added as a potential replacement for hydrogen in the permeances experiments, was no longer necessary. Furthermore, He had notably different gas permeation behaviour to hydrogen, indicating that the initial judgement that the similarity between these two gases may make them equivalent in terms of gas permeances was, in fact, incorrect. Errors estimated using linear approximation by partial differentiation where an equation was used [Error Propagation article accessed

2013], or based purely on measurement equipment error otherwise. In all cases errors represent the worst case scenario.

Sample	**Mass fraction reduced** ±0.0042	**Nominal coating thickness (µm)**	**m_{YSZ} (mg)** ±1 mg
B.01	0.999	10	72.3
B.02	0.998	10	78.4
C.01	0.998	150	1,054.1
C.02	1.000	150	891.5
D.01	0.999	50	331.2
D.02	1.000	50	331.7

Table 12-6. Summary of permeameter AEC sample fabrication parameters. All samples reduced at 1,000 °C (ramp only). The m_{Ni}, m_{Ni+NiO}, MFO, $m_{reduced}$, m_{loss} and m_{Ni+YSZ} were omitted as they add nothing to the discussion hereunder.

Fabrication data (Table 12-6.) was included to emphasise the reproducibility of the process. Compare with the results presented in section 9.6.1 and section 11.3. The samples utilised for permeametry are therefore representative of anode–electrolyte complexes fabricated as described in the specified sections of this thesis, other than two additional nominal coating thicknesses (estimated based on deposition rate).

Gas	**Ar**		**H_2**		**5 vol.%H_2**		**Air mix**	
Sample B.01 (10 µm)								
t_0 [s] ± 1 s	0	0	0	0	0	0	0	0
$p^{0,Norm}$ [kPa] ± 0.064 kPa	200.4	200.1	199.5	199.5	198.8	198.7	199.7	199.5
t_1 [s] ± 1 s	30	30	30	30	30	30	30	30
$p^{t1,Norm}$ [kPa] ± 0.064 kPa	120.1	118.8	69.60	61.71	118.6	118.4	111.4	108.8
t_2 [s] ± 1 s	60	60	60	60	60	60	60	60
$p^{t2,Norm}$ [kPa] ± 0.064 kPa	81.30	80.24	33.83	23.02	79.38	89.55	68.82	68.03
t_3 [s] ± 1 s	120	120	120	120	120	120	120	120
$p^{t3,Norm}$ [kPa] ± 0.064 kPa	36.47	36.27	8.537	3.674	36.82	38.37	28.31	28.21
t_4 [s] ± 1 s	300	300	300	300	300	300	300	300
$p^{t4,Norm}$ [kPa] ± 0.064 kPa	4.827	4.988	-0.108	-0.270	4.522	4.520	2.323	2.323
t_5 [s] ± 1 s	600	600	441	322	600	600	`600	600
$p^{t5,Norm}$ [kPa] ± 0.064 kPa	-0.109	-0.108	-0.324	-0.324	-0.108	-0.108	-0.270	-0.270
t_6 [s] ± 1 s	921	895			896	883	739	726
$p^{t6,Norm}$ [kPa] ± 0.064 kPa	-0.325	-0.325			-0.323	-0.323	-0.324	-0.324

Gas	**Ar**		**H_2**		**5 vol.%H_2**		**Air mix**	
Sample B.02 (10 µm)								
t_0 [s] ± 1 s	0	0	0	0	0	0	0	0
$p^{0,Norm}$ [kPa] ± 0.064 kPa	198.5	198.5	199.0	199.0	198.3	198.38	199.0	199.1
t_1 [s] ± 1 s	30	30	30	30	30	30	30	30
$p^{t1,Norm}$ [kPa] ± 0.064 kPa	111.5	111.0	80.27	57.23	110.0	109.8	102.5	101.2
t_2 [s] ± 1 s	60	60	60	60	60	60	60	60
$p^{t2,Norm}$ [kPa] ± 0.064 kPa	71.47	69.65	37.68	22.42	68.79	69.54	60.16	59.75
t_3 [s] ± 1 s	120	120	120	120	120	120	120	120
$p^{t3,Norm}$ [kPa] ± 0.064 kPa	30.65	30.04	9.164	3.934	29.23	29.67	22.59	22.38
t_4 [s] ± 1 s	300	300	300	300	300	300	300	300
$p^{t4,Norm}$ [kPa] ± 0.064 kPa	2.903	2.740	-0.108	-0.270	2.580	2.634	1.294	1.240
t_5 [s] ± 1 s	600	600	577	383	600	600	`600	600
$p^{t5,Norm}$ [kPa] ± 0.064 kPa	-0.215	-0.215	-0.323	-0.323	-0.215	-0.215	-0.270	-0.270
t_6 [s] ± 1 s	765	762			752	769	674	659
$p^{t6,Norm}$ [kPa] ± 0.064 kPa	-0.322	-0.323			-0.322	-0.323	-0.323	-0.324
Sample C.01 (150 µm)								
t_0 [s] ± 1 s	0	0	0	0	0	0	0	0
$p^{0,Norm}$ [kPa] ± 0.064 kPa	199.3	198.8	198.9	199.7	199.2	198.9	198.9	199.5
t_1 [s] ± 1 s	30	30	30	30	30	30	30	30
$p^{t1,Norm}$ [kPa] ± 0.064 kPa	141.3	141.2	96.87	90.69	141.2	140.9	134.4	135.0
t_2 [s] ± 1 s	60	60	60	60	60	60	60	60
$p^{t2,Norm}$ [kPa] ± 0.064 kPa	107.0	107.0	56.24	51.80	106.8	106.6	96.97	97.20
t_3 [s] ± 1 s	120	120	120	120	120	120	120	120
$p^{t3,Norm}$ [kPa] ± 0.064 kPa	63.64	64.08	22.39	20.05	62.66	62.62	53.46	53.08
t_4 [s] ± 1 s	300	300	300	300	300	300	300	300
$p^{t4,Norm}$ [kPa] ± 0.064 kPa	15.54	15.47	1.724	1.458	14.88	14.76	10.12	9.990
t_5 [s] ± 1 s	600	600	600	600	600	600	600	600
$p^{t5,Norm}$ [kPa] ± 0.064 kPa	1.511	1.509	-0.270	-0.270	1.348	1.346	0.484	0.486
t_6 [s]	1,800	1,550	673	625	1,410	1,645	994	949

Gas	**Ar**		**H_2**		**5 vol.%H_2**		**Air mix**	
± 1 s								
$p^{t6,Norm}$ [kPa] ± 0.064 kPa	-0.270	-0.269	-0.323	-0.324	-0.270	-0.323	-0.269	-0.270
Sample C.02 (150 µm)								
t_0 [s] ± 1 s	0	0	0	0	0	0	0	0
$p^{0,Norm}$ [kPa] ± 0.064 kPa	202.0	202.0	202.6	202.4	210.6	201.8	202.2	202.3
t_1 [s] ± 1 s	30	30	30	30	30	30	30	30
$p^{t1,Norm}$ [kPa] ± 0.064 kPa	137.8	138.9	88.44	87.428	138.5	138.5	131.2	132.3
t_2 [s] ± 1 s	60	60	60	60	60	60	60	60
$p^{t2,Norm}$ [kPa] ± 0.064 kPa	101.8	103.0	48.83	48.63	101.8	102.0	92.70	92.78
t_3 [s] ± 1 s	120	120	120	120	120	120	120	120
$p^{t3,Norm}$ [kPa] ± 0.064 kPa	57.32	59.11	18.56	18.00	57.42	57.85	48.21	48.18
t_4 [s] ± 1 s	300	300	300	300	300	300	300	300
$p^{t4,Norm}$ [kPa] ± 0.064 kPa	11.58	12.51	1.095	1.039	11.80	11.91	7.823	7.768
t_5 [s] ± 1 s	600	600	556	555	600	600	600	600
$p^{t5,Norm}$ [kPa] ± 0.064 kPa	0.710	0.874	-0.328	-0.328	0.710	0.710	0.109	0.109
t_6 [s] ± 1 s	1,204	1,139			1,158	1,108	855	883
$p^{t6,Norm}$ [kPa] ± 0.064 kPa	-0.328	-0.328			-0.328	-0.328	-0.328	-0.328
Sample D.01 (50 µm)								
t_0 [s] ± 1 s	0	0	0	0	0	0	0	0
$p^{0,Norm}$ [kPa] ± 0.064 kPa	200.6	200.3	200.6	200.5	200.4	200.8	200.6	200.8
t_1 [s] ± 1 s	30	30	30	30	30	30	30	30
$p^{t1,Norm}$ [kPa] ± 0.064 kPa	121.6	121.48	91.13	70.99	120.0	121.3	113.7	114.3
t_2 [s] ± 1 s	60	60	60	60	60	60	60	60
$p^{t2,Norm}$ [kPa] ± 0.064 kPa	79.97	79.70	47.65	30.18	78.32	79.02	69.01	69.16
t_3 [s] ± 1 s	120	120	120	120	120	120	120	120
$p^{t3,Norm}$ [kPa] ± 0.064 kPa	32.95	32.46	11.45	3.581	31.48	31.46	24.00	23.91
t_4 [s] ± 1 s	300	300	300	248	300	300	300	300
$p^{t4,Norm}$ [kPa] ± 0.064 kPa	0.326	0.326	-0.271	-0.271	0.217	0.163	-0.163	-0.217
t_5 [s]	519	459			421	408	358	350

Gas	**Ar**		**H_2**		**5 vol.%H_2**		**Air mix**	
± 1 s								
$p^{t5,Norm}$ [kPa] ± 0.064 kPa	-0.271	-0.271			-0.271	-0.272	-0.272	-0.272
Sample D.02 (50 µm)								
t_0 [s] ± 1 s	0	0	0	0	0	0	0	0
$p^{0,Norm}$ [kPa] ± 0.064 kPa	200.7	200.7	200.8	200.865	200.7	200.8	200.8	200.8
t_1 [s] ± 1 s	30	30	30	30	30	30	30	30
$p^{t1,Norm}$ [kPa] ± 0.064 kPa	146.7	146.6	101.4	101.4	146.5	146.1	140.3	140.6
t_2 [s] ± 1 s	60	60	60	60	60	60	60	60
$p^{t2,Norm}$ [kPa] ± 0.064 kPa	113.9	113.3	61.33	62.31	113.3	112.8	103.9	104.1
t_3 [s] ± 1 s	120	120	120	120	120	120	120	120
$p^{t3,Norm}$ [kPa] ± 0.064 kPa	69.62	68.75	25.49	25.71	68.78	68.67	58.17	58.129
t_4 [s] ± 1 s	300	300	300	300	300	300	300	300
$p^{t4,Norm}$ [kPa] ± 0.064 kPa	16.36	15.93	1.903	1.740	15.66	15.60	10.17	10.17
t_5 [s] ± 1 s	600	600	600	579	600	600	600	600
$p^{t5,Norm}$ [kPa] ± 0.064 kPa	0.924	0.816	-0.272	-0.272	0.816	0.761	0.054	0.109
t_6 [s] ± 1 s	1,030	972			911	905	780	770
$p^{t6,Norm}$ [kPa] ± 0.064 kPa	-0.272	-0.272			-0.272	-0.272	-0.272	-0.272

Table 12-7. Permeameter measurements in relevant gas mixes. The pressures given are normalised to 20 °C. Repeat measurements are shown in adjacent columns for the same gas.

As previously the pressure drop was plotted against time for each pair of repeats, with a different plot for every combination of gas type and sample. Figure 12-13. shows two such plots (from a total of 24 that can be found in Appendix L: All Permeametry Plots).

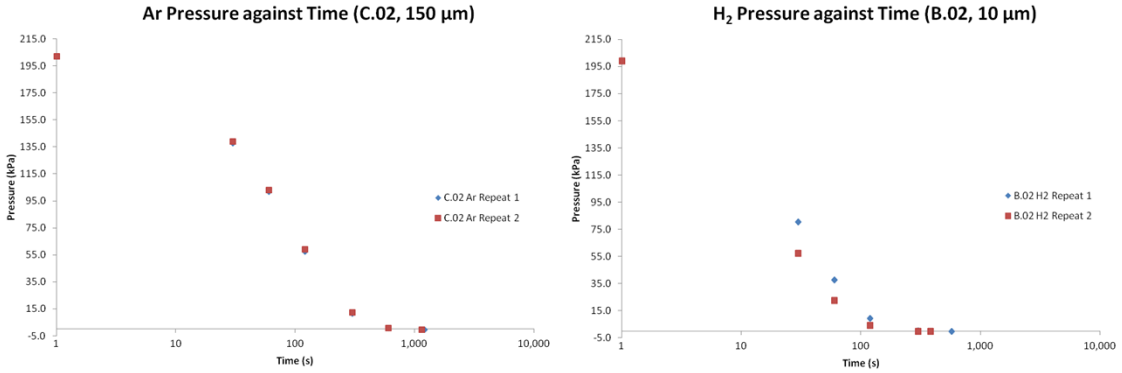

Figure 12-13. Pressure drop against time showing repeat variance for the same sample for each gas. Two exemplars are shown of a total of 24 plots (see Appendix L: All Permeametry Plots). The errors (based on measurement error) are too small to be visible.

The plot on the left is a typical exemplar from this set of graphs, while the plot on the right shows the largest scatter in the data among these 24 graphs. Notable clear trends, even with the sample with the largest scatter, are once more clearly visible. In almost all instances the repeat measurements show excellent repeatability, being virtually indistinguishable, as before for those measurements on anodes (without the deposited electrolyte). Unfortunately, as was the case before, no explanation presents itself to account for the visible scatter: the error calculated according to the sensor manufacturer's error analysis does not account for it. As explained previously there may be a partial explanation (see discussion after Figure 12-8.).

The overwhelming majority of the data suggests reproducibility is very good. For this second set of permeametry experiments the underlying anodes were all made identically (with the high temperature, short dwell reduction scheme). This particular variant was selected as it presents the greatest gas permeances (see the anode results discussed previously: section 12.6.1) and so would be of minimum impediment to gas flow. Thus, even without the application of a model to separate the gas fluxes, one may directly judge the electrolyte gas tightness from the data. It also presents the electrolyte with a 'worst case scenario' (at least for electrolyte gas tightness) by having an elevated underlying gas flux. The results very clearly show the effect of increasing thickness: lower gas permeability. The generally excellent repeatability of the measurements suggests one may reasonably use mean values.

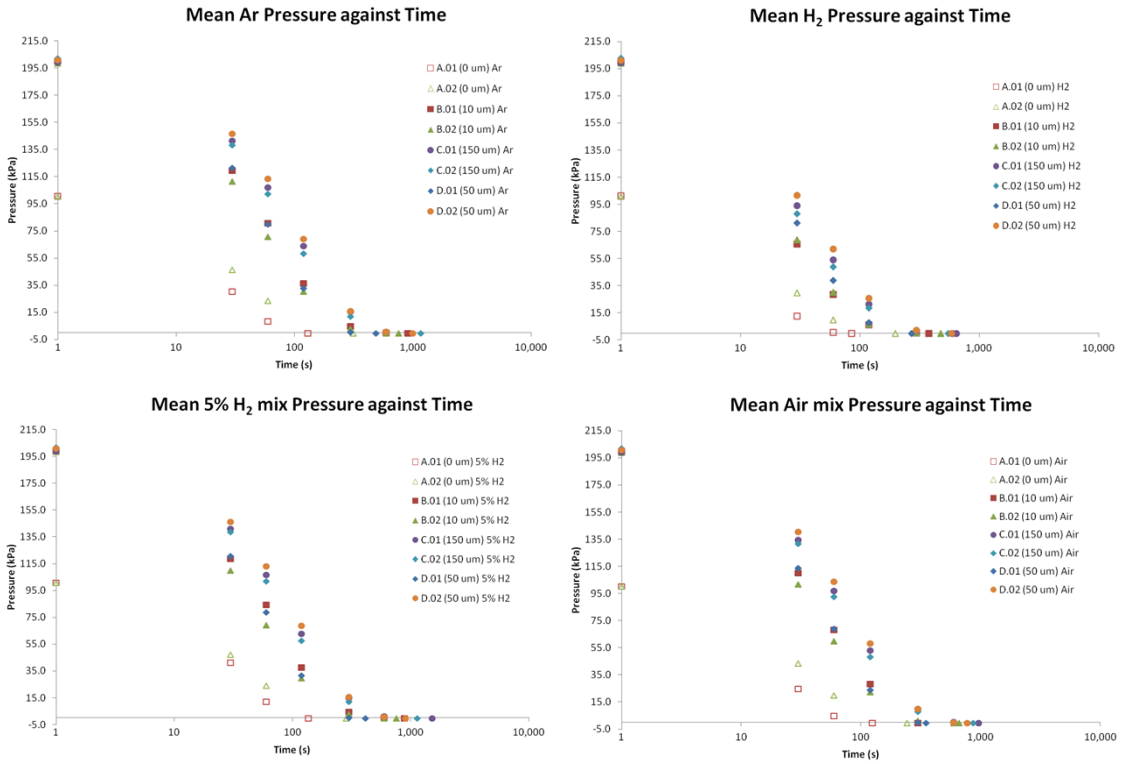

Figure 12-14. Mean pressure drop with time through anode-electrolyte complex organised by gas showing data points by sample and repeat. Note the anode was included for reference (as a 0 µm electrolyte).

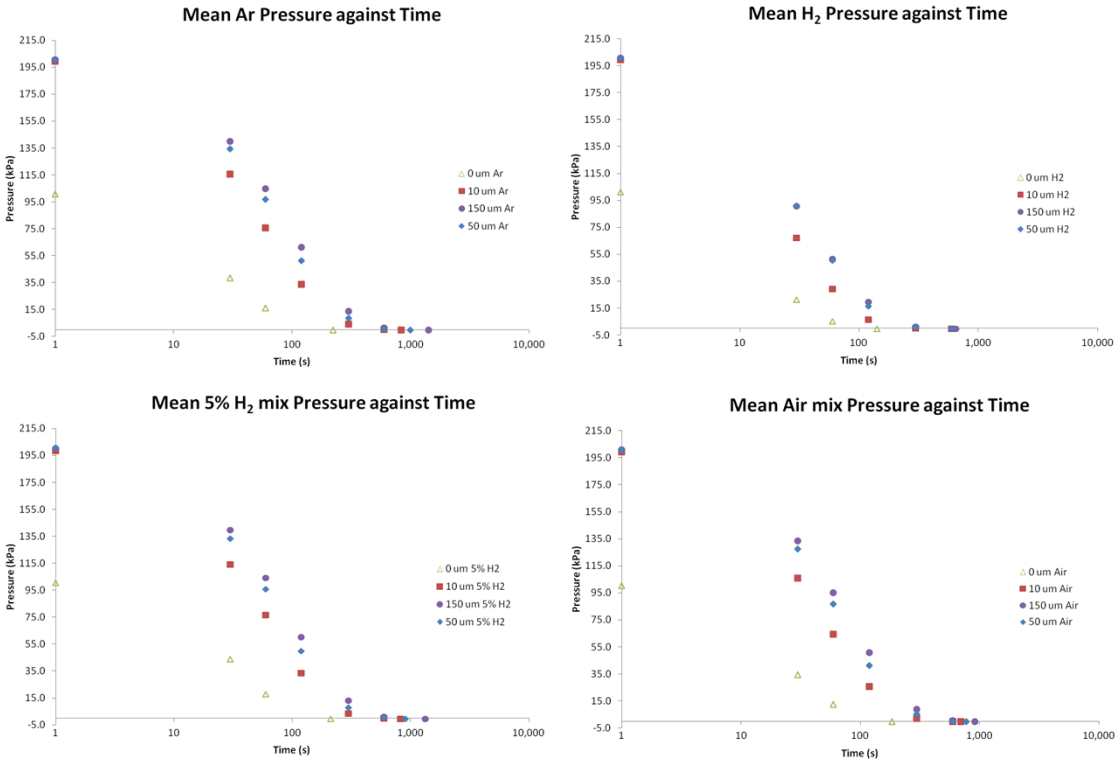

Figure 12-15. Mean pressure drop with time through anode-electrolyte complex organised by gas showing data points by electrolyte thickness. Note the anode was included for reference (as a 0 μm electrolyte).

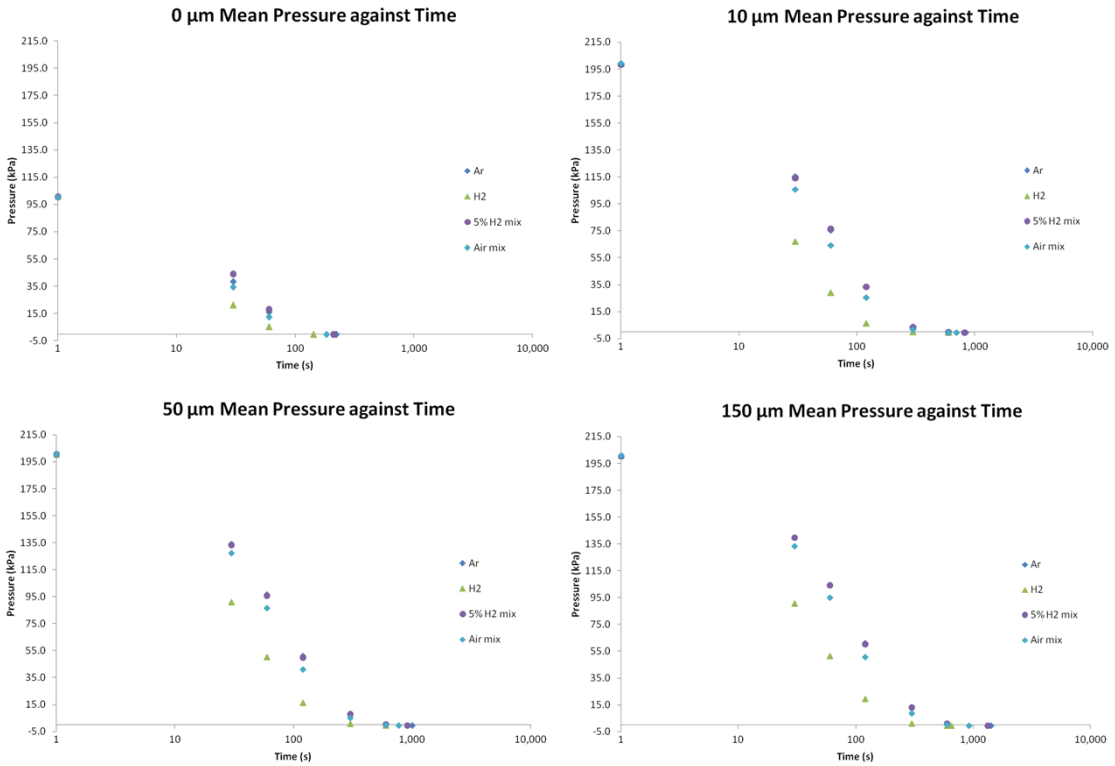

Figure 12-16. Mean pressure drop with time through anode-electrolyte complex organised by electrolyte thickness showing data points by gas. Note the anode was included for reference (as a 0 µm electrolyte).

The simplest graphs, pressure drop against time with a single plot per combination of gas and sample showing both repeats, reveal that there is sufficient variance between samples with the same thickness to overlap the range of results of other electrolyte thicknesses. The overlap of the 50 µm and the 150 µm data indicates that they are not sufficiently different to resolve completely; i.e. the electrolyte thickness has a relatively limited influence, at least at the thicknesses considered. The variance in the anode microstructure that leads to the scatter in its data contributes to the overlap. The trends shown when plotting as described in the next paragraph (one sample per plot / one electrolyte thickness per plot, all gasses shown) indicates that despite the overlap the thickness has a clear effect.

A notable trend exists in the plots of mean pressure over time, where each of the four plots are arranged to show all samples of a single gas averaging the data for repeats: thinner electrolytes result in greater permeance of all relevant gases. The data conforms to a single mathematical model, however, unlike the anode permeance results. The results are as expected, with hydrogen consistently displaying the fastest pressure drop to atmospheric and air, Ar and the 5% H_2 (balance Ar) mix being very close.

The same data may be plotted but arranged such that each graph shows all gases for a single sample. The expected trend noted in the preceding paragraph is now even more visible.

As with the anode the same methodology applied to the pressure drop plots was employed for the analysis of the calculated permeances. As the method was the same the steps shown for the pressure drop analysis will not be repeated. The aforementioned microstructural effect on the permeance of the 5% H_2 mix was not observed for the anode-electrolyte samples. While it is certainly possible that for this set of six samples there was no such effect (being stochastic in nature) it is more likely that, as noted above, the effect is suppressed for anodes reduced at 1,000 °C. Instead, the plots shown (Figure 12-17.) demonstrate the typical results achieved, divided by electrolyte thickness.

Gas	**Mean Permeance ±s ($molm^{-2}s^{-1}Pa^{-1}$)**		**Mean by electrolyte thickness ±s**
Sample	*B.01*	*B.02*	*10 µm*
Ar	$9.967\times^{-6}$ ±$1.754\times^{-7}$	$1.012\times^{-5}$ ±$3.998\times^{-8}$	$1.005\times^{-5}$ ±$1.376\times^{-7}$
H_2	$2.396\times^{-5}$ ±$3.998\times^{-6}$	$2.266\times^{-5}$ ±$3.832\times^{-6}$	$2.331\times^{-5}$ ±$3.284\times^{-6}$
5 vol.%H_2	$9.157\times^{-6}$ ±$3.943\times^{-8}$	$1.027\times^{-5}$ ±$2.674\times^{-8}$	$9.715\times^{-6}$ ±$6.454\times^{-7}$
Air mix	$1.139\times^{-5}$ ±$3.096\times^{-8}$	$1.258\times^{-5}$ ±$9.046\times^{-8}$	$1.199\times^{-5}$ ±$6.906\times^{-7}$
Sample	*D.01*	*D.02*	*50 µm*
Ar	$1.866\times^{-5}$ ±$8.507\times^{-8}$	$7.105\times^{-6}$ ±$6.619\times^{-8}$	$1.288\times^{-5}$ ±$6.669\times^{-6}$
H_2	$2.462\times^{-5}$ ±$5.833\times^{-6}$	$1.297\times^{-5}$ ±$2.057\times^{-7}$	$1.880\times^{-5}$ ±$7.524\times^{-6}$
5 vol.%H_2	$2.057\times^{-5}$ ±$9.667\times^{-7}$	$7.234\times^{-6}$ ±$2.005\times^{-9}$	$1.390\times^{-5}$ ±$7.717\times^{-6}$
Air mix	$1.488\times^{-5}$ ±$1.710\times^{-7}$	$8.494\times^{-6}$ ±$5.311\times^{-9}$	$1.169\times^{-5}$ ±$3.689\times^{-6}$
Sample	*C.01*	*C.02*	*150 µm*
Ar	$6.344\times^{-6}$ ±$1.149\times^{-7}$	$8.500\times^{-6}$ ±$1.385\times^{-7}$	$7.422\times^{-6}$ ±$1.249\times^{-6}$
H_2	$1.173\times^{-5}$ ±$5.988\times^{-7}$	$1.587\times^{-5}$ ±$5.979\times^{-8}$	$1.380\times^{-5}$ ±$2.417\times^{-6}$
5 vol.%H_2	$6.430\times^{-6}$ ±$4.910\times^{-8}$	$8.587\times^{-6}$ ±$3.135\times^{-8}$	$7.509\times^{-6}$ ±$1.246\times^{-6}$
Air mix	$7.440\times^{-6}$ ±$2.615\times^{-7}$	$1.011\times^{-5}$ ±$2.637\times^{-9}$	$8.776\times^{-6}$ ±$1.550\times^{-6}$

Table 12-8. Tabulated calculated gas fluxes (permeances) in relevant gas mixes for AEC. The values given use the average temperature and non-normalised pressure. Of the three variants calculated this was the least modified or corrected and therefore deemed most representative despite increased scatter. Permeances calculated with average temperature and normalised pressure or normalised temperature and normalised pressure (in effect compensating to STP) did not differ significantly but were deemed less representative.

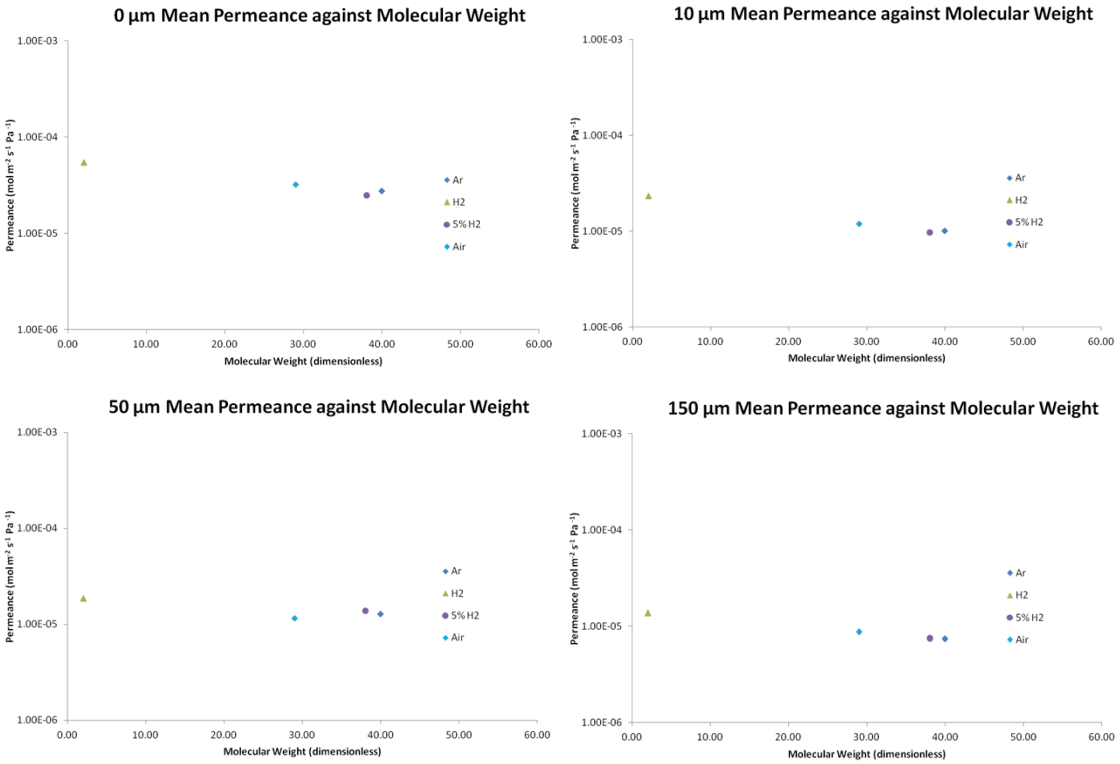

Figure 12-17. Mean gas permeance through AEC against molecular weight, organised by electrolyte thickness (note that the 0 m refers to data from anode samples A.01 and A.02).

Figure 12-18. plots permeance against molecular weight for all gases, all samples and all repeats (measured data points, not means) including data from the solid Ni tube and anodes (samples A01 and A.02) for facile comparison. The graph on the right hand side has a log-scale ordinate that more clearly shows the separation between solid Ni tubes and the two reduction schemes. As before, two sets of permeance plots were created and analysed against weight: atomic weight and molecular weight. Similar to the anode there was no difference in behaviour between the two, and the molecular weight was deemed ‘more correct’ and is shown here, as explained previously.

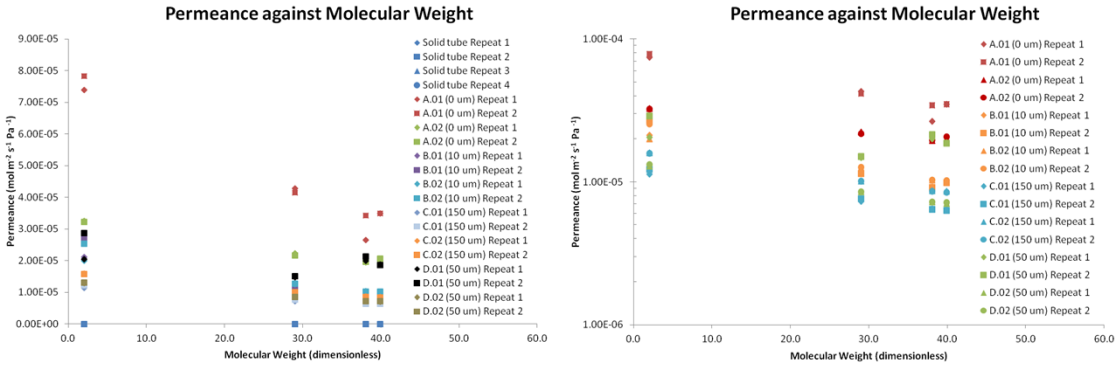

Figure 12-18. Gas permeance against molecular weight for all gases, all samples and all repeats (measured data points, not means) including data from the solid Ni tube and anodes (samples A01 and A.02) for facile comparison. Graph on the right is log-scaled on the ordinate (in this case the data for solid tubes was omitted) and colour-coded to more easily distinguish different electrolyte thicknesses.

The behaviour is exponential with molecular (and atomic) weight, shown by its linear behaviour when plotted with a log-scale ordinate. This is consistent with the anode results, and entirely expected. The same comments regarding a definite, though weak, thickness effect in the discussion for the anode-electrolyte pressure drop plots apply once more, with no evidence of additional mechanisms or phenomena. Perhaps the only addition to be made is that the 5% H_2 mix is the only one where the behaviour from the 50 μm and 150 μm is reversed. There is insufficient data to be certain this is more than simply stochastic. Samples with a 50 μm thick electrolyte have a large scatter, behaving like samples with a 10 μm thick electrolyte in some instances and in others like ones with a 150 μm thick electrolyte. The author believes 50 μm could be some critical thickness, perhaps an effect of an increasingly columnar coating (from a relatively disordered one).

Overall the gas permeance is reduced by an order of magnitude by the deposition of a thicker electrolyte (from 0 μm to 150 μm). The biggest difference is approximately half an order of magnitude and occurs with the addition of the 10 μm electrolyte intended for this design. As noted for the anode the gas has only a small influence on the overall permeance, indicating that chasms are sufficiently wide for permeance not to be influenced much by the size of the transported atoms. This suggests that it is the number of channels (i.e. extent of connected pore network) that predominantly determines gas permeance rather than the nature of the gas.

The measurement deviation of sample repeats was much less than the scatter in the measured permeances for different samples. Thus, the measured differences in permeance for samples fabricated by the same reduction scheme are due to stochastic variation in the manufacture.

As with the anode permeance the same analysis (via a fresh set of some 48 graphs for the AEC) was repeated with atomic radius and then also covalent radius as the abscissa. No new information was revealed in this way and the plots are therefore omitted.

The membranes reported by Menzler *et al.* (2013) were created as a gas separation membrane, but the results provide an interesting comparison with those reported here. The range of gas permeances for these membrane structures, which is considered an excellent separation membrane with high selectivity and high gas flow (permeance) [Menzler *et al.* 2013] at best are several orders of magnitude lower than my design (see figure below).

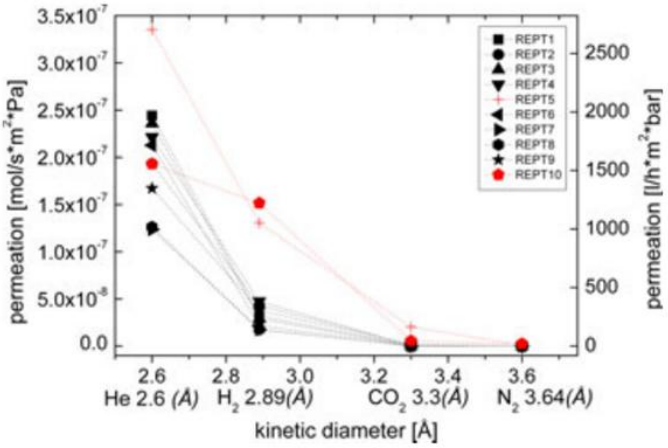

Figure 12-19. Gas permeance against kinetic diameter of several test gases for a series of 10 membranes with a SiO_2 top layer (that enhances selectivity) [Menzler *et al.* 2013].

According to Othman *et al.* (2010) a membrane can be considered gas tight if the nitrogen permeance is close to 1×10^{-10} mol m^{-2} s^{-1} Pa^{-1}. Their electrolytes had at worst a nitrogen permeance of 0.96×10^{-10} mol m^{-2} s^{-1} Pa^{-1}, and so may safely be considered gas tight. The measured air permeance through the anode-electrolyte complex for this project was approximately 1×10^{-5} mol m^{-2} s^{-1} Pa^{-1} for the same thickness of electrolyte (10 μm), approximately 5 orders of magnitude too much to be considered gas tight.

An example with contradictory conclusions considered the electrolyte gas tight with a gas flux through it of less than 1.36×10^{-3} mol m^{-2} s^{-1} Pa^{-1} of air at room temperature and was 4 μm thick [Haydn *et al.* 2014], much higher than Othman *et al.* (2010). This was a complex multi-layer structure. Haydn *et al.* (2014) reported that single layer electrolytes exhibited gas fluxes half on order of magnitude greater or more. By this definition the electrolyte of this project would be considered gas tight. I do not consider this to be a realistic conclusion (furthermore Haydn *et al.* (2014) adopt unusual nomenclature and units that made the gas flux appear far smaller than in fact it was). Haydn *et al.* (2014) report conclusions that are highly unsatisfactory in this respect, and appear to be misleading.

Unfortunately the electrolyte is unacceptably permeable to the gases of interest leading to a significant loss in performance – victim, as it were, of the very porous anode. The electrolyte microstructure does offer some resistance, as evidenced by the decreasing permeances with increasing electrolyte thickness. However, by its very nature the deposition of YSZ via EB-PVD is highly conformal leading to large cracks as the deposited coating conforms to the crack on the extremely porous underlying microstructure of the anode. Micrographs of this are omitted because the structure is nearly identical to the surface morphology of the reduced samples (see Figure 8-67., Figure 8-68., Figure 8-73., Figure 8-79. and Figure 8-85.).

12.7.2 Conclusions

The repeat anode-electrolyte complex pressure drop measurements show excellent repeatability, much as before for those measurements on anodes. The overwhelming majority of the data suggests reproducibility is also very good. The conditions prepared present a 'worst case scenario' for electrolyte gas tightness; having an elevated underlying gas flux through a very permeable anode. Increasing electrolyte thickness lowers gas permeance. However, there is sufficient variance between samples with the same thickness to overlap the range of results of other electrolyte thicknesses. The overlap of the 50 μm and the 150 μm data indicates that they are not sufficiently different to resolve completely. Yet despite the overlap, thickness has a clear effect. *Ergo*, the electrolyte thickness has a relatively limited influence (at least at the thicknesses considered). The variance in the anode microstructure that leads to the scatter in its data more than likely contributes to this overlap. The results are as expected, with hydrogen consistently displaying the fastest pressure drop to atmospheric and air, Ar and the 5% H_2 (balance Ar) mix exhibiting very similar behaviour to each other.

The anode-electrolyte complex permeance is exponential with molecular (and atomic) weight (linear when plotted with a log-scale ordinate). This is consistent with the anode results, and entirely expected. The same comments regarding a definite, though weak, thickness effect above apply once more. Samples with a 50 μm thick electrolyte have a large scatter, behaving like samples with a 10 μm thick electrolyte in some instances and in others like ones with a 150 μm thick electrolyte. The author believes this could be indicative of some critical thickness, perhaps an effect of an increasingly columnar coating (from a relatively disordered one). As noted for the anode the gas has only a small influence on the overall permeance, suggesting that chasms in the coating are sufficiently wide for permeance to be relatively uninfluenced by the size of the transported species. It is therefore the number of channels that determines gas permeance rather than the nature of the gas.

From a gas transport perspective the anode is controlling the gas fluxes, with the electrolyte thickness having only a minor influence. Therefore, there is a clear incentive to continue with optimising for the thinnest possible electrolyte with a modified microstructure to improve gas tightness.

12.8 Summary

Precise and accurate measurement of the permeance of relevant gases through fuel cells and their components, particularly as opposed to porosity measurement, was made possible by the design and fabrication of a permeameter and measurement procedure. Measurements were successfully carried out with several gas mixes on a number of samples spanning the manufactured properties of interest. Pressure drop over time proved a very useful tool alongside calculated gas permeances for understanding gas permeation.

The rig is common to all the measurements. Measurements with a solid Ni tube constituting the measurement limits of the rig. These limits are very small, better, in fact, than predicted demonstrating the effectiveness of a relatively simple rig built almost entirely of off-the-shelf components, and also highlighting its potential value to similar studies.

The gas has little effect on the permeance. The microstructure dominated gas permeance implying that chasms are sufficiently wide for permeance not to be influenced much by the size of the transported atoms. Therefore, it is the number of channels that determines gas permeance rather than the nature of the gas.

From a gas transport perspective the anode is controlling the gas fluxes, with the electrolyte thickness having only a minor influence. There is a clear incentive, then, to continue with optimising for the thinnest possible electrolyte with a modified microstructure to improve gas tightness. As Coddet *et al.* (2014) neatly expressed "the challenge of depositing a thin electrolyte layer on a porous substrate appears as a key point of the process."

It is enlightening to calculate the gas fluxes expected for real components fabricated as described (see chapters 8 and 9) for temperatures of interest at the intended operating pressures. For the anode the total membrane area is $\approx 1.814\times10^{-3}$ m^2 and the maximum measured hydrogen permeance is approximately $J_{max} = 6\times10^{-5}$ mol m^{-2} s^{-1} Pa^{-1}.

Therefore, assuming the pressure remains close to 1.01 bar (the initial test pressure of the pressure drop with time measurements):

$\dot{n}_{max}^{anode}$ = 10.99×10^{-3} mol s^{-1}

Now $P\dot{V} = \dot{n}RT$, so at four temperatures of interest (at an assumed pressure difference of 1.013 bar plus a back pressure of 0.097 bar during operation as anodes in the fuel cell; see also section 13.2):

T (°C)	400	600	800	1,000
$\dot{V}$ **(m^3 s^{-1})**	5.59×10^{-4}	7.19×10^{-4}	8.83×10^{-4}	1.05×10^{-3}
$\dot{V}$ **(litres min^{-1})**	33.54	43.12	52.99	62.88

Table 12-9. Hydrogen flux through manufactured anodes at 400 °C, 600 °C, 800 °C and 1,000 °C.

To the author's knowledge, this anode design outperforms others in the literature in terms of gas permeance, even at low temperature. The result of this should be very low anodic concentration polarisation. As noted earlier the performance degradation over time under operating conditions has not been assessed, and would be a worthy endeavour in and of itself.

From equation (4.62) it is possible to calculate the maximum current of the fuel cell. A few assumptions must be made. First, it was assumed that the permeance of water vapour through the anode is approximately the same as that of hydrogen (H_2) (it was assumed the high temperature would lead to a significant proportion of free H^+ and OH^- ions). The permeance of oxygen through the cathode is likewise assumed to not be limiting. Based on the maximum hydrogen flux and the cell active area the maximum current is 4.229 A. The current calculated represents the maximum current based on anode concentration. Once practical currents have been measured it is possible to use this equation to estimate the gas fluxes noted: useful from a permeametry standpoint as it forms the minimum acceptable gas permeance of those gasses.

For the anode-electrolyte complex the total membrane area exposed is the same as for the anode alone and the maximum measured hydrogen permeance is approximately J_{max} = 3×10^{-5} mol m^{-2} s^{-1} Pa^{-1}.

Therefore, assuming the pressure remains close to 1.01 bar:

$\dot{n}_{max}^{anode}$ = 5.57×10^{-3} mol s^{-1}

As before using $P\dot{V} = \dot{n}RT$ at the four temperatures of interest:

T (°C)	400	600	800	1,000
$\dot{V}$ **(m^3 s^{-1})**	2.81×10^{-4}	3.64×10^{-4}	4.48×10^{-4}	5.31×10^{-4}
$\dot{V}$ **(litres min^{-1})**	16.85	21.85	26.86	31.87

Table 12-10. Hydrogen flux through manufactured anode-electrolyte samples at 400 °C, 600 °C, 800 °C and 1,000 °C.

The electrolyte microstructure does offer some resistance, as evidenced by the decreasing permeances with increasing electrolyte thickness. However, by its very nature the deposition of YSZ via EB-PVD is highly conformal leading to large cracks as the deposited coating conforms to the crack on the extremely porous underlying microstructure of the anode. The solution is thus likely to be found in modifying the electrolyte microstructure.

Essentially the addition of the intended 10 μm electrolyte halves the gas flux (compared to the anode alone). It is however, still far higher than acceptable – victim, as it were, of the very porous anode. Although by no means ideal the electrolyte would certainly function in this state, albeit with reduced performance compared to a gas tight one, mainly in terms of a lower OCV.

The use of permeance measurement is potentially very useful in large scale manufacture to quickly test batches throughout the production process. For instance, by sampling one or more random anodes from the production line immediately after reduction and test their permeance in a select gas. Then repeat after the electrolyte is deposited. Rejects should be easily re-processed and even if not can be caught early enough to save a great deal of money later in the process.

13 Design and Construction of Test Rig

Testing the fabricated fuel cells required a bespoke experimental platform, generally referred to as the test rig, fuel cell test rig or FC test rig.

13.1 Background

A standard for solid oxide fuel cell performance testing, even an informal one, is yet to be established. Certain groups, Suzuki *et al.* for instance, follow a seemingly well-established set of guidelines created for their own use. However varied the details in the literature may be a few common elements stand out. Firstly, electrical performance is nearly always assessed both by Electrochemical Impedance Spectroscopy and I–V plots. Secondly, gas flows are generally not carefully controlled, and exhaust composition is rarely measured. While understandable (this is more challenging than it sounds, see later) the result is that efficiency is calculated purely based on the fuel utilization estimated from the electrical performance – and not verified.

Commercial systems to test fuel cells exist, for example those manufactured by SOFCPower (models for both planar and tubular geometries are available). While hardly exorbitant their cost was deemed excessive for this project as it was, essentially, the pilot to a new area of research at Cranfield University. Thus, one had to be designed and constructed in-house.

13.2 FC Test Rig Specifications and Design

The design of the bespoke test rig was worked on in parallel to other experimental areas from the very beginning of this project and continued to evolve as difficulties were resolved and occasionally new ones emerged. This somewhat unconventional approach was taken to ensure the test rig does not artificially constrain the fuel cell design (in cases where the rig is designed before the cells are fully realised) nor the reverse where the fuel cell design inhibits finding elegant solutions to test rig challenges (possible when the fuel cell design is established before a fuel cell test rig design concept).

The basic specifications are that the rig must operate at sustained temperatures in excess of 1,000 °C (ideally continuously for 24 h periods) under a hydrogen atmosphere inside the fuel cell and fuel line, air on the outside of the fuel cell, and a mixture of hydrogen and water vapour in the exhaust line. Additionally, the setup must provide means to connect at least two thermocouples to monitor *in situ* the temperature of the fuel cell, as well as sufficient wires for 4-probe electrical connection. The overall rig must

furthermore be gas tight at all relevant operating temperatures both to prevent unwanted gas mixing internally and also prevent any hot gases from escaping the test chamber.

The design of the test rig, which is the bulk of this chapter, is divided into sections by the task that part of the design is required to fulfil. For instance, the furnace and temperature control are described together. The rig itself was housed in the corrosion lab of the National High Temperature Surface Engineering Laboratory (B57 at Cranfield University) to take advantage of the available gas extraction, cooling, safety systems, and gas manifolding resources, not to mention the considerable (and invaluable) experience of staff there.

13.2.1 Furnace and Temperature Control

The furnace was a vertical tubular furnace with a bespoke 316 stainless steel inner tube (made in-house at Cranfield), open at the top. The heating elements were Ni, Cr, Al, Fe alloy wire (commercial name Fecralloy) with a power of 5.5 kW capable of maintaining a maximum continuous operating temperature of 1,100 °C made by Carbolite. Note the furnace tube itself could only withstand sub-800 °C for sustained operation without damage (such as the FC performance test runs). The furnace was secured into a mild steel frame constructed in house consisting of welded box sections.

Temperature control was via a separate controller (Eurotherm 815P I, in a control box made in-house and designed by Tim Pryor). The large thermal mass of the furnace is the limiting factor on heating and cooling rates rather than the controller (as it is a metal furnace tube rather than an alumina or alumina-lined one relatively rapid heating and cooling rates are possible, limited only by the thermal mass of the furnace).

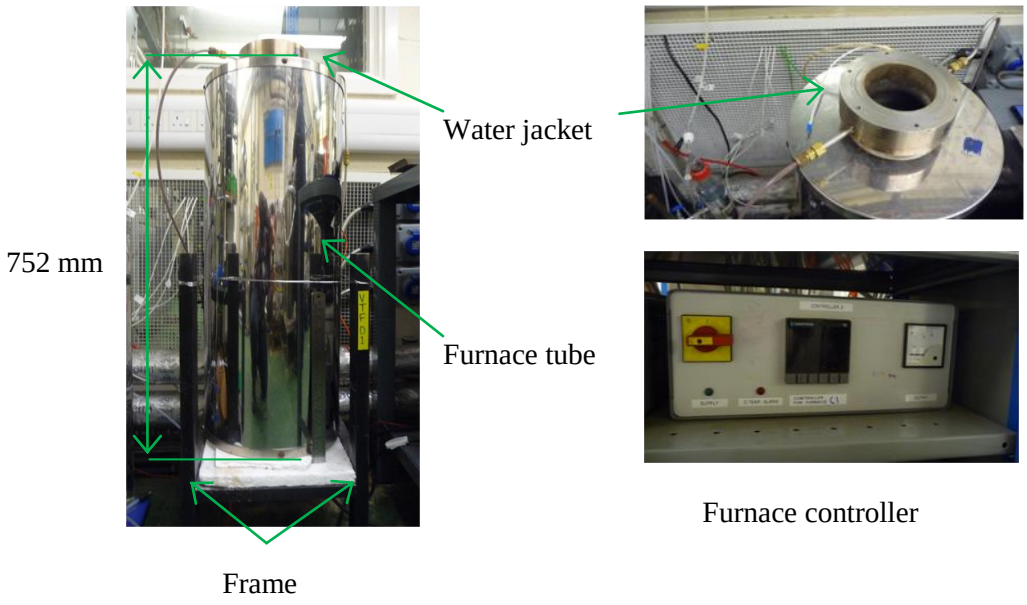

Figure 13-1. Photographs of furnace, support frame and controller.

13.2.2 Gas Metering

Gases were supplied via a mass flow controller or separate manifold, both integral parts of the Corrosion Laboratory, according to the needs of the particular gas line. Gas lines were extended to reach the SOFC test rig and connect directly into the four gas pipes that come through the furnace end cap: air supply (a SS pipe extending to the bottom of the furnace enabling the air to be heated and flow up over the fuel cell), air exhaust, fuel inlet (flows directly into the fuel cell, the pipe connecting to the cell under test in the hot zone near the bottom of the furnace) and fuel exhaust (a U-shaped pipe that connects to the other end of the fuel cell and then exhausted through the top of the rig into a Davey lamp to burn off unspent fuel, this in turn was connected to the exhaust extraction system).

For improved safety the rig was designed to operate with bubblers at the air exhaust and fuel exhaust to create back pressures as follows: A bubbler with a small head of water was fitted to the fuel exhaust downstream of the rig to prevent gas from flowing back into the test rig (fed with fuel at atmospheric pressure). A second, much larger, bubbler was fitted to the air exhaust downstream of the rig to create a slight differential pressure across the fuel cell; this differential pressure means that any leaks will be of air into the cell tube rather than hydrogen into the chamber filled with air. The bubblers created back pressures of up to 1.7 kPa and 6.8 kPa, respectively.

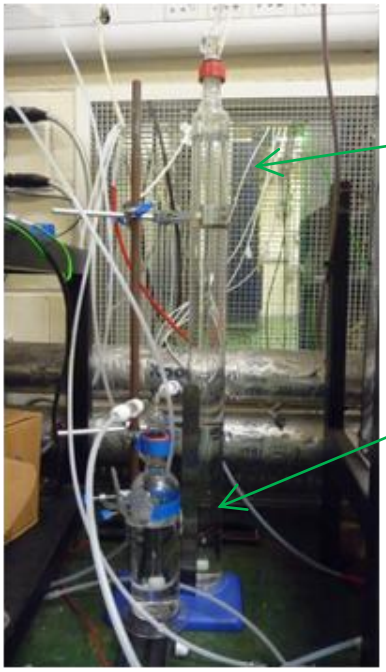

Figure 13-2. Air and fuel exhaust bubbles for overpressure control.

13.2.3 Electrical Connection

There are two elements: first, the electricity generated by the fuel cell required electrical connections to complete the circuit (indeed the reader may recall that a fuel cell does

not generate power unless it is connected to an external circuit); second, electrochemical impedance spectroscopy (EIS) is a powerful tool very commonly used in the characterization of fuel cells of all types. Both of these can be fulfilled by a potentiostat (or galvanostat) with impedance analyser [Macdonald and Johnson, Raistrick, Franceschetti and Macdonald, McKubre and Macdonald, Macdonald, and Wagner from the excellent book edited by Barsoukov and Macdonald (2005)]. For this project I was fortunate enough to have access to a high-end device combining all three: a potentiogalvanostat with impedance analyser (VersaSTAT 3F). The VersaSTAT is programmed and controlled by PC connected via USB, and comes with a proprietary software package enabling this as well as to assist analysis (VersaSTUDIO).

The resistive losses incurred by requiring relatively long wires to connect the VersaSTAT 3F to the fuel cell can be compensated for by using four-point (also called four-probe or four-terminal) measurements. Long wires were needed. Partly because this sensitive and expensive piece of equipment must remain outside of the corrosion lab proper, but also because special consideration must be given to the high temperature connections necessary in the fuel cell furnace itself. The end cap of the furnace, the furnace itself and the frame that supports it are all grounded both for safety and to avoid interference with electrical measurements.

Connection to the fuel cell was achieved as follows: the anode connection consisted of a Ni wire discharge welded onto a machined truncated cone of Ni that was lowered vertically down the fuel inlet and wedges itself in place at temperature in a pseudo-interference fit; a second connection to the anode side is made by a length of high temperature wire (K-type thermocouple wire) tightly coiled around the SS adapter that joins the fuel cell, that connects to the exposed anode at each end, to the rig and emerging from the end cap through a gas-tight multiple feedthrough (Swagelock); the cathode terminal's main current bearing connection consisted of a coil of Pt wire (thickness estimated based on maximum likely current output of the fuel cell) wound snugly around the SOFC and clamped into a conducting rod, the requisite length of which was determined by the furnace temperature profiles (temperature with depth).

The conducting rod, referred to as the current collector rod, was a Ni rod aluminized in-house by a CVD process leaving 40 mm of each end uncoated. The same process was a possible solution to difficulty sealing the fuel cell to the test rig, and is described in more detail in that section. Each end was machined to form a clamp tightened by a stainless steel bolt. The high temperature end (that is, the one in the hot zone of the furnace and positioned as near as possible to the SOFC) was electroplated with a few microns of Pt, and employed an alumina nut and bolt rather than stainless steel. Suitability of this solution was confirmed via an oxidation test of a short section of Ni rod coated in the same way. Observing the growth (or lack thereof) of an oxide is a good indication of the process (CVD aluminising and diffusion heat treatment) success

or failure to create a protective layer. The interaction of aluminised and Pt plated Ni becomes a platinum aluminide after heat treatment (under similar conditions to operating conditions) [Angenete 2002]. In this manner a minimal length of relatively thick Pt wire was used rather than the metre or more required otherwise. The NiAl and Pt were of course necessary to protect the current collection at the anode side at operating temperatures since these would be in an oxidising atmosphere. The second cathode connection was the same as the secondary anode terminal, but instead coiled around the SOFC near the cathode current collection terminal. In all cases where the contacts consisted of a coiled wire a second piece of high temperature wire (a 80:20 NiCr alloy, commercial name Nichrome) was used to cinch it in place. This technique has been tested, and, if employed with care, is effective even at temperatures in excess of 800 °C.

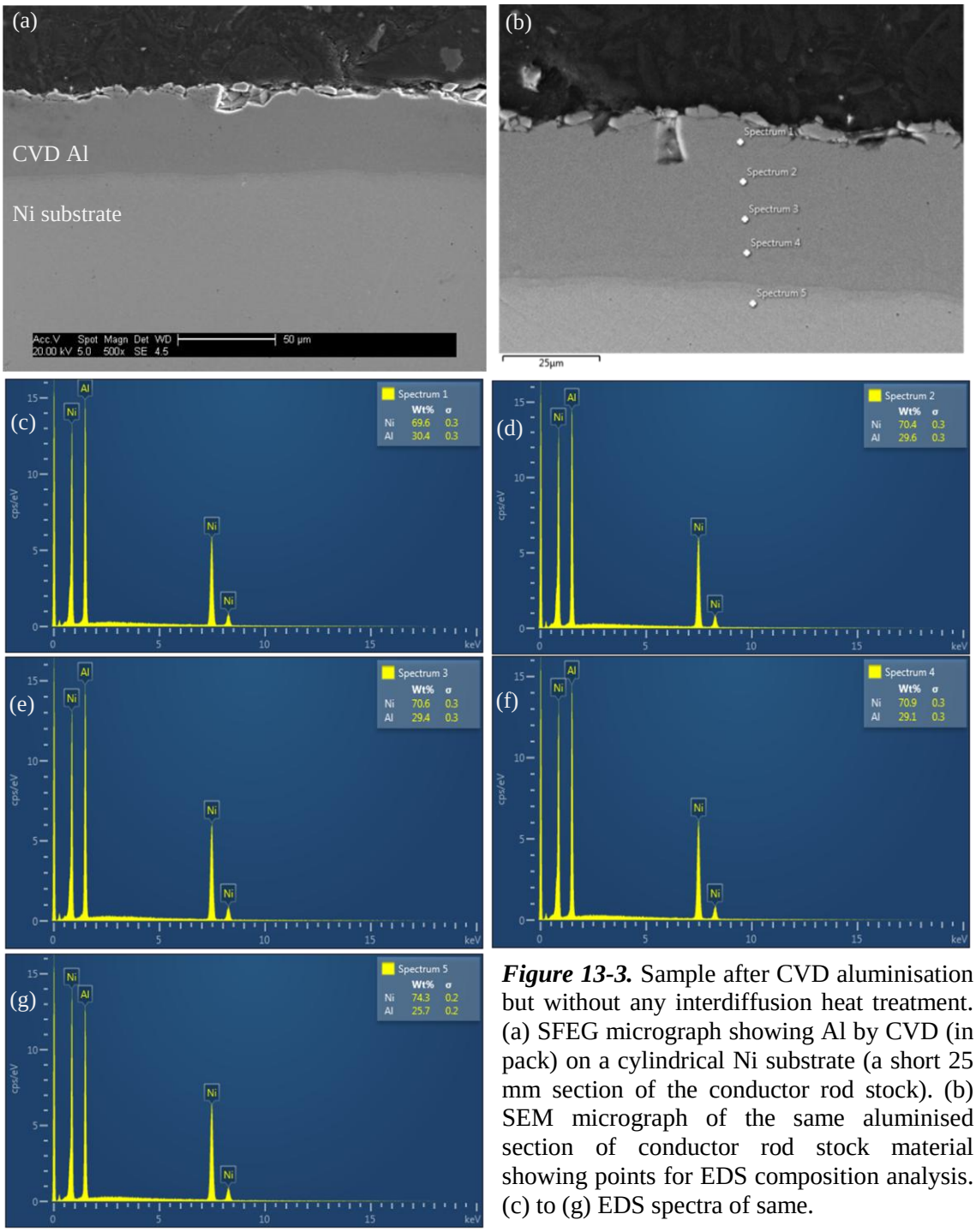

Figure 13-3. Sample after CVD aluminisation but without any interdiffusion heat treatment. (a) SFEG micrograph showing Al by CVD (in pack) on a cylindrical Ni substrate (a short 25 mm section of the conductor rod stock). (b) SEM micrograph of the same aluminised section of conductor rod stock material showing points for EDS composition analysis. (c) to (g) EDS spectra of same.

Figure 13-3. shows a sample that was aluminised but not heat treated. Notice that there is significant inward diffusion of aluminium, though this will be mixed phases. Figure 13-4. is of the same format, showing the results of the heat treatment recommended by Craig (2010). Unfortunately, the conductor rod itself was too large to fit in the vacuum furnace necessitating the exploration of other possible solutions. A further sample was created to this end but heat treated under Ar in a larger controlled atmosphere-furnace

large enough for the conductor rod (this was the same furnace used for all reduction work carried out for this thesis). The results are shown in Figure 13-5.

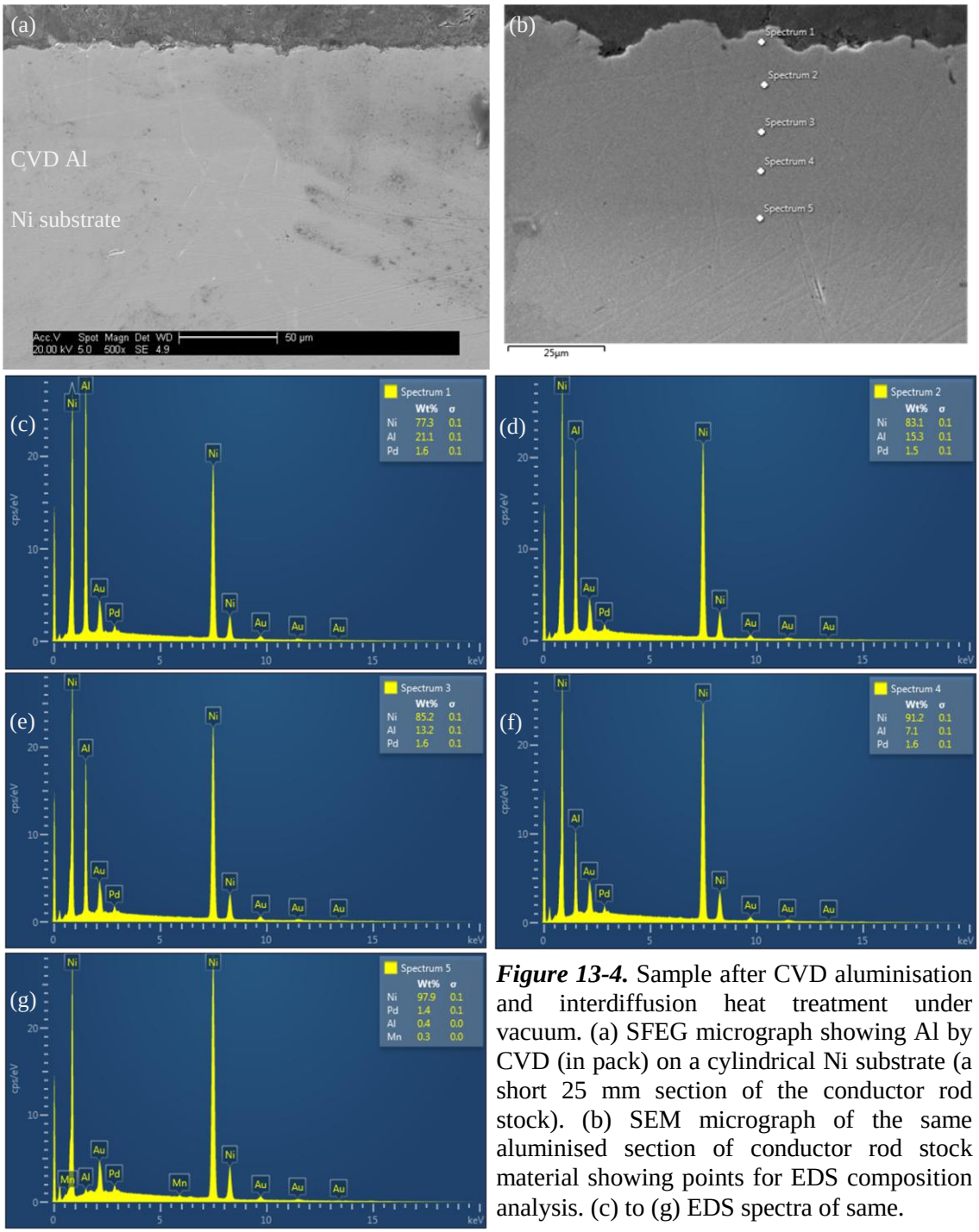

Figure 13-4. Sample after CVD aluminisation and interdiffusion heat treatment under vacuum. (a) SFEG micrograph showing Al by CVD (in pack) on a cylindrical Ni substrate (a short 25 mm section of the conductor rod stock). (b) SEM micrograph of the same aluminised section of conductor rod stock material showing points for EDS composition analysis. (c) to (g) EDS spectra of same.

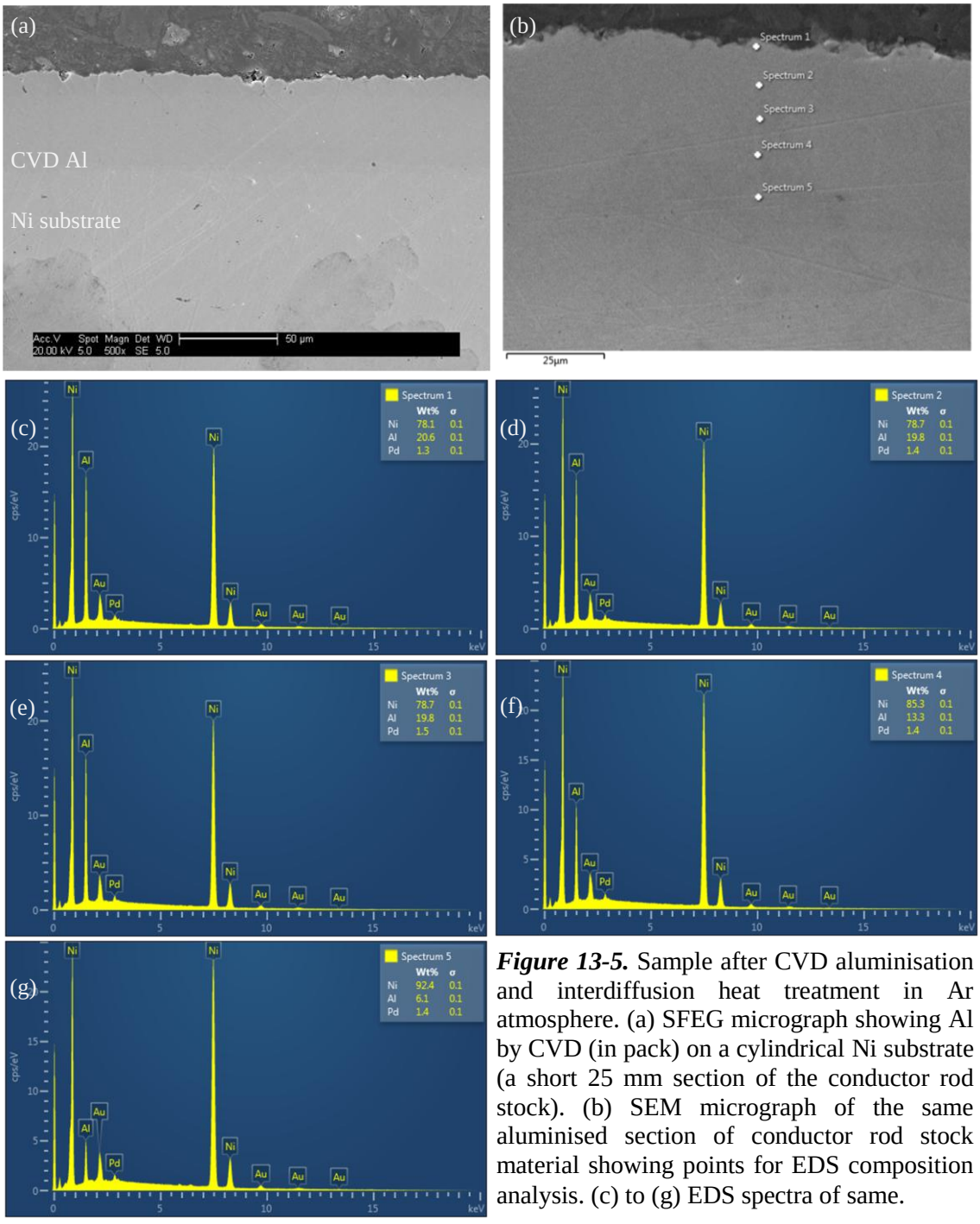

Figure 13-5. Sample after CVD aluminisation and interdiffusion heat treatment in Ar atmosphere. (a) SFEG micrograph showing Al by CVD (in pack) on a cylindrical Ni substrate (a short 25 mm section of the conductor rod stock). (b) SEM micrograph of the same aluminised section of conductor rod stock material showing points for EDS composition analysis. (c) to (g) EDS spectra of same.

As Figure 13-4. and Figure 13-5. show the heat treatment (which diffuses the coating and produces NiAl phase), is effective both under vacuum and in an Ar atmosphere. Thus, carrying out the diffusion heat treatment under Ar (circumventing the small size of the vacuum furnace) will create an oxidation resistant intermetallic to protect the Ni conductor rod during operation.

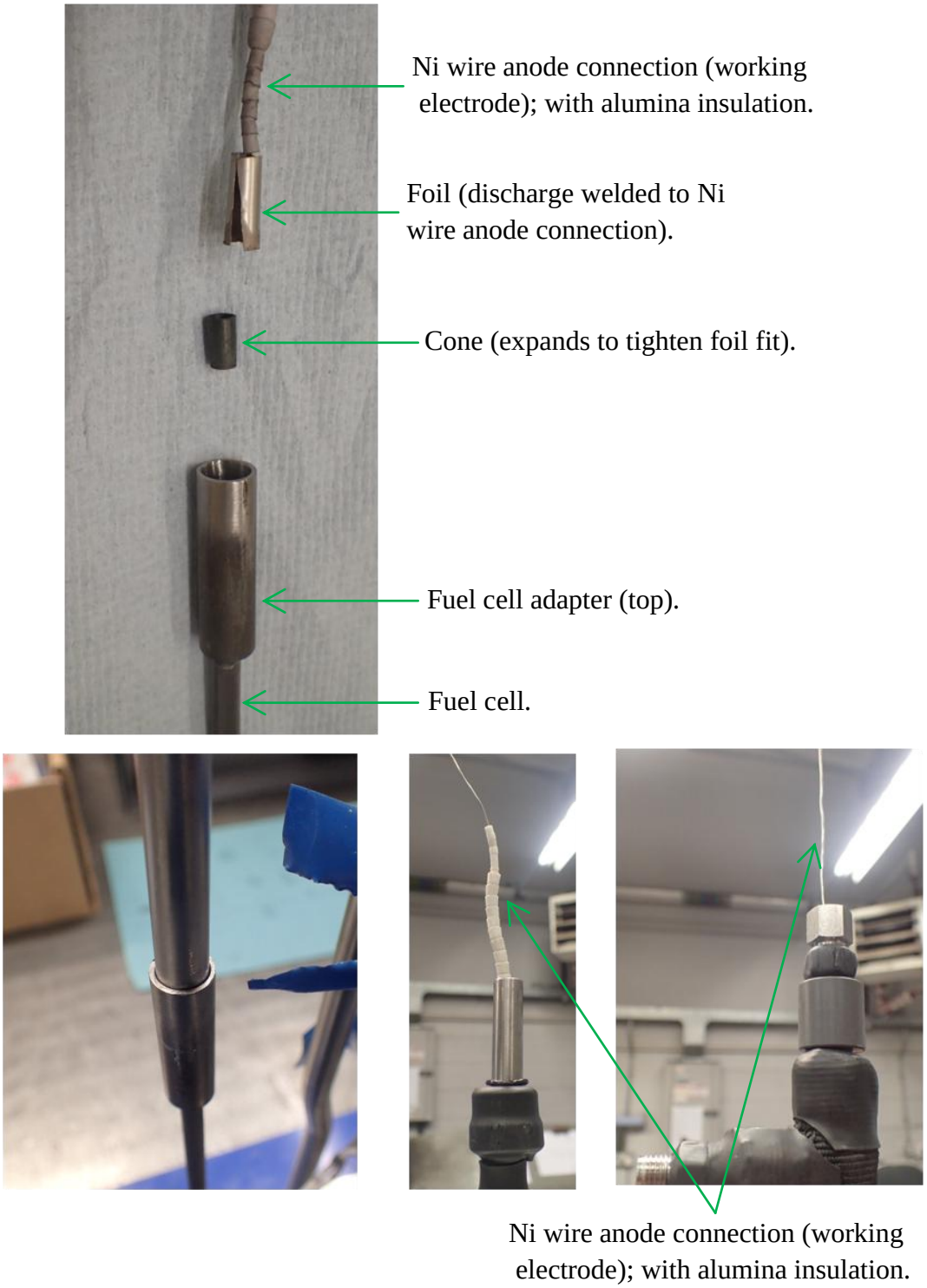

Figure 13-6. Anode electrical connections (cone and foil arrangement).

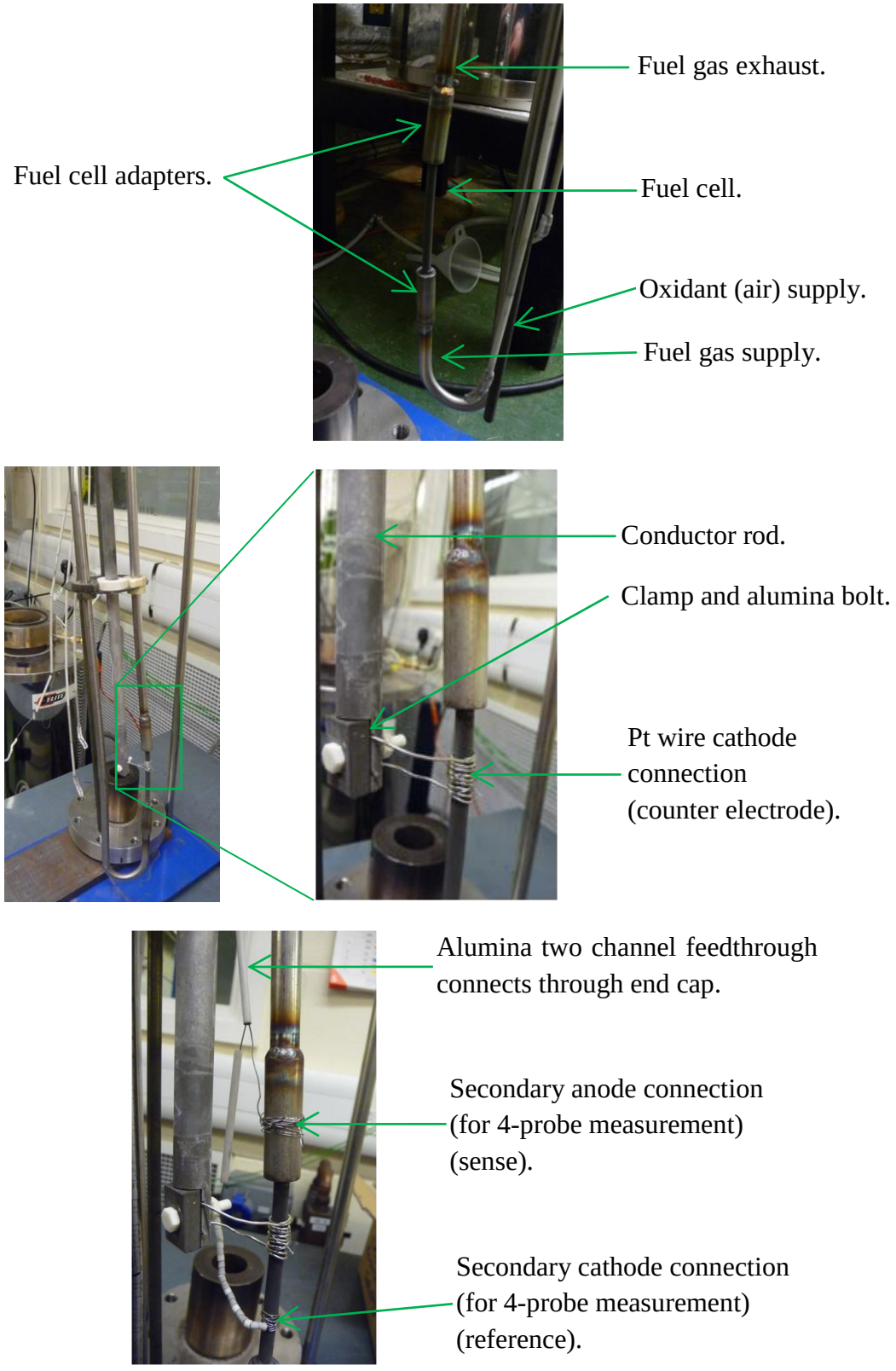

Figure 13-7. Cell gas and electrical connections.

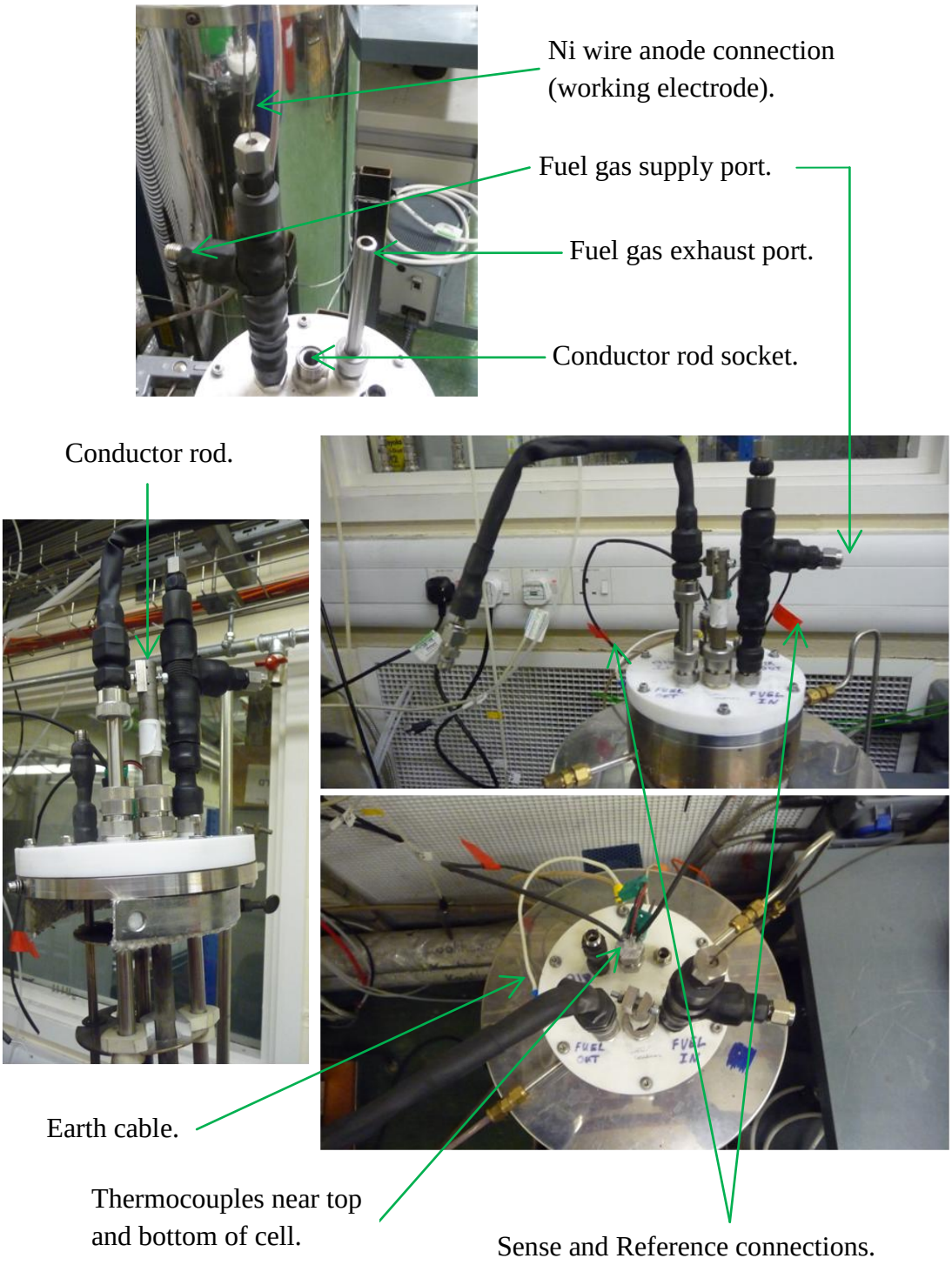

Figure 13-8. End cap layout and connections (gas and electric).

13.2.4 Furnace Temperature Profile

The following are average temperature profiles for the temperatures of interest of the fuel cell test rig furnace. They were used to calibrate the furnace controller and in addition provided crucial information guiding the positioning of the fuel cell (and attendant pipework and electrical connections) to ensure the fuel cell was in the hottest

part of the furnace across the entire length of the fuel cell. Temperature measurement was via a handheld meter and K-type thermocouple.

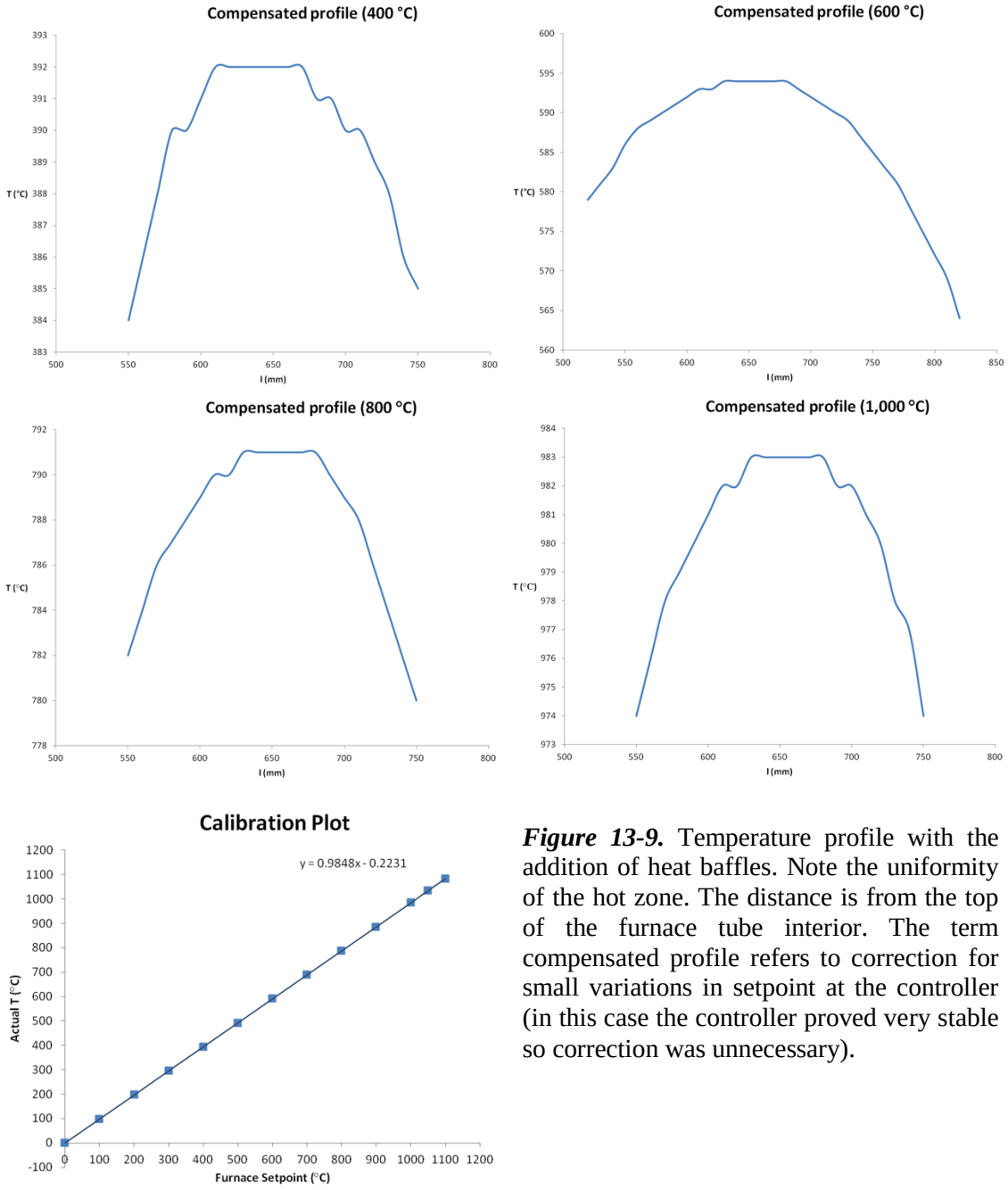

Figure 13-9. Temperature profile with the addition of heat baffles. Note the uniformity of the hot zone. The distance is from the top of the furnace tube interior. The term compensated profile refers to correction for small variations in setpoint at the controller (in this case the controller proved very stable so correction was unnecessary).

Such an exercise was important because the temperature in a furnace is not uniform and needs to be measured to determine the hot zone (a spatial volume at the maximum actual temperature that approaches, often closely, the temperature setpoint on the controller). These measurements allow calculation of a correction factor (usually in the form of a simple linear regression model) to ensure that the actual temperature is the desired one. An additional subtlety is determining what temperature to calibrate to in

such a way as to ensure an adequate volume is heated. In this case, the hot zone must be as uniform as possible over the length of the fuel cell. The addition of heat baffles (a necessary feature that impedes convective heat transfer to protect the end cap from excessive temperature) significantly modifies the temperature profile. Their addition requires an iterative process of positioning internal components and furniture for the gas lines, fuel cell and electrical connections and refinement of the baffle positions alternating with new temperature profiles. After a couple of iterations the ideal positing of all components was determined. An added benefit of introducing heat baffles is more gradual temperature changes in the vicinity of the maximum temperature – or put differently, a longer hot zone with only 1 or 2 degrees variation across the entire length.

13.2.5 Sealing the SOFC to the Test Rig

Preventing hydrogen fuel leak into the main chamber is crucial both to safety and performance. Additionally this must be done in such a manner to prevent damage to the fuel cell. Ideally such a system would not be permanent and thus reusable. As shown in Figure 13-10., below, the design went through a number of iterations. No reusable option was deemed feasible (such designs tend to be bulky, too bulky to fit inside the furnace available given the gas feeding and electrical connections also necessary). As such a permanent seal was designed, that required the minimum machining possible (e.g. rod stock chosen such that the outer dimensions required no machining at all).

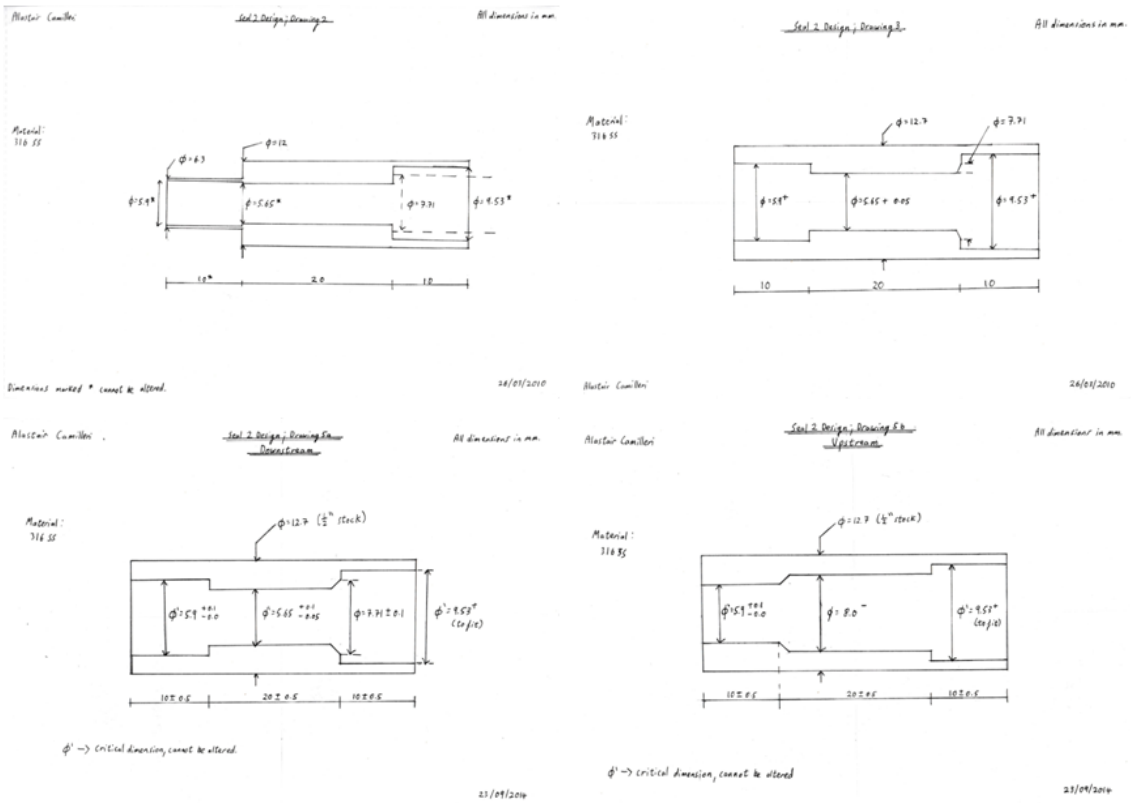

Figure 13-10. Scanned part drawings showing evolution of adapter design (only the most pertinent iterations shown). All dimensions in mm.

The functioning of the seal is straightforward: the part acts as an adapter connecting the 5.9 mm OD fuel cell (the 10 mm length of exposed anode at each end) to standard 3/8” stainless steel gas pipes. The adapters themselves could be conveniently machined from 316 SS, providing sufficient high temperature oxidation resistance to run the planned tests. The seal was formed by a permanent bond. Two techniques were required. Ordinary TIG/MIG or arc welding was adequate to join the adapters to the SS gas pipes. However, selecting (or in this case developing) a suitable method to join the fuel cells to the adapters was more involved.

This most closely resembles a bell-and-spigot joint. This design is only intended for use with the test rig because of the requirement to test single cells under varying conditions and obtain as much data as possible. For eventual prototypes the cell stacks, or perhaps more aptly called current modules since they provide far more significant currents than voltages (making them essentially current sources), would be sealed to fuel supply and exhaust as units rather than individual cells – preferably by laser or microplasma welding – to a faceplate. The final assembly would bear a strong resemblance to a steam locomotive boiler.

Of the scarce mentions of seal design in the tubular solid oxide fuel cell literature the one most commonly associated with high temperature cells (over 800 °C) is the use of a ceramic cement, though often this must be inferred from the context and test setup [Suzuki *et al.* 2008a]. Aremco 552 is purpose-designed for solid oxide fuel cell high temperature sealing, and was also used by the cited source. However, it did not form a gas tight bond when tested. Furthermore, bond quality (both strength and reproducibility) were found to be poor. Several simple tests were carried out consisting of attempting to bond a short section of as-delivered Ni200 tube into a SS part that corresponded to half an adapter piece. Gas tightness was tested by connecting the tube end via silicone hose to an Ar supply line and submerging the assembly in isopropanol. After a few attempts following the manufacturer’s published instructions several more were made with an improved process suggested by the manufacturer (personal correspondence). The strength and reproducibility were both improved however no gas seal could be achieved. The Aremco 552 paste was therefore rejected. The best results achieved in testing the Aremco 552 paste are shown in Figure 13-11. below.

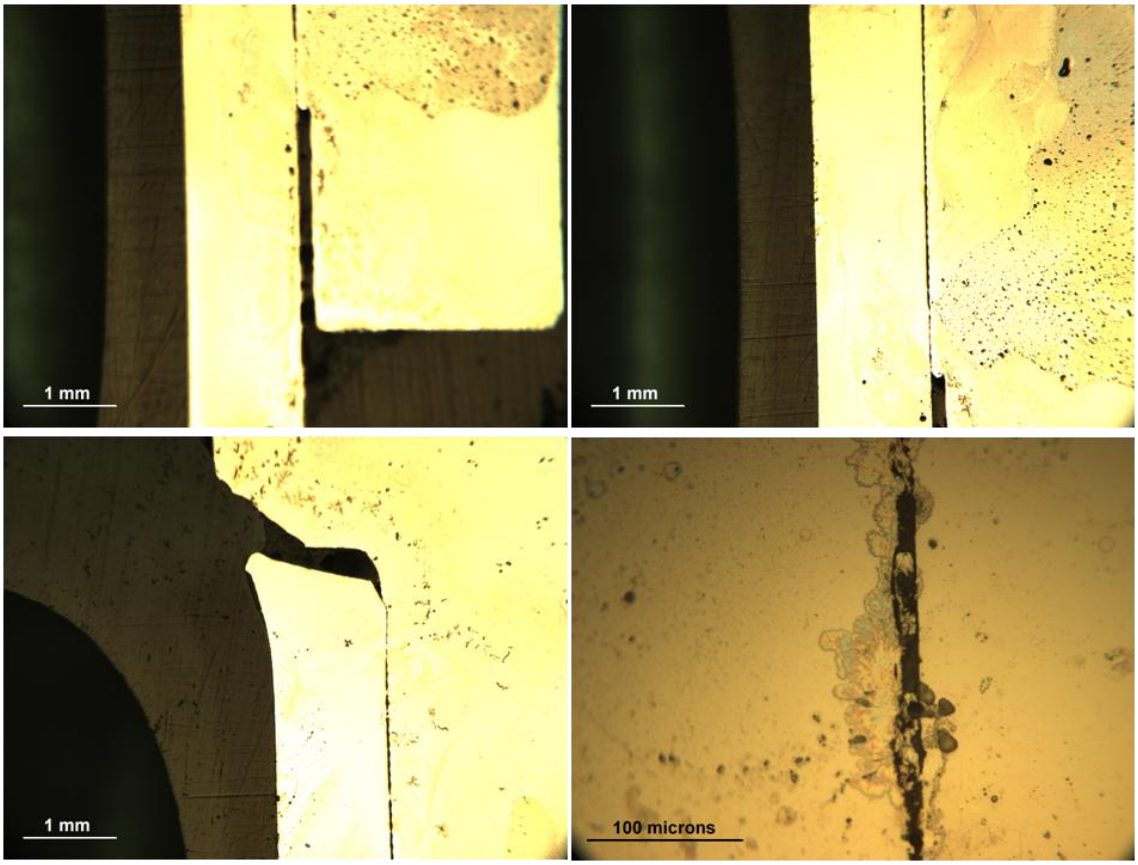

Figure 13-11. Aremco 552 ceramic paste trials. Shown is the most successful attempt bonding a solid (as-delivered) Ni200 tube into a piece of SS bored to match the test rig adapters (Images taken with a Nikon optical microscope with camera and AcQuis image acquisition system).

Conventional welding techniques must be rejected because of the small dimensions of the cell.

However, two unconventional welding techniques were (and indeed still are) deemed very promising. The more exotic of these is also the most suitable joining technique this author has come across – microplasma welding. The salient characteristics of the technique are: very narrow HAZ (heat affected zone) and rapid welding speed (minimising heat absorbed; in this case by the fuel cell). It is suitable for components from 0.1 mm to 1.0 mm thick, limiting its usefulness in many applications but making it ideal for fine workpieces or delicate components. It is capable of welding stainless steels. The recommended shielding gas for austenitic SS is up to 20 vol.% H_2, balance Ar.

No microplasma facilities were available at Cranfield University, nor for outsourcing economically. It did not therefore prove possible to employ this technique for the project. However, the author still considers this the most suitable option. Laser welding offers similar advantages and while generally employed to replace conventional welding

can be tuned to smaller work pieces. Adaptation in this way is highly system dependant, and will not be possible in all cases. While it was possible to trial laser welding in a laboratory at Canfield University it did not prove possible to employ this to join fuel cells to the test rig. The trials were very promising and, with some development to reduce the HAZ (and thereby minimise risk of damage to the cell), the technology is a strong contender for full scale manufacture connecting individual cells into stack arrangements with a mechanically strong, thermally resistant and gas tight bond.

High temperature brazing was another possible solution. It had the advantage of being readily available at Cranfield. This was trialled in parallel with the ceramic cement and welding discussed previously. High temperature brazes have one insurmountable obstacle for this application – they must be heated to a higher temperature than that they will be exposed to during operation. Thus, in order to bond the fuel cells into the SS adapters the parts would need to be exposed to significantly higher temperatures than the maximum operating temperature. While this need only be local heating the small size of components leads to a larger-than-necessary, and far greater than desirable, section that would be exposed to these temperatures. This would inevitably result in uncontrolled microstructural changes. Furthermore, creating a sufficiently elevated localised temperature proved practically very difficult. All attempts made burnt trough the fuel cell before the SS reached sufficient temperature to melt a high temperature braze.

Another possible technique for joining fuel cells to the test rig pipework is diffusion bonding. It will be explained in some detail for reasons that will become clear momentarily. Diffusion bonding is a microdeformation solid phase bonding technique that is finding application in more and more diverse areas [Dunkerton 1990]. In its most basic form it involves holding components together under load at elevated temperature in an inert atmosphere. The inert atmosphere is required to prevent the formation of diffusion-inhibiting oxides. The load is intended only to deform asperities and close voids so is far lower than the bulk yield stress. The temperatures used range from $0.5T_m - 0.8T_m$ where T_m is the melting point of the material in Kelvin (the lowest melting point if there are several). Bond times are usually at least an hour. Surface finish of the mating surfaces is crucial since the materials must come into atomic contact to bond properly [Dunkerton 1990].

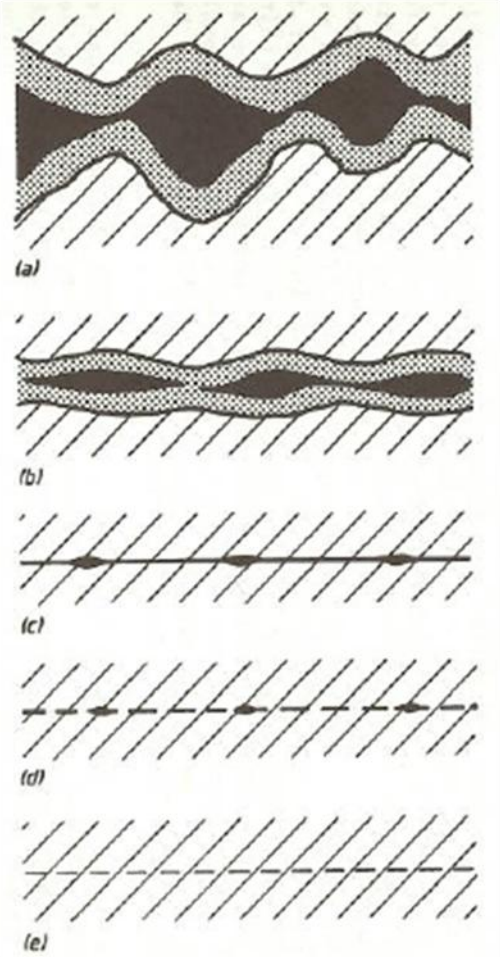

Figure 13-12. The mechanism of diffusion bonding: (a) Initial 'point' contact and oxide contaminant layer; (b) Asperity yielding and some creep leading to a thinner oxide and large voids; (c) After the first yielding and creep, some voids remain with a very thin oxide layer; (d) Continued vacancy diffusion eliminates the oxide layer, leaving a few small voids till the final stage; (e) bonding process is complete [Dunkerton 1990].

Diffusion bonding relies on the combination of two mechanisms to join materials. The first mechanism is hot pressing that uses viscoplastic deformation of surface asperities to bring the mating surfaces into more complete contact. The second mechanism is diffusion (bulk and grain boundary) of material across the rapidly shrinking gap to close voids and form a permanent bond. At no point is there any liquid phase involved in the process. The lack of a liquid phase is one reason the process is quite slow since all voids need to be closed by what effectively amounts to creep. Diffusion bonding and pressure assisted sintering are very similar processes: same mechanism but the purpose differs. It is possible to diffusion bond without assistance from pressure, just as it is possible to sinter without it – only it takes much longer.

In diffusion bonding the materials are brought sufficiently close for short range interatomic forces to influence the process. This involves both intimate contact of the

mating surfaces and the removal or reduction of diffusion barriers. Large plastic deformations are avoided in diffusion bonding, but localised plastic flow must be created by the interface geometry and friction in order to form a bond. The diffusion bonding process is a slow one but has many advantages [Bienvenu *et al.* 1987]:

1. Absence of melting and related defects (for example microporosity, segregation of elements upon recrystallisation). Also there is no heat-affected zone as would be seen with welding, since the entirety of both materials is held at uniform temperature. Some authors make reference to an analogous diffusion-affected zone.
2. Properties at the joint are the same as of the bulk. There is no change in material properties or the formation of phases or intermetallic compounds at the interface.
3. Capable of bonding different materials, not just metals. One very useful application is the joining of metals to ceramics or cermets.
4. Uses relatively low temperatures (two-thirds of the melting temperature of the material with the lowest melting point is typical).

However, it is usually limited to joining parts only a few square centimetres in cross-section because diffusion bonding tends to require isostatic or uniaxial pressing under controlled atmospheres or vacuum to prevent the formation of oxides that may interfere with the process and weaken the bond [Bienvenu *et al.* 1987].

There are minimum pressures and temperatures to give satisfactory bonds between materials [Bienvenu *et al.* 1987]. The effect of temperature is stronger than that of stress [Bienvenu *et al.* 1987]. The minimum temperature depends greatly on the solvus of the species (boundary between completely solid and mixed solid and liquid or completely liquids phases of the phase diagram). The optimal temperature depends on the relative stress and also the oxidation characteristics of the materials [Bienvenu *et al.* 1987]. The latter is important because it dictates the tendency of the material to form diffusion-inhibiting compounds.

Diffusion bonding results in a clear interface area between the materials, with properties necessarily somewhat weaker at the interface than in the bulk. This is because there is little recrystallisation so the interface is a mechanical singularity – properties change suddenly from one set to another across a few grains (in theory across a grain boundary) [Bienvenu *et al.* 1987]. This is especially true when different materials are joined. While the diffusion-affected zone is a weak spot in the material it remains a very strong bond [Bienvenu *et al.* 1987]. More important to the properties of the bond (especially bond strength) is the presence of diffusion-inhibiting impurities and the formation of minor phases [Bienvenu *et al.* 1987]. For the modelling of the diffusion bonding process the interested reader is referred to Wallach and Hill [1987].

Diffusion bonding is a high temperature process, and as such may affect changes to the microstructure. See the cited references for details. The most common effects are: grain growth (and exaggerated grain growth at the interface is a sign of a good bond according to Bienvenu *et al.* 1987), recrystallisation and modification of secondary and tertiary phases at the interface, changes in composition at the interface, and penetration of one material into the other (rather than forming a clear bond interface).

There is one serious impediment to the application of simple diffusion bonding for our purposes: the overall manufacturing process of the fuel cells makes machining the adapter parts to sufficient fit for 'dry' diffusion bonding a somewhat unrealistic prospect. Each end of every cell would need to be carefully measured and adapters machined to match by precision milling (rather than conventional turning on a lathe) to account for any slight out of roundness as well as matching dimensions exactly. As such, in lieu of a better alternative, it was decided to create a modified diffusion bonding process.

There exists a modification to diffusion bonding (sometimes considered a separate process) that introduces liquid phase to facilitate bonding. This is often referred to as liquid phase bonding. The technique is superficially similar to brazing, but the liquid phase is not generally a composition dissimilar to the mating surfaces. General liquid phase bonding will not be discussed further in this work as it was a novel (and to the best of the author's knowledge entirely new and unique) approach that was taken, explained below.

The first hurdle was determining a suitable material. Such a material must be stable at high temperature when exposed to both oxidising and reducing conditions, must readily form a liquid phase that will fill the gap between the fuel cell and adapter thereby conformably joining the two, and naturally the material must also be capable of forming a gas tight seal. The highly innovative component came about directly as a result of the search for suitable liquid phase materials: the use of combustion synthesis to create high temperature intermetallics via a relatively low temperature heat treatment.

As with the oxidation-reduction treatment to create porous anodes I cannot say for certain what inductive path led to this process. I can certainly say that discussion with Mark Craig (then a post doctoral researcher in the same group) and subsequently his doctoral thesis had a strong influence. It is because of his work and its behaviour under the expected operating conditions that the formation of nickel aluminides (NiAl) was of such interest.

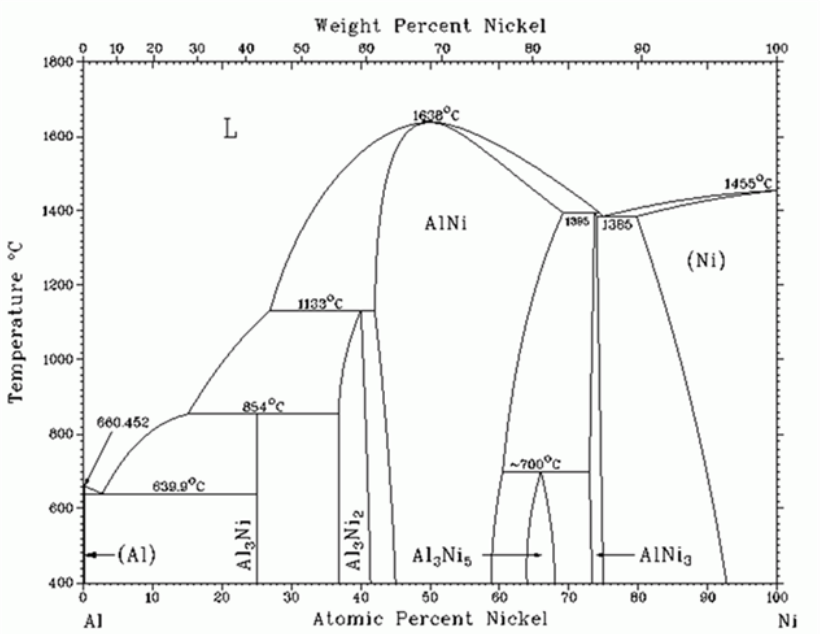

Figure 13-13. The Ni-Al binary phase diagram. Note the intermetallics $NiAl_3$, Al_3Ni_2 and $AlNi_3$.

The formation of all nickel aluminide compounds is exothermic, with an enthalpy of formation ranging from -51.3 kJ/g-atom ($Ni_{0.61}Al_{0.39}$) to -61.2 kJ/g-atom ($Ni_{0.505}Al_{0.495}$) varying by composition as shown in parenthesis [Craig 2010]. Craig's thesis gives tabulated enthalpies of formation ordered by nickel aluminide phase/composition ($NiAl_3$, Ni_2Al_3, etc.) including melting point and UCL and LCL (upper composition limit and lower composition limit respectively).

From a figure in Craig (2010) that plots the enthalpy of formation of other aluminides (NiAl ranging from -38 kJ/g-atom to -67 kJ/g-atom) four other useful compounds appear: YAl (from Y_3Al_2 -40 kJ/g-atom to YAl_2 -50 kJ/g-atom); ZrAl (from $ZrAl_3$ -48 kJ/g-atom to $ZrAl_2$ -52 kJ/g-atom); CrAl (from Cr_2Al -11 kJ/g-atom to $CrAl_3$ -12 kJ/g-atom); and FeAl (from FeAl -28 kJ/g-atom to $FeAl_3$ -30 kJ/g-atom). These are of particular interest to diffusion bonding the fuel cell into the stainless steel (316) adapters described because: firstly, while the sputtered aluminium is on the Ni anode it is in contact with the electrolyte (containing Yttrium and Zirconium) which may form aluminides, also if the deposition resulted in an oxygen deficient coating (something unintended but not especially unlikely with EB-PVD). Secondly because in diffusion bonding with the stainless steel (containing Fe and Cr) may form aluminides also that may have a detrimental effect on the process by overheating the joint and damaging it.

Recall from eqution (4.4) that $\Delta G = \Delta H - T\Delta S$. "The enthalpy of formation is the main driving force for intermetallic formation as entropy values and change in T are thought to have a minimal effect on the formation of an ordered compound." [Craig

2010] ΔG is therefore taken as equal to ΔH, and, again after Craig (2010), $\Delta H_{reaction} = \Delta H_{products} - \Delta H_{reactants}$.

The ICON heat treatment, developed by Craig (2010), capitalises on the exothermic heat of formation to assist with interdiffusion: creating a β-NiAl layer. He was also able to determine that the addition of Cr does not deleteriously affect the composition. The reaction is a type of Combustion Synthesis (also known as Self Propagating High Temperature Synthesis). Craig (2010) gives a good review in brief, and cites several sources the interested reader is encouraged to consult. The interdiffusion works by a net inward movement of Al [Craig 2010], that is, into the Ni substrate (in this case the ends of the fuel cell to be joined to the SS adapters). The heat treatment was carried out in a vacuum furnace as follows [Craig 2010] (vacuum furnace was pumped to 5×10^{-6} mbar before the heat treatment):

Ramp (°C/min)	Target T (°C)	Dwell (min)
10	620	60
10	820	60
40	0	END

Table 13-1. ICON Heat Treatment (at 5×10^{-6} mbar).

Craig's (2010) work with DSC (Differential Scanning Calorimetry) indicated that the heat treatment may also work as intended in a simpler form: a continuous ramp from room temperature to just 660 °C. As a result of Craig's work the heat treatment used to test the formation of NiAl as a means to bond the fuel cell (at the exposed Ni ends) to the SS adapters employed a heat treatment consisting of a ramp from room temperature to 660 °C (3 °C per min), then cooled back to room temperature at the same rate. The heat treatment was carried out in a 100 vol.% H_2 atmosphere at low flow (the minimum flow at which the Davey lamp could operate safely burning off the exhaust). The hydrogen served to lower the oxygen partial pressure and prevent the formation of alumina during the heat treatment replacing the vacuum furnace whose interior was too small. The intermetallics formed by the heat treatment provide good oxidation protection ensuring a stable gas seal in use.

The next hurdle was determining a suitable method to introduce aluminium into the bond in a way that is facile, conforms to the geometry of the joint and is amenable to the required heat treatment. Craig (2010) utilised CVD to aluminise Ni superalloy substrates prior to heat treatment for interdiffusion (taking advantage of combustion synthesis), although in this case the NiAl was a surface coating rather than a bonding agent. CVD was not suitable in this case because the adverse processing conditions were very likely to damage the fuel cells (particularly by altering microstructure). Furthermore, the effect of the carrier gases is unknown.

A surprisingly simple solution presented itself. Al catering foil is high purity and of very uniform thickness. The material available was measured to be 10 μm thick by micrometer (variance was negligible for the purposes of this work). Several trials were carried out in which the foil was cut into a strip 10 mm wide and wrapped tightly around one end of the fuel cell end (the exposed 10 mm of anode) and carefully inserted into the SS adapter. The fit between any given cell end and any given adapter varied such that the exact length of Al foil had to be determined each time by trial and error, the excess being cut from over-long strips. Generally approximately 2–2.5 layers of foil resulted in a tight fit. A tighter fit is beneficial because it facilitates bonding. After both ends were prepared in this way each test cell was placed in a long ceramic boat and heat treated as described in a horizontal tube furnace. Initially heat treatment was carried out under Ar (as this was previously shown to be an acceptable substitute for the vacuum furnace) in lowering p_{O_2} without deleterious effects.

The process was somewhat fiddly but worked well, consistently creating very strong bonds. However, the process did not result in a gas tight seal. This was tested by immersing the assembly, sealed with a silicone plug at one end and connected to a helium bottle at the other, in a measuring cylinder of isopropanol. It was subsequently repeated with a modified heat treatment – a ramp to 700 °C with a 30 min dwell. The results were unfortunately the same. A third attempt was made, re-heat-treating this sample. A solution of water (6 ml), isopropanol (4 ml) and 200 mg (2 wt.%) ammonium chloride (NH_4Cl) was prepared and added, by pipette, to the joint. This was then heat treated a second time, in a different furnace (a vertical tube furnace) with the same heat treatment. The gas was changed to a 5 vol.% H_2 (balance Ar) mix. The intention was to use the highly reactive salt to remove surface oxygen from the Al foil that was believed to be impeding the foil from melting and subsequently diffusing into the Ni sufficiently to create the desired bond. Although the leak was slightly reduced the seal still leaked significantly.

The initial tests carried out showed that Al foil was not sufficiently conformal to fill the space between the cell and the adapter for bonding to take place across a sufficient portion of the cross section at sufficient sites along the length to prevent gas transport. At least to some extent this can be attributed to surface oxides preventing the Al from melting. This resulted in small gaps creating a connected network through the bond along the long axis. The network proved porous enough to reject this process for the purpose of creating gas tight seals between the fuel cells and test rig pipework. The use of a NH_4Cl solution was beneficial but insufficient by itself.

An alternative means to supply Al to create the intermetallic was needed. The salt solution described above was mixed with fine Al powder (5 μm, Alfa Aesar) to create a slurry. This was coated in several thin layers directly onto the Ni tube ends, which were then assembled into the SS adapters before drying completely and heat treated as

previously (700 °C, 30 min dwell, vertical tube furnace, 5 vol.% H_2 (balance Ar) gas mix). The leak was reduced: finer bubbles indicating a more closed network. The result was still unacceptably permeable, however. A further attempt was made using a thicker slurry, approaching the consistency of thick cream. The heat treatment was altered to 750 °C for 1 h, under 5 vol.% H_2 (balance Ar). Modifying the heat treatment in this manner would ensure all of the aluminium powder melted to give the bonding the best possible chance of both creating an intermetallic with the Ni as well as fill all spaces with material. The result was very small bubbles, and possibly a slight reduction in overall leak rate but still far from gas tight. Thus far the process, using Al, did not result in reproducible gas tightness.

Concurrently with developing the process the formation of intermetallics and the bond microstructure were analysed by SEM and EDS. Refer to Figure 13-14. and Figure 13-15. respectively.

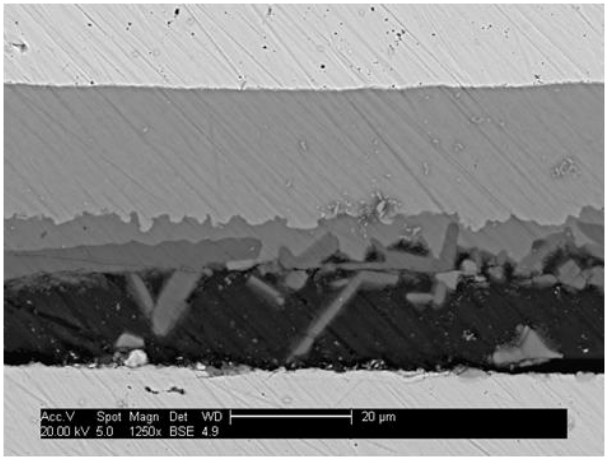

Figure 13-14. SEM micrograph of cell-adapter seal with Al powder. Note the different phases visible by use of a back scatter detector (and the resulting atomic number contrast).

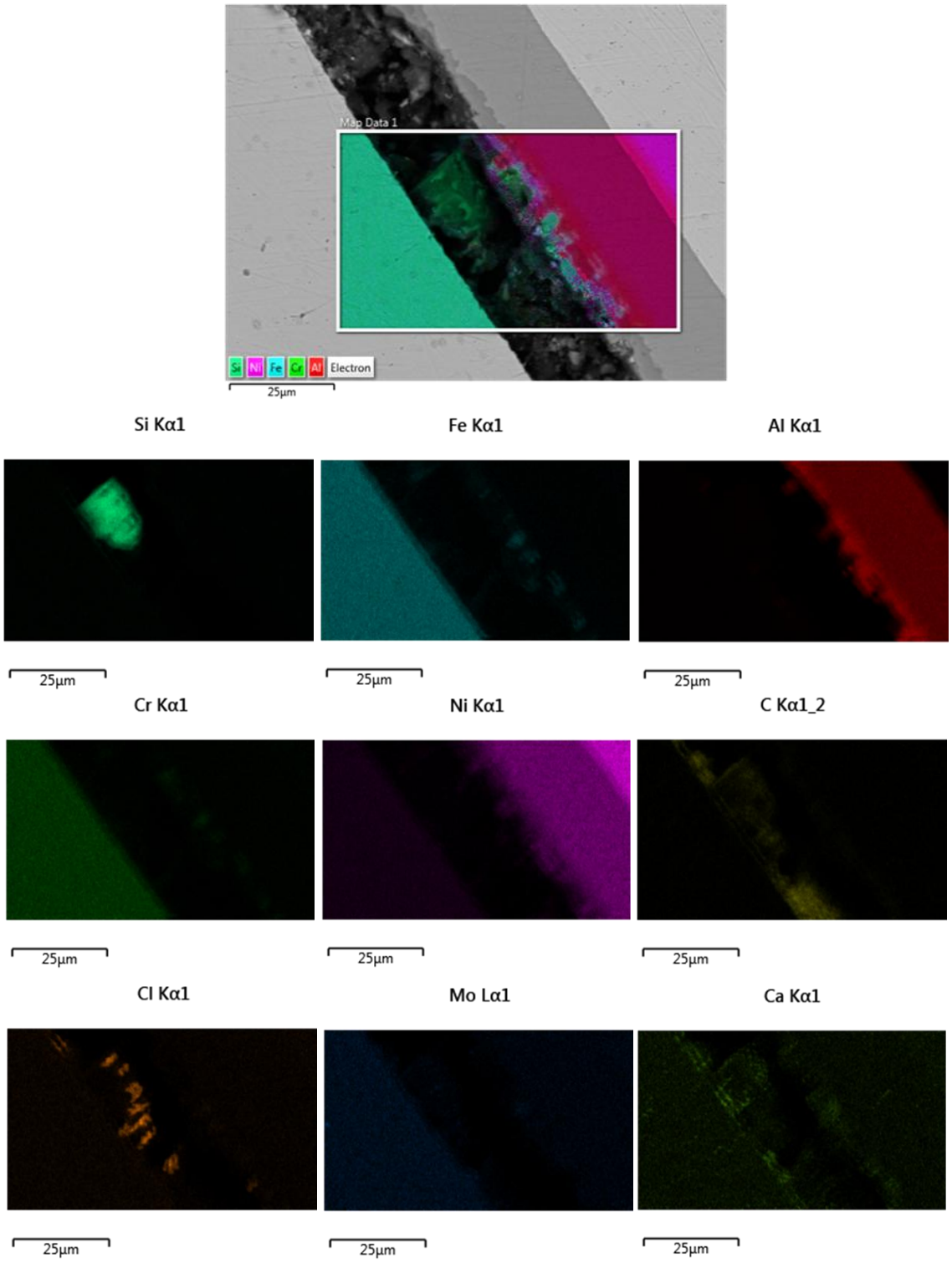

Figure 13-15. EDS of cell-adapter seal with Al foil.

The author believes that the aluminium failed in some of the powder to break through the inevitable thin alumina shell of the particles. Thus the aluminium powder would have to some degree sintered together rather than melted. This was sufficient to impede good wetting of molten Al on the two surfaces and thence deleteriously effect the

slurry's ability to reproducibly create a continuous intermetallic phase and hence a gas tight seal.

It was back to the drawing board to some extent. The process worked surprisingly well, and several proof-of-concept tests showed potential in other applications (particularly where gas tightness is unimportant). However, the gas tightness was still a critical hurdle to overcome. After some discussion with Professor John Nicholls it was decided to search for other potentially adequate materials. These would be assessed initially based on their binary phase diagram with Ni. The selection criterion used was a relatively low melting temperature. Lead was immediately rejected, without even consulting its phase diagram, due to the dangers posed by working with Pb at high temperatures. Tin was found to be the only promising and practical candidate. The binary phase diagram of Sn and Ni revealed that it forms, like Al, high temperature intermetallic phases. The first of these forms at just 300 °C, ideal for initial testing of the new material. Sn also forms an intermetallic phase resistant to very high temperatures; 1,264 °C for Ni_3Sn_2.

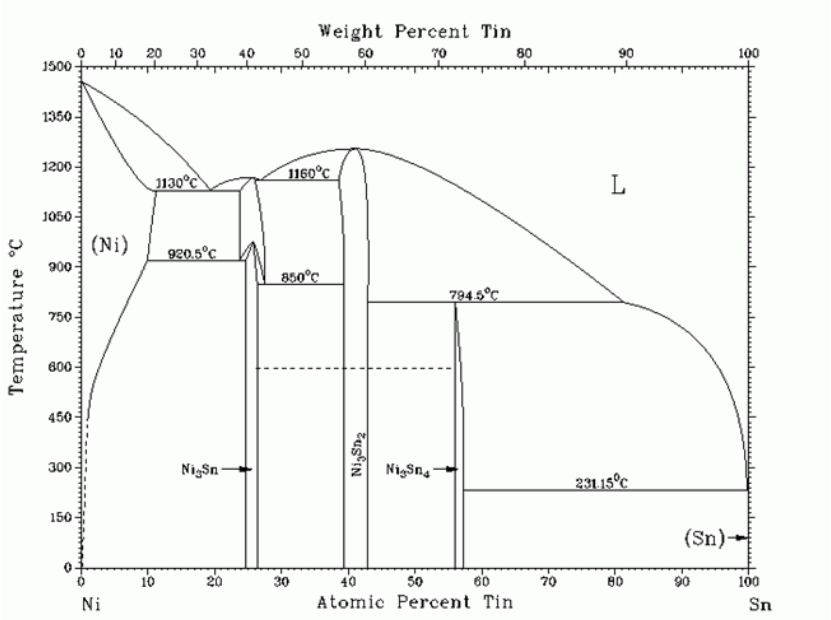

Figure 13-16. The Ni-Sn binary phase diagram. Note the intermetallics Ni_3Sn_2 and Ni_3Sn_4.

A thicker slurry was prepared once more. This time using Sn powder (44 μm, Alfa Aesar) and a saturated solution of NH_4Cl salt in distilled water. The prepared solution was added to the dry powder by pipette, in increments of 3 or 4 ml, mixing thoroughly, until the desired consistency was achieved. The first test was to determine whether the new material would result in a physical bond by combined liquid phase and diffusion bonding. The sample and adapter joined by the new paste formulation were heat treated as follows: ramp at 6 °C per min to 400 °C and slow cool (no dwell). The test would

also reveal whether the Sn-based paste could create a strong bond and gas tight seal thanks to the low molten viscosity and improved wetting of Sn over Al on stainless steel. The result was a mechanically sound bond, even with a cell that was rather out of round used for the express purpose of ascertaining how closely the cell must fit the adapters with this new slurry formulation. Even more promising the bubbler test showed the system still leaked, but only through the cell itself (see chapter 1 – the permeameter) not through the seal – at long last a solution was found.

The same sample was then re-heat-treated to reach the Ni_3Sn_2 intermetallic. According to the Ni-Sn binary phase diagram the second intermetallic – the one of interest – requires heat treatment to above 795 °C to form. The sample was heated to 800 °C (same ramp as previously) with a 12 min dwell in a 5 vol.% H_2 (balance Ar) gas mix to prevent oxidation. No deleterious reactions with Ni (the anode) or YSZ (the electrolyte) were observed. The process was therefore deemed suitable for bonding cells to the SS adapters necessary to connect the cell to the test rig.

The subsequent round of testing had a twofold objective: assess reproducibility of fabricating a gas tight seal by this method and more thoroughly measure the quality of the seal. Gas tightness was determined by permeametry, as discussed and described in chapter 1, a technique that would comprehensively demonstrate the ability to create a gas tight seal. The same permeametry setup was used except a solid Ni tube was used to exclude gas permeance through the cell from the measurement and the parts were joined together by this, as yet unnamed, procedure. There were three consecutive failures, each leaked very badly. The Sn coated the solid Ni tube away from the SS adapter pieces leaving voids in the joint. This was attributed to poor wettability on SS relative to pure nickel. The test was attempted a fourth time replacing the SS permeametry parts with new ones manufactured from Ni200 rod stock. The result was a complete success. An initial bubble test in isopropanol showed the seal to be completely gas tight up to 1.5 bar of He. Higher pressures were not attempted to prevent damage (since the sample was intended for permeametry). Permeametry likewise showed no detectable gas permeance using pure hydrogen over several days.

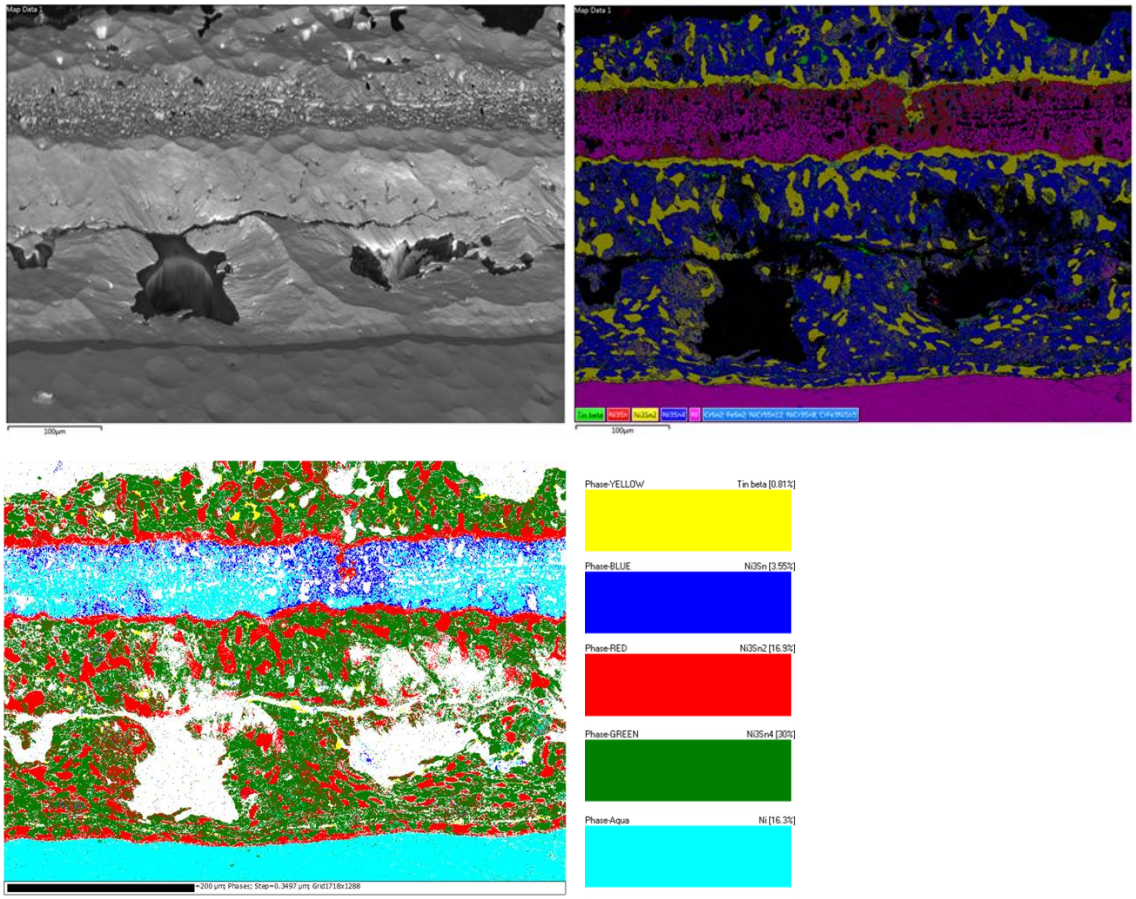

Figure 13-17. EBSD of cell-adapter seal with Sn slurry. Note the presence of bonding slurry inside the fuel cell (above the porous Ni area at the top of the micrographs, especially visible with EBSD phase-colouring).

As before the bond microstructure was analysed by SEM and EBSD, shown in Figure 13-17. Some of the paste appears to be on the inside of the tube (above the porous Ni anode in the figure). This indicates too much may have been used in preparation for heat treatment or that it flowed around the cell inside the closed-end permeametry fitting. The sample appears to have been damaged during sample preparation. Recall that the tube was a cell (and therefore the portion shown is a porous Ni tube). As such the voids evident in the upper Ni area are not damage but the normal appearance of the extremely porous anodes. Most likely due to mounting in a hot press with Bakelite (required for cutting cross-sections). The FC tube end near the site of the joint buckled, belling outwards. Generally this method of sample mounting was avoided because of the fragility of thin walled samples such as those used throughout this project. However, it was found to be an acceptable method to prepare samples for microscopy and EBSD for the adaptors since the area of interest is joined into a sufficiently sturdy stainless steel or Ni part (the adapters or permeametry fittings). It is not clear why this proved insufficient on this occasion although a longer than usual exposed section of tube may have been the determining factor. There is microstructural evidence in Figure 13-17. supporting damage during mounting as opposed to during the bonding process. The

cracks show no sign of healing and are therefore most likely post-heat treatment. The buckled tube end attests to sufficient pressure being exerted in the tube to cause the damage noted. Furthermore, the adapters seem to have been machined to a poorer finish possibly contributing to the damage. It is less clear why this sample contains many more voids, and of a generally larger diameter, than previous cases. It is worth reiterating that the voids did not prevent a gas tight seal from being created nor significantly impact the mechanical strength required for assembly into the rig and cell testing.

As the EBSD results in Figure 13-17. show the majority phase of the intermetallic was Ni_3Sn_4 (T_m = 794 °C). However, it is clear that the more desirable Ni_3Sn_2 (T_m = 1,160 °C) was in the process of forming. The temperature for the heat treatment was therefore adequate but the dwell time insufficient for complete transformation to the Ni_3Sn_2 phase. This need not concern us overmuch since the test rig furnace has a large thermal mass and therefore ramps to temperature very slowly. For those elevated temperatures where the Ni_3Sn_2 phase is required (i.e. operating temperature is above 794 °C) are expected to undergo the necessary transformation of intermetallic phase from Ni_3Sn_4 to Ni_3Sn_2. Some pure tin infiltrated the porous anode section at the joint area. Tin is sufficiently conductive to have an insignificant effect on the electrical performance of the cell provided it remains at the ends and does not diffuse significantly into the cell proper (i.e. towards the middle) where it has an unknown effect on the electrochemical reactions at the anode side and may also diffuse into the electrolyte.

Potentially also of interest is the area where the cell appears to have been infiltrated by Ni_3Sn_2 apparently filling several large connected pores. The importance of this, if any, is unclear. It is rather interesting that the pores formed during the oxidation-reduction process to create the anode are sufficiently large to allow molten tin to enter.

As a final proof-of-concept test an anode-electrolyte tube was used to repeat the previous test (AEC.20/03/15-125;10;0.3.1100(1000)-F.04). In this case, due to the permeable nature of the AEC, permeametry would be of little help in assessing the bond. Instead bubbling in IPA (same procedure and pressure as before) showed that indeed the seals were gas tight and the only gas bubbles visible were from the AEC surface. The main reason for utilising the permeametry fittings rather than test rig adapters, however, was to ascertain whether it would be safe to run the cells for electrical and electrochemical testing. The bond is gas tight as demonstrated. However, the electrolyte is not. Therefore, we must acknowledge there are additional safety considerations to operation of these fuel cells. Primarily it was necessary to determine whether any of the unused fuel (hydrogen) leaking through the cell ignited upon contact with oxygen will merely burn, much like a gas lamp with the flame remaining near the ‘wick’ or form a rapidly expanding gas front (an explosion). Unused fuel leaking into the oxygen to a sufficient concentration to ignite is a likely occurrence during higher

temperature tests once the partial pressure of hydrogen in the oxygen containing gas is greater than 20%).

In order to test this hydrogen was flowed into the sample. The exhaust route was through the AEC walls (since the permeametry end cap is closed). The hydrogen was ignited via a lit splint and the gas flow rate varied while the resulting flame was observed closely. The sample was enclosed by a mesh shield (the same sort used on Davey lamps) to confine the flame. This was dubbed a burner test. Figure 13-18., below, shows a selection of photographs demonstrating that the flame remains close to the cell surface, The cells, therefore, are safe to test. The results are even clearer on video, but the photographs shown suffice to show this.

A stock of stainless steel adapters had already been produced (dating back to the previous plan to rely on laser welding once it proved viable). It was necessary to modify these so the mating surfaces were Ni, as discussed above. Electroplating was the most facile technique. A Ni wire was used as anode, suspended inside the adapter bore, to evenly plate the inner bore that forms the gas seal. This was insulated along its whole length to prevent short circuits save for approximately 15 mm arranged to plate the 10 mm bond surface at one end of the adapter. Only a Ni strike was used. Normally the strike is used immediately prior to plating in Watt's solution or one of several alternative recipes [discussion with Lluis Isern Arrom, a fellow PHD student, who also carried out the plating]. Ni strike yields a coating 3–5 μm thick, which was deemed sufficient as a surface modification. The solutions are given in Appendix M: Ni Plating Recipes. Plating was at 5 Adm^{-2} for a duration of 15 min.

Once the adapters were bonded to a cell it was then welded (by conventional techniques) to the pipework and assembled into the FC test rig end cap. The cell is suspended vertically in the furnace, with all components attached to the end cap. The use of a U-shaped exhaust attached independently from the fuel inlet to the end cap meant there would be next to no mechanical loading on the cell due to thermal expansion of dead weight of components. At this point all connections were made (two main conducting paths and two secondary for four probe measurement of electrical and electrochemical performance, and two thermocouples: one near the top of the cell and one near the bottom). Subsequently the whole assembly (end cap, cell, stainless steel gas lines and all sensing connections and probes) was lowered into the furnace which could then be sealed and tests started.

13.3 Conclusions

A bespoke test rig was designed and built to accommodate the tubular cells designed and meet testing needs. A critical part of this was the development of a novel process to

bond the adapters necessary to connect the fuel cell to standard size gas pipes in a way that was both mechanically sound and gas tight while accommodating any slight out-of-roundness of the fabricated cells.

Furthermore, it was shown that even with the additional safety requirements imposed by the potential of unused fuel ignition inside the cells the test setup is expected to operate safely throughout testing.

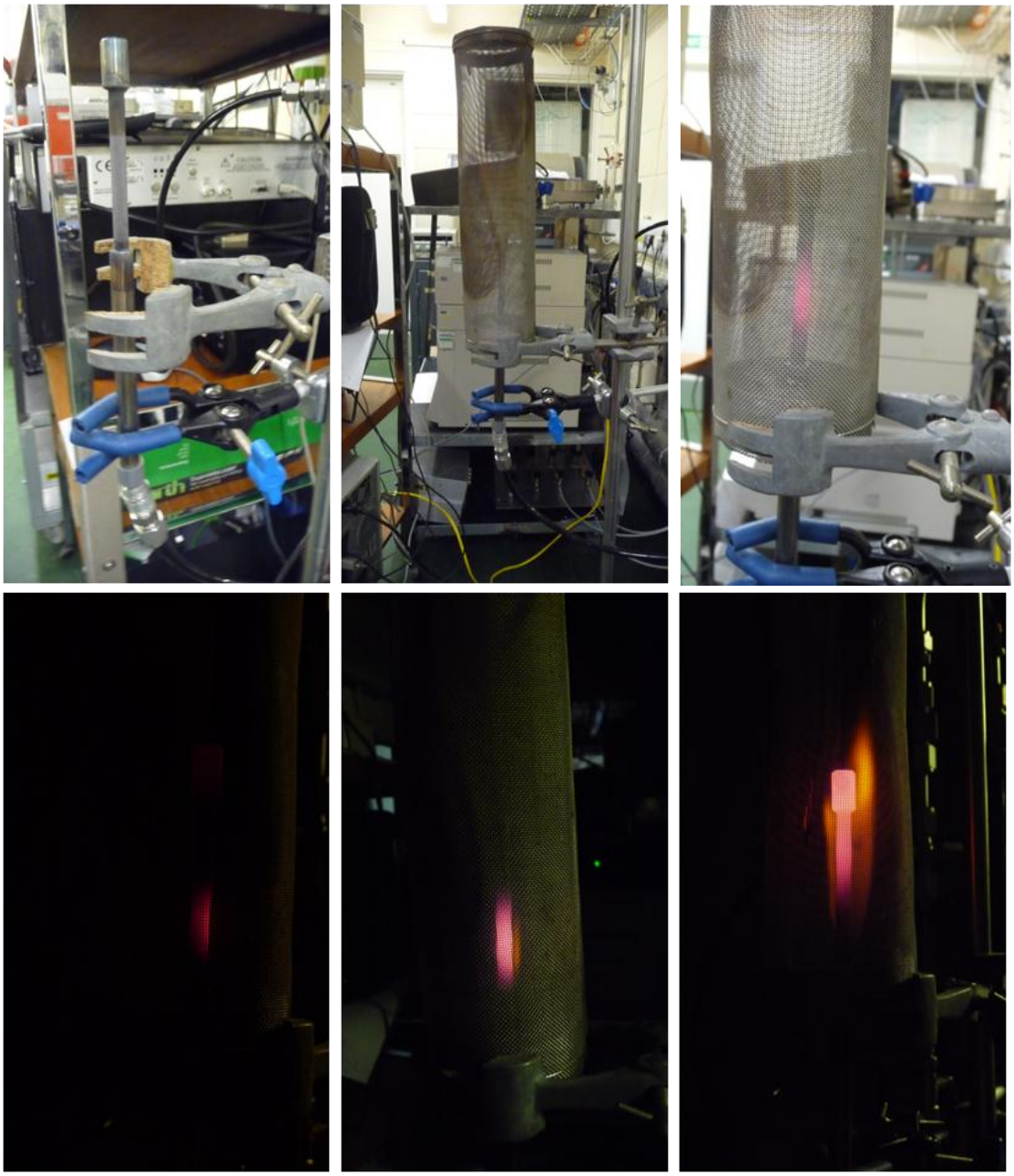

Figure 13-18. Burner test photographs. Top row: setup; Bottom row from low H_2 flow rate (just sufficient to maintain flame) to high H_2 flow rate (approximately 2 litres per min). Note: hydrogen flames are very difficult to observe in lit conditions.

14 Fuel Cell Electrical and Electrochemical Performance Testing

Camilleri (2009) successfully demonstrated the creation of a complete μ-tubular SOFC by a method very similar to that used in this project. However, only two such demonstrators were fabricated (as a single batch) due to time constraints and their performance as fuel cells (electrical and electrochemical) could not be assessed with the facilities available. For this project a bespoke testing rig was created. The electrical parameters of interest were measured via potentiogalvanostat with integrated frequency response analyzer (FRA) in conjunction with a software package for electrical and electrochemical analysis (VersaSTAT 3F and VersaStudio software from AMATEK UK/Princeton Applied Research). Perhaps somewhat unexpectedly at this stage there was no clearly optimal manufacturing route – only a small number of likely ones.

14.1 Objective and background

First and foremost determining the optimal (for FC performance) reduction process is a design concern. As discussed in detail in the anode fabrication chapter (8.13) the two extremes of the reduction parameters explored result in significantly different microstructures. At the time it was believed that permeametry would then determine which of the two was optimal for creating anodes (i.e. resulted in the greatest permeance to the relevant gases). However, although a clear leader in terms of gas permeance emerged (1,000 °C, ramp only; see section 12.6.2) the results do not encompass anode requirements entirely, but only gas transport. The different microstructures presented by these two reduction conditions have two further roles to play: surface area for hydrogen dissociation and (coupled with the electrolyte) creating the three phase boundary at which the fuel cell reaction takes place. Both are a function of the internal surface area of the anode, so it is possible that despite inferior gas permeance exhibited by the low temperature reduction (400 C, 15 h dwell; see section 12.6.2) the resulting anode may be superior as it offers a greater surface area due to a larger, more widely distributed, pore network consisting mostly of the smaller pores among those observed (c.100 nm).

Secondly, one must consider electrolyte fabrication. As demonstrated in section 9.5.1, reproducibility remains sub-optimal. However, as stated elsewhere, this is a limitation of the coater available rather than an inherent limitation of EB-PVD, and is therefore a relatively easily surmountable obstacle. For the purposes of testing my design of μ-tubular fuel cells this presents somewhat of a challenge. Ideally two electrolyte thicknesses as set out in the objectives of this project would have been reproducibly fabricated. Planning the experiments by DoE (similar to the tier 2 electrolyte deposition experiments; section 9.6) would have then enabled an optimal fabrication route to be

established factoring in reduction parameters and electrolyte thickness (having already optimised both processes in terms of fabrication) for the best possible fuel cell performance. However, since it was not possible to fully control the electrolyte thickness between 5 μm and 15 μm one must instead compare performance of the two reduction schemes alone, treating each cell as having a nominal 10 μm electrolyte thickness with a rather large proportional error (c. ±5 μm). Furthermore, the electrolyte is not gas tight. This leads to a significant reduction in performance as fuel combusts rather than reacting electrochemically.

It can be argued that the described comparison (that neglects to address different electrolyte thicknesses) is not as robust as it could be. A suitable counter-argument is randomness: by fabricating a relatively large number of fuel cells for each reduction scheme and randomly selecting cells to test from each set, a reasonable representative average performance is achievable even with very few actual experiments. In any case, poor robustness or not, the experiments form a valid first tier of electrical and electrochemical performance testing, including information on how significant the performance loss is due to the low gas tightness of the electrolytes.

14.2 Electrical and Electrochemical Experiments

The fuel cells for testing were manufactured as set out in chapter 11. The bespoke rig's design and construction is described in section 13.2. What follows is the description of the battery of tests performed on the (randomly selected) complete cells. One cell was selected from those with each of the two types of anodes (the two reduction schemes) Each sample underwent a series of measurements at four nominal temperatures: 400 °C, 600 °C, 800 °C and 1,000 °C. Repeat measurements (four to six) were carried out at each temperature of interest.

Prior to taking any actual measurements the temperature was allowed to reach steady state conditions for a few minutes at the desired temperature (the large thermal mass of the furnace is helpful because it dampens any temperature fluctuations experienced by the cell). Note that during settling (as well as ramping up to temperature or cooling down) no fuel flows and therefore the cell was not generating electricity. The heating and cooling times were long enough to preclude completing a cycle from 400 °C to 1,000 °C in a single working day, so each cycle was spread over two days. Also, the time required to complete each set of measurements was negligible compared to heating and cooling times. Taking measurements on the heating cycle and cooling overnight was preferred. Intermediate to long term performance, which would be altered by microstructure changes, was beyond the scope of this project.

The measurements taken at each temperature were automated via the VersaStudio software, running the programmed tasks once the desired temperature has been reached and allowed to settle. The programmed sequence of tasks (measurements, checks, analysis, etc.) follows:

1. Measure open circuit voltage (OCV)
2. Potentiostatic Electrochemical Impedance Spectroscopy (EIS): Frequency Range 10 kHz – 1 Hz, Perturbation voltage 10 mV_{RMS}, 10 points per decade.
3. Galvanostatic Electrochemical Impedance Spectroscopy (EIS): Frequency Range 10 kHz – 1 Hz, Perturbation current 100 μA_{RMS}, 10 points per decade.

In all cases the oxidant was simulated air supplied at slightly over atmospheric pressure for safety reasons as covered in sections 13.2.2 and 13.2.5. The supply was the same as that for the permeametry experiments. Air was supplied at a nominal flow rate of 50 ±5 sccm (2.82×10^{-5} $\pm0.28\times10^{-5}$ kg s^{-1}). The fuel gas was the same pure hydrogen mix (from BOC) used for the reduction experiments and permeametry. It was supplied at a nominal flow rate of 100 ±10 sccm (1.43×10^{-6} $\pm0.14\times10^{-6}$ kg s^{-1}), a stoichiometric mix with the oxidant.

The system includes a number of important parameters that are maintained at static values (inherent to the system design): the gas pressures (hydrogen and air) are determined (and fixed) by the bubblers to 1.7 ±0.2 kPa and 6.8 ±0.7 kPa, respectively; the fuel and oxidant flow rates are set by mass flow controller channels with the flow rates noted above (controller automatically adjusts to maintain these values).

Note that the inlet and exhaust pressures (fixed by the bubblers as noted above) and the total inlet and exhaust flow rates (both mass and volume, obviously) are nominally equal. They would only differ in case of leaks outside of the system (conservation of mass). To simplify the necessary measurements (i.e. obviate the need for measuring the noted parameters at the exhaust also) the FC test rig was leak tested after installing each new cell for testing and making all connections (and sealing the furnace) but prior to commencing the experiment.

14.3 Results & Discussion

The resulting measurements are summarised in Table 14-1., Table 14-2. and Table 14-4. below; tabulating nominal and actual temperature (near top of cell and near bottom of cell), OCV (10 measurements taken by the VersaSTAT per repeat and generally 6 repeats per sample at each temperature), the hydrogen flow rate, and the air flow rate. Measurement error is based on instrument manuals and thermocouple datasheets. Table 14-2. summarises Table 14-1. showing the corrected mean and error for each sample at each temperature. The EIS (electrochemical impedance spectroscopy) results are not

easily tabulated, and are instead best shown in their standard form (semi-circular plots of Z_{Re} against Z_{Imm} called Nyquist plots).

The ADC ranges employed were ±10 mV (300 nV resolution) and ±100 mV (3 μV resolution). The applied perturbation current has an accuracy of ±0.2% of the reading (max. 100 μA). Input impedance is >12 TΩ in parallel with <5 pF. Voltage measurement has a minimum resolution of ±6 μV and an accuracy of ±0.2% of the reading. DC current measurement depends on current range but is at worst <0.5% FSO at the currents observed. For full hardware specifications the interested reader is referred to the VersaSTAT 3F hardware manual (available at Princeton Applied Research's website for download free of charge).

It was found that the four-probe measurements were unreliable or of dubious credibility (a zero OCV was the most common cause for concern followed by the occasional negative OCV). For sample A.03 the fourth probe was found to be in poor contact with the anode upon unloading. It was assumed to have worked itself loose as a result of thermal cycling. In the case of sample G.04 the fourth probe was found firmly attached in place at the conclusion of the experiments, yet similar OCV results were observed. More instances of a negative OCV measurement occurred, with fewer zero values and for approximately one repeat at each temperature a believable OCV was measured (in line with the 3-probe measurements at the same temperature). Due to this the analysis is based on the 3-probe OCV data.

In a fuel starved condition the OCV should drop to zero according to the anode-limiting current density given by equation (4.64). In order to enumerate what that limiting current density is we use Fick's First Law to calculate $D_{A(eff)}$ from the measured flux (see chapter 1):

$$J_A = -D_{A(eff)} \frac{\mathrm{dC}}{\mathrm{dx}} \qquad (14.1)$$

Where:

J_A = gas flux through the anode (mol m^{-2} s^{-1} Pa^{-1})
$D_{A(eff)}$ = effective gas diffusivity through the anode ($m^2 s^{-1}$)
C = concentration (mol m^{-3})
x = distance, in this case the anode thickness (m)

Now $P\dot{V} = \dot{n}RT$:

$$\frac{\dot{n}}{\dot{V}} = C = \frac{p_{A,H_2}}{RT} \qquad (14.2)$$

Therefore,

$$J_{A,H_2} = -D_{A(eff)} \frac{P}{RTx} \quad (14.3)$$

$$J_{A,H_2} = -D_{A(eff)} \frac{P}{RTt_A} \quad (14.4)$$

Where:

$t_A =$ anode thickness (m)

Equation (4.64) becomes:

$$i_{As} = 2\mathcal{F}J_{A,H_2} \quad (14.5)$$

The anode limiting current density is therefore $i_{As} = 1.285\times10^6$ Am^{-2}. *Ergo*, the low OCV is not due to operation at or near the anode limiting current density.

In order to ensure any observed voltages were unlikely to be spurious, the test routine was performed on a cell at temperature prior to introducing the oxidant. Under such conditions solid oxide fuel cell operation is not possible. No OCV was detected without the oxidant flow, therefore subsequent OCV readings under test conditions (including with both fuel and oxidant) indicate cell operation.

Operating Temperature (°C) ±3 °C	**OCV (mV) ±0.2%**					
PT-AEC.13/03/15-125;10;0.3.1100(400)[1000]-A.03						
400	*Repeat 1*	*Repeat 2*	*Repeat 3*	*Repeat 4*	*Repeat 5*	*Repeat 6*
	0.9197	1.226	0.9197	1.226	1.226	0.9197
	0.9197	1.226	0.9197	0.9197	0.9197	1.226
	1.226	1.226	0.9197	1.226	1.226	1.226
	1.226	1.226	0.9197	1.226	0.9197	1.226
	1.226	1.226	0.9197	1.226	6.130	1.226
	1.226	1.226	0.9197	1.226	1.226	1.226
	0.9197	1.226	0.9197	0.9197	1.226	1.226
	1.226	1.226	0.9197	1.226	1.226	1.226
	0.9197	1.226	0.9197	1.226	1.226	1.226
	0.9197	1.226	0.9197	1.226	1.226	1.226
μ	*1.073*	*1.226*	0.9197	*1.165*	*1.104*	*1.196*
σ	*0.162*	*0*	*0*	*0.129*	*0.215*	*0.097*
600	*Repeat 1*	*Repeat 2*	*Repeat 3*			
	0.9197	96.00	99.07			
	0.9197	96.00	99.37			
	0.9197	97.23	99.07			

Operating Temperature (°C) ±3 °C	**OCV (mV) ±0.2%**					
	0.9197	97.84	99.07			
	0.9197	99.07	99.07			
	0.9197	99.37	99.37			
	0.9197	99.37	99.37			
	0.9197	99.68	99.07			
	0.9197	99.37	98.76			
	0.9197	99.37	98.76			
μ	*0.9197*	*98.33*	*99.10*			
σ	*0*	*1.45*	*0.23*			
800	*Repeat 1*	*Repeat 2*	*Repeat 3*	*Repeat 4*	*Repeat 5*	
	1.840	0.9197	1.840	1.840	1.840	
	1.840	0.9197	1.840	1.840	1.840	
	1.840	0.9197	1.840	1.840	1.840	
	1.840	0.9197	1.840	1.840	1.840	
	1.840	1.226	1.840	1.840	1.840	
	1.840	1.226	1.840	1.840	1.840	
	1.840	0.9197	1.840	1.840	1.840	
	1.840	1.226	1.840	1.840	1.840	
	1.840	0.9197	1.840	1.840	1.840	
	1.840	0.9197	1.840	1.840	1.840	
μ	*1.840*	*1.012*	*1.840*	*1.840*	*1.840*	
σ	*0*	*0.148*	*0*	*0*	*0*	
1,000	*Repeat 1*	*Repeat 2*	*Repeat 3*	*Repeat 4*	*Repeat 5*	
	1.840	1.840	1.840	1.840	1.840	
	1.840	1.533	1.840	1.840	1.840	
	1.840	1.533	1.840	1.840	1.840	
	1.840	1.533	1.840	1.840	1.840	
	1.840	1.840	1.840	1.840	1.840	
	1.840	1.840	1.840	1.840	1.840	
	1.840	1.840	1.840	1.840	1.840	
	1.840	1.840	1.840	1.840	1.840	
	1.840	1.533	1.840	1.840	1.840	
	1.840	1.840	1.840	1.840	1.840	
μ	*1.840*	*1.717*	*1.840*	*1.840*	*1.840*	
σ	*0*	*0.158*	*0*	*0*	*0*	
PT-AE.20/03/15-125;10;0.3.1100(1000)[1000]-G.04						
400	*Repeat 1*	*Repeat 2*	*Repeat 3*	*Repeat 4*	*Repeat 5*	*Repeat 6*
	0.9197	0.9197	0.9197	0.9197	0.9197	1.226
	0.9197	0.9197	0.9197	0.9197	0.9197	1.226

Operating Temperature (°C) ±3 °C	**OCV (mV) ±0.2%**					
	0.9197	0.9197	0.9197	0.9197	0.9197	1.226
	0.9197	0.9197	0.9197	0.9197	0.6130	1.226
	0.9197	0.9197	0.9197	0.9197	0.9197	1.226
	0.9197	0.9197	0.9197	0.9197	0.9197	1.226
	0.9197	0.9197	0.9197	0.9197	0.9197	1.226
	0.9197	0.6130	0.9197	0.9197	0.9197	1.226
	0.9197	0.9197	0.9197	0.9197	0.6130	1.226
	0.9197	0.9197	0.9197	0.9197	0.9197	1.226
μ	*0.9197*	*0.8890*	*0.9197*	*0.9197*	*0.8584*	*1.226*
σ	*0*	*0.0970*	*0*	*0*	*0.1293*	*0*
600	*Repeat 1*	*Repeat 2*	*Repeat 3*	*Repeat 4*	*Repeat 5*	*Repeat 6*
	1.533	1.533	1.226	1.840	1.840	1.533
	1.840	1.533	1.226	1.840	1.840	1.533
	1.533	1.840	1.226	1.840	1.840	1.840
	1.533	1.840	1.226	1.840	1.533	1.840
	1.533	1.840	1.226	1.533	1.840	1.533
	1.840	1.840	1.226	1.840	1.533	1.533
	1.533	1.533	1.226	1.840	1.840	1.533
	1.840	1.840	1.226	1.533	1.840	1.840
	1.533	1.840	1.226	1.840	1.840	1.533
	1.840	1.840	1.226	1.840	1.840	1.840
μ	*1.656*	*1.748*	*1.226*	*1.778*	*1.778*	*1.656*
σ	*0.158*	*0.148*	*0*	*0.129*	*0.129*	*0.158*
800	*Repeat 1*	*Repeat 2*	*Repeat 3*	*Repeat 4*	*Repeat 5*	*Repeat 6*
	1.840	1.840	2.147	1.840	2.147	0.3063
	2.147	2.147	2.147	2.147	2.147	0.3063
	2.147	1.840	2.147	2.147	2.147	0.3063
	2.147	1.840	1.840	2.147	2.147	0.3063
	2.147	1.840	2.147	2.147	2.147	0
	2.147	2.147	1.840	2.147	2.147	0.3063
	2.147	2.147	2.147	2.147	2.147	0.3063
	2.147	1.840	2.147	2.147	2.147	0.3063
	2.147	2.147	2.147	2.147	2.147	0
	2.147	1.840	1.840	2.147	2.147	0.3063
μ	*2.116*	*1.963*	*2.055*	*2.116*	*2.147*	*0.2450*
σ	*0.097*	*0.158*	*0.148*	*0.097*	*0*	*0.1293*
1,000	*Repeat 1*	*Repeat 2*	*Repeat 3*	*Repeat 4*	*Repeat 5*	*Repeat 6*
	1.840	1.840	1.840	4.293	1.840	1.840
	1.840	1.840	1.840	4.293	1.840	1.840

Operating Temperature (°C) ±3 °C	**OCV (mV) ±0.2%**					
	1.840	1.840	1.840	4.293	1.840	1.840
	1.840	1.840	1.840	4.293	1.840	1.840
	1.840	1.840	1.840	4.293	1.840	1.840
	1.840	1.840	1.840	4.293	1.840	1.840
	1.840	1.840	1.840	4.293	1.840	1.840
	1.840	1.840	1.840	4.293	1.840	1.840
	1.840	1.840	1.840	4.293	1.840	1.840
	1.840	1.840	1.840	4.293	1.840	1.840
μ	*1.840*	*1.840*	*1.840*	*4.293*	*1.840*	*1.840*
σ	*0*	*0*	*0*	*0*	*0*	*0*

Table 14-1. Open circuit voltage data showing the 10 automated repeats divided by repeat measurement sets and temperature from the 3-probe measurement data. (Mean $\boldsymbol{\mu}$ and standard deviation $\boldsymbol{\sigma}$ included).

In order to separate those data points that are outliers from the remainder, especially given the small number of OCV values appearing at each temperature, a combination of statistical techniques was employed to validate probable outliers. Those data points validated as outliers (outside ±3σ, 99.9% confidence interval) were excluded and the mean recalculated (as well as its standard deviation). Next those data points between 2σ and 3σ were excluded (if any occurred) to determine, with a 95% confidence interval, which were outliers (if any). In these cases a new mean and standard deviation was calculated excluding these data points to determine which data points falling between 2σ and 3σ were correctly identified as outliers. If any occurred these were removed and new, corrected, mean and standard deviation calculated. The procedure was repeated iteratively as necessary. See Appendix Q: OCV Arrhenius Plots for detailed analysis of the OCV at each temperature (mean, mode, standard deviation discussion, data subsets, etc.) and any relevant implications.

On two occasions the statistical analysis revealed a repeat that was in its entirety a subset (see Table 14-2.). This either relates to the VersaSTAT's quantisation or occurred for some other, currently unknown, reason. The data is sound, however, and should not be neglected.

It is important to note that A.03 was the first sample tested and part way through a superior method was developed and it was decided to take additional measurements with 2 and 3-probe connections in addition to the original planned 4-probe measurements as well as double the number of repeat measurements. The 600 °C data was the last recorded chronologically speaking, and it was part way through this sequence of measurements that the cell failed completely. The final two sets of data with much higher OCV than otherwise observed may therefore be spurious.

Determining a reasonable mean OCV at 600 °C for A.03 is less straightforward. Clearly (see Table 14-1.) a simple mean is insufficient; the statistical method employed detects no outliers when obviously there are two distinct subsets. I decided to ignore the lesser subset treating the majority group as the main data set, with the other as a subset.

In addition for each sample at each temperature the batch to batch error was calculated. It was determined that there was no significant contribution to the overall error from the testing procedure (several repeat batches). It was found that the OCV measurements were highly repeatable and therefore the mean values have been used for further analysis of the cell performance (Table 14-2.).

Operating Temperature (°C) ±3 °C	**Summary of mean OCV (mV) ±0.2%**			
	A.03		*G.04*	
	μ (mV)	σ (mV)	μ (mV)	σ (mV)
400	1.12	±0.15	0.92 [1.23]	±0 [±0]
600	*	*	1.64	±0.23
800	1.84 [1.01]	±0 [±0.15]	1.77	±0.7
1,000	1.84	±0	1.84	±0

Table 14-2. Summary of mean OCV and standard deviation (data subsets in brackets). *These values are based on only three repeat sets, shortly prior to the failure of this sample and were considered unreliable.

Considering the reproducibility (that is, determining whether the results are significantly different for the two samples – representative of the two reduction schemes – at each temperature) is the next analytical step. If these are not significantly different (using the Student T test) we can treat them as a single large data set (continuing to exclude outliers as discussed) for further analysis. For the earlier discussion outliers were worth noting as clusters of outliers (entire repeats forming subsets of data) but going forward the subsets should be dismissed as outliers.

The Student T tests were of an independent two sample form, with unequal sample size and equal variance. The equal variance case is justified by the fact that the data samples were obtained from cells manufactured with the same techniques and materials. As noted immediately above the final data sets were used having excluded outliers and subsets.

Nominal Temperature (°C)	p-value	Significance
400	1.51×10^{-15}	There is a significant difference between samples (>99.9% confidence).
600	–	Could not test as there was only one reliable data set.
800	0.23	There is NO significant difference between samples (>99.9% confidence).
1,000	0.17	There is NO significant difference between samples (>99.9% confidence).

Table 14-3. Summary of sample reproducibility testing (via independent, 2 sample, unequal sample size, equal variance Student T tests); excludes outliers and data subsets identified previously.

The results summarised in Table 14-3. indicate that at the lower temperatures the cell microstructure has much greater influence on performance than at elevated ones. This suggests that there is a divide between grain boundary-dominated (low temperature) and bulk-dominated (high temperature) transport. Such behaviour is consistent with Arrhenius-type behaviour and the shift to a bulk-diffusion-dominated system occurring at approximately 0.4 T_m (homologous). Such an outcome was to be expected because of the different reduction schemes of the two samples (see Permeametry in chapter 1 for details on the gas transport effects). At this stage it was not possible to determine if the performance difference is due solely to the anode microstructure or the electrolyte air leak exclusively or whether a combination of the two. To determine that additional samples with the same two anode types but with gas tight electrolytes is required. It remains worthwhile to note that at the very least the electrical and electrochemical performance reflects the processing in some deterministic way.

Operating Temperature (°C) ±3 °C		**Mean OCV (mV) ±0.2%**	$\dot{m}_{H_2}^{inlet}$ **(kg s^{-1}) ±2%**	$Q_{H_2}^{inlet}$ **(cm^3 s^{-1}) ±2 cm^3 s^{-1}**	$\dot{m}_{air}^{inlet}$ **(kg s^{-1}) ±2%**	Q_{air}^{inlet} **(cm^3 s^{-1}) ±2 cm^3 s^{-1}**
T_1	**T_2**					
PT-AEC.13/03/15-125;10;0.3.1100(400)[1000]-A.03						
400.9	393.0	1.12 ±0.15	1.86×10^{-6}	99.9	2.82×10^{-5}	50.0
606.0	598.3	(1.64 – 1.66)	1.43×10^{-6}	100.0	2.15×10^{-5}	49.9
800.0	791.4	1.84 ±0	1.17×10^{-6}	100.1	1.77×10^{-5}	50.0
995.0	985.7	1.84 ±0	9.89×10^{-7}	100.0	1.49×10^{-5}	49.9
PT-AE.20/03/15-125;10;0.3.1100(1000)[1000]-G.04						
404.3	399.3	0.92 ±0	1.85×10^{-6}	100.1	2.80×10^{-5}	50.0
592.5	589.3	1.64 ±0.23	1.45×10^{-6}	100.1	2.18×10^{-5}	50.0
800.2	796.4	1.77 ±0.70	1.17×10^{-6}	100.0	1.76×10^{-5}	49.9
976.7	972.6	1.84 ±0	1.00×10^{-6}	100.0	1.51×10^{-5}	50.0

Table 14-4. Mean open circuit voltage and test parameters. One representative repeat was selected for each combination of sample and temperature for inclusion in the table from the 3-probe measurement data. The OCV in parenthesis was estimated based on the linear regression of an Arrhenius plot (explained later).

As discussed the measured OCV values for sample A.03 at 600 °C were found to be questionable. In Table 14-4. the most probable values, the range of values reflects the two most representative models. The details on the Arrhenius plot and how this was used to create various linear regression models is later in this discussion section.

A second main area of analysis was the impedance characteristic of the cells via the numerous impedance spectra recorded. Kumpulainen *et al.* (2002), Macdonald (2005), Macdonald and Johnson (2005), McKubre and Macdonald (2005), Raistrick *et al.* (2005), Wagner (2005), Milewski and Miller (2006) and Kulikovsky *et al.* (2010) were helpful in this regard. As previously set out the 3-probe experiments proved the most credible, and it was this impedance data that was preferred for analyses. The author is grateful to the technical staff of Princeton Applied Research, particularly Ing. Dirk Moens, for their assistance in attempting to understand the results obtained. All recorded 3-probe spectra may be found in Appendix P: Electrochemical Impedance Spectroscopy. The spectra were unfortunately not interpretable. There was no bias between galvanostatic or potentiostatic measurements. Particularly strange was the

negative imaginary impedance. Such strongly inductive behaviour could not be explained. See Appendix P: Electrochemical Impedance Spectroscopy for details.

There was a single instance where the Nyquist plot closely resembled what one would expect (1,000 °C in galvanostatic mode, a data set determined to be an outlier from the OCV data) yet the impedances were very different from the rest and very high compared to all other EIS plots (by over three orders of magnitude). Refer to Figure 14-1. Even this, then, had to be discarded.

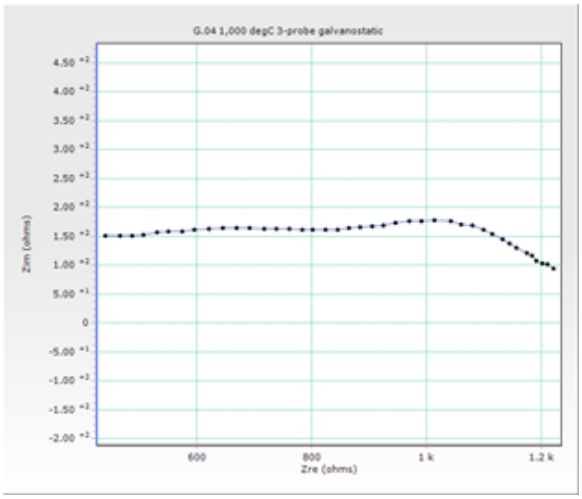

Figure 14-1. Galvanostatic mode Nyquist plot at 1,000 °C of sample PT-AE.20/03/15-125;10;0.3.1100(1000)[1000]-G.04. Note that this repeat was identified statistically as an outlier despite its resemblance to a classic Nyquist plot for an SOFC. Furthermore, note the very high impedances recorded.

Although unable to interpret it at this time the EIS plots (that is not obviously too noisy to interpret at all) showing overwhelmingly inductive behaviour (negative imaginary impedance) appear to be the characteristic Nyquist plots for the cells tested based on the large number of these that occurred (Appendix P: Electrochemical Impedance Spectroscopy).

Calculation and interpretation of the fuel utilization in conjunction with exhaust gas analysis had been planned. However, the lack of electrolyte gas tightness meant that analysis of the exhaust gases would add no further understanding to the permeametry work nor would it be helpful in characterising cell performance. Consequently the calculated fuel utilization, which could be verified experimentally via exhaust gas analysis, was not considered helpful. Furthermore, the poor cell performance means a calculated fuel utilization and detailed characterization of I-V data was likewise not considered beneficial. Despite certain important areas of cell characterization proving impractical as a consequence of the poor cell performance one important factor remains: proof of concept. The dramatic reduction from an expected OCV of approximately 1 V to the values discussed shows how great the influence of the electrolyte gas tightness

was. Statistically demonstrating that the OCV is not noise but an electrochemical process with measurable trends is significant.

There is a little-publicised type of fuel cell in which the fuel and oxidant mix freely, passing over a single chamber comprising cathode, electrolyte and anode. It has some advantages over planar designs that match tubular designs (particularly the simplified sealing), with the added advantage of a simplified structure allowing more compact stack design [Fabbri *et al*. 2010]. This paper however, does not make any mention of tubular designs for comparison. Many of the advantages mentioned in that work are shared with tubular designs, or are perhaps more accurately limitations of planar designs.

That design is sufficiently similar to the situation with the cells tested as part of this project that comparison is worthwhile. Fabbri *et al*. (2010) tackled the problem of a low OCV due to oxygen reacting chemically rather than electrochemically by engineering the electrolyte to have greater selectivity (through material selection) for electrochemical rather than thermochemical reaction. The resulting best OCV was 0.53 V at 550 °C with 40% C_3H_8 (propane) and 60% O_2 at 360 mL/min [Fabbri *et al*. 2010] (it is not reported if the proportions are by mass or volume; however, both were reported as dry synthetic gases). Therefore, engineering the materials for maximum selectivity is necessary for a cell with a very porous electrolyte to achieve a useful OCV – via the use of a different electrolyte material altogether. For example, a proton conducting perovskite-type oxide electrolyte such as yttrium-doped barium zirconate (BZY), employed by Fabbri *et al*. (2010). Processing BZY into dense films is challenging because of the highly refractory nature of the material [Fabbri *et al*. 2010], in line with the other electrolyte materials for SOFCs whether gadolinia-doped ceria of yttria-stabilised zirconia. A problem the authors get around by using a PVD technique: Pulsed Laser Deposition (PLD); that offers similar advantages to EB-PVD. The electrodes were specifically designed for proton conducting electrolyte single chamber SOFCs since both aspects do not work well with the usual SOFC materials (in single chamber cells they need a high selectivity to ensure the correct reaction (only) takes place at each electrode, similarly the materials need to be adapted to proton conduction since their roles are effectively reversed) [Fabbri *et al*. 2010], involving composite electrodes including a proportion of BZY. Note that sintering was required to create the electrodes, and a reduction step was needed to convert NiO into Ni at the anode after depositing the electrolyte by PLD. For further details on materials and fabrication please refer to the cited work.

The reported OCV is significantly less than that achieved by conventional (non-SC) SOFCs, attributed by the authors to imperfect selectivity of the anode and cathode towards hydrocarbon partial oxidation and partial reduction respectively [Fabbri *et al*. 2010]. This is not really surprising as it is one of the main limitations to SC-SOFC

performance. The presence of water vapour (in the form of humidified gases) reduced the OCV to 0.35 V at 550 °C, attributed to alteration of the gas shift reaction in favour of fuel partial oxidation (and a residual oxygen concentration) [Fabbri *et al*. 2010]. Their work shows how it is possible to create a working SOFC without gas separation, and that even when engineered to operate in this way the OCV is approximately half that of a state of the art µ-tubular SOFC. It also highlights the great impact on OCV based on lack of selectivity for the electrochemical reaction pathway pathway that applies irrespective of fuel and oxidant (although the actual OCVs naturally will differ).

Readers interested in single-chamber SOFC technology and development are referred to the extensive review by Kuhn and Napporn (2010). Of particular relevance to the point made above is the importance of catalysis and selectivity at the electrodes since both are exposed to the same gas atmosphere [Kuhn and Napporn 2010].

Arrhenius plots may be used to determine whether cell operation is controlled by diffusion mechanisms (the plot is a straight line); the diffusion control is a combination of ionic conduction and the effect of electrolyte porosity. An Arrhenius-type graph is also a convenient way of estimating the activation energy. If the data fits an Arrhenius model the equation of the line may be used to calculate a reasonable approximation for what the OCV for A.03 at 600 °C should be. In this case the Arrhenius model treats the cell as a single process. It is worth bearing in mind that the transport through the electrolyte dominates SOFC performance considerations so this is essentially an Arrhenius plot for the oxygen transport as measured by the voltage generated.

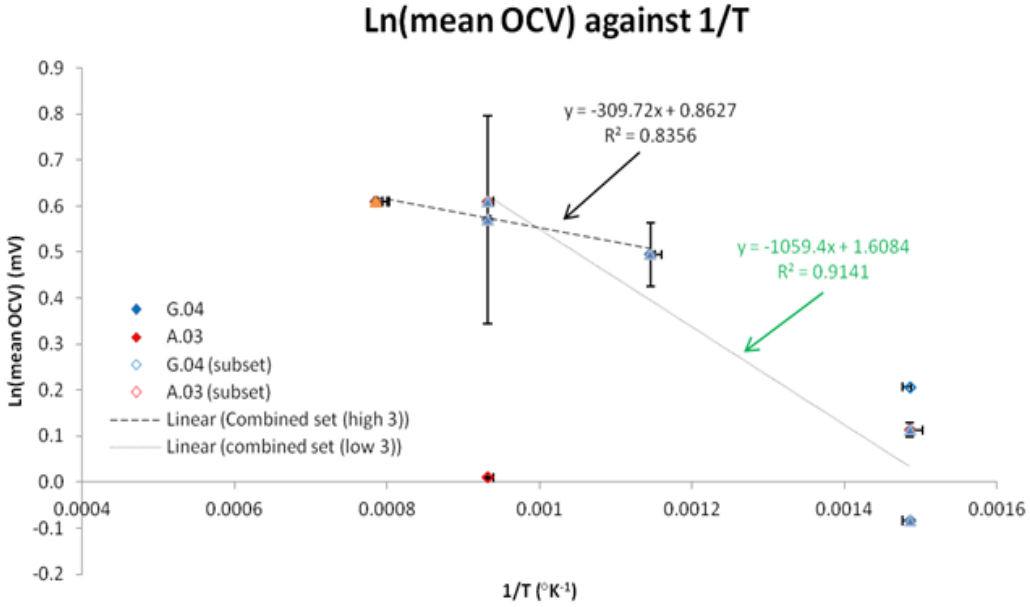

Figure 14-2. Arrhenius-type plot for OCV. Note due to the uncertainty of this data discussed previously no point was plotted for A.03 at 600 °C.

The temperature error in Figure 14-2. and Figure 14-3. (below) shows the upper and lower bounds for each nominal operating temperature. The voltage error was calculated for each data point and is the Ln of that point's relative error (i.e. Ln (OCV) / (±σ / OCV). For the majority of points the error bars are too small to be clearly visible. The A.03 data at 800 °C has a much smaller error than the A.04 data, which has the greatest error of all the OCV data. The largest error is on a single sample which may be linked to manufacture, possibly specifically the anode reduction scheme. However, confirming this would require testing additional samples. Furthermore, at the intermediate temperatures the error is greater for G.04 than A.03.

Observation of the distribution of points and a linear fit of each sample separately as well as combined into a larger single dataset (neither shown here but see Appendix Q: OCV Arrhenius Plots) indicated that the situation was more complex. The resulting linear fits were not good and by observation of the plotted data points it became apparent that there may be two mechanisms. Considering the by-sample plots a different transport mechanism appears to dominate at 400 °C. The difference between the two samples at 400 °C highlights a microstructural effect due to different reduction schemes that becomes less significant (smaller difference in mean OCV) with increasing temperature. The fact that the microstructural influence diminishes and becomes nearly insignificant by 800 °C and the activation energies calculated as described below reflects one or more thermodynamic processes responsible for generating the measured OCV. This was presumed to be electrochemical oxidation of hydrogen but may be linked to a combustion effect or the Seebeck effect (additional temperature measurements inside the cell are required to ascertain this – the test rig was missing that capability).

The temperatures of interest could be conveniently divided into two: a set containing the higher three (1,000 °C, 800 °C and °600 C) and another containing the lower three (800 °C, 600 °C and 400 °C). Data from the two samples were combined and a linear fit for each temperature set was plotted. The former is a bulk diffusion-dominated regime while the latter is a surface diffusion-dominated regime. The result can be seen in Figure 14-2. In addition the two subsets identified previously were added to the Arrhenius plot. A.03's subset is clearly an outlier while the G.04 subset is near enough to the other mean OCV data points at 400 °C that it may be relevant.

The very good linear fits indicate that there are indeed two regimes to consider and that in both cases behaviour is strongly diffusion-controlled. Confirming that the upper 3 are bulk diffusion-controlled, which is the expected behaviour for an SOFC operating at 550 °C or higher, serves to support the hypothesis that despite a low OCV (due to the air leak through the electrolyte) the cells do indeed function as such. The appearance of another diffusion-controlled regime at lower temperatures (which implies it is surface diffusion-dominated) is interesting. This result demonstrates that although performance

is poor some oxygen may be transported via surface-diffusion to the three phase boundary and react electrochemically.

From Figure 14-2. the transition temperature appears to be around 730 °C (the intersection of the two lines). It was not known at this stage what exact temperature the shift occurs at but was expected to be around 600 °C based on the appearance of the Arrhenius plot and the fact that it is at around this temperature that bulk transport of oxygen through zirconia becomes viable for fuel cell operation as evidenced by intermediate temperature SOFCs (IT-SOFCs) operating successfully at 550–650 °C. The ability to conveniently divide into two temperature regimes was no coincidence. Refining the transition time can be done in much the same manner as for oxidation (see section 8.4) but requires more data than is available at the time of writing.

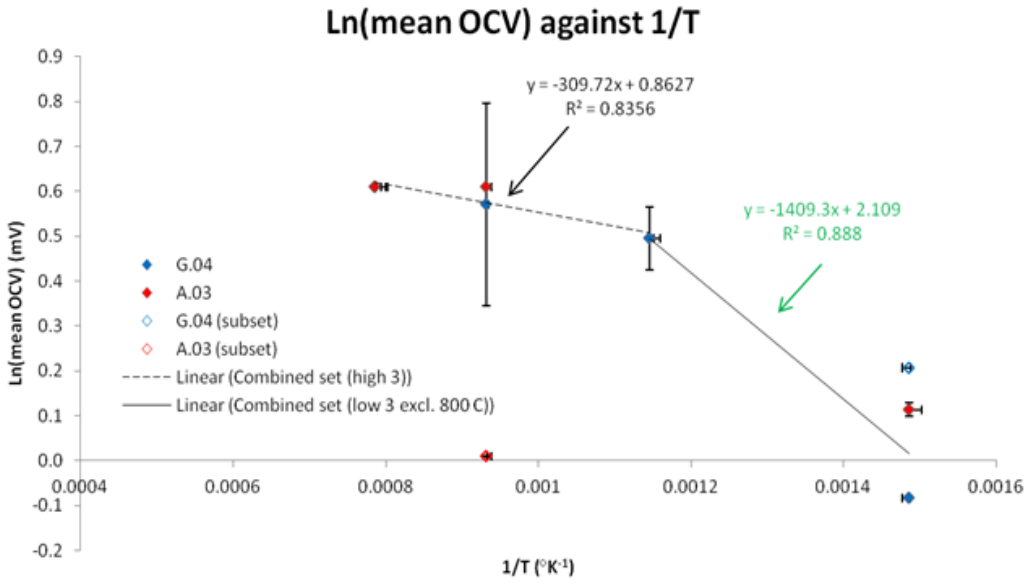

Figure 14-3. Arrhenius-type plot for OCV (excluding 800 °C from the lower temperature regime). Note due to the uncertainty of this data discussed previously no point was plotted for A.03 at 600 °C.

In Figure 14-3. we assume that the transition from surface-dominated to bulk-dominated diffusion occurs at 600 °C (as noted we have reason to expect the transition to be in the range 550–650 °C). This is possibly a better rendition of what the two gradients should look like, at least in the absence of the additional data necessary to rigorously determine the transition temperature.

The linear regression models can be used to estimate where the A.03 600 °C point should lie, and thence an approximate OCV. From the combined sets of Figure 14-2. we obtain an OCV of 1.66 mV (high 3) and 1.49 mV (low 3). If we exclude the data points at 800 °C from the low 3 combined set and use the low 3 model from Figure 14-3. the OCV rises to 1.64 mV. Compare these values to the mean OCV for A.03: 1.64 ±0.23

mV. The sequence of those three steps implies that the transition is close to 600 °C. Note the large bias that the error at 800 °C adds: bringing the calculated OCV to 1.49 mV where once excluded this rises to around 1.6 mV (1.64 or 1.66 mV). The similar values obtained for the high 3 (recall this includes the 800 °C data) and the low 3 assuming a transition temperature at 600 °C, indicates that the transition temperature may well be above 600 °C, possibly in the region of 650–700 °C (note that the gradient of the high 3 model means the transition temperature is liable to be closer to 700 °C than 600 °C).

The $0.4T_m$ for zirconia, 912–922 °C, is another comparison point for where the transition from bulk to surface is anticipated (depends on Y_2O_3 doping with the lowest temperature being for fully stabilised and the highest for pure ZrO_2). Note while this mechanism transition is generally in the region of $0.4T_m$ to $0.6T_m$ it can be as low as $0.3T_m$ (i.e. a transition at 616–623 °C, depending on doping). A transition temperature in the region of 650–700 °C is entirely feasible, but so is a considerably higher range. It is the author's hypothesis that the determining factor will be the degree of porosity in the electrolyte. In this case it is high, and somewhat counter-intuitively this leads to short diffusion paths through grains and therefore a suppressed transition temperature range. As noted earlier, further experimentation is required to verify.

By comparison the first model (see Appendix Q: OCV Arrhenius Plots) that treats each sample separately but does not subdivide by temperature into low 3 and high 3 results in a calculated OCV of 1.47 mV. This is significantly different highlighting the importance of separating the bulk and surface contributions.

Other useful information that can be derived from an Arrhenius plot is activation energies. In this instance the activation energy, E_a, refers to the activation energy for oxygen transport through porous YSZ. For the high temperature combined set E_a= 2.575 kJmol^{-1}, and for the low temperature set E_a= 8.808 kJmol^{-1}. Both values are low, implying that the surface-transport contribution is highly significant. It appears to dominate over the bulk transport trough the electrolyte due to the low gas tightness; much of the bulk transport channel is effectively bypassed. The large surface cracks of the anode and resulting cracks through the electrolyte lead to much greater gas permeance and thus oxygen availability at all sites. Therefore, diffusion distances whether near surface or bulk are considerably shorter.

Oxygen exchange and diffusion in the near-surface and bulk of YSZ was studied by de Ridder *et al.* (2003). In their work they separated near surface and bulk contributions with the assistance of SIMS (secondary ion mass spectroscopy). The near-surface E_a= 3.2 eV and the bulk E_a= 1.1 eV.

In converting between $Jmol^{-1}$ and eV it is important to note that $R = k_B N_A$ where R is the universal gas constant (8.3140 $J\ K^{-1}mol^{-1}$), k_B is Boltzmann's constant ($1.3806\times10^{-23}\ J\ K^{-1}$) and N_A is Avogadro's constant ($6.0221\times10^{23}\ mol^{-1}$). Thus, there is a factor N_A difference between activation energies given in $Jmol^{-1}$ (traditional for chemistry and engineering) and eV (traditional for physics). The difference is due to the former being expressed in terms of energy per mole and the latter energy per atom/molecule. The high 3 combined set has an equivalent E_a= 0.0267 eV and the low 3 combined set E_a= 0.0913 eV. There is a factor of 35 between near-surface from Ridder *et al.* (2003) and the low temperature set (presumed to be surface dominated), and a factor of 41 between the bulk and high temperature set (normally presumed to be bulk transport dominated).

Opitz *et al.* (2011) employed Pt electrodes on YSZ to investigate the oxygen exchange mechanism. The Pt microelectrodes were of carefully defined sizes, and varying their size and the testing temperature allowed determination of two temperature regimes with different geometric dependencies of the polarization [Opitz *et al.* 2011]. At 550–700 °C the rate limiting step was found to be an elementary step at the TPB (three-phase boundary) with an approximate activation energy of 1.6 eV [Opitz *et al.* 2011]. At lower temperatures (300–400 °C) the rate limiting elementary step was linked to the electrode area, with an approximate activation energy of 0.2 eV [Opitz *et al.* 2011]. These correspond to two parallel reaction paths for electrochemical oxygen exchange. While the electrodes Opitz *et al.* (2011) employed are very similar to those of the cells (in their case 300 nm of Pt in the form of circular microelectrodes of varying diameter – from 10–200 microns – deposited by sputtering with a photolithographic mask) they used (100) single crystals of YSZ whereas the deposited electrolytes of this project are of course polycrystalline. However, since their investigations concentrate at the TPB between the oxygen and the YSZ–Pt interface this should not deter meaningful comparison to the tested cells. In the temperature range of relevance (the high temperature regime in the cited study) a TPB length-dependent rate limiting step with an activation energy of 1.6 eV was observed [Opitz *et al.* 2011].

The authors were able to preclude the 0.2 eV activation energy linked to electrode area (and therefore a surface process) from the adsorption/desorption of oxygen onto platinum (in the form of dissociated atoms) [Opitz *et al.* 2011]. Instead they ascribe it to oxygen diffusion through the Pt film along Pt grain boundaries acting in parallel to the TPB length-dependent higher activation energy step [Opitz *et al.* 2011] (hence the combination leads to a lower activation energy at lower temperature).

A TPB length-dependent rate limiting step with an activation energy of 1.6 eV [Opitz *et al.* 2011] matches well with the E_a= 3.2 eV near-surface contribution and E_a= 1.1 eV contribution activation energies determined by de Ridder *et al.* (2003). The calculated activation energies for the tested cells (E_a= 0.0267 eV for high 3 combined set and E_a=

0.0913 eV for low 3 combined set) are not easily reconciled with published values. Such low activation energies imply an altogether different rate-controlling step.

The values calculated in this study suggest there is no rate-controlling energy barrier to the breakdown of O_2 into monoatomic oxygen – in fact, the rate-limiting step appears to be the arrival/residence of O_2 to available surface sites. Oxygen is more likely than hydrogen because the presence of water vapour occurs in the vicinity of the Ni whereas the activation energy values suggest a connection with YSZ based on comparison with the cited literature sources.

The impinging rate of oxygen at the Pt surface shows Arrhenius type behaviour at temperatures in excess of 200 °K [Opitz *et al.* 2011]. Depending on the kinetic energy of the impinging oxygen molecule activation energies of the sticking coefficient, $E_{sticking}$, between 0.04 and 0.13 eV were reported [Opitz *et al.* 2011]. The activation energies calculated for the cells tested fit well in this range, implying then that it is the rate controlling step.

This work cannot categorically define the rate-controlling process for the tested cells but the literature validates activation energies of the order of magnitude observed, and furthermore validates a rate-controlling step associated with the arrival/residence of oxygen rather than its conduction through the electrolyte.

14.4 Conclusions

The measured OCVs are far lower than anticipated based on the literature (even considering the lack of electrolyte gas tightness) even so they were measureable. As discussed the OCV measurements were highly repeatable. Sample reproducibility *viz-a-vis* performance could not be tested since only a single sample from each reduction scheme was tested. However, the differences highlighted by Student T tests are consistent with the microstructural differences (and therefore manufacturing differences) despite insufficient data to prove causality.

Based on the regression models the OCV for A.03 at 600 °C should be between 1.64 mV (from low temperature combined set excluding 800 °C) and 1.66 mV (from high 3 combined set).

The activation energies calculated for the cells in combination with the cited literature sources suggests that the arrival/residence of oxygen is the rate controlling step – there is no rate-controlling energy barrier to the breakdown of O_2 into monoatomic oxygen nor a rate-controlling energy barrier to ionic conduction.

The expected capacitive EIS behaviour of the cells tested in this study did not occur. In our own mind we do not understand the meaning of, nor possible interpretation of, negative imaginary impedances in the context of a fuel cell.

While it is not certain at the time of writing, the fuel cells fabricated as described in this thesis do not seem to benefit from an operating temperature above 800 °C. Given the thin electrolyte combined with the overall low performance (due to air leaks through the electrolyte) this fact is not especially surprising. It would be very interesting to see whether this changes or not once a robust technique for ensuring adequate electrolyte gas tightness has been developed experimentally (beyond proof of concept stage).

The data acquired makes it quite clear there is a marked difference, creating two temperature regimes of operation. These results demonstrate there was some elecrtrochemical aspect: not enough to be cetain the device is functioning as a fuel cell but enough to conclude that some electrochemical behaviour was taking place (rather than combustion alone). Further refinement of electrolyte manufacture is necessary to achieve the anticipated µ-tubular SOFC performance.

15 Conceptual Development and Manufacturing Vision

Fuel cells have achieved only limited market proliferation. Many designs take little account of large scale manufacture and target applications (see chapter 2 and chapter 3). The mass manufacture of microtubular cells has been an integral part of the high level design elements of this project. Some ideas on how this might be achieved are discussed below. This chapter must be seen as a conceptual discussion that both informed this project and should continue to inform any future development of this design, including many elements of possible research discussed in further work (chapter 17).

15.1 Production Scale Out Discussion

The nature of fuel cell stacks makes them readily scalable for various applications by both increasing stack size and combining stacks together. It is especially desirable to target more than one potential application and design a stack that can be readily combined to fulfil another application, e.g. a stack for domestic use (2 kW_{AC}, V_{DC} 75 V, I_{DC} 27 A, V_{AC} 230 V, I_{AC} 12 A via electronic inverters typical of PV solar panels) could be scaled out to light industrial use (20 kW_{AC}) by combining ten stacks arranged in series and/or parallel to provide greater current and/or potential as needed for the application packaged together with the balance of plant as an entirely new product. Such a product would not affect the manufacture of the cell stacks and would thus require little additional investment to manufacture once developed (new enclosure, BOP, and so on). One possible stacking arrangement was shown in Figure 3-6.

Assuming a tight packed stacking arrangement as shown in that example, and that the overall stack is to be tubular the following arrangements based on tube stacking are possible:

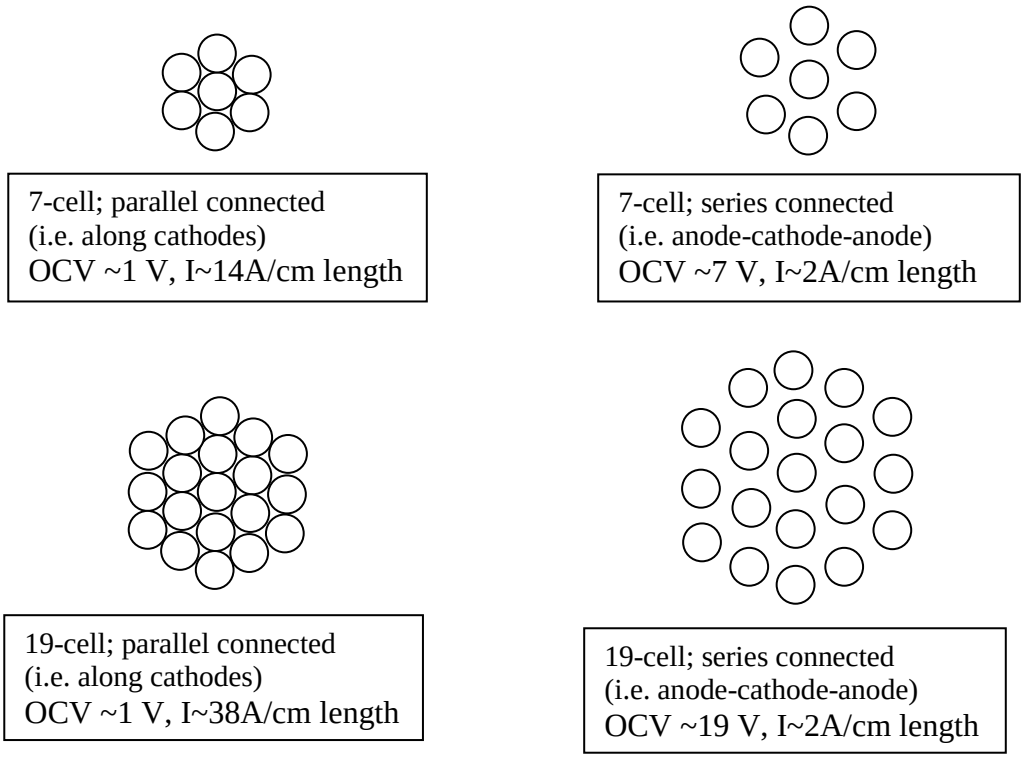

Figure 15-1. Examples of cell packing arrangements.

Obviously stacks need not be complete cylinders, but for the sake of the discussion this is assumed to be the most convenient arrangement. The machined end-plates of the stack enclosure would control the spacing between cells. They could be kept in close contact leading to a parallel connection or held slightly apart to create a series connection with the addition of insulators. The above also assumes performance comparable to state-of-the-art tubular cells, particularly Funahashi *et al.* (2008 and 2009) and Suzuki *et al.* (2009a). Reaching that stage, of course, requires this design progress through further iterations of optimization as well as establishing a mass-manufacture-friendly method to eliminate gas leakage through the electrolyte.

Stacks with an output current of approximately 38 A/cm length are fairly impractical. Seven cell, series-connected mini-stacks appear to be a useful building block requiring 11 such units, each with an active length of 12 cm for the domestic unit: a DC supply of 77 V at 24 A. As will be seen, this is also a convenient building block size from a mass manufacture standpoint. It is, however, far simpler to connect stacks in series than individual cells, even if close packing results in losses and additional interconnects are required (a scenario that is not expected to occur but is certainly possible). Using the 7-cell parallel arrangement, a 6 cm active cell length would generate 84 A. This would allow a 24 V supply (24 cells) to be employed (2.02 kVA), giving a unit suitable as an APU (auxiliary power unit) for mobile applications. Of the proposed 19-cell configurations on the serial connected one offers significant utility; for instance 38 V at 54 A (a 2×3 series/parallel design) with each cell having an active area of 9 cm.

15.2 Concept Model for Multi-Chamber Machine Manufacture of Cells

This is a descriptive type model and commentary detailing the possibility of manufacturing cells on a large (mass-production) scale using a single machine with multiple chambers. Automating the process control is straightforward and is of some benefit. Of far greater interest is material handling automation – which is a significant challenge despite the very short distances involved due to the needs of the processing in terms of pressures, gas compositions, and temperatures. Although it may appear more accurate to refer to this as a single production line than a single machine I would stress the integrated nature of the envisioned process and its centralised control and high potential level of automation. Therefore the term multi-chamber machine is preferred. The focus is on requirements for such to be possible, process sequence and benefits.

From the manufacturing perspective the entire cell fabrication process lends itself to batch production. Basing the final product (as well as developing from the initial one a line of products to meet needs in several market sectors) on standardised unit sizes rearranged and connected as needed can be served well by batch manufacture of the individual cells. What follows is a conceptual model of the workflow combined with an example of how this might be achieved by a single multi-chamber machine with fully automated material handling and minimal manual labour requirements.

The model began as some notes and musing during my MSc project, later incorporated into the thesis [Camilleri 2009]. It has evolved since then through further discussion with, among others, Professor John Nicholls, Tony Gray and Tim Pryor taking advantage of their experience with various relevant furnaces and coaters, and some additional pondering. While this may at first seem time and effort that might have been more productively used the exercise is in fact not only of direct benefit to the project by ensuring that the design remains ‘manufacturable’ (although not to the level of detail of DfM, Design for Manufacture), but also provides a vital supporting strut to the thesis in demonstrating, albeit with words alone, how to scale fabrication of cells of this design out to commercially useful quantities.

The fabrication process for individual cells can be conveniently divided into a process for each component (anode, electrolyte, and cathode) as follows: oxidation-reduction process, deposition of YSZ electrolyte, and deposition of Pt (or other) cathode, respectively. The process as a whole is described in detail in chapter 11. The reproducibility (using laboratory scale equipment) has been analysed also (chapter 1).

The oxidation-reduction process to convert commercially available nickel tubes into porous anodes requires a furnace capable of operating at up to 1,100 °C with a controlled chamber atmosphere. These capabilities are a normal part of any EB-PVD coater with the addition of a hydrogen line for the reduction step and modification for higher furnace temperature being necessary. As for the process itself; the furnace is heated to 1,100 °C, requiring up to 6 h. Then the tubes are moved into the chamber either from outside or preferably automatically from an adjacent sub-chamber (which will be re-filled during the oxidation-reduction cycle with the next batch). The tubes are oxidised, potentially for as little as a few minutes (see section 17.1) but more likely for up to 42 h, with the chamber filled with air to atmospheric pressure. The temperature is cooled to the reduction temperature of 1,000 °C, while the chamber is evacuated, possibly after being evacuated with the vacuum pump and then filled with argon three times for more traditional (and slower) argon purges that omit the evacuation between cycles (in which case five repeats are needed). One could go further and utilise two separate furnaces for oxidation and reduction with a load lock to feed batches into each (or from one to the other). This would maintain the furnace environment for oxidation and reduction as well as minimise the gas purge and material transfer to the load lock(s). Notice that for this hypothetical system the high temperature no dwell reduction scheme was selected because of the short cycle time and superior gas permeability. Once 1,000 °C has been reached, hydrogen flow is started, and then cut off once reduction is complete. This will require some dwell time since the gas is introduced after reaching the reduction temperature (unlike reducing in a separate furnace), but will certainly be far less than 11.5 h which is the time required to heat from 400 °C to 1,000 °C then cool back to room temperature. The time will be considerably shorter should it prove acceptable to transfer to the first intermediate chamber at an elevated temperature (ideally close to 850 °C). The chamber is subsequently purged up to five times with argon (it is not possible to use the evacuation method because this may damage vacuum pumps if the chamber gas is hydrogen). It is expected that the controlled cooling from oxidation temperature to reduction temperature will take no more than 100 minutes, and the two purge processes require a total of 30 minutes to complete.

The EB-PVD process deposits a few microns of YSZ forming the fuel cell electrolyte. The exact thickness is expected to be no more than 10 µm. PVD is a rapid process, taking at most 5 minutes to deposit such a thickness of YSZ. Once the oxidation-reduction process is complete the PVD chamber is evacuated to a suitable deposition pressure (around $1x10^{-5}$ mbar). The pump-down takes about 8 h with most of the atmosphere in the chamber evacuated within the first hour or so (the 80/20 rule of thumb applies quite well to pumping down vacuum chambers). In the meantime the chambers (intermediate and PVD) are heated to 850 °C. Once complete, the cells having been transferred from the intermediate chamber to the deposition chamber, and this last pumped-down to the deposition pressure, and the deposition temperature having been reached, the deposition process itself starts. The electron gun raises the substrate

temperature to 1,000 °C as required for deposition, with a shutter to ensure there is no uncontrolled deposition prior to establishing a melt pool (see sections 9.6.1 and 17.2). As such by using an intermediate chamber pumped-down to a similarly intermediate pressure, the time needed for the first batch of the week is not diminished, however a higher production rate is enabled by reducing the time needed to evacuate between batches (since the intermediate and PVD chambers work in tandem). After deposition the anode-electrolyte tubes are transferred to another intermediate chamber and finally to the cathode deposition chamber. These last two steps are explained in the next paragraph.

A convenient technique for depositing the cathode (especially a platinum one) is by sputtering. This is done at room temperature under vacuum. In order to create a porous structure a higher pressure than usual is used as described previously (chapter 10). It is desirable to have an intermediate chamber used for cooling prior to cathode deposition that is pumped to a pressure that is close to the required sputtering pressure. This has the benefit of both increasing the overall throughput as well as minimizing pumping energy since the intermediate chamber can cycle between the a pressure near the PVD pressure and another near the sputtering pressure, leaving these two chambers with a shortened pump-down to their respective pressures and able to work in parallel by de-coupling PVD and sputtering chambers. Once the anode-electrolyte tubes have cooled to room temperature, they are transferred to the sputtering station and this is pumped down to the correct deposition pressure in an inert atmosphere (Ar or N_2 purge gas). Since the cathode is to be very thin, as thin as a few hundred nanometres (if made of Pt), to a few microns (if alternative material is less catalytically active and/or electronically conducting than Pt) the deposition itself is not expected to take longer than 15–30 minutes. After sputtering the batch of (now complete) cells is transferred to a final intermediate chamber at a somewhat higher pressure before being transferred to one near atmospheric pressure for unloading. In this final chamber the pressure is brought up to the surrounding atmospheric conditions (both temperature and pressure) in air, a process taking about 1 h. The completed cells are then removed, ready to be assembled into stacks, the whole process having taken less than 76 h from cold, i.e. the first batch of the week (note however that this includes an estimated 11.5 h maximum time for reduction where it is expected this will be 1 h at most).

A note on batch size: Commercial large scale manufacture using PVD and sputtering equipment uses holders mounted on carousels that rotate both on their own axis and on a central axis in the machine's deposition chamber to ensure uniform deposition thickness. The exact number of work parts a carousel carries depends on the size of the deposition chamber and the part geometry; varying degrees of clearance may be needed to ensure uniform deposition. Occasionally the carousel will also rotate the individual parts on their respective holders. Assuming a fairly large scale of manufacture it is

reasonable to expect 15 tubes per carousel and 5 carousels in the deposition chamber for a total of 75 cells per batch.

A note on timing: Following the process as described above and with the noted equipment, manual (that is human) work hours are only required for the initial loading of nickel tubes and final unloading of complete cells, plus any necessary monitoring. This has not been taken into account because it is highly variable and is furthermore dependent on minutiae such as exact carousel design and the number of cells produced per batch. The 76 h is therefore purely machine time, and more than a little approximate as it is based in the time taken for a refined research process extrapolated to mass manufacture. In any case the machine time is the majority of the time on a highly automated system such as this. However, the system is designed such that it will not take 76 h per batch! Rather it takes 76 h for the first batch to emerge. In reality each time a batch completes a step of the process and moves on to the next chamber another takes its place in the previous chamber. This will not necessarily be immediate because of necessary changes in temperature, pressure and atmosphere (gas composition) between chambers. Intermediate chambers are used to reduce this time. For instance, rather than the carousels moving directly from the sputtering chamber to the unloading station they move to an intermediate chamber first (labelled intermediate 3 in Figure 15-2.). This is because sputtering may be at room temperature but is at a vacuum pressure. Without the intermediate chamber once sputtering is complete the chamber must be brought up to atmospheric pressure before moving the carousels to the unloading station, then pumping this back down to the sputtering pressure for the next batch. With the use of an intermediate chamber evacuated to nearly the sputtering pressure the sputtering chamber can be used in short order after the carousels are transferred to it since the time needed to evacuate to sputtering pressure from an already high vacuum pressure is obviously less than doing so from atmospheric pressure. In the meantime the intermediate chamber is pumped up to atmospheric pressure, unloaded, and evacuated once more. The aim in choosing the intermediate pressure is to find one that can be reached rapidly (pumping times are not linear with desired pressure). Thus, the intermediate chamber cycles from atmospheric pressure to some 80% of the desired vacuum pressure and the sputtering chamber cycles between the sputtering pressure and one that is slightly higher. It may well be feasible to reduce some of the processing times, particularly whatever technique is eventually used to create the cathode for large scale manufacture since sputtering is a relatively slow process (and even then it may be possible to reduce the time to 5 minutes). See also the figure below (Figure 15-3.).

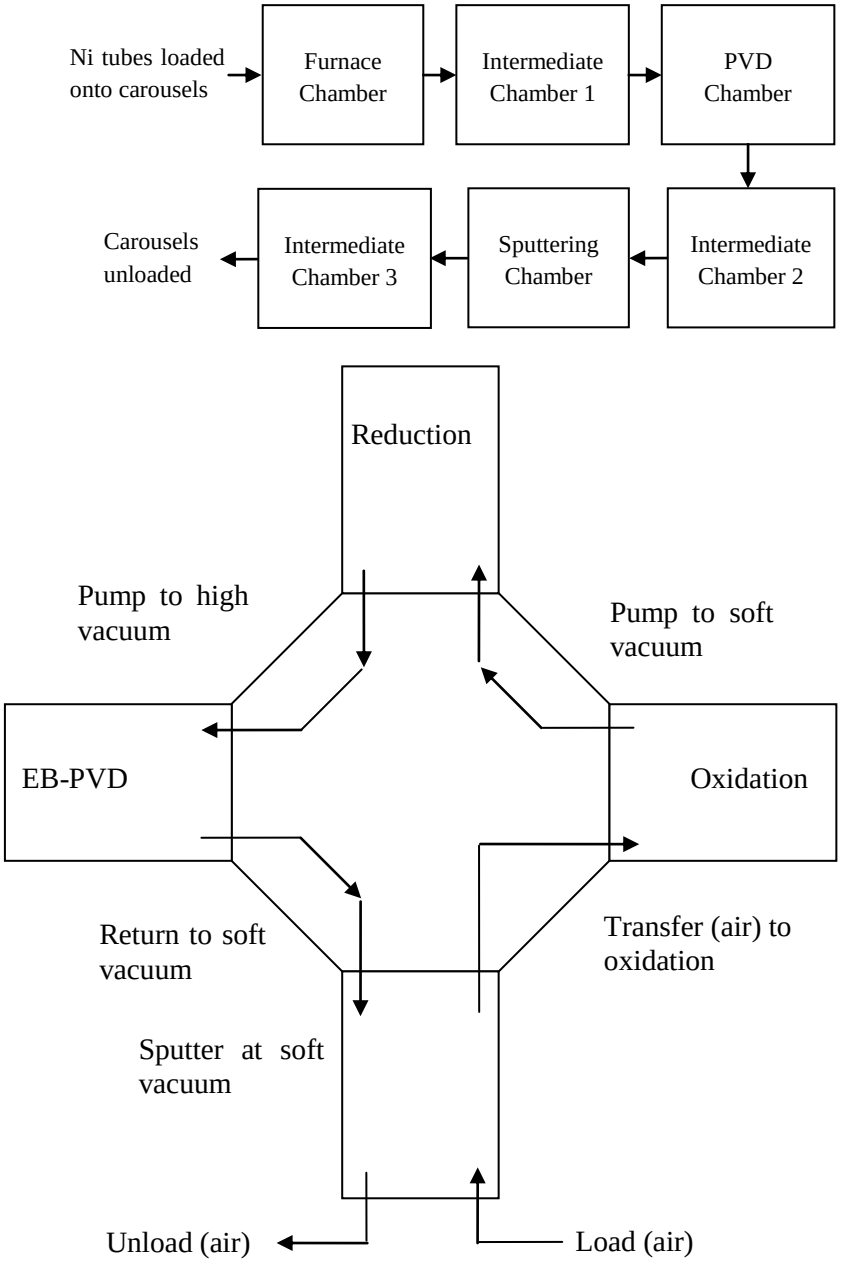

Figure 15-2. Single-Multi-Chamber-Machine Cell Manufacture process flow and schematic for a machine with rotating material handling feed and load locks.

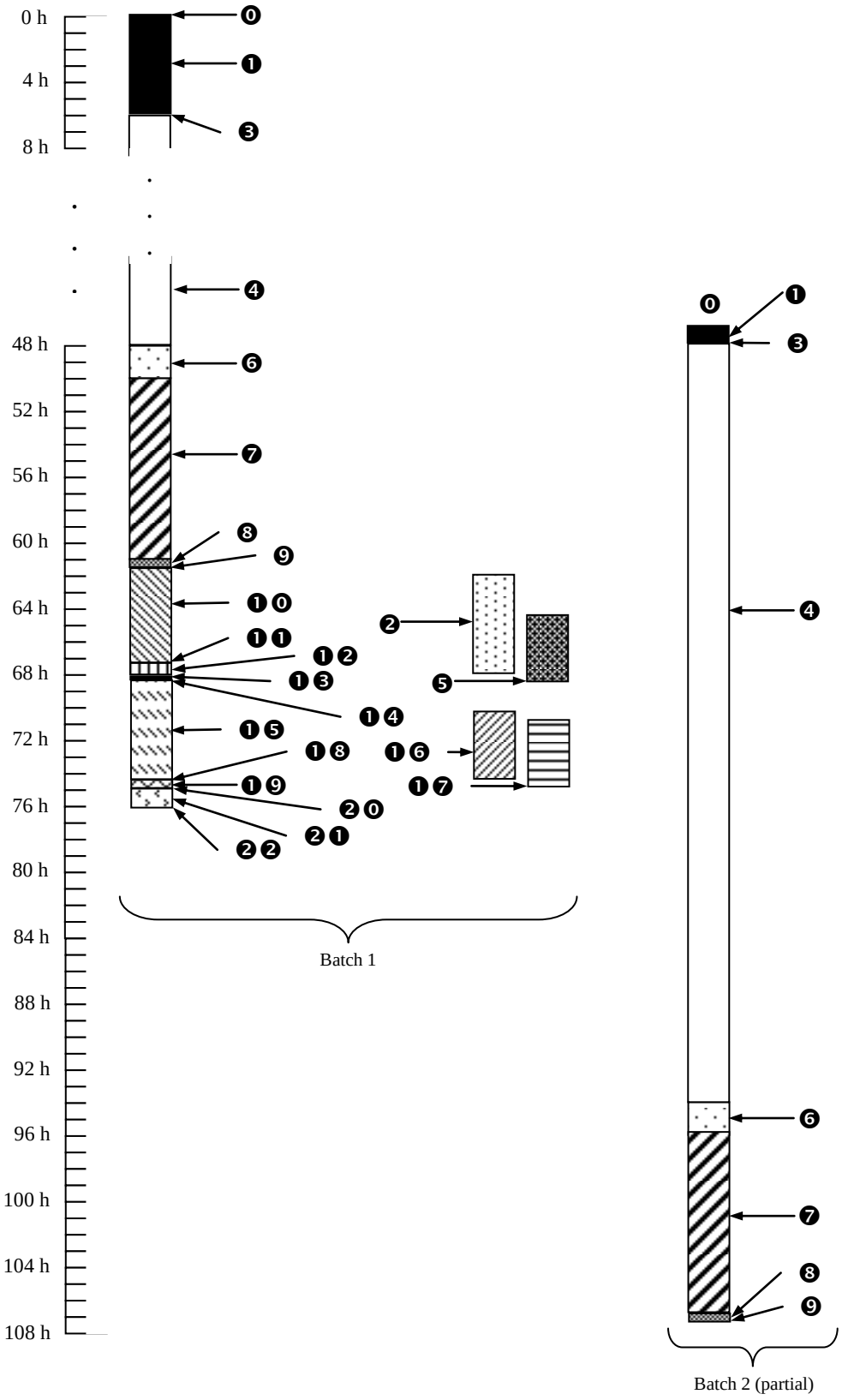

Figure 15-3. Single-Multi-Chamber-Machine Cell Manufacture Gantt-chart type depiction of manufacturing process. The figure shows the first batch of the week and one subsequent one (with the necessary process modifications).

Key:	
⓿ Ni tubes are pre-loaded onto carousels.	❶❷ Final evacuation of PVD chamber.
❶ Furnace heated to 1,100 °C.	❶❸ YSZ electrolyte deposited.
❷ PVD chamber evacuated and heated to 850 °C.	❶❹ Carousels transferred to intermediate chamber 2.
❸ Carousels moved into furnace chamber.	❶❺ Intermediate chamber 2 cooled to 25 °C.
❹ Ni tubes oxidised.	❶❻ Sputtering chamber evacuated.
❺ Intermediate chamber 2 evacuated and heated to 850 °C.	❶❼ Intermediate chamber 3 evacuated.
❻ Cooled to 1,000 °C & evacuated and purged (Ar) x3.	❶❽ Carousels transferred to sputtering chamber.
❼ Ni tubes reduced.	❶❾ Cathode sputtered.
❽ Purged (Ar) x5.	❷⓿ Carousels transferred to intermediate chamber 3.
❾ Carousels transferred to intermediate chamber 1.	❷❶ Intermediate chamber 3 pumped to atmospheric.
❶⓿ Intermediate 1 evacuated and heated to 850 °C.	❷❷ Carousels transferred to unloading station.
❶❶ Carousels transferred to PVD chamber.	

Table 15-1. Key to Figure 15-3.

Even without optimising the production process further an additional 71 h are required for a batch of cells to be made. Assuming work is started at 08:00 on Monday, that work continues for 24 h each day, and that all chambers are left to cool at atmospheric pressure over the weekend, by 11:00 on Sunday a total of 150 cells (2 batches) are completed. This leads to approximately 10 batches per month of continuous operation (750 cells).

Notice that the greatest improvement is to be had by reducing the oxidation time, reduction time (although recall the 11.5 h used here is the worst case scenario) and making clever use of intermediate chambers. The overestimation of the reduction time alone represents a significant time saving since it represents over 15% of the total.

The EU has published a 4,000 €/kW SOFC target system cost for 2020 (FCH-JU accessed 2018). According to a paper by Staffell and Green (2013) and NELLHI (NELLHI accessed 2018) the profitable customer price should be less than 1,000 €/kW. Similar targets were set in the US by the Department of Energy: 1,000 $/kW (equivalent to 848 €/kW) [Staffell and Green 2013]. Sale prices are typically 30-50 times the target sale price even when mass produced [Staffell and Green 2013]. Staffell and Green (2013) review the disparity in target price and sale prices and quantify the minimum feasible price for a typical 1 kW natural gas CHP system. “Based on the findings, even a heroic effort by industry is unlikely to reduce the price of small domestic-scale systems to the $1,000/kW mark.” [Staffell and Green 2013] A far more realistic 2020 target is 3,000–5,000 $/kW (equivalent to 2,550–4,240 €/kW) [Staffell and Green 2013]. This is in line with the FCH-JU findings. The detailed review by Staffell and Green (2013) is highly recommended reading.

The total active area cell is ≈ 18.14 cm^2. Assuming the design once further optimised reaches a typical performance of 0.5 Wcm^{-2} a 1 kW stack would require 111 cells. This sets a maximum per cell cost of € 36.04 (£ 31.51) to meet the FCH-JU target. Based on the estimates made in chapter 11 the current design costs a maximum of £ 30.38 per cell

(using unreasonably high energy consumption assumptions to elucidate a worst-case-scenario and a batch size of just 8). A system as described in section 15.2 could produce 75 cells per batch (conservative estimate made above) to as much as 128 cells per bath (based on very large scale mass manufacture EB-PVD coaters). In these cases the cost per cell is closer to £ 17.70–17.10.

A multi-chamber system similar to but somewhat larger than the one described in section 15.2 has a total capital cost of c.10 million GBP with chambers sufficiently large to process batches of about 128 cells [private communication with Professor John Nicholls, cost of large commercial EB-PVD coater]. Amortising the coater over 10 years using a simple linear model results in a £ 1 million p.a. cost.

Based on personal experience with and around vacuum coaters and the building space required to house them, ancillary functions (e.g. gas storage, extraction and cooling systems) and staff a floor area of approximately 600 m^2 is suitable for large scale manufacture. Approximately a third of this is office space, a third laboratory (manufacturing) space and a third industrial (warehousing). Typical rent figures for 2017 were found for these types of buildings for prime industrial estate or areas in industrial areas of the UK (concentrating on the Midlands and East Midlands). Office space rental is typically 350 GBP/m^2 [Statistica.com a, accessed 2018]. Industrial space rental in prime industrial estate areas is an average of 88 GBP/m^2 [Statistica.com a, accessed 2018]. Finally, laboratory space is approximately 332 GBP/m^2 [Plymouthsciencepark.com, accessed 2018]. Total rental cost would be of the order of £ 154,000.

Assuming a small SME level of manufacture a staff of approximately 10 people is reasonable. Cost of equipment per annum is approximately 1/3 of labour cost. An additional 100% of this added to the labour cost factors overheads and ancillary staff. This amounts to a total of £ 4 million p.a. This is sufficiently significant to motivate searching for suitable sites away from the UK.

Working for about 220 days per year produces 5,500-9,300 cells per year (equivalent to about 50-80 complete 1 kW stacks) reckoning by the two batch sizes noted. The total annualised cost is therefore estimated to be £ 6.94–7.0 million. Thus, in order to meet the EU target costs need to be significantly reduced. However, it is important to note that for this first estimate cost the processing time for both oxidation and reduction is probably greatly overestimated, unreasonably high energy costs were assumed (lacking better data) and £ 12.15 per cell represents the commercial cost of thin walled Ni tubes from a supplier that caters to specialty and research rather than mass manufacture. Both are expected to be much lower.

The preceding section sought to present what a complete manufacturing process for large scale production of microtubular solid oxide fuel cells of the design presented in this thesis could look like in broad strokes. The high capital investment of such a system is offset by the gains in manufacture volume and minimising labour costs. Such a route is preferable to many others in order to reduce manufacturing costs sufficiently for successful commercialization based on similar manufacturing challenges (e.g. turbine blades for gas turbines).

15.3 Roadmap to Mass Manufacture

The following is a roadmap that seeks to bridge the work covered in this thesis to mass manufacture in the form presented in above (section 15.2).

- Completed proof-of-concept of basic design (work presented in this thesis).
- Research and optimise graded anodes via EB-PVD (for proposed methods see section 17.1).
- Improve control, of electrolyte thickness, research thinner electrolytes, explore and then optimise additional technique(s) to achieve gas tightness (see section 17.2).
- Select between ceramic or cermet materials for cathode in line with future developments (e.g. LSM), establish sputtering/EB-PVD manufacture, and optimise this (both for cell performance and for mass manufacture).
- Achieve graded cathode for optimal results (subject to investigative work into the value of a graded cathode for a µ-tubular SOFC).
- Explore series and parallel stack designs (e.g. 7-cell series stack – a 'potential' stack and a 7-cell parallel stack – a 'current' stack) and optimise these for low connection resistance, packing density, and manufacture, excluding BOP at this stage. See discussion in section 15.2.
- Select an initial target application and develop prototype unit (consisting of several stacks and BOP).
- Design plant necessary for manufacture.

Build/redevelop manufacturing facilities and allow due time to work out kinks and attempt to further optimise. Integral to this is BOP and enclosure (especially insulation and control elements) design and optimization (once more for both performance and mass manufacture) of prototype.

16 Conclusion

The first four parts of this chapter acts as the counterpart to chapter 5 (Summary of Contributions to Science) and tabulates for clarity the objectives reached. Each of these four also describes the extent of optimization carried out on the process and resulting fuel cell components. The fifth part draws to a close the thesis as a whole. It is, however, by no means the end of pertinent research on this design. Chapter 17 outlines the next steps, including additional optimization iterations and/or routes on a by-component basis.

16.1 Anode

Anode		
Requirements	**Gaps in Knowledge/ Novelty in this Project**	**Objectives Achieved**
Porous (min. 30%-40%)	Oxidation-reduction is a novel way to create anodes with a connected network of pores.	Demonstrated excellent reproducibility of the technique for creating porous metallic Ni anodes with through porosity. Gas permeance performance is excellent with very weak influence of gas type/size (see chapter 1). Both reduction schemes result in suitable anodes. A higher reduction temperature reduces the necessary dwell time and leads to overall superior gas permeance. However, it also complicates the achievement of a gas-tight electrolyte (see chapter 1).
	Complete oxidation not well understood (actual oxide thickness, mass and oxidation rate strays from classical model).	A modified Wagnerian model closely matched experimental oxidation data indicating there are no significant deviations from the fundamental model despite through oxidation violating two of its assumptions (see 8.1 to 8.8). The mechanism transitions to a second parabolic mechanism with a much lower k_p. The microstructure, however, differs from some reports, as discussed. Much seemingly contradictory information reported in the literature was successfully disentangled and an improved understanding of Ni oxidation achieved.
Catalyst for hydrogen dissociation	Catalyst performance	It is possible that the very fine porosity will lead to very large surface areas and better catalysis – incidental to the technique rather than a separate endeavour. A good indicator would be a particularly low activation polarization. The poor electrochemical performance (see chapter 14) rendered determination of catalytic performance untenable.
Fabrication/ processing costs	No quantified assessment of the manufacturing cost (or materials for that matter) exists, merely claims.	Circumstances prevented a completely accurate auditing. Nevertheless a reasonable estimation was reached (see 11.4.1)

Table 16-1. Anode contributions achieved.

The oxidation process has been optimised with the initial proviso of oxidation at 1,100 °C (indeed the initial work presented in this thesis can be considered a first iteration optimization of similar work in Camilleri (2009), optimising for minimum time). An initial pass, though one that cannot be considered a comprehensive iteration, at further

oxidation time optimization was carried out at an increased temperature of 1,150 °C with very promising results.

The reduction process opened several important options. The resulting morphology is eminently suited to the SOFC anodes whether the reduction process is optimised for low reduction temperature or short reduction dwell time. The latter yields quantifiably superior gas permeance. Yet, as discussed in chapter 1, the former was more than suitable also. It is therefore a matter of selecting which route is optimal for large scale manufacture based upon the approach taken. The exploration of both routes resulted in optimization towards both minimum processing temperature and minimum processing time (though separately). The resulting anodes have thus benefitted from a combination of optimization iterations targeting the processing steps and the component's performance (namely gas permeance). Further optimization of the anode as well as its manufacture is discussed in chapter 17.

16.2 Electrolyte

Electrolyte		
Requirements	**Gaps in Knowledge/ Novelty in this Project**	**Objectives Achieved**
Gas tight (to both H_2 and O_2).	Disorder in the first few µm leads to a non-columnar structure which is believed be gas tight.	The permeametry work (chapter 1) demonstrates this is only the case with anodes electrolytes thicker than the intended 10 µm. Some gas transport resistance was measured, but this was far from gas tightness. OCV was therefore expected to be low. As discussed in that chapter, however, much of this may be attributed to the anode surface morphology and its effect on the highly conformal electrolyte as deposited by EB-PVD. Solutions are proposed in chapter 17.
	Having demonstrated it is possible to manufacture 10 µm. Next is optimization of the process and pushing to find lower limit (thinner electrolyte leads to lower losses).	It did not prove possible with the existing setup to control deposition thickness to a sufficient degree to reliably manufacture sub-10 µm thick electrolytes. Some samples were produced with 6–7 µm electrolytes, demonstrating it is possible, but occurred by chance rather than design. The results discussed in chapter 9 show promise for the creation of thinner electrolyte subject to improved deposition control.
High ionic conductivity.	Effect of columnar texturing on cathode side unknown. Possibly will enhance conductivity (large surface area).	The lack of interpretable Nyquist plots hampered investigating this possibility.
	A high operating temperature is needed for sufficient ionic conduction (hence the HT requirement of YSZ electrolyte cells). Thinner electrolytes relieve this requirement.	The results of chapter 14 show that a comparable OCV was generated at as low as 400 °C, rising steadily with operating temperatures. There is some evidence that operating in excess of 800 °C offers no additional benefit.
Intimate contact with electrodes.	Behaviour of EB-PVD YSZ electrolyte deposition onto porous Ni anode.	Micrographical evidence indicates strongly adhering and highly conformal interfaces. Electrical performance is an indicator of uniformity and intimacy of electrolyte-electrode contact. The insufficient gas tightness of the electrolyte makes it difficult to ascribe any performance loss to interfacial effects.
	Behaviour of sputtered Pt cathode deposition onto columnar YSZ electrolyte.	
Fabrication/ processing costs.	No quantified assessment of the manufacturing costs (or materials for that matter) exist, merely claims.	As noted (chapter 5) due to the complications of the coater using several three-phase power supplies only the material costs were assessed. This amounts to approximately £ 0.95 per fuel cell (see 11.4.2 for details).

Table 16-2. Electrolyte contributions achieved.

The deposition process has been optimised via a modified Design of Experiments route for processing parameters and also assessed for reproducibility. As discussed in chapter 9 it was not possible to iterate further on electrolyte thickness due to the lack of a shutter. Electrolyte thickness is the most significant optimization iteration(s) remaining.

16.3 Cathode

Cathode		
Requirements	**Gaps in Knowledge/ Novelty in this Project**	**Objectives Achieved**
Porous (min. 30%-40%).	Is a very thin (c. 300 nm) layer of Pt sufficient for gas transport?	Previous experience (Camilleri 2009) combined with rate run experiments determined the necessary sputtering parameters to achieve a c. 300 nm conformal approximately 40% porous cathode. This was expected to provide sufficient gas transport, i.e. result in a low cathodic concentration polarization. Micrographs clearly show the thin highly conformal porous cathode.
	Is the cathodic activation polarization as low as expected?	The lack of Nyquist plots that are interpretable meant this could not be determined with certainty at the time of writing. However, the exceedingly low activation energies suggest that it is the arrival/residence of oxygen that is the rate limiting step. *Ergo*, the cathodic activation polarization is likely even lower than anticipated.
Provide electronic conduction.	Is a very thin (c. 300 nm) layer of Pt adequate for electronic conduction?	The average resistance for the porous Pt was found to be $296.67 \pm 213.87\ \Omega$. Comparison to bulk Pt shows in increase in bulk resistivity of two orders of magnitude due to porosity. Measured resistance variance agrees with the expected thickness variation of sputtered coatings. This simple design of cathode was deemed adequate for the purview of this project.
Catalyst for oxygen dissociation.	Catalyst performance.	As noted in chapter 5 Pt is an excellent catalyst for oxygen dissociation (among many other reactions). It was expected that the very fine porosity resulted in very large surface areas and better catalyst performance (seen as a lower cathodic activation polarization). This was not investigated separately (since the selected cathode was merely to enable testing of the anode-electrolyte design) but EIS results and activation energy calculations suggest the activation polarization was remarkably low.
	Behaviour	
Fabrication/ processing costs.	No quantified assessment of the manufacturing cost (or materials for that matter) exists, merely claims.	As the cathode employed was an enabler rather than integral part of the design (as it was focussed on the anode-electrolyte complex) this aspect was relatively unimportant. A basic audit, however, is included in chapter 11.

Table 16-3. Cathode contributions achieved.

The cathode was not optimised in any way since it was necessary for the electrical performance testing of the completed cells but was not a component investigated in detail during this project. However, it is possible that with such thin cathodes Pt is indeed suitable and high pressure sputtering may benefit from process optimization. Similarly, further study may indicate optimizations possible for cathode thickness.

16.4 General

General (i.e. not component-specific)		
Requirements	**Gaps in Knowledge/ Novelty in this Project**	**Objectives Achieved**
Evaluate performance of cells by experiment.	The performance of these particular cells obviously was unknown.	The planned comprehensive analysis of cell performance including I-V curves, impedance spectroscopy, power-current density plots, fuel utilization plotted against both current density and power output, was halted for the reasons given in chapter 14. The fabricated devices do, however, perform as SOFCs with temperature dependent OCV and some interesting implications based on the Arrhenius plots generated. The low electrochemical performance was expected once permeametry results showed the lack of gas tightness of the electrolyte and revealed probable causes (see chapter 1). Measured OCVs were highly repeatable. Despite the inability (small sample size) to prove causality significant performance differences could be attributed with confidence to cell microstructure.
Economics of fuel cells.	Detailed investigation into fuel feasibility and the economics of fuel cells, taking into consideration infrastructure and economics. This is crucial because it concretely justifies an approach that does not follow current trends as well as defining the niche such products are able to fill in the energy market.	This was reviewed in detail in chapters 1 and 2. From this review the most suitable target market for microtubular SOFCs was deemed to be domestic and small scale (e.g. residential, light industrial) CHP or electrical supply. Success in these markets would allow expansion into other markets. Of particular interest are grid-independent and load balancing applications.
Assessing fabrication process consistency.	Reproducibility is an acknowledged weakness in the fabrication of micro- and nano-scaled devices, and becomes increasingly important as size is reduced. No relevant literature source so much as makes mention of this, let alone attempts to assess it.	The manufacture of both the component layers (e.g. anode) and complete cell fabrication, as discussed at length in chapter 11, shows excellent reproducibility. The one major weakness is the electrolyte thickness. The addition of shutters is a straightforward solution, although one that was not available with the current setup of the coater (the modification, while relatively simple would interfere with other ongoing work and was therefore deemed unfeasible). The reproducibility of the performance was also discussed in terms of gas transport in sections 12.6.1 and 12.7.1.

Table 16-4. General contributions achieved.

The cells tested reveal a working prototype with superior anodes in need of improvement in electrolyte gas tightness. Testing of additional prototypes without further optimization was not undertaken because of the limited usefulness such data would hold. The evidence cannot at this stage validate the use of EB-PVD for the creation of YSZ electrolyte for µ-tubular SOFCs. However, the poor gas tightness could not be attributed to the fabrication technique chosen either. Further scientific investigation is required to ascertain what is necessary to create optimal electrolytes by a modified EB-PVD technique or by the addition of a further manufacturing step before the viability of electrolytes manufactured in this way can be conclusively determined.

The author believes this will be found to be true provided manufactured volumes are sufficiently large to offset the high capital cost of equipment.

16.5 Overall Conclusions

The metallic Ni anodes designed, fabricated and tested over the course of this project offer excellent performance (by the yardstick of the experiments undertaken – long term performance remains unknown and activation polarization could not be determined to a justifiable precision due to the gas leakage through the electrolyte). The highly porous microstructure with its large gas permeance was both a hallmark success of this work and also the cause of the single greatest loss of electrochemical performance (see 8.14, 12.6 and 14.3). As described in chapter 9 (especially sections 9.5.1, 9.6.1 and 9.7) and section 12.7, the highly conformal EB-PVD processing route for the electrolyte leads to a deposited morphology that closely follows the large surface cracks of the anode leading to poor electrolyte gas tightness and the concomitant loss of electrical performance but showed that the devices did indeed operate as fuel cells. Chapter 17 proposes solutions that were envisaged early on, as some loss of gas tightness was anticipated due to the columnar morphology (not the success of the anode!).

EB-PVD has proved a viable deposition technique for the creation of very thin YSZ electrolytes for μ-tubular SOFCs. The method is not without flaws but the most significant of these is expected to be solvable by either one of the solutions proposed in section 17.2 (or perhaps a combination of both). Electrolytes fabricated this way were shown to be highly reproducible, with overall thickness requiring some improvement as discussed in sections 9.5 through 9.7 (along with how such is likely to be achieved) in order to achieve sub-10 μm electrolytes (recall some samples had 5 μm electrolytes).

Of unexpected interest is the variation on gas permeance achievable via selection of reduction scheme (section 12.6 through 12.8). The upper and lower limits, as identified in this work, were explored continuing the discussion of low-temperature-long-dwell against high-temperature-short-dwell from initial anode manufacture (*viz.* morphology and reproducibility in particular), through to the influence this has on gas permeance and to the effect on electrical and EIS characteristics of the cells. The route to future optimization is clear and the mass manufacture benefits of this design amply justify continued development.

17 Further Work

Some of the ideas recorded below are purely in the interest of furthering science. Others are more directed, either optimising some part of the fabrication process even further or modifications to enhance performance (that the author refers to as performance optimization or optimization for performance).

17.1 Further Development of the Anode

a. Oxidation at higher temperature has the benefit of significantly speeding up manufacture. The only concerns are discovering at what point does the added cost of moving to higher temperature outweigh the increase in productivity and whether there are any deleterious microstructural effects in moving to a higher temperature. The former requires metering the energy and material consumption of both the oxidation and reduction steps of the process more closely than was possible on this project. The latter was partly explored in section 11.4.1. However, the number of samples was small. I propose a systematic study akin to the other oxidation experiments, exploring a few dwells with at least five samples per dwell and maybe also investigating more than one additional temperature; 1,150 °C and 1,200 °C for example. Based on the literature temperatures equal to or greater than 1,200 °C are likely to be less than successful (see section 8.1).
b. Of great interest would be tracing the movement of oxygen in the samples. This can be done by isotopic study: a known amount of an oxygen isotope (typically O^{18}) is introduced to the oxidant at a known composition. Samples are then analysed by secondary ion mass spectroscopy (SIMS). Unfortunately, this equipment is not available at Cranfield University. However, collaboration with another university is certainly not too arduous to organise. Such a study would answer questions as to where oxidation begins, how far do the anions travel, where they dissociate from cations and what concentrations result in vapour phase transport.
c. The reduction step would benefit from a similar isotope analysis study. This would show whether predominantly hydrogen infiltrates the surface and reduces the NiO or whether NiO interdiffusion brings it to a reactive surface. Furthermore, such a study could help improve understanding of the processes occurring at the TPB of anode-electrolyte and fuel gas.
d. Reduction at even just 400 °C is not only possible but entirely feasible from a process standpoint. The lower temperature easing furnace requirements and resulting in a considerably safer process. Exploring this low temperature limit further would be of value from a manufacture standpoint. As such it constitutes a

further optimization of the anode for manufacture. It may also reveal pertinent information about hydrogen transport in a permeable Ni matrix that would be of use in designing and modelling SOFCs. Another question of great interest is whether a lower temperature at significantly longer dwell is more economical than no dwell at 1,000 °C – not only in monetary terms but in efficient usage of energy (and the environmental impact of the manufacturing process) as well as estimated overheads, wages, etc.

e. The flow rate of the reducing gas is another parameter that may benefit from optimization. Treating this as another process variable would extend the comparison of processes (in terms of mass fraction reduced, for example) into three dimensions: temperature, dwell time and gas flow rate. The dwell times can be restricted to only include those that result in complete reduction and a suitable microstructure, the addition of gas flow rate as a parameter being a further stage of optimization rather than a new investigation.
f. The overall resistivity of a structure created via oxidation-reduction in this way needs to be assessed (since the technique is new). This involves carrying out accurate resistance measurements for a statistically meaningful number of samples for (at least) the two competing extremes of the reduction scheme. Such data can then be compared to bulk values. It is also useful in calculating ohmic polarization.
g. As remarked a few times in the main body of this thesis, cermet anodes offer a number of not-to-be-overlooked advantages compared to either ceramic or metallic ones. My intention was always to move towards this despite it not being feasible at the time of this project to reconfigure the EB-PVD system to do so. One possible route to achieve cermet anodes is to create metallic anodes on Ni tubes with thinner walls and then co-deposit Ni and 7YSZ, grading gradually from 100% Ni to 100% 7YSZ over a thin metallic portion, a smooth transition from anode to electrolyte the greatly extends the TPB. Similar work was reported by Meng *et al.* (2009), in which they compare uniform cermet anodes and graded ones, both created by EB-PVD, with 1 Ni ingot and 1 YSZ ingot (each with their own beam and therefore melt pool). An interesting question arises as to how much more 7YSZ would need to be deposited to form a suitable electrolyte. Perhaps an electrolyte *per se* is no longer needed. Another possible technique is to make metallic anodes as per the technique described in this thesis and subsequently employ ion implantation to add 7YSZ into the anode creating a cermet. It may prove impossible to create a graded anode in this manner, but may offer a more rapid manufacturing process. Certainly an alternative worthy of investigation.
h. Ancillary to the above is experimenting with the integration of some elements of a Cu-GDC system. Cu–CGO and Cu–Ni–CGO anodes exhibit mixed ionic and electronic conductivity [Shaikh *et al.* 2015, Mahato *et al.* 2015]. CeO_2–based anode materials show sufficient catalytic activity and good electronic

conductivity due to change from Ce^{4+} to Ce^{3+} in reducing atmospheres [Shaikh *et al.* 2015]. In addition, Cu–ceria based anodes have high resistance to carbon deposition [Shaikh *et al.* 2015, Mahato *et al.* 2015]. Cu is helpful as it has a higher electronic conductivity than Ni and is not sufficiently catalytic for hydrocarbons to form carbon deposits on the anode (carbon fouling). It is not sufficiently catalytic for the oxidation of hydrogen however, this depends entirely on the ceria (or CGO) content [Shaikh *et al.* 2015]. The drawbacks, however, are significant. Ceria is not nearly as stable as Ni or Ni-YSZ at high temperature and the Cu tends to sinter into aggregate phases rather than remain dispersed. Hence, while promising these modifications require careful investigation prior to integration. Particularly because unfortunately Shaikh *et al.* in their cited review contradict themselves saying both that Ni is "an inert metal" and also that it possesses a "high electronic conductivity and catalytic activity". So some of their analysis is likely not sound, and these dubious elements have been excluded. The review by Mahato *et al.* (2015) confirms the other information from Shaikh *et al.* (2015).

17.2 Further Development of the Electrolyte

a. The implementation of a shutter would allow experiments both refining the deposition process for even better reproducibility (another level of optimization for manufacture) and also investigate the creation of ever-thinner electrolytes (a level of performance optimization). How thin is sufficient? Is there effectively no limitation so we may create pseudo-single chamber SOFCs with nanoscopic component thicknesses?
b. The deleterious gas fluxes through the electrolyte needs to be rectified. A sol gel infiltration treatment as proposed by Meng *et al.* (2008) is worth assessing. Laser re-melting of the electrolyte surface prior to cathode deposition could work too [Coddet *et al.* 2014]. Additionally, by altering the rotation of sample holders to a back-and-forth type it is possible to create herringbone or zigzag morphologies rather than columnar ones. The author believes this may introduce sufficient resistance to gas transport to solve the problem. It has the advantage over a post-treatment in that it occurs as part of the deposition process rather than as an additional step – valuable for mass manufacture – although it has an associated cost in increasing the time required to deposit the electrolyte. The technique is certainly worth investigating. Till some solution is found performance of this design will remain severely curtailed. This concept is supported by the work of Haydn *et al.* (2014), described hereunder. Their cells are built on a metal substrate manufactured by powder metallurgy (see Figure 17-1.).

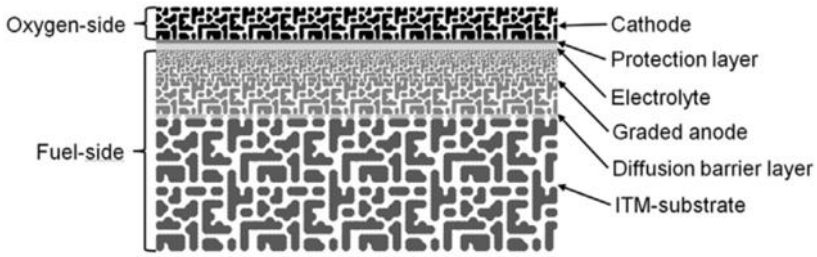

Figure 17-1. Schematic cross-section of the metal supported cell created by Haydn *et al.* [after Haydn *et al.* 2014].

Their work is an apt comparison. The most relevant details are given here. The porous metallic substrate (an oxygen dispersion strengthened Fe26 Cr (Mo, Ti), Y_2O_3) is 1 mm thick. A graded anode is deposited in top of this that is 1–2 µm of GDC by reactive magnetron sputtering that acts as a diffusion barrier to prevent Ni diffusion into the metal support and the diffusion of Fe and Cr into the anode, then a 40–70 µm cermet anode of Ni–8YSZ with a porosity gradient by screen printing and sintering. The anode must be flat and smooth to enable the deposition of a thin gas-tight electrolyte later on top of it. On top of this is the 8YSZ electrolyte, 4–5 µm thick, deposited by a physical vapour deposition process called gas flow sputtering ('high' deposition rate up to 10 µm h^{-1} and high process pressures of about 0.5 mbar). On this is another layer of GDC, 1–2 µm thick, deposited by reactive magnetron sputtering that prevents the formation of electrically insulting Sr–Zr phases between the electrolyte and the cathode during operation. An LSCF cathode is the final layer, deposited by screen printing and sintering to a thickness of 20–60 µm. interestingly the cathode is allowed to sinter during the opening phases of operation (at 700 °C – 850 °C) rather than by a separate sintering step. The parts of most interest are those dealing with the electrolyte gas tightness.

Essentially alternating layers of metallic zirconium-yttrium and YSZ were deposited by switching on or off the oxygen flow [Haydn *et al.* 2014] (rather like intentionally depositing an oxygen deficient coating with EB-PVD by turning off the gas supply). The metallic layers do not conduct oxygen ions. However, either via a heat treatment to oxidise them or during operation at high temperature they will convert to YSZ, and therefore function as an electrolyte [Haydn *et al.* 2014]. The authors' discovered that this way gas tightness is greatly improved: from 0.3 mbar dm^3 s^{-1} cm^{-2} for their design with single layer electrolytes to 0.03 mbar dm^3 s^{-1} cm^{-2} for multilayer ones [Haydn *et al.* 2014]. Can this be achieved by EB-PVD? I certainly believe so. Unfortunately, they only tested gas permeance with air, so what improvement, if any, is to be had for smaller molecules like hydrogen remains unknown. The authors further note that the anode topology strongly impacts the resulting microstructure (and gas tightness) of the electrolyte, especially if the electrolyte is a single oxide layer. I have found much the same (see chapter 1), and agree completely with them that

a graded anode with fewer smaller pores at the anode-electrolyte interface would improve gas tightness.

c. It may be fruitful to use the existing DoE data and carry out ANOVA analysis as another way to determine factor significances – via variances rather than on the delta as was done for this study. One may reasonably expect ANOVA to help discern which deposition factors are the most important.

17.3 Further Development of the Cathode

a. A re-evaluation of current cathode materials (whichever conform to the *de facto* state-of-the-art) is necessary to take this design forward. The considerable interest in this area of fuel cell research around 2010 has resulted in many contributions to the literature that merit careful reading [cf. Connor (2010) and the Proceedings of the 9th European Solid Oxide Fuel Cell Forum more generally]. Once the above is concluded novel deposition techniques that favour mass manufacture are to be developed and tested; then integrated into the design presented in this thesis and evaluated. Subsequently, some optimization in manufacturing process and performance is highly desirable prior to developing the final design. Of greatest priority are creating the thinnest cathode possible that is still fit for purpose and designing a method for the mass manufacture of graded cathodes. In conjunction with the latter the benefit to performance and various costs will need to be carefully assessed.

b. The development of a cermet cathode, especially a graded one, may provide similar benefits to a graded anode. Such work is of lower priority than the anode, however, since the cathodic concentration polarization is less significant than the anodic concentration polarization. The benefits may be worth the added cost and complexity, but require careful study. I would propose beginning by co-sputtering Pt and YSZ onto the electrolyte. The composition can be controlled dynamically during deposition to create a graded structure with mostly zirconia at the cathode-electrolyte interface and mostly platinum at the outermost surface of the cathode. Platinum can be supplanted by any other material deemed superior, with the only adjustments necessary coming from an altered deposition rate of the new material.

c. Given a thin layer Pt cathode (300 nm) appears sufficient it would be worthwhile fully investigating their creation via sputtering porous films. Such a study would resemble chapter 8 in determining optimal deposition parameters, with follow-up permeametry to analyse gas transport performance. Additionally investigation of deposition efficiency and improvement via jigging is critical to such a design alternative. Could nanoscopic Pt cathodes prove economically viable once scaled out?

17.4 Further Permeametry

a. Extend the dataset to statistically significant numbers. Ideally a single repeat and many samples. However, the nature of the experiments means it is more practical to find a compromise between number of samples and repeats per sample. While the author does not expect any significant changes to the trends observed or conclusions drawn such an undertaking would allow the determination of a realistic standard deviation and mean for the data, particularly for the error that otherwise relies on measurement errors that are more uncertain than one often encounters because of the way they stack in this case (e.g. temperature error affects both the sensor reading and supply voltage output, the latter also affects the sensor error).
b. Additional measurements that could prove useful (and would certainly be of scientific interest) are measurements of select reduction step dwells that do not produce a fully reduced sample. Potentially, a sample need not be fully reduced to be sufficiently permeable to the relevant gases for use in fuel cells. Of particular interest, due to the advantages of low temperature reduction, would be the ramp only (0 h dwell) and a few short dwells of samples reduced at 400 °C.
c. At the other end of the spectrum permeametry is a powerful tool in both assessing and understanding the deterioration of performance with operation of solid oxide fuel cells. With reference to the work I have carried out it would be interesting (and useful in performance degradation studies) to carry out measurements similar to the above for samples exposed to temperatures (manufacture or operating) for far longer dwells than needed to produce porous anodes / for realistic operating time scales.
d. In addition to gathering more permeance data for the relevant gases with anodes and anode-electrolyte complexes the same should be done on complete fuel cells.
e. It is not practical to attempt to separate the electrolyte (or the cathode) from the anode for permeametry measurements since these component layers are too fragile to be free-standing membranes. A means of using the data to separate component permeances is highly desirable. A suitable model could be found in the literature. A suitable alternative is to create an equivalent circuit. The author believes that heat transfer is a close equivalent, in terms of creating an equivalent circuit, to gas fluxes though a membrane and it may therefore be permissible to model each component as a parallel resistor (subject to verification, of course).
f. As noted in the permeametry chapter (chapter 1) this technique has great potential for in line testing of fuel cells manufactured at a very large scale. It would be beneficial then to develop a method (including modifications of the existing permeametry rig design) to evaluate whether a manufactured component (anode, anode-electrolyte complex, and finally complete cell) is within tolerances.

Bibliography and Reference List

Al-Qattan A., Abdelrahman E.-S. and Kholoud A.-A. (2014), "Solid oxide fuel cell application in district cooling"; *Journal of Power Sources*; vol 257; pg 21–26.

Anderson H. U. and Tietz F. (2003), “Interconnects”. In Singhal S. C. and Kendall K. (Ed.) *High Temperature Solid Oxide Fuel Cells: Fundamentals, Design and Applications*, Elsevier Advanced Technology, Oxford, UK (pg. 173–195).

Angenete J. (2002), “Aluminide diffusion coatings for Ni based superalloys”; *Doktorsavhandlingar vid Chalmers Tekniska Hogskola*; issue 1803.

Armstrong E. N., Duncan K. L., Oh D. J., Weaver J. F. and Wachsman E. D. (2011), "Determination of Surface Exchange Coefficients for LSM, LSCF, YSZ, GDC Constituent Materials in Composite SOFC Cathodes"; *Journal of The Electrochemical Society*; vol 158; issue 5; pg B492–B499.

Atkinson A. and Taylor R.I. (1978), "The self-diffusion of Ni in NiO and its relevance to the oxidation of Ni"; *Journal of Materials Science*; vol 13; issue 2; pg 427-432.

Atkinson A. and Taylor R.I. (1979), "The diffusion of Ni in the bulk and along dislocations in NiO single crystals"; *Philosophical Magazine A*; vol 39; issue 5; pg 581-595.

Atkinson A., Taylor R.I. and Hughes A.E. (1982), "A quantitative demonstration of the grain boundary diffusion mechanism for the oxidation of metals"; *Philosophical Magazine A*; vol 45; issue 5; pg 823-833.

Bacon F. T. (March 15, 1960), "Porous Nickel Electrode"; *United States Patent Office*; Patent Number 2,928,783.

Betts J. (2005), Introduction to Ceramic Engineering, Lecture notes.

Bienvenu Y., Massart T., Van Wouw L., Jeandin M. and Morrison A. (1987), “The Metallurgy of Diffusion Bonding”. In Pearce R. (Ed.) *Diffusion Bonding: Proceedings of an International Conference held at Cranfield Institute of Technology 7-8 July 1987*, Printed by Paul Ellerington, Keysoe, UK (pg. 33–43).

Bin Z. (2009), "Solid Oxide Fuel Cell (SOFC) technical challenges and solutions from nano-aspects"; *International Journal of Energy Research*; vol 33; issue 13; pg 1126-1137.

Bischoff B. L., Suton T. G. and Armstrong T. R. (2007), “Tubular Solid Oxide Fuel Cell Current Collector”; International Patent WO2007005675 (A1); 11th January 2007.

Bove R. and Ubertini S. (2006), "Modeling solid oxide fuel cell operation: Approaches, techniques and results"; *Journal of Power Sources*; vol 159; pg 543–559.

Brault P., Caillard A., Thomann A. L. Mathias J., Charles C., Boswell R. W., Escribano S., Durand J. and Sauvage T. (2004), "Plasma sputtering deposition of platinum into porous fuel cell electrodes"; *Journal of Physics D: Applied Physics*; vol 37; pg 3419–3423.

Burchell T. D., Contescu C. I. and Gallego N. C. (2016), “Activated carbon fibres for gas storage”. In *Activated Carbon Fiber and Textiles*, Woodhead Publishing (pg. 305-335).

Camilleri A. F. (2009), *Microtubular Solid Oxide Fuel Cell Design and Prototype*, MSc Thesis, Cranfield University.

Ceramic Fuel Cells BlueGen: http://www.ceramicfuelcells.co.uk/en/technology/gennex-module/ (author unknown, accessed 21st October 2014).

Chang K.-S., Lin Y.-F. and Tung K.-L. (2011), "Insight into the grain boundary effect on the ionic transport of yttria-stabilized zirconia at elevated temperatures from a molecular modeling perspective"; *Journal of Power Sources*; vol 196; issue 22; pg 9322–9330.

Chatterjee R., Banjeree S., Banjeree S. and Gosh D. (2012), "Reduction of Nickel Oxide Powder and Pellet by Hydrogen"; *Transactions of the Indian Institute of Metals*; vol 65; issue 3; pg 265–273.

Chen E. (2003), “History”. In Hoogers G. (Ed.) *Fuel Cell Technology Handbook*, CRC Press, New York, USA (pg. 2-1–2-40).

Chen E. (2003), “Thermodynamics and Electrochemical Kinetics”. In Hoogers G. (Ed.) *Fuel Cell Technology Handbook*, CRC Press, New York, USA (pg. 3-1–3-30).

Chen F., Yang C. and Jin C. (June 18, 2013), "Method to fabricate high performance tubular solid oxide fuel cells"; *United States Patent Office*; Assignee University of South Carolina, Patent Number 8,465,797.

Chian C. and Li K. (2008), "Yttria-Stabilised Zirconia (YSZ)-Based Hollow Fiber Solid Oxide Fuel Cells"; *Industrial & Engineering Chemistry Research*; vol 47; issue 5; pg 1506–1512.

Cho H. J. and Choi G. M. (2009), "Fabrication and characterization of Ni-supported solid oxide fuel cell"; *Solid State Ionics*; doi:10.1016/j.ssi.2008.12.041.

Chuprina V. G. and Shalya I. M. (2004), "Oxidation processes for alloys in the Ni-Zr system. III. Oxidation of NiZr"; *Powder Metallurgy and Metal Ceramics*; vol 43, issue 9-10; pg 504–512.

ClearEdge Power article: http://en.wikipedia.org/wiki/ClearEdge_Power (accessed 21st October 2014).

Coddet P., Liao H. and Coddet C. (2014), "A review on high power SOFC electrolyte layer manufacturing using thermal spray and physical vapour deposition technologies"; *International Journal of Advanced Manufacturing*; vol 2; pg 212-221.

Connor P. (2010), *Proceedings of the 9th European Solid Oxide Fuel Cell Forum*, June 29 – July 2 2010, Lucerne (Switzerland), Published by the European Fuel Cell Forum 2010.

Craig M. (2010), "Manufacture of Novel Intermetallic Bond Coats from the Electroplating of Ionic Liquids", PhD Thesis, Cranfield University.

Dal Grande F., Thursfield A. and Metcalfe I. S. (2008), "Morphological control of electroless plated Ni anodes: Influence on fuel cell performance"; *Solid State Ionics*; vol 179, issue 35–36; pg 2042–2046.

Douglass D. L. (1995), "A Critique of Internal Oxidation in Alloys During the Post-Wagner Era"; Oxidation of Metals; vol 44; issue 1–2; pg 81–111.

Dunkerton S.B. (1990), "Diffusion Bonding – An Overview". In Stephenson D.J. (Ed.) Diffusion Bonding 2: Proceedings of the 2nd International Conference in Diffusion Bonding held at Cranfield Institute of Technology 28-29 March 1990, Elsevier Applied Science, London, UK (pg. 1–12).

Eisenberg M. (1963), "Thermodynamics of Electrochemical Fuel Cells". In Mitchell W. Jr. (Ed.) *Fuel Cells* (pg. 17-64). From Baddour R. F. (Ed.) *Chemical Technology: A Series of* Monographs, Volume 1. Academic Press, New York and London.

Error Propagation article (for error estimation by partial derivatives): http://en.wikipedia.org/wiki/Error_propagation (author unknown, accessed 25th August 2013).

Fabbri E., D'Epifanio A., Sanna S., Di Bartolomeo E., Balestrino G., Licoccia S. and Traversa E. (2010), "A novel single chamber solid oxide fuel cell based on chemically stable thin films of Y-doped BaZrO3 proton conducting electrolyte"; *Energy & Environmental Science*; vol 3; pg 618–621.

Farrugia M. (2005), Thermodynamics I, Lecture notes.

FCH-JU Fuel Cells and Hydrogen – Joint Undertaking: http://www.fch.europa.eu/ (accessed April 2018).

Frost H. J. and Ashby M. F. (1982), *Deformation-Mechanism Maps; The Plasticity and Creep of Metals and Ceramics*, Pergamon Press.

Fujinaga K., Aikawa S., Kuroishi M., Saito T., Abe T., Suzuki K. and Takeuchi H. (2004), "Cylindrical Solid Oxide Fuel Cell (SOFC) Generator"; International Patent JP2004119300 (A); 15th April 2004.

Funahashi Y., Suzuki T., Fujishiro Y., Shimamori T. and Awano M. (2007), "Optimization of Configuration for Cube-Shaped SOFC Bundles"; *ECS Transactions*; vol 7; issue 1; pg 643–649.

Funahashi Y., Shimamori T., Suzuki T., Fujishiro Y. and Awano M. (2008), "Microstructure Control of Cathode Matrices for the Cube-Type SOFC Bundles"; *ECS Transactions*; vol 28; issue 4; pg 195–202.

Funahashi Y., Shimamori T., Suzuki T., Fujishiro Y., and Awano M. (2009). "New Fabrication Technique for Series-Connected Stack With Micro Tubular SOFCs"; *Fuel Cells*; vol 9; issue 5; pg 711–716.

Gadow R., Killinger A., Candel Ruiz A., Weckmann H., Öllinger A. and Patz O. (Feb 5th 2018), "Investigation on HVOF-Technique for Fabrication of SOFCs (Solid Oxide Fuel Cells) Electrolyte Layers"; *researchGate.net;* https://www.researchgate.net/publication/268275794_Investigation_on_HVOF-Technique_for_Fabrication_of_SOFCs_Solid_Oxide_Fuel_Cells_Electrolyte_Layers.

Galwey A. K. (2012), "Theory of solid-state thermal decomposition reactions"; *Journal of Thermal Analysis and Calorimetry*; vol 109; pg 1625–1635.

Ghirlando R. (2004), Engineering Science – Thermodynamics, Lecture notes.

Gibbs Free Energy article: http://en.wikipedia.org/wiki/Gibbs_free_energy (accessed 13th October 2014).

Gillett J. E., Dederer J. T., Zafred P. R. and Collie J. C. (April 21, 1998), "Solid Oxide Fuel Cell Generator With Removable Modular Fuel Cell Stack Configurations"; *United States Patent Office*; Assignee Westinghouse Electric Corporation, Patent Number 5,741,605.

Gillett J. E., Zafred P. R., Riggle M. W. and Litzinger K. P. (June 11, 2013), "Generator module architecture for a large solid oxide fuel cell power plant"; *United States Patent Office*; Assignee Siemens Energy Inc., Patent Number 8,460,838.

Glenn Research Center: https://www.nasa.gov/centers/glenn/technology/fuel_cells.html (accessed 17th August 2017).

Gorin E. and Recht H. L. (1963), "High Temperature Fuel Cells". In Mitchell W. Jr. (Ed.) *Fuel Cells* (pg. 193–252). From Baddour R. F. (Ed.) *Chemical Technology: A Series of* Monographs, Volume 1. Academic Press, New York and London.

Grew K. N., Joshi A. S., Peracchio A. A. and Chiu W. K. S. (2010), "Pore-scale investigation of mass transport and electrochemistry in a solid oxide fuel cell anode"; *Journal of Power Sources*; vol 195; pg 2331–2345.

Grove W. R. (1839), "On Voltaic Series and the Combination of Gases by Platinum"; *Phil. Mag. (Ser. 3)*; vol 14.

Hancock P. (1976), "Influence of vacancy production on the mechanical properties of nickel and nickel-chromium alloys" in Smallman and Harris (Ed.) *Vacancies 76*, The Metal Society, London (pg. 215–223).

Hart D. and Bauen A. (2003), "Fuel Cell Fuel Cell Cycles". In Hoogers G. (Ed.) *Fuel Cell Technology Handbook*, CRC Press, New York, USA (pg. 12-1–12-23).

Hass D. D., Slifka A. J. and Wadley H. N. G. (2001), "Low Thermal Conductivity Vapor Deposited Zirconia Microstructures"; *Acta Materialia*; vol 49; pg 973–983.

Hatada S. (2007), "Solid Oxide Fuel Cell Stack And Its Operation Method"; International Patent JP2004119300 (A); 9th August 2007.

Hauch A., Ebbesen S. D., Jensen S. H. and Morgensen M. (2008), "Solid Oxide Electrolysis Cells: Microstructure and Degradation of the Ni/Yttria-Stabilized Zirconia Electrode"; *Journal of the Electrochemical Society*; vol 155; issue 11; pg B1184–B1193.

Haugsrud R. (2001), "High-Temperature Oxidation of Ni-20 wt.% Cu from 700 to 1100 °C"; *Oxidation of Metals*; vol 55; issue 5/6; pg 571–583.

Haugsrud R. (2003), "On the high-temperature oxidation of nickel"; *Corrosion Science*; vol 45, issue 1; pg 211–235.

Haydn M., Ortner K., Franco T., Uhlenbruck S., Menzler N. H., Stöver D., Bräuer G., Venskutonis A., Sigl L. S., Buchkremer H.-P. and Vaßen R. (2014), "Multi-layer thin-film electrolytes for metal supported solid oxide fuel cells"; *Journal of Power Sources*; vol 256; pg 52–60.

Heath C. E. and Sweeney W. J. (1963), "Kinetics and Catalysis in Fuel Cells". In Mitchell W. Jr. (Ed.) *Fuel Cells* (pg. 65–128). From Baddour R. F. (Ed.) *Chemical Technology: A Series of* Monographs, Volume 1. Academic Press, New York and London.

Hexis Galileo 1000N: http://www.hexis.com/de/galileo-1000-n (author unknown, accessed 21st October 2014).

Holmes R. A., Zafred P. R., Gillett J. E., Draper R., Lau L. K., Basel R. A., Cather R. L., Doshi V. B. and Toms J. M. (December 2, 2003), "Low-Cost Atmospheric SOFC Power Generation System"; *United States Patent Office*; Assignee Westinghouse Electric Corporation, Patent Number 6,656,623.

Honda FCX Clarity official website: http://automobiles.honda.com/fcx-clarity/ (author unknown, accessed 17th October 2014).

Hoogers G. (2003a), "Introduction". In Hoogers G. (Ed.) *Fuel Cell Technology Handbook*, CRC Press, New York, USA (pg. 1-1–1-5).

Hoogers G. (2003b), "The Fueling Problem: Fuel Cell Systems". In Hoogers G. (Ed.) *Fuel Cell Technology Handbook*, CRC Press, New York, USA (pg. 5-1–5-23).

Hoogers G. (2003c), "Stationary Power Generation". In Hoogers G. (Ed.) *Fuel Cell Technology Handbook*, CRC Press, New York, USA (pg. 8-1–8-30).

Hoogers G. (2003d), “Outlook: The Next Five Years”. In Hoogers G. (Ed.) *Fuel Cell Technology Handbook*, CRC Press, New York, USA (pg. 13-1–13-3).

Huang K. and Ruka R. J. (May 8, 2012), "Tubular solid oxide fuel cells with porous metal supports and ceramic interconnections"; *United States Patent Office*; Assignee Siemens Energy Inc., Patent Number 8,173,322.

Huntz A. M., Andrieux M. and Molins R. (2006), "Relation between the oxidation mechanism of nickel, the microstructure and mechanical resistance of NiO films and the nickel purity I. Oxidation mechanism and microstructure of NiO films"; *Material Science and Engineering A*; vol 415; pg 21–32.

Hussain M. M., Li X. and Dincer I. (2009), "A general electrolyte-electrode-assembly mode for the performance characteristics of planar anode-supported solid oxide fuel cells"; *Journal of Power Sources*; vol 189; pg 916–928.

Hwang S.-H., Choi W. M. and Lim S. K. (2016), "Hydrogen storage characteristics of carbon fibers derived from rice straw and paper mulberry"; *Materials Letters*; vol 167; pg 18-21.

Ishihara T., Sammes N. M. and Yamamoto O. (2003), “Electrolytes”. In Singhal S. C. and Kendall K. (Ed.) *High Temperature Solid Oxide Fuel Cells: Fundamentals, Design and Applications*, Elsevier Advanced Technology, Oxford, UK (pg. 83–117).

Ismail A. F. and Shilton S. J. (c.1997), "The Practical use of Resistance Modeling to Interpret the Gas Separation Properties of Hollow Fiber Membranes"; *Jurnal Teknologi*; vol 32; issue F; pg 93–101.

Ivers-Tiffée E. and Virkar A. V. (2003), “Electrode Polarisations”. In Singhal S. C. and Kendall K. (Ed.) *High Temperature Solid Oxide Fuel Cells: Fundamentals, Design and Applications*, Elsevier Advanced Technology, Oxford, UK (pg. 229–260).

James A. S., Young S. J. and Matthews A. (1995), "An investigation into the use of a simple model for thickness uniformity on horizontal surfaces to describe thickness variations on vertical substrates"; *Surface and Coatings Technology*; vol 74–75; pg 306-311. [Note this paper is the culmination of a series of four on the subject of coating thickness variation and was used under the assumption that the final paper contained the most developed model.]

Jou S. and Wu T.-H. (2008), "Thin porous Ni-YSZ films as anodes for a solid oxide fuel cells"; *Journal of Physics and Chemistry of Solids*; vol 69; pg 2804–2812.

Kato T., Kashihara T., Nozaki K., Endo E. and Iimura Y. (2008), "Investigation of Initial SOFC Market in Japan"; *ECS Transactions*; vol 12; issue 1; pg 755–762.

Kendall K., Minh N. Q. and Singhal S. C. (2003), "Cell and Stack Designs". In Singhal S. C. and Kendall K. (Ed.) *High Temperature Solid Oxide Fuel Cells: Fundamentals, Design and Applications*, Elsevier Advanced Technology, Oxford, UK (pg. 197–228).

Khaleel M. A., Lin Z., Singh P., Surdoval W. and Collin D. (2004), "A Finite Element Analysis Modeling Tool for Solid Oxide Fuel Cell Development: Coupled Electrochemistry, Thermal and Flow Analysis in MARC®"; *Journal of Power Sources*; vol 130; issue 1–2; pg 136–148.

Khaleel M. A. and Selman J. R. (2003), "Cell, Stack and System Modelling". In Singhal S. C. and Kendall K. (Ed.) *High Temperature Solid Oxide Fuel Cells: Fundamentals, Design and Applications*, Elsevier Advanced Technology, Oxford, UK (pg. 291–331).

Khalid F. A., Hussain N. and Shahid K. A. (1999), "Microstructure and morphology of high temperature oxidation in superalloys"; *Material Science and Engineering A: Structural Materials*; vol 265, issue 1–2; pg 87–94.

Kjeang E., Djilali N. and Sinton D. (2009), "Advances in Microfluidic Fuel Cells". In Zhao T. S. (Ed.) *Micro Fuel Cells*, Elsevier Academic Press (pg. 104–108).

Kuhn M. and Napporn T. W. (2010), "Single-Chamber Solid Oxide Fuel Cell Technology – From Its Origins to Today's State of the Art"; *Energies*; vol 3; pg 57–134.

Kulikovsky A., Oetjen H.-F. and Wannek Ch. (2010), "A Simple and Accurate Method for High-Temperature PEM Fuel Cell Characterisation"; *Fuel Cells*; vol 3; pg 363–368.

Kumpulainen H., Peltonen T., Koponen U., Bergelin M., Valkiainen M. and Wasberg M. (2002), "In situ voltammetric characterization of PEM fuel cell catalyst layers"; *Research Notes T2137*; VTT Tiedotteita (URL: http://www.inf.vtt.fi/pdf/).

Larminie J. and Dicks A. (2003), *Fuel Cell Systems Explained 2nd Edition*, Wiley.

Lee B.-T., Song H.-Y., Kim J.-H., and Rahman A. H. M. E. (2008), "Method of Manufacturing Micro-Channel Tubular Solid Oxide Fuel Cell Using Multi-Pass Extrusion Process"; International Patent WO2008093995 (A1); 7th August 2008.

Li H., Czerwinski F., Zhilyaev A. and Szpunar J. A. (1997), "Computer Modelling the Diffusion of Ni in NiO at High Temperatures"; *Corrosion Science*; vol 39; issue 7; pg 1211–1219.

Liu Y.-X., Wang S.-F., Hsu Y.F. and Jasinski P. (2017), "Characteristics of $La_{0.8}Sr_{0.2}Gd_{0.9}Mg_{0.2}O_{3-\delta}$–supported micro-tubular solid oxide fuel cells with bi-layer and tri-layer electrolytes"; *Journal of the Ceramic Society of Japan*; vol 125; issue 4; pg 236-241.

L'vov B. and Galwey A. (2012), "The mechanism and kinetics of NiO reduction by hydrogen"; *Journal of Thermal Analysis and Calorimetry*; vol 110; pg 601–610.

Macdonald J. R. (2005), "Data Analysis". In Barsoukov E. and Macdonald J. R. (Ed.) *Impedance Spectroscopy Theory, Experiment, and Applications*, Wiley, New Jersey, USA (pg. 188–204).

Macdonald J. R. and Johnson W. B. (2005), "Fundamentals of Impedance Spectroscopy". In Barsoukov E. and Macdonald J. R. (Ed.) *Impedance Spectroscopy Theory, Experiment, and Applications*, Wiley, New Jersey, USA (pg. 1–26).

Marino K. A., Hinnemann B. and Carter E. A. (2011), "Atomic-scale insight and design principles for turbine engine thermal barrier coatings from theory"; *Proceedings of the National Academy of Sciences of the USA*; vol 108; issue 14; pg 5480–5487.

Matsumoto M., Wada K., Yamaguchi N., Kato T. and Matsubara H. (2008), "Effects of substrate rotation speed during deposition on the thermal cycle life of thermal barrier coatings fabricated by electron beam physical vapor deposition"; *Surface Coatings and Technology*; vol 202; pg 3507–3512.

Maus H., Glanz U., Satet R., Oehler G., Schwegler L., Hagemann B., Bluthard A. and Hirth E. (November 5, 2013), "Method for production of a solid oxide fuel cell (SOFC)"; *United States Patent Office*; Assignee Robert Bosch GmbH, Patent Number 8,574,791.

McCarty D. "Fuel-Cell producer ClearEdge Power Files for Bankruptcy"; Bloomberg News URL: http://www.bloomberg.com/news/2014-05-02/fuel-cell-producer-clearedge-power-files-for-bankruptcy.html (accessed 21st October 2014).

McEvoy A. (2003), "Anodes". In Singhal S. C. and Kendall K. (Ed.) *High Temperature Solid Oxide Fuel Cells: Fundamentals, Design and Applications*, Elsevier Advanced Technology, Oxford, UK (pg. 149–171).

McKubre M. C. H. and Macdonald D. D. (2005), “Impedance Measurement Techniques”. In Barsoukov E. and Macdonald J. R. (Ed.) *Impedance Spectroscopy Theory, Experiment, and Applications*, Wiley, New Jersey, USA (pg. 129–168).

Meng B., Sun Y., He X. D. and Peng J. H. (2009), "Fabrication and characterisation of Ni-YSZ anode functional coatings by electron beam physical vapor deposition"; *Thin Solid Films*; doi:10.1016/j.tsf.2009.03.098.

Meng B., Xiaodong H., Sun Y. and Mingwei L. (2008), "Preparation of YSZ electrolyte coatings for SOFC by electron beam physical vapor deposition combined with a sol infiltration treatment"; *Materials Science and Engineering B*; doi:10.1016/j.mseb.2008.03.002.

Menzler N. H., Han F., van Gestel T., Schafbauer W., Schulze-Küppers F., Baumann S., Uhlenbruck S., Meulenberg W. A., Blum L. and Buchkremer H. P. (2013), "Application of Thin-Film Manufacturing Technologies to Solid Oxide Fuel Cells and Gas Separation Membranes"; *International Journal of Applied Ceramic Technology*; vol 10; issue 3; pg 421–427.

Mert S. O., Ozcelik Z. and Dincer I. (2015), "Comparative assessment and optmization of fuel cells"; *International Journal of Hydrogen Energy*; vol 40; issue 24; pg 7835–7845.

Milewski J. and Miller A. (2006), "Influences of The Type and Thickness of Electrolyte on Solid Oxide Fuel Cell Hybrid System Performance"; *Journal of Fuel Cell Science and Technology*; vol 3; issue 4; pg 396–402.

Mitchell W. Jr. (1963), “Introduction”. In Mitchell W. Jr. (Ed.) *Fuel Cells* (pg. 1-16). From Baddour R. F. (Ed.) *Chemical Technology: A Series of* Monographs, Volume 1. Academic Press, New York and London.

Mogensen M. and Hendriksen P. V. (2003), “Testing of Electrodes, Cells and Short Stacks”. In Singhal S. C. and Kendall K. (Ed.) *High Temperature Solid Oxide Fuel Cells: Fundamentals, Design and Applications*, Elsevier Advanced Technology, Oxford, UK (pg. 261–289).

Monzón H., Laguna-Bercero M. A., Larrea A., Arias B. I., Várez A. and Levenfeld B. (2014), "Design of industrially scalable microtubular solid oxide fuel cells based on an extruded support"; *International Journal of Hydrogen Energy*; vol 39; issue 10; pg 5470–5476.

Moulson A. J. and Herbert J. M. (2008), *Electroceramics*, Second Edition, Wiley, Sussex, UK (pg. 173–196).

Neirinck B, Fransaer J., Van der Beist O. and Vleugels J. (2008), "A novel route to produce porous ceramics"; *Journal of the European Ceramic Society*; pg 63–79.

NELLHI: http://www.nellhi.eu/ (accessed April 2018).

Opila E. J. and Jacobson N. S. (2011), "Stability of Materials in High Temperature Water Vapor: SOFC Applications"; *Advances in Solid Oxide Fuel Cells VI*; vol 29; pg 833–836.

Opitz A. K., Lutz A., Kubicek M., kubel F., hutter H. and Fleig J. (2011), "Investigation of the oxygen exchange mechanism on Pt/yttria stabilized zirconia at intermediate temperatures: Surface path versus bulk path"; *Electrochimica Acta*; vol 56; issue 27; pg 9727–9740.

Ormerod R. M. (2003), "Fuels and Fuel Processing". In Singhal S. C. and Kendall K. (Ed.) *High Temperature Solid Oxide Fuel Cells: Fundamentals, Design and Applications*, Elsevier Advanced Technology, Oxford, UK (pg. 333–361).

Othman M. H. D., Wu Z., Droushiotis N., Doraswami U., Kelsall G. and Li K. (2010), "Single-step fabrication and characterisations of electrolyte/anode dual-layer hollow fibres for micro-tubular solid oxide fuel cells"; *Journal of Membrane Science*; vol 3; doi:10.1016/j.memsci.2010.01.050.

Panteix P. J., Baco-Charles V., Tailhades Ph., Rieu M., Lenormand P., Ansart F. and Fontaine M. L. (2009), "Elaboration of metallic compacts supports of SOFC"; *Solid State Sciences*; vol 11; issue 2; pg 444–450.

Piccardo P., Amendola R., Fontana S., Chevalier S., Caboches G. and Gannon P. (2009), "Interconnect materials for next-generation solid oxide fuel cells"; *Journal of Applied Electrochemistry*; vol 30; issue 4; pg 545–551.

Pichonat T. (2009), "MEMS-Based Micro Fuel Cells as Promising Power Sources for Portable Electronics". In Zhao T. S. (Ed.) *Micro Fuel Cells*, Elsevier Academic Press (pg. 51–97).

Pieraggi B. and Rapp R. A. (1988), "Stress generation and vacancy annihilation during scale growth limited by cation-vacancy diffusion"; *Acta Metallurgica*; vol 36; issue 5; pg 1281–1289.

Plymouthsciencepark.com Laboratory space UK – rental 332 GBP/m^2: http://plymouthsciencepark.com/rent-office-space/laboratory-space/ (accessed May 2018).

Pomfret M. B., Eigenbrodt B. C. and Walker R.A. (2008), "Interfacial Resistivity of Yttria Stabilized Zirconia in Operating Solid Oxide Fuel Cells"; *ECS Transactions*; vol 11; issue 27; pg 111–120.

Rabat H. and Brault P. (2008), "Plasma Sputtering Deposition of PEMFC Porous Carbon Platinum Electrodes"; *Fuel Cells*; vol 8, issue 25; pg 81–86.

Raistrick I. D., Franceschetti D. R. and Macdonald J. R. (2005), "Theory". In Barsoukov E. and Macdonald J. R. (Ed.) *Impedance Spectroscopy Theory, Experiment, and Applications*, Wiley, New Jersey, USA (pg. 1–26).

de Ridder M., van Welzenis R.G., Brongersma H. H. and Kreissig U. (2003), "Oxygen exchange and diffusion in the near surface of pure and modified yttria-stabilized zirconia"; *Solid State Ionics*; vol 158; pg 67–77.

Rosa C. J. (1982), "The High Temperature Oxidation of Nickel"; *Corrosion Science*; vol 22; issue 12; pg 1081–1088.

Ruiz-Morales J. C., Pena-MartĺnezJ., Canales-Vázquez J., Savaniu C. and Nunez P. (2009), "Cost-Effective Microstructural Engineering of Solid Oxide Fuel Cell Components for Planar and Tubular Designs"; *Journal of the American Ceramic Society*; vol 92; issue 1; pg 276–279.

Sammes N., Murray T., Brown M. and Ziegler W. (2011), "Electrode-Supported Solid State Electrochemical Cell"; Canadian Intellectual Property Office CA 2447855; 12th April 2011.

Sammes N., Pusz J., Smirnova A., Mohammadi A., Serincan F., Ziaoyu Z., Awano M., Suzuki T., Yamaguchi T., Fujishiro Y. and Funahashi Y. (2009), "The Properties and Performance of Micro-Tubular (Less then 1 mm OD) Anode Supported Solid Oxide Fuel Cells"; *Ceramic Engineering and Science Pro*; pg 29–39.

Sarkar P. R., Rho H., Johanson L. and Yamarte L. (2004), "Metal-supported Tubular Fuel Cell"; US Patent WO2004/012287; 5th February 2004.

Schœnbein C. F. (1839), "On the Voltaic Polarisation of certain Solid and Fluid Substances"; *Phil. Mag. (Ser. 3)*; vol 14.

Scott M., Bell S., Bannister M., Cleaver K., Cridland D., Dadachanji F., Farley R., Greaves P., Harris R., Pragnell R., Wilkin M. and Wortley P. (1996), *A Guide to the Measurement of Humidity*, Published by the National Physical Laboratory (UK) and the Institute of Measurement & Control.

Schütze M. (1997), *Protective Oxide Scales and their Breakdown*, Wiley.

Shaikh S. P. S., Muchtar A. and Somalu M. R. (2015), "A review on the selection of anode materials for solid-oxide fuel cells"; *Renewable and Sustainable Energy Reviews*; vol 51; pg 1–8.

Siemens-Westinghouse Research Archives: http://www.nfcrc.uci.edu/2/ACTIVITIES/RESEARCH_STUDIES/RESEARCH_ARCHIVES/westinghouse.aspx (accessed 12th January 2010).

Singhal S. C. and Kendall K. (2003), "Introduction to SOFCs". In Singhal S. C. and Kendall K. (Ed.) *High Temperature Solid Oxide Fuel Cells: Fundamentals, Design and Applications*, Elsevier Advanced Technology, Oxford, UK (pg. 1–22).

Soysal D., Arnold J., Szabo P., Henne R. and Ansar S. A. (2013), "Thermal Plasma Spraying Applied in Solid Oxide Fuel Cells"; *Journal of Thermal Spray Technology*; vol 22; issue 5; pg 588-598.

Staffell I. and Green R. (2013), "Cost of domestic fuel cell micro-CHP systems"; *International Journal of Hydrogen Energy*; vol 38; issue 2; pg 1088-1102.

Statistica.com a Office space UK – rental 350 GBP/m^2/year in city: https://www.statista.com/statistics/323013/uk-real-estate-prime-office-rent-prices-in-selected-cities/ (accessed May 2018).

Statistica.com b Industrial space UK – rental 88 GBP/m^2 in prime industrial estate: https://www.statista.com/statistics/323030/prime-industrial-rent-costs-in-the-united-kingdom-uk/ (accessed May 2018).

Suzuki T., Funahashi Y., Hasan Z., Yamaguchi T., Fujishiro Y. and Awano M. (2008a), "Fabrication of needle-type micro SOFCs for micro power devices"; *Electrochemistry Communications*; vol 10; pg 1563–1566.

Suzuki T., Funahashi Y., Yamaguchi T., Fujishiro Y. and Awano M. (2008b), "New Stack Design of Micro-tubular SOFCs for Portable Power Sources"; *Fuel Cells*; vol 8; issue 6; pg 381–384.

Suzuki T., Funahashi Y., Yamaguchi T., Fujishiro Y. and Awano M. (2008c), "Effect of Anode Microstructure on the Performance of Micro Tubular SOFCs"; *Solid State Ionics*; vol 180; pg 546–549.

Suzuki T., Funahashi Y., Yamaguchi T., Fujishiro Y. and Awano M. (2009a), "Development of Fabrication/Integration for Micro Tubular SOFCs". In Zhao T. S. (Ed.) *Micro Fuel Cells*, Elsevier Academic Press (pg. 141–177).

Suzuki T., Hasan Z., Funahashi Y., Yamaguchi T., Fujishiro Y. and Awano M. (2009b), "Impact of Anode Microstructure on Solid Oxide Fuel Cells"; *Science*; vol 325; pg 852–855.

Tan X., Liu Y. and Li K. (2005), "Mixed Conducting Ceramic Hollow-Fiber Membranes for Air Separation"; *American Institute of Chemical Engineers*; vol 51; issue 7; pg 1991–2000.

Thome T., Pham Van L. and Cousty J. (2004), "Evolution of yttria-stabilized zirconia (100) surface morphology"; *Journal of the European Ceramic Society*; vol 24; pg 841–846.

Thompsett D. (2003), "Catalysts for the Proton Exchange Membrane Fuel Cell". In Hoogers G. (Ed.) *Fuel Cell Technology Handbook*, CRC Press, New York, USA (pg. 6-1–6-23).

Thomson C. B. and Randle V. (1997), "The effects of strain annealing on grain boundaries and secure triple junctions in nickel 200"; *Journal of Materials Science*; vol 32; pg 1909–1914.

Tsipis E. V. and Kharton V. V. (2008a), "Electrode materials and reaction mechanisms in solid oxide fuel cells: a brief review. I. Performance-determining factors"; *Journal of Solid State Electrochemistry*; vol 12; issue 1; pg 1039–1060.

Tsipis E. V. and Kharton V. V. (2008b), "Electrode materials and reaction mechanisms in solid oxide fuel cells: a brief review. II. Electrochemical behavior vs. materials science aspects"; *Journal of Solid State Electrochemistry*; vol 12; issue 1; pg 1367–1450.

Tsunoda T. (2005), "Fuel Cell"; International Patent EP1532704 (A2); 25th May 2005.

Tsunoda T. and Izumi M. (2009), "Fuel Cell and Fuel Cell Stack"; International Patent EP2026394 (A2); 18th February 2009.

van Gerwen R. J. F. (2003), “Systems and Applications”. In Singhal S.C. and Kendall K. (Ed.) *High Temperature Solid Oxide Fuel Cells: Fundamentals, Design and Applications*, Elsevier Advanced Technology, Oxford, UK (pg. 363–392).

Venables John A. (2000), *Introduction to Surface and Thin Film Processes*, Wiley.

Wagner N. (2005), “Fuel Cells”. In Barsoukov E. and Macdonald J. R. (Ed.) *Impedance Spectroscopy Theory, Experiment, and Applications*, Wiley, New Jersey, USA (pg. 497–537).

Wallach E.R. and Hill A. (1987), “Modelling of Diffusion Bonding”. In Pearce R. (Ed.) *Diffusion Bonding: Proceedings of an International Conference held at Cranfield Institute of Technology 7-8 July 1987*, Printed by Paul Ellerington, Keysoe, UK (pg. 9–16).

Wei W.-C. J. (2008), "Development of Micro-Solid Oxide Fuel Cells (Micro- SOFCs)"; *Advanced Materials Research*; vol 51; pg 111–115.

Winkler W. (2003), “Thermodynamics”. In Singhal S. C. and Kendall K. (Ed.) *High Temperature Solid Oxide Fuel Cells: Fundamentals, Design and Applications*, Elsevier Advanced Technology, Oxford, UK (pg. 53–82).

Wynveen R. A. (1963), “Research Techniques for Fuel Cell Application”. In Mitchell W. Jr. (Ed.) *Fuel Cells* (pg. 193–252). From Baddour R.F. (Ed.) *Chemical Technology: A Series of* Monographs, Volume 1. Academic Press, New York and London.

Xing J.J., Takeguchi M., Tanaka M. and Nakayama Y. (2012), "Reduction of a NiO Thin Film deposited by PLD on a single crystal YSZ (111) substrate"; *Journal of Material Science*; vol 47; issue 13; pg 5254–5262.

Yakabe H., Hishinuma M., Uratani M., Matsuzaki Y. and Yasuda I. (2000), "Evaluation and modeling of performance of anode-supported solid oxide fuel cell"; *Journal of Power Sources*; vol 86; pg 423–431.

Yang C., Li W., Zhang S., Bi L., Peng R., Chen C. and Liu W. (2009), "Fabrication and characterization of an anode-supported hollow fiber SOFC"; *Journal of Power Sources*; vol 187; issue 1; pg 90–92.

Yashima M., Kakihana M. and Yoshimura M. (1996), "Metastable-stable phase diagrams in the zirconia-containing systems utilized in solid-oxide fuel cell application"; *Solid State Ionics*; vol 86–88; pg 1131–1149.

Yokokawa H. and Horita T. (2003), “Cathodes”. In Singhal S.C. and Kendall K. (Ed.) *High Temperature Solid Oxide Fuel Cells: Fundamentals, Design and Applications*, Elsevier Advanced Technology, Oxford, UK (pg. 119–147).

Yoo S. J., Cho Y.-H., Park H.-S., Lee J. K. and Sung Y.-E. (2008), "High utilisation of Pt nanocatalysts fabricated using a high=pressure sputtering technique"; *Journal of Power Sources*; vol 178; pg 547–553.

Young D. J. (2016), *High Temperature Oxidation and Corrosion of Metals, Second Edition*, Published by Elsevier Science.

Zafred P. R. and Gillett J. E. (April 24, 2012), "Fuel cell integral bundle assembly including ceramic open end seal and vertical and horizontal thermal expansion control"; *United States Patent Office*; Assignee Siemens Energy Inc., Patent Number 8,163,433.

Zaitsev A. I. and Zaitseva N. E. (2002), "Pressure of the Saturated Vapor of Nickel at High Temperatures"; *High Temperature*; vol 70; issue 2; pg 225–230.

Zhao H., Yu F., Bennett T. D. and Wadley H. N.G. (2006), "Morphology and thermal conductivity of yttria-stabilized zirconia coatings"; *Acta Materialia*; vol 54; pg 5195–5207.

Zhou C. H., Ma H. T. and Wang L. (2008), "Effect of Mechanical Loading on Oxidation Kinetics and Oxide-Scale Failure of Pure Ni"; *Oxidation of Metals*; vol 70, issue 5–6; pg 287–294.

CRANFIELD UNIVERSITY

ALASTAIR CAMILLERI B. Eng. (Hons.) MSc. (Cranfield)

DEVELOPMENT OF MICROTUBULAR SOLID OXIDE FUEL CELLS
DESIGN, FABRICATION AND PERFORMANCE

Appendices

SCHOOL OF AEROSPACE TRANSPORT AND MANUFACTURING (SATM)

PhD Thesis
Nov 2009 – Aug 2017

Supervisors: Prof. John Nicholls

Submission: 25th August 2017

Appendices

Appendix A: Activity Coefficient Calculations

Calculation of the activity coefficient is based on the equations and data given in Speight, J. G. (2005), *Lange's Handbook of Chemistry* (16th Edition), McGraw-Hill. Online version available at: http://knovel.com/web/portal/browse/display?_EXT_KNOVEL_DISPLAY_bookid=1347&VerticalID=0 Accessed 02/06/2009.

Generally the activity coefficient is defined as the ratio of the chemical activity of any substance to its molar concentration. Although it is not possible to measure an individual ionic activity coefficient, f_i, of a particular species i, it may be estimated using the Debye-Hückel equation:

$$-\log f_i = \frac{0.5115 z_i^2 \sqrt{I_i}}{I_i + 0.3291 a \sqrt{I_i}}$$

Where: f_i= coefficient of activity of species i $(no\ units)$
z_i = ionic charge of species i $(no\ units)$
I_i = ionic strength of species i $(M = mol/litre)$
a = ionic radius (Å)

The ionic strength, I_i, is given by the following relation:

$$I_i = \frac{1}{2} \sum c_i z_i^2$$

Where c_i is the molarity of species $(M = mol/litre)$.

At moderate ionic strength it is usual to introduce the correction factor bI_i as shown below. The factor b depends on the solution and temperature. For instance it is 0.2 for water at 25 ℃.

$$-\log f_i = \frac{0.5115 z_i^2 \sqrt{I_i}}{I_i + 0.3291 a \sqrt{I_i}} - bI_i$$

With regards the activity of water, it is usually quoted as unity [Water Activity website: http://www.wateractivity.org/theory.html Accessed 02/06/2009.

Appendix B: Characterisation of As-delivered Nickel (Ni200) Tubes

In all cases where nickel tubes were used these were 99.5% pure nickel (Ni200) nominal OD 5.9 mm, nominal wall thickness 125 μm from Goodfellow Cambridge Ltd., unless specified otherwise. Below is the information supplied by Goodfellow regarding the nickel tube:

Outside Diameter:	5.9 mm
Wall Thickness:	0.125 mm
Purity:	99.5%
Inside Diameter:	5.65 mm
Temper:	Hard
Typical Analysis:	Al 100, Co 600, Cr 100, Cu 100, Fe 400, Mg 800, Mn 200, Si 100, Ti 100, C 100, S 25 (all in ppm)
Tolerances	
Outside Diameter:	±5%
Wall Thickness:	±10%
Length:	<100 mm ±1 mm ≥100 mm +5%/-1%

The tubes are manufactured by cold drawing through a die on a mandrel. They are delivered in this strained, cold-worked state giving a hard temper [telephone discussion with supplier].

The length of tubes ordered depended on what was most cost effective. Typically this meant 200 mm long. The tubes were then cut into shorter sections as needed using a precision saw, and finished using 1200 grit SiC paper to smooth the cut ends. As noted in the various experimental sections before any experiment the tubes were cleaned ultrasonically in an acetone bath.

During the process of designing the jig for EB-PVD YSZ deposition and the test rig it was noted that there were frequent difficulties in getting parts to mate with acceptable tolerances. As a result, I thought it best to determine some basic characteristics of the tube like roundness, standard deviation of radii (inner and outer) and so on. The two obvious alternatives to achieve this are outlined here. The first is manually measuring the wall thickness, inner diameter (the bore) and outer diameter using optical or mechanical methods (e.g. a Vernier caliper). To obtain roundness this would have to be repeated at least twice for each sample at 90° to each other, and ideally four times (at 45° to each other). In addition this would need to be repeated for several samples for any sort of statistical analysis. The second alternative is using an image analysis (IA) system of some kind to collect data points then calculate the relevant diameters. Such a

system was available on campus and is used regularly to measure the degree of corrosion on samples where rather than two surfaces (inner and outer) as is the case for the tubes, the interface of substrate and corroded surface and the thickness of corrosion product are measured.

After some discussion with Professor John Nicholls, Peter West and Joy Sumner (the last two having considerable experience with the IA system) it seemed that image analysis was the most suitable approach. The reasons for selecting this technique are that it is faster and less prone to error than manually taking readings with a Vernier calliper, and also that data is automatically in digital form (as a .txt file) facilitating calculations and further manipulation.

In addition to data collected to assess roundness, it was decided to ascertain variation in diameter along the axis of the tubes. To that end the samples for IA were prepared as follows: Three as-delivered 200 mm long Ni200 tubes were selected at random. For each of these a section 10 mm long was cut from each end and the middle. Each trio of samples (from a single tube) were mounted together in resin (Struers Epofix resin and hardener – room temperature cure), and polished to 2400 grit and finally finished with colloidal silica paste. An autopolisher (Buehler Motopol automatic grinder/polisher) was used to ensure flatness of the mounted samples. The procedure resulted in samples well suited to image analysis having excellent contrast between the mounting material and the samples. Measurements were taken at twenty positions around the circumference of each tube, equally spread 18° apart based on the centre of the section determined by the IA system. Co-ordinates for the inner and outer surface were taken for each of these 20 locations. All the data (essentially co-ordinates for a multitude of points) were analysed using a spreadsheet. The results collated below are from these spreadsheets (one per sample).

The information shown includes: a graph showing all the data points as well as two solid circles representing what the ideal inner and outer radii would look like, this gives a facile visual assessment of how far the points are from their ideal position (i.e. on a perfect circle of the nominal dimensions); a plot of the wall thickness variation; the mean inner and outer radii and their standard deviations (computed from the variance of each data point). For reference the nominal inner radius is 2825 µm and the nominal outer radius is 2950 µm.

Appendix C: Complete Oxidation Results Tables

Tier 1

Sample	**t (h)** ±0.01 h	**m_{Ni} (mg)** ±1 mg	**m_{Ni+NiO} (mg)** ±1 mg	**m_{gain} (mg)** ±2 mg	**Mass fraction oxidised** ±0.001	**z (µm)** ±0.23 µm
Batch A						
OT-A.13/07/10-125.1100-A.01	0.017 (1 min)	467.4	469.4	2.0	0.789	1.54
OT-A.13/07/10-125.1100-A.02	0.033 (2 min)	475.3	480.6	5.3	0.795	4.07
OT-A.13/07/10-125.1100-A.03	0.083 (5 min)	479.6	487.2	7.6	0.798	5.83
OT-A.13/07/10-125.1100-A.04	0.167 (10 min)	474.1	485.3	11.2	0.804	8.60
OT-A.13/07/10-125.1100-A.05	0.333 (20 min)	464.8	480.2	15.4	0.812	11.82
OT-A.13/07/10-125.1100-A.06	1.000	467.9	494.6	26.7	0.831	20.50
OT-A.13/07/10-125.1100-A.07	2.000	490.7	529.9	39.2	0.849	30.09
OT-A.14/07/10-125.1100-A.08	5.000	543.5	583.6	40.1	0.844	30.78
OT-A.15/07/10-125.1100-A.09	9.000	530.8	583.8	53.0	0.864	40.69
OT-A.15/07/10-125.1100-A.10	16.000	537.4	618.4	81.0	0.904	62.18
OT-A.14/07/10-125.1100-A.11	20.000	477.0	571.2	94.2	0.941	72.32
OT-A.15/07/10-125.1100-A.12	42.000	561.7	686.5	124.8	0.960	95.81
Batch B						
OT-A.13/07/10-125.1100-B.01	0.017 (1 min)	478.9	481.8	2.9	0.791	2.23
OT-A.13/07/10-125.1100-B.02	0.033 (2 min)	475.4	480.9	5.5	0.795	4.22
OT-A.13/07/10-125.1100-B.03	0.083 (5 min)	468.6	477.0	8.4	0.800	6.45
OT-A.13/07/10-125.1100-B.04	0.167 (10 min)	508.4	520.4	12.0	0.804	9.21
OT-A.13/07/10-125.1100-B.05	0.333 (20 min)	464.8	480.2	15.4	0.812	11.82
OT-A.13/07/10-125.1100-B.06	1.000	486.9	514.6	27.7	0.830	21.27
OT-A.13/07/10-125.1100-B.07	2.000	487.4	526.1	38.7	0.848	29.71
OT-A.14/07/10-125.1100-B.08	5.000	536.2	583.1	46.9	0.855	36.00
OT-A.15/07/10-125.1100-B.09	9.000	536.0	591.2	55.2	0.867	42.38
OT-A.15/07/10-125.1100-B.10	16.000	541.2	616.2	75.0	0.895	57.58
OT-A.14/07/10-125.1100-B.11	20.000	464.2	559.0	94.8	0.946	72.78
OT-A.15/07/10-125.1100-B.12	42.000	544.7	673.5	128.8	0.972	98.88
Batch C						
OT-A.13/07/10-125.1100-C.01	0.017 (1 min)	492.1	496.1	4.0	0.792	3.07
OT-A.13/07/10-125.1100-C.02	0.033 (2 min)	468.6	473.2	4.6	0.793	3.53
OT-A.13/07/10-125.1100-C.03	0.083 (5 min)	479.1	486.5	7.4	0.798	5.68
OT-A.13/07/10-125.1100-C.04	0.167	476.8	487.7	10.9	0.804	8.37

Sample	t (h) ±0.01 h	m_{Ni} (mg) ±1 mg	m_{Ni+NiO} (mg) ±1 mg	m_{gain} (mg) ±2 mg	Mass fraction oxidised ±0.001	z (µm) ±0.23 µm
	(10 min)					
OT-A.13/07/10-125.1100-C.05	0.333 (20 min)	474.0	488.4	14.4	0.810	11.06
OT-A.13/07/10-125.1100-C.06	1.000	485.9	511.6	25.7	0.827	19.73
OT-A.13/07/10-125.1100-C.07	2.000	507.4	545.1	37.7	0.844	28.94
OT-A.14/07/10-125.1100-C.08	5.000	592.4	642.5	50.1	0.852	38.46
OT-A.15/07/10-125.1100-C.09	9.000	537.1	590.0	52.9	0.863	40.61
OT-A.15/07/10-125.1100-C.10	16.000	526.4	603.1	76.7	0.900	58.88
OT-A.14/07/10-125.1100-C.11	20.000	533.4	608.2	74.8	0.896	57.42
OT-A.15/07/10-125.1100-C.12	42.000	534.4	650.8	116.4	0.957	89.36
Batch D						
OT-A.13/07/10-125.1100-D.01	0.017 (1 min)	503.7	508.2	4.5	0.793	3.46
OT-A.13/07/10-125.1100-D.02	0.033 (2 min)	476.6	482.1	5.5	0.795	4.22
OT-A.13/07/10-125.1100-D.03	0.083 (5 min)	492.4	500.4	8..0	0.799	6.14
OT-A.13/07/10-125.1100-D.04	0.167 (10 min)	494.1	506.3	12.2	0.805	9.37
OT-A.13/07/10-125.1100-D.05	0.333 (20 min)	502.0	517.3	15.3	0.810	11.75
OT-A.13/07/10-125.1100-D.06	1.000	492.9	519.0	26.1	0.827	20.04
OT-A.13/07/10-125.1100-D.07	2.000	494.7	531.3	36.6	0.844	28.10
OT-A.14/07/10-125.1100-D.08	5.000	542.8	583.4	40.6	0.845	31.17
OT-A.15/07/10-125.1100-D.09	9.000	553.6	609.6	56.0	0.865	42.99
OT-A.15/07/10-125.1100-D.10	16.000	538.2	611.8	73.6	0.893	56.50
OT-A.14/07/10-125.1100-D.11	20.000	529.0	606.0	77.0	0.900	59.11
OT-A.15/07/10-125.1100-D.12	42.000	530.4	656.6	126.2	0.973	96.88
Batch E						
OT-A.15/07/10-125.1100-E.01	0.017 (1 min)	569.5	572.4	2.9	0.790	2.23
OT-A.15/07/10-125.1100-E.02	0.033 (2 min)	550.4	553.8	3.4	0.791	2.61
OT-A.15/07/10-125.1100-E.03	0.083 (5 min)	539.8	545.1	5.3	0.793	4.07
OT-A.15/07/10-125.1100-E.04	0.167 (10 min)	551.6	559.1	7.5	0.796	5.76
OT-A.15/07/10-125.1100-E.05	0.333 (20 min)	538.8	548.2	9.4	0.799	7.22
OT-A.15/07/10-125.1100-E.06	1.000	538.1	557.8	19.7	0.815	15.12
OT-A.15/07/10-125.1100-E.07	2.000	534.9	558.7	23.8	0.821	18.27
OT-A.14/07/10-125.1100-E.08	5.000	561.4	601.7	40.3	0.842	30.94
OT-A.15/07/10-125.1100-E.09	9.000	550.2	610.1	59.9	0.871	45.98
OT-A.15/07/10-125.1100-E.10	16.000	538.0	617.6	79.6	0.902	61.11
OT-A.14/07/10-125.1100-E.11	20.000	523.6	606.1	82.5	0.910	63.33
OT-A.15/07/10-125.1100-E.12	42.000	563.5	688.4	124.9	0.960	95.88

Table C–1. Mass gain, mass fraction oxidized and oxide thickness of Ni tube oxidation at 1,100 °C. All batches of Tier 1 shown.

Tier 2

Sample	**t (h)** ±0.01 h	**m_{Ni} (mg)** ±1 mg	**m_{Ni+NiO} (mg)** ±1 mg	**m_{gain} (mg)** ±2 mg	**Mass fraction oxidised** ±0.001	**z (µm)** ±0.23 µm
Batch A						
OT-A.10/06/11-125.1100-A.13	1.083 (65 min)	493.2	522.6	29.4	0.833	22.57
OT-A.10/06/11-125.1100-A.14	1.167 (70 min)	492.6	520.6	28.0	0.830	21.50
OT-A.10/06/11-125.1100-A.15	1.333 (80 min)	492.4	521.4	29.0	0.832	22.26
OT-A.10/06/11-125.1100-A.16	1.667 (100 min)	478.0	510.9	32.9	0.840	25.26
OT-A.10/06/11-125.1100-A.17	2.333 (140 min)	494.9	534.5	39.6	0.849	30.40
Batch B						
OT-A.10/06/11-125.1100-B.13	1.083 (65 min)	487.2	511.6	24.4	0.825	18.73
OT-A.10/06/11-125.1100-B.14	1.167 (70 min)	532.1	561.6	29.5	0.829	22.65
OT-A.10/06/11-125.1100-B.15	1.333 (80 min)	480.4	509.7	29.3	0.834	22.49
OT-A.10/06/11-125.1100-B.16	1.667 (100 min)	491.4	524.0	32.6	0.838	25.03
OT-A.10/06/11-125.1100-B.17	2.333 (140 min)	483.2	529.7	46.5	0.861	35.70
Batch C						
OT-A.10/06/11-125.1100-C.13	1.083 (65 min)	493.9	541.1	47.2	0.861	36.23
OT-A.10/06/11-125.1100-C.14	1.167 (70 min)	497.1	525.6	28.5	0.831	21.88
OT-A.10/06/11-125.1100-C.15	1.333 (80 min)	491.6	520.7	29.1	0.832	22.34
OT-A.10/06/11-125.1100-C.16	1.667 (100 min)	496.3	529.4	33.1	0.838	25.41
OT-A.10/06/11-125.1100-C.17	2.333 (140 min)	510.1	535.8	25.7	0.825	19.73
Batch D						
OT-A.29/07/11-125.1100-D.13	1.083 (65 min)	494.8	521.5	26.7	0.828	20.5
OT-A.29/07/11-125.1100-D.14	1.167 (70 min)	490.1	515.9	25.8	0.827	19.81
OT-A.29/07/11-125.1100-D.15	1.333 (80 min)	528.6	558.8	30.2	0.831	23.18
OT-A.29/07/11-125.1100-D.16	1.667 (100 min)	499.7	532.8	33.1	0.838	25.41
OT-A.29/07/11-125.1100-D.17	2.333 (140 min)	495.8	536.7	40.9	0.851	31.40

Sample	t (h) ±0.01 h	m_{Ni} (mg) ±1 mg	m_{Ni+NiO} (mg) ±1 mg	m_{gain} (mg) ±2 mg	Mass fraction oxidised ±0.001	z (µm) ±0.23 µm
Batch E						
OT-A.29/07/11-125.1100-E.13	1.083 (65 min)	487.7	513.7	26.0	0.828	19.96
OT-A.29/07/11-125.1100-E.14	1.167 (70 min)	478.1	503.4	25.3	0.827	19.42
OT-A.29/07/11-125.1100-E.15	1.333 (80 min)	497.6	526.4	28.8	0.831	22.11
OT-A.29/07/11-125.1100-E.16	1.667 (100 min)	499.4	532.3	32.9	0.838	25.26
OT-A.29/07/11-125.1100-E.17	2.333 (140 min)	507.9	548.7	40.8	0.849	31.32

Table C–2. Mass gain, mass fraction oxidized and oxide thickness of Ni tube oxidation at 1,100 °C. All batches of Tier 2 shown.

Tier 3

All batches shown in Chapter 1.

Tier 4

Sample	t (h) ±0.01 h	m_{Ni} (mg) ±1 mg	m_{Ni+NiO} (mg) ±1 mg	m_{gain} (mg) ±2 mg	Mass fraction oxidised ±0.001	z (µm) ±0.23 µm
Batch A						
OT-A.15/11/12-125.1100-A.18	0.667 (40 min)	499.5	519.4	19.9	0.817	15.28
OT-A.16/11/12-125.1100-A.19	2.667 (160 min)	494.4	535.8	41.4	0.852	31.78
OT-A.27/11/12-125.1100-A.20	3.000	472.3	517.0	44.7	0.860	34.32
OT-A.05/02/13-125.1100-A.21	3.333 (200 min)	496.9	547.7	50.8	0.866	39.00
OT-A.07/02/13-125.1100-A.22	4.000	487.4	539.5	52.1	0.870	40.00
OT-A.22/02/13-125.1100-A.23	3.667 (220 min)	492.1	540.9	48.8	0.864	37.46
OT-A.27/02/13-125.1100-A.24	7.000	494.9	558.4	63.5	0.887	48.75
Batch B						
OT-A.15/11/12-125.1100-B.18	0.667 (40 min)	484.0	503.4	19.4	0.817	14.89
OT-A.16/11/12-125.1100-B.19	2.667 (160 min)	475.1	514.7	39.6	0.851	30.40
OT-A.27/11/12-125.1100-B.20	3.000	471.8	516.6	44.8	0.860	34.39
OT-A.05/02/13-125.1100-B.21	3.333 (200 min)	500.2	551.3	51.1	0.866	39.23
OT-A.07/02/13-125.1100-B.22	4.000	489.5	543.0	53.5	0.872	41.07
OT-A.22/02/13-125.1100-B.23	3.667 (220 min)	494.5	539.9	45.4	0.858	34.85

Sample	t (h) ±0.01 h	m_{Ni} (mg) ±1 mg	m_{Ni+NiO} (mg) ±1 mg	m_{gain} (mg) ±2 mg	Mass fraction oxidised ±0.001	z (µm) ±0.23 µm
OT-A.27/02/13-125.1100-B.24	7.000	534.5	606.7	72.2	0.892	55.43
Batch C						
OT-A.15/11/12-125.1100-C.18	0.667 (40 min)	490.7	510.5	19.8	0.817	15.20
OT-A.16/11/12-125.1100-C.19	2.667 (160 min)	495.3	536.2	40.9	0.851	31.40
OT-A.27/11/12-125.1100-C.20	3.000	475.5	520.9	45.4	0.861	34.85
OT-A.05/02/13-125.1100-C.21	3.333 (200 min)	502.6	551.0	48.4	0.861	37.16
OT-A.07/02/13-125.1100-C.22	4.000	499.9	554.1	54.2	0.871	41.61
OT-A.22/02/13-125.1100-C.23	3.667 (220 min)	497.5	543.0	45.5	0.858	34.93
OT-A.27/02/13-125.1100-C.24	7.000	499.1	567.1	68.0	0.893	52.20
Batch D						
OT-A.15/11/12-125.1100-D.18	0.667 (40 min)	496.9	518.4	21.5	0.820	16.51
OT-A.16/11/12-125.1100-D.19	2.667 (160 min)	482.3	522.4	40.1	0.851	30.78
OT-A.27/11/12-125.1100-D.20	3.000	473.3	518.3	45.0	0.860	34.55
OT-A.05/02/13-125.1100-D.21	3.333 (200 min)	495.1	543.3	48.2	0.862	37.00
OT-A.07/02/13-125.1100-D.22	4.000	497.7	550.0	52.3	0.868	40.15
OT-A.22/02/13-125.1100-D.23	3.667 (220 min)	490.6	538.3	47.7	0.862	36.62
OT-A.27/02/13-125.1100-D.24	7.000	498.9	566.0	67.1	0.891	51.51
Batch E						
OT-A.15/11/12-125.1100-E.18	0.667 (40 min)	492.5	513.4	20.9	0.819	16.04
OT-A.16/11/12-125.1100-E.19	2.667 (160 min)	484.6	526.5	41.9	0.854	32.17
OT-A.27/11/12-125.1100-E.20	3.000	478.7	523.8	45.1	0.860	34.62
OT-A.05/02/13-125.1100-E.21	3.333 (200 min)	498.2	546.2	48.0	0.861	36.85
OT-A.07/02/13-125.1100-E.22	4.000	483.1	534.6	51.5	0.870	39.54
OT-A.22/02/13-125.1100-E.23	3.667 (220 min)	496.0	544.3	48.3	0.862	37.08
OT-A.27/02/13-125.1100-E.24	7.000	493.4	556.0	62.6	0.885	48.06

Table C–3. Mass gain, mass fraction oxidized and oxide thickness of Ni tube oxidation at 1,100 °C. All batches of Tier 4 shown.

Appendix D: Oxidation Micrographs

This appendix shows the full set of SEM micrographs from which the representative examples shown in section 8.3 through 8.7 were drawn. While this does not represent all the micrographs taken of these samples it does represent all points of interest in full detail. For discussion of these results please refer to the aforementioned sections of the thesis.

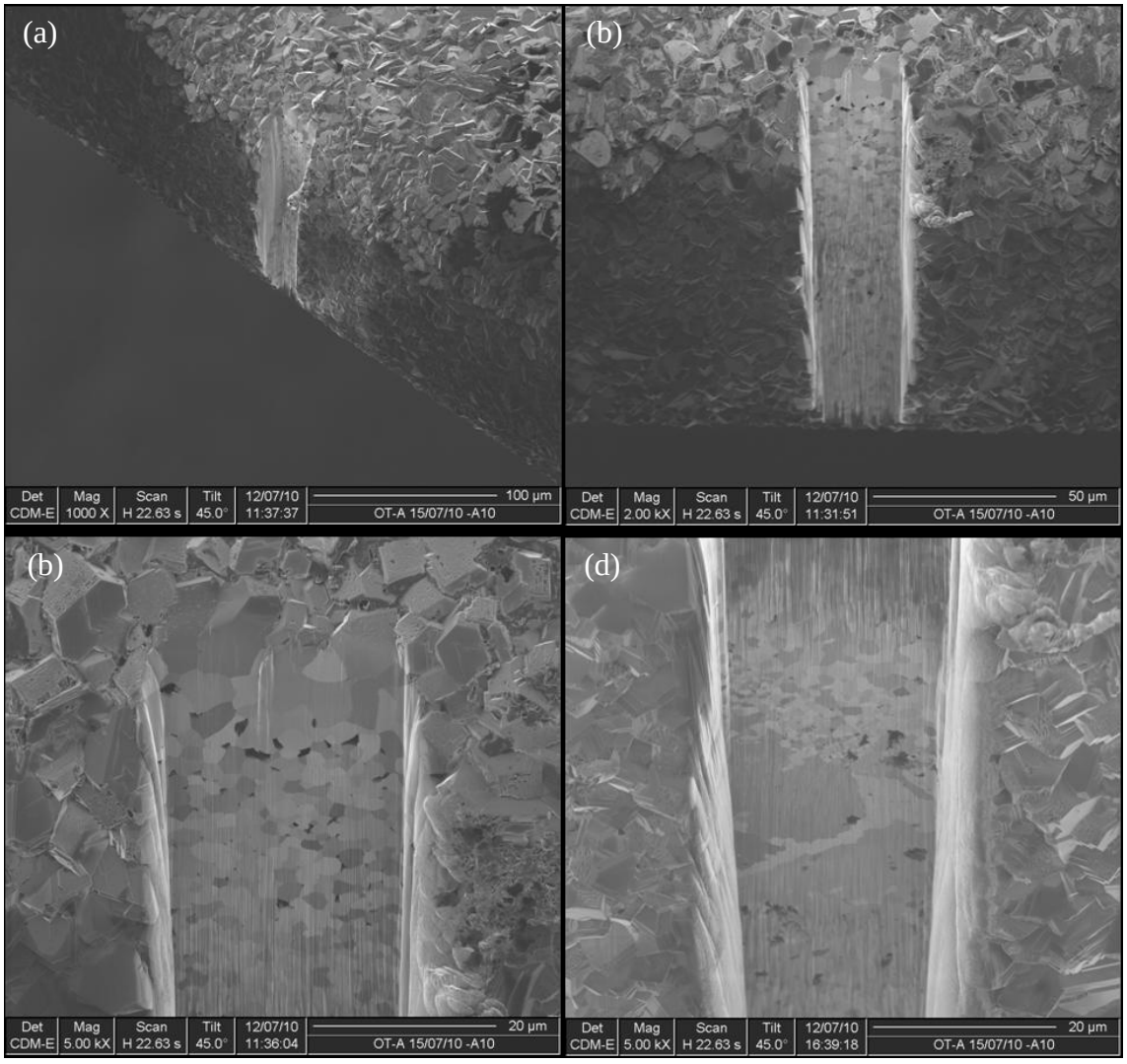

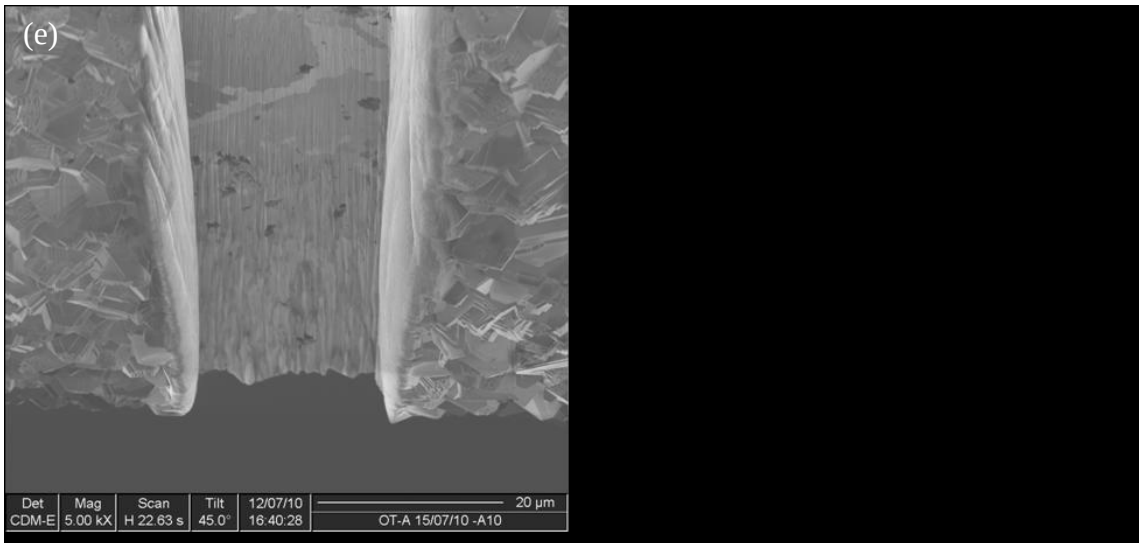

Figure D–1. FIB micrographs of a sample (sample OT-A-15/07/10-125.1100-A.10) 90.4% oxidised showing milled trench. This was done in order to obtain a representative cross-sectional area for high resolution SEM imaging (see below). Micrographs (a) and (b) show the milled trench, (c) the upper portion, (d) the middle and (e) the lower part of the trench. Notice the large pores visible even at this magnification. Also note that (as expected) they appear in distinct layers parallel to the surfaces. Some areas show heavy waterfalling due to the great depth of the trench which was milled from outer surface (top of images) to the inner surface of the tube (bottom of images).

Figure D–2. FIB micrographs of of a sample (sample OT-A-14/07/10-125.1100-E.11) 91.0% oxidised showing milled trench. Similarity to above images confirms the reproducibility.

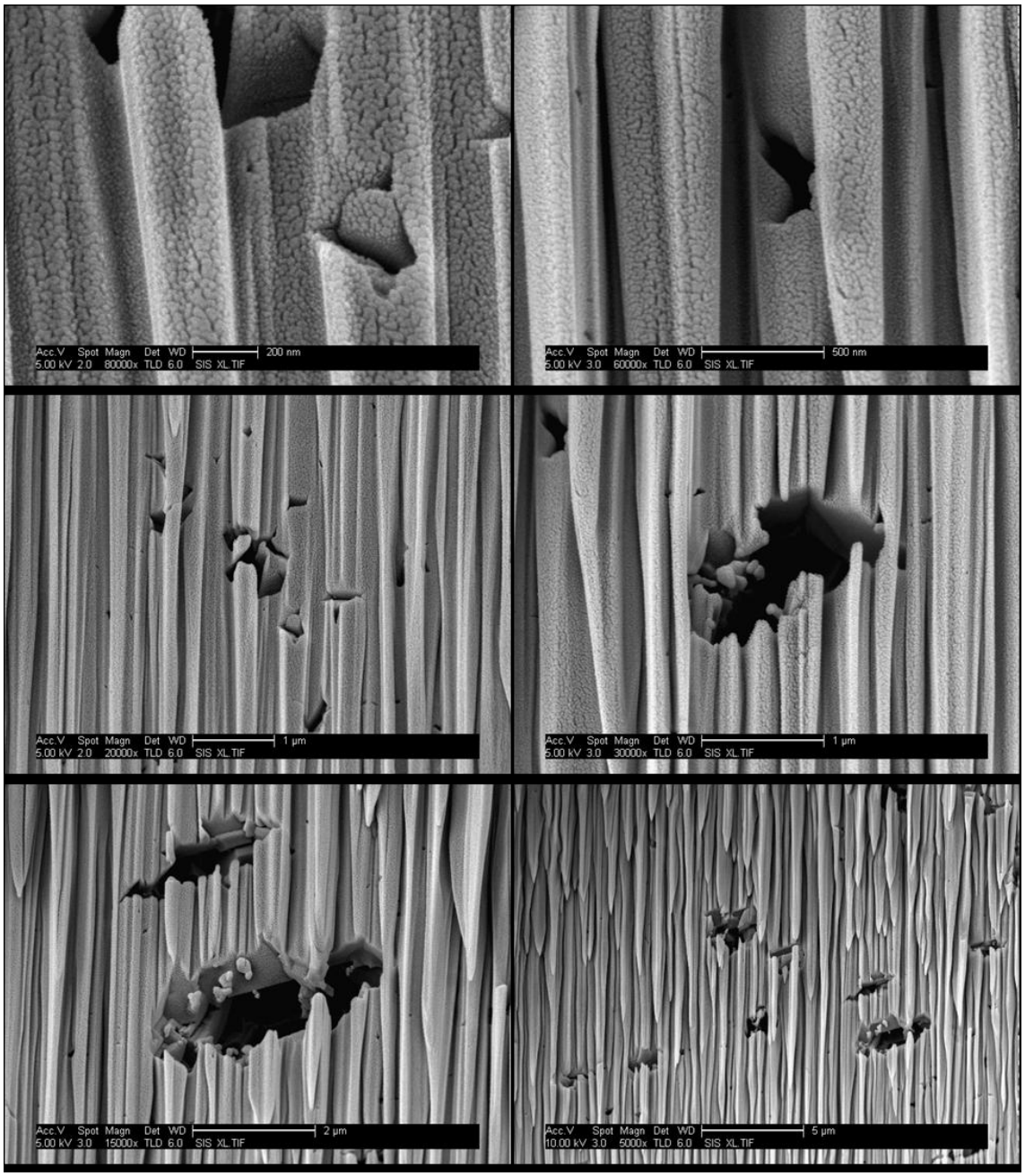

Figure D–3. SEM micrographs showing pores (ordered smallest to largest) around the middle of a 90.4 wt.% oxidised NiO tube (sample OT-A.15/07/2010-125.1100-A.10). Note that a Au-Pd coating was used to enable the high resolution imaging. The grains of the coating are visible in some images appearing somewhat as scales.

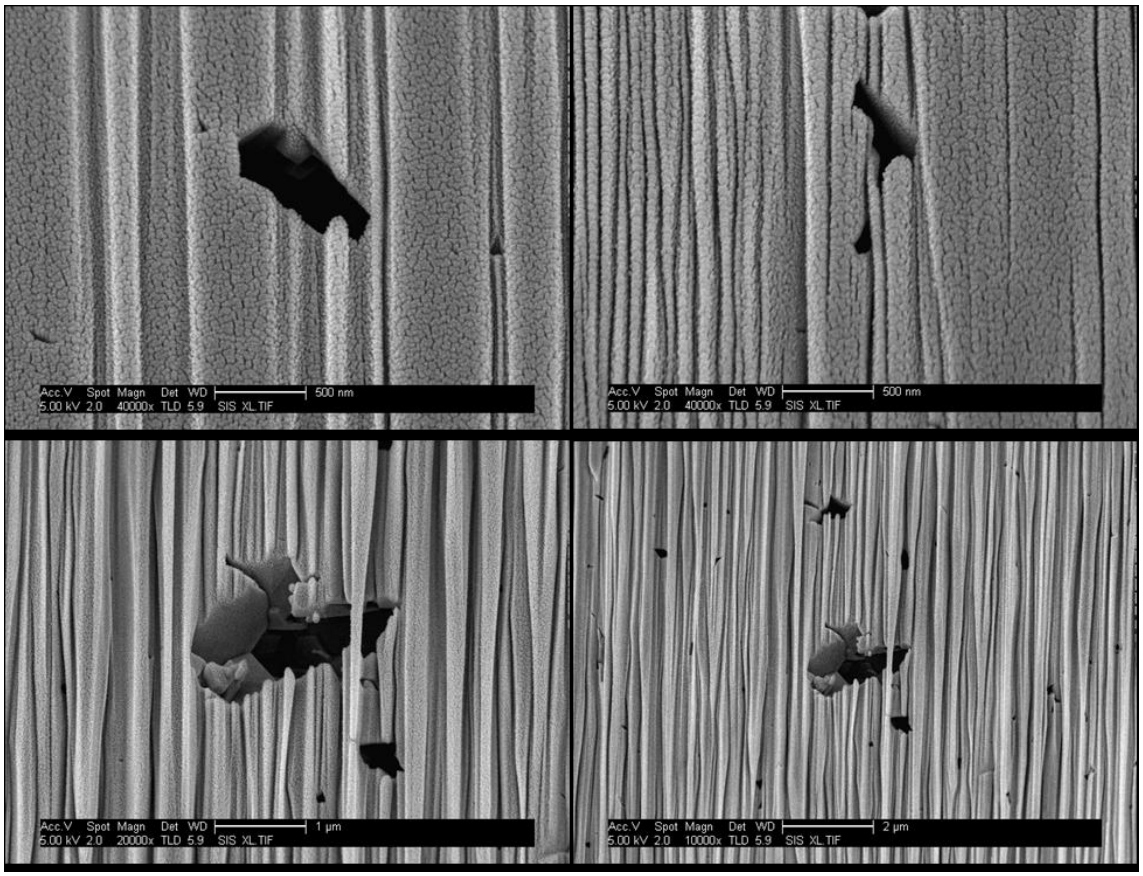

Figure D–4. SEM micrographs showing pores (ordered smallest to largest) near the outside edge of a 90.4 wt.% oxidised NiO tube (sample OT-A.15/07/2010-125.1100-A.10). Note that a Au-Pd coating was used to enable the high resolution imaging. The grains of the coating are visible in some images appearing somewhat as scales.

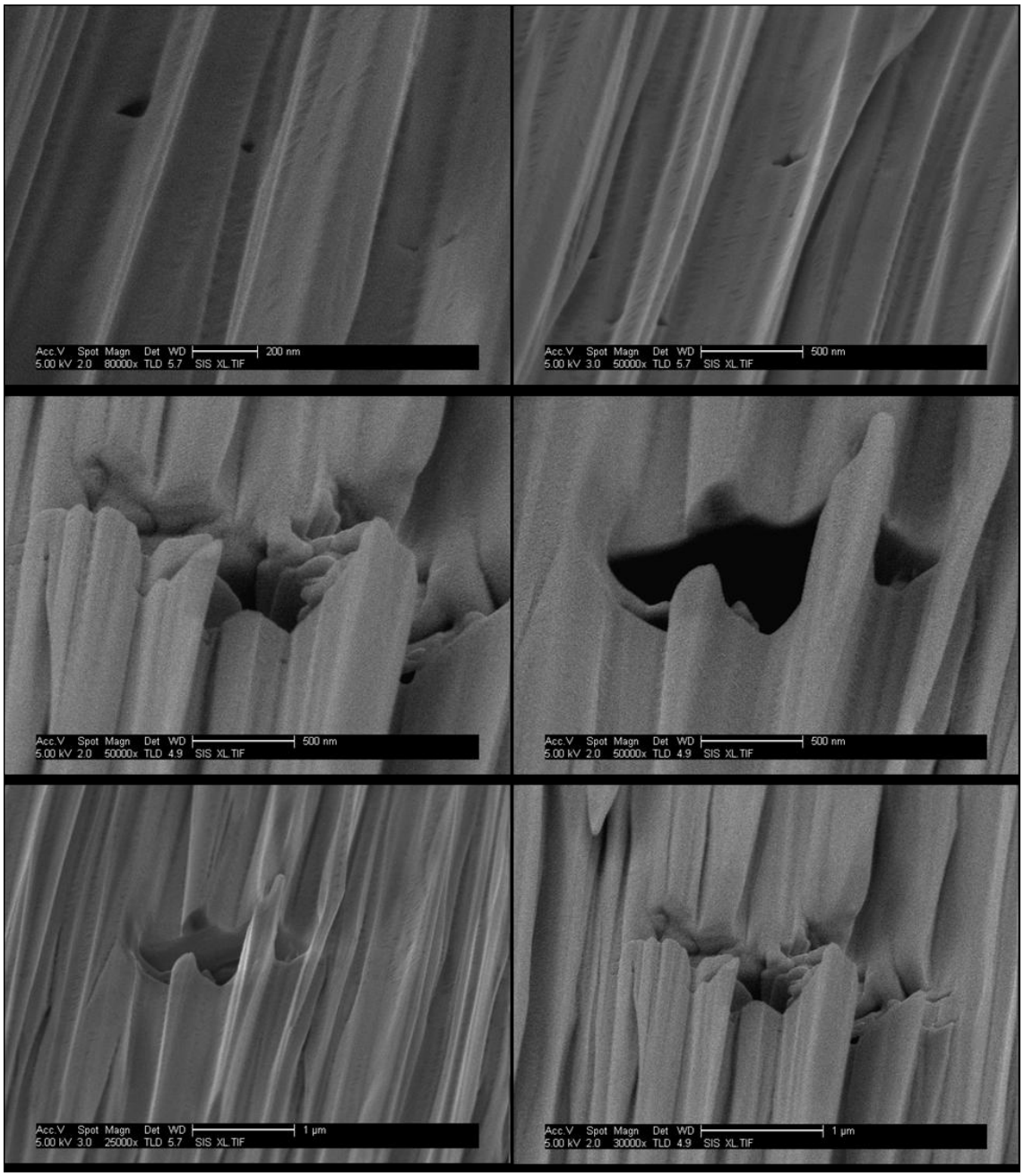

Figure D–5. SEM micrographs showing pores (ordered smallest to largest) near the inside edge of a 91.0 wt.% oxidised NiO tube (sample OT-A.15/07/2010-125.1100-E.11). Note that a Au-Pd coating was used to enable the high resolution imaging. The grains of the coating are visible in some images appearing somewhat as scales.

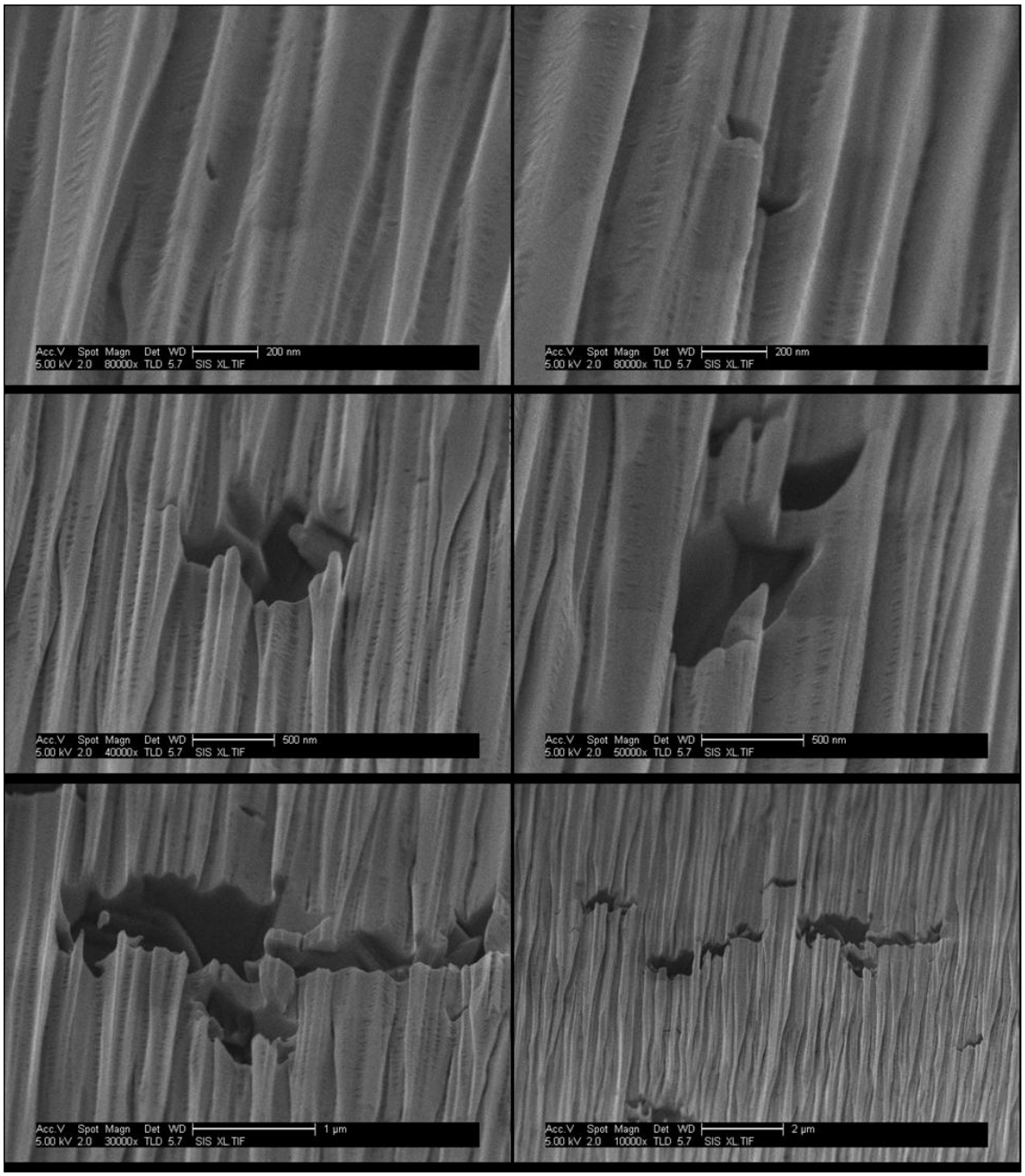

Figure D–6. SEM micrographs showing pores (ordered smallest to largest) around the middle of a 91.0 wt.% oxidised NiO tube (sample OT-A.15/07/2010-125.1100-E.11). Note that a Au-Pd coating was used to enable the high resolution imaging. The grains of the coating are visible in some images appearing somewhat as scales.

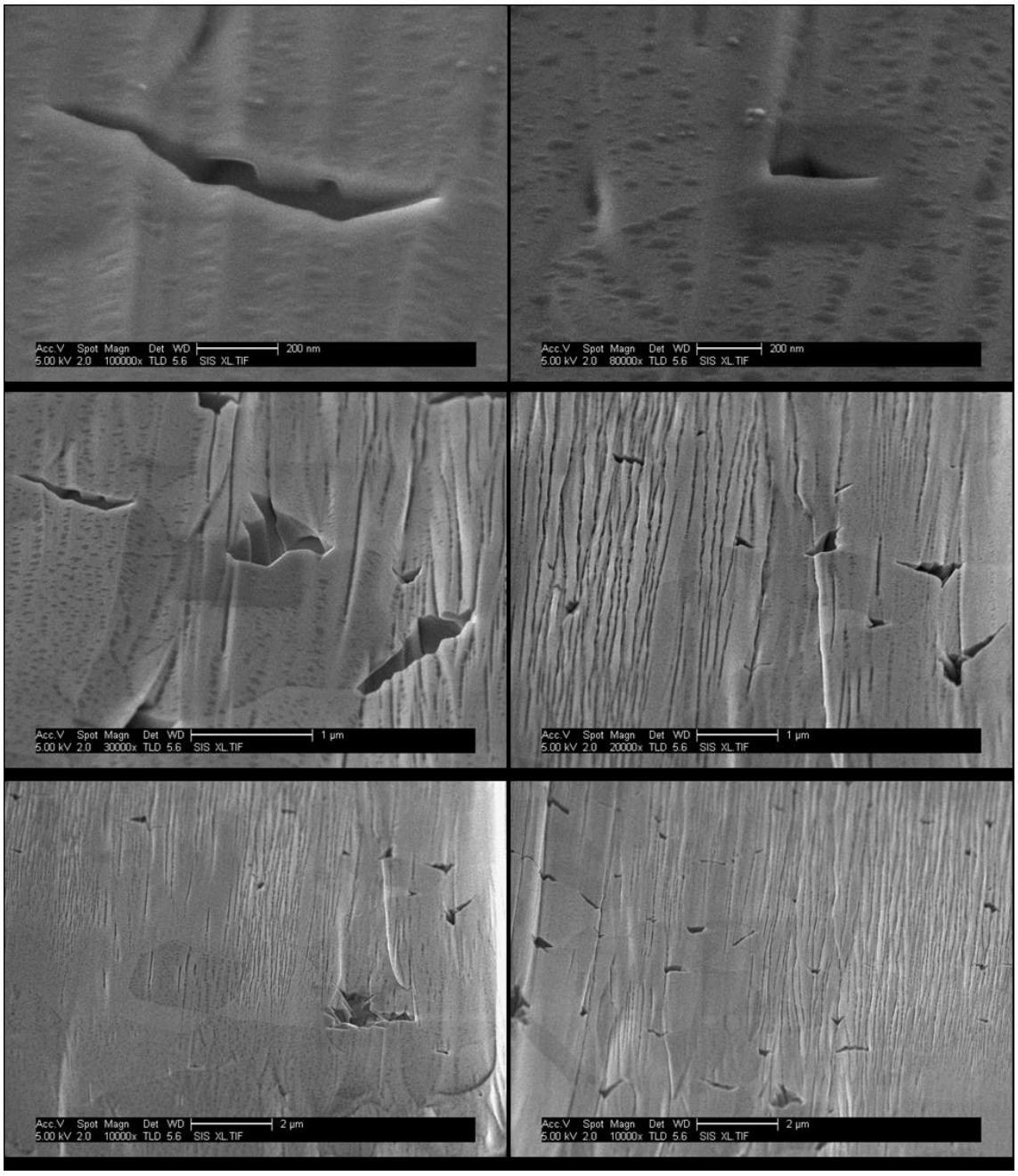

Figure D–7. SEM micrographs showing pores (ordered smallest to largest) near the outside edge of a 91.0 wt.% oxidised NiO tube (sample OT-A.15/07/2010-125.1100-E.11). Note that a Au-Pd coating was used to enable the high resolution imaging. The grains of the coating are visible in some images appearing somewhat as scales.

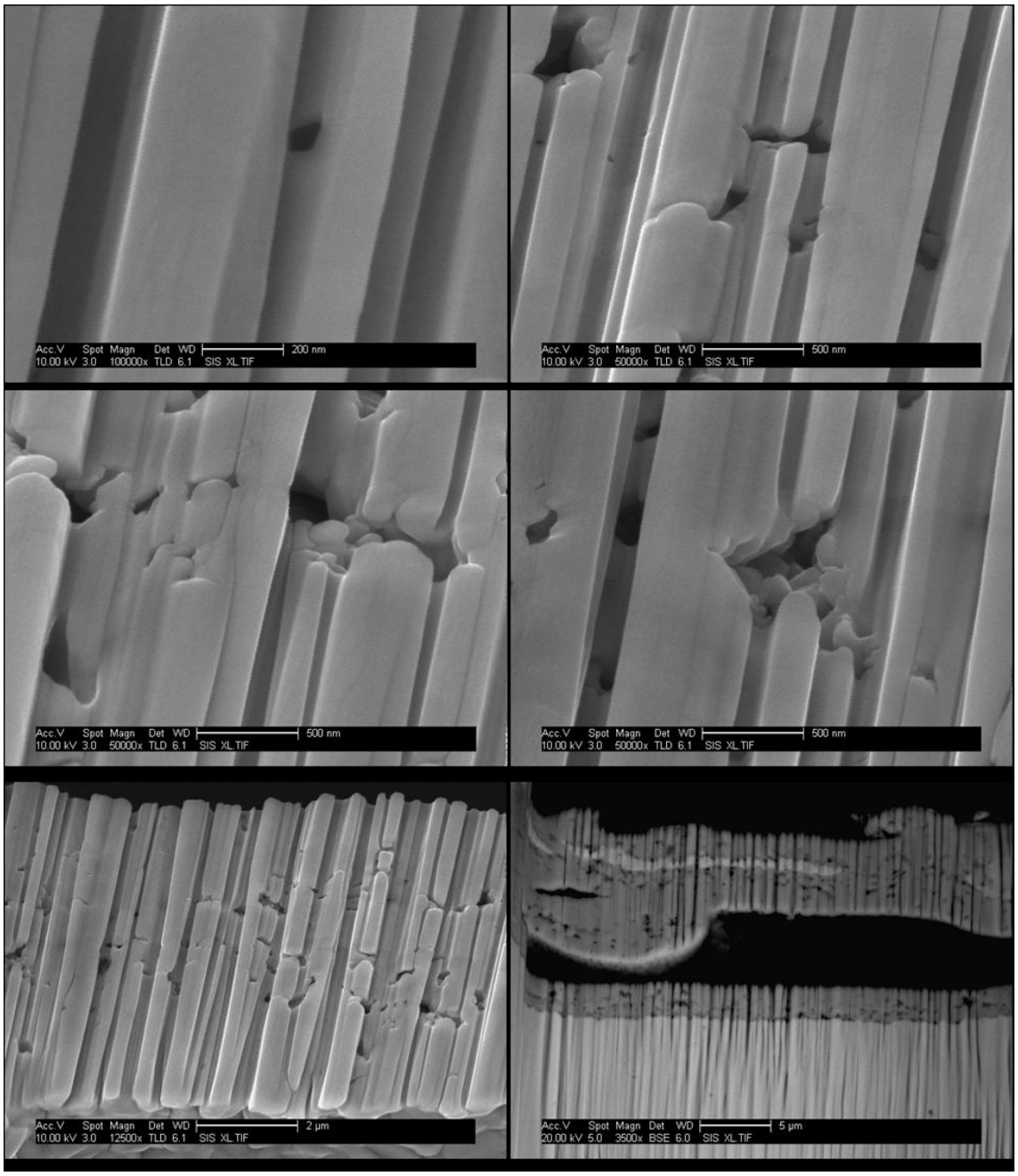

Figure D–8. SEM micrographs showing pores (ordered smallest to largest) near the inside edge of a 79.2 wt.% oxidised NiO tube (sample OT-A.15/07/2010-125.1100-C.01). This particular sample had a large void near the surface; probably a manufacturing defect. It is interesting to observe the oxidation from both sides of the upper portion leaving an unoxidised part near the middle. Note that a Au-Pd coating was used to enable the high resolution imaging. The grains of the coating are visible in some images appearing somewhat as scales.

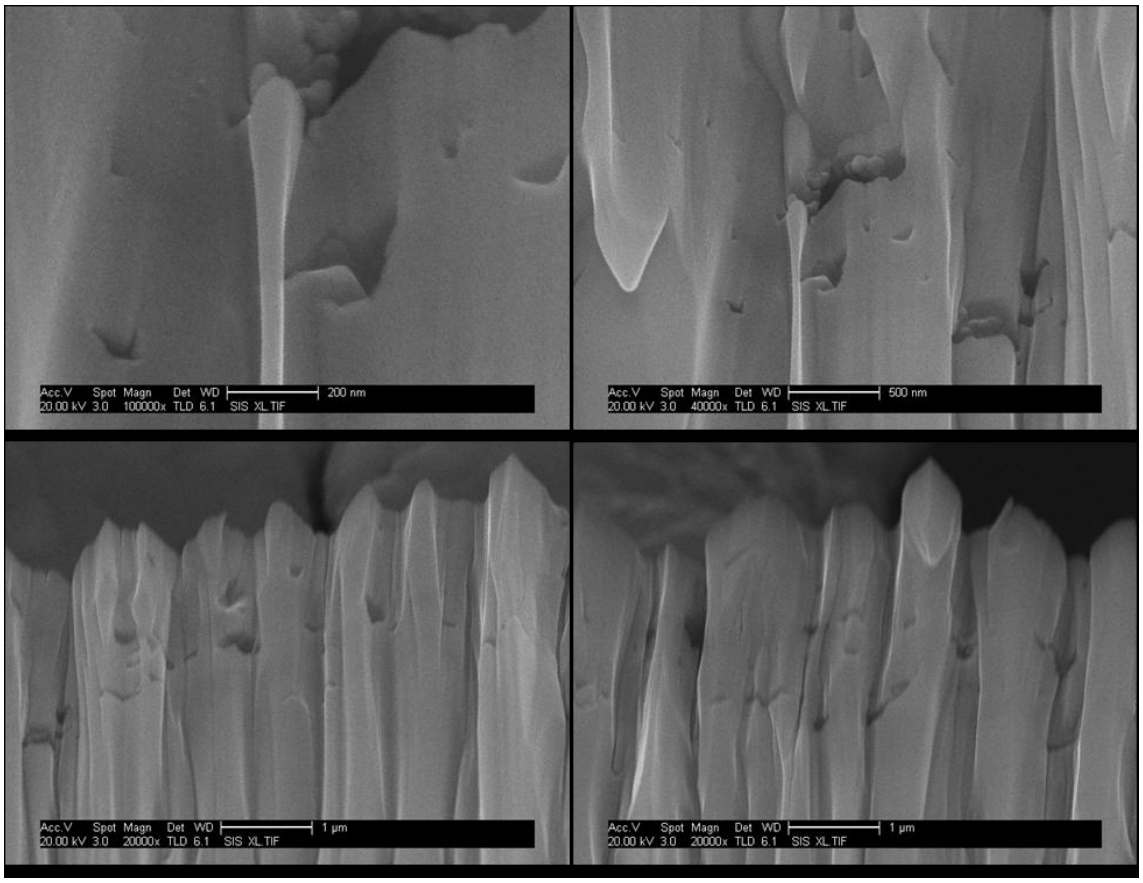

Figure D–9. SEM micrographs showing pores (ordered smallest to largest) near the outside edge of a 79.3 wt.% oxidised NiO tube (sample OT-A.15/07/2010-125.1100-D.01).

Appendix E: Oxidation Sample Furnace Positions and Schedule

Tier 1

The plus sign in the sample furnace position identifies samples in the same ceramic boat. Also tabulated is the oxidation schedule used (optimised for shortest furnace usage as this was a frequently needed furnace).

Toward furnace door	**At rear of furnace**
A.01+B.01, C.01+D.01, E.01	A.05+B.05, C.05+D.05, E.05
A.02+B.02, C.02+D.02, E.02	A.06+B.06, C.06+D.06
A.03+B.03, C.03+D.03, E.03	A.07+B.07, C.07+D.07
A.04+B.04, C.04+D.04, E.04	A.09+B.09, C.09+D.09, E.09
E.06	
E.07	
A.08+B.08, C.08+D.08, E.08	
A.10+B.10, C.10+D.10, E.10	
A.11+B.11, C.11+D.11, E.11	A.12+B.12, C.12+D.12, E.12

Table E–1. Sample positions in furnace (Tier 1).

Time	**Samples**	**Load / Unload**
Day 01		
10:00	A.01+B.01, A.02+B.02, A.03+B.03, A.04+B.04, A.05+B.05, A.06+B.06, A.07+B.07	Load
10:01	A.01+B.01	Unload
10:02	A.02+B.02	Unload
10:05	A.03+B.03	Unload
10:10	A.04+B.04	Unload
10:20	A.05+B.05	Unload
11:00	A.06+B.06	Unload
12:00	A.07+B.07	Unload
12:00	C.01+D.01, C.02+D.02, C.03+D.03, C.04+D.04, C.05+D.05, C.06+D.06, C.07+D.07	Load
12:01	C.01+D.01	Unload
12:02	C.02+D.02	Unload
12:05	C.03+D.03	Unload
12:10	C.04+D.04	Unload
12:20	C.05+D.05	Unload
13:00	C.06+D.06	Unload
14:00	C.07+D.07	Unload
16:00	A.11+B.11, A.12+B.12, C.11+D.11, C.12+D.12, E.11, E.12	Load
Day 02		
10:00	A.11+B.11, C.11+D.11, E.11	Unload
10:00	A.08+B.08, C.08+D.08, E.08	Load
15:00	A.08+B.08, C.08+D.08, E.08	Unload

Time	Samples	Load / Unload
17:00	A.10+B.10, C.10+D.10, E.10	Load
Day 03		
09:00	A.10+B.10, C.10+D.10, E.10	Unload
10:00	A.09+B.09, C.09+D.09, E.09	Load
10:00	A.12+B.12, C.12+D.12, E.12	Unload
10:00	E.01, E.02, E.03, E.04, E.05	Load
10:01	E.01	Unload
10:02	E.02	Unload
10:05	E.03	Unload
10:10	E.04	Unload
10:20	E.05	Unload
12:00	E.06, E.07	Load
13:00	E.06	Unload
14:00	E.07	Unload
19:00	A.09+B.09, C.09+D.09, E.09	Unload

Table E–2. Oxidation schedule (Tier 1).

Tier 2

As noted in section 8.4, the samples from this (and subsequent tiers) of oxidation experiments were supported on individual wire jigs rather than in pairs in ceramic boats.

Toward furnace door	At rear of furnace
A.13, B.13, C.13	A.17, B.17, C.17
A.14, B.14, C.14	A.16, B.16, C.16
A.15, B.15, C.15	
D.13, E.13	D.17, E.17
D.14, E.14	D.16, E.16
D.15, E.15	

Table E–3. Sample positions in furnace (Tier 2).

Time	Samples	Load / Unload
Day 01		
14:00	A.13, B.13, C.13, A.17, B.17, C.17	Load
15:05	A.13, B.13, C.13	Unload
15:05	A.14, B.14, C.14	Load
16:15	A.14, B.14, C.14	Unload
16:15	A.15, B.15, C.15	Load
16:20	A.17, B.17, C.17	Unload
16:20	A.16, B.16, C.16	Load
17:35	A.15, B.15, C.15	Unload
18:00	A.16, B.16, C.16	Unload
Day 02		
11:00	D.13, E.13, D.17, E.17	Load

Time	Samples	Load / Unload
12:05	D.13, E.13	Unload
12:05	D.14, E.14	Load
13:15	D.14, E.14	Unload
13:15	D.15, E.15	Load
13:20	D.17, E.17	Unload
13:20	D.16, E.16	Load
14:35	D.15, E.15	Unload
15:00	D.16, E.16	Unload

Table E–4. Oxidation schedule (Tier 2).

Tier 3

Not recorded.

Tier 4

As noted in section 0, the samples from tier of oxidation experiments were supported on individual wire jigs.

Toward furnace door	At rear of furnace
A.18, B.18, C.18	D.18, E.18
A.19, B.19, C.19	D.19, E.19
A.20, B.20, C.20	D.20, E.20
A.21, B.21, C.21	D.21, E.21
A.22, B.22, C.22	D.22, E.22
A.23, B.23, C.23	D.23, E.23
A.24, B.24, C.24	D.24, E.24

Table E–5. Sample positions in furnace (Tier 4).

Time	Samples	Load / Unload
Day 01		
14:00	A.18, B.18, C.18, D.18, E.18	Load
14:40	A.18, B.18, C.18, D.18, E.18	Unload
Day 02		
09:15	A.19, B.19, C.19, D.19, E.19	Load
11:55	A.19, B.19, C.19, D.19, E.19	Unload
[Period with no furnaces available.]		
Day 13		
13:45	A.20, B.20, C.20, D.20, E.20	Load
16:45	A.20, B.20, C.20, D.20, E.20	Unload
[Period with no furnaces available followed by Christmas holidays.]		

Time	Samples	Load / Unload
Day 51		
12:00	A.21, B.21, C.21, D.21, E.21	Load
15:20	A.21, B.21, C.21, D.21, E.21	Unload
Day 53		
10:00	A.22, B.22, C.22, D.22, E.22	Load
14:40	A.22, B.22, C.22, D.22, E.22	Unload
Day 68		
09:30	A.23, B.23, C.23, D.23, E.23	Load
13:10	A.23, B.23, C.23, D.23, E.23	Unload
Day 73		
09:30	A.24, B.24, C.24, D.24, E.24	Load
16:30	A.24, B.24, C.24, D.24, E.24	Unload

Table E–6. Oxidation schedule (Tier 4).

Appendix F: Horizontal Hydrogen Furnace SOP

The following is a copy of the SOP developed with Tim Pryor for use of this furnace. This is a typical part of the process of risk assessment (in addition to the RA) step, standardised at Cranfield University with all relevant documentation available to staff and students on the intranet. This SOP was included because the restrictions it places on the experiments undertaken as part of this project constrain what was possible, as discussed elsewhere.

SAS SSE SOP 029
Hydrogen heat treatment furnace (HTF 7)
Standard Operating Procedure

General precautions

When used with pure hydrogen or another flammable gas mix this process should not be run when periodic monitoring is not possible, eg. outside of normal working hours, unless authorisation is obtained and in which case the process must be seen to stabilise during the daytime before it is left over-night etc..
Risk assessment B57/G07/NiO tube reductions covers the use of this equipment in accordance with this SOP using hydrogen gas. Any activity that falls well outside of this risk assessment will need to be assessed on its own merits.

Trained operators only to use this equipment. Activities must comply with SSE SOP 42 (PGTC SOP 027); “Working in the High Temperature Corrosion Lab”.

Caution: Extreme heat, radiated heat, hot surfaces, invisible flame, live elements, **explosive gases**. Wear protective clothing: Furnace gloves, eye protection, lab coat, robust foot ware, long sleeves and long trousers.

Furnaces fitted with silicon carbide (SiC) elements and/or ceramic work tubes should be heated and cooled gradually to prevent thermal shock damage.

Allow for temperature off-set when programming. Re-check the off-set if thermocouples disturbed. Be aware of the uniform “hot zone”, re-check this if elements changed, work tube changed/ moved, insulation bungs moved etc.

Measures must be taken to prevent contamination from corrosive chemicals/ organics; Clean samples, use clean crucibles/ furniture, use clean loading/ unloading tools. Obtain permission before exposing anything other than steel, Ni, Cr, Al metallic samples or inert ceramics. If you need to use wire in the furnace; only use high temperature wire.

Tube furnaces do not have door interlocks. This means that, particularly in SiC element furnaces, it is potentially possible, if using a fine wire unload tool, to make contact with live elements. If this situation applies to you isolate element power, take great care and consider other methods of removing your samples.

Do not place hot loading tools onto painted or other polymer coated surfaces.

Ensure any end bungs and internal heat baffles are positioned correctly after loading.

Stop test if an interruption to power supply, air extraction or chilled water circuit is predicted.

Maintenance should be conducted by experienced staff only.

Procedure

Pre-checks and sample loading:

Check cooling water is on. Pressure can be checked by observing gauges in oxidation lab.
Check extraction to burner hood is sufficient.

This furnace must be load/ unloaded cold and the hydrogen atmosphere introduced before heating starts.

Ensure gas feed system is connected to appropriate gas supplies and that there is sufficient supply reserve.

The chamber must be thoroughly purged with inert gas (usually argon or nitrogen) before hydrogen/ hydrogen mix is introduced and again before furnace is opened to atmosphere. **Failure to do this could lead to an explosion.**

Samples to be mounted on suitable furniture (ceramic brick) and loaded into hot zone. Take care not damage internal thermocouple in roof of furnace.

Fit thermal plug with tip of metallic handle flush with tube opening.

Check condition of O-ring, fit and secure end cap, connect gas line.

Leak test and pre-treatment purge:

The chamber is sealed at each end with a gas inlet valve (blue) at the front, and gas outlet valve (to burner) and vacuum outlet at the rear.

The gas is fed via a 2-way selector and a rotameter. This enables the supply gas to be switched between inert purge gas (usually argon) and process gas (hydrogen/ hydrogen-argon mix) and the flow rate to be controlled.

Pass a small amount of purge gas into the chamber to flush the gas line. With outlet closed fill chamber to 0.5 bar and turn off gas supply closing blue inlet valve.
Tap pressure gauge and observe pressure. Leave for approx 5 minutes and then tap and check gauge again. There should have been no drop in pressure.
Turn off inlet valve and outlet valve and pump down with vacuum pump. Close rotameter and gas selector valve and gently open blue inlet valve to evacuate back to selector. When base pressure reached as indicated on gauge, close vac valve and turn off pump. Tap pressure gauge and observe pressure. Leave for approx 5 minutes and then tap and check gauge again. There should have been no rise in pressure.

Restart vac pump and open vac valve. When base pressure reached as indicated on gauge, maintain pumping for a short while.
Slowly introduce purge gas and then close vac valve and turn off pump.
Back-fill with purge gas to ≈+0.25 bar.
Turn off gas supply and repeat pump-down.
Slowly introduce purge gas and then close vac valve and turn off pump.
Repeat back-fill with purge gas to ≈+0.25 bar.

Turn off gas supply and repeat pump-down for last time. When base pressure reached as indicated on gauge, maintain pumping for a short while.
Close vac valve and turn off vac pump. Select process gas and slowly open rotameter to start back-fill with process gas. **Do not run hydrogen through vacuum pump as this could cause an explosion.**

Back fill until gauge pressure just positive, and reduce gas flow to normal test flow rate. Slowly open outlet valve to allow gas out to the flare and so to drop the chamber pressure to ≈ atmospheric. Re-adjust the flow rate if needed. If using a flammable gas composition the flare (burner) should be lit at this point.
The outlet valve should be opened sufficiently to ensure a pressure rise does not occur during heating.

<u>Lighting the burner:</u>
Set gas flow to normal test rate (usually ≈150ccm) allow a few seconds for flow to stabilise as chamber pressure drops. Lift off Davey gauze. Light a splint away from the burner or any gas lines. Carefully introduce splint to burner nozzle spiral to ignite gas.
Pure hydrogen burns with a near invisible flame, so it may be necessary to turn off lab lights to see if it gas is ignited. Once flame is stable, replace Davey gauze wearing furnace glove and take extreme care not to burn hand with flame or hot nozzle.

Programme furnace controller and run process:

This furnace must be heated and cooled on a controlled ramp rate to avoid thermal shocking the alumina work tube (chamber). Up to around 800 °C a rate of 5°C/ minute can be used, for temperatures above this the rate should be reduced to 3°C/minute.

The furnace and work tube have an absolute max temperature of 1400 °C but the life will be significantly reduced if run for long periods at this temperature. Check that all components are compatible with your desired operating conditions. (At time of writing the monitoring thermo-couple is an N-type and max test temp should be limited to 1250 °C.)

The gas flow is to be maintained throughout heat and cool cycle.

Periodically monitor the burner, gas flow, pressure, water cooling, temperature and general conditions during the process, especially at highest set temperature. When using a flammable gas initiate the start time such that the process reaches maximum temperature during the working day and monitor frequently during heat up.

Post treatment purge and unloading:

The furnace should purged and unloaded only when cool.

Check furnace controller and monitor t/c for temperature and check controller has completed program.

Change gas selector to purge gas to flush-out the chamber. Running gas at test flow rate; run until burner extinguishes indicating no flammable gas is remaining. Then continue purge for at least 3x volume changes (if not using flammable gas go straight to 3x volume changes).

At time of writing; Work chamber = 7.5cm dia x 120cm long ≈ 5.3 litres.

Once purged; close rotameter and gas selector valve, turn off gas inlet valve.
Disconnect gas line and remove front cap.
Remove and safely stow thermal plug.
Remove samples taking care not damage internal thermocouple in roof of furnace.
Take care thermal masses may mean large items are still too hot to touch even if the furnace is “cool”.- Allow time for samples and furniture to cool before handling; wear gloves, use IR thermometer to check temperature.

When the equipment is not to be used for a day or so the sample support furniture (brick) and thermal plug are best stored in the furnace with the front cap in place to keep contamination out.

Water cooling and gas fed lines can be isolated for longer periods of redundancy.

Emergency shut-down procedure

Switch gas selector to purge gas.

Increase gas flow to max range on rotameter.

Make sure outlet valve is fully open.

If possible isolate flammable process gas at valve on gas line outlet.

Follow emergency procedures as detailed in SSE SOP 42 (PGTC SOP 027).

If the furnace needs to be cooled it must either be ramped down steadily or the chamber purged to clear flammable gas first.

N.B. Switching off the power to the furnace when hot would cause thermal shock to the alumina work tube which could result in sudden escape of explosive gas. This should be avoided unless absolutely necessary.

Upon building evacuation; if possible turn off gas supplies from gas store.

Appendix G: Complete Reduction Results Tables

Tier 1

Sample	$t_{oxidised}$ (h) ±0.01 h	m_{Ni} (mg) ±1 mg	m_{Ni+NiO} (mg) ±1 mg	m_{gain} (mg) ±2 mg	Mass fraction oxidised ±0.0012	$t_{reduced}$ (h) ±1 s	$m_{reduced}$ (mg) ±1 mg	m_{loss} (mg) ±2 mg	Mass fraction reduced ±0.0344
Reduction at 600 °C									
RT-A.23/03/11-125.1100(600)-F.01 D	42	197.3	251.0	53.7	1.000	ramp	244.3	6.8	0.126
RT-A.23/03/11-125.1100(600)-G.01 M	42	182.3	232.1	49.8	1.000	ramp	224.9	7.1	0.143
RT-A.23/03/11-125.1100(600)-H.01 U	42	206.0	262.1	56.1	1.000	ramp	255.4	6.8	0.120
RT-A.30/03/11-125.1100(600)-I.01 D	42	202.0	256.9	54.9	0.999	ramp	252.2	4.9	0.089
RT-A.30/03/11-125.1100(600)-J.01 M	42	205.3	261.4	56.1	1.001	ramp	256.2	5.1	0.090
RT-A.30/03/11-125.1100(600)-K.01 U	42	208.3	265.0	56.7	1.000	ramp	260.0	5.1	0.090
RT-A.21/06/11-125.1100(600)-F.03 D	42	196.3	249.8	53.5	1.000	2	241.7	8.1	0.152
RT-A.21/06/11-125.1100(600)-G.03 M	42	199.4	253.7	54.3	1.000	2	245.4	8.4	0.154
RT-A.21/06/11-125.1100(600)-H.03 U	42	192.7	245.1	52.4	0.999	2	237.4	7.8	0.149
RT-A.09/05/11-125.1100(600)-I.02 D	42	200.8	255.5	54.7	1.000	2	232.4	23.1	0.423
RT-A.09/05/11-125.1100(600)-J.02 M	42	199.8	254.3	54.5	1.000	2	230.3	24.0	0.440
RT-A.09/05/11-125.1100(600)-K.02 U	42	194.5	247.6	53.1	1.000	2	216.4	31.1	0.586
Reduction at 800 °C									
RT-A.25/05/11-125.1100(800)-L.01 D	42	200.2	254.8	54.6	1.000	ramp	219.2	35.6	0.652
RT-A.25/05/11-125.1100(800)-M.01 M	42	182.5	232.2	49.7	1.000	ramp	196.3	36.0	0.723
RT-A.25/05/11-125.1100(800)-N.01 U	42	213.9	272.4	58.5	1.001	ramp	221.5	50.7	0.867
RT-A.01/06/11-125.1100(800)-O.01 D	42	194.6	247.6	53.0	1.000	ramp	237.0	10.7	0.201
RT-A.01/06/11-125.1100(800)-P.01 M	42	205.9	261.8	55.9	0.999	ramp	250.5	11.5	0.206
RT-A.01/06/11-125.1100(800)-Q.01 U	42	199.5	253.7	54.2	0.999	ramp	242.5	11.4	0.210
RT-A.08/06/11-125.1100(800)-L.02 D	42	199.6	254.0	54.4	1.000	2	245.1	8.9	0.164
RT-A.08/06/11-125.1100(800)-M.02 M	42	192.9	245.6	52.7	1.000	2	236.2	9.3	0.176
RT-A.08/06/11-125.1100(800)-N.02 U	42	191.7	243.9	52.2	1.000	2	232.7	11.3	0.216
RT-A.08/06/11-125.	42	193.9	246.9	53.0	1.001	2	238.4	8.4	0.158

Sample	**$t_{oxidised}$ (h)** ±0.01 h	**m_{Ni} (mg)** ±1 mg	**m_{Ni+NiO} (mg)** ±1 mg	**m_{gain} (mg)** ±2 mg	**Mass fraction oxidised** ±0.0012	**$t_{reduced}$ (h)** ±1 s	**$m_{reduced}$ (mg)** ±1 mg	**m_{loss} (mg)** ±2 mg	**Mass fraction reduced** ±0.0344
1100(800)-O.02 D									
RT-A.08/06/11-125.1100(800)-P.02 M	42	189.8	241.6	51.8	1.000	2	233.3	8.2	0.159
RT-A.08/06/11-125.1100(800)-Q.02 U	42	209.3	266.4	57.1	1.000	2	257.4	9.0	0.157
Reduction at 1,000 °C									
RT-A.13/07/11-125.1100(1000)-R.01 D	42	203.1	258.3	55.2	0.999	ramp	247.2	11.3	0.204
RT-A.13/07/11-125.1100(1000)-S.01 M	42	212.0	269.5	57.5	0.999	ramp	257.6	12.2	0.212
RT-A.13/07/11-125.1100(1000)-T.01 U	42	220.9	280.8	59.9	0.999	ramp	268.1	13.0	0.217
RT-A.20/08/13-125.1100(1000)-U.01 D	42	205.1	260.9	55.8	1.000	ramp	249.1	11.9	0.214
RT-A.20/08/13-125.1100(1000)-V.01 M	42	184.7	234.9	50.2	0.999	ramp	223.4	11.7	0.232
RT-A.20/08/13-125.1100(1000)-W.01 U	42	187.0	237.9	50.9	1.000	ramp	226.6	11.4	0.224
RT-A.18/07/11-125.1100(1000)-R.02 D	42	203.4	258.8	55.4	1.000	2	235.0	23.9	0.431
RT-A.18/07/11-125.1100(1000)-S.02 M	42	203.8	259.1	55.3	0.999	2	233.0	26.4	0.477
RT-A.18/07/11-125.1100(1000)-T.02 U	42	208.1	264.8	56.7	1.000	2	238.7	26.1	0.461
RT-A.20/08/13-125.1100(1000)-U.02 D	42	208.0	264.8	56.8	1.000	2	238.1	26.6	0.468
RT-A.20/08/13-125.1100(1000)-V.02 M	42	177.4	225.8	48.4	1.000	2	201.0	24.8	0.512
RT-A.20/08/13-125.1100(1000)-W.02 U	42	188.2	239.4	51.2	1.000	2	212.6	26.9	0.526
RT-A.01/10/13-125.1100(1000)-R.04 D	42	210.2	267.5	57.3	1.000	10	212.1	55.4	0.967
RT-A.01/10/13-125.1100(1000)-S.04 M	42	190.1	241.9	51.8	1.000	10	191.4	50.5	0.975
RT-A.01/10/13-125.1100(1000)-T.04 U	42	189.4	241.0	51.6	1.000	10	191.8	49.2	0.954
RT-A.09/10/13-125.1100(1000)-U.04 D	42	195.2	248.5	53.3	1.000	10	205.4	43.0	0.807
RT-A.09/10/13-125.1100(1000)-V.04 M	42	211.4	269.2	57.8	1.001	10	221.3	47.7	0.826
RT-A.09/10/13-125.1100(1000)-W.04 U	42	206.2	262.6	56.4	1.001	10	215.4	47.0	0.834
RT-A.18/09/13-125.1100(1000)-R.03 D	42	195.3	248.5	53.2	1.000	15	195.4	53.1	0.999
RT-A.18/09/13-125.1100(1000)-S.03 M	42	189.7	241.4	51.7	1.000	15	189.7	51.7	1.000
RT-A.18/09/13-125.1100(1000)-T.03 U	42	194.4	247.3	52.9	1.000	15	194.5	52.9	1.000
RT-A.24/09/13-125.1100(1000)-U.03 D	42	195.9	249.3	53.4	1.000	15	196.1	53.2	0.996

Sample	$t_{oxidised}$ (h) ±0.01 h	m_{Ni} (mg) ±1 mg	m_{Ni+NiO} (mg) ±1 mg	m_{gain} (mg) ±2 mg	Mass fraction oxidised ±0.0012	$t_{reduced}$ (h) ±1 s	$m_{reduced}$ (mg) ±1 mg	m_{loss} (mg) ±2 mg	Mass fraction reduced ±0.0344
RT-A.24/09/13-125. 1100(1000)-V.03 M	42	205.1	261.1	56.0	1.000	15	205.2	55.8	0.997
RT-A.24/09/13-125. 1100(1000)-W.03 U	42	190.8	242.8	52.0	1.000	15	191.0	51.8	0.996

Table G–1. Mass loss and mass fraction reduced of Tier 1 reduction. All temperatures reduced in 5% H_2 (balance Ar) shown. D, M, U after the sample code indicates whether it was downstream, in the middle or upstream with respect to the gas supply (respectively).

Tier 2

Sample	$t_{oxidised}$ (h) ±0.01 h	m_{Ni} (mg) ±1 mg	m_{Ni+NiO} (mg) ±1 mg	m_{gain} (mg) ±2 mg	Mass fraction oxidised ±0.0005	$t_{reduced}$ (h) ±1 s	$m_{reduced}$ (mg) ±1 mg	m_{loss} (mg) ±2 mg	Mass fraction reduced ±0.0042
Reduction at 400 °C									
RT-A.04/03/13-125. 1100(400)-FF.01 U	42	498.7	634.7	136.0	1.000	ramp	509.5	125.2	0.920
RT-A.04/03/13-125. 1100(400)-FG.01 M	42	499.4	635.5	136.1	1.000	ramp	525.5	110.0	0.809
RT-A.04/03/13-125. 1100(400)-FH.01 D	42	492.7	627.2	134.5	1.000	ramp	504.9	122.1	0.908
RT-A.05/04/13-125. 1100(400)-FI.01 U	42	476.6	606.4	129.8	1.000	ramp	483.3	123.2	0.949
RT-A.05/04/13-125. 1100(400)-FJ.01 M	42	487.3	620.0	132.2	1.000	ramp	495.1	125.0	0.942
RT-A.05/04/13-125. 1100(400)-FK.01 D	42	482.3	613.6	131.3	1.000	ramp	489.3	124.5	0.948
RT-A.26/03/13-125. 1100(400)-FF.02 U	42	489.3	622.8	133.5	1.000	0.017 (1 min)	497.6	125.1	0.937
RT-A.26/03/13-125. 1100(400)-FG.02 M	42	496.8	632.2	135.4	1.000	0.017 (1 min)	504.5	127.8	0.944
RT-A.26/03/13-125. 1100(400)-FH.02 D	42	488.7	622.0	133.3	1.000	0.017 (1 min)	496.7	125.2	0.939
RT-A.05/04/13-125. 1100(400)-FI.02 U	42	486.4	619.0	132.6	1.000	0.017 (1 min)	494.5	124.5	0.939
RT-A.05/04/13-125. 1100(400)-FJ.02 M	42	488.4	621.4	133.0	1.000	0.017 (1 min)	497.8	123.7	0.930
RT-A.05/04/13-125. 1100(400)-FK.02 D	42	490.7	624.4.	133.7	1.000	0.017 (1 min)	500.2	124.3	0.929
RT-A.07/05/13-125. 1100(400)-FF.03 U	42	493.4	627.9	134.5	1.000	0.167 (10 min)	500.0	127.9	0.951
RT-A.07/05/13-125. 1100(400)-FG.03 M	42	497.5	632.9	135.4	1.000	0.167 (10 min)	503.9	129.2	0.954
RT-A.07/05/13-125. 1100(400)-FH.03 D	42	491.3	625.2	133.9	1.000	0.167 (10 min)	498.0	127.2	0.950
RT-A.07/05/13-125. 1100(400)-FI.03 U	42	505.0	642.8	137.8	1.000	0.167 (10 min)	512.6	130.1	0.944
RT-A.07/05/13-125. 1100(400)-FJ.03 M	42	487.8	620.7	132.9	1.000	0.167 (10 min)	494.4	126.4	0.951
RT-A.07/05/13-125. 1100(400)-FK.03 D	42	490.0	623.4	133.4	1.000	0.167 (10 min)	496.8	126.8	0.950

Sample	$t_{oxidised}$ (h) ±0.01 h	m_{Ni} (mg) ±1 mg	m_{Ni+NiO} (mg) ±1 mg	m_{gain} (mg) ±2 mg	Mass fraction oxidised ±0.0005	$t_{reduced}$ (h) ±1 s	$m_{reduced}$ (mg) ±1 mg	m_{loss} (mg) ±2 mg	Mass fraction reduced ±0.0042
RT-A.17/05/13-125.1100(400)-FF.04 U	66.5	484.0	615.9	131.9	1.000	1	491.0	124.9	0.947
RT-A.17/05/13-125.1100(400)-FG.04 M	66.5	488.4	621.5	133.1	1.000	1	495.3	126.2	0.949
RT-A.17/05/13-125.1100(400)-FH.04 D	66.5	475.9	605.4	129.5	1.000	1	482.8	122.8	0.949
RT-A.17/05/13-125.1100(400)-FI.04 U	66	485.8	618.3	132.5	1.000	1	492.4	125.8	0.950
RT-A.17/05/13-125.1100(400)-FJ.04M	66	475.5	602.9	127.4	0.996	1	480.2	124.9	0.981
RT-A.17/05/13-125.1100(400)-FK.04 D	66	468.6	596.4	127.8	1.000	1	475.5	120.8	0.946
RT-A.12/06/13-125.1100(400)-FF.05 U	66	474.6	604.1	129.5	1.000	5	480.0	124.0	0.957
RT-A.12/06/13-125.1100(400)-FG.05 M	66	478.9	609.5	130.6	1.000	5	484.3	125.2	0.958
RT-A.12/06/13-125.1100(400)-FH.05 D	66	492.9	627.3	134.4	1.000	5	498.7	128.6	0.957
RT-A.12/06/13-125.1100(400)-FI.05 U	42	477.9	610.7	132.8	1.004	5	483.2	125.0	0.941
RT-A.12/06/13-125.1100(400)-FJ.05 M	42	481.8	615.2	133.4	1.003	5	487.5	125.6	0.942
RT-A.12/06/13-125.1100(400)-FK.05 D	42	490.0	624.1	134.1	1.001	5	495.8	127.8	0.953
RT-A.17/07/13-125.1100(400)-FF.06 U	42	485.6	617.8	132.2	1.000	15	489.5	128.5	0.972
RT-A.17/07/13-125.1100(400)-FG.06 M	42	490.4	623.8	133.4	1.000	15	494.4	129.7	0.972
RT-A.17/07/13-125.1100(400)-FH.06 D	42	501.4	637.8	136.4	1.000	15	505.5	132.6	0.972
RT-A.17/07/13-125.1100(400)-FI.06 U	42	502.7	639.5	136.8	1.000	15	506.8	132.9	0.972
RT-A.17/07/13-125.1100(400)-FJ.06 M	42	499.3	635.2	135.9	1.000	15	503.4	132.0	0.971
RT-A.17/07/13-125.1100(400)-FK.06 D	42	506.2	644.0	137.8	1.000	15	510.4	133.8	0.971
Reduction at 600 °C									
RT-A.28/11/12-125.1100(600)-R.01 U	42	464.3	591.0	126.7	1.000	ramp	466.5	124.4	0.982
RT-A.28/11/12-125.1100(600)-S.01 M	42	499.2	635.4	136.2	1.000	ramp	501.6	133.7	0.982
RT-A.28/11/12-125.1100(600)-T.01 D	42	493.2	627.8	134.6	1.000	ramp	495.6	132.1	0.981
RT-A.19/02/13-125.1100(600)-U.01 U	42	501.9	638.7	136.8	1.000	ramp	504.1	134.6	0.984
RT-A.19/02/13-125.1100(600)-V.01 M	42	496.7	632.0	135.3	1.000	ramp	498.9	133.2	0.985
RT-A.19/02/13-125.1100(600)-W.01 D	42	491.8	625.9	134.1	1.000	ramp	494.0	131.9	0.983
RT-A.19/02/13-125.	42	503.0	640.2	137.2	1.000	0.033	505.1	135.0	0.984

Sample	$t_{oxidised}$ (h) ±0.01 h	m_{Ni} (mg) ±1 mg	m_{Ni+NiO} (mg) ±1 mg	m_{gain} (mg) ±2 mg	Mass fraction oxidised ±0.0005	$t_{reduced}$ (h) ±1 s	$m_{reduced}$ (mg) ±1 mg	m_{loss} (mg) ±2 mg	Mass fraction reduced ±0.0042
1100(600)-R.02 U						(2 min)			
RT-A.19/02/13-125.1100(600)-S.02 M	42	503.6	640.9	137.3	1.000	0.033 (2 min)	505.6	135.3	0.985
RT-A.19/02/13-125.1100(600)-T.02 D	42	493.3	627.8	134.5	1.000	0.033 (2 min)	495.4	132.4	0.984
RT-A.04/03/13-125.1100(600)-U.02 U	42	476.3	606.2	129.9	1.000	0.033 (2 min)	478.5	127.6	0.983
RT-A.04/03/13-125.1100(600)-V.02 M	42	501.4	638.1	136.7	1.000	0.033 (2 min)	503.7	134.4	0.983
RT-A.04/03/13-125.1100(600)-W.02 D	42	490.3	623.8	133.5	1.000	0.033 (2 min)	492.3	131.7	0.986
Reduction at 800 °C									
RT-A.16/10/12-125.1100(800)-L.01 U	42	493.8	628.6	134.8	1.000	ramp	494.3	134.1	0.995
RT-A.16/10/12-125.1100(800)-M.01 M	42	476.5	606.7	130.2	1.000	ramp	477.1	129.3	0.993
RT-A.16/10/12-125.1100(800)-N.01 D	42	490.7	624.6	133.9	1.000	ramp	491.1	133.4	0.996
RT-A.23/10/12-125.1100(800)-O.01 U	42	492.4	626.7	134.3	1.000	ramp	493.0	133.6	0.995
RT-A.23/10/12-125.1100(800)-P.01 M	42	487.9	620.9	133.0	1.000	ramp	488.5	132.4	0.996
RT-A.23/10/12-125.1100(800)-Q.01 D	42	494.6	629.4	134.8	1.000	ramp	495.1	134.3	0.997
RT-A.23/10/12-125.1100(800)-L.02 U	42	481.0	612.0	131.0	1.000	1	481.3	130.8	0.999
RT-A.23/10/12-125.1100(800)-M.02 M	42	484.7	617.0	132.3	1.000	1	485.2	131.6	0.995
RT-A.23/10/12-125.1100(800)-N.02 D	42	481.8	613.0	131.2	1.000	1	482.1	131.0	0.999
RT-A.05/10/13-125.1100(800)-O.02 U	42	488.4	621.4	133.0	1.000	1	488.7	132.8	0.999
RT-A.05/02/13-125.1100(800)-P.02 M	42	503.1	639.7	136.6	0.999	1	503.1	137.2	1.004
RT-A.05/02/13-125.1100(800)-Q.02 D	42	502.0	638.8	136.8	1.000	1	502.2	136.7	0.999
Reduction at 1,000 °C									
RT-A.06/06/12-125.1100(1000)-F.01 U	137.5	491.8	625.8	134.0	1.000	5	492.2	133.7	0.998
RT-A.06/06/12-125.1100(1000)-G.01 M	137.5	494.2	626.6	132.4	0.996	5	492.8	136.1	1.028
RT-A.06/06/12-125.1100(1000)-H.01 D	137.5	482.6	602.5	119.9	0.981	5	473.8	140.4	1.171
RT-A.09/10/12-125.1100(1000)-I.01 U	42	489.9	622.3	132.4	0.998	5	489.6	133.9	1.011
RT-A.09/10/12-125.1100(1000)-J.01 M	42	507.8	646.0	138.2	1.000	5	508.0	138.2	1.000
RT-A.09/10/12-125.1100(1000)-K.01 D	42	483.3	614.9	131.6	1.000	5	483.5	131.6	1.000

Sample	$t_{oxidised}$ (h) ±0.01 h	m_{Ni} (mg) ±1 mg	m_{Ni+NiO} (mg) ±1 mg	m_{gain} (mg) ±2 mg	Mass fraction oxidised ±0.0005	$t_{reduced}$ (h) ±1 s	$m_{reduced}$ (mg) ±1 mg	m_{loss} (mg) ±2 mg	Mass fraction reduced ±0.0042
RT-A.12/06/12-125.1100(1000)-F.02 U	42	492.6	626.7	134.1	1.000	ramp	492.9	134.0	0.999
RT-A.12/06/12-125.1100(1000)-G.02 M	42	499.7	634.3	134.6	0.997	ramp	498.8	137.1	1.019
RT-A.12/06/12-125.1100(1000)-H.02 D	42	498.9	635.9	137.0	1.002	ramp	500.0	134.9	0.985
RT-A.09/10/12-125.1100(1000)-I.02 U	42	495.7	630.8	135.1	1.000	ramp	496.0	134.8	0.998
RT-A.09/10/12-125.1100(1000)-J.02 M	42	490.8	624.3	133.5	1.000	ramp	490.7	133.9	1.003
RT-A.09/10/12-125.1100(1000)-K.02 D	42	474.2	603.4	129.2	1.000	ramp	474.4	129.1	0.999
RT-A.02/07/12-125.1100(1000)-F.03 U	42	473.6	587.4	113.8	0.975	1	461.6	141.1	1.240
RT-A.02/07/12-125.1100(1000)-G.03 M	42	493.5	628.0	134.5	1.000	1	493.7	134.3	0.999
RT-A.02/07/12-125.1100(1000)-H.03 D	42	496.8	630.1	133.3	0.997	1	495.3	136.9	1.027
RT-A.16/10/12-125.1100(1000)-I.03 U	42	479.5	610.2	130.7	1.000	1	479.6	130.6	0.999
RT-A.16/10/12-125.1100(1000)-J.03 M	42	483.3	615.0	131.7	1.000	1	483.3	131.8	1.000
RT-A.16/10/12-125.1100(1000)-K.03 D	42	488.5	621.6	133.1	1.000	1	488.6	133.1	1.000

Table G–2. Mass loss and mass fraction reduced of Tier 2 reduction. All temperatures reduced in 100% H_2 shown. U, M, D after the sample code indicates whether it was upstream, in the middle or downstream with respect to the gas supply (respectively).

Appendix H: Reduction Micrographs

This appendix shows the full set of SEM micrographs from which the representative examples shown in section 8.12 were drawn. While this does not represent all the micrographs taken of these samples it does represent all points of interest in full detail. For discussion of these results please refer to the aforementioned section of the thesis.

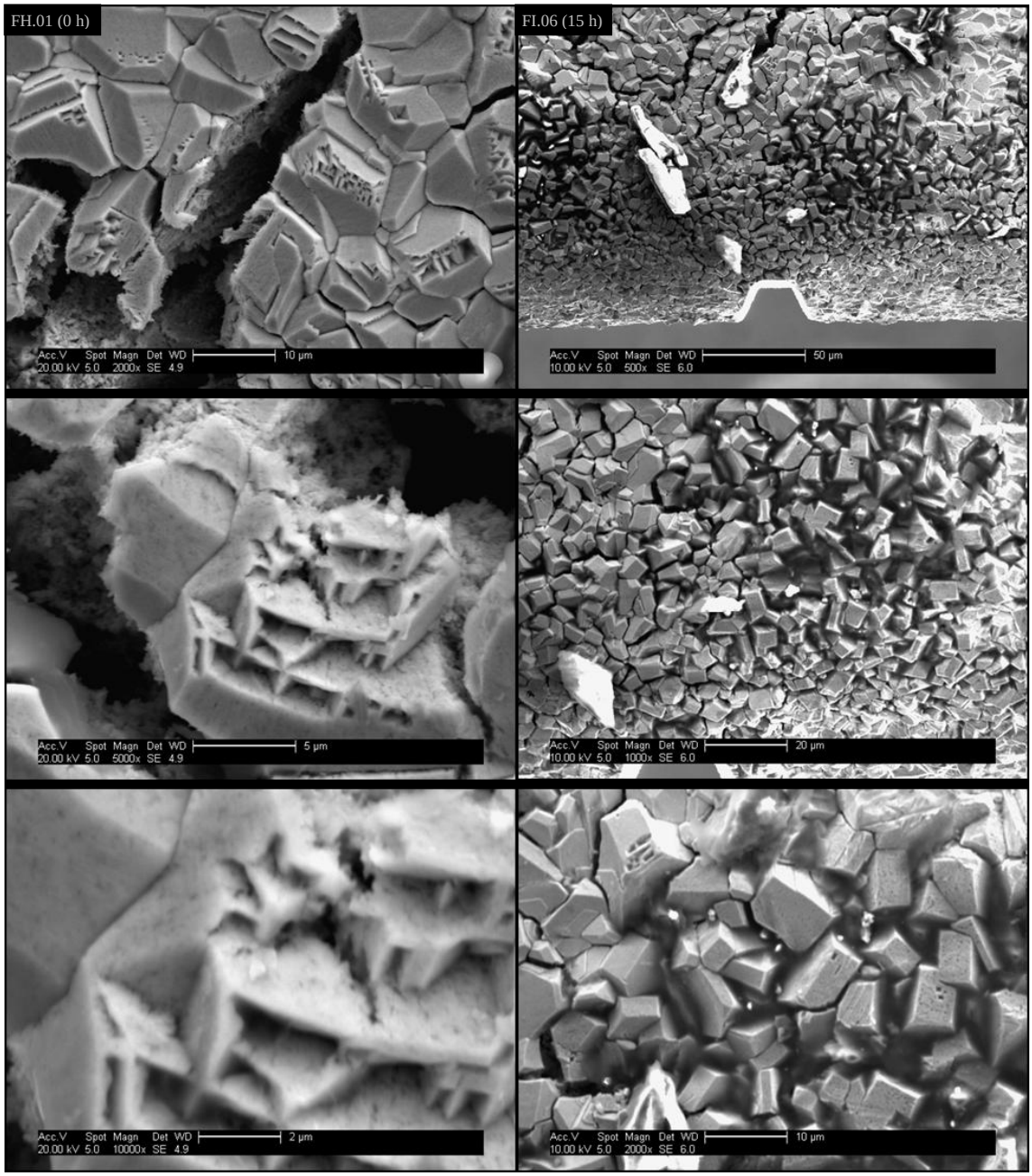

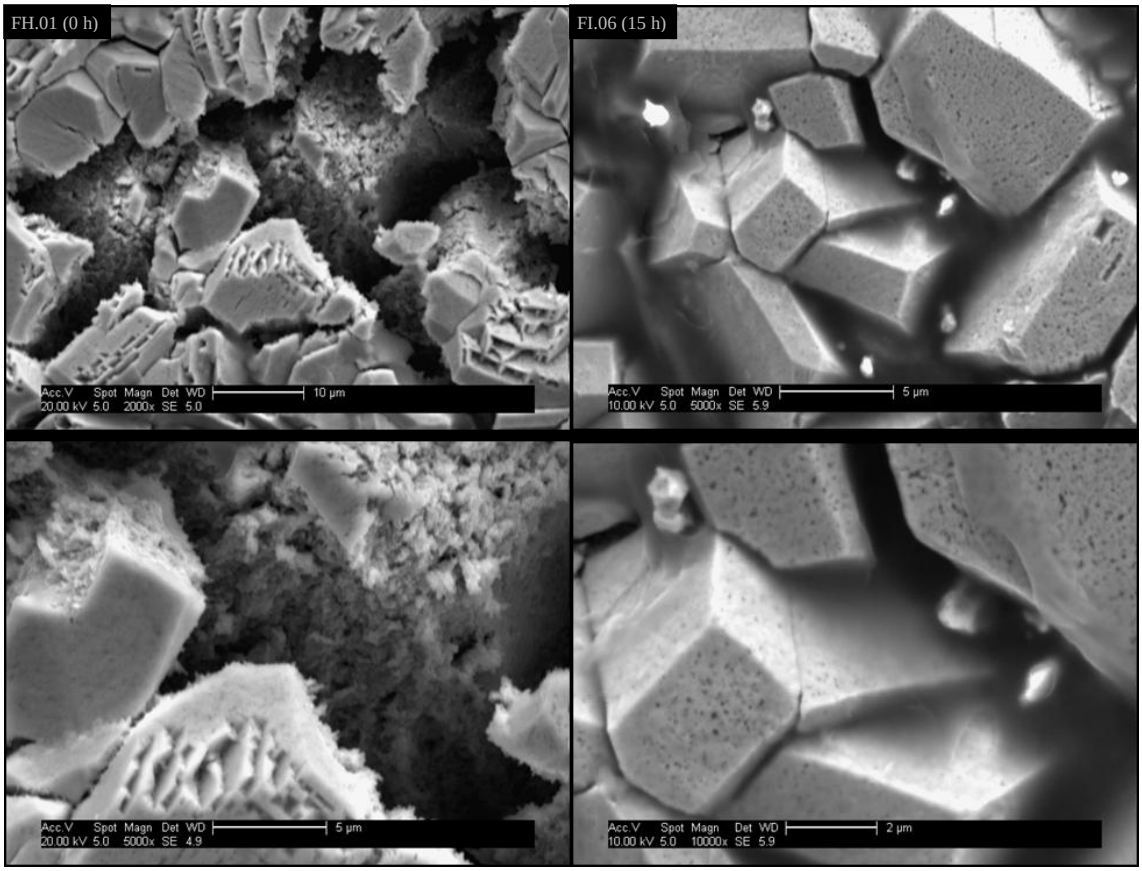
FH.01 (0 h)
Acc.V Spot Magn Det WD
20.00 kV 5.0 2000x SE 5.0
10 µm
FI.06 (15 h)
Acc.V Spot Magn Det WD
10.00 kV 5.0 5000x SE 5.9
5 µm
Acc.V Spot Magn Det WD
20.00 kV 5.0 5000x SE 4.9
5 µm
Acc.V Spot Magn Det WD
10.00 kV 5.0 10000x SE 5.9
2 µm

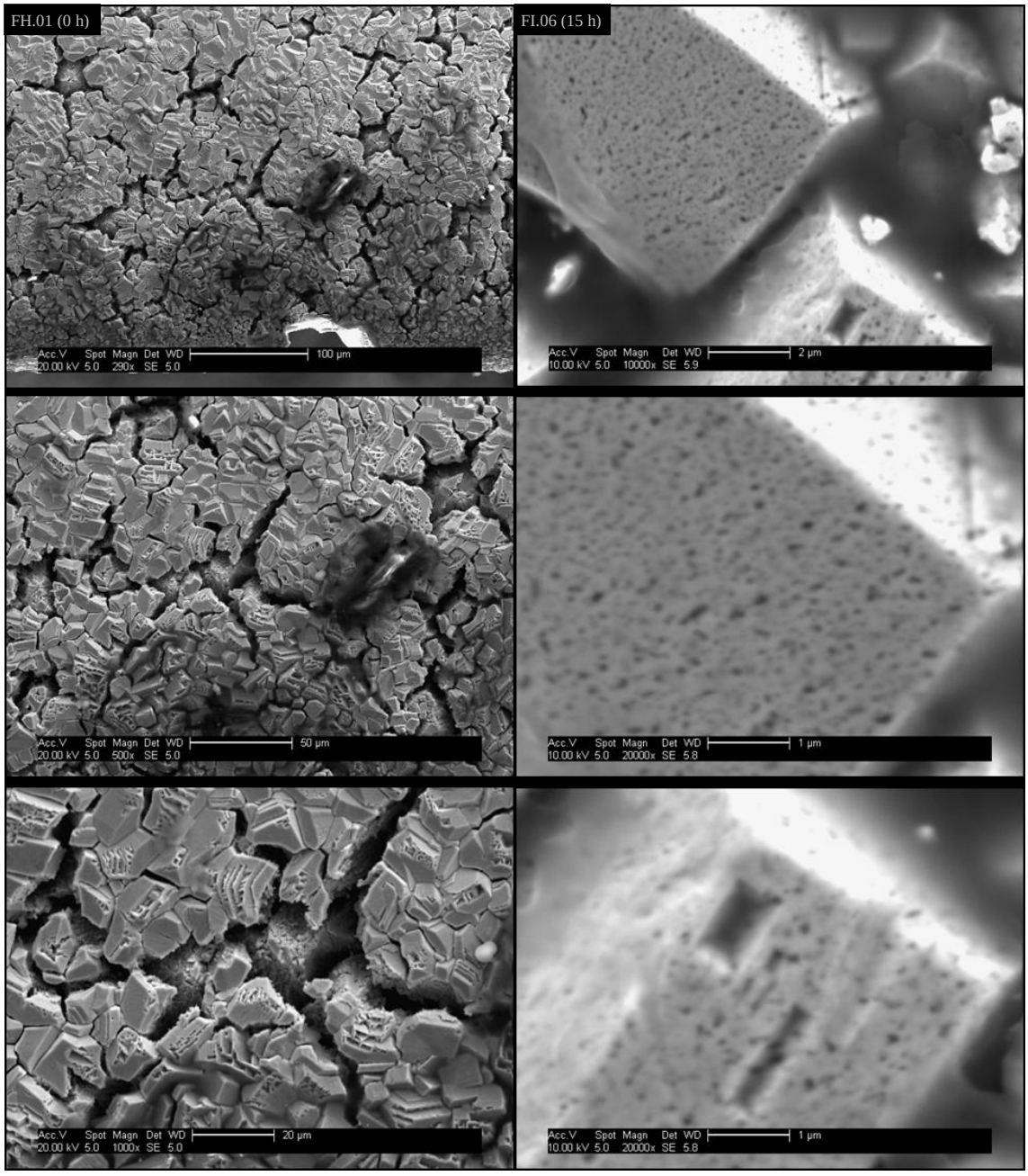
FH.01 (0 h)
FI.06 (15 h)
Acc.V Spot Magn Det WD 100 µm
20.00 kV 5.0 290x SE 5.0
Acc.V Spot Magn Det WD 2 µm
10.00 kV 5.0 10000x SE 5.9
Acc.V Spot Magn Det WD 50 µm
20.00 kV 5.0 500x SE 5.0
Acc.V Spot Magn Det WD 1 µm
10.00 kV 5.0 20000x SE 5.8
Acc.V Spot Magn Det WD 20 µm
20.00 kV 5.0 1000x SE 5.0
Acc.V Spot Magn Det WD 1 µm
10.00 kV 5.0 20000x SE 5.8

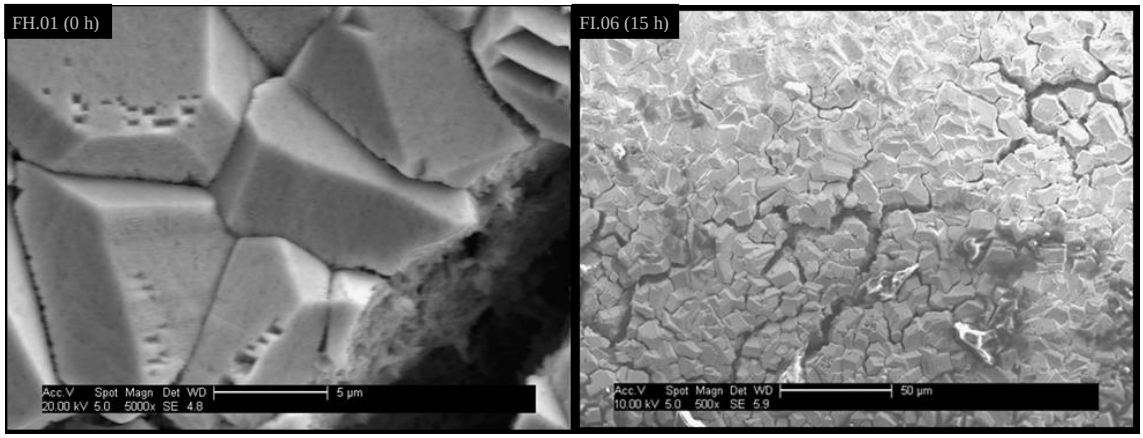
FH.01 (0 h)
FI.06 (15 h)
Acc.V Spot Magn Det WD 5 µm
20.00 kV 5.0 5000x SE 4.8
Acc.V Spot Magn Det WD 50 µm
10.00 kV 5.0 500x SE 5.9

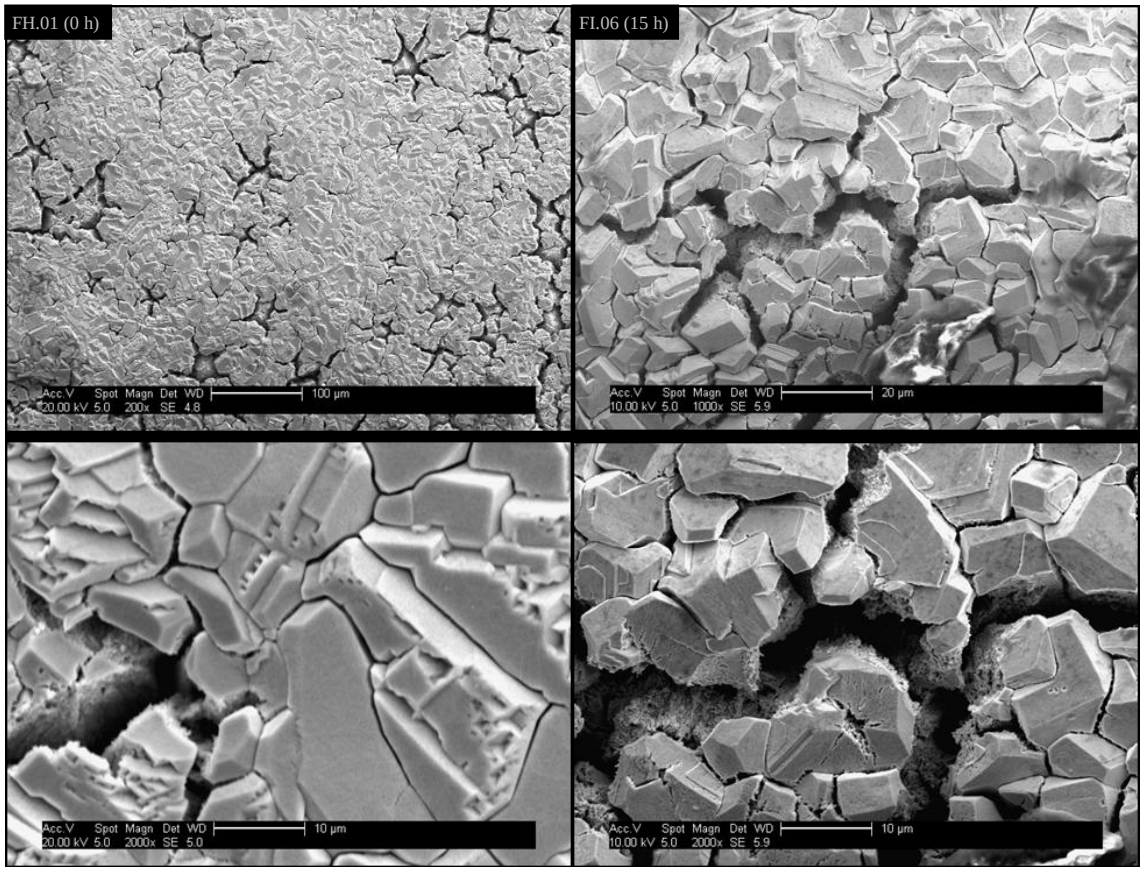
FH.01 (0 h)
Acc.V Spot Magn Det WD
20.00 kV 5.0 200x SE 4.8
100 µm
FI.06 (15 h)
Acc.V Spot Magn Det WD
10.00 kV 5.0 1000x SE 5.9
20 µm
Acc.V Spot Magn Det WD
20.00 kV 5.0 2000x SE 5.0
10 µm
Acc.V Spot Magn Det WD
10.00 kV 5.0 2000x SE 5.9
10 µm

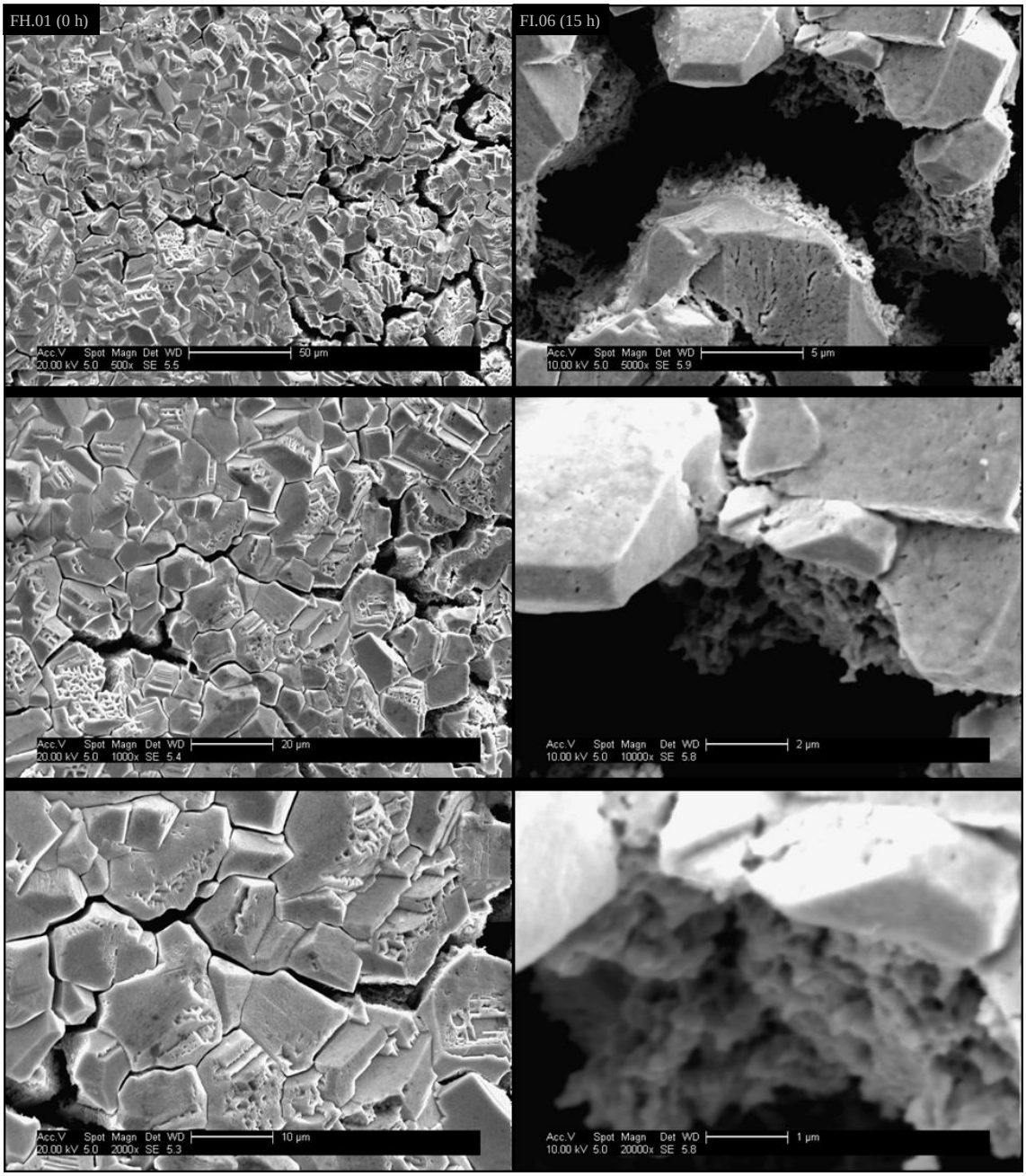
FH.01 (0 h)
FI.06 (15 h)
Acc.V Spot Magn Det WD 50 µm
20.00 kV 5.0 600x SE 5.5
Acc.V Spot Magn Det WD 5 µm
10.00 kV 5.0 5000x SE 5.9
Acc.V Spot Magn Det WD 20 µm
20.00 kV 5.0 1000x SE 5.4
Acc.V Spot Magn Det WD 2 µm
10.00 kV 5.0 10000x SE 5.8
Acc.V Spot Magn Det WD 10 µm
20.00 kV 5.0 2000x SE 5.3
Acc.V Spot Magn Det WD 1 µm
10.00 kV 5.0 20000x SE 5.8

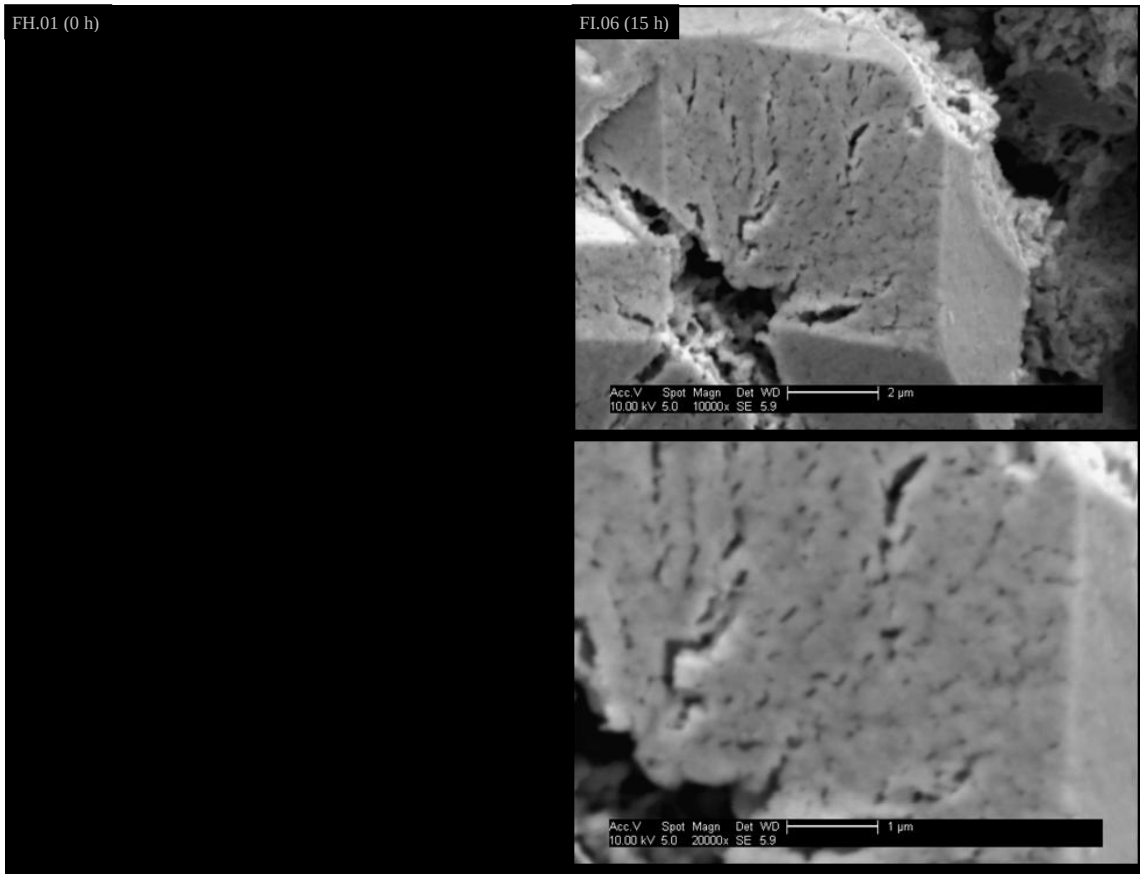

Figure H–1. SEM micrographs of the surface morphology of samples reduced at 400 °C. Images are ordered: from top to bottom in order of increasing apparent magnification; left column is 0 h dwell (ramp only – the minimum possible) and right column is 15 h dwell (nominally fully reduced). Samples: RT-A.04/03/13-125.1100(400)-FH.01 (downstream) and RT-A.17/07/13-125.1100(400)-FI.06 (upstream).

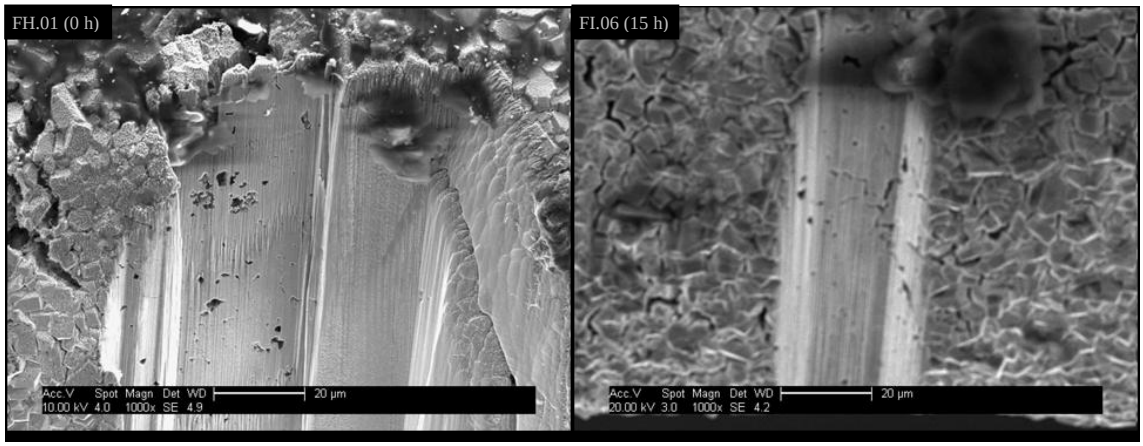

Figure H–2. SEM micrographs showing the overall cross-section of samples reduced at 400 °C. Images are ordered: left column is 0 h dwell (ramp only – the minimum possible) and right column is 15 h dwell (nominally fully reduced). Samples: RT-A.04/03/13-125.1100(400)-FH.01 (downstream) and RT-A.17/07/13-125.1100(400)-FI.06 (upstream).

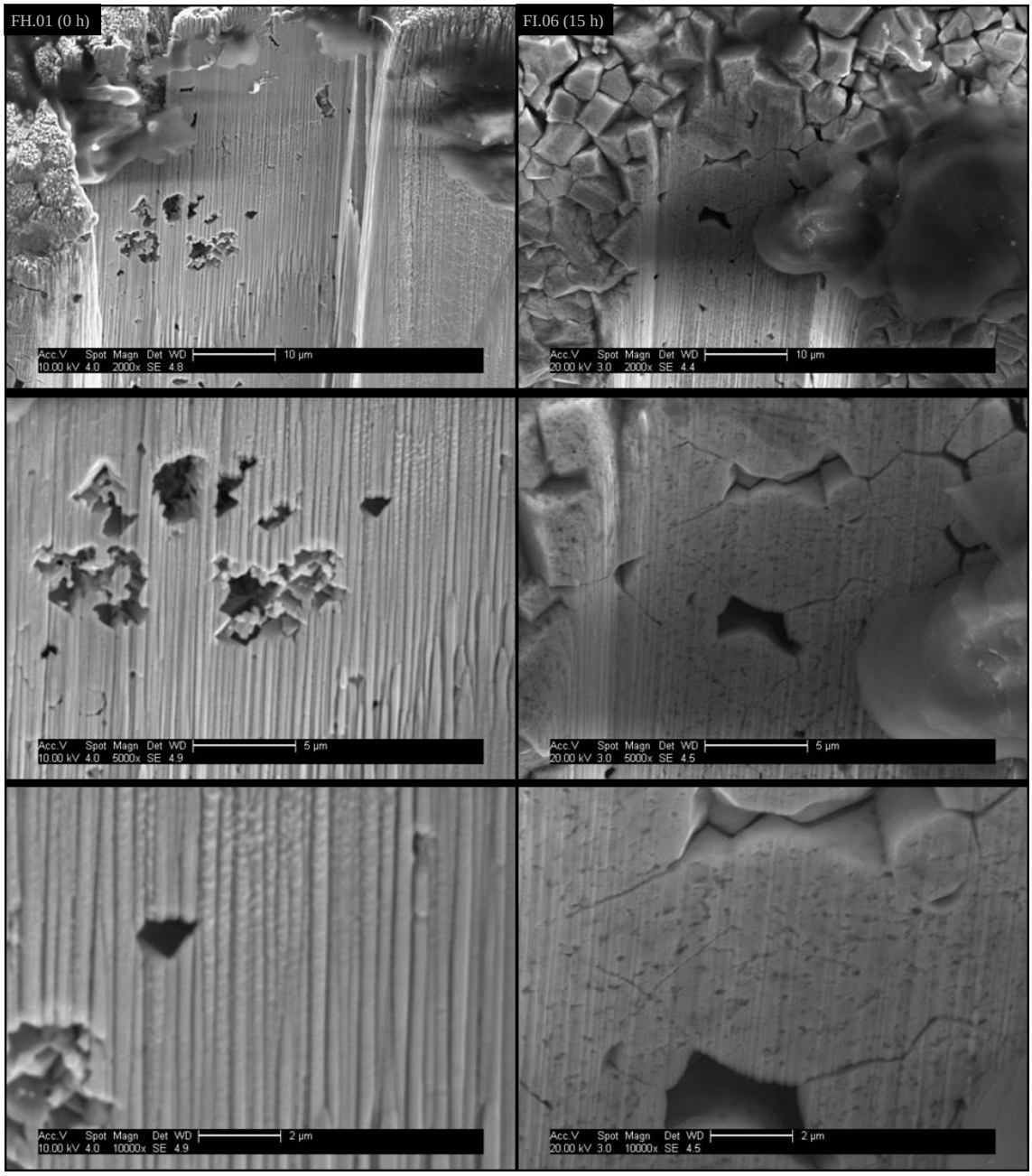
FH.01 (0 h)
FI.06 (15 h)
Acc.V Spot Magn Det WD 10 µm
10.00 kV 4.0 2000x SE 4.8
Acc.V Spot Magn Det WD 10 µm
20.00 kV 3.0 2000x SE 4.4
Acc.V Spot Magn Det WD 5 µm
10.00 kV 4.0 5000x SE 4.9
Acc.V Spot Magn Det WD 5 µm
20.00 kV 3.0 5000x SE 4.5
Acc.V Spot Magn Det WD 2 µm
10.00 kV 4.0 10000x SE 4.9
Acc.V Spot Magn Det WD 2 µm
20.00 kV 3.0 10000x SE 4.5

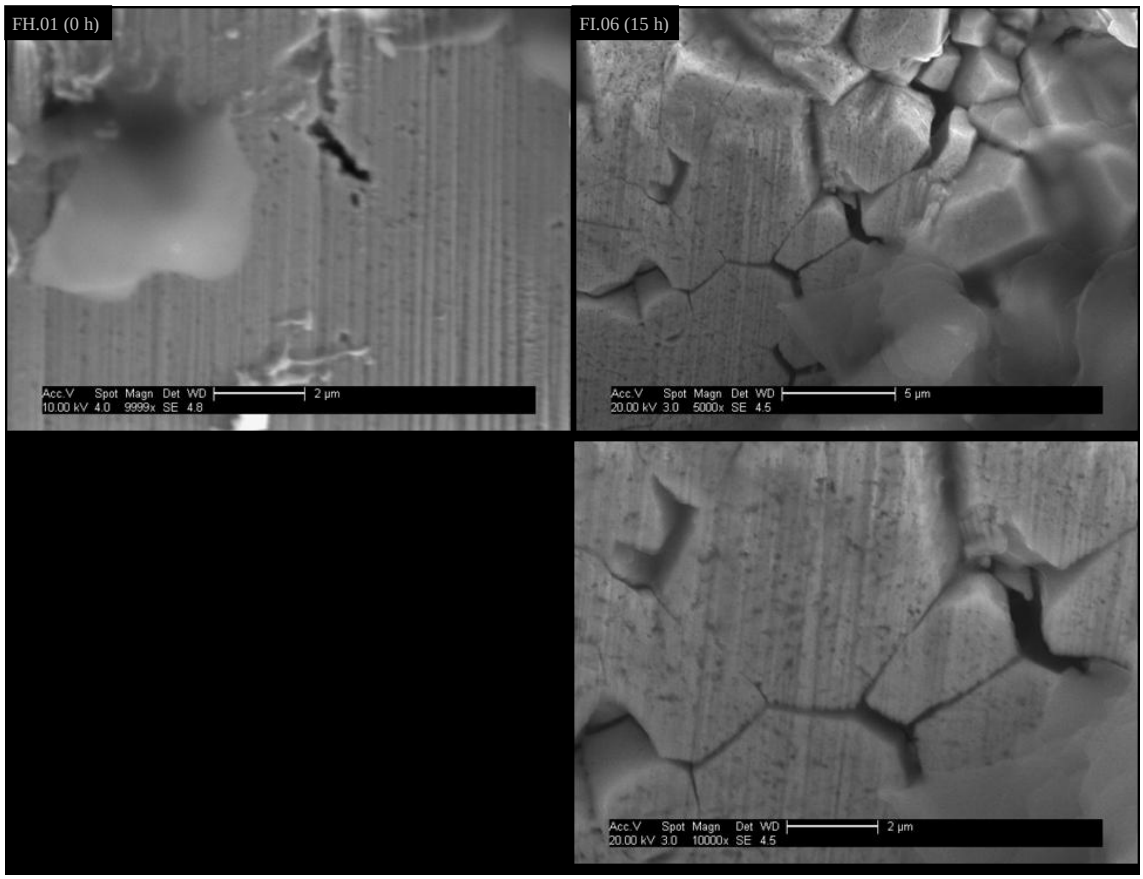

Figure H–3. SEM micrographs showing the cross-section near the outer edge of samples reduced at 400 °C. Images are ordered: from top to bottom in order of increasing apparent magnification; left column is 0 h dwell (ramp only – the minimum possible) and right column is 15 h dwell (nominally fully reduced). Samples: RT-A.04/03/13-125.1100(400)-FH.01 (downstream) and RT-A.17/07/13-125.1100(400)-FI.06 (upstream).

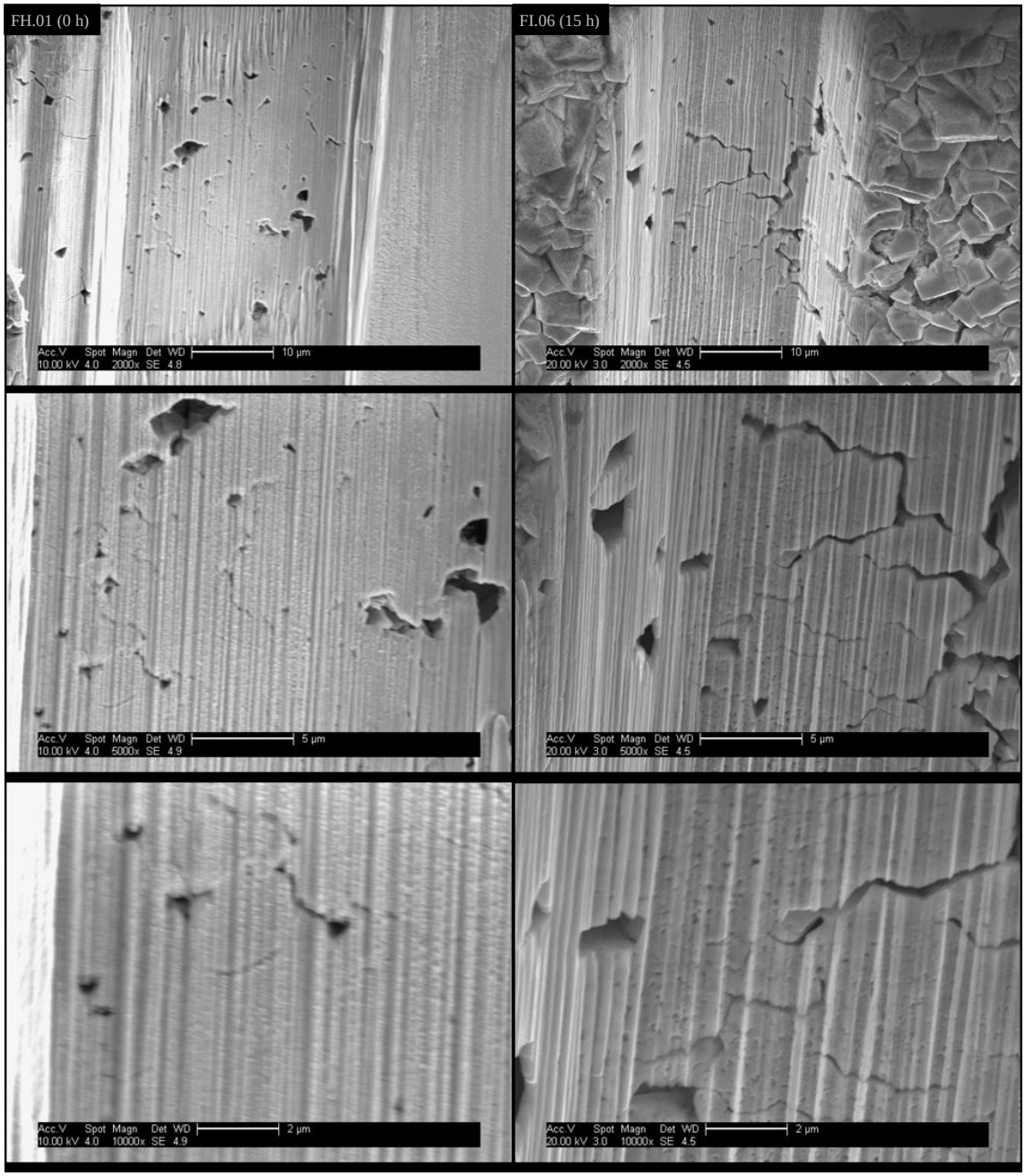

Figure H–4. SEM micrographs showing the cross-section near the middle of samples reduced at 400 °C. Images are ordered: from top to bottom in order of increasing apparent magnification; left column is 0 h dwell (ramp only – the minimum possible) and right column is 15 h dwell (nominally fully reduced). Samples: RT-A.04/03/13-125.1100(400)-FH.01 (downstream) and RT-A.17/07/13-125.1100(400)-FI.06 (upstream).

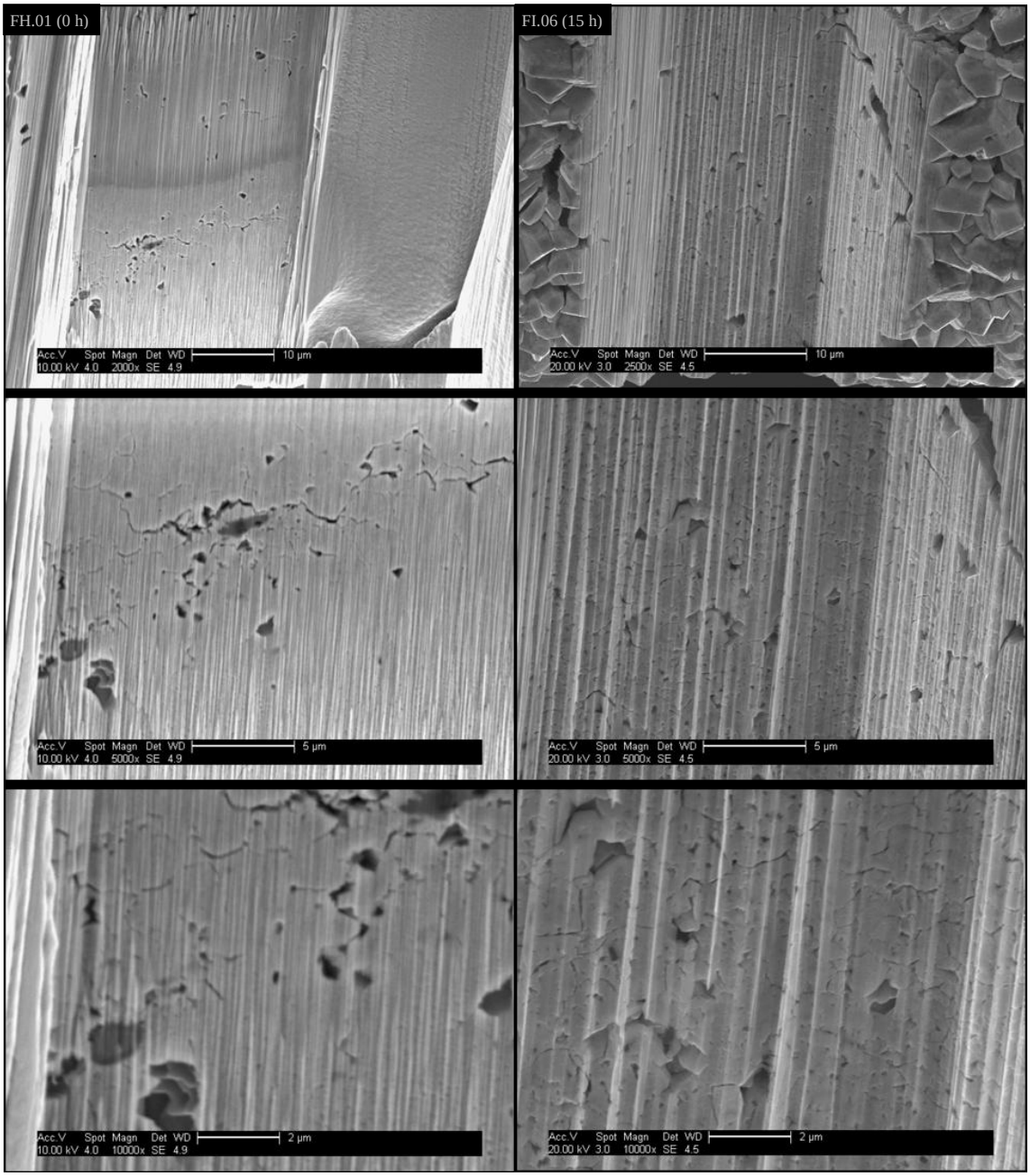
FH.01 (0 h)
FI.06 (15 h)
Acc.V Spot Magn Det WD 10 µm
10.00 kV 4.0 2000x SE 4.9
Acc.V Spot Magn Det WD 10 µm
20.00 kV 3.0 2500x SE 4.5
Acc.V Spot Magn Det WD 5 µm
10.00 kV 4.0 5000x SE 4.9
Acc.V Spot Magn Det WD 5 µm
20.00 kV 3.0 5000x SE 4.5
Acc.V Spot Magn Det WD 2 µm
10.00 kV 4.0 10000x SE 4.9
Acc.V Spot Magn Det WD 2 µm
20.00 kV 3.0 10000x SE 4.5

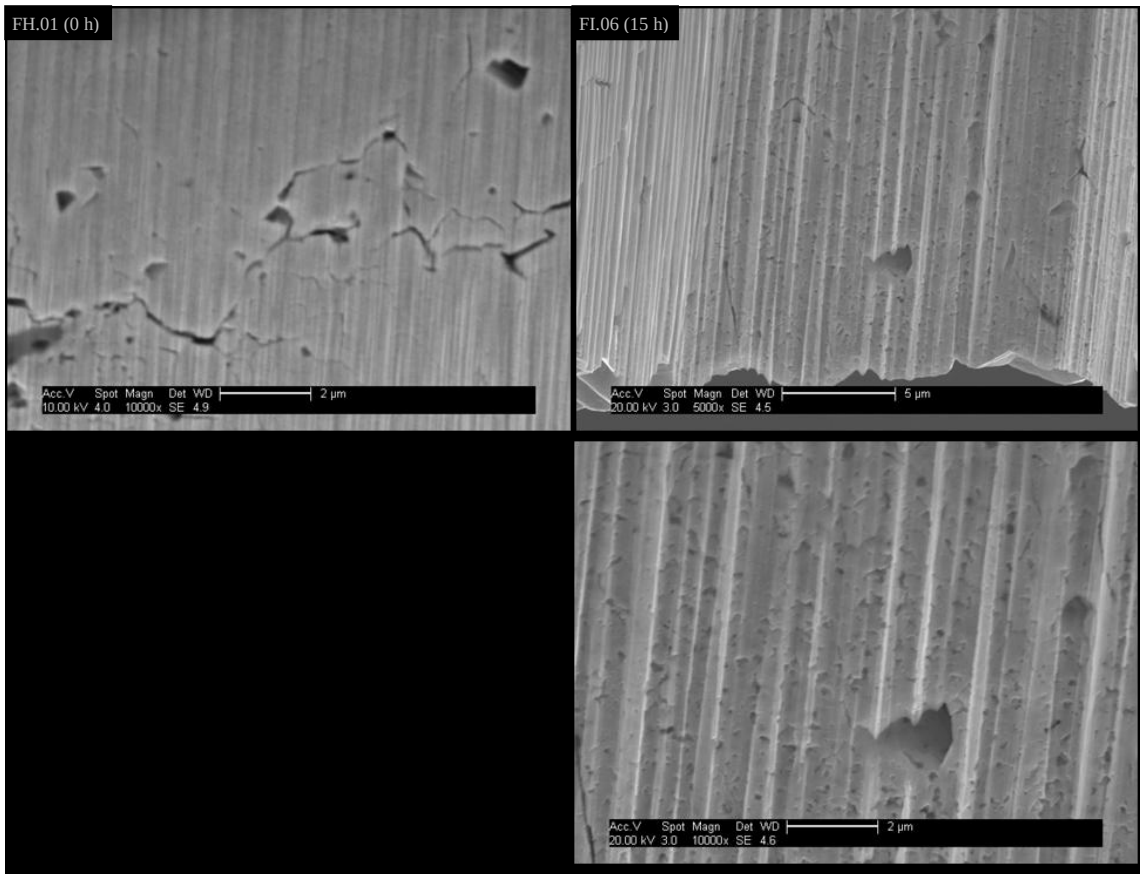

Figure H–5. SEM micrographs showing the cross-section near the inner edge of samples reduced at 400 °C. Images are ordered: from top to bottom in order of increasing apparent magnification; left column is 0 h dwell (ramp only – the minimum possible) and right column is 15 h dwell (nominally fully reduced). Samples: RT-A.04/03/13-125.1100(400)-FH.01 (downstream) and RT-A.17/07/13-125.1100(400)-FI.06 (upstream).

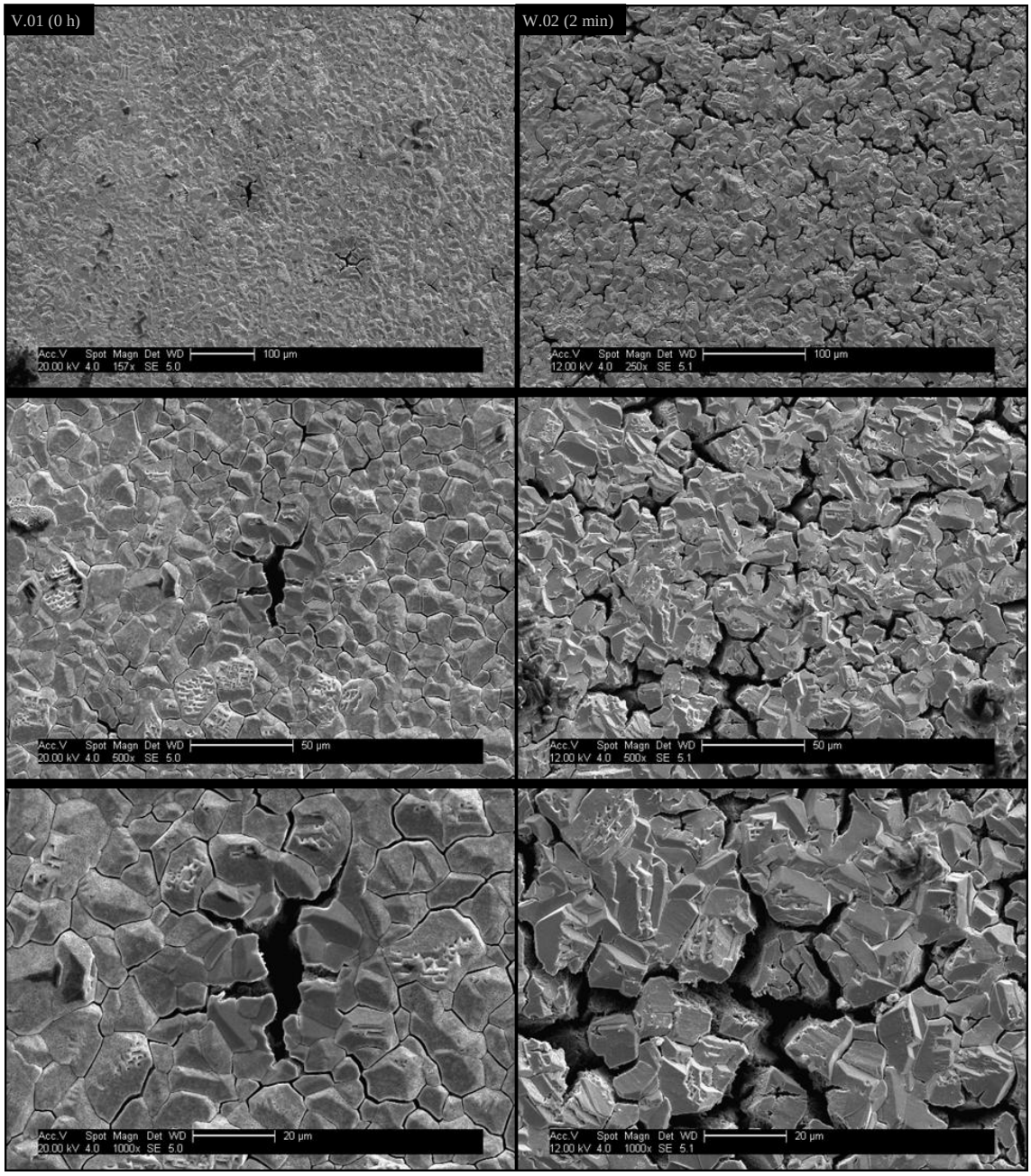
V.01 (0 h)
W.02 (2 min)
Acc.V Spot Magn Det WD 100 µm
20.00 kV 4.0 157x SE 5.0
Acc.V Spot Magn Det WD 100 µm
12.00 kV 4.0 250x SE 5.1
Acc.V Spot Magn Det WD 50 µm
20.00 kV 4.0 500x SE 5.0
Acc.V Spot Magn Det WD 50 µm
12.00 kV 4.0 500x SE 5.1
Acc.V Spot Magn Det WD 20 µm
20.00 kV 4.0 1000x SE 5.0
Acc.V Spot Magn Det WD 20 µm
12.00 kV 4.0 1000x SE 5.1

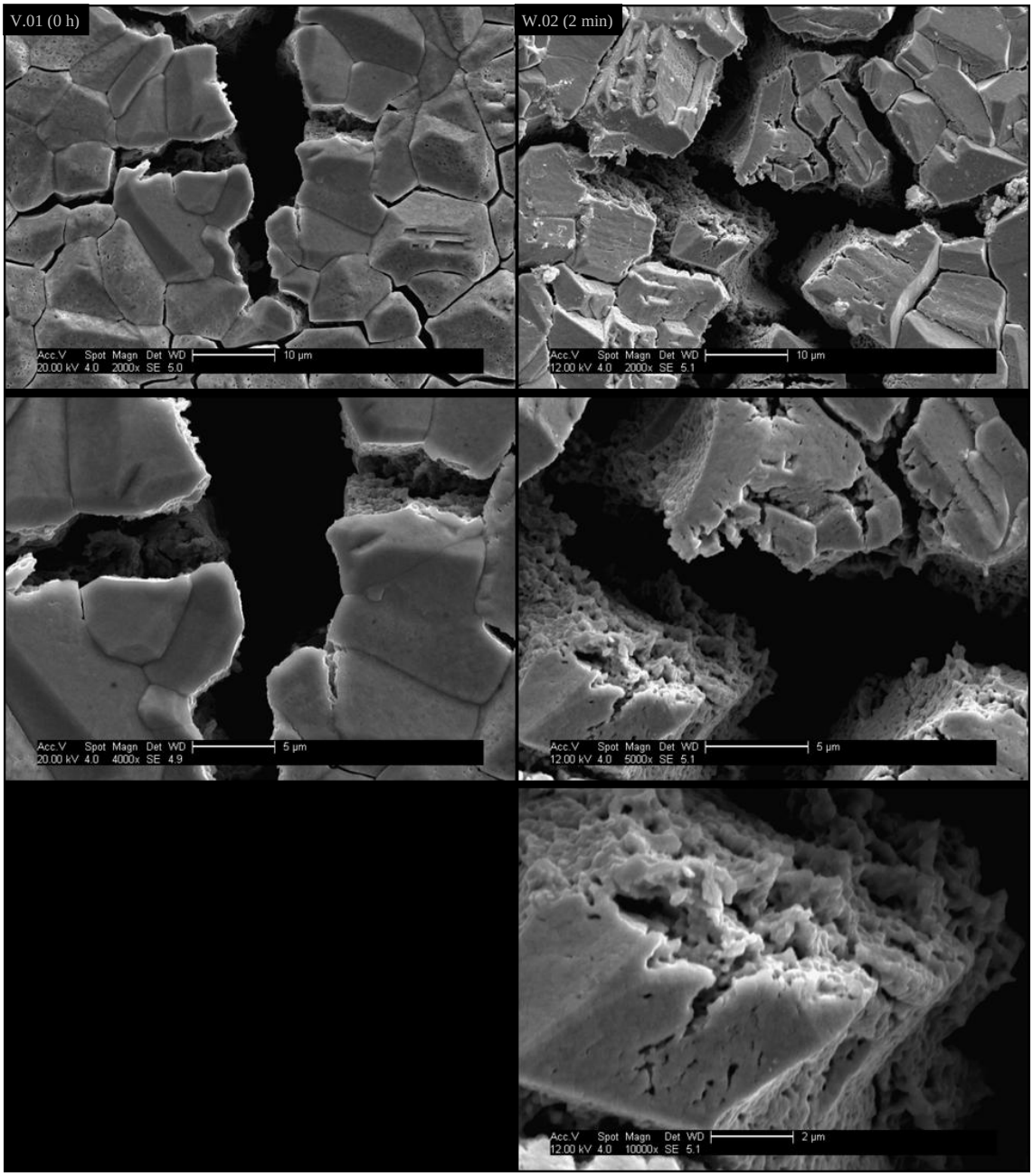
V.01 (0 h)
W.02 (2 min)
Acc.V Spot Magn Det WD
20.00 kV 4.0 2000x SE 5.0
10 µm
Acc.V Spot Magn Det WD
12.00 kV 4.0 2000x SE 5.1
10 µm
Acc.V Spot Magn Det WD
20.00 kV 4.0 4000x SE 4.9
5 µm
Acc.V Spot Magn Det WD
12.00 kV 4.0 5000x SE 5.1
5 µm
Acc.V Spot Magn Det WD
12.00 kV 4.0 10000x SE 5.1
2 µm

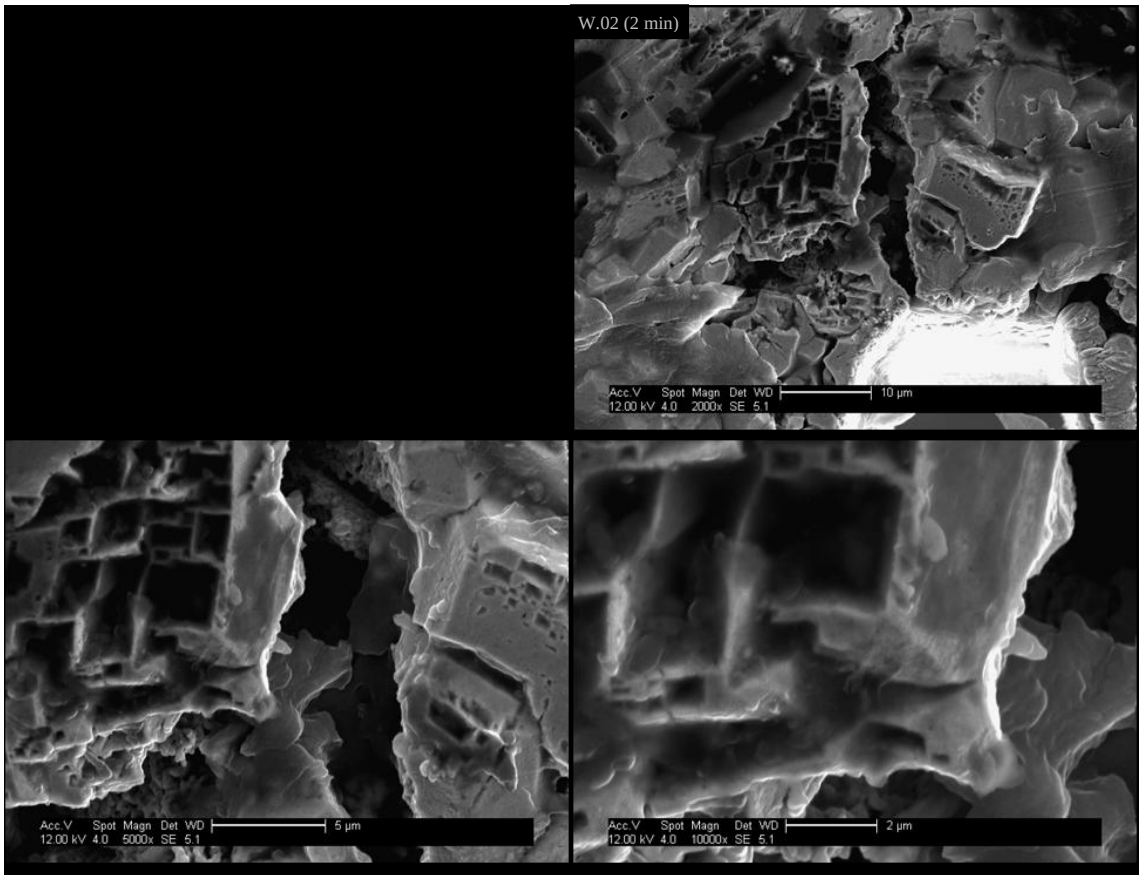

Figure H–6. SEM micrographs of the surface morphology of samples reduced at 600 °C. Images are ordered: from top to bottom in order of increasing apparent magnification; left column is 0 h dwell (ramp only – the minimum possible) and right column is 2 min dwell (nominally fully reduced). Samples: RT-A.19/02/13-125.1100(600)-V.01 (midstream) and RT-A.04/03/13-125.1100(600)-W.02 (downstream).

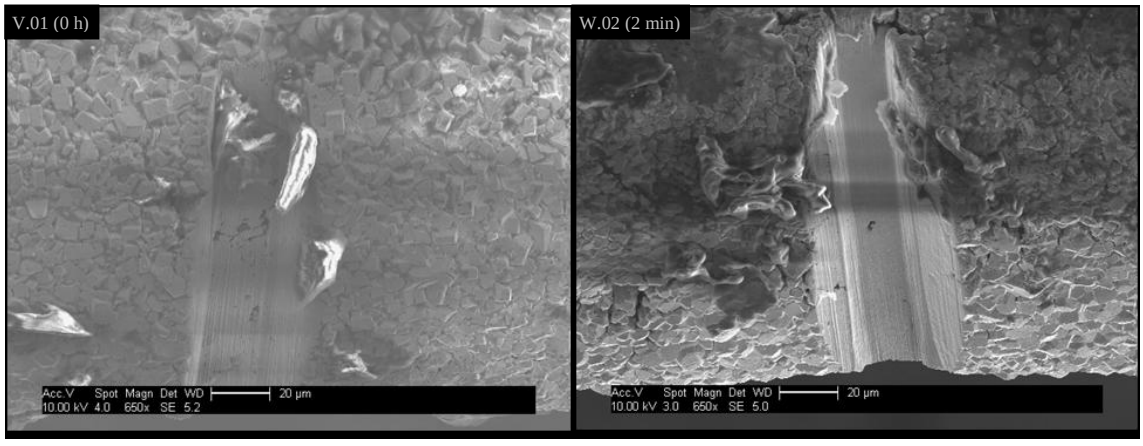

Figure H–7. SEM micrographs showing the overall cross-section of samples reduced at 600 °C. Images are ordered: left column is 0 h dwell (ramp only – the minimum possible) and right column is 2 min dwell (nominally fully reduced). Samples: RT-A.19/02/13-125.1100(600)-V.01 (midstream) and RT-A.04/03/13-125.1100(600)-W.02 (downstream).

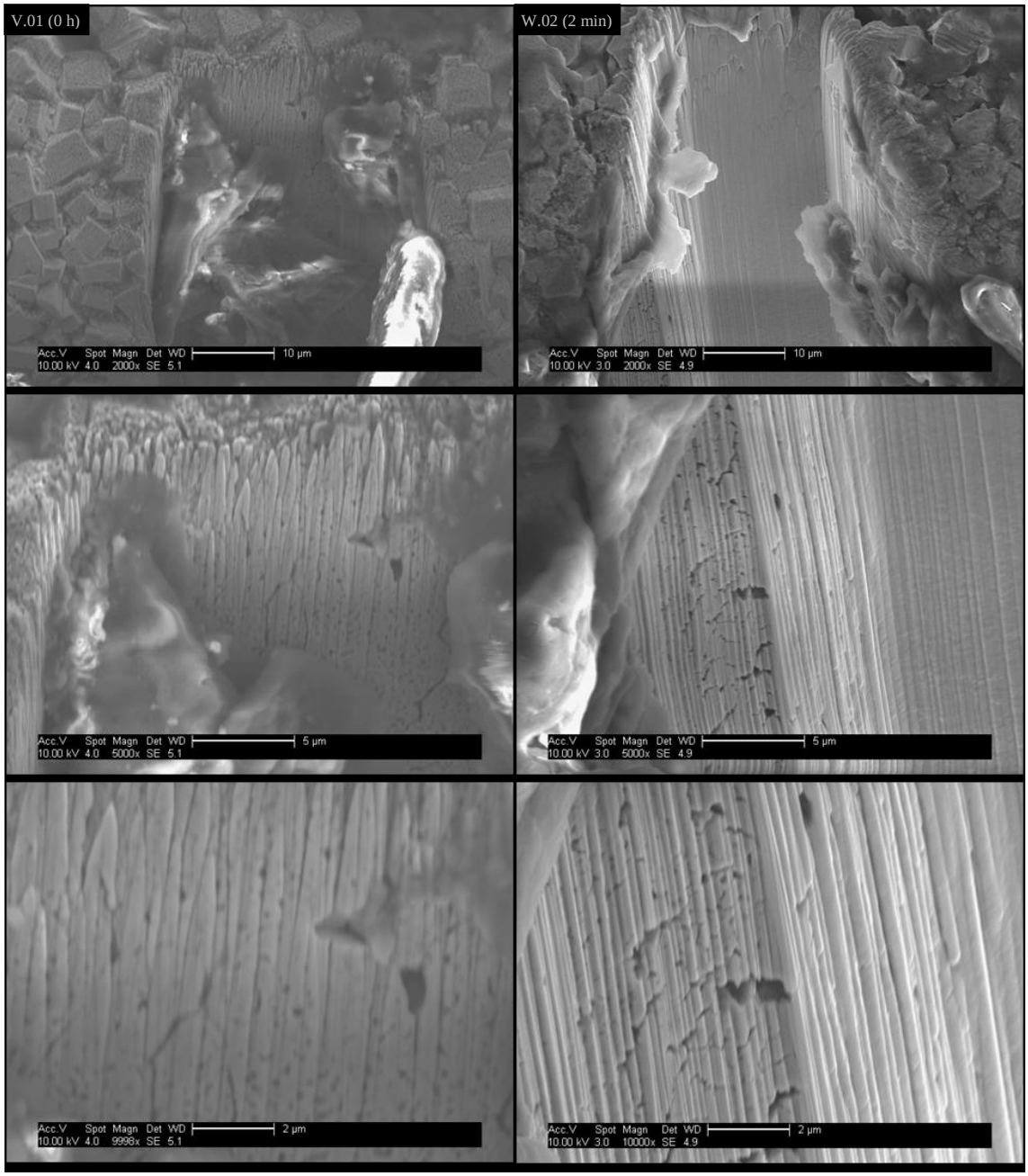

Figure H–8. SEM micrographs showing the cross-section near the outer edge of samples reduced at 600 °C. Images are ordered: from top to bottom in order of increasing apparent magnification; left column is 0 h dwell (ramp only – the minimum possible) and right column is 2 min dwell (nominally fully reduced). Samples: RT-A.19/02/13-125.1100(600)-V.01 (midstream) and RT-A.04/03/13-125.1100(600)-W.02 (downstream). Note that part of the trench appears to have become clogged with debris from an unknown source that was not removed by rinsing the sample with acetone prior to imaging by SEM. This obscures some images yet sufficient detail remains visible.

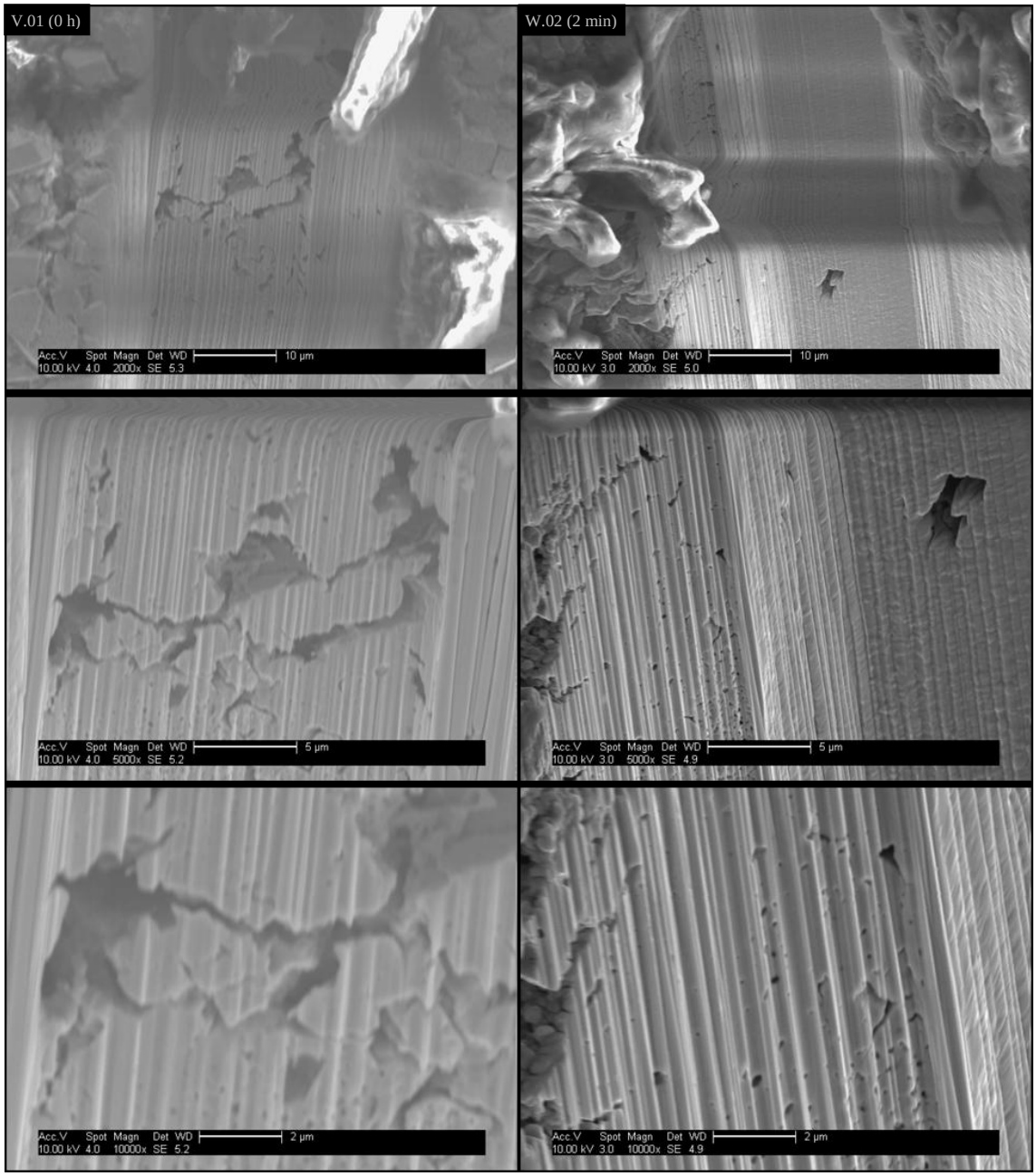
V.01 (0 h)
W.02 (2 min)
Acc.V Spot Magn Det WD 10 µm
10.00 kV 4.0 2000x SE 5.3
Acc.V Spot Magn Det WD 10 µm
10.00 kV 3.0 2000x SE 5.0
Acc.V Spot Magn Det WD 5 µm
10.00 kV 4.0 5000x SE 5.2
Acc.V Spot Magn Det WD 5 µm
10.00 kV 3.0 5000x SE 4.9
Acc.V Spot Magn Det WD 2 µm
10.00 kV 4.0 10000x SE 5.2
Acc.V Spot Magn Det WD 2 µm
10.00 kV 3.0 10000x SE 4.9

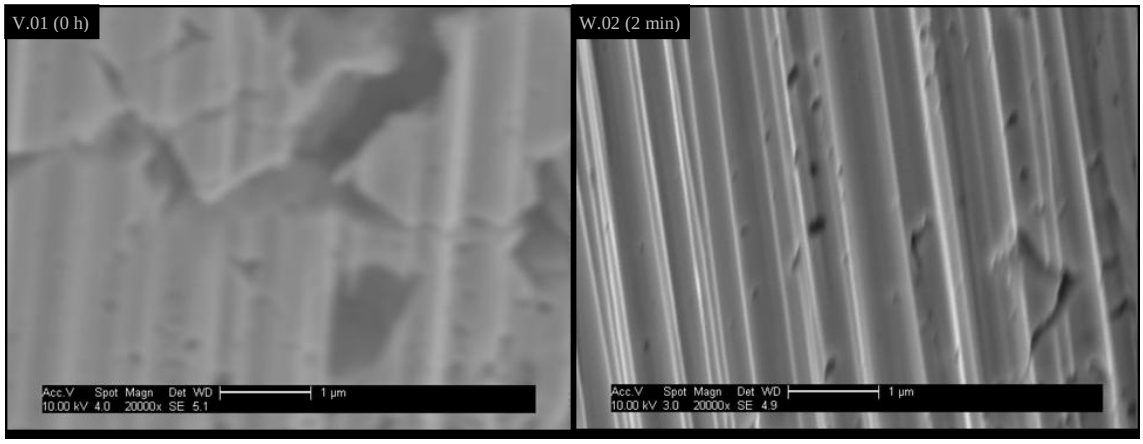

Figure H–9. SEM micrographs showing the cross-section near the middle of samples reduced at 600 °C. Images are ordered: from top to bottom in order of increasing apparent magnification; left column is 0 h dwell (ramp only – the minimum possible) and right column is 2 min dwell (nominally fully reduced). Samples: RT-A.19/02/13-125.1100(600)-V.01 (midstream) and RT-A.04/03/13-125.1100(600)-W.02 (downstream).

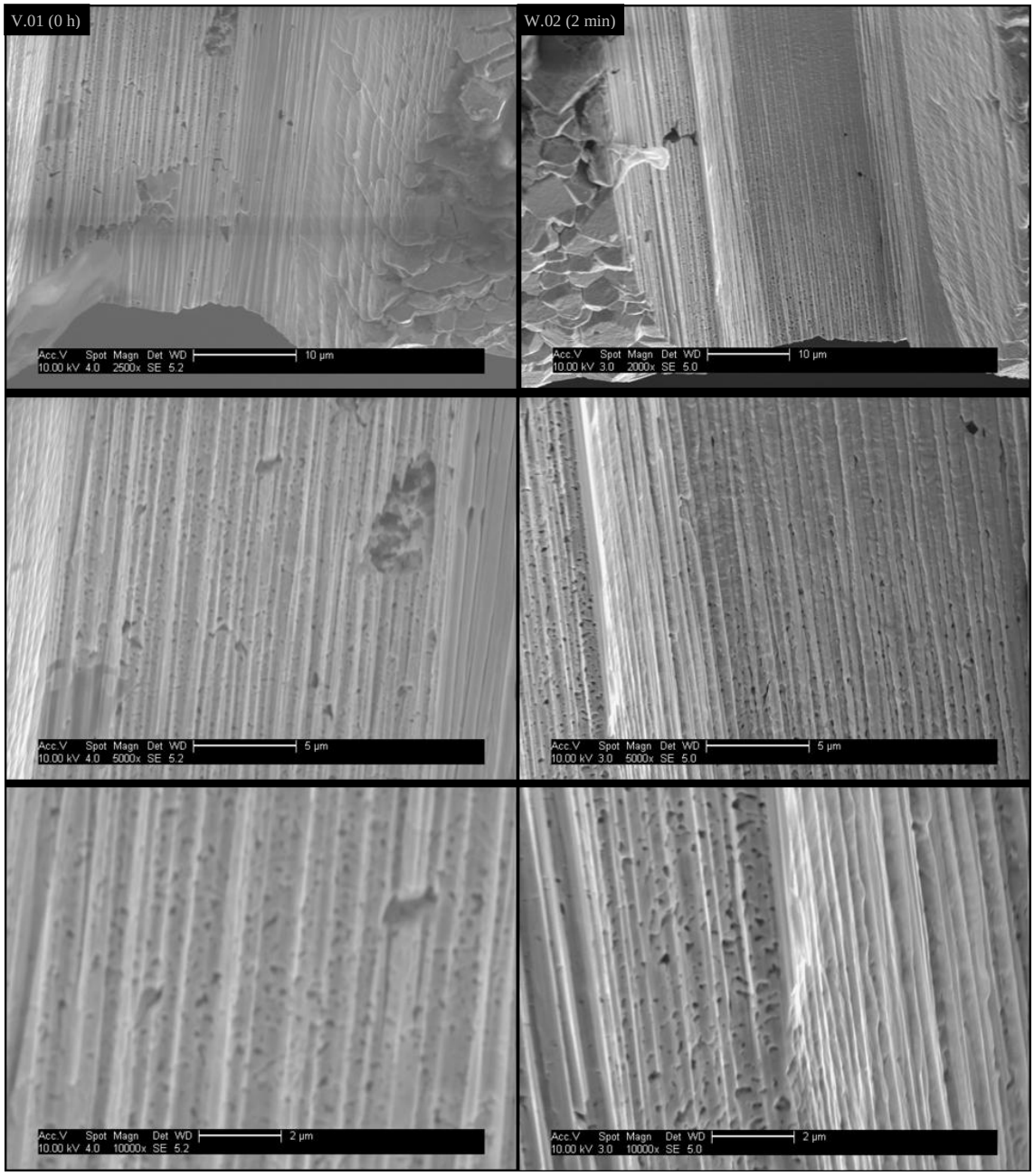
V.01 (0 h)
W.02 (2 min)
Acc.V Spot Magn Det WD 10 µm
10.00 kV 4.0 2500x SE 5.2
Acc.V Spot Magn Det WD 10 µm
10.00 kV 3.0 2000x SE 5.0
Acc.V Spot Magn Det WD 5 µm
10.00 kV 4.0 5000x SE 5.2
Acc.V Spot Magn Det WD 5 µm
10.00 kV 3.0 5000x SE 5.0
Acc.V Spot Magn Det WD 2 µm
10.00 kV 4.0 10000x SE 5.2
Acc.V Spot Magn Det WD 2 µm
10.00 kV 3.0 10000x SE 5.0

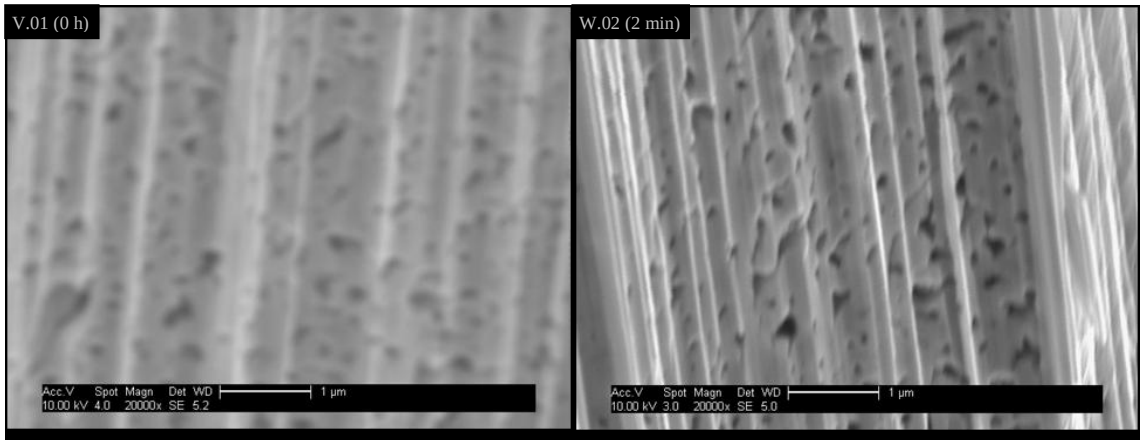

Figure H–10. SEM micrographs showing the cross-section near the inner edge of samples reduced at 600 °C. Images are ordered: from top to bottom in order of increasing apparent magnification; left column is 0 h dwell (ramp only – the minimum possible) and right column is 2 min dwell (nominally fully reduced). Samples: RT-A.19/02/13-125.1100(600)-V.01 (midstream) and RT-A.04/03/13-125.1100(600)-W.02 (downstream).

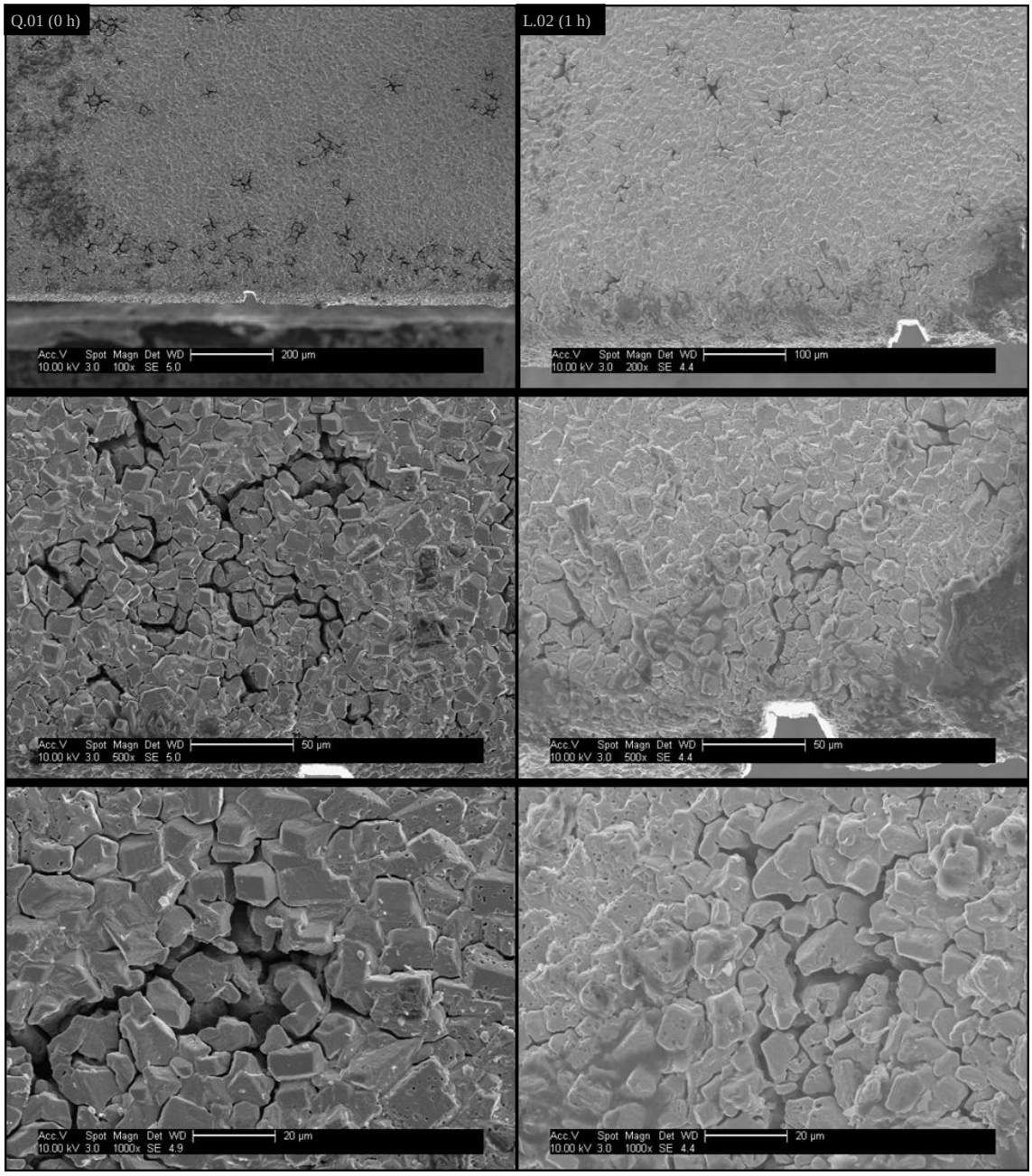
Q.01 (0 h)
L.02 (1 h)
Acc.V Spot Magn Det WD 200 µm
10.00 kV 3.0 100x SE 5.0
Acc.V Spot Magn Det WD 100 µm
10.00 kV 3.0 200x SE 4.4
Acc.V Spot Magn Det WD 50 µm
10.00 kV 3.0 500x SE 5.0
Acc.V Spot Magn Det WD 50 µm
10.00 kV 3.0 500x SE 4.4
Acc.V Spot Magn Det WD 20 µm
10.00 kV 3.0 1000x SE 4.9
Acc.V Spot Magn Det WD 20 µm
10.00 kV 3.0 1000x SE 4.4

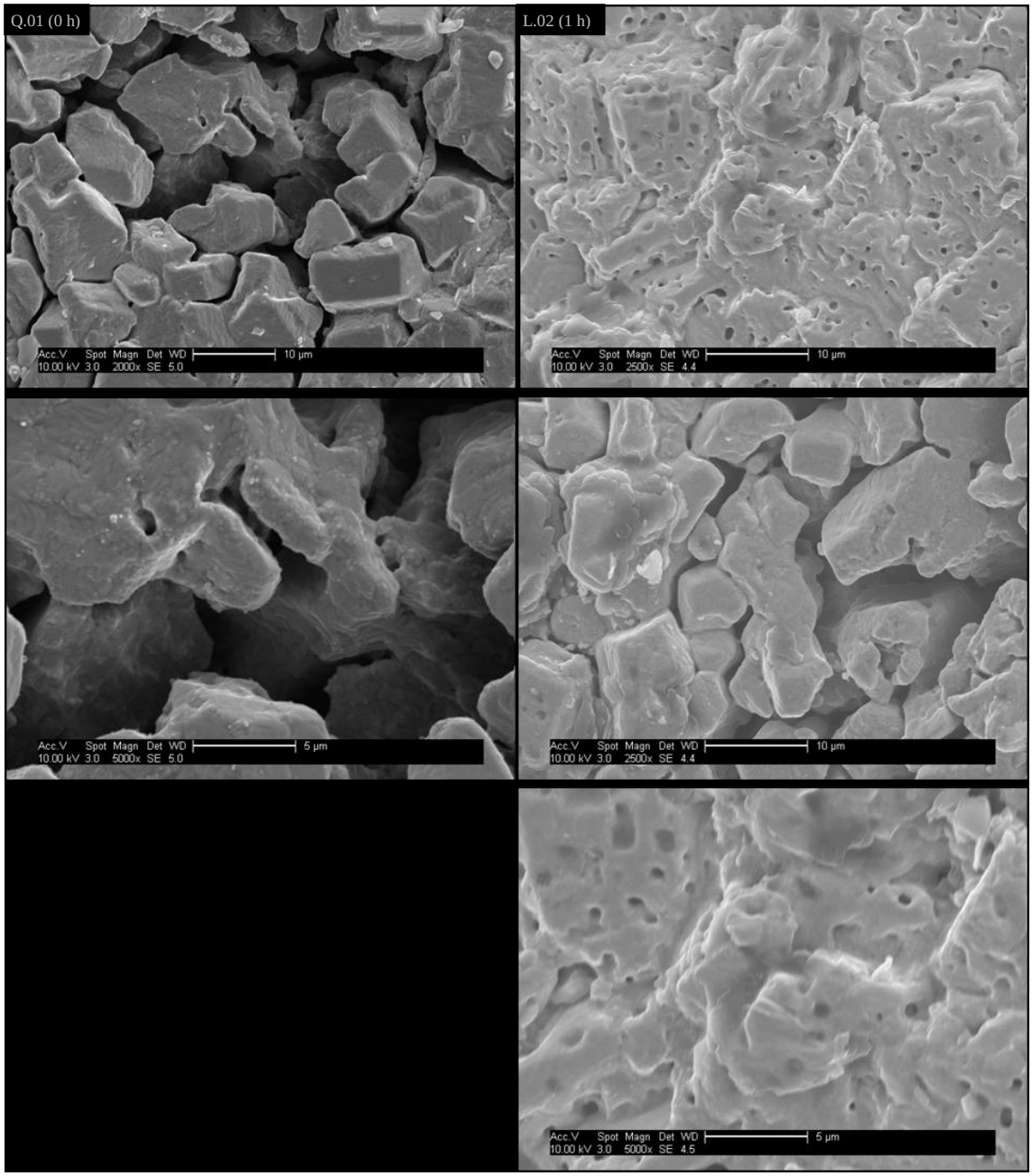
Q.01 (0 h)
L.02 (1 h)
Acc.V Spot Magn Det WD 10 µm
10.00 kV 3.0 2000x SE 5.0
Acc.V Spot Magn Det WD 10 µm
10.00 kV 3.0 2500x SE 4.4
Acc.V Spot Magn Det WD 5 µm
10.00 kV 3.0 5000x SE 5.0
Acc.V Spot Magn Det WD 10 µm
10.00 kV 3.0 2500x SE 4.4
Acc.V Spot Magn Det WD 5 µm
10.00 kV 3.0 5000x SE 4.5

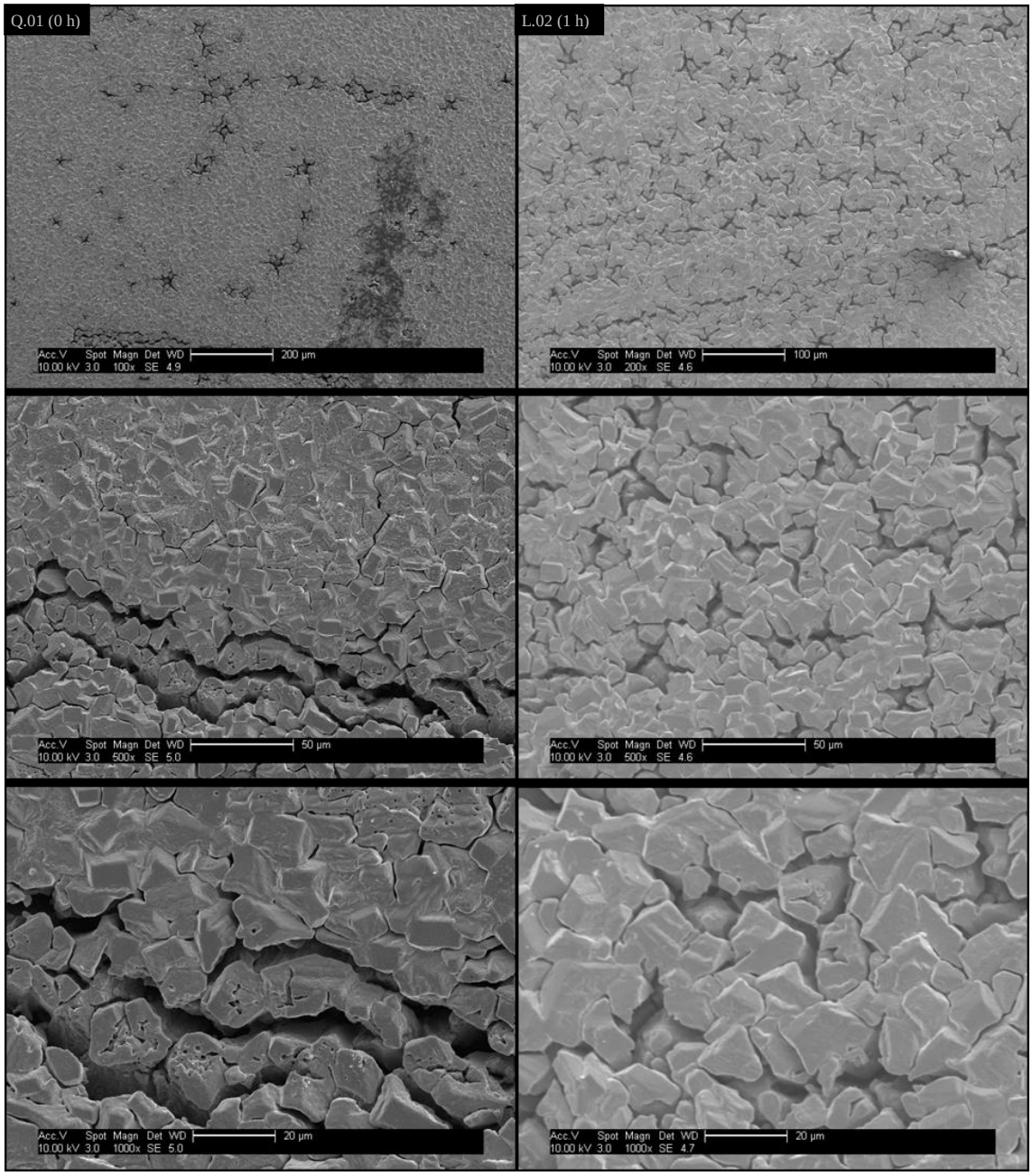
Q.01 (0 h)
L.02 (1 h)
Acc.V Spot Magn Det WD 200 µm
10.00 kV 3.0 100x SE 4.9
Acc.V Spot Magn Det WD 100 µm
10.00 kV 3.0 200x SE 4.6
Acc.V Spot Magn Det WD 50 µm
10.00 kV 3.0 500x SE 5.0
Acc.V Spot Magn Det WD 50 µm
10.00 kV 3.0 500x SE 4.6
Acc.V Spot Magn Det WD 20 µm
10.00 kV 3.0 1000x SE 5.0
Acc.V Spot Magn Det WD 20 µm
10.00 kV 3.0 1000x SE 4.7

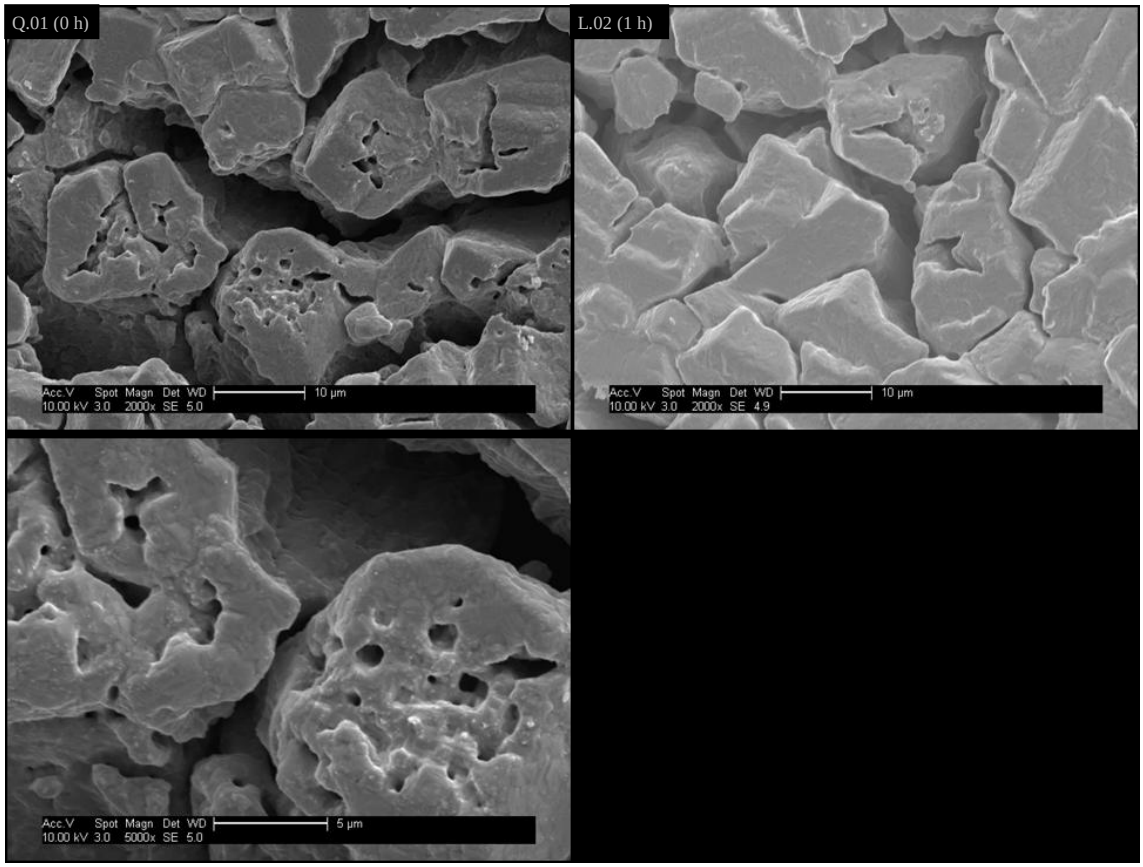
Q.01 (0 h)
Acc.V Spot Magn Det WD
10.00 kV 3.0 2000x SE 5.0
10 µm
L.02 (1 h)
Acc.V Spot Magn Det WD
10.00 kV 3.0 2000x SE 4.9
10 µm
Acc.V Spot Magn Det WD
10.00 kV 3.0 5000x SE 5.0
5 µm

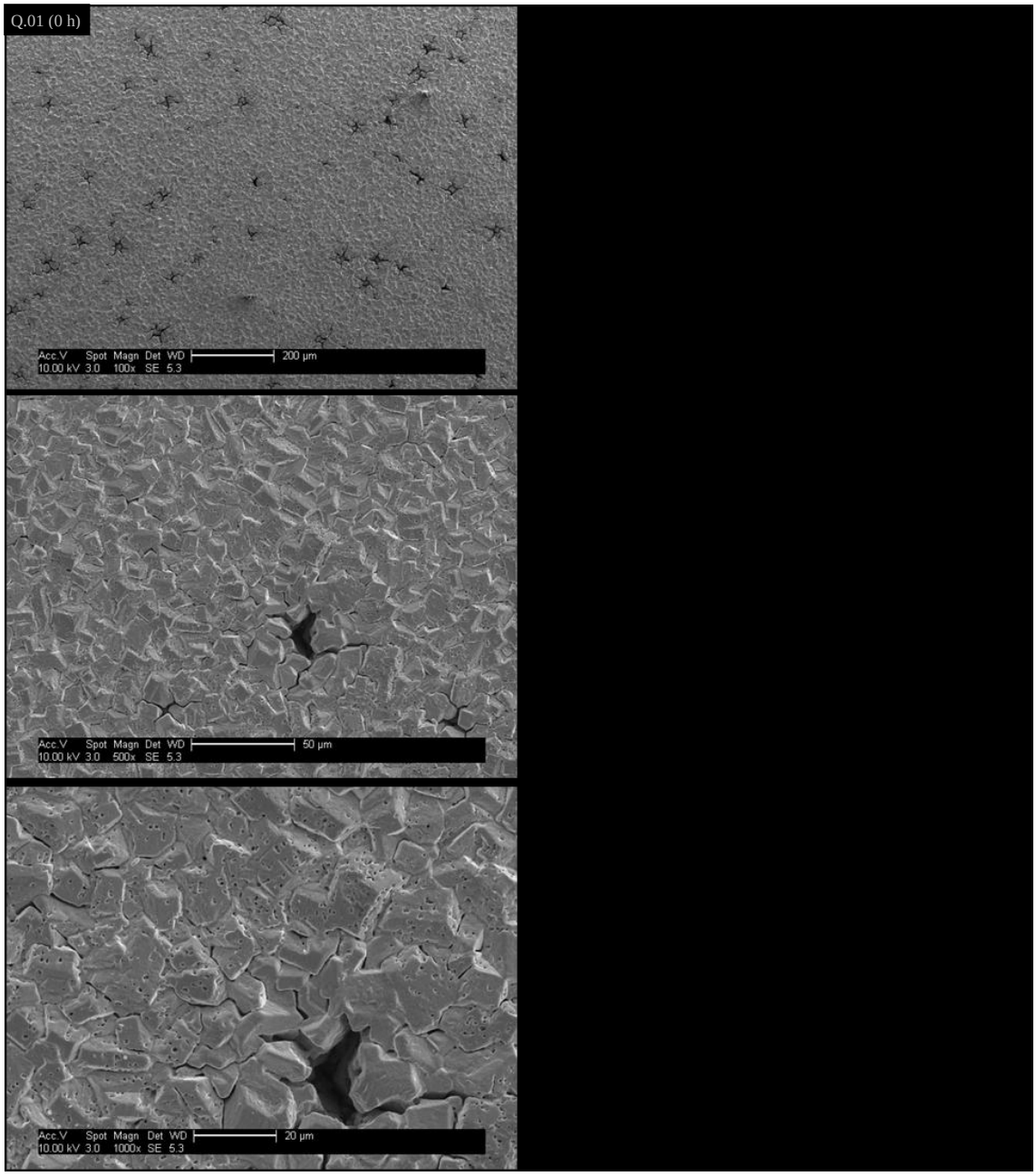
Q.01 (0 h)
Acc.V Spot Magn Det WD 200 µm
10.00 kV 3.0 100x SE 5.3
Acc.V Spot Magn Det WD 50 µm
10.00 kV 3.0 500x SE 5.3
Acc.V Spot Magn Det WD 20 µm
10.00 kV 3.0 1000x SE 5.3

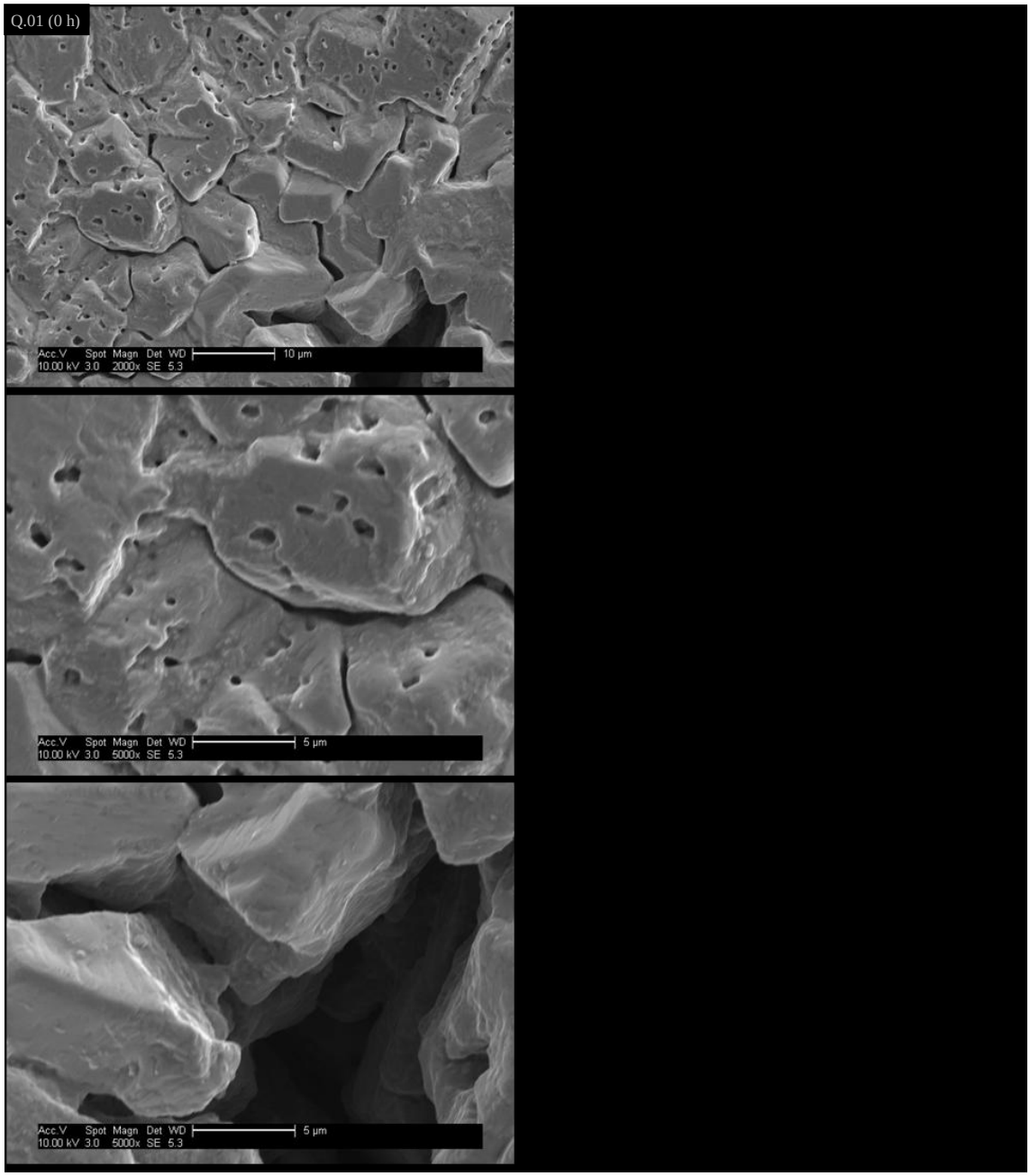

Figure H–11. SEM micrographs of the surface morphology of samples reduced at 800 °C. Images are ordered: from top to bottom in order of increasing apparent magnification; left column is 0 h dwell (ramp only – the minimum possible) and right column is 1 h dwell (nominally fully reduced). Samples: RT-A.23/10/12-125.1100(800)-Q.01 (downstream) and RT-A.23/10/12-125.1100(800)-L.02 (upstream). Both samples were coated with a few nm of AuPd by sputtering to improve resolution. The coating was omitted on those samples analysed initially because previous experience showed such coatings are visible at higher magnifications (appearing similar to reptile scales) potentially obscuring important details; pores 100 nm across or smaller. A new coater enabled coatings to be deposited that are not visible in these micrographs and do not obscure even very small pores.

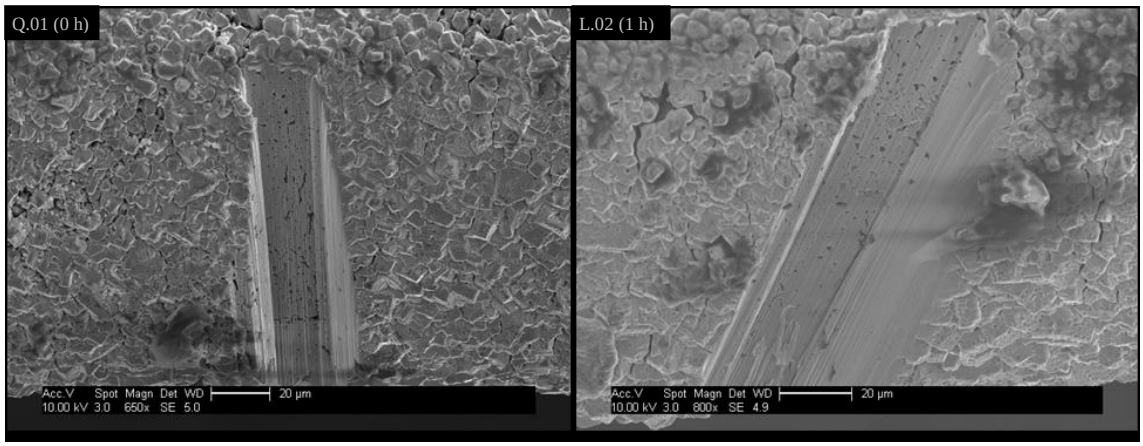

Figure H–12. SEM micrographs showing the overall cross-section of samples reduced at 800 °C. Images are ordered: left column is 0 h dwell (ramp only – the minimum possible) and right column is 1 h dwell (nominally fully reduced). Samples: RT-A.23/10/12-125.1100(800)-Q.01 (downstream) and RT-A.23/10/12-125.1100(800)-L.02 (upstream). Both samples were coated with a few nm of AuPd by sputtering to improve resolution. The coating was omitted on those samples analysed initially because previous experience showed such coatings are visible at higher magnifications (appearing similar to reptile scales) potentially obscuring important details; pores 100 nm across or smaller.

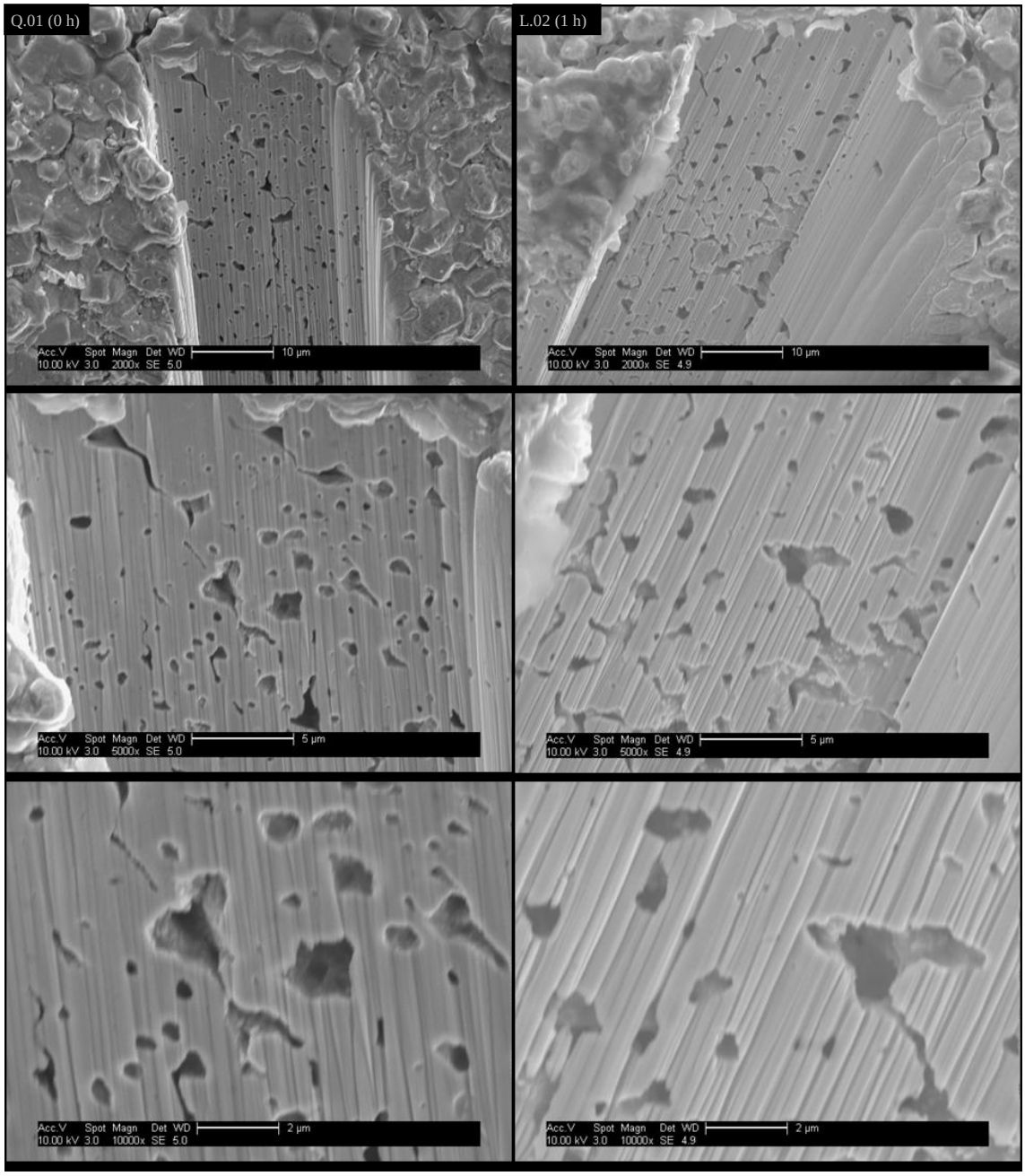

Figure H–13. SEM micrographs showing the cross-section near the outer edge of samples reduced at 800 °C. Images are ordered: from top to bottom in order of increasing apparent magnification; left column is 0 h dwell (ramp only – the minimum possible) and right column is 1 h dwell (nominally fully reduced). Samples: RT-A.23/10/12-125.1100(800)-Q.01 (downstream) and RT-A.23/10/12-125.1100(800)-L.02 (upstream). Both samples were coated with a few nm of AuPd by sputtering to improve resolution. The coating was omitted on those samples analysed initially because previous experience showed such coatings are visible at higher magnifications (appearing similar to reptile scales) potentially obscuring important details; pores 100 nm across or smaller.

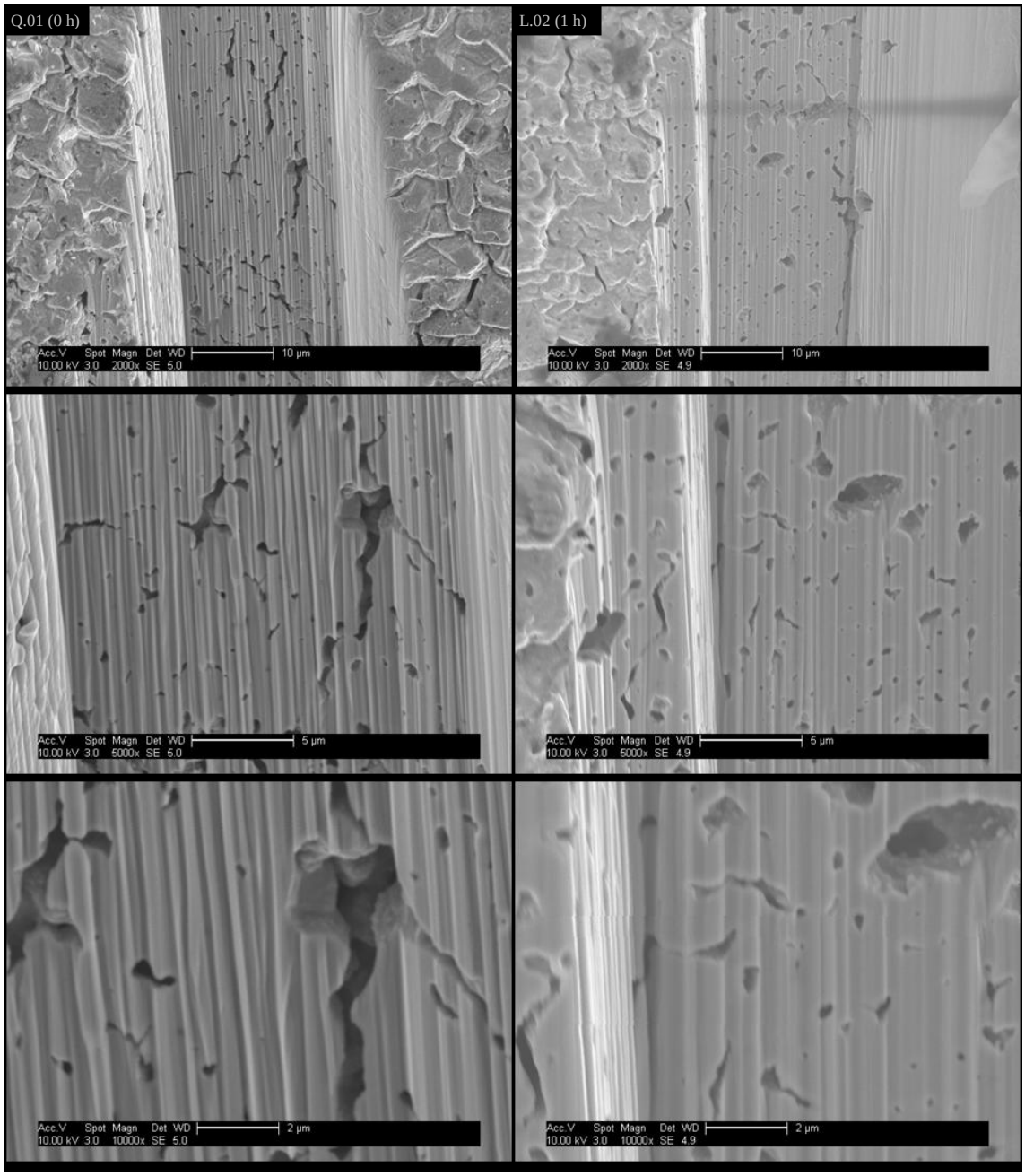

Figure H–14. SEM micrographs showing the cross-section near the middle of samples reduced at 800 °C. Images are ordered: from top to bottom in order of increasing apparent magnification; left column is 0 h dwell (ramp only – the minimum possible) and right column is 1 h dwell (nominally fully reduced). Samples: RT-A.23/10/12-125.1100(800)-Q.01 (downstream) and RT-A.23/10/12-125.1100(800)-L.02 (upstream). Both samples were coated with a few nm of AuPd by sputtering to improve resolution. The coating was omitted on those samples analysed initially because previous experience showed such coatings are visible at higher magnifications (appearing similar to reptile scales) potentially obscuring important details; pores 100 nm across or smaller.

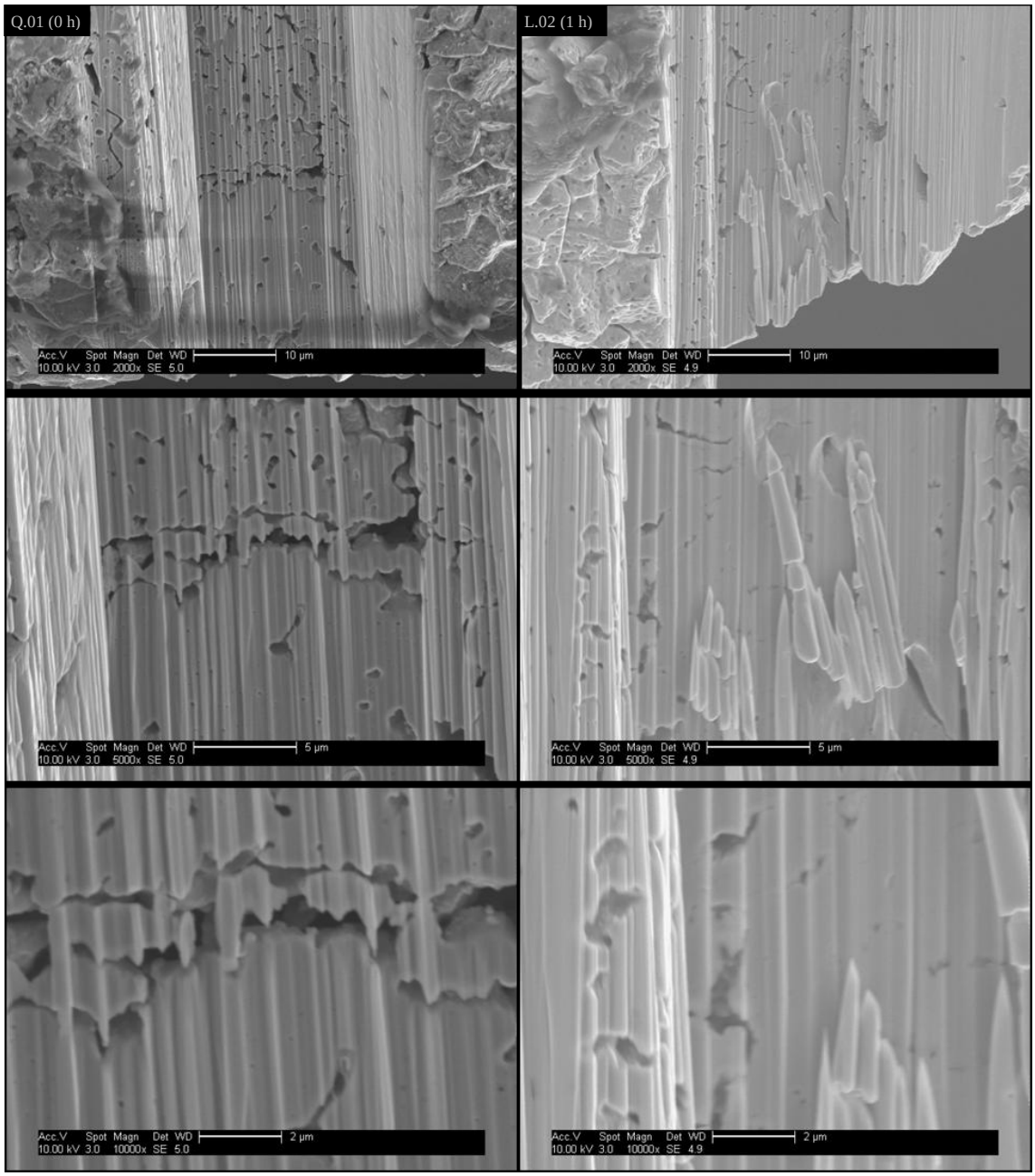
Q.01 (0 h)
L.02 (1 h)
Acc.V Spot Magn Det WD 10 µm
10.00 kV 3.0 2000x SE 5.0
Acc.V Spot Magn Det WD 10 µm
10.00 kV 3.0 2000x SE 4.9
Acc.V Spot Magn Det WD 5 µm
10.00 kV 3.0 5000x SE 5.0
Acc.V Spot Magn Det WD 5 µm
10.00 kV 3.0 5000x SE 4.9
Acc.V Spot Magn Det WD 2 µm
10.00 kV 3.0 10000x SE 5.0
Acc.V Spot Magn Det WD 2 µm
10.00 kV 3.0 10000x SE 4.9

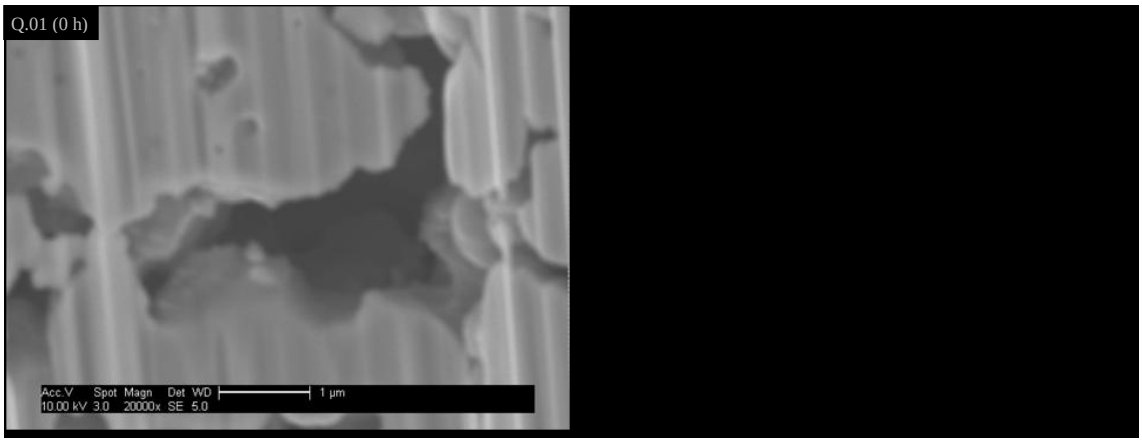

Figure H–15. SEM micrographs showing the cross-section near the inner edge of samples reduced at 800 °C. Images are ordered: from top to bottom in order of increasing apparent magnification; left column is 0 h dwell (ramp only – the minimum possible) and right column is 1 h dwell (nominally fully reduced). Samples: RT-A.23/10/12-125.1100(800)-Q.01 (downstream) and RT-A.23/10/12-125.1100(800)-L.02 (upstream). Both samples were coated with a few nm of AuPd by sputtering to improve resolution. The coating was omitted on those samples analysed initially because previous experience showed such coatings are visible at higher magnifications (appearing similar to reptile scales) potentially obscuring important details; pores 100 nm across or smaller.

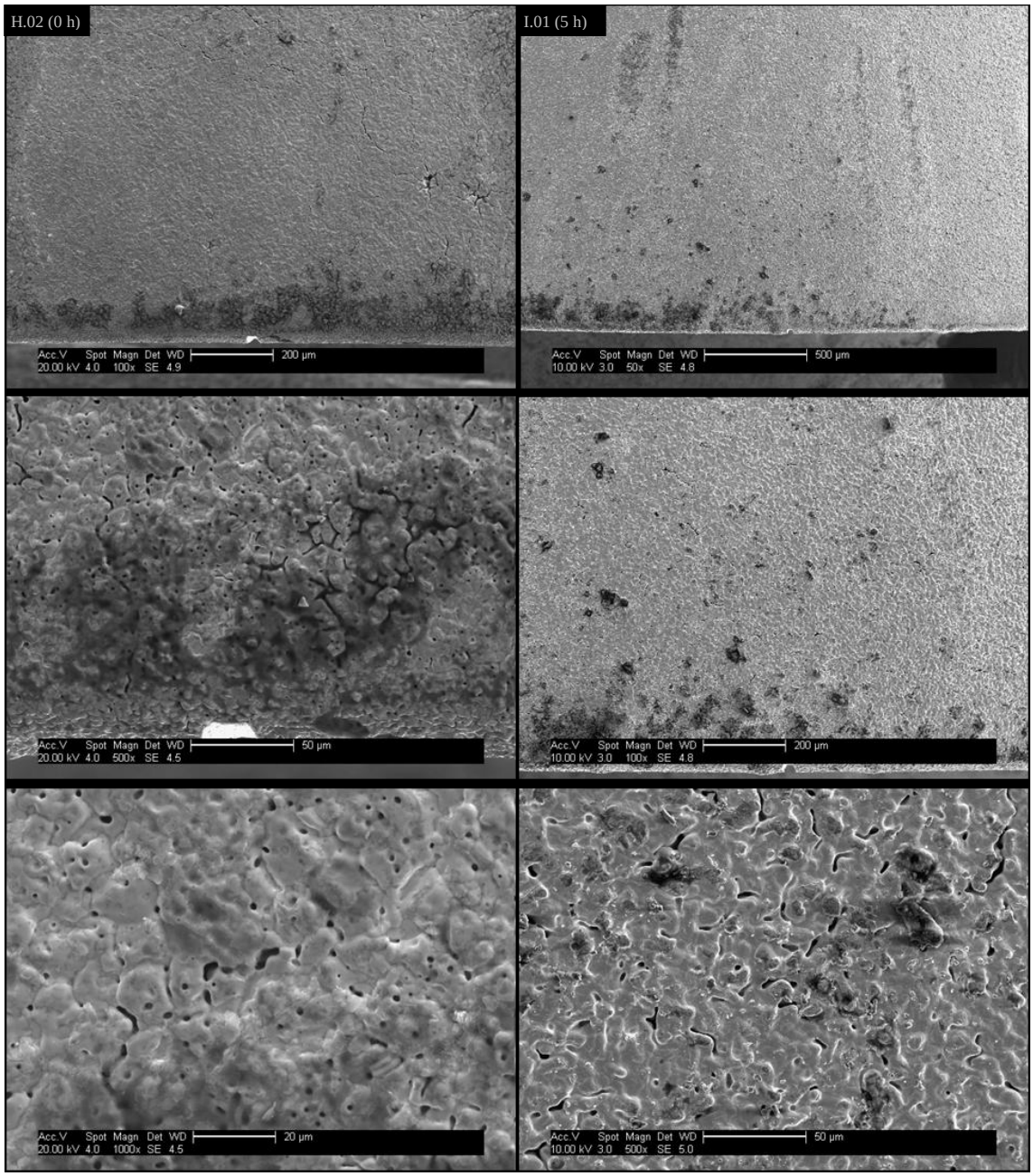
H.02 (0 h)
I.01 (5 h)
Acc.V Spot Magn Det WD 200 µm
20.00 kV 4.0 100x SE 4.9
Acc.V Spot Magn Det WD 500 µm
10.00 kV 3.0 50x SE 4.8
Acc.V Spot Magn Det WD 50 µm
20.00 kV 4.0 500x SE 4.5
Acc.V Spot Magn Det WD 200 µm
10.00 kV 3.0 100x SE 4.8
Acc.V Spot Magn Det WD 20 µm
20.00 kV 4.0 1000x SE 4.5
Acc.V Spot Magn Det WD 50 µm
10.00 kV 3.0 500x SE 5.0

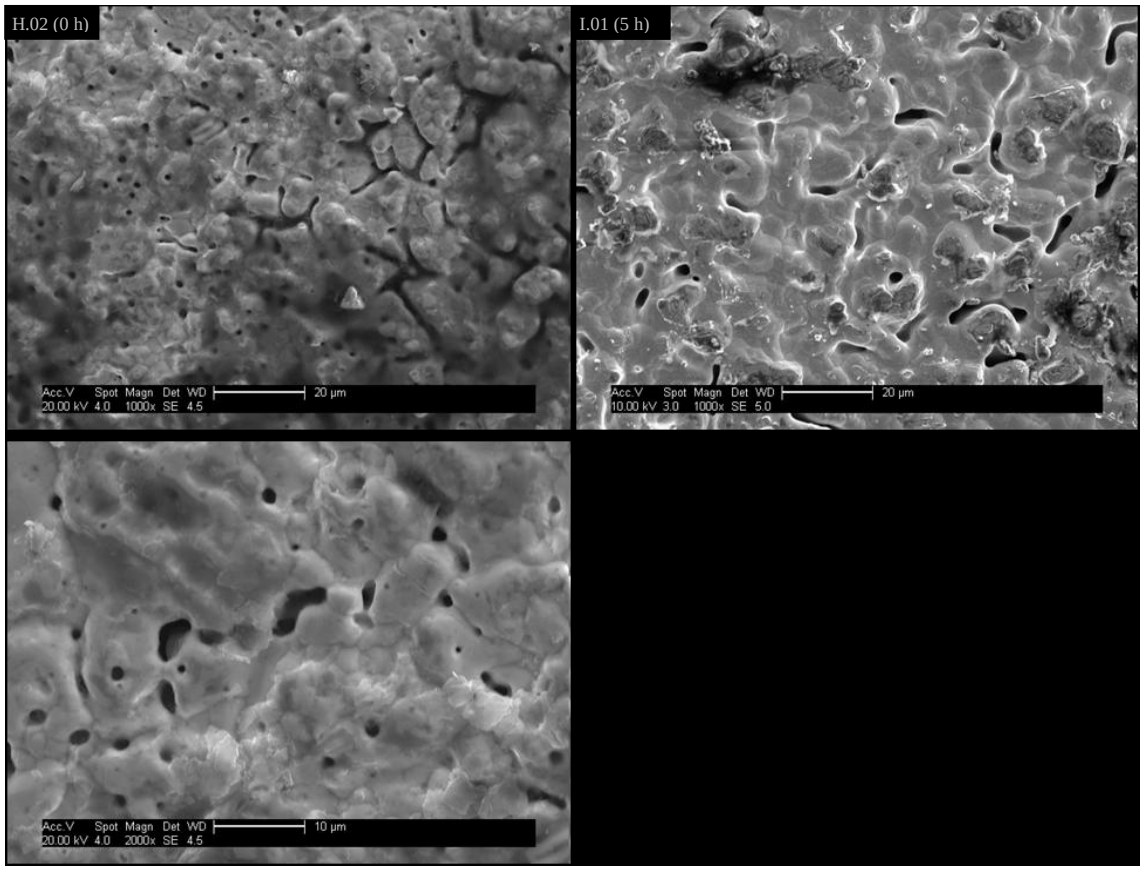
H.02 (0 h)
Acc.V Spot Magn Det WD
20.00 kV 4.0 1000x SE 4.5
20 µm
I.01 (5 h)
Acc.V Spot Magn Det WD
10.00 kV 3.0 1000x SE 5.0
20 µm
Acc.V Spot Magn Det WD
20.00 kV 4.0 2000x SE 4.5
10 µm

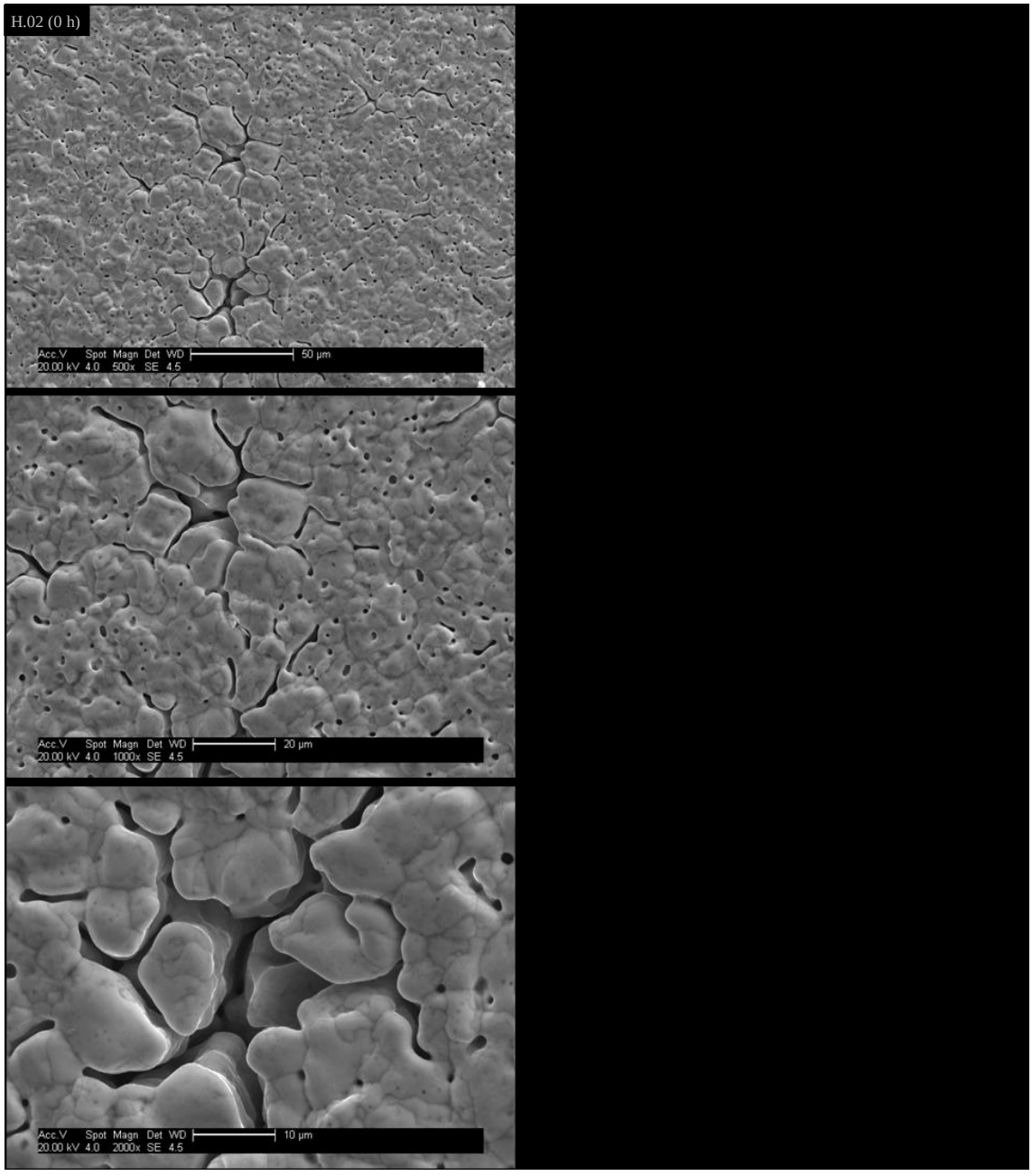
H.02 (0 h)
Acc.V Spot Magn Det WD 50 µm
20.00 kV 4.0 500x SE 4.5
Acc.V Spot Magn Det WD 20 µm
20.00 kV 4.0 1000x SE 4.5
Acc.V Spot Magn Det WD 10 µm
20.00 kV 4.0 2000x SE 4.5

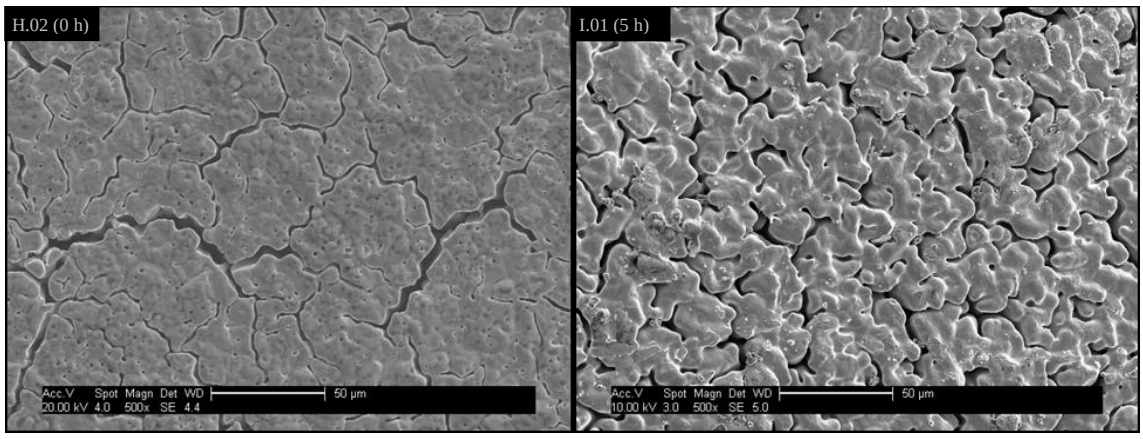
H.02 (0 h)
Acc.V Spot Magn Det WD 50 µm
20.00 kV 4.0 500x SE 4.4
I.01 (5 h)
Acc.V Spot Magn Det WD 50 µm
10.00 kV 3.0 500x SE 5.0

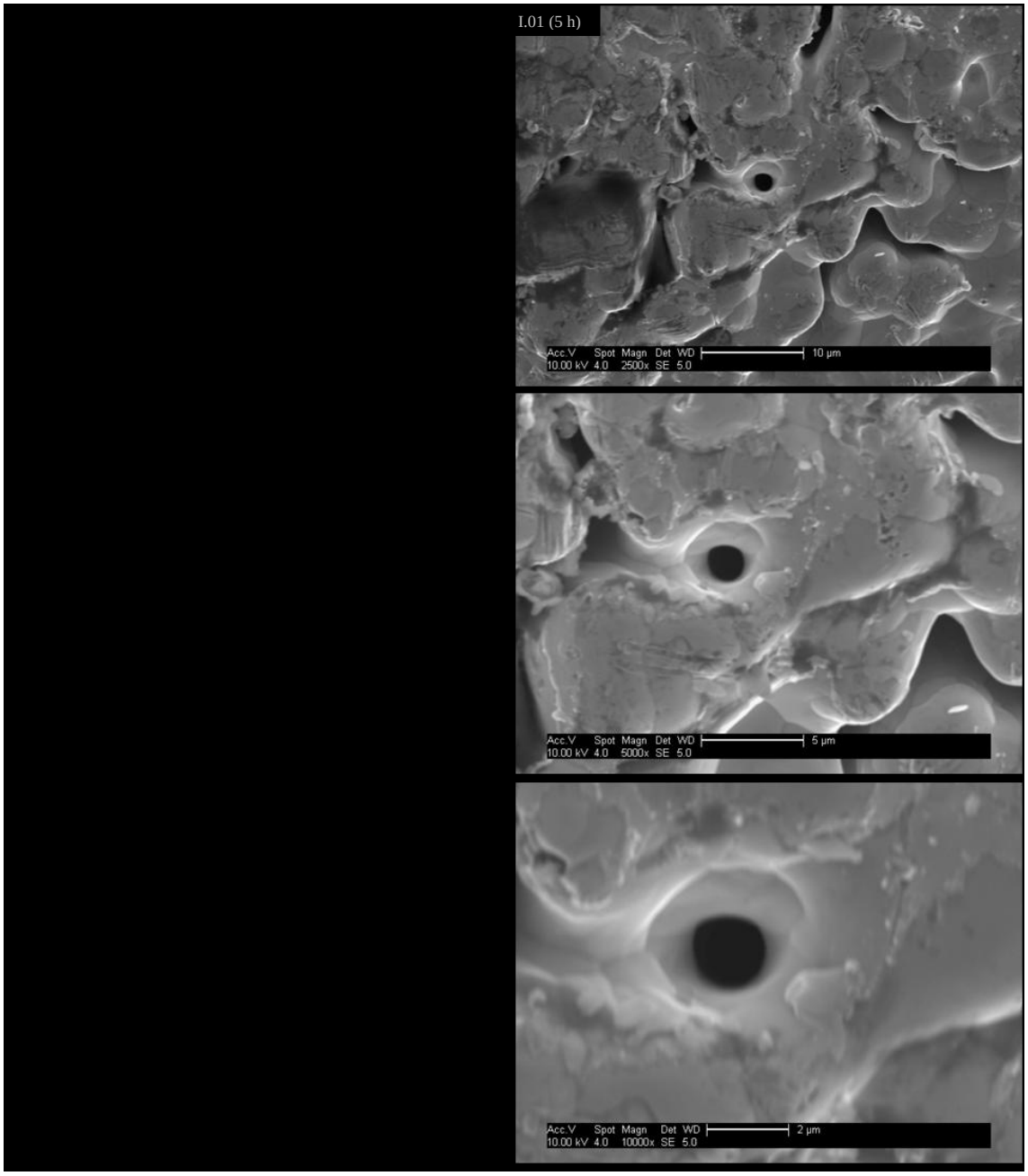

Figure H–16. SEM micrographs of the surface morphology of samples reduced at 1,000 °C. Images are ordered: from top to bottom in order of increasing apparent magnification; left column is 0 h dwell (ramp only – the minimum possible) and right column is 5 h dwell (nominally fully reduced). Samples: RT-A.12/06/12-125.1100(1000)-H.02 (downstream) and RT-A.09/10/12-125.1100(1000)-I.01 (upstream). I.01 was coated with a few nm of AuPd by sputtering to improve resolution. The coating was omitted on those samples analysed initially because previous experience showed such coatings are visible at higher magnifications (appearing similar to reptile scales) potentially obscuring important details; pores 100 nm across or smaller.

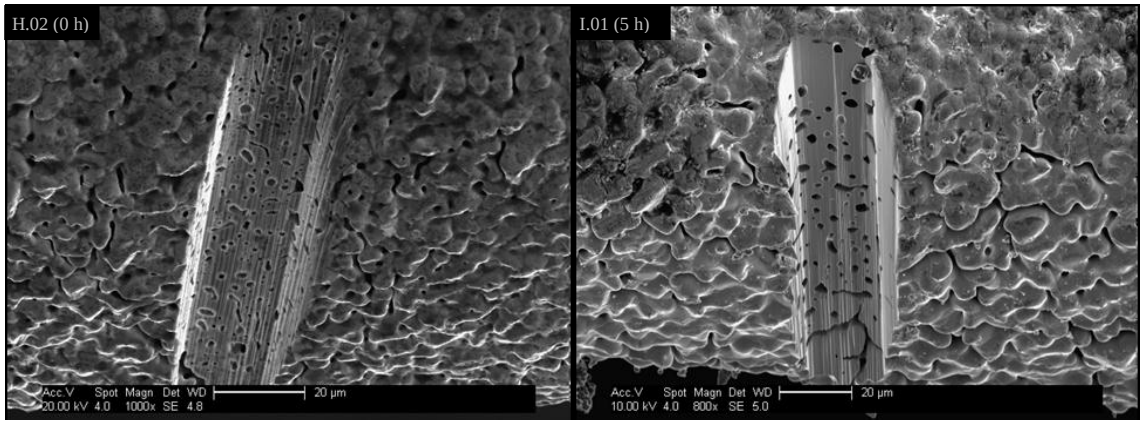

Figure H–17. SEM micrographs showing the overall cross-section of samples reduced at 1,000 °C. Images are ordered: left column is 0 h dwell (ramp only – the minimum possible) and right column is 5 h dwell (nominally fully reduced). Samples: RT-A.12/06/12-125.1100(1000)-H.02 (downstream) and RT-A.09/10/12-125.1100(1000)-I.01 (upstream). I.01 was coated with a few nm of AuPd by sputtering to improve resolution. The coating was omitted on those samples analysed initially because previous experience showed such coatings are visible at higher magnifications (appearing similar to reptile scales) potentially obscuring important details; pores 100 nm across or smaller.

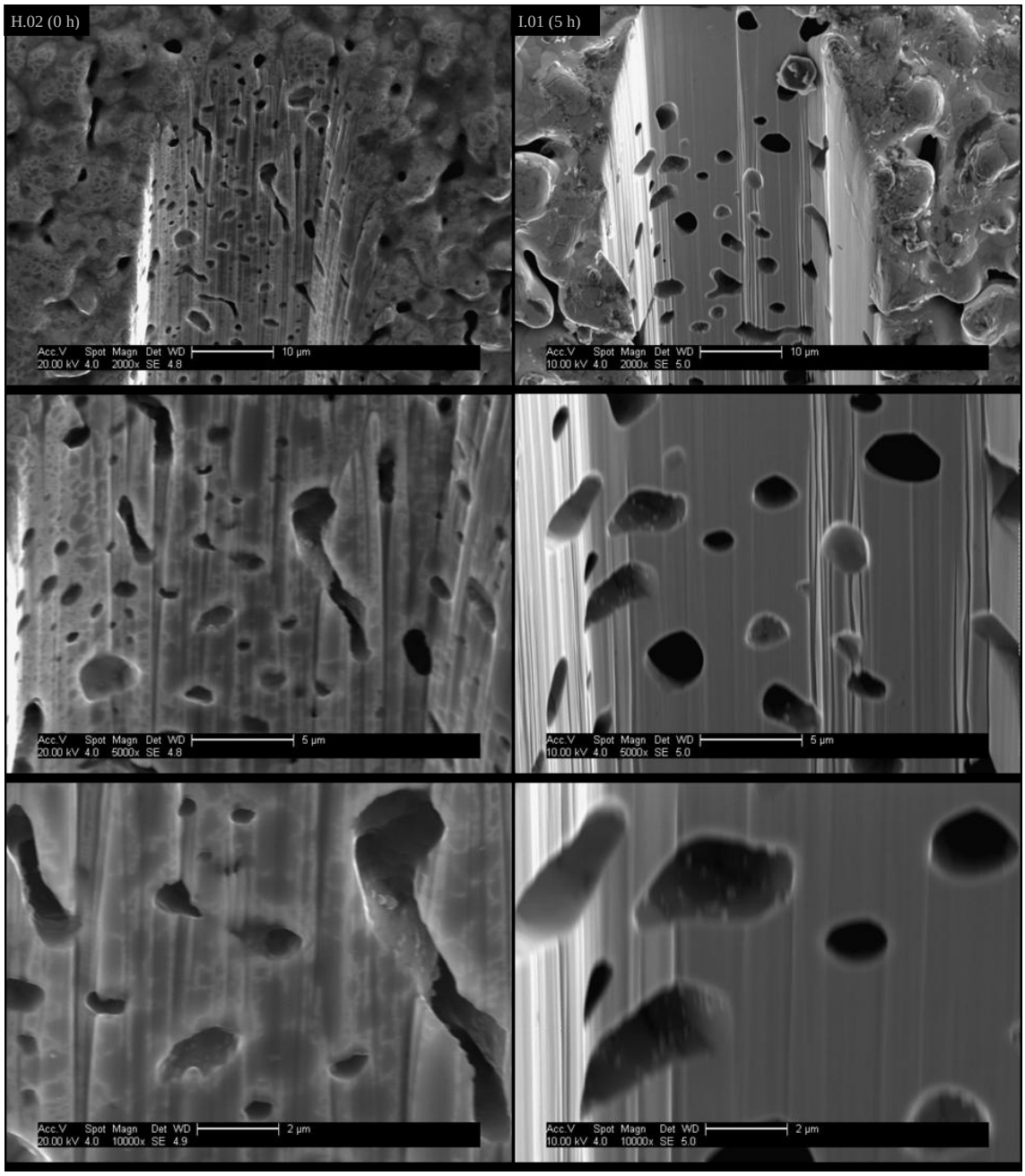

Figure H–18. SEM micrographs showing the cross-section near the outer edge of samples reduced at 1,000 °C. Images are ordered: from top to bottom in order of increasing apparent magnification; left column is 0 h dwell (ramp only – the minimum possible) and right column is 5 h dwell (nominally fully reduced). Samples: RT-A.12/06/12-125.1100(1000)-H.02 (downstream) and RT-A.09/10/12-125.1100(1000)-I.01 (upstream). I.01 was coated with a few nm of AuPd by sputtering to improve resolution. The coating was omitted on those samples analysed initially because previous experience showed such coatings are visible at higher magnifications (appearing similar to reptile scales) potentially obscuring important details; pores 100 nm across or smaller.

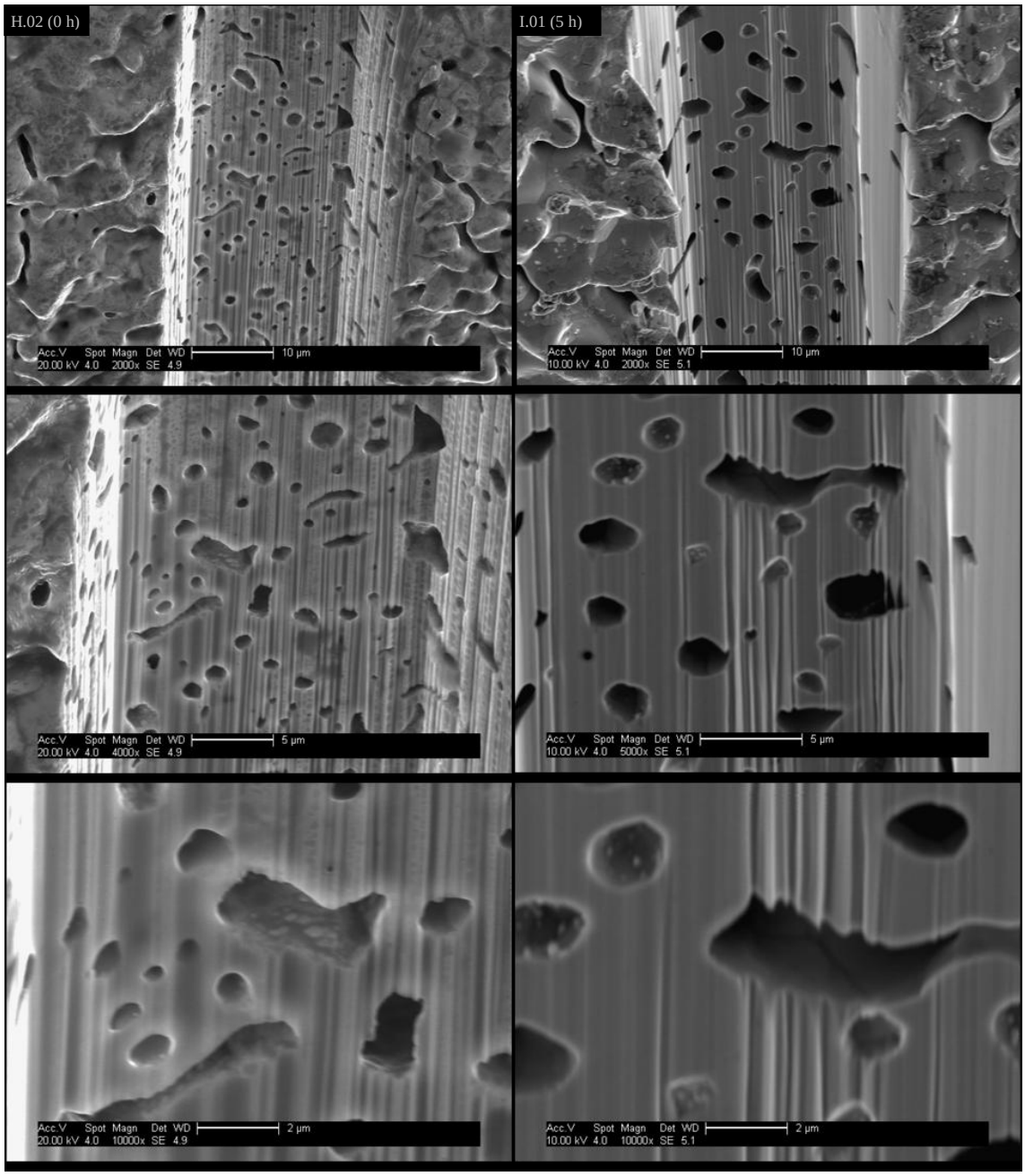

Figure H–19. SEM micrographs showing the cross-section near the middle of samples reduced at 1,000 °C. Images are ordered: from top to bottom in order of increasing apparent magnification; left column is 0 h dwell (ramp only – the minimum possible) and right column is 5 h dwell (nominally fully reduced). Samples: RT-A.12/06/12-125.1100(1000)-H.02 (downstream) and RT-A.09/10/12-125.1100(1000)-I.01 (upstream). I.01 was coated with a few nm of AuPd by sputtering to improve resolution. The coating was omitted on those samples analysed initially because previous experience showed such coatings are visible at higher magnifications (appearing similar to reptile scales) potentially obscuring important details; pores 100 nm across or smaller.

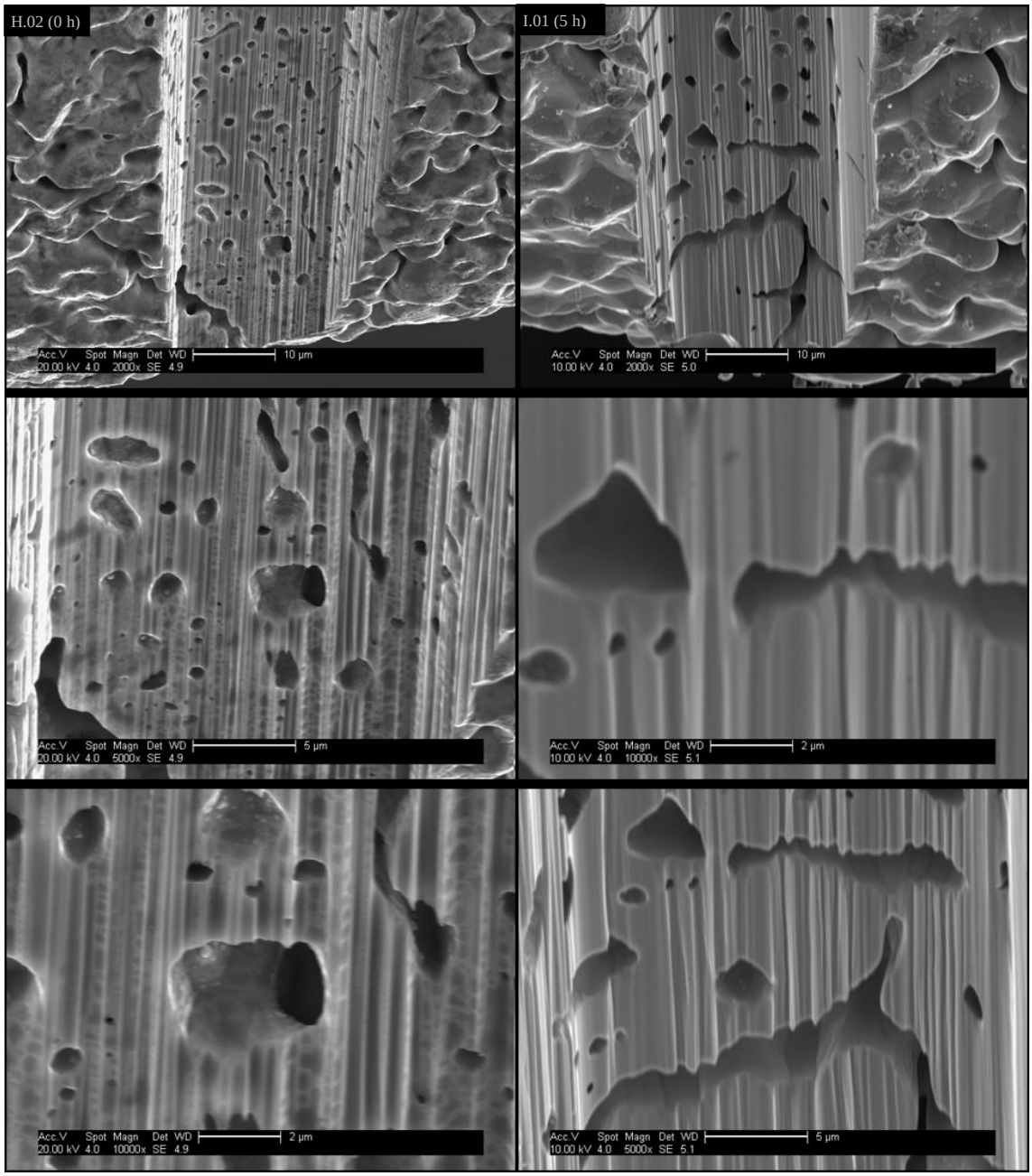
H.02 (0 h)
I.01 (5 h)
Acc.V Spot Magn Det WD 10 µm
20.00 kV 4.0 2000x SE 4.9
Acc.V Spot Magn Det WD 10 µm
10.00 kV 4.0 2000x SE 5.0
Acc.V Spot Magn Det WD 5 µm
20.00 kV 4.0 5000x SE 4.9
Acc.V Spot Magn Det WD 2 µm
10.00 kV 4.0 10000x SE 5.1
Acc.V Spot Magn Det WD 2 µm
20.00 kV 4.0 10000x SE 4.9
Acc.V Spot Magn Det WD 5 µm
10.00 kV 4.0 5000x SE 5.1

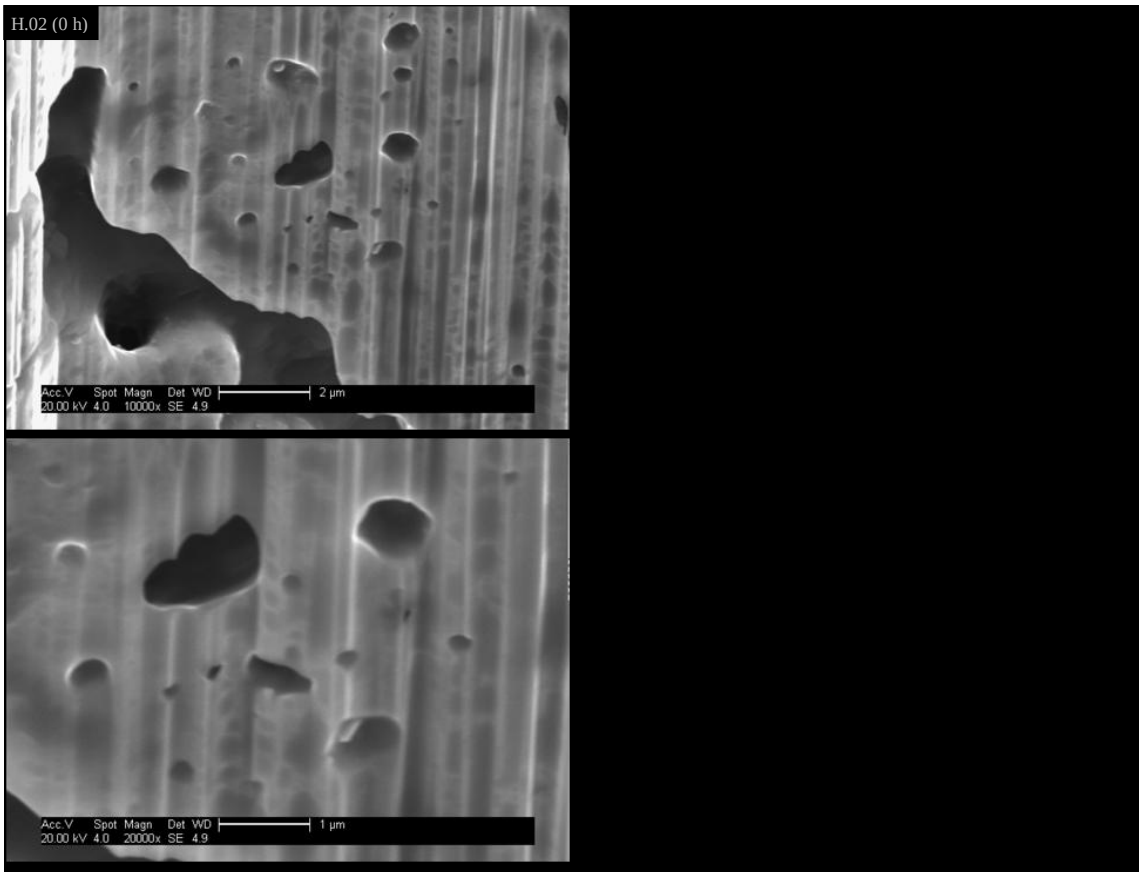

Figure H–20. SEM micrographs showing the cross-section near the inner edge of samples reduced at 1,000 °C. Images are ordered: from top to bottom in order of increasing apparent magnification; left column is 0 h dwell (ramp only – the minimum possible) and right column is 5 h dwell (nominally fully reduced). Samples: RT-A.12/06/12-125.1100(1000)-H.02 (downstream) and RT-A.09/10/12-125.1100(1000)-I.01 (upstream). I.01 was coated with a few nm of AuPd by sputtering to improve resolution. The coating was omitted on those samples analysed initially because previous experience showed such coatings are visible at higher magnifications (appearing similar to reptile scales) potentially obscuring important details; pores 100 nm across or smaller.

Appendix I: SOP for the Deposition of YSZ Coatings

The following is a copy of the SOP developed by Tony Gray. This SOP was included because the restrictions it places on the experiments undertaken as part of this project constrain what was possible as well as having a strong influence on the coating thickness reproducibility (discussed in chapter 9).

Equipment

The evaporation equipment used in the deposition of thermal barrier coatings is a modified Electrotech 680 square chambered ion plater. The vacuum station consists of an upper chamber and a lower chamber, each having it's own pumping system of diffusion pump and mechanical pump. Between the two chambers is a separation plate enabling the two chambers to maintain different pressures. Whilst processing, the upper chamber will be at the process pressure, while the lower chamber will be at a lower pressure, to enable the electron beam gun to operate.

The upper chamber accommodates the furnace and substrate manipulation system. There are facilities for two substrates to rotate above the source at a nominal distance of 15 cm and at a rotation speed of between 0 and 60 RPM. The lower chamber incorporates the filament assembly and high voltage components of the electron beam gun. It also houses the rotation and elevation mechanisms of the ingot.

The evaporation source is a modified standard single hearth Temescal electron beam gun. There is a 33 mm hole drilled in the base of the crucible to allow the ceramic ingots to rotate and rise within the hearth. The gun is driven by a Temescal CV14 power supply capable of operating the gun at a maximum power of 14 kW.

Operation

The two chambers are brought up to atmosphere. The required ingot is loaded into the gun hearth (in this case 7 mol.% Y_2O_3 stabilised ZrO_2) and the height of the ingot adjusted to the operating position. The substrates are loaded on to the substrate holders, after they have been cleaned in acetone. The substrate holders are then bolted on to the rotating substrate stations. The furnace is positioned around the substrates and electrically connected. Both chambers are then evacuated to a pressure of below $5x10^{-5}$ mbar. The furnace is then switched on and allowed to heat up to above 860 °C. The process gas (90% oxygen, 10% argon) is then admitted to the upper chamber and this chamber is allowed to settle at about 7×10^{-3} torr. The substrates are rotated at a speed of 10 RPM. After this the electron beam gun is switched on and the beam played on the surface of the ingot. The emission current of the gun is slowly increased until the top of the ingot is molten and optimum evaporation occurs. This is normally with an

accelerating voltage of 10 kV and an emission current of 5.5 to 6 A. The temperature of the substrates is then allowed to rise to 1000 °C and the pressure in the upper chamber to$1–10^{-2}$ torr.

These conditions are maintained throughout the evaporation process until the required thickness of coating is achieved, in this case a period of 4 min 6 s. When the coating is considered thick enough the electron beam gun is turned off. The process gas is switched off as is the furnace and the substrate rotation. The substrates are allowed to cool and both chambers are pumped down. When the substrates have reached a temperature of below 100 °C the chambers are brought up to atmosphere and the substrates are unloaded.

Appendix J: DoE Factor Significance Plots

The following are organised by factor (temperature, chamber pressure, etc.).

Factor significance: Temperature

Recall that the results are actually for 2 ‘unit cells’ side by side along the temperature axis. For analysis an overall plot is shown initially, followed by plots per DoE ‘unit cell’.

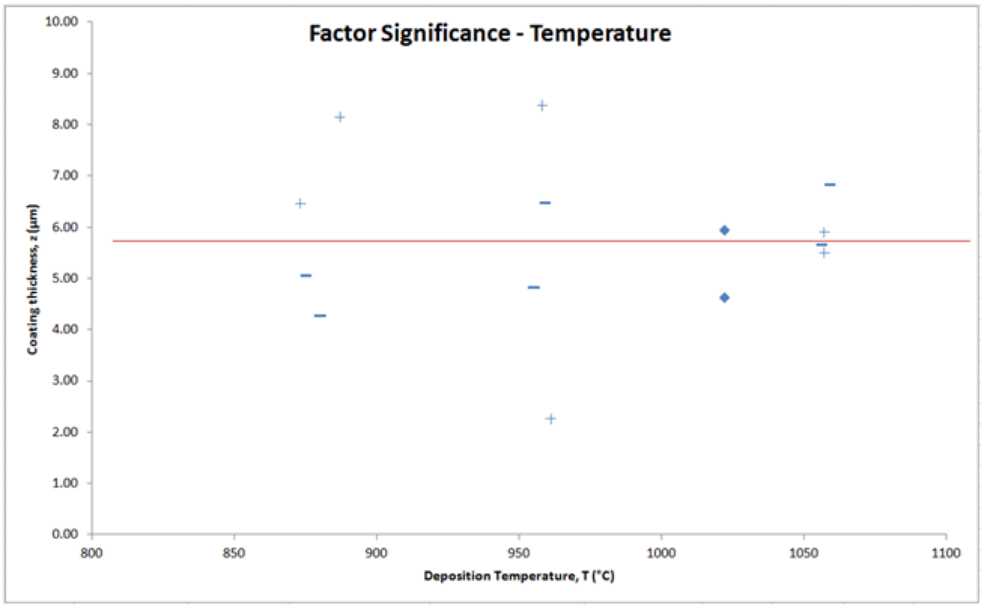

Points with the low chamber pressure setting are denoted by a '-'. Diamonds are the middle setting and a '+' denotes the high chamber pressure setting.

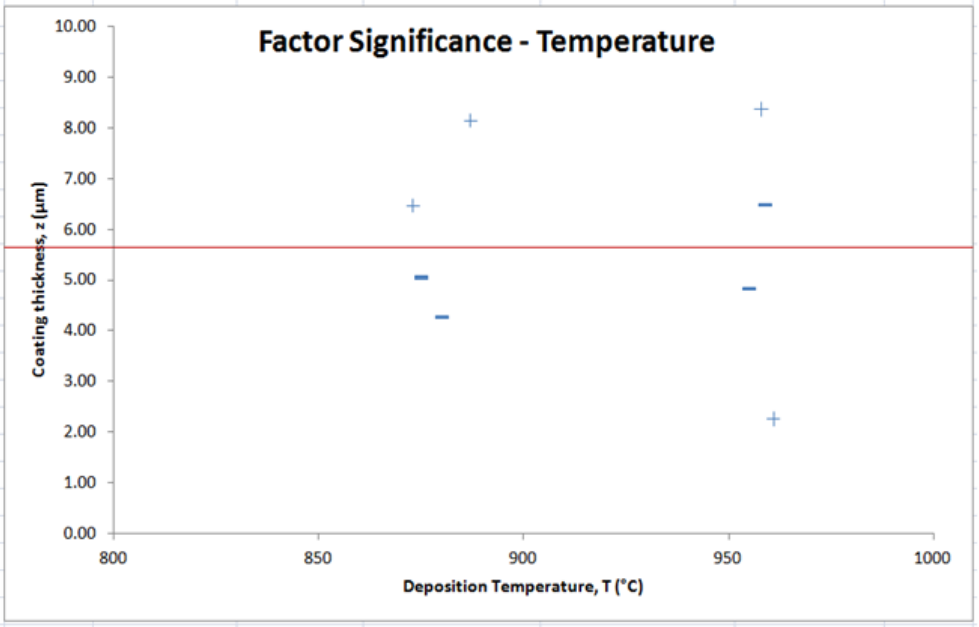

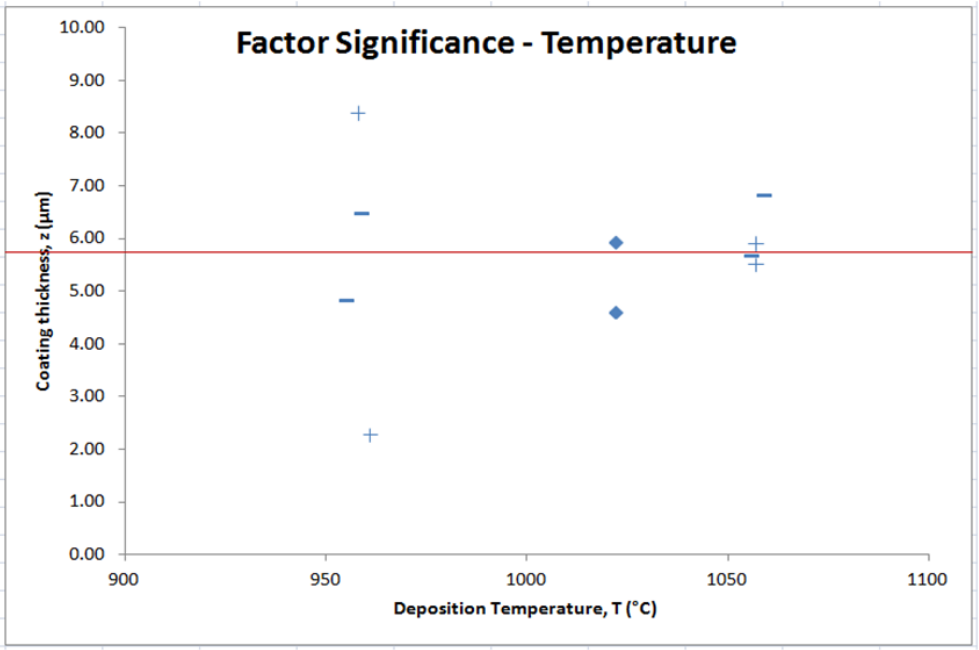

Points with the low chamber pressure setting are denoted by a '-'. Diamonds are the middle setting and a '+' denotes the high chamber pressure setting.

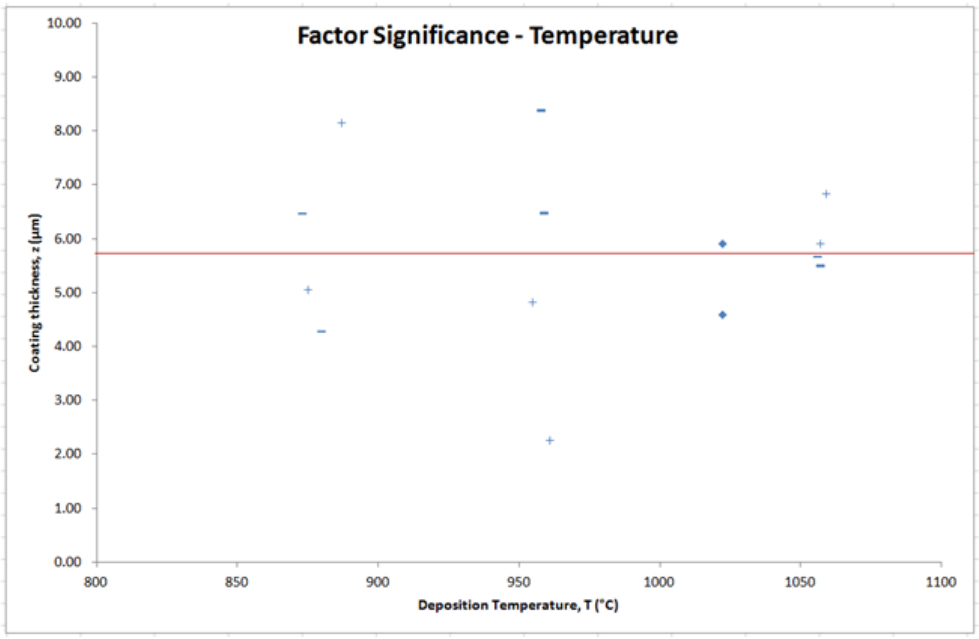

Points with the low sample rotation speed setting are denoted by a '-'. Diamonds are the middle setting and a '+' denotes the high sample rotation speed setting.

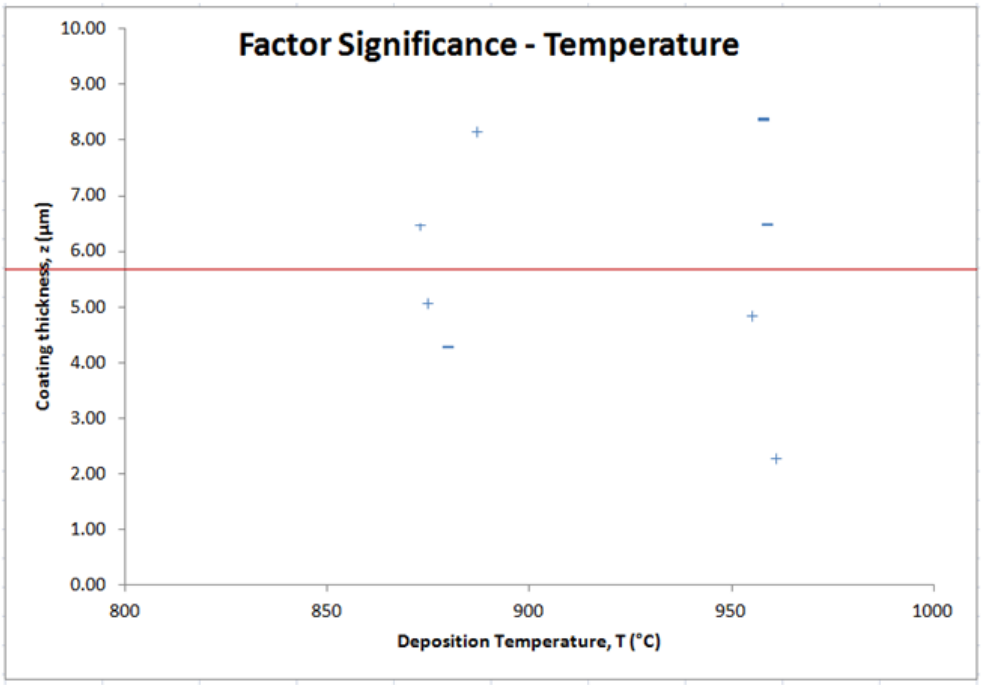

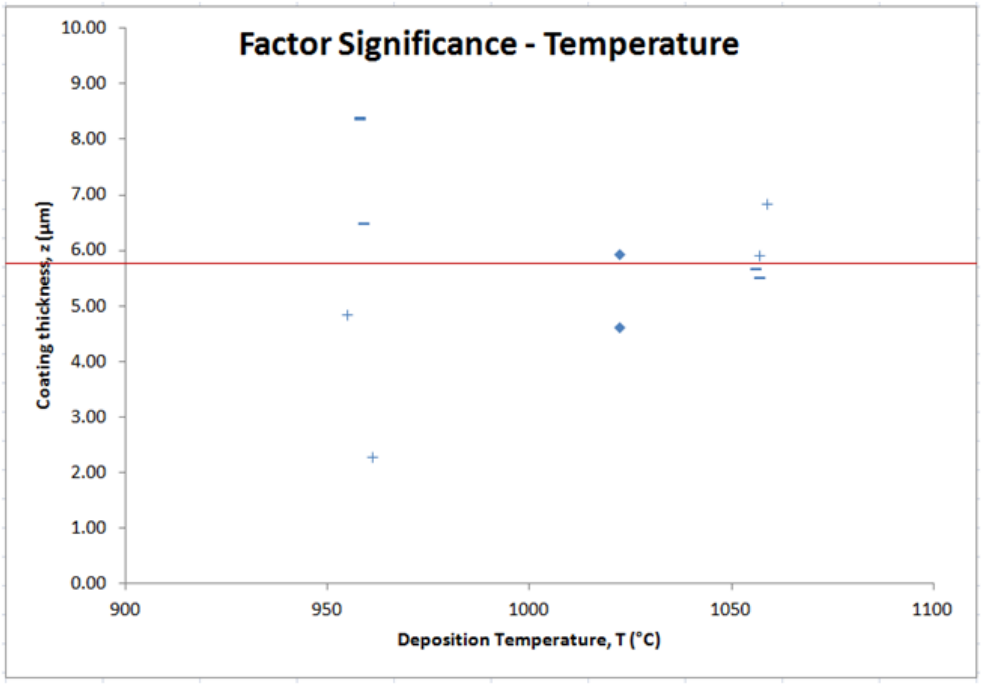

Points with the low sample rotation speed setting are denoted by a '-'. Diamonds are the middle setting and a '+' denotes the high sample rotation speed setting.

Factor significance: Pressure

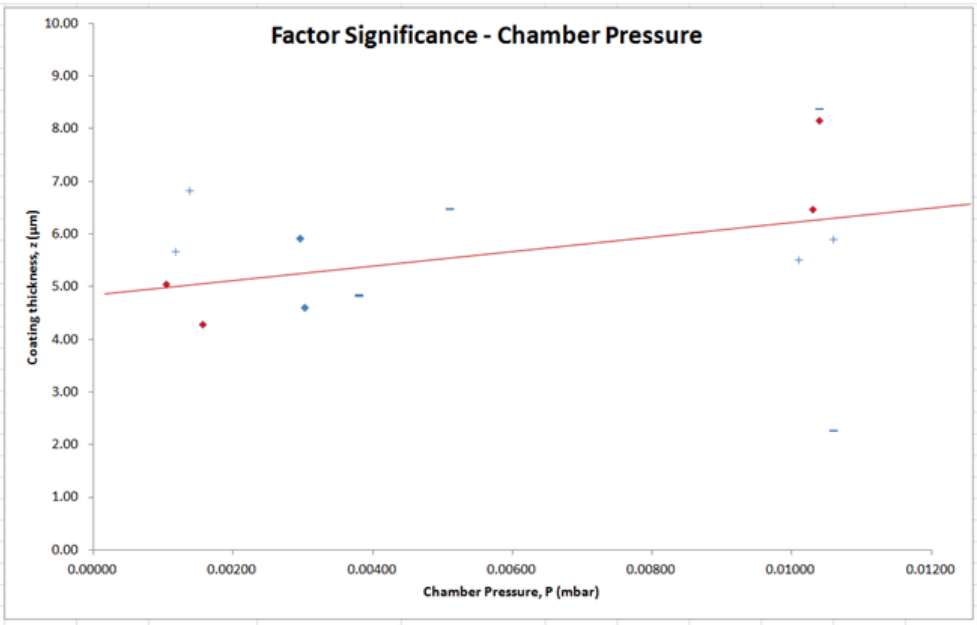

Points with the low temperature setting are denoted by a '-'. Diamonds are the middle setting and a '+' denotes the high temperature setting. Samples in red are at 850 °C.

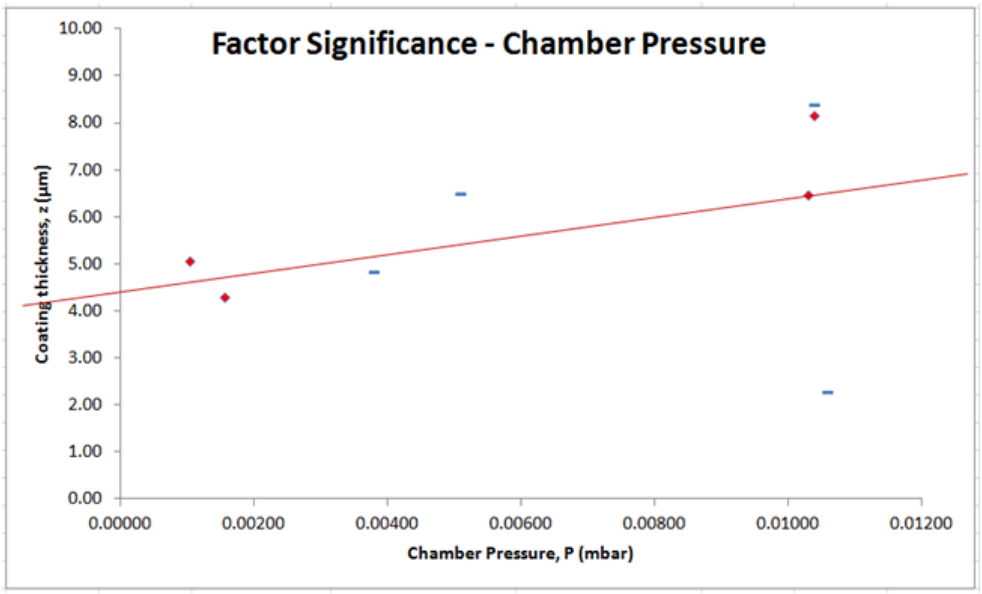

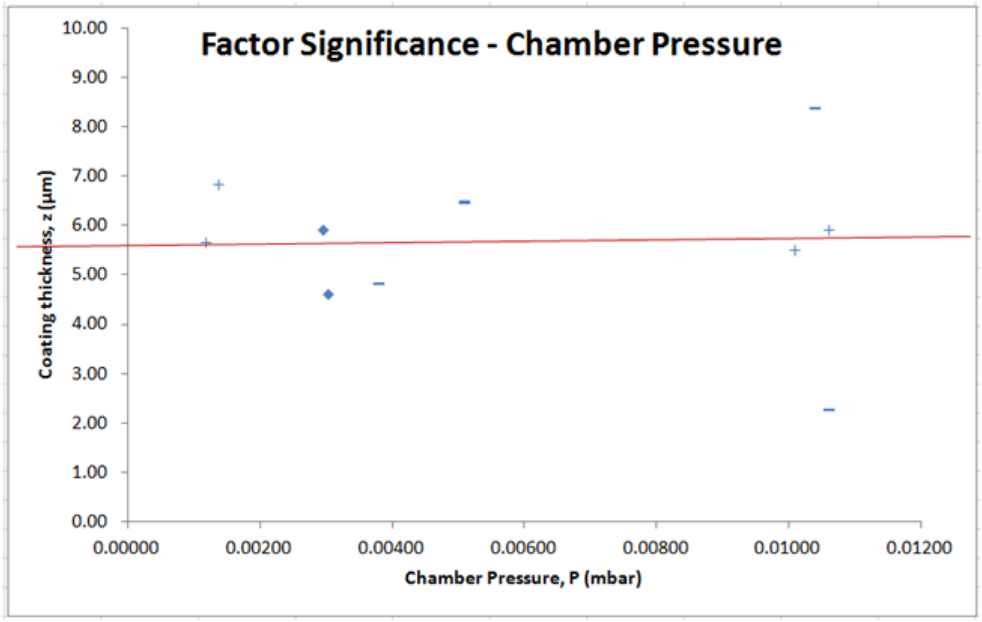

Points with the low temperature setting are denoted by a '-'. Diamonds are the middle setting and a '+' denotes the high temperature setting. Samples in red are at 850 °C.

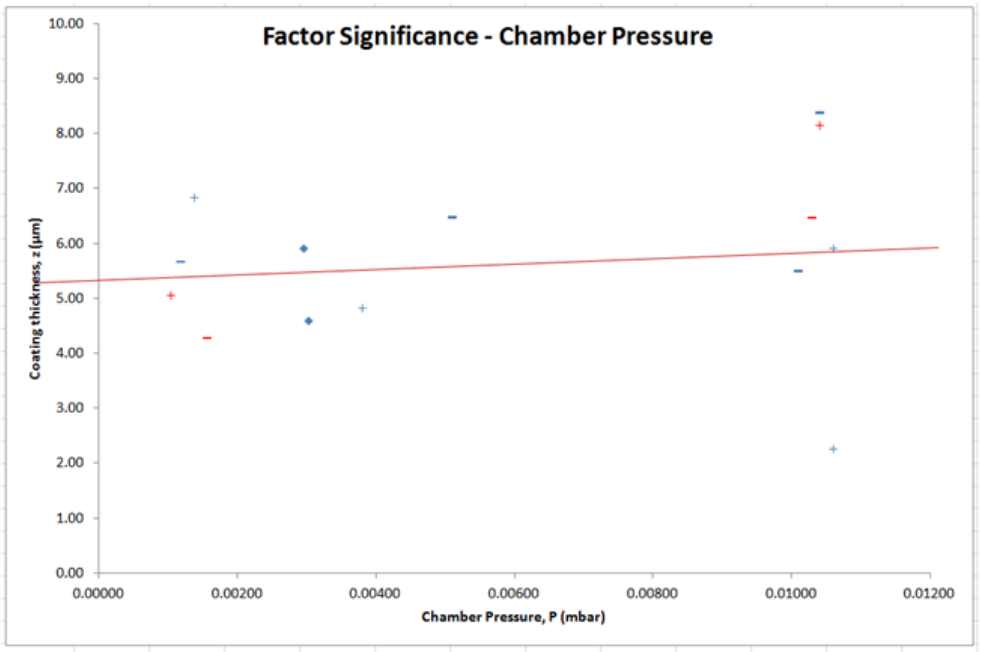

Points with the low sample rotation speed setting are denoted by a '-'. Diamonds are the middle setting and a '+' denotes the high sample rotation speed setting. Samples in red are at 850 °C (circles instead of '-' for low rotation speed, diamonds for high).

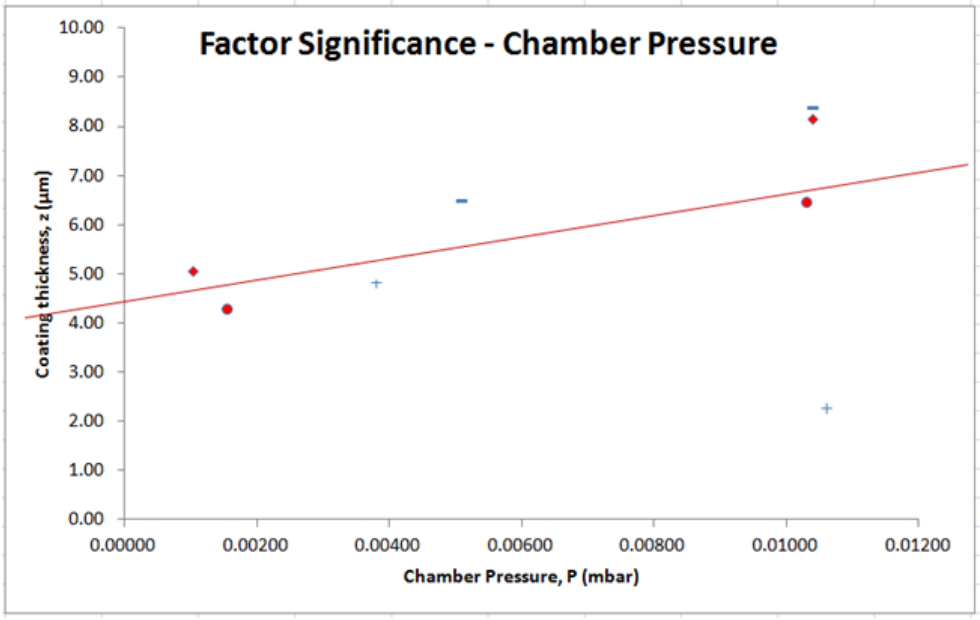

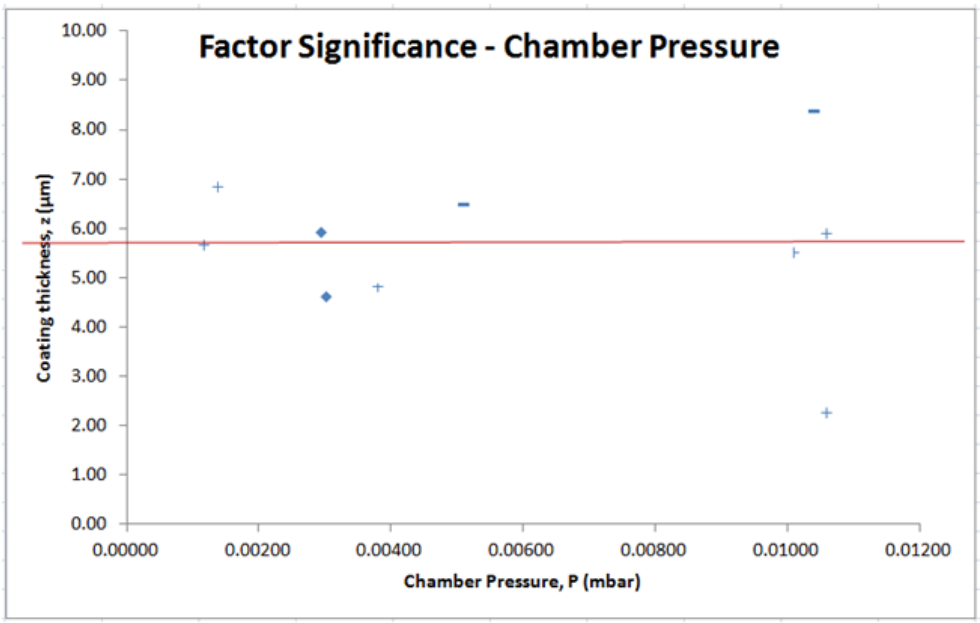

Points with the low sample rotation speed setting are denoted by a '-'. Diamonds are the middle setting and a '+' denotes the high sample rotation speed setting. Samples in red are at 850 °C (circles instead of '-' for low rotation speed, diamonds for high).

Factor significance: Rotation Speed

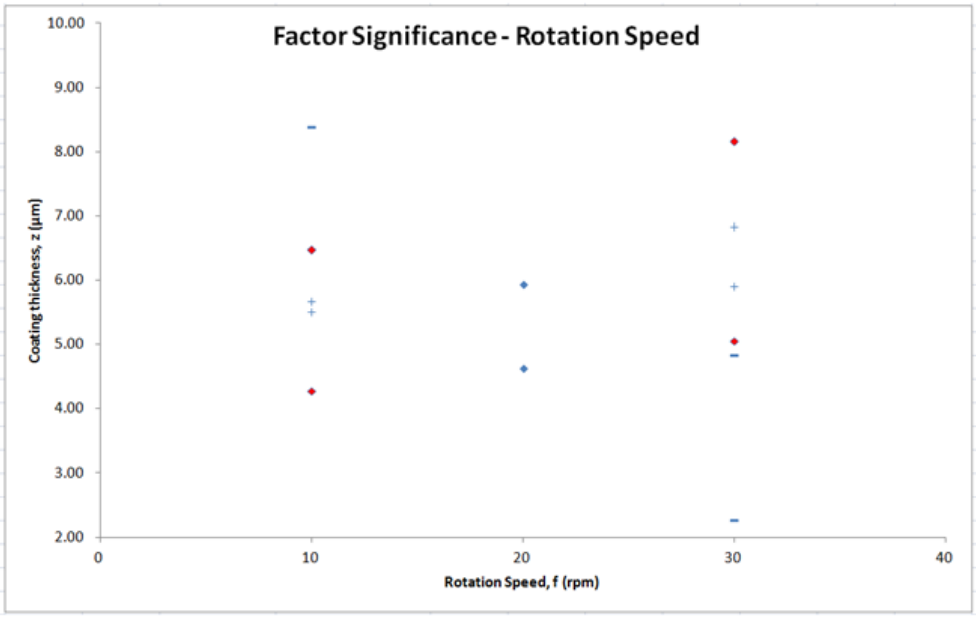

Points with the low temperature setting are denoted by a '-'. Diamonds are the middle setting and a '+' denotes the high temperature setting. Samples in red are at 850 °C.

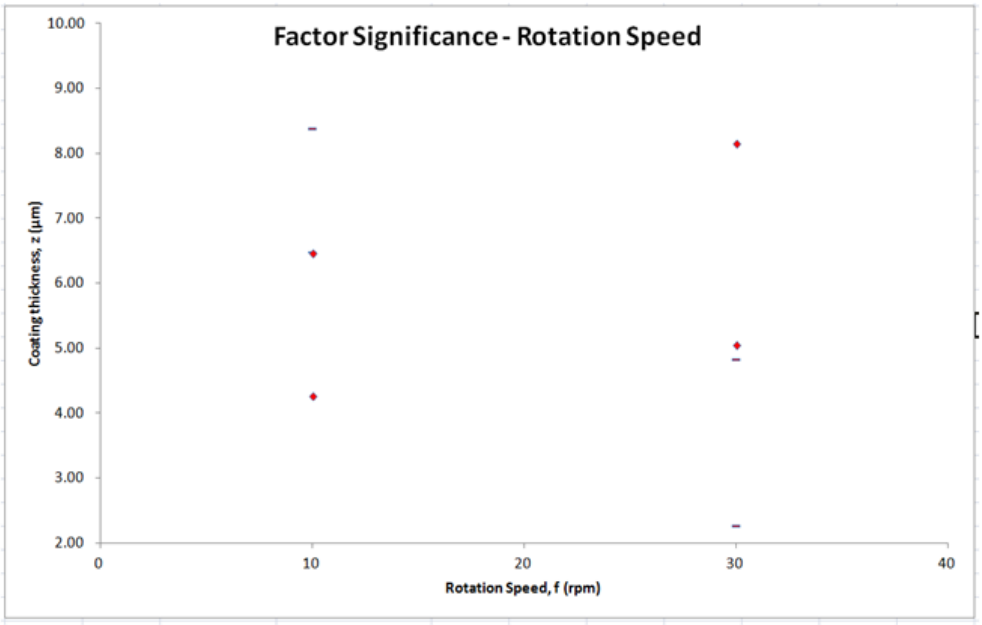

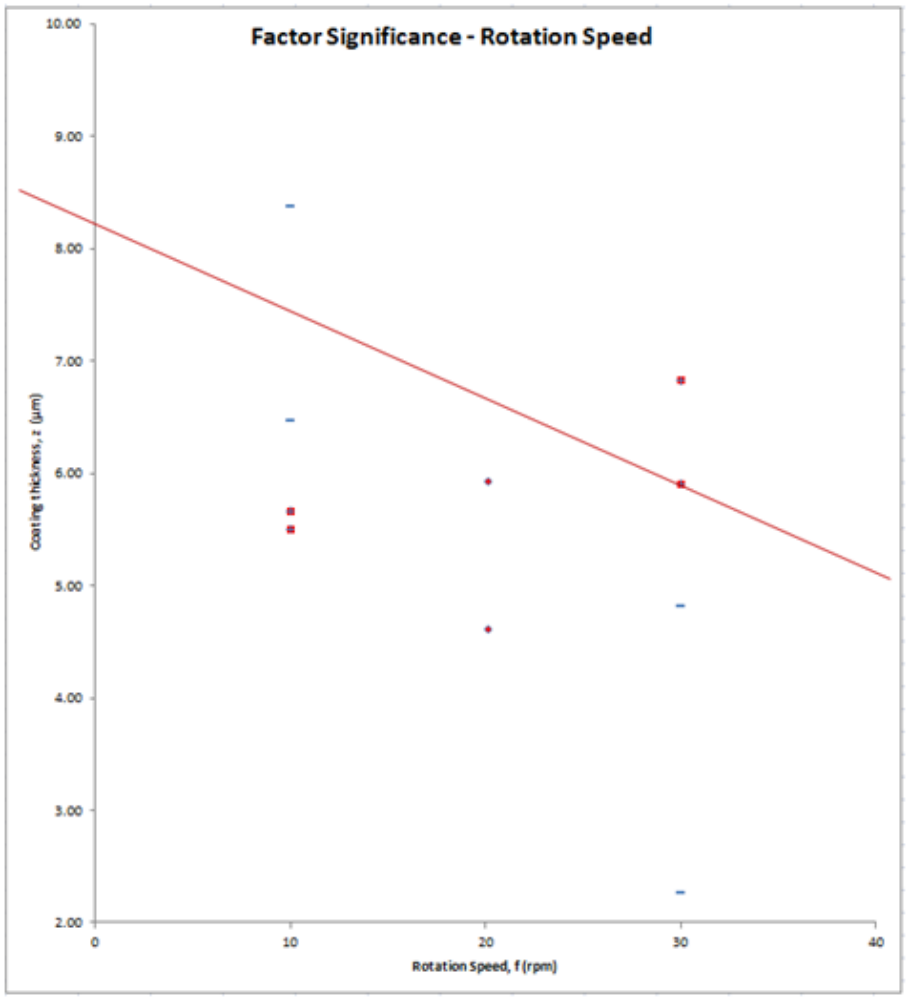

Points with the low temperature setting are denoted by a '-'. Diamonds are the middle setting and a '+' denotes the high temperature setting. Samples in red are at 850 °C.

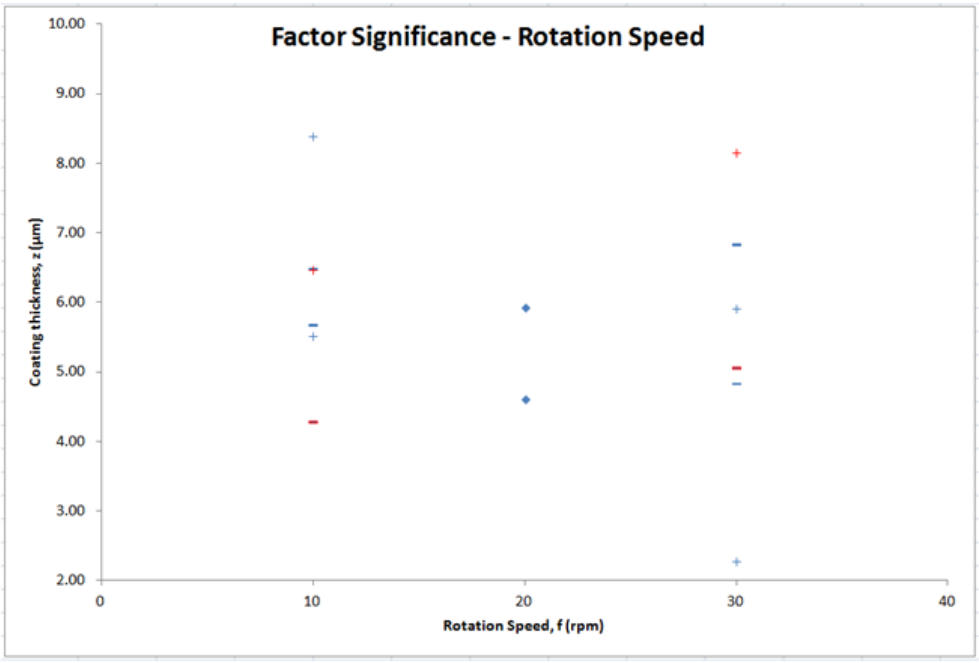

Points with the low chamber pressure setting are denoted by a '-'. Diamonds are the middle setting and a '+' denotes the high temperature setting. Samples in red are at 850 °C.

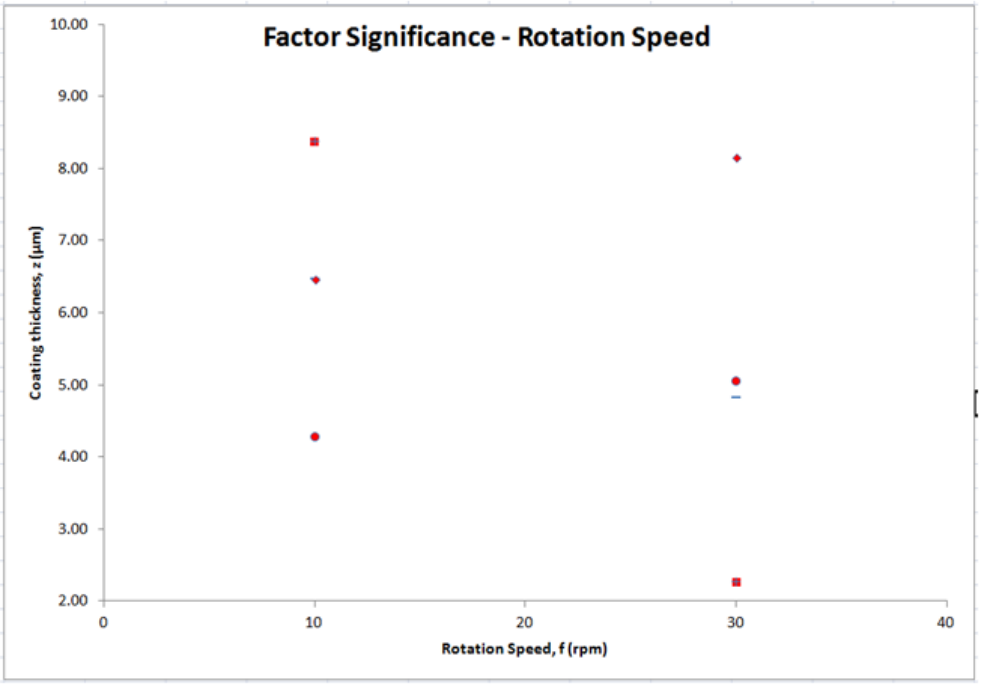
Factor Significance - Rotation Speed
Coating thickness, z (µm)
10.00
9.00
8.00
7.00
6.00
5.00
4.00
3.00
2.00
0
10
20
30
40
Rotation Speed, f (rpm)

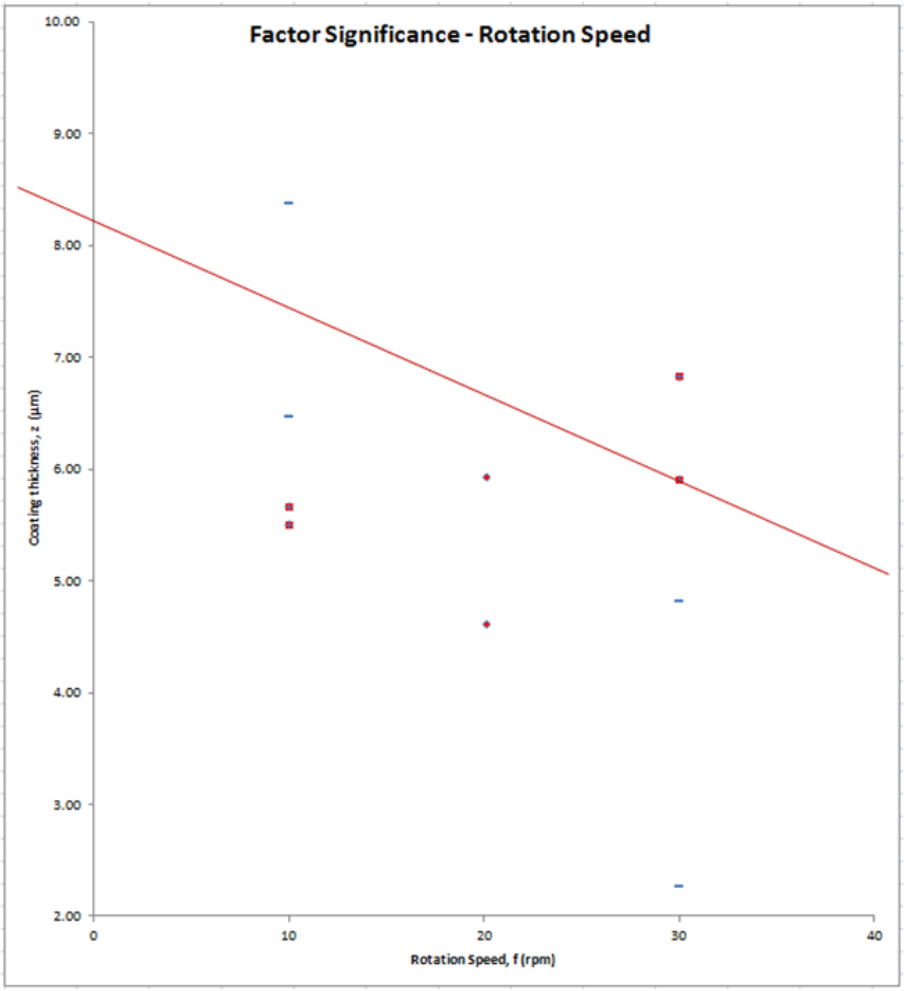
Factor Significance - Rotation Speed
Coating thickness, z (µm)
10.00
9.00
8.00
7.00
6.00
5.00
4.00
3.00
2.00
0
10
20
30
40
Rotation Speed, f (rpm)

Points with the low chamber pressure setting are denoted by a '-'. Diamonds are the middle setting and a '+' denotes the high chamber pressure setting. Samples in red are at 850 °C (circles instead of '-' for low chamber pressure, diamonds for high).

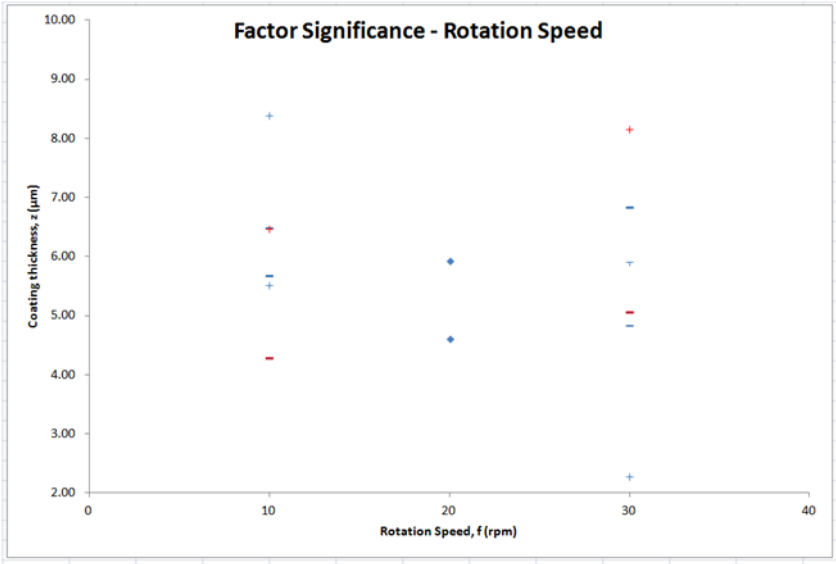

Points with the low chamber pressure setting are denoted by a '-'. Diamonds are the middle setting and a '+' denotes the high chamber pressure setting. Samples in red are at 850 °C.

Points in the figures below with the low chamber pressure setting are denoted by a '-'. Diamonds are the middle setting and a '+' denotes the high chamber pressure setting. Samples in red are at 850 °C (circles instead of '-' for low chamber pressure, diamonds for high).

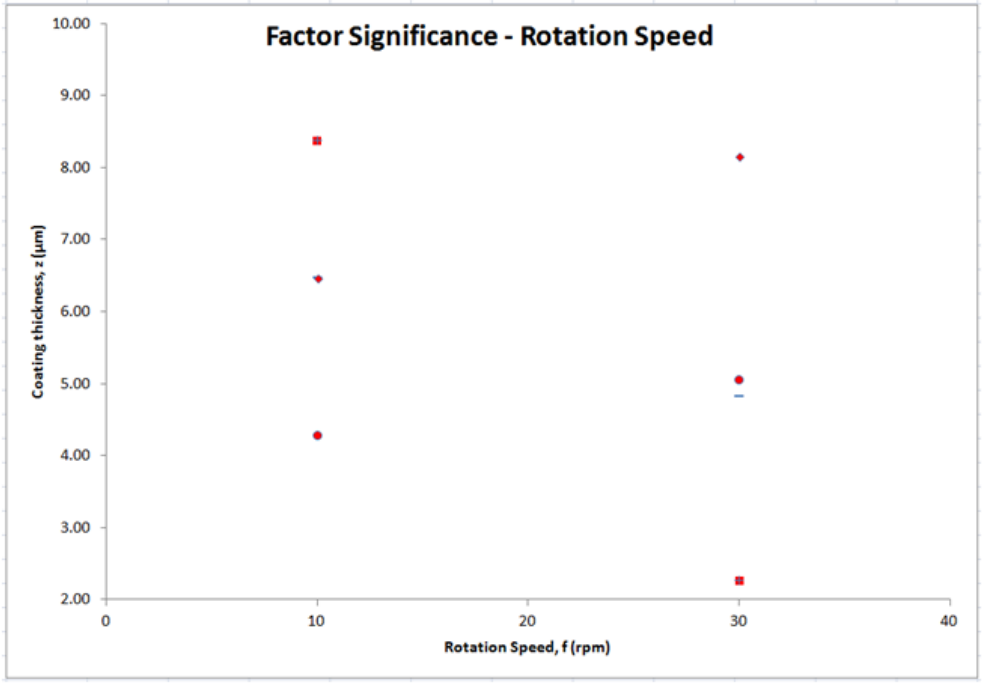
Factor Significance - Rotation Speed
Coating thickness, z (µm)
10.00
9.00
8.00
7.00
6.00
5.00
4.00
3.00
2.00
0
10
20
30
40
Rotation Speed, f (rpm)

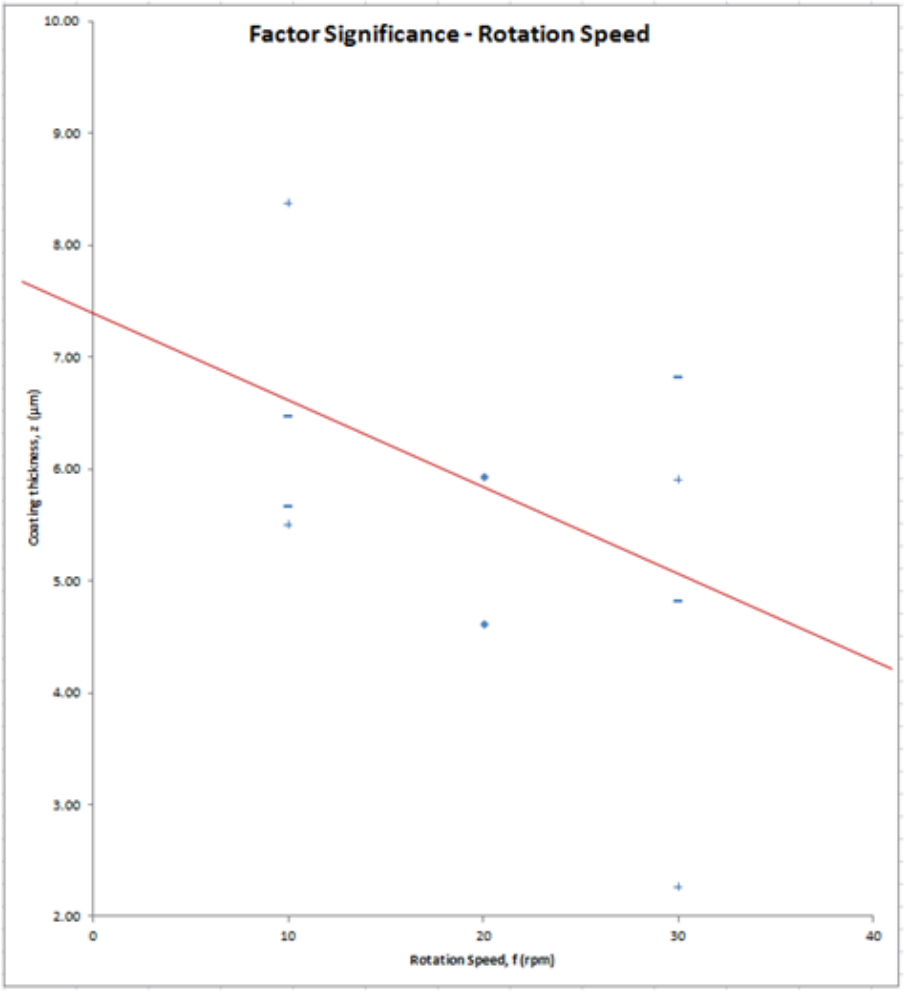
Factor Significance - Rotation Speed
Coating thickness, z (µm)
10.00
9.00
8.00
7.00
6.00
5.00
4.00
3.00
2.00
0
10
20
30
40
Rotation Speed, f (rpm)

Appendix K: Permeameter SOP

The following is a copy of the SOP developed by the author and approved by Tim Pryor for use of the bespoke permeameter built in-house. This is a typical part of the process of risk assessment (in addition to the RA) step, standardised at Cranfield University with all relevant documentation available to staff and students on the intranet. This SOP was included because of the effect of the procedure on experimental flow, as discussed in chapter 1.

SAS SSE SOP 078
Permeability measurement rig
Standard Operating Procedure

General precautions

When used with pure hydrogen or another flammable gas mix this procedure should not be run if periodic monitoring is not possible, e.g. outside normal working hours, unless authorisation is obtained (in which case the process must be seen to stabilise during the daytime before it is left overnight).

Risk assessment RA570066A covers the use of this equipment in accordance with this SOP. Any activity that falls well outside of this risk assessment will need to be assessed on its own merits.

Trained operators only to use this equipment. Activities must comply with SSE SOP 42 (PGTC SOP 027); "Working in the High Temperature Corrosion Lab" if set up to operate within that laboratory. If the permeameter (permeability measurement rig) is to be used outside of the corrosion lab the local SOP should be adhered to.

Caution: **Explosive gases**.
Wear protective clothing: Eye protection, lab coat, robust footwear, long sleeves and long trousers.

Measures must be taken to prevent contamination from corrosive chemicals/ organics; Clean samples, use clean crucibles/ furniture, use clean loading/ unloading tools. Obtain permission before exposing anything other than metallic samples or inert ceramics. Ensure any solvents used are dried off before using the rig.

The permeability measurement rig does not have an interlock. Ensure that the test chamber is returned to room pressure and the pressure sensor power supply is switched off before removing samples.

Maintenance should be conducted by experienced staff only.

Procedure

Pre-checks and sample loading:

Leak test sample after it is glued (with an appropriate epoxy resin) to an end cap and adapter matching the 3/8" pipe fittings (e.g. with a helium leak detector).

Check mating surfaces on test cell are clean to ensure a good seal.

Ensure gas feed system is connected to appropriate gas supplies and that there is sufficient supply reserve.

Connect gas line and pressure sensor ports.

Leak test and pre-treatment purge:

The chamber is sealed with a pair of gas pipes at the front, both located at the front face of the test cell, one (bottom) to pressurise the sample and the other (top) connected to the chamber to measure the chamber pressure.

Note: The measurements are based on a differential pressure, with a positive pressure applied to the sample-holding inlet, leaving the rest of the chamber at atmospheric pressure and measuring the increase as gas permeates from inside the sample tube into the chamber.

The gas is fed from the gas manifold or direct from a cylinder where necessary.

Leak Test:

All valve numbers refer to the diagram below.

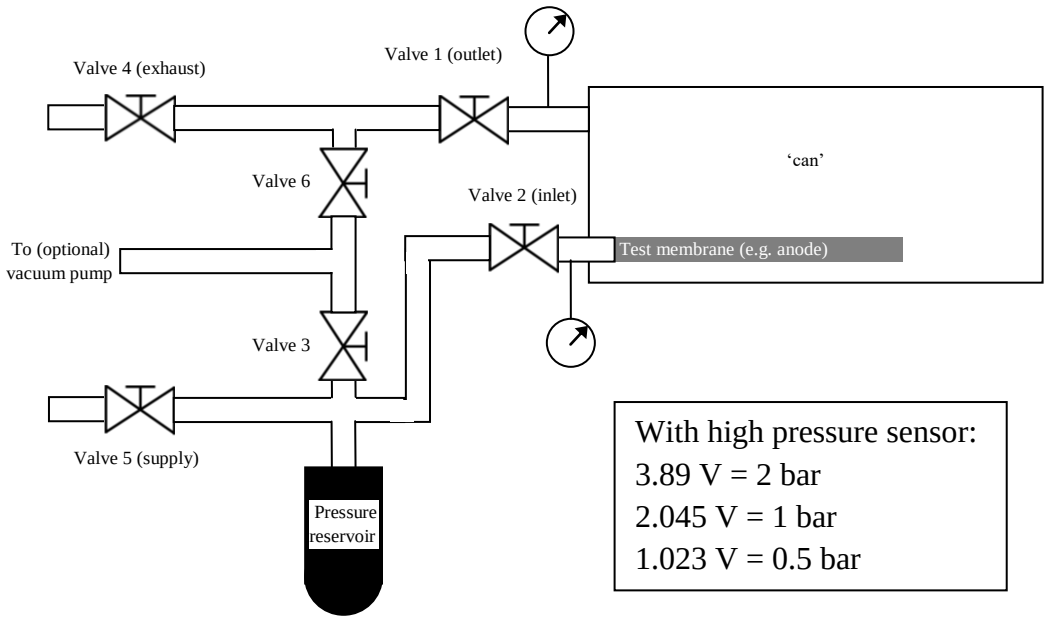

With the sample loaded in place.

The gas supply is connected to 5 (the supply valve). A single line will carry both the purge gas and the test gas(es) to the rig. Switching between gases is achieved using a 4-

position valve on this single gas line. In turn this is connected to the gas manifold/s lines. Before beginning the line needs to be purged. Do this by closing valves 1 and 2, opening valves 3–6 and passing a small amount of argon through the system.

Note: The pressures are limited to ones suitable for the permeametry and sensors using throttle valves/ a bubbler at the mass flow control end.

Initially valves 1–3 and 5 are open, 4 is closed, and unless a vacuum pump is used valve 6 is left open throughout.
Back fill with argon or helium till desired permeametry pressure (normally 0.5 bar = 50 kPa).
Close all valves including the gas supply valve (5) then open valve 4 to vent the exhaust line.
Measure the pressure with both the 0–250 kPa sensor and the 0–50 kPa sensor. Doing so with both (one at each pressure take off) is necessary to check the two isolated portions of the rig (the test chamber itself via the pressure take off port near valve 1 and the plumbing via the pressure take off near valve 2).
Leave for approx 15 minutes and then measure again. There should have been no drop in pressure.

Alternatively use the helium leak detector instead of a timed pressure drop is this is available.

Pre-Test Purge:
Open valves 1–4 to vent the system to close to atmospheric pressure.
Close valve 4, open 5 and back fill with argon to 0.5 bar gauge.
Close valve 5.
Open valve 4 again to vent the system a second time.
Close valve 4, open valve 5 and back fill again to 0.5 bar gauge.
Close valve 5.
Open valve 4 again to vent the system a third time.

Changing to Permeametry Gas:
At this stage valves 1–4 are open and 5 is closed.
Switch from the purge gas to the process gas at the gas selector valve. If using a flammable test gas attach the anti-flashback orifice to valve 4.
Close valve 4, open 5 and back fill with the test gas to 0.5 bar gauge.
Close valve 5.
Open valve 4 to vent the system.
Close valve 4, open 5 and back fill with the test gas to 0.5 bar gauge.
Close valve 5.
Open valve 4 to vent the system a second and final time.

Close valve 4, open 5 and back fill with the test gas to the test pressure.
Close valve 5.
Close valves 2 and 3.
Open valves 1 and 4.
Allow the pressure to drop to atmospheric, checking the pressure take offs near valve 1.
Record this pressure, at pressure take off near valve 2.
Open valve 2 and begin timing for the pressure-drop-over-time permeametry.
Close the supply gas valve and leave system for the desired time (notice the rig uses a pressure reservoir, but the supply is switched off otherwise there will not be any pressure drop!).
Take the second pressure reading (from the pressure take off near valve 2). The second measurement should be taken before the pressures have completely equalised. Doing so allows calculation of the volume of gas passed.

Post-Permeametry Purge:
After measurements valves 1, 2 and 4 are open and valves 3, 5 and the supply valve are closed.
Open valve 3 and allow reservoir, sample and chamber to vent.
Close valve 4.
Switch from the process gas to the purge gas at the gas selector valve.
Open the gas supply valve.
Slowly open valve 5 and back fill with argon to 0.5 bar gauge.
Close valve 5.
Open valve 4 to vent the system to atmosphere.
Close valve 4, open 5 and back fill again to 0.5 bar gauge.
Close valve 5.
Open valve 4 again to vent the system a second time.
Close valve 4, open 5 and back fill again to 0.5 bar gauge.
Close valve 5.
Open valve 4 again to vent the system a third and final time.
Close the gas supply valve.

Unloading:
Disconnect the gas supply line from the permeameter.
Switch off the pressure sensor power supply.
Disconnect the pressure sensor ports (optional).
Only at this point begin unloading.

Permeametry or Leak Testing?
NB: the rig and SOP are designed so the gas permeating through the membrane passes into a larger volume of Ar ensuring the ability to safely carry out permeametry experiments with gases like hydrogen.

The rig is designed to either pressurise the membrane from the inlet side (valve 2) or the chamber side (valve 1). As such which port is fitted with which sensor depends on the type of experiment carried out. To use the rig with the original equations (designed to reflect pressure drops) the sensor should be at the pressure take off nearest that side of the membrane.

For normal permeametry measurements use the 0–50 kPa sensor at the pressure take off near the inlet valve (valve 2) for maximum accuracy. The high pressure sensor can be used as a check of measurements (note it is less accurate at low pressure differences so the other sensor should be used for recorded readings.

The rig can also be utilised to measure leaks across a nominally impermeable membrane. This is achieved using the 0–250 kPa sensor at pressure take off near the inlet valve instead of the low pressure one. However, do not exceed 0.5 bar in the leak test and purge procedures as this may damage the 0–0.5 bar sensor (now attached near valve 1 for the second pressure measurement during leak testing and to check purging).

Other notes:
At time of writing; Chamber has an internal volume of 251.58 cc measured with a 60 mm length of SS rod, 3/8" OD plugging the aperture for the tubular membrane/sample, measured from the outside edge of the fitting.

When the equipment is not scheduled for use immediately close all valves and store the inlet plug inside to prevent contamination.

Emergency shut-down procedure

In case of emergency:

- Isolate the gas supply by closing the gas supply valve and valve 5.
- Stop outflow of gas (if necessary) by closing valve 4.

Upon building evacuation; if possible turn off gas supplies from gas store.

Hydraulic Leak Test

This was a test carried out before any measurements using the rig were made, proofing the chamber safety at pressure. NB: No sensors were connected to prevent damage and the valves and fittings were not tested (these are rated to high pressure by the manufacturer). In essence, the hydraulic test checks the integrity of the test chamber's welds.

A stainless steel tube (with both ends left open) was used in place of a sample. Wire was used to hold components together and prevent parts coming apart (possibly violently) under pressure should any seals, welds or fittings fail.

The chamber was filled with water (letting bubbles out) up till atmospheric pressure (i.e. 0 bar gauge). A manual pump was used to pressurise with water to verify the integrity of the vessel (the ‘can’). A calibrated pressure gauge (part of the hydraulic tester) was used to measure the pressure.

The entire test was recorded on video, with frequent still images of the gauge and setup. The most important images are reproduced below:

Held at 8 bar. The gauge connector developed a slight leak, otherwise no leaks. The connector was reinforced for better sealing.

Held at 10 bar with no detectable leaks. Test end.

Appendix L: All Permeametry Plots

All the plots referred to in the chapter are presented here for reference, including any exemplars explicitly shown as part of the discussion.

Pressure Drop with Time: Anode

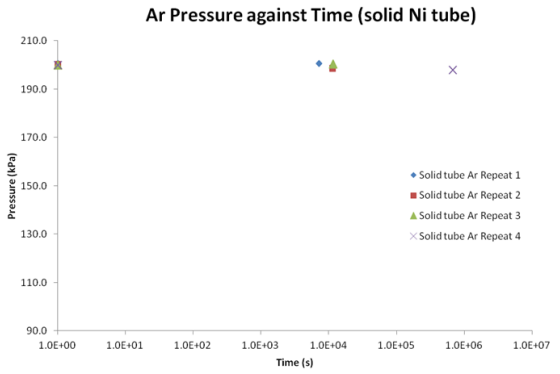

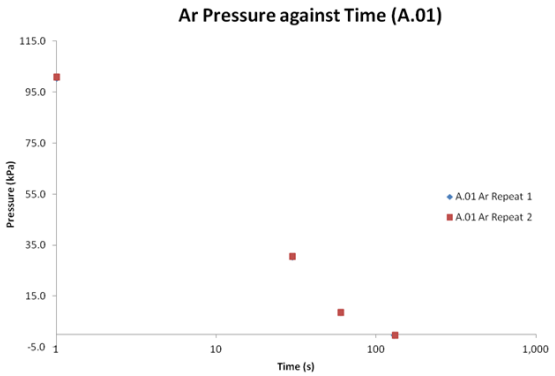

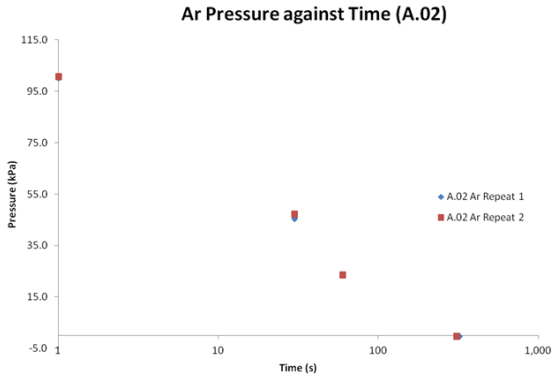

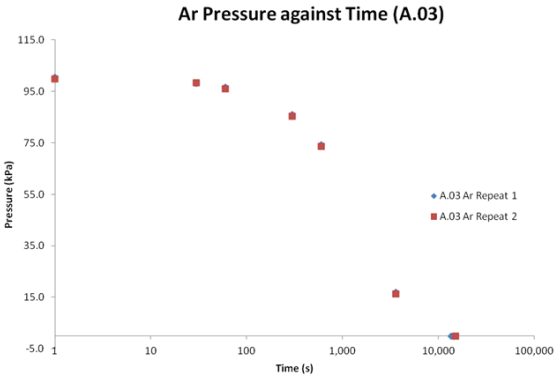

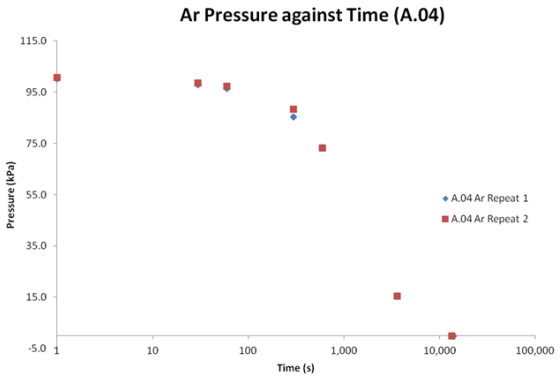

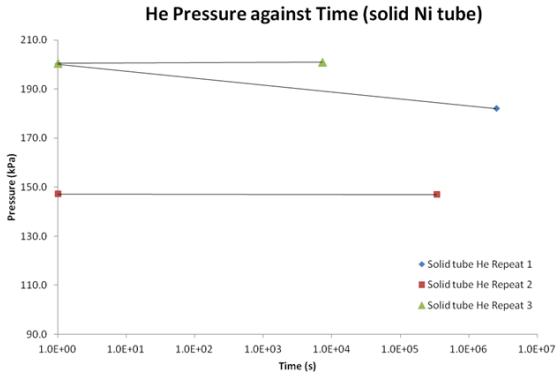
He Pressure against Time (solid Ni tube)
Pressure (kPa)
210.0
190.0
170.0
150.0
130.0
110.0
90.0
1.0E+00
1.0E+01
1.0E+02
1.0E+03
1.0E+04
1.0E+05
1.0E+06
1.0E+07
Time (s)
Solid tube He Repeat 1
Solid tube He Repeat 2
Solid tube He Repeat 3

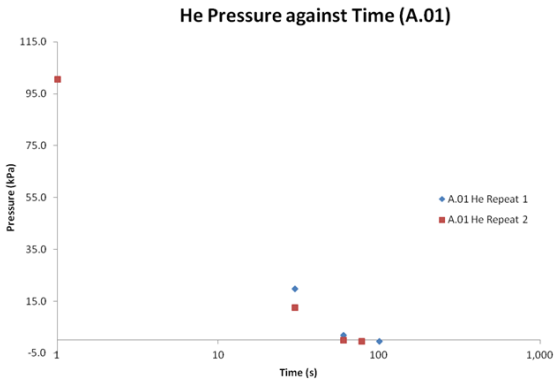
He Pressure against Time (A.01)
Pressure (kPa)
115.0
95.0
75.0
55.0
35.0
15.0
-5.0
1
10
100
1,000
Time (s)
A.01 He Repeat 1
A.01 He Repeat 2

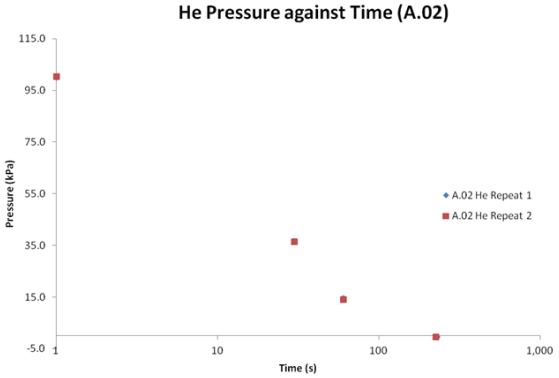
He Pressure against Time (A.02)
Pressure (kPa)
115.0
95.0
75.0
55.0
35.0
15.0
-5.0
1
10
100
1,000
Time (s)
A.02 He Repeat 1
A.02 He Repeat 2

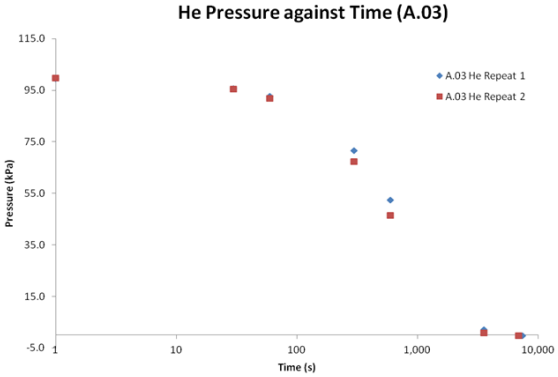
He Pressure against Time (A.03)
Pressure (kPa)
115.0
95.0
75.0
55.0
35.0
15.0
-5.0
1
10
100
1,000
10,000
Time (s)
A.03 He Repeat 1
A.03 He Repeat 2

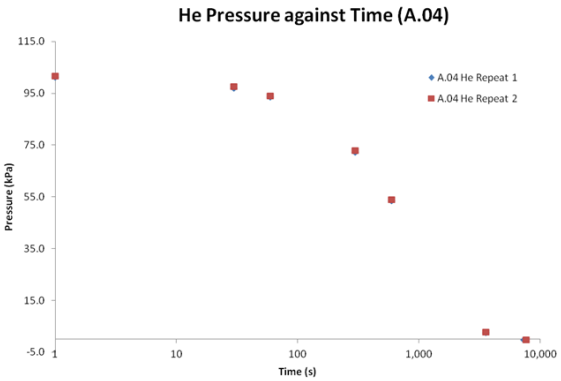
He Pressure against Time (A.04)
Pressure (kPa)
115.0
95.0
75.0
55.0
35.0
15.0
-5.0
1
10
100
1,000
10,000
Time (s)
A.04 He Repeat 1
A.04 He Repeat 2

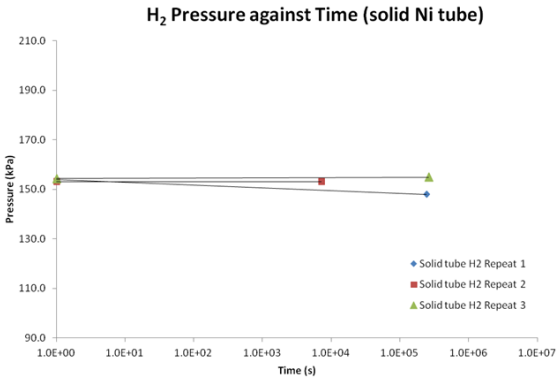
H2 Pressure against Time (solid Ni tube)
Pressure (kPa)
Time (s)
Solid tube H2 Repeat 1
Solid tube H2 Repeat 2
Solid tube H2 Repeat 3

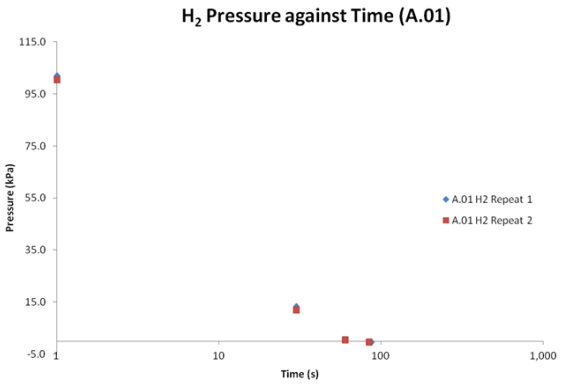
H2 Pressure against Time (A.01)
Pressure (kPa)
Time (s)
A.01 H2 Repeat 1
A.01 H2 Repeat 2

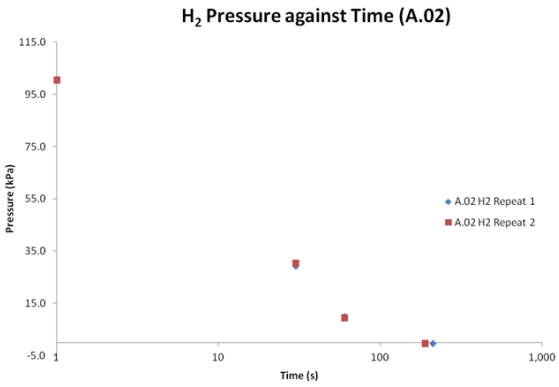
H2 Pressure against Time (A.02)
Pressure (kPa)
Time (s)
A.02 H2 Repeat 1
A.02 H2 Repeat 2

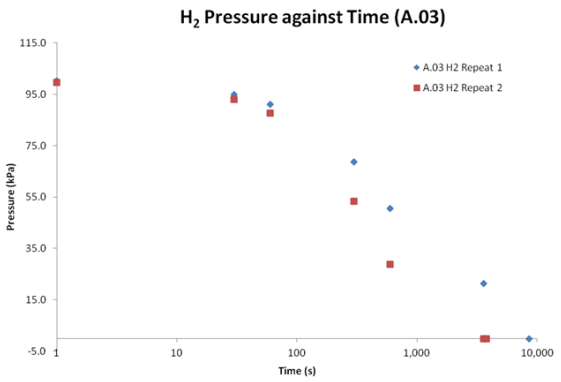
H2 Pressure against Time (A.03)
Pressure (kPa)
Time (s)
A.03 H2 Repeat 1
A.03 H2 Repeat 2

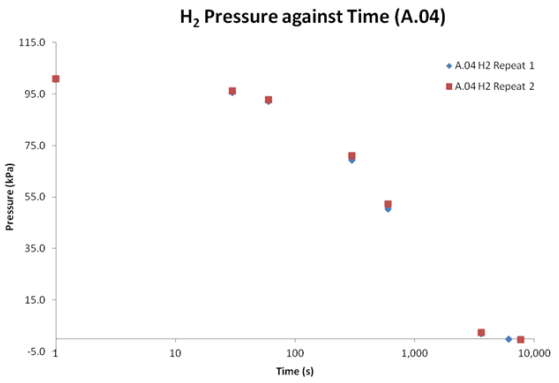
H2 Pressure against Time (A.04)
Pressure (kPa)
Time (s)
A.04 H2 Repeat 1
A.04 H2 Repeat 2

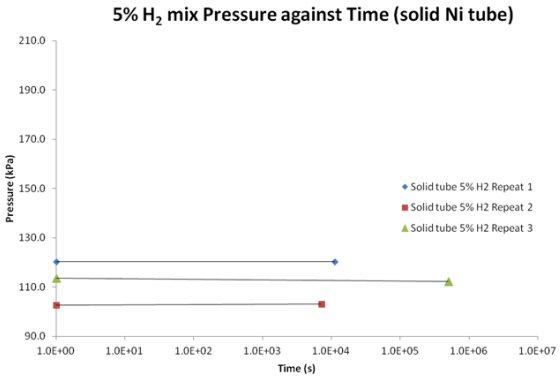
5% H2 mix Pressure against Time (solid Ni tube)
Pressure (kPa)
Time (s)
Solid tube 5% H2 Repeat 1
Solid tube 5% H2 Repeat 2
Solid tube 5% H2 Repeat 3

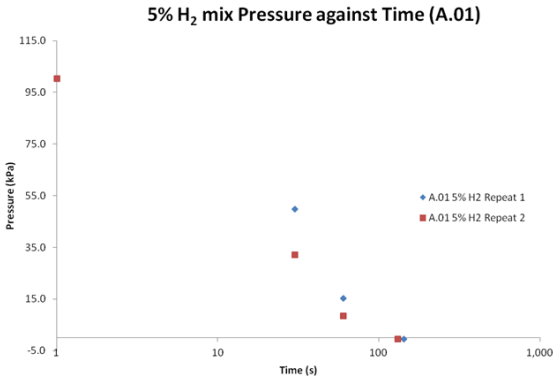
5% H2 mix Pressure against Time (A.01)
Pressure (kPa)
Time (s)
A.01 5% H2 Repeat 1
A.01 5% H2 Repeat 2

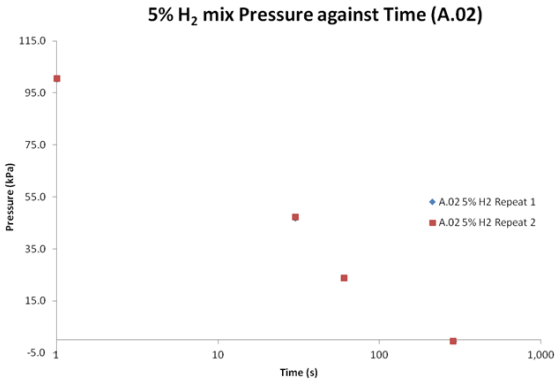
5% H2 mix Pressure against Time (A.02)
Pressure (kPa)
Time (s)
A.02 5% H2 Repeat 1
A.02 5% H2 Repeat 2

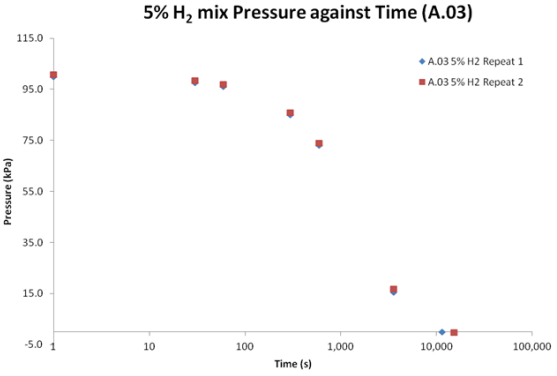
5% H2 mix Pressure against Time (A.03)
Pressure (kPa)
Time (s)
A.03 5% H2 Repeat 1
A.03 5% H2 Repeat 2

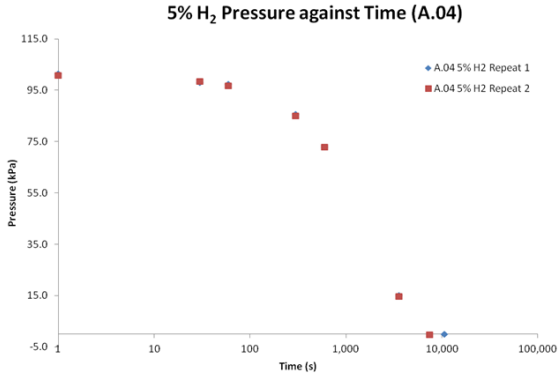
5% H2 Pressure against Time (A.04)
Pressure (kPa)
Time (s)
A.04 5% H2 Repeat 1
A.04 5% H2 Repeat 2

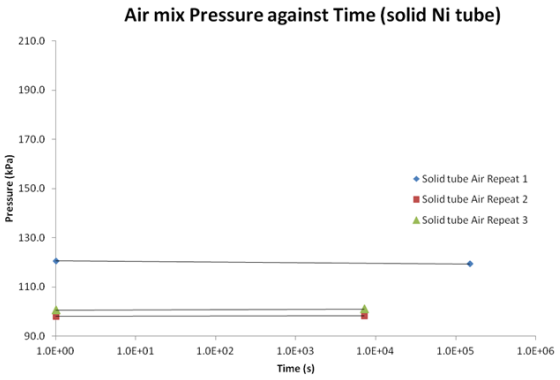
Air mix Pressure against Time (solid Ni tube)
Pressure (kPa)
Time (s)
Solid tube Air Repeat 1
Solid tube Air Repeat 2
Solid tube Air Repeat 3

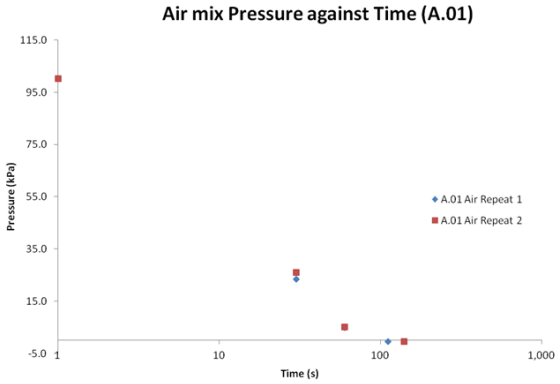
Air mix Pressure against Time (A.01)
Pressure (kPa)
Time (s)
A.01 Air Repeat 1
A.01 Air Repeat 2

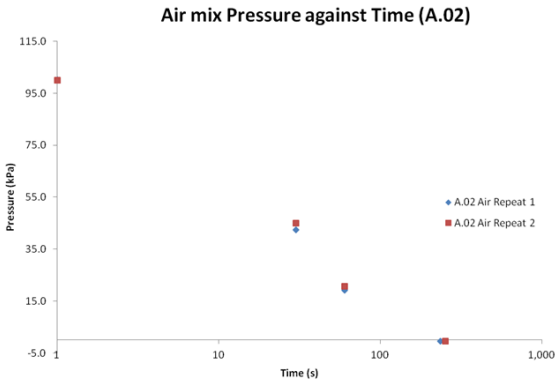
Air mix Pressure against Time (A.02)
Pressure (kPa)
Time (s)
A.02 Air Repeat 1
A.02 Air Repeat 2

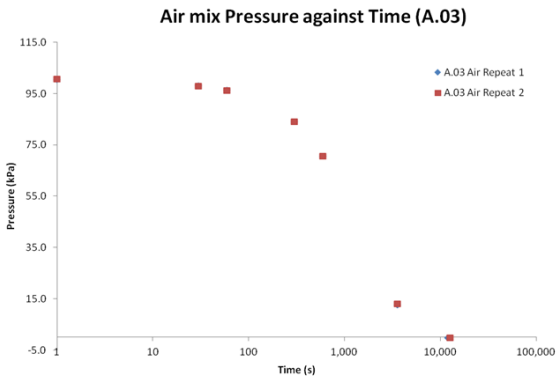
Air mix Pressure against Time (A.03)
Pressure (kPa)
Time (s)
A.03 Air Repeat 1
A.03 Air Repeat 2

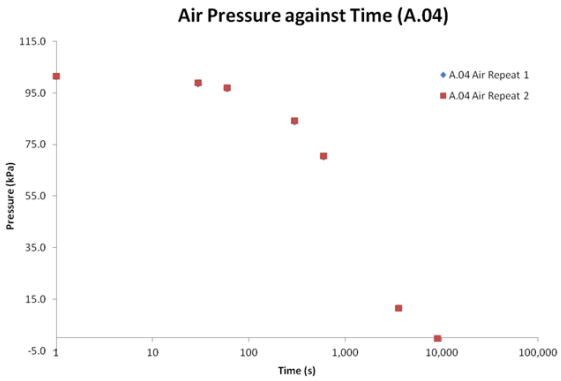
Air Pressure against Time (A.04)
Pressure (kPa)
Time (s)
A.04 Air Repeat 1
A.04 Air Repeat 2

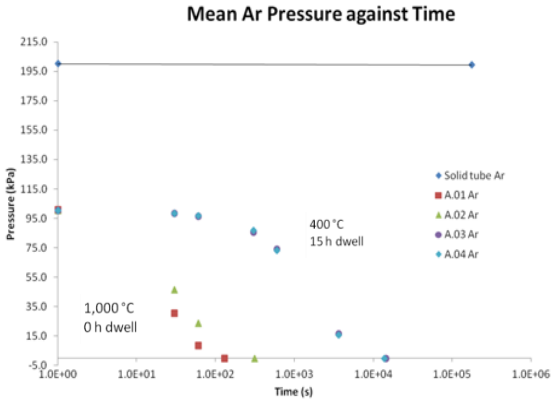
Mean Ar Pressure against Time
Pressure (kPa)
Time (s)
Solid tube Ar
A.01 Ar
A.02 Ar
A.03 Ar
A.04 Ar
400 °C
15 h dwell
1,000 °C
0 h dwell

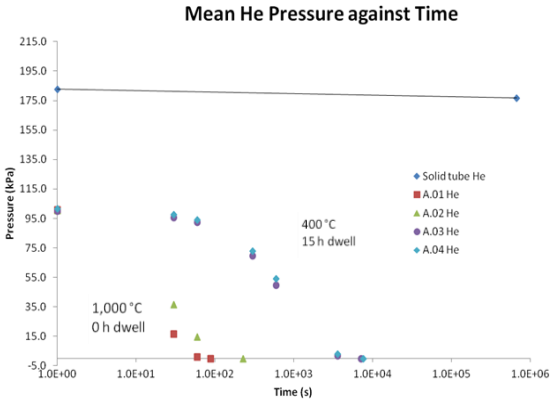
Mean He Pressure against Time
Pressure (kPa)
Time (s)
Solid tube He
A.01 He
A.02 He
A.03 He
A.04 He
400 °C
15 h dwell
1,000 °C
0 h dwell

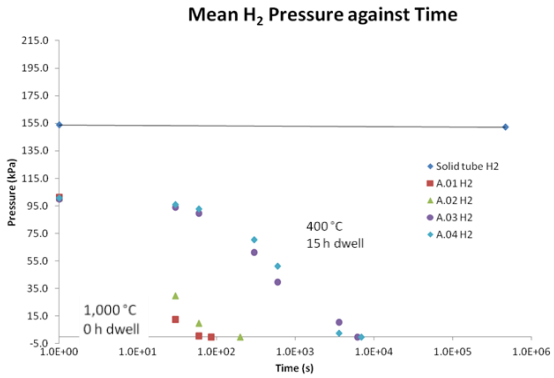
Mean H2 Pressure against Time
Pressure (kPa)
Time (s)
Solid tube H2
A.01 H2
A.02 H2
A.03 H2
A.04 H2
400 °C
15 h dwell
1,000 °C
0 h dwell

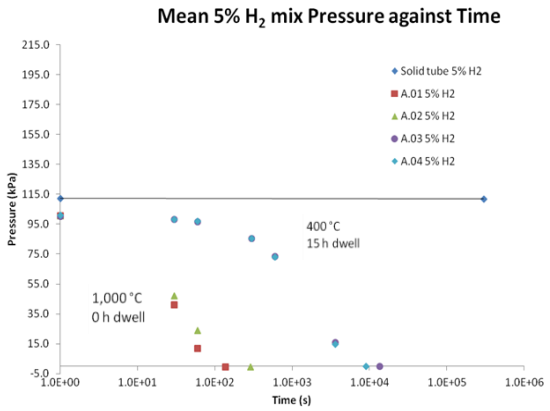
Mean 5% H2 mix Pressure against Time
Pressure (kPa)
Time (s)
Solid tube 5% H2
A.01 5% H2
A.02 5% H2
A.03 5% H2
A.04 5% H2
400 °C
15 h dwell
1,000 °C
0 h dwell

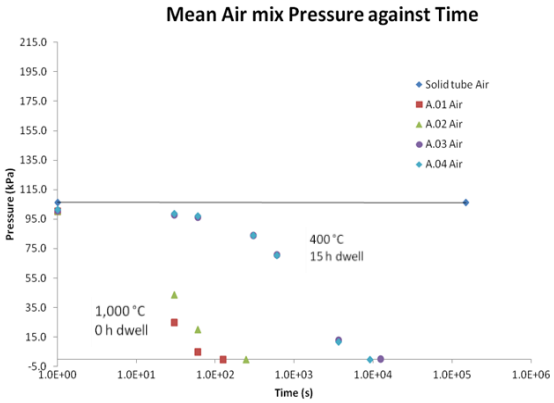
Mean Air mix Pressure against Time
Pressure (kPa)
Time (s)
Solid tube Air
A.01 Air
A.02 Air
A.03 Air
A.04 Air
400 °C
15 h dwell
1,000 °C
0 h dwell

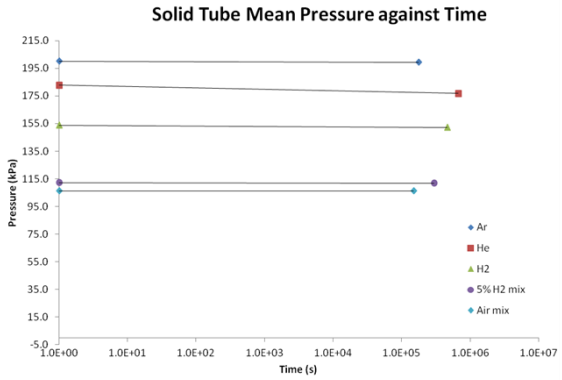
Solid Tube Mean Pressure against Time
Pressure (kPa)
215.0
195.0
175.0
155.0
135.0
115.0
95.0
75.0
55.0
35.0
15.0
-5.0
1.0E+00
1.0E+01
1.0E+02
1.0E+03
1.0E+04
1.0E+05
1.0E+06
1.0E+07
Time (s)
Ar
He
H2
5% H2 mix
Air mix

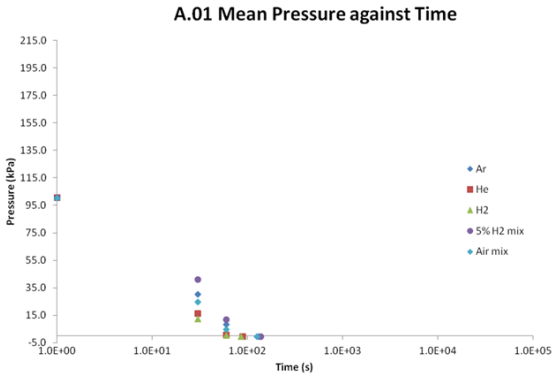
A.01 Mean Pressure against Time
Pressure (kPa)
215.0
195.0
175.0
155.0
135.0
115.0
95.0
75.0
55.0
35.0
15.0
-5.0
1.0E+00
1.0E+01
1.0E+02
1.0E+03
1.0E+04
1.0E+05
Time (s)
Ar
He
H2
5% H2 mix
Air mix

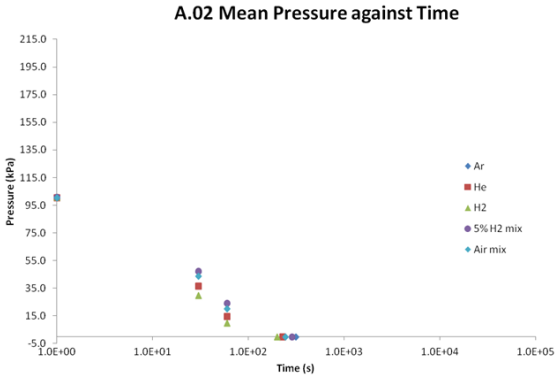
A.02 Mean Pressure against Time
Pressure (kPa)
215.0
195.0
175.0
155.0
135.0
115.0
95.0
75.0
55.0
35.0
15.0
-5.0
1.0E+00
1.0E+01
1.0E+02
1.0E+03
1.0E+04
1.0E+05
Time (s)
Ar
He
H2
5% H2 mix
Air mix

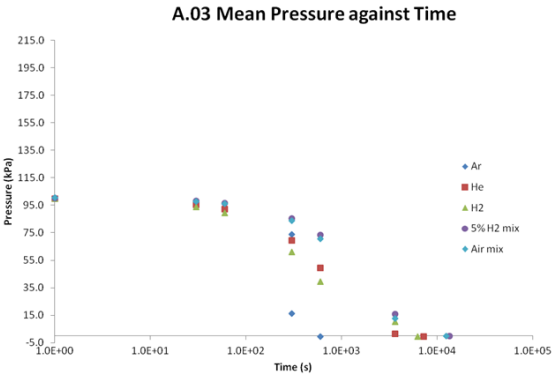
A.03 Mean Pressure against Time
Pressure (kPa)
215.0
195.0
175.0
155.0
135.0
115.0
95.0
75.0
55.0
35.0
15.0
-5.0
1.0E+00
1.0E+01
1.0E+02
1.0E+03
1.0E+04
1.0E+05
Time (s)
Ar
He
H2
5% H2 mix
Air mix

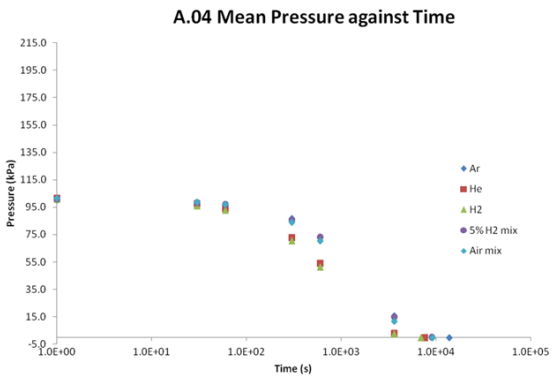
A.04 Mean Pressure against Time
Pressure (kPa)
215.0
195.0
175.0
155.0
135.0
115.0
95.0
75.0
55.0
35.0
15.0
-5.0
1.0E+00
1.0E+01
1.0E+02
1.0E+03
1.0E+04
1.0E+05
Time (s)
Ar
He
H2
5% H2 mix
Air mix

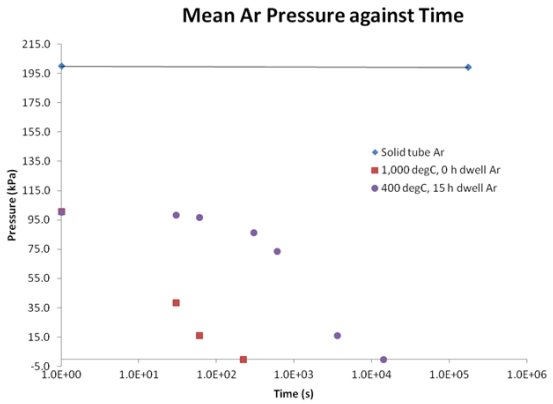
Mean Ar Pressure against Time
Pressure (kPa)
Time (s)
Solid tube Ar
1,000 degC, 0 h dwell Ar
400 degC, 15 h dwell Ar

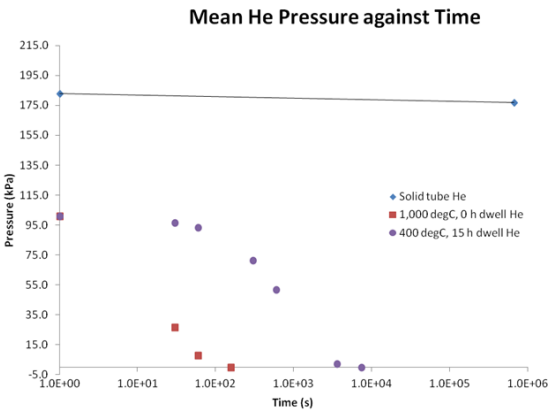
Mean He Pressure against Time
Pressure (kPa)
Time (s)
Solid tube He
1,000 degC, 0 h dwell He
400 degC, 15 h dwell He

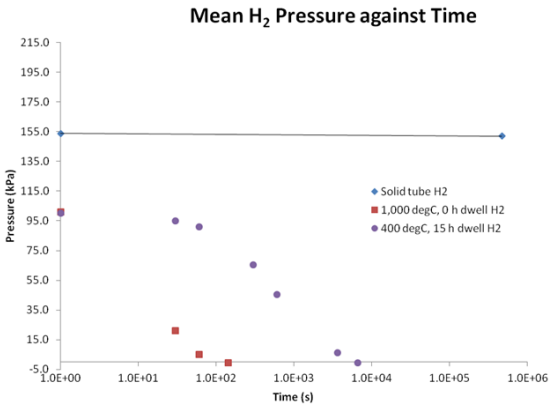
Mean H2 Pressure against Time
Pressure (kPa)
Time (s)
Solid tube H2
1,000 degC, 0 h dwell H2
400 degC, 15 h dwell H2

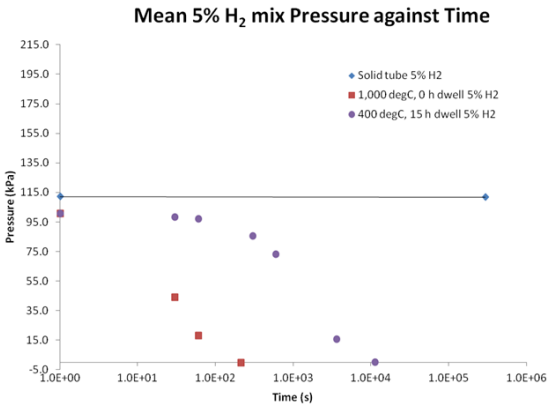
Mean 5% H2 mix Pressure against Time
Pressure (kPa)
Time (s)
Solid tube 5% H2
1,000 degC, 0 h dwell 5% H2
400 degC, 15 h dwell 5% H2

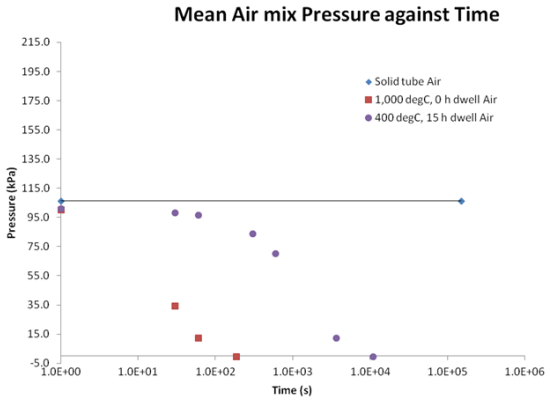
Mean Air mix Pressure against Time
Pressure (kPa)
Time (s)
Solid tube Air
1,000 degC, 0 h dwell Air
400 degC, 15 h dwell Air

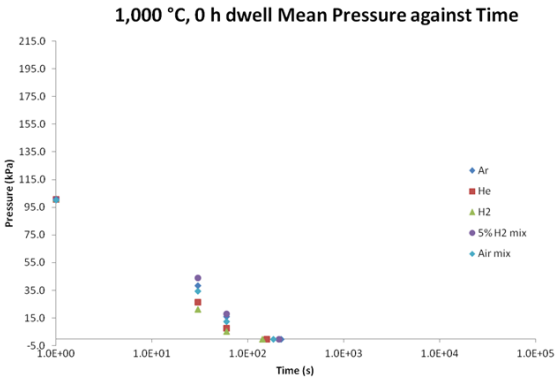
1,000 °C, 0 h dwell Mean Pressure against Time
Pressure (kPa)
Time (s)
Ar
He
H2
5% H2 mix
Air mix

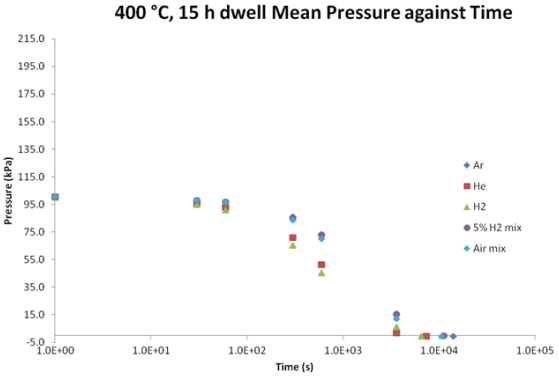
400 °C, 15 h dwell Mean Pressure against Time
Pressure (kPa)
Time (s)
Ar
He
H2
5% H2 mix
Air mix

Pressure Drop with Time: Anode-Electrolyte Complex

In the interest of space about a third of the plots used for analysis were not included (those showing single samples and single gasses) since comparing them on a single plot is more useful.

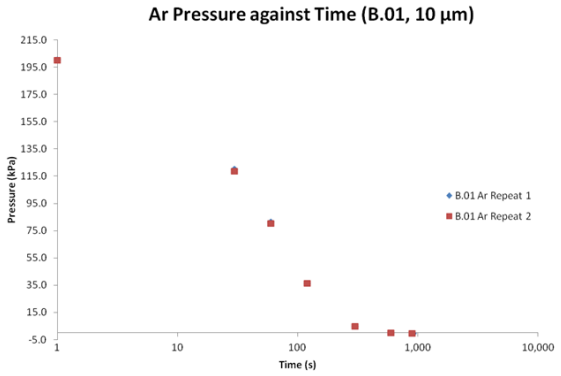

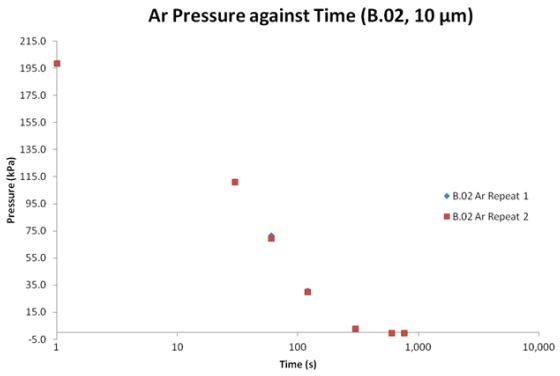

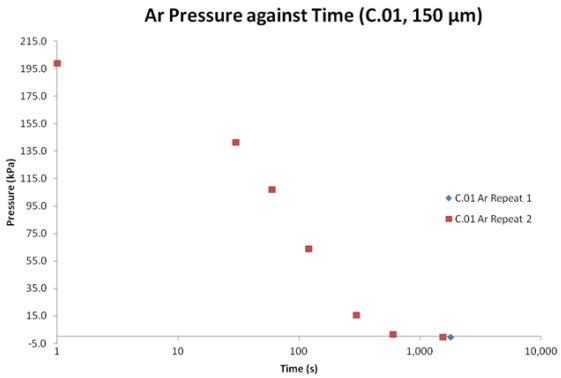

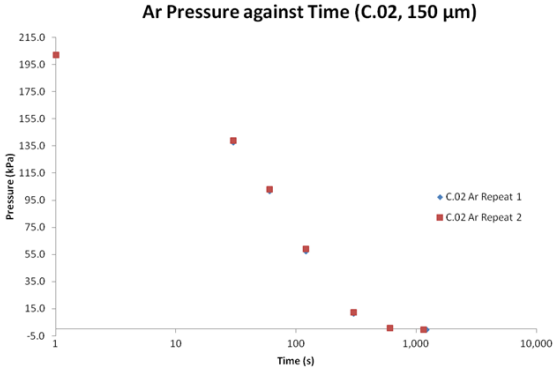

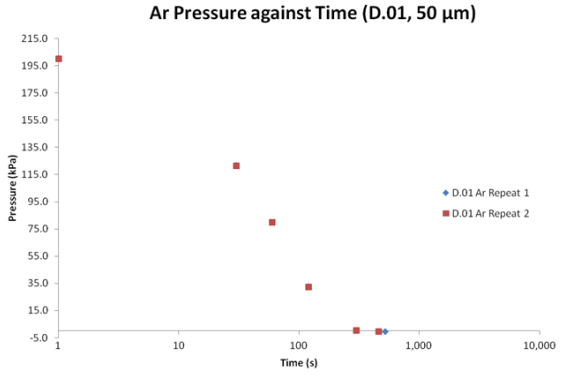

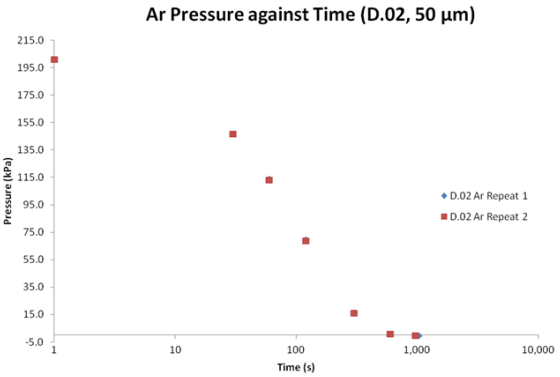

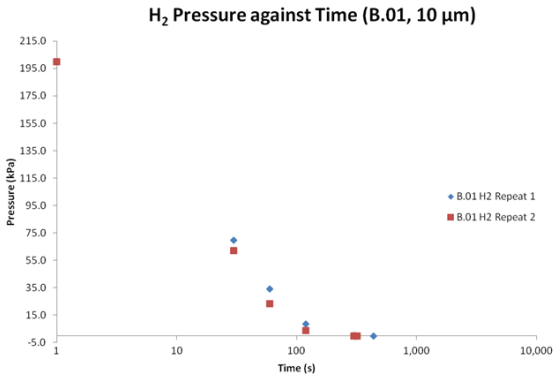
H2 Pressure against Time (B.01, 10 µm)
Pressure (kPa)
215.0
195.0
175.0
155.0
135.0
115.0
95.0
75.0
55.0
35.0
15.0
-5.0
1
10
100
1,000
10,000
Time (s)
B.01 H2 Repeat 1
B.01 H2 Repeat 2

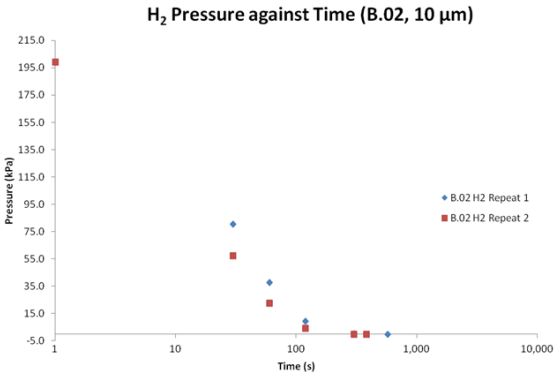
H2 Pressure against Time (B.02, 10 µm)
Pressure (kPa)
215.0
195.0
175.0
155.0
135.0
115.0
95.0
75.0
55.0
35.0
15.0
-5.0
1
10
100
1,000
10,000
Time (s)
B.02 H2 Repeat 1
B.02 H2 Repeat 2

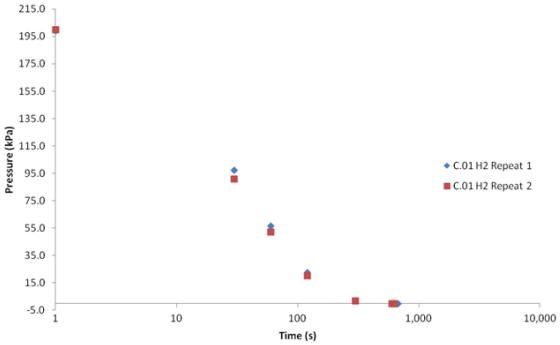
H2 Pressure against Time (C.01, 150 µm)
Pressure (kPa)
215.0
195.0
175.0
155.0
135.0
115.0
95.0
75.0
55.0
35.0
15.0
-5.0
1
10
100
1,000
10,000
Time (s)
C.01 H2 Repeat 1
C.01 H2 Repeat 2

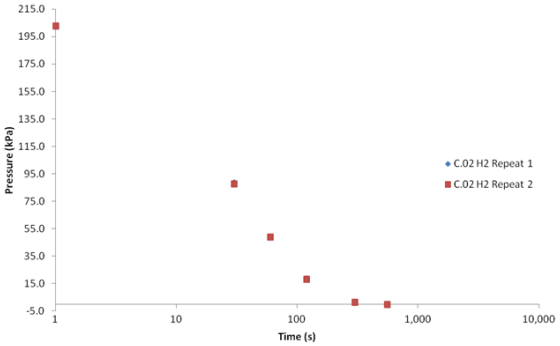
H2 Pressure against Time (C.02, 150 µm)
Pressure (kPa)
215.0
195.0
175.0
155.0
135.0
115.0
95.0
75.0
55.0
35.0
15.0
-5.0
1
10
100
1,000
10,000
Time (s)
C.02 H2 Repeat 1
C.02 H2 Repeat 2

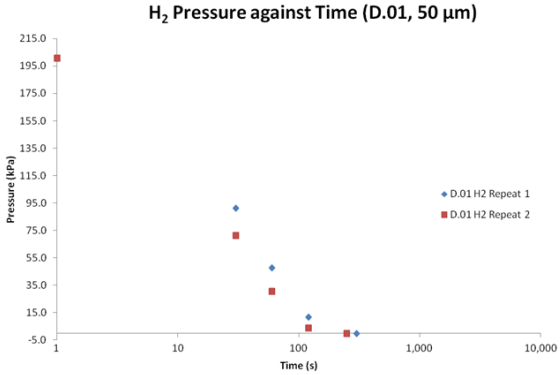
H2 Pressure against Time (D.01, 50 µm)
Pressure (kPa)
215.0
195.0
175.0
155.0
135.0
115.0
95.0
75.0
55.0
35.0
15.0
-5.0
1
10
100
1,000
10,000
Time (s)
D.01 H2 Repeat 1
D.01 H2 Repeat 2

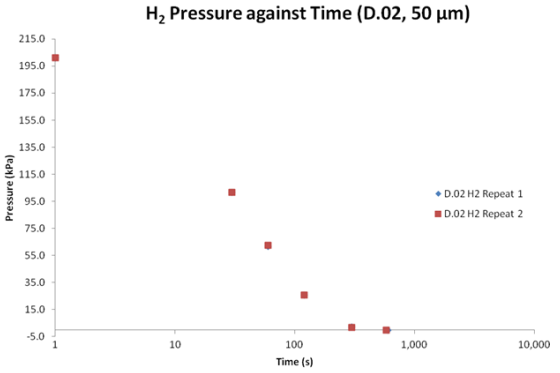
H2 Pressure against Time (D.02, 50 µm)
Pressure (kPa)
215.0
195.0
175.0
155.0
135.0
115.0
95.0
75.0
55.0
35.0
15.0
-5.0
1
10
100
1,000
10,000
Time (s)
D.02 H2 Repeat 1
D.02 H2 Repeat 2

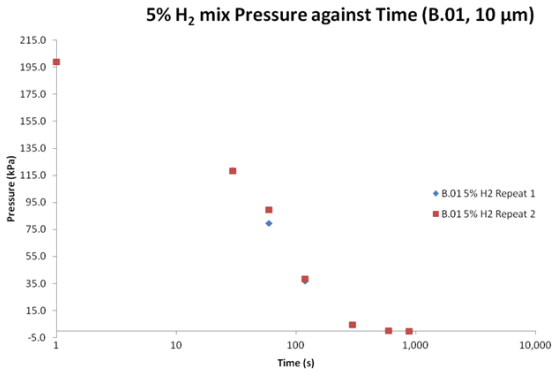
5% H2 mix Pressure against Time (B.01, 10 µm)
Pressure (kPa)
215.0
195.0
175.0
155.0
135.0
115.0
95.0
75.0
55.0
35.0
15.0
-5.0
1
10
100
1,000
10,000
Time (s)
B.01 5% H2 Repeat 1
B.01 5% H2 Repeat 2

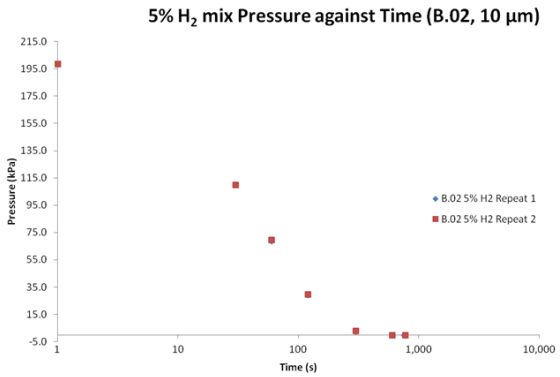
5% H2 mix Pressure against Time (B.02, 10 µm)
Pressure (kPa)
215.0
195.0
175.0
155.0
135.0
115.0
95.0
75.0
55.0
35.0
15.0
-5.0
1
10
100
1,000
10,000
Time (s)
B.02 5% H2 Repeat 1
B.02 5% H2 Repeat 2

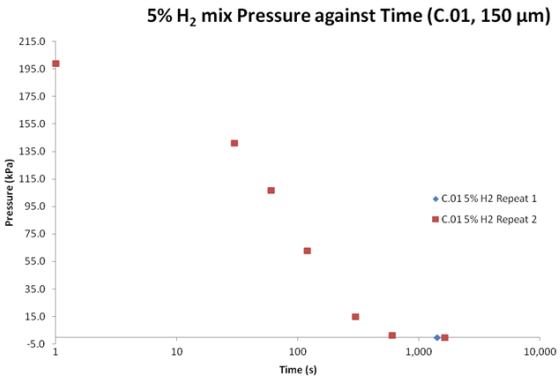
5% H2 mix Pressure against Time (C.01, 150 µm)
Pressure (kPa)
215.0
195.0
175.0
155.0
135.0
115.0
95.0
75.0
55.0
35.0
15.0
-5.0
1
10
100
1,000
10,000
Time (s)
C.01 5% H2 Repeat 1
C.01 5% H2 Repeat 2

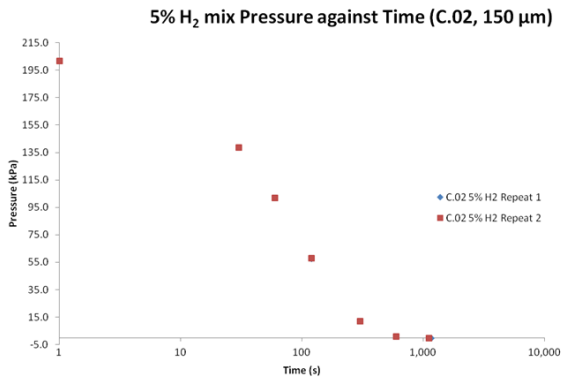
5% H2 mix Pressure against Time (C.02, 150 µm)
Pressure (kPa)
215.0
195.0
175.0
155.0
135.0
115.0
95.0
75.0
55.0
35.0
15.0
-5.0
1
10
100
1,000
10,000
Time (s)
C.02 5% H2 Repeat 1
C.02 5% H2 Repeat 2

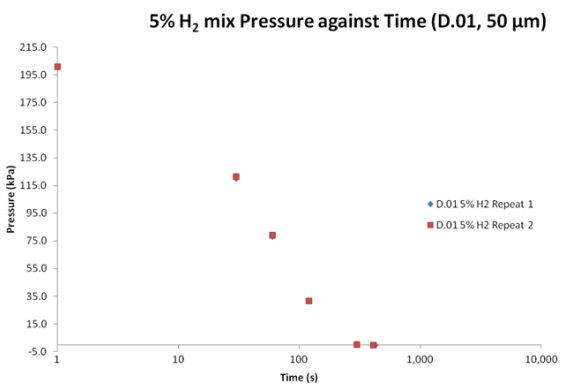
5% H2 mix Pressure against Time (D.01, 50 µm)
Pressure (kPa)
215.0
195.0
175.0
155.0
135.0
115.0
95.0
75.0
55.0
35.0
15.0
-5.0
1
10
100
1,000
10,000
Time (s)
D.01 5% H2 Repeat 1
D.01 5% H2 Repeat 2

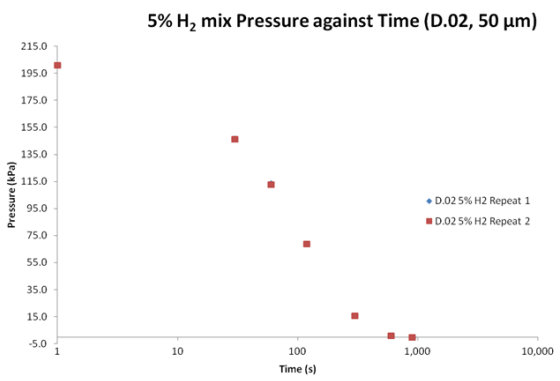
5% H2 mix Pressure against Time (D.02, 50 µm)
Pressure (kPa)
215.0
195.0
175.0
155.0
135.0
115.0
95.0
75.0
55.0
35.0
15.0
-5.0
1
10
100
1,000
10,000
Time (s)
D.02 5% H2 Repeat 1
D.02 5% H2 Repeat 2

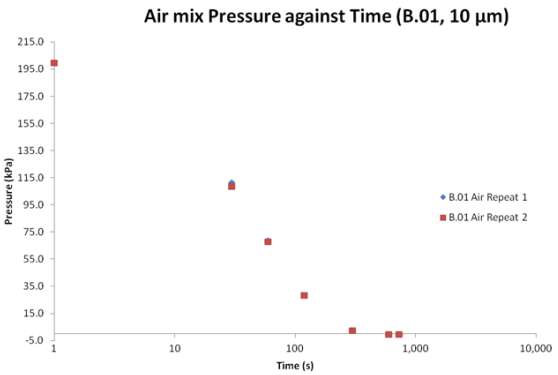
Air mix Pressure against Time (B.01, 10 µm)
Pressure (kPa)
215.0
195.0
175.0
155.0
135.0
115.0
95.0
75.0
55.0
35.0
15.0
-5.0
1
10
100
1,000
10,000
Time (s)
B.01 Air Repeat 1
B.01 Air Repeat 2

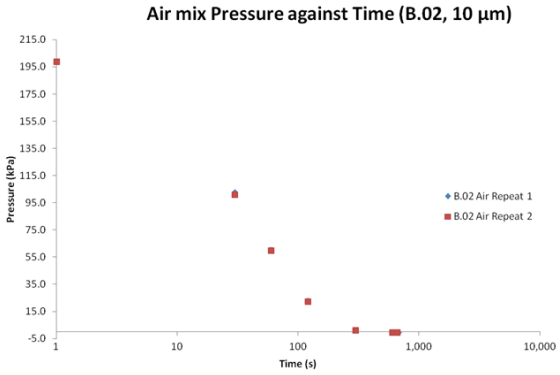
Air mix Pressure against Time (B.02, 10 µm)
Pressure (kPa)
215.0
195.0
175.0
155.0
135.0
115.0
95.0
75.0
55.0
35.0
15.0
-5.0
1
10
100
1,000
10,000
Time (s)
B.02 Air Repeat 1
B.02 Air Repeat 2

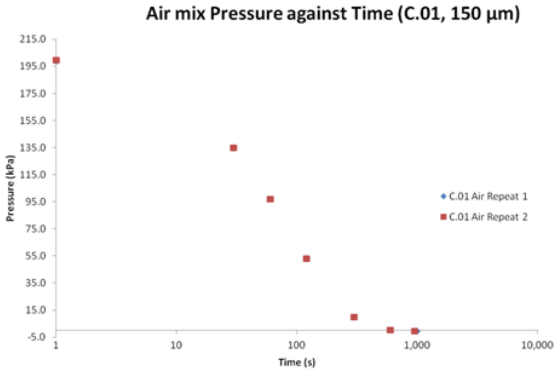
Air mix Pressure against Time (C.01, 150 µm)
Pressure (kPa)
215.0
195.0
175.0
155.0
135.0
115.0
95.0
75.0
55.0
35.0
15.0
-5.0
1
10
100
1,000
10,000
Time (s)
C.01 Air Repeat 1
C.01 Air Repeat 2

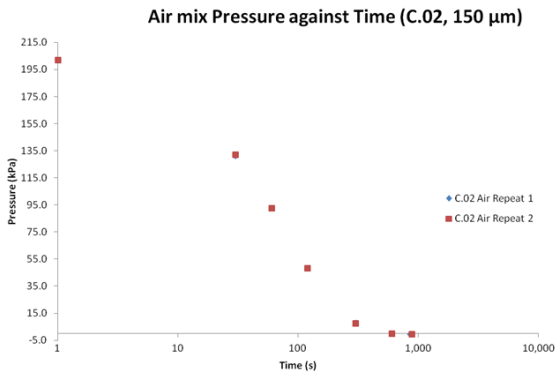
Air mix Pressure against Time (C.02, 150 µm)
Pressure (kPa)
215.0
195.0
175.0
155.0
135.0
115.0
95.0
75.0
55.0
35.0
15.0
-5.0
1
10
100
1,000
10,000
Time (s)
C.02 Air Repeat 1
C.02 Air Repeat 2

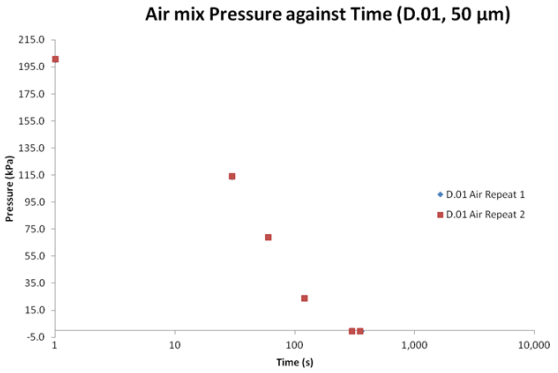
Air mix Pressure against Time (D.01, 50 µm)
Pressure (kPa)
215.0
195.0
175.0
155.0
135.0
115.0
95.0
75.0
55.0
35.0
15.0
-5.0
1
10
100
1,000
10,000
Time (s)
D.01 Air Repeat 1
D.01 Air Repeat 2

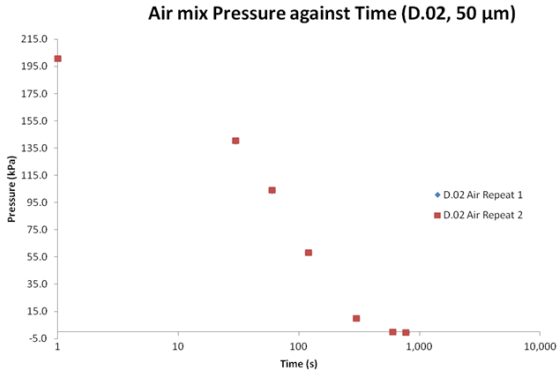
Air mix Pressure against Time (D.02, 50 µm)
Pressure (kPa)
215.0
195.0
175.0
155.0
135.0
115.0
95.0
75.0
55.0
35.0
15.0
-5.0
1
10
100
1,000
10,000
Time (s)
D.02 Air Repeat 1
D.02 Air Repeat 2

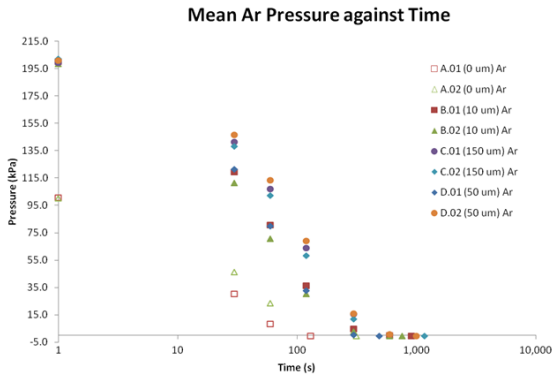
Mean Ar Pressure against Time
Pressure (kPa)
Time (s)
A.01 (0 um) Ar
A.02 (0 um) Ar
B.01 (10 um) Ar
B.02 (10 um) Ar
C.01 (150 um) Ar
C.02 (150 um) Ar
D.01 (50 um) Ar
D.02 (50 um) Ar

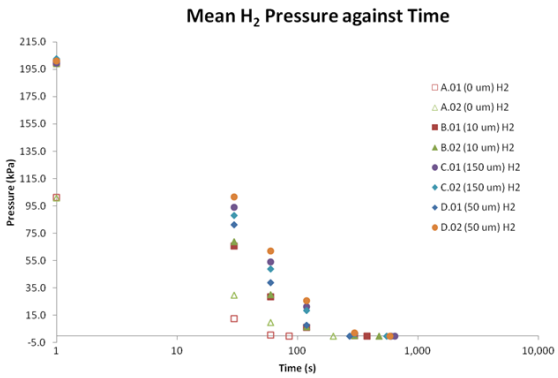
Mean H2 Pressure against Time
Pressure (kPa)
Time (s)
A.01 (0 um) H2
A.02 (0 um) H2
B.01 (10 um) H2
B.02 (10 um) H2
C.01 (150 um) H2
C.02 (150 um) H2
D.01 (50 um) H2
D.02 (50 um) H2

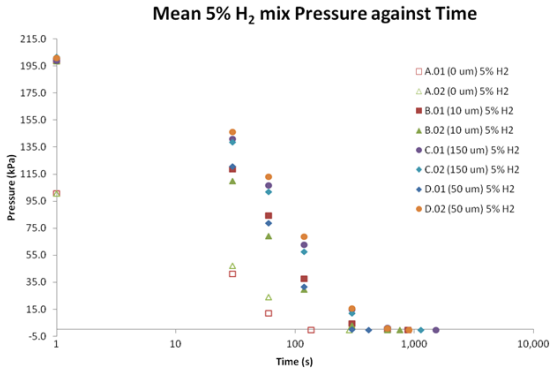
Mean 5% H2 mix Pressure against Time
Pressure (kPa)
Time (s)
A.01 (0 um) 5% H2
A.02 (0 um) 5% H2
B.01 (10 um) 5% H2
B.02 (10 um) 5% H2
C.01 (150 um) 5% H2
C.02 (150 um) 5% H2
D.01 (50 um) 5% H2
D.02 (50 um) 5% H2

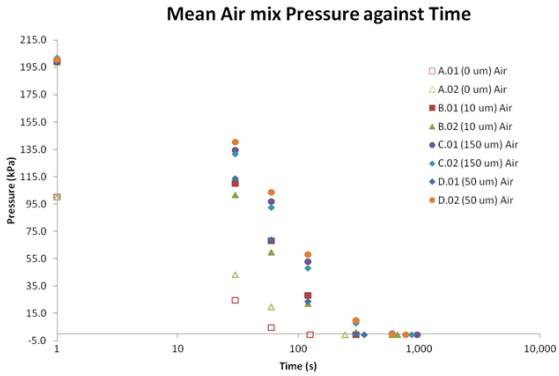
Mean Air mix Pressure against Time
Pressure (kPa)
Time (s)
A.01 (0 um) Air
A.02 (0 um) Air
B.01 (10 um) Air
B.02 (10 um) Air
C.01 (150 um) Air
C.02 (150 um) Air
D.01 (50 um) Air
D.02 (50 um) Air

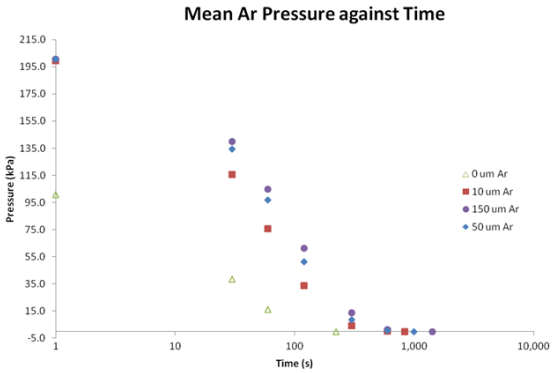
Mean Ar Pressure against Time
Pressure (kPa)
Time (s)
0 um Ar
10 um Ar
150 um Ar
50 um Ar

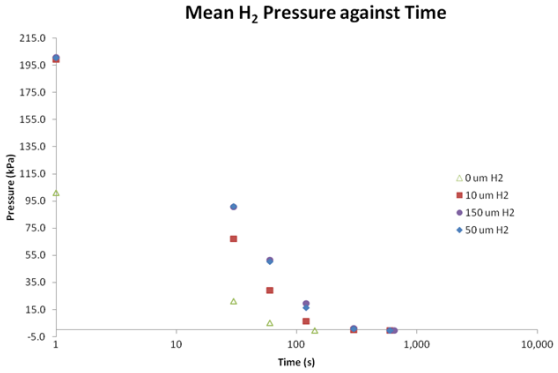
Mean H2 Pressure against Time
Pressure (kPa)
Time (s)
0 um H2
10 um H2
150 um H2
50 um H2

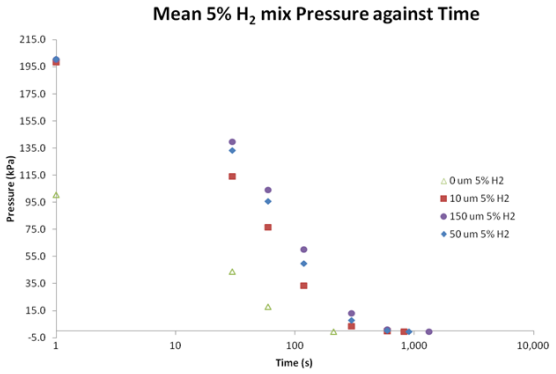
Mean 5% H2 mix Pressure against Time
Pressure (kPa)
Time (s)
0 um 5% H2
10 um 5% H2
150 um 5% H2
50 um 5% H2

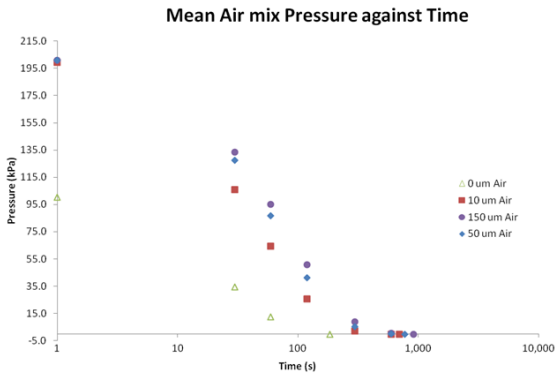
Mean Air mix Pressure against Time
Pressure (kPa)
Time (s)
0 um Air
10 um Air
150 um Air
50 um Air

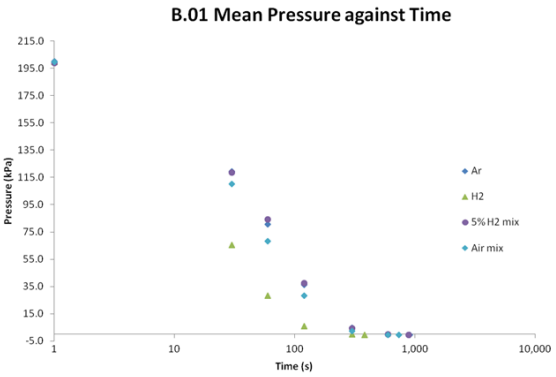
B.01 Mean Pressure against Time
Pressure (kPa)
215.0
195.0
175.0
155.0
135.0
115.0
95.0
75.0
55.0
35.0
15.0
-5.0
1
10
100
1,000
10,000
Time (s)
Ar
H2
5% H2 mix
Air mix

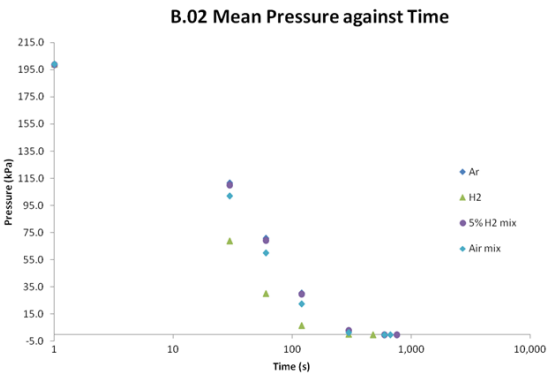
B.02 Mean Pressure against Time
Pressure (kPa)
215.0
195.0
175.0
155.0
135.0
115.0
95.0
75.0
55.0
35.0
15.0
-5.0
1
10
100
1,000
10,000
Time (s)
Ar
H2
5% H2 mix
Air mix

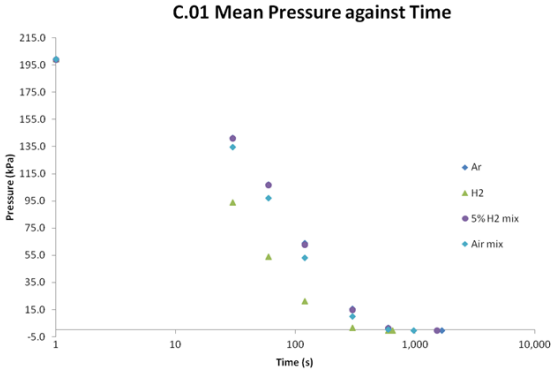
C.01 Mean Pressure against Time
Pressure (kPa)
215.0
195.0
175.0
155.0
135.0
115.0
95.0
75.0
55.0
35.0
15.0
-5.0
1
10
100
1,000
10,000
Time (s)
Ar
H2
5% H2 mix
Air mix

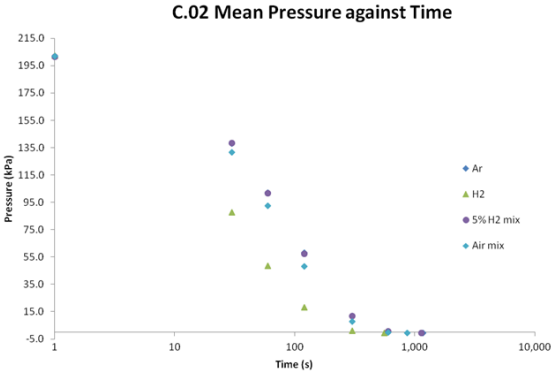
C.02 Mean Pressure against Time
Pressure (kPa)
215.0
195.0
175.0
155.0
135.0
115.0
95.0
75.0
55.0
35.0
15.0
-5.0
1
10
100
1,000
10,000
Time (s)
Ar
H2
5% H2 mix
Air mix

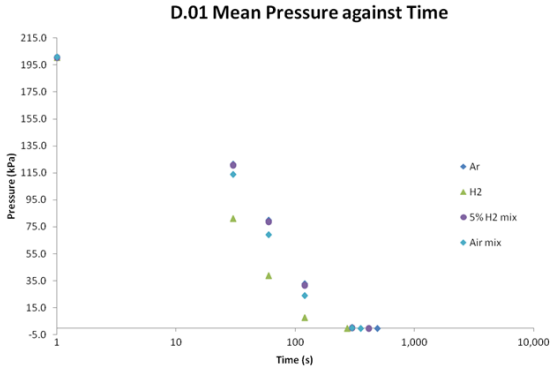
D.01 Mean Pressure against Time
Pressure (kPa)
215.0
195.0
175.0
155.0
135.0
115.0
95.0
75.0
55.0
35.0
15.0
-5.0
1
10
100
1,000
10,000
Time (s)
Ar
H2
5% H2 mix
Air mix

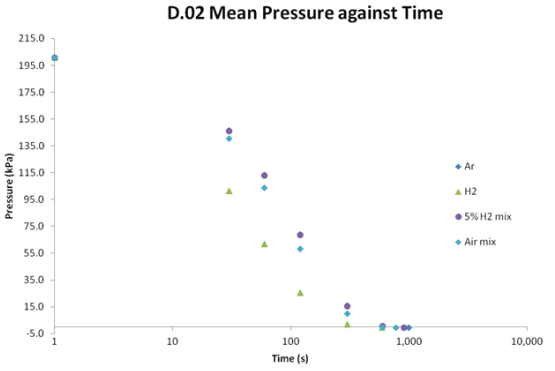
D.02 Mean Pressure against Time
Pressure (kPa)
215.0
195.0
175.0
155.0
135.0
115.0
95.0
75.0
55.0
35.0
15.0
-5.0
1
10
100
1,000
10,000
Time (s)
Ar
H2
5% H2 mix
Air mix

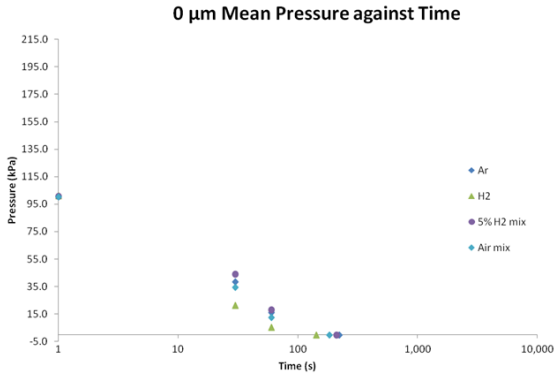
0 µm Mean Pressure against Time
Pressure (kPa)
215.0
195.0
175.0
155.0
135.0
115.0
95.0
75.0
55.0
35.0
15.0
-5.0
1
10
100
1,000
10,000
Time (s)
Ar
H2
5% H2 mix
Air mix

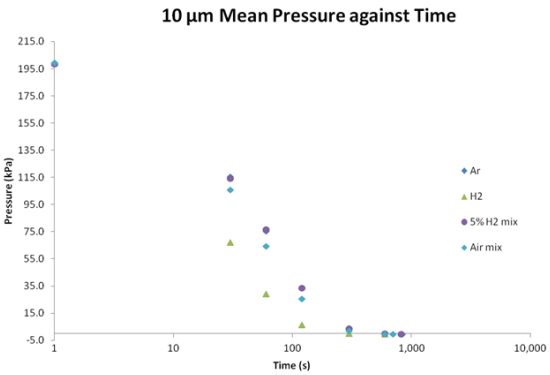
10 µm Mean Pressure against Time
Pressure (kPa)
215.0
195.0
175.0
155.0
135.0
115.0
95.0
75.0
55.0
35.0
15.0
-5.0
1
10
100
1,000
10,000
Time (s)
Ar
H2
5% H2 mix
Air mix

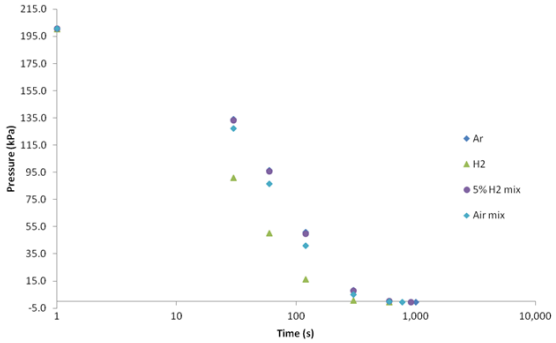
50 µm Mean Pressure against Time
Pressure (kPa)
215.0
195.0
175.0
155.0
135.0
115.0
95.0
75.0
55.0
35.0
15.0
-5.0
1
10
100
1,000
10,000
Time (s)
Ar
H2
5% H2 mix
Air mix

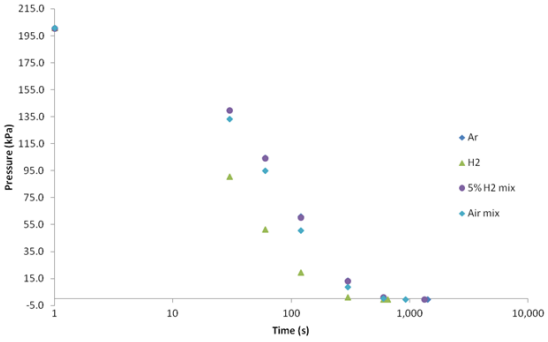
150 µm Mean Pressure against Time
Pressure (kPa)
215.0
195.0
175.0
155.0
135.0
115.0
95.0
75.0
55.0
35.0
15.0
-5.0
1
10
100
1,000
10,000
Time (s)
Ar
H2
5% H2 mix
Air mix

Permeance: Anode

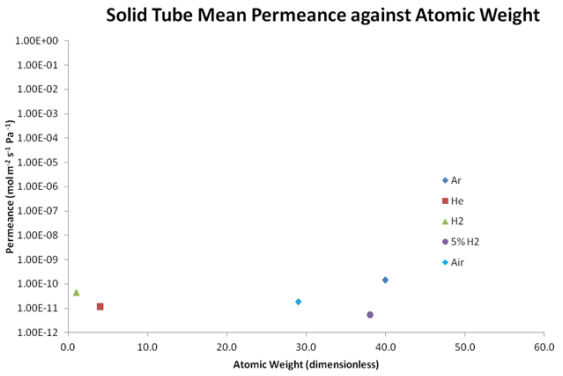

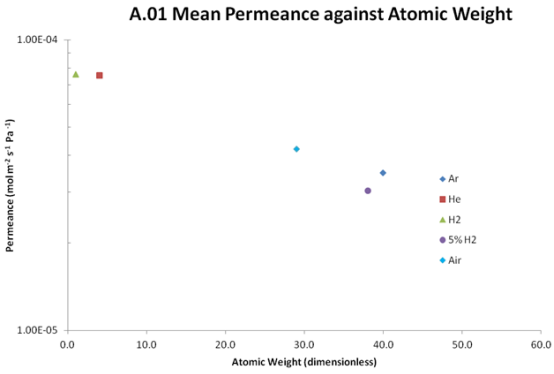

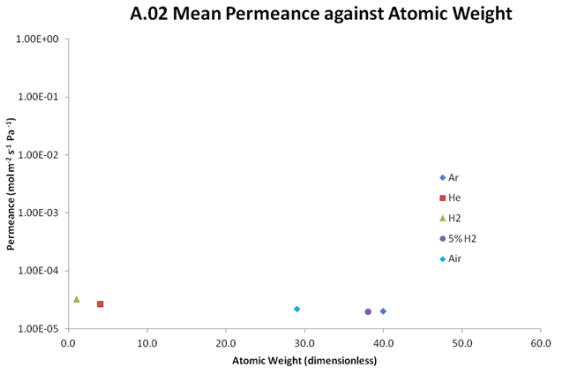

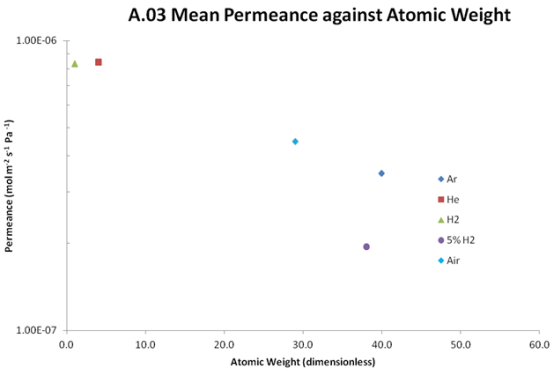

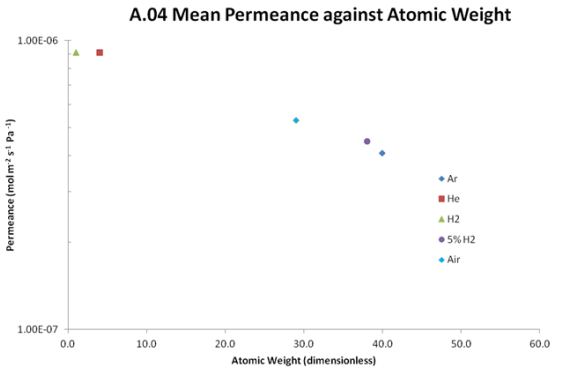

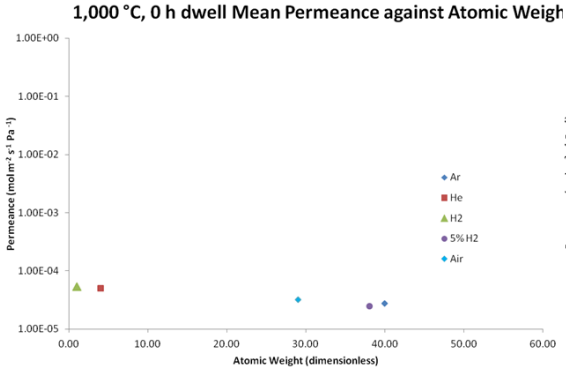

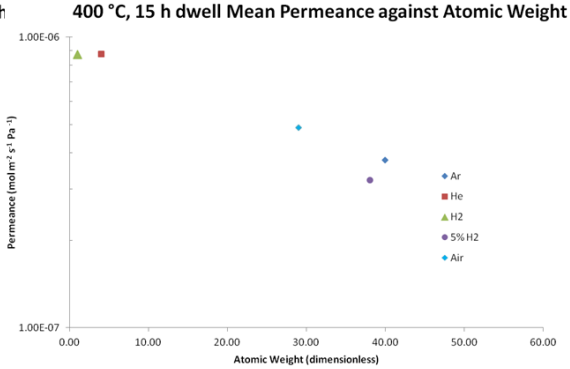

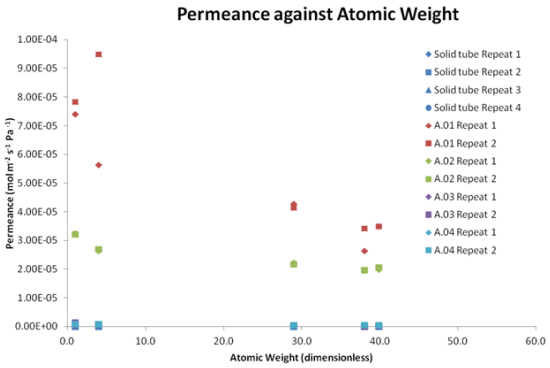
Permeance against Atomic Weight
Permeance (mol m-2 s-1 Pa-1)
Atomic Weight (dimensionless)
Solid tube Repeat 1
Solid tube Repeat 2
Solid tube Repeat 3
Solid tube Repeat 4
A.01 Repeat 1
A.01 Repeat 2
A.02 Repeat 1
A.02 Repeat 2
A.03 Repeat 1
A.03 Repeat 2
A.04 Repeat 1
A.04 Repeat 2

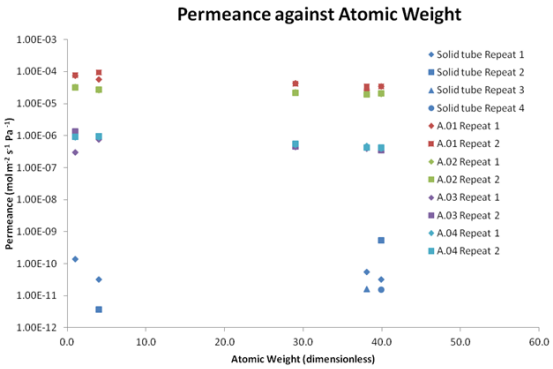
Permeance against Atomic Weight
Permeance (mol m-2 s-1 Pa-1)
Atomic Weight (dimensionless)
Solid tube Repeat 1
Solid tube Repeat 2
Solid tube Repeat 3
Solid tube Repeat 4
A.01 Repeat 1
A.01 Repeat 2
A.02 Repeat 1
A.02 Repeat 2
A.03 Repeat 1
A.03 Repeat 2
A.04 Repeat 1
A.04 Repeat 2

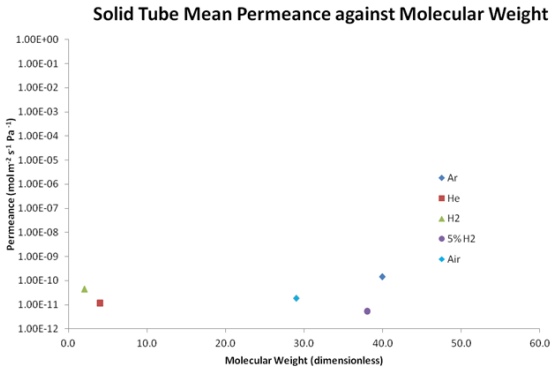
Solid Tube Mean Permeance against Molecular Weight
Permeance (mol m-2 s-1 Pa-1)
Molecular Weight (dimensionless)
Ar
He
H2
5% H2
Air

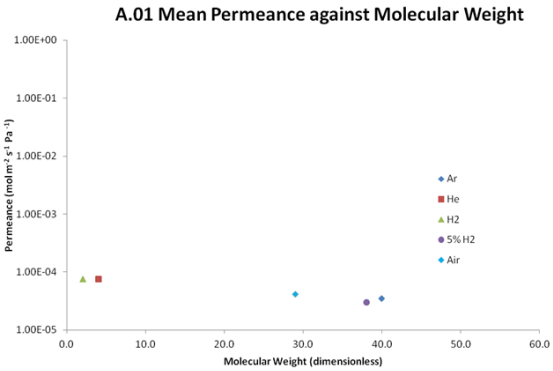
A.01 Mean Permeance against Molecular Weight
Permeance (mol m-2 s-1 Pa-1)
Molecular Weight (dimensionless)
Ar
He
H2
5% H2
Air

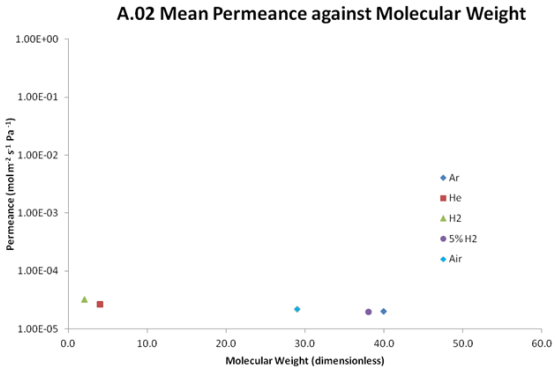
A.02 Mean Permeance against Molecular Weight
Permeance (mol m-2 s-1 Pa-1)
Molecular Weight (dimensionless)
Ar
He
H2
5% H2
Air

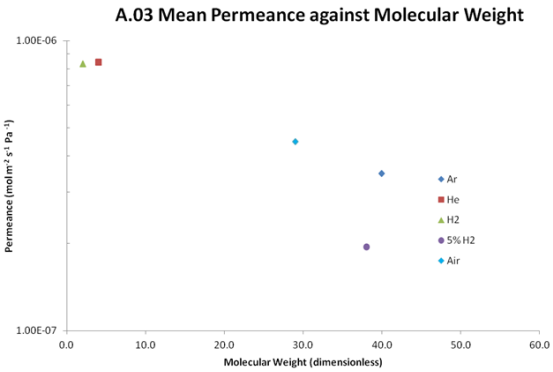
A.03 Mean Permeance against Molecular Weight
Permeance (mol m-2 s-1 Pa-1)
Molecular Weight (dimensionless)
Ar
He
H2
5% H2
Air

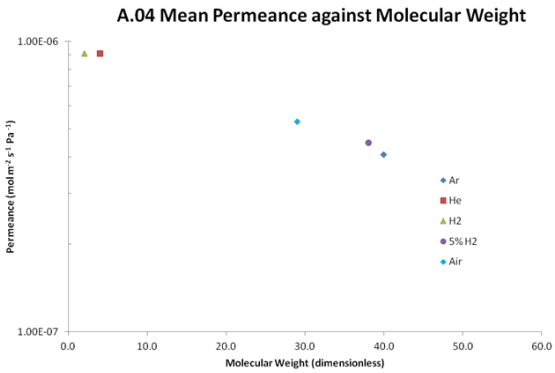
A.04 Mean Permeance against Molecular Weight
Permeance (mol m-2 s-1 Pa-1)
Molecular Weight (dimensionless)
Ar
He
H2
5% H2
Air

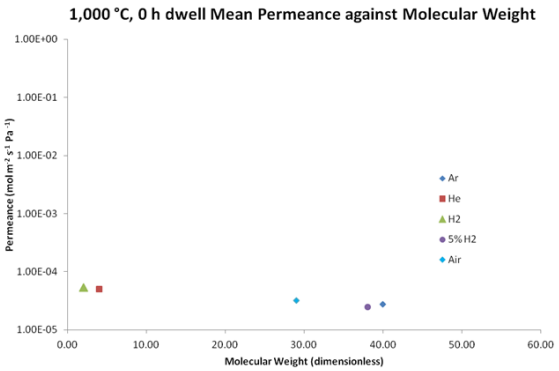
1,000 °C, 0 h dwell Mean Permeance against Molecular Weight
Permeance (mol m-2 s-1 Pa-1)
1.00E+00
1.00E-01
1.00E-02
1.00E-03
1.00E-04
1.00E-05
0.00
10.00
20.00
30.00
40.00
50.00
60.00
Molecular Weight (dimensionless)
Ar
He
H2
5% H2
Air

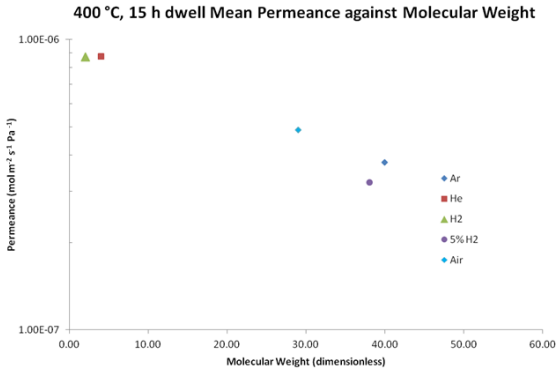
400 °C, 15 h dwell Mean Permeance against Molecular Weight
Permeance (mol m-2 s-1 Pa-1)
1.00E-06
1.00E-07
0.00
10.00
20.00
30.00
40.00
50.00
60.00
Molecular Weight (dimensionless)
Ar
He
H2
5% H2
Air

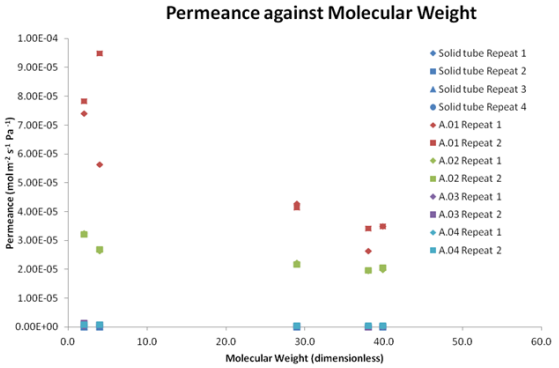
Permeance against Molecular Weight
Permeance (mol m-2 s-1 Pa-1)
1.00E-04
9.00E-05
8.00E-05
7.00E-05
6.00E-05
5.00E-05
4.00E-05
3.00E-05
2.00E-05
1.00E-05
0.00E+00
0.0
10.0
20.0
30.0
40.0
50.0
60.0
Molecular Weight (dimensionless)
Solid tube Repeat 1
Solid tube Repeat 2
Solid tube Repeat 3
Solid tube Repeat 4
A.01 Repeat 1
A.01 Repeat 2
A.02 Repeat 1
A.02 Repeat 2
A.03 Repeat 1
A.03 Repeat 2
A.04 Repeat 1
A.04 Repeat 2

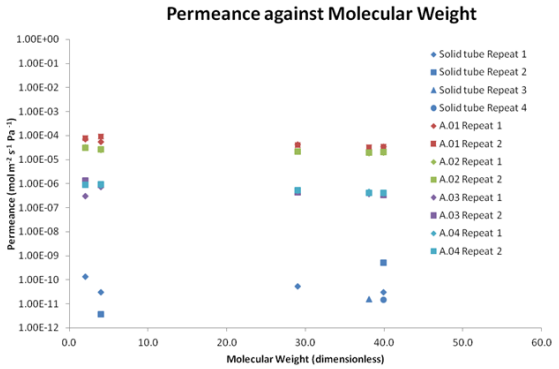
Permeance against Molecular Weight
Permeance (mol m-2 s-1 Pa-1)
1.00E+00
1.00E-01
1.00E-02
1.00E-03
1.00E-04
1.00E-05
1.00E-06
1.00E-07
1.00E-08
1.00E-09
1.00E-10
1.00E-11
1.00E-12
0.0
10.0
20.0
30.0
40.0
50.0
60.0
Molecular Weight (dimensionless)
Solid tube Repeat 1
Solid tube Repeat 2
Solid tube Repeat 3
Solid tube Repeat 4
A.01 Repeat 1
A.01 Repeat 2
A.02 Repeat 1
A.02 Repeat 2
A.03 Repeat 1
A.03 Repeat 2
A.04 Repeat 1
A.04 Repeat 2

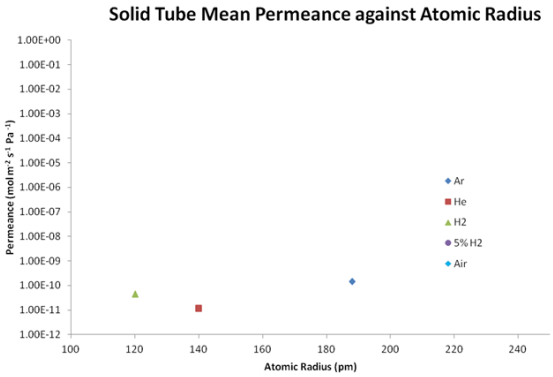
Solid Tube Mean Permeance against Atomic Radius
Permeance (mol m-2 s-1 Pa-1)
1.00E+00
1.00E-01
1.00E-02
1.00E-03
1.00E-04
1.00E-05
1.00E-06
1.00E-07
1.00E-08
1.00E-09
1.00E-10
1.00E-11
1.00E-12
100
120
140
160
180
200
220
240
Atomic Radius (pm)
Ar
He
H2
5%H2
Air

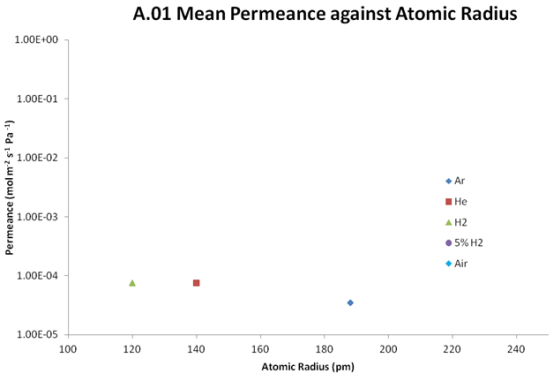
A.01 Mean Permeance against Atomic Radius
Permeance (mol m-2 s-1 Pa-1)
1.00E+00
1.00E-01
1.00E-02
1.00E-03
1.00E-04
1.00E-05
100
120
140
160
180
200
220
240
Atomic Radius (pm)
Ar
He
H2
5%H2
Air

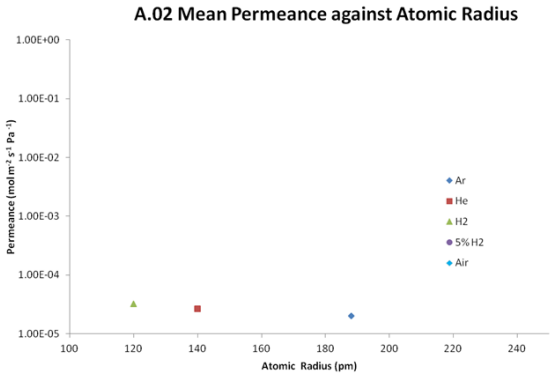
A.02 Mean Permeance against Atomic Radius
Permeance (mol m-2 s-1 Pa-1)
1.00E+00
1.00E-01
1.00E-02
1.00E-03
1.00E-04
1.00E-05
100
120
140
160
180
200
220
240
Atomic Radius (pm)
Ar
He
H2
5%H2
Air

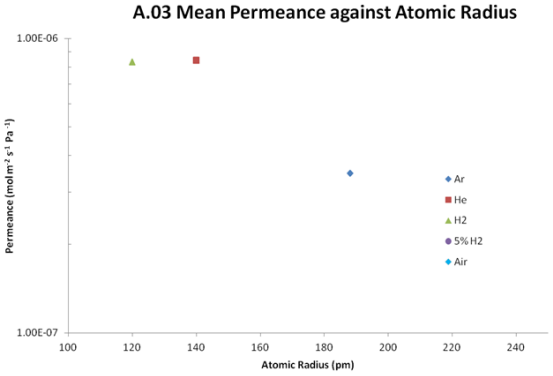
A.03 Mean Permeance against Atomic Radius
Permeance (mol m-2 s-1 Pa-1)
1.00E-06
1.00E-07
100
120
140
160
180
200
220
240
Atomic Radius (pm)
Ar
He
H2
5%H2
Air

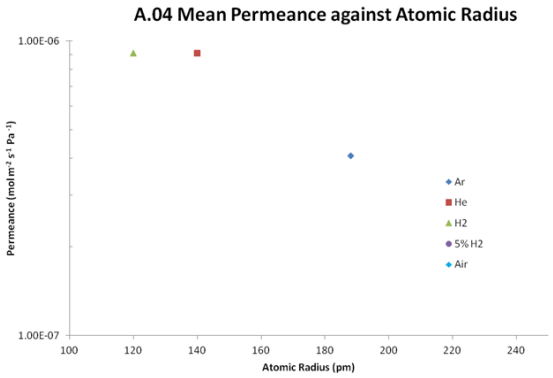
A.04 Mean Permeance against Atomic Radius
Permeance (mol m-2 s-1 Pa-1)
1.00E-06
1.00E-07
100
120
140
160
180
200
220
240
Atomic Radius (pm)
Ar
He
H2
5%H2
Air

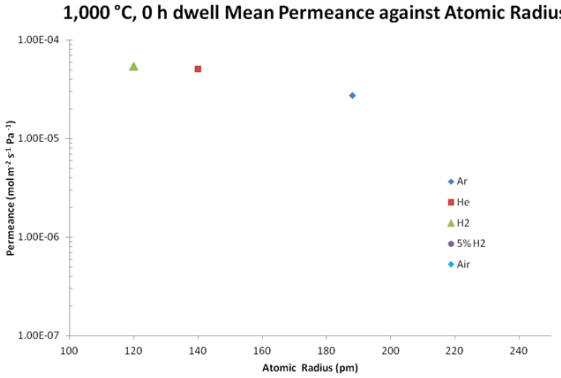
1,000 °C, 0 h dwell Mean Permeance against Atomic Radius
Permeance (mol m-2 s-1 Pa-1)
1.00E-04
1.00E-05
1.00E-06
1.00E-07
100
120
140
160
180
200
220
240
Atomic Radius (pm)
Ar
He
H2
5%H2
Air

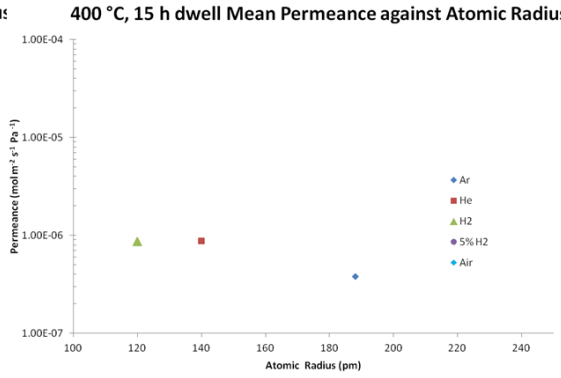
400 °C, 15 h dwell Mean Permeance against Atomic Radius
Permeance (mol m-2 s-1 Pa-1)
1.00E-04
1.00E-05
1.00E-06
1.00E-07
100
120
140
160
180
200
220
240
Atomic Radius (pm)
Ar
He
H2
5%H2
Air

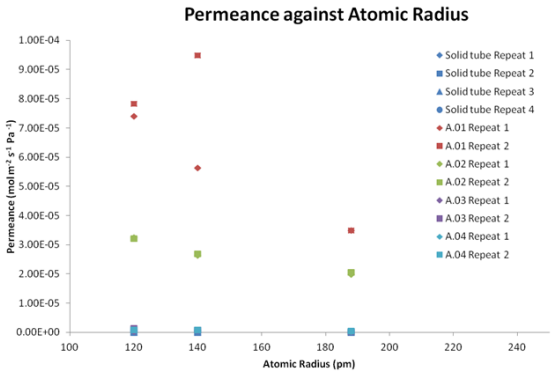
Permeance against Atomic Radius
Permeance (mol m-2 s-1 Pa-1)
Atomic Radius (pm)
Solid tube Repeat 1
Solid tube Repeat 2
Solid tube Repeat 3
Solid tube Repeat 4
A.01 Repeat 1
A.01 Repeat 2
A.02 Repeat 1
A.02 Repeat 2
A.03 Repeat 1
A.03 Repeat 2
A.04 Repeat 1
A.04 Repeat 2

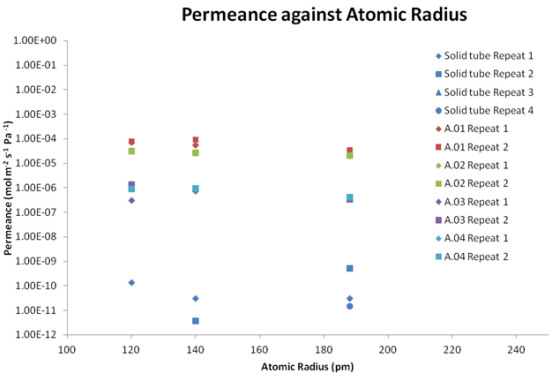
Permeance against Atomic Radius
Permeance (mol m-2 s-1 Pa-1)
Atomic Radius (pm)
Solid tube Repeat 1
Solid tube Repeat 2
Solid tube Repeat 3
Solid tube Repeat 4
A.01 Repeat 1
A.01 Repeat 2
A.02 Repeat 1
A.02 Repeat 2
A.03 Repeat 1
A.03 Repeat 2
A.04 Repeat 1
A.04 Repeat 2

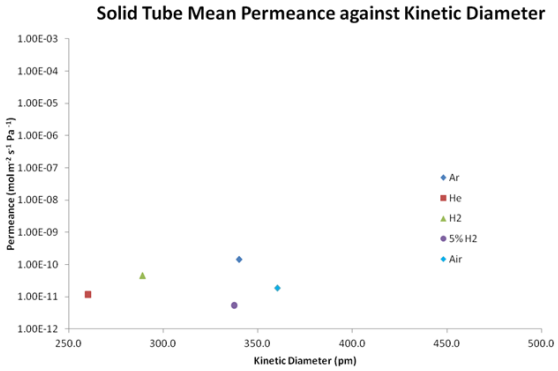
Solid Tube Mean Permeance against Kinetic Diameter
Permeance (mol m-2 s-1 Pa-1)
Kinetic Diameter (pm)
Ar
He
H2
5% H2
Air

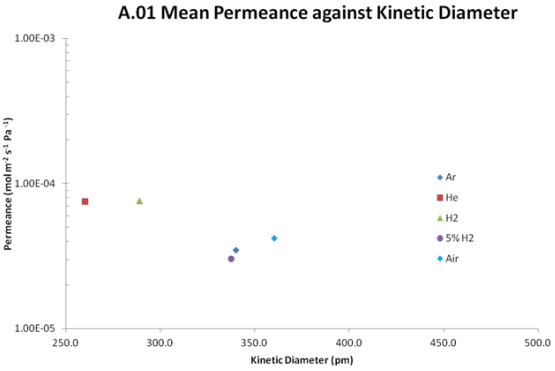
A.01 Mean Permeance against Kinetic Diameter
Permeance (mol m-2 s-1 Pa-1)
Kinetic Diameter (pm)
Ar
He
H2
5% H2
Air

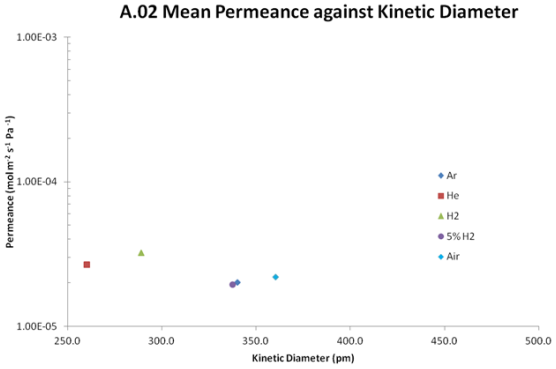
A.02 Mean Permeance against Kinetic Diameter
Permeance (mol m-2 s-1 Pa-1)
Kinetic Diameter (pm)
Ar
He
H2
5% H2
Air

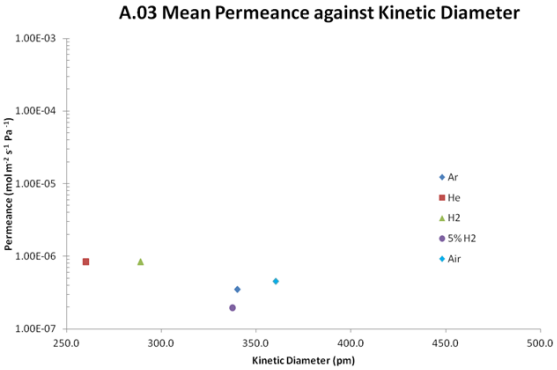
A.03 Mean Permeance against Kinetic Diameter
Permeance (mol m-2 s-1 Pa-1)
Kinetic Diameter (pm)
Ar
He
H2
5% H2
Air

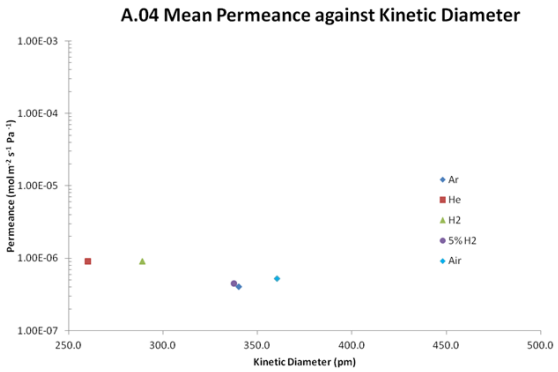
A.04 Mean Permeance against Kinetic Diameter
Permeance (mol m-2 s-1 Pa-1)
Kinetic Diameter (pm)
Ar
He
H2
5% H2
Air

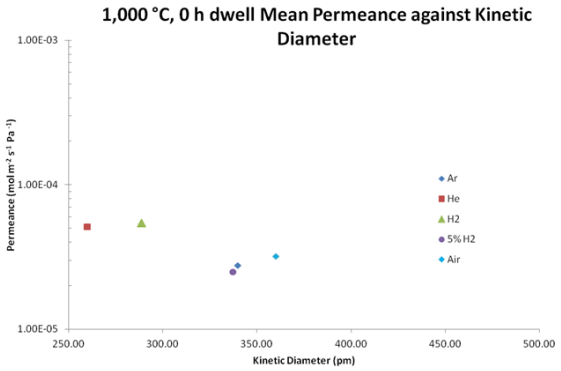
1,000 °C, 0 h dwell Mean Permeance against Kinetic Diameter
Permeance (mol m-2 s-1 Pa-1)
1.00E-03
1.00E-04
1.00E-05
250.00
300.00
350.00
400.00
450.00
500.00
Kinetic Diameter (pm)
Ar
He
H2
5% H2
Air

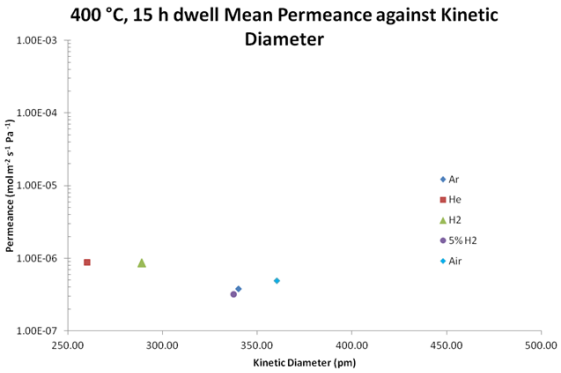
400 °C, 15 h dwell Mean Permeance against Kinetic Diameter
Permeance (mol m-2 s-1 Pa-1)
1.00E-03
1.00E-04
1.00E-05
1.00E-06
1.00E-07
250.00
300.00
350.00
400.00
450.00
500.00
Kinetic Diameter (pm)
Ar
He
H2
5% H2
Air

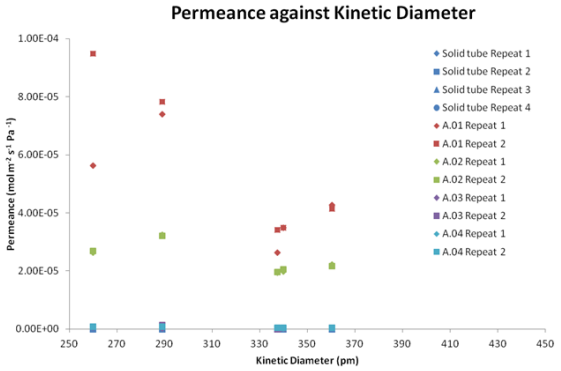
Permeance against Kinetic Diameter
Permeance (mol m-2 s-1 Pa-1)
1.00E-04
8.00E-05
6.00E-05
4.00E-05
2.00E-05
0.00E+00
250
270
290
310
330
350
370
390
410
430
450
Kinetic Diameter (pm)
Solid tube Repeat 1
Solid tube Repeat 2
Solid tube Repeat 3
Solid tube Repeat 4
A.01 Repeat 1
A.01 Repeat 2
A.02 Repeat 1
A.02 Repeat 2
A.03 Repeat 1
A.03 Repeat 2
A.04 Repeat 1
A.04 Repeat 2

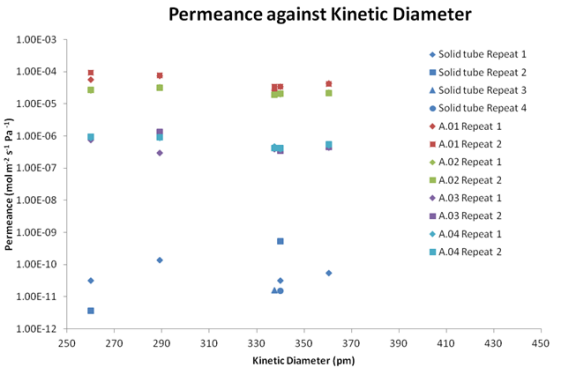
Permeance against Kinetic Diameter
Permeance (mol m-2 s-1 Pa-1)
1.00E-03
1.00E-04
1.00E-05
1.00E-06
1.00E-07
1.00E-08
1.00E-09
1.00E-10
1.00E-11
1.00E-12
250
270
290
310
330
350
370
390
410
430
450
Kinetic Diameter (pm)
Solid tube Repeat 1
Solid tube Repeat 2
Solid tube Repeat 3
Solid tube Repeat 4
A.01 Repeat 1
A.01 Repeat 2
A.02 Repeat 1
A.02 Repeat 2
A.03 Repeat 1
A.03 Repeat 2
A.04 Repeat 1
A.04 Repeat 2

Permeance: Anode-Electrolyte Complex

In the interest of space about a third of the plots used for analysis were not included (those showing single samples and single gasses), since comparing them on a single plot is more useful.

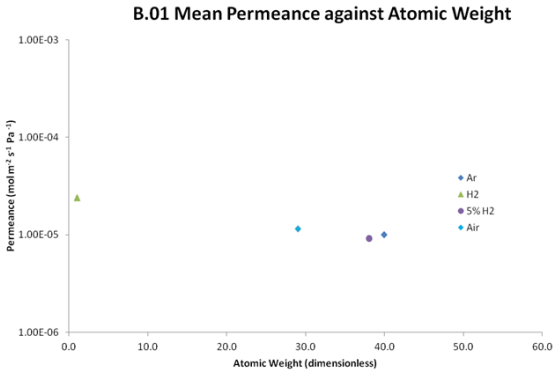

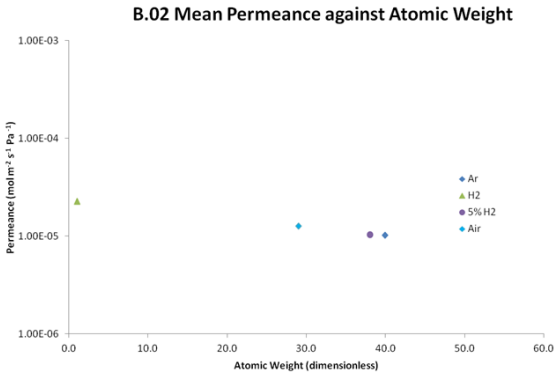

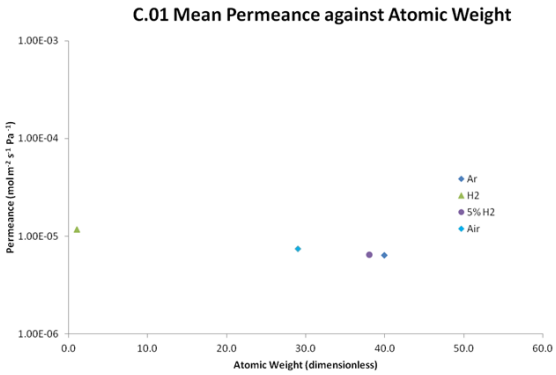

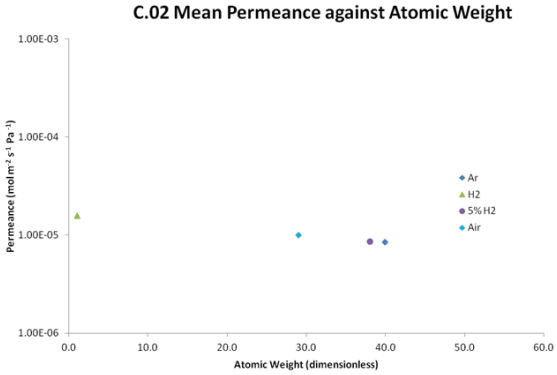

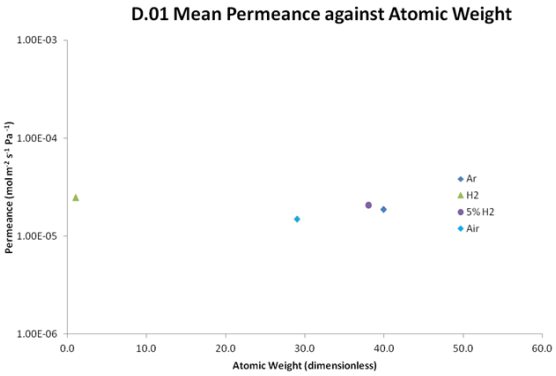

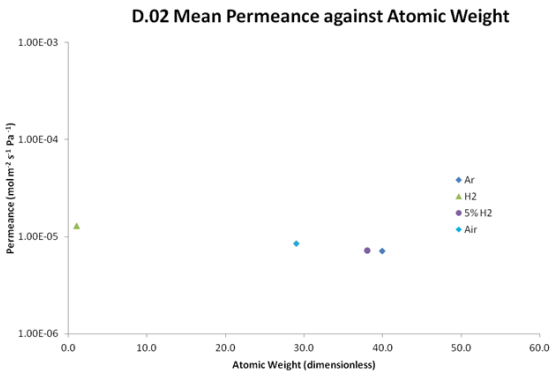

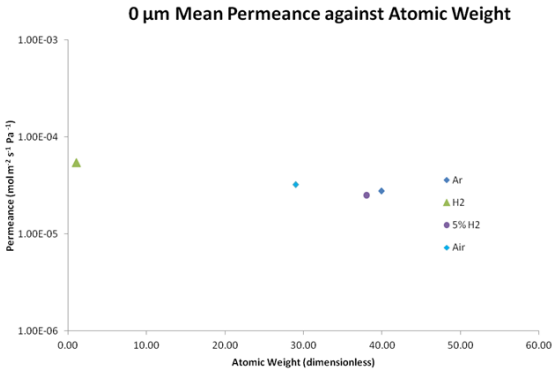
0 µm Mean Permeance against Atomic Weight
Permeance (mol m-2 s-1 Pa-1)
1.00E-03
1.00E-04
1.00E-05
1.00E-06
0.00
10.00
20.00
30.00
40.00
50.00
60.00
Atomic Weight (dimensionless)
Ar
H2
5% H2
Air

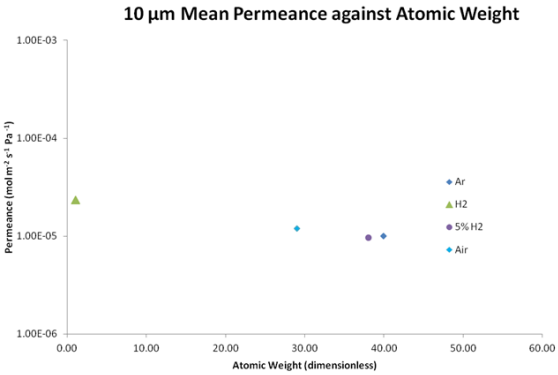
10 µm Mean Permeance against Atomic Weight
Permeance (mol m-2 s-1 Pa-1)
1.00E-03
1.00E-04
1.00E-05
1.00E-06
0.00
10.00
20.00
30.00
40.00
50.00
60.00
Atomic Weight (dimensionless)
Ar
H2
5% H2
Air

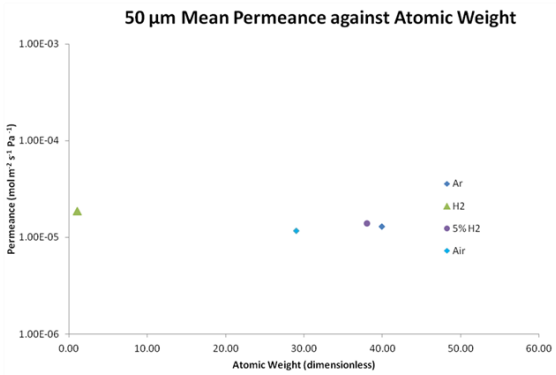
50 µm Mean Permeance against Atomic Weight
Permeance (mol m-2 s-1 Pa-1)
1.00E-03
1.00E-04
1.00E-05
1.00E-06
0.00
10.00
20.00
30.00
40.00
50.00
60.00
Atomic Weight (dimensionless)
Ar
H2
5% H2
Air

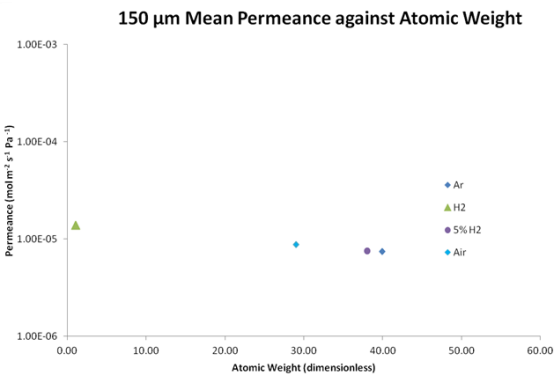
150 µm Mean Permeance against Atomic Weight
Permeance (mol m-2 s-1 Pa-1)
1.00E-03
1.00E-04
1.00E-05
1.00E-06
0.00
10.00
20.00
30.00
40.00
50.00
60.00
Atomic Weight (dimensionless)
Ar
H2
5% H2
Air

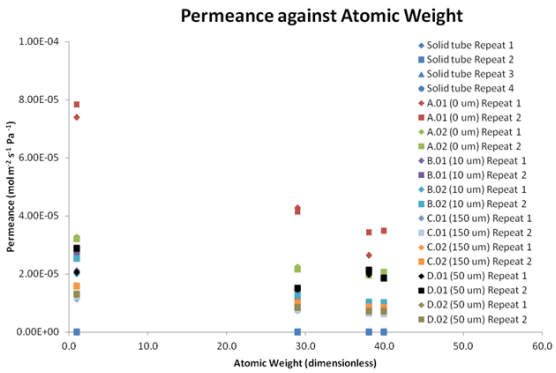
Permeance against Atomic Weight
Permeance (mol m-2 s-1 Pa-1)
1.00E-04
8.00E-05
6.00E-05
4.00E-05
2.00E-05
0.00E+00
0.0
10.0
20.0
30.0
40.0
50.0
60.0
Atomic Weight (dimensionless)
Solid tube Repeat 1
Solid tube Repeat 2
Solid tube Repeat 3
Solid tube Repeat 4
A.01 (0 um) Repeat 1
A.01 (0 um) Repeat 2
A.02 (0 um) Repeat 1
A.02 (0 um) Repeat 2
B.01 (10 um) Repeat 1
B.01 (10 um) Repeat 2
B.02 (10 um) Repeat 1
B.02 (10 um) Repeat 2
C.01 (150 um) Repeat 1
C.01 (150 um) Repeat 2
C.02 (150 um) Repeat 1
C.02 (150 um) Repeat 2
D.01 (50 um) Repeat 1
D.01 (50 um) Repeat 2
D.02 (50 um) Repeat 1
D.02 (50 um) Repeat 2

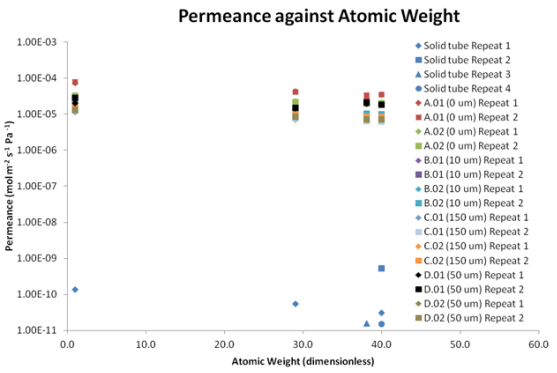
Permeance against Atomic Weight
Permeance (mol m-2 s-1 Pa-1)
1.00E-03
1.00E-04
1.00E-05
1.00E-06
1.00E-07
1.00E-08
1.00E-09
1.00E-10
1.00E-11
0.0
10.0
20.0
30.0
40.0
50.0
60.0
Atomic Weight (dimensionless)
Solid tube Repeat 1
Solid tube Repeat 2
Solid tube Repeat 3
Solid tube Repeat 4
A.01 (0 um) Repeat 1
A.01 (0 um) Repeat 2
A.02 (0 um) Repeat 1
A.02 (0 um) Repeat 2
B.01 (10 um) Repeat 1
B.01 (10 um) Repeat 2
B.02 (10 um) Repeat 1
B.02 (10 um) Repeat 2
C.01 (150 um) Repeat 1
C.01 (150 um) Repeat 2
C.02 (150 um) Repeat 1
C.02 (150 um) Repeat 2
D.01 (50 um) Repeat 1
D.01 (50 um) Repeat 2
D.02 (50 um) Repeat 1
D.02 (50 um) Repeat 2

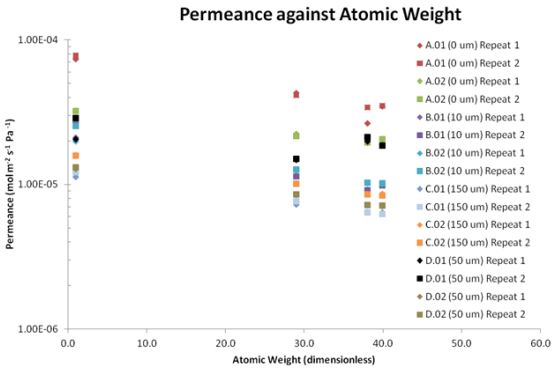
Permeance against Atomic Weight
Permeance (mol m-2 s-1 Pa-1)
1.00E-04
1.00E-05
1.00E-06
0.0
10.0
20.0
30.0
40.0
50.0
60.0
Atomic Weight (dimensionless)
A.01 (0 um) Repeat 1
A.01 (0 um) Repeat 2
A.02 (0 um) Repeat 1
A.02 (0 um) Repeat 2
B.01 (10 um) Repeat 1
B.01 (10 um) Repeat 2
B.02 (10 um) Repeat 1
B.02 (10 um) Repeat 2
C.01 (150 um) Repeat 1
C.01 (150 um) Repeat 2
C.02 (150 um) Repeat 1
C.02 (150 um) Repeat 2
D.01 (50 um) Repeat 1
D.01 (50 um) Repeat 2
D.02 (50 um) Repeat 1
D.02 (50 um) Repeat 2

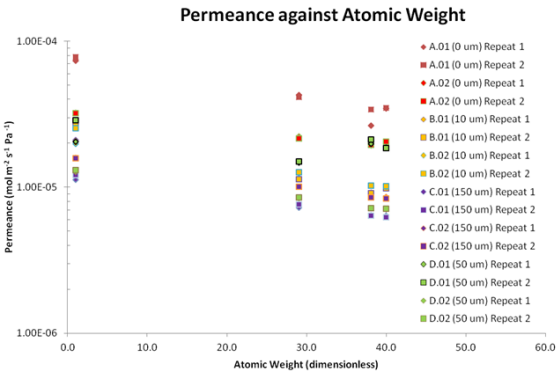
Permeance against Atomic Weight
Permeance (mol m-2 s-1 Pa-1)
1.00E-04
1.00E-05
1.00E-06
0.0
10.0
20.0
30.0
40.0
50.0
60.0
Atomic Weight (dimensionless)
A.01 (0 um) Repeat 1
A.01 (0 um) Repeat 2
A.02 (0 um) Repeat 1
A.02 (0 um) Repeat 2
B.01 (10 um) Repeat 1
B.01 (10 um) Repeat 2
B.02 (10 um) Repeat 1
B.02 (10 um) Repeat 2
C.01 (150 um) Repeat 1
C.01 (150 um) Repeat 2
C.02 (150 um) Repeat 1
C.02 (150 um) Repeat 2
D.01 (50 um) Repeat 1
D.01 (50 um) Repeat 2
D.02 (50 um) Repeat 1
D.02 (50 um) Repeat 2

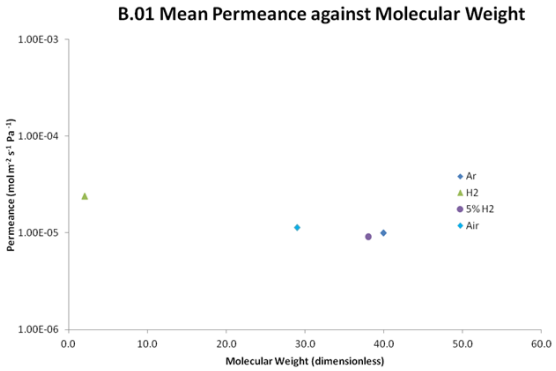
B.01 Mean Permeance against Molecular Weight
Permeance (mol m-2 s-1 Pa-1)
1.00E-03
1.00E-04
1.00E-05
1.00E-06
0.0
10.0
20.0
30.0
40.0
50.0
60.0
Molecular Weight (dimensionless)
Ar
H2
5% H2
Air

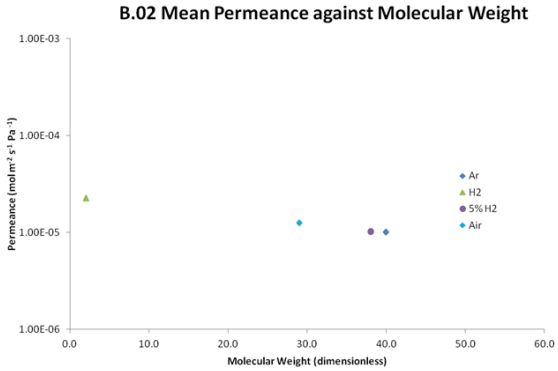
B.02 Mean Permeance against Molecular Weight
Permeance (mol m-2 s-1 Pa-1)
1.00E-03
1.00E-04
1.00E-05
1.00E-06
0.0
10.0
20.0
30.0
40.0
50.0
60.0
Molecular Weight (dimensionless)
Ar
H2
5% H2
Air

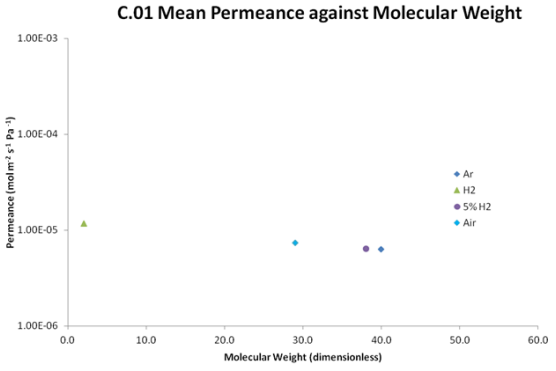
C.01 Mean Permeance against Molecular Weight
Permeance (mol m-2 s-1 Pa-1)
1.00E-03
1.00E-04
1.00E-05
1.00E-06
0.0
10.0
20.0
30.0
40.0
50.0
60.0
Molecular Weight (dimensionless)
Ar
H2
5% H2
Air

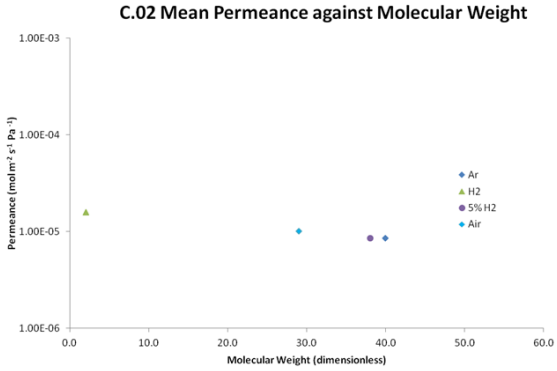
C.02 Mean Permeance against Molecular Weight
Permeance (mol m-2 s-1 Pa-1)
1.00E-03
1.00E-04
1.00E-05
1.00E-06
0.0
10.0
20.0
30.0
40.0
50.0
60.0
Molecular Weight (dimensionless)
Ar
H2
5% H2
Air

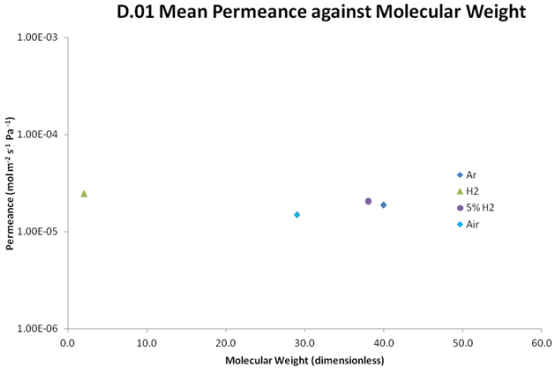
D.01 Mean Permeance against Molecular Weight
Permeance (mol m-2 s-1 Pa-1)
1.00E-03
1.00E-04
1.00E-05
1.00E-06
0.0
10.0
20.0
30.0
40.0
50.0
60.0
Molecular Weight (dimensionless)
Ar
H2
5% H2
Air

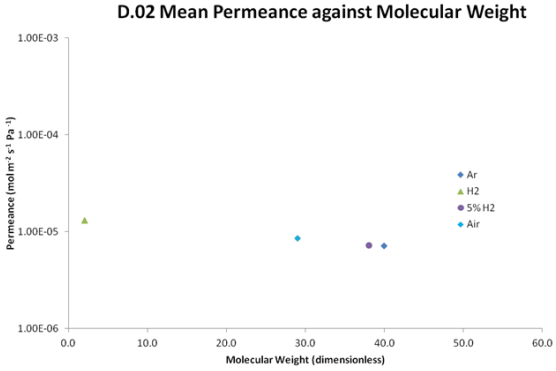
D.02 Mean Permeance against Molecular Weight
Permeance (mol m-2 s-1 Pa-1)
1.00E-03
1.00E-04
1.00E-05
1.00E-06
0.0
10.0
20.0
30.0
40.0
50.0
60.0
Molecular Weight (dimensionless)
Ar
H2
5% H2
Air

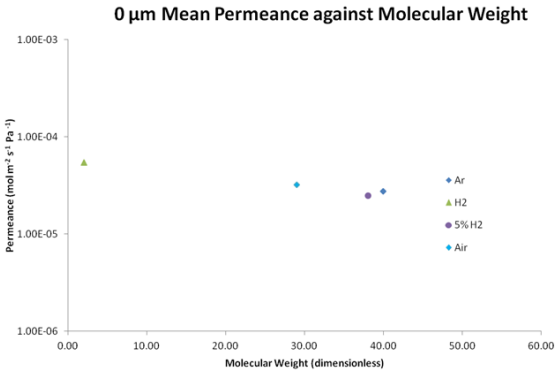
0 µm Mean Permeance against Molecular Weight
Permeance (mol m-2 s-1 Pa-1)
1.00E-03
1.00E-04
1.00E-05
1.00E-06
0.00
10.00
20.00
30.00
40.00
50.00
60.00
Molecular Weight (dimensionless)
Ar
H2
5%H2
Air

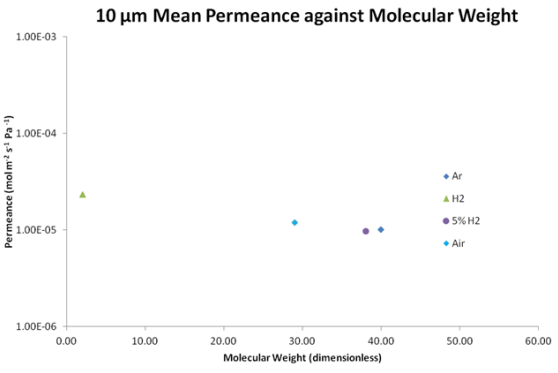
10 µm Mean Permeance against Molecular Weight
Permeance (mol m-2 s-1 Pa-1)
1.00E-03
1.00E-04
1.00E-05
1.00E-06
0.00
10.00
20.00
30.00
40.00
50.00
60.00
Molecular Weight (dimensionless)
Ar
H2
5%H2
Air

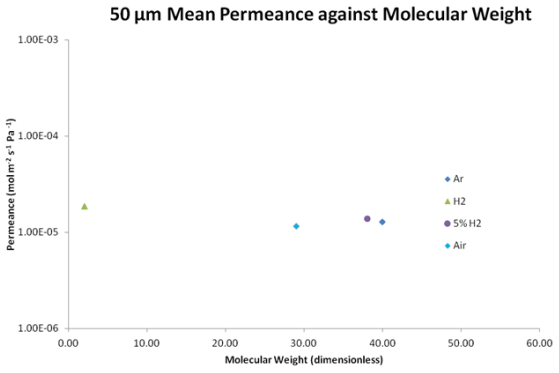
50 µm Mean Permeance against Molecular Weight
Permeance (mol m-2 s-1 Pa-1)
1.00E-03
1.00E-04
1.00E-05
1.00E-06
0.00
10.00
20.00
30.00
40.00
50.00
60.00
Molecular Weight (dimensionless)
Ar
H2
5%H2
Air

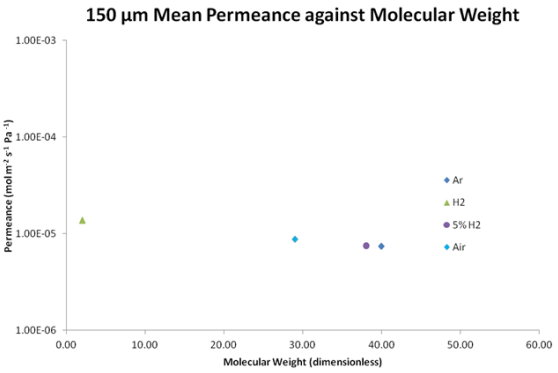
150 µm Mean Permeance against Molecular Weight
Permeance (mol m-2 s-1 Pa-1)
1.00E-03
1.00E-04
1.00E-05
1.00E-06
0.00
10.00
20.00
30.00
40.00
50.00
60.00
Molecular Weight (dimensionless)
Ar
H2
5%H2
Air

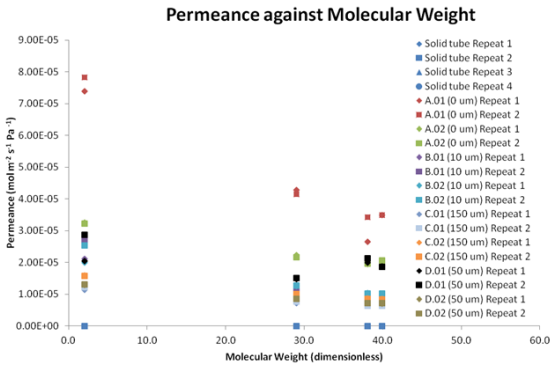
Permeance against Molecular Weight
Permeance (mol m-2 s-1 Pa-1)
9.00E-05
8.00E-05
7.00E-05
6.00E-05
5.00E-05
4.00E-05
3.00E-05
2.00E-05
1.00E-05
0.00E+00
0.0
10.0
20.0
30.0
40.0
50.0
60.0
Molecular Weight (dimensionless)
Solid tube Repeat 1
Solid tube Repeat 2
Solid tube Repeat 3
Solid tube Repeat 4
A.01 (0 um) Repeat 1
A.01 (0 um) Repeat 2
A.02 (0 um) Repeat 1
A.02 (0 um) Repeat 2
B.01 (10 um) Repeat 1
B.01 (10 um) Repeat 2
B.02 (10 um) Repeat 1
B.02 (10 um) Repeat 2
C.01 (150 um) Repeat 1
C.01 (150 um) Repeat 2
C.02 (150 um) Repeat 1
C.02 (150 um) Repeat 2
D.01 (50 um) Repeat 1
D.01 (50 um) Repeat 2
D.02 (50 um) Repeat 1
D.02 (50 um) Repeat 2

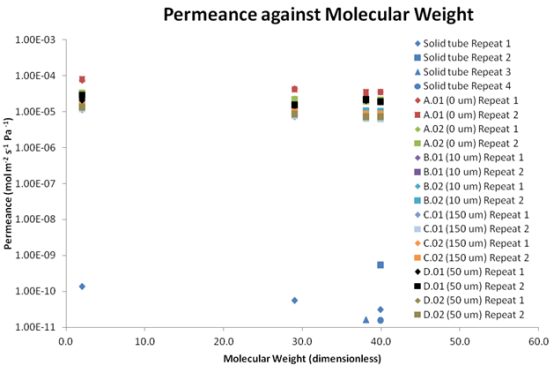
Permeance against Molecular Weight
Permeance (mol m-2 s-1 Pa-1)
1.00E-03
1.00E-04
1.00E-05
1.00E-06
1.00E-07
1.00E-08
1.00E-09
1.00E-10
1.00E-11
0.0
10.0
20.0
30.0
40.0
50.0
60.0
Molecular Weight (dimensionless)
Solid tube Repeat 1
Solid tube Repeat 2
Solid tube Repeat 3
Solid tube Repeat 4
A.01 (0 um) Repeat 1
A.01 (0 um) Repeat 2
A.02 (0 um) Repeat 1
A.02 (0 um) Repeat 2
B.01 (10 um) Repeat 1
B.01 (10 um) Repeat 2
B.02 (10 um) Repeat 1
B.02 (10 um) Repeat 2
C.01 (150 um) Repeat 1
C.01 (150 um) Repeat 2
C.02 (150 um) Repeat 1
C.02 (150 um) Repeat 2
D.01 (50 um) Repeat 1
D.01 (50 um) Repeat 2
D.02 (50 um) Repeat 1
D.02 (50 um) Repeat 2

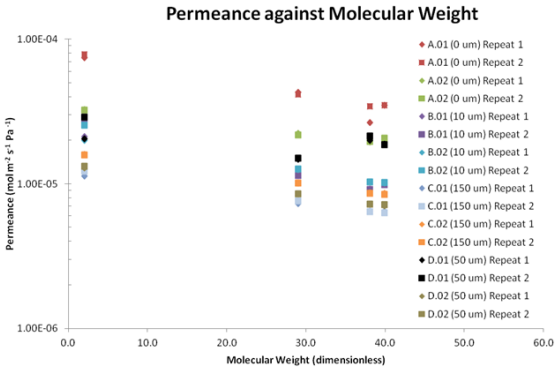
Permeance against Molecular Weight
Permeance (mol m-2 s-1 Pa-1)
1.00E-04
1.00E-05
1.00E-06
0.0
10.0
20.0
30.0
40.0
50.0
60.0
Molecular Weight (dimensionless)
A.01 (0 um) Repeat 1
A.01 (0 um) Repeat 2
A.02 (0 um) Repeat 1
A.02 (0 um) Repeat 2
B.01 (10 um) Repeat 1
B.01 (10 um) Repeat 2
B.02 (10 um) Repeat 1
B.02 (10 um) Repeat 2
C.01 (150 um) Repeat 1
C.01 (150 um) Repeat 2
C.02 (150 um) Repeat 1
C.02 (150 um) Repeat 2
D.01 (50 um) Repeat 1
D.01 (50 um) Repeat 2
D.02 (50 um) Repeat 1
D.02 (50 um) Repeat 2

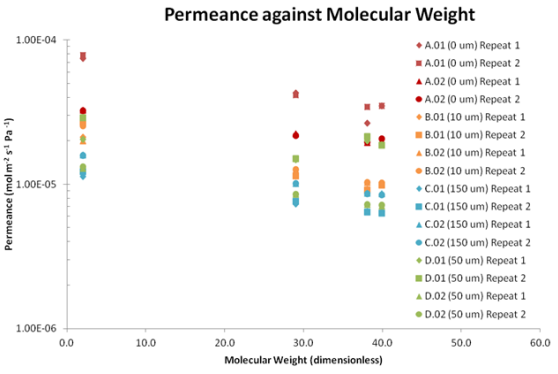
Permeance against Molecular Weight
Permeance (mol m-2 s-1 Pa-1)
1.00E-04
1.00E-05
1.00E-06
0.0
10.0
20.0
30.0
40.0
50.0
60.0
Molecular Weight (dimensionless)
A.01 (0 um) Repeat 1
A.01 (0 um) Repeat 2
A.02 (0 um) Repeat 1
A.02 (0 um) Repeat 2
B.01 (10 um) Repeat 1
B.01 (10 um) Repeat 2
B.02 (10 um) Repeat 1
B.02 (10 um) Repeat 2
C.01 (150 um) Repeat 1
C.01 (150 um) Repeat 2
C.02 (150 um) Repeat 1
C.02 (150 um) Repeat 2
D.01 (50 um) Repeat 1
D.01 (50 um) Repeat 2
D.02 (50 um) Repeat 1
D.02 (50 um) Repeat 2

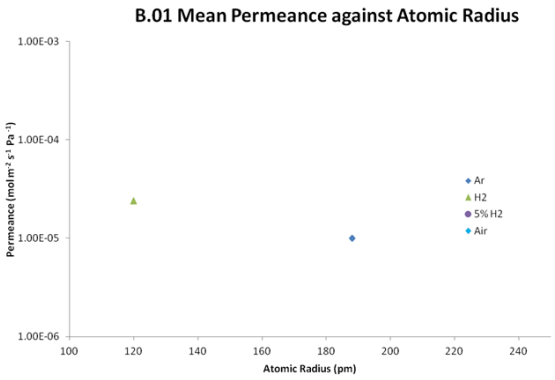
B.01 Mean Permeance against Atomic Radius
Permeance (mol m-2 s-1 Pa-1)
1.00E-03
1.00E-04
1.00E-05
1.00E-06
100
120
140
160
180
200
220
240
Atomic Radius (pm)
Ar
H2
5% H2
Air

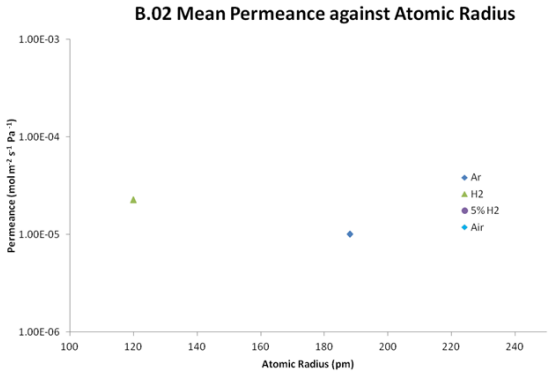
B.02 Mean Permeance against Atomic Radius
Permeance (mol m-2 s-1 Pa-1)
1.00E-03
1.00E-04
1.00E-05
1.00E-06
100
120
140
160
180
200
220
240
Atomic Radius (pm)
Ar
H2
5% H2
Air

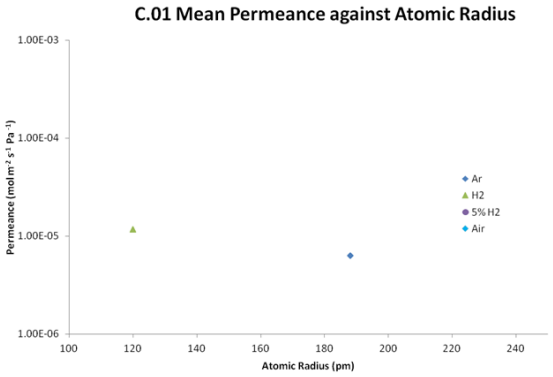
C.01 Mean Permeance against Atomic Radius
Permeance (mol m-2 s-1 Pa-1)
1.00E-03
1.00E-04
1.00E-05
1.00E-06
100
120
140
160
180
200
220
240
Atomic Radius (pm)
Ar
H2
5% H2
Air

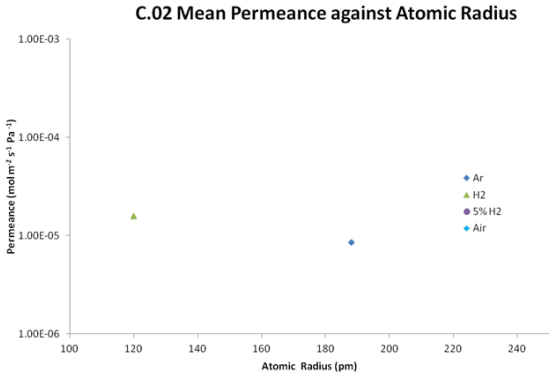
C.02 Mean Permeance against Atomic Radius
Permeance (mol m-2 s-1 Pa-1)
1.00E-03
1.00E-04
1.00E-05
1.00E-06
100
120
140
160
180
200
220
240
Atomic Radius (pm)
Ar
H2
5% H2
Air

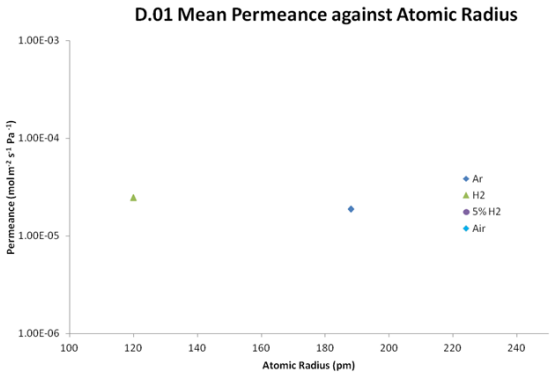
D.01 Mean Permeance against Atomic Radius
Permeance (mol m-2 s-1 Pa-1)
1.00E-03
1.00E-04
1.00E-05
1.00E-06
100
120
140
160
180
200
220
240
Atomic Radius (pm)
Ar
H2
5% H2
Air

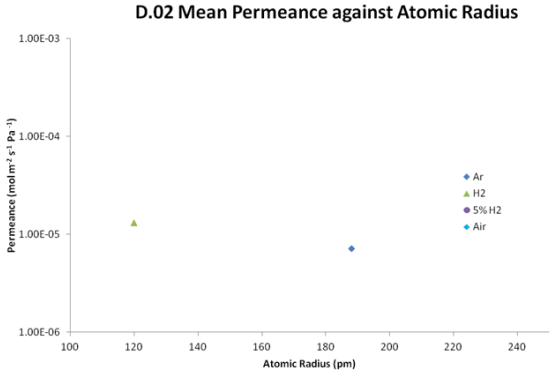
D.02 Mean Permeance against Atomic Radius
Permeance (mol m-2 s-1 Pa-1)
1.00E-03
1.00E-04
1.00E-05
1.00E-06
100
120
140
160
180
200
220
240
Atomic Radius (pm)
Ar
H2
5% H2
Air

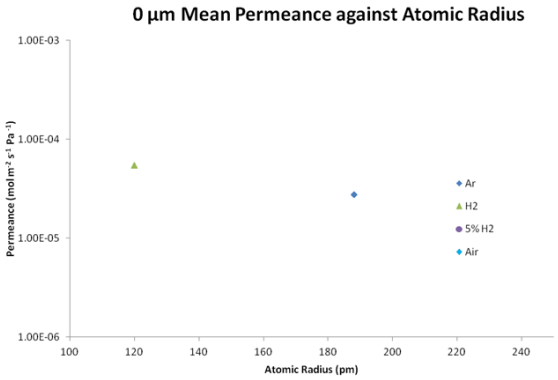
0 µm Mean Permeance against Atomic Radius
Permeance (mol m-2 s-1 Pa-1)
1.00E-03
1.00E-04
1.00E-05
1.00E-06
100
120
140
160
180
200
220
240
Atomic Radius (pm)
Ar
H2
5% H2
Air

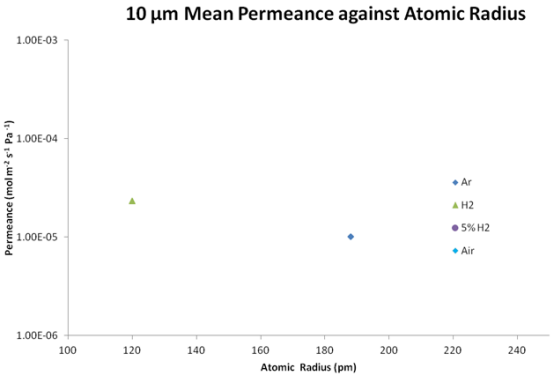
10 µm Mean Permeance against Atomic Radius
Permeance (mol m-2 s-1 Pa-1)
1.00E-03
1.00E-04
1.00E-05
1.00E-06
100
120
140
160
180
200
220
240
Atomic Radius (pm)
Ar
H2
5% H2
Air

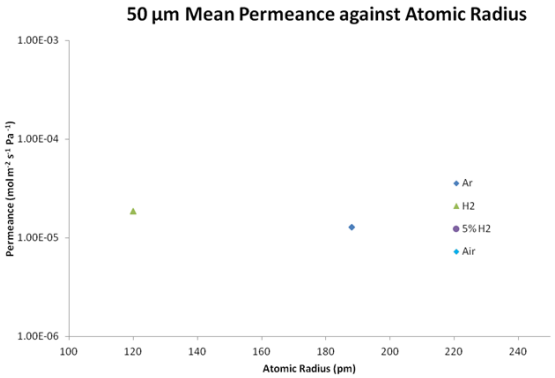
50 µm Mean Permeance against Atomic Radius
Permeance (mol m-2 s-1 Pa-1)
1.00E-03
1.00E-04
1.00E-05
1.00E-06
100
120
140
160
180
200
220
240
Atomic Radius (pm)
Ar
H2
5% H2
Air

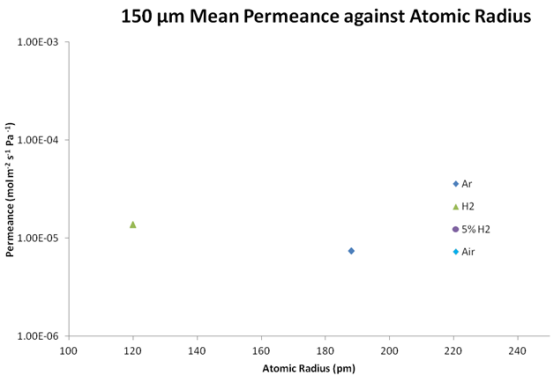
150 µm Mean Permeance against Atomic Radius
Permeance (mol m-2 s-1 Pa-1)
1.00E-03
1.00E-04
1.00E-05
1.00E-06
100
120
140
160
180
200
220
240
Atomic Radius (pm)
Ar
H2
5% H2
Air

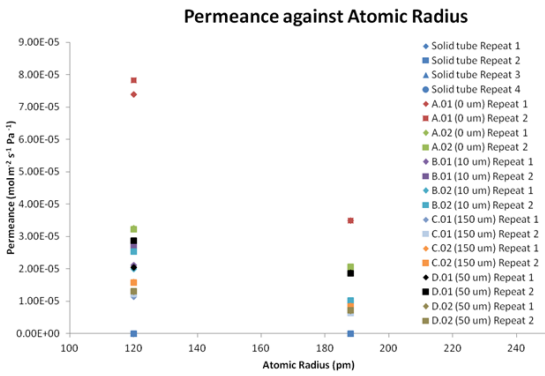
Permeance against Atomic Radius
Permeance (mol m-2 s-1 Pa-1)
9.00E-05
8.00E-05
7.00E-05
6.00E-05
5.00E-05
4.00E-05
3.00E-05
2.00E-05
1.00E-05
0.00E+00
100
120
140
160
180
200
220
240
Atomic Radius (pm)
Solid tube Repeat 1
Solid tube Repeat 2
Solid tube Repeat 3
Solid tube Repeat 4
A.01 (0 um) Repeat 1
A.01 (0 um) Repeat 2
A.02 (0 um) Repeat 1
A.02 (0 um) Repeat 2
B.01 (10 um) Repeat 1
B.01 (10 um) Repeat 2
B.02 (10 um) Repeat 1
B.02 (10 um) Repeat 2
C.01 (150 um) Repeat 1
C.01 (150 um) Repeat 2
C.02 (150 um) Repeat 1
C.02 (150 um) Repeat 2
D.01 (50 um) Repeat 1
D.01 (50 um) Repeat 2
D.02 (50 um) Repeat 1
D.02 (50 um) Repeat 2

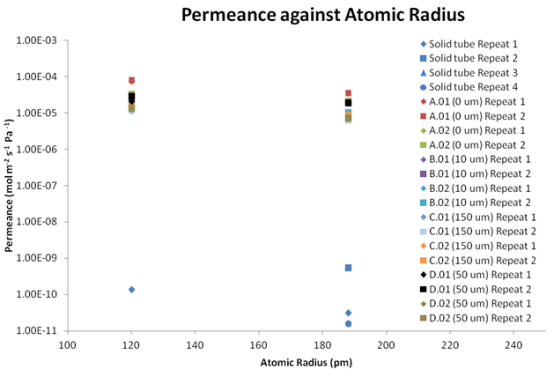
Permeance against Atomic Radius
Permeance (mol m-2 s-1 Pa-1)
1.00E-03
1.00E-04
1.00E-05
1.00E-06
1.00E-07
1.00E-08
1.00E-09
1.00E-10
1.00E-11
100
120
140
160
180
200
220
240
Atomic Radius (pm)
Solid tube Repeat 1
Solid tube Repeat 2
Solid tube Repeat 3
Solid tube Repeat 4
A.01 (0 um) Repeat 1
A.01 (0 um) Repeat 2
A.02 (0 um) Repeat 1
A.02 (0 um) Repeat 2
B.01 (10 um) Repeat 1
B.01 (10 um) Repeat 2
B.02 (10 um) Repeat 1
B.02 (10 um) Repeat 2
C.01 (150 um) Repeat 1
C.01 (150 um) Repeat 2
C.02 (150 um) Repeat 1
C.02 (150 um) Repeat 2
D.01 (50 um) Repeat 1
D.01 (50 um) Repeat 2
D.02 (50 um) Repeat 1
D.02 (50 um) Repeat 2

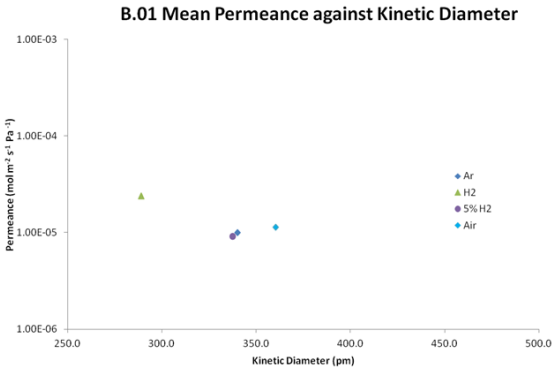
B.01 Mean Permeance against Kinetic Diameter
Permeance (mol m-2 s-1 Pa-1)
1.00E-03
1.00E-04
1.00E-05
1.00E-06
250.0
300.0
350.0
400.0
450.0
500.0
Kinetic Diameter (pm)
Ar
H2
5% H2
Air

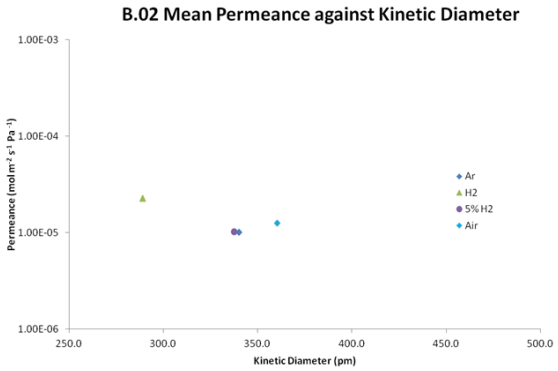
B.02 Mean Permeance against Kinetic Diameter
Permeance (mol m-2 s-1 Pa-1)
1.00E-03
1.00E-04
1.00E-05
1.00E-06
250.0
300.0
350.0
400.0
450.0
500.0
Kinetic Diameter (pm)
Ar
H2
5% H2
Air

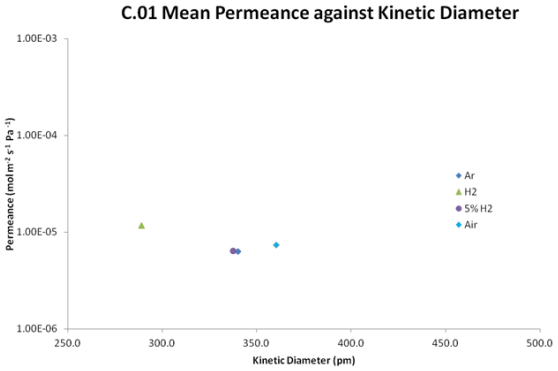
C.01 Mean Permeance against Kinetic Diameter
Permeance (mol m-2 s-1 Pa-1)
1.00E-03
1.00E-04
1.00E-05
1.00E-06
250.0
300.0
350.0
400.0
450.0
500.0
Kinetic Diameter (pm)
Ar
H2
5% H2
Air

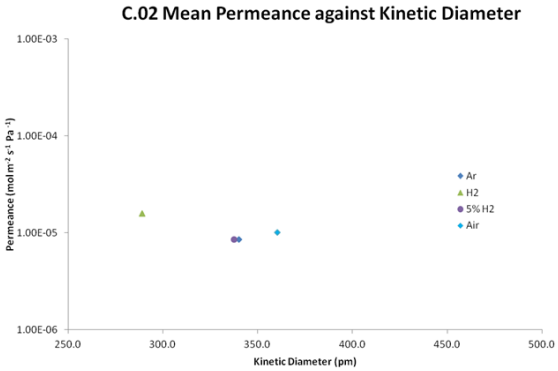
C.02 Mean Permeance against Kinetic Diameter
Permeance (mol m-2 s-1 Pa-1)
1.00E-03
1.00E-04
1.00E-05
1.00E-06
250.0
300.0
350.0
400.0
450.0
500.0
Kinetic Diameter (pm)
Ar
H2
5% H2
Air

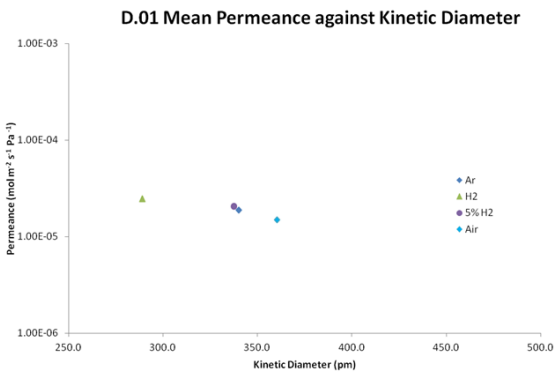
D.01 Mean Permeance against Kinetic Diameter
Permeance (mol m-2 s-1 Pa-1)
1.00E-03
1.00E-04
1.00E-05
1.00E-06
250.0
300.0
350.0
400.0
450.0
500.0
Kinetic Diameter (pm)
Ar
H2
5% H2
Air

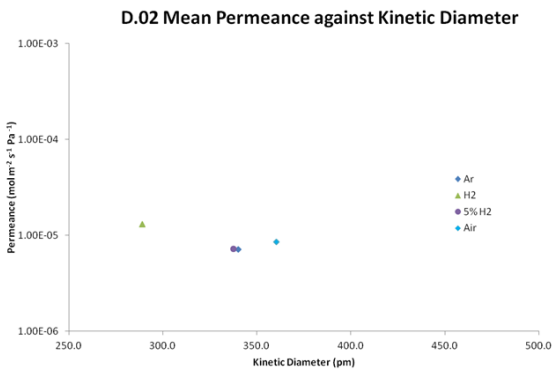
D.02 Mean Permeance against Kinetic Diameter
Permeance (mol m-2 s-1 Pa-1)
1.00E-03
1.00E-04
1.00E-05
1.00E-06
250.0
300.0
350.0
400.0
450.0
500.0
Kinetic Diameter (pm)
Ar
H2
5% H2
Air

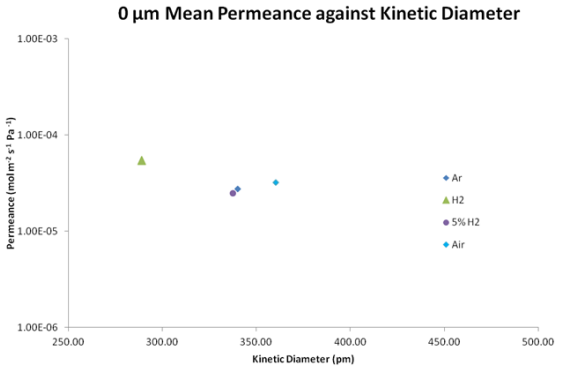
0 µm Mean Permeance against Kinetic Diameter
Permeance (mol m-2 s-1 Pa-1)
1.00E-03
1.00E-04
1.00E-05
1.00E-06
250.00
300.00
350.00
400.00
450.00
500.00
Kinetic Diameter (pm)
Ar
H2
5% H2
Air

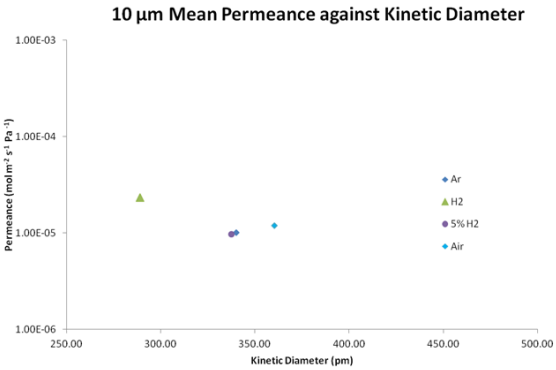
10 µm Mean Permeance against Kinetic Diameter
Permeance (mol m-2 s-1 Pa-1)
1.00E-03
1.00E-04
1.00E-05
1.00E-06
250.00
300.00
350.00
400.00
450.00
500.00
Kinetic Diameter (pm)
Ar
H2
5% H2
Air

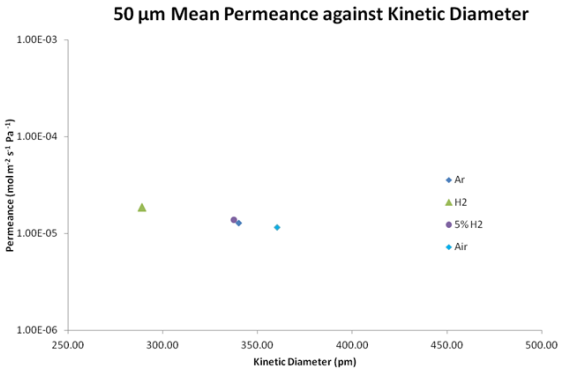
50 µm Mean Permeance against Kinetic Diameter
Permeance (mol m-2 s-1 Pa-1)
1.00E-03
1.00E-04
1.00E-05
1.00E-06
250.00
300.00
350.00
400.00
450.00
500.00
Kinetic Diameter (pm)
Ar
H2
5% H2
Air

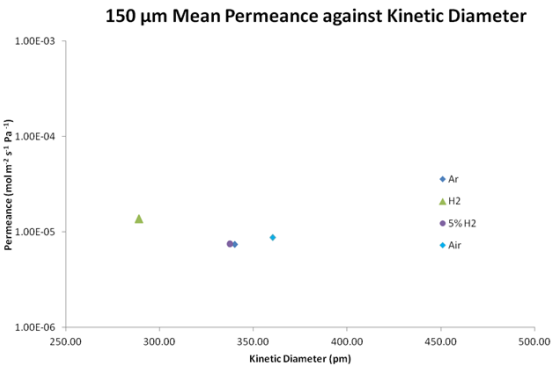
150 µm Mean Permeance against Kinetic Diameter
Permeance (mol m-2 s-1 Pa-1)
1.00E-03
1.00E-04
1.00E-05
1.00E-06
250.00
300.00
350.00
400.00
450.00
500.00
Kinetic Diameter (pm)
Ar
H2
5% H2
Air

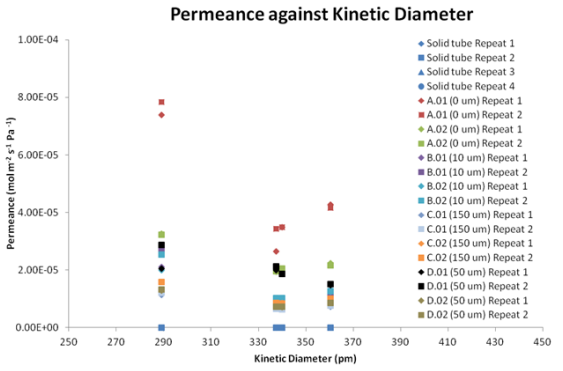
Permeance against Kinetic Diameter
Permeance (mol m-2 s-1 Pa-1)
1.00E-04
8.00E-05
6.00E-05
4.00E-05
2.00E-05
0.00E+00
250
270
290
310
330
350
370
390
410
430
450
Kinetic Diameter (pm)
Solid tube Repeat 1
Solid tube Repeat 2
Solid tube Repeat 3
Solid tube Repeat 4
A.01 (0 um) Repeat 1
A.01 (0 um) Repeat 2
A.02 (0 um) Repeat 1
A.02 (0 um) Repeat 2
B.01 (10 um) Repeat 1
B.01 (10 um) Repeat 2
B.02 (10 um) Repeat 1
B.02 (10 um) Repeat 2
C.01 (150 um) Repeat 1
C.01 (150 um) Repeat 2
C.02 (150 um) Repeat 1
C.02 (150 um) Repeat 2
D.01 (50 um) Repeat 1
D.01 (50 um) Repeat 2
D.02 (50 um) Repeat 1
D.02 (50 um) Repeat 2

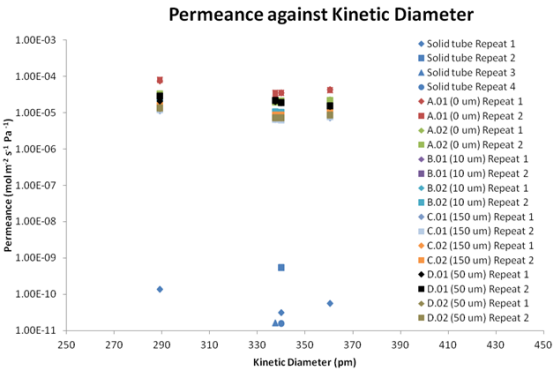
Permeance against Kinetic Diameter
Permeance (mol m-2 s-1 Pa-1)
1.00E-03
1.00E-04
1.00E-05
1.00E-06
1.00E-07
1.00E-08
1.00E-09
1.00E-10
1.00E-11
250
270
290
310
330
350
370
390
410
430
450
Kinetic Diameter (pm)
Solid tube Repeat 1
Solid tube Repeat 2
Solid tube Repeat 3
Solid tube Repeat 4
A.01 (0 um) Repeat 1
A.01 (0 um) Repeat 2
A.02 (0 um) Repeat 1
A.02 (0 um) Repeat 2
B.01 (10 um) Repeat 1
B.01 (10 um) Repeat 2
B.02 (10 um) Repeat 1
B.02 (10 um) Repeat 2
C.01 (150 um) Repeat 1
C.01 (150 um) Repeat 2
C.02 (150 um) Repeat 1
C.02 (150 um) Repeat 2
D.01 (50 um) Repeat 1
D.01 (50 um) Repeat 2
D.02 (50 um) Repeat 1
D.02 (50 um) Repeat 2

Appendix M: Ni Plating Recipes

Ni Plating Solutions:

Ni Strike (usually before Watt's)
Conditions:- pH n/a; T = T_{room}; i = 2.5–10 Adm^{-2}
Solution:- $NiCl_2$ 240 g/litre and HCl (32%) 250 ml/litre.

Watt's Solution
Conditions:- pH n/a; T = 50 °C; i = 2.5–10 Adm^{-2}
Solution:- Ni_3SO_4 330 g/litre, $NiCl_2$ 45 g/litre and H_3BO_3 38 g/litre.

All–Chloride [Modern Electroplating by Schleisinger]
Conditions:- pH 1–4; T = 50–70 °C; i = 2.5–10 Adm^{-2}
Solution:- $NiCl_2$ 225–300 g/litre and H_3BO_3 30–35 g/litre.

All–Sulphate [Modern Electroplating by Schleisinger]
Conditions:- pH 1.5–4; T = 38–70 °C; i = 1–10 Adm^{-2}
Solution:- Ni_3SO_4 225–410 g/litre and H_3BO_3 30–45 g/litre.

Sulphate/Chloride [Modern Electroplating by Schleisinger]
Conditions:- pH 1.5–2.5; T = 43–52 °C; i = 2.5–15 Adm^{-2}
Solution:- Ni_3SO_4 150–225 g/litre, $NiCl_2$ 150–225 g/litre and H_3BO_3 30–45 g/litre.

Appendix N: Material Data Tables

Reported values for material properties varies considerably. This is especially the case for linear coefficients of thermal expansion probably as a result of differing test conditions (not always reported with the data). These tables represent the raw data set found in the literature as reported by different sources (books, websites and journal articles). The average value of each property used for calculations is given at the conclusion of each table. Averages are simple arithmetic means.

Salient Nickel properties. The nominal alloy in all cases was Ni 200 (99% pure Ni).

Density, ρ (g/cm^3)	**Young's Modulus, E (GPa)**	**Poisson's Ratio, γ**	**Linear CTE, α (K^{-1})**	**Resistivity, ρ (Ω.m)**	**Source & Notes**
8.88	207	0.31	13.1x10^{-6} (at 300 K)	0.64x10^{-7}	www.MatWeb.com (cited as 100% Ni)
8.89			13.3x10^{-6} (300-373 K)	0.96x10^{-7}	www.MatWeb.com (other manufacturer)
8.91				0.8x10^{-7}	www.MatWeb.com (other manufacturer)
			15-18x10^{-6} (assumed at 800+ K)		Cho and Choi (2009)
			16.5x10^{-6} (assumed at 800+ K)		Tsipis and Kharton I (2008)
			12.7x10^{-6} (at 300 K) 16.8x10^{-6} (at 800 K)	0.69x10^{-7}	Shackelford 5th Edition
8.89	204	0.31	13.3x10-6 (at 300 K)	0.95x10^{-7}	Callister 6th Edition
8.89	**205.5**	**0.31**	**13.1x10^{-6} (at 300 K) 16.6x10^{-6} (at 800 K)**	**0.96x10^{-7} (at 300 K) 0.808x10^{-7} (overall avg.)**	**Average**

Table N–1. Ni material properties.

Melting point: 1728 K [Zaitsev and Zaitseva (2001)]

Salient NiO properties.

ρ_{NiO} = 7,450 kg m^{-3}

Salient Platinum properties. The nominal alloy in all cases was commercially pure Pt (99.99% pure Pt).

Density, ρ (g/cm^3)	Young's Modulus, E (GPa)	Poisson's Ratio, γ	Linear CTE, α (K^{-1})	Resistivity, ρ (Ω.m)	Source & Notes
21.45	171	0.39	9.1x10^{-6} (at 300 K)	1.06x10^{-7}	Callister 6th Edition
21.45	171	0.39	9.1x10^{-6} (at 300 K)	1.06x10^{-7}	www.MatWeb.com
21.45	**171**	**0.39**	**9.1x10^{-6} (at 300 K)**	**1.06x10^{-7}**	**Average**

Table N–2. Pt material properties.

Salient YSZ properties. The nominal composition for the system in all cases was 8YSZ (8 mol% Yttria, balance Zirconia). Unless otherwise noted it has been assumed the manufacturing to be sintering based. [3YSZ included for comparison only, 3YSZ and unknown compositions not considered in averaging properties.]

Density, ρ (g/cm^3)	Young's Modulus, E (GPa)	Poisson's Ratio, γ	Linear CTE, α (K^{-1})	Resistivity, ρ (Ω.m)	Source & Notes
			11x10^{-6}		Zhao *et al.* (2006) (EB-PVD)
			2x10^{-6}		Hass *et al.* (2001) (EB-PVD)
			10x10^{-6} (300-1273 K)		Tsipis and Kharton II (2008)
5.85			9.5x10^{-6} (at 300 K)	1.2 (at 873 K) 0.3 (at 973 K) 0.2 (at 1073 K) 0.1 (at 1173 K) 0.05 (at 1273 K)	www.MatWeb.com
6 (at 0% porosity)			8x10^{-6} (at 573 K) 10x10^{-6} (at 1173 K)		www.MatWeb.com (other manufacturer)
6.6	160		10.5x10^{-6} (at 300 K)		www.MatWeb.com (unknown composition)
6.1	205		10.9x10^{-6} (at 300 K)		www.MatWeb.com (unknown composition, other manufacturer)
6.05 (at 0% porosity)	200	0.31	10.3x10^{-6} (at 300 K)	1x10^{7}	www.MatWeb.com (unknown composition, other manufacturer) Weibull Modulus = 22
6.02	210	0.23	10.3x10^{-6} (300-1273 K)	1x10^{11} 200 (at 773 K) 10 (at 1273 K)	www.MatWeb.com (unknown composition, other manufacturer)

Density, ρ (g/cm^3)	Young's Modulus, E (GPa)	Poisson's Ratio, γ	Linear CTE, α (K^{-1})	Resistivity, ρ (Ω.m)	Source & Notes
6	205	0.31	9.6x10^{-6} (at 300 K)	1x10^{10}	Callister 6th Edition (3YSZ)
6			9.9x10^{-6} (at 300 K)	2.8 (at 873 K) 1 (at 973 K) 0.5 (at 1073 K) 0.3 (at 1173 K) 0.2 (at 1273 K)	www.MatWeb.com (3 YSZ)
				10 (at 1073 K)	
6.025 (at 0% porosity) 5.925 (overall average)	**193.75 (excluding only 3YSZ)**	**0.27 (excluding only 3YSZ)**	**8.125x10^{-6} (at 300 K) 9x10^{-6} (at 573 K) 10x10^{-6} (at 1173 K) 10x10^{-6} (at 1273 K)**	**5x10^{10} (at 300 K) 1.2 (at 873 K) 0.3 (at 973 K) 0.2 (at 1073 K) 0.1 (at 1173 K) 0.05 (at 1273 K)**	**Average**

Table N–3. YSZ material properties.

Electrolyte Material	Conductivity at 1,000 ℃ (S/cm)		Bending Strength (MPa)	Linear coefficient of thermal expansion, α ($10^{-6}/K$)
	As sintered	After annealing		
3YSZ	0.059	0.050	1200	10.8
8YSZ	0.13	0.09	230	10.5
9YSZ	0.13	0.12	n/a	n/a

Table N–4. Selected electrical and mechanical properties of YSZ [adapted from Ishihara *et al*. 2003].

Salient Stainless Steel properties. The nominal alloy in all cases was Austenitic 316 (C 0.03-0.08%, Cr 16-18%, Fe 61.8-72%, Mn 0.2-2%, Mo 1.88-3%, Ni 10-14%, N ≤0.13%, P 0.045-0.2%, Si ≤1%, S 0.03-0.1%).

Density, ρ (g/cm^3)	Young's Modulus, E (GPa)	Poisson's Ratio, γ	Linear CTE, α (K^{-1})	Resistivity, ρ (Ω.m)	Source & Notes
8.0	193		16.0x10^{-6} (till 373 K) 16.2x10^{-6} (till 588 K) 17.5x10^{-6} (till 813 K)	7.4x10^{-7} (at 295 K)	www.MatWeb.com (cited as 316 SS bar/sheet/plate, annealed)
8.0	193		16.6x10^{-6} (till 373 K) 17.5x10^{-6} (till 588 K) 18.2x10^{-6}	7.4x10^{-7} (at 295 K)	www.MatWeb.com (other manufacturer, cited as AISI 316F SS sheet, annealed)

Density, ρ (g/cm^3)	**Young's Modulus, E (GPa)**	**Poisson's Ratio, γ**	**Linear CTE, α (K^{-1})**	**Resistivity, ρ (Ω.m)**	**Source & Notes**
			(till 813 K)		
8.0	193		16.6x10^{-6} (till 373 K) 17.5x10^{-6} (till 588 K) 18.2x10^{-6} (till 813 K)	7.4x10^{-7} (at 295 K)	www.MatWeb.com (other manufacturer, cited as AISI 316F SS bar, annealed)
8.0	193			7.4x10^{-7} (at 295 K)	www.MatWeb.com (other manufacturer, cited as AISI 316L SS sheet, annealed)
8.0	193			7.4x10^{-7} (at 295 K)	www.MatWeb.com (other manufacturer, cited as AISI 316L SS strip, annealed)
7.92	196		16.0x10^{-6} (till 373 K) 16.2x10^{-6} (till 588 K) 17.5x10^{-6} (till 813 K)	7.4x10^{-7} (at 295 K)	www.MatWeb.com (other manufacturer, cited as AISI 316N SS sheet, annealed)
7.92	196		16.0x10^{-6} (till 373 K) 16.2x10^{-6} (till 588 K) 17.5x10^{-6} (till 813 K)	7.4x10^{-7} (at 295 K)	www.MatWeb.com (other manufacturer, cited as AISI 316N SS bar, annealed)
					Shackelford 5th Edition
					Callister 6th Edition
7.98	**193.86**	**0.3**	**16.24x10^{-6} (till 373 K) 16.72x10^{-6} (till 588 K) 17.78x10^{-6} (till 813 K)**	**7.4x10^{-7} (at 295 K)**	**Average**

Table N–5. Stainless steel material properties.

Thermal conductivity, k (W/mK)	Melting Point, T_m (°K)	Maximum Continuous Service Temperature, T_{MAX} (°K)	Elongation, ε (%)	Source & Notes
16.3 (at 373 K)	1643-1673	1198	50	www.MatWeb.com (cited as 316 SS bar, annealed)
14.4 (at 373 K)	1643-1673	1198	60	www.MatWeb.com (other manufacturer, cited as AISI 316F SS sheet, annealed)
14.4 (at 373 K)	1643-1673	1198	57	www.MatWeb.com (other manufacturer, cited as AISI 316F SS bar, annealed)
	1643-1673	1198	50	www.MatWeb.com (other manufacturer, cited as AISI 316L SS sheet, annealed)
	1643-1673	1198	50	www.MatWeb.com (other manufacturer, cited as AISI 316L SS strip, annealed)
16.1 (at 373 K)	1643-1673	1198	48	www.MatWeb.com (other manufacturer, cited as AISI 316N SS sheet, annealed)
16.1 (at 373 K)	1643-1673	1198	55	www.MatWeb.com (other manufacturer, cited as AISI 316N SS bar, annealed)
				Shackelford 5th Edition
				Callister 6th Edition
15.46 (at 373 K)	**1643-1673**	**1198**	**52.857**	**Average**

Table N–6. Stainless steel material properties (continued).

Salient INCONEL properties. The nominal alloy in all cases was INCONEL 600 (C 0.15 %, Cr 14-17%, Cu 0.5%, Fe 6-10%, Mn 1%, Ni 72%, Si 0.5%, S 0.015%).

Density, ρ (g/cm^3)	**Young's Modulus, E (GPa)**	**Poisson's Ratio, γ**	**Linear CTE, α (K^{-1})**	**Resistivity, ρ (Ω.m)**	**Source & Notes**
8.47	1.455? (at 293 K) [based on UTS 655 MPa and Elongation at break 45%] 1.309? (at 823 K) [based on UTS 550 MPa and Elongation at break 42% at 823 K]		13.3x10^{-6} (till 373 K)	10.3x10^{-7} (at 295 K)	www.MatWeb.com (cited as INCONEL 600, annealed)
					Shackelford 5th Edition
					Callister 6th Edition
8.47	**1.455 (at 293 K) 1.309 (at 823 K)**	**0.3?**	**13.3x10^{-6} (till 373 K)**	**10.3x10^{-7} (at 295 K)**	**Average**

Table N–7. Inconel material properties.

Thermal conductivity, k (W/mK)	**Melting Point, T_m (°K)**	**Maximum Continuous Service Temperature, T_{MAX} (°K)**	**Elongation, ε (%)**	**Source & Notes**
14.9 (at 293 K)	1627-1686	??	45 (at 293 K) 42 (at 823 K)	www.MatWeb.com (cited as INCONEL 600, annealed)
				Shackelford 5th Edition
				Callister 6th Edition
14.9 (at 293 K)	**1627-1686**	**??**	**45 (at 293 K) 42 (at 823 K)**	**Average**

Table N–8. Inconel material properties (continued).

Diffusion Coefficients.

Diffusion coefficient D for H_2O molecules in N_2 given by: D = 0.204(T/273)2.072

Appendix O: Thermodynamic Data for Selected Chemical Compounds

Compound	**Common Name**	**Molar Mass ($g\ mol^{-1}$)**	**ΔH_f ($kJ\ mol^{-1}$)**	**ΔG_f ($kJ\ mol^{-1}$)**
H_20 (l)	water	18.02	-285.83	-237.13
H_20 (g)	water (steam)	18.02	-241.82	-228.57
CH_4	methane	16.04	-74.81	-50.72
C_3H_6 (g)	propane	42.08	20.42	62.78
C_4H_{10} (g)	butane	58.13	-126.15	-17.03
C_8H_{18} (l)	octane	114.23	-249.90	6.4
C_8H_{18} (l)	iso-octane	114.23	-255.10	-
CH_3OH (l)	methanol	32.04	-238.66	-166.27
CH_3OH (g)	methanol	32.04	-200.66	-161.96
C_2H_5OH (l)	ethanol	46.07	-277.69	-174.78
C_2H_5OH (g)	ethanol	46.07	-235.10	-168.49
CO	carbon monoxide	28.01	-110.53	-137.17
CO_2	carbon dioxide	44.01	-393.51	-394.36
H_2	hydrogen	2.02	0	0
O_2	oxygen	32.00	0	0

Table O–1. Thermodynamic data for selected chemical compounds.

Note: Tabulated are the standard heat (enthalpy) of formation, ΔH_f, and the Gibbs free energy, ΔG_f, at 10^5 Pa and 298 K.

Source: Hoogers G. (Ed.) *Fuel Cell Technology Handbook*, CRC Press, New York, USA.

Appendix P: Electrochemical Impedance Spectroscopy

This appendix compiles all the EIS plots associated with the 3-probe fuel cell testing experiments. The Nyquist plots are divided by temperature as well as whether in galvanostatic or potentiostatic mode. Both tested samples are included. The 2- and 4-probe Nyquist plots yield somewhat unreliable data.

The Nyquist plots yielded highly unexpected and unusual results. In almost all cases where the galvanostatic mode was employed the result was a star-shaped plot that defies any interpretation other than being very noisy (while it was suggested that the root cause may be an unintended connection to ground the setup makes this unlikely and no evidence was found after testing to indicate connections had shifted and possibly shorted). In more specific terms these extremely noisy plots from galvanostatic mode EIS occurred in 6 of 7 cases at 400 °C, 4 of 4 at 600 °C, 4 of 5 at 800 °C and 6 of 7 at 1,000 °C. In potentiostatic mode they occur not at all at 400 °C, in 3 of 5 cases at 600 °C, 0 of 6 at 800 °C and 1 of 6 at 1,000 °C. Therefore, while their occurrence may be linked strongly to galvanostatic mode EIS this is not likely causal. This was the most common result (25 of 45 EIS plots; 56%), with no bias evident due to temperature or sample. Figure P-1. (below) shows an exemplar of each sample at the same temperature.

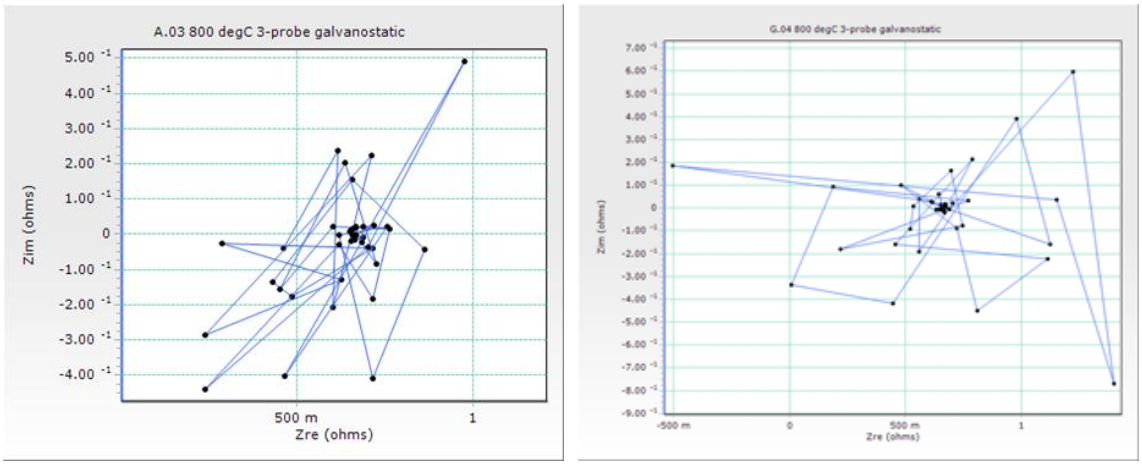

Figure P-1. One exemplar at 800 °C of galvanostatic mode Nyquist plot from sample PT-AEC.13/03/15-125;10;0.3.1100(400)[1000]-A.03 (left) and PT-AE.20/03/15-125;10;0.3.1100(1000)[1000]-G.04 (right).

The second most common result (19 of 45 EIS plots; 42%) consisted of a near-linear behaviour with little variance in real impedance commencing near zero imaginary impedance (at the high frequency end) and trending strongly towards an increasingly negative imaginary impedance (at the low frequency end). Figure P-2. (below) shows an exemplar of each sample at the same temperature. The Nyquist plot took on this form in galvanostatic mode in 1 of 7 EIS plots at 400 °C, 0 of 4 at 600 °C, 1 of 5 at 800 °C, and

0 of 7 at 1,000 °C. Most occurrences were for potentiostatic EIS: 5 of 5 at 400 °C, 2 of 5 at 600 °C, 6 of 6 at 800 °C and 5 of 6 at 1,000 °C. Such strongly inductive behaviour of the sample could not be explained.

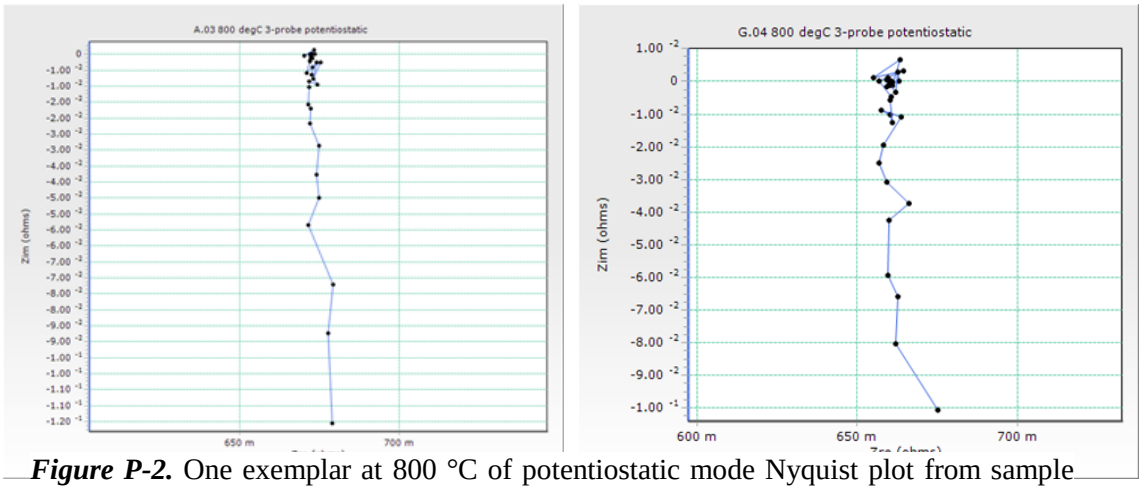

Figure P-2. One exemplar at 800 °C of potentiostatic mode Nyquist plot from sample PT-AEC.13/03/15-125;10;0.3.1100(400)[1000]-A.03 (left) and PT-AE.20/03/15-125;10;0.3.1100(1000)[1000]-G.04 (right).

The first case may indicate some form of avalanche ionisation effect similar to that occurring in the breakdown of a diode. In other words, the sudden increase in current due to this breakdown effect during the impedance measurements results in inductive impedance with frequency. The author would not expect such behaviour but testing such a hypothesis was well beyond the scope of this thesis. There is a fairly strong possibility that the result is linked to digitization errors of the potentiogalvanostat.

In the semiconductor industry inductors are created from conductor and insulator elements via geometrical arrangement of layer structures (the same as used to create capacitive elements, and are what gives rise to the capacitive traits of SOFCs). It is feasible, therefore, that a similar situation has occurred due to the somewhat fractured nature of the electrolyte in the second case. This too is an untested hypothesis at this stage, however.

400 °C

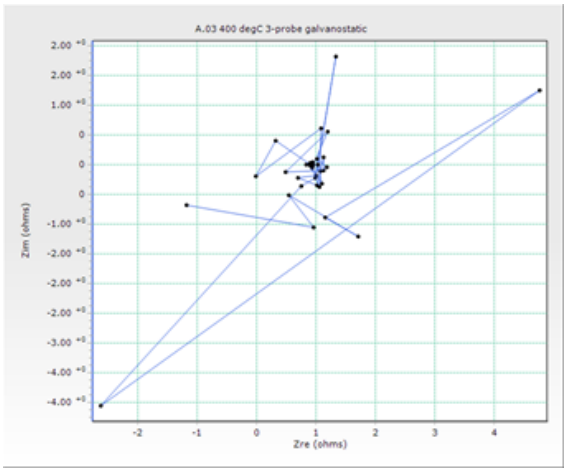
A.03 400 degC 3-probe galvanostatic
Zim (ohms)
Zre (ohms)

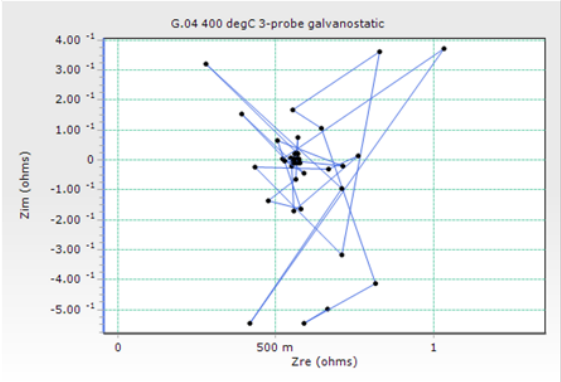
G.04 400 degC 3-probe galvanostatic
Zim (ohms)
500 m
Zre (ohms)

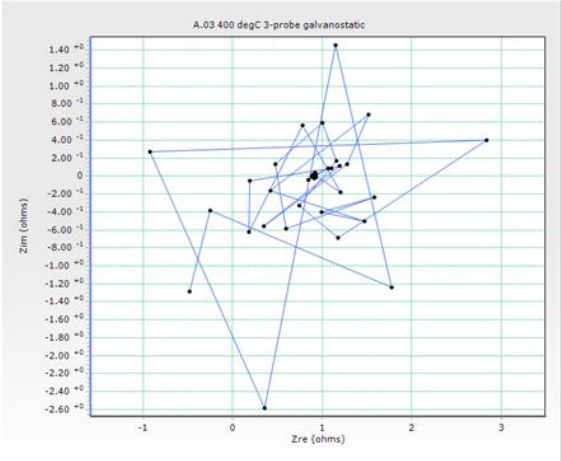
A.03 400 degC 3-probe galvanostatic
Zim (ohms)
Zre (ohms)

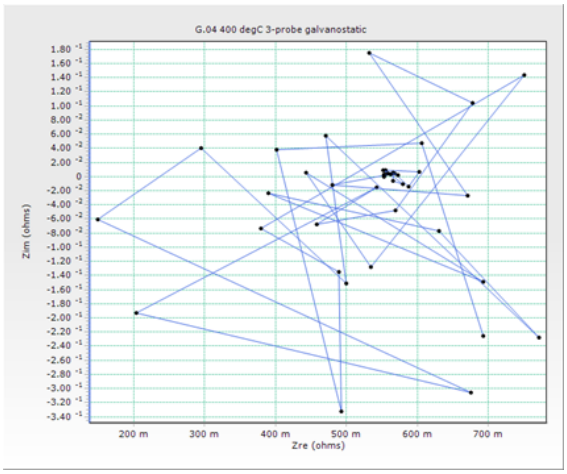
G.04 400 degC 3-probe galvanostatic
Zim (ohms)
200 m
300 m
400 m
500 m
600 m
700 m
Zre (ohms)

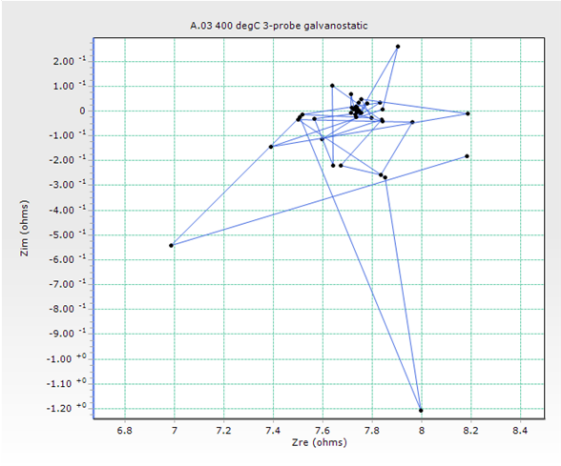
A.03 400 degC 3-probe galvanostatic
Zim (ohms)
Zre (ohms)

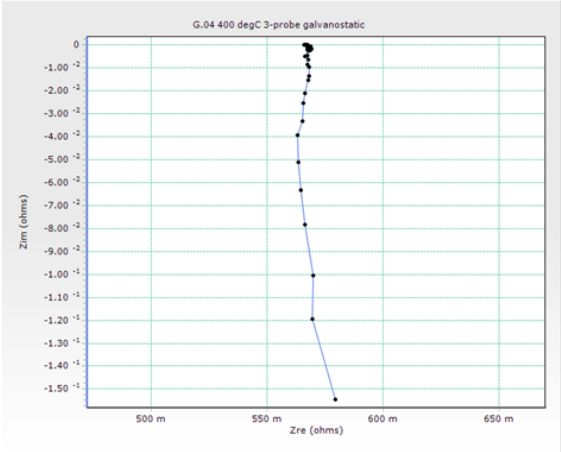
G.04 400 degC 3-probe galvanostatic
Zim (ohms)
Zre (ohms)

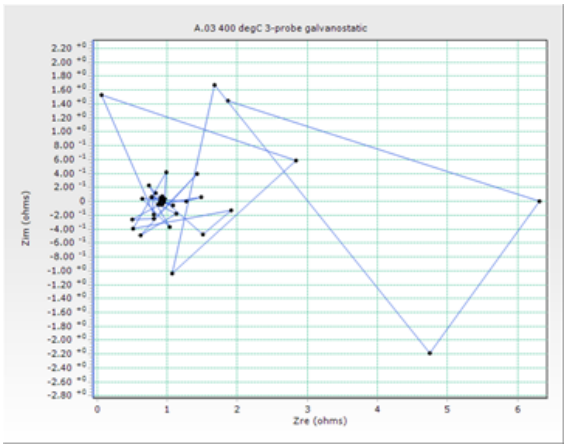
A.03 400 degC 3-probe galvanostatic
Zim (ohms)
Zre (ohms)

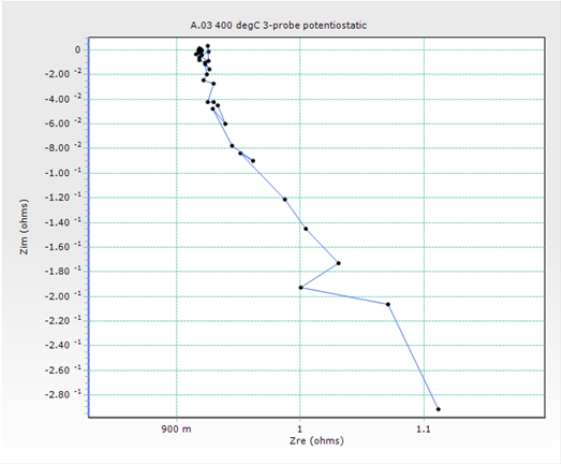
A.03 400 degC 3-probe potentiostatic
Zim (ohms)
Zre (ohms)
900 m
1
1.1

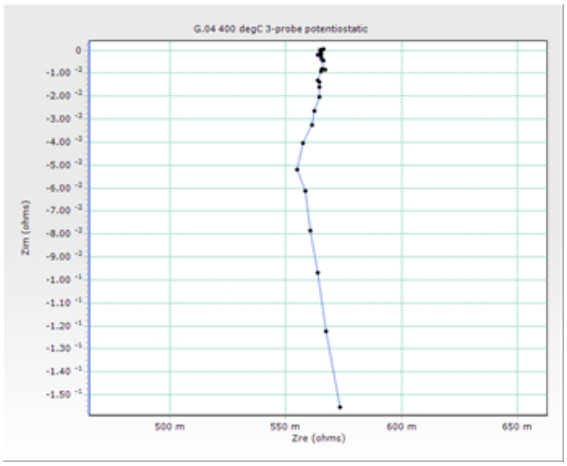
G.04 400 degC 3-probe potentiostatic
Zim (ohms)
Zre (ohms)
500 m
550 m
600 m
650 m

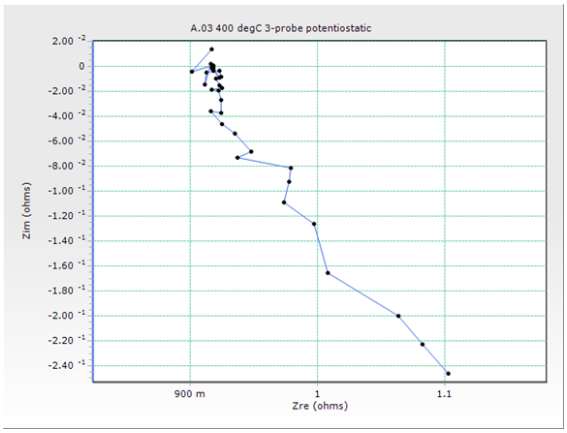
A.03 400 degC 3-probe potentiostatic
Zim (ohms)
Zre (ohms)
900 m
1
1.1

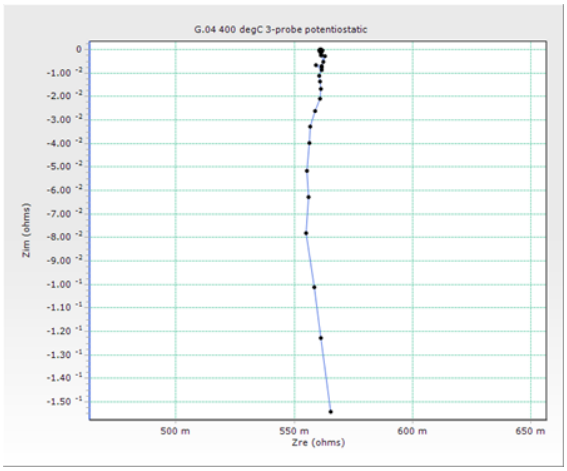
G.04 400 degC 3-probe potentiostatic
Zim (ohms)
Zre (ohms)
500 m
550 m
600 m
650 m

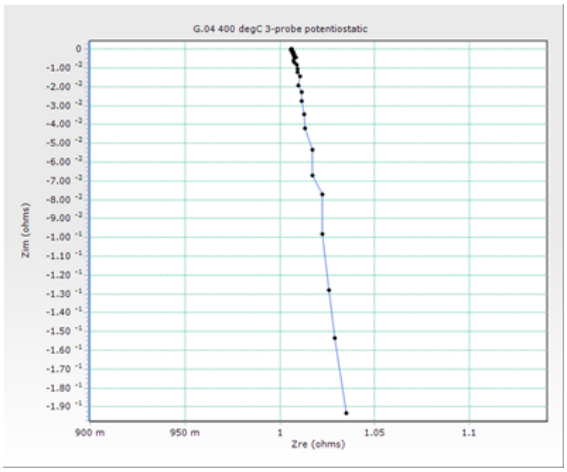
G.04 400 degC 3-probe potentiostatic
Zim (ohms)
Zre (ohms)
900 m
950 m
1
1.05
1.1

600 °C

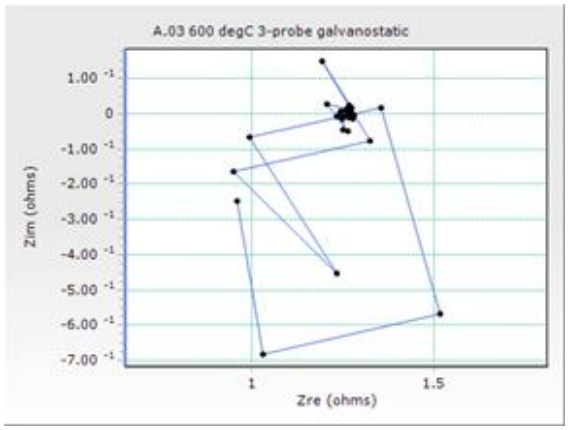
A.03 600 degC 3-probe galvanostatic
Zim (ohms)
Zre (ohms)

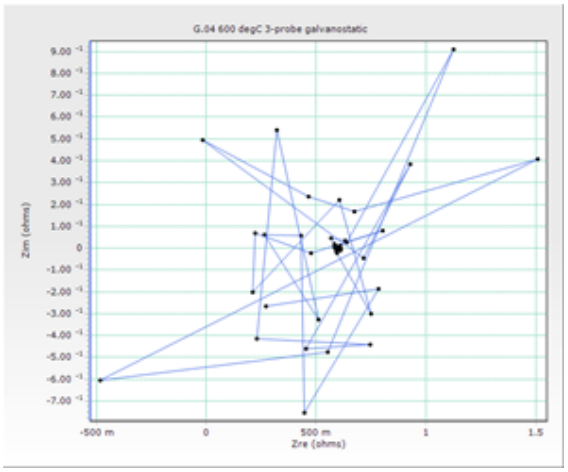
G.04 600 degC 3-probe galvanostatic
Zim (ohms)
Zre (ohms)

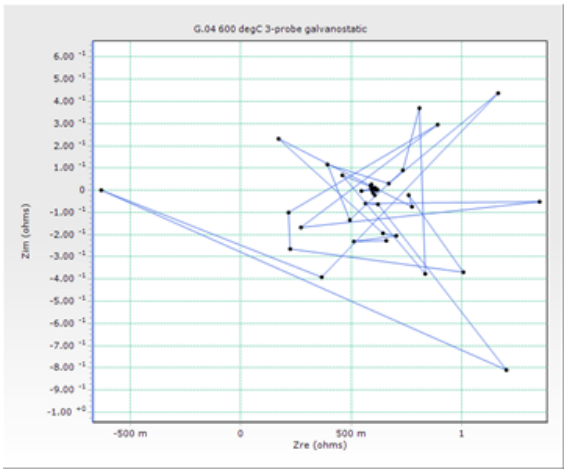
G.04 600 degC 3-probe galvanostatic
Zim (ohms)
Zre (ohms)

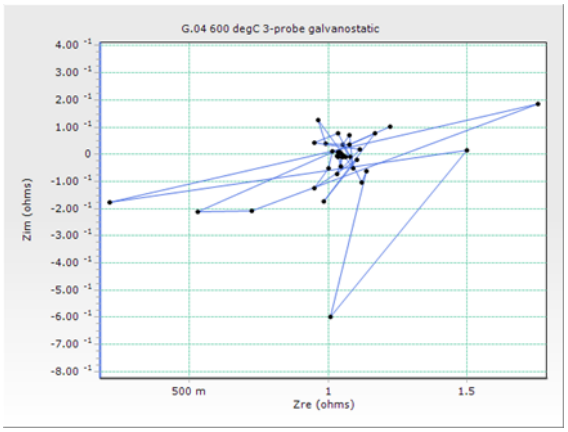
G.04 600 degC 3-probe galvanostatic
Zim (ohms)
Zre (ohms)

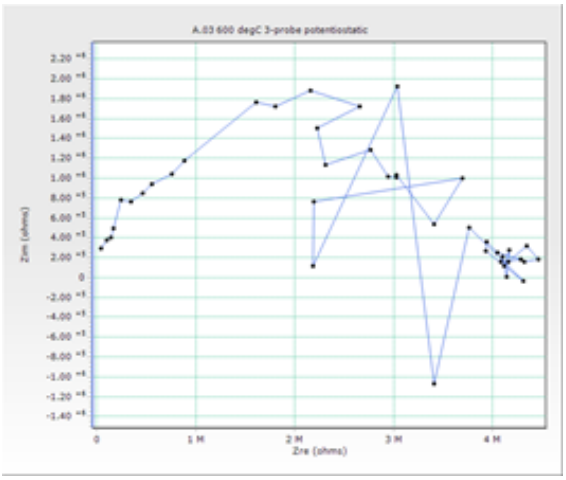
A.03 600 degC 3-probe potentiostatic
Zim (ohms)
Zre (ohms)

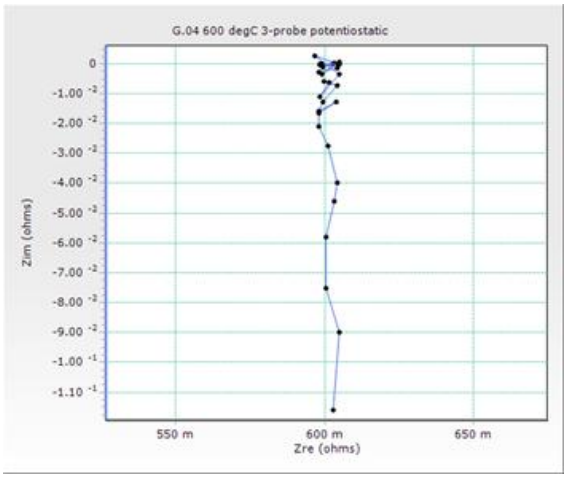
G.04 600 degC 3-probe potentiostatic
Zim (ohms)
550 m
600 m
650 m
Zre (ohms)

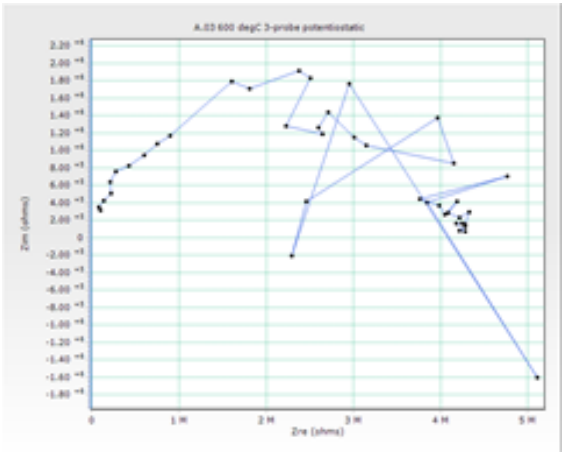
A.03 600 degC 3-probe potentiostatic
Zim (ohms)
Zre (ohms)

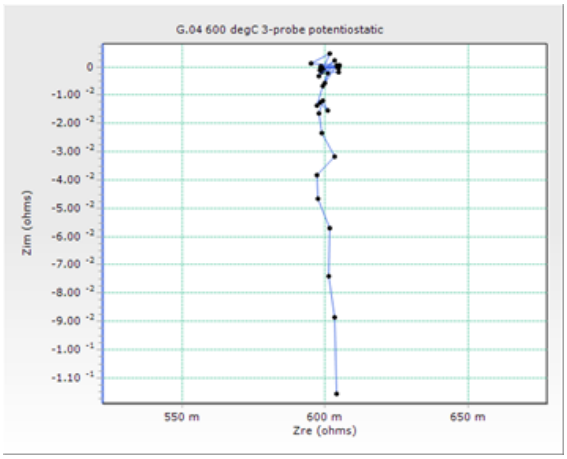
G.04 600 degC 3-probe potentiostatic
Zim (ohms)
550 m
600 m
650 m
Zre (ohms)

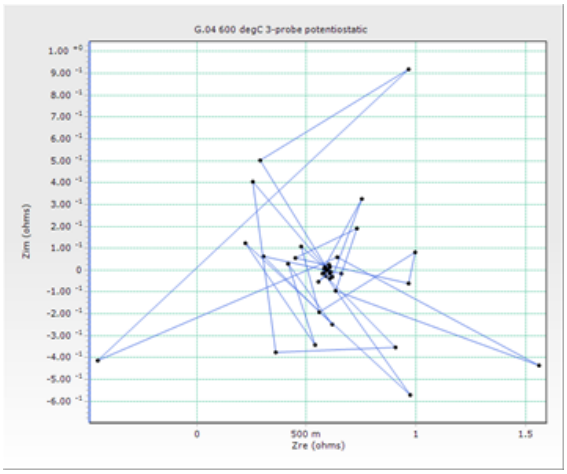
G.04 600 degC 3-probe potentiostatic
Zim (ohms)
Zre (ohms)

800 °C

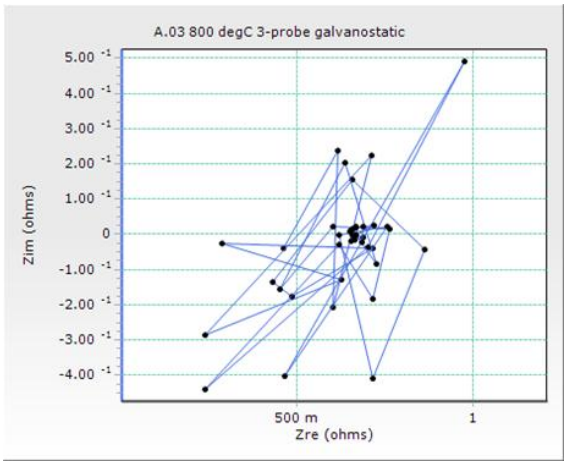
A.03 800 degC 3-probe galvanostatic
Zim (ohms)
Zre (ohms)
500 m
1

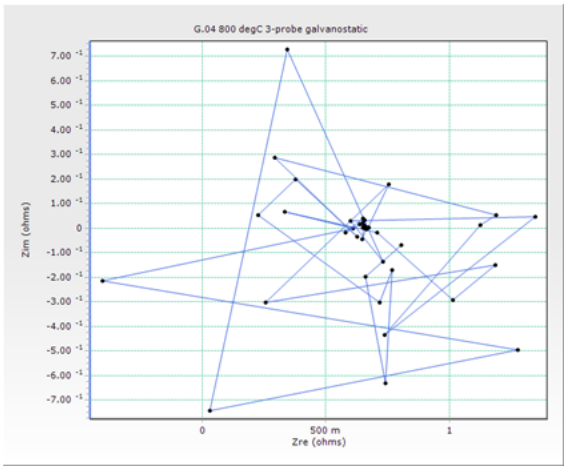
G.04 800 degC 3-probe galvanostatic
Zim (ohms)
Zre (ohms)
0
500 m
1

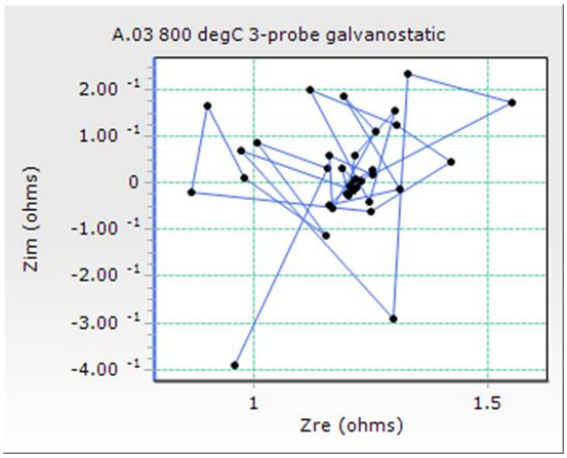
A.03 800 degC 3-probe galvanostatic
Zim (ohms)
Zre (ohms)
1
1.5

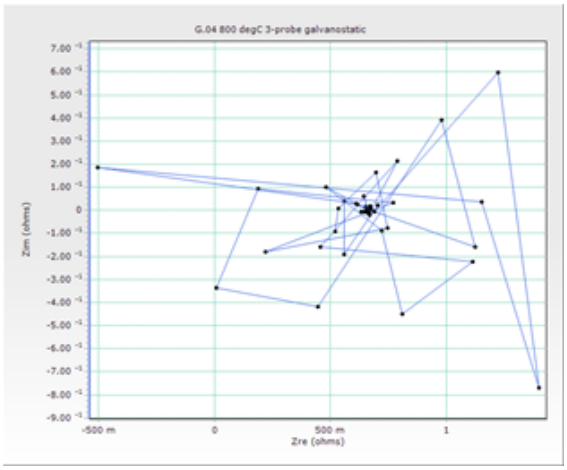
G.04 800 degC 3-probe galvanostatic
Zim (ohms)
Zre (ohms)
-500 m
0
500 m
1

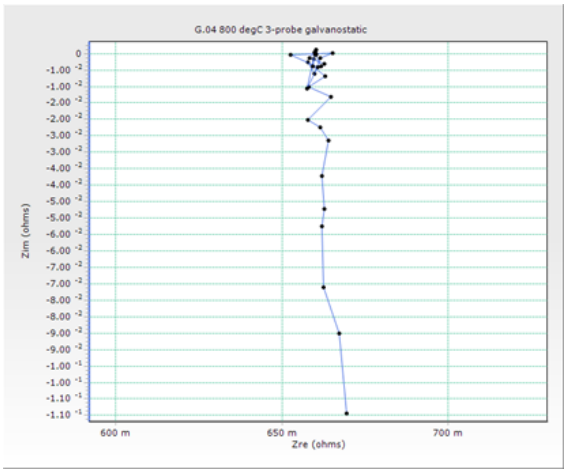
G.04 800 degC 3-probe galvanostatic
Zim (ohms)
Zre (ohms)
600 m
650 m
700 m

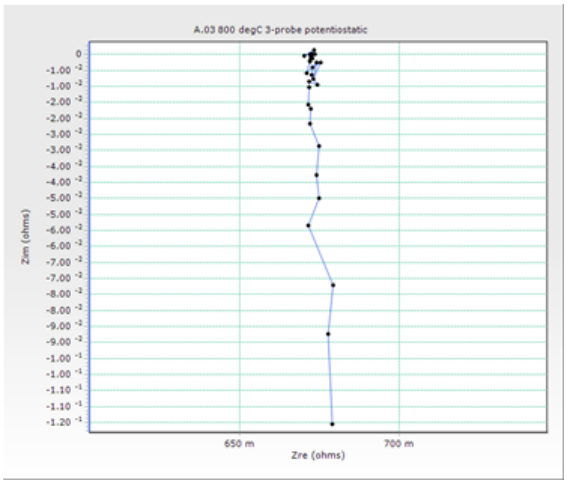
A.03 800 degC 3-probe potentiostatic
Zim (ohms)
650 m
700 m
Zre (ohms)

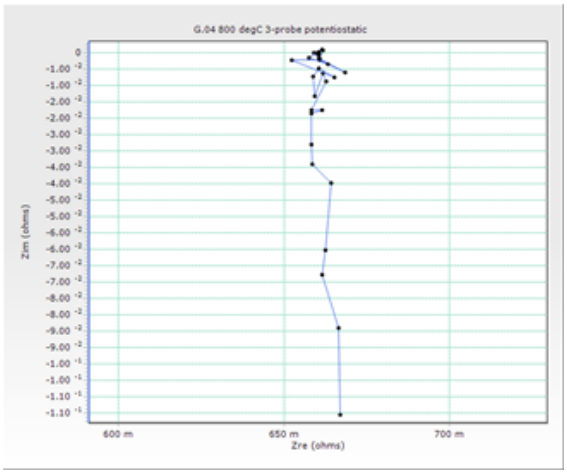
G.04 800 degC 3-probe potentiostatic
Zim (ohms)
600 m
650 m
700 m
Zre (ohms)

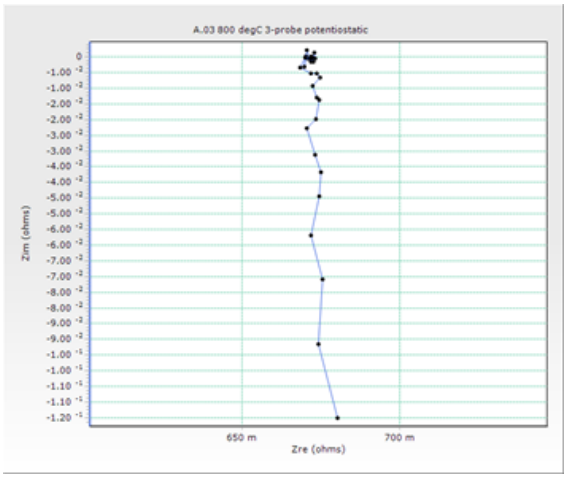
A.03 800 degC 3-probe potentiostatic
Zim (ohms)
650 m
700 m
Zre (ohms)

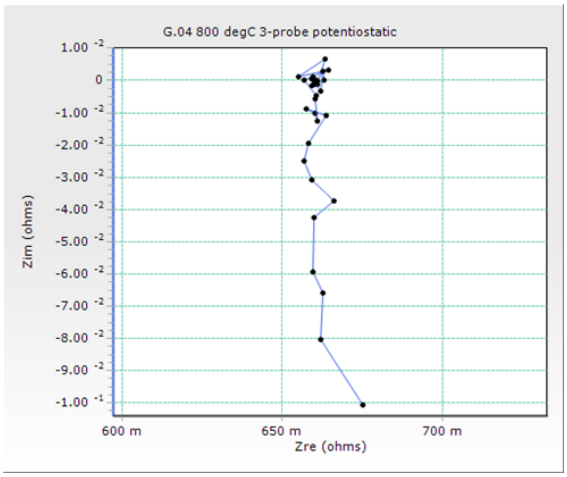
G.04 800 degC 3-probe potentiostatic
Zim (ohms)
600 m
650 m
700 m
Zre (ohms)

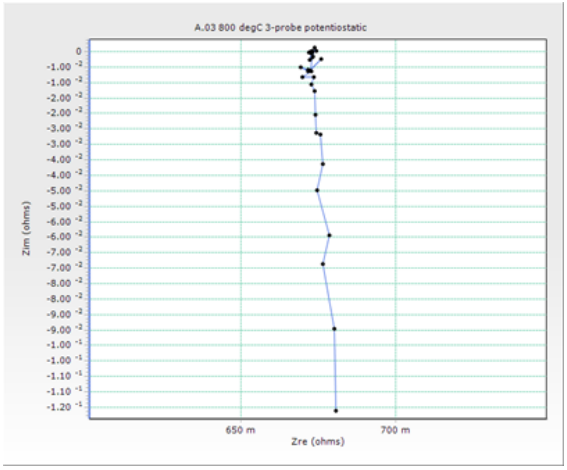
A.03 800 degC 3-probe potentiostatic
Zim (ohms)
650 m
700 m
Zre (ohms)

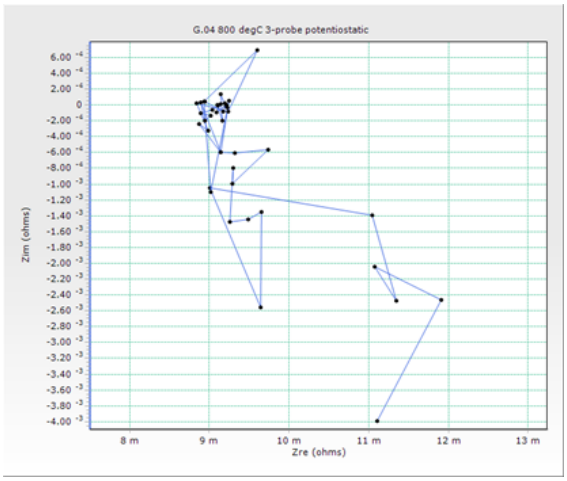
G.04 800 degC 3-probe potentiostatic
Zim (ohms)
8 m
9 m
10 m
11 m
12 m
13 m
Zre (ohms)

1,000 °C

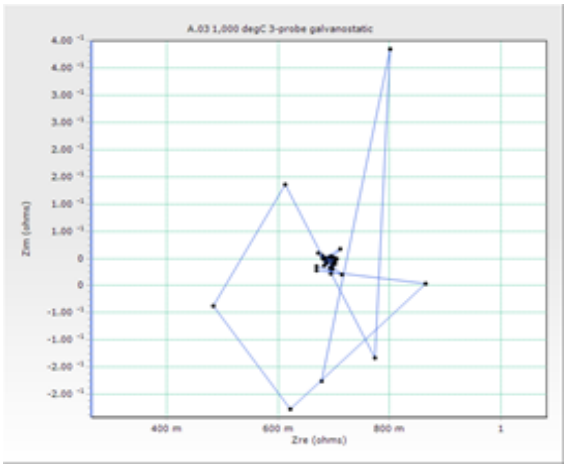
A.03 1,000 degC 3-probe galvanostatic
Zim (ohms)
Zre (ohms)

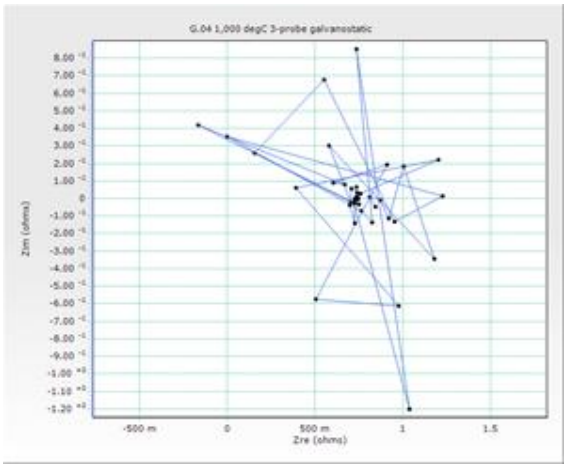
G.04 1,000 degC 3-probe galvanostatic
Zim (ohms)
Zre (ohms)

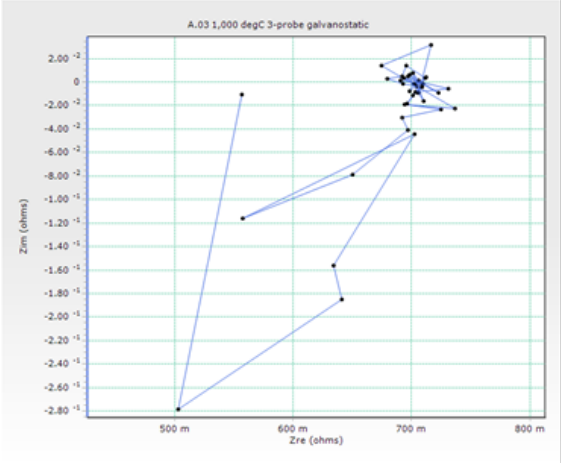
A.03 1,000 degC 3-probe galvanostatic
Zim (ohms)
Zre (ohms)

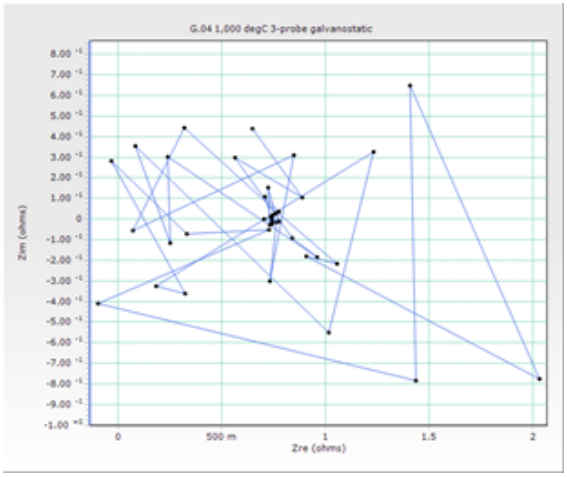
G.04 1,000 degC 3-probe galvanostatic
Zim (ohms)
Zre (ohms)

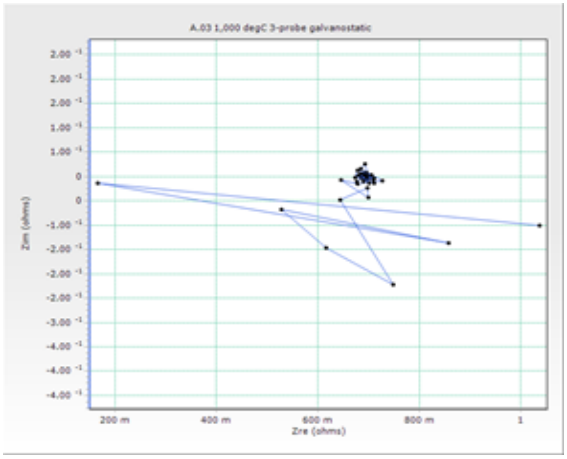
A.03 1,000 degC 3-probe galvanostatic
Zim (ohms)
Zre (ohms)

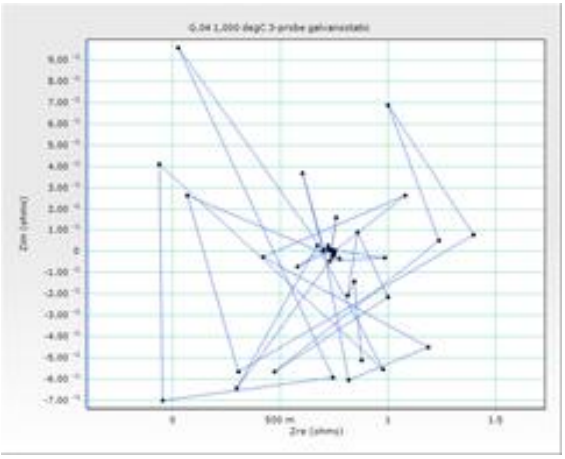
G.04 1,000 degC 3-probe galvanostatic
Zim (ohms)
Zre (ohms)

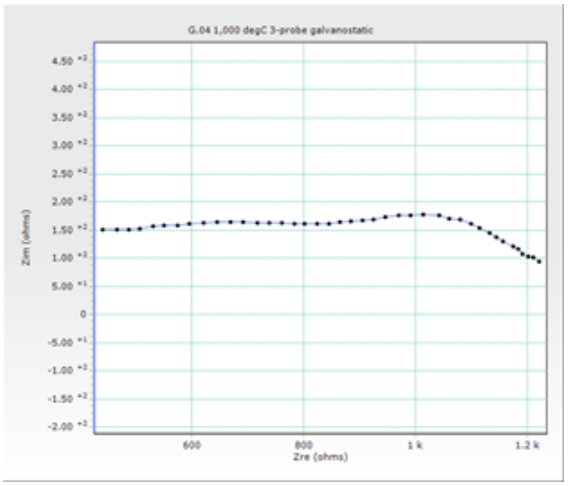
G.04 1,000 degC 3-probe galvanostatic
Zim (ohms)
Zre (ohms)
600
800
1 k
1.2 k

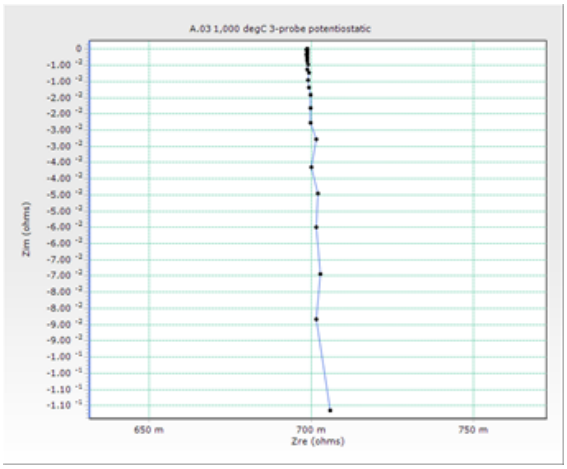
A.03 1,000 degC 3-probe potentiostatic
Zim (ohms)
650 m
700 m
750 m
Zre (ohms)

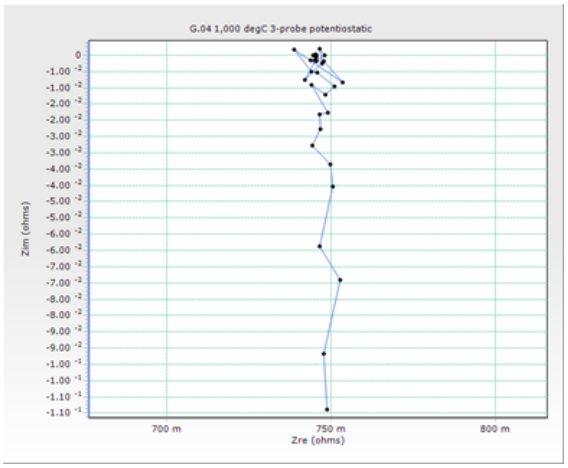
G.04 1,000 degC 3-probe potentiostatic
Zim (ohms)
700 m
750 m
800 m
Zre (ohms)

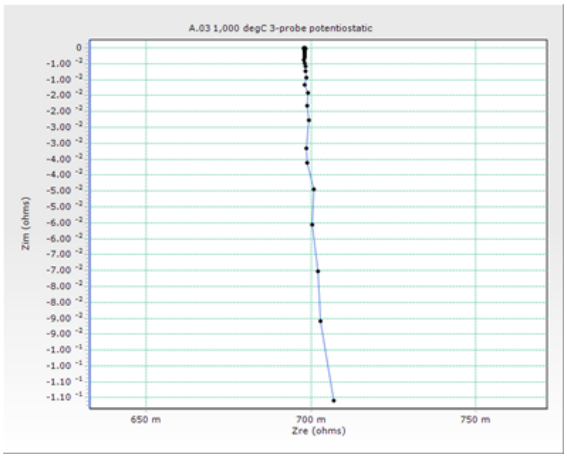
A.03 1,000 degC 3-probe potentiostatic
Zim (ohms)
650 m
700 m
750 m
Zre (ohms)

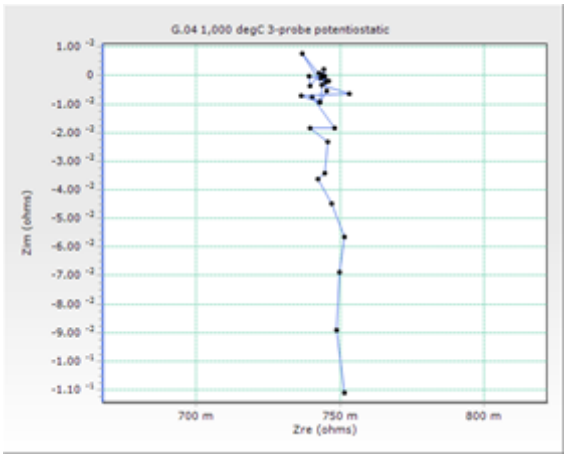
G.04 1,000 degC 3-probe potentiostatic
Zim (ohms)
700 m
750 m
800 m
Zre (ohms)

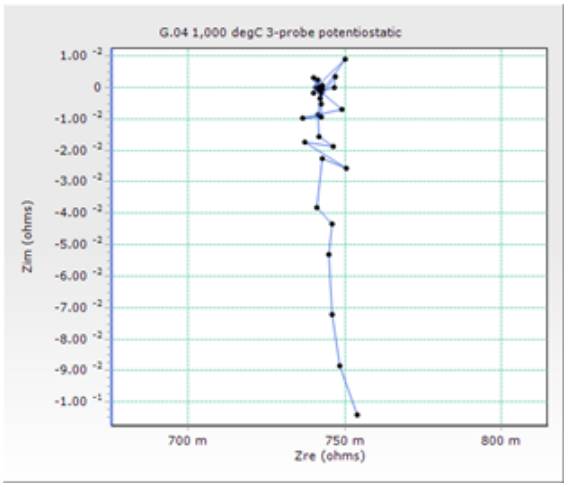
G.04 1,000 degC 3-probe potentiostatic
Zim (ohms)
Zre (ohms)
700 m
750 m
800 m

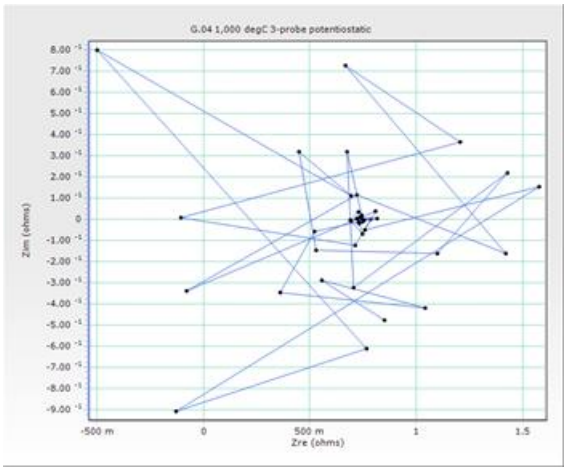
G.04 1,000 degC 3-probe potentiostatic
Zim (ohms)
Zre (ohms)
-500 m
0
500 m
1
1.5

Appendix Q: OCV Arrhenius Plots

What follows is analysis divided by temperature of the measured OCV value (mode, range, standard deviation) and some related commentary deemed valuable enough to include but not critical to the discussion on electrochemical performance. Note this is after statistically identifying and removing outliers.

At 400 °C the mean OCV ranges from 0.92±0 mV to 1.23±0 mV for A.03 and 0.86±0.13 mV to 1.23±0 mV for G.04. The standard deviations range from ±0 mV to a maximum of ±0.22 mV for A.03 and ±0 mV to a maximum of ±0.13 mV for G.04. It is important to note however that only two OCV values were measured for both A.03 and G.04: 0.92 mV and 1.23 mV (67 and 49 of 120 data points respectively). Overall A.03 had a higher mode (1.23 mV) and G.04 a lower mode (0.92 mV). Furthermore the overall standard deviation considering both samples was very low (mode ±0 mV, maximum ±0.22 mV). Repeatability was therefore excellent. In addition there was probably no significant sample-to-sample variance (insufficient number of samples to state with greater confidence). After excluding outliers as explained above the mean OCV is 1.12±0.15 mV for A.03 and 0.92±0.0 mV for G.04. In the case of the latter the statistical analysis revealed that repeat 6 in its entirety is a subset whose mean OCV is 1.23±0 mV. This either relates to the VersaSTAT's quantisation or occurred for some other, currently unknown, reason. The data is sound, however, and should not be neglected.

At 600 °C the mean OCV ranges from 0.92±0 mV to 99.1±0.23 mV for A.03 and 1.23±0 mV to 1.78±0.13 mV for G.04. The standard deviations range from ±0 mV to a maximum of ±1.45 mV for A.03 and ±0 mV to a maximum of ±0.16 mV for G.04. It is important to note that A.03 was the first sample tested and part way through a superior method was developed and it was decided to take additional measurements with 2 and 3-probe connections in addition to the original planned 4-probe measurements as well as double the number of repeat measurements. The 600 °C data was the last recorded chronologically speaking, and it was part way through this sequence of measurements that the cell failed completely. The final two sets of data with much higher OCV than otherwise observed may therefore be spurious. Just three OCV values were measured for G.04: 1.23 mV, 1.53 mV and 1.84 mV (10, 19 and 31 of 60 data points respectively). Of these 1.23 mV occurred only for one repeat. Overall A.03 did not have sufficient data at this temperature, being the final set and failing part way through testing (hence the few repeats). G.04 had a mode of 1.84 mV. Furthermore the overall standard deviation considering both samples was at least an order of magnitude smaller than the mean. After excluding outliers as explained above the mean OCV is 1.64±0.23 mV for G.04. Determining a reasonable mean OCV at 600 °C for A.03 is less straightforward. Clearly (see Table 14-1.) a simple mean is insufficient; the statistical

method employed detects no outliers when obviously there are two distinct subsets. I decided to ignore the lesser subset treating the majority group as the main data set, with the other as a subset. The mean OCV is then 98.71±1.09 mV. The first repeat in its entirely was a subset with a mean of 0.92±0 mV.

At 800 °C the mean OCV ranges from 1.01±0.15 mV to 1.84±0 mV for A.03 and 0.31±0.13 mV to 2.15±0 mV for G.04. The standard deviations range from ±0 mV to a maximum of ±0.15 mV for A.03 and ±0 mV to a maximum of ±0.10 mV for G.04. Just three OCV values were measured for A.03: 0.92 mV, 1.23 mV and 1.84 mV (7, 3 and 40 of 50 data points respectively). Of these 0.92 mV and 1.23 mV occurred in a single repeat. Just three OCV values were measured for G.04: 0.31 mV, 1.84 mV and 2.15 mV (8, 11 and 39 of 60 data points respectively). Of these 0.31 mV occurred in a single repeat that also contained two 0 V OCV measurements. Overall A.03 had a lower mode (1.84 mV) and G.04 a higher one (2.15 mV). Furthermore the overall standard deviation considering both samples was very low (mode ±0 mV, maximum ±0.15 mV). Repeatability was therefore excellent. A.03 displayed notably better repeatability (though with a lower OCV) than G.04; sample-to-sample variance is in this case difficult to assess for both the aforementioned limited number of samples and also the difference in repeatability between the two samples. After excluding outliers as explained above the mean OCV is 1.84±0 mV for A.03 and 1.77±0.70 mV for G.04. In the case of the former the statistical analysis revealed that repeat 2 is wholly a subset whose mean OCV is 1.01±0.15 mV. This either relates to the VersaSTAT's quantisation or occurred for some other, currently unknown, reason. The data is sound, however, and should not be neglected.

At 1,000 °C the mean OCV ranges from 1.72±0.16 mV to 1.84±0 mV for A.03 and 1.84±0 mV to 4.30±0 mV for G.04. The standard deviations range from ±0 mV to a maximum of ±0.16 mV for A.03 and ±0 mV for G.04. It is important to note however that only three OCV values were measured for both A.03 and G.04: 1.53 mV, 1.84 mV and 4.30 mV (4, 96 and 10 of 110 data points respectively). Overall both samples had a mode of 1.84 mV. Furthermore the overall standard deviation considering both samples was very low (mode ±0 mV, maximum ±0.16 mV; the former being by far the most common). Thus, repeatability was excellent. There was no significant sample-to-sample variance (can be stated with confidence despite the small number of samples tested). There was however one repeat measurement using sample G.04 with a significantly greater OCV: 4.30±0 mV; a potentially significant result. After excluding outliers as explained above the mean OCV is 1.84±0 mV for A.03 and 1.84±0 mV for G.04.

The second part of this appendix shows the linear fit of each sample separately (first plot) as well as combined into a larger single dataset (second plot).

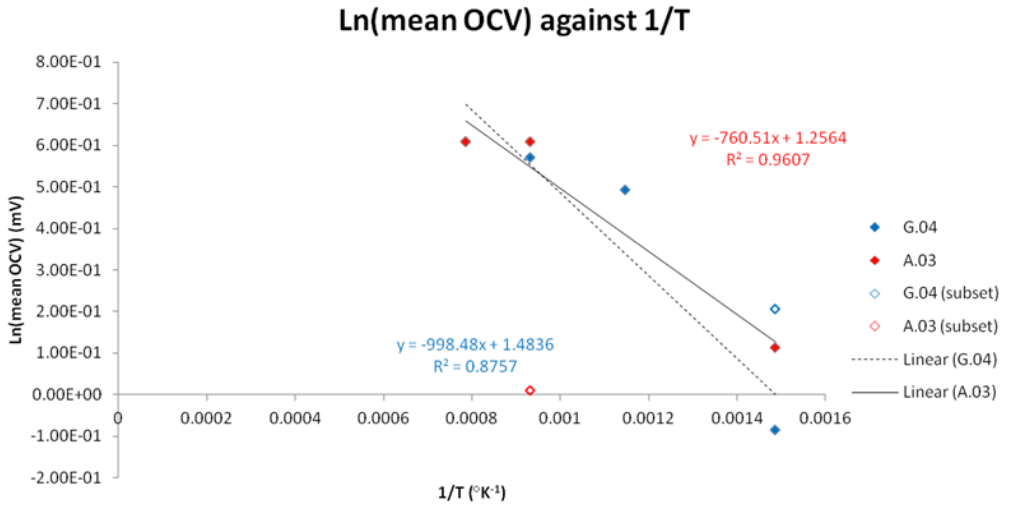

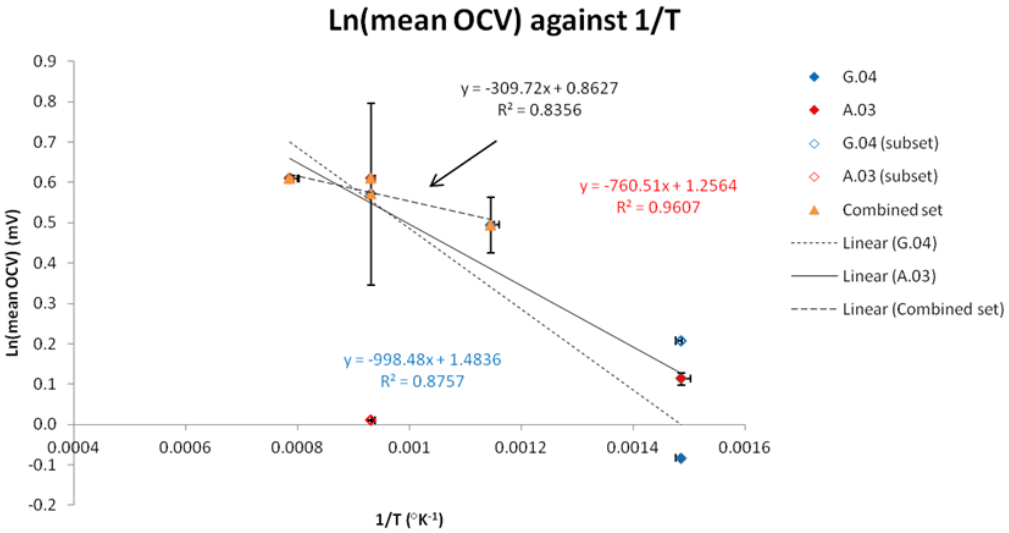

The following plot sows linear fits by sample, and the following combined sets: high 3 temperatures, low 3 temperatures, low 3 temperatures and G.04 outlier subset (see legend). Keeping the by-sample plots shows that there is a different mechanism at the lowest temperature (which stabilizes at about 600 °C to a common diffusion mechanism). The difference at 400 °C highlights the effect of the different microstructure at this low temperature (different reduction schemes) that becomes less significant with increasing temperature.

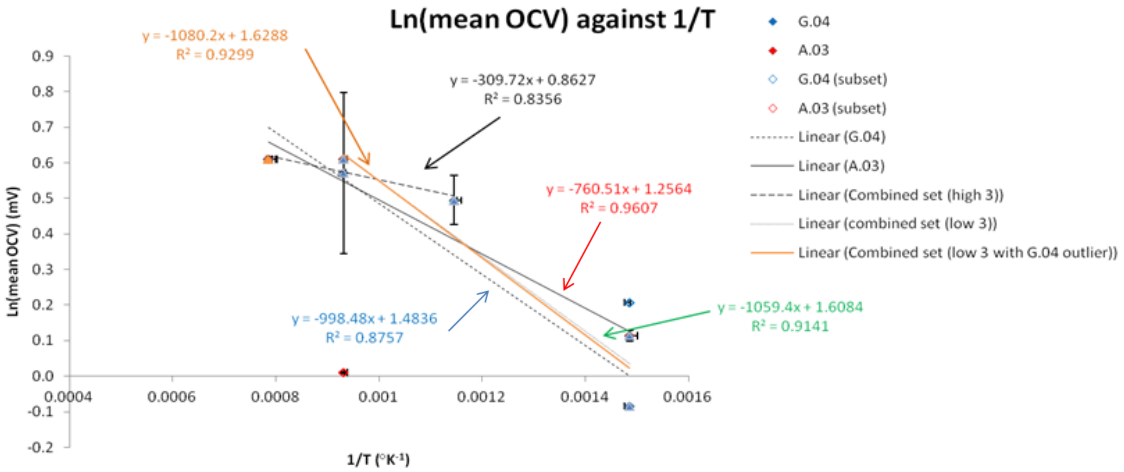

A.03 linear fit (R^2 = 0.9607) calculated OCV at 600 °C 1.4705 mV.
Combined set (high 3) (R^2 = 0.8356) calculated OCV at 600 °C 1.6619 mV.
Combined set (low 3) (R^2 = 0.9141) calculated OCV at 600 °C 1.4850 mV.
Combined set (low 3 and G.04 outlier) (R^2 = 0.9299) calculated OCV at 600 °C 1.45 mV.

Now doing the same but excluding G.04 at 800 °C instead results in:

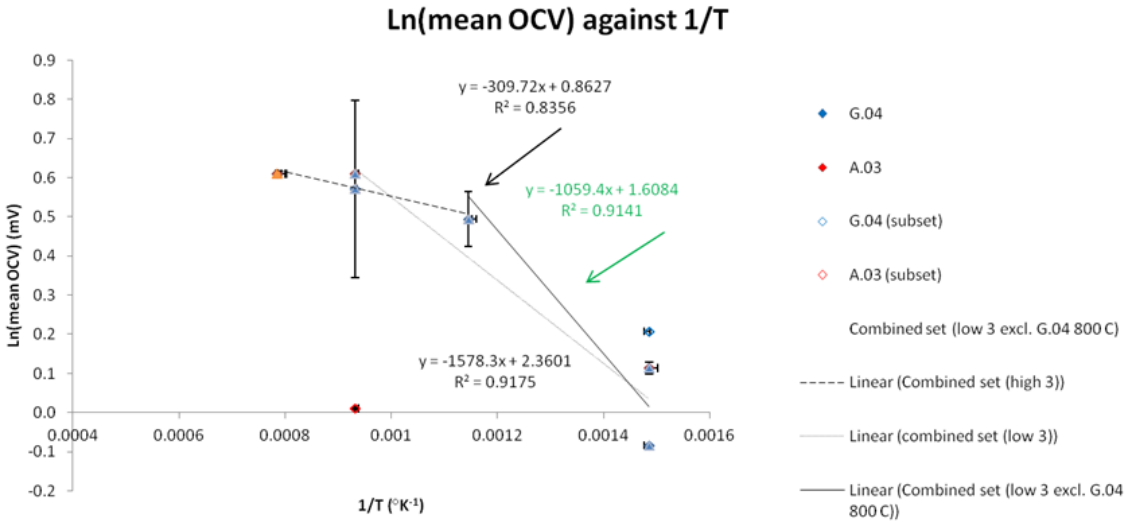

Combined set (low 3 and G.04 outlier at 800 °C) (R^2 = 0.9175) calculated OCV at 600 °C 1.7384 mV.

Appendix R: Sample Code

$$\alpha - \beta . dd/mm/yy - a; b; etc. T - \{add\ other\ elements\ here\} B. \#. X$$

α - Experiment type. DT for material deposition test. OT for oxidation test. RT for reduction test. IA for image analysis. PM for permeability measurement. PT for performance testing.

β - SOFC components involved/fabricated. A for anode, E for Electrolyte, C for cathode, I for interconnect, gA for graded anode, gC for graded cathode, D for as delivered. e.g. AE ⇒ anode and electrolyte

$dd/mm/yy$ - Date experiment/test carried out.

$a; b; etc.$ - Component layer thicknesses in microns

T - Operating or deposition temperature in ℃. If there is more than one relevant temperature the second is given in parenthesis. e.g. reduction experiments have the oxidation temperature first – 1100(800) would be oxidised at 1100 ℃ and subsequently reduced at 800 ℃. Where an operating temperature is given the batch letter and sample number are used to distinguish differing processing.

B - Batch letter. A, B, C, etc.

- Sample number. 01, 02, 03, etc.

X - Characterisation/performance measurements. X for XRD, S for SEM (normally the sample is FIB milled first), P for in-house fabricated permeameter, I for current, V for voltage, M for mass, Z for impedance spectra, R for resistance, C for confocal microscope (R_A), K for mass spectra, D for dew point measurement (water content in exhaust), A for image analyser. e.g. XS ⇒ XRD and SEM, $SIVMZR$ ⇒typical performance analysis.

The whole code can be a bit unwieldy. An abbreviated from consisting of the experiment type, date, batch letter and sample number (e.g. $MT - 01/07/09 - A.04$) or just the batch letter and sample number (e.g. $A.04$) have been used where context is sufficiently clear.